

AD-A274 655



125

Laboratory Plasma Studies

Final Report
SAIC 93/1229

November 30, 1993



Science Applications International Corporation
An Employee-Owned Company

DTIC
ELECTE
JAN 12 1994
S A

This document has been approved
for public release and sale; its
distribution is unlimited.

752P8 94-01377



94 1 11 166

1710 Goodridge Drive, P.O. Box 1303, McLean, Virginia 22102 (703) 821-4300

Other SAIC Offices: Albuquerque, Boston, Colorado Springs, Dayton, Huntsville, Las Vegas, Los Angeles, Oak Ridge, Orlando, Palo Alto, San Diego, Seattle, and Tucson

**Best
Available
Copy**

Laboratory Plasma Studies

Final Report

SAIC 93/1229

November 30, 1993

Submitted to:

**Dr. Arne Fliflet
Beam Physics Branch - Code 6790
Plasma Physics Division
Naval Research Laboratory
Washington, DC 20375-5000**

Prepared by:

**Contributing Authors Include: Ellis Hyman, Principal Investigator,
Avraham Bar-Shalom, Paul Boris, Jin Choi, Alban Deniz, Demosthenes
Dialetis, Bahman Hafizi, Nicholas Krall, Victor Granatstein,
Dennis Papadopoulos, Alex Velikovich**

Prepared Under:

Contract No. N00014-89-C-2111

TABLE OF CONTENTS

I.	TECHNICAL DISCUSSION	1
A.	NIKE KrF Laser Support	1
B.	Microwave and Millimeter Wave Experiments-1	14
C.	Microwave and Millimeter Wave Experiments-2	15
D.	Studies of Novel Accelerator Concepts and Free Electron Lasers	19
E.	Studies for the Modified Betatron Accelerator (MBA)	20
F.	PHAROS III Studies	24
G.	Electron Beam Diagnostics	25
H.	Microwave Energy Deposition in the Upper Atmosphere	25
I.	Visualization Tools and Parallel Processing for Physics Applications	26

Accession For	
NTIS CRA&I	<input checked="" type="checkbox"/>
DTIC TAB	<input type="checkbox"/>
Unannounced	<input type="checkbox"/>
Justification	
By	
Distribution /	
Availability Codes	
Dist	Avail and/or Special
A-1	

I. TECHNICAL DISCUSSION

The work performed by Science Applications International Corporation (SAIC) on this contract, "Laboratory Plasma Studies," Contract Number N00014-89-C-2111, SAIC Project Number 01-0157-13-0988, encompasses a wide range of topics in experimental, computational, and analytical laboratory plasma physics. The accomplishments described in this report were in support of the programs of the Beam Physics Branch (Code 6790) and the Plasma Physics Division of the Naval Research Laboratory (NRL) and cover the period 25 March 1989 to 30 September 1993. In the following subsections we will describe each of the topics investigated and the results obtained. Much of the research work has resulted in journal publications and NRL Memorandum Reports in which the investigation is described in detail. These reports are included as Appendices to this Final Report.

A. NIKE KrF Laser Support

SAIC scientists and engineers have played a major role in supporting the design, construction, and testing of the Krypton Fluoride Laser (NIKE) Facility at NRL. This effort has also been supported by SAIC consultants: Mr. Orville Barr of Pharos Technical Enterprises, Drs. Alex Velikovich, Avraham Bar Shalom, and Nicholas Krall. When completed NIKE will produce intensities in excess of 2×10^{14} Watts/cm² on flat foils for laser plasma experiments related to direct drive inertial confinement fusion. The primary goal of NIKE is to produce uniform, high intensity illumination on target, with a goal of less than 2% RMS distortion in the desired focal profile. During the past year we achieved a major milestone, demonstrating the required uniformity with the penultimate laser amplifier in the NIKE system. To our knowledge, this is the most uniform laser illumination ever produced. Additionally, this laser produced the 120 Joules required to drive the final amplifier stage, which will eventually produce greater than 5 kJ of output. If the focal profile uniformity can be maintained (and all indications are that it will) NIKE will be the first laser to meet the theoretically predicted intensity uniformity requirements of direct drive ICF.

SAIC's responsibility has been the design, specification, testing and implementation of the optical/optomechanical system. A large portion of the optical paper design was previously completed by R. Lehmberg of NRL. Details of the laser front end were completed by SAIC in collaboration with S. Obenschain of NRL. Optical components then had to be specified and procured to assure that the system would be true to the design. This procurement is nearing completion. Approximately two-thirds of the optical system is in operation and recently we have demonstrated seven times diffraction limited performance at 248 nm. This is in excellent agreement with predictions from the optical design codes. The remainder of the components to complete the optical system are now arriving and being tested.

Optomechanical design required stable mounts that do not distort the optics. Because of the large number of optics components in the system (~350) it was also required that these mounts be inexpensive. Mounts for each optical component were designed, prototyped, and tested before large quantities were made. All of these mounts have met the stability requirements and, in most cases, have cost less than originally estimated. In conjunction with mechanical engineers, SAIC supervised the design and fabrication of structures for mounting large numbers of individual optics. These structures had to provide rigid mounting to reduce vibration of optical components. They were then tested to assure adequate performance as they were delivered.

The majority of work has involved characterization, modification and operation of the laser system. Diagnostics have been developed and added to the system as required for laser beam characterization. SAIC has made significant changes to the laser oscillator, which improved overall system performance and was crucial to attaining the high energy uniform focal profiles mentioned above. The laser is beginning to operate on a routine basis and SAIC personnel continue to be involved in planning and performing experiments.

The following specific contributions are described below.

NIKE laser oscillator and focal profile diagnostics SAIC collaborated with Steve Obenschain of NRL to develop and test two methods for producing

uniform laser focal profiles. This profile is to be amplified and used to perform flat-target direct-drive fusion experiments, which require a very uniform profile. In addition, methods to attenuate and measure the focal profile with high accuracy were developed and tested.

The first method involved the development of a novel oscillator configuration with large angular divergence. It is described in a paper entitled, "A KrF oscillator system with uniform profiles," which has been accepted for publication. The proofs are included as Appendix A in this report. The paper also describes the method to attenuate the beam and measure the focal profile to high accuracy.

The second method involved illuminating a Lambertian diffuser with spatially incoherent light and using the far-field of the diffuser as the uniform profile. This is presently installed in the NIKE laser.

Pulse slicing Another important milestone was completed by SAIC as follows. We sliced a 4 ns pulse out of the 30 ns oscillator output. We used two Pockels cells in series between crossed polarizers. With a 60 times diffraction limited beam, we were able to obtain an energy contrast of 3000:1. We determined that the pulse slicing system did not appreciably distort the beam. We were also able to partially compensate for the stress-induced birefringence of the crystal by imposing a low electric field parallel to the direction of propagation of the light. The NIKE laser will deliver a 4 ns pulse to the target. The high contrast ratio is necessary to avoid prepulse, which could degrade the laser fusion experiments.

Laser bandwidth measurement SAIC measured the spectral profile of the KrF oscillator with a grating spectrometer and found that the full width at the half-maximum points is 0.3 nm. With an echelle spectrometer, E.A. McLean and C. Pawley of NRL collaborated with SAIC to measure the bandwidth of the oscillator at various stages of amplification through the 20 cm amplifier. The full width at the half-maximum points is 0.2 nm, and the bandwidth decreases as the beam is amplified. The RMS deviation of the focal profile due to its incoherence is $(\tau/T)^{1/2}$, where τ is the laser coherence time, and T is the pulse width. Because beam uniformity is very important for direct-

drive laser fusion, it is important to know the bandwidth when optimizing the laser uniformity. For example, if it is necessary to get a smoother focal profile, one could broaden the bandwidth, and therefore would need to be able to monitor the bandwidth.

Computerized data acquisition, archival, retrieval, and display SAIC designed, tested, implemented, and used a computerized data acquisition system using IEEE-488 instruments and the Unix operating system. The system allows the user to take data from a set of instruments (cameras, oscilloscopes, etc.), and simultaneously archive and display the data. In addition, the data can be retrieved from disk for later analysis.

The archival and retrieval software is written in ANSI C, and runs on SCO Unix, DEC Ultrix, and SUNOS 4.1. The analysis and display software is written in Interactive Data Language (IDL), a commercial product from Research Systems, Inc.

SAIC has trained various members of the NIKE group in its use. It is now being routinely used by the NIKE group, and it is planned to be used for the plasma physics experiments.

Smooth beam amplification SAIC has worked with NRL personnel to amplify the uniform beam through the 20 cm aperture amplifier (over 100 J in 4 ns). The results, obtained in August 1993, were presented by Tom Lehecka of SAIC at the APS meeting. The abstract follows:

Production of Uniform Laser Illumination with the NIKE Laser.*

T. LEHECKA, A.V. DENIZ, J. HARDGROVE, *Science Applications International Corp.*, S.E. BODNER, K.A. GERBER, R.H. LEHMBERG, E.A. McLEAN, S.P. OBENSCHAIN, C.J. PAWLEY, M.S. PRONKO, J.D. SETHIAN, J.A. STAMPER, *Plasma Physics Division, Naval Research Laboratory*: NIKE is a KrF laser at the Naval Research Laboratory designed to produce uniform illumination on flat targets for hydrodynamic and laser plasma interaction experiments. The goals for NIKE include $> 2 \times 10^{14} \text{W/cm}^2$ intensity on target ($> 2 \text{kJ}$, 4 ns, 600 μm diameter) and less than 2% RMS fluence nonuniformities. Approximately one-half of the final system is operational and is currently being tested. To date we have produced more than 120 J in a 4 ns pulse with 4% peak to valley linear tilts and 2% RMS deviation from a flat top profile. Modifications are being made to reduce this below the desired 2% peak to valley tilt level. Experimental results and future plans will be presented.

*This work is sponsored by the U.S. Department of Energy.

Laser beam nonuniformity effects from random phase distortion and nonlinear optical processes An investigation was performed in collaboration with NRL scientists to determine the magnitude of laser profile distortion due to random amplitude and phase nonuniformities, nonlinear refraction, and self-seeded stimulated rotational Raman scattering. The investigation included both numerical simulations and experimental measurements. This was reported at the SPIE Conference on Laser Coherence Control: Technology and Applications, January 1993 and is included in this report in Appendix B.

A number of earlier papers, posters, or talks in which SAIC participated include:

"Design and Development of the NIKE 20-cm Aperture KrF Amplifier," a poster presented at the Conference on Lasers and Electro-Optics (CLEO) in Anaheim, CA, May 1990 (CWF45).

"Production of Flat KrF Laser Focal Profiles with Echelon Free-Induced Spatial Incoherence," a poster presented at the above CLEO Meeting (CWF47).

"Large Aperture Discharge Excited KrF Laser Amplifier Development for the NIKE Laser Facility," a paper presented at the above CLEO Meeting (CWG4).

"Optomechanical Considerations for the NIKE Laser," a paper presented at the KrF Laser Technology Workshop in Banff, Alberta, Canada, September 1990.

"Overview of the NIKE Laser Facility," a paper presented at the IAEA Technical Committee Meeting on Drivers for Inertial Confinement Fusion in Osaka, Japan, April 1991.

"Energy Deposition and Extraction from the NIKE 200 -cm KrF Amplifier," a poster presented May 1991 at the Conference on Lasers and Electro-Optics (CLEO) in Baltimore (CWF43).

"NIKE Laser Optical Design and Propagation Issues," a paper presented at the above CLEO Meeting (CTUI5).

"Production of Flat KrF Focal Profiles for Laser Fusion Experiments," a paper presented at the above CLEO meeting (CTUI6).

"High Fidelity Amplification of Light Using Induced Spatial Incoherence for Laser Fusion," a paper presented at the above CLEO Meeting, May 1992, in Anaheim, CA (CTHI9).

"Calculation of Focal Spot Distortion in the NIKE Laser," a paper presented at the above CLEO Meeting (CFA2).

"Overview of the NIKE KrF Laser Facility," a paper presented at the IIIrd Workshop on KrF Laser Technology at the Rutherford Appleton Laboratory in Great Britain, November 1992.

"Effects of Random Phase Distortion and Non-Linear Optical Processes on NIKE Laser Beam Uniformity," a paper presented at the above Rutherford Appleton Laboratory Meeting.

"The NIKE Optical System," a paper presented at the above Rutherford Appleton Laboratory Meeting.

"An ISI Oscillator System with Uniform Profiles," a paper presented at the above Rutherford Appleton Laboratory Meeting.

"The NIKE KrF Laser Facility," a paper presented at the Division of Plasma Physics Meeting of the American Physical Society, November 1992 in Seattle, WA.

Mirror control system SAIC developed a mirror control system for the NIKE laser system; the system controls more than 600 mirrors from a PC located in the NIKE control room. The system was required to involve low power consumption for low heat dissipation, have low outgassing, and provide easy user operation. A stepper motor was selected for our linear actuators to

move the mirrors along the X and Y axes. A motor driver card was developed that can drive 8 motors per card and allows for multiple cards per card cage. A card cage is placed at each mirror array location in the propagation bay where it performs the function of moving the stepper motors in the linear actuators.

In addition to the manual control an automatic system was developed in which a camera system acquires the image of the laser beam, calculates the centroid of the beam and determines the distance required to move the beam to the center of the mirror.

An active damping system is currently being developed to stabilize the 20 and 60 cm mirrors from both ground vibration and large movements due to the effects of the large magnetic fields being used with these KrF lasers. Currently a preliminary prototype has been developed so that NRL will be able to evaluate several different real time control systems.

Control system design and implementation The NIKE laser's controls are implemented in split system consisting of a Modicon 984-485 programmable logic controller (PLC) executing critical control logic and U.S. Data's Factory Link graphical operator interface running on a PC.

During this period tasks have included the following, among others:

Modification and expansion of the oscillator room logic and interfaces.

Control of the 60-cm high-voltage equipment.

Control of the 60-cm magnet power supply.

Expansion of the access controls to include the alleyways outside the facility and motion detectors in the amplifier room.

Adding data recording of power-system parameters for trouble-shooting support.

Adding the third operator display monitor.

Automating the log-in process.

All changes are documented and backed-up. Backups are kept at NIKE and at Pharos.

There have been a few minor problems to resolve during this period. Included are the following:

The PC for FactoryLink was too small and slow. The replacement NRL provided was incompatible with our hardware, particularly the multiple VGA display adapters. I found another PC that met all requirements.

FactoryLink slowed down when the real-time trending displays were added for the operator, to the point that it could not sustain the desired one-second update rate. Some tasks were moved to the PLC, the priority of some tasks was adjusted, and the earliest parts of the display logic were generally cleaned up some. The display update is now reliably once-per-second again. More cleanup will be needed as the controls expand, but we are well over the hump now.

The PLC's remote I/O processor in the amplifier room crashed three times with failure in the 60-cm high voltage system. The problem was traced to an unavoidable ground loop in an 18-inch coaxial cable buried in our cabinet. This was fixed so that now one can take a Tesla coil directly to this coax cable without looking up the processor, although there is about a 3 percent change causing it to halt for about one second. No further problems caused by high-voltage arcs have been observed.

The PLC ran out of logic memory long before we expected it to. The problem was that we had inadvertently specified the wrong memory module for it. Modicon shipped us the correct one for a couple of hundred dollars and the small one in trade. Now the PLC memory is running about 50-percent utilization.

On-going tasks include the following:

Integration of the propagation bay into the safety system.

Addition of the south Marx bank on the 60-cm amplifier.

Automation of gas and vacuum controls for the 20-cm and 60-cm amplifiers.

Providing an integrated, automatic shot sequencer, including interfacing with the data acquisition system.

Switching the 60-cm amplifier to the UVC power supply.

Expansion into the target area.

Supporting on-going installation and testing of laser system components and subsystems.

Target area controls planning Preliminary plans have been made to extend the control system's tentacles into the target area. These should gel quickly as the target area construction is completed.

Amplifier magnet construction, installation, and testing The magnet coils were designed about three years ago. During this period they were fabricated, installed, tested, and are now in regular use. Tasks included the following:

- Inspecting the magnet coils often during fabrication and participating in their installation and testing.
- Designing and installing the power supply interface to the control system.
- Analyzing the fabricator's field mapping data for NRL.
- Reviewing the electrical installation for proper grounding.
- Calculating and measuring power line distortion caused by the power supply. As a result, we installed various constant voltage transformers and back-up power supplies.

Our original cooling estimates were incorrect and thus the magnet's operation is limited to a lower duty cycle than planned. We designed an

improved cooling system, but the duty-cycle limitation has not been a problem so NRL hasn't installed the improved system.

The power supply proved sensitive to interference from the adjacent high voltage equipment, so we added appropriate shielding and filtering to solve the problem.

60-cm amplifier test support We have provided as-needed support throughout the installation and testing of the 60-cm amplifier. Included are the following:

Designing and installing most of the control interfaces.

Trouble-shooting the Physics International controls and correcting the design to work with two Marx generators.

Trouble-shooting the UVC power supply when it failed. We found five bad solder joints and several failed resistors, but UVC eventually traced the problem to a failed high-voltage capacitor.

Helping with the vacuum system and just about everywhere else non-mechanical.

Three major remaining tasks on the 60-cm amplifier are the following:

Bringing up the UVC power supply again, since it has been repaired. We expect it will not tolerate the power line notching produced by the magnet power supply. A line filter for it does not look economically attractive. Remaining alternatives are time-staggering the two power supplies or running in separate power for the UVC supply.

Getting the vacuum and gas controls into the control system.

Bringing up the south Marx generator. We have redesigned PI controls so they will function properly with both Marx generators, but we have not yet installed the changes.

Safety We provide limited safety consulting to the NIKE project. This activity has included the following:

Review of class 3b HeNe laser hazards,

safety walk-through,

contracting DOE and NASA facilities concerning inert-gas-filled spaces, and

interviewing potential safety consultants.

The second and last items are continuing.

Program management consultation At NRL's request, Orville Barr of Pharos Technical Enterprises and a consultant to SAIC served as an outside reviewer of dry-runs for the DOE ICFAC KrF laser program review. He also attended the review. Most comments were provided verbally, but one written summary also was provided. He provided comments on plans for the review, starting several months before the actual review dates. He also provided comments on NRL's plans for an earlier (December 1992) DOE review of part of LLNL's ICG program.

Investigation of electron deposition and kinetic instability in an e-beam-driven KrF laser A study of various Monte Carlo treatments of e-beam deposition was completed. In addition to the different results of the diverse models, neglect of return currents due to boundary conditions or electron density buildup was investigated. The details of this analysis are presented in Appendix C of this report.

Strongly coupled plasma effects Possible stabilization of Rayleigh-Taylor (RT) instability of ablatively accelerated foils caused by strongly coupled plasma (SCP) effects has been analyzed as a general concept, as possible explanation of earlier NRL experiments (Grun et al., Phys. Rev. Lett., 1987), and as a reason to pursue further experimental research on SCP. The stabilizing influence of SCP effects, such as modification of equation-of-state,

plasma viscosity, thermal conductivity, surface tension and mechanical rigidity (in the case of plasma phase transition to the condensed state), estimated from above in a most generous way, has been found insufficient for suppressing RT instability, in particular, in the case of the experiment cited above. An alternative explanation has been suggested for lack of observed perturbation growth in the short-wave range in this experiment.

A report entitled "On possible stabilization of ablatively accelerated foils by strongly coupled plasma effects" has been completed and presented to NRL. The report includes some new analytic results, in particular, those of Sect. 3 (viscosity of a light fluid has been shown to be a stabilizing factor only as long as the effective Atwood number differs from unity), and in Sect. 4 (RT dispersion curves for a partly frozen fluid layer have been obtained). A detailed discussion of the '87 NRL experiment concluding that its seemingly surprising results could be accounted for within conventional hydrodynamic theory, are presented. The full report is included here as Appendix D.

A new approach to stabilization of ablatively accelerated foils, attempting to combine the advantages of the snowplow and dynamic stabilization mechanisms has been suggested.

Stability of a shock-wave-driven acceleration of a plane stratified layer has been studied using the linearized Chester-Chisnell-Whitham (CCW) equation. A shock wave propagating in the direction of increasing density has been shown to be absolutely stable (amplitudes of perturbations decrease with increased distance traveled by the shock wave). Since the CCW approximation is not justified for the planar piston problem (which is the most important one in the context of laser fusion studies), self-similar solutions of gasdynamic equations for the case of stratified density have been constructed. There are some indications that the above conclusion concerning stability would not be changed if the stability of these exact solutions was studied. A numerical experiment aimed at elucidating this point has been suggested.

Opacity calculations Several important steps were taken to develop a mechanism for reliably carrying out opacity calculations relevant to the NIKE program. We make use of a technique developed by SAIC consultant, Bar-

Shalom, that employs Super Transition Arrays and is known as the STA method. The following elements were completed.

Configuration interaction In this work the theory that facilitates for the first time the inclusion of configuration interaction (CI) in the calculation of emission and absorption LTE spectra was developed. The theory is combined with the STA method, bypassing the need for huge numbers of matrix diagonalizations. Analytical expressions for the corrected intensities of super-transition arrays due to CI were obtained. These analytic expressions serve as working formulas in the STA codes and in addition, reveal a priori the conditions under which CI effects are significant (Bar-Shalom et al., 1993a).

Orbital relaxation The treatment of orbital relaxation was improved. At first for each super array the potential was optimized for the initial super-configuration only. This was good enough for transition energies of the order of the temperature. But comparison with measurements (Bar-Shalom, et al., 1993b) has shown that for transitions of higher energy there is a need also to optimize the potential of the upper super-configuration. This improvement was applied to the code in a few steps and now the comparison with the available experiments is satisfactory.

Scattering The treatment of the scattering of photons was improved by including two correlation effects: one due to exchange and the other due to Coulomb interaction (Boercker, 1987). These effects are important in cases where scattering is a dominant mechanism, i.e. high temperatures and high photon energies.

Low temperature cases When the atom is almost neutral the Average Atom (AA) model overestimates the contribution of negative ions (especially for Hydrogen) since in this case the electrostatic interaction between the electrons, which is ignored in the Boltzman factor in the AA model, is comparable to the interaction with the nucleus. A special procedure which ignores negative ions has been developed.

Line shapes The line shape of the individual line is approximated by a Voigt profile. The parameters needed for this profile are the intensity, the line

center, Gaussian width and Lorentzian width. The intensity and the line center are obtained from STA calculations, the Gaussian width is the root mean square of the STA and Doppler widths. The Lorentzian width due to collisions with electrons is calculated by the method proposed by Dimitrijevic and Konjevic [1980]. We have improved the Lorentzian width determination using the proper radial integrals and a different method for evaluating the collisional cross section. Care is taken to include the line far wings in cases where they contribute significantly to the opacity. For this purpose a new algorithm was added to the procedure for calculating the Voigt profile.

B. Microwave and Millimeter Wave Experiments-1

At the start of this contract period a K_a -band gyrotron oscillator experiment was completed. Using a 1-1.35 MeV multikiloampere beam from a pulse line accelerator it generated approximately 250 MW at 35 GHz in a circular TE_{62} mode with a peak efficiency greater than 10%. Details of this experiment are included in this report in Appendix E, previously published in Physics of Fluids B (1990).

An experiment was carried out using a gyrotron configuration in which the electron beam current exceeded the vacuum space-charge-limited value. This limit was circumvented by introducing background plasma produced by an array of four plasma guns positioned immediately downstream of the electron gun anode. Details of this experiment have been published in Applied Physics Letters in 1990; the paper is included in this report as Appendix F.

A gyrokystron amplifier experiment was performed. The device operated at an accelerating voltage of 1 MV, consisted of two cavities with fundamental mode TE_{111}^0 , and demonstrated a linear gain of 15 dB, an unsaturated output power ~40 kW, and intracavity gain and power ~ 4dB higher. The second cavity tracked the driver cavity over a range of 300 MHz around a center frequency of 35 GHz. This investigation was described in detail in IEEE Transactions on Plasma Science (1990) and is included in this report in Appendix G.

C. Microwave and Millimeter Wave Experiments-2

Efforts to increase the bandwidth of millimeter wave rf amplifiers are of critical importance for applications such as high resolution radar/communications and missile jammers for Navy measure/countermeasure systems. In most applications, tenth of kilowatts of rf power generated from low magnetic field and low beam power is required in the frequency range of the Ka-band (26 - 40 GHz) and W-band (75 - 110 GHz). Today's most commercially available microwave tubes such as helix TWTs and coupled cavity TWTs do not meet the Navy's tube development program needs of rf power > 20 kW for millimeter wave radiation.

Gyro-TWT amplifiers can produce much higher power than the linear beam devices due to a relatively large circuit dimension and thus higher beam power injection in the circuit. Any uniform waveguide cannot produce an instantaneous bandwidth of more than 3%, unless the waveguide is loaded with dielectric slabs or with a periodic structure so that the wave phase velocity becomes constant over a wide frequency range in the slow wave region ($v_{ph} < c$). Tapering the waveguide is another way of obtaining continuous phase synchronism of beam and waveguide mode in the fast wave region ($v_{ph} > c$). SAIC in collaboration with NRL researchers has designed two gyro-TWT amplifiers that produce Ka-band radiation power of 50 kW in the frequency range 29 - 36 GHz and W-band millimeter radiation of 10 kW, using a low magnetic field.

I. Dielectric loaded slow wave cyclotron amplifier (SWCA)

With dielectric slabs inserted in the waveguide, the waveguide cutoff frequency is shifted down and the waveguide becomes so much less dispersive that the rf phase velocity is below the speed of light. The dielectric loaded slow wave cyclotron amplifier is designed so that a constant wave group velocity is maintained over a wide frequency range when the wave group velocity in the dielectric loaded waveguide is close to the beam axial velocity in the slow wave region ($v_{ph} < c$). The amplifier is operated with low external magnetic field (lower by a factor of 2 compared to fast wave gyro-devices) and wide bandwidth (> 20 %) in the Ka-band frequency range.

In the design of the amplifier, there are several issues to take into account: (1) high quality electron beam formation and propagation, (2) amplifier stability and performance, (3) broadband rf coupler and vacuum window, and (4) dielectric heating.

The designed interaction is a first harmonic TE_{x10} -even interaction to reduce mode competition and enhance interaction efficiency. A strong second harmonic gyro-BWO of a TE_{x10} -odd mode might limit the bandwidth of the amplifier. A two-stage circuit with a sever has been configured to achieve stable operation of the SWCA without oscillations in the higher order modes. Another reason that a sever is inevitable in the circuit is that, since the dielectric mode converter is designed such that only TE_{x10} -even mode in the dielectric loaded circuit can couple with the TE_{10} mode in the standard Ka-band waveguide, all other hybrid modes might be excited by a beam instability and would be completely trapped in the circuit. Using a non-linear slow-time-scale code developed by NRL (Ganguly and Alm, 1990), SAIC examined the large signal performance on the two-stage SWCA. It predicts a saturated efficiency of 17 % (output power > 50 kW), a gain of 28 dB, and bandwidth of 20 % (29 - 36 GHz) at $V = 60$ kV, $I = 5$ A, $a = 1$, $\Delta v_z/v_z = 2$ % (Choi et al., 1992). The efficiency is very sensitive to the velocity spread. This is because the SWCA interaction takes place at large values of the propagation constant, $k_{||}$. The paper by Choi et al is included in this report as Appendix H.

One of the main concerns in the dielectric loaded circuit was an issue of electron beam interception on the dielectric and charge drain-off. Since the peak rf field is located in the dielectric in the slow wave region, the beam should be propagated close to the dielectric surface for high efficiency. However, in practice, a beam radius (or, a Larmor radius in an axis-encircling beam) can not be more than $0.9 d$ because of difficulties in aligning a beam axis to a magnetic field axis and in having a straight field axis. In the present design, a 30 mil clearance between a beam and a dielectric surface was chosen. SAIC developed a double ridged circuit to prevent electron beam bombardment on dielectrics. It consists of two dielectrics lined on the waveguide narrow walls and four metal ridges next to the dielectrics. Beam-wave coupling in the ridged circuit is expected to be stronger than the circuit without ridges because a peak electric field shifts from the dielectric region to the vacuum region.

Rf couplers in the SWCA should have a broadband coupling characteristic. In addition, a return loss on each component has to be better than the gain of the amplifier. Both a directional coupler and a mode converter were designed by SAIC so that the maximum rf power can be transferred into the desired mode in the circuit, TE_{x10} -even mode. Cold-tests on the 1.5" long compact directional coupler show a coupling value of -0.4 dB in the frequency range of 22.4 to over 40 GHz, which corresponds to -3 dB bandwidth of 60% (Choi et al., 1993a). A broadband rf vacuum window should cover the bandwidth of the amplifier. In addition, the window material is chosen for good thermal conduction with low heat loss. SAIC designed and cold-tested a broadband rf window which is a three step $1/4$ wavelength long BeO dielectric [Choi, et al., 1993a]. Cold-tests on the rf vacuum window show a return loss of better than -20 dB in the frequency range of 24 - 37 GHz.

The dielectric material chosen is a Transtar (99.9 % of Al_2O_3). It has a relative dielectric constant of 10.1, low loss tangent (10^{-4}), and very high bulk breakdown field (~ 190 kV/cm). It is known that the dielectric properties change temperature. It has been pointed out by SAIC that the temperature change due to a finite loss tangent and the risk of electron beam heating on the dielectric could result in rf pulse shortening. Therefore we suggest monitoring the temperature rise during experiments. A circuit has to be designed for good heat conduction to the outside. The paper by Choi et al (1993a) is included in this report as Appendix I.

II. Frequency multiplied harmonic gyro-TWT amplifier

Broadening bandwidth in the fast wave interaction is achievable by tapering both waveguide and magnetic field along the axis. A frequency multiplied harmonic gyro-TWT amplifier has unique features that will meet the requirements of the Navy electronic countermeasure system. It is designed to operate the amplifier at a low magnetic field that can be provided by a PPM (periodic permanent magnet) while the bandwidth can be maintained over 10% (90 - 100 GHz) in W-band. The interaction circuit consists of two linearly tapered waveguides of rectangular cross-section separated by a uniform drift section. The two stage configuration is used to isolate the input and output signals and to enhance the gain and efficiency by pre-bunching the beam. The concept of "frequency multiplier" was first introduced in the US by SAIC and

NRL researchers (Choi et al, 1993b); a low frequency drive signal (Ka-band) is injected in the tapered input section to modulate the gyrating beam and amplified radiation in the tapered output section is extracted with frequencies (W-band) increased by a factor of the harmonic numbers. The beam-circuit clearance in the output circuit is tight since the operating mode is chosen to be the lowest rectangular waveguide mode. Due to such a tight beam clearance, the output circuit was designed to be of square cross-section. Longitudinal slots parallel to the desired electric field were needed to radiate the undesired polarized TE₁₀ mode from the circuit and be absorbed in the lossy dielectric slabs. For maximum radiation of the undesired polarization without affecting the desired TE₁₀ mode, the slot width should be 4 to 6 mils and the thickness in the range of 30 - 40 mils. The clearance for a hot beam ($\Delta v_z/v_z = 2\%$) changes from 10 mils (at the location with the smallest width) to 20 mils along the output circuit. This corresponds to a beam filling factor of 50 - 68%, which is acceptable for a W-band circuit. It is crucial that the magnet provides a straight field over the circuit length for good beam propagation. There is no concern about beam interception in the input section because the circuit width, which determines cutoff frequencies, is made three times wider than the output circuit width. The details of this work are described in Choi et al (1993b) which is included in this report as Appendix J.

SAIC examined the performance of the frequency multiplied harmonic gyro-TWT amplifier by the use of a large signal code that was developed by NRL researchers (Ganguly and Ahn, 1984). The code predicts a saturated gain of 30 dB, an efficiency of 10% corresponding to 10 kW radiation output in the frequency range of 90 - 100 GHz at $\Delta v_z/v_z = 2\%$, 50 kV, 2 A, $a = 1$ to 1.4. Input (Ka-band) and output (W-band) couplers will be multi-hole directional couplers similar to that mentioned in the SWCA. A coupling value of better than - 0.4 dB over 70 - 110 GHz is predicted by a 3-D electromagnetic code, HFSS (HP High Frequency Structure Simulator User's Reference, 1992). A W-band rf vacuum window will be a three step $1/4$ wavelength BeO. HFSS simulations show a return loss better than - 25 dB in the frequency range of 90 - 100 GHz. A paper submitted to the IEEE Plasma Science Journal entitled, "Design of a 50 kW, Broad Ka-Band Slow-Wave Cyclotron Amplifier" is included in this report as Appendix K.

D. Studies of Novel Accelerator Concepts and Free Electron Lasers

1. Magnicon Amplifier

The magnicon employs a scanning beam that is obtained by the passage of a magnetized pencil beam from an electron gun through a deflection system to generate microwave radiation. The magnicon has the potential of extremely high efficiency and is therefore a candidate to power future high-gradient radio-frequency accelerators. We have employed a combination of analytical methods and numerical codes to study and design a magnicon amplifier for operation at X-band (11.4 GHz) at NRL. Cold tests of the cavities are in progress at the magnicon laboratory.

2. Diffraction of Directed Beams

Propagation of directed beams of electromagnetic radiation is of interest in a number of applications including power beaming and remote sensing. A number of researchers have proposed and analyzed novel electromagnetic wavepacket forms, claiming superior propagation characteristics as compared to conventional Gaussian wavepackets. We have made a detailed analysis of these proposals. Our conclusion is that in every case a careful comparison reveals that the claimed superior propagation property is unfounded. These results have been described in more detail in two publications: (1) Journal of the Optical Society of America A (1991) and (2) Physical Review Letters (1991). They are included in this report as Appendices L and M respectively.

3. Synchrotron-Betatron Parametric Instability in Free-Electron Lasers

It is shown that the nonlinear coupling of the synchrotron motion and the betatron oscillation of electrons in free-electron lasers leads to an instability which grows exponentially in time. This parametric instability is of a different physical character from those analyzed previously. This work has been described in more detail in two publications: in Physical Review A (1990) and in Nuclear Instruments and Methods in Physics Research A (1990), which are included in this report as Appendices N and O respectively.

4. Electron-Beam Quality in Free-Electron Lasers

The beam quality requirement in free-electron lasers (FEL) is often expressed as $\lambda = \pi \epsilon$, where λ is the wavelength and ϵ is the unnormalized emittance. We have obtained a generalization of this expression valid for an FEL in the gain guiding regime of operation. This work has been described in more detail in a publication in Nuclear Instruments and Methods in Physics Research A (1990), which is included in this report in Appendix P.

5. Effect of Tapering in Free-Electron Lasers

We have performed numerical simulations of a high-power free-electron laser. We have shown that tapering improves the quality of the optical beam by reducing the growth of sidebands. Additionally, we find that as the tapering rate increases, the effect of refractive guiding is significantly reduced. This work has been described in detail in two publications: (1) Physical Review Letters (1990) and (2) Nuclear Instruments and Methods in Physical Research A (1990), which are included in this report as Appendices Q and R respectively.

E. Studies for the Modified Betatron Accelerator (MBA)

SAIC made substantial contributions to the analysis and simulation of NRL's modified betatron accelerator (MBA) experiment up to the time that the program was terminated in mid 1992. Much of the work is included in the NRL Memorandum Report entitled, "Final Report, The NRL Modified Betatron Accelerator Program," NRL/MR/6793-92-7161 (1992) included in this report as Appendix S. Specific elements of SAIC's contributions are described below.

1. Using the Poisson code, a Poisson equation solver, SAIC designed the extractor component compatible with the extraction scheme that was to be implemented for the beam extraction in the MBA. The scheme for the ring extraction was based on three stages. During the first stage, the ring is displaced radially outward by mismatching the vertical magnetic field to the electron energy with a local time dependent magnetic field ($\tau = 5-10 \mu\text{sec}$). During the second stage, a local vertical magnetic field disturbance, generated by the agitator coil, transforms the ring into a helix in the toroidal direction. The minor radius of the helix increases with each passage through the agitator coil ($\tau = 40-60 \text{ nsec}$). Finally, during the third stage, the electrons reach the

extractor (the component designed by SAIC), which has the property that it cancels out the external magnetic fields transverse to its axis. Thus, the electron ring unwinds into a straight beam ($\tau = 2\text{nsec}$). This work has been described in more detail in a presentation given at a technical review workshop in June 1989. It is included here as Appendix T.

2. SAIC made extensive calculations for the design of the stellarator windings that were implemented in the MBA and led to the successful acceleration of the beam. It can be shown that, due to the large values of the stellarator field index at the initial stage of the acceleration, the beam confinement is improved with strong focusing. Initially, stellarator and torsatron winding configurations were considered. Both configurations have advantages and shortcomings. The stellarator configuration was finally selected not only because of the small net vertical field and the lower current per winding but also because it was compatible with the contemplated extraction scheme. The stellarator current must be appropriately chosen; otherwise it may cause an unstable behavior of the beam centroid due to the integer resonances of the bounce and strong focusing modes of the stellarator windings (see, for example, Fig. 23, on p. 121 of the final report in Appendix S). Further details can be found in two papers: (1) Proceedings of SPIE (1990) included here in Appendix U and (2) Physical Review Letters (1990) - Appendix V.

SAIC analyzed and interpreted the experimental data from the acceleration experiments that were associated with the cyclotron resonances present in the device during acceleration. The experimental results were also consistent with the excitation of the electron-cyclotron instability, which is caused by the coupling of the electron-cyclotron mode with the TE_{11} waveguide mode of the torus. Attempts were made to measure the poloidal and toroidal fields of the electromagnetic modes inside the torus. Measurements with wideband probes yielded null results. Therefore, the beam loss was attributed to the crossing of the electron cyclotron resonances, i.e., when the ratio of the toroidal to the vertical magnetic fields becomes an integer. The excitation of these resonances is due to field errors in the toroidal or vertical external magnetic fields. Additional details of this work can be found in Appendix V, referred to above, and in a paper published in Physics of Fluids (1991) and included in this report as Appendix W.

4. The diffusion of the magnetic field through a toroidal conducting shell was studied under the assumption of small aspect ratio. The external field that diffuses into the toroidal shell can have an arbitrary field index and magnetic flux on the minor axis of the torus. The diffused field, field index, magnetic flux and wall current were computed analytically and compared with the numerical results from the TRIDIF code. Three time constants determine the evolution in time of the diffusion process, namely, the L/R time, τ_0 , the diffusion time, τ_1 , and $\tau_2 = \tau_1/2$. The delay time depends linearly on τ_0 , τ_1 , and also on the flux condition of the external field. The agreement between the theoretical and numerical results was quite good. A measurement of the delay time in the toroidal chamber of the NRL modified betatron gave a delay time equal to approximately 34 μsec , i.e., less than 10% smaller than the theoretical value of 37 μsec . The main conclusion of the study was that the diffusion process in a toroidal conducting shell is much more complicated than that in a conducting cylinder. Therefore, the results for a cylinder cannot be generalized to apply to a toroidal device. This work has been described in more detail in a publication in the Journal of Applied Physics (1991) and is included here as Appendix X.

5. The diffusion of the self magnetic fields of an electron beam through a resistive toroidal chamber was studied. The computed image fields were used in explaining the resistive beam trapping in the MBA immediately after the beam injection. The resistive trapping is due to the negative radial component of the image magnetic field of the beam that acts on its centroid, when such a beam moves poloidally inside a resistive chamber. This field component crossed with the axial (toroidal) velocity of the beam produces a poloidal force, which is in the opposite direction to the poloidal motion of the beam. In the absence of strong focusing and when the self-fields dominate the external fields (high-current regime), the poloidal force in conjunction with the axial (toroidal) magnetic field drives the beam to the wall (drag instability). However, in the presence of strong focusing the direction of the poloidal motion can be reversed and the beam spirals to the minor axis. Two modifications were introduced to the original resistive trapping model. First, the beam motion is not limited near the minor axis and therefore nonlinear effects and the fast diffusion times become important. Second, in order to take into account the intermediate motion of the beam that was omitted in the calculation of the image fields of

the beam, the wall surface resistivity was completed using the skin depth that corresponds to the frequency of the intermediate mode and not the actual thickness of the chamber. With these modifications, the revised model of resistive trapping is in agreement with the experimental observations. Further details concerning this investigation can be found in two papers: (1) Physical Review A (1991) included here as Appendix Y and (2) an NRL Memorandum Report (1991) presented here in Appendix Z.

6. Beam trapping in the modified betatron could be achieved by means of a localized bipolar electric field pulse rather than a magnetic field pulse that was actually used in the experiment. The pulseline that generates the bipolar electric pulse was constructed and tested but was not installed in the MBA. SAIC's contribution in the paper by J. Mathew et al. was the computation of the eigenfunctions and eigenvalues in a toroidal cavity that supports quasi-TE and quasi-TM modes. This paper is included here as Appendix AA and was published as an NRL Memorandum Report (1992).

7. SAIC investigated the dynamic behavior of an electron ring close to a cyclotron resonance in a modified betatron accelerator. In the presence of a vertical field error, there is a threshold value of the field error amplitude that separates two distinct regimes. Below threshold (Fresnel regime) and for zero initial perpendicular velocity, the perpendicular velocity increases by a finite amount as the resonance is crossed. The increase, as well as the time it takes to cross the resonance, are inversely proportional to the square root of the acceleration rate. Above threshold (lock-in-regime), the perpendicular velocity is proportional to the square root of the acceleration rate and increases with the square root of time while $\gamma\beta_\theta$ remains on the average constant, where γ is the relativistic factor and β_θ is the ratio of the ring toroidal velocity to the velocity of light. Therefore the ring locks into the resonance. The threshold is predicted by the slow equations of motion that were derived by averaging out the fast cyclotron motion. The origin is the nonlinear dependence of $\gamma\beta_\theta$ on the perpendicular velocity and the fact that the cyclotron frequency is inversely proportional to $\gamma\beta_\theta$. Possible ways to increase the threshold were studied. One possible way is to increase the acceleration rate, since it was shown that the threshold value is proportional to the 3/4 power of the acceleration rate. Another possible way is dynamic stabilization, i.e., the addition of a small time-

dependent field to the main toroidal field, which provides an effective increment to the acceleration rate if it has a negative time derivative during the resonance crossing. Finally, the multiple crossing of the same resonance was analyzed in the presence of dynamic stabilization with some interesting results (see, for example, Fig. 14 in the paper in Phys. Rev. 47, 2043 (1993), included here as Appendix BB. Additional details have been presented in two SPIE Proceedings (1991 and 1992) included respectively in Appendices CC and DD and in an NRL Memorandum Report (1992) included in Appendix EE.

F. PHAROS III Studies

Several studies were carried out by SAIC researchers in support of PHAROS III Nd-glass laser experiments performed at NRL. In one study the effect of induced spatial incoherence (ISI), a beam smoothing technique to provide highly uniform illumination for direct-drive laser fusion, in suppressing certain deleterious plasma instabilities was investigated. Suppression had been noted for stimulated Raman scattering (SRS) and stimulated Brillouin scattering (SBS). In these experiments ISI reduced $3 \omega_0/2$ emission from laser-irradiated targets at $0.53 \mu\text{m}$. However, the mechanism appears to differ from suppression of SRS or SBS. This has been described in more detail in a publication in Physics of Fluids B (1991), included in this report as Appendix FF.

An experiment to investigate instability mechanisms in laser-produced plasma jets was carried out at NRL. It used the beams from the PHAROS III Nd-glass laser operating at wavelength 1054 nm , employed 2 ns pulses with energies between 30 and 300 J . Dramatic structuring instabilities developed with growth rates much larger than characteristic of Rayleigh-Taylor or Kelvin-Helmholtz. The results represented the first detailed observations of large-scale-length electron-ion hybrid instabilities in a laser-produced plasma. This work has been published in Physics of Fluids B (1992) and is included here as Appendix GG.

An experiment to investigate the large Larmor radius regime was carried out. The plasma is formed by placing a small Al disk target in the focal region of one or two beams of the PHAROS III Nd laser. In this regime in which the expansion speed is sub-Alfvenic the experiment demonstrated linear and

nonlinear properties of a flutelike instability. The observations are similar to those from barium releases in the Active Magnetospheric Particle Tracer Experiment (AMPTE) and from the Combined Release and Radiation Effects Satellite (CRRES) magnetospheric barium releases. This work is described in detail in a publication in Physics of Fluids B (1993) and appears here in Appendix HH.

G. Electron Beam Diagnostics

The NRL SuperIBEX accelerator produces an intense relativistic electron beam ($I \approx 15 \text{ kA}$, $E \approx 5 \text{ MeV}$). SAIC researchers played a major role in developing a Faraday cup to measure time-dependent relativistic electron beam profiles. Details of this diagnostic and the experimental measurements are described in the Review of Scientific Instruments (1991); the publication is included in this report in Appendix II.

H. Microwave Energy Deposition in the Upper Atmosphere

During the last contract period the utilization of microwaves and lasers developed at the Plasma Physics Division of the Naval Research Laboratory to accomplish remote monitoring of the atmosphere, stratosphere and ionosphere was assessed. Results of the ongoing effort were often presented orally during the duration of the contract. An important milestone of the effort was the invention of a novel technique for optical diagnostic of the minority atmospheric constituents in the troposphere and the stratosphere. A brief description of the technique follows:

The technique relies on excitation of atoms and molecules of minority species by electron impact during and following impulsive atmospheric breakdown. Radio waves in the 2-15 GHz range generated on the ground and focused using a 34 meter dish at the relevant atmospheric altitude can trigger breakdown if the combination of pulse length and effective radiation power (ERP) exceeds a threshold whose value depends on a combination of atmospheric and microwave parameters. Electron fluxes with energy up to 30 eV are produced during the ionizing pulse. During both the energization stage and the cooling stage the electrons deposit their energy in the atmospheric atoms and molecules. The excited atoms and molecules radiate part of this

energy as prompt or delayed emissions in the visible, UV and IR bands. By measuring the emission rate due to minority species whose diagnosis is desired and by comparing them to the emissions from majority species such as O₂ their mixing ratio can be determined and monitored with high accuracy. Altitude profiles can be determined by changing the focal spot of the microwaves. The technique allows for measurement of winds and atmospheric turbulence by following the after glow transport.

During the past contract period a strawman facility was designed. The facility was based on 10 GHz microwaves focused by a 34 meter dish at 30-50 km altitude. Pulse lengths of the order 10-50 nanoseconds were required for power of the order of a few Gigawatts. A strawman diagnostic system was also designed. Photometers as well as lidars were considered. An assessment of the capability of such a system indicated that it can detect species with mixing ratios below one particle per trillion. Experimental parameters for a laboratory proof of principle were also determined. Comprehensive analysis is presented in a paper accepted for publication by the Journal of Geophysical Research.

I. Visualization Tools and Parallel Processing for Physics Applications

The following outline describes visualization tools, software development and other support provided by SAIC to NRL researchers for a variety of physics applications.

1. SAIC designed a 3D visualization tool to model the position in space of magnetic windings around a half-torus accelerator. The data for the magnetic windings' location in space came from the input deck to the Mafco magnetic field solver code. By using this input deck SAIC was able to produce images that were directly related to the proposed experimental setup. After debugging the visualization code, SAIC used it to analyze the location of the windings and to determine if the windings were correctly terminated. These terminations were impossible to locate without the use of the visualization software because their location was represented by several input parameters and mathematical functions. This software provided a check for the Mafco input parameters.

2. SAIC also improved the IDL point plotting package and supplied a user's tutorial for this package.
3. SAIC researched potential graphical interfaces to determine the optimal setup for executing acoustical simulations.
4. SAIC developed a series of software tools for manipulating the GDEM soundspeed database. These tools made it possible to update the database and to account for physical phenomena such as the movement of the Gulf stream. SAIC also designed and developed tools to map regions of the ocean and to graphically display their sound speed profiles. It is now possible to examine specific latitude and longitude locations and to determine the sound speed profile at each location. This tool was used to add the region of the Tasman sea to the GDEM database in order to numerically study this region.
5. SAIC ported several computer codes from the VAX environment to the SGI workstations. This conversion involved replacing VAX specific FORTRAN code, interfacing with newly developed SGI graphics routines and solving problems arising from VMS-UNIX incompatibilities.
6. SAIC developed a point plotting package for the SGI workstations to handle visualizing lineplotted data and providing output to the Tektronic color printer.
7. SAIC integrated their point plotting package into a simulated-annealing propagation code. The resulting code generated a multi-window display which graphically kept track of several key variables at run time. This animation provides scientists with a method for determining the accuracy of their model in real time. This code was successfully used to analyze data during an at-sea experiment.
8. SAIC created software to generate a 3-D representation of the GDEM sound speed database. The results generated by this program were

used as input to a 3D visualization program which was also improved by SAIC.

9. SAIC developed a conversion program on the VAX to read output data collected from a matched-field processing run and created a file that could be viewed by graphics code on the SGI workstations. To facilitate the data transfer between the VAX and the SGI workstations, SAIC implemented the TRANSL8 software. SAIC has subsequently translated several other data files into an SGI format.
10. SAIC developed comprehensive documentation for their point plotting package to allow stand-alone use at sea.
11. SAIC integrated the HITS ship-location database with the matched-field processing (MFP) code so that ship noise could be more accurately modeled in propagation simulations. This integration involved modifying the MFP code and porting mathematical library functions from the IMSL library. Several random ship distributions were created using this software. Graphical descriptions were then generated to depict these ship distributions as well as the average ship distributions as reported by HITS. These descriptions were combined with the MFP command file to create target detection simulations. These combinations were tested for several cases with varying source levels and ship distributions. The results were used to help determine the position of experiments in order to minimize the interference due to ship noise.
12. SAIC tested framemaker and instructed government personnel in the use of this desktop publishing software. SAIC also served as a reference for scientists and analysts to deal with issues concerning the use and applications of the UNIX operating system.
13. SAIC (in collaboration with NRL and PSI) continued a major research effort using the Connection Machine 200 under the 6.0 version of CMFortran. This effort involved upgrading several existing routines

and solving incompatibility problems arising due to the differences in the SUN and SGI operating platforms.

14. The team included the backscatter correction in the Wide Area Rapid Acoustical Prediction (WRAP) model and implemented this version on the Connection Machine 200.
15. The team redesigned the connection machine code to take advantage of some parallel structures that needed representation in polar coordinates. The connection machine architecture had drastically limited the Cartesian model because several times more grid points were needed to describe the area in Cartesian coordinates and because the Cartesian layout caused many processors to attempt to collide when accessing data arrays. This conflict was avoided in the polar model because redundant grid points were eliminated when describing the 256x256 millimeter Cartesian grid. The algorithms were also tailored toward the other coordinate system. In polar coordinates the radials were independent so that each radial could be calculated in parallel. This parallel structure allowed processors to be used to calculate several acoustical modes at once. This savings in processor allocation increased the performance of the backscattered wrap model several times.
16. SAIC designed a series of cshell scripts to analyze data collected at sea. These scripts automated many of the repetitive data processing programs. By using this method, several man-weeks were saved. Subsequently, SAIC modified several of the scripts to increase efficiency for other projects as well.
17. Sediment Inversion Model: SAIC used the Simulated-Annealing method for perturbing parameters to determine the optimal model for ocean sediment properties in the specified region. After perturbing the parameters the model generated a file containing the acoustic modes. This mode file propagated the signal from source to receiver along the path used for taking the experimental data. The model then generated a transmission loss plot along the

experiment's track. The simulated transmission loss (TL) array was then compared against the experimental TL curve. Based on the results of this comparison the parameters were kept or rejected and the process restarted. A cooling schedule was set up limiting the number of changes in parameters to be accepted based on how many time steps the program has advanced. The model yielded some promising results.

18. At-Sea Experiment Track Determination Simulation: SAIC used the Parabolic Equation model for acoustic propagation monitored by Kevin Heaney to determine the difference in accuracy of transmission loss data taken for several radials at different angular spacing. This information was used to determine the experiment's track in order to maximize spacing between radials while minimizing loss of accuracy. This project is still in progress and has generated graphical manipulation spinoffs.
19. Focalization Code: SAIC used a trial source determination method which locates a source when limited environmental data is available. While this technique is not reliable if information is available for source (or receiver) location only, it is quite successful with specific information available at both source and receiver locations.
20. Global Positioning: SAIC tested the data collection process of the Global Positioning System (GPS) and wrote a users manual that enabled scientists to set up and collect data for several at-sea experiments.
21. SAIC automated several programs to perform repetitive tasks and to enable the codes to handle their own operation. This automation saves time and increases productivity.
22. SAIC interfaced the acoustical Parabolic Equation code with a graphical software application so that the program generated animated graphics as the acoustic modes propagate in range. These animations were used as a video for presentation.

23. SAIC was first author on a paper that appeared in Shock Waves, Proceedings of the 18th International Symposium on Shock Waves, (1992) entitled "Enhanced Mixing from Shock-Generated Turbulence in Dusty Air," by P. Boris, J. Boris, R. Hubbard, E. Oran, and S. Slinker. This paper is included in this report as Appendix JJ.

24. SAIC, working with PSI and NRL, continued modeling reverberation properties using the Connection Machine Backscatter-Wrap code. The paper, "Reverberation Modeling with the Adiabatic Normal Mode Model Applications to the ARSRP Experiment," by D. Dacol, P. Boris, E. Jennings, and E. Kim, shows the reverberation information graphically. This paper is included here as Appendix KK.

Several other papers have resulted from the work described above. They are included in the Appendices as follows:

"Hydrodynamic Simulations of Beam-Generated Turbulence in Channels," P. Boris, J. Boris, R. Hubbard, E. Oran, J. Picone, S. Slinker; NRL Memorandum Report 6677, "NRL 1989 Beam Propagation Studies in Support of the ATA Multi-Pulse Propagation Experiment." SAIC also presented number iii. at the DARPA SDIO Charged Particle Review 1990 as a poster. See Appendix LL.

"Beam Propagation in Channels," R.F. Hubbard, S.P. Slinker, R.D. Taylor, R.F. Fernsler, A.W. Ali, G. Joyce, and P. Boris; NRL Memorandum Report 6675: "NRL Beam Propagation Theory Studies in Support of SuperIBEX, PULSERAD, RADLAC, PURE, and DELPHI." See Appendix MM.

"Foil Focusing for Transport and Conditioning," R. Fernsler, R. Hubbard, S. Slinker, P. Boris, Proceedings of 1989 DARPA/SDIO/Services Charged Particle Beam Propagation Review. See Appendix NN.

Two additional contributions: "Wire Cells I: Vacuum" in Appendix OO and "Beam Stability and Range Extension Predictions for the ATA Multi-Pulse Propagation Experiment" in Appendix PP.

References

A. K. Ganguly and S. Ahn, IEEE Trans. on Electron devices **31**(4), p. 474-480, 1984.

A. K. Ganguly and S. Ahn, Phys. Rev. A **42**(6), p 3544-3554, 1990.

J. J. Choi, G. S. Park, S. Y. Park, C. M. Armstrong, R. H. Kyser, and M. L. Barsanti, "Broad-Band Gyro-Amplifier Research at NRL," Proc. of 17-th Int. Conf. on Infrared and Millimeter Waves, Invited Paper, SPIE Volume 1927, pp. 314 - 317, Dec. 14 - 17, 1992

J. J. Choi, C. M. Armstrong, A. K. Ganguly, and M. L. Barsanti, "Wideband Millimeter Wave Gyro-Amplifiers," 2nd Annual Vacuum Electronic Review, June 1993a.

J. J. Choi, G. S. Park, S. Y. Park, C. M. Armstrong, A. K. Ganguly, R. H. Kyser, and M. L. Barsanti, "Wideband Gyro-TWT Amplifier Experiments," Proc. of 18th Int. Conf. on Infrared and Millimeter Waves, Sept. 1993b.

A. Bar-Shalom, J. Oreg, and W.H. Goldstein, to be published in J. Quant. Spectr. Radia. Transfer, 1993.

A. Bar-Shalom, J. Oreg, J.F. Seely, U. Feldman, C.M. Brown, B.A. Hammel, R.W. Lee, and C.A. Black, *Atomic Processes in Plasmas*, San Antonio, Texas, 1993.

D.B. Boercker, Astroph. J. **316**, L95, 1987.

M.S. Dimitrijevic and N. Konjevic, J. Quant. Spectr. Radiat. Transfer **24**, 451, 1980.

APPENDIX A

A KrF Oscillator System with Uniform Profiles

IMPORTANT

1. Please correct the proofs carefully; the responsibility for detecting errors rests with the author.
 2. Restrict corrections to instances in which the proof is at variance with the manuscript
 3. Recheck all reference data
 4. A charge will be made for extensive alterations
 5. Return proofs by airmail within 3 days of receipt
- Thank you.

Optica Communications (1993) 000-000
North-Holland

OPTICS
COMMUNICATIONS

Full length article

A KrF oscillator system with uniform profiles

A.V. Deniz

Science Applications International Corporation, McLean, VA 22102, USA

and

S.P. Obenschain

Plasma Physics Division, U.S. Naval Research Laboratory, Washington, DC 20375, USA

Received 1 June 1993; revised manuscript received 19 August 1993

A KrF oscillator system that has produced highly uniform flat-top focal distributions is described. The oscillator system is part of a large laser system that will utilize the echelon-free induced spatial incoherence technique to obtain uniform illumination of planar targets for fusion research. With this system, focal profiles with small long scale length nonuniformities have been obtained. The nonuniformity was determined by performing a least-squares fit to a series of profiles, and calculating the deviation of each fit from a flat-top profile. With a linear fit, the deviation averaged over the series is $\pm 0.5\%$, and with a quadratic fit, it is $\pm 1.4\%$. Details of the oscillator system configuration, focal uniformity measurement techniques, and resulting focal profiles are presented.

1. Introduction

One of the requirements for high-gain direct-drive inertial confinement fusion is a highly symmetric implosion of the spherical fuel pellet. Ablation pressure nonuniformities less than a few percent are thought to be required. If an ultraviolet wavelength is used (which couples more efficiently to the target than longer wavelengths), then there is only modest lateral smoothing of the ablation pressure [1]. Therefore, success with direct drive laser fusion requires the development of techniques for highly uniform illumination of fuel pellets. It is perhaps impossible with today's technology to have a uniform focal illumination with a nearly diffraction limited beam. Progress has instead been made by methods that employ controlled spatial and temporal incoherence with focal profiles that are smooth when averaged over many temporal coherence times [2-11]. These smoothing techniques have been shown to reduce laser plasma instabilities [12-18]. However, with existing high energy glass lasers, peak-to-valley focal nonuniformities still are typically $\sim 10\%$ with these techniques [9-11].

The NIKE KrF laser system [19-21] currently under construction at the Naval Research Laboratory, is being built to have focal profiles that are uniform enough to produce ablation pressures flat to within 2% on planar targets. NIKE will use the echelonfree induced spatial incoherence (EFISI) technique [3] to produce 60 time diffraction limited flat-top focal profiles with at least two kilojoules in 4 ns on target.

The EFISI technique is illustrated in fig. 1. An oscillator with spatially incoherent output illuminates an object aperture, whose image is relayed by the two lenses to the image plane. Light from each point in the object aperture illuminates an aperture at the Fourier plane with the same intensity. The light passes through the object aperture, is amplified at the Fourier plane, and is then focused at the image

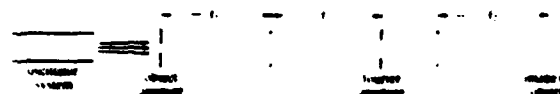


Fig. 1. A simplified schematic of the echelon-free induced spatial incoherence technique.

plane. With the EFISI technique, the image profile would not be strongly affected by the spatial non-uniformity of the amplifier gain because light from each point in the object aperture is amplified by the same amount. Also, because the image is already many times diffraction limited, it will not be strongly affected by the phase aberrations of the laser system.

There are several requirements that the oscillator must meet:

(i) The light at the object aperture must have sufficient spatial incoherence (divergence) to fill the Fourier aperture.

(ii) The oscillator output must have sufficient temporal incoherence to produce a time-averaged smooth profile.

(iii) The light at the object and Fourier apertures must produce a uniform flat-top profile at the image plane.

(iv) The light from each point in the object aperture must illuminate the Fourier aperture with the same profile.

Requirements (i) through (iii) are perhaps straightforward. Requirement (iv) is necessary so that the focal profile be insensitive to gain nonuniformities of an amplifier located at the Fourier plane. These requirements are discussed in the next section.

Here we report on a KrF oscillator system with unconventional resonator optics that has come close to meeting the above requirements. This oscillator, with a two stage Pockels cell pulse slicer, produces 4 ns flat-top focal profiles (using an $f/130$ lens) with tilts on the order of 1% and the temporal coherence time of 0.6 ps. When a nonuniform amplifier gain was simulated by blocking half the Fourier aperture, the tilts were still less than 3%. This system approached the focal uniformity goals for the NIKE laser.

In this oscillator, the laser medium is imaged back onto itself by the resonator optics. Thus a photon that makes a large angle with the longitudinal axis will still pass through the laser medium, even after many transits (unless the angle is so large that the finite size of the laser chamber windows blocks it). The output of this oscillator therefore has greater angular divergence than the output of an oscillator with conventional stable resonator optics. In addition, the Fourier aperture is illuminated more nearly uni-

formly by each point in the object aperture, as required by the EFISI technique.

The next section describes the oscillator setup in greater detail and presents its measured characteristics. Section 3 presents details of the pulse slicing system. Section 4 presents details of the imager used to measure the profiles. Section 5 presents the focal profiles and the algorithms used to evaluate them. Section 6 summarizes the results and presents the conclusions.

2. The oscillator system

As mentioned in the introduction, the oscillator output must be spatially incoherent so that it can produce a beam that is many times diffraction limited. The focal profile does not then depend strongly on the phase errors encountered during propagation. The focal profiles presented are 60 times diffraction limited, although the NIKE system has been designed to propagate beams which are up to 120 times diffraction limited without vignetting. If both the object and Fourier apertures are circular, then the beam is N_d times diffraction limited with

$$N_d = Dd/\lambda f, \quad (1)$$

where D is the Fourier aperture diameter, d is the object aperture diameter, λ is the wavelength of the light (248 nm), and f is the focal length of the lens between the object and Fourier apertures.

The second requirement is that the oscillator output be temporally incoherent. At any given time, the focal profile is a complicated speckle pattern. After one coherence time, it is a different pattern. The measured profiles are time-integrated, so that if the measurement is made over more coherence times, then both the shot-to-shot variation due to the speckle and the random variation from one coherence zone to the next ^{are} decreased. The coherence time must be short enough so that these variations are not too large.

The third requirement is that light from each part of the object aperture illuminate the Fourier aperture with the same angular energy distribution. This requirement can be stated more precisely as follows: Let $I(x, k)$ be the time-averaged intensity profile at point k within the Fourier aperture due to light from

several coherence zones (which have a size of $\sim d/60$) around point x in the object aperture. The requirement becomes

$$\nabla_x f(x, k) = 0. \quad (2)$$

Note that $f(x, k)$ need not also be uniform across the Fourier aperture. If eq. (2) is satisfied, then the focal profile will be flat, even if the light is subjected to nonuniform amplification at the Fourier aperture.

Equation (2) can be checked by placing a small pinhole in the object aperture and measuring the time-averaged intensity profile at the Fourier aperture. The resulting Fourier intensity profile should be the same regardless of where the pinhole is placed within the object aperture. Adherence to eq. (2) can also be checked by blocking various regions of the Fourier aperture, and observing whether or not the image maintains its flat-top shape. The latter method was used in this work.

Figure 2 shows the optical setup for the oscillator used for the results presented here. The oscillator optics image the laser medium back onto itself. All the oscillator configurations investigated used a $1 \text{ cm} \times 2 \text{ cm} \times 80 \text{ cm}$ discharge pumped KrF laser medium. The rear optics consist of a positive lens and a high-reflectivity flat mirror with an aperture, and the front optic is a 50% reflectivity flat mirror. The distance between each mirror and the lens is equal to the focal length of the lens (1 m). Light from point a inside the laser medium will be imaged, after reflection by both the front and rear optics, at point b . This property of imaging the laser medium back onto itself produces a large angular divergence.

Conventional discharge oscillator optics did not satisfy these requirements. A stable resonator setup consisting of a flat front mirror and a rear mirror with a large radius of curvature (5 m, 10 m, and ∞) was tested. While the image of the object aperture was flat, the angular divergence was too small to produce the required 60 times diffraction limited beam.

The front of the laser medium (which is approx-

imately 10 cm from the chamber window) was relayed with a telescope to the object aperture. This geometry was found empirically to produce the flat-test images. The image was not as flat when the center of the discharge was imaged onto the object aperture, or when the object aperture was $\sim 50 \text{ cm}$ from the front oscillator mirror outside the oscillator (no telescope was used in the latter case).

The images produced by this setup had flat-top focal profiles, but with residual tilts on the order of 10% in the vertical direction. This was most likely due to irregularities in the laser cell and/or electrodes. The tilts also varied during the oscillator pulse. Finally, there was a short-to-short variation of the tilts, presumably caused by irreproducibilities of the discharge.

All profile tilts were substantially reduced by adding the telescope system shown in fig. 3. The oscillator output was split into two beams and then recombined. One beam passed through a single telescope, and the image was inverted. The other beam traveled the same distance but passed through two telescopes, and the image was not inverted. Combining the beams at the object aperture resulted in images with a very small tilt ($\sim 1\%$), independent of when the oscillator pulse was sliced. The tilts of the profiles also had a very small short-to-short variation.

The rear reflector of the oscillator, which is located close to a Fourier plane, was apertured to limit the angular divergence of the output at the object aperture. This affected the concavity of the profile at the image plane (after passing through the Fourier aperture). Decreasing the angular divergence by placing a smaller aperture at the rear reflector tended to make the image concave up, while increasing the divergence had the opposite effect. With no rear reflector aperture, the image was slightly concave down.

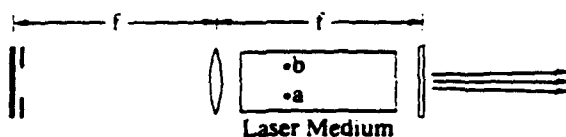


Fig. 2. The optical setup for the oscillator.

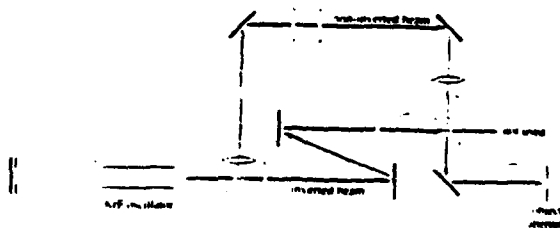


Fig. 3. The optical setup for the oscillator and telescopes.

The rear reflector aperture was made smaller until the concavity was nearly eliminated. For the results in this work, the divergence from the object aperture was limited to ~ 8 mrad in the vertical direction, and ~ 14 mrad in the horizontal direction. This divergence is sufficient to overfill the Fourier aperture, which requires only 5 mrad.

The object aperture diameter of 3 mm was limited by the transverse dimension of the laser medium (1 cm by 2 cm), and the Fourier aperture size was limited by the size of the Pockels cells to $0.5 \text{ cm} \times 0.5 \text{ cm}$, which implies a focal length of 1 m. The required angular divergence of the oscillator is $60\lambda/d \sim 5$ mrad, which is less than the measured angular divergence.

Two KD*P Pockels cells in series were used to slice a 4 ns pulse out of the 30 ns oscillator output. The setup is shown in fig. 4. A pair of dielectric polarizers polarized the beam horizontally before the object aperture. The beam then passes through the Fourier aperture, the two Pockels cells, and the remaining sets of dielectric polarizers. The energy contrast ratio, defined as the ratio of the transmitted fluences with and without voltage applied to the Pockels cells, was 3000 to 1.

3. The imager

The imager is a cooled, slow-scan, two-dimensional charge coupled device (CCD) camera. It is capable of measuring the energy profiles to an accuracy of better than 1%, and it has a spatial resolution of 384 by 576. The camera parameters are shown in table 1. The CCD is coated with a phosphor in order to increase its quantum efficiency at 248 nm to ~ 0.25 .

The imager has a vacuum window to prevent formation of frost on the CCD. This window has an anti-reflection coating on each surface with a power re-

Table 1
Parameters of the CCD camera.

Parameter	Value
Format	384 by 576 pixels
Pixel size	$23 \mu\text{m}$ by $23 \mu\text{m}$
Readout noise	25 electrons
Charge transfer efficiency	0.99998
Full well capacity	160000 electrons/pixel
Quantum efficiency	0.25 at 248 nm
Dark current	15 electrons/sec/pixel
Exposure time	0.1 s
Digitizer resolution	12 bits
CCD temperature	-45°C
Window thickness	1.0 cm
Window reflectivity	0.25%, each surface

flectivity of 0.25% at $\lambda = 248 \text{ nm}$, 0° incidence. This introduced a negligible error in the measurement of the profile because the coherence length of the light ($1.9 \times 10^{-2} \text{ cm}$) was much shorter than the window thickness.

For temporally coherent light, the noise in a cooled CCD measurement is due mainly to the statistical nature of the photoelectric process (the electron shot noise) and the preamplifier noise. For the measurements presented the signal was large enough that the preamplifier noise was negligible. Because the number of photoelectrons in one pixel for several measurements of identical light levels has a Poisson distribution, the electron shot noise σ_{ccd} for one measurement is

$$\sigma_{\text{ccd}} = \sqrt{N_e} \quad (3)$$

The noise in one pixel is independent of the noise in another.

In addition to the noise in the CCD measurement, there is a random variation σ_i associated with the temporal incoherence of light. If a pixel in the detector is smaller than a spatial coherence zone, then

$$\sigma_i = N_e (\tau/T)^{1/2} \quad (4)$$

where T is the laser pulse length, τ is the coherence time, N_e is the average number of photoelectrons in the pixel measured in time T , and σ_i is the shot-to-shot RMS variation of the signal in electrons. In this case, there is correlation in the measurements of adjacent pixels. If on the other hand there are N_c coherence zones in a pixel, then

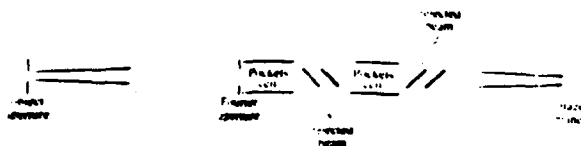


Fig. 4. The pulse slicing system.

$$\sigma_i = N_e (\tau / N_e T)^{1/2} \quad (5)$$

In this case, the random variation for adjacent pixels is independent. The bandwidth ($\approx 1/\tau$) of the oscillator has been measured to be 1.6 THz, which gives a coherence time of 0.6 ps. Because the random variation associated with the incoherence is not correlated with the CCD measurement noise, the total random variation σ_i in electrons of the number of electronics in a pixel is given by

$$\sigma_i^2 = \sigma_i^2 + \sigma_{\text{ccd}}^2 \quad (6)$$

Because a typical CCD exhibits a nonuniform response to light, the camera was calibrated by illuminating it with a uniform light source (fig. 5). The oscillator was used as a light source for a commercial integrating sphere. This has the advantage of calibrating the camera for the same wavelength and approximately the same pulse length used in the measurements. The camera was placed ~ 1 m from the output aperture of the sphere. At that distance, the variation in light across the CCD surface from a lambertian surface is theoretically 1.5×10^{-4} . In an actual setup, the variation will probably be greater: the camera and integrating sphere might not be perfectly aligned, there might be spurious reflections, and the light output from the integrating sphere might not be perfectly uniform.

In order to test the calibration technique, the camera was calibrated at different positions. The distance between the camera and the integrating sphere was varied from 0.4 m to 1.6 m, the camera was moved ± 3 mm perpendicular to a line between it and the sphere, and the camera was rotated about that line. The greatest change in the calibration was a 0.3% spatial tilt across the 8.83 mm width of the sensor. This corresponds to a systematic error of less



Fig. 5. Calibration of the camera. The oscillator illuminates an integrating sphere. A negative lens (not shown) is used to spread out the input light to avoid damaging the integrating sphere. A tube (not shown) is used in order to reduce stray light. Apertures inside the tube are necessary in order to reduce stray reflections.

than 0.1% in the calculation of the tilt of a 2 mm diameter profile.

During the calibration, there will be the random variation in the measurements given by eq. (6). There were several coherence zones in each pixel, so eq. (5) was used to calculate the random variation due to the incoherence of light. The size δ of a coherence zone at the CCD is approximately

$$\delta = \lambda l / D_1 \quad (7)$$

where λ is the wavelength of light and l is the distance between the CCD and the integrating sphere output aperture, which has a diameter D_1 . For $\lambda = 248$ nm, $l = 1$ m, and $D_1 = 5$ cm, δ is 4.96 μm . Using the pixel size from the table, the value of N_e (to be used in eq. (5)) is $(23 \mu\text{m} / 4.96 \mu\text{m})^2 = 21.5$.

In order to measure the noise, the output from the integrating sphere was measured 64 times. After correcting for variation in the total energy falling on the CCD, the noise-to-signal ratio (σ_i / N_e) for a given pixel was calculated. At a signal level of 6.6×10^4 electrons, the result ranged from 2.5×10^{-3} to 3.0×10^{-3} , compared to an expected value (from eq. (6)) of 3.8×10^{-3} ($T = 30$ ns, $\tau = 0.6$ ps, and $N_e = 21.5$). This indicates that the camera is capable of measuring the profiles with low noise.

The calibration was determined by summing 64 measurements (with the background subtracted) of the integrating sphere output (flat fields). The average signal level was 1.5×10^5 electrons, or 3825 counts. The calibration factor C_i for pixel i is given by

$$C_i = \frac{1}{N_p f_i} \sum_{j=1}^{N_p} f_j \quad (8)$$

where N_p is the number of pixels on the CCD, and f_i is the summed flat field signal at pixel i . Because f_i is a sum of 64 measurements, the relative error of C_i calculated by eq. (6) due to the error in f_i is reduced by a factor of 8 from 2.8×10^{-3} to 3.5×10^{-4} .

The relative energy e_i falling on pixel i is given by

$$e_i = C_i (s_i - b_i) \quad (9)$$

where s_i and b_i are respectively the signal and background at pixel i . The signal levels of the profiles presented in the next section are 6.0×10^4 electrons, or ~ 1500 counts, while the background levels (which are due to the camera) are ~ 50 counts. This implies

that the RMS measurement error due to the electron shot noise and the calibration error is 0.4% for one pixel. When observing longer scale length focal profile nonuniformities that cover many pixels, one can reduce this error by averaging over more than one pixel.

4. The profiles

The object aperture is imaged onto the camera through a lens, the Fourier aperture, the pulse slicing system, a demagnifying telescope, and focusing lens. A schematic of the experimental arrangement without the demagnifying telescope is shown in fig. 4. The telescope is located before the second lens, which focuses the beam onto the camera after attenuation by two reflections by uncoated surfaces and transmission through a 95% flat reflector. The telescope demagnifies the image of the object aperture from 3 mm to 2 mm diameter.

The measured profiles were analyzed with the following algorithm:

- (i) Determine the centroid (x_c, y_c) of the profile.
- (ii) Find the edges of the flat region of the horizontal and vertical cross-sections through the centroid.
- (iii) For the flat region of each cross-section: (a) Perform a linear least-squares fit, and calculate the variation of the fit from a flat-top (tilt). (b) Perform a quadratic least-squares fit, and calculate the mean-to-peak variation of the fit from a flat-top. (c) Calculate the RMS deviation of the measured cross-section from the fits.

The centroid is determined by

$$x_c = \frac{\sum_{i=1}^{N_p} x_i e_i}{\sum_{i=1}^{N_p} e_i}, \quad (10)$$

where x_i is the x position of pixel i . The calculation of y_c is analogous. The edges of the flat region of a cross-section is determined by the following algorithm:

- (i) Find the pixels l and r where the measured value of the cross-section is just greater than a specified fraction f_0 of the maximum value.
- (ii) The edges of the flat region at l pixels from l and r towards the center of the cross-section. For ex-

ample, if l is the pixel on the left edge of the profile, and pixel numbers increase from left to right, the flat region is between pixels $l+t$ and $r-t$, inclusive.

For the results presented, f_0 was 0.25, and t was 5 (the cross-section of the profile is 85 pixels across). The results do not depend strongly on f_0 or t .

Three aspects of the profiles were evaluated. First, the 4 ns pulse was taken at different times during the oscillator output to check whether the object aperture illumination uniformity changed in time. It was found that the tilts of the profiles do not vary appreciably during the oscillator output. Second, a series of profiles were taken at the same time during the oscillator output to determine the shot-to-shot variation of the profiles. It was found that the observed shot-to-shot RMS variation of the tilts was consistent with the spatial and temporal incoherence of the light. It was also found that the variation of the linear fit from a flat-top profile (a measure of tilt) averaged over the series was $\pm 0.5\%$, and of the quadratic fit (a measure of peaking or concavity) was $\pm 1.4\%$. Finally, the Fourier aperture was partially blocked to simulate the effects of a nonuniform gain in an amplifier. The profiles were found to be insensitive to this partial blocking; blocking half the Fourier aperture changed tilts of the profile by only a few percent.

Figure 6 shows a typical profile and its cross-sections. The RMS deviation of the measurement from the linear least-squares fit is 1.0% along the vertical direction and 0.8% along the horizontal. If the profile were flat, the deviation would be the same as the total random variation σ_y (given by eq. (6)) in each datum. Because a pixel is smaller than a coherence zone, eq. (4) can be used to calculate the variation due to the incoherence of the light. With a coherence time of 0.6 ps, a pulse length of 4 ns, and a signal of 6×10^4 electrons, the expected RMS relative variation of each datum is 1.3%. This indicates that the observed deviation is probably due to the CCD shot noise error and the variation of the light energy due to the laser incoherence and the finite averaging time.

Figure 7 shows the tilts of the cross-sections as a function of time during the oscillator output. Eight images were recorded for seven times spaced 5 ns apart during the oscillator output, for a total of 56 images. Each point on the graphs is the tilt of the horizontal or vertical cross-section of one image. Note

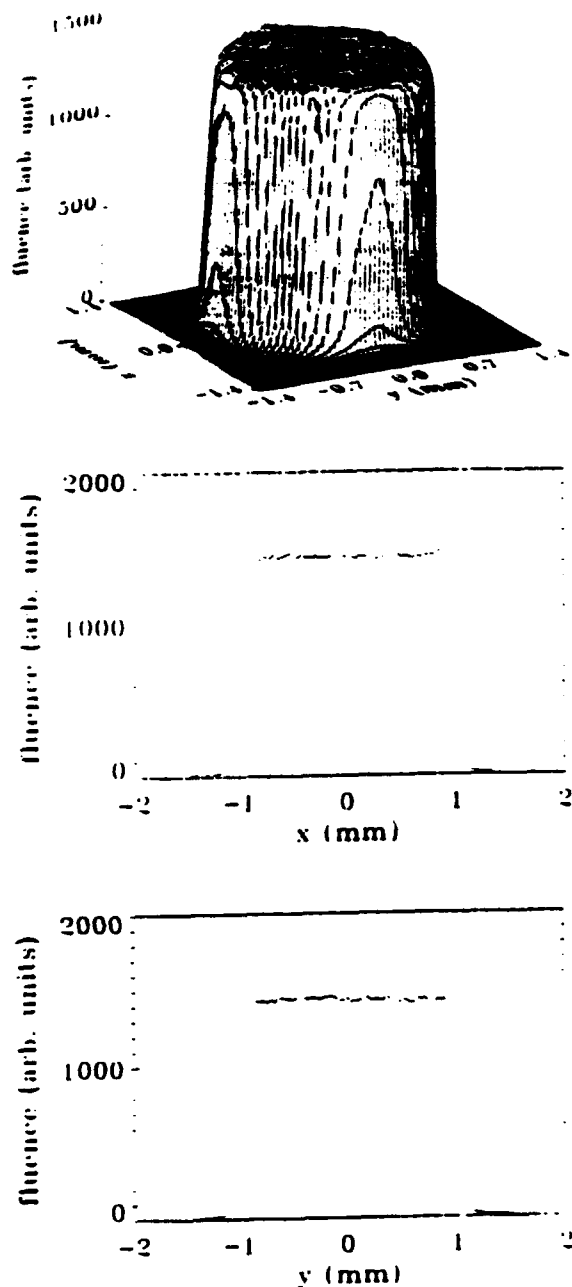


Fig. 6. A typical profile and its cross-sections: (a) three-dimensional view, (b) horizontal cross-section through the centroid, and (c) vertical cross-section through the centroid.

that the time variation is negligible. Therefore, the output of the oscillator does not vary appreciably when averaged over 4 ns.

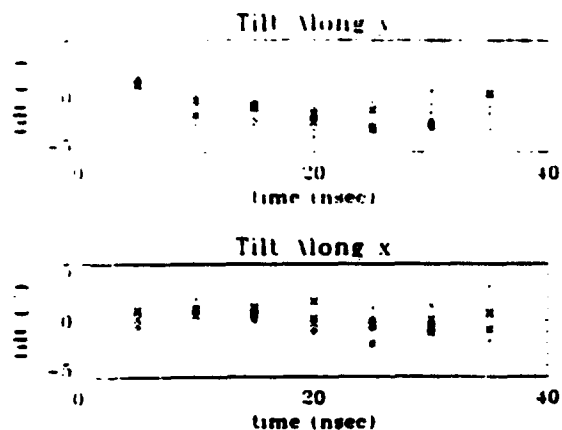


Fig. 7. Tilts of the cross-sections as a function of time during the oscillator output.

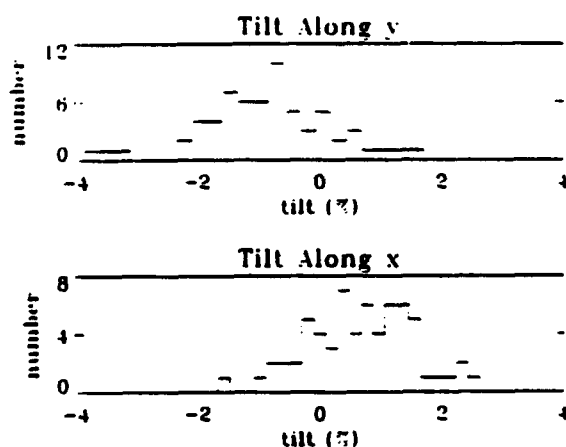


Fig. 8. A histogram of the tilts of the linear fits to the profiles with the Fourier aperture completely unblocked.

Figure 8 is a histogram of the tilts for 64 images. Note that the average tilt is very nearly zero; it is -0.75% along the vertical direction, and 0.75% along the horizontal. The RMS variation of the tilt is 1% , which is close to the expected value of 0.7% (this is calculated in the appendix). The RMS variation of the tilt of a single beam of fig. 3 is $\sim 5\%$ along the vertical direction and $\sim 1\%$ along the horizontal. The larger variation along the vertical direction for a single beam indicates that the telescopes shown in fig. 3 are effective in reducing the shot-to-shot variation of the tilt. Furthermore, the average tilt of a single

beam is 5 to 10%, which indicates that the telescopes are also effective in reducing the average tilt.

Figure 9 is a histogram of the mean-to-peak variation of the quadratic fit from a flat-top profile for the 64 images. The mean averaged over the images is $\pm 1.4\%$ along the vertical direction, and $\pm 0.6\%$ along the horizontal. The variation is larger along the vertical direction because there is more shot-to-shot variation of the concavity of the profile, which is not reduced by the telescopes.

Figure 10 shows the tilts of the cross-sections with

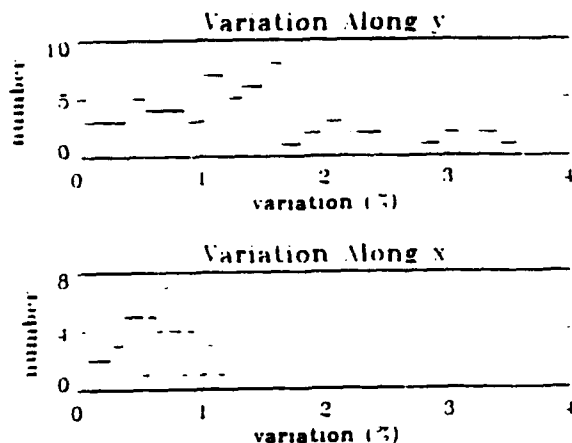


Fig. 9. A histogram of the mean-to-peak variation of the quadratic fits from a flat-top profile with the Fourier aperture completely unblocked.

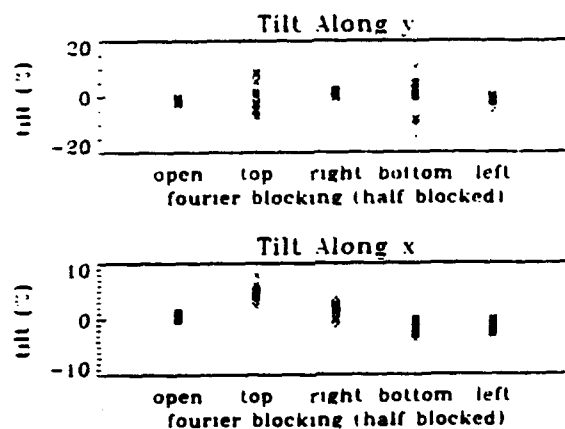


Fig. 10. Variation of the tilts of the cross-section when different parts of the Fourier aperture are blocked.

different parts of the Fourier aperture blocked in order to simulate nonuniform amplifier gain. Sixteen images were recorded with (i) the Fourier aperture completely unblocked, (ii) the top half of the Fourier aperture blocked, (iii) the right half blocked, (iv) the bottom half blocked, and (v) the left half blocked, for a total of 80 images. Note that the average tilt changed by a few percent. Note also that when the top or bottom of the Fourier aperture was blocked, the shot-to-shot variation of the tilt of the vertical cross-section increased, because different parts of the inverted and noninverted beams were blocked. The two beams were not exact inverses of each other, and the tilt of one did not cancel the tilt of the other. This larger shot-to-shot variation does not occur in the horizontal direction because the angular divergence of the oscillator output in the horizontal direction is larger than the divergence in the vertical direction.

5. Summary

A laser oscillator system has been developed with a 4 ns pulse output, 3000 to 1 energy contrast ratio, and flat focal profile. Its angular divergence is large enough to produce 60 times diffraction-limited images. The coherence time was 0.6 ps, and the pulse duration was 30 ns. The focal images of 4 ns slices of the beam had the desired flat cross-sections (tilts of $\sim 1\%$). The shape of the focal profile should not depend strongly on the gain profiles of the laser amplifiers if they are placed at the Fourier aperture of the EFISI system. This was tested by partially blocking the Fourier aperture and observing that the shape of the focal profile was not strongly affected (the tilts were typically on the order of a few percent). The top, bottom, left, and right halves of the Fourier aperture were blocked. Partially blocking the Fourier aperture simulates an extremely nonuniform amplifier gain; typical nonuniformities of actual amplifiers used in the NIKE laser are only approximately 20%.

The oscillator system described here comes close to fulfilling the goals for the NIKE system. The existing system is now being used to test the ability of the NIKE system to maintain uniform focal profiles after several stages of amplification. In future work,

we will attempt obtain more nearly uniform beams which are less affected by partial blocking of the Fourier aperture. We will also attempt to produce more than 60 times diffraction limited beams, so that phase aberrations in the laser system will have even less effect on the focal profile.

Acknowledgements

We would like to thank our colleagues for useful discussions and assistance: Mark S. Pronko, Robert H. Lehmberg, Thomas Lehecka, Carl J. Pawley, Warren Webster, Julius Goldhar, and Andrew J. Schmitt. The data was archived on disk using a modified version of National Center for Supercomputer Activities' Hierarchical Data Format. This work was supported by the United States Department of Energy.

Appendix

This appendix presents a calculation of the variance of the slope of the linear least-squares fit. The variance is determined by the variance of the data used to calculate the slope. The random variation of each datum in the measured profile is due to both the CCD measurement noise and the random variation associated with the temporal incoherence of the light. The CCD measurement noise is due mainly to the electron shot noise, and is given by eq. (3). The random variation due to the incoherence is given by eq. (4) or (5). The total random variation σ_y (given by eq. (6)) causes the calculated slope m to have a variance σ_m^2 .

In order to calculate σ_m , let y_α be a set of N_f random variables, and $y_{\alpha i}$ be the value of sample i of y_α . Let x_α be a set of N_f numbers. The y_α are the measurements at position x_α ; N_f is the number of pixels across the profile. Define

$$\bar{y}_\alpha = \frac{1}{N_f} \sum_{i=1}^{N_f} y_{\alpha i}, \quad (11a)$$

$$\sigma_{\alpha\beta}^2 = \frac{1}{N_f} \sum_{i=1}^{N_f} (y_{\alpha i} - \bar{y}_\alpha)(y_{\beta i} - \bar{y}_\beta), \quad (11b)$$

$$\beta_1 = \sum_{\alpha=1}^{N_f} x_\alpha, \quad (11c)$$

$$\beta_2 = \sum_{\alpha=1}^{N_f} x_\alpha^2, \quad (11d)$$

where N_f is the number of profiles measured. Note that the x_α can be chosen so that β_1 is zero. Note also that in this case, eq. (11d) can be approximated by an integral. Let L be the diameter of the profile, and let $\Delta x = L/N_f$. Then

$$\beta_2 = \frac{N_f}{L} \sum_{\alpha=1}^{N_f} x_\alpha^2 \Delta x, \quad (12)$$

$$\approx \frac{N_f}{L} \int_{-L/2}^{L/2} x^2 dx \quad (13)$$

$$\approx N_f L^2 / 12. \quad (14)$$

The variance will be calculated by first using the standard formula for the slope of the linear least-squares fit to a set of data. The variance will depend on $\sigma_{\alpha\beta}^2$. However, $\sigma_{\alpha\beta}^2$ will be negligible if the pixels α and β are not close together, because the size of a coherence zone is approximately the same size as a pixel. Using a rough approximation, the ratio σ_m/σ_y is calculated.

The slope m of the linear least-squares fit to the data pairs (x_α, y_α) is a random variable given by (after setting $\beta_1 = 0$):

$$m = \frac{1}{\beta_2} \sum_{\alpha=1}^{N_f} x_\alpha y_\alpha. \quad (15)$$

Let σ_m^2 be the variance of m . Because x_α is a number (rather than a random variable),

$$\sigma_m^2 = \frac{1}{\beta_2^2} \sum_{\alpha=1}^{N_f} \sum_{\beta=1}^{N_f} x_\alpha x_\beta \sigma_{\alpha\beta}^2. \quad (16)$$

For the results presented, there are 60 coherence zones and 85 pixels across a profile; each coherence zone spans approximately one pixel. In addition, $\sigma_1 \sim 750$ electrons (from eq. (4), with $T=4$ ns, $\tau=0.6$ ps, and $N_e=6.0 \times 10^6$ electrons), while $\sigma_{\text{meas}} \sim 250$ electrons (from eq. (3)). The total variation at one pixel is therefore (eq. (6)) ~ 790 electrons, which is a relative variation of 1.3×10^{-2} . Because the variation due to the measurement (σ_{meas}) is independent for each pixel, while the variation due to the incoh-

oh
st

erence of light (σ_y) is somewhat correlated, the rather arbitrary assumption can be made:

$$\begin{aligned}\sigma_{\alpha\beta}^2 &= \sigma_{\alpha\alpha}^2, & \text{if } \alpha = \beta, \\ &= k\sigma_{\alpha\alpha}^2, & \text{if } |\alpha - \beta| = 1, \\ &= 0, & \text{otherwise.}\end{aligned}\quad (17)$$

Equation (16) then becomes

$$\sigma_m^2 = \frac{1}{\beta_2^2} \sum_{\alpha=1}^{N_f} (x_\alpha^2 + kx_{\alpha-1}x_\alpha + kx_{\alpha+1}x_\alpha) \sigma_{\alpha\alpha}^2, \quad (18)$$

where $x_\alpha = 0$ for $\alpha = 0$ and $\alpha = N_f + 1$ so that there is no contribution from the nonexistent points 0 and $N_f + 1$.

Because the signal level is nearly the same for all points on the profile, the variances of each of the y_α will all be approximately equal:

$$\sigma_{11}^2 = \sigma_{22}^2 = \dots = \sigma_{N_f}^2. \quad (19)$$

Then

$$\frac{\sigma_m}{\sigma_y} = \frac{1}{\beta_2} \left[\sum_{\alpha=1}^{N_f} (x_\alpha^2 + kx_{\alpha-1}x_\alpha + kx_{\alpha+1}x_\alpha) \right]^{1/2}. \quad (20)$$

With $x_\alpha x_{\alpha-1} \approx x_\alpha^2$,

$$\frac{\sigma_m}{\sigma_y} \approx \left(\frac{1+2k}{\beta_2} \right)^{1/2}. \quad (21)$$

Approximating β_2 by $N_f L^2/12$, this becomes

$$\frac{\sigma_m}{\sigma_y} \approx \frac{2\sqrt{3}}{L} \left(\frac{1+2k}{N_f} \right)^{1/2}. \quad (22)$$

For a 2 mm diameter image with $N_f = 85$ and $k = 0.5$, $\sigma_m/\sigma_y = 0.27/\text{mm}$. With $\sigma_y/N_s = 1.3 \times 10^{-2}$, $\sigma_m/N_s = 3.5 \times 10^{-3}/\text{mm}$, or a 0.7% shot-to-shot RMS variation of the tilt of the profile. With $k = 0.75$, $\sigma_m/\sigma_y = 0.30/\text{mm}$, and with $k = 0.25$, $\sigma_m/\sigma_y = 0.23/\text{mm}$. This indicates that the value of k does not strongly affect the RMS variation of the tilts.

References

- [1] S.E. Bodner, *J. Fusion Energy* 1 (1981) 221.
- [2] R.H. Lehmborg and S.P. Obenschain, *Optics Comm.* 46 (1983) 27.
- [3] R.H. Lehmborg and J. Goldhar, *Fusion Tech.* 11 (1987) 532.
- [4] Ximing Deng, Xiangchun Liang, Zezun Chen, Wenyan Yu and Renyong Ma, *Appl. Optics* 25 (1986) 377.
- [5] A.J. Gardner and J.H. Gardner, *J. Appl. Phys.* 60 (1986) 6. *SCHMITT John*
- [6] S. Skupsky, R.W. Short, T. Kessler, R.S. Craxton, S. Letzring and J.M. Soures, *J. Appl. Phys.* 66 (1989) 3456.
- [7] D.G. Colombant and A.J. Schmitt, *J. Appl. Phys.* 67 (1990) 2303.
- [8] Y. Kato, K. Mima, N. Miyanaga, S. Arinaga, Y. Kitagawa, M. Nakatsuka and C. Yamanaka, *Phys. Rev. Lett.* 53 (1984) 1057.
- [9] D. Veron, G. Thiell and C. Gouedard, *Optics Comm.* 97 (1993) 259.
- [10] D.M. Penington, M.A. Henesian, H.T. Powell, C.E. Thompson and T.L. Weiland, *Conf. on Lasers and electro-optics, 1993, Technical Digest Series, Vol. 11* (1993).
- [11] H. Nakano, K. Tsubakimoto, N. Miyanaga, M. Nakatsuka, T. Kanabe, H. Azechi, T. Jitsuno and S. Nakei, *J. Appl. Phys.* 73 (1993) 2122.
- [12] S.P. Obenschain, J. Grun, M.J. Herbst, K.J. Kearney, C.K. Manka, E.A. McLean, A.N. Mostovych, J.A. Stamper, R.R. Whitlock, S.E. Bodner, J.H. Gardner and R.H. Lehmborg, *Phys. Rev. Lett.* 56 (1986) 2807.
- [13] J. Grun, M.H. Emery, C.K. Manka, T.N. Lee, E.A. McLean, A. Mostovych, J. Stamper, S. Bodner, S.P. Obenschain and B.H. Ripen, *Phys. Rev. Lett.* 58 (1987) 2672.
- [14] A.N. Mostovych, S.P. Obenschain, J.H. Gardner, J. Grun, K.J. Kearney, C.K. Manka, E.A. McLean and C.J. Pawley, *Phys. Rev. Lett.* 59 (1987) 1193.
- [15] S.P. Obenschain, C.J. Pawley, A.N. Mostovych, J.A. Stamper, J.H. Gardner, A.J. Schmitt and S.E. Bodner, *Phys. Rev. Lett.* 62 (1989) 768.
- [16] O. Willi, T. Afshar-rad and S. Coe, *Phys. Fluids B* 2 (1990) 1318.
- [17] T.A. Peyser, C.K. Manka, S.P. Obenschain and K.J. Kearney, *Phys. Fluids B* 3 (1991) 1479.
- [18] D.K. Bradley, J.A. Delettretz and C.P. Verdon, *Phys. Rev. Lett.* 68 (1992) 2774.
- [19] C.J. Pawley et al., *Proc. Intern. Conf. on Lasers '90*, eds. D.G. Harris and J. Herbelin (1991) p. 491.
- [20] M.S. Pronko et al., *Proc. Intern. Conf. on Lasers '91*, eds. F.J. Duarte and D.G. Harris (1992) p. 691.
- [21] S.E. Bodner et al., *Fourteenth Intern. Conf. on Plasma physics and controlled nuclear fusion research, IAEA-CN-36/B-2-1(C)*, (1992).

Appendix B

Effects of Random Phase Distortion and Nonlinear Optical Processes on Laser Beam Uniformity with Induced Spatial Incoherence (ISI)

**Effects of random phase distortion and nonlinear optical processes on
laser beam uniformity with induced spatial incoherence (ISI)**

R. H. Lehmberg, S. P. Obenschain, C. J. Pawley, M. S. Pronko

Naval Research Laboratory, Plasma Physics Division, Laser-Plasma Branch
Washington, DC 20375

A. V. Deniz and T. Lehecka

Science Applications International Corporation
McLean, VA 22102

ABSTRACT

One of the key requirements for direct-drive laser fusion is a laser whose focal profile is sufficiently smooth and controllable to produce highly symmetric implosions. To achieve this, the NIKE laser will implement the echelon-free ISI technique, in which the desired focal profile is formed at the output of a spatially and temporally incoherent oscillator, then imaged through the laser amplifiers onto the target. Because the amplifiers are located in the quasi far-field of the oscillator, their large scalelength gain and phase nonuniformities will have little effect on the image as long as the light remains highly incoherent. However, small scalelength phase aberrations and nonlinear optical processes must be minimized to maintain good control over the image. After a brief description of the NIKE system, this paper reports on numerical simulations and measurements of profile distortion due to random amplitude and phase nonuniformities, nonlinear refraction, and self-seeded stimulated rotational Raman scattering, and describes the steps being taken to control these effects.

1. INTRODUCTION

The NIKE laser is a KrF facility currently under construction at the Naval Research Laboratory to address technological and physics issues of direct-drive laser fusion. It is designed to ablatively accelerate thin planar foil targets under conditions close to the operating regime envisioned for a high gain pellet. High pellet gain can be achieved only if peak to valley nonuniformities of the ablation pressure are less than 2%. For direct-drive, this requires a laser whose focal spot distribution is highly smooth and controllable because UV light allows only modest smoothing of irradiance nonuniformities by lateral energy flow in the underdense plasma surrounding the pellet.

To produce such a beam, NIKE is implementing the echelon-free ISI technique¹ illustrated in Fig. 1. A broad bandwidth temporally and spatially incoherent oscillator (e.g. an amplified spontaneous emission source) uniformly illuminates an apodized aperture, which imposes the desired *time-averaged* intensity profile on the beam. This profile is imaged onto the target by relaying its quasi far-field through the amplifier chain; i.e., the focal distribution at the target is controlled directly by changing the diameter and spatial profile of the apodized aperture. At the quasi far-field, the information needed to produce the focal distribution is encoded in large optical field angles, or equivalently, in a multitude of small coherence zones. It therefore remains relatively insensitive to the large scale gain and phase nonuniformities that are invariably imposed by the amplifiers and their associated optical components. In NIKE, the image will normally subtend an angular width $\Delta\theta = 60$ times diffraction limit (XDL), thus giving coherence zones of 1/60th the beam diameter.

Image distortion can be easily pre-compensated at the oscillator as long as it remains relatively small and reproducible. In general, low distortion requires that $\Delta\theta$ remain large compared to the angular perturbations introduced by phase aberrations within the laser. The NIKE optical design, which is described briefly in Section 2, allows nearly complete compensation of all systematic phase aberrations, such as astigmatism, coma, and spherical aberration. Distortion due to random phase nonuniformities, gain nonuniformities, and nonlinear optical processes is calculated in Section 3.

The instantaneous focal spot intensity produced by incoherent beam smoothing schemes such as ISI^{1,2} is rapidly fluctuating, highly nonuniform speckle. It approaches a smooth profile $F(x)$ only when averaged over intervals much longer than the laser coherence time $t_c = 1/\Delta\nu$, where $\Delta\nu$ is the bandwidth. For fusion applications, t_c must be much shorter than the time required for the target to react hydrodynamically to the speckle. Calculations indicate that $t_c \approx 1$ psec is short enough to provide the required ablation pressure uniformity once the steady-state blowoff plasma is formed; however, shorter coherence times are desirable to reduce imprinting of the laser nonuniformities onto the target *before* the plasma forms.³ KrF amplifiers have sufficient $\Delta\nu$ to easily achieve this,⁴ but the optical system must be capable of transporting such bandwidths without distorting the focal profile. The NIKE optical system is designed to accommodate a bandwidth up to 5 THz ($t_c \approx 0.2$ psec) with negligible chromatic aberration. It achieves this by using mostly reflective optics at the larger apertures, and by using large F-number lenses and chromatic correction in the front end optics.

2 NIKE OPTICAL SYSTEM DESIGN

The laser is a 56 beam angularly-multiplexed system designed to illuminate a planar foil target with 2-3 kJ in a 3-4 nsec pulse.⁵ A schematic view of the optical train is shown in Fig. 2. The present oscillator comprises a commercial KrF discharge module, plus image inverting and beam combining optics; it produces a 1.6 THz spatially-multimode beam of ~ 80 XDL divergence and nearly uniform time-averaged intensity.^{6,7} Because most of the planar target experiments will require a flat-top focal distribution, the oscillator currently uses a hard aperture of 3 mm diameter. Figure 3 shows an image of the oscillator beam, using a 4 nsec slice of the pulse and a pair of lenses with a 60 XDL pupil and 1.5 X magnifying telescope located at the far-field plane between them. Eventually, the output of the oscillator will be split into two beam lines with independently adjustable ISI apertures and pulse shaping systems. The main line will provide 44 beams optimized for 3-4 nsec direct target illumination, while the second line will provide up to 12 beams of 5-6 nsec pulsewidth optimized for diagnostic X-ray backlighting.

The far-field distribution $f(x)$ of the main oscillator beam $F(x)$ is image-relayed through the pulse-shaping optics, a commercial discharge preamplifier, and a large aperture (4×4 cm²) discharge preamplifier. (The relay telescopes between these elements are not shown explicitly in Fig. 2.) A pair of neutral chromatic correction doublets, each consisting of a MgF₂ convex lens and a fused silica concave lens, can be placed at the input and output of the second preamplifier when broader bandwidth operation is desired. The beam is then split and relayed into an array of three parallel 4×4 cm² discharge amplifiers identical to the one used in the preceding stage. (The fourth module of the array shown in Fig. 2 will be used to amplify the X-ray backlighter beams.) Each of these modules has produced over 2 J in 15 nsec, with negligible distortion of the oscillator image profile.⁷ The output beams are split twofold and differentially delayed by a stack of 8 folded image-relaying telescopes of unequal length and 2:1 magnification. An additional array of time delay mirrors again splits each of these beams to create 28 sequential beams, then feeds them to the 4×7 input array of the angularly-multiplexed amplifier chain.

The angularly-multiplexed amplifier chain will comprise two double-passed e-beam pumped stages and the associated transport optics. The diverging mirrors of the input array expand the 28 beams and overlap them at the concave rear mirror of the 20×20 cm² amplifier. Within the 125 nsec extraction time of these sequential beams, this amplifier has produced 150 J output for an input energy < 1 J. A 50% beamsplitter at the output will create an additional 28 beams, which will be relayed through a 120 nsec delay line (a 1:1 off-axis reflecting telescope) that images the beamsplitter onto an adjacent re-entrant mirror. The resulting 56 sequential beams, which will extend over 240 nsec, will be overlapped at the concave rear mirror of the 60

x 60 cm² final amplifier by a single 4 x 14 array of identical planar mirrors and double-passed diverging lenses. This amplifier is expected to provide ~5 kJ output within 240 nsec.

A final 4 x 14 array of diverging mirrors will recollimate the output beams with 15 x 15 cm² widths, and direct them via the demultiplexing mirrors to the target chamber. The 44 (coincident) interaction beams will be focused onto the planar target through a 7 x 7 array of lenses, while the remainder will serve as backlighters. The backlighter beams will come from the upper and lower rows at the recollimation array, where the shadowing losses in the final amplifier are large (12% to 22%). For the target interaction beams, these losses range from 0 to 19%.

Field angle divergences within the optical system are determined by the focusing lens array and the required spot size on target. Most target interaction experiments will require a spot diameter of 600 μ m in order to achieve the desired intensities ($\sim 2 \times 10^{14}$ W/cm²) with 3-4 nsec pulsewidths. The lenses were chosen to be 6 meter focal length, which will allow a reasonable depth of field around focus with the 2.2 meter wide 7 x 7 array. These conditions require a field angle divergence $\Delta\theta_F = 100 \mu$ rad; the normalized divergence of the 15 cm incident beams will therefore be $\Delta\theta = \Delta\theta_F / (248 \text{ nm} / 15 \text{ cm}) = 60 \text{ XDL}$, as stated above.

The NIKE optical design allows virtually complete compensation of each beam for all *systematic* phase aberrations (including a small amount of spherical aberration) over a 5 THz bandwidth.⁸ Astigmatism and coma due to the off-axis optics will be compensated by tilting the lenses in the intermediate and focusing arrays - typically by angles less than 3°. Without this correction, the combined astigmatism and coma could be in excess of 15 XDL in some of the beams. The lens tilt angles need not be adjusted or maintained with high precision; spot diagrams show nearly complete compensation even for angular perturbations of 1-2 mrad.

As indicated in Fig. 2, the front end encoding telescopes are designed to image the far-field profile $f(x)$ to the vicinity of the final amplifier, but not to the 20 cm (driver) amplifier. Imaging onto both stages would require the intermediate array to be replaced by either a pair of monolithic relay telescopes (resulting in excessive multiplexing angles at the driver) or a cumbersome 4 x 14 array of smaller telescopes and turning mirrors. This is unnecessary because the large beam sizes ensure that the two amplifiers remain optically close to one another for all field angles of interest. With the final amplifier acting as the aperture stop of the system, and a 60 XDL angular divergence, the chief ray displacement at the driver will remain within ± 4 mm. The main penalty for this approach is a lower effective fill factor (65%) at the driver. Although both of these amplifiers will be slightly overfilled in order to suppress ASE, the usable portion of the beams (i.e., the part that eventually clears the aperture stop) must underfill the driver amplifier to avoid vignetting. The NIKE optical system is designed to handle field angle divergences up to 120 XDL without vignetting.

3. ANALYSIS OF IMAGE QUALITY

Although the optical design allows for correction of systematic phase aberrations, there are several other factors that can also distort the image. These include (i) amplifier gain nonuniformities, (ii) phase distortion due to random optical surface imperfections, air turbulence, and transient refractive index variations in the KrF amplifiers, and (iii) nonlinear optical effects such as self-phase modulation and stimulated rotational Raman scattering. This section will estimate the distortion due to these effects, and describe the steps being taken to control it.

3.1 Amplifier gain nonuniformities

Because the driver amplifier is not imaged to the aperture stop, a nonuniformity in its gain profile $G_d(x)$ can partially imprint itself onto the focal spot $F(\theta)$, as illustrated in Fig. 4. (For simplicity, this figure omits the front-end optics and the large beam size variations between the driver amplifier and focusing lens.) Nonuniformity in the beam profiles from the discharge preamplifier array (Fig. 2) may also cause some imprinting because the beams split off after each of the folded telescopes are delayed by different amounts, and therefore cannot all be imaged exactly to the aperture stop at the final amplifier.

The lowest order correction to the ideal focal profile $F_0(\theta)$ is a tilt $F_1(\theta)$ of fractional value

$$F_1(\theta)/F_0(\theta) = -x_{cd} \cdot \langle \nabla_{\perp} \ln(G_d) \rangle_d - x_{cf} \cdot \langle \nabla_{\perp} \ln(f) \rangle_f, \quad (1)$$

where x_{cd} and x_{cf} are the respective chief ray displacements at the driver amplifier and far-field image planes ($x_{cd}, x_{cf} \approx -\theta$), and $f(x)$ is the image of the beam profile at the last discharge amplifier (without the gain nonuniformity imposed by the driver). The brackets denote averages over transverse coordinates scaled to the 60 cm aperture D_a and weighted by the normalized output beam profile \hat{I}_a of the final amplifier; i.e.,

$$\langle \nabla_{\perp} \ln(G_d) \rangle_d = (D_a/D_d) \int \hat{I}_a(x) \nabla_{\perp} \ln[G_d(xD_d/D_a)] d^2x, \quad (2a)$$

$$\langle \nabla_{\perp} \ln(f) \rangle_f = (D_a/D_f) \int \hat{I}_a(x) \nabla_{\perp} \ln[f(xD_f/D_a)] d^2x, \quad (2b)$$

$$\int \hat{I}_a(x) d^2x = 1, \quad (2c)$$

where D_d and D_f are the *usable* beam widths (as defined in the preceding section) at the driver amplifier and far-field plane, respectively.

In the case of primary interest, where F_0 is a flat-top profile of width $\Delta\theta$, and \hat{I}_a also remains approximately uniform ($\approx 1/D_a^2$) within aperture D_a , the fractional tilt along the x direction reduces to⁸

$$\Delta_x F_1/F_0 \approx (\Delta x_{cd}/D_d) \langle \Delta_x G_d/G_d \rangle + (\Delta x_{cf}/D_f) \langle \Delta_x f/f \rangle. \quad (3)$$

Here Δx_{cd} and Δx_{cf} are the chief ray divergences corresponding to $\Delta\theta$ (Fig. 4), and the bracketed quantities (assumed to be less than 1) are the fractional variations across the aperture in the x direction of quantities averaged along the y direction. At the driver stage, where $\Delta x_{cd} \approx 8$ mm for $\Delta\theta = 60$ XDL and the usable beam width is $D_d = 16$ cm, a 20% gain imbalance would contribute only 1% to the fractional tilt. For the beams whose far-field image planes lie farthest from the aperture stop in each direction, $\Delta x_{cf}/D_f \approx \pm 0.8\%$. Thus, even a 2:1 variation in $f(x)$ would produce tilts of magnitude $< 0.4\%$, which would be nearly cancelled by other beams whose far-field planes are located on the opposite side of the final amplifier. In both terms of Eq.(3), the tilts due to the first group of 28 beams would be largely cancelled by those of the second, which are inverted by the 120 nsec delay telescope.

The second order correction is a quadratic curvature $F_2(\theta)$ whose fractional value $F_2(\theta)/F_0(\theta)$ is proportional to the factors $(x_{cd}/D_d)(x_{cd}/D_d)$, $(x_{cd}/D_d)(x_{cf}/D_f)$, and $(x_{cf}/D_f)(x_{cf}/D_f)$. With the small values of $\Delta x_{cd}/D_d$ and $\Delta x_{cf}/D_f$ shown above, $|F_2(\theta)|/F_0(\theta) < 1\%$ as long as large fractional variations of $G_d(x)$ and $f(x)$ do not occur on scalelengths much shorter than the usable beam widths. This condition can be satisfied only if those usable widths underfill all of the amplifiers except the final stage.

3.2 Phase distortion

Random phase distortion is expected to arise primarily from surface imperfections of the large aperture optics in the recollimated beams, the two e-beam pumped amplifiers, and the optical feed paths between them. Most of the corresponding distortion from the small front end optics will be astigmatism and coma, which can be corrected using the lens tilting procedure discussed previously.

At present, the total random phase distortion $\phi(x)$ is described by a statistical model that lumps it into two independent components; i.e.,

$$\phi(x) = \phi_{15}(x) + \phi_{60}(x), \quad (4)$$

where $\phi_{15}(x)$ is the contribution to the ~15 cm beams imposed by the driver amplifier, beamsplitter, delay telescope, and recollimated output paths, while $\phi_{60}(x)$ comes from the 60 cm mirror and windows of the final amplifier. These functions are summations over randomly-phased Fourier modes that are periodic within the 15 and 60 cm beamwidths. This restriction ignores lower spatial frequency variations, such as phase tilts, lensing, and astigmatism, which can be corrected by the intermediate array lenses and the beam steering and focusing optics. Using optical surface specifications and interferometric data on the 60 cm windows and 20 cm amplifier mirror, we first calculate the total rms phase variations $(\phi_{15})_{rms}$, $(\phi_{60})_{rms}$ and the phase gradients $(\nabla\phi_{15})_{rms}$, $(\nabla\phi_{60})_{rms}$. All of the optical elements are assumed statistically independent, with double contributions from the double-pass amplifier windows. Because of the periodicity restriction along each transverse direction, the total value of $(\phi_{15})_{rms}$ had to be reduced to $(15 \text{ cm}/2\pi) (1/\sqrt{2}) (\nabla\phi_{15})_{rms}$ in order to keep $(\nabla\phi_{15})_{rms}$ within its specified value. To construct statistical realizations of $\phi_{15}(x)$ and $\phi_{60}(x)$, the model starts with a pair of 2D arrays of initially independent normally distributed random numbers, then repeatedly filters them in k-space (using Gaussian filter functions) and re-scales them until they satisfy the specified rms values. This model can be easily updated as more phase measurements become available.

Using the simulated $\phi(x)$ and again assuming that \bar{I}_a is approximately uniform, we evaluate the point-spread function $P(\theta)$ at the target plane, including the effect of diffraction from the 60 cm final amplifier aperture. Figure 5 shows a typical result. In this example, the effective diameter $\Delta\theta_R$ (i.e., the circle that encloses 50% of the energy) is 9 XDL, which is still small compared to the 60 XDL image. The 90% energy diameter is 18.5 XDL, which agrees with the corresponding 15-20 XDL value estimated by Berggren⁹ using a different model for the phase distortion.

Phase distortion introduced by air turbulence and thermal gradients is controlled by enclosing most of the NIKE optical chain in a hermetically-sealed double-wall propagation bay whose walls, ceiling, and floor are maintained at uniform temperature to within $\pm 1^\circ\text{C}$.⁵ Preliminary measurements using a 10 cm diameter 633 nm beam propagating over an 80 meter air path show that the focal spot remains nearly diffraction-limited. For most shots, the centroid of the spot remained within a region comparable to 3 μm (the diffraction limit $1.22\lambda/D$ of 248 nm light), as shown in Fig. 6. Moreover, some of this displacement is known to arise from vibrations and drift in the mirrors. The absence of strong steering effects in a 10 cm beam suggests that atmospheric distortion is likely to remain small in the larger beams around the 60 cm amplifier.

Under NIKE operating conditions, transient refractive index (TRI) effects are expected to arise primarily from F₂ burnup¹⁰ in the e-beam pumped amplifiers. Smaller but significant contributions can also come from plasma dispersion, absorbing trimers, and the KrF excimer itself. Estimates give phase shifts that increase to 1.7-3.2 waves toward the end of the e-beam pulse. If the e-beam deposition profile peaks in the center of the amplifier, the TRI phase shift will produce a weak (1.5-3 XDL) time-dependent defocusing effect, which can be partially compensated in each beam by adjusting the focusing lenses at the target chamber. An update of these estimates will soon be possible, using far-field measurements at the output of the 20 cm amplifier.

Using the point-spread function, one can relate the distorted and undistorted image profiles by the usual convolution

$$F(\theta) = \int P(\theta - \theta') F_O(\theta') d^2\theta', \quad (5)$$

where the approximation $P(\theta, \theta') \cong P(\theta - \theta')$ is well satisfied in the NIKE optical system because the phase distortion occurs optically close to the aperture stop. As long as $P(\theta)$ remains narrow compared to $F_O(\theta)$ (i.e., $\Delta\theta_R \ll \Delta\theta$ in Fig. 4), its main effect is to round-off the edge of the flat-top profile, reducing the intensity in a zone of fractional width $\Delta\theta_R/\Delta\theta$ around the perimeter.⁸ This is shown in Figs. 7a-c for the $\Delta\theta_R = 9$ XDL simulation in Fig. 5. The distorted image (7c) is closely approximated by a Fermi-Dirac distribution function

$$F(\theta) \equiv \left[1 + \exp\left(\frac{|\theta| - \Delta\theta/2}{\Delta\theta_R/4}\right) \right]^{-1} \quad (6)$$

3.3 Nonlinear optical effects

Self phase modulation (SPM) and stimulated rotational Raman scattering (SRRS) may also distort the image because these processes can respond to the rapidly changing stochastic fluctuations of the beam, and thus directly affect the spatial coherence zones. The effect of SPM can be partially characterized by the average nonlinear phase shift

$$B = B_1 + B_2, \quad B_i = n_{2i} \int \langle I \rangle_z dz, \quad (7)$$

where B_1 arises from atmospheric propagation, B_2 arises from the final focusing lenses and target chamber windows, $n_{2i} = n_{21}, n_{22}$ are the nonlinear refractive coefficients, and $\langle I \rangle_z$ is the intensity averaged over time and the transverse coordinates ($\langle I \rangle_z = 70\text{--}100 \text{ MW/cm}^2$ in the recollimated output beams). In general, SPM tends to broaden the image profile and introduce curvature in the central portion when B significantly exceeds 0.2. The magnitude of the perturbation is proportional to B^2 . SRRS arises entirely from propagation in air, and can be characterized by the gain factors

$$G_j = g_j \int \langle I \rangle_z dz, \quad (8)$$

where g_j is the steady-state convective gain coefficient of the j th transition. For the 50-100 m high intensity air paths in NIKE, $G_j = 10\text{--}15$, which is approximately a factor of 2-3 below normal threshold. However, self-seeding will tend to enhance SRRS, especially at bandwidths greater than 2 THz; this was recently demonstrated by experiments at LANL.¹¹

Image distortion due to these nonlinear processes is being studied using a simulation code NIKEBEAM, which also includes diffraction and linear losses in the long atmospheric paths, plus two-photon absorption in the focusing lenses and target windows. Ignoring group velocity dispersion, we use the paraxial wave equation for the complex optical field amplitude $E(x_\perp, z, t)$ and the driven oscillator equation for the (real) susceptibility $Q_j(x_\perp, z, t)$ due to the j th SRRS transition:

$$(\partial/\partial z + v_g^{-1}\partial/\partial t + \alpha - i\nabla_\perp^2/2k_0)E = i\beta|E|^2E + i\sum_j Q_j E \quad (9a)$$

$$(\partial^2/\partial t^2 + 2\Gamma_j\partial/\partial t + \omega_j^2)Q_j = \omega_j\Gamma_j g_j |E|^2. \quad (9b)$$

Here, v_g is the group velocity, α is the linear loss coefficient, $k_0 = 2\pi/\lambda$, $\text{Re}(\beta) = n_2/2$, and $\text{Im}(\beta)$ is half the two-photon absorption coefficient; ω_j and Γ_j are, respectively, the frequency and damping coefficient of the j th SRRS transition. NIKEBEAM evaluates the time-averaged focal spot intensity by formally integrating Eqs.(9a,b) up to second order in $\int \langle I \rangle_z dz$ for the SPM and SRRS contributions. The zeroth order term is the linearly distorted profile $F(\theta)$ found from Eq.(5). For the chaotic multimode light used in echelon-free ISI, we factorize all products of the zeroth order complex field amplitudes according to Gaussian statistics.

Image distortion calculations were carried out assuming either an air or pure Ar atmosphere in the propagation bay. The lenses and windows were assumed to be fused silica with the measured nonlinear parameters $n_2 = 140 \text{ cm/TW}$ ($2 \times 10^{-14} \text{ esu}$) and $2\text{Im}(\beta) = 60 \text{ cm/TW}$.¹² At present, there is still considerable uncertainty on the size of n_2 in air around 248 nm. The most thorough measurement, which examined self-focusing in a high pressure cell, yielded $n_2 = 0.31 \text{ cm/TW}$ ($2.9 \times 10^{-16} \text{ esu}$) at 308 nm.¹³ The SRRS coefficients g_j , ω_j , and Γ_j included all N_2 transitions from $J = 0$ to 16 and O_2 transitions from $J = 1$ to 15.¹⁴ For chaotic light, the main effect of SRRS is an increase in the effective value of n_2 , especially at broader optical bandwidths. Combining the above measurement with the contribution from Eq.(9b), one finds that the effective value of n_2

increases from ≈ 0.4 cm/TW at bandwidths < 1 THz to ≈ 0.5 cm/TW at 3 THz. There do not appear to be any published values of n_2 in Ar around 248 nm, so a calculation was carried out using dispersion formulas of Hellwarth, et. al.¹⁵ to obtain $n_2 \approx 0.05$ cm/TW.

Figure 7d shows the perturbed image profile for the case where the high power beams propagate in air. This example simulates the beam with the longest high intensity pathlength (effectively about 93 m at 90 MW/cm²), giving $B_1 \approx 0.31$ and $B_2 \approx 0.06$. An overall rounding effect due to the nonlinear optical processes is clearly evident, especially when compared to the zeroth order profile (Fig. 7c), which shows only the edge rounding arising from the linear phase distortion.

Figure 8a shows the image profiles for the same beam as in Fig 7, but propagating in Ar. With B_1 now only 0.04 and no SRRS, the perturbed profile is virtually indistinguishable from the zeroth order case, and remains flat to within 2% over the central 2/3 of its radius. Target interaction simulations indicate that some of the edge rounding may be beneficial because it reduces plasma turbulence that would otherwise develop around a sharp discontinuity. If it becomes necessary to extend the flat portion, however, it could be accomplished by using phase-correction optics in the front end, or by increasing the image size beyond 60 XDL (at the expense of intensity). Because the image retains good azimuthal symmetry, it may also be possible to extend the flat portion just by adjusting the oscillator profile F_O to pre-compensate some of the distortion. Figure 8b shows an example of this compensation, which is accomplished by placing a uniform weakly-absorbing disk of 48 XDL diameter just beyond the oscillator hard aperture.

Additional NIKEBEAM simulations indicate that curved profiles relevant to a multibeam spherical illumination facility are less susceptible to linear and nonlinear phase distortion than the top-hat function. Figure 9 shows an example of this, using the profile $F_O(\theta) = (1 - \theta^2/\theta_0^2)^{1/2}$. For a lens of focal length f and a pellet of radius $R = f \theta_0$ and polar angle $\Theta_p = \sin^{-1}(f \theta/R)$, this profile would produce an energy deposition proportional to $\cos^2 \Theta_p$ in the limit where R remains large compared to the width of the underdense plasma. This would allow highly uniform energy deposition in a multibeam spherical illumination geometry.¹⁶

4. DISCUSSION

The NIKE optical system is designed to incorporate echelon-free ISI to produce a smooth and controllable focal profile for laser-target interaction experiments. This design allows complete compensation of chromatic and off-axis aberrations over a 5 THz bandwidth. Calculations of beam distortion due to gain nonuniformities, optical imperfections, air turbulence, transient refractive indices, and nonlinear optical effects indicate that time-averaged nonuniformities of 1-2% should be possible over the central 2/3 of the target beam profile if an argon or helium fill is used in the propagation bay. Although the propagation bay is designed to accommodate either an Ar or He gas fill, experiments will be performed in the near future to better quantify the nonlinear effects before committing to an inert gas atmosphere.

The calculations presented here are applicable to the 1-2 THz bandwidths at which NIKE is currently operating. In order to accurately model broader bandwidths, NIKEBEAM will be generalized to include group velocity dispersion in the long atmospheric propagation paths. At broader bandwidths (~ 5 THz), this effect is expected to decrease the profile distortion due to the nonlinear optical effects.

5. ACKNOWLEDGEMENTS

The authors wish to thank J. Dahlburg (NRL), R. Berggren (LANL) and P. McLaughlin (Sinclair Optics) for helpful comments and suggestions. This work is supported by the U. S. Department of Energy

6. REFERENCES

1. R. H. Lehmberg, and J. Goldhar, "Use of incoherence to produce smooth and controllable irradiation profiles with KrF fusion Lasers," *Fusion Technology*, Vol. 11, pp. 532-541 (1987)
2. R. H. Lehmberg and S. P. Obenschain, "Use of induced spatial incoherence for uniform illumination of laser fusion targets," *Opt. Commun.* Vol. 46, pp. 27-31 (1983); R. H. Lehmberg, A. J. Schmitt and S. E. Bodner, "Theory of induced spatial incoherence," *J. Appl. Phys.*, Vol. 62, pp. 2680-2701 (1987)
3. M. H. Emery, J. H. Gardner, R. H. Lehmberg, and S. P. Obenschain, "Hydrodynamic target response to an induced spatial incoherence-smoothed laser beam," *Phys. Fluids B*, Vol. 3, pp. 2640-2650 (1991)
4. R. C. Sze, S. J. Thomas, N. A. Kurnit, and C. W. Patterson, "Wide bandwidth control studies for the advanced Aurora KrF fusion laser front end," 1990 *Conference on Lasers and Electro-Optics*, OSA Technical Digest Series, Vol. 7, paper CWF46 (Optical Society of America, Wash. DC, 1990)
5. S. P. Obenschain, et al, "Overview of the NIKE KrF laser facility," *IAEA Technical Committee Meeting on Drivers for Inertial Confinement Fusion* (Osaka, Japan, 1991) paper IV-4
6. A. V. Deniz, M. S. Pronko, S. P. Obenschain and R. H. Lehmberg, "Production of flat KrF focal profiles for laser fusion experiments," 1991 *Conference on Lasers and Electro-Optics*, OSA Technical Digest Series, Vol. 10, paper CTu16 (Optical Society of America, Wash. DC, 1991)
7. M. S. Pronko and A. V. Deniz, "High fidelity amplification of light using induced spatial incoherence for laser fusion," 1992 *Conference on Lasers and Electro-Optics*, OSA Technical Digest Series, Vol. 12, paper CTh19 (Optical Society of America, Wash. DC, 1992)
8. R. H. Lehmberg and T. Lehecka, "NIKE laser optical design and propagation issues," *IAEA Technical Committee Meeting on Drivers for Inertial Confinement Fusion* (Osaka, Japan, 1991) paper PII-7
9. R. R. Berggren (Los Alamos National Laboratory), private communication
10. S.F. Fuighum, D.W. Trainor and C.H. Appel, "Transient refractive index measurements in XeF laser gas mixtures," *IEEE J. Quantum Electron.*, Vol. QE-25, pp. 955-963 (1989)
11. N. A. Kurnit, et al, "Raman scattering of variable bandwidth KrF laser radiation in long air paths," 1992 *Conference on Lasers and Electro-Optics*, OSA Technical Digest Series, Vol. 12, paper CFA2 (Optical Society of America, Wash. DC, 1992)
12. I. N. Ross, W. T. Toner, C. J. Hooker, J. R. M. Barr and I. Coffey, "Nonlinear properties of silica and air for picosecond ultraviolet pulses," *J. Modern Optics*, Vol. 37, pp. 555-573 (1990)
13. Y. Shimoji, A. T. Fay, R. F. S. Chang, and N. Djeu, "Direct measurement of the nonlinear refractive index of air," *J. Opt. Soc. Am. (B)*, Vol. 6, pp. 1994 - 1998 (1989)
14. C. J. Herring, M. J. Dyer, and W. K. Bischel, "Temperature and density dependence of the linewidths and line shifts of the rotational Raman lines in N₂ and H₂," *Phys. Rev. A*, Vol 34, pp. 1944 -1951 (1986); K. S. Jammu, G. E. St. John, and H. L. Walsh, "Pressure broadening of the rotational Raman lines of some simple gases," *Can. J. Phys.*, Vol. 44, pp. 797-814 (1966); N. A. Kurnit (Los Alamos National Laboratory), private communication
15. R. W. Hellwarth, D. M. Pennington, and M. A. Henessian, "Indices governing optical self-focusing and self-induced changes in the state of polarization in N₂, O₂, H₂, and Ar gases," *Phys. Rev. A*, Vol. 41, pp. 2766-2777 (1990)
16. A. J. Schmitt, "Absolutely uniform illumination of laser fusion pellets," *Appl. Phys. Lett.*, Vol. 44, pp. 399-401 (1984)

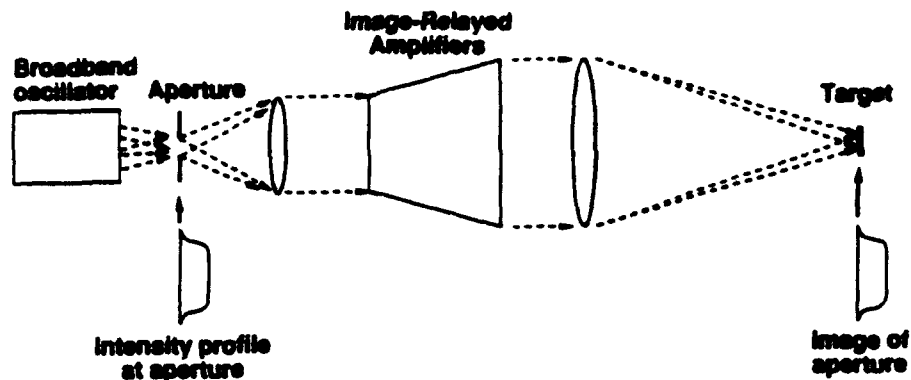


Fig. 1 Echelon-free induced spatial incoherence concept, showing image-relayed amplifiers placed at the quasi far-field of the oscillator aperture

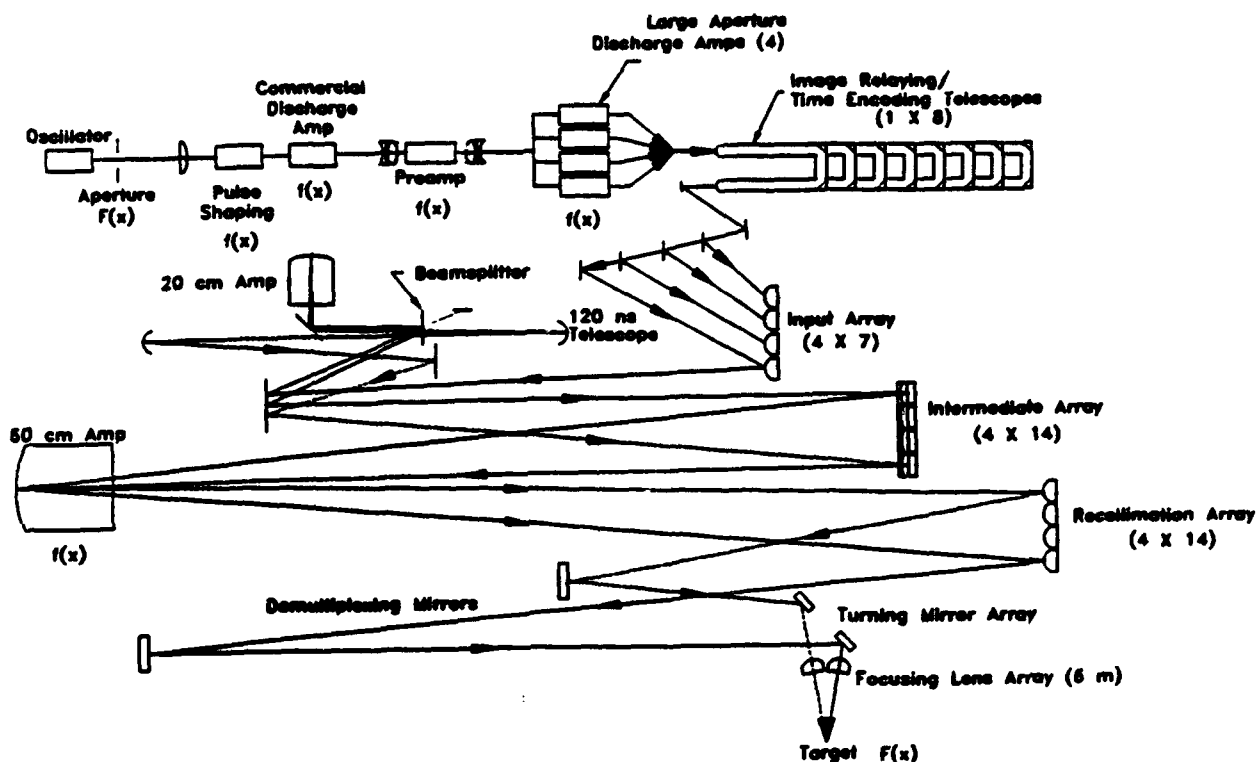


Fig. 2 Schematic view of the NIKE laser optical system

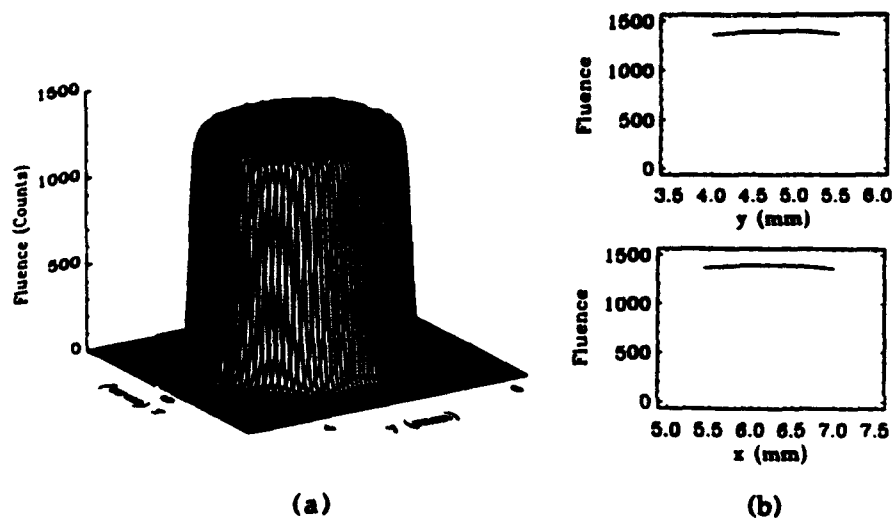


Fig. 3 Typical image of a 4 nsec slice of the oscillator beam profile: (a) isometric view, (b) horizontal and vertical slices

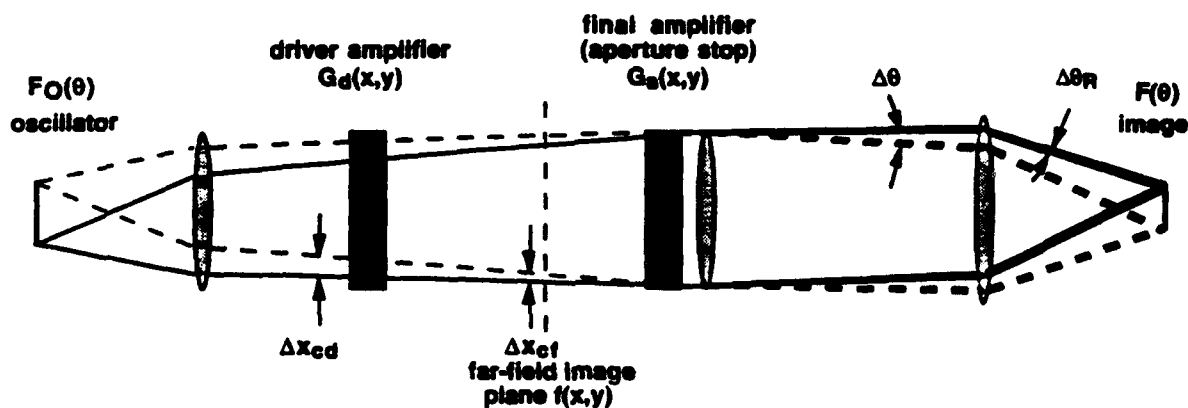


Fig. 4 Illustration of image distortion: Amplifiers displaced from the far-field plane can partially imprint their gain nonuniformities, while beam divergence $\Delta\theta_R$ due to random phase uniformities can blur the image.

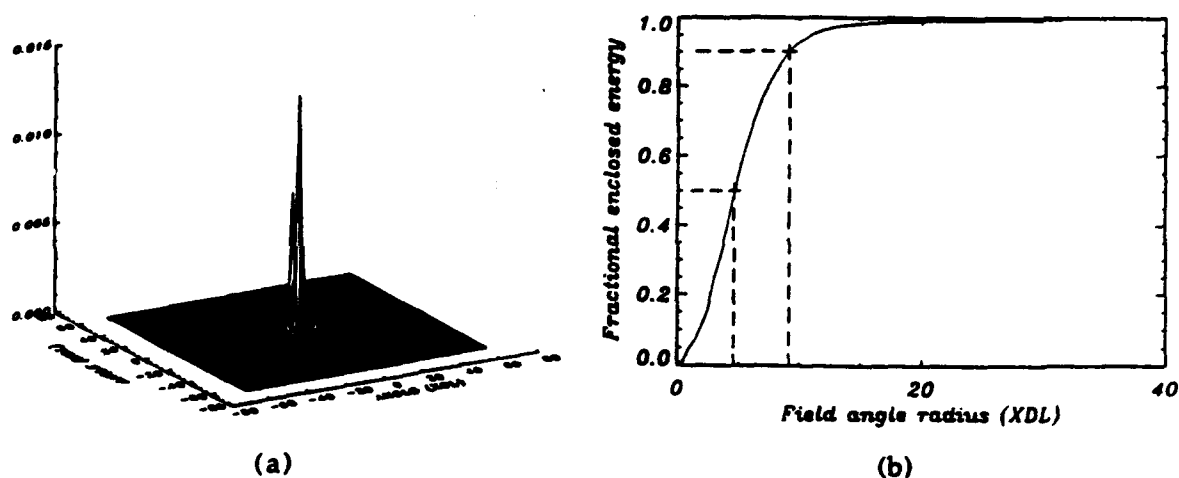


Fig. 5 Point-spread function $P(\theta)$ at the image plane, calculated from typical random phase distortion $\phi(x)$: (a) isometric view, (b) fractional energy enclosed within a circle of angular radius θ , centered at the centroid

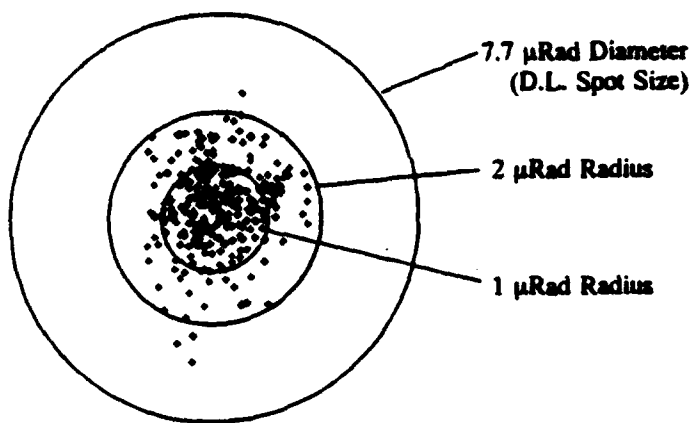
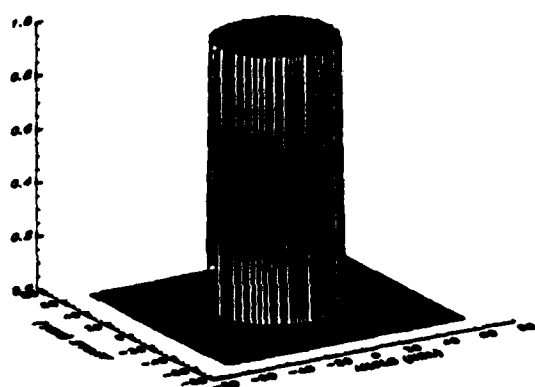
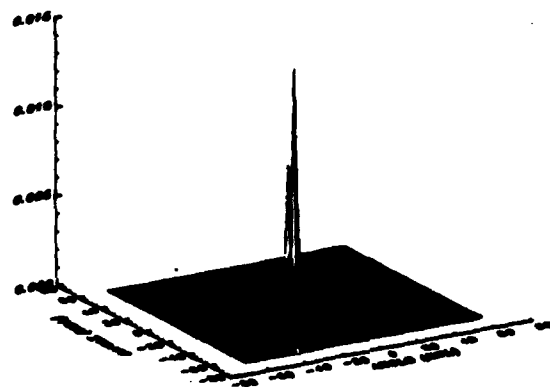


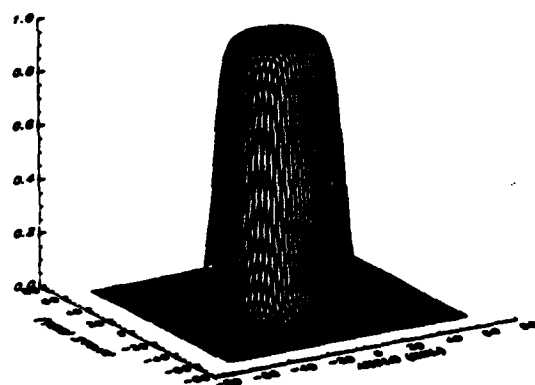
Fig. 6 Drift of the focal spot centroid of a 10 cm diameter 633 nm beam propagating over an 80 m air path in the NIKE propagation bay. The diffraction-limited focal spot diameter is 7.7 μ rad at 633 nm and 3.0 μ rad at 248 nm.



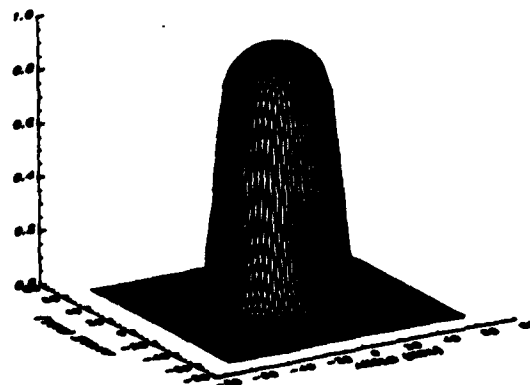
(a)



(b)

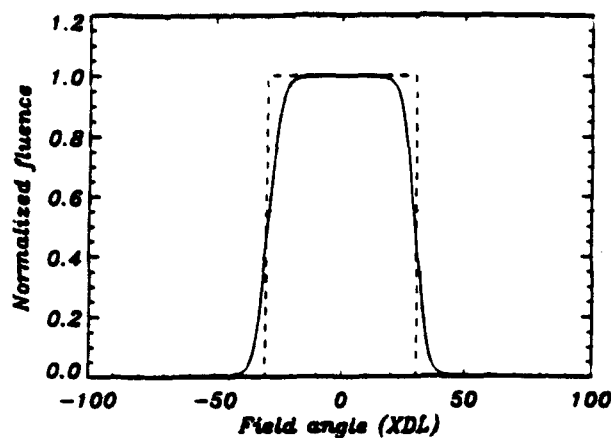


(c)

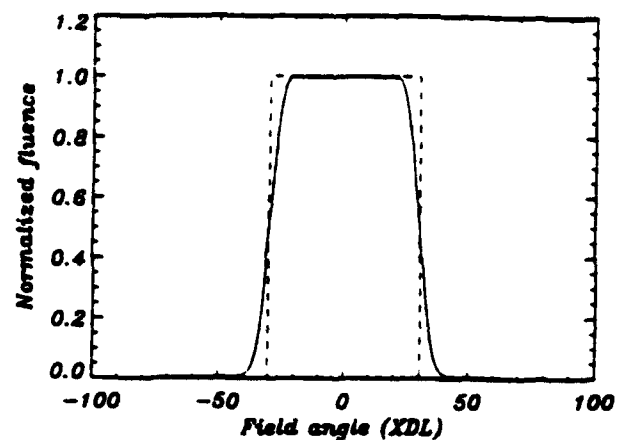


(d)

Fig. 7 Comparison of simulated time-averaged beam profiles at the image plane: (a) ideal 60 XDL image (i.e., object), (b) point-spread function, (c) image distorted only by random phase nonuniformities, and (d) image also perturbed by nonlinear phase distortion with effective total $B = B_1 + B_2 = 0.37$

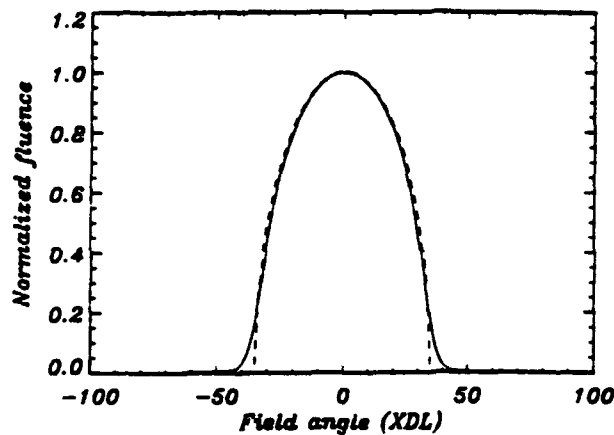


(a)

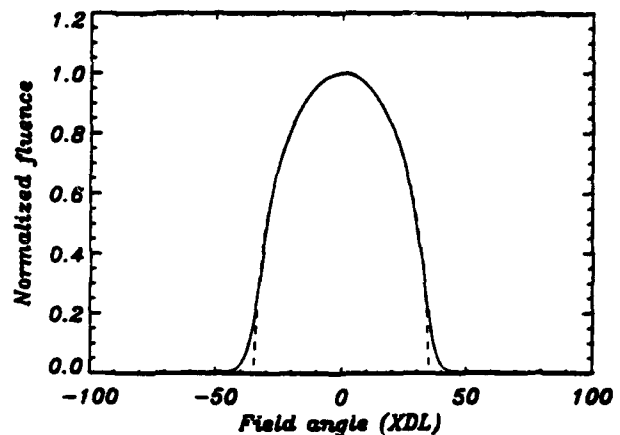


(b)

Fig. 8 Image profiles for the same propagation conditions as in Fig 7, except that the air is replaced by Ar: Dashed lines show the ideal (object) profile, solid lines include both linear and nonlinear phase distortion, and the (nearly indistinguishable) dotted lines include only the linear distortion. (a) hard aperture at the oscillator and (b) hard aperture followed by the pre-correction described in the text



(a)



(b)

Fig. 9 Same as Fig. 8, except that the ideal image profile (dashed line) is of the form $F_O(\theta) = (1 - \theta^2/\theta_O^2)^{1/2}$ and the oscillator pre-correction in 9b is provided by a soft aperture.

Appendix C

Electron Deposition and Kinetic Stability in an E-Beam-Driven KrF Laser

KRALL ASSOCIATES

KA-90-03

**ELECTRON DEPOSITION AND
KINETIC STABILITY IN AN
e-BEAM-DRIVEN KrF LASER**

**Prepared by
Nicholas A. Krall**

**Prepared for
Naval Research Laboratory
Washington, D.C. 20375**

January 9, 1990

1. SUMMARY

The tasks set out for this project centered on the adequacy of Monte Carlo numerical techniques for calculating electron beam deposition and the ultimate plasma state in a KrF laser. We find that there are a variety of choices to be made in determining the physics to be included in the Monte Carlo code to be used, even within the framework of an integrated system of user codes such as the ITS. With suitable choice of the code version, the deposition can be calculated with high reliability and accuracy. This finding is described in detail in Appendix A, along with a code developed by Krall Associates for this study.

The question of the final plasma state is another matter. The strong dependence of various poorly known atomic cross sections on energy is known to produce a nonMaxwellian electron distribution which is not reproduced by existing codes. While this is of some importance in determining laser output, a more crucial question may be the generation of return currents and concomitant electric fields from deposition of excess electrons. We have calculated the stability for a model kinetic equilibrium, and find that current-driven instability can onset for current density in the range of $5-10 \text{ A/cm}^2$; with some theoretical interpretation of apparently dissimilar experiments, it can be argued that this instability has been observed in the laboratory. This study is described in detail in Appendix B.

Finally, these results were presented in-depth at a meeting at NRL on December 20, 1989. Viewgraphs from that presentation are appended as Appendix C.

2. FUTURE DIRECTIONS

The discussions at NRL made it clear that although the instability discovered during this study might be of a type identified in other experiments, the nonlinear behavior, i.e., the effect of the instability on the system, should be strikingly different. This immediately suggests the direction which follow-up work on the stability study should take:

- Determine the nonlinear behavior of the instability
- Determine the scaling of the growth rate of the instability
- Estimate the spatial structure of the turbulence.

Previous observations of this instability were in discharge-driven lasers with or without a stabilizing e-beam. The consequences of the instability was to terminate the discharge, by presenting the external circuit with a complete mismatch. In the present case, the fact that the discharge is entirely beam driven might have the consequence that the instability will degrade the performance of the laser, rather than terminating the discharge. This is why the details of the instability--structure and nonlinear behavior--become so important. If the scaling and control of this turbulence is understood, then the effect of instability might be minimized even if the instability itself cannot be avoided.

APPENDIX A

KRALL ASSOCIATES

KA-89-07
June 1989

INTERIM REPORT

ELECTRON BEAM DEPOSITION IN A KrF LASER

Prepared by

**Nicholas A. Krall
Krall Associates**

Prepared for

**Naval Research Laboratory
and
Science Applications International Corp.**

under

Contract No. N00014-86-C-2499

June 26, 1989

TABLE OF CONTENTS

<u>Section</u>		<u>Page</u>
1	BACKGROUND INFORMATION	1
	1.1 Sources	1
	1.2 Discussion	1
2	LITERATURE SEARCH AND ANALYSIS	4
3	THE TIGER SERIES OF MONTE CARLO CODES	6
	3.1 Overview of the ITS Code Package	7
4	A SIMPLIFIED MODEL OF e-BEAM PROPAGATION	10
5	RETURN CURRENTS, LASER PERFORMANCE, AND OTHER DETAILS . . .	17
6	IONIZATION INSTABILITY IN THE NRL EXPERIMENTS	20
7	RECOMMENDATIONS	22

1. BACKGROUND INFORMATION

1.1 SOURCES

Jonah Jacobs, Science Research Lab, Inc.

John A. Halbleib, Sandia National Lab

Julius Goldhar, University of Maryland

Thomas Johnson, U.S. Military Academy

Alan Hunter, Thermoelectric Corporation (Western Research)

Roger Haas, University of California at Davis

1.2 DISCUSSION

Over a period of several days I initiated discussion with the scientists listed above, on the following topics:

- How is e-beam deposition in a KrF laser presently calculated?
- What physics is included in these calculations?
- Under what conditions are these calculations expected to fail?
- Is there any experimental evidence that suggests that Monte Carlo calculations break down when used to calculate deposition?
- What physics uncertainty actually does affect predicted laser performance?

From these conversations a number of points emerged, including the following:

There are well documented Monte Carlo models developed as user codes and widely available. In particular, the ITS (TIGER) series of codes, developed at Sandia National Laboratory by John Halbleib and others, have been used by the Science Research Laboratory, Inc. This code, along with SANDYL, EGS, ETRAN, and related models, have been compared with each other over energy ranges from 10 keV to 1 GeV. They produce similar results,

with discrepancies attributed to the fact that each of these models has a number of versions, with increasingly detailed physics in each. The most popular versions used in practice were one-dimensional, with stopping power and straggling effects dominant.

Some analytic models have been constructed both as a gross check on the Monte Carlo calculation and as a quick way to do parameter variation studies. The disagreement between the semi-analytic models and MC becomes noticeable at $\Delta E \sim E$, i.e., when most of the energy has already been deposited.

Return currents due to boundary conditions or electron density buildup are not calculated by any of the standard models. The codes are single particle calculations, and electrostatic effects are generally ignored. The effect of an externally produced electric field on the beam itself is sometimes included, but not the self-consistent field, including return current, avalanche, etc.

Atomic chemistry, such as F_2 attachment, is a strong effect in depleting the free electron density. The cross sections for some of these atomic processes have more uncertainty than the error in the deposition codes. In fact, this emphasizes one of the difficulties in KrF modelling. In the XeF system, F_2 dissociates into F almost solely by direct electron impact. By contrast, in KrF systems dissociation by electron attachment is a significant process, as well as other processes. Many models do not even include direct impact dissociation, although this process may account for about one third of the production of F. The rates for these processes depend on the energy distribution of low energy electrons, which is non-Maxwellian because the energy dependence of the electron attachment rate selectively depletes the electron distribution. This can be crucial, for example, because high power deposition and subsequently large electron densities leads to burnup of F_2 , which becomes strongly dependent on the dissociative attachment rate.

The biggest uncertainty in modelling the electron beam is in calculating the properties of the beam that enters the gas region of the laser. Transport from the electron gun to and through the foils and into the laser is not particularly reliable, especially for large guns. Besides the complexities in the electrode and virtual electrode regions, non-uniformities in the beam develop in the drift region, scattering in the foils affects the beam entering the laser, effects due to a second beam entering the geometry of the first gun can be important, and partial reflection can take place throughout the system.

In summary, uncertainties in atomic chemistry and transport and beam breakup before entering the active region are more fundamental questions than beam deposition itself.

2. LITERATURE SEARCH AND ANALYSIS

The physics base for deposition calculation stems from early work of Landau and more extensively by Bethe and his collaborators. Early papers reviewed include:

H. A. Bethe, M. Rose, and L. P. Smith, "The Multiple Scattering of Electrons," Proc. Am. Phil. Soc. 78, 573 (1938).

L. Landau, "On the Energy Loss of Fast Particles by Ionization," Journal of Physics VIII, 201 (1944).

H. A. Bethe and J. H. Jacob, "Diffusion of Fast Electrons in the Presence of an Electric Field," Phys. Rev. A 16, 1952 (1977).

These papers calculate the energy distribution of electrons after traversing a given distance in terms of ionization cross sections, and calculate the effect of multiple scattering on the transmission of a collimated beam, with and without energy loss. For thick targets, the transmitted intensity is proportional to $1/L$, L being the thickness of the target. The absorption process has three stages. Initially the beam loses energy but is not much deflected. After substantial energy loss the electron velocity is nearly random, and a diffusion approximation is a valid description of electron motion. The intermediate region between straight line and diffusion is difficult to treat, and a direct transition between the two limits is often assumed.

Later work showed that for thick targets the simplifications of Bethe et al. led to fairly poor approximations of the electron distribution function at various depths. In principle this would have an impact on deposition predictions because attachment rates are dependent on $f_e(E)$. In practice, the uncertainties in rate coefficients and their dependence on $f(E)$ outweigh the uncertainties in the calculation of $f(E)$ itself. Some of the literature analyzed includes:

R. Marshak, "The Milne Problem for a Large Plane Slab with Constant Source and Anisotropic Scattering," Phys. Rev. 72, 47 (1947).

H. Snyder and W. Scott, "Multiple Scattering of Fast Charged Particles," Phys. Rev. 76, 220 (1949).

M. Wang and E. Guth, "On the Theory of Multiple Scattering, Particularly of Charged Particles," Phys. Rev. 84, 1092 (1951).

H. Bethe, "Moliere's Theory of Multiple Scattering," Phys. Rev. 89, 1256 (1953).

L. Spencer, "Theory of Electron Penetration," Phys. Rev. 98, 1597 (1955).

J. Jacob, "Multiple Electron Scattering Through a Slab," Phys. Rev. A 8, 226 (1973).

M. Tekula and J. Jacob, "Diffusion of Fast Electrons in the Presence of a Magnetic Field," Appl. Phys. Lett. 41, 432 (1982).

3. THE TIGER SERIES OF MONTE CARLO CODES

The Integrated TIGER Series (ITS) of coupled electron/photon Monte Carlo transport codes is a widely used software package permitting state-of-the-art Monte Carlo solution of the linear time-independent electron scattering problem. The ITS has been developed as a user code, and can be run with or without macroscopic electric and magnetic fields of arbitrary spatial dependence. A virtue of this series is that the user can select one of eight codes to run on a machine from one of four major vendors. Physical rigor is attained by employing the best available cross section data, along with a very complete physical model for describing the production and transport of the electron photon cascade from 1 GeV to 1 keV. The code can be tailored to a variety of specific applications.

The TIGER codes are time independent, multidimensional, and multimaterial codes, based primarily on the ETRAN code (M. Berger and S. Seltzer, CCC-107, ORNL, 1968), which combines microscopic photon transport with a macroscopic random walk treatment of electron transport. The base codes of the series are TIGER, CYLTRAN, and ACCEPT, which differ primarily in dimensionality and geometry. TIGER is a 1-D, multilayer code, CYLTRAN uses 3-D particle trajectories and an axisymmetric cylindrical material geometry, and ACCEPT is a general 3-D transport code.

These base codes were designed to study transport at source energies from a few tens of MeV down to 1.0 and 10.0 keV for electrons and photons, respectively. Fluorescence and Auger processes are only allowed for the K-shell of the highest atomic number element in a given material.

For some applications it is desirable to have a more detailed model of the low energy transport. Code variants called TIGERP and CYLTRANP add a more elaborate ionization/relaxation model originally developed for a code called SANDYL, and extends photon transport down to 1.0 keV.

Another option called CYLTRANM combines the collisional transport of CYLTRAN with transport in macroscopic electric and magnetic fields of arbitrary spatial dependence using a Runge-Kutta-Fehlberg algorithm to integrate the Lorentz force equations. An important modification of this algorithm led to the development of the ACCEPTM code which combines the collisional transport of the

ACCEPT code with macroscopic field transport. In addition to these models, SPHERE and SPHEM are two special purpose codes that are restricted to multiple concentric spherical shells without and with macroscopic field transport, respectively.

This left eight separate code packages to maintain. Five of these--TIGER, CYLTRAN, ACCEPT, TIGERP, and SPHERE--have been publicly released and are disseminated through the Radiation Shielding Information Center at Oak Ridge National Laboratory. CYLTRANM, CYLTRANP, and ACCEPTM are not publicly released, but are maintained locally for use at Sandia. Maintaining multiple code packages became quite burdensome for the developers as well as for users. As a result, important modifications were no longer implemented in a timely fashion. Furthermore, the multiplicity of packages resulted in uneven development of the various codes, such that each code can have unique features not yet implemented in the other codes.

It is in order to remedy this situation that the ITS (The Integrated TIGER Series) was developed. The full implementation of this series has superseded all other versions of the TIGER series codes.

3.1 OVERVIEW OF THE ITS CODE PACKAGE

The ITS consists of four essential elements:

- (1) XDATA - The electron/photon cross section data file
- (2) XGEN - The cross section generation program
- (3) ITS - The Monte Carlo program file
- (4) UPEML - A machine portable update emulator

The heart of ITS is the Monte Carlo program file. The combined program library file was obtained by integrating the eight codes of Table 1 in such a way as to minimize the repetition of coding that is common to two or more of these codes. This process led quite naturally to the development of a new code, ACCEPTP. In ACCEPTP, the improved low-energy physics of the SANDYL code has been added to the ACCEPT code. Each of the eight member codes will run on any of four machines--CRAY, CDC, VAX (double precision), or IBM (double precision). Although

the codes have only been tested on these four machines, the use of FORTRAN 77 (i.e., American National Standard FORTRAN, ANSI X3.9-1978) should facilitate installation on other machines as well. Additional cross section data and associated logic allow transport from 1.0 keV to 1.0 GeV for both electrons and photons. A new free-format, order-independent input procedure based on descriptive keywords and maximum use of defaults and internal error checking has resulted in a very simple and user-friendly input scheme. Integration of the various codes has resulted in the availability of additional common options for each code. Also, a general restart option has been added. In an attempt to conform to modern programming practices, a complete line-by-line rewrite of the codes was carried out with emphasis on implementing the top-down block-if structure of FORTRAN 77. Finally, options are available for plotting the problem geometry in ACCEPT, ACCEPTP, ACCEPTM, and CYLTRANM, and, in the case of the latter two codes, for plotting electron trajectories in regions where macroscopic fields exist.

Table 1. ITS member codes.

Standard Codes	Enhanced Ionization/Relaxation (P-Codes)	Macroscopic Fields (M-Codes)
TIGER (1-D)	TIGERP	
CYLTRAN (2-D/3-D)	CYLTRANP	CYLTRANM
ACCEPT (3-D)	ACCEPTP	ACCEPTM

The moral of this discussion is that a user code exists which is elaborate enough to handle very general problems, and is well maintained and documented. However, there are two problems with this situation:

- If you are given a result based on ITS, it is important to inquire as to what version is being used, in terms of both dimensionality and physics, especially low energy physics.
- If self-consistent electric fields and the currents they generate are important, a calculation outside the framework of ITS is required.

4. A SIMPLIFIED MODEL OF e-BEAM PROPAGATION

To get a feeling for the evolution of e-beam deposition theory, we built a working model based on the 1938 papers referenced above. The treatment was relativistic; the model divides the laser into n parallel slabs of gas of thickness $dx = g/n$. Following Bethe we use the singular solution to the transport equations, $V_2 = V_1/(1 + 3x/2\lambda)$, to calculate the energy of electrons emitted from the slab in terms of the energy entering the slab (V_1) and the mean free path based on the cross sections for scattering at that energy, $\lambda = \lambda(V_1, \text{gas parameters})$.

When the energy is reduced to an amount comparable to the original energy, it can be shown that scattering has produced a sufficiently uncollimated beam that a diffusion approximation to subsequent transport is more realistic than straight-line slowing. At that point the current out of a slab is given by $J = J_0[1 - \phi(x/\tau_0^{1/2})]$, where ϕ is the error function, x is the penetration distance, and $\tau_0 = (1/6)\int_0^s \lambda ds'$, with s the actual electron path length. This can be written in reasonable approximation by an expansion of the error integral, $V(j) = V(j-1) - V(1)X \exp(-(j-1 - 0.5)^2 X^2 \pi)$, where i is the index of the slab at which the electron energy is about half its original value, and $X = dx/\lambda$ where λ is a mean free path.

A listing of the KA code is contained in Table 2; results of several runs are shown in Figures 1-3, compared with Monte Carlo calculations. The abrupt transition between straight-line slowing and diffusion, employed in the KA code following Bethe's original suggestion, produces a less uniform deposition profile than the Monte Carlo code. This is a reasonable reflection of smooth vs. abrupt changes of physics model in adjacent regions. Even so, the agreement is pretty good.

Parameter runs show that the results are sensitive to the scattering cross section in the regions near each boundary; there is also some sensitivity to the cross over point between slowing and diffusion. But the general trend shows, as we said above, that energy deposition is not as big an issue as the low energy distribution of scattered electrons, which is going to be inaccurate as much because of uncertainties in the cross sections and rates at those energies as it is because of approximate treatment of slowing and diffusion.

Table 2. A Program to Calculate Electron Energy Deposition in a Gas Laser

```

real e(20),v(20),de(20),de2(20)
real kev
real j
character ENDH
character*3 BEG
character BEGX(3)
equivalence (BEG,BEGX)
character c
real b(3)

CALL SETSCREEN(begx,endh)

write(*,*) beg,'USE,NRL1.AID',endh
pause ' '
write(*,*) beg,'USE,NRL2.AID',endh

CALL PARAMETERS(beg,g,kev,j,p,a,bb,cc,n,endh)

**Begin the deposition calculation
v(1) = 1.9e9*kev**.5 *sqrt(1.+kev/1.e3)/(1.+2.*kev/1.e3)
e(1) = kev
dx = g/n
**Assume an incoming current of 1 electron/cm
**e = energy(kev)/electron; (J*A/q)*e kev/sec incoming energy
det = 0.
**For 1 electron use Ne = 1/gV (e/cm); Later use J(kA) to get Ne
en0 = 1./v(1)/g
**
en0 = j/v(1)/1.5e3
dt = e(1)*v(1)*g*en0

do 10 i = 2,n+1
  xgen = 0.79e2*p/(e(i-1)+10.)**2*((1.+2.e-3*e(i-1))/(1.+
$      1.e-3*e(i-1)))**2*log(64.*(e(i-1)+10.))
  v(i) = v(i-1)/(1.+1.5*xgen*dx)
  e(i) = e(i-1)/(1.+1.5*xgen*dx)**2
**de = ev/sec/cm deposited in dx; det = total energy/sec deposited in G
  de(i-1) = (e(i-1) - e(i))/dx
  det = det + de(i-1)*dx
  if(e(i) .ge. kev/1.4) go to 10
  do 14 j = i+1,n+1
    x = 1.1*dx*xgen
    v(j) = v(j-1)-v(i)*x*exp(-((j-i-.5)*x)**2*3.14)
    e(j) = e(j-1)*(v(j)/v(j-1))**2
    de(j-1) = (e(j-1)-e(j))/dx
    det = det + de(j-1)
  14 continue
  go to 19
10

```

```

10  continue
19  do 20 i = 1,n
      de2(i) = de(i) + de(n+1-i)
20  continue

```

**** Print Output**

```

      do 30 i = 1,n
        x = float(i)*dx
        print 130, x,v(i),e(i),de(i),de2(i)
130    format(' ',f4.1,9x,e10.2,2x,e10.2,4x,e10.2,4x,e10.2)
        write(6,130)x,v(i),e(i),de(i),de2(i)
30    continue

      print 140,det,dt
      write(6,140)det,dt
140    format(' ',/, ' Energy deposited/s = ',f7.1,' kev. Energy expende
$d/s = ',f7.1,' kev. (1 el./s)')
      print 150,a,bb,cc
      write(6,150)a,bb,cc
150    format(' ', 'a = ',f6.3,' bb = ',f5.3,' cc = ',f5.3)
      end

```

**** The calling rule for Hi Screens**

```

SUBROUTINE SETSCREEN(begx,endh)
character endh
character begx(3)
BEGX(1) = CHAR(19)
BEGX(2) = CHAR(255)
BEGX(3) = CHAR(1)
ENDH = CHAR(1)
return
end

```

**** Input parameters from the screen**

```

SUBROUTINE PARAMETERS(beg,g,kev,j,p,a,bb,cc,n,endh)
real kev
real j
character ENDH
character*3 beg
3  write(*,*) beg,'SCREEN,*',endh
   read(*,4) rcode
4  format(a03)
5  format(f8.1)
6  format(i5)
   write(*,*) beg,'recover,g',endh
   read(*,5) g
   write(*,*) beg,'recover,kev',endh
   read(*,5) kev
   write(*,*) beg,'recover,j',endh

```

```

read(*,5) j
write(*,*) beg,'recover,p',endh
read(*,5) p
write(*,*) beg,'recover,a',endh
read(*,5) a
write(*,*) beg,'recover,bb',endh
read(*,5) bb
write(*,*) beg,'recover,cc',endh
read(*,5) cc
write(*,*) beg,'recover,n',endh
read(*,6) n
open (unit=6, file='nrl.run')
write (6,100)p,j,kev,g
100  format(' ','P = ',f4.1,' atm, J = ',f6.1,' kamps, Energy = ',f6.1,
$' kev, gap = ',f4.1,' cm',/)
print 100, p,j,kev,g
write(*,*) beg,'USE,NRL3.AID',endh
write(*,*) beg,'DISPLAY,P,=',p,endh
write(*,*) beg,'DISPLAY,kev,=',kev,endh
write(*,*) beg,'DISPLAY,J,=',j,endh
write(*,*) beg,'DISPLAY,G,=',g,endh
print 110
110  format(' ',///)
write(6,120)
120  format(' ',2x,'distance',7x,'Ve(cm/s)',5x,'Ee',11x,'En Dep',10x,'2
$-beams',/)
return
end

```

P = 1.5 atm, J = 10.0 kamps, Energy = 250.0 kev, gap = 30.0 cm

distance	Ve(cm/s)	Ee	En Dep	2-beams
.9	.22E+11	.25E+03	.17E+02	.17E+02
3.8	.21E+11	.22E+03	.18E+02	.18E+02
5.6	.19E+11	.19E+03	.19E+02	.19E+02
7.5	.17E+11	.15E+03	.12E+02	.13E+02
9.4	.16E+11	.13E+03	.11E+02	.13E+02
11.3	.15E+11	.11E+03	.92E+01	.12E+02
13.1	.13E+11	.90E+02	.75E+01	.11E+02
15.0	.12E+11	.76E+02	.59E+01	.10E+02
16.9	.11E+11	.65E+02	.44E+01	.10E+02
18.8	.11E+11	.57E+02	.33E+01	.11E+02
20.6	.10E+11	.51E+02	.23E+01	.12E+02
22.5	.96E+10	.46E+02	.16E+01	.13E+02
24.4	.93E+10	.43E+02	.11E+01	.13E+02
26.3	.91E+10	.41E+02	.71E+00	.19E+02
28.1	.89E+10	.40E+02	.45E+00	.18E+02
30.0	.88E+10	.39E+02	.27E+00	.17E+02

Energy deposited/s = 159.1 kev. Energy expended/s = 250.0 kev. (1 el./s)
a = 1.000 bb = 1.000 cc = 1.000

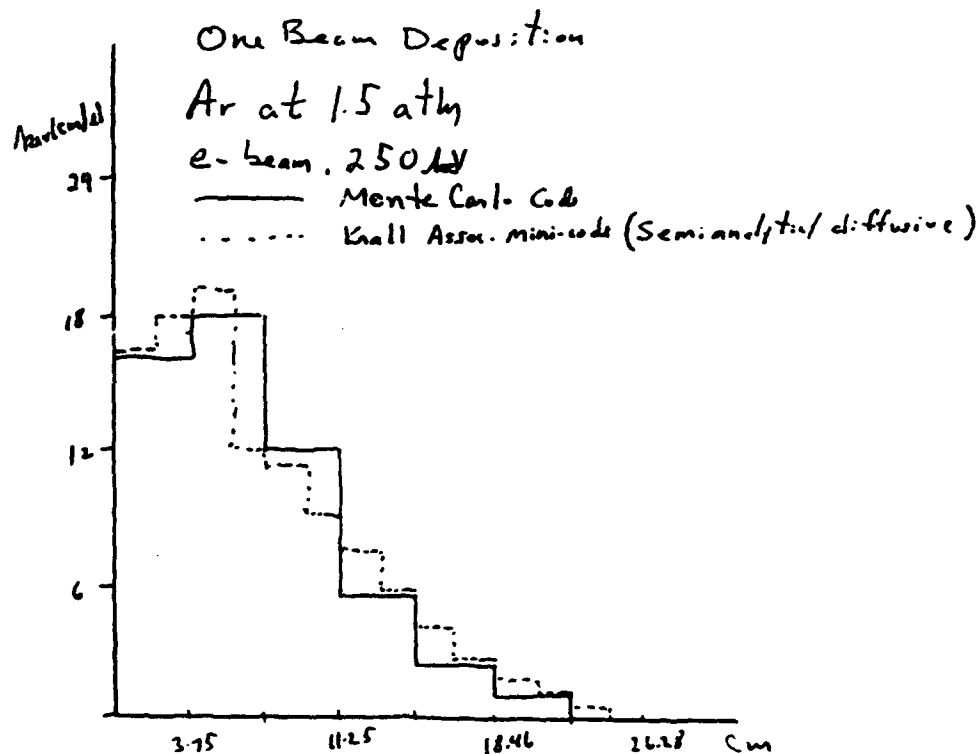


Figure 1. Dissipation of a single 250 keV beam.

P = 2.0 atm, J = 10.0 kamps, Energy = 250.0 kev, gap = 20.0 cm

distance	Ve(cm/s)	Ee	En Dep	2-beams
(.4	.22E+11	.25E+03	.22E+02	.23E+02
2.9	.21E+11	.22E+03	.23E+02	.25E+02
4.3	.19E+11	.18E+03	.25E+02	.27E+02
5.7	.17E+11	.15E+03	.16E+02	.19E+02
7.1	.16E+11	.13E+03	.14E+02	.19E+02
8.6	.15E+11	.11E+03	.12E+02	.18E+02
10.0	.13E+11	.88E+02	.98E+01	.17E+02
11.4	.12E+11	.74E+02	.76E+01	.17E+02
12.9	.11E+11	.63E+02	.57E+01	.18E+02
14.3	.11E+11	.55E+02	.41E+01	.19E+02
15.7	.99E+10	.49E+02	.29E+01	.19E+02
17.1	.95E+10	.45E+02	.20E+01	.27E+02
18.6	.92E+10	.42E+02	.13E+01	.25E+02
20.0	.90E+10	.40E+02	.85E+00	.23E+02

Energy deposited/s = 177.8 kev. Energy expended/s = 250.0 kev. (1 el./s)
a = 1.000 bb = 1.000 cc = 1.000

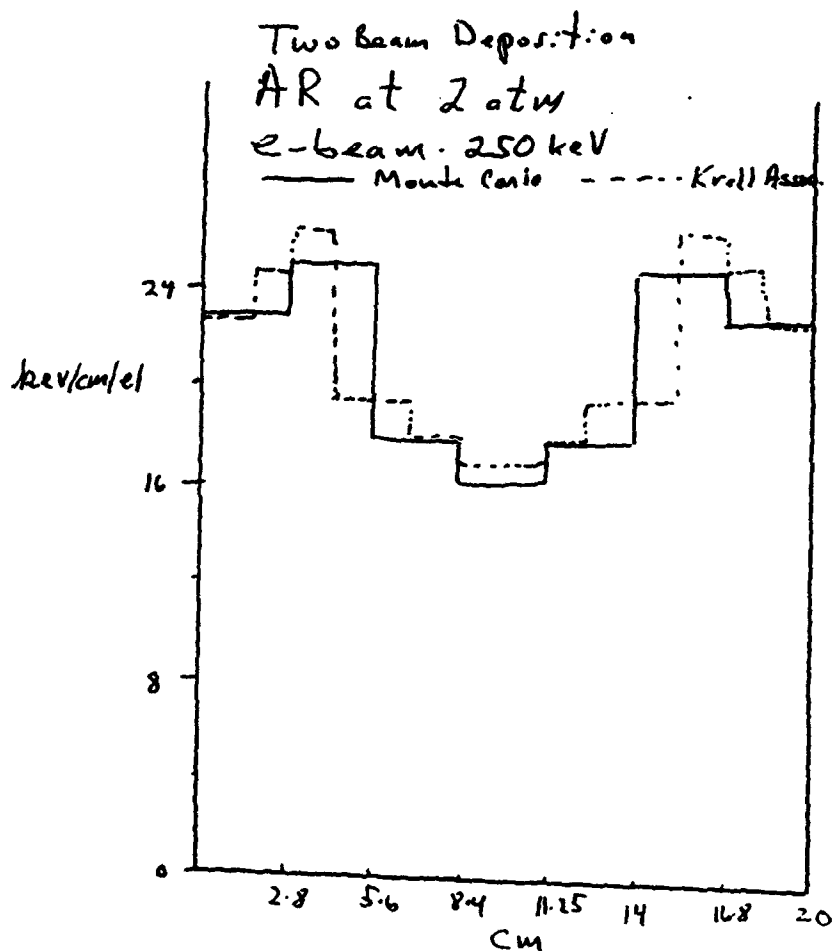


Figure 2. Dissipation of two 250 keV beams.

P = 2.0 atm, J = 10.0 kamps, Energy = 285.0 kev, gap = 20.0 cm

distance	Ve (m/s)	Re	En Dep	2-beams
.7	.23E+11	.29E+03	.21E+02	.23E+02
3.3	.22E+11	.25E+03	.22E+02	.25E+02
5.0	.20E+11	.21E+03	.23E+02	.28E+02
6.7	.18E+11	.18E+03	.15E+02	.21E+02
8.3	.17E+11	.15E+03	.14E+02	.21E+02
10.0	.15E+11	.13E+03	.12E+02	.21E+02
11.7	.14E+11	.11E+03	.97E+01	.21E+02
13.3	.13E+11	.91E+02	.77E+01	.21E+02
15.0	.12E+11	.79E+02	.60E+01	.21E+02
16.7	.11E+11	.69E+02	.45E+01	.28E+02
18.3	.11E+11	.61E+02	.33E+01	.25E+02
20.0	.10E+11	.56E+02	.24E+01	.23E+02

Energy deposited/s = 183.8 kev. Energy expended/s = 285.0 kev. (1 el./s)
a = 1.000 bb = 1.000 cc = 1.000

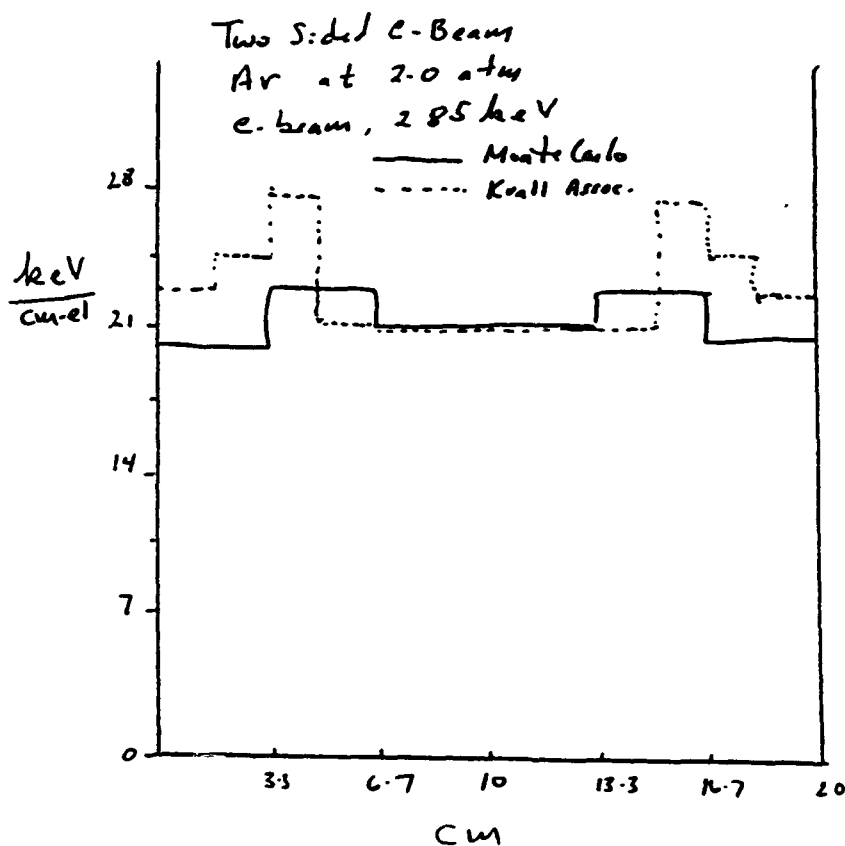


Figure 3. Dissipation of two 285 keV beams.

5. RETURN CURRENTS, LASER PERFORMANCE, AND OTHER DETAILS

A number of conversations, discussions, and literature analyses dealt with "anomalies" in laser performance. My initial approach was to look for specific cases where conventional treatments of laser deposition failed to agree with experiment. This didn't produce any showstoppers, so I broadened it a bit to look at any vagaries in laser performance related to electrons interacting with KrF.

One useful discussion was with Alan Hunter of Thermoelectric Corp. He made a number of useful points based on his previous experience:

- The most common reasons for breakdown in Monte Carlo modelling are unrelated to the M.C. method itself. They include:
 - Neglect of relativistic corrections
 - Errors in calculating scattering in all foils
 - Inaccurate modelling in the gun and electrode region for 2-beam systems, where penetration of one beam into the opposite gun can cause reflection, nonuniform lateral fields, and similar complications
- The Japanese have constructed analytic fits to M.C. calculations, at energies up to 20 MeV, which are purportedly useful in parameter variation and modelling. Examination of these papers showed work of about the same level as the KA code described in the previous section, except they showed more emphasis on curve fitting rather than on physics models. All of this showed general satisfaction with the use of M.C. for deposition calculation.
- More detailed simulations track beam propagation, energy deposition, species pumping down to a fraction of an eV; these show difficulties in modelling that transcend the calculation of uniform volumetric power deposition. This is because the rate of electron attachment to F_2 is strongly dependent on the low energy electron distribution

$f(E)$, with the cross section going from a very large value at $E = 0$ to a very small value at 0.03 eV. Electrostatic fields from charge buildup have a dominant effect on the low energy part of $f(E)$. Return currents reduce the electrostatic field, and directly influence the low energy part of $f(E)$. A self-consistent solution to the determination of $f(E,t)$ in the energy region below a few eV is beyond the scope of simulations done to date.

- There have been comments by experimentalists that indicate the electron penetration is less in experiments than predicted by the M.C. codes. This is consistent with the notion that electric field buildup has a macroscopic effect on total energy deposition per cm.

In addition to those comments, other information relevant to return currents and/or laser performance include the following:

- Comments by Dr. J. Jacobs of SRL indicated his belief that return currents would be small due to enhanced electron attachment to F_2 . In my opinion, that argument emphasizes the point I've been making. Electric fields and return currents dominate the electron distribution $f(E)$ at low energies, which directly affects attachment, which has a big effect on the gas kinetics. So return currents are an important effect, especially if attachment keeps them artificially low.
- Research at AVCO by Mangano et al. showed the effect of return currents in a single beam system by using various boundary conditions. With a transparent grid boundary, a magnetic field developed in the gap, consistent with a one-sided current. When the grid is replaced by a solid insulator, the magnetic field quickly decays, indicating the presence of a counter current which cancels most of the e-beam current.

- Conversation with Roger Haas at UC Davis emphasized the fact that it is well known that the electron distribution following e-beam deposition is non-Maxwellian. At low energy the first break in the distribution from Maxwellian is due to F_2 attachment, at nearly zero energy. Another break in $f(E)$ can occur at energies corresponding to the ionization threshold of Ar, at about 0.4 eV.
- Dr. Haas also pointed out several other potential dangers when return currents become strong. Electron heating by the return current can be substantial, further altering the low energy distribution of electrons.
- In addition to these general and various effects, a specific danger emerged, namely that buildup of a background electric field would generate a return current sufficient to drive the well known ionization instability (see, e.g., "Stability of Excimer Laser Discharges," Roger A. Haas, in Applied Atomic Collision Physics, Vol. 3, Academic Press, 1982).

6. IONIZATION INSTABILITY IN THE NRL EXPERIMENTS

Experimental development of discharge excited excimer lasers has shown that their performance characteristics are limited by an ionization instability. The instability leads to a collapse or filamentation of the discharge, usually terminating laser operation after a few tens of nanoseconds. The same process can affect high power e-beam driven discharges, in that the buildup of electric fields will drive a return current which may reproduce the phenomenology found in discharge driven devices.

The onset conditions for the ionization instability depend on a local imbalance between electron production processes and loss processes in the discharge. Because the e-beam also produces ionization, it can have a significant effect tending to quench the instability, besides being the source of the currents which tend to drive the instability. In discharge systems the instability occurs under the conditions for optimized laser performance. Whether the beam damping will be enough to stabilize the mode depends on a detailed accounting of the beam ionization rates and the F_2 electron attachment rates.

The importance of the ionization instability would be that it produces a striated or collapsed discharge, with the plasma forming alternating layers of high and low density, with planes of constant density oriented normal to the e-beam. It is possible to get some ideas of when these effects might come into play. Using

$$\nabla \cdot E = 4\pi n_e e$$

and noting that during the kinetic phase where the (deposited) electron density is increasing with time

$$n_e = \left(\frac{1}{E_0} \frac{dE_e}{dx} \right) \frac{I_0 t}{eA}$$

where dE_e/dx is the energy deposited per cm, E_0 is the original energy, and I_0/Ae is the number of electrons entering the laser per second. This gives

$$E = 4\pi I_0 t \int (I/E_0)(dE_e/dx) dx$$

$$I_{\text{Return}} = I_0 4\pi\sigma t \int (I/E_0)(dE_e/dx) dx$$

where

$$\sigma = n_e e^2 / m_e \nu_{ne}$$

is the conductivity and ν_{ne} is the collision frequency of electrons with background materials. The time to develop a return current comparable with the beam current is

$$t = \frac{m_e \nu}{4\pi n_e e^2} = \frac{m_e n_0 \sigma n_e \nu}{4\pi n_e e^2}$$

which for electron densities in the range 10^{13} cm^{-3} is 10's of nanoseconds or less. However, it may not be necessary for $I_R \geq I_0$ to trigger ionization instability, and a calculation of the steady state current will doubtless be more significant than the condition $I_R = I_0$. It is clear that since this balance between currents and rates is crucial to stability, a self-consistent model is essential.

7. RECOMMENDATIONS

At this point in the study, my opinion is that as a general technique for calculating energy deposition, the Monte Carlo code is potentially adequate. "Potentially" is because the code exists in many versions; it is necessary for the researcher to take care both in calculating electron propagation in the gun-electrode-drift-foil region as well as using the code version best adopted to KrF, particularly the low energy physics package.

There are at least two issues more vital than simple deposition. First is that the laser performance will depend critically on the low energy (\leq few eV) electron distribution and the rates for attachment, etc., at those energies. Neither of these is particularly well determined; this lack may be too difficult to remedy in a reasonable time frame for KrF development.

The second issue is that of ionization instability produced by the return currents and electrostatic fields generated during e-beam deposition. It may be possible to impact this problem with a small study at the level indicated in the cover letter to this report. What has to be done is the following:

- Develop a simple model for electric field (E) buildup, taking into account the mobility of electrons after deposition and loss to the boundaries.
- Estimate $I_R(t)$ from the fields determined in the above model.
- Apply the stability calculation to a KrF system with the E/n determined above.
- Estimate the stabilizing effect of ionization produced by the e-beams.

This can be as complicated a problem as one chooses to make it, but I believe an estimate can be obtained with three to four weeks work which will show under what conditions an e-beam driven KrF system might arguably be unstable due to this return current effect, and what choice of parameters would tend to avoid it.

APPENDIX B

KRALL ASSOCIATES

KA-89-17

**STABILITY OF A HIGH POWER
e-BEAM-DRIVEN KrF LASER**

Prepared by

Nicholas A. Krall

Krall Associates
Del Mar, CA 92014

Prepared for

Naval Research Laboratory
Washington, D.C. 20375

December 20, 1989

I. INTRODUCTION

The stability of excimer laser discharges¹ has been studied for many years.²⁻⁷ It is well known that performance characteristics and scalability are limited by an ionization instability, produced by a local imbalance between electron production rates and loss processes. In this instability, a local increase in electron density leads to a state where the ionization rate (electron production) exceeds the loss rate of electrons by direct processes (attachment) or indirect processes (metastable quenching). The instability leads to a collapse or filamentation of the discharge, terminating operation after a few tens of nanoseconds. It has been shown^{2,5} that sustaining the discharge by a high energy electron beam adds to the stability, if a significant fraction of the total power deposited in the laser is supplied by the electron beam.

An understanding of the parameter range for beam-induced stability is clouded by the effect the beam can have on the equilibrium, in addition to its effect on the stability of a given equilibrium. Thus, for example, Reference 7, which gives an excellent survey of excimer laser stability, reports a stability criterion (Ref. 7, Eq. (19)), $S_{eb} > n_e n_1 k_{1i}$ as the minimum ionization rate by the beam for stability (S is ionization rate due to the beam, n_e the electron density, n_1 the density of the first excimer excited state, and k_{1i} the rate of ionization from the excimer excited state).^{1,2} On the other hand, experiments and analysis²⁻⁵ reported in Ref. 7, Eq. (27), find that stability of this type of discharge requires $S_{eb} < n_F^3 k_a^2 k_q / 4nk_{11}k_{01}$, where n_F is the density of F_2 , k_a is the attachment coefficient for $e + F_2 \rightarrow F + F^-$, k_q is the rate for quenching the metastable state n_1 by F_2 , n is the total gas density, and k_{01} is the rate for excitation of the metastable state n_1 by electron impact.

The reason for a stability range rather than a stability limit lies among other possibilities in the dependence of the electron density n_e and the rate coefficients k_{01} , etc., on S_{eb} , and on E/n which also depends on S_{eb} .

In this report we describe research on the stability of a high power output KrF laser system in which the high energy e-beam dominates both the equilibrium and stability of the discharge, i.e., in which the discharge is maintained by the e-beam rather than electrically. The elements we consider are (1) the bifurcated equilibria possible in this system, (2) the return currents and E/n produced by the electrons deposited by those currents, and (3) the stability of the more likely equilibrium, as a function of beam current. As a guide in the stability analysis, we follow closely Reference 6, which also specifically recognizes the influence of separate stability phenomena and equilibria phenomena in calculating the threshold for stability in beam sustained systems.⁶

2. RETURN CURRENTS AND RELATED PHENOMENOLOGY OF AN e-BEAM-DRIVEN KrF LASER

A significant phenomenon in a KrF system driven by a high power electron beam is that electron deposition can create a substantial charge density, leading to an electric field and current typical of a discharge laser. This current can affect the operating point of the laser as well as its stability. In this section we derive some of the features of a laser dominated by e-beam deposition.

Beam electrons deposited in the laser set up an electric field whose potential is given by

$$\nabla^2 \phi = 4\pi e n_{eb} \quad , \quad (1)$$

since the secondaries produced by ionization, etc., are balanced by an equal charge density of ions. This potential drives part of the dense cloud of slow secondary electrons out of the system, reducing the charge density. In equilibrium the return current J_r equals the beam current J_b . Although the current is determined by the beam current, the electric potential and unbalanced charge density to support it is determined by the conductivity of the gas.

Note that in the absence of return currents, the electron density increase due to beam deposition is

$$n_e \text{ (due to beam electrons)} = j_b \left(\frac{A}{cm^2} \right) \frac{x \ 6 \times 10^{18} \text{ electrons}}{L(cm)} \frac{1}{cm^3-s} \quad , \quad (2)$$

where j_b is the electron beam current. For a pulse length of 100 ns, gap width of 10 cm, and current of 50 A/cm², Eq. (2) would give an excess electron density

and corresponding electric field of

$$n_e(\text{beam}) = 3 \times 10^{12} \text{ cm}^{-3} ,$$

$$E(\text{beam}) = 10^{10} \text{ Volts/meter} ,$$

which would drive a current far in excess of the beam current.⁸ So a return current is absolutely required to reduce the charge imbalance and maintain a self-consistent electric field.

To estimate the electric field in steady state, we assume that the plasma current balances the beam current, so the field is given by

$$E = I_b(\text{A}) R(\text{ohms})/L(\text{m}) \quad . \quad (3)$$

The resistivity can be expressed in terms of the background gas density and the electron density and temperature,⁸ giving the familiar (for gas discharge physics) form

$$\frac{E}{n} = 3 \times 10^{15} \frac{\sqrt{T_e(\text{eV})} j_{eb}(\text{A/cm}^2)}{n_e(\text{cm}^{-3})} \text{ Townsends} , \quad (4)$$

where n is the neutral gas density and $1 \text{ Td} = 10^{-17} \text{ V-cm}^2$. This is a normal level of E/n for discharge driven lasers, showing that the effect of return currents in these high powered beam driven discharges is substantial.

The result Eq. (4) assumes steady state. The buildup of E with time can be calculated from the rate of electron deposition Eq. (2) giving

$$E = 4\pi I_b t \int (1/E_b)(dE_b/dx) dx \quad , \quad (5)$$

$$I_{\text{Return}} = I_b 4\pi \sigma t \int (1/E_b)(dE_b/dx) dx \quad , \quad (6)$$

which shows that a current comparable to the beam current develops in a time

$$t = 10^{-15} n_0/n_e \text{ s} \quad , \quad (7)$$

where n_0 is the neutral gas density. This short time scale means that the assumption of steady state is a good one, and that Eq. (4) is a reasonable estimate of E/n . The excess electron density consistent with the calculated electric field can be obtained from Eq. (1), giving

$$n_e(\text{excess}) = 2 \times 10^4 \left(\frac{n_0}{n_e} \right) j_b \text{ cm}^{-3} \quad . \quad (8)$$

Since typically $n_0/n_e = 10^4$ and $j_b < 10^2 \text{ amps/cm}^2$, it is clear that the excess of electrons produced by the beam is not of high enough density to affect the kinetics.

For later reference, we estimate the ionization rate due to the beam deposition. Assume E_b is the beam energy per electron, and that during deposition eE_b goes into ionizing the gap. Take E_i to be the ionization energy. Then from Eq. (2) the total energy density which goes into ionization per second is

$$E_T \left(\frac{\text{eV}}{\text{cm}^3 \cdot \text{s}} \right) = 6 \times 10^{18} \frac{j(\text{A/cm}^2)}{L(\text{cm})} \epsilon E_b(\text{eV}) = E_i \frac{dn_e}{dt} \quad (9)$$

and the electron production rate becomes

$$S_{eb} = 6 \times 10^{18} \frac{\epsilon j(\text{A/cm}^2)}{L(\text{cm})} \frac{E_b}{E_i} \frac{eI}{\text{cm}^3 \cdot \text{s}} \quad (10)$$

This will be used in both equilibrium and stability calculations below.

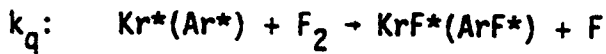
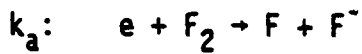
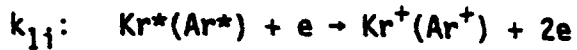
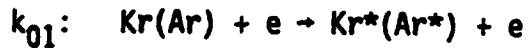
3. EQUILIBRIUM IN A KrF LASER

We consider a simplified model for the KrF system, with the densities and atomic processes as listed in Table 1.

Table 1. Elements of the KrF kinetics model.

Densities:	electron	Kr-ground state	(Kr+Ar)Metastables	Argon	F ₂
	n_e	n_k	n_1	n_0	n_F

Rates and processes:



The equilibrium equations, similar to Reference 7, are then

$$\frac{dn_e}{dt} = S_{eb} + k_{11}n_1n_e - k_a n_F n_e, \quad (11)$$

$$\frac{dn_1}{dt} = S_M + k_{01}n_en_0 - k_{11}n_en_1 - k_q n_1 n_F, \quad (12)$$

where S_M is the rate of production of metastables by the e-beam, given for argon by⁷ $S_m = S_{eb}/3.5$.

Solving with $dn/dt = 0$ gives the coupled equations

$$n_e = \frac{S_{eb}}{n_F k_a - n_1 k_{1i}} \quad , \quad (13)$$

$$n_1 = \frac{n_0 n_e k_{01} + S_m}{n_e k_{1i} + n_F k_q} \quad , \quad (14)$$

and solving gives the equilibrium electron density

$$n_e = \frac{n_F^2 k_a k_q - S k_{1i} \pm [(n_F^2 k_a k_q - S k_{1i})^2 - 4 S_{eb} n_F k_q M]^{1/2}}{2M} \quad , \quad (15)$$

$$M = n_0 n_e k_{01} - n_F k_a k_{1i} \quad , \quad (16)$$

$$S = S_{eb} + S_m \quad .$$

There are several branches of equilibria

a. $S_{eb} \ll n_F^2 k_a k_q / k_{1i}$

a1. $n_F k_a < n_0 k_{01}$

In this branch of weak beam equilibria, there are two solutions to Eq. (15), namely,

$$n_{e1} = S_{eb}/n_F k_a \quad , \quad (17)$$

and

$$n_{e2} = \frac{n_F^2 k_a k_q (1 - \frac{S_{eb} n_0 k_{01} k_{1i}}{n_F^2 k_a^2 k_q})}{n_0 k_{01} k_i - n_F k_a k_{1i}} \quad (18)$$

From both branches, using the limiting S_{eb} for case a,

$$S_{eb} < \frac{n_F^3 k_q k_a^2}{4 n_0 k_{01} k_{1i}} \quad \text{for equilibrium} \quad . \quad (19)$$

This is the same as Eq. (4), Reference 5, where it is listed as a stability condition.

There is a strong beam solution to the equilibrium equation (15), namely $S > n_F^2 k_q k_a / k_{1i}$. This limit will not give a real, positive value for the electron density unless S_{eb} is actually somewhat higher, giving the following regime.

$$b. \quad S_{eb} > 4 n_F k_q n_0 k_{01} / k_i \quad , \quad n_F k_a > n_0 k_{01}$$

This limit has an electron density which to lowest order is independent of S_{eb} ,

$$n_e \approx n_F k_q / k_i \quad . \quad (20)$$

This limit gives an electron density independent of S_{eb} ; to reach it requires transiting a parameter range which may be unstable as in discharge driven cases where n_e is also independent of S_{eb} , or may not have an equilibrium, with Eq. (15) giving negative or complex n_e . It is beyond the scope of the present study to examine this density range, not usually considered in the existing literature.¹⁻⁷ Nevertheless, it may be worth further study to determine if this region can in fact be accessed in a real system, and whether it would be desirable from a stability standpoint to do so.

4. STABILITY OF AN e-BEAM DRIVEN KrF LASER

We consider a system with n_e given by Eq. (17), S_{eb} limited as in case a, and E/n given by Eq. (4). In analyzing the stability of the e-beam pumped KrF systems, we use the following values⁶ for kinetic rate coefficients, defined in Table 2.

Table 2. Rate coefficients for the kinetic model in Table 1.

Metastable ionization	$k_{1i} = 6 \times 10^{-8} \text{ cm}^3/\text{s}$
Electron attachment	$k_a = 4.3 \times 10^{-9} (E/n)^{-0.63}$
Metastable quenching	$k_q = 7.5 \times 10^{-10} \text{ cm}^3/\text{s}$
Metastable production	$k_{01} = \text{fn } (E/n, n_e/n) \sim 10^{-11} - 10^{-13}$

Long⁶ gives a set of empirical curves for k_{01} as a function of E , n , n_e . We use a crude fit to his curves for the purpose of estimating critical parameter ratios,

$$k_{01} = 2.5 \times 10^{-13} (E/n)^{3/2} \quad \text{for } n_e/n = 3 \times 10^{-6} \quad . \quad (21)$$

Figure 1 shows the parametric dependence on n_e/n .

Stability is calculated by perturbing the electron and excited excimer densities, $n_e = n_e^0 + n_e^1 \exp(-i\omega t)$, $n_1 = n_1^0 + n_1^1 \exp(-i\omega t)$, substituting into Eqs. (11)-(12) and linearizing. The fact that the metastable production rate k_{01} is a strong function of E and n_e must be recognized by writing

$$k_{01} = k_{01}^0 + k_{01}^1 \exp(-i\omega t) \quad , \quad (22)$$

$$k_{01}^1 = \frac{\partial k_{01}}{\partial E} E^1 + \frac{\partial k_{01}}{\partial n_e} n_e^1 \quad . \quad (23)$$

The perturbed field E^1 can be obtained as follows. There are two special cases of the relation between the current, voltage, and external circuit. One is the voltage limited case, where a change in the discharge impedance changes the current. In that case,

$$k_{01}^1 \text{ (Voltage limited)} = \frac{\partial k_{01}}{\partial n_e} n_e^1 \quad . \quad (24)$$

A second limit is current limited, where a change in discharge impedance causes a change in the voltage, the current held constant. For constant current, $J = en_e V_e$, so

$$\frac{n_e^1}{n_e} + \frac{1}{V_e} \frac{\partial V_e}{\partial n_e} n_e^1 + \frac{1}{V_e} \frac{\partial V_e}{\partial E} E^1 = 0$$

and

$$k_{01}^1(\text{current limited}) = - \frac{\partial k_{01}}{\partial E} \left[\frac{1 + \left(\frac{1}{V_e} \frac{\partial V_e}{\partial n_e} \right) n_e}{\frac{1}{V_e} \frac{\partial V_e}{\partial E}} \right] n_e^1 + \frac{\partial k_{01}}{\partial n_e} n_e^1. \quad (25)$$

From Figure 1, k_{01} varies more strongly with E than with n_e , so an increase in electron density causes a decrease in the metastable production rate coefficient for the current limited case, while for the voltage limited case, k_{01}^1 and n_e^1 are in phase, $\partial k_{01}/\partial n_e > 0$.

Linearizing the kinetic equations (11)-(12) about a small perturbation $-e(-i\omega t)$ gives the stability condition ($\text{Im } \omega \geq 0$)

$$\frac{S_{eb}}{n_e} k_q n_F > k_{01} n_e \left[k_{1i} n_0 \left(1 + \frac{k_{01}^1 n_e}{k_{01} n_e^1} \right) - k_a n_F \right]. \quad (26)$$

The value of k_{01}^1/n_e^1 depends on whether the discharge is voltage or current limited. On a sufficiently long time scale the current will be constant, determined by the beam deposition rate. But on a shorter instability time scale, a variation in the impedance will produce a variation in the current, since the density of excess electrons has not changed. Thus we consider first the voltage limited case. In that case $k_{01}^1/n_e^1 > 0$, and the right-hand side of (26) is positive. It may appear that (26) then gives a lower limit on S_{eb} for stability. However, if the dependence of n_e on S_{eb} is included from Eq. (17), the stability condition gives instead an upper limit on S_{eb} ,

$$S_{eb} < \frac{n_F^3 k_q k_a^2}{n_0 k_{01} k_{1i}} \quad \text{for stability}, \quad (27)$$

which is comparable to the limit on S_{eb} from equilibrium constraints.

Using Eqs. (4) and (10), taking $\epsilon = 1/2$, and estimating $k_{01} = 10^{-12}$ gives

$$j_{eb} < 2 \times 10^{-26} \frac{n_F^3 L E_1}{n_0 E_b} \left(\frac{10^{-12}}{k_{01}} \right) \frac{\text{Amps}}{\text{cm}^2} \quad (28)$$

It is instructive to compare this result with the result obtained assuming a current limited discharge. In that case, k_{01}^1/n_e^1 is negative and the discharge is stable to the uniform perturbation assumed above for any beam density. However, as has been noted in Reference 6, experiments show that current limited discharges are also unstable, but to a disturbance that produces filamentation in the current. Figure 2 shows data indicating the stable operating regimes in this limit. Equation (4) and the equilibrium equation (17) can be used to estimate $E/N - 5 \text{ Td}$ which corresponds to stable e-beam currents less than 5-10 $\text{A/cm}^2/\text{amagat}$, which is comparable to that obtained from Eq. (27).

The point in both of these cases is that the E/n which develops is only weakly sensitive to j_{eb} , since it is proportional to j_{eb}/n_e and $n_e - j_{eb}$ in equilibrium. Both theoretically and experimentally, a fixed E/n is only stable up to a critical beam current, given approximately by either Eq. (27) or Figure 2.

5. CONCLUSION AND SUMMARY

In previous studies, both experimental and theoretical, it has been shown that discharge-driven KrF lasers are subject to an ionization instability driven by multistep ionization processes involving the metastable states of Kr or Ar. In the present study it is shown that a sufficiently intense e-beam driven laser can also be subject to these instabilities.

The mechanism is that the electrons deposited by the beam create a local charge imbalance which, due to finite conductivity, sets up an electric field of comparable size to that which drives discharge lasers unstable. Just as the e-beam current has a maximum stable value in a discharge laser, it has a similar stable value in an e-beam driven laser. The primary effect of the electric field is to increase the rate coefficient for metastable production by electron bombardment.

Both volume and striated modes of instability are possible. We have treated the volume mode analytically and referred to experiment for the striated mode. Both give similar current levels for stability. To extend the stability range, Eq. (27) suggests increasing the density of F_2 , and/or tailor the e-beam pulse to compensate for the loss of F_2 during the experiment. Raising n_0 can also increase the stability range. This may seem to contradict Eq. (27), but in fact $k_{11} \sim n_0^{-3/2}$, so that higher n_0 increases the stable S_{eb} . The same trend obtains for the striation instability, as seen in Figure 2, where decreasing n_F reduces the stable current. We recognize that there is an optimal n_F for maximum output, but the stability constraint should be folded into the choice of this parameter.

Finally, the dependence of electron temperature T_e on beam current has been neglected as beyond the scope of the present calculation. This could influence the E/N produced by a given current, and change S_{eb}^{max} . A more detailed treatment of the dependence of the metastable production rate k_{01} on electric field and on electron density should also be carried out if more precise results are desired. But the present work demonstrates the physics and points to a stability limit due to e-beam induced return currents.

ACKNOWLEDGMENT

This work was supported by SAIC under a contract to the Naval Research Laboratory. We especially thank Dr. Steve Bodner, NRL, for his support and encouragement.

REFERENCES

1. M. Rokni and J. H. Jacob in Applied Atomic Collision Physics, H. S. W. Massey, E. W. McDaniel, and B. Bendersen, eds., Vol. 3 (Academic Press, New York, 1982), pp. 273-317.
2. J. D. Daugherty, in Principles of Laser Plasmas, (G. Bekefi, ed.), Chapter 9, pp. 369-419 (Wiley, New York), 1976.
3. J. D. Daugherty, J. A. Mangano, and J. H. Jacob, Appl. Phys. Lett. **28**, 581-583 (1976).
4. R. T. Brown and W. L. Nighan, Appl. Phys. Lett. **32**, 730-733 (1978).
5. R. T. Brown and W. L. Nighan, Appl. Phys. Lett. **35**, 142-144 (1979).
6. W. H. Long, J. Appl. Phys. **50**, 168-172 (1979).
7. R. A. Haas in Applied Atomic Collision Physics, H. S. W. Massey, E. W. McDaniel, and B. Bendersen, eds., Vol. 1 (Academic Press, New York, 1982), pp. 423-451.
8. N. A. Krall and A. W. Trivelpiece, Principles of Plasma Physics, (McGraw-Hill, New York, 1973), pp. 330-331.
9. L. R. Peterson and J. E. Allen, J. Chem. Phys. **56**, 6068 (1972).

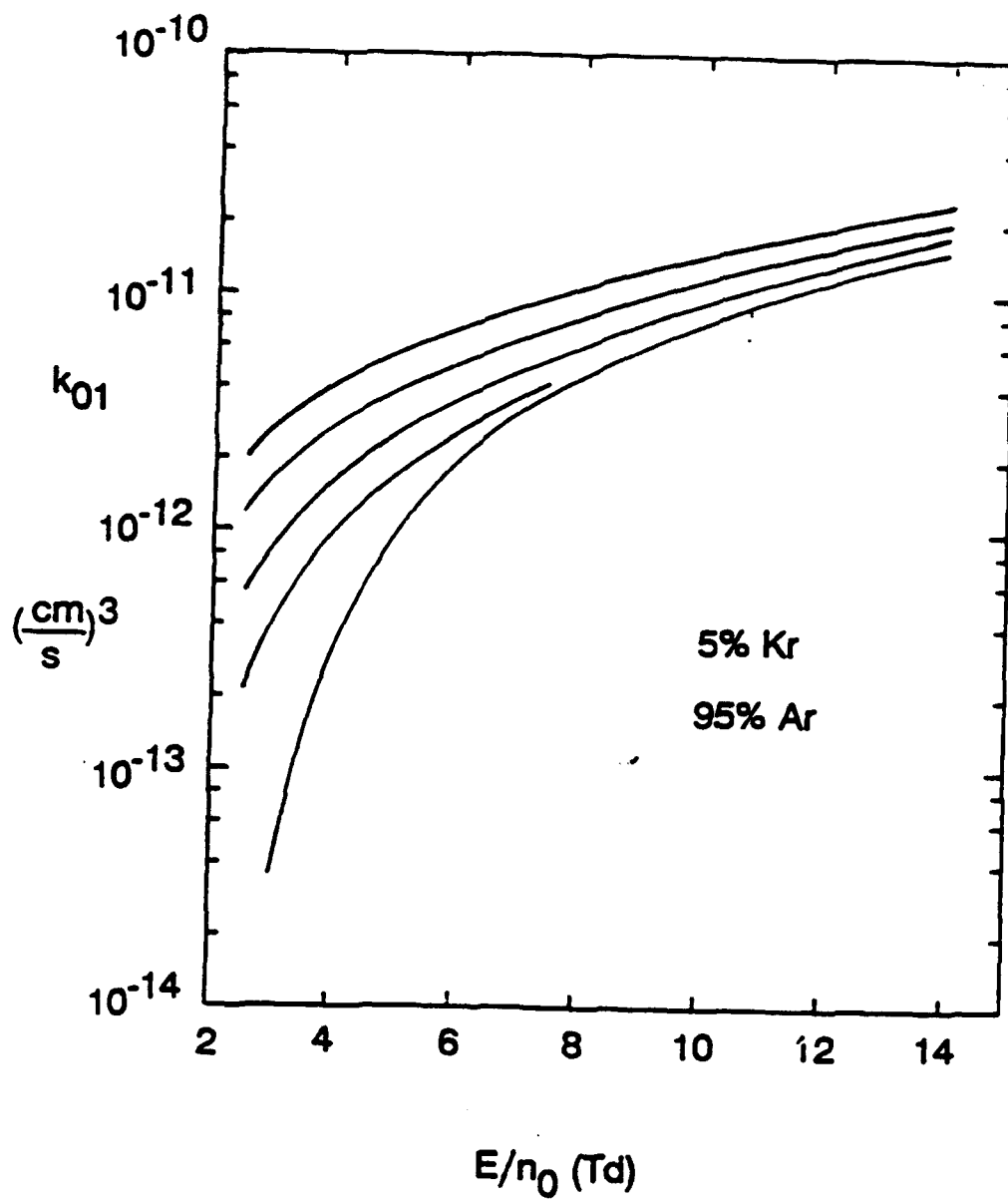


Figure 1. Metastable production rate. Parameters for the curves from top to bottom are $n_e/n_0 = 3 \times 10^{-5}$, 10^{-5} , 3×10^{-6} , 10^{-6} , 0.

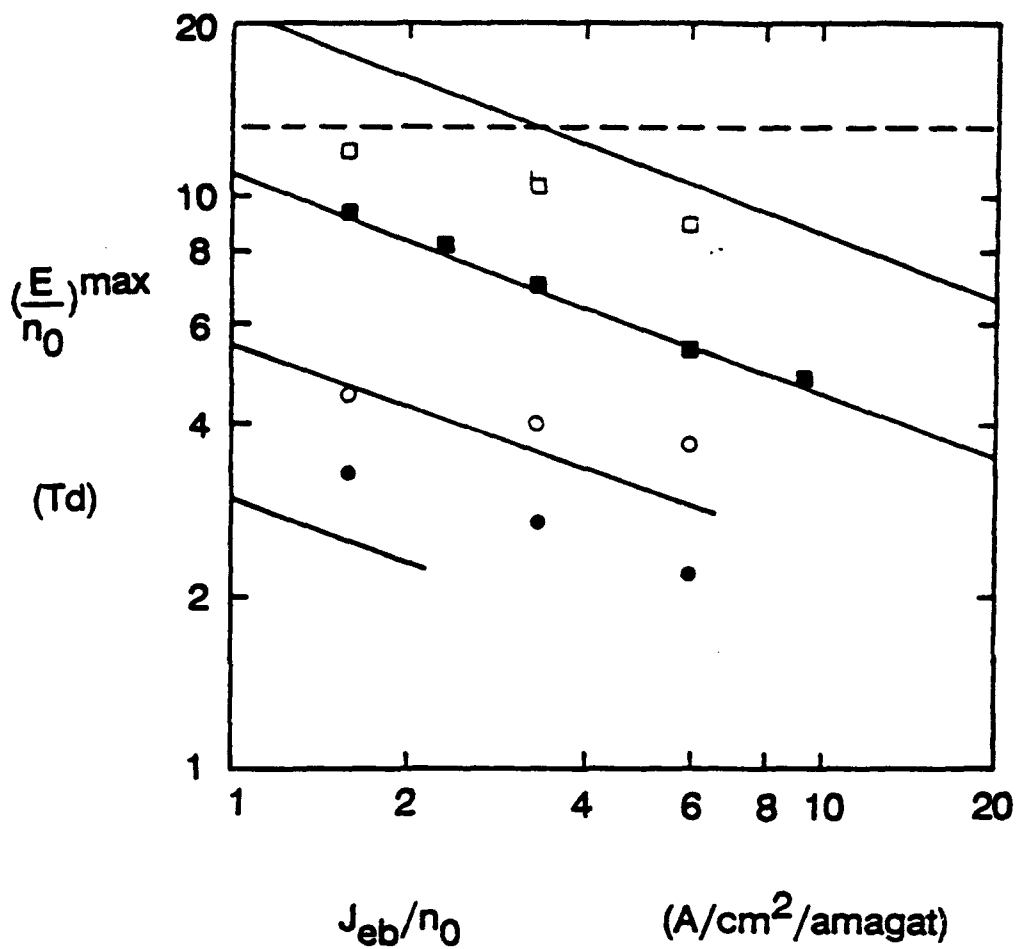


Figure 2. Maximum E/n_0 for stable discharge operation. The symbols are experimental data for $n_1/n_0 = 0.35\%$ (\square), 0.175% (\blacksquare), 0.088% (\circ), and 0.044% (\bullet).

APPENDIX C

**VIEWGRAPHS FROM
PRESENTATION AT NRL
DECEMBER 20, 1989**

KRALL

ASSOCIATES

Physics of e-beam deposition

- Analyze the physics content and adequacy of Monte Carlo deposition models

- Calculate the stability properties due to return currents in an e-beam driven KrF laser

Monte Carlo questions

- How is e-beam deposition in a KrF laser presently calculated?
- What physics is included in these calculations?
- Under what conditions are these calculations expected to fail?
- Is there any experimental evidence that suggests that Monte Carlo calculations break down when used to calculate deposition?
- What physics uncertainty actually does affect predicted laser performance?

KRALL ASSOCIATES

Tasks and Methodology

1. Survey of and discussion with a number of scientists expert in e-beam deposition calculations and/or KrF and other excimer laser systems.
2. Search for literature which follows from and expands on the information acquired in (1).
3. Acquisition of documentation for TIGER and SANDYL; TIGER is a widely used publicly available Monte Carlo code, existing in several versions. SANDYL is a related model, developed about ten years earlier. Several treatments from SANDYL have been incorporated into TIGER, in particular its elaborate ionization/relaxation model.
4. Analysis of TIGER/SANDYL, with emphasis on the base literature for e-beam deposition.
5. Construction of a simple computer code based on range-energy physics near the initial beam energy, and diffusion physics at the proper point of the slowing down process, as originally suggested by Bethe et al. (1938) and Landau (1944); this code was run as a test of the much more exotic Monte Carlo calculations. Agreement turned out to be fairly decent.
6. Estimate of sensitivity of deposition performance to details of the physics model, and a beginning examination of the sensitivity of laser performance to other details.
7. Calculation of a bound on the time scale for return current buildup, and discussion of possible effects of this current.
8. Preparation of an interim report summarizing the findings to date.
9. A diffusion calculation to determine the return current level as a function of beam and laser parameters.
10. A stability calculation (ionization instability) for a KrF laser with self-consistent return current.

KRALL

ASSOCIATES

Findings

Well documented user codes are available

Many codes cross-checked with each other

Analytic models give further check

Return currents, field buildup not included

External E-B fields included, but not

self-consistent fields

KRALL

ASSOCIATES

Major uncertainties

Atomic chemistry

Rates: attachment, impact dissociation, etc.

Dependence on $f(v_i)$

$f(v_i)$ - non Maxwellian due to $k(v_i)$

Beam properties

Transport to and through the foil

Non-uniformities in drift region

Second beam can enter the first gun

Partial reflection

Table 1. IIS member codes.

Standard Codes	Enhanced Ionization/Relaxation (P-Codes)	Macroscopic Fields (M-Codes)
TIGER (1-D)	TIGERP	
CYLTRAN (2-D/3-D)	CYLTRANP	CYLTRANM
ACCEPT (3-D)	ACCEPTP	ACCEPTM

Time independent, multi-d, multi-material; photon + random walk electron transport

Base code: transport at source energy ≤ 10 Mev $\rightarrow 1.0$ keV

Variants: more detailed low energy transport
 Macroscopic B-fields and E-fields and/or collisional transport
 Spherical shell models

KRALL ASSOCIATES

Sensitivity Test - KA Model

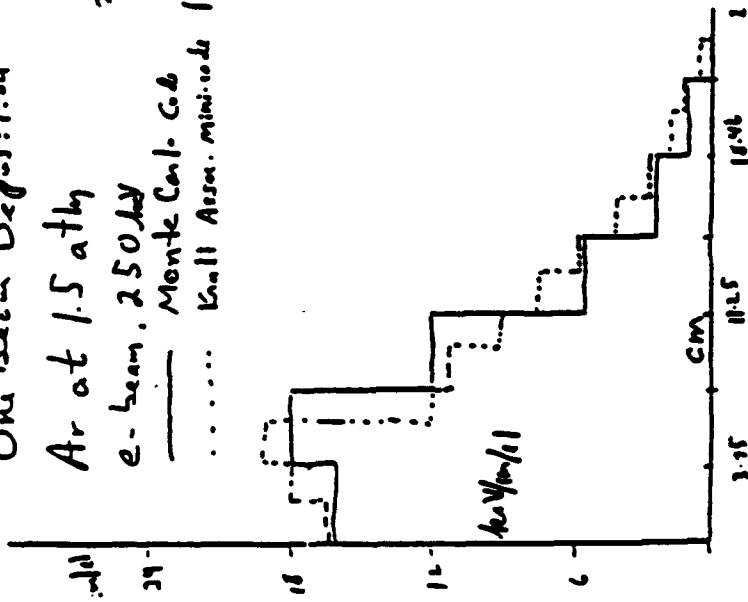
One Beam Deposition

Ar at 1.5 atw

e-beam, 250keV

— Monte Carlo

..... Krall Assoc.



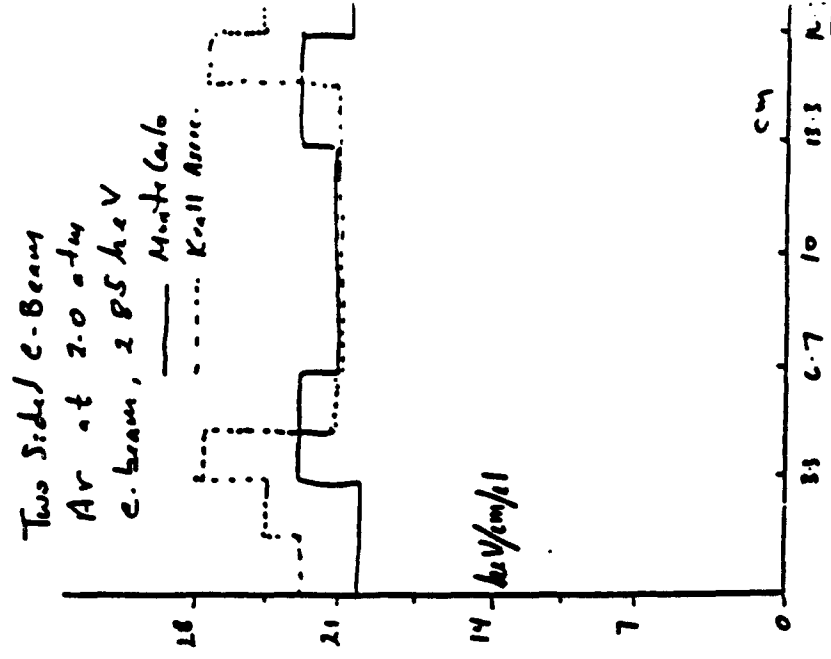
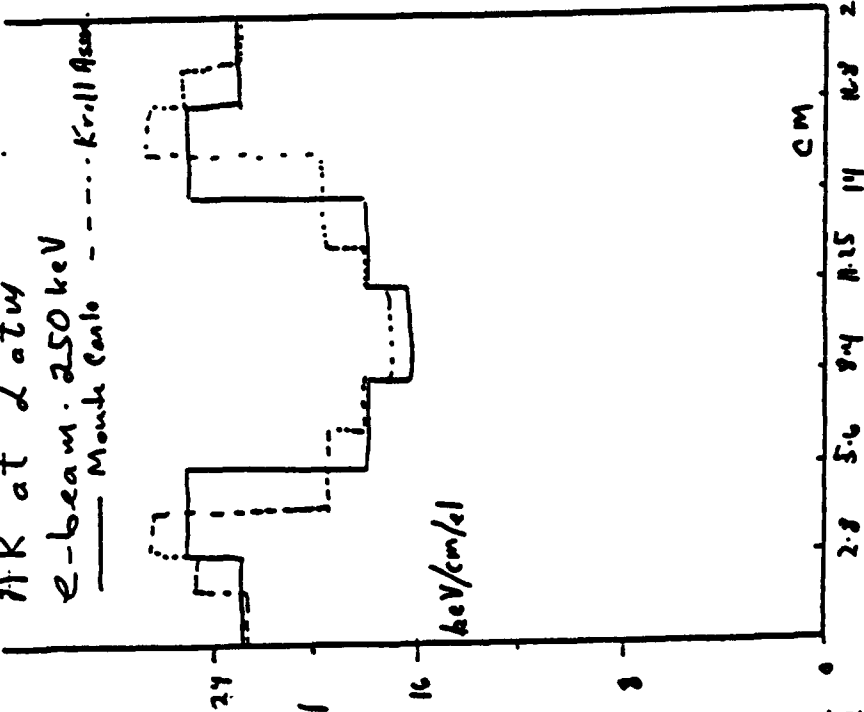
Two Beam Deposition

AR at 2 atw

e-beam, 250keV

— Monte Carlo

..... Krall Assoc.



Conclude: Sensitive to σ_{wall} , crossover from slowing to diffusion;
Gross deposition profile not an issue.

KRALL

ASSOCIATES

Conclusions

Fidelity of Monte Carlo predictions depends on what version is used. Can be very good.

Self consistent fields and currents require calculation outside M.C. framework, at present

Distribution of low-energy electrons is inaccurate more due to rate uncertainties than to

Monte Carlo inadequacies

KRALL

ASSOCIATES

Return Currents and Ionization Instability

Approach:

Calculate electron buildup,

E-field buildup,

Current flow.

Determine kinetic equilibrium properties.

Calculate volumetric stability.

Compare parameter range with striation instability experiments.

- Electron buildup: n_e (due to beam electrons) = $j_b \left(\frac{A}{cm^2} \right) \frac{6 \times 10^{18} \text{ electrons}}{L(cm)^3} \text{ cm}^{-3} \cdot s$
- If unneutralized, $n_e \sim 3 \times 10^{12} \text{ cm}^{-3}$, $E \sim 10^{10} \text{ V/m}$ in 100 ns
- \therefore Return current is essential
- Equilibrium, $E = IR/L \Rightarrow \frac{E}{n} = 3 \times 10^{15} \frac{J_e(\text{eV}) j_{eb}(\text{A/cm}^2)}{n_e(\text{cm}^{-3})}$ Townsends
- Time scale for buildup: $E \sim I_b t$, $I_R \sim 4\pi\sigma I_b t$; $I_R \sim I_b$ in $10^{-15} \frac{1 \text{ b.s}}{n_e}$
- Excess electron in equilibrium: $\tilde{n}_{ex} \sim 2 \times 10^9 (n_b/n_e) j_b \text{ cm}^{-3} \ll n_e$

Electron production rate from $E_T \sim j_e E_b/L = E_i dn_e/dt$

$$S_{eb} = 6 \times 10^{18} \frac{\epsilon j(\text{A/cm}^2)}{L(\text{cm})} \frac{E_b}{E_i} \frac{e}{cm^3 \cdot s}$$

KRALL ASSOCIATES

Kinetic Model for $E_g + \text{stability}$

Densities:	electron	Kr-ground state	(Kr+Ar)Metastables	Argon	F_2
	n_e	n_k	n_1	n_0	n_f
Rates and processes:					
k_{01} :	$Kr(Ar) + e \rightarrow Kr^+(Ar^+) + e$	Metastable ionization		$k_{11} = 6 \times 10^{-8} \text{ cm}^3/\text{s}$	
k_{11} :	$Kr^+(Ar^+) + e \rightarrow Kr^+(Ar^+) + 2e$	Electron attachment		$k_a = 4.3 \times 10^{-9} (E/n)^{-0.63}$	
k_a :	$e + F_2 \rightarrow F + F^-$	Metastable quenching		$k_q = 7.5 \times 10^{-10} \text{ cm}^3/\text{s}$	
k_q :	$Kr^+(Ar^+) + F_2 \rightarrow KrF^+(ArF^+) + F$	Metastable production		$k_{01} = f n (E/n, n_e/n) = 10^{-11} - 10^{-13}$	

$$\frac{dn_e}{dt} = S_{eb} + k_{11}n_1n_e - k_a n_f n_e$$

$$\frac{dn_1}{dt} = S_M + k_{01}n_e n_0 - k_{11}n_e n_1 - k_q n_1 n_f$$

KRALL

ASSOCIATES

Equilibrium

$$n_e = \frac{n_{fa}^2 k_q - sk_{11} + [(n_{fa}^2 k_q - sk_{11})^2 - 4s_{eb} n_{fk} M]^{1/2}}{2H}$$

$$M = n_0 n_{e01} - n_{fa} k_{11}$$

$$S = S_{eb} + S_m$$

a. $S_{eb} < n_{fa}^2 k_q / k_{11}$

b. $S_{eb} > 4n_{fa} k_q n_{0k01} / k_{11}$, $n_{fa} k_a > n_{0k01}$

a1. $n_{fa} k_a < n_{0k01}$

$$n_e \approx n_{fa} k_q / k_{11}$$

$$n_{e1} = S_{eb} / n_{fa} k_a$$

$$n_{e2} = \frac{n_{fa}^2 k_q (1 - \frac{S_{eb} n_{0k01} k_{11}}{n_{fa}^2 k_q})}{n_{0k01} k_{11} - n_{fa} k_{11}}$$

$$S_{eb} < \frac{n_{fa}^3 k_q^2}{4n_{0k01} k_{11}}$$

for equilibrium

KRALL

ASSOCIATES

Stability

a.

$$n_e = n_e^0 + n_e' \exp(-i\omega t) ; n_i = n_i^0 + n_i' \exp(-i\omega t) ; h_{01} = h_{01}^0 + h_{01}'$$

$$h_{01}' = \frac{\partial h_{01}}{\partial E} E' + \frac{\partial h_{01}}{\partial n_e} n_e'$$

Voltage limited, $E' = 0$

$$h_{01}' = \frac{\partial h_{01}}{\partial n_e} n_e'$$

$$\text{Current limited } E' = -\frac{n_i v_b - \frac{\partial h_{01}}{\partial E} n_i'}{\frac{\partial h_{01}}{\partial E}}$$

$$h_{01}' = \left\{ \frac{\partial h_{01}}{\partial n_e} - \frac{\partial h_{01}}{\partial E} \left[1 + \frac{\partial \frac{\partial h_{01}}{\partial E}}{\frac{\partial h_{01}}{\partial E}} \right] \right\} n_e'$$

$$\text{Voltage limited: } \frac{S_{eb}}{n_e} k_q n_F > k_{01} n_e [k_{11} n_0 (1 + \frac{k_{01} n_e}{k_{01} n_e}) - k_a n_F]$$

$$S_{eb} < \frac{n_F^3 k_q^2}{n_0 k_{01} k_{11}}$$

for stability

$$J_{eb} < 2 \times 10^{-26} \frac{n_e^3}{n_0} \frac{E_i}{E_b} \left(\frac{10^{-12}}{h_{01}} \right)$$

Current limited: Stable to volume mode, unstable to h_{11} striations

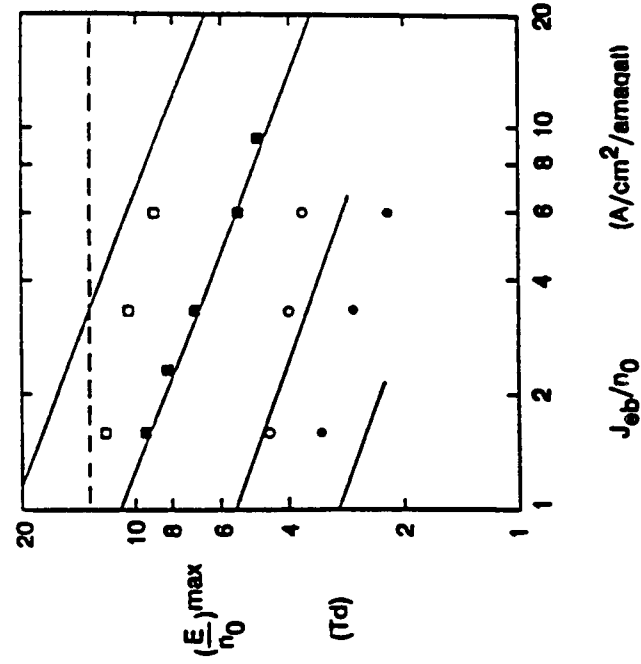


Figure 1. Metastable production rate. Parameters for the curves from top to bottom are $n_0/n_0 = 3 \times 10^{-5}$, 10^{-5} , 3×10^{-6} , 10^{-6} , 0.

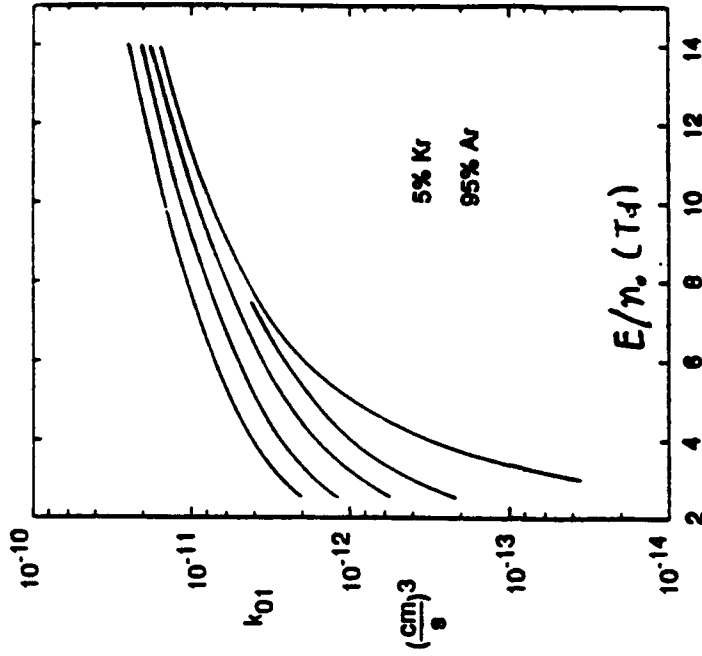


Figure 2. Maximum E/n_0 for stable discharge operation. The symbols are experimental data for $n_1/n_0 = 0.35\%$ (□), 0.175% (■), 0.088% (○), and 0.044% (●).

Example: $M_F = 10^{16}$, $n_0 = 10^{19}$, $E_b = 250$ keV. $j \lesssim 10$ A/cm² ($k_{01} = 10^{-12}$)

KRALL

ASSOCIATES

Conclusions

Experiment and theory find ionization instabilities in E-discharges

j_{eb} sets up a return current and self-consistent E/n_0 .

E/n_0 is comparable to that in electric discharge systems

\therefore There is a critical (maximum) current for stability

$$j_{max} \sim n_F^3 L ; \quad j_{max} \text{ is sensitive to}$$

$$j_{max} \sim 10^2 \text{ A/cm}^2$$

for typical Krf
parameters

n_F, L, E_b but especially to

$\Lambda_{e0}, (E/n, n_e/n)$, which is

known empirically over some
range of parameters, but depends
on T_e and f_{low} and other details.

Appendix D

On Possible Stabilization of Ablatively Accelerated Foils by Strongly Coupled Plasma Effects

**On possible stabilization of ablatively accelerated
foils by strongly coupled plasma effects**

A. L. Velikovich

Laboratory for Plasma Research
University of Maryland
College Park, MD 20742

Abstract: Possible stabilization of Rayleigh-Taylor (RT) instability of ablatively accelerated foils caused by strongly coupled plasma (SCP) effects has been analyzed as a general concept, as possible explanation of earlier NRL experiments (Grun et al., Phys. Rev. Lett., 1987), and as a reason to pursue further research on SCP physics. The stabilizing influence of SCP effects, such as modification of equation of state, plasma viscosity, thermal conductivity, surface tension, and mechanical rigidity (the last two mechanisms correspond to possible plasma phase transition into a condensed state), estimated from above in a most generous way, have been found insufficient for suppressing RT instability, in particular, in the case of experiment cited above. Alternative explanations for lack of observed perturbation growth in the short-wavelength range in this experiment are discussed.

1. Introduction

Rayleigh-Taylor instability of ablatively accelerated targets is known to be a major problem for the direct-drive concept of laser fusion. Ability to suppress the RT instability is a prerequisite for making this concept feasible.

Unfortunately, with high-temperature ablated plasma much lighter than the dense accelerated layers, the effective Atwood number A is very close to unity, and we have therefore to deal with the most dangerous kind of RT instability. It is known that for $A = 1$ the dominating instability mode of a layer supported by the pressure of a massless fluid against gravity, is the so-called global RT mode, whose growth rate equals \sqrt{gk} (g is acceleration, k is the perturbation wavenumber), and is therefore independent of the density and pressure profiles, equation-of-state (EOS) of accelerated material, etc.^{1,2} It is easy to explain independence of the equation-of-state: the global RT mode corresponds to purely interchange, divergence-free perturbations, volume of any plasma particle being constant in time. Consequently, compressibility of those particles is never tested (this is why the growth rate does not depend on the equation-of-state), and no energy is required for compression (thus this mode is the fastest one). The independence of the flow profiles, though not so evident (e.g., see³ and the comment⁴), is nevertheless an established fact. If one aims at suppressing the RT instability, no simple rearrangement of the fluid profiles and the EOS would help. The very nature of the perturbed flow should be changed in a radical way.

Of course, the RT instability of an ablatively accelerated foil is not exactly the same as that of a plane layer in a gravitational field. Flow of plasma particles through the unstable zone and non-uniformity of the acceleration profile should both contribute to stabilization.⁵ However, this stabilization is not particularly effective for large perturbation wavelengths, the decrease in growth rate being given by a factor of about 0.9. Here again, variation of the fluid profiles and properties within an order of magnitude is not likely to produce a major stabilizing effect. For stabilization, one should use mechanisms capable of changing the perturbed flow qualitatively.

The aim of this paper is to investigate whether the required stabilization could be produced by the strongly coupled plasma effects. Indeed, the ablatively accelerated plasmas (especially the cold, dense layers) are known to be non-ideal, strongly coupled, with the values of the coupling parameter Γ typically in the range between 1 and 10.^{6,7} In principle, the SCP effects could substantially modify all the plasma properties, from its kinetic coefficients to the EOS. Plasma phase transition to a liquid-like (and even solid) state is not excluded also.

Particular attention is to be paid to the still unexplained experimental results of Ref. 8, where no appreciable growth has been observed for short-wavelength perturbations with $\lambda = 50 \mu\text{m}$, whereas observed growth rates for long-wavelength perturbations ($\lambda = 100$ and $150 \mu\text{m}$) were quite close to the classical \sqrt{gk} . Though this result has not been confirmed by subsequent experiments, the experimental conditions of ⁸ also never have been reproduced exactly. The possibility, however small, that this experiment has accidentally produced conditions favorable for suppressing the growth of short-wavelength perturbations (maybe, by some SCP mechanisms) should be carefully analyzed.

Though physics of strongly coupled plasmas has been an area of extensive research

for several decades, there is still some uncertainty in calculations of basic SCP parameters and kinetic coefficients like compressibility, viscosity or thermal conductivity, even in the extensively studied case of a hydrogen-like (fully ionized) SCP. Considerably less is known about partially ionized SCP, where additional collective effects are possible due to overlapping of the wave functions of bound electrons in neighbouring atoms. The SCP realized in laser-fusion experiments appear to belong mainly to this latter type.

Quantitative theoretical studies of laser-produced SCP are particularly difficult (and their results accordingly uncertain) since the coupling parameter Γ , often being of order of (and greater than) unity, cannot be made very large. Indeed,

$$\Gamma = \frac{(Ze)^2}{a_i T} = 8.6 \frac{Z^2 (n/5 \cdot 10^{22} \text{ cm}^{-3})^{1/3}}{T \text{ (eV)}}, \quad (1)$$

where T is the plasma temperature, n is the ion density, $a_i = (3/4\pi n)^{1/3}$ is the "mean ion radius". We see that it is very difficult to produce laser plasmas with Γ greater than, say, 20. Indeed, increasing ion number density of a singly ionized plasma to 10^{24} cm^{-3} , one can gain a factor about 3; however, this degree of compression is hardly possible without plasma heating to several eV, the net result being rather a decrease of Γ . Whenever Z is greater than unity, the contribution of the Z^2 factor is usually more than compensated by the corresponding increase in temperature, so that for a pusher-fuel interface one can hardly expect Γ to be greater than 3 to 5.

The general characteristics of strongly coupled plasmas are "cold" and "dense". However the degree $1/3$ in Eq. (1) indicates that when one needs to produce a SCP with very large Γ , it could (and, in effect, should) have very low density and low temperature. Indeed, pure ion or electron plasmas can exist only at low density (recombination of a two-component plasma at low temperatures would be inevitable). A decrease in density by 14 orders of magnitude from the solid-state level to $(1 - 2) \cdot 10^8 \text{ cm}^{-3}$ accompanied by decrease in temperature by 6-7 orders of magnitude from 1 eV to 1-10 mK in experiments with laser-cooled ions in Penning traps (e.g., see Refs. 9, 10) results in overall increase in Γ , which could achieve a few hundred. The same refers to the 2-D systems of strongly-coupled electrons, also produced at cryogenic temperatures^{11,12}: in the range of typical electron densities 10^7 to 10^{10} cm^{-2} (which corresponds to the same values of a_i as number densities per unit volume 10^{11} to 10^{15} cm^{-3}) high values of Γ are obtained at the temperatures about 0.1-1 K.

Therefore, laser-produced strongly coupled plasmas fall into the most uncomfortable range of the SCP parameters, where one cannot make use of reliable theoretical results obtained in the limit of very large Γ . However, filling the corresponding (very large) gap in the theory of SCP is certainly beyond the scope of the present report. My main goal is to estimate whether the SCP effects could be sufficient to suppress RT instability in the experiments with laser ablative acceleration of thin foils, conditions of the NRL experiment⁸ being an important example and a reference point.

For this, a complete theory is not required. The SCP effects could be estimated from above, the estimates being based on very simple considerations.

For instance, there is still no reliable theory to predict the threshold value of Γ required for so-called plasma phase transition from a partially ionized gas to a liquid-like state. This

type of transition, first discussed in^{13,14}, may be related to some results of LLNL shock-wave experiments.¹⁵ Without going into details, we may assume that the strongly coupled plasma indeed turns into a liquid state, - and then estimate the possible contribution of corresponding stabilizing factors, like surface tension (Sect. 2) or enhanced viscosity (Sect. 3) to suppression of the RT instability.

Though within the range of Γ covered by laser-fusion experiments plasma freezing and formation of solid crystal structure stabilizing the flow appear to be unlikely, one has still to allow for this possibility. However, the Young's modulus of this crystal, if one is formed, could be estimated from above, too, as well as possible contribution of the presence of a frozen layer to the overall stabilization (Sect. 4).

The influence of SCP modification of the plasma equation-of-state and thermal conductivity on suppression of the RT instability is briefly discussed in Sect. 5.

In Section 6, the still unexplained results of Ref. 8, possible contribution of SCP effects to observed unusual stability and some alternative explanations are discussed. Section 7 summarizes the results.

2. Surface tension

Let us assume that a relatively cold ablatively accelerated plasma is turned into a liquid state as a result of a plasma phase transition^{13,14}. This implies that a surface of the liquid, and hence, surface tension appears. Surface tension is known to be an effective mechanism for suppressing the RT instability. The cut-off perturbation wavelength for this mechanism equals

$$\lambda_{min} = 2\pi \left(\frac{S/\rho}{g} \right)^{1/2}, \quad (2)$$

where S is the surface tension, and ρ is the density of the fluid¹⁶. Short-wavelength perturbations with $\lambda < \lambda_{min}$ do not grow; on the other hand, perturbations whose wavelengths are sufficiently long compared to λ_{min} , are not affected.

The exact value of surface tension S is not easily calculated even for the most simple and thoroughly studied liquids like liquid argon or liquid sodium: discrepancy between the theoretical results and measured values is typically within 30 to 50%¹⁷. However, S could be estimated from above in a relatively simple way. Indeed, the additional energy needed to pull a particle - molecule or atom - from the volume to the surface (that is, surface energy per particle) is needed to break some of the bonds, since a particle on the surface has less neighbors than one in the volume. Nevertheless, it still has some neighbors, it is still bound to the fluid. This amount of energy is clearly several times less than the energy ϵ needed to extract a particle from the fluid (evaporation energy per particle). Then the estimate for S is

$$S < S_m = \epsilon n^{2/3}, \quad (3)$$

where the factor $n^{2/3}$ is number density of particles per unit area of the liquid surface.

Let us verify that Eq. (3) is indeed a reliable estimate from above. For liquid argon at $T = 84$ K ($\epsilon = 0.067$ eV = 785 K/ k_B , $n = 2.1 \cdot 10^{22}$ cm⁻³) we have: $S = 13$ dyn/cm, $S_m = 82$ dyn/cm. For liquid nitrogen at $T = 63$ K ($\epsilon = 0.058$ eV = 676 K/ k_B , $n = 1.9 \cdot 10^{22}$ cm⁻³): $S = 12$ dyn/cm, $S_m = 66$ dyn/cm. For liquid sodium at $T = 371$ K ($\epsilon = 1.03$ eV = 12000

K/k_B , $n = 2.4 \cdot 10^{22} \text{ cm}^{-3}$): $S = 191 \text{ dyn/cm}$, $S_m = 1373 \text{ dyn/cm}$ (all the data from¹⁷). Hence, S_m overestimates S by factor 5 to 7, as it should.

For a strongly coupled plasma, the characteristic energy per particle is

$$\epsilon_{SCP} = \frac{(Ze)^2}{a_i} = \Gamma T. \quad (4)$$

In particular, the evaporation energy, if nonzero, should be of the same order of magnitude. Hence, the required estimate from above for surface tension of a strongly coupled plasma is obtained by substituting (4) into (3):

$$S_m = (4\pi/3)^{1/3} (Ze)^2 n. \quad (5)$$

We can check up whether this is indeed an estimate from above for surface tension of a SCP by comparing (5) with the numerical results obtained within the framework of the density functional theory for surface energy of a classical one-component plasma.¹⁸ This approach yields quite good estimates for surface tensions of simple liquid metals. Formulation of the one component plasma problem (ions in the field of rigid compensating charge background, the latter having a step-function density profile) allows one to calculate surface energy for any values of Γ , even for low ones, which would not normally correspond to a liquid state of a SCP.

Surface energy E_s is normalized in¹⁸, to produce a dimensionless characteristic equal to

$$U_s = \frac{E_s}{a_i n T}. \quad (6)$$

Substituting into Eq. (6) $E_s = S_m$, where S_m is given by (5), we obtain: $U = 1.6 \cdot \Gamma$. With Γ varying in the range from 3 to 30, this estimate for U varies between 5 and 50. However, the results of¹⁸ (as well as those obtained by other authors and cited therein) yield the values for U in this range of Γ well below unity, mostly about 0.5. This confirms that (5) is indeed an estimate from above for S .

We can now substitute (5) into (2) to obtain the estimate from above for λ_{min} :

$$\lambda_{min} < \frac{2^{4/3} \pi^{7/6}}{3^{1/6}} \frac{Ze}{(m_i g)^{1/2}} = \frac{3Z}{[A \cdot (g/10^{14} \text{ cm/sec}^2)]^{1/2}} \mu\text{m}, \quad (7)$$

A being the atomic mass of the accelerated plasma.

Equation (7) demonstrates that possible stabilizing effect of surface tension is limited to very short waves. Let us estimate its right-hand side for the experimental conditions of.⁸ This experiment had been performed with polystyrene foils (average atomic mass A is about 6) at temperatures below 3 eV (hence, Z is not likely to exceed unity) and typical acceleration $g = 8.5 \cdot 10^{14} \text{ cm/sec}^2$. Equation (7) demonstrates, that surface tension stabilization could be effective there for wavelengths smaller than (or, at least, of order of) $0.4 \mu\text{m}$. Stabilization of perturbations with $\lambda = 50 \mu\text{m}$ by this mechanism therefore appears impossible.

For the sake of completeness, however, the only result that does not fit into the described scheme should also be cited. I refer to surface tension at pusher-fuel interface,

calculated in¹⁹ by means of particle simulation. This calculation has been done for pusher plasma with $\Gamma = 3$, $T = 200$ eV, $Z = 5$ (that is, $n = 1.1 \cdot 10^{24}$ cm⁻³) and fuel plasma with $Z = 1$ at temperature and pressure equilibrium with it (which corresponds to $n = 3.3 \cdot 10^{24}$ cm⁻³). The plasma with moderate value of Γ , of course, is not supposed to turn into liquid state. Here, the surface tension emerges as an interface effect, just like contact potential. [To provide quasi-neutrality, electron density should be higher at the pusher side of the interface by factor $2Z/(Z + 1) = 1.8$, and to maintain this in thermodynamic equilibrium, potential on the fuel side should be accordingly lower]. The calculated contact potential is indeed very close to plasma temperature T expressed in eV.

Estimating the surface tension, one would naturally expect something of order of $S = T \cdot n^{2/3}$. For the above conditions, this amounts to $7 \cdot 10^6$ dyn/cm, and the value of the quantity S/ρ , relevant for stabilization, about $6.6 \cdot 10^5$ cm³/sec². However, the result of¹⁹ reads:

$$S/\rho^3 = 3 \cdot 10^8 \text{ cm}^3/\text{sec}^2, \quad (8)$$

Dimensionality of the right-hand side of Eq. (8) indicates an error in the left-hand side: the power of ρ should be -1, not -3 [this is also suggested by Eq. (2)]. If we attempt to correct Eq. (8) accordingly, then we are left with enormous value of surface tension, 500 times greater than the above estimate (it corresponds to the energy required for pulling one additional ion to the surface from the fuel side of about 100 keV!). If correct, this would mean suppression of the RT instability at the pusher-fuel interface for perturbation wavelengths below 30 μ m with $g = 10^{15}$ cm/sec², - in other words, almost complete stabilization of this interface. Importance of this discovery for laser fusion studies would need no explanation.

In my opinion, however, the value of S/ρ cited in Ref. 19, is simply erroneous. This is indirectly confirmed by the fact that none of the authors of¹⁹ did mention it in any of the subsequent publications. In particular, no stabilizing effect of surface tension has been discussed in their papers about RT instability on the pusher-fuel contact surface of stagnating targets^{20,21}, where a surface tension term of order of (8) would have drastically changed most of the results.

3. Viscosity

Here we consider possible stabilizing influence of viscosity. It is well known that plasma viscosity given by the classical, Braginskii's formulae²², which is proportional to $T^{5/2}$, is very small at comparatively low temperatures characteristic of ablatively accelerated targets, and therefore definitely insufficient for stabilization. However, plasma transition into a liquid-like state should also be considered (see above), and viscosity of a liquid is larger than that of a gas. It should be estimated whether the liquid viscosity could be large enough to suppress the RT instability effectively.

Dimensionality of kinematic viscosity is [length squared/time] - that is, it equals the square of characteristic length l_0 divided per characteristic time τ_0 :

$$\nu = l_0^2/\tau_0, \quad (9)$$

To make a reasonable estimate with (9), one should define l_0 and τ_0 in an appropriate way for a liquid.

For this purpose, the results of conventional theory of simple liquids are used. Recall that the main structural properties of simple liquids are determined by "harsh repulsion that appears at short range and has its physical origin in the overlap of the outer electron shells",¹⁷ whereas the long-range attractive forces, which vary much more smoothly with the distance between the particles, form essentially uniform background and provide stability of the fluid. The strength of repulsion is represented, for instance, by the high negative power of r in the known 12-6 potential of Lennard-Jones

$$U(r) = 4\epsilon \left[\left(\frac{\delta}{r} \right)^{12} - \left(\frac{\delta}{r} \right)^6 \right], \quad (10)$$

where ϵ is the depth of potential well, and δ is the collision diameter, which corresponds to separation between the particles for which potential $U(r)$ has a minimum. The natural unit of time τ_0 associated with the potential (10) is¹⁷

$$\tau_0 = \left(\frac{m\delta^2}{48\epsilon} \right)^{1/2}, \quad (11)$$

where m is the mass of an atom (ion) or a molecule, and the large numerical factor 48 emerges as product of 4 and 12, when $U(r)$ given by (10) is differentiated. This factor decreases τ_0 and hence increases viscosity given by (9). The gas-kinetic estimates of kinematic viscosity, performed without this factor, yield reasonable values for gaseous plasmas,²² but would underestimate viscosity of a liquid by about an order of magnitude. The characteristic energy ϵ is estimated below by temperature T , which appears to provide a correct order of magnitude for most cases.

To assess the value of the parameter δ in a conservative way, minimizing the risk of underestimating it, let us assume

$$\delta = 2a_i, \quad (12)$$

where $a_i = (3/4\pi n)^{1/3}$, as above, n being the number density of atoms or molecules in the simple fluid. Substituting (11), (12) into (9), we obtain a very simple formula

$$\nu = \frac{2^{7/3} 3^{5/6}}{\pi^{1/3}} \left(\frac{T}{m} \right)^{1/2} n^{-1/3} = 9 \cdot 10^{-4} \frac{[T(K)]^{1/2}}{\rho^{1/3} A^{1/6}} \text{ cm}^2/\text{sec}, \quad (13)$$

where ρ is the density of the liquid, A is the atomic mass.

Indeed, Eq. (13) provides quite reasonable estimates for kinematic viscosity of simple fluids. For liquid argon at $T = 84$ K ($\rho = 1.36$ g/cm³, $A = 39$), estimate (13) yields $4 \cdot 10^{-3}$ cm²/sec, whereas the measured value is $2 \cdot 10^{-3}$ cm²/sec. For liquid nitrogen at $T = 63$ K ($\rho = 0.87$ g/cm³, $A = 28$) we have 4.3 and $4.4 \cdot 10^{-3}$ cm²/sec, respectively. For liquid sodium at $T = 371$ K ($\rho = 0.92$ g/cm³, $A = 23$) - 10 and $7.6 \cdot 10^{-3}$ cm²/sec. For water at $T = 293$ K ($\rho = 1$ g/cm³, $A = 18$) - 9.5 and $10 \cdot 10^{-3}$ cm²/sec. For mercury at $T = 293$ K ($\rho = 13.6$ g/cm³, $A = 201$) - 3 and $1.2 \cdot 10^{-3}$ cm²/sec. For alcohol at $T = 293$ K ($\rho = 0.81$ g/cm³, $A = 46$) - 1 and $2.2 \cdot 10^{-2}$ cm²/sec.

It should be stressed that applicability of the estimate (13) is limited to simple liquids only. One can see that dependence of the right-hand side of (13) on both ρ and A is rather

weak, implying that all simple liquids at the same temperature should have comparable kinematic viscosities. This assumption is obviously not true when applied, say, to glycerine, whose kinematic viscosity at room temperature exceeds that of water by almost 3 orders of magnitude. For large, especially organic, molecules, both our estimates of l_0 and τ_0 fail: these molecules represent long chains or other structures, whose spatial dimensions are much larger than one can estimate from their known number density. In addition, their interaction is not described by some simple pair potential like (10), because these structures are capable by interacting by many different links simultaneously. Hence, the effective values of l_0 could be much larger and those of τ_0 - much smaller than estimated above, which would result in much larger viscosity.

However, at present there is no indication (and no apparent reason to believe) that strongly coupled plasmas at moderate values of Γ form large multi-ion structures like organic molecules, and this possibility will not be discussed below. This type of collective behavior will be partly addressed in the next Section, where we deal with frozen plasma substance, viscosity being replaced by rigidity, a much stronger effect. For the moment, we continue to work with the estimate (13).

It is interesting to compare (13) with the available theoretical results of calculation of shear viscosity for strongly coupled plasmas, cited in.²³ A dimensionless parameter (reduced viscosity η^*) used in²³ is defined as

$$\eta^* = \frac{\nu}{\omega_p a_i^2}, \quad (14)$$

where $\omega_p = [4\pi n(Ze)^2/m]^{1/2}$, ν and a_i meaning the same as above - kinematic viscosity and mean ion radius, respectively. Substituting expression (13) into (14), we obtain the following estimate for η^* :

$$\eta^* = 8/\Gamma^{1/2}. \quad (15)$$

Comparing (15) with the results cited in²³, we see that (13) indeed represents an estimate from above. Though various theoretical estimates for η^* spread over a broad range, and differ by factor exceeding 4 for some values of Γ , they all are considerably lower than that given by (15). For Γ equal to 4, 10 and 20, ratio of the right-hand side of (15) to the largest of these estimates (0.23, 0.102, and 0.097) equals 17, 25, and 12, respectively.

Now we can use (13) to estimate the range of wavelengths effectively stabilized by the viscous mechanism under typical conditions of ablative acceleration. It is well known that viscosity, unlike surface tension, does not suppress RT instability completely: rather, it substantially decreases the growth rates for sufficiently short wavelengths, whose wavenumbers are of order of (or greater than) $k = k_m = (g\nu^2)^{1/3}$.¹⁶ The corresponding characteristic wavelength λ_m is found from (13):

$$\begin{aligned} \lambda_m &= 2^{23/9} 3^{5/9} \pi^{7/9} (T/mg)^{1/3} n^{-2/9} \\ &= 0.5 \left[\frac{T(\text{eV})}{A(g/10^{14} \text{cm/sec}^2)} \right]^{1/3} \left(\frac{n}{5 \cdot 10^{22} \text{cm}^{-3}} \right)^{-2/9} \mu\text{m}. \end{aligned} \quad (16)$$

These are evidently too short wavelengths for effective stabilization of ablatively accelerated targets. In particular, substituting into (16) the characteristic values estimated for⁸

($T = 2.4$ eV, $A = 6$, $g = 8.5 \cdot 10^{14}$ cm/sec², n about $5 \cdot 10^{22}$ cm⁻³), we see that the viscous stabilizing mechanism could be effective for wavelengths well below $1 \mu\text{m}$. Recall that (13) (as compared to rigorous SCP calculations) overestimates kinematic viscosity by an order of magnitude. To provide appreciable stabilization of perturbations with $\lambda = 50 \mu\text{m}$, the kinematic viscosity should be larger at least by 3 orders of magnitude than estimated by (13) - this is about the same difference as between viscosities of water and glycerine. One can conclude that if the strongly coupled plasma were a simple fluid, the results of⁸ are impossible to explain by viscous stabilization.

To make the discussion complete, let us study now another possible method of using viscosity for stabilization. We can consider an interface between relatively cold accelerated plasma, where most of the mass is concentrated, and hot low-density plasma, whose kinematic viscosity could be high. In other words, an interface can separate regions where inertia and viscosity, respectively, dominate. One can try to find out whether this way of distributing viscosity and inertia could stabilize the interface.

In the first paper where the influence of viscosity on the eigenmodes of an interface between to incompressible fluid has been studied,²⁴ it was correctly stated that decay of wave motion at the interface between two fluids due to viscosity was much more pronounced than in the case of a single fluid surface. The explanation is: "When there is a wave motion at the interface between two non-viscous fluids, the tangential velocities at the interface are different; in viscous motion, they must be the same. ... We have the result that, in general, wave motion at the interface between two fluids dies away much more rapidly than in the case of a single fluid." Since then, no particular attention has been paid to the influence of viscosity distribution between the two sides of the interface. The calculations aimed at interpretation of experimental results were done mainly for the typical case of the total viscosity acting in the heavy fluid, as in the case of glycerine-air interface (e.g., see²⁵). In the classical monograph¹⁶ influence of viscosity on development of the RT instability is studied assuming equal kinematic viscosities at both sides of the interface, $\nu_1 = \nu_2$ - "one would not expect that any of the essential features of the problem would be obscured by this simplifying assumption"¹⁶. Though the latter statement is basically correct, it is instructive to show how the distribution of kinematic viscosities over the two fluids affects the overall stabilization.

To do this, we start with the exact dispersion relation, derived in²⁴ and reproduced in¹⁶. It would be convenient to use dimensionless variables. Let us express the growth rate σ as $\sigma^2 = gk\mu^2$, where μ is a dimensionless eigenvalue (real values of μ correspond to unstable modes). Let the characteristic kinematic viscosity ν be distributed as follows: $\nu_1 = (1-s)\nu$, $\nu_2 = s\nu$ (the latter corresponds to heavy fluid), $0 \leq s \leq 1$. Dimensionless wavenumber expressed in units of $(g/\nu^2)^{1/3}$ is denoted by κ . Then the dispersion equation can be presented as

$$\frac{1}{2}(\mu^2 - A)[q_1 + q_2 - 2 + A(q_1 - q_2)] + \mu^2(1 - A^2) - \mu\kappa^{3/2}(1 - A - 2s)[q_1 - q_2 + A(q_1 + q_2 - 2)] - \kappa^3(1 - A - 2s)^2(q_1 - 1)(q_2 - 1) = 0, \quad (17)$$

where

$$q_1 = \left[1 + \frac{\mu}{\kappa^{3/2}(1-s)}\right]^{1/2}, \quad q_2 = \left(1 + \frac{\mu}{\kappa^{3/2}s}\right)^{1/2},$$

$A = (\rho_2 - \rho_1)/(\rho_2 + \rho_1)$ being the Atwood number.

Instead of solving Eq. (17), it is convenient to obtain the dispersion curves in a parametric form, which could be easily done without solving anything, in the same way as done in¹⁶ for $\nu_1 = \nu_2$. For this, we denote $y = \mu/\kappa^{3/2}$, and rewrite (17) as a system:

$$\kappa^3 = \frac{M(y)}{N_1(y) + N_2(y) + N_3(y)}, \quad (18)$$

$$\sigma = y \cdot \kappa^2, \quad (19)$$

where

$$\begin{aligned} M(y) &= A[q_1 + q_2 + A(q_1 - q_2)], \\ N_1(y) &= y^2 \cdot [q_1 + q_2 + A(q_1 - q_2 - 2A)], \\ N_2(y) &= 2y(2s + A - 1)[q_1 - q_2 + A(q_1 + q_2 - 2)], \\ N_3(y) &= -2(2s + A - 1)^2(q_1 - 1)(q_2 - 1); \\ q_1 &= \left(1 + \frac{y}{1-s}\right)^{1/2}, \quad q_2 = \left(1 + \frac{y}{s}\right)^{1/2}, \end{aligned}$$

parameter y varies from 0 to ∞ and the growth rate σ in (19) is expressed in appropriate units of $(\nu/g^2)^{1/3}$.

Though it is quite easy to study the general case, the two following limiting cases are particularly instructive. Let us first suppose $s \rightarrow 0$ (all the viscosity is assigned to a light fluid). Then Eq. (18) is reduced to

$$\kappa^3 = \frac{A}{y^2 + 2(1-A)(y+1-\sqrt{y+1})}. \quad (20)$$

For long perturbation wavelengths ($y \gg 1$) the second term in the denominator of the right-hand side of Eq. (20) is small compared to the first one, hence $\kappa^3 \simeq A/y^2$, and substituting it into (19), we find:

$$\sigma \simeq (A\kappa)^{1/2} \quad (21),$$

that is, the classical RT growth rate is reproduced asymptotically. In the opposite limiting case of short wavelengths ($y \ll 1$) the second term dominates, and we obtain:

$$\sigma \simeq \frac{A}{1-A} \kappa^{-1}, \quad (22)$$

which means that the growth rate decreases as κ^{-1} for large wavenumbers.

However, the asymptotic expression (22) is obviously invalid for $A = 1$. Returning to (20) we find that in this case the second term vanishes identically, so that the right-hand side of (21) (where $A = 1$) represents the growth rate (exactly, not approximately). Consequently, in this particular case there is no viscous stabilization, though viscosity is nonzero!

Consider now the case of massless fluid 2 ($A=1$) without assuming $s = 0$. We obtain instead of (20):

$$\kappa^3 = \frac{A}{y^2 + 4s(y + s - s\sqrt{y+1})}. \quad (23)$$

Here again, for long wavelengths expression (21) (with $A = 1$) is reproduced, whereas for short wavelengths

$$\sigma = \frac{1}{2s(2-s)} \kappa^{-1}. \quad (24)$$

In general, this is similar to (22). However, (24) is invalid for $s = 0$. Returning to (23), we conclude that this case corresponds to absence of stabilization, the classical RT growth rate being the exact eigenvalue - in agreement with the above.

Therefore viscosity of infinitely light fluid does not contribute to stabilization: with $A = 1$, only viscosity of heavy fluid matters. Similarly, if only viscosity of the light fluid is appreciable, its stabilizing effect vanishes in the limit $A \rightarrow 1$. To make the latter statement more precise, one can use Eqs. (19)-(20) to calculate the wavelength λ_{max} corresponding to maximum growth rate. Assuming $1 - A \ll 1$, we find that

$$\lambda_{max} \simeq \lambda_m [\sqrt{2}(1-A)]^{2/3}. \quad (25)$$

For instance, with $A = 0.9$ we find that the wavelengths effectively stabilized by viscosity are about 4 times shorter than predicted by the simple estimate, which is based on dimensionality [namely: wavelengths shorter than or of order of $\lambda_m = 2\pi(\nu^2/g)^{1/3}$]-and correct almost always - except the limiting case discussed above. This is illustrated by Fig. 1, where growth rates σ are plotted for $s = 0$ (all the viscosity attributed to the light fluid) as functions of dimensionless wavenumber κ . The curves are marked by respective Atwood numbers. With A close to unity, stabilization is accordingly less effective.

The above discussion indicates that viscous stabilization of ablatively accelerated targets in some sandwich configuration, with large viscosity of a relatively light layer, would be much more difficult than one might have expected without this analysis, the effective viscosity being diminished by factor of order of $(1-A)^{1/3}$.

4. Rigidity

In Section 1 a transition of a strongly coupled plasma into solid state has been mentioned. Here we are going to consider stabilizing effect which might be caused by rigidity of some frozen layer of the accelerated plasma.

It should be stressed that freezing of a SCP with Γ below 20 seems extremely unlikely. To show this, let us make the most simple estimate of the freezing temperature, based on the known Lindemann melting criterion.²⁶ The latter states that a crystalline solid melts when average displacement of atoms (ions) due to thermal motion $\langle r \rangle$ exceeds a certain fraction ϵ_L of the interatomic distance (for most metals, ϵ_L is about 0.2). Let us estimate melting temperature of a crystalline SCP, using the Einstein's oscillatory model to assess the displacements:

$$\frac{1}{2} k \langle r \rangle^2 = \frac{3}{2} T, \quad (26)$$

where k is the effective elastic coefficient, whose dimensionality is [energy/length squared]. For SCP, the latter should be therefore of order of

$$k = \frac{(Ze)^2}{a_i^3}. \quad (27)$$

Substituting (27) into (26), we can express Lindemann criterion as an equality for Γ (for lower values of Γ a solid phase cannot exist):

$$\Gamma > 3/\epsilon_L^2 \quad (28)$$

With $\epsilon_L = 0.2$ we find: $\Gamma > 75$. This appears to be a very low estimate. Both theoretical and experimental results available indicate that freezing occurs for Γ well over 100. (For instance, Wigner crystallization in 2-D systems of electrons is observed at $\Gamma = 135$, see.¹² For a strongly coupled one-component plasma, first-order freezing transition is predicted at $\Gamma = 178 - 180$ ^{27,28}). Though exact evaluation of freezing temperature very complicated (liquid and solid energy curves are almost parallel near the transition point, a metastable glass phase can emerge, etc.), freezing at Γ about 20 appears to be unlikely. However, even this slight chance should be accounted for in an appropriate way.

To do this, let us consider perturbations of an isothermal layer of ideal gas. The gas occupies space between $z = 0$ and $z = d$ in a constant gravitational field g directed toward negative z and is supported from below by the pressure of a massless fluid, exhibiting thereby a RT instability. The sound speed c_0 is constant due to uniformity of temperature. We introduce a length scale $H = 2c_0^2/g$ and note that unperturbed profiles of both pressure and density are exponential (Boltzmann's equilibrium), with characteristic height $H_B = H/2\gamma$, γ being the adiabatic exponent of the gas. (The limit of incompressible fluid corresponds to $c_0, H, \gamma \rightarrow \infty$.) A dimensionless eigenvalue μ is introduced in the same way as above: $\sigma^2 = gk\mu^2$, σ being the growth rate.

Performing a standard perturbation analysis [the exponential factor $\exp(ikz + \sigma t)$ is omitted below], we find vertical displacement ξ :

$$\xi = C_1 \exp(k\kappa_1 z) + C_2 \exp(k\kappa_2 z), \quad (29)$$

where

$$\kappa_{1,2} = \frac{1}{kH} \left(1 \pm \sqrt{k^2 H^2 + 2\mu^2 kH + 1} \right),$$

(in the limit of incompressible fluid $\kappa_1 = 1$, $\kappa_2 = -1$), the constants C_1 and C_2 being determined by the boundary conditions. Pressure perturbation in a fluid particle is given by

$$\delta p = -\rho^{(0)} c_0^2 \frac{\mu^2 (d\xi/dz) + k\xi}{\mu^2 + kH/2}, \quad (30)$$

where $\rho^{(0)}$ is unperturbed density. We are interested in instability modes, with real μ , so that the denominator in the expression for δp is nonzero.

We suppose the lower boundary ($z = 0$) to be free, that is, $\delta p(0) = 0$. This boundary condition allows one to present (29) in the form

$$\xi = (\mu^2 \kappa_2 + 1) \exp(k \kappa_1 z) - (\mu^2 \kappa_1 + 1) \exp(k \kappa_2 z), \quad (31)$$

which contains no arbitrary constants (an arbitrary factor is inessential) except the eigenvalue μ to be determined from the boundary condition at the upper boundary.

The most simple case is free upper boundary:

$$\delta p(d) = 0. \quad (32)$$

Substituting (30), (31) into (32), we obtain:

$$(\mu^2 \kappa_1 + 1)(\mu^2 \kappa_2 + 1) = 0, \quad (33)$$

which is easily shown to be equivalent to $\mu^4 = 1$, or

$$\sigma = \sqrt{gk} \quad (33a)$$

$$\sigma = -\sqrt{gk} \quad (33b)$$

and

$$\sigma = \pm i\sqrt{gk} \quad (33c)$$

(the sonic solution $\mu^2 = -kH/2$, which is the same as $\sigma = \pm ic_0 k$ is discarded here, because it makes denominator of the right-hand side of Eq. (30) vanish). Here the exponentially growing solution (33a) represents the global RT mode. Both it and the exponentially decaying mode (33b) correspond to perturbations, exponentially decreasing with increased distance from the lower surface. There are also two oscillatory solutions (33c), which represent surface (Rayleigh) waves localized near the upper boundary of the fluid, the corresponding eigenfunctions exponentially decreasing with increased distance from it.

The case of upper boundary represented by a rigid ceiling corresponds to the boundary condition

$$\xi(d) = 0. \quad (34)$$

Substituting (31) into (34), we obtain the dispersion relation in the form

$$\ln \frac{\mu^2 \kappa_1 + 1}{\mu^2 \kappa_2 + 1} = \frac{2d}{H} \sqrt{k^2 H^2 + 2\mu^2 kH + 1}. \quad (35)$$

Equation (35) is easily solved in the limit of incompressible fluid ($\kappa_{1,2} = \pm 1$, the right-hand side of (35) equal to $2kd$): $\mu^2 = \tanh(kd)$. Thus for the exponentially growing solution the growth rate is given by

$$\sigma = [gk \tanh(kd)]^{1/2}. \quad (36)$$

For short waves ($kd \gg 1$, $\tanh(kd) \simeq 1$) expression (33a) is reproduced, as it should be: the corresponding eigenfunctions decay at short distance (of order of $1/k$) from the

unstable boundary and do not "feel" the presence of the ceiling. For long waves ($kd \ll 1$, $\tanh(kd) \simeq kd$) there is some stabilizing effect:

$$\sigma \simeq k\sqrt{gd}, \quad (37)$$

the growth rate is proportional to k , not to $k^{1/2}$, that is, the smaller k , the more pronounced is the stabilizing effect. Essentially the same result is found for finite γ , without the simplifying assumption of incompressibility: σ is proportional to k for small k , whereas for large k it is given by (33a).

Let us suppose now that the fluid is bounded from above by a layer of solid material. The latter cannot be regarded as absolutely rigid (no material is rigid in a gravitational field of order of 10^{14} cm/sec²). Rather, it should be considered elastic, and the fluid equations should be solved simultaneously with the equation of motion of the layer (elastic plate) on the top. The latter can be written in the form²⁹

$$\rho_m h \frac{\partial^2 \xi}{\partial t^2} + D \Delta^2 \xi = \delta p, \quad (38)$$

where ρ_m is the density of the plate, h is its thickness, Δ is the Laplace operator, δp [see (30)] is taken for $z = d$,

$$D = \frac{Eh^3}{12(1 - \sigma_p^2)} \quad (39)$$

is the so-called flexural rigidity or cylindrical rigidity of the plate, E being the Young's modulus, and σ_p - the Poisson's ratio of the plate material.

After some algebra, we obtain the dispersion relation in the form similar to (35):

$$\ln \frac{(\mu^2 \kappa_1 + 1)B_2}{(\mu^2 \kappa_2 + 1)B_1} = \frac{2d}{H} \sqrt{k^2 H^2 + 2\mu^2 kH + 1}. \quad (40)$$

Here

$$B_{1,2} = \gamma(\mu^2 \kappa_{1,2} + 1) + [\mu^2 + (kl)^3](\mu^2 + kH/2),$$

and

$$l = h \left(\frac{E}{12(1 - \sigma_p^2)\rho_m gh} \right)^{1/3}$$

We see that in the limit of infinitely high rigidity of the plate $l \rightarrow \infty$ $B_2/B_1 \rightarrow 1$, and Eq. (40) is reduced to (35), as it should be.

To study the effect of finite rigidity, we again suppose the fluid to be incompressible. This allows us to present (40) as a quadratic equation:

$$\mu^4[\alpha + \tanh(kd)] + \mu^2\alpha[\beta - \tanh(kd)] - (\alpha\beta + 1)\tanh(kd) = 0, \quad (41)$$

where

$$\alpha = (\rho_m / \rho^{(0)})kh, \quad \beta = (kl)^3,$$

and the value of unperturbed density $\rho^{(0)}$ is taken at $z = d$.

Note that the terms containing α and β represent different kinds of influence of the top plate on the dispersion relation. The term α accounts for additional inertia due to loading the top of the fluid with some material which is not a fluid. The term β is proportional to D and represents rigidity. We see that due to high power of k [which stems from the Δ^2 term in the equation of motion (38)] β is negligible in the long-wavelength limit, no matter how large the cylindrical rigidity is, and therefore, rigidity does not effectively contribute to stabilization. Solving (41) in the limit $k \rightarrow 0$, we find the growth rate

$$\sigma = \sqrt{A_{eff} g k}, \quad (42)$$

where the effective Atwood number

$$A_{eff} = \frac{1}{1 + (\rho_m h / \rho^{(0)} d)}. \quad (43)$$

Therefore, the stabilizing effect of rigidity is reducing the growth rate by a numerical factor of order unity (namely, by square root of the effective Atwood number (43)). To make this effect large (and A_{eff} accordingly small), most of the target mass should be frozen, which is hardly possible.

On the other hand, in the short-wavelength limit (large β) the classical RT growth rate (33a) is asymptotically approached, and though stabilization by elastic plate on top in this limit is almost as effective as stabilization by rigid ceiling, the latter is not effective at all, see above.

To plot the dispersion curves, we must estimate l . The Young's modulus (whose dimensionality is energy/volume) would be correctly estimated by density of binding energy (e.g., for most metals binding energy per ion is about 10 eV, and number density of ions - about $5 \cdot 10^{22} \text{ cm}^{-3}$, the product of the two numbers, 0.8 Mbar, being indeed close to their Young's moduli), that is, by n times the right-hand side of Eq. (4)

$$E = n \frac{(Ze)^2}{a_i} = \Gamma n T. \quad (44)$$

Recall that the Poisson's ratio σ_p for most materials is below 0.3, so that the denominator of (39) is at least about 8. The energy density given by (44) is not likely to be more than one order of magnitude higher than the pressure $\rho_m g h$ at the interface between the plate and the fluid. Therefore, h would be a reasonable estimate for l , rather an estimate from above. Substituting h instead of l into the definition of β , we can solve Eq. (41) and plot the dispersion curves.

The curves are presented in Fig. 2. Here the growth rate σ expressed in units of $\sqrt{g/d}$, is plotted versus $\kappa = kd$. Curve 1 corresponds to (33a) (no stabilization), curve 4 - to (36) (rigid ceiling). The curves 2 and 3 are plotted for $h = d$, and the ratio $\rho_m h / \rho^{(0)} d$ equal to 1 and 2, respectively. Though these parameters appear to be quite generous (more than a half of the target mass is supposed to be frozen), stabilization - that is, the difference between curve 1 and curves 2, 3, - is not particularly impressive. This is, of course, due to the fact mentioned above: for low k , the dispersion curves 2 and 3 behave like curve 1, and not like curve 4, whereas for large k all of them behave similarly.

Consequently, even if partial freezing of the ablatively accelerated plasma is supposed (which is itself very questionable), there is no reason to believe it would be effective for suppressing the RT instability of the target.

5. Compressibility and thermal conductivity

Modification of the equation-of-state and of plasma thermal conductivity (the reason why the two are combined is explained below) is not likely to produce any appreciable stabilizing effect. Basically, there are two reasons for this. First, both effects are relatively small. Second, they appear to have a wrong sign.

It is known (mainly from astrophysical works like³⁰) that in a linear stability problem formulated for planar geometry parallel heat conductivity could be accounted for in the perturbation equations derived for ideal fluid, with renormalized adiabatic exponent γ :

$$\gamma \rightarrow \gamma_{eff} = \gamma \frac{Pe + 1/\gamma}{Pe + 1}, \quad (45)$$

where the parameter Pe (Peclet number) is defined as

$$Pe = \sigma/k^2 \chi_T, \quad (46)$$

χ_T being the temperature conductivity. The parameter Pe depends on plasma density and temperature, and is therefore a function of σ and z . Note that when $\gamma_{eff}(z; \sigma)$ is substituted into the perturbation equations, the corresponding boundary-value problem is no longer self-adjoint. Now γ enters the equations together with γ^2 , so that the eigenvalue γ must be complex (together with Pe and γ_{eff}). However, in the limit of very high parallel thermal conductivity $Pe \rightarrow 0$ we have: $\gamma_{eff} \rightarrow 1$. This is a real value, so that one may conclude that the influence of parallel heat conductivity, whenever it is large, is in effectively increasing compressibility of the fluid by decreasing γ .

It has been shown in³¹, that the instability growth rate σ increases with decreasing γ . A rigorous foundation of this result is found in³², where the inequality $\partial\sigma/\partial\gamma \leq 0$ is derived from the energy principle under quite general assumptions. A simple qualitative explanation is given in³¹, where the RT instability is compared to the instability of an inverted pendulum. If the pendulum is rigid, then all its parts move at the same angular velocity. However, if it consists of parts capable of falling separately, like a brick smokestack, then it is faster destroyed by a small perturbation. Note that this analogy is adequate only when the global RT mode cannot develop - otherwise, it is the rigid pendulum that falls faster. The increase in growth rate is limited anyway. For the problem considered above (isothermal plasma in the upper half-space supported from below by the pressure of a massless fluid) the increase of growth rate due to decrease of γ from ∞ to 1 is about 25%, see³³.

The starting point of the above discussion was the effective increase in compressibility due to parallel thermal conductivity. All of this is equally applicable to modification of the equation of state due to the SCP effects. The attraction between electrons and ions tends to decrease pressure at the given temperature, and hence, increase compressibility, which could slightly increase the instability growth rates. However, we have seen that even opposite sign of the SCP effects, making the accelerated fluid incompressible, would

not help much. Therefore no more details are needed to conclude that any possible SCP-related modification of plasma compressibility and thermal conductivity would not provide a stabilizing effect, simply because both compressibility and heat conductivity have little effect on the growth rates of dominating eigenmodes.

6. Interpretation of the '87 experiment

In the experiment⁸ no growth rate for the ablative RT instability was experimentally observed at 50- μm perturbation wavelength, though 100- and 150- μm RT modes grew at predicted rates. These results have been surprising for many people involved in laser fusion research, and remain largely unexplained since '87.

In my opinion, experimental results of⁸, accurate as they are, do not represent conclusive, unambiguous evidence for the lack of growth of the 50- μm mode. The conclusion is largely a matter of interpretation. Recall that the experimental and numerical work⁸ addressed several important issues at once, studying the dependence of the growth rates on the wavelength, laser irradiance profile [either smoothed or not by the induced spatial incoherence (ISI) method], and position of the grooves on the front or rear side of the target. However, the experimental data is limited both in amount and, which is even more important, in observation time compared to the e-folding time of the RT instability. Due to all of this, interpretation of the experimental data is far from being straightforward.

The two following points appear to be particularly important.

First, the observed lateral redistribution of mass over the target surface is not necessarily a trademark of the RT instability. Under the experimental conditions of⁸, the redistribution should take place without any instability, being caused only by the shape of the target.

Second, if the observation time does not exceed many (not just 2-3) e-folding times of the dominating instability mode, then the inherent uncertainty of the estimate of a growth rate is very large.

Let us elaborate starting with the first point. Consider acceleration of a target with grooves on its front side (Fig. 3). Suppose we are able to eliminate instability of the laser-irradiated surface by introducing an (imaginary) thin foil F , which transmits applied pressure but suppresses instability. (The same could be done with a glass filled by water, covered by a sheet of paper and then turned upside down). Note that light and heavy (that is, thin and thick) parts of the target would still have different velocities and accelerations, since they are driven by essentially the same ablative pressure p . The light parts are accelerated faster, rising above the heavy ones in the effective gravitational field g . The accelerated material (which at this stage could be regarded as something quite close to an incompressible fluid) would flow in the lateral direction (v vectors), trying to arrange the fluid level at an equipotential surface, as it should be in equilibrium in a gravitational field. This means loss of mass per unit area in the light parts of the target, and gain in the heavy side. Thus development of an instability is simulated, though no real instability is present.

Consider now acceleration of a target with grooves on its rear side (Fig. 4). Now the upper fluid level in the heavy parts is higher than that in the light parts, initially by the depth of the grooves Δh . This creates a lateral flow from the heavy parts to the light ones. However, the light parts move faster, rising the upper fluid level accordingly. Acceleration

g is inversely proportional to initial thickness, hence

$$\frac{\Delta(gt^2/2)}{gt^2/2} = \frac{\Delta g}{g} = \frac{\Delta h}{h}, \quad (45)$$

where h is the average thickness of the target, g is average acceleration. The time required for the light parts to catch up the upper level of the heavy ones is found from $\Delta(gt^2/2) = \Delta h$, which implies $gt^2/2 = h$ [see (45)], or

$$t = \sqrt{2h/g}. \quad (46)$$

On the other hand, the lateral fluid flow trying to establish its equilibrium upper level is carried by gravitational waves in a "shallow water", whose wavelength λ is much greater than the effective depth h , and velocity is³⁴

$$v = \sqrt{gh}. \quad (47)$$

[this is the same as Eq. (37) with inverted sign of g].

The width of the heavy part of the square-wave pattern is $\lambda/2$. Mass flows out from both sides of it, so that lateral mass redistribution is expected to complete during the time interval (46), if

$$vt > \lambda/4, \quad (48)$$

or

$$\lambda < 4\sqrt{2}h. \quad (49)$$

Substituting here $h = 10 \mu\text{m}$ ⁸, we find: $\lambda < 56 \mu\text{m}$. Thus the observed lack of growth of the 50- μm mode (with 100- and 150- μm modes growing all right) may be not much of a surprise.

In the real experiment⁸ there was no foil F stabilizing the front surface. And here we come to the second point mentioned above. Indeed, we observe (when we do) a perturbation growth. How can we know that this is a growth of a given particular mode? This question is easily answered only for some numerical works, when an unperturbed state is time-independent, so that if one perturbs the system and can wait long enough, he can reasonably expect to single out the exponentially growing dominating mode. With dynamic, time-dependent unperturbed states, everything is much more complicated. For instance, the unstable modes may form a continuous spectrum, without any particular mode dominating³⁵. A general method which allows one to find the fastest-growing mode numerically³⁶ requires enormous amount of calculations even for unperturbed states represented by exact analytic formulae. With a more or less arbitrary initial perturbation, the dominating mode remains for a while camouflaged by all sorts of other, stable and unstable modes, and it is often impossible to trace it in the numerical solution of an initial-value problem. This is why specially prepared initial conditions ("quiet start", etc.) are used in most numerical studies of the RT instability to control the development of the dominant mode from the very start.

The paper⁸ presents no details of the numerical calculations done with the FAST2D code to inquire into this matter further. However, the initial state of the target (square-wave pattern) is well known. With the grooves on the rear side (all the experiments with 50- μm mode have been done in this geometry), most of the initial perturbation is localized near the stable upper surface, and therefore contributes mainly to the stable (oscillatory) eigenmodes (33c), and only partly - to the unstable one (33a), see Fig. 5. The running waves (33c) tend to spread perturbation over the whole rear surface. The phase velocity corresponding to the surface waves (33c) is

$$v = \sqrt{g/k}, \quad (50)$$

where $k = 2\pi/\lambda$. Substituting (50) into (48), we obtain: there is enough time for effective spreading of the perturbation over the whole surface, if

$$\lambda < \frac{16}{\pi} h, \quad (51)$$

which is, of course, almost the same as (49) (for $h = 10 \mu\text{m}$ we find: $\lambda < 50 \mu\text{m}$, as it should be). The only difference is that (49) corresponds to rigid bottom F , and (51) - to the case when the bottom is replaced by a RT unstable free surface, but only the oscillating (stable) eigenmodes are excited initially.

Some of the effects discussed here should have been found in numerical simulation of⁸. Though the discussion of numerical results in⁸ is very brief and certainly not sufficient to make conclusions here, this seems to be the case. For instance, the code does not make difference whether the initial perturbations are on the front or the back for 100- μm mode, whereas for the 50- μm mode the perturbation growth is delayed with the grooves on the rear side. Consequently, Fig. 2 of⁸, where observed growth for $\lambda = 100 \mu\text{m}$, grooves on the front side (upper) is compared to no growth for $\lambda = 50 \mu\text{m}$, grooves on the rear side (lower) hardly represents equal growth opportunities for the two wavelengths: the 50- μm mode has been given no chance to develop in the optimal configuration of our Fig. 3.

The above considerations do not aim at providing a comprehensive interpretation of the experimental results given in⁸. All this has been presented only in order to demonstrate that seemingly surprising lack of growth of the 50- μm mode in⁸ could be accounted for within quite conventional concepts. To make everything absolutely clear, to answer all the questions, a good deal of experimental, theoretical and numerical efforts is still required.

7. Conclusion

It has been demonstrated that the strongly coupled plasma effects are insufficient for suppressing ablative RT instability under the typical conditions, which range from the '87 NRL experiment⁸ to the planned NIKE experiments. It has been shown also that no unusual effects (including the SCP effects) may be really needed to account for the seemingly surprising experimental results of⁸, though both new experimental studies and careful analysis are needed to achieve a full understanding.

The aforesaid does not mean that I doubt if further research on the SCP phenomena is really necessary in the context of laser fusion program. Actually, quite the opposite is true. This study has convinced me that the SCP-related effects are the least known in the

field of plasma physics relevant to laser fusion. Consequently, the uncertainty due to poor knowledge of the SCP effects is likely to determine the overall accuracy of many numerical results. One can hardly expect to increase accuracy by refining the hydrodynamic, atomic and optical components of the codes, as long as some of the basic plasma parameters might be known only to a factor of order unity. If the NIKE program aims at quantitative study and detailed understanding, the SCP research should definitely be a part of it.

However, varying any of the plasma parameters within one order of magnitude, being enough to make noticeable changes of the flow profiles, opacity, hydrodynamic efficiency of acceleration, etc., is not sufficient to suppress the RT instability. In my opinion, the latter is possible only with the aid of the so-called hydrodynamic mechanisms which affect the only parameter relevant for the RT - that is, the acceleration g . But discussion of this issue is certainly beyond the scope of the present report.

References

1. K. O. Mikaelian, Phys. Rev. Lett **48**, 1793 (1982).
2. N. A. Inogamov, Prikl. Mekh. Tekh. Fiz. **5**, 110 (1985).
3. D. H. Munro, Phys. Rev. A **38**, 1433 (1988).
4. V. V. Bychkov, M. A. Liberman, and A. L. Velikovich, Phys. Rev. A **42**, 5031 (1990).
5. H. Takabe, K. Mima, L. Montierth, and R. L. Morse, Phys. Fluids **28**, 3676 (1985).
6. A. N. Mostovych, K. J. Kearney, J.A. Stamper, and A. J. Schmitt, Phys. rev. Lett. **66**, 612 (1991).
7. A. N. Mostovych, K. J. Kearney, J. A. Stamper, in *Strongly Coupled Plasma Physics*, edited by S. Ichimaru (North-Holland, Amsterdam, 1990), pp. 589-600.
8. J. Grun, M. E. Emery, C. K. Manka, T. N. Lee, E. A. McLean, A. Mostovych, J. Stamper, S. Bodner, S. P. Obenschain, and B. H. Ripin, Phys. Rev. Lett. **58**, 2673 (1987).
9. S. L. Gilbert, J. J. Bollinger, and D. J. Wineland, Phys. Rev. Lett. **60**, 2022 (1988).
10. L. R. Brewer, J. D. Prestage, J. J. Bollinger, W. M. Itano, D. J. Larson, and D. J. Wineland, Phys. Rev. A **38**, 859 (1988).
11. V. S. Edel'man, Pis'ma Zh. Eksp. Teor. Fiz. **25**, 422 (1977).
12. C. C. Grimes and G. Adams, Phys. Rev. Lett. **42**, 785 (1979).
13. L. Landau and J. Zeldovich, Acta Physicochimica U.R.S.S. **18**, 194 (1943).
14. G. E. Norman and A. N. Starostin, Teplofiz. vys. temp. **8**, 413 (1970).
15. W. J. Nellis, A. C. Mitchell, M. van Thiel, C. J. Devine, and R. J. Trainor, J. Chem. Phys. **79**, 1480 (1983).
16. S. Chandrasekhar, *Hydrodynamic and Hydromagnetic Stability* (Dover Publications, New York, 1981).
17. J. P. Hansen and I. R. McDonald, *Theory of Simple Liquids* (Academic Press, New York, 1987).
18. M. Hasegawa and M. Watabe, op. cit. in⁷, pp. 201-212.
19. H. Furukawa, K. Nishihara, M. Kawaguchi, H. Sakagami, T. Hiramatsu, and H. Yasui, op. cit. in⁷, pp. 613-616.
20. H. Sakagami and K. Nishihara, Phys. Rev. Lett. **65**, 432 (1990).
21. H. Sakagami and K. Nishihara, Phys. Fluids B **2**, 2715 (1990).
22. S. I. Braginskii, in *Reviews of Plasma Physics*, Vol. I (Consultants Bureau, New York, 1965), p. 205.
23. S. Ichimaru, H. Iyetomi, and S. Tanaka, Phys. Reports **149**, 91 (1987).
24. W. J. Harrison, Proc. London Math. Soc. **6**, 396 (1908).
25. R. Bellman and R. H. Pennington, Quart. Appl. Math. **12**, 151 (1954).
26. F. Lindemann, Phys. Z. **11**, 609 (1910).
27. W. L. Slattery, G. D. Doolen, and H. E. DeWitt, Phys. Rev. A **26**, 2255 (1982).

28. S. Ogata and S. Ichimaru, *Phys. Rev. A.* **36**, 5451 (1987).
29. L. D. Landau and E. M. Lifshitz, *Theory of Elasticity* (Pergamon, London, 1959).
30. G. Torricelli-Ciamponi, V. Ciampolini, and C. Chiuderi, *J. Plasma Phys.* **37**, 175 (1987).
31. I. B. Bernstein and D. L. Book, *Phys. Fluids* **26**, 453 (1983).
32. W. A. Newcomb, *Phys. Fluids* **26**, 3246 (1983).
33. D. Parks, *Phys. Fluids* **26**, 448 (1983).
34. L. D. Landau and E. M. Lifshitz, *Hydrodynamics* (Pergamon, London, 1959).
35. A. I. Kleev and A. L. Velikovich, *Plasma Phys. Contr. Fusion* **32**, 763 (1990).
36. A. I. Kleev and A. L. Velikovich, *XIX International Conference on Phenomena in Ionized Gases, Belgrade, Yugoslavia, 10-14 July 1989, Contributed Papers* (Faculty of Physics, University of Belgrade, 1989), Vol. 4, p. 834.

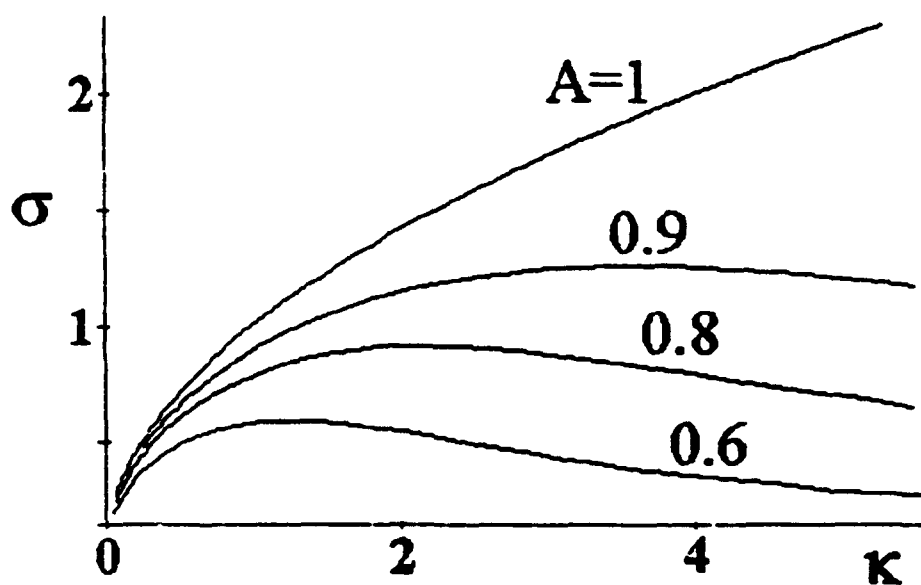


Fig. 1

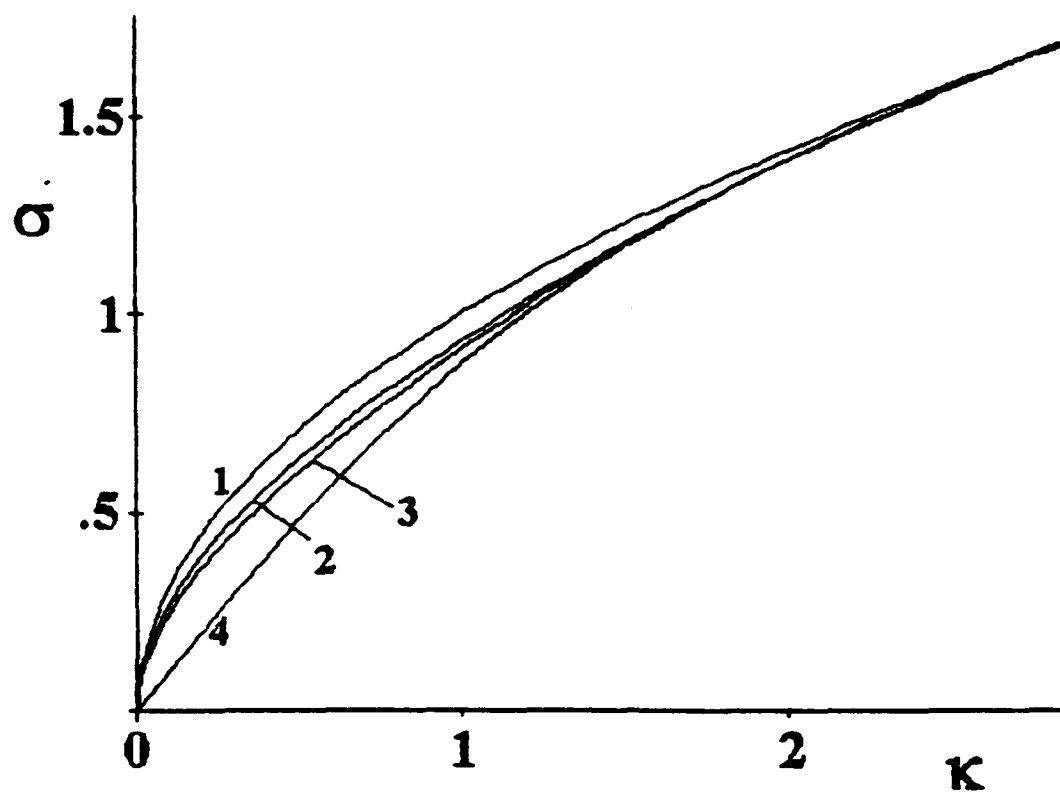


Fig. 2

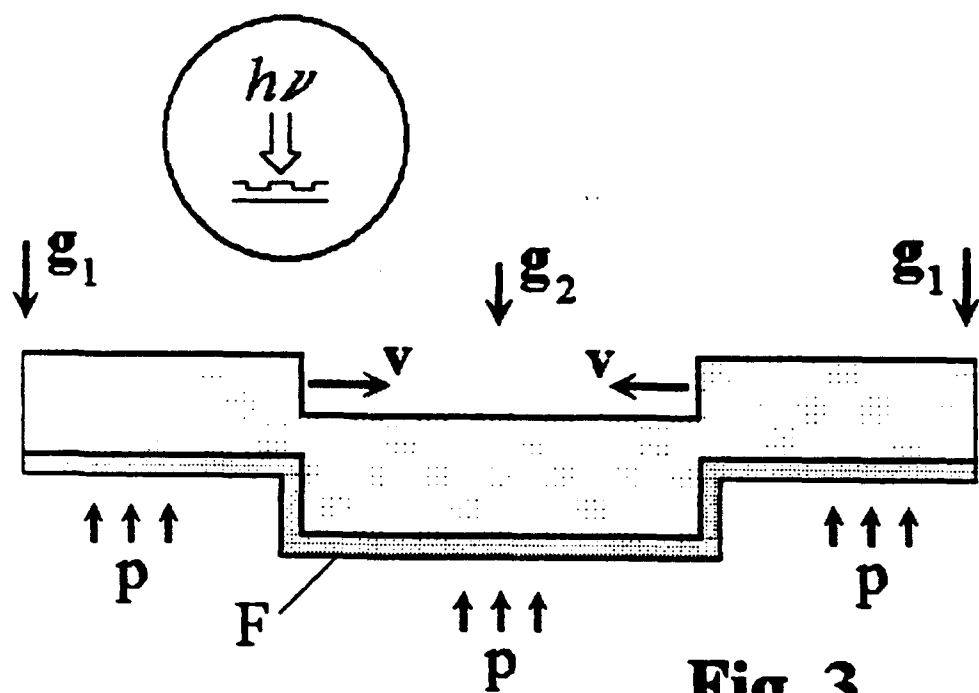


Fig. 3

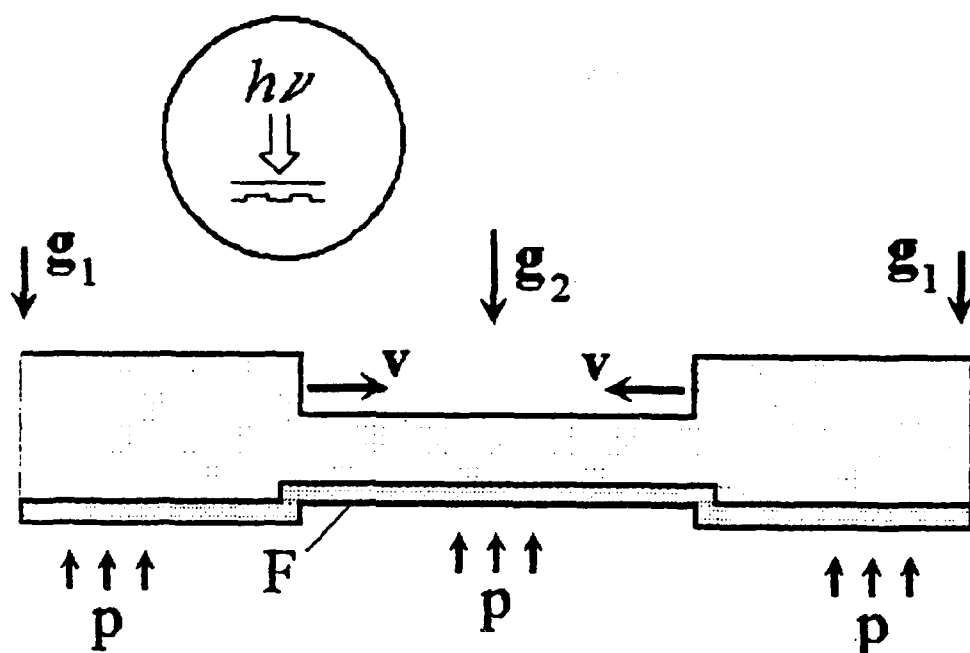


Fig. 4

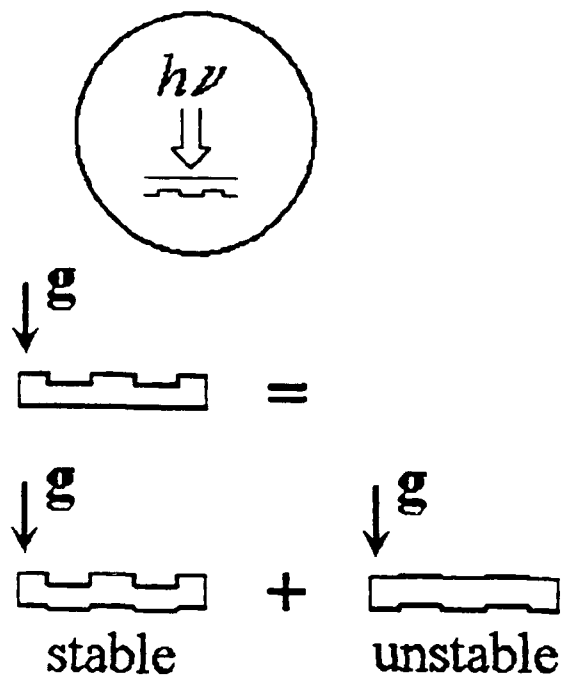


Fig. 5

Appendix E

Megavolt, Multikiloamp K_α Band Gyrotron Oscillator Experiment

Megavolt, multikiloamp K_u band gyrotron oscillator experiment

W. M. Black,^(a) S. H. Gold, A. W. Fliflet, D. A. Kirkpatrick,^(b) W. M. Manheimer,
R. C. Lee,^(c) V. L. Granatstein,^(d) D. L. Hardesty, A. K. Kinkead, and M. Sucky^(c)

Beam Physics Branch, Plasma Physics Division, Naval Research Laboratory, Washington, DC 20375-5000

(Received 15 February 1989; accepted 7 September 1989)

A K_u -band gyrotron oscillator experiment using a 1–1.35 MeV, multikiloampere beam from a pulse line accelerator has produced approximately 250 MW at 35 GHz in a circular TE_{62} mode with a peak efficiency exceeding 10%. Time-dependent simulation studies have been used to predict the behavior of a high-peak-power, short-pulse gyrotron in this parameter range. The simulations demonstrate the occurrence of such phenomena as hard excitation of the gyrotron as a result of the time dependence of the voltage pulse. The experimental results are in reasonable agreement with the predictions of theory.

I. INTRODUCTION

Gyrotron oscillators have proved to be efficient sources of very high-power radiation in the microwave and millimeter-wave regimes. Conventional gyrotrons use thermionic cathodes, with typical operating currents of ≤ 50 A at voltages of ≤ 100 keV, and have demonstrated hundreds of kilowatts of average power at efficiencies approaching 50%. However, some future applications of millimeter-wave radiation, such as radars and high-energy linear electron (and positron) accelerators, may require substantially higher-peak power levels than have been produced using conventional thermionic microwave tube technologies. The pursuit of higher microwave powers inevitably requires the application of higher beam powers, implying operation at higher currents and/or voltages. Gyrotron scaling to high-current, high-voltage operation is relatively favorable,¹ and a number of high-voltage (> 250 kV) gyrotron experiments have been reported in recent years that take advantage of the substantially higher currents and voltages available for short pulses (typically, ≤ 100 nsec) from pulse line accelerators driving plasma-induced field emission cathodes. Among these are a set of experiments from the Lebedev Physics Institute of the Soviet Union that demonstrated 23 MW at 40 GHz in a linearly polarized (i.e., nonrotating) TE_{13} mode with 5% efficiency, using a 350 keV electron beam.² Studies of gyrotrons driven by pulse line accelerators or Marx generators have also been carried out at the University of Michigan³ and at the University of Strathclyde in the United Kingdom.⁴

In 1984, a program was initiated at the Naval Research Laboratory to investigate very high-power gyrotron oscillators driven by intense relativistic electron beams. These experiments were designed to operate in K_u band, with the principal interest at 35 GHz. Prior to the present work, these experiments were carried out on a compact Febetron pulser capable of producing a 600 kV, 6 kA, 55 nsec pulse into a 100 Ω matched load.

^(a) Also at Electrical and Computer Engineering Department, George Mason University, Fairfax, Virginia 22021.

^(b) Science Applications International Corporation, McLean, Virginia 22102.

^(c) JAYCOR, Inc., Vienna, Virginia 22180.

^(d) Electrical Engineering Department, University of Maryland, College Park, Maryland 20742.

A key requirement for intense beam gyrotrons, unlike most other high-power microwave devices driven by intense relativistic electron beams, is to produce an electron beam with a large amount of momentum transverse to the applied axial magnetic field. The progress of this series of experiments has been marked by an evolution in the means by which this is accomplished. The earliest series of experiments produced the required beam α , where α is the ratio of transverse to parallel momentum, by emitting electrons across magnetic field lines at the cathode to produce some initial nonzero value of α and then adiabatically compressing the beam into the gyrotron cavity to increase α while positioning the beam to couple to the desired waveguide mode. These experiments operated at approximately 350 kV and 800 A, and produced 20 MW of output power at 35 GHz with 8% efficiency in a "whispering-gallery" TE_{62} mode.⁵

When this approach was found to lack flexibility, a new approach was implemented, in which the diode was designed to emit primarily along the direction of the axial magnetic field, i.e., to produce a low initial beam α , and the α was then sharply increased by transit through a localized nonadiabatic dip in the axial field, produced by a "pump" magnet, before being adiabatically compressed into the gyrotron cavity. This allowed the use of a very simple diode geometry, and the pump magnet provided a separate experimental control for beam α that greatly increased the experimental flexibility.

For this second series of experiments, the Febetron pulser was operated at its full rated charge voltage and mismatched upward at the diode to produce voltages of up to 900 kV. Because of the high impedance of the pulser, it was impossible to employ relatively low impedance diodes, such as diodes with beam-scraper anodes, without substantially reducing the operating voltages. The experiments were therefore carried out in a foil-less geometry employing a magnetic-field-immersed, cylindrical graphite cathode with a sharpened edge, in which the cylindrical vacuum vessel served as the anode. In this geometry, the diode produces a beam current determined by the space-charge limited flow of the annular beam within the cylindrical vacuum enclosure in the vicinity of the cathode. In general, this was more current than could be effectively employed in the experiment. In addition, because of emission from the sharpened edge of the

cathode, the beam possesses a relatively large spread in pitch angle.

Single-particle simulations demonstrate that the pump magnet has the effect of greatly magnifying any initial spread in electron velocity pitch angle. Fortunately, gyrotron oscillators are not very sensitive to such spreads. However, a large electron beam pitch angle spread limits the average beam α ; as the strength of the pump magnet is increased, the highest α portion of the resulting particle distribution function will be reflected during the subsequent adiabatic compression phase. The use of a "pump" magnet to increase the average beam α to a level sufficient to drive the gyrotron interaction invariably resulted in the loss of a sizable fraction of the beam current. Optimum high-power operation generally occurred with pump strengths resulting in the loss of half or more of the total beam current between the diode and the gyrotron cavity. Current loss occurred as a result of electron mirroring during the adiabatic compression stage, due in part to the effects of beam space charge on the electron beam kinetic energy, and in part to the effects of pitch-angle spread in the beam. It was not clear precisely where the reflexing electrons were collected, or whether they caused a space-charge buildup that affected the performance of the diode.

The second series of experiments was carried out in both whispering-gallery TE_{m2} modes and linearly polarized TE_{1n} modes.^{6,7} Results included a peak power of 100 MW at 35 GHz at 8% efficiency in a rotating TE_{62} mode and a peak power of 35 MW at 35 GHz in a "linearly polarized" (i.e., nonrotating) TE_{13} mode through use of a slotted gyrotron cavity. The gyrotron signal frequency could be step tuned over the range 28–49 GHz in a sequence of TE_{m2} modes by variation of the axial magnetic field. Results were in general agreement with the predictions of steady-state gyrotron theory, with theoretical values of power and efficiency typically being larger than experimental values by about a factor of 2. However, due to the nonideal voltage waveform provided by the Febetron pulser, the typical microwave pulse length was only 15 nsec.

In order to extend these experiments to higher power and longer pulse, as well as to gain some flexibility in the diode design in order to produce a better quality electron beam, these experiments were moved to the VEBA pulse line accelerator,⁸ which can operate at voltages exceeding 1.5 MV and has a 20 Ω output impedance and a 55 nsec full width at half-maximum (FWHM) pulse, of which approximately 40 nsec is relatively flat ($\pm 3\%$ – 5%). These new experiments initially employed a very similar experimental setup to that utilized previously in the Febetron experiments, except that the $Q = 250$, TE_{62} cavity of the 100 MW experiments was replaced by a slightly shorter cavity with a cold-cavity Q of 180. However, the best results have been achieved by replacing the foil-less diode geometry with a beam scraper diode. In these experiments, the peak output power has been increased to approximately 275 MW at 35 GHz in a TE_{62} mode, a factor of 3 increase over that reported from the previous work. The peak efficiency was increased to $\sim 14\%$, a 50% increase over that reported previously. In addition, as a result of the improved voltage waveform, the

microwave emission has occurred during a 40 nsec interval of approximately constant current and voltage, rather than being a transient effect at a time of rapidly varying current and voltage, as was the case with the Febetron pulser, thus permitting a better comparison with the predictions of theory.

II. EXPERIMENTAL SETUP

The 1.5 MeV VEBA pulse line accelerator with 20 Ω output impedance and 55 nsec voltage pulse was used to generate a multikiloampere annular electron beam by explosive plasma formation from a graphite cathode immersed in a uniform axial magnetic field provided by the main solenoidal magnet. Figure 1 illustrates the experimental geometry. A hollow ringlike cathode is placed from 1–2.2 cm from a graphite anode plate with an annulus cut into it to match the cathode ring. The annulus is interrupted in two places by radial graphite struts, in order to support the central region of the anode plate. The mean diameter of the annulus was 3.34 cm, and its radial extent was 1.5 mm. Emission takes place from the rounded edge of a hollow cathode, and a small fraction of the total current is extracted from the diode through an annular slot in the graphite anode. The anode functions in part as an emittance filter, since it scrapes off the inner and outer edges of the annular electron beam produced by the cathode, and in part as a control grid, since changes in the cathode-anode gap are a reliable means to control the beam current, which is space-charge limited. Typically, 25–35 kA of cathode current is produced, with roughly 90% being scraped off before leaving the diode.

The initial transverse momentum is expected to be low, because the emission is predominantly along the direction of the applied magnetic field. Downstream, the transverse momentum is induced by transit through a localized depression in the axial field, which is produced by the "pump" magnet. The operation of the pump magnet is described in more de-

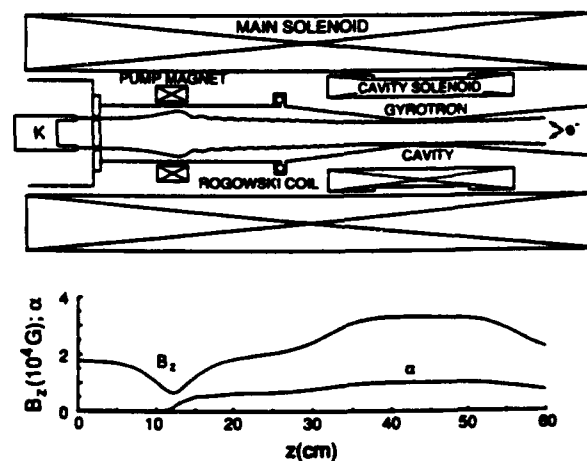


FIG. 1. Scale drawing of the high-voltage gyrotron, showing the diode region, the inner wall of the experiment, and the gyrotron cavity, and indicating the location of the various magnetic field coils. A calculated single-particle electron trajectory through the magnetic field profile is superimposed on the experimental geometry, and the magnetic field profile and beam α as a function of z are shown below.

tail in Ref. 6. Finally, the beam is adiabatically compressed to its final radius by the cavity solenoid. The overall magnetic field profile through the experiment, a calculated single-particle electron trajectory, and the calculated α as a function of axial position z along that trajectory are shown in Fig. 1. The electron trajectory, which is shown superimposed on the scale drawing of the experiment, is calculated for a single electron emitted in the axial direction at the cathode tip in the realistic fields produced by the experimental coil configuration. For this calculation, the current through the pump magnet was selected to produce a final α of 1 at the gyrotron cavity. A Rogowski coil positioned between the pump magnet and the gyrotron cavity measures the net current into the gyrotron. The current loss from the diode to the cavity, as measured by the Rogowski coil, is reduced to approximately 10%–15% under typical conditions of gyrotron operation, unlike the loss of 50% or more of the beam that was observed with foil-less diode geometries. This is an indication that the beam quality has been improved by the new diode geometry. This small fraction of reflected electrons is most likely to be collected on the downstream side of the anode scraper plate, thereby preventing a buildup of space charge anywhere in the system.

In order to achieve separate adjustment of the electron transverse momentum, the magnetic compression ratio, and the final magnetic field in the gyrotron cavity, each of the three magnets (i.e., the pump magnet, the cavity solenoid, and the main magnet) is powered by a separate capacitor bank discharge. By a proper selection of pump magnet strength and compression ratio, the beam diameter can be adjusted to couple to the desired TE_{62} mode in the cavity while the electron velocity pitch ratio α is increased to a value near unity. The cavity itself is cylindrically symmetric with a diameter of 3.2 cm and has a calculated cold-cavity Q of 180 for the TE_{62} mode. Beyond the cavity there is a 5° output taper transition to a 120 cm long drift tube with diameter of 14 cm. Finally, a 1 m long output horn is terminated with a 32 cm diam output window.

The microwave measurement system consists of two separate detection channels, each composed of calibrated "in-band" WR-28 components, including filters, attenuators, and directional couplers, and beginning with a small microwave aperture antenna positioned within 1 cm of the output window. One aperture is maintained at a fixed position on the output window, while the second is scanned. A bandpass filter limits the detected signal to a narrow frequency band (1.6 GHz FWHM) centered at 35 GHz. These diagnostics as well as the overall experimental setup are described in greater detail in Ref. 6. The changes affecting the present work are in the diode region, the cavity Q , and the currents, voltages, and magnetic fields employed in the experiment.

III. EXPERIMENTAL RESULTS AND DISCUSSION

The waveforms for the diode voltage, diode current, cavity current, and 35 GHz microwave pulses for a "typical" discharge are shown in Fig. 2. The improved voltage waveform and beam quality, compared to that described in Ref. 6, have generally permitted high-power microwave pulses with

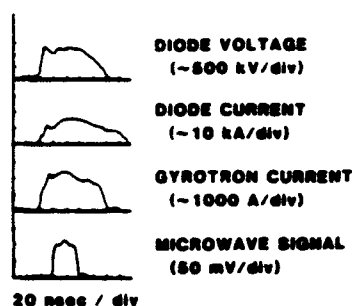


FIG. 2. Measured experimental waveforms as a function of time.

a duration of up to 40 nsec, nearly matching the duration of the flat portion of the high-voltage pulse applied to the diode. However, the microwave pulse is subject to large discharge-to-discharge variation in amplitude and pulse shape. A set of measurements were conducted as a function of beam energy, magnetic field, magnetic compression ratio, and pump field amplitude, in order to find the optimum operating parameters.

Figure 3 shows a scan of the output mode of the device as a function of radius in both $|E_r|^2$ and $|E_\theta|^2$ with a cavity magnetic field of $B_0 = 32$ kG, a current of 2.5 kA, and a peak diode voltage of 1.2 MV. The estimated experimental uncertainties are ± 1.5 kG on the magnetic field, ± 0.1 kA on the instantaneous current measured by the Rogowski coil, and ± 0.1 MV on the diode voltage, including the effect of voltage ripple during the voltage flat top. (The net current will be lower if current interception takes place between the Rogowski coil and the gyrotron cavity. Fluorescent screen data taken subsequent to the microwave measurements suggest that up to 20% of the current may have been intercepted under these experimental conditions.) For an average beam α of 1, the peak beam kinetic energy should be corrected downward by approximately 50 keV because of space-charge depression.

The normalized beam radius (i.e., the ratio of the beam guiding center radius r_0 to the cavity wall radius r_w) for this scan was approximately 0.725. However, there was some spread in the electron guiding centers due to beam thickness (reflecting the 1.5 mm width of the anode annulus) and finite decentering of the beam in the gyrotron cavity. This radius is close to optimum for coupling to the circularly polarized TE_{62} mode counter-rotating to the sense of electron gyration in the axial magnetic field. However, in the vicinity of 35 GHz, the beam will also couple to the $TE_{10,1}$ and TE_{14} modes, and more weakly to the TM_{23} and TM_{04} modes. The general shape of the measured profile in Fig. 3 fits reasonably well to the TE_{62} mode for both the radial and azimuthal polarizations of the rf electric field, and is similar to that of Ref. 6. The peaks at small values of the radii may be due to parasitic excitation of the TM_{04} mode. Mode purity at the output window may also be reduced by mode conversion in the 5° output taper and horn. For instance, mode conversion to the TE_{01} mode might explain the higher than expected peak in $|E_r|^2$ near the wall.

For the data of Fig. 3, the measured mode pattern can be

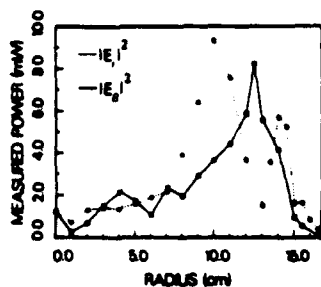


FIG. 3. Scan of output power versus radius, in both radial and azimuthal polarizations, across the output window.

used to calculate the total gyrotron power by integrating over the output window, and correcting for the measured losses in the detection system. This procedure has been described in detail elsewhere.⁶ The power estimate, which is based on the average of several discharges per position in the scan, is 160 MW. Following the radial scan, further data was taken with the pickup at a fixed radial position at the maximum of the mode pattern shown in Fig. 3. By assuming that the ratio of the power at this location in the mode to the total integrated power across the mode remains constant, we find a single-discharge peak output power of 275 MW, with 250 MW being measured on several occasions. The single-discharge efficiencies, based on the Rogowski coil measurements of beam current, varied from 9% to 14%. Based on error bars in the averaging process and in the calibration of the various multiplicative factors, the overall uncertainty of the power values is estimated to be less than 3 dB.

Figure 4 shows starting current and output isopower curves for the gyrotron interaction with the counter-rotating TE_{62} mode, calculated from a steady-state model⁹ for $B_0 = 32$ kG. To simplify the model, the beam current is assumed to scale as $V^{1.5}$ with a maximum value of 2.5 kA at 1.15 MV. (Based on a numerical solution to the equations presented by Miller,¹⁰ the relativistically correct current scaling for an infinite planar cathode-anode gap varies from $V^{1.5}$ at low voltage to $V^{1.44}$ at the peak voltage of 1.15 MV.)

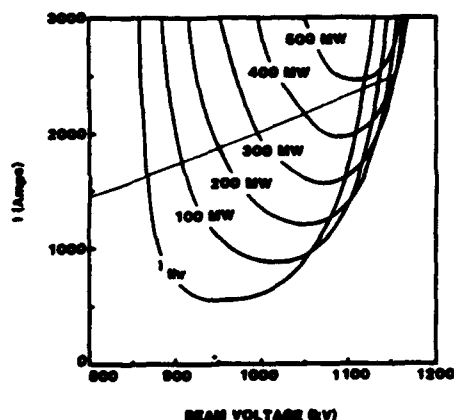


FIG. 4. Gyrotron starting current and isopower curves for the counter-rotating TE_{62} mode as a function of beam voltage, assuming $r_s/r_a = 0.725$, $B_0 = 32$ kG, and that the beam α is proportional to V , with $\alpha = 1$ at 1.15 MeV. A beam line is included, with the current assumed to scale as $V^{1.5}$, with a maximum value $I = 2.5$ kA at 1.15 MeV.

Based on single-particle simulations of the effect of the pump magnet, followed by adiabatic compression on the beam electrons, the beam α is assumed to scale linearly with V , with a maximum value of $\alpha = 1$ at 1.15 MV. The starting current and isopower curves are calculated assuming a half-sinusoidal rf-field profile along the cavity axis with a length of 3.5 cm and a hollow beam with a radius, normalized to the cavity wall radius, of 0.725. The dotted line models the behavior of the electron beam current during the rise of the voltage waveform. The effect of increasing voltage on the coupling to this mode may be inferred from this figure. As the voltage (and current) rise to their flat-top values, the interactions will begin at the left of the figure, where the beam line crosses the threshold current line labeled I_{th} , and then progressively tune to higher powers as the voltage and current continue to rise. The line ends at 2.5 kA and 1.15 MeV, and corresponds to predicted operation outside of the starting current curve, i.e., in the "hard excitation" regime, with a peak power of approximately 400 MW. Aside from the peak power predictions, which exceed the experimental value by approximately a factor of 2, this simulation is in reasonable agreement with the experimental observations. Furthermore, small changes in the assumed scaling relationships will not change these basic results. It is interesting to note that conventional low-voltage (< 100 kV), long pulse thermionic gyrotrons have been observed to drop below theoretical powers and efficiencies by comparable factors at high currents. (See, for example, Kreischer *et al.*¹¹)

In order to better understand the time-dependent nature of the gyrotron operation, as illustrated in Fig. 2, we have carried out a set of slow-time-scale single-mode time-dependent simulations of gyrotron operation for the approximate experimental conditions corresponding to the measurements shown in Fig. 3. Figure 5 shows a series of time-dependent simulations of the gyrotron operation,¹² employing a

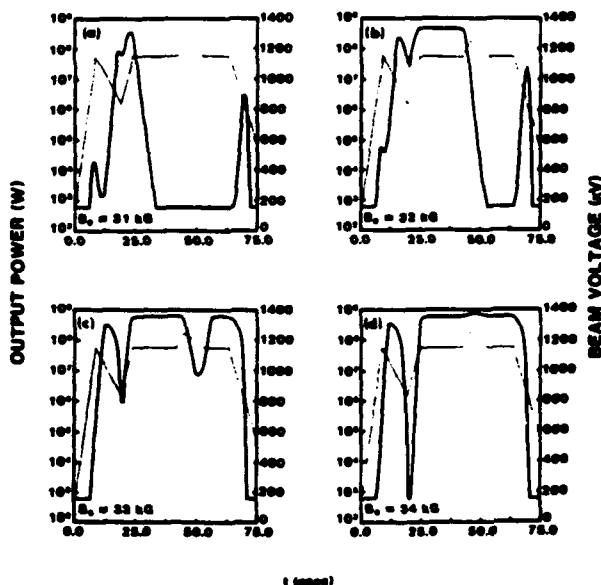


FIG. 5. Single-mode slow-time-scale time-dependent simulations of gyrotron operation in the counter-rotating TE_{62} mode for a simulated VIBA voltage waveform, assuming $r_s/r_a = 0.725$, $\alpha \propto V$ with $\alpha = 1$ at 1.15 MeV, and $I \propto V^{1.5}$ with $I = 2.5$ kA at 1.15 MeV. Runs with four values of B_0 are shown: (a) 31 kG, (b) 32 kG, (c) 33 kG, and (d) 34 kG.

simulated VEBA voltage waveform that models the leading edge of the pulse, the duration of the approximately flat portion of the voltage waveform, and a "typical" short-duration voltage "spike" during the "flat top." These simulations employ the same sinusoidal rf-field profile used for the steady-state simulations, and assume the same dependence of current and beam α on voltage. For the four runs shown, only the magnetic field was varied. At the lowest magnetic field, $B_0 = 31$ kG [Fig. 5(a)], the microwave signal occurs only during the rise and fall of the voltage waveform, and there is no interaction at the voltage flat top. The next case [Fig. 5(b)], for $B_0 = 32$ kG, corresponds to the steady-state simulations of Fig. 4. In this case, the microwave signal grows substantially during the leading edge of the voltage pulse and persists up to the voltage flat top. Figure 5(b) demonstrates that the full voltage of the flat top, corresponding to the upper end point of the beam line in Fig. 4, results in a highly detuned state of the gyrotron interaction, corresponding to "hard excitation." This is evident because the short-duration voltage spike modeled at approximately 45 nsec detunes the interaction further, causing the output power to fall off dramatically, and the power does not begin to recover until the voltage falls below the flat-top voltage. This case agrees well with the steady-state simulation of Fig. 4, and the peak power predicted by this simulation exceeds the best experimental value by approximately a factor of 2, as in Fig. 4. At $B_0 = 33$ kG [Fig. 5(c)], the voltage flat top no longer corresponds to hard excitation, since the microwave signal falls off during the voltage spike, but then recovers during the remainder of the flat top. Finally, at $B_0 = 34$ kG [Fig. 5(d)], the simulation shows that the microwave power follows the voltage signal for the duration of its flat portion including the voltage spike, and the power actually increases during the voltage spike.

For the assumed voltage waveform, the best agreement between the experimental microwave signals and the predictions of the single-mode time-dependent code, as a function of magnetic field, occurs at the experimental value of $B_0 = 32$ kG. However, the experimental values have error bars, as noted previously. In addition, the predictions of the time-dependent simulation depend in part on the exact shape of the axial rf-field profile assumed for the interaction, and small variations in the assumed length of the sinusoidal profile, or in substituting an approximately equivalent Gaussian profile for the sinusoid, will change the required values of the externally applied axial magnetic field by one to two kilogauss. The time-dependent simulations of Fig. 5 suggest that the microwave signal should last longer and reach higher power as the magnetic field is increased beyond the best experimental value of $B_0 = 32$ kG. In general, this is not observed in the laboratory. A possible explanation for this experimental observation lies in the area of mode competition. Specifically, as the magnetic field is increased, it becomes increasingly probable that a higher frequency mode will start oscillation during the rise of the voltage waveform, and will interfere with the startup of the TE_{62} mode at 35 GHz. The most likely competing mode in this situation is the counter-rotating TE_{72} mode. Time-dependent simulations carried out for the TE_{72} mode indicate that it should begin to

compete with the startup of the TE_{62} mode at approximately 34 kG. A thorough analysis of the effects of mode competition and other transient phenomena on the operation of a high-voltage gyrotron would require the use of true multi-mode simulations, such as the fast-time-scale particle-in-cell simulations carried out by Lin *et al.* for the parameters of Ref. 6.¹³

In summary, a 35 GHz gyrotron oscillator driven by an intense relativistic electron beam has successfully operated at voltages exceeding 1 MeV and currents of several kiloamps to produce peak output power levels of up to a quarter of a GW in a TE_{62} mode and peak efficiencies exceeding 10% (up to 14%). By comparison, an earlier experiment operating at approximately 800 keV and 1.6 kA at the same frequency in the same mode achieved 100 MW at 8% efficiency. Furthermore, in contrast to the previous experimental work, the emission has taken place during a time of approximately constant current and voltage, facilitating the comparison between theory and experiment. The improved interaction efficiency compared to the earlier experiments is attributed to the use of an apertured diode, in place of the foil-less diode configuration used previously, which has allowed better control of the current injected into the gyrotron and better beam quality. Time-dependent simulations have been carried out to investigate the behavior of high-peak-power, short-pulse gyrotron operation in this parameter range. The simulations demonstrate the occurrence of such phenomena as hard excitation of the gyrotron as a result of the time dependence of the voltage waveform. Overall experimental operation is in general agreement with the predictions of theory, with the best experimental powers within a factor of 2 of the theoretical predictions.

ACKNOWLEDGMENTS

This work was supported in part by the Office of Naval Research. This work was also supported in part by the Office of Innovative Science and Technology of the Strategic Defense Initiative Organization and managed by the Harry Diamond Laboratories.

¹See National Technical Information Service Document No. ADA-157746 [Naval Research Laboratory Memorandum Report 5598 (1985) by A. W. Fliflet]. Copies may be ordered from the National Technical Information Service, Springfield, Virginia 22161. The price is \$6.95 plus a \$3.00 handling fee.

²S. N. Voronkov, V. I. Kremensov, P. S. Strelkov, and A. G. Shkvarunets, *Zh. Tekh. Fiz.* 52, 106 (1982) [*Sov. Phys. Tech. Phys.* 27, 68 (1982)]. Also, V. V. Bogdanov, S. N. Voronkov, V. I. Kremensov, P. S. Strelkov, V. Yu. Shafer, and A. G. Shkvarunets, *Zh. Tekh. Fiz.* 53, 106 (1983) [*Sov. Phys. Tech. Phys.* 28, 61 (1983)].

³R. M. Gilgenbach, J. G. Wang, J. J. Choi, C. A. Outten, and T. A. Spencer, in *Conference Digest of the 13th International Conference on Infrared and Millimeter Waves*, edited by R. J. Temkin (SPIE, Bellingham, WA, 1988), pp. 362-363.

⁴A. D. R. Phelps, T. Garvey, and A. S. Hameedi, *Int. J. Electron.* 57, 1141 (1984).

⁵S. H. Gold, A. W. Fliflet, W. M. Manheimer, W. M. Black, V. L. Granatstein, A. K. Kinkad, D. L. Hardesty, and M. Sacy, *IEEE Trans. Plasma Sci.* PS-13, 374 (1985).

⁶S. H. Gold, A. W. Fliflet, W. M. Manheimer, R. B. McCowan, W. M. Black, R. C. Lee, V. L. Granatstein, A. K. Kinkad, D. L. Hardesty, and M. Sacy, *Phys. Fluids* 30, 2226 (1987).

⁷S. H. Gold, A. W. Fliflet, W. M. Manheimer, R. B. McCowan, R. C. Lee,

- V. L. Granatstein, D. L. Hardesty, A. K. Kinkad, and M. Sucky, *IEEE Trans. Plasma Sci.* **PS-14**, 142 (1988).
- ⁸J. R. Bettis, J. K. Burton, R. K. Parker, S. H. Gold, M. Herndon, R. H. Jackson, A. K. Kinkad, A. H. Guenther, and E. J. Kobice, *IEEE Trans. Nucl. Sci.* **NS-28**, 3091 (1981).
- ⁹A. W. Fliflet, M. E. Read, K. R. Chu, and R. Seeley, *Int. J. Electron.* **53**, 305 (1982).
- ¹⁰R. B. Miller, *An Introduction to the Physics of Intense Charged Particle*

- Beams* (Plenum, New York, 1982), pp. 42-45.
- ¹¹K. E. Kreischer, T. L. Grimm, A. W. Mobius, and R. J. Temkin, in *Conference Digest of the 13th International Conference on Infrared and Millimeter Waves*, edited by R. J. Temkin (SPIE, Bellingham, WA, 1988), pp. 179-180.
- ¹²A. W. Fliflet and W. M. Manheimer, *Phys. Rev. A* **39**, 3432 (1989).
- ¹³A. T. Lin, C.-C. Lin, Z. H. Yang, K. R. Chu, A. W. Fliflet, and S. H. Gold, *IEEE Trans. Plasma Sci.* **PS-14**, 135 (1988).

Appendix F

Measurement of Plasma-Neutralized Super-Vacuum Currents in a Gyrotron Configuration

Measurement of plasma-neutralized super-vacuum currents in a gyrotron configuration

D. A. Kirkpatrick,^{a)} S. H. Gold, W. M. Manheimer,^{b)} W. M. Black,
A. K. Kinkaid, D. L. Hardesty, K. W. Killian, and M. Sucky^{c)}

Beam Physics Branch, Plasma Physics Division, Naval Research Laboratory, Washington, DC 20375-5000

(Received 4 January 1990; accepted for publication 18 May 1990)

Experimental results are reported on the transport of an electron beam with current in excess of the vacuum space-charge-limited value, in a configuration directly applicable to gyrotron oscillators. The vacuum space-charge limit is circumvented by the introduction of a neutralizing background plasma which is produced by an array of four plasma guns placed immediately downstream of the electron gun anode.

A high-power microwave device typically consists of an intense relativistic electron beam driving a beam-wave interaction in an evacuated cavity or interaction volume. This includes slow-wave devices such as backward-wave oscillators (BWOs)^{1,2} and relativistic klystrons, and fast-wave devices such as gyrotrons^{3,4} and free-electron lasers.^{5,6} A fundamental limit to the power of such devices can be obtained by multiplying their theoretical interaction efficiency by the maximum beam power that can be propagated. For a particular voltage and geometry, the maximum beam power is set by the vacuum limiting current. This limit on the beam current arises from the fact that the electron beam loses an amount of energy corresponding to the capacitive voltage drop between the electron beam and the conducting boundary.

Recently there has been much interest in exceeding the space-charge limit in high-power microwave devices, notably the gyrotron and BWO.⁷⁻⁹ The space-charge limit is severe in the gyrotron due to the nature of the gyrotron interaction, which is more favorable when the beam α is large ($\alpha = \beta_\perp/\beta_\parallel$, the ratio of perpendicular to parallel velocities). The space-charge-limiting current for a cold annular beam of vanishing thickness is given by¹⁰

$$I_{LO} = I_A \frac{\gamma_0 [1 - (1 - \beta_{z0}^2)^{1/3}]^{3/2}}{2 \ln(R_w/R_{beam})}, \quad (1)$$

where I_A is the Alfvén current (17.07 kA), $\gamma_0 = 1 + (eV_0/m_0c^2)$ is the relativistic factor associated with the electron energy in the absence of any space-charge depression, $\beta_{z0} = v_{z0}/c$, v_{z0} is the electron axial velocity prior to any space-charge depression, R_w is the radius of the conducting boundary, and R_{beam} is the radius of the electron beam. The large beam α which is desirable for operation of the gyrotron corresponds to low β_{z0} and therefore low limiting currents.

One possible means to circumvent this obstacle is to use a neutral background plasma to short out the self-electric field of the electron beam. This concept of a neutralizing background plasma has been investigated exten-

sively in the Soviet Union,⁷ and has recently been the focus of some investigations with regard to the BWO.⁹ In order for the background plasma to cancel the effects of the electron beam self-electric field, the density of the neutral plasma must be greater than the density of the beam electrons, so that sufficient background electrons may be expelled from the region of the transiting electron beam to provide for space-charge neutralization.

In this letter we report on the achievement of super-vacuum currents (beam currents in excess of the vacuum space-charge limit) in a configuration directly applicable to gyrotron oscillators. The experimental arrangement is shown in Fig. 1. The VEBA pulseline accelerator ($V \sim 0.6$ – 2.5 MV, $I \sim 20$ – 100 kA, $\tau \sim 60$ ns) is used to energize an electron gun which produces an annular electron beam. The electron gun consists of a hollow cylindrical cathode and an anode mask with an annular aperture. Both the cathode and the anode are fabricated from reactor-grade graphite. The annulus in the anode mask has an inner radius of 1.6 cm and outer radius of 1.9 cm. The cathode-anode gap is 2.1 cm. Directly downstream from the anode mask is a Rogowski coil which measures the emitted beam current on each accelerator pulse. Immediately following is an array of four plasma guns,¹¹ equally spaced in azimuth. The plasma guns are individually energized by an array of four 0.22 μ F capacitors which are typically charged to 14 kV. The entire system is immersed in a uniform 10 kG axial guide magnetic field, produced by an external solenoid. In addition, as shown in Fig. 1, there is a field reversed, thin-solenoid "dip" magnet which is used to spin up the electron beam,¹² and a Helmholtz pair positioned symmetrically about the cavity region. In these experiments the cavity region is composed of a simple straight wall drift space. The magnetic-field in the center of the cavity region is 29 kG.

The plasma density produced in the cavity region has been characterized by 70 GHz quadrature microwave interferometry and by time-integrated photography of the light emitted by the plasma. The photographs of the light emitted by the plasma in the cavity region indicate that while the plasma is relatively uniform in the azimuthal direction, significant nonuniformity exists in the radial direction, with the peak density being close to the cavity wall. Close inspection of the interferometry data shows the

^{a)}Permanent address: Science Applications International Corporation, McLean, VA 22102.

^{b)}Code 4707, Plasma Physics Division, Naval Research Laboratory.

^{c)}Permanent address: JAYCOR, Inc., Vienna, VA 22180.

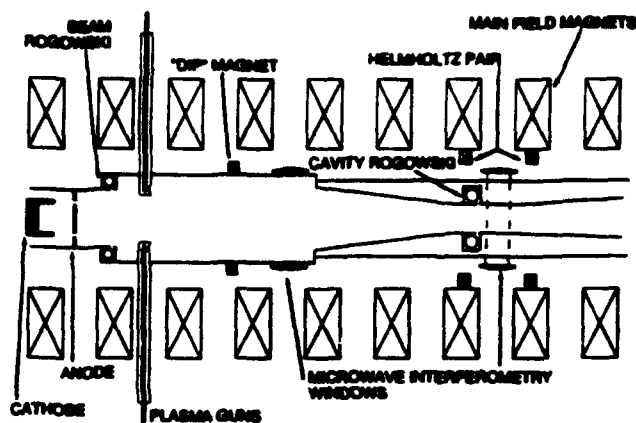


FIG. 1. Schematic layout of the VEBA plasma-neutralized gyrotron experiment, showing the magnet positions, inner conducting wall, vacuum chamber, microwave interferometry windows, plasma guns, and cathode-anode positions.

presence of cutoff-level densities early in the plasma pulse, when the line-averaged plasma density is computed to be about 10^{13} cm^{-3} . Since the plasma cutoff for our 70 GHz interferometer occurs at $n_p = 6 \times 10^{13} \text{ cm}^{-3}$, this would suggest peak densities on the order of a factor of five greater than the line-averaged densities. The data presented here are obtained with line-averaged plasma densities in the range $1.5\text{--}5 \times 10^{11} \text{ cm}^{-3}$, corresponding to peak background plasma densities in the range $0.8\text{--}3 \times 10^{12} \text{ cm}^{-3}$.

The achievement of super-vacuum currents is demonstrated by measuring the beam current transported through the cavity region with and without the background neutralizing plasma, while varying the amplitude of the "dip" magnet. These data are shown in Fig. 2(a), where we plot the measured cavity current against the amplitude of the "dip" magnet for both the vacuum and plasma-neutralized cases. For the plasma-neutralized case the data represent the maximum measured signals across a sample of neutral plasma densities. This step is necessary because with too little plasma background the beam is not neutralized, while with too much plasma background the beam current is partially neutralized and the Rogowski measurement gives an artificially low account of the beam current. Similarly, as the "dip" magnitude increases, the average beam axial velocity decreases, which results in an increase in the local number density of beam electrons. The higher number density of beam electrons requires a greater background plasma density to provide for neutralization. The variation of the plasma density is achieved by varying the time delay between the firing of the plasma guns and the firing of the accelerator. For our measured beam parameters, and using the estimated beam alpha, the peak number density of the beam electrons is in the range $1\text{--}3 \times 10^{12} \text{ cm}^{-3}$. Combined with our previous estimate of the relative nonuniformity of the neutral background plasma, the condition for neutralization of $n_b \approx n_p$ appears to be well met.

The variation of α with the amplitude of the dip magnet is shown in Fig. 2(b). Here we plot the average and

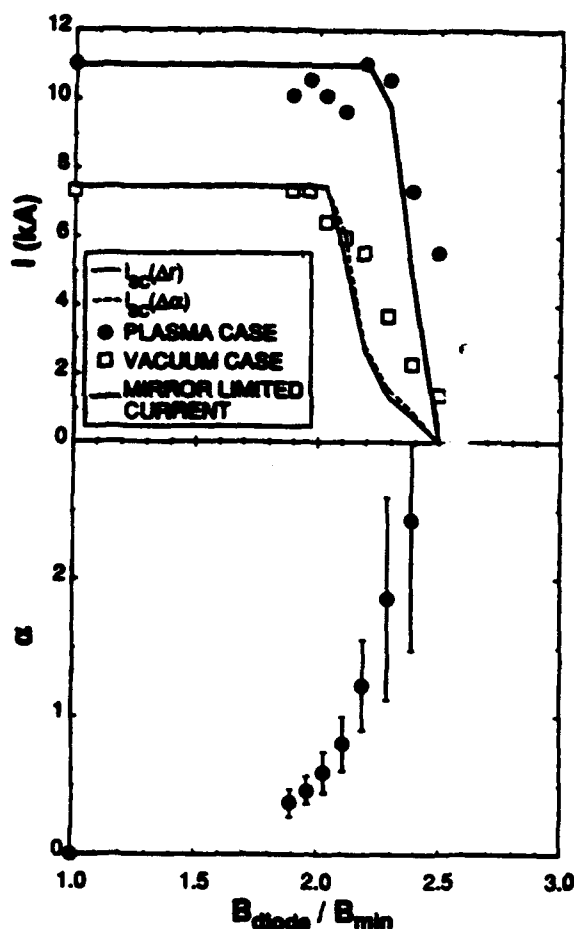


FIG. 2. Current measured by the Rogowski coil positioned in the cavity region, for the vacuum case (open circles) and for the plasma-neutralized case (solid circles), shown with the calculated vacuum space-charge-limiting current for a beam of nonzero thickness (dotted line), the calculated vacuum space-charge-limiting current for a beam with nonzero thermal spread (thin line), and the calculated transmitted current for an ensemble of noninteracting electrons (bold line).

spread in α for the calculated trajectories of an ensemble of noninteracting particles, using the measured magnetic fields and electron beam voltage. The calculated transmitted current for these single particle ensembles is shown in Fig. 2(a) as the "mirror limiting current." In this case, the loss of current is due wholly to mirroring of individual particles in the region of the magnetic compression. It can be seen that there is good agreement between this curve and the measured data for the plasma neutralized case. Similarly, we can use the calculated beam alpha to calculate space-charge-limiting current for a zero-temperature beam of nonzero thickness,¹⁰

$$I_{sc}(\Delta r) = I_{LO} \frac{G(r_0/r_w, 0)}{G(r_0/r_w, \Delta r/r_w)}, \quad (2)$$

and the space-charge-limiting current for a zero-thickness beam with a nonzero thermal spread in velocity¹³

$$I_{sc}(\Delta \alpha) = I_{LO} [f(\alpha_+) + f(\alpha_-)]. \quad (3)$$

In these equations, r_0 is the mean radius of the electron beam, Δr is the radial beam thickness, r_w is the radius of the conducting boundary, G is an involved function of r_0 ,

r_w and Δr , and $f(\alpha_+)$ and $f(\alpha_-)$ are involved functions of the maximum and minimum α of electrons in the beam distribution function. For these calculations a simple uniform distribution extending from $\alpha = \alpha_-$ to $\alpha = \alpha_+$ is assumed. Both the $I_{sc}(\Delta r)$ and $I_{sc}(\Delta \alpha)$ curves are seen to agree reasonably well with the measured data for the vacuum case. It should be noted that for pump amplitudes corresponding to an average beam α of 1 to 2, the presence of the neutralizing plasma results in an increase in the beam current propagated through the cavity by a factor of about 3.

The calculations of $I_{sc}(\Delta r)$, $I_{sc}(\Delta \alpha)$, and the mirror limiting current shown in Fig. 2(a) are obtained using a very simple electron beam distribution function. The inner and outer radii of the electron beam correspond to the inner and outer radii of the anode mask aperture. The velocity distribution assumes a uniform spread in initial diode α ranging from 0 to 0.1. This range gave good agreement for both the roll-over point of the mirror limiting current, and for the space-charge-limited current in the case of no pump field. Deviations of the theoretical curves from the data, for both the vacuum and plasma-neutralized cases, are probably due to the details of the electron beam distribution function which are grossly simplified in the calculations. Further, no accounting has been made of the possibility of diamagnetic effects associated with the high α beam, nor do the calculations consider the effect of space charge on the "spinning up" of the electron beam by the pump magnet.

In conclusion, we have demonstrated transport of beam currents in excess of the vacuum space-charge limit in a plasma-filled, gyrotron-type cavity. For values of the beam α in the range of 1–2 the increase in electron beam current is approximately a factor of 3. Comparison of the measured transmitted vacuum current with the theoretical vacuum space-charge-limited current shows good agreement. In the case of the plasma-neutralized measurements, we obtain good agreement from a simple calculation of magnetic mirroring of an ensemble of noninteract-

ing electrons, where the ensemble is taken to represent a uniform, low initial temperature, annular beam of radial dimensions given by the anode mask. The higher intracavity beam currents achieved with the aid of the neutralizing background plasma should enable higher power operation in existing intense beam gyrotron designs.¹⁴

The authors would like to acknowledge the assistance of B. Weber of NRL with the use of the plasma gun, setup of the microwave interferometry, and associated data analysis programs. This work was supported by the Office of Naval Research.

¹Y. Carmel, J. Ivera, R. E. Kribel, and J. Nation, *Phys. Rev. Lett.* 33, 1278 (1974).

²N. Kovalev, M. I. Petelin, M. D. Raizer, A. V. Smorgonskii, and L. E. Tsopp, *Pis'ma Zh. Eksp. Teor. Fiz.* 18, 232 (1973) [*JETP Lett.* 18, 138 (1973)].

³V. L. Granatstein, *Int. J. Electron.* 57, 787 (1984).

⁴S. P. Bugaev, V. I. Kanavets, A. I. Klimov, and V. A. Cherepanin, *Pis'ma Zh. Tekh. Fiz.* 9, 1385 (1983) [*Sov. Tech. Phys. Lett.* 9, 596 (1983)].

⁵J. Fajana, G. Bekeš, Y. Z. Yin, and B. Lax, *Phys. Fluids* 28, 1995 (1985).

⁶T. J. Orzechowski, B. Anderson, W. M. Fawley, D. Promitz, E. T. Scharlemann, S. M. Yarema, D. Hopkins, A. C. Paul, A. M. Sessler, and J. Wurtele, *Phys. Rev. Lett.* 54, 889 (1985).

⁷M. V. Kuzlev, A. A. Rukhadze, P. S. Streikov, and A. G. Shkvarunets, *Fiz. Plazmy* 13, 1370 (1987) [*Sov. J. Plasma Phys.* 13, 793 (1987)].

⁸V. I. Kurilko, V. I. Kucharov, and A. O. Ostrovskii, *Zh. Tekh. Fiz.* 51, 1415 (1981) [*Sov. Phys. Tech. Phys.* 26, 812 (1981)].

⁹Y. Carmel, K. Minami, R. A. Kels, W. W. Destler, V. L. Granatstein, D. Abe, and W. L. Lou, *Phys. Rev. Lett.* 62, 2389 (1989).

¹⁰A. K. Ganguly and K. R. Chu, *Int. J. Infrared Millimeter Waves* 5, 103 (1984).

¹¹R. J. Comisso, D. D. Hinselwood, J. M. Neri, W. F. Oliphant, and B. V. Weber, *NRL Memo Report 6057*, Naval Research Laboratory, Wash. DC 20375-5000 (1987).

¹²S. H. Gold, A. W. Fliflet, W. M. Manheimer, R. B. McCowan, W. M. Black, R. C. Lee, V. L. Granatstein, A. K. Kinkad, D. L. Hardesty, and M. Suty, *Phys. Fluids* 30, 2226 (1987).

¹³T. Antonsen and B. Levush, *Int. J. Electron.* 61, 871 (1986).

¹⁴W. M. Black, S. H. Gold, A. W. Fliflet, D. A. Kirkpatrick, W. M. Manheimer, R. C. Lee, V. L. Granatstein, D. L. Hardesty, A. K. Kinkad, and M. Suty, *Phys. Fluids B* 2, 193 (1990).

Appendix G

Millimeter-Wave Gyroklystron Amplifier Experiment Using a Relativistic Electron Beam

Millimeter-Wave Gyroklystron Amplifier Experiment Using a Relativistic Electron Beam

STEVEN H. GOLD, SENIOR MEMBER, IEEE, ARNE W. FLIFLET, MEMBER, IEEE,
WALLACE M. MANHEIMER, SENIOR MEMBER, IEEE, DOUGLAS A. KIRKPATRICK,
W. MURRAY BLACK, MEMBER, IEEE, ALLEN K. KINKEAD, DELBERT L. HARDESTY,
AND MARK S. SUCY

Abstract—A fundamental mode TE_{011} two-cavity intense-beam gyroklystron amplifier experiment, operating at an accelerating voltage of 1 MV, is reported. The two cavities that were tested are designed to serve as bunching cavities for a high-power output cavity. The two-cavity amplifier has demonstrated a linear gain of 15 dB and an unsaturated output power of ~40 kW, with the intracavity gain and power ~4 dB higher. The frequency of the second cavity has been found to track the frequency of the driven cavity over a range of 300 MHz around a center frequency of 35 GHz. Stable amplifier operation was achieved with beam currents as large as 150 A and a velocity pitch ratio (v_z/v_x) of 0.36. The stable operating range was limited by spurious oscillation in the TE_{012} mode. Theoretical calculations indicate that higher gains might be attainable if this mode could be suppressed.

I. INTRODUCTION

THE GYROTRON oscillator has proved to be a highly efficient source of high-power millimeter-wave radiation. Much of the research on gyrotron oscillators has been motivated by the need to develop sources for cyclotron resonance heating of fusion plasmas [1]. However, there are a variety of applications in which the requirements for frequency and phase control are more demanding than for the fusion application. An example of this is the requirements imposed on the driver tubes for high-power linear electron or positron accelerators, in which a large number of separate microwave sources must be in close phase synchronism to properly drive a long chain of acceleration cavities [2]. Another example is the requirements imposed on separate sources which will be combined for high-power-directed energy applications, such as when each source drives a separate element of a phased array antenna. For such applications, the gyroklystron amplifier has a number of natural advantages over the single-cavity

gyrotron oscillator. With an amplifier, the required phase and frequency coherence should be attainable, and in addition, because of the possibility of controlling beam pre-bunching before entry into the final cavity where microwave power is produced, higher efficiency operation should be possible. Furthermore, by using multiple gyroklystron cavities, higher stable gain should be achievable than in gyro-traveling-wave amplifiers (see [3] and references therein).

A number of previous gyroklystron amplifier experiments have been reported in the literature. Symons and Jory [4] discuss a 50 kW, 28 GHz gyroklystron with 40 dB gain that employed a circular TE_{011} input cavity and a TE_{021} output cavity. It operated at 80 kV with an 8 A beam current, and achieved a saturated efficiency near 10%. Significant difficulty was reported in this device with spurious oscillations in the input cavity and beam tunnel. This oscillation was suppressed by resistive loading of the undesired modes. Symons and Jory also reported a second harmonic gyroklystron experiment, operating at 50 kV and 5 A, that produced 20 kW at 10.4 GHz. This device also experienced significant problems with oscillation in spurious modes. More recently, Bollen *et al.* [5] have reported a 50 kW, 4.5 GHz three-cavity gyroklystron amplifier operating at 35 kV and 5–10 A in a rectangular TE_{101} mode that achieved 30% efficiency. This device avoided mode competition by operating in the fundamental mode of rectangular cavities, with drift spaces that were cut off at the operating frequency.

In recent years, gyrotron oscillator operation has been extended to very high peak power (hundreds of megawatts) by employing high voltage (≥ 1 MeV) intense (≥ 1 kA) relativistic electron beams from pulseline accelerators [6]. There has been no corresponding extension reported for gyroklystron amplifiers. This paper reports the results of an initial experimental study of the operation of a two-cavity gyroklystron amplifier with fundamental mode cylindrical cavities operating near 1 MeV at relatively low current (≥ 100 A). It was carried out at 35 GHz using a 50 ns beam from a pulseline accelerator. The two cavities were designed to serve as the bunching cavities for a higher power final output stage, which was intended to operate as a phase-locked oscillator [7]. How-

Manuscript received March 9, 1990; revised July 11, 1990. This work was supported by the Office of Naval Research.

S. H. Gold, A. W. Fliflet, W. M. Manheimer, A. K. Kinkead, and D. L. Hardesty are with the Beam Physics Branch, Plasma Physics Division, Naval Research Laboratory, Washington, DC 20375.

D. A. Kirkpatrick is with the Science Applications International Corporation, McLean, VA 22102.

W. M. Black is with the Beam Physics Branch, Plasma Physics Division, Naval Research Laboratory, Washington, DC 20375 and the Department of Electrical and Computer Engineering, George Mason University, Fairfax, VA 22021.

M. S. Sucky is with Jaycor, Inc., Vienna, VA 22180.
IEEE Log Number 9040081.

ever, theoretical modeling and initial experimental measurements demonstrated that the accelerator voltage waveform ($\pm 5\%$ voltage ripple) was inadequate to demonstrate phase-locking of the output cavity. For the final parameters of the present experiment, the output cavity was found to behave as a "primed" oscillator; i.e., to oscillate only when the first cavity was driven. It was found to have a peak output power of approximately 1 MW (based on near-field measurements at the center of the mode pattern), but to exhibit strong temporal modulation that was inconsistent with the observation of phase-locked operation. This amplitude modulation had a 4-ns periodicity that seemed to match the period of the $\pm 5\%$ ripple on the voltage waveform. In light of this, the present study was intended to test the stability of the bunching cavities and to demonstrate linear amplification of the drive signal, with definitive tests of the output cavity postponed pending the availability of a new accelerator with an improved voltage waveform.

II. APPARATUS

These experiments were carried out on the VEBA pulseline accelerator [8]. Fig. 1 shows a schematic diagram of the experiment. An 8-mm-diam. solid electron beam was produced by an apertured diode which made use of beam scraping to produce a low-velocity spread beam with low initial transverse momentum [9]. The diode operated in a uniform axial magnetic field of ~ 7.8 kG. The transverse momentum required for the gyrotron interaction was induced by transit through a one-period untapered bifilar helical wiggler magnet with 4-cm length, followed by adiabatic compression of the beam by means of a rise in the axial magnetic field to a final value of ~ 25 kG. After compression, the beam was designed to overfill the 4.32-mm-diam. beam tunnel leading to the first cavity in order to correct for the decentering induced by passage through the wiggler magnet. The excess current was deposited on the walls of a graphite down-taper. The final beam current was monitored by a Rogowski coil (not shown) at the entrance to the beam tunnel. The final axial magnetic field needed for the device was determined by the resonance condition for the first harmonic cyclotron-maser interaction in the cavities, while the field in the vicinity of the wiggler magnet was chosen somewhat above the gyroresonant value [10]. This was due to produce the required beam α , where $\alpha = v_{\perp}/v_{\parallel}$ is the ratio of transverse to axial velocity, without inducing large momentum spread, which would be deleterious to the operation of the gyrokystron.

The gyrokystron has two slotted cylindrical TE_{111} bunching cavities of identical design (but slightly different cold test properties), separated by a 4-cm-long drift space. Following the second cavity, an additional 4-cm-long drift space leads to a TE_{121} slotted output cavity. Each cavity has a separate vacuum enclosure lined with microwave absorbing material, so that energy leakage from the slots will not couple back to the slots, or to another cavity. The bunching cavities can be accessed

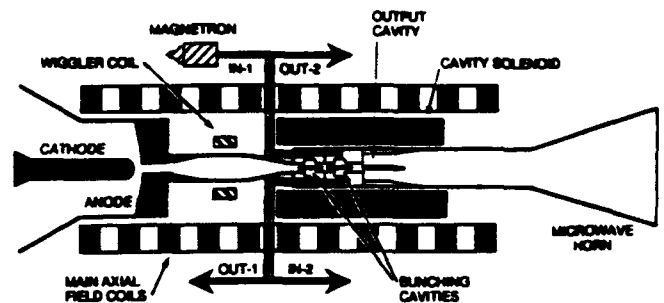


Fig. 1. Schematic diagram of the gyrokystron experiment.

through the coupling apertures, which are labeled in Fig. 1 as "IN-1" and "IN-2," respectively, and through the sampling apertures, labeled "OUT-1" and "OUT-2." Fig. 2 shows the details of the bunching cavity design, including the location of these apertures and of the slots used to control oscillation and mode competition. Fig. 2 also shows the calculated axial RF-field profile for the TE_{111} and TE_{112} modes of the bunching cavities. The bunching cavity diameter is 5.33 mm, the nominal cavity length (not including field penetration into the drift spaces) is 7.5 mm, and the drift space diameter is 4.32 mm. The calculated isolation of each cavity from leakage fields of the adjacent cavities exceeds 100 dB for the TE_{111} mode, not including the additional losses due to the presence of slots. The present work deals only with the operation of the bunching cavities.

The bunching cavities were designed to operate at a total Q of 200, where Q is the cavity quality factor. The Q of each bunching cavity is given by

$$Q^{-1} = Q_{\text{int}}^{-1} + Q_{\text{ext}}^{-1} \quad (1)$$

where Q_{int} is the internal cavity quality factor, determined principally by slot and ohmic losses, and Q_{ext} is the quality factor determined solely by losses through the cavity coupling aperture. It is convenient to define the coupling β as $\beta = Q_{\text{int}}/Q_{\text{ext}}$. In terms of this parameter, the fraction \mathcal{R} of the incident power reflected from the coupling aperture at resonance is given by [11]

$$\mathcal{R} = \frac{(1 - \beta)^2}{(1 + \beta)^2} \quad (2)$$

A value of β less than one is considered *undercoupled*, while a value greater than one is considered *overcoupled*. *Critical coupling* is defined as a coupling β of 1, a condition for which \mathcal{R} goes to zero. For $\beta \sim 1$, a drive signal in the coupling arm should couple almost completely into the cavity.

The bunching cavity design called for $\beta \sim 1$; i.e., $Q_{\text{int}} \sim Q_{\text{ext}} \sim 400$. A pair of opposing axial shots, each of 44° transverse extent, was used to lower Q_{int} to 400 for the TE_{111} mode, while assisting in suppressing other competing modes [7]. The length of these slots is three times the nominal cavity length (see Fig. 2) in order to extend everywhere that the TE_{111} mode has substantial RF fields. The ohmic Q of the cavities is high compared to the Q

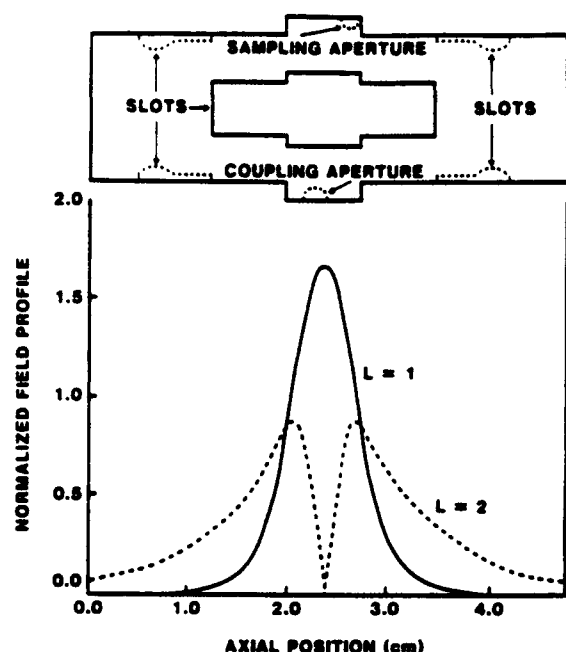


Fig. 2. Schematic of the bunching cavities, indicating the location of apertures and slots and calculated axial profile functions for the TE_{111} and TE_{112} modes of the bunching cavities. (The calculated profiles do not include the effects of the four "keyhole slots, which are expected to suppress the wings of the $L = 2$ axial profile function.)

associated with the slots and may be neglected. The presence of these slots also permits tuning of the resonant frequency of each cavity (to slightly higher frequencies) by transverse compression of the cavities.

The coupling apertures were designed to approximate critical coupling to the cavity (i.e., $Q_{ext} \sim 400$), while the sampling apertures were designed so as not to significantly load the cavities. For a particular (measured) reflected signal, (2) can be used to calculate two possible values for β which are reciprocals of each other. However, the measurement does not indicate which of these is the correct value. The remaining uncertainty can be resolved by slotted line measurements of the phase of the standing wave in the coupling arm. The procedure used to ensure nearly critical coupling began before the final cavity brazing took place. Each cavity was initially cold-tested with a very small coupling aperture ($\beta \ll 1$). The cavity Q -value and reflected signal were then determined and the coupling aperture progressively enlarged until the Q dropped by approximately a factor of two and the reflected signal at resonance dropped to near zero. At the conclusion of this process, each bunching cavity demonstrated a resonance within a few tens of MHz of 35 GHz accompanied by a large (~ 20 dB) dip in the reflected signal at resonance. At this point, the final cavity brazing was performed. The cold tests were then reverified, yielding center frequencies of 35.03 and 34.86 GHz for the first and second cavities, respectively. (The absolute accuracy of these two frequencies is $\sim 0.1\%$, or ± 35 MHz, but the precision of the measurements is ~ 5 MHz, which permits an accurate determination of the frequency difference between the cavities.) This frequency difference

would correspond to a $25\mu\text{m}$ difference in the diameter of the two cavities. In addition, the coupling to each cavity was nearly critical.

The desired cold cavity frequency of the gyrokystron was 35.06 GHz (based on a predicted hot cavity frequency shift of approximately $+0.5\%$ [7] and the calculated 35.2 GHz operating frequency of the TE_{121} output cavity). Each bunching cavity was then tuned to this frequency by transverse compression by means of separate clamps. However, cavity deformation affects both the center frequency and value of Q . Following the tuning process, the approximate quality factors of the two cavities (the average of measurements performed driving the large and small apertures) were $Q_1 = 230$ and $Q_2 = 140$. The lower Q -value for the second cavity resulted in part from the greater amount of compression needed to tune this cavity to the desired frequency. At the final cavity tunings, the dip in the reflected signal for the first cavity was 18.6 dB, while the dip in the reflected signal for the second cavity was 11.6 dB. Based on the slotted-line measurements, each of the cavities was undercoupled. Hence the value of β for the first cavity was 0.79, and for the second cavity was 0.58. For the first cavity, this means that the internal quality factor was 410. For the second cavity, this means that only $\sim 37\%$ of the power generated in the cavity would escape from IN-2.

As in the previous gyrokystron devices, a critical design consideration was to avoid oscillation in either the operating mode of the bunching cavity or in other spurious modes. Oscillation in the design mode was avoided through control of the cavity Q -values by means of slot and aperture loading. Since the two bunching cavities were designed to operate in the fundamental TE_{11} mode of cylindrical cavities, no mode competition was possible from higher order transverse modes in the first harmonic. The cavities were also designed for stability in higher-order transverse modes coupling in higher harmonics of the cyclotron frequency [7]. However, analysis showed that a higher order axial mode of the bunching cavities, the TE_{112} mode at approximately 40.4 GHz, would be difficult to suppress. This mode could only be weakly cut off in the drift space separating the cavities because of the need to propagate the electron beam. As a result, the axial profile function of the TE_{112} mode extended substantially farther into the drift space than that of the TE_{111} mode, resulting in a substantially lower starting current. In order to further suppress the TE_{112} mode without loading down the TE_{111} mode excessively, additional pairs of 7.5-mm-long slots (see Fig. 2) were placed in the walls of the cutoff sections. These slots begin just beyond the main cavity slots, but are at an angle of 90° to them. The combination of large slots at 90° intervals in different regions of the cutoff sections was intended to limit the axial extent of the RF fields of the TE_{112} mode of the cavity. They were also intended to substantially lower the Q of the TE_{11} mode of the drift spaces, of any polarization, as well as of other modes that might occur at higher harmonics of the cyclotron frequency, in order to prevent the buildup

of oscillation in the drift spaces. The design of the entire RF circuit is discussed in detail by Fliflet *et al.* [7].

Despite these measures, an important limitation to the available parameter space of these gain measurements was the need to avoid exciting the TE_{112} mode. As predicted, too high a beam α , or too high a magnetic field, would cause this mode to oscillate during the flat portion of the VEBA voltage waveform, during which the amplification measurement at ~ 35 GHz must take place. The presence of this mode both at high α and at a high magnetic field was verified by determining that an observed oscillating mode produced power that could propagate through a short section of the V -band waveguide, with cutoff frequency of 40.0 GHz, but not through a section of the W -band waveguide, with cutoff frequency of 59.35 GHz. Limiting operation to lower magnetic fields and lower beam α in order to avoid exciting this mode moved the 35 GHz operation to relatively large detunings and lower gains, compared to the optimum values predicted for this circuit by Fliflet *et al.* [7].

III. THEORY

Early results on the small-signal theory of the gyro-klystron were reported by Ergakov and Moiseev [12] and Symons and Jory [4]. A nonlinear analysis of the two-cavity gyro-klystron has been given by Ganguly and Chu [13], and a small-signal self-consistent field theory of the multicavity gyro-klystron has been given by Ganguly *et al.* [14]. A small-signal theory of the multicavity gyro-klystron based on Gaussian axial profiles for the cavity electric fields and expressed in terms of well-known gyrotron normalized parameters has been given by Tran *et al.* [15]. The theory of the phase-locked gyrotron with a prebunching cavity has been treated in the small-signal approximation, including finite temperature effects, by Manheimer [16], and in the nonlinear regime by Fliflet and Manheimer [17]. The theoretical approach given in [15] has been used to calculate the small-signal gain for the present configuration in the cold beam approximation. The phase bunching of the beam at the entrance to the second cavity is characterized by the bunching parameter,

$$q = \sqrt{\pi} F_1 \mu_1 e^{-(\mu_1 \Delta/4)^2} [\sqrt{3} \mu_1/2 + \mu_d] \quad (3)$$

where F_1 , μ_1 , and Δ are the normalized peak electric field amplitude, interaction length, and resonance detuning parameters for the first cavity, and μ_d is the normalized length of the drift section. The normalized amplitude of the RF electric field induced in the second cavity by the phase-bunched is given by

$$F_2 = \sqrt{\pi} I_2 \mu_2 e^{-(\mu_2 \Delta/4)^2} J_1(q) \cdot \left[\sin \psi + \frac{\mu_2^2 \Delta/4 - 1}{\sqrt{3} \mu_1/2 + \mu_d} \cos \psi \right] \quad (4)$$

where I_2 and μ_2 are the normalized current and length parameters for the second cavity, ψ is essentially the phase difference between the RF fields in the first and second cavities, and J_1 is a regular Bessel function of the first

kind. For a linearly polarized TE_{1n} circular waveguide mode, an on-axis beam, and the fundamental harmonic interaction, the normalized quantities are defined according to

$$I_i = \left[\frac{2}{\pi} \right]^{5/2} \frac{|e| \mu_0}{4 m_0 c} \frac{Q_i}{\gamma_0 \beta_{\perp 0}^4} \frac{\lambda}{d_i} \frac{1}{(x_i^2 - 1)} \frac{1}{i(x_i)} I_0 \quad (5)$$

$$\mu_i = \frac{\beta_{\perp 0}^2}{\pi} \frac{d_i}{\beta_{10} \lambda} \quad (6)$$

$$\Delta = \frac{2}{\beta_{\perp 0}^2} \left(1 - \frac{\Omega}{\omega} \right) \quad (7)$$

$$F_i = \frac{2|e|}{m_0 c^2} \frac{r_{wi}}{\gamma_0 \beta_{\perp 0}^3 x_i} E_i \quad (8)$$

where the subscript i is the cavity index, e and m_0 are the electron charge and rest mass, μ_0 is the free-space permeability, c is the speed of light, x_i is a zero of J'_1 , λ is the free-space wavelength, d_i is the effective interaction length, $\beta_{\perp 0}$ and β_{10} are the average transverse and axial electron velocities normalized to c , γ_0 is the relativistic energy factor, Q_i is the cavity quality factor, r_{wi} is the cavity wall radius, E_i is the peak cavity RF field, I_0 is the beam current, Ω is the relativistic cyclotron frequency, and ω is the wave frequency. Except as noted, all quantities are expressed in MKS units. Equation (4) agrees with the result given in [15], except for the presence of the term proportional to $\cos \psi$. This term was not included in [15] or [7], which both assume operation at detunings (magnetic fields) for which $\mu^2 \Delta/4 \approx 1$. This is a conventional choice for obtaining a high threshold current for self-oscillation of the bunching cavity, but unnecessarily restricts the generality of the result. The intracavity gain is calculated by relating F_2 to F_1 using (3) and (4) and noting that the power generated by the second cavity (P_2) is related to the power injected into the first cavity (P_{in}) as

$$P_2 = P_{in} \frac{F_2^2 Q_{int}}{F_1^2 Q_2} \quad (9)$$

However, the power coupled *out* of the second cavity is given by

$$P_{out} = P_{in} \frac{F_2^2 Q_{int}}{F_1^2 Q_{2ext}} \quad (10)$$

Here Q_{int} corresponds to the internal quality factor of the first cavity, and Q_{2ext} refers to the external quality factor (the Q associated with the coupling aperture) of the second cavity. Note that the cavity lengths do not appear in (9) and (10) because μ_1 and μ_2 are equal.

IV. EXPERIMENTAL RESULTS

The principal measurements were a straightforward gain measurement and a frequency comparison between the first and second cavities. Measurements were carried out

as a function of the drive frequency applied to the first cavity and as a function of experimental parameters. The diode voltage "flat-top" was 950 ± 50 keV (with 5% ripple), the beam current was 150 ± 20 A, and the calculated beam α was 0.36. The beam α was calculated using a fully relativistic single particle simulation that calculates electron particle trajectories in the combination of solenoidal fields and fields due to the wiggler windings. The wiggler fields were calculated from a complete Biot-Savart solution of the fields due to a one-period untapered wiggler coil with realistic closures at each end.

The frequency of the second cavity was tracked by a heterodyne diagnostic as the driver magnetron frequency was varied. To do this, the signal from OUT-2, after attenuation, was split by a 3-dB coupler, and half of it was combined in a balanced mixer with a local oscillator (an IMPATT diode) whose frequency could be tuned separately from the frequency of the driver magnetron. The magnetron and the IMPATT frequencies were monitored by separate frequency meters whose relative calibration was determined by cold test. By this means, the difference frequency Δf_0 between the drive signal and local oscillator signal could be determined for each separate experimental discharge. The experimental value of Δf for the output of the second bunching cavity, when the first bunching cavity was driven at a known frequency, was determined by analysis of the signal from the balanced mixer which was recorded on an analog oscilloscope. The maxima and zero crossings of the mixer signal were used to count the full and fractional "beats" of the local oscillator frequency against the output frequency of the second cavity during a central 20 ns central interval within the output pulse length. The number of cycles of the beat signal divided by the reference time interval yields an experimental measure of Δf .

Fig. 3 shows a measurement of the variation of the second cavity output frequency as a function of the frequency of the driver magnetron, with the local oscillator frequency held fixed. This data was taken with a cavity magnetic field of 26.6 kG. The plot actually compares the measured beat frequency Δf between the local oscillator (at 35.23 ± 0.02 GHz) and the second cavity output frequency as the first cavity drive frequency was varied between 34.98 and 35.27 GHz. The solid line indicates the predicted beat frequency Δf_0 . This data indicates that the frequency of the signal in the second bunching cavity tracks the drive frequency of the first bunching cavity; i.e., that the gyrokystron circuit is amplifying the signal injected into the first cavity. (In the absence of the beam, there is no measurable leakage between the two cavities at the drive frequencies.)

The amplification factor is measured by determining the ratio of the power generated in the second cavity, as monitored through the coupling port IN-2 (see Fig. 1), to the power injected into the first cavity through the coupling port labeled IN-1, as monitored by the sampling port OUT-1. This determination depends sensitively on the calibration of the coupling factors of the various apertures

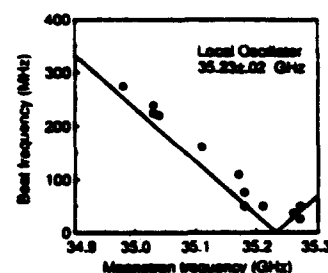


Fig. 3. Measured beat frequency between the local oscillator and second cavity output frequency as a function of the drive frequency of the first cavity. The solid line is the calculated beat frequency based on the measured difference between the local oscillator and magnetron frequencies.

on the first and second bunching cavities. The cold tests were carried out as follows: At critical coupling, essentially all of the drive signal at the coupling aperture flows into the first cavity and is dissipated in the other cavity losses, in this case dominated by the cavity slots. Cold tests were used to determine the ratio of the power injected into IN-1 to the power detected at OUT-1. To determine the power generated in the second cavity, it was assumed that only 37% of the power was coupled out of port IN-2, while the remainder was delivered to the internal cavity losses, dominated by the cavity slots (see the discussion in Section II). Thus the measured signal was multiplied by 2.7.

Fig. 4 plots the linear gain between the first and second cavities as a function of the axial magnetic field at a drive frequency of 35.19 GHz, along with the predicted gain. Since the second cavity was designed as a bunching cavity rather than an output cavity, the gain was defined in terms of the intracavity power P_2 rather than the output power P_{out} . The experimental data were taken by varying the field provided by the cavity solenoid while keeping the main axial magnetic field fixed. Each point in the figure represents a single experimental discharge. The measured gain peaks in the vicinity of 28.5 kG. The highest-single-discharge gain factor is $\sim 90\times$, corresponding to a gain of approximately 19 dB. Based on the difficulty in calibrating the various cavity coupling factors, the uncertainty in this value is at least 3 dB. (The corresponding gain measured in terms of the power coupled out of the second cavity is ~ 15 dB.) The highest intracavity powers in the second cavity were in the range of 50 to 100 kW (20 to 40 kW coupled out), while typical first cavity drive powers were in the range of 1 to 2 kW.

The predicted gain shown in Fig. 4 is calculated from (9). It is found by optimizing (4) with respect to ψ , which corresponds to driving the system close to the cavity resonant frequency. The calculations assume a 950 keV, 150 A, $\alpha = 0.36$ beam. In obtaining this curve, the Bessel function $J_1(q)$ in (4) was approximated by $q/2$. From approximately 22 to 28.5 kG, theory and experiment agree moderately well. The experiment actually does slightly better than the theoretical model in this range of magnetic fields. (It should be noted that small changes in the experimental values of current, voltage, magnetic field, and

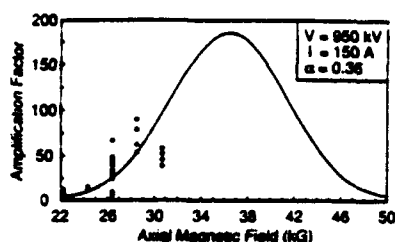


Fig. 4. Experimental power gain of the gyrokystron as a function of the axial magnetic field. The points plot the ratio of the intracavity power of the second cavity to the drive power injected into the first cavity for individual experimental discharges. The solid line is the predicted gain, corresponding to a 950 keV, 150 A, $\alpha = 0.36$ beam.

beam α could produce 50% changes in the predicted gain.) Theory shows the gain to continue to rise at higher magnetic fields, while the data show the gain rolling over. This is believed to be due to the onset of oscillation of the TE_{112} mode. Data taken at still higher magnetic fields show clear evidence of this oscillation. Thus the substantially higher gains predicted at higher magnetic fields are inaccessible due to mode competition. Future efforts will concentrate on achieving stable operation of the third cavity (output cavity), and achieving stable three-cavity gyrokystron amplifier operation.

V. DISCUSSION

We have carried out a fundamental-mode two-cavity K_a -band gyrokystron amplifier experiment driven by a 1 MeV, 150 A electron beam from a pulsedline accelerator. The two cavities were intended to serve as bunching cavities for a higher power output cavity. We have demonstrated that the output frequency of the second cavity tracks the drive frequency over the range from 35.0 to 35.3 GHz and have found a regime of stable amplification. The peak gain was 15 dB, measured to the output of the second cavity, or 19 dB, if defined in terms of the increase in intracavity electric fields, which is the relevant parameter for the intermediate bunching cavity of a gyrokystron. This performance is in reasonable agreement with the predictions of theory. The peak intracavity power in the second cavity was ~ 100 kW. This value was limited by the available drive power and did not correspond to saturation. More than half of this power flowed into slot losses that were intended to stabilize the second cavity as a bunching cavity, rather than to optimize it as an output cavity. As a result, the peak output power was ~ 40 kW. The available parameter space for amplifier operation was limited by the excitation of parasitic oscillation of the competing TE_{112} mode, as predicted by theory [7]. This problem could have been mitigated somewhat by a small reduction in the diameter of the drift spaces. Despite this limitation, these measurements have demonstrated the feasibility of operating gyrokystron amplifiers with megavolt electron beams. In addition, they have demonstrated the feasibility of using multiple bunching cavities to increase the RF fields available for beam

bunching. The resulting increase in bunching would make possible a higher gain in a gyrokystron amplifier, or a larger locking bandwidth in a gyrokystron oscillator.

ACKNOWLEDGMENT

The authors are grateful for useful discussions with Prof. V. L. Granatstein and R. Fischer.

REFERENCES

- [1] A. C. England and H. Hsuan, "Electron cyclotron heating in tokamaks and tokamak reactors," in *Wave Heating and Current Drive in Plasma*, V. L. Granatstein and P. L. Colestock, Eds. New York: Gordon and Breach, 1985, pp. 459-509.
- [2] V. L. Granatstein *et al.*, "Design of gyrotron amplifiers for driving 1 TeV e^-e^- linear colliders," *IEEE Trans. Nucl. Sci.*, vol. NS-32, pp. 2957-2959, 1985.
- [3] L. R. Barnett *et al.*, "Absolute instability competition and suppression in a millimeter-wave gyrotron traveling-wave tube," *Phys. Rev. Lett.*, vol. 63, pp. 1062-1065, 1989.
- [4] R. S. Symons and H. R. Jory, "Cyclotron resonance devices," in *Advances in Electronics and Electron Physics*, Vol. 55, L. Marton and C. Marton, Eds. New York: Academic, 1981, pp. 1-75.
- [5] W. M. Bollen, A. H. McCurdy, B. Arfin, R. K. Parker, and A. K. Ganguly, "Design and performance of a three-cavity gyrokystron amplifier," *IEEE Trans. Plasma Sci.*, vol. PS-13, pp. 417-423, 1985.
- [6] W. M. Black *et al.*, "Megavolt, multi-kiloamp K_a -band gyrotron oscillator experiment," *Phys. Fluids B*, vol. 2, pp. 193-198, 1990.
- [7] A. W. Fliflet, S. H. Gold, and W. M. Manheimer, "Design of a high voltage multi-cavity 35 GHz phase-locked gyrotron oscillator," *Int. J. Electron.*, vol. 67, pp. 111-130, 1989.
- [8] J. R. Bettis *et al.*, "Laser-triggered switch modification to VEBA," *IEEE Trans. Nucl. Sci.*, vol. NS-28, pp. 3091-3093, 1981.
- [9] S. H. Gold, D. L. Hardesty, A. K. Kinkad, L. R. Barnett, and V. L. Granatstein, "A high-gain 35 GHz free-electron laser amplifier experiment," *Phys. Rev. Lett.*, vol. 52, pp. 1218-1221, 1984.
- [10] L. Friedland, "Electron beam dynamics in combined guide and pump magnetic fields for free electron laser applications," *Phys. Fluids*, vol. 23, pp. 2376-2382, 1980.
- [11] J. C. Slater, *Microwave Electronics*. New York: Van Nostrand, 1950, chap. 5.
- [12] V. S. Ergakov and M. A. Moiseev, "Theory of synchronization of oscillations in a cyclotron-resonance maser monotron by an external signal," *Izv. Vyssh. Uchebn. Zaved. Radiofiz.*, vol. 18, pp. 120-131, 1975; also, *Radiophys. Quantum Electron.*, vol. 18, pp. 89-96, 1975.
- [13] A. K. Ganguly and K. R. Chu, "Analysis of two-cavity gyrokystron," *Int. J. Electron.*, vol. 51, pp. 503-520, 1981.
- [14] A. K. Ganguly, A. W. Fliflet, and A. H. McCurdy, "Theory of multicavity gyrokystron amplifier based on a Green's function approach," *IEEE Trans. Plasma Sci.*, vol. PS-13, pp. 409-416, 1985.
- [15] T. M. Tran, B. G. Danly, K. E. Kreischer, J. B. Schutkeker, and R. J. Temkin, "Optimization of gyrokystron efficiency," *Phys. Fluids*, vol. 29, pp. 1274-1281, 1986.
- [16] W. M. Manheimer, "Theory of the multi-cavity phase locked gyrotron oscillator," *Int. J. Electron.*, vol. 63, pp. 29-47, 1987.
- [17] A. W. Fliflet and W. M. Manheimer, "Nonlinear theory of phase-locking gyrotron oscillators driven by an external signal," *Phys. Rev. A*, vol. 39, pp. 3432-3443, 1989.

*



Steven H. Gold (M'86-SM'88) was born in Philadelphia, PA, on September 3, 1946. He received the B.A. degree in physics from Haverford College, Haverford, PA, in 1968, and the M.S. and Ph.D. degrees in physics in 1970 and 1978 from the University of Maryland, College Park. His Ph.D. dissertation topic was an experimental study of plasma turbulence in a high-voltage theta pinch by means of collective laser scattering.

From 1978 to 1980 he held a National Research Council Resident Research Associateship

with the Laser Plasma Branch of the Plasma Physics Division at the Naval Research Laboratory (NRL), Washington, DC. During this period, he studied energy transport through laser-accelerated thin-foil targets using optical diagnostic techniques. Since 1980 he has been a Research Physicist in the Plasma Physics Division at NRL, where he has studied the generation of high-power coherent millimeter-wave radiation from gyrotrons, cyclotron autoresonance masers, and free-electron lasers driven by intense relativistic electron beams. He has published more than 25 papers on these and other topics, and holds two patents and a Statutory Invention Registration. His present position is Supervisory Research Physicist and Head of the Intense Beam Microwave Generation Section of the Beam Physics Branch.

Dr. Gold presently serves on the Executive Committee (ExCom) of the IEEE Nuclear and Plasma Sciences Society's Plasma Science and Applications Committee. He is an Associate Editor of the IEEE TRANSACTIONS ON PLASMA SCIENCE and was Guest Editor of its second Special Issue on "High-Power Microwave Generation" in 1988. He is a member of the Plasma Physics Division of the American Physical Society.

*



Arne W. Fliflet (M'86) was born in Aiken, SC, on December 22, 1947. He received the B.Sc. degree in physics from Duke University, Durham, NC, in 1970, and the Ph.D. degree in physics from the University of Virginia, Charlottesville, in 1975. His thesis topic was the application of the Many Body Perturbation Theory to atomic photoionization.

From 1975 to 1979 he was a Research Fellow in the Chemistry and Chemical Engineering Division of the California Institute of Technology, where he worked on theoretical approaches to low energy electron-molecule collision processes. During this time he also served as a Consultant to the Laser Division of the Lawrence Livermore National Laboratory. From 1979 until 1982 he was a Project Scientist with B-K Dynamics, Inc. in Rockville, MD, where he developed theoretical models for gyrotron oscillators. In 1982 he joined the Naval Research Laboratory (NRL), Washington, DC, as a Research Physicist in the High Power Electromagnetic Radiation Branch. He is currently Head of the Long Pulse Electron Cyclotron Maser Section of the Beam Physics Branch of the Plasma Physics Division of the NRL. Current research interests include conventional and quasi-optical CW gyrotrons, high-voltage pulsed gyrotrons, phase-locked gyrotrons, and Cyclotron Auto-Resonance Maser oscillators and amplifiers.

Dr. Fliflet is a member of the Plasma Physics Division of the American Physical Society.

*



Wallace M. Manheimer (M'59-SM'69) was born in New York City. He received the S.B. degree (physics) from the Massachusetts Institute of Technology, Cambridge, where he also received the Ph.D. degree, also in physics.

From 1967 until 1970 he was on the research staff and Physics Department faculty at MIT. Since 1970 he has been at the Plasma Physics Division of the Naval Research Laboratory (NRL), Washington, DC. Until 1984 he was in the Plasma Theory Branch and worked in high-altitude nuclear effects, inertial fusion, magnetic fusion, advanced accelerators, and radiation sources. From 1984 to 1989 he was the Head of the High Power Electromagnetic Radiation Branch, which did research in gyrotrons, cyclotron auto resonance masers, and the effect of high-power electromagnetic radiation on military systems. Since July 1989 he has been the Senior Scientist for Fundamental Plasma Processes at NRL.

*

Douglas A. Kirkpatrick was born in Paris, France, on May 16, 1959. He received the B.S. degree in physics and mathematics from the College of William and Mary, Williamsburg, VA, in 1980, and the Ph.D. degree in physics from the Massachusetts Institute of Technology, Cambridge, in 1988.

After graduation he joined Science Applications International Corporation, where he is a Research Scientist with the Applied Physics Operation.

His research interests include free electron lasers, electron-beam dynamics, electron-beam generation, gyrotrons, and plasma-filled microwave devices.

*



W. Murray Black (M'71) received the B.S. degree in electrical engineering from the University of Virginia in 1962, the M.S.E.E. degree in 1967 and the Ph.D. degree in electrical engineering in 1971, both from The Pennsylvania State University.

In 1971 he joined the faculty of George Mason University, where he is currently Chairman of the Electrical and Computer Engineering Department. He is also a Consultant in the High Power Electromagnetic Radiation Branch of the Plasma

Physics Division of the Naval Research Laboratory. He has recently conducted research and published papers involving the development of high-power radiation sources such as gyrotrons and relativistic magnetrons.

Dr. Black is a member of the APS, the ASEE, Sigma Xi, and Tau Beta Pi.

*



Allen K. Kinkad was born in Bristol, TN, on May 31, 1935. He attended the School of Mechanical Engineering, East Tennessee State University, Johnson City, from 1958 to 1962, and completed additional courses in electrical engineering and electronics at George Washington University, Washington, DC.

From 1958 to 1962 he was employed in the Engineering Design Section of the Raytheon Aerospace Division. From 1962 through 1965 he was employed at the Apollo Space Craft Division of the North American Aviation Company, where he was involved in the engineering support effort for the Apollo Program. Since 1966, he has been employed at the Naval Research Laboratory, Washington, DC, where he helped build and operate large electron beam pulse generators such as Gamble I, Gamble II, Triton, and Veba. He is currently working on millimeter-wave gyrotron and CARM experiments.

*



Delbert L. Hardesty was born in Akron, OH, on December 2, 1951. He attended the United Electronics Institute in Cuyahoga Falls, OH, from 1969 to 1971.

Since 1980 he has been an Electronics Technician in the Beam Physics Branch of the Plasma Physics Division at the Naval Research Laboratory Washington, DC, where he has assisted in the operation of a variety of high-power microwave generation experiments using pulsedline accelerators, including VEBA and TRITON.

*



Mark S. Sucey was born in Washington, DC, on April 13, 1950. He received the A.A.S. degree in mechanical engineering from Northern Virginia Community College in 1978.

He joined the staff of Jaycor as an Associate Editor in 1980. He has participated in the Light Ion Beam Program and the Free Electron Laser Program at the Naval Research Laboratory (NRL). He is currently working on the NRL High Power Microwave Program.

APPENDIX H

Broad-Band Gyro-Amplifier Research at NRL

BROAD-BAND GYRO-AMPLIFIER RESEARCH AT NRL

J. J. Choi*, G. S. Park[†], S. Y. Park[†], C. M. Armstrong,

R. H. Kyser[‡], and M. L. Barsanti

Naval Research Laboratory, Code 6840, Washington, D.C. 20375-5000

INTRODUCTION

The high power handling capability of millimeter wave gyro-amplifiers makes these devices attractive for applications such as high resolution radar, long range space communication, and plasma heating. The Vacuum Electronics Branch at NRL is making continuing efforts to develop stable, broadband (> 15 %) millimeter wave gyro-amplifiers operating at low beam voltage (< 100 kV). Two configurations are being investigated: a two-stage tapered gyrotron-traveling-wave-tube amplifier (gyro-TWT), and a two-stage slow wave cyclotron amplifier (SWCA). The growth mechanism in the two-stage gyro-TWT is based on phase synchronism between the relativistic cyclotron motion of a gyrating beam and a fast guided wave, leading to the azimuthal phase bunching (cyclotron resonance maser instability); whereas wave growth in the SWCA occurs when the gyrating beam is in synchronism with a slow guided wave, resulting in axial bunching (Weibel instability). A two-stage Ka-band gyro-TWT has been assembled and experiments are currently underway to demonstrate stable, high power, broadband amplification. An initial design study on a Ka-band two-stage SWCA with a sever has been completed. A high quality axis-encircling beam (60 kV, 5 amps, $\Delta v_z/v_z \leq 2\%$ at $v_t/v_z = 1$) is employed in the slow wave circuit. Characteristics of cold-test rf components are described.

TWO-STAGE TAPERED GYRO-TWT AMPLIFIER

Previous experiments on the single-stage Ka-band tapered gyro-TWT at NRL¹ have demonstrated high power (~5 kW), millimeter wave amplification with an instantaneous bandwidth > 30%. As is usual in single-stage distributed amplifiers without severs, gain in this device was limited by the impedance mismatch between the RF amplifying circuit and the vacuum window. In order to increase the stable gain while reducing the amplifier's sensitivity to circuit match, a two-stage tapered gyro-TWT has been designed and built.

The experimental setup of the two stage tapered gyro-TWT is depicted in Figure 1. An annular electron beam is produced from a thermionic cathode of a double anode MIG. The initial beam velocity ratio, $\alpha = v_t/v_z$, is adjusted from 0.5 to 1 at the entrance of the tapered circuit by adjustment of the mod anode voltage and the magnetic field at the cathode. The cathode voltage is typically -33 kV DC and the mod anode voltage (-10 ~ -20 kV) is pulsed at 60 Hz. The circuit consists of three sections: a linearly down-tapered rectangular waveguide input section, a 1" long waveguide cutoff section ($f_{co} = 39.4$ GHz), and a linearly up-tapered rectangular waveguide output section. The rf signal from a frequency synthesizer and a 50 W TWTA is injected into the input section through a directional coupler. The rf amplified in the input section is reflected at the cutoff section and coupled back to a matched load through the directional coupler. The amplified rf power in the output section is extracted directly through a smooth transition to Ka-band waveguide. The width of the circuit varies from 0.24" ($f_{co} = 24.6$ GHz) to 0.15" ($f_{co} = 39.4$ GHz) along the 8" axial length in the input section and from 0.15" to 0.24" along the 12" axial length in the output section. The circuit height throughout its axial extent remains constant at 0.14". The total length is the same as that in the single-stage gyro-TWT and the input and output tapering lengths are selected so that oscillations are not expected in the amplifier. The grazing condition for beam-wave synchronism can be maintained over a wide frequency range by tapering an external magnetic field along both tapered circuits. The grazing magnetic field is related to beam and circuit parameters through $B = \gamma f_{co} / (2.8 \gamma_z)$ in kG, where γ_z is $(1 - (v_z/c)^2)^{-1/2}$ and f_{co} is in GHz. Such a precise non-linear tapered field, as shown in Figure 1, is produced by a computer controlled, 14-coil superconducting magnet system based on a magnet current synthesizing code. As will be shown below, the instantaneous bandwidth of a two-stage gyro-TWT is very sensitive to the axial velocity spread. Thus, in order to produce a low velocity spread beam from the double anode MIG, three water-cooled trim coils are added in the gun region to insure a flat field at the cathode.

A directional coupler to inject RF power in the input section was designed based on Bethe's coupling theory using Chebyshev coupling distribution (7 element and 6 array)². A broad wall coupling of the Ka-band waveguide was chosen because it produces a broader bandwidth than a narrow wall coupling. In order to increase the coupling strength, rectangular holes with rounded corners are used. Figure 2 shows a coupling strength measurement, obtained from a HP8510B network analyzer. Measurements show a coupling value of -1.5 dB, a return loss < -27 dB, and a bandwidth of 43 % (24.1 - 37.4 GHz); these are in good agreement with the simulation using the 3-D electromagnetic code, HFSS³. Two vacuum windows and DC-breaks for monitoring beam currents in the circuit and collector are made of mica films with thickness less than 1 mil.

*SAIC, McLean, VA 22102

[†]Omega-P, Inc., New Haven, CT 06520

[‡]B-K Systems, Inc., Rockville, MD 20850

Cold test measurement on the window shows a reflection of less than -23 dB, which satisfies the amplifier stability condition (Gain < Reflection) in both the input and output sections.

Simulation results for the amplifier performance obtained from a non-linear code⁴ predict a two-stage gain of -30 dB, an electronic efficiency of 20-30 %, and an instantaneous bandwidth of 10-15 % for $\Delta v_z/v_z = 2\%$. In contrast to the single-stage gyro-TWT, the bandwidth is seen to be very sensitive to axial velocity spread, although the efficiency is less sensitive.

TWO-STAGE SLOW WAVE CYCLOTRON AMPLIFIER

Another broadband millimeter wave gyro-device is the slow wave cyclotron amplifier. In this device, a constant group velocity can be maintained over a wide frequency range when a waveguide is appropriately loaded. The SWCA interaction occurs over the frequency band where the wave group velocity is close to the beam axial velocity in the slow wave region ($v_{ph} < c$). Two types of slow wave circuits have been considered: a metallic disk loaded waveguide⁵ and a dielectric loaded waveguide⁶. As an initial experiment, the dielectric loaded circuit was chosen because the amplifier is operated in the lowest TE mode (TE_{x10} -even) and is thus free from mode competition, and because the required magnetic field in the circuit is lower (e.g., -7 kG for a Ka-band operation).

Figure 3 shows a cross-section view of the dielectric loaded circuit. Two dielectric slabs line the narrow walls in the circuit. Transtar⁷ (Al_2O_3 (99.9 %), $\epsilon_r = 10.1$) was chosen because of its low loss tangent ($\sim 10^{-4}$) and its high dielectric strength (~ 190 kV/cm). An irregular circuit is chosen such that the fundamental beam line does not intersect any undesired higher order hybrid modes in the operating frequency range (28 - 36 GHz). As shown in Figure 4, the measured wave dispersion characteristics are in good agreement with the prediction.

A compact (~ 6 cm long) input directional coupler was designed for high coupling value and wide bandwidth. The difference from the gyro-TWT coupler is in that the coupling holes are arrayed with an 8 element, 4 array distribution and thus the coupling strength and the bandwidth are increased with fewer holes. Measurements show a coupling value of -0.4 dB over a 60 % bandwidth (22.7 to > 40 GHz) and a minimum directivity of 45 dB. Table 1 shows the comparison between theory, code, and cold-test results. It was also observed in the simulation that, by reducing the coupling wall thickness from 10 mils to 5 mils, a more compact (~ 4 cm long) coupler can be designed with the coupling strength and flatness as good as the present coupler.

The HFSS-code was utilized to design a mode convertor to couple a fast wave injected from the directional coupler into the slow wave in the circuit. The mode convertor employs two tapered sections. In the first, linearly tapered dielectrics in uniform Ka-band waveguide convert a fast wave TE_{10} mode into a slow wave TE_{x10} -even mode. In the second, both dielectrics and surrounding metallic waveguide are tapered to match with the smaller circuit dimension. Simulations predict pure mode conversion (coupling value ~ -0.02 dB) and low return loss (~ -30 dB) in the frequency range of 22 - 36 GHz. Figure 5 illustrates the difference in the mode conversion efficiency between the irregular dielectric and regular dielectric loading (ie. simple rectangular cross-section). Note that there is mode conversion to a hybrid mode at ~ 33 GHz where the hybrid mode has the same phase velocity as the TE_{x10} -even mode.

Since the maximum RF field is located in the dielectric in the slow wave region, the beam should be propagated close to the dielectric surface for strong coupling. The clearance between the beam and the dielectric in the circuit is ~ 30 mils for a cold beam. Thus, it is possible for a highly energetic beam to be intercepted by the circuit. Arrays of thin wires on the dielectric surface could drain charge buildup. However, simulations show that hybrid modes become very dense near the operating mode when such wires are present, resulting in undesired mode competition. Therefore, a thin conducting film of tantalum is sputtered on to the dielectric surface to drain the space charge. It is also possible that heating of the dielectric due to electron beam bombardment can cause a change in the properties of the dielectric. Cold-test measurements show a 2% increase of the dielectric constant at 200 °C, which was observed similarly in other dielectric materials⁸. Therefore, temperature rise should be monitored during experiments, and circuit cooling may have to be applied.

A non-linear theory⁹ was used to examine the performance of a single-stage amplifier in the small and large signal regions. As shown in Figure 6, the efficiency is very sensitive to beam axial velocity spread. This is because the Weibel instability takes place at large values of the axial propagation constant in the slow wave region. The saturation length is different for $\Delta v_z/v_z = 0, 2, 4\%$. The circuit length was chosen to maximize the gain and efficiency at $\Delta v_z/v_z = 2\%$. A triple pole piece center-post gun¹⁰, designed at Litton and currently in assembly, will be used to produce a high quality axis-encircling beam with a low velocity spread (60 kV, 5 amps, $\Delta v_z/v_z < 2\%$).

As seen in the dispersion relation (Figure 4), oscillation at the second harmonic TE_{x10} -odd mode can exist in the long single-stage circuit. In addition, the odd mode and all the hybrid modes would be completely trapped in the circuit because the dielectric mode convertor is designed such that only TE_{x10} -even mode can couple with the TE_{10} mode. A threshold current of the gyro-BWO in the dielectric loaded slow wave circuit¹¹ is expressed as

$$I_{th} = \frac{4\pi\epsilon_0 mc^3}{e} \frac{\gamma_1^3}{2\beta_1^2} \frac{k_z L_2}{(k_c L_1)^4} \frac{g^3 \Gamma}{J_s^2(x_0)}$$

where $g = 1.9733/L_2$, $k_c = ((\omega/c)^2 - k_z^2)^{1/2}$, $x_0 = k_c r_L$, L_1 = circuit half width, L_2 = circuit height, L_z = circuit length normalized by L_1 , s = harmonic number, and Γ is defined in reference 12. Figure 7 illustrates the threshold currents versus interaction length. It is clear that a sever is necessary for a stable operation of the amplifier at high gain. Backward wave growth (negative phase/group velocity) was observed in a particle-in-cell code, MAGIC¹³ when there was no sever; this is consistent with the prediction from linear theory. The length and tapering angle of two lossy dielectrics for the sever were optimized by the use of HFSS. The code predicts a wave attenuation of better than -25 dB and low reflection (< -30 dB) in the operating frequency range.

Large signal calculations of the two-stage SWCA predict an efficiency of 10-15 %, a gain of 23 - 25 dB, and an instantaneous bandwidth of 15 - 20 % for an input section length = 13.6 cm, output section length = 14.1 cm, sever length = 2 cm, input power = 200W, and $\Delta v_z/v_z = 2$ %. The results from the slow time-scale non-linear code agree with MAGIC simulations for a cold beam.

CONCLUSION

Cold-tests on each component of the two-stage tapered gyro-TWT have been completed. Hot-test of the circuit with a 33 kV, 0.5 - 1 amp beam is currently underway to demonstrate stable high gain broadband amplification.

A design study on the SWCA has been performed to conduct Ka-band experiments on a broadband millimeter wave amplifier with a low magnetic field. An axis-encircling beam with low velocity spread is designed to amplify Ka-band radiation with a power > 30 kW and an instantaneous bandwidth > 15 %. One of the main difficulties in the SWCA experiment will be beam propagation through the circuit.

ACKNOWLEDGEMENTS

The authors would like to acknowledge useful discussions with Drs. J. Hirshfield and V. Granatstein. This work is supported by the Office of Naval Technology.

REFERENCES

- ¹G.S. Park, et. al., IEDM Technical Digest, p. 779-781, 1991
- ²R. Levy, Advances in Microwaves, Vol. 1, ed. by L. Young, 1966
- ³HP High Frequency Structure Simulator, Version A.02.01, Hewlett Packard Co. and Ansoft Co.
- ⁴A. K. Ganguly, et. al., Int. J. Electronics, 53(6), p. 641-658, 1982
- ⁵J. Y. Choe, et. al., Int. J. of Electronics, 53(6), p. 729-741, 1982
- ⁶H. Guo, et. al., Phys. Rev. Lett. 49(10), p. 730-733, 1982
- ⁷Ceradyne, Inc. Costa Mesa, CA
- ⁸W. E. Courtney, IEEE Trans. Microwave Theory and Tech., MTT-18(8), p. 476-485, 1970
- ⁹A. K. Ganguly, et. al., Phys. Rev. A, 42(6), p. 3544-3554, 1990
- ¹⁰G. P. Scheitrum, et. al., IEEE Int. Conf. on Plasma Science, 1991
- ¹¹J. J. Choi, et. al., to be published
- ¹²A. K. Ganguly, et. al., NRL Memo Report 4215, 1980
- ¹³B. Goplen, et. al., MAGIC User's Manual (MRC), Newington, VA, 1989

Table 1. directional coupler designed by 8-element/4-array Chebyshev method

	coupling value (dB)	min. directivity (dB)	3dB bandwidth (GHz)
theory	0	45.4	24 - 42
HFSS	- 0.2	43	22 - 42
cold test	- 0.4	45	22.7 - >40

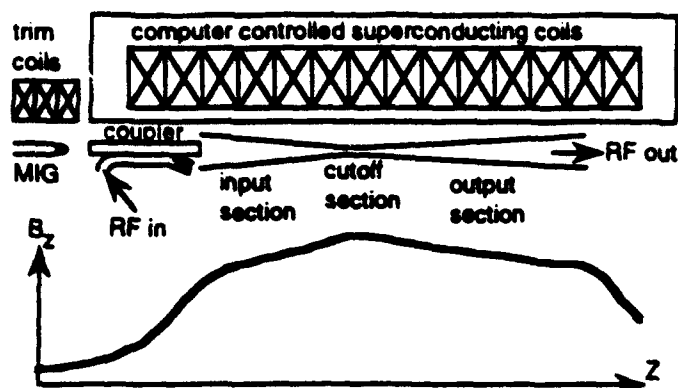


Figure 1. Experimental setup of a two-stage tapered gyro-TWT

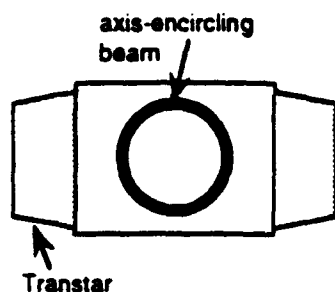


Figure 3. Irregular dielectric loaded circuit

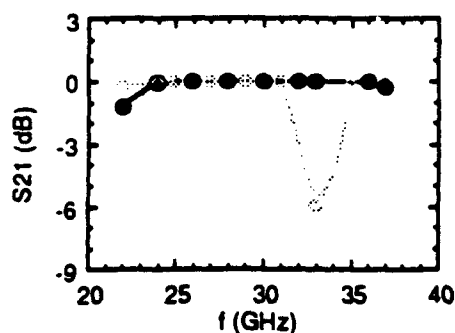


Figure 5. Mode convertor with regular and irregular dielectrics. (○ = regular, ● = irregular)

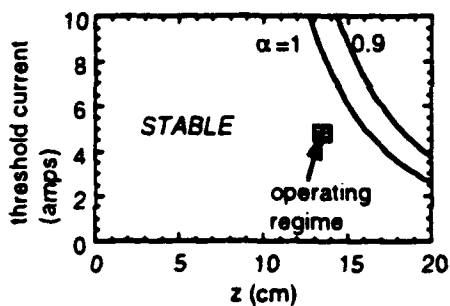


Figure 7. Oscillation threshold current vs axial length for a second harmonic TEx10-odd mode.

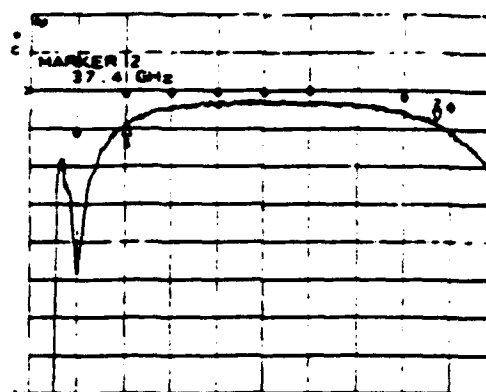


Figure 2. Coupling measurement of a directional coupler ($f_{\text{start}}=20$ GHz, $f_{\text{stop}}=40$ GHz, $R_{\text{ref}}=0$ dB, 5 dB/div). Dots are values obtained from HFSS-simulations.

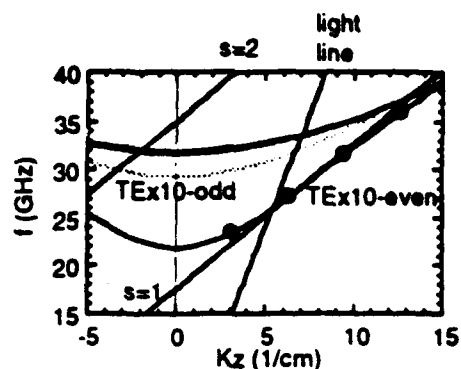


Figure 4. Uncoupled dispersion relations (Dots are measured values.)

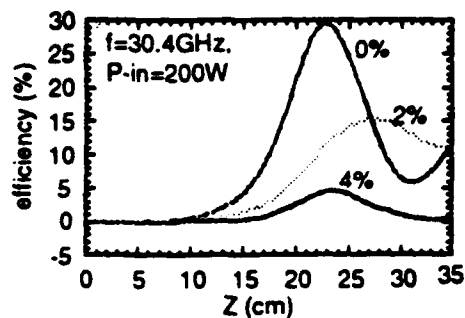


Figure 6. Efficiency vs axial length for a single-stage circuit.

APPENDIX I

Wideband Millimeter Wave Gyro-Amplifiers

WIDEBAND MILLIMETER WAVE GYRO-AMPLIFIERS†

**J. J. Choi*, C. M. Armstrong, A. K. Ganguly, and
M. L. Barsanti**

**Naval Research Laboratory, Vacuum Electronics Branch
Washington, D.C. 20375**

Gyro-TWT amplifier configurations are under investigation to demonstrate broadband ($> 10\%$), multi-kilowatt, millimeter wave generation with low beam voltage (< 60 kV) and low magnetic field (< 1.4 Tesla) for electronic warfare applications. Wideband rf amplification can be achieved by either loading the waveguide to slow down the rf phase velocity of the wave or tapering the waveguide along the axial distance. Three configurations are under study: (1) a broadband W-band harmonic tapered gyro-TWT amplifier, (2) a dielectric loaded slow wave cyclotron amplifier, and (3) a folded waveguide gyro-TWT amplifier.

The broadband harmonic tapered gyro-TWT concept under study is an extension of the Ka-band two-stage tapered gyro-TWT experiment at NRL [1]. The use of tapered waveguide allows wideband interaction along the circuit. As shown in Figure 1, the interaction circuit consists of two linearly tapered circuits of rectangular cross-section separated by a uniform drift section. The input circuit is designed to operate in the fundamental cyclotron harmonic, while the output stage operates in the third harmonic. A two stage configuration is used to isolate the input and output signals and to enhance the gain and efficiency by pre-bunching the beam. The circuit is placed in a nonlinearly tapered external magnetic field which is maintained synchronously at each axial position. Efficient interaction occurs over a broad frequency range when the magnetic field is held near the grazing condition along the circuit. A Ka-band drive signal is injected in the input section to modulate the axis-encircling beam as in the previous two-stage tapered gyro-TWT. However, in the output section, the waveguide width is designed so that the waveguide mode is in phase synchronism with the third harmonic beam cyclotron mode. As a result, amplified radiation in the output section is extracted at frequencies increased by the harmonic number ($s = 3$) over the drive signal. To insure single mode operation, the waveguide operates in the lowest order mode, TE_{10} , in both the input and output sections of the amplifier.

One of key issues for the W-band harmonic gyro-TWT is beam formation and transport. A triple pole piece, center-post electron gun [2] originally designed for the NRL gyropeniotron experiment, will be used to produce a high quality axis-encircling beam for the tapered harmonic experiment. Since the operating mode is the lowest rectangular waveguide mode interacting with the third harmonic beam cyclotron mode, the beam-circuit clearance in the output circuit is tight.

To alleviate the beam clearance problems in the output stage and to allow the use of a single sidewall coupler, an overmoded slotted square waveguide is used. To suppress the undesired polarization in the square guide, lossy dielectrics are placed adjacent to the waveguide slots. For a hot beam in the square output guide, the beam clearance varies from 10 mils (at the narrow end) to 20 mils along the output circuit. This corresponds to a beam filling factor of 50 - 68 %. It is crucial, therefore, that the magnet provide a straight field over the circuit length for good beam propagation. Since the circuit width in the input section is three times wider than the output circuit, beam interception in the input section is not expected to be a problem.

The performance of the harmonic tapered gyro-TWT amplifier has been examined using a self-consistent slow-time-scale nonlinear code [3]. A detailed description can be found in reference 4. Simulation parameters are: beam voltage - 50 kV, current - 2 A, input rf power - 10 W, initial beam velocity ratio at the entrance of the input stage - 1. The simulated efficiency and output power of the amplifier are shown in Figure 2 as a function of frequency for various axial velocity spreads ($\Delta v_z/v_z$) of the electron beam. Gain in the input and output stages are also plotted in Figure 3. The peak efficiency is seen to decrease from 13 % to 8.5 % as $\Delta v_z/v_z$ increases from 0 to 4 %, while the 3 dB bandwidth decreases from 15% to 6%. At $\Delta v_z/v_z = 2$ %, the saturated efficiency is approximately 12 % (corresponding to 12 kW) with a bandwidth of 10 % from 90 - 100 GHz.

A proof-of-principle tapered harmonic experiment is currently underway. Broadband rf vacuum windows have been designed for Ka-band (input window) and W-band (output window). The windows consist of three sections of 1/4 wavelength BeO. Figure 4 shows the return loss measurement for the Ka-band vacuum window. The return loss is observed to be better than - 20 dB in the frequency range of 23.5 - 37.2 GHz (bandwidth = 46 %), which agrees very well with the prediction from a 3-D electromagnetic code, HFSS [5]. A broadband rf directional coupler for the experiment has been designed using Chebyshev impedance transformation theory and Bethe coupling theory [6]. A Ka-band directional coupler has been fabricated using EDM (electrical discharge machining) for cold-test. Figure 5 shows the forward coupling measurement obtained from a HP 8510B network analyzer. Measurements show a coupling value of -0.4 dB over 22.7 to > 40 GHz (BW \geq 60 %), minimum directivity of 40 dB, and return loss of < -25 dB, in good agreement with HFSS predictions.

The second wideband gyro-device concept under study is a dielectric loaded slow wave cyclotron amplifier. By the use of a loaded circuit, a constant group velocity can be maintain over a wide frequency range in the slow wave region therefore providing the possibility for wideband operation. Figure 6 shows a cross-section view of a ridged rectangular circuit which is loaded with two dielectric slabs. A high quality axis-encircling beam (60 kV, 5 A, $\alpha = 1$) couples with the slow waveguide mode, TE_{x10} -even mode in this device. The dielectric height is less than that in the beam tunnel to insure that the fundamental beam line does not intersect any undesired higher

order hybrid modes (such as TM_x modes) in the operating frequency range of interest. The ridged circuit has some advantages over a regular rectangular shape in that (1) the dielectric slabs can be protected from beam interception, and (2) the peak electric field is shifted from inside the dielectric to near the ridges in the beam tunnel. Thus the beam-wave coupling is expected to be improved.

A linear theory [7] predicts second harmonic backward wave oscillations of the TE_{x10} -odd mode in the single stage circuit. In order to suppress the gyro-BWO oscillation, the circuit must be severed. Large signal calculations of the two-stage SWCA predict a saturated efficiency of $\sim 17\%$ (50 kW output power), a gain of ~ 28 dB, and an instantaneous bandwidth of $\sim 20\%$ (29 - 36 GHz) for input power = 150 W, $B = 7$ kG, and $\Delta v_z/v_z = 2\%$. Note that although the SWCA operates at the fundamental cyclotron harmonic interaction the magnetic field is reduced by a factor of 2 compared with conventional fast wave gyro-devices due to the large doppler shift in the electron cyclotron frequency. The results from the slow time-scale non-linear code are found to agree with the simulations by the particle-in-cell code, MAGIC [8]. The design of the SWCA tube has been completed and parts are on order for hot-test. Detailed design calculations for the device can be found in reference 7.

Another wideband gyro-device concept which has recently been investigated is the folded (H-plane bend) waveguide gyro-TWT. As illustrated in Figure 7, the device is configured so that an axis-encircling electron beam exchanges energy with a transverse electromagnetic wave as it passes successively through the narrow walls of a metallic serpentine structure. The major advantages of the folded waveguide gyro-TWT amplifier include; (1) natural rf separation from the spent electron beam, thus easily applicable for operation with a depressed collector for efficiency enhancement, (2) potentially high average power handling capability, (3) simple input and output coupling, and (4) low cost of fabrication. Potential shortcomings for the device include reduced gain per unit length over continuous interaction schemes and bandwidth reduction due to backward wave and/or stop band oscillations.

Figure 8 shows the normalized gain function in a cavity structure as a function of the linear theory detuning parameter for two cases; (a) gyro-klystron type cavity in which case the beam propagates along the long dimension (L) of the cavity, and (b) the case of the folded waveguide in which case the beam propagates along the short dimension (A) of the cavity. The detuning parameters are defined as $(\omega - \omega_c/\gamma - k_z v_z)(L/v_z)$ for the case (a) and $(\omega - \omega_c/\gamma - k_x v_x)(A/v_x)$ for case (b), where ω_c/γ is the relativistic cyclotron frequency, $k_z = \pi/L$, $k_x = \pi/A$, A = cavity width, L = cavity length ($3A$), and v_x and v_z are the beam axial velocity. As depicted in Figure 8, the linear magnitude of the gain function for case (b) is lower by a factor of 10. This is primarily due to the reduction in the interaction length for the folded waveguide case.

In order to examine the large signal performance of the folded waveguide gyro-TWT, the configuration has been modeled and simulated using the PIC code MAGIC. In the simulation, the

transverse and axial length of the serpentine structure was set so that the rf "effective" axial (beam propagation direction) phase velocity was reduced to $[\ell/(\ell+h)]v_{ph} = 0.9 v_{ph}$, where v_{ph} is the phase velocity of an unfolded waveguide and ℓ and h are defined in Figure 7. The beam current was set at 0.5 A, which is less (by a factor 10) than the designed beam current of 5 A, to reduce the beam potential depression effects observed in the 2-D simulation. In the simulations, a high power drive signal of 3 kW was injected to save simulation space and time for saturation. As a result the high power rf injection, a strong electron azimuthal phase bunching was observed after only 4 passes through the folded waveguide circuit. Figure 9 illustrates MAGIC outputs; gain and electronic efficiency versus the number of beam passes through the serpentine waveguide. The saturated electronic efficiency is $\sim 12\%$. The linear gain of the device is expected to be around 1.6 dB/cm for a beam current of 5A.

A cold-test model of the folded waveguide has been fabricated. A beam hole with a diameter of 86 mils was made on the narrow walls of the folded waveguide by wire EDM. A larger hole for high beam power can be accommodated, however, at the expense of the increased rf mismatch near the stop bands. Cold test measurements show a return loss of -12 dB at the stop-bands where the space harmonic modes intersect and -20 dB in the propagation bands. The stopband frequency and spacing are in good agreement with HFSS simulations. In order to increase the spacing between the stop bands, a double ridged circuit is proposed for which broadband ($>10\%$) operation may be possible. The dispersion relation for the ridged folded waveguide gyro-TWT is depicted in Figure 10. Future work includes the study of the threshold conditions for the onset of backward wave gyrotron oscillations for the space harmonics and the development of a slow-time scale non-linear simulation code.

† Work supported by ONR.

*SAIC, McLean, VA 22102

REFERENCES

- [1] J. J. Choi, et. al., Conf. Digest on Infrared and Millimeter wave Conf., p. 314 - 317, 1992
- [2] G. P. Scheitrum, et. al., IEEE Int. Conf. on Plasma Science, 1991
- [3] A. K. Ganguly, et. al., Int. J. Electronics, 53(6), p. 641-658, 1982
- [4] J. J. Choi, et. al. to be published
- [5] HP High Frequency Structure Simulator, Version A.02.01, Hewlett Packard Co. and soft Co.
- [6] H. A. Bethe, Phys. Rev. 66(7), p 163 - 182, 1944
- [7] J. J. Choi, et. al., to be published
- [8] B. Goplen, et. al., MAGIC User's Manual (MRC), Newington, VA, 1993

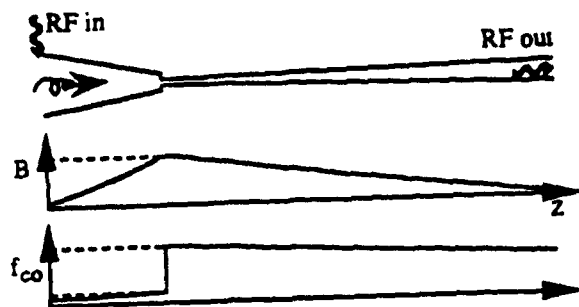


Figure 1. Schematic of the broadband tapered harmonic gyro-TWT amplifier with magnetic field and cutoff frequency axial profiles.

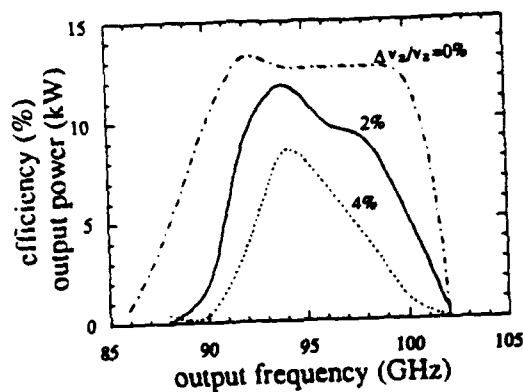


Figure 2. Efficiency and output power versus output frequency for various velocity spreads.

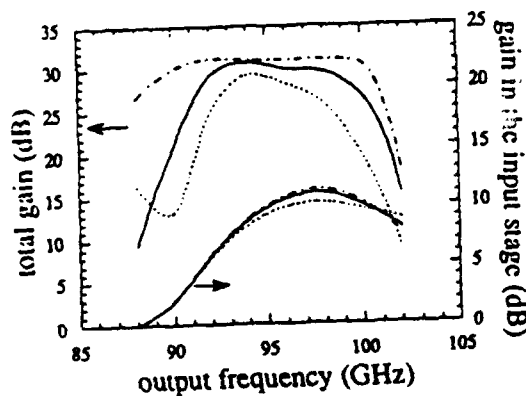


Figure 3. Gain versus output frequency for various velocity spreads. (a long dashed line for $\Delta v_z/v_z=0\%$, a solid line for 2%, and a short dashed line for 4%)

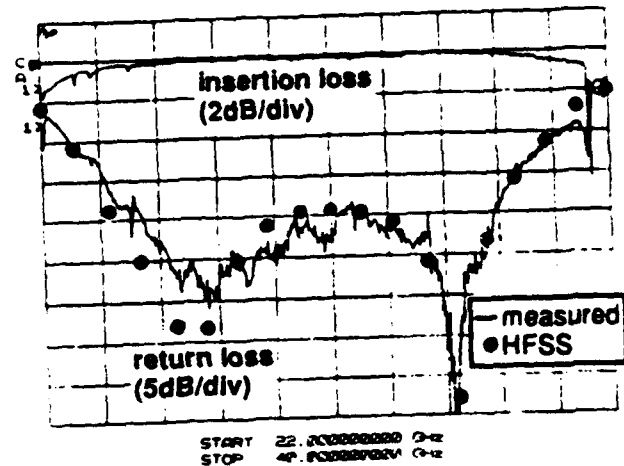


Figure 4. Return loss measurement of the input rf vacuum window.

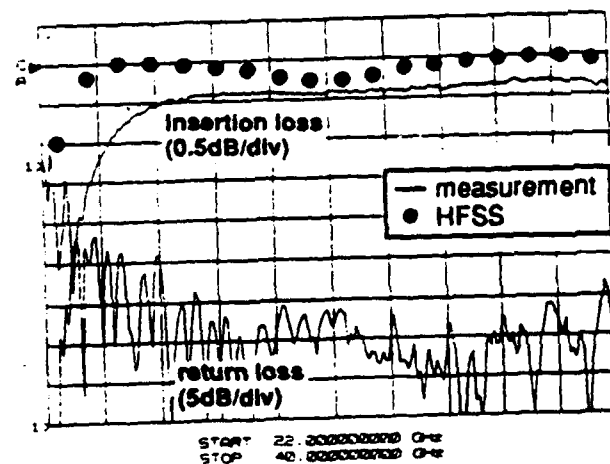


Figure 5. Cold-test results on the input directional coupler

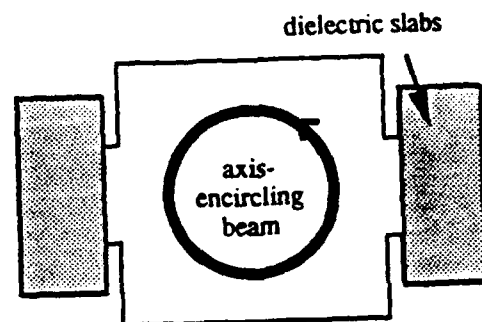


Figure 6. Cross section view of a ridged slow wave circuit.

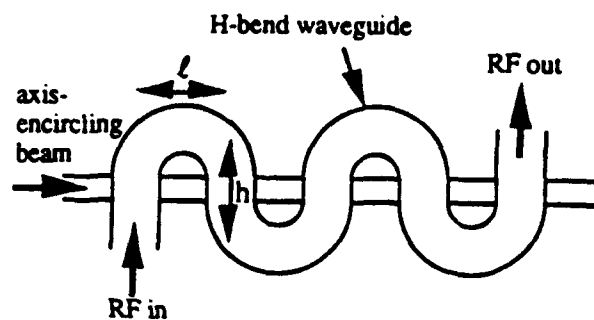


Figure 7. Folded waveguide gyro-TWT

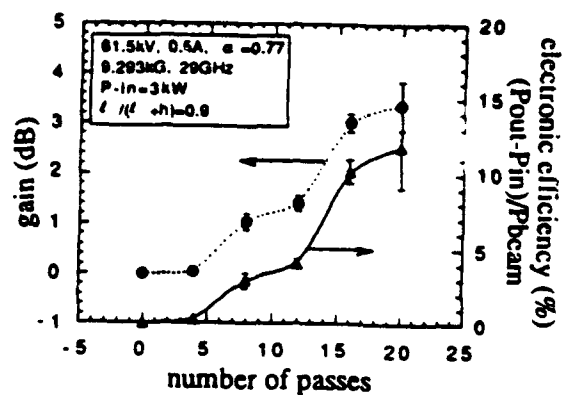


Figure 9. MAGIC results for a folded waveguide gyro-TWT

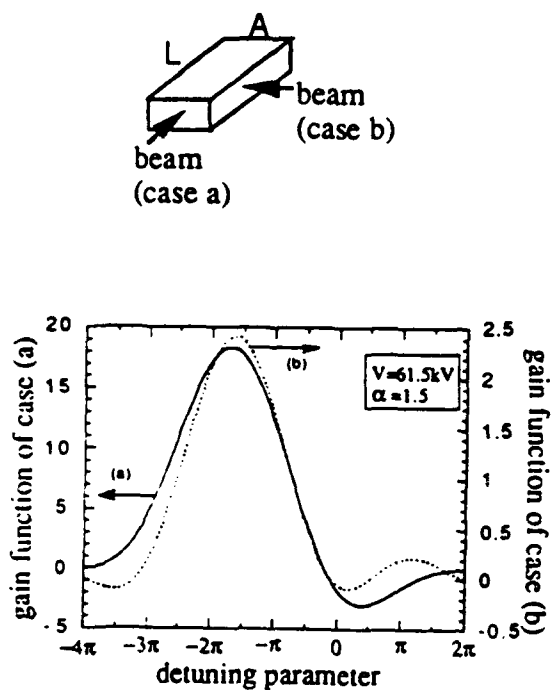


Figure 8. Normalized gain functions in a cavity structure versus detuning parameters

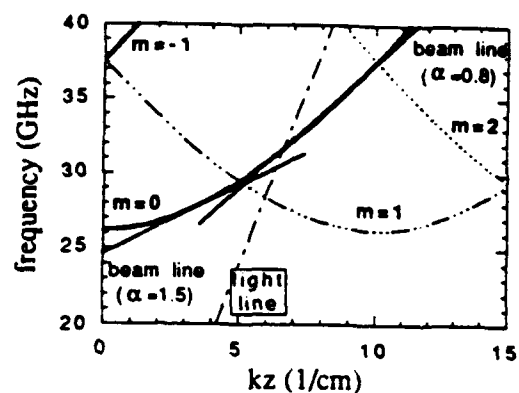


Figure 10. Uncoupled dispersion relations of a ridged folded waveguide gyro-TWT (m denotes index of space harmonics)

APPENDIX J

Wideband Gyro-TWT Amplifier Experiments

WIDEBAND GYRO-TWT AMPLIFIER EXPERIMENTS

J. J. Choi*, G. S. Park[†], S. Y. Park[‡], C. M. Armstrong, A. K. Ganguly,
R. H. Kyser[§], and M. L. Barsanti
Naval Research Laboratory, Code 6840, Washington, D.C. 20375

INTRODUCTION

Research on broadband, multi-kilowatt millimeter wave gyro-TWT amplifiers operating at low beam power (< 300 kW) is attractive for applications such as electronic warfare, radar, and communications. In order to achieve wideband rf amplification in gyro-devices, the waveguide is either tapered along the axial distance or loaded with disks or dielectric. Two Ka-band gyro-TWT amplifiers are considered; (1) a tapered rectangular waveguide and (2) a dielectric loaded rectangular waveguide. A frequency multiplied harmonic interaction in tapered waveguide is also investigated for W-band rf amplification.

TWO-STAGE TAPERED GYRO-TWT AMPLIFIER

Previous experiments on the single-stage Ka-band tapered gyro-TWT at NRL¹ have demonstrated high power (~ 5 kW), millimeter wave amplification with an instantaneous bandwidth $> 30\%$. It was found that gain in the single stage amplifier was limited by reflection-type oscillations caused by the rf mismatch in the vacuum window. Separation of the input section from the output section will stabilize such oscillations.

A two-stage Ka-band gyro-TWT has been assembled and experiments are currently underway. Preliminary experimental results show that there is some beam interception in the multihole directional coupler due to insufficient magnetic compression of the small orbit beam (33 kV, 1 A) produced by the MIG. An improved input coupler is designed for better beam clearance and wider coupling bandwidth. A 3-D electromagnetic code (HFSS)² predicts a coupling value of -0.4 dB and a bandwidth of 60 % (22 GHz - 40 GHz).

Numerical results obtained from a slow-time scale non-linear code³ predict a two-stage gain of ~ 30 dB, an electronic efficiency of 20 - 30 %, and an instantaneous bandwidth of 10 - 15 % for $\Delta v_z/v_z = 2$ %. In contrast to the single-stage gyro-TWT, the bandwidth is expected to be very sensitive to axial velocity spread.

RIDGED SLOW WAVE CYCLOTRON AMPLIFIER

A dielectric loaded rectangular waveguide can provide a constant group velocity over a wide frequency range. Figure 1 shows a cross-section view of the ridged circuit loaded with two dielectric slabs. A high quality axis-encircling beam⁴ (60 kV, 5 A, $\alpha = 1$) couples with the slow wave. The dielectric height is less than that in the beam tunnel to insure that the fundamental beam line does not intersect any undesired higher order hybrid modes in the operating frequency range. The ridged circuit has some advantages over a regular rectangular shape. First, the dielectric slabs can be protected from beam interception. Secondly, the peak electric field is shifted from inside the dielectric to near the ridges in the beam tunnel. Thus the interaction coupling is expected to be improved.

Large signal calculations of the two-stage ridged SWCA predict a saturated efficiency of ~ 17 %, a gain of ~ 28 dB, and an instantaneous bandwidth of ~ 20 % (29 - 36 GHz) for input power = 150 W, $B = 7$ kG, and $\Delta v_z/v_z = 2$ %. The results from the slow time-scale non-linear code agree with MAGIC⁵ simulations for a cold beam.

A broadband rf window has been designed by the use of the HFSS code. It consists of three sections of $1/4$ wavelength BeO. As shown in Figure 2, the return loss is better than -15 dB in the frequency range of 23.5 - 37.2 GHz (bandwidth = 46 %).

FREQUENCY MULTIPLIED HARMONIC GYRO-TWT AMPLIFIER

The operation of a "frequency multiplier" broadband harmonic gyro-TWT amplifier configuration is also under investigation. Figure 3 depicts the schematic of the amplifier, and the axial profiles of the non-linear tapered magnetic field (9 - 13 kG) and the circuit cutoff frequency. A Ka-band frequency drive signal is injected in the tapered fundamental input section to modulate the axis-encircling beam (50 kV, 2 A), as in the two-stage tapered gyro-TWT. However, in the tapered output section, the waveguide width is designed so that the waveguide mode is in phase synchronism with the third harmonic beam cyclotron mode. As a result, amplified radiation in the tapered output section is extracted at frequencies increased by the harmonic number. The operating waveguide mode is the lowest order mode, TE₁₀, in both the input and output sections of the amplifier.

*SAIC, McLean, VA 22102

[†]Omega-P, Inc., New Haven, CT 06520

[§]B-K Systems, Inc., Rockville, MD 20850

A self-consistent slow-time scale non-linear code has been used to simulate the amplifier performance. The calculated efficiency and output power are shown in Figure 4 as a function of frequency for various axial velocity spreads of the electron beam. The efficiency drops slowly as the beam velocity spread increases but the instantaneous bandwidth shrinks more rapidly. Simulations also show that the amplifier operation is insensitive to the guiding center spread. At $\Delta v_z/v_z = 2\%$, the saturated efficiency and gain are $\sim 12\%$ and ~ 30 dB. The bandwidth is predicted to be $\sim 10\%$ with output frequency in the range of 90 - 100 GHz. A drive signal of ~ 10 W in the 30 - 33 GHz frequency range is sufficient to saturate the output power in the frequency range of 90 - 100 GHz.

CONCLUSION

Experiments on the Ka-band two-stage tapered gyro-TWT amplifier are underway with the improved input directional coupler. The ridged SWCA has been designed to conduct Ka-band experiments operating at a low magnetic field. The frequency multiplied harmonic gyro-TWT has been investigated to produce W-band radiation with $\sim 10\%$ instantaneous bandwidth. Both the SWCA and the harmonic gyro-TWT require an axis-encircling beam with low velocity spread.

ACKNOWLEDGMENTS

This work is supported by the Office of Naval Research.

REFERENCES

- ¹G.S. Park, et. al., IEDM Technical Digest, p. 779-781, 1991
- ²HP High Frequency Structure Simulator, Version A.02.01, Hewlett Packard Co. and Ansoft Co.
- ³A. K. Ganguly, et. al., Int. J. Electronics, 53(6), p. 641-658, 1982
- ⁴G. P. Scheitrum, et. al., IEEE Int. Conf. on Plasma Science, 1991
- ⁵B. Goplen, et. al., MAGIC User's Manual (MRC), Newington, VA, 1989

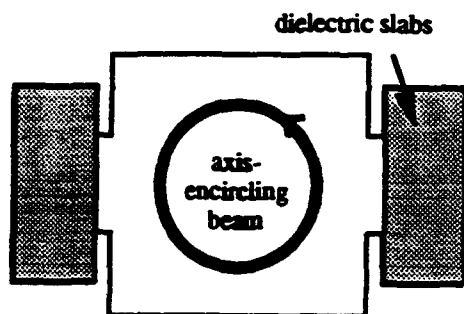


Figure 1. Cross section view of the ridged slow wave circuit.

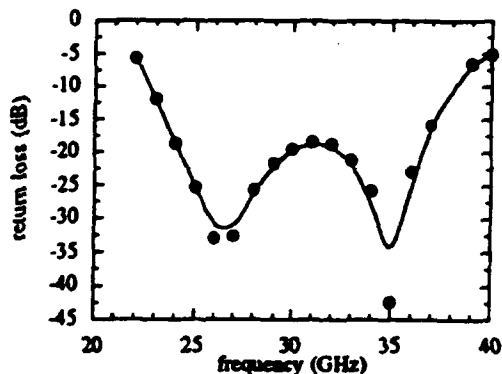


Figure 2. Return loss of the BeO window.

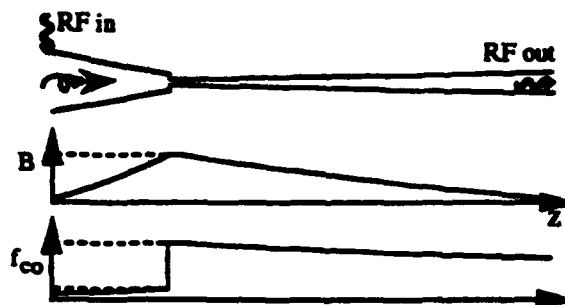


Figure 3. Schematic of the broadband frequency multiplied harmonic gyro-amplifier with magnetic field and cutoff frequency axial profiles.

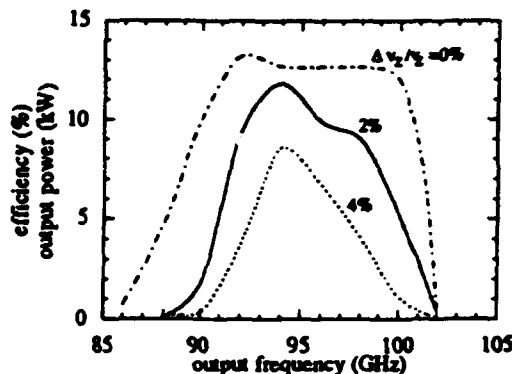


Figure 4. Efficiency and output power versus output frequency for various velocity spreads.

APPENDIX K

Design of a 50 kW, Broad Ka-Band Slow Wave Cyclotron Amplifier

DESIGN OF A 50 kW, BROAD Ka-BAND SLOW WAVE CYCLOTRON AMPLIFIER

J. J. Choi*, C. M. Armstrong, A. K. Ganguly, and M. L. Barsanti

Naval Research Laboratory, Vacuum Electronics Branch, Washington, D.C. 20375

ABSTRACT

A two-stage slow wave cyclotron amplifier is investigated to demonstrate a high power, stable, and broad Ka-band radiation source, operating at a low beam power (~ 60 kV, ~ 5 amps) and a low magnetic field (~ 7 kG). A linear theory predicts that the second harmonic gyro-BWO is competing in the amplifier and can be stabilized by inserting a sever in the interaction circuit. A slow-time-scale non-linear code, with a sever included, predicts a saturated gain of 24 - 28 dB, an efficiency of 15 - 17 %, and an instantaneous bandwidth of 15 - 20 % at a beam axial velocity spread of 2 %. A broadband rf coupler and a mode converter are designed by the use of a 3-D electromagnetic, finite element code. Measured rf characteristics are in good agreement with predictions.

*SAIC, McLean, VA 22102

I. INTRODUCTION

Increasing demands on broadband radiation sources in millimeter and submillimeter wavelengths for applications such as high resolution radar/communications¹ make gyrotron devices attractive because of their high power handling capability. The Vacuum Electronics Branch at NRL is making continuing efforts in the development of stable, broad (bandwidth > 20 %) Ka-band gyro-amplifiers operating at a low beam power (< 100 kV, < 5 amps). One of the recent gyro-amplifier experiments is a tapered single-stage gyro-TWT amplifier². It has demonstrated a saturated power of 5 kW and an instantaneous bandwidth > 30% in the Ka-band frequency range. As in usual single-stage amplifiers without severs, however, the gain was limited by the traveling wave mismatch between the RF amplifying circuit and the vacuum window. A two-stage tapered gyro-TWT³ reduces sensitivity on the wave mismatch and enhances the amplifier gain without gain fluctuation with frequency.

Gyro-devices such as tapered gyro-TWT amplifiers are operated at a very high external magnetic field, e.g., 9 - 14 kG to produce Ka-band radiation. Harmonic operations in gyro-peniotrons⁴ and gyro-TWTs with a vane structure⁵ are proposed to overcome such a high magnetic field requirement. Another concept on a millimeter wave gyro-device operating at a low magnetic field is a dielectric loaded slow wave cyclotron amplifier (SWCA). The beam-wave instability in the SWCA (called Weibel instability⁶) takes place when the gyrating beam is in resonance in phase with a slow waveguide mode and an axial bunching due to a $\vec{v}_\perp \times \vec{B}$ force dominates where \vec{v}_\perp is a beam perpendicular momentum and \vec{B} is a rf magnetic field. It is shown that the Weibel instability competes with a cyclotron resonance maser instability: azimuthal bunching dominates in a fast wave region and axial bunching dominates in a slow wave region⁷. One advantage of the SWCA over the harmonic gyro-devices is that a SWCA interaction range can be designed to be broadband because a constant wave group velocity is maintained over a wide frequency range when the waveguide is loaded such that the wave group velocity is close to the beam

axial velocity in the slow wave region ($v_{ph} < c$). In addition, a fundamental cyclotron mode can couple to the lowest waveguide mode, thus less mode competition is expected.

Linear theories on the dielectric loaded slow wave cyclotron amplifier were reported for both a rectangular waveguide⁸ and a circular waveguide⁹ in early 1980s. The experiment at Yale proved the principle of the slow wave cyclotron interaction in a higher order mode, TE_{01} circular waveguide mode¹⁰. However, the interaction circuit was not optimized due to the lack of a large signal non-linear theory of the beam-wave interaction. Further, the bandwidth of the amplifier was not as wide as expected, probably due to low beam quality with large axial velocity spread and mode competition with other hybrid modes and backward wave oscillations. No other experimental result on the SWCA was published.

Recently, a slow-time-scale non-linear code¹¹ has been developed for the SWCA. The present paper describes, by the use of the non-linear code, detailed design studies on a two-stage SWCA with a view to demonstrate a stable, broadband millimeter wave gyro-amplifier with high gain. Amplifier stability in the second harmonic gyro-BWO was examined from a linear theory. To demonstrate the wide bandwidth of the amplifier, a rf input coupler was designed for a high directivity and a high coupling value over a broadband frequency range. A compact multi-hole directional coupler has been constructed, based on a Chebyshev coupling theory¹² and a Bethe's coupling theory¹³. Cold-test measurements show good agreement with theoretical predictions and simulation results from a 3-D electromagnetic, finite element code (HFSS¹⁴).

II. DISPERSION CHARACTERISTICS

A proposed experimental configuration is shown in Figure 1. Since the Larmor radius of a gyrating beam is larger at smaller magnetic field, an axis-encircling beam is used to couple the lowest mode of a dielectric lined rectangular circuit. A high quality axis-encircling beam is produced from a triple-pole-piece center-posted gun¹⁵. A ratio of

perpendicular velocity to parallel velocity, $\alpha = v_{\perp}/v_{\parallel}$, is externally controlled by a bias voltage applied to two electrodes placed directly after the cathode and magnetic fields in the pole piece region. As shown in Figure 1, two dielectric slabs line the narrow walls in the circuit. Transtar¹⁶ (Al_2O_3 (99.9 %), relative dielectric constant (ϵ_r) = 10.1) was chosen because of low loss tangent ($\sim 10^{-4}$) and high dielectric strength (~ 190 kV/cm). Wave dispersion characteristics of a dielectric lined rectangular waveguide are generally described by LSE (longitudinal section electric) and LSM (longitudinal section magnetic) modes¹⁷. LSE_x ($E_x = 0$) and LSM_x ($H_x = 0$) modes are often referred as TE_x and TM_x modes respectively where electric fields for LSE_x and magnetic fields for LSM_x can be either symmetric or asymmetric with respect to $x = 0$ plane. Using the boundary conditions of $E_{\text{tan}}^0 = E_{\text{tan}}^d = 0$ on conductor and $E_{\text{tan}}^0 = E_{\text{tan}}^d$, $H_{\text{tan}}^0 = H_{\text{tan}}^d$, $\epsilon_0 E_{\text{norm}}^0 = \epsilon_d E_{\text{norm}}^d$, $\mu_0 H_{\text{norm}}^0 = \mu_d H_{\text{norm}}^d$ on vacuum-dielectric interface where 0 and d denote vacuum and dielectric regions respectively, one can get dispersion relations as

$$\begin{aligned} k_{nm} \tan k_{nm} d - k'_{nm} \cot k'_{nm} w &= 0 \\ k_{nm} \cot k_{nm} d + k'_{nm} \cot k'_{nm} w &= 0 \end{aligned} \quad \text{Equ. 1}$$

for even symmetry TE_{xnm} , odd symmetry TE_{xnm} modes, and

$$\begin{aligned} \epsilon_r k_{nm} \tan k_{nm} d + k'_{nm} \tan k'_{nm} w &= 0 \\ \epsilon_r k_{nm} \cot k_{nm} d - k'_{nm} \tan k'_{nm} w &= 0 \end{aligned} \quad \text{Equ. 2}$$

for even symmetry TM_{xnm} , odd symmetry TM_{xnm} modes respectively. Here, k_{nm} is $((2\pi f/c)^2 - (m\pi/L_y)^2 - k_{\parallel}^2)^{1/2}$, k'_{nm} is $(\epsilon_r(2\pi f/c)^2 - (m\pi/L_y)^2 - k_{\parallel}^2)^{1/2}$, k_{\parallel} is an axial propagation constant, $\epsilon_r = \epsilon_d/\epsilon_0$, d is the distance from center to dielectric, w is dielectric thickness, and L_y is height. The subscript n is the n -th root of the dispersion relations.

The lowest mode, TE_{x10} -even, was chosen as an operating mode. The only non-zero electric field of the TE_{x10} -even mode is an E_y -component, given by

$$\begin{aligned} E_y^0 &= A_m \frac{jk_{||}}{\epsilon_0} \cos k_{nm} x \\ E_y^d &= A_m \frac{jk_{||} \cos k_{nm} d}{\epsilon_0 \sin k_{nm} w} \sin k'_{nm} (L_x - |x|) \end{aligned} \quad \text{Equ. 3}$$

where $L_x = d + w$ and A_m is constant. As shown in Figure 2, it is interesting to note that a peak electric field of the TE_{x10} -even mode shifts into a dielectric region as frequency increases. This is different from the case of an empty metallic waveguide in which a transverse electric field profile is independent of frequency. It indicates that a beam-wave coupling strength in the slow wave structure is weak in a high frequency region, as will be also shown in non-linear simulations later.

The slow waveguide mode becomes unstable when in phase synchronism with a beam cyclotron mode, given by

$$\omega = s \frac{\Omega_c}{\gamma} + k_{||} \beta_{||} c \quad \text{Equ. 4}$$

where s is a harmonic number, ω_c/γ is a relativistic cyclotron frequency and $\beta_{||}$ is a beam axial velocity. Uncoupled dispersion relations of a fundamental beam mode and six lowest waveguide modes in a regular rectangular dielectric lined circuit are calculated using Equ. 1 and Equ. 2 and plotted in Figure 3. It is also shown that HFSS simulations on dispersion relations are in good agreement with the calculation. Note that the TM_{x11} mode intersect with the designed TE_{x10} -even mode at ~ 33 GHz. An irregular circuit, as the cross-section view is shown in Figure 1, is designed so that the fundamental beam mode does not intersect with any undesired TM_x modes in band. The dielectric height is less than the beam tunnel and tapered down by 5° to raise cutoff frequencies of the TM_x modes without

affecting the TE_x modes. Waveguide dispersion curves of the irregular circuit obtained from the HFSS code are presented in Figure 4.

An experimental verification was performed by the use of a HP 8510B network analyzer to check the validity of the code results on the dispersion characteristics. A rf signal couples in and out from an enclosed cavity by means of two small coupling holes to avoid perturbation of the resonant peaks. As shown in Figure 4, measured resonant frequencies of the TE_{x10p} -even modes (axial mode index, $p = 1, 2, 3$, and 4) are in good agreement with the prediction. This measurement also provides a measured value of the dielectric constant of Transtar, $\epsilon_r = 10.1$.

III. STABILITY ANALYSIS AND CIRCUIT DESIGN

A self-consistent slow-time-scale non-linear code¹¹ has been used to simulate the performance of a single stage SWCA. In this formulation, the electromagnetic field is expanded as a superposition of unperturbed TE modes of an empty waveguide. Maxwell's equations are averaged over a wave period, allowing a series of slow-time-scale equations to be derived for the evolution of the amplitude and phase of each TE mode as driven by an electron beam in an external guide magnetic field. In general, the guide magnetic field is axisymmetric but nonuniform. The modes are coupled through their mutual nonlinear interaction with the ensemble of beam electrons. The wave-period averaging allows multi-mode interactions to be considered provided the frequencies are integral multiples of a fundamental frequency, and provided the time average is done over the fundamental wave period. In this case, the particles that enter the interaction region at times separated by integral multiples of the fundamental wave period will execute identical trajectories even though they interact with many modes. The time-averaged field equations are integrated simultaneously with the three dimensional Lorentz force equations that determine the particle orbits. No averaging is done for the orbit equations. The trajectory of each particle is calculated by summing contributions from each mode. The non-linear equations for

gyrotron traveling wave amplifiers including the effects of guiding center motion and axial velocity spread. The theory can be easily extended to include a nonuniform guide magnetic field. In the simulation, all other modes except a TE_{x10} -even mode are assumed to be absent and ohmic loss of a dielectric material is ignored.

Since the peak RF field is located in the dielectric in the slow wave region, the beam should be propagated close to the dielectric surface for high efficiency. However, in practice, a beam radius (or, a Larmor radius in a axis-encircling beam) can not be more than $0.9d$ because of difficulties in aligning a beam axis to a magnetic field axis and in having a straight field axis. In the present design, a 30 mil clearance between a beam and a dielectric surface is chosen. To compensate the weak interaction due to such a large clearance for beam propagation, a longer interaction length or a higher input power would be required for saturation. Increasing the input power for saturation is limited by the threshold breakdown power of a dielectric and power handling capability of waveguide. Figure 5 shows the difference of saturation lengths between the case of a 30 mil clearance and 15 mil clearance where a beam axial velocity spread, $\Delta v_{||}/v_{||} = 2\%$ is assumed for both cases. The interaction length for the case of 30 mil clearance is about 30 % longer, compared with the case of 15 mil clearance. Note that the saturated efficiencies are about the same for the two cases. Figure 6 illustrates a large signal efficiency versus axial length for $\Delta v_{||}/v_{||} = 0\%$, 2 %, and 4 %. The efficiency is very sensitive to the velocity spreads. This is because the SWCA interaction takes place in the large value of propagation constant, $k_{||}$. An interaction circuit length, $L_z = 27$ cm, is determined where a maximum efficiency occurs at $\Delta v_{||}/v_{||} = 2\%$.

As seen in the dispersion relation in Figure 4, a possible oscillation in the second harmonic TE_{x10} -odd mode exists in such a long single-stage SWCA circuit. A universal equation for a gyro-BWO threshold condition is derived in other literature¹⁸. A BWO threshold current or length is predicted by solving

$$\sum_{i=1}^3 \left(1 - \frac{2\Delta/3}{\delta\bar{k}_i - \Delta/3}\right) \cdot \exp(j\delta\bar{k}_i \bar{L}_z) = 0 \quad \text{Equ. 5}$$

where Δ is a detuning parameter, $\Delta = \bar{k}_\parallel + (\bar{\omega} - s\Omega_c / \gamma) / \beta_\parallel$, and \bar{L}_z is an interaction length normalized by L_x . The three $\delta\bar{k}_i$ values are roots of a cubic equation,

$$\delta\bar{k}(\delta\bar{k} - \Delta)^2 + \epsilon^3 = 0 \quad \text{Equ. 6}$$

where the coupling constant, ϵ , is related to all beam and circuit parameters. A general solution of Equ. 5 is $g\bar{L}_z = 1.9733$ where g is related to ϵ through

$$g^3 = \frac{\epsilon(k_{nm}L_x)^4}{2\beta_\parallel^2 k_\parallel L_x} \quad \text{Equ. 7}$$

A linear theory⁸ of the slow wave cyclotron interaction predicts a coupling constant of

$$\epsilon = \frac{eI_b}{8\epsilon_0 m_0 c^3} \frac{\beta_\perp^2}{\gamma\beta_\parallel} \frac{L_x}{L_y \Theta} \{1 + J_0(2k_c r_0)\} \{J'_s(k_c r_L)\}^2 \quad \text{Equ. 8}$$

where $4\pi\epsilon_0 m_0 c^3 / e = 17.1$ kA, L_y is a circuit height, r_0 is a beam radius, r_L is a beam Larmor radius. A dimensionless quantity, Θ , for odd-symmetry modes such as a TE_{xn0} -odd mode is given as

$$\Theta = \frac{d}{d+w} \left(1 - \frac{\sin 2k_{nm}d}{2k_{nm}d}\right) + \frac{\epsilon}{\epsilon_0} \frac{w}{d+w} \frac{k_{nm}^2 \cos^2 k_{nm}d}{k_{nm}'^2 \cos^2 k_{nm}'w} \left(1 - \frac{\sin 2k_{nm}'w}{2k_{nm}'w}\right) \quad \text{Equ. 9}$$

For even-symmetry modes, $\sin 2k_{nm}d$ is replaced with $-\sin 2k_{nm}d$ and $\cos^2 k_{nm}d$ with $\sin^2 k_{nm}d$. From Equ. 7 and Equ. 8, a threshold current of gyro-BWO in the second harmonic TE_{x10} -odd mode interaction is derived as

$$I_{th} = \frac{4\epsilon_0 m_0 c^3 \gamma \beta_1^3}{e} \frac{k_{||} L_y}{\beta_1^2 (k_{nm} L_x)^4} \frac{g^3 \Theta}{\{1 + J_0(2k_{nm} r_0)\} \{J'_s(k_{nm} r_L)\}^2} \quad \text{Equ. 10}$$

where a cold beam is assumed. Figure 7 illustrates threshold currents versus interaction circuit length for $\alpha = 0.6, 0.8$, and 1. Since a single-stage circuit with an interaction length of 27 cm is predicted to excite the second harmonic gyro-BWO, a two-stage circuit with a sever is employed for stable operation of the amplifier at high gain. A circuit length of each section is determined to be shorter than the threshold length corresponding to the operating beam current of 5 amps.

The slow-time-scale non-linear code used for examining the single stage SWCA has been modified to design a two-stage circuit with a sever. In the code, rf electric fields are set at zero in the sever region. Since a saturation length or power depends on an input frequency, all the following simulations were optimized at a frequency of 30.4 GHz. Figure 8 shows gain and efficiency versus input rf power where $\Delta v_{||}/v_{||} = 2\%$, input section = 13.6 cm, sever = 1.5 cm, and output section = 14.1 cm. Saturation occurs at the input power of 200 watts. The dependence of electronic efficiency on a sever length is depicted in Figure 9. A sever length of 1 - 2.5 cm is determined to be an optimum length. As shown in Figure 10, large signal simulations of the two-stage SWCA predict an efficiency of $\sim 15\%$, gain of ~ 24 dB, and an instantaneous bandwidth of $\sim 15\%$ where $\Delta v_{||}/v_{||} = 2\%$. Table 1 summarizes the design parameters of the two-stage SWCA.

A 2-1/2-D particle-in-cell (PIC) code, MAGIC¹⁹ simulation with a cold beam is performed to compare with the large signal results from the slow-time-scale non-linear code. The PIC code includes a fast-time-scale phenomena and space charge effects which

are assumed to be negligible in the non-linear code. MAGIC is capable of modeling and simulating the SWCA circuit because both the axis-encircling beam and the E_y -component of TE_{x10} modes are symmetric along y-axis. A sever is modeled with two lossy dielectrics lined on the side walls which resistivity changes gradually along axis so that a return loss is negligible. A TE_{x10} -even mode with frequency = 30.4 GHz and input power = 147 W is launched at the beam entrance. As shown in the MAGIC output plots in Figure 11, an injected rf field keeps growing in the input section until it encounters the sever in which rf power is attenuated by - 23 dB. A bunched electron beam passes through the sever and gives up its kinetic energy to a rf energy in the output section until saturation. Rf growth becomes saturated at ~ 26 cm, which is in good agreement with a saturation length of 26.3 cm predicted from the non-linear code. Energy re-absorption to the electron beam after saturation is seen as well. This is because, as mentioned early, the circuit length for saturation is optimized at $\Delta v_{||}/v_{||} = 2\%$. Both a frequency spectrum and a transverse mode pattern confirm a single TE_{x10} -even mode at 30.4 GHz. An amplified rf power is obtained by calculating a slope in Figure 11(b), which is an energy gained from rf to an electron beam divided by a time period. The calculated gain of 25.6 dB agrees with 26 dB obtained from the non-linear simulation. The small discrepancy could be due to the difference in modeling the sever: in the non-linear code, the whole sever region assumes zero field whereas, in the MAGIC, rf attenuates gradually as in an actual tapered sever. No gyro-BWOs were excited as expected. More MAGIC simulations with different input powers are presented in Figure 12, showing good agreements between the particle-in-cell code and the slow-time-scale non-linear code.

When a high energetic electron beam is intercepted in the circuit, an rf amplification would no longer last because a temperature rise in the dielectric changes the dielectric properties. Another source of a temperature rise is in a finite loss tangent of Transtar. Power dissipation is written as

$$P_{dsp} = \frac{1}{2} \omega \epsilon_r \epsilon_0 \tan \delta \int_V |E|^2 dv$$

Equ. 11

where $\tan \delta$ is loss tangent, E is given in Equ. 3, and integration is over dielectric volume. For loss tangent of 10^{-4} , the ratio of a dissipated power in the dielectric power to a total power in the circuit is calculated to be -23 dB, which is significant in the operation with a high duty cycle. The sensitivity of the amplifier performance on the change of a dielectric constant was examined. As shown in Figure 13, an efficiency and bandwidth of the amplifier drop by half when the dielectric constant is changed by $\sim 2\%$. A cold-test has been performed to observe a dielectric constant change as a function of temperature by measuring cavity resonant frequencies of a TE_{x104} -even mode. A thermal expansion of the cavity metal enclosure and the dielectric was taken into account in calculating a dielectric constant. As shown in Figure 14, the dielectric constant of 10.08 at room temperature changes to 10.23 at 200 °C, which was observed similarly in other dielectric materials²⁰. Therefore, temperature rise should be monitored during experiments, and circuit cooling may have to be applied.

In order to drain the space charge off in case of electron beam bombardment, a conducting material should be applied on the dielectric. Arrays of thin wires on the dielectric surface perpendicular to the electric field direction would cure the charge buildup problem. However, HFSS simulations predict that hybrid modes become very dense near the operating mode, resulting in undesired mode competition. A thin conducting film which thickness is much less than a skin depth is sputtered on the dielectric surface to drain the space charge off.

IV. RIDGED SLOW WAVE CIRCUIT

A ridged irregular circuit, as shown in Figure 15(a), is proposed. It consists of two dielectrics lined on the narrow walls and four metal ridges next to dielectrics. Dielectric

height is less than beam tunnel as before, so that TM_x modes can not be supported in the circuit in the operating frequency range. One of the major advantages is that the metal ridges prevent electron beam bombardment on dielectrics. Therefore, one can design the circuit of shorter length and tighter clearance between beam and dielectric. In addition, beam-wave coupling in the ridged circuit is expected to be stronger than the circuit without ridges because a peak electric field shifts from inside dielectric to near ridges. Electric field distributions for the cases of a regular circuit and a ridged circuit are shown in Figure 15(b). With a 20 mil clearance, the large signal non-linear simulations are performed assuming a regular circuit. It predicts an efficiency of 17 %, a gain of 28 dB, and an instantaneous bandwidth of 20 % (29 - 36 GHz) where input section = 9.3 cm, output section = 13.9 cm, sever = 1.2 cm, input power = 90 W, and $\Delta v_{||}/v_{||} = 2$ %. A dispersion curve of a TE_{x10} mode in the ridged circuit is not significantly affected by the ridges and the irregular dielectric shaping. Even broader band operation than the predicted bandwidth (> 20 %) may be possible because a constant group velocity of the TE_{x10} -even mode extends to the high frequency regime. A drawback of the ridged circuit would be rf breakdown across the ridges and thus it is not suitable for extremely high power applications. However, HFSS simulation predicts that the peak electric field around the ridges are ~ 30 kV/cm for rf power of 50 kW, which is less than the breakdown threshold field in vacuum (~ 100 kV/cm).

V. BROADBAND RF COUPLER

A rf coupler in the SWCA should have a broadband coupling characteristic. A direct side wall coupling on the dielectric lined circuit by a multi-hole directional coupler was considered, in which scheme undesired oscillations in the coupling region may be avoided if a length can be designed to be short. However, since a coupling hole spacing is a quarter-wavelength and becomes shorter by a factor of $(\epsilon_r)^{1/2}$ than a regular metallic waveguide, a number of small holes are required to have a high coupling value. As a

result, a total longitudinal length may become longer than a circuit length. In the present design, as shown in Figure 1, an input rf power is coupled into the dielectric lined circuit by two steps: (i) the rf signal from a frequency synthesizer is coupled through a broadwall multihole directional coupler in rectangular Ka-band waveguides, and (ii) the fast wave in the Ka-band waveguide converts into a slow wave in the circuit. The amplified rf in the output section can be coupled out either directly through the mode converter to a Ka-band waveguide, or through a directional coupler so that beam is separated from rf. Both a directional coupler and a mode converter are designed so that the maximum rf power can be transferred into the desired mode in the circuit, TE_{x10} -even mode. Further, a return loss on each component has to be designed to meet the amplifier stability condition, $G > L + R_{in} + R_{out}$, where G is an amplifier gain, L is a circuit ohmic loss, R_{in} is a reflection in the input end and R_{out} is a reflection in the output end.

A compact (~ 6 cm long) input directional coupler was designed for high forward coupling strength and wide bandwidth in a Ka-band frequency range, based on the 8 element/4 array Chebyshev theory and the Bethe's coupling theory. Consider a wave incident on port 1 as shown in Figure 16(a). In general, for a n -hole distribution, a backward coupling amplitude seen on port 3 is given by

$$A_{back} = \sum_{i=1}^n a_i e^{-2j(i-1)\phi} \quad \text{Equ. 12}$$

where ϕ is a phase difference between two adjacent holes and a_i is a coupling amplitude of a i -th hole. For a 8-hole distribution ($n = 8$), a backward coupling amplitude is written as

$$|A_{back}| = 2\{a_1 T_7(\cos\phi) + a_2 T_5(\cos\phi) + a_3 T_3(\cos\phi) + a_4 T_1(\cos\phi)\} \quad \text{Equ. 13}$$

where the 8 holes are assumed to be symmetric, or $|a_i| = |a_{9-i}|$, and a property of a Chebyshev polynomial function, $T_n(\cos\phi) = \cos n\phi$, is used. In order to have a

Chebyshev equal ripple directivity over a given frequency band, Equ. 13 is required to be equal to $A_0 T_{n-1}(\cos\phi / \cos\phi_0)$ where A_0 is a maximum amplitude of a backward coupling. From this equality, a Chebyshev taper of coupling amplitude is derived in terms of $\cos\phi_0$.

Superposition of Chebyshev arrays yields a high coupling strength and broad bandwidth in a limited coupling area. The unknown parameter, ϕ_0 , is determined from the condition of equal coupling strength of a uniform hole array. A distribution of 8 elements and a superposition of 4 arrays are illustrated in Figure 16(b). To have equal coupling amplitude in the uniform region, it requires $a_1 + a_4 = a_2 + a_3$. This determines the ϕ_0 -value. Note that the quantity, $(a_1 + a_4)$, represents a coupling amplitude per hole in the uniform hole region. Since, in a rectangular waveguide, two rows of a longitudinal multi-hole coupling array can be placed, a total coupling amplitude is 32 times $(a_1 + a_4)$. For instance, a forward coupling of 0 dB requires a coupling per hole of -30.1 dB for 32 identical holes.

With a total coupling value given, a hole size and a hole location are determined from the Bethe's small hole coupling theory. For two identical rectangular waveguides, a coupling amplitude through a single hole is given by

$$A_{\text{coupling}} = j \frac{64\pi R^6}{3L_a L_b \lambda_g} \left[\left\{ \pm 1 - \frac{1}{2} \left(\frac{\lambda_g}{\lambda} \right)^2 - \left(\frac{\lambda_g}{2L_a} \right)^2 \right\} \sin^2 \frac{\pi \zeta}{L_a} + \left(\frac{\lambda_g}{2L_a} \right)^2 \right]$$

Equ. 14

where λ_g is a guided wavelength given as $c/[f(1-(f_{c0}/f)^2)^{1/2}]$, R is a radius of a circular coupling hole, ζ is the distance from waveguide side wall to center of hole, and L_a and L_b are waveguide width and height respectively. The upper (lower) sign denotes forward (backward) coupling amplitude. Since the Bethe's theory was developed with the assumption of coupling through a small hole which thickness is negligible, a correction for

a large area of the coupling aperture is necessary for a better estimation of the required coupling strength. The thickness of the coupling wall makes significant effects on the coupling strength because of the exponential attenuation of rf in the coupling wall given by²¹

$$A_{\text{thick}} = \exp\left(-\frac{2\pi t f_{\text{co}}}{c} \sqrt{1 - \left(\frac{f}{f_{\text{co}}}\right)^2}\right)$$

Equ. 15

where t is a coupling wall thickness and f_{co} is a cutoff frequency in a rectangular waveguide. A coupling amplitude correction due to the resonance effect²¹ in the hole given by

$$A_{\text{reson}} = \frac{1}{1 - \left(\frac{f}{f_{\text{co}}}\right)^2}$$

Equ. 16

should be also considered, where f_{co} is the cutoff frequency of a fundamental mode in a circular coupling hole. The effective coupling amplitude is the sum of all three, or

$$A_{\text{eff}} = A_{\text{coupling}} + A_{\text{thick}} + A_{\text{reson}}$$

Equ. 17

In Figure 17, a coupling strength of each circular hole, A_{eff} , is plotted as a function of a hole location, ζ , for various hole radii where frequency is a mid-frequency, 32.9 GHz. There are several choices of hole radius to meet the required coupling strength of each hole of -30.1 dB. In order to examine coupling flatness over frequency, A_{eff} versus frequency for various hole radii is plotted in Figure 18. Note that coupling of each hole becomes weaker as frequency is away from the cutoff frequency. Since the multi-hole directional

coupler is designed for a broad bandwidth with minimum ripples in band, a hole radius is determined at $2R/L_a = 0.368$ or $R = 0.131$ cm. Other tapered hole radii are determined similarly from the Chebyshev taper of the coupling amplitude, discussed early. It is interesting to note that coupling strength of each hole

A minimum directivity (where a directivity in dB unit is defined as $D = 20 \log(A_{fwd}/A_{back})$) is estimated from

$$D_{min} = 20 \log T_{n-1} \left(\frac{1}{\cos \phi_0} \right) \quad \text{Equ. 18}$$

where a forward coupling amplitude is $|A_{fwd}| = A_0 T_{n-1}(1 / \cos \phi_0)$ and $-1 \leq T_{n-1} \leq 1$ is used. A hole spacing is determined from $\lambda_g/4$ where frequency is a center frequency of minimum and maximum frequency obtained from the inequality. And, a coupling bandwidth (minimum and maximum frequency) is obtained through

$$\phi_0 \leq \frac{2\pi\ell}{\lambda_g} \leq \pi - \phi_0 \quad \text{Equ. 19}$$

where ℓ is a hole spacing. Table 2 summarizes design parameters of a multi-hole directional coupler.

To compare the coupling theory and the finite element code, HFSS, the coupler was simulated where rectangular holes with rounded corners are used instead of circular holes in order to increase the coupling strength. Simulation results, as shown in Table 3, are in good agreement with the coupling theories. Based on the designed parameters, a directional coupler was fabricated using electrical discharge machining. Figure 19 shows a forward coupling measurement obtained from a HP 8510B network analyzer. Measurements show a coupling value of -0.4 dB over 22.7 to > 40 GHz ($BW \geq 60\%$), minimum directivity of 40 dB, and return loss of < -25 dB, which are in good agreement of

the predictions. Note that the coupling flatness covers the whole Ka-band frequency range. It was also observed in the HFSS simulation as well as the coupling theory that, by reducing the coupling wall thickness from 10 mil to 5 mil, a more compact (4 cm long) coupler with a hole distribution of 8 elements and 3 arrays can be designed with the coupling strength and flatness as good as the present coupler.

The waveguide mode coupled through the directional coupler is a TE_{10} fast wave. In order to convert the TE_{10} fast wave mode to the operating TE_{x10} -even mode, a mode converter is necessary between the directional coupler and the circuit. The mode converter has two symmetric dielectric slabs which facilitates the propagation of the TE_{x10} -even mode. The converter employs two tapered sections; (1) a linear taper of two dielectrics in the uniform Ka-band waveguide where a fast wave TE_{10} mode converts into a slow wave TE_{x10} -even mode, and (2) both tapered dielectrics and surrounding metallic waveguide to match with the smaller circuit dimension. HFSS simulations predict pure mode conversion (coupling value ~ -0.02 dB) and low return loss (~ -30 dB) in the frequency range of 22 - 36 GHz. Figure 20 illustrates the difference in the mode conversion efficiency between two mode converters with an irregular dielectric shaping and a regular dielectric with square-corners lined in the rectangular waveguide. Note that, for the mode converter with a regular dielectric shaping, there is a mode conversion to a TM_{x11} -even mode at ~ 33 GHz where the TM_{x11} -even mode has the same phase velocity with the TE_{x10} -even mode (as seen in Figure 3). Since the dielectric mode converter is designed such that only TE_{x10} -even mode in the dielectric loaded circuit can couple with the TE_{10} mode in the standard Ka-band waveguide, all other hybrid modes which might be excited from beam instability would be completely trapped in the circuit. This is another reason that a sever is inevitable in the circuit.

VI. CONCLUSIONS

A design study on the two-stage SWCA has been performed to conduct experiments on broadband millimeter wave generation at a low magnetic field. A high quality axis-encircling beam with low velocity spread is incorporated in the dielectric lined slow wave circuit. To stabilize a gyro-BWO in the second harmonic TEx10-odd mode predicted by a linear theory, a two-stage circuit with a severs is designed. Slow-time-scale non-linear simulations of the two-stage SWCA with a 30 mil clearance predict an efficiency of ~ 15 % , gain of ~ 24 dB (saturated output power ~ 50 kW), and an instantaneous bandwidth of ~ 15 % at input power = 200 W and $\Delta v/v = 2$ %.

A compact multi-hole directional coupler with high coupling strength over a wide frequency range was designed and fabricated to inject RF power in the input section. Measurements show a coupling value of - 0.4 dB over a 60 % bandwidth (22.7 to > 40 GHz) and a minimum directivity of 45 dB, which is in good agreement with both theoretical predictions and HFSS simulations. The HFSS-code was utilized to design a mode converter to couple a fast wave injected from the directional coupler into the slow wave in the circuit. Simulations show pure mode conversion (coupling value ~ - 0.02 dB) and low return loss (~ - 30 dB) in the frequency range of 22 - 37 GHz. One of the main difficulties in the SWCA experiment will be beam propagation through the circuit.

A ridged slow wave circuit is predicted to be more practical because there is less chance of electron beam interception directly on the dielectrics. Since the electric field is enhanced near the ridges, the coupling strength becomes strong even in the slow wave interaction region. By increasing electron beam filling percentage in the beam tunnel, one can design for high gain (~ 28 dB) with shorter interaction length. A detailed large signal performance of the ridged circuit will be investigated in the future.

ACKNOWLEDGEMENTS

The authors would like to acknowledge useful discussions with Drs. S. Y. Park, V. L. Granatstein and J. L. Hirshfield. This work is supported by the Office of Naval Technology.

REFERENCES

- ¹J. Benford and J. Swegle, High-Power Microwaves, Artech House, 1992
- ²G. S. Park, S. Y. Park, R. H. Kyser, C. M. Armstrong, and A. K. Ganguly, Technical Digest of the International Electron Devices Meeting, p. 779-781, 1991
- ³J. J. Choi, G. S. Park, S. Y. Park, C. M. Armstrong, R. H. Kyser, and M. L. Barsanti, Invited Paper, Conf. Digest on Infrared and Millimeter wave Conf., Dec., 1992
- ⁴A. K. Ganguly, S. Ahn, and S. Y. Park, Int. J. Electronics, **65**(3), p 597 - 618, 1988
- ⁵C. K. Chong, D. B. McDermott, A. J. Balkcum, and N. C. Luhmann, IEEE Trans. on Plasma Science **20**(3), p 176 - 187, 1992
- ⁶E. S. Weibel, Phys. Rev. Lett. **2**(83), 1959
- ⁷K. R. Chu and J. L. Hirshfield, Phys. Fluids **21**(3), 1978
- ⁸A. K. Ganguly and K. R. Chu, NRL Memo Report 4215, 1980
- ⁹K. R. Chu, A. K. Ganguly, V. L. Granatstein, J. L. Hirshfield, S. Y. Park, and J. M. Baird, Int. J. Electronics **51**(4), p. 493 - 502, 1981
- ¹⁰H. Guo, L. Chen, H. Karen, J. L. Hirshfield, S. Y. Park, and K. R. Chu, Phys. Rev. Lett. **49**(10), p. 730-733, 1982
- ¹¹A. K. Ganguly and S. Ahn, Phys. Rev. A **42**(6), p 3544-3554, 1990
- ¹²R. Levy, Advances in Microwaves, Vol. 1, ed. by L. Young, p. 115 - 209, 1966
- ¹³H. A. Bethe, Phys. Rev. **66**(7), p 163 - 182, 1944
- ¹⁴HP High Frequency Structure Simulator User's Reference, 1992
- ¹⁵G. P. Scheitrum and R. True, IEEE Int. Conf. on Plasma Science, June, 1991
- ¹⁶Ceradyne, Inc. Costa Mesa, CA
- ¹⁷C. A. Balanis, Advanced Engineering Electromagnetics, John Wiley & Sons, 1989

18A. K. Ganguly, to be published

19B. Goplen, L. Ludeking, D. Smithe, and G. Warren, MAGIC User's Manual (MRC),
Newington, VA, 1991

20W. E. Courtney, IEEE Trans. Microwave Theory and Tech. MTT-18(8), p. 476-485,
1970

21S. B. Cohn, Proc. IRE 40, p 697 - 699, 1952

FIGURE CAPTIONS

Figure 1. Proposed experimental configuration for a two-stage slow wave cyclotron amplifier. A cross-section of an irregular dielectric lined circuit is also shown.

Figure 2. Transverse electric field distribution of TE_{x10p} -even modes where p is an axial mode index.

Figure 3. Calculated uncoupled dispersion relations of a regular dielectric lined circuit (TE_{x10} -even, TM_{x11} -even, TM_{x11} -odd, TE_{x10} -odd, TE_{x11} -even, TE_{x11} -odd in the order of lowest cutoff frequency). The filled square, open circle, open triangle, filled triangle, filled circle, and cross denote the dispersion relations of TE_{x10} -even, TM_{x11} -even, TM_{x11} -odd, TE_{x10} -odd, TE_{x11} -even, and TE_{x11} -odd respectively, obtained from HFSS simulations.

Figure 4. Uncoupled dispersion relations of an irregular dielectric lined circuit, obtained from HFSS simulations (TE_{x10} -even, TE_{x10} -odd, TM_{x11} -even, TM_{x11} -odd modes from the lowest cutoff mode). Dots are measured cavity resonance frequencies of TE_{x10p} -even modes where cavity dimensions are $d = 0.123$ cm, $w = 0.097$ cm, $L_y = 0.246$ cm, and $L_z = 1$ cm.

Figure 5. Difference of saturation lengths between the cases of a 30 mil clearance and 15 mil clearance where $\Delta v_{||}/v_{||} = 2\%$ for both cases. Optimum design parameters are $d = 0.153$ cm, $w = 0.095$ cm, $L_y = 0.246$ cm, $B = 6.81$ kG, $\alpha = 0.82$, and input power for

saturation = 200 W at $f = 30.4$ GHz for the case of 30 mil clearance; and $d = 0.123$ cm, $w = 0.097$ cm, $L_y = 0.246$ cm, $B = 6.86$ kG, $\alpha = 0.95$, and input power = 170 W at $f = 32$ GHz for the case of 15 mil clearance.

Figure 6. Efficiency of a single-stage SWCA as a function of interaction length for $\Delta v_{||}/v_{||} = 0\%$, 2% , and 4% .

Figure 7. Threshold currents of the second harmonic TE_{x10} -odd gyro-BWO as a function of interaction circuit length for $\alpha = 0.6$, 0.8 , and 1 . The operating region for a two-stage SWCA is shown.

Figure 8. Gain and efficiency of a two-stage SWCA versus input rf power where $\Delta v_{||}/v_{||} = 2\%$.

Figure 9. Dependence of electronic efficiency on sever length where $\Delta v_{||}/v_{||} = 2\%$ and input power = 200 W.

Figure 10. Efficiency and gain of a two-stage SWCA as a function of frequency for $\Delta v_{||}/v_{||} = 2\%$ and input power = 200 W.

Figure 11. Typical MAGIC outputs of a two-stage SWCA simulation: (a) electric field growth along axial length at $t = 4$ nsec, (b) energy gained from rf to electron beam versus time (negative slope corresponds to rf amplification). A TE_{x10} -even mode with 200 W is launched at left end and propagates toward right.

Figure 12. Comparison between MAGIC and slow-time-scale non-linear simulations. Dots are gain obtained from MAGIC simulations.

Figure 13. Sensitivity of amplifier efficiency on the change of dielectric constant where $\Delta v/v = 2\%$ and input power = 200 W.

Figure 14. Measured cavity resonant frequency shifts of a TE_{x104} -even mode and the corresponding dielectric constant values as a function of temperature. The frequency, 35.679 GHz, is a measured value at room temperature.

Figure 15. (a) cross-section of a ridged slow wave circuit, (b) electric field profiles of a regular and ridged circuits.

Figure 16. (a) Model of a multi-hole directional coupler, (b) layout of 8 elements of coupling holes and superposition scheme of 4 arrays where a_i is the i -th coupling amplitude of 5 different holes.

Figure 17. Coupling strength per hole versus normalized hole location ($2\zeta/L_a$) for various hole radii where frequency is 32.9 GHz.

Figure 18. Coupling strength per hole versus frequency for various radii where hole location is $2\zeta/L_a = 0.393$.

Figure 19. Measured forward coupling values obtained from a HP 8510B network analyzer. Dots are the HFSS-simulated coupling values. Frequency sweeps from 20 GHz to 40 GHz. Vertical scale is 3 dB/div.

Figure 20. Mode conversion efficiencies obtained from HFSS simulations: (a) an irregular dielectric lined circuit, and (b) a regular dielectric lined circuit.

Table 1. Summary of two-stage SWCA design parameters

axis-encircling beam

$V \sim 60$ kV

$I \sim 5$ A

$B \sim 7$ kG

$\alpha \sim 0.8$

$\Delta v_z/v_z = 2$ %

length of input section = 13.6 cm

length of output section = 14.1 cm

length of sever = 1.5 cm

dielectric thickness = 0.095 cm

circuit width (L_x) = 0.248 cm

circuit height (L_y) = 0.246 cm

dielectric = Transtart (Al_2O_3 , 99.9%, $\epsilon_r = 10.1$)

input power for saturation = 200 W

saturated output power = 50 kW

large signal gain = 24 dB

large signal efficiency = 15 %

instantaneous bandwidth = 15 % (29 - 34 GHz)

Table 2. Design parameters of a multi-hole directional coupler

coupling value = 0 dB

number of holes per row = 20

coupling per hole = 30.1 dB

hole radius = 0.131 cm

hole location from the narrow wall of waveguide = 0.14 cm

hole spacing = 0.297 cm

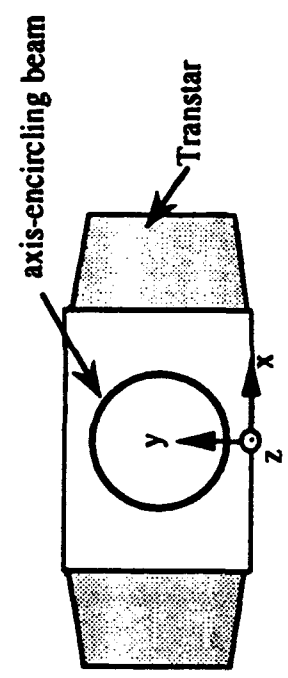
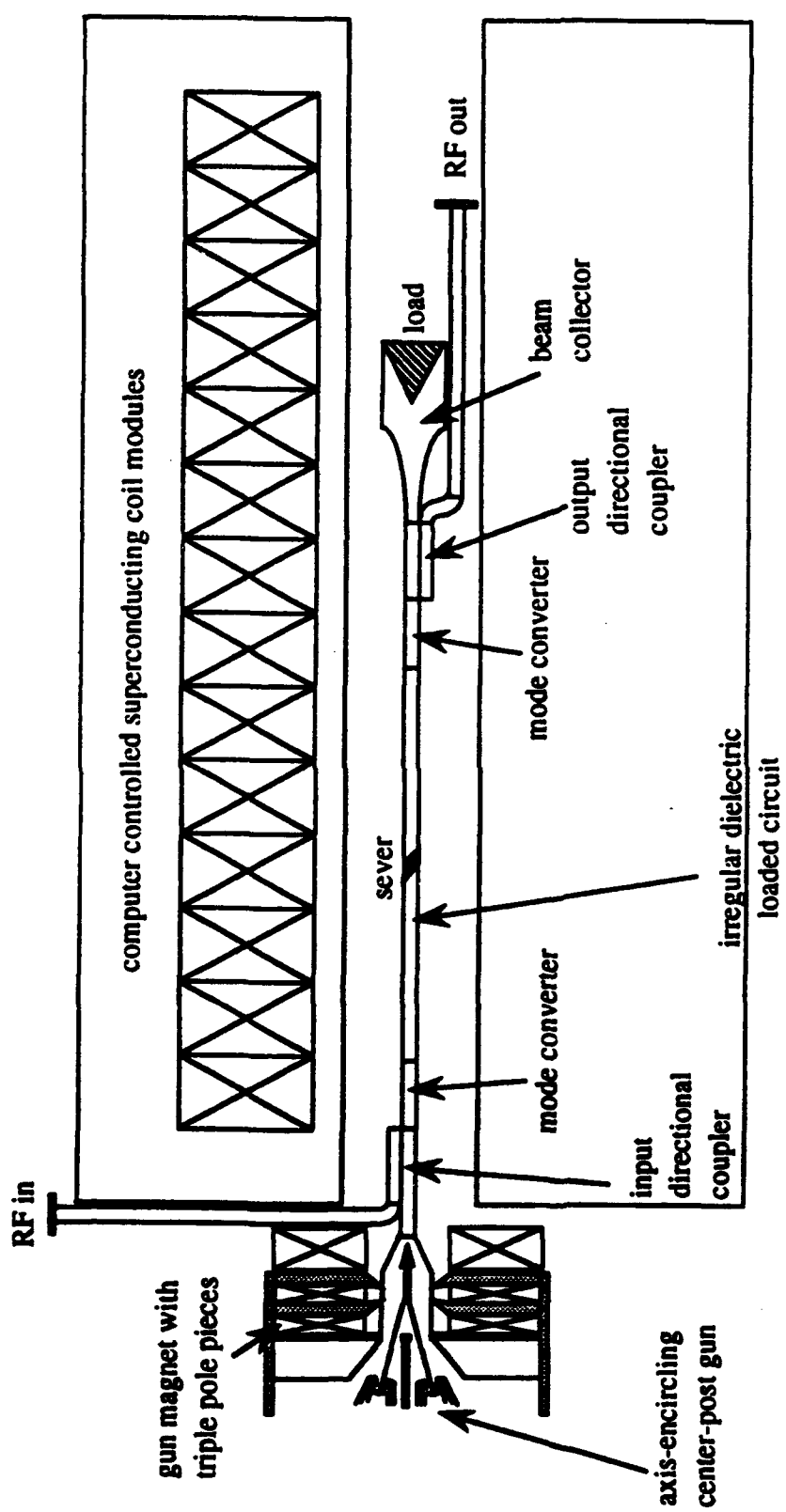
thickness of coupling wall = 0.025 cm

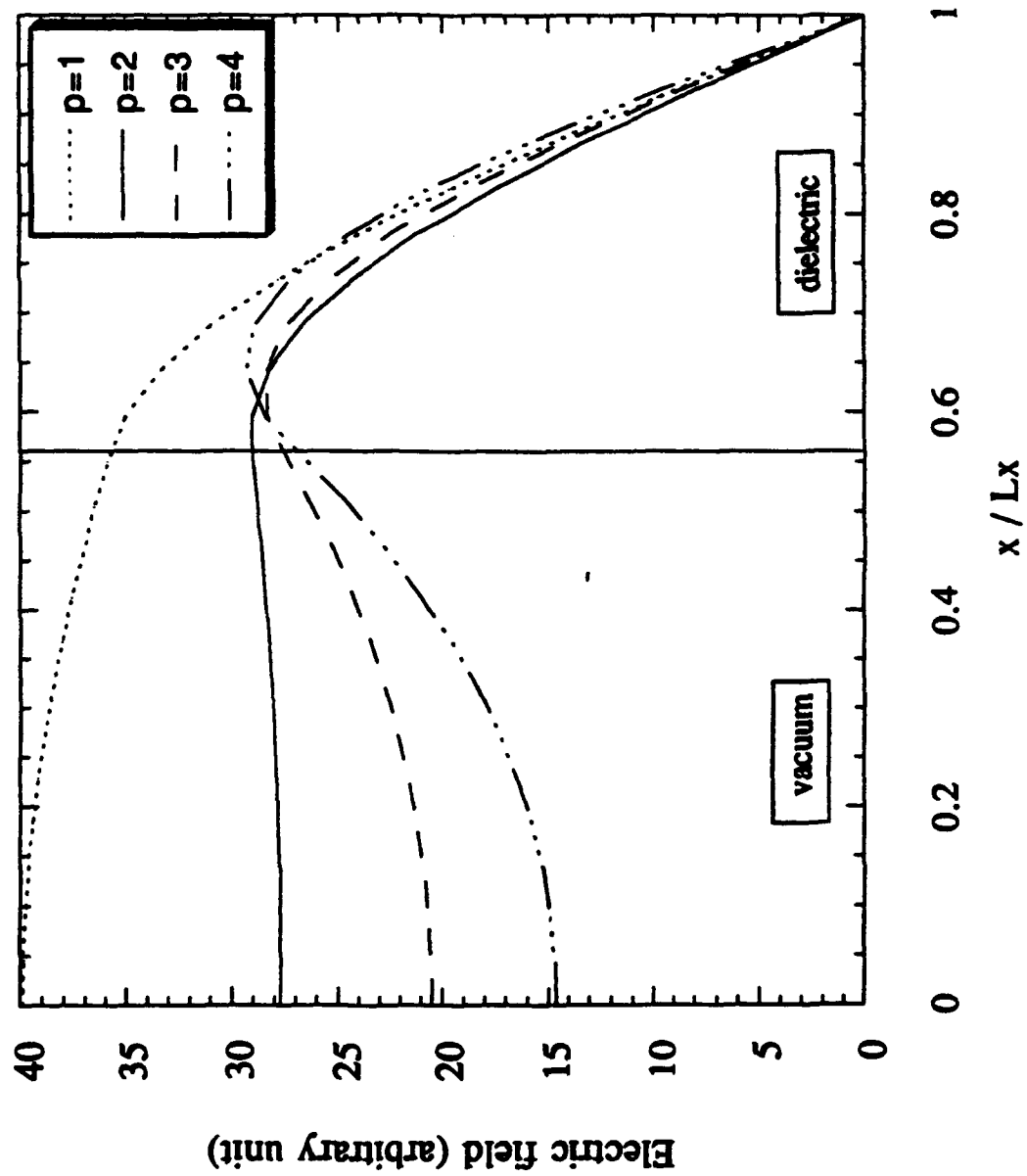
bandwidth = 24 - 42 GHz

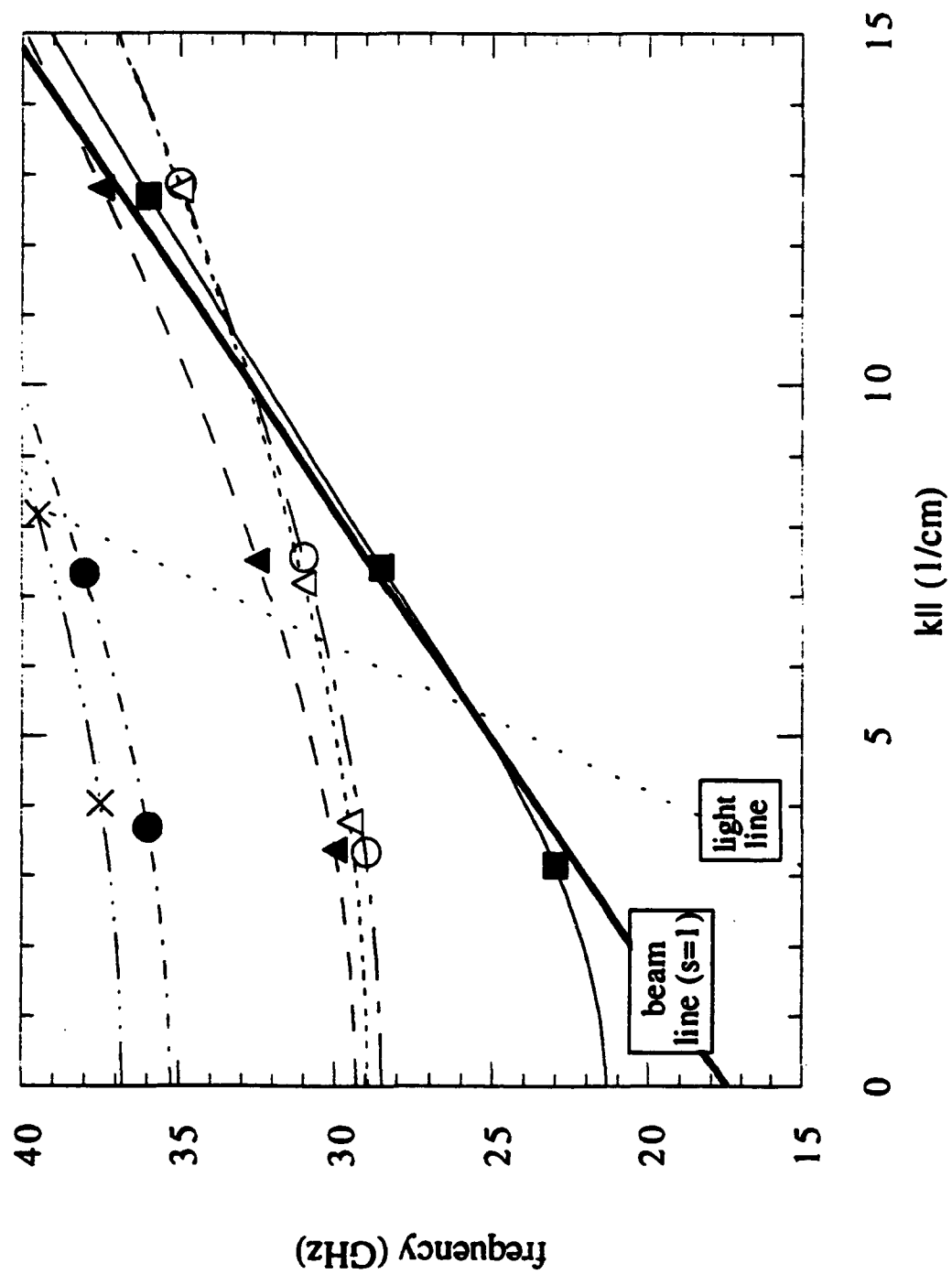
minimum directivity = 45 dB

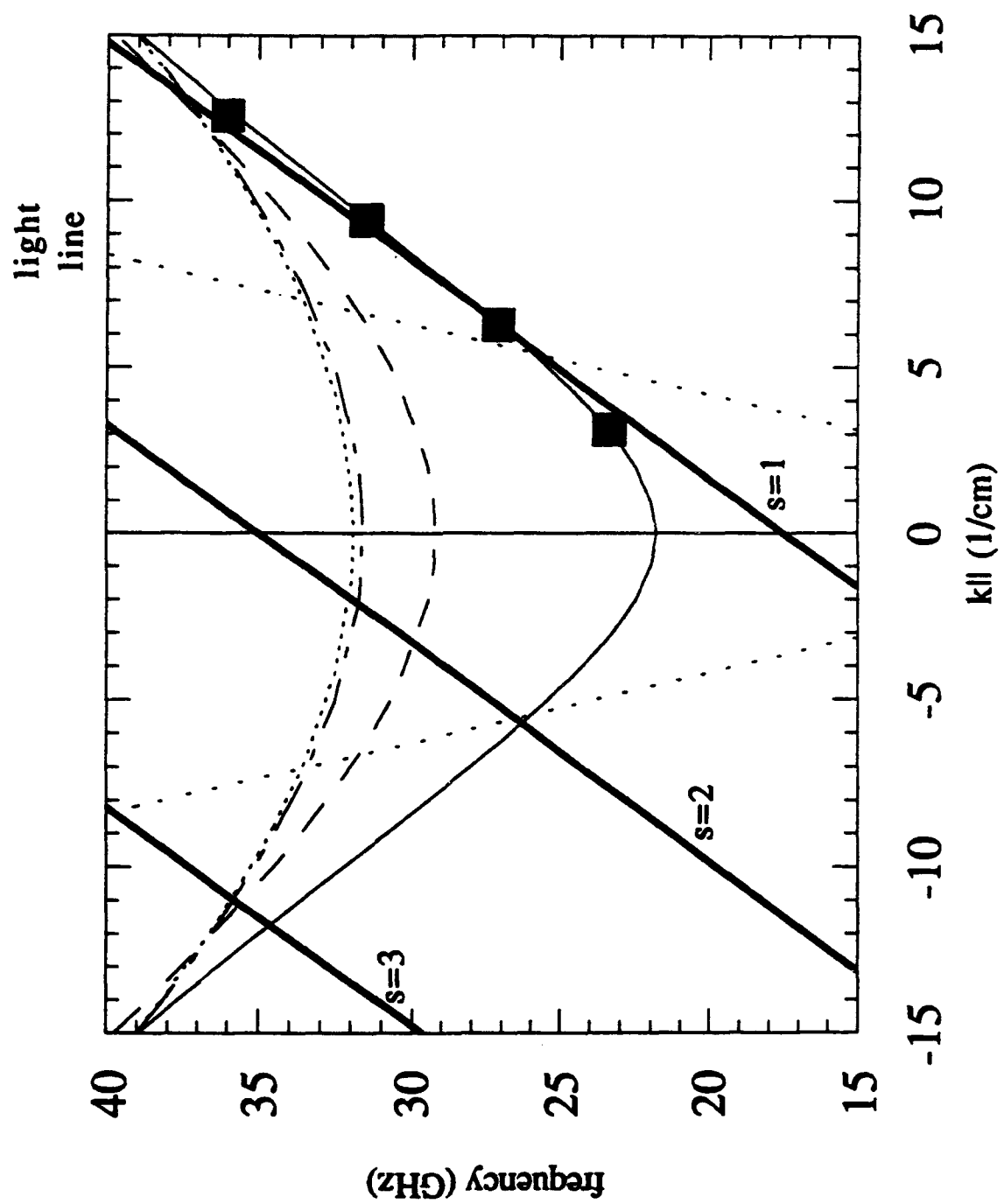
Table 3. Comparison between theory, simulations and measurements on a multi-hole directional coupler

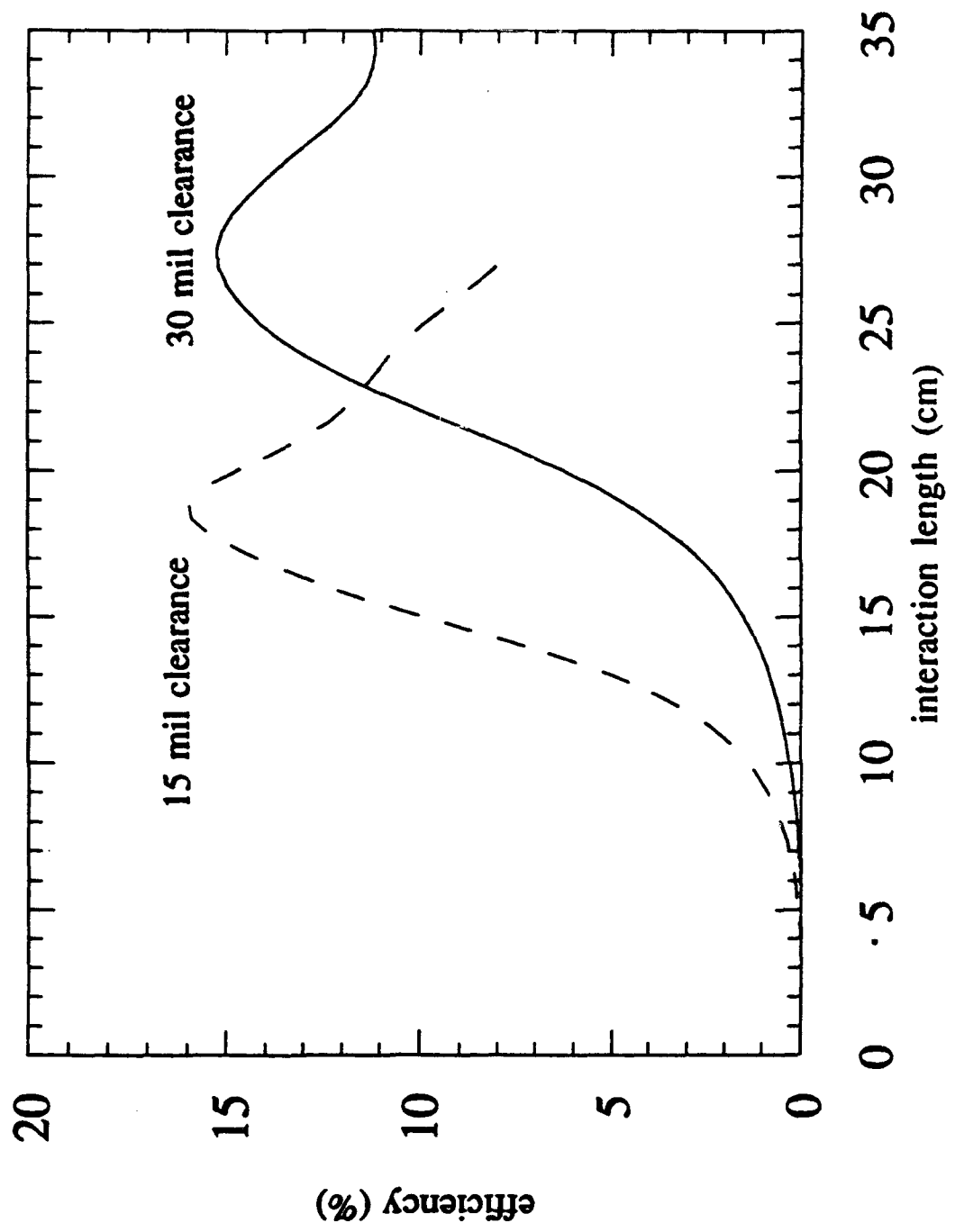
	coupling value (dB)	min. directivity (dB)	3dB bandwidth (GHz)
theory	0	45.4	24 to 42
HFSS	- 0.2	43	22 to 42
cold test	- 0.4	45	22.7 to > 40

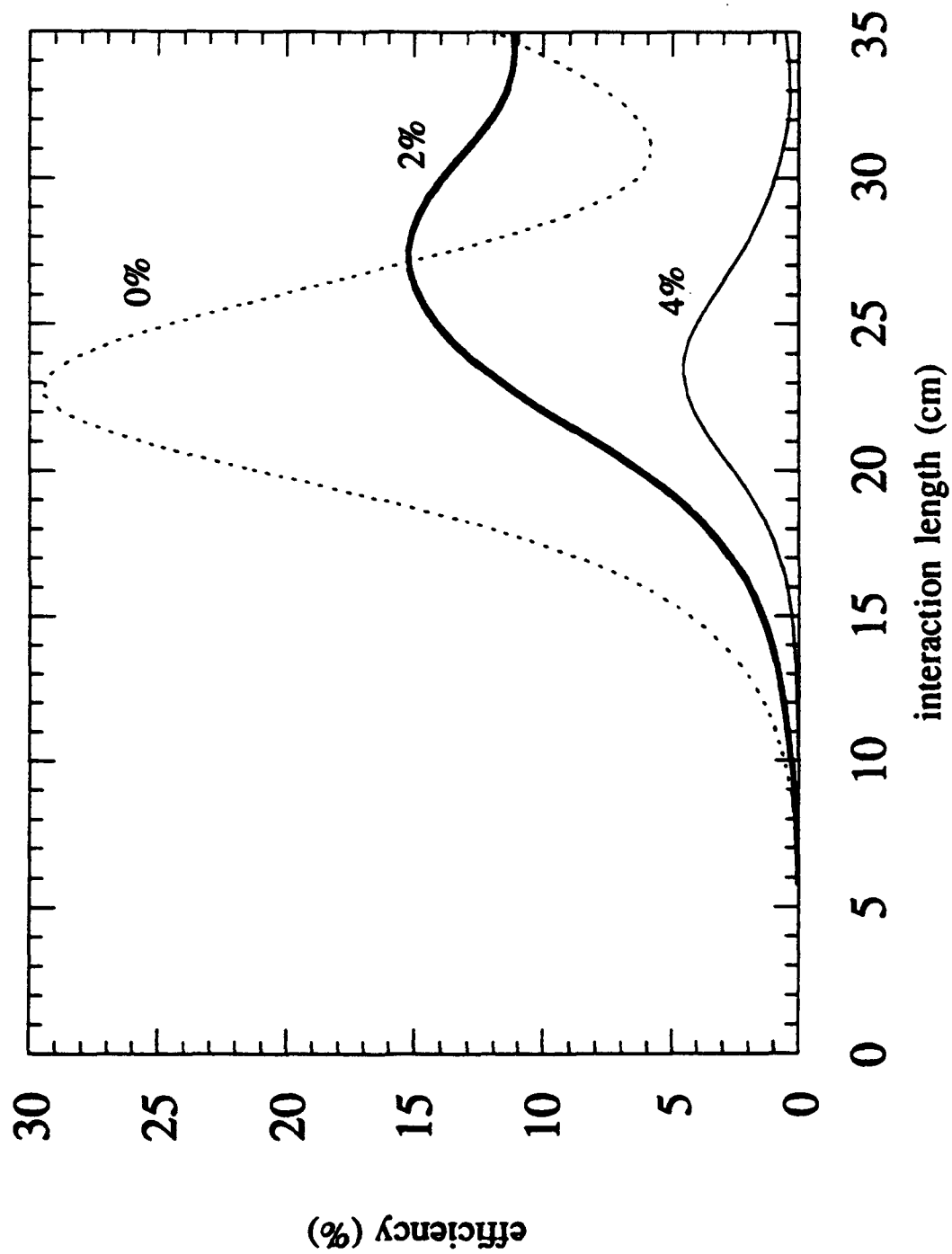


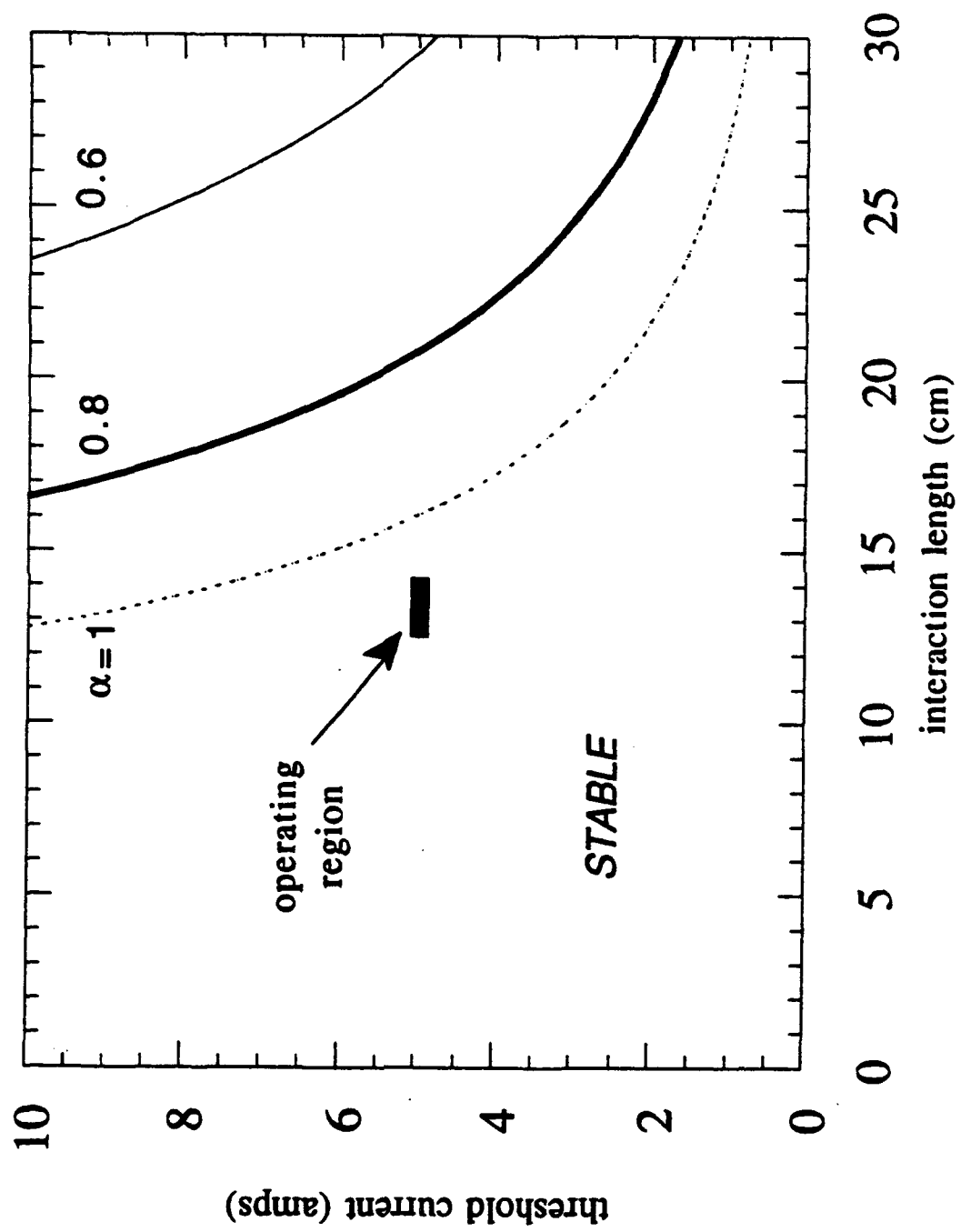


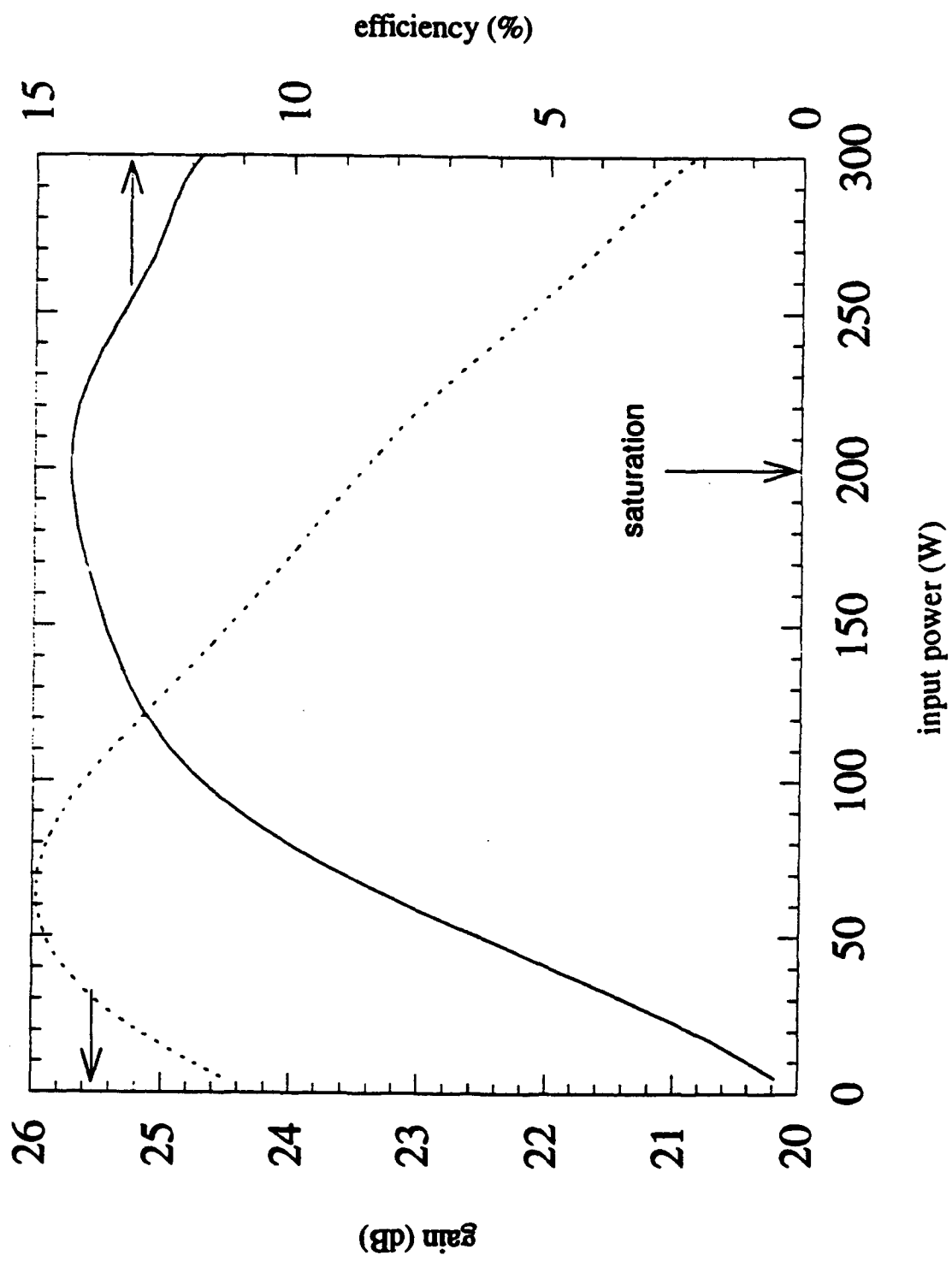


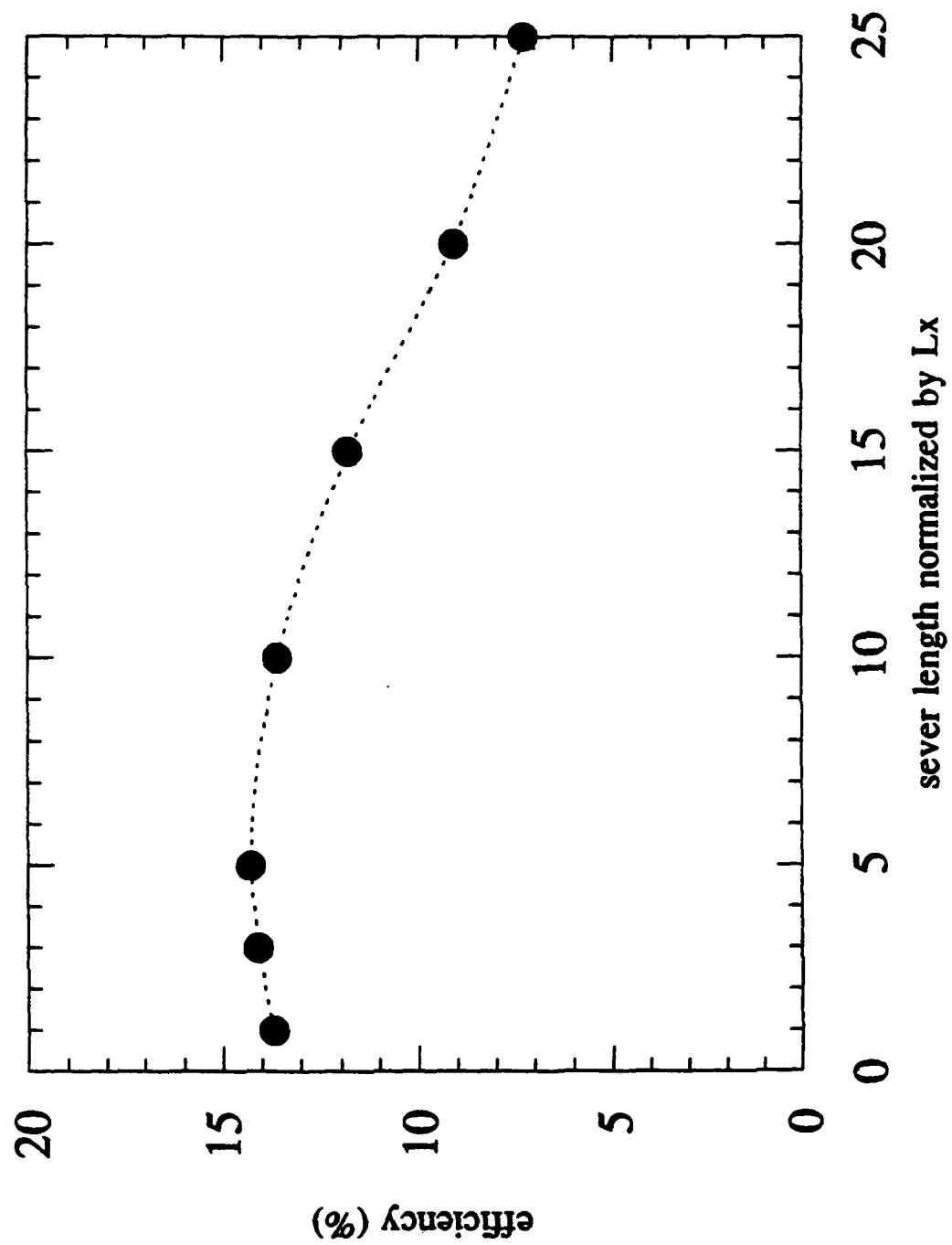


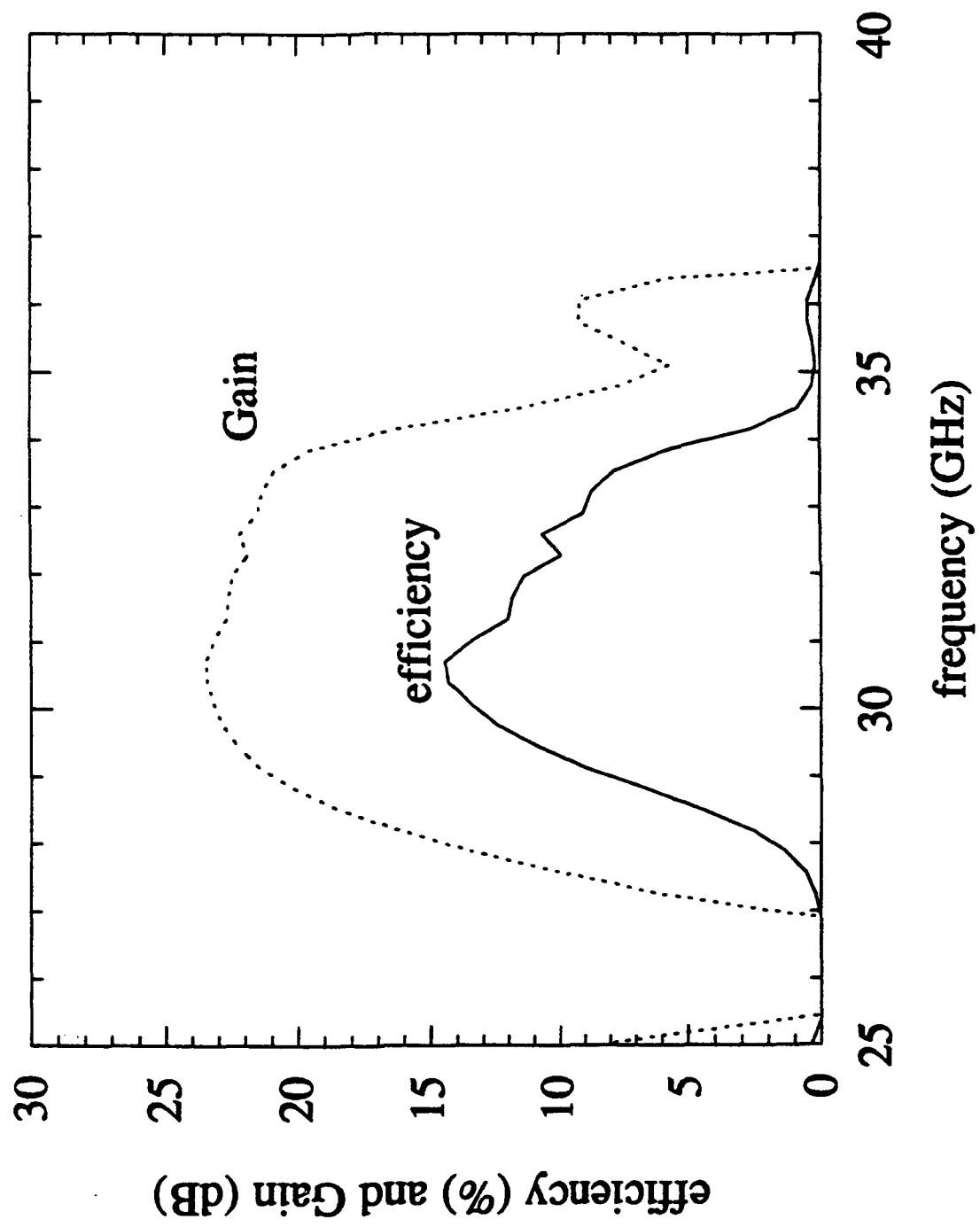


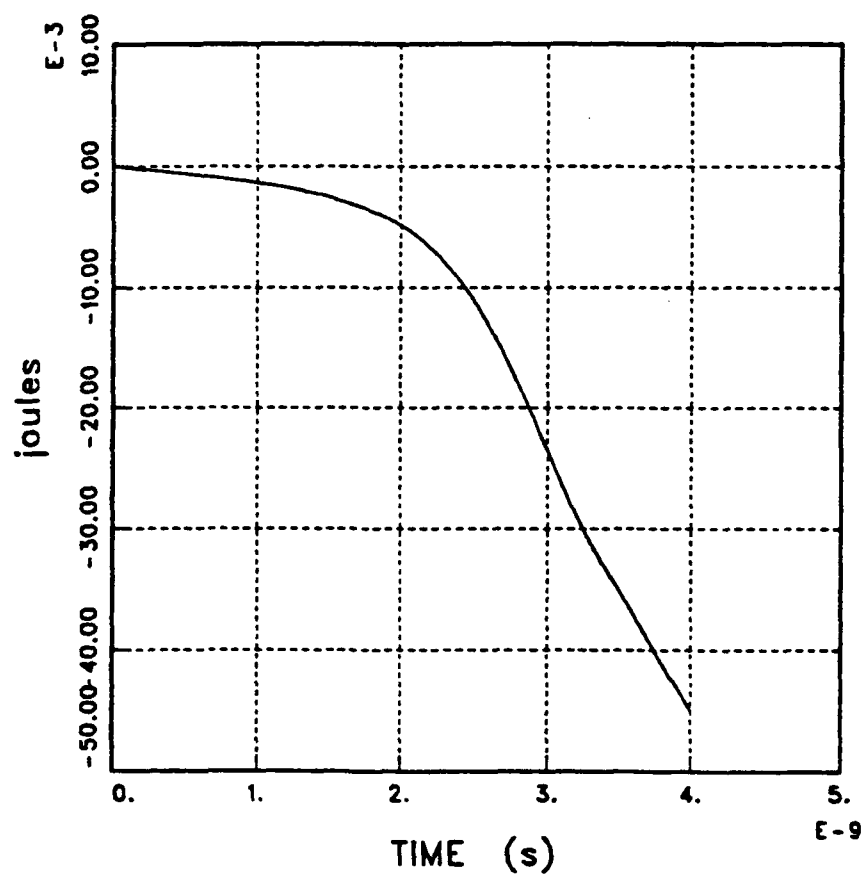
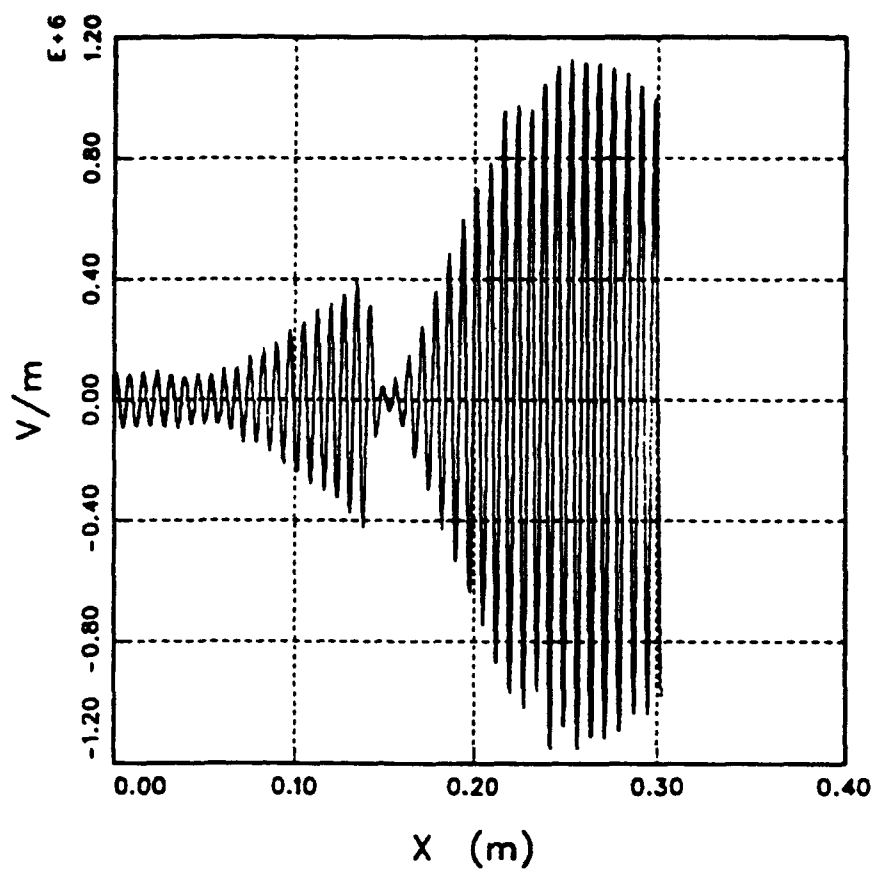


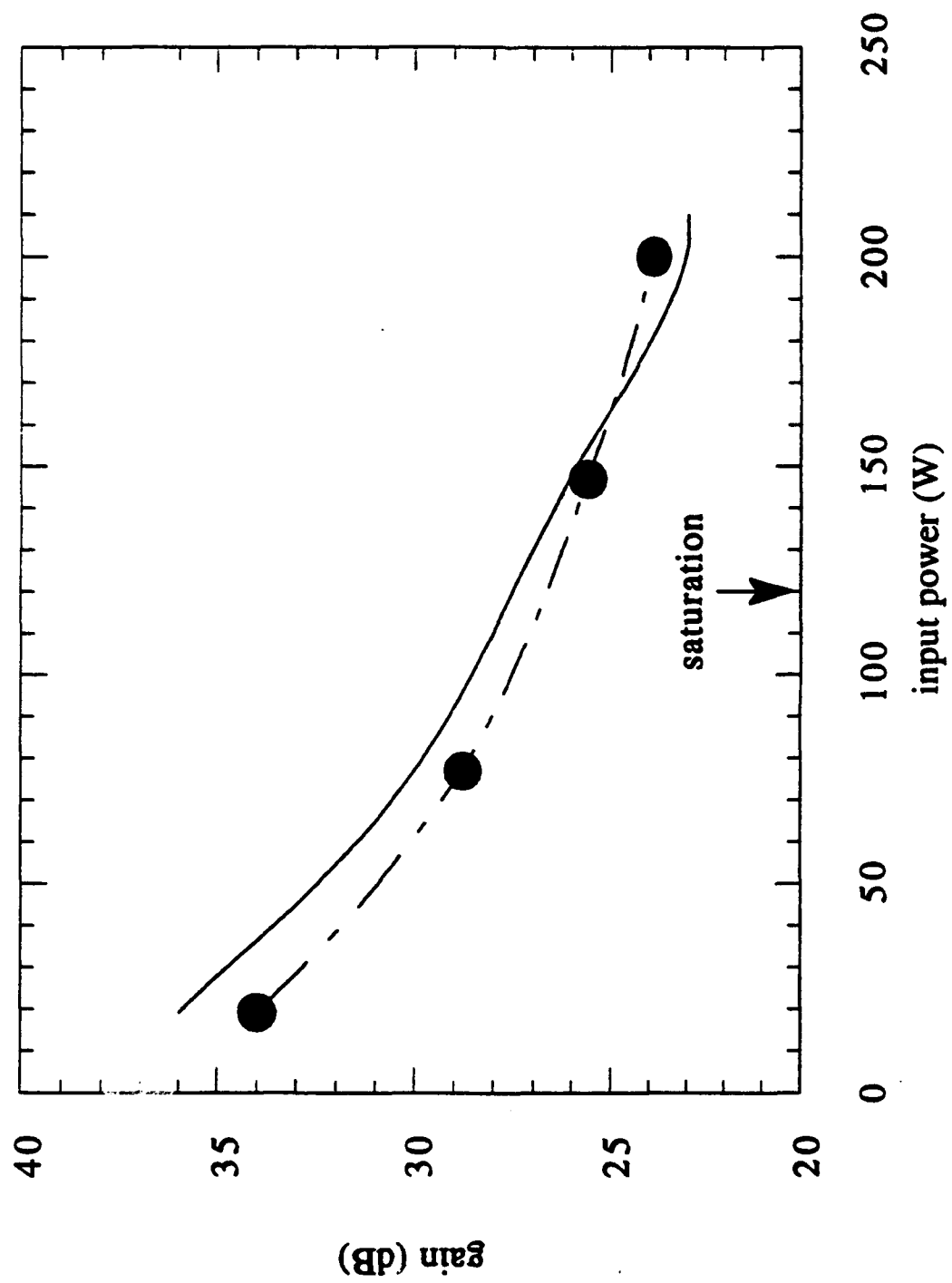


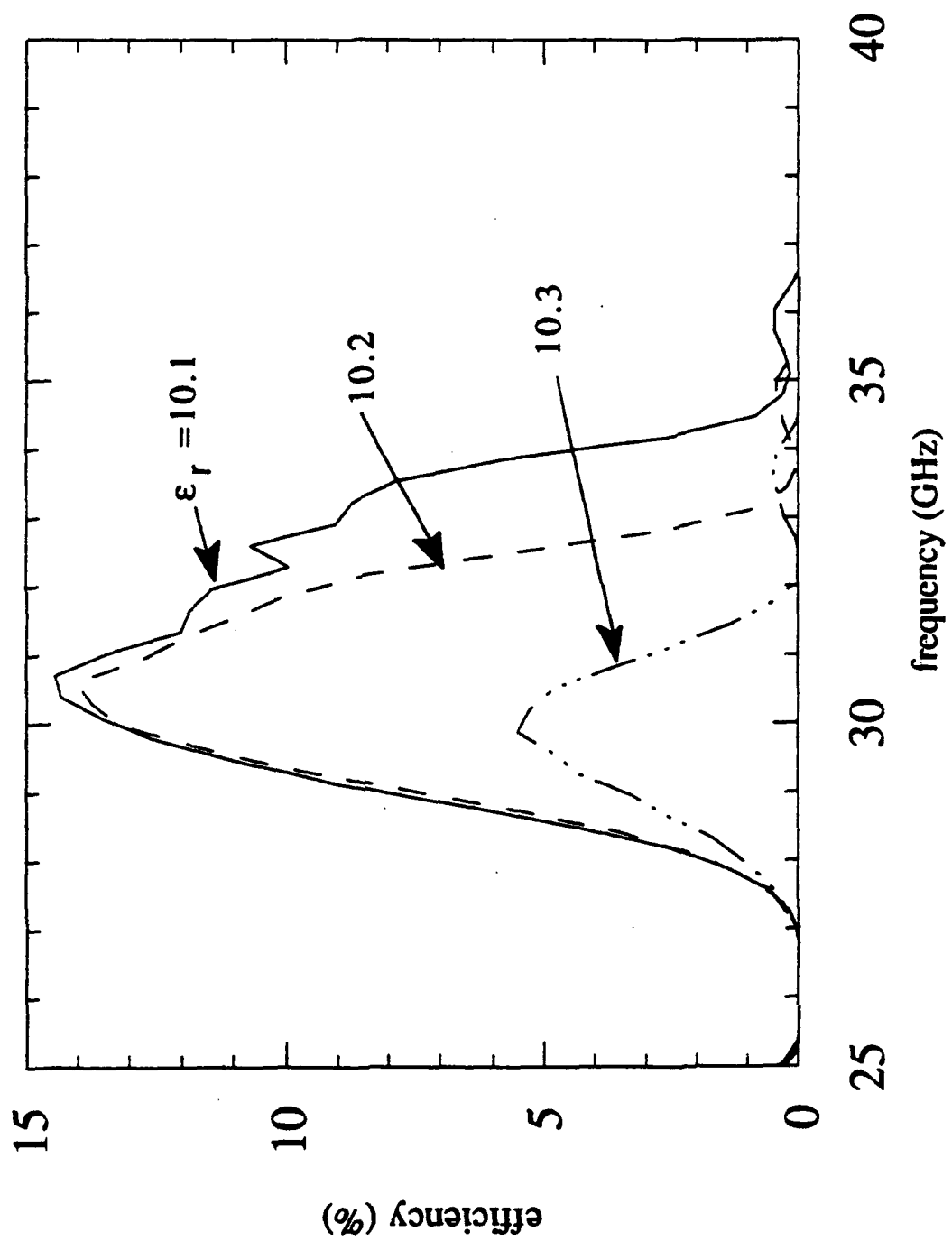


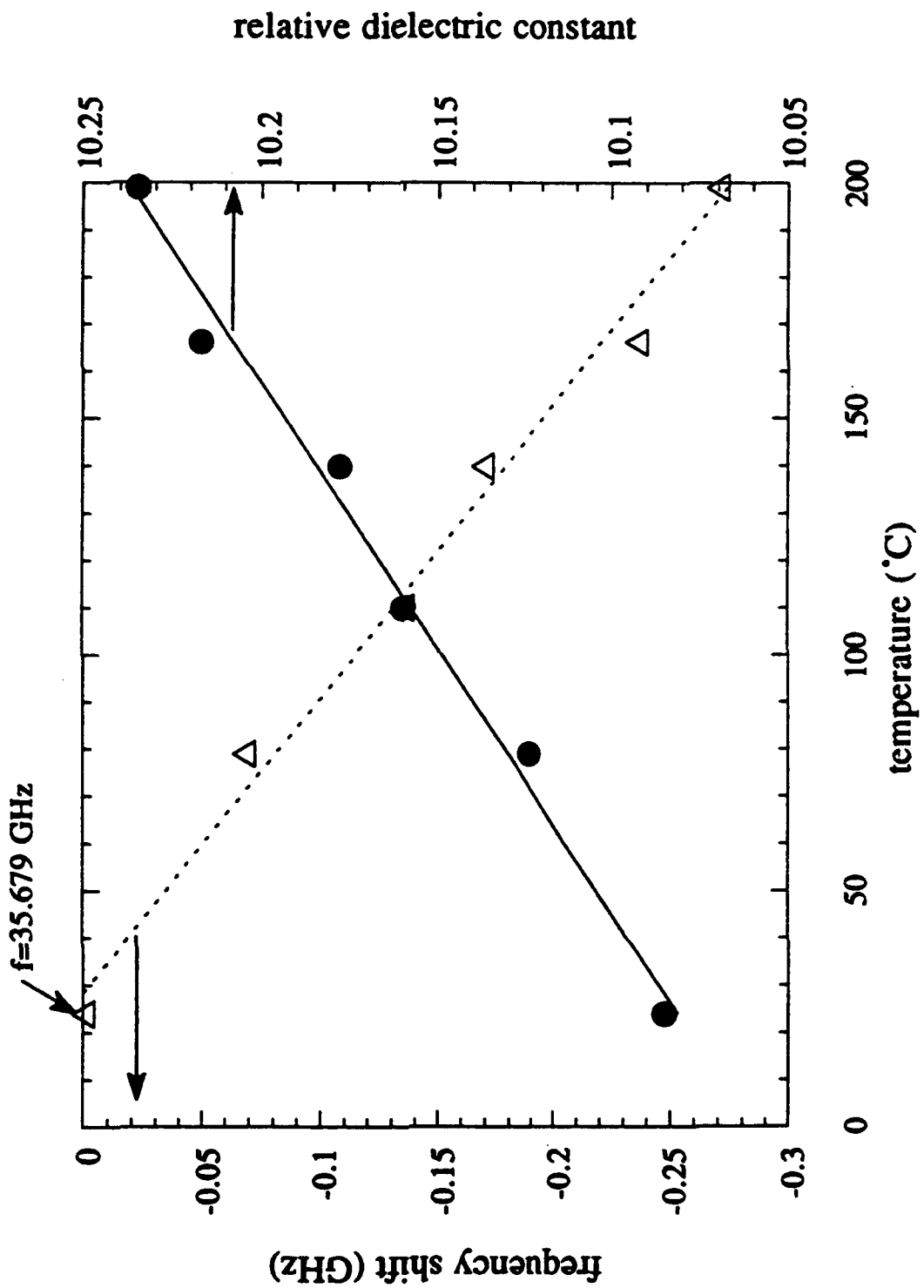


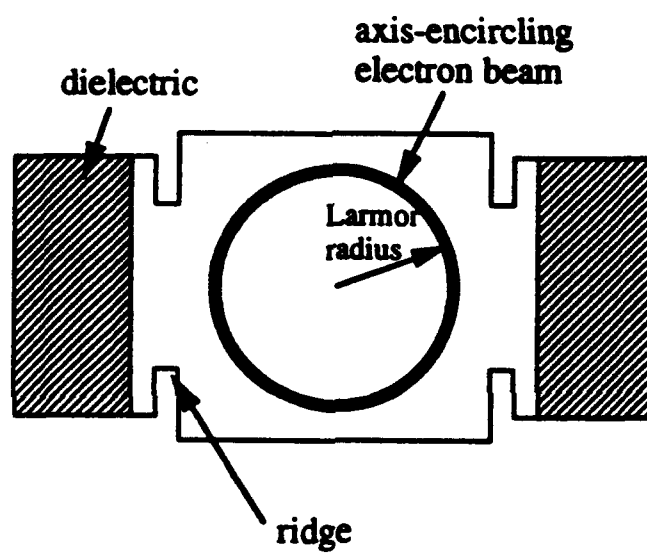


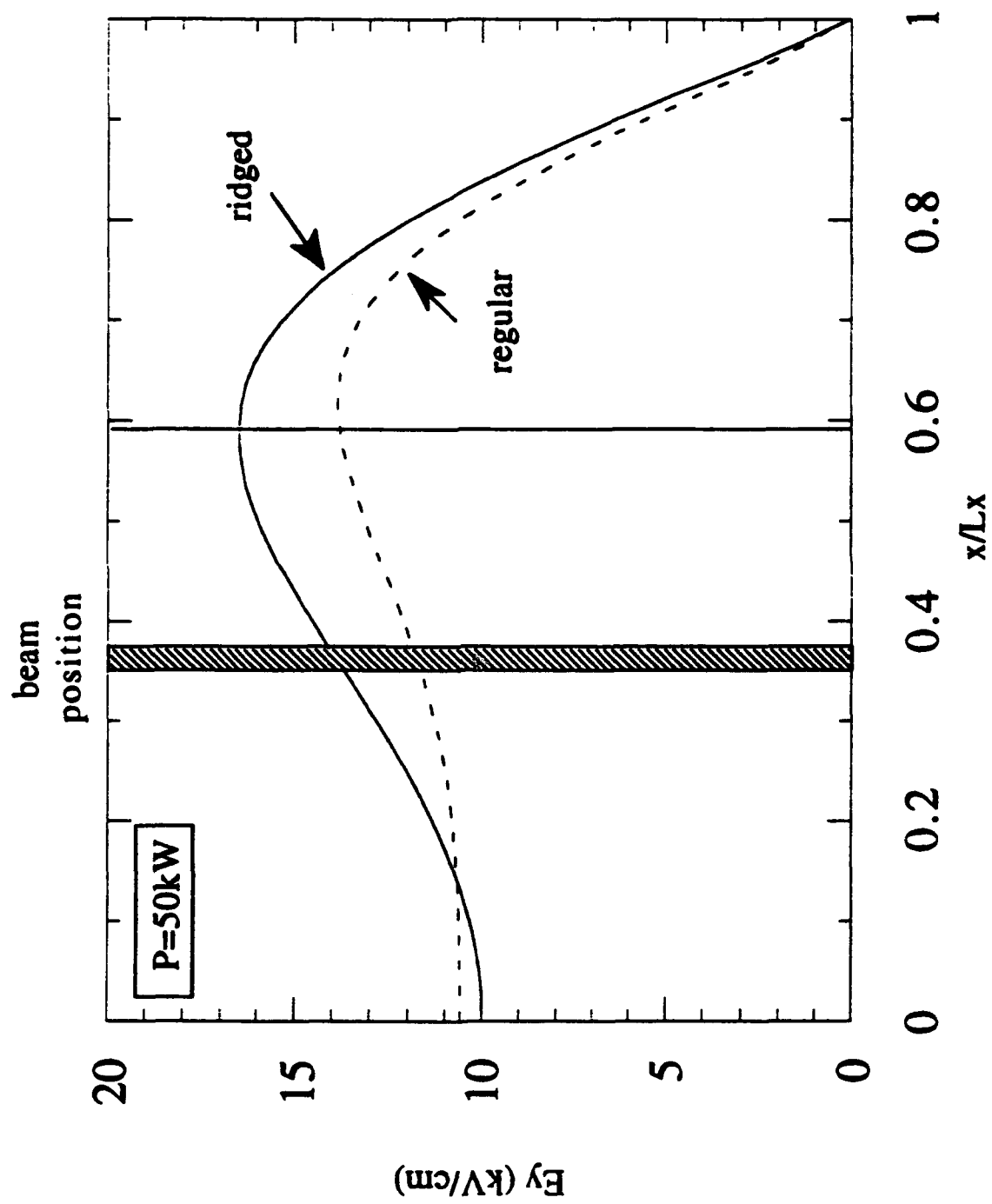




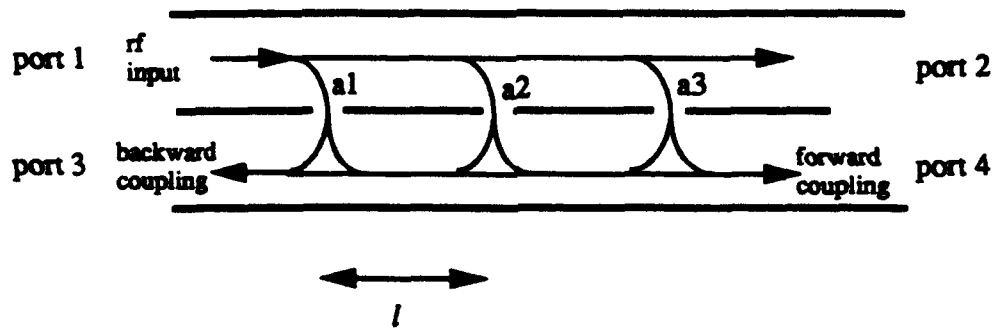




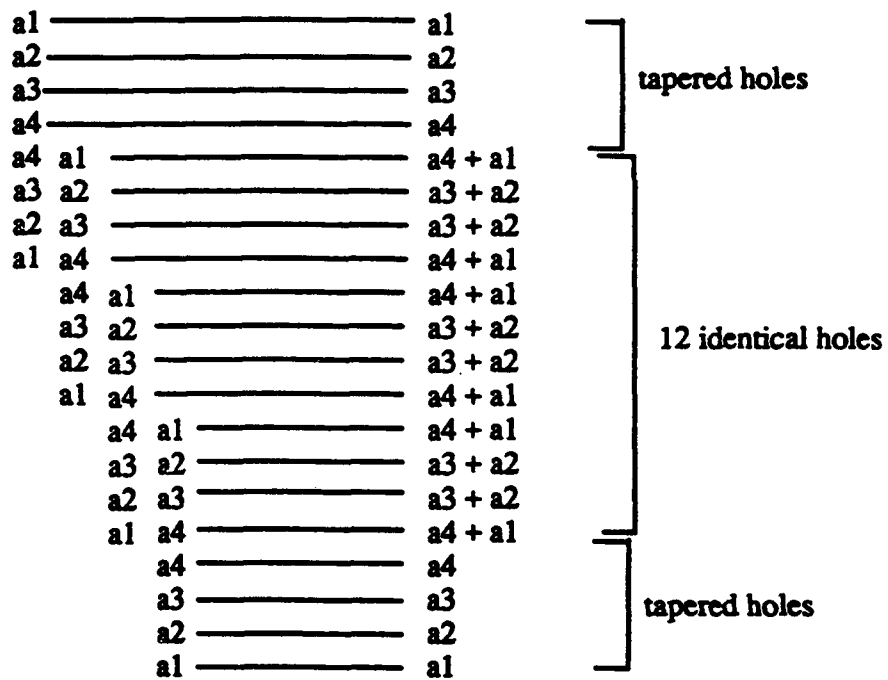


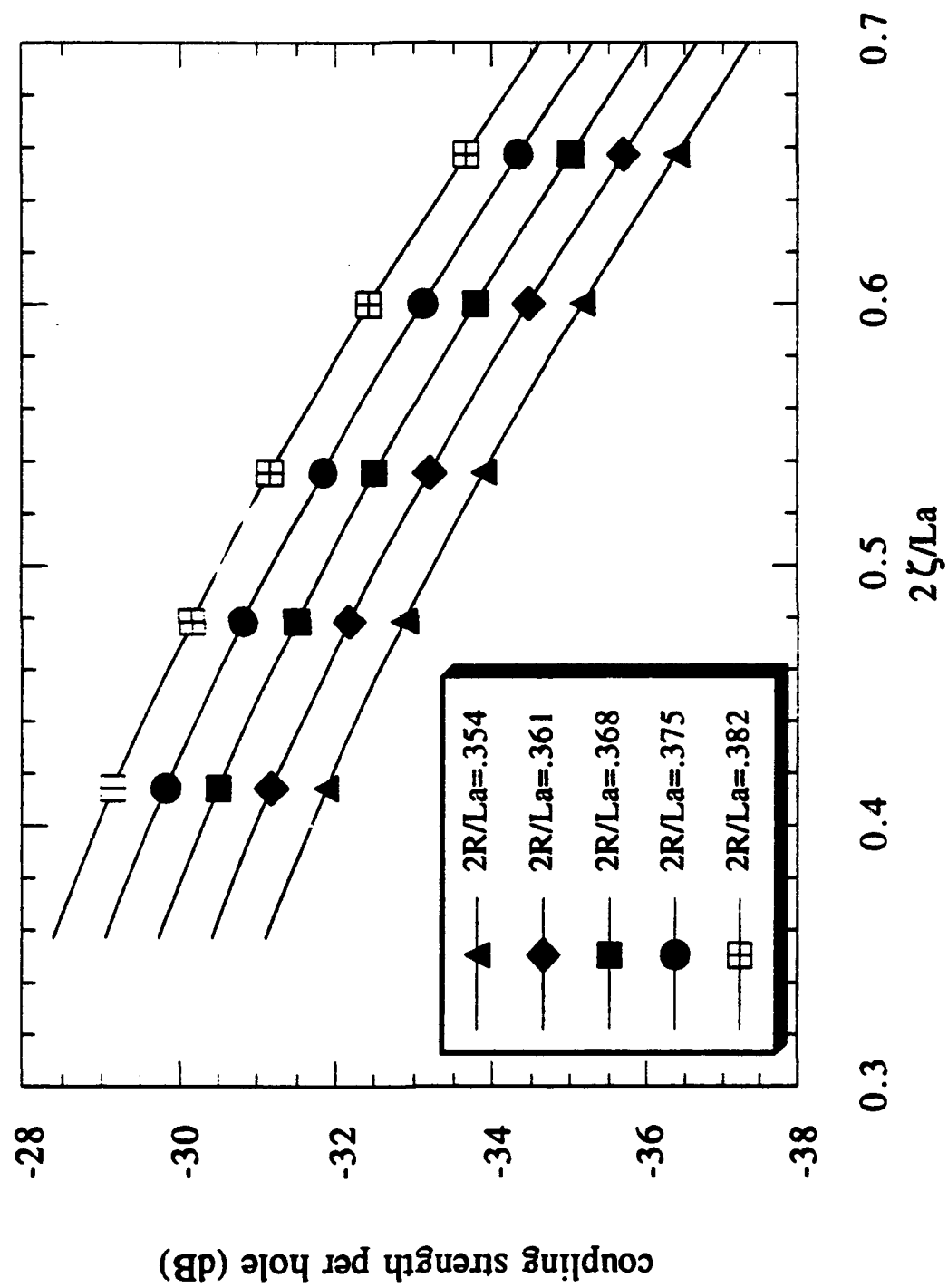


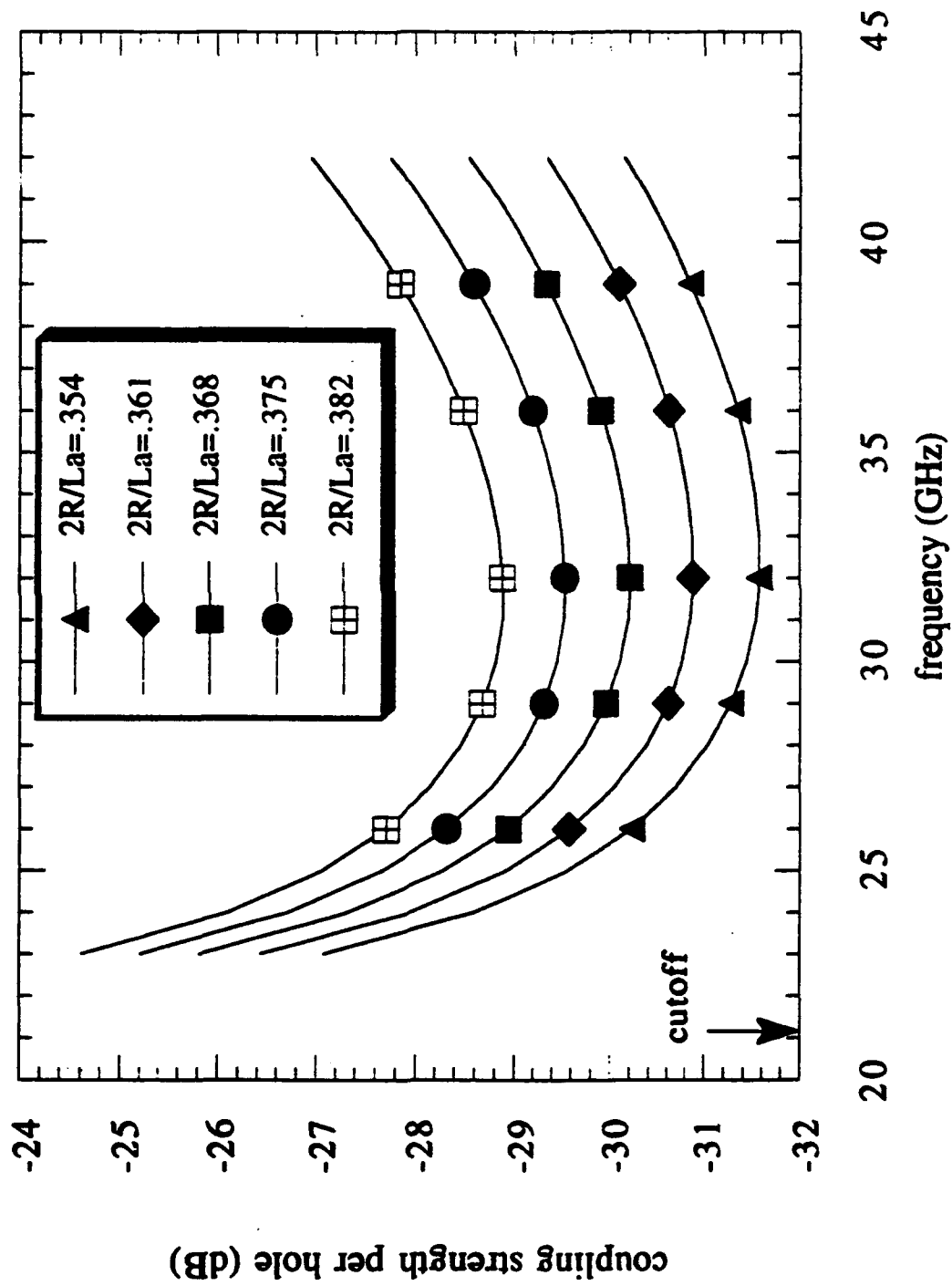
(a)

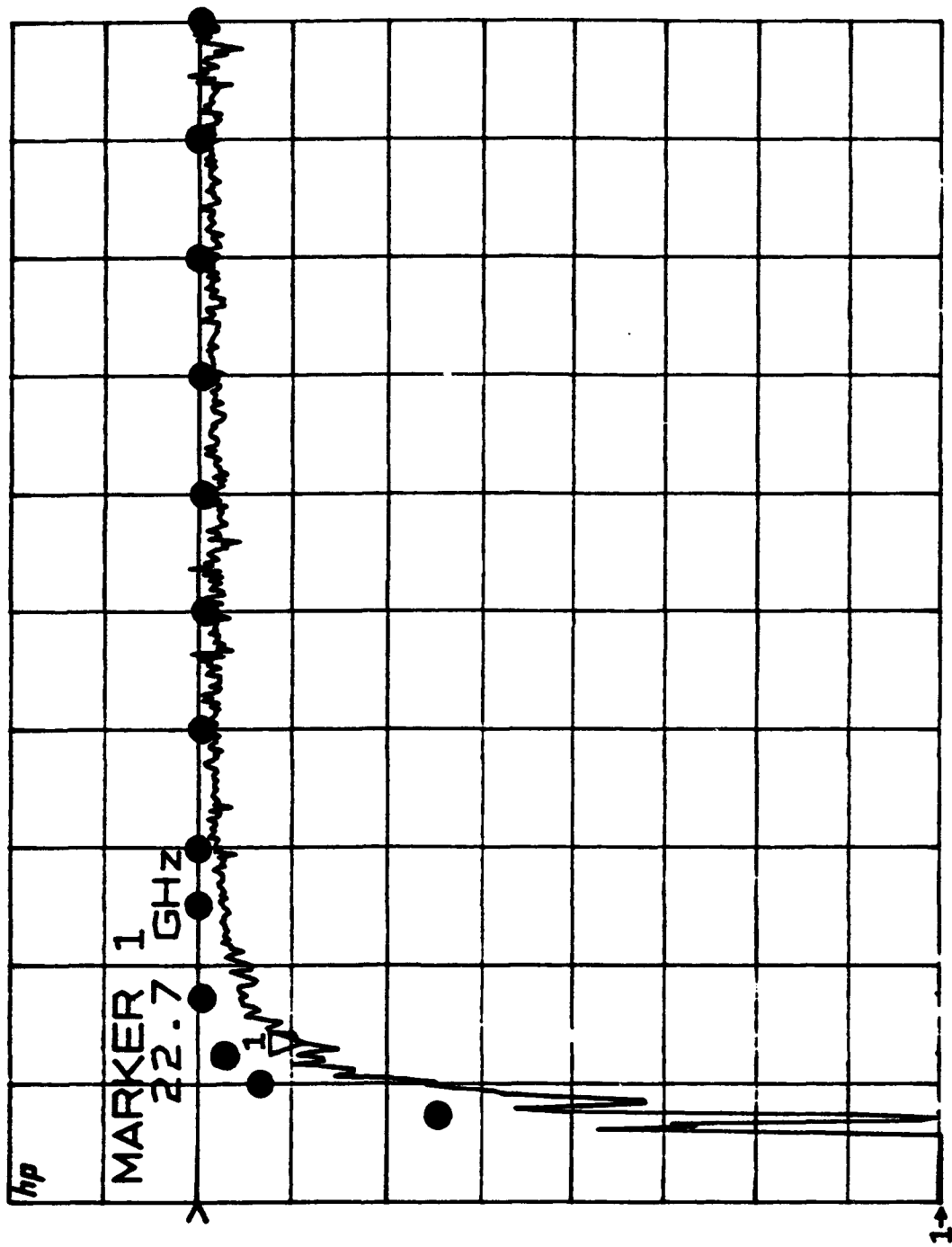


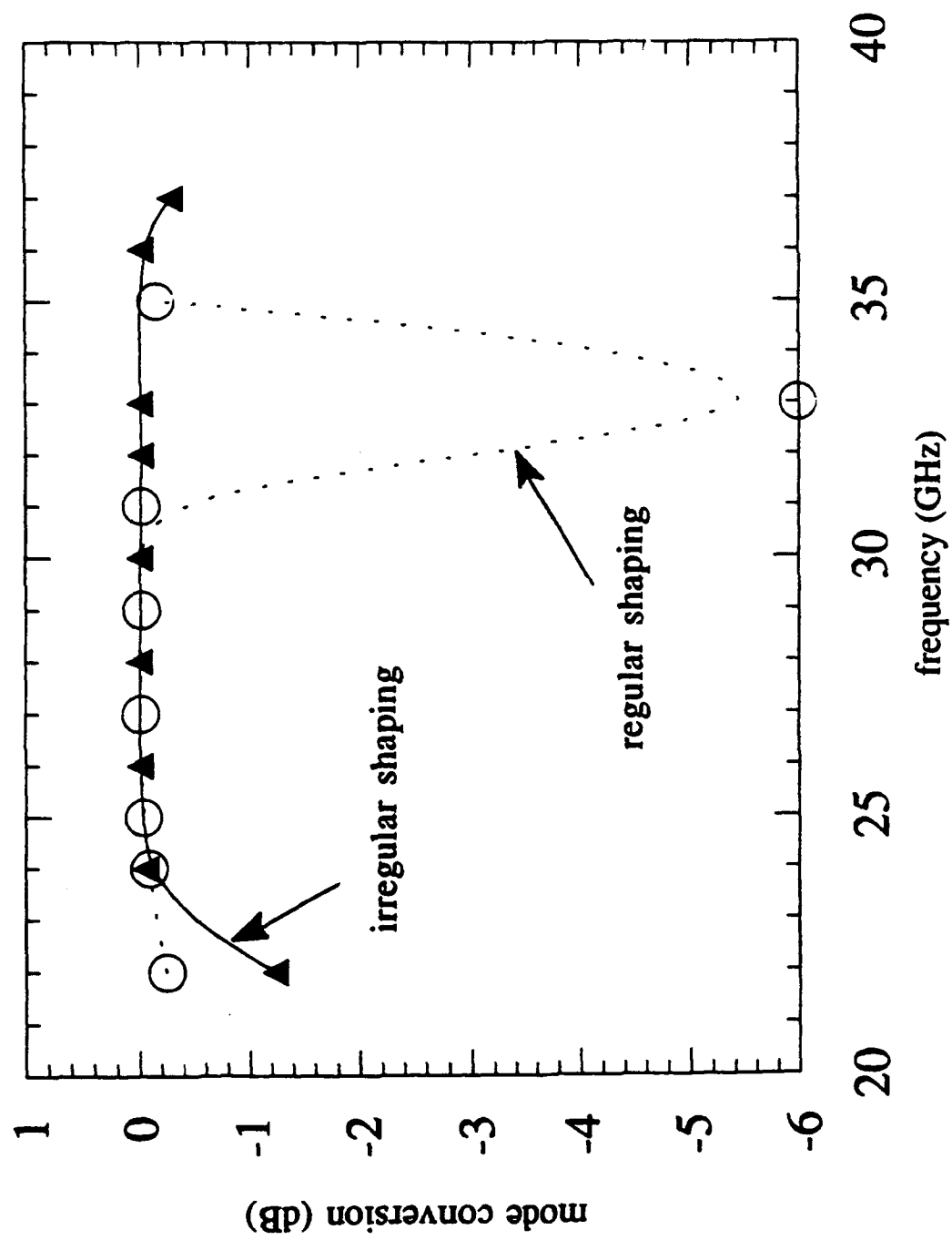
(b)











Appendix L

Diffraction Effects in Directed Radiation Beam

Diffraction effects in directed radiation beams

R. Hafizi* and P. Sprangle

Beam Physics Branch, Naval Research Laboratory, Washington, D.C. 20375-5000

Invited paper; received February 20, 1990; accepted November 1, 1990

A number of proposed applications of electromagnetic waves require that the radiation beam maintain a high intensity over an appreciable propagation distance. These applications include, among others, power beaming, advanced radar, laser acceleration of particles, and directed-energy sources. The quest to achieve these objectives has led to a resurgence of research on diffraction theory. We present a survey and critique of the analyses and experimental tests of solutions of the wave equation in connection with so-called diffractionless and other directed radiation beams. The examples discussed include electromagnetic missiles, Bessel beams, electromagnetic directed-energy pulse trains, and electromagnetic bullets.

1. INTRODUCTION AND SUMMARY

Diffraction is a fundamental characteristic of all wave fields, be they photons, electrons, etc. The effect of diffraction is typically manifested when an obstacle is placed in the path of a beam. On an observation screen some distance away from the obstacle, one observes a rather complicated modulation of the time-average intensity in the vicinity of the boundary separating the illuminated region from the geometrical shadow cast by the obstacle.^{1,2}

In many applications it would be highly desirable to propagate a beam over a long distance without an appreciable drop in the intensity. As an example we cite the possibility of accelerating particles to ultrahigh energies by utilizing high-power laser beams. Although the accelerating gradient in many of these schemes is extremely large, the actual distance over which the particle and laser beams maintain an appreciable overlap is limited. The overlap is reduced because of the diffraction of the laser beam, and as a result the net gain in the particle energy is limited.

With the use of high-power lasers and microwave sources, diffraction of radiation beams with finite transverse dimensions has become a problem of special importance. As an example, consider laser radiation of frequency ω emanating from a cavity oscillating in the fundamental transverse Gaussian mode. How far will this beam propagate in a turbulence-free atmosphere? More to the point, how fast is the falloff in the intensity of this laser beam?

The answer to this question is well known.³ The scale length for the falloff in intensity is given by the Rayleigh range, defined by

$$Z_R = \pi w_0^2 / \lambda, \quad (1)$$

where w_0 is the minimum spot size, or radius, of the beam, and $\lambda = 2\pi c/\omega$ is the wavelength. The minimum spot size w_0 is also known as the waist of the radiation beam. The falloff of the beam intensity as it propagates in space is a consequence of the fact that initially the beam was constrained to a finite waist w_0 . Diffraction then causes the beam to spread in the lateral direction and, from energy conservation, the intensity must drop off correspondingly. In the limit of an

infinitely wide beam, $w_0 \rightarrow \infty$, the Rayleigh range is infinite, there is no diffraction, and the intensity is constant.

A natural way to propagate a beam over long distances is to increase the Rayleigh range by employing a wider beam or shorter-wavelength radiation. Clearly the width of the beam is limited by the energy source available for pumping the lasing medium, and short-wavelength lasers (x rays and beyond) are not currently available. As a result, over the past several years there has been an upsurge in research on such fundamental topics as propagation and diffraction properties of radiation beams.⁴⁻³⁸ Briefly, the question being asked is as follows: "Can diffraction be overcome?" What follows is a summary of our review of diffractionless and other directed radiation beams:

(1) Electromagnetic missiles (Section 4): Experiments indicate the possibility of generating wave packets with a broad frequency spectrum. The high-frequency end of the spectrum determines the furthest distance the missile can propagate, in complete accord with our understanding of diffraction.

(2) Bessel beams (Section 5): A Bessel beam is a particular, monochromatic solution of the wave equation. Bessel beams propagate no farther than Gaussian beams or plane waves with the same transverse dimensions, and, contrary to previous assertions, Bessel beams are not resistant to the diffractive spreading commonly associated with all wave propagation.

(3) Electromagnetic directed-energy pulse trains (Section 6): These are particular, broadband solutions of the wave equation. We show that the experiment and the numerical studies of these pulses are consistent with conventional diffraction theory, and, contrary to previous assertions, these pulses do not defeat diffraction.

(4) Electromagnetic bullets (Section 7): Electromagnetic bullets are solutions of the wave equation that are confined to a finite region of space in the wave zone. The ultimate goal of the research has been to determine the source function that leads to a prescribed form for the bullet in the wave zone. Although the mathematical framework for this has been established, no concrete example has appeared in the literature.

Sections 2 and 3 begin with a review of basic diffraction theory, and our findings and conclusions are summarized in Section 8.

After the completion of our research we became aware of a number of related studies. In a review of diffraction-free propagation, Godfrey arrived at conclusions similar to ours regarding electromagnetic missiles, Bessel beams, and electromagnetic directed-energy pulse trains.³⁹ Ananov presented a concise and revealing analysis of Bessel beams and noted that, in order to increase the propagation range, it is necessary to illuminate the transmitter (aperture) as uniformly as possible.⁴⁰ In connection with this point, Barakat's variational analysis of apodization problems in the context of Fraunhofer diffraction is noteworthy.⁴¹

2. ELECTROMAGNETIC WAVE DIFFRACTION

Consider the radiation beam from a cavity of radius d . The wave vector is given by $k_1 \hat{e}_z$, corresponding to propagation predominantly in the z direction, and the magnitude of the spread in the wave vector in the transverse direction is denoted by Δk_\perp , with $k_1 \gg \Delta k_\perp$. The angular spread of the radiation relative to the z axis is

$$\theta \approx \Delta k_\perp / k_1. \quad (2)$$

On an observation screen at a distance z , the radius of the illuminated region is given by

$$w \approx d + \theta z. \quad (3)$$

The first term on the right-hand side of this expression indicates the width of the region illuminated according to geometrical optics. Beyond this region lies the region of the geometrical shadow, and the second term in expression (3) indicates the extent to which this region is illuminated because of diffraction of light. The distance Z over which the angular spread leads to a falloff in the intensity is given by $d + \theta Z = 2d$, or

$$Z = d/\theta. \quad (4a)$$

The distance Z may be regarded as the scale length for diffractive spreading of the beam.

As a first example, suppose that the transverse distribution of intensity in the beam is uniform. This is the case when plane waves are apertured. If the radius of the aperture is d , from a fundamental result of Fourier analysis, $\Delta k_\perp d \approx 1$. The angular spread is therefore given by $\theta \approx \lambda / 2\pi d$, where $\lambda \approx 2\pi/k_1$ is the wavelength. For this intensity distribution, one thus finds that

$$Z_p \approx 2\pi d^2/\lambda. \quad (4b)$$

For the case in which the transverse intensity distribution is a Gaussian, $\exp(-r^2/w_0^2)$, of width w_0 , we have $\Delta k_\perp \approx 1/w_0$, and the angular spread of the beam is of the order of $\theta \approx \lambda / 2\pi w_0$. In this case $d = w_0$, and hence

$$Z_G \approx 2\pi w_0^2/\lambda, \quad (4c)$$

which is twice the Rayleigh range Z_R defined in Eq. (1).

Clearly, diffraction is simply the physical manifestation of the well-known result of Fourier analysis relating the spreads in wave-vector space to the corresponding widths in real space, $\Delta k_i \Delta x_i \approx 1$ for $i = 1, 2, 3$. As a result, Eq. (4a)

expresses a fundamental relation that we shall make use of repeatedly in order to interpret the results of theory and experiment on so-called diffractionless radiation beams.

3. DIFFRACTION ZONES (HUYGENS'S PRINCIPLE)

According to Huygens's principle, each point on a given wave front acts as a source of secondary wavelets. The field at a point P is given by the sum over the wavelets. If $u(r) \exp(-i\omega t)$ is the amplitude on an aperture, an approximate solution of the scalar wave equation at P is given by^{1,2}

$$\psi_P(x, t) = (i\lambda)^{-1} \exp(-i\omega t) \int_{\text{aperture}} dS' u(r') R^{-1} \exp(i\omega R/c), \quad (5)$$

where $R = [(x - x')^2 + (y - y')^2 + z^2]^{1/2}$ is the distance between the area element dS' on the aperture and the point P , as shown in Fig. 1.

In the Fresnel approximation the binomial expansion of R may be used to simplify Eq. (5) to

$$\psi_P \approx (i\lambda z)^{-1} \exp[i\omega(z/c - t)] \times \int_{\text{aperture}} dS' u(x', y') \exp \left[i \frac{\omega}{c} \left(\frac{x'^2 + y'^2}{2z} - \frac{xx' + yy'}{z} \right) \right]. \quad (6)$$

For plane waves incident upon an aperture with linear dimension d , there are two physically interesting limits for approximating expression (6):

(1) Fraunhofer diffraction (far-field or wave-zone region): If

$$z \gg d^2/\lambda, \quad (7)$$

one may neglect the quadratic terms in the exponent of expression (6), and the wavelets from the entire wave front at the aperture contribute to the field at P . In the Fraunhofer region ψ_P is simply the Fourier transform of the amplitude at the diffracting aperture.

(2) Fresnel diffraction (near-field region): In the other limit,

$$z < d^2/\lambda, \quad (8)$$

it is necessary to retain the quadratic terms in the exponent

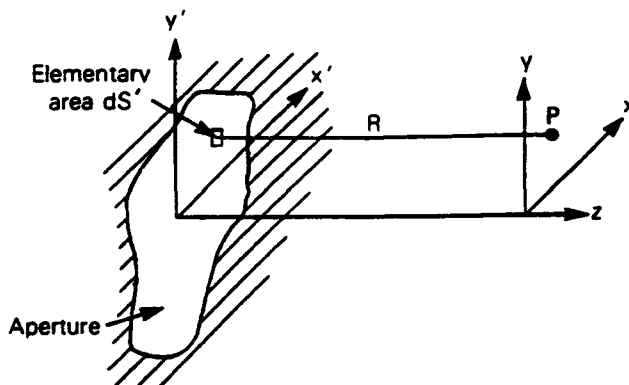


Fig. 1. Radiation diffracted by an aperture in an opaque screen. The distance between the element of area dS' on the aperture and the point of observation P is denoted by R .

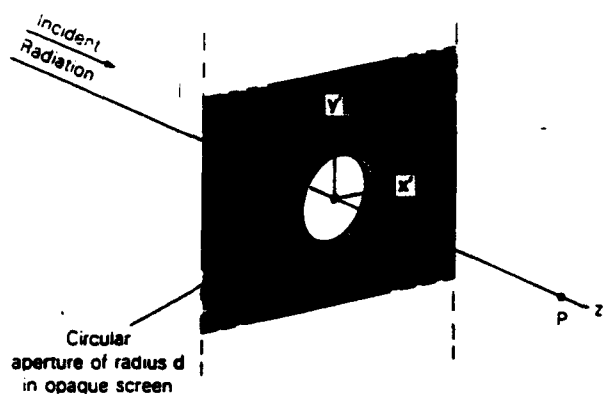


Fig. 2. Diffraction through a circular opening of radius d in an opaque screen. The point of observation P lies on the symmetry axis.

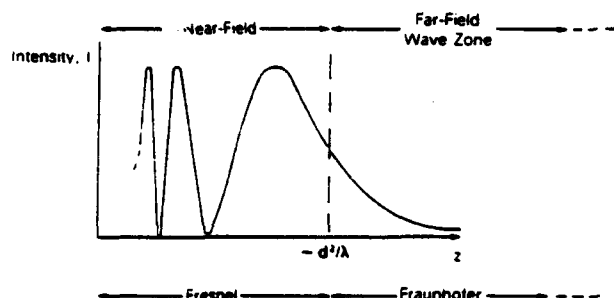


Fig. 3. Intensity profile on the axis of symmetry of a circular aperture of radius d . The point of demarcation between near-field and far-field regions is $\sim d^2/\lambda$.

of expression (6), and the wavelets from a limited portion of the wave front at the aperture make the dominant contribution to the field at P . In this case the integration in expression (6) may be taken to be over the entire $z = 0$ plane.

For plane waves incident upon a circular aperture of radius d (Fig. 2), making use of Eq. (5), we find that the exact field on the axis of symmetry is given by $\psi_P \propto \exp(-i\omega t) \cdot [\exp(i\omega z/c) - \exp[i\omega(d^2 + z^2)^{1/2}/c]]$, and the intensity $I \propto \psi_P \psi_P^*$ is

$$I \propto 1 - \cos[\omega[(d^2 + z^2)^{1/2} - z]/c]. \quad (9)$$

Figure 3 is a schematic plot of the intensity function [expression (9)] indicating in particular the transition between the Fresnel and the Fraunhofer regions. Note that the intensity drops off precipitously beyond $z \approx 2\pi d^2/\lambda$, consistent with the scale length defined by expression (4b).

We proceed now to examine the research on new solutions of the wave equation, with particular emphasis on their diffraction properties.

4. ELECTROMAGNETIC MISSILES

A. Theory

Consider first the case of a field, termed a missile, that falls off more slowly than the usual $1/R$ law. The inventive step is the use of a broad frequency spectrum. Depending on the spectrum, the falloff with R may be as slow as desired.¹⁴⁻²⁴

To appreciate the nature of this field, note that, for an arbitrary source distribution within a region \mathcal{A} as shown in

Fig. 4, the energy delivered to a screen S , integrated over all time, is

$$\epsilon(S, R) = \int_{-\infty}^{\infty} dt \int_{\text{screen}} dS \hat{n} \cdot c(\mathbf{E} \times \mathbf{B})/4\pi,$$

where \hat{n} is a unit vector normal to the screen and \mathbf{E} and \mathbf{B} are the electric and the magnetic fields, respectively. For a source with a bounded frequency spectrum, a screen of fixed area S , and for sufficiently large R , $\epsilon(S, R) \sim 1/R^2$, according to well-known results.⁴²

The current density for the electromagnetic missile described in Ref. 14, $\mathbf{J}(\mathbf{r}, t) = \delta(z)f(t)\hat{e}_z$, $r < d$, is confined to a disk of radius d , where $r = (x^2 + y^2)^{1/2}$ is the radial coordinate and $f(t)$ is a given function of time. If $\tilde{A}(\omega)$ and $\tilde{J}(\omega)$ denote the Fourier transforms of the vector potential and the current density, respectively, then $\tilde{A}(\omega) = \int d^3r \tilde{J}(\omega) \exp(i\omega R/c)/cR$ is a solution of the wave equation.⁴² In the present case, $\tilde{J}(\omega) = \delta(z)\tilde{f}(\omega)\hat{e}_z$, and the vector potential on the axis of symmetry is given by

$$\tilde{A}(\omega) = \frac{2\pi}{c} \tilde{f}(\omega) \int_0^d dr r (r^2 + z^2)^{-1/2} \exp\left[i \frac{\omega}{c} (r^2 + z^2)^{1/2}\right] \hat{e}_z.$$

Making use of this expression for $\tilde{A}(\omega)$, we find that the Poynting flux along the z axis integrated over all time, $U(z) = \int dt \hat{e}_z \cdot c(\mathbf{E} \times \mathbf{B})/4\pi$, is given by

$$U = c^{-1} [1 + z(z^2 + d^2)^{-1/2}] \int_0^\infty d\omega |\tilde{f}(\omega)|^2 \times \left(1 - \cos\left\{\frac{\omega}{c} [(z^2 + d^2)^{1/2} - z]\right\}\right). \quad (10)$$

Note the resemblance between expression (9) and the integrand of Eq. (10). Expression (9) is for a monochromatic field and is based on the Huygens-Fresnel principle, while Eq. (10) is obtained from a rigorous solution of the full wave equation.

In the limit $z \rightarrow \infty$ in Eq. (10), for a fixed frequency ω , $\cos[(\omega/c)[(z^2 + d^2)^{1/2} - z]] \rightarrow \cos(\omega d^2/2cz) \rightarrow 1$, and the integrand tends to zero. From Fig. 3, this result means that the contribution of this frequency to the expression in Eq. (10) lies in the far-field region and is thus negligible. At a given large z we can therefore write

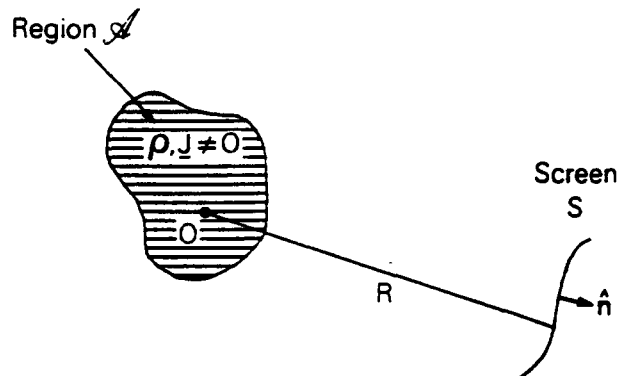


Fig. 4. Bounded region \mathcal{A} inside which there is a distribution of charge $\rho(\mathbf{r}, t)$ and current $\mathbf{J}(\mathbf{r}, t)$. The origin of coordinate system 0 lies inside \mathcal{A} . The distance between 0 and a point on the screen is R . The unit vector normal to the screen is denoted by \hat{n} .

$$U \simeq \frac{2}{c} \int_{2cz/d^2}^{\infty} d\omega |\tilde{f}(\omega)|^2 [1 - \cos(\omega d^2/2cz)].$$

We see that the most important contribution is from the high-frequency end of the spectrum, for which the given point z lies in the near-field, Fresnel zone. The contributions from all the lower-frequency components will have decayed to negligible values before reaching the given z . While the eventual falloff of any frequency component is as $1/z$, the falloff of the time-integrated Poynting flux for the wave packet depends on how rapidly $|\tilde{f}(\omega)|$ decays or $\omega > 2cz/d^2$. As an example, consider a source with a frequency spectrum¹⁴

$$\tilde{f}(\omega) \propto [1 + (\omega/\omega_0)^2]^{-(1+2\epsilon)/4},$$

where $\epsilon > 0$. We note that this spectrum is not an analytic function in the upper half of the ω plane. The singularity in the upper half-plane is a reflection of the unrealistic character that $f(t)$ extends over the entire time domain $-\infty < t < \infty$. For this hypothetical spectrum the time-integrated Poynting flux falls off as $U \propto 1/z^2$, which can be as slow as desired by taking the limit $\epsilon \rightarrow 0$. Consistent with this, the amplitude varies as $z^{1/2-\epsilon}$, and the pulse width decreases as $1/z$.²³ In the time domain the function $f(t)$ is symmetric with respect to $t \rightarrow -t$. Evaluating the inverse Fourier transform of $\tilde{f}(\omega)$, one finds that $f(t) \sim t^{(2\epsilon-3)/4} \exp(-\omega_0 t)$ for $t \gg 1/\omega_0$. For $\epsilon > 1/2$ and $t \ll 1/\omega_0$, $f(t) \rightarrow \text{constant}$. However, for the more interesting case of $\epsilon < 1/2$, $f(t) \rightarrow t^{-1/2}$ when $t \ll 1/\omega_0$, indicating a singularity initially.^{15,24}

For a realistic, or practical, frequency distribution the important issue of truncation of the spectrum at a finite frequency has been addressed by Wu *et al.*²⁴ Naturally, it is found that truncating the spectrum at a frequency f_{max} limits the maximum propagation range to a distance of the order of the Rayleigh range corresponding to f_{max} .

B. Experiment (Electromagnetic Missiles)

The difficulties involved in an experimental study of electromagnetic missiles stem from the need to generate pulses with extremely short rise times and suitably shaped wave fronts.¹⁸ An antenna was used to generate a pure spherical wave, which formed the primary pulse, and the field reflected from a parabolic dish of radius 0.61 m (2 ft) formed the secondary pulse. The pulses were detected by a specially designed sensor. The primary pulse was found to fall off as $1/z^2$, the energy decaying by $1/16$ when the sensor was moved from 1.22 m (4 ft) to 4.88 m (16 ft) from the source. This falloff occurred because the antenna, being a point source, generated spherical wave fronts. The pulse reflected from the parabolic dish was found to resemble that of a circular disk, similar to that studied in Subsection 4.A. Over the same distance, the energy in this electromagnetic missile was found to decay by just under $1/2$. This behavior and the diminishing pulse width have been found to be in accord with analytical predictions.¹⁸

These experimental results indicate that a suitably tailored pulse shape can be designed to have an energy-decay rate essentially limited by the highest frequencies present in the pulse generator, in complete accordance with the elementary notions of diffraction of light. Propagation of a composite pulse in free space is a dispersive process. As the

beam propagates, the lowest-frequency components diffract away first.

The generation and transmission of energy by electromagnetic missiles is severely limited by the practical means of launching wave packets with extremely short rise times and pulse widths.

5. BESSEL BEAMS

A. Theory

An example of a so-called diffractionless electromagnetic beam is a Bessel beam. We note that a particular solution of the scalar wave equation

$$\left(\nabla^2 - c^{-2} \frac{\partial^2}{\partial t^2}\right) \psi(x, t) = 0$$

is

$$\psi = \exp[i(k_1 z - \omega t)] \times \int_{\theta_0}^{2\pi+\theta_0} d\theta A(\theta) \exp[ik_{\perp}(x \cos \theta + y \sin \theta)] \quad (11)$$

for arbitrary θ_0 and $A(\theta)$, provided that $\omega^2 = c^2(k_1^2 + k_{\perp}^2)$. Here, k_1 and k_{\perp} denote the magnitudes of the components of the wave vectors parallel and orthogonal to the z axis, respectively, and $\lambda = 2\pi/(k_1^2 + k_{\perp}^2)^{1/2}$ is the wavelength. Since the z dependence in Eq. (11) is separated from the x and y dependences, the solution is clearly diffractionless in the sense that the time-average intensity is independent of z . In fact, the intensity is constant for all z and all t .

Durnin considers the case in which $A(\theta) = 1$.²⁵ In this case, if one makes use of the expansion $\exp(i\theta \sin \theta) = \sum_n J_n(\theta) \exp(in\theta)$, where J_n is the ordinary Bessel function of the first kind of order n ,⁴³ Eq. (11) simplifies to $\psi = 2\pi J_0(k_{\perp} r) \exp[i(k_1 z - \omega t)]$, where $r = (x^2 + y^2)^{1/2}$ is the radial variable.

Making use of the properties of the Bessel function,⁴³ one can show that the energy content, $\int dr r J_0^2(k_{\perp} r)$, integrated over any transverse period, or lobe, is approximately the same as that in the central lobe. This point will be important in our interpretation of the diffractive properties of Bessel beams.

B. Experiment (Bessel Beams)

A Bessel beam has an infinite number of lobes and therefore has infinite energy. In the laboratory an approximation to this ideal beam is realized by clipping the beam beyond a certain radius. The question is, given the finite transverse size, how well is the diffractionless property preserved.

To answer this question Durnin *et al.*²⁶ compared the propagation of a clipped Bessel beam with a Gaussian beam. (See also Ref. 27.) The full width at half-maximum (FWHM) of the Gaussian was taken to be equal to the FWHM of the central lobe of the Bessel beam. In the experiment the on-axis intensity of each beam was measured along the axis of symmetry. The Bessel beam was claimed²⁶ to be "resistant to the diffractive spreading commonly associated with all wave propagation" since its intensity was observed to remain approximately constant for a much long-

er distance than the Gaussian beam. The idea of a diffraction-free beam was further reinforced by using a geometrical optics argument in order to obtain a formula for the propagation distance of the central lobe of the Bessel beam.

We shall now reconsider this comparison. The wavelength of the radiation was $\lambda = 6328 \text{ \AA}$. For the Gaussian beam $\exp(-r^2/w_0^2)$, w_0 was equal to 0.042 mm, corresponding to a FWHM of 0.07 mm. For the Bessel beam $J_0(k_\perp r)$, k_\perp was equal to 41 mm^{-1} , corresponding to a FWHM for the central lobe of 0.07 mm. The beams were apertured to a radius $d = 3.5 \text{ mm}$. The following order-of-magnitude discussion is based on expressions (2)–(4); a more rigorous analysis is presented in Appendix A. The angular spread due to the natural width of the Gaussian beam is $\theta = \lambda/2\pi w_0$, and expression (3) takes the form $w = w_0 + (\lambda/2\pi w_0)z$, where the first term in this expression is w_0 , rather than d , since the energy of the Gaussian is concentrated in the central peak. The scale length for diffraction is the same as that given by expression (4c), namely, $Z_G \approx 2\pi w_0^2/\lambda = 1.75 \text{ cm}$. The natural angular spread of the Bessel beam is $\theta \approx k_\perp \lambda/2\pi$, and expression (3) takes the form $w = d + (k_\perp \lambda/2\pi)z$, where the first term represents the radius of the aperture since the energy in each lobe is approximately the same and the lobes all affect the propagation of the Bessel beam. The scale length for diffraction is, therefore, given by $d + (k_\perp \lambda/2\pi)Z_B = 2d$, or $Z_B \approx 2\pi d/k_\perp \approx 85 \text{ cm}$, which is consistent with the experimental observation.

In the transverse plane the lobes of the Bessel beam diffract away sequentially starting with the outermost one. The outermost lobe diffracts in a distance of the order of $2\pi^2/\lambda k_\perp^2$, which is approximately equal to Z_G . The next lobe diffracts away after a distance of the order of $2Z_G$. This process continues until the central lobe, which diffracts away after a distance $\sim NZ_G$, where N denotes the number of lobes within the aperture. In the experiment $N \approx 50$, implying a propagation distance of the order of $50Z_G$ for the central lobe of the Bessel beam, which is consistent with the measured value. Measurements of the on-axis intensity displayed by Durnin *et al.* obviously fail to reveal the gradual deterioration of the transverse beam profile. However, by careful examination of Fig. 2 of Ref. 25, we find that the numerical plots are consistent with such having occurred. Therefore the Bessel beam is not "resistant to the diffractive spreading commonly associated with all wave propagation."²⁶ Our interpretation points out the significance of each successive lobe's having approximately the same energy. The central lobe persists as long as there are off-axis lobes compensating for its energy loss, and hence the comparison with the narrower Gaussian beam in Ref. 26 is of little significance.

Let us now consider the power-transport efficiency of the beams.²⁸ We note that, utilizing the full width of the aperture, a Gaussian beam propagates a distance of the order of NZ_B , i.e., N times farther than the Bessel beam. Consequently, in terms of diffraction-free propagation distance per unit energy, the two beam profiles are equally efficient. However, by appropriately curving the wave front, one can focus nearly all the power of the Gaussian beam on a target of dimension w_0 in a distance Z_B . Hence, for this purpose, a Gaussian beam would be significantly better than the Bessel beam employed by Durnin *et al.*

6. ELECTROMAGNETIC DIRECTED-ENERGY PULSE TRAINS

A. Theory

Electromagnetic directed-energy pulse trains are particular solutions of Maxwell's equations.^{29–34} The research on these pulse trains resulted from earlier studies of focus wave modes.^{5–13} To discuss these, we make the change of variables $\xi = z - ct$ and $\tau = t$ and transform the wave equation

$$(\nabla^2 - c^{-2}\partial^2/\partial t^2)\Psi = 0$$

into the form

$$(\nabla_\perp^2 + \frac{2}{c} \frac{\partial^2}{\partial \xi \partial \tau} - c^{-2}\partial^2/\partial \tau^2)\Psi = 0.$$

Making the assumption that

$$\Psi = \psi(\xi, r, \tau)\exp(i\omega\xi/c) \quad (12)$$

leads to an equation for the complex envelope ψ :

$$\left(\nabla_\perp^2 + 2i\omega c^{-2} \frac{\partial}{\partial \tau} + \frac{2}{c} \frac{\partial^2}{\partial \tau \partial \xi} - c^{-2} \frac{\partial^2}{\partial \tau^2}\right)\psi = 0.$$

Here r denotes the radial variable and ∇_\perp is the differential operator in the plane z constant. If $\psi(\xi, r, \tau)$ varies slowly compared with the characteristic scales $1/\omega$ and c/ω , the second derivative of the envelope function may be neglected, and the wave equation reduces to

$$\left(\nabla_\perp^2 + 2i\omega c^{-2} \frac{\partial}{\partial \tau}\right)\psi \approx 0. \quad (13)$$

Expression (13) is an extremely useful approximation to the full-wave equation in a vacuum. Note that the full-wave operator is of the hyperbolic type, whereas the reduced-wave operator is of the parabolic type. For this reason, expression (13) is sometimes referred to as the parabolic approximation to the wave equation.

A particular solution of expression (13) is given by

$$\psi = C \frac{w_0}{w} \exp[-i \tan^{-1}(\tau/\tau_R) - (1 - i\tau/\tau_R)r^2/w^2], \quad (14a)$$

where C is a constant,

$$w = w_0[1 + (\tau/\tau_R)^2]^{1/2} \quad (14b)$$

is the spot size, w_0 is the waist, and

$$\tau_R = \omega w_0^2/2c^2 \quad (14c)$$

is related to the Rayleigh range $Z_R = \omega w_0^2/2c$ by $\tau_R = Z_R/c$.

References 29–33 make use of the variables transformation

$$\xi = z - ct, \quad \eta = z + ct$$

in the wave equation in order to reduce it to the form

$$\left(\nabla_\perp^2 + 4 \frac{\partial^2}{\partial \eta \partial \xi}\right)\Psi = 0.$$

Representing Ψ in the form

$$\Psi = \psi(\eta, r)\exp(i\omega\xi/c) \quad (15)$$

leads, without any approximation, to an equation for ψ :

$$\left(\nabla_{\perp}^2 + 4i \frac{\omega}{c} \frac{\partial}{\partial \eta}\right) \psi = 0. \quad (16)$$

A particular solution of Eq. (16) is given by

$$\psi = C \frac{w_0}{w} \exp[-i \tan^{-1}(\eta/\eta_R) - (1 - i\eta/\eta_R)r^2/w^2], \quad (17a)$$

where C is a constant,

$$w = w_0[1 + (\eta/\eta_R)^2]^{1/2}, \quad (17b)$$

and

$$\eta_R = \omega w_0^2/c \quad (17c)$$

is related to the Rayleigh range $Z_R = \omega w_0^2/2c$ by $\eta_R = 2Z_R$.

Some remarks on the solutions in Eqs. (14) and (17) are in order. First, Eqs. (14) are solutions of the parabolic approximation to the full wave equation. On the other hand, Eqs. (17) are exact solutions of the full equation. Second, there is a factor-of-2 difference between the scale length $c\tau_R$ in Eq. (14c) and the scale length η_R in Eq. (17c). Third, the solution of Eqs. (17) has infinite energy. Finally, the exact solution in Eq. (15) consists of a pulse traveling to the left that is modulated by a plane wave moving to the right.

To examine the last two points, we may combine Eqs. (15) and (17) in order to form a fundamental Gaussian pulse Ψ_k with parameter $k = \omega/c$:

$$\Psi_k(r, z, t) = \exp(ik\eta) \frac{\exp(-kr^2/V)}{4\pi i V}, \quad (18)$$

where

$$\frac{1}{V} = \frac{1}{A} - \frac{i}{R}, \quad A = z_0 + \xi^2/z_0, \quad R = \xi + z_0^2/\xi,$$

and z_0 is constant.²⁹⁻³³ From Refs. 29-33, Eq. (18) represents a pulse traveling to the right that is modulated by a plane wave moving to the left. With an appropriate weight function, it can be shown that the Ψ_k for all k form a complete set of basis functions, each with total energy proportional to $\int d^3r |\Psi_k|^2 \rightarrow \infty$. Just as in the case of Fourier synthesis with plane waves, a general finite-energy pulse may be obtained by superposing the various Ψ_k according to a weight function $F(k)$; that is,

$$\begin{aligned} f(r, z, t) &= \int_0^\infty dk \Psi_k(r, z, t) F(k) \\ &= \frac{1}{4\pi i(z_0 + i\xi)} \int_0^\infty dk F(k) \exp(-ks), \end{aligned} \quad (19a)$$

where

$$s = -i\eta + \frac{r^2}{z_0 + i\xi}. \quad (19b)$$

Equation (19a) indicates that $f(r, z, t)$ is proportional to the Laplace transform of $F(k)$.

B. Modified Power-Spectrum Pulse: Numerical Study
References 29-33 examined in detail the pulse corresponding to a modified power spectrum (MPS). With a slight redefinition of constants, the spectrum has the form

$$F(k) = 4\pi i \beta H(k - k_c) \exp[-(k - k_c)L], \quad (20a)$$

where β and L are constants, $H(x)$ is the Heaviside function, and the spectrum is nonvanishing for wave numbers exceeding the cutoff value k_c . Substituting Eq. (20a) into Eq. (19), one obtains

$$f(r, z, t) = \left\{ \frac{\beta}{z_0 + i\xi} \frac{\exp[ik_c \eta - k_c r^2/(z_0 + i\xi)]}{L + r^2/(z_0 + i\xi) - i\eta} \right\}. \quad (20b)$$

The real part of this function defines the MPS pulse. From Eq. (20b) we note that z_0 is a measure of the axial extent of the pulse, which is equivalent to a frequency of the order of c/z_0 . This frequency is the upper bound of the spectrum in Ziolkowski's examples and is much greater than the cutoff frequency ck_c . The radial profile of the MPS pulse at the pulse center, $\xi = 0$, has the form

$$f(r, z) = \frac{\beta}{z_0} \frac{\exp(2ik_c z - k_c r^2/z_0)}{L + r^2/z_0 - 2iz}. \quad (20c)$$

In the numerical studies the pulse was replicated by superposing the fields from a planar array of discrete points, each of which was driven by a function specified by the MPS form on some z constant plane.³¹ The parameters were $L = 6.0 \times 10^{15}$ cm, $\beta = 6.0 \times 10^{15}$, $z_0 = 1.667 \times 10^{-3}$ cm, and $k_c = 1.667 \times 10^{-6}$ cm⁻¹. The spectrum was approximately flat up to 200 GHz, becoming negligible beyond $\sim c/z_0 = 18$ THz. The pulse generated in this manner was propagated forward and compared with the exact form in Eq. (20b) at several locations along the z axis. The minimum radius of the array required to replicate the exact pulse form at 1, 10, 100, and 1000 km was determined. From the results of Refs. 29-33 we estimate the corresponding radii of the antenna to be approximately 0.5, 5, 50, and 500 m, respectively.

We shall examine these results by asking the following question: What is the scale length for diffraction of the MPS pulse? The pulse has a Gaussian radial profile, as indicated in Eq. (20c), with a width $w_0 = (z_0/k_c)^{1/2} = 31.6$ cm, and therefore Ziolkowski calculates a Rayleigh range $\pi w_0^2/\lambda = 0.21$ km for the 200-GHz component.³¹ This, however, is not the appropriate scale length for diffraction of the MPS pulse. The correct scale length is given by $2\pi w_0 d/\lambda$, where the antenna dimension d always exceeds w_0 . The point here is that the Rayleigh range based on the waist w_0 , as calculated by Ziolkowski,^{30,31} is valid only at the pulse center $\xi = 0$. Away from the plane $\xi = 0$ the effective waist increases, as indicated by Eq. (20b), and the actual diffraction length is therefore longer than $\pi w_0^2/\lambda$. This explains why the pulse propagates farther than the Rayleigh range defined in terms of w_0 . To calculate the actual diffraction length, we note that the perpendicular wave-number (k_{\perp}) spectrum given in Ref. 31 indicates that the smallest k_{\perp} is of the order of $1/w_0$. Hence an estimate for the diffraction angle is $\lambda/2\pi w_0$. The width of the radiation beam given by Eq. (3) can be written as $w = d + (\lambda/2\pi w_0)z$, where d is the radius of the array or antenna. The scale length for diffraction is then simply

$$Z_{MPS} = 2\pi w_0 d/\lambda. \quad (21)$$

Note the similarity between the diffraction length in Eq. (21) and the scale length for diffraction of the Bessel beam. $Z_B = 2\pi d/k_{\perp} \lambda$, derived in Subsection 5.B. The resemblance is a reflection of the fact that in both cases the pulse energy is

spread over the entire radius d of the aperture, which is much larger than the nominal waist of the beam w_0 .

According to Eq. (21), the larger the radius of the array, the longer is the distance of propagation of the pulse, consistent with the numerical values quoted above. Indeed, from the numbers the ratio of the propagation distance to the antenna radius is equal to 2000. Equating this to Z_{MPS}/d , from Eq. (21) we find that the corresponding frequency is 300 GHz. Since this frequency is well within the cutoff of the pulse spectrum, we have a persuasive indication that the MPS pulse does not defeat diffraction as claimed by Ziolkowski.³⁰

C. Modified Power-Spectrum Pulse: Experiment

Ziolkowski *et al.* have performed a water-tank experiment to demonstrate the properties of a MPS acoustic pulse.³² The pulse was generated by a 6×6 cm² square array. The MPS pulse parameters were $L = 300.0$ m, $\beta = 300.0$, $z_0 = 4.5 \times 10^{-4}$ m, and $k_c = 2.0$ m⁻¹. From these parameters one finds that the pulse width w_0 is equal to 1.5 cm. The experiment indicated that a Gaussian pulse with an initial width equal to 1.5 cm suffered a greater transverse spreading than the MPS pulse.

This experiment may be examined in the light of the discussion leading to Eq. (21). The expression in Eq. (21) gives the scale length for the falloff in the intensity of a pulse that is generated by an array (i.e., antenna) of radius d . Since the square array is 6 cm \times 6 cm, we take the parameter d to be equal to 3 cm. Note that the speed of sound in water is 1.5×10^3 m/sec; the wavelength of the dominant frequency in the pulse, 0.6 MHz, is $\lambda = 2.5$ mm. From this, the actual diffraction scale length Z_{MPS} is 1.1 m. This is consistent with the experimental observation that the MPS pulse propagated a distance of 1 m without significant spreading. Comparing the MPS pulse generated by a 6 cm \times 6 cm array with a Gaussian pulse having a waist of 1.5 cm is inappropriate. A Gaussian beam with spot size equal to the array radius used in the experiment would propagate a distance $\pi d^2/\lambda \simeq Z_{MPS}$, i.e., as far as the MPS pulse.

We note from Eq. (21) that, in general, a Gaussian beam with an appropriately curved wave front and an initial spot size equal to the antenna dimension transfers nearly all the power onto a target of dimension w_0 in a distance of the order of Z_{MPS} . Such a Gaussian beam therefore transfers more power on the target than the corresponding MPS pulse.

7. ELECTROMAGNETIC BULLETS

In this section we shall discuss solutions of the wave equation that are confined to a finite region of space in the wave zone and are termed electromagnetic bullets. We consider solutions of the wave equation

$$(\nabla^2 - c^{-2}\partial^2/\partial t^2)f(\mathbf{r}, t) = -\rho(\mathbf{r}, t), \quad (22)$$

where the source term $\rho(\mathbf{r}, t)$ is assumed to be nonzero for a finite time interval $-T < t < T$. In this problem there are two cases of interest:

Case (a) is the direct source problem (initial value problem). In this case the solution for $t < -T$ is given, and the solution for $t > T$ is sought.

Case (b) is the inverse source problem. Here, the solution

of the homogeneous wave equation for $|t| > T$ is known, and one seeks the source term appropriate to this solution. This case is of particular interest since it would enable one to find the time-dependent source for a prescribed radiation field.

Subsections 7.A–7.D summarize the extensive research of Moses and Prosser^{34–36} on this subject. For a brief description of the properties of a bullet, the reader is referred to Subsection 7.D.

A. Nonuniqueness of the Inverse Source Problem

In this subsection we indicate the reason for the nonuniqueness of the inverse source problem.³⁵ By making use of the eigenfunctions of the curl operator, we may solve the electromagnetic vector-field wave equation along essentially the same lines as the one-dimensional problem. The discussion in this subsection is therefore confined to the one-dimensional wave equation in order to avoid the complications of multidimensional effects.

Let $f_+(x, t) = f(x, t)$ denote the solution of Eq. (22) for $t > T$ and $f_-(x, t) = f(x, t)$ denote the solution for $t < -T$. It is well known that the solution of the source-free initial value problem for $t > T$ in terms of the values of the function $f_+(x, t)$ at $t = T$ and the velocity $(\partial/\partial t)f_+(x, t)$ at $t = T$ is expressible in terms of a propagator $G(x; t)$:

$$f_+(x, t) = \int dx' [G(x - x'; t - T) \frac{\partial}{\partial t} f_+(x', t = T) + f_+(x', t = T) \frac{\partial}{\partial t} G(x - x'; t - T)]. \quad (23a)$$

Similarly, the solution of the source-free final value problem for $t < -T$ in terms of $f_-(x, t)$ at $t = -T$ and $(\partial/\partial t)f_-(x, t)$ at $t = -T$ is given by

$$f_-(x, t) = \int dx' [G(x - x'; t + T) \frac{\partial}{\partial t} f_-(x', t = -T) + f_-(x', t = -T) \frac{\partial}{\partial t} G(x - x'; t + T)]. \quad (23b)$$

The propagator G can be written in terms of the Heaviside function H as follows:

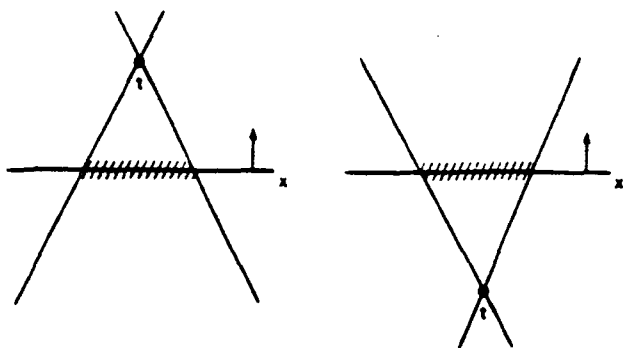
$$G(x; t) = \frac{1}{2} \text{sgn}(t) H(c^2 t^2 - x^2) = \frac{1}{2} [H(x + ct) - H(x - ct)]. \quad (24)$$

That is, G may be expressed as the difference between the advanced and the retarded Green functions. As a result, $f_+(x, t)$ is influenced only by points x at $t = T$ that lie in the backward light cone of the observation instant; similarly, $f_-(x, t)$ is influenced only by points x at $t = -T$ that lie in the forward light cone of the observation instant, as indicated in Fig. 5.

Let us now consider the effect of the source on the solution of the wave equation. We define two auxiliary functions,

$$\tilde{\rho}(k, t) = (2\pi)^{-1/2} \int_{-\infty}^{\infty} dx \rho(x, t) \exp(-ikx), \quad (25)$$

$$\tilde{f}(k, \sigma, t) = \tilde{f}(k, \sigma, -T) \exp[-i\sigma c|k|(t + T)] + \frac{i\sigma}{2|k|} \times \exp(-i\sigma c|k|t) \int_{-T}^t dt' \tilde{\rho}(k, t') \exp(i\sigma c|k|t'), \quad (26)$$



BACKWARD LIGHT CONE

FORWARD LIGHT CONE

Fig. 5. Backward and forward light cones of an event t , indicating the causal properties of the propagator $G(x; t)$.

where $\sigma = +1, -1$ distinguishes the two directions of propagation along the x axis. Note that $\tilde{\rho}(k, t)$ is simply the spatial Fourier transform of $\rho(x, t)$. In terms of the two auxiliary functions, it is simple to show that

$$f(x, t) = (2\pi)^{-1/2} \int_{-\infty}^{\infty} dk \tilde{f}(k, \sigma, t) \exp(ikx)$$

is a solution of the inhomogeneous wave equation in Eq. (22). The solutions for $t < -T$ and for $t > T$ are then given by

$$f_{\pm}(x, t) = (2\pi)^{-1/2} \int_{-\infty}^{\infty} dk \tilde{f}(k, \sigma, \pm T) \times \exp[ikx + i\sigma c|k|(\pm T - t)]. \quad (27)$$

Equation (27) expresses the solution of the wave equation in terms of \tilde{f} evaluated at $\pm T$. This function is related to the source ρ by Eqs. (25) and (26). Equation (23), on the other hand, expresses the same solutions in terms of f and $(\partial/\partial t)f$ evaluated at $\pm T$. Hence one would expect to be able to relate $\tilde{f}(k, \sigma, \pm T)$ to f and $(\partial/\partial t)f$ evaluated at $\pm T$. Indeed, the formula connecting $\tilde{f}(k, \sigma, T)$ and f_{+} is

$$\tilde{f}(k, \sigma, T) = (8\pi)^{-1/2} \int_{-\infty}^{\infty} dx \times \left[f_{+}(x, t = T) + i \frac{\sigma}{|k|} \frac{\partial}{\partial t} f_{+}(x, t = T) \right] \exp(-ikx), \quad (28)$$

and $\tilde{f}(k, \sigma, -T)$ is obtained in terms of f_{-} by Fourier inversion of Eq. (27) evaluated at $t = -T$. Thus, in the direct source problem, $f_{+}(x, t)$ is obtained by specifying either $f_{+}(x, t)$ and $(\partial/\partial t)f_{+}(x, t)$ evaluated at $t = T$ or $f(x, -T)$ and $\rho(x, t)$.

We now turn to the inverse source problem. Inverse problems, in general, have been the subject of extensive research in many branches of physics. In our case we wish to determine the source from a knowledge of the field generated by that source. Supposing that $f_{\pm}(x, t)$ and T are known, we can determine $\tilde{f}(k, \sigma, \pm T)$ from Eqs. (27) and (28). Letting the upper limit of integration of Eq. (26) equal T , one can apparently obtain the temporal Fourier transform $s(k, \omega)$ of $\tilde{\rho}(k, t)$, where

$$s(k, \omega) = (2\pi)^{-1/2} \int_{-T}^T dt \tilde{\rho}(k, t') \exp(i\omega t').$$

The source function is then given by

$$\rho(x, t) = (2\pi)^{-1} \int_{-\infty}^{\infty} dk \int_{-\infty}^{\infty} d\omega s(k, \omega) \exp(ikx - i\omega t).$$

Thus, if $s(k, \omega)$ were known for all k and all ω , we could determine $\rho(x, t)$. However, referring to Eq. (26), we notice that $s(k, \omega)$ is known only for $\omega = \pm c|k|$, which is not sufficient to permit us to reconstruct $\rho(x, t)$. This complication is intimately connected with the nonuniqueness of the inverse problem.

Moses has shown that specification of the time dependence of the source is sufficient to guarantee a unique solution.³⁵ As a concrete example, if $\rho(x, t) = \rho_e(x)h_e(t) + \rho_o(x)h_o(t)$, where h_e is an even function of t and h_o is an odd function of t and both are essentially arbitrary, then a complete solution of the inverse problem for $\rho_e(x)$ and $\rho_o(x)$ is possible. It must be stressed, however, that this assumed form for the source function is a sufficient but unnecessary condition for the solvability of the inverse problem.

Without going into details we cite the example given in Ref. 35. For simplicity, taking the time dependence to be of the form $h_e(t) = \delta(t)$, $h_o(t) = \delta'(t)$, where the prime is d/dt , and assuming the field to be of the form

$$f_{+}(x, t) = \sin[k(x - ct)], \quad -a < x - ct < a, \quad ka = n\pi,$$

we find that the source function is given by

$$\rho(x, t) = -[k\delta(t)\cos(kx) - c^{-1}\delta'(t)\sin(kx)], \quad -a < x < a.$$

Note that the source is confined to a finite region of space. This important attribute for any physically realizable source function is not in general guaranteed for the inverse source problem. [We should point out that the source function given by Moses is erroneous because of a sign error in evaluating the Fourier transform of $h_o(t)$ [Eq. (2.36') of Ref. 35].]

B. Solution of the Three-Dimensional Wave Equation in the Wave Zone

The general solution of the source-free three-dimensional wave equation is³⁶

$$f(\mathbf{r}, t) = (2\pi)^{-3/2} \int d^3k \exp(i\mathbf{k} \cdot \mathbf{r} - i\sigma ckt) \tilde{f}(\mathbf{k}, \sigma), \quad (29)$$

where $\sigma = \pm 1$ and $k = |\mathbf{k}|$. In spherical coordinates θ and ϕ are used to denote the polar and the azimuthal angles, respectively, of the wave vector \mathbf{k} . Making use of the method of stationary phase, we can show that

$$\lim_{r \rightarrow \infty} \exp(i\mathbf{k} \cdot \mathbf{r}) = \frac{2\pi i}{kr \sin \theta} [-\exp(ikr)\delta(\theta - \theta_r)\delta(\phi - \phi_r) + \exp(-ikr)\delta(\theta - \theta_r')\delta(\phi - \phi_r')], \quad (30)$$

where (θ_r, ϕ_r) are the angles in the cone along the $+z$ axis and (θ_r', ϕ_r') are the angles in the cone along the $-z$ axis.⁴⁴ We shall define cones more precisely in the following discussion. Substituting Eq. (30) into Eq. (29), we find that the field in the wave zone is given by

$$f(\mathbf{r}, t) = (8\pi)^{-1/2} r^{-1} \text{Im} \int_0^T dk [\exp[ik(r - ct)] \tilde{f}(k, \theta_r, \phi_r) - \exp[ik(r + ct)] \tilde{f}(k, \theta_r', \phi_r')]. \quad (31)$$

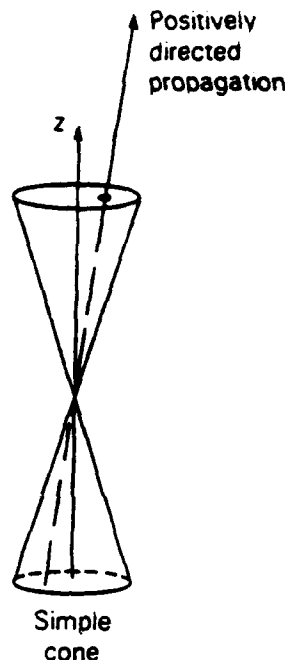


Fig. 6. Simple cone consisting of two associated solid angles and the two-sheeted cone that they subtend. One solid angle lies in the positive hemisphere and the other in the negative hemisphere relative to the indicated direction of the z axis. Positively directed propagation proceeds from the negative hemisphere to the positive hemisphere.

Remarkably, Eq. (31) shows that the general solution of the three-dimensional wave equation in the wave zone is, apart from the factor $1/r$, a superposition of one-dimensional wave motion, expressed as functions of $r - ct$ and $r + ct$. Moreover, if initially $f(r, t)$ is confined to a given solid angle, $\hat{f}(k, \theta, \phi)$ will be significant for k lying within that angle and, from Eq. (31), the solution in the wave zone will also be confined to the same angle. For the purposes of interpretation it is convenient to consider propagation in cones, as indicated in Fig. 6. In particular, an electromagnetic field in a cone is defined as one that is completely confined to a cone in the wave zone.

C. Exact Solution of the Wave Equation from the Solution in the Wave Zone (Radon Transforms)

The purpose of this subsection is to point out that, given the solution of the wave equation in the wave-zone region, it is possible to determine the solution everywhere.^{36,37} In particular, one seeks the initial conditions $f(r, t)$ and $(\partial/\partial t)f(r, t)$ at $t = T$. This is referred to as the inverse initial value problem.

The solution of the inverse initial value problem is discussed in Ref. 36 for a particularly simple case. A systematic treatment of the general problem is possible by using radon transforms.³⁷

The radon transform $F(k, \hat{n})$ of a function $f(r)$ is obtained by integrating f over all planes $r \cdot \hat{n} = \text{constant}$:

$$F(k, \hat{n}) = \int d^3r f(r) \delta(r \cdot \hat{n} - k),$$

where \hat{n} is a unit vector.⁴⁵ The usual radon transform is

defined as an integral over planes whose normals vary over a unit sphere. In general, the function $f(r)$ defines some internal distribution (such as density) of an object, and $F(k, \hat{n})$ is the projected distribution, or the profile, of the object on the plane $r \cdot \hat{n} = \text{constant}$. The radon transform is a useful tool in image reconstruction from projections, with applications in computerized axial tomography, radio astronomy, remote sensing, etc.

A refinement of the usual definition of the radon transform shows that only the transform over a hemisphere, which may consist of disjointed parts, is sufficient to reconstruct the original function. It can then be shown that the task of obtaining an exact solution of the three-dimensional wave equation from the solution in the wave zone reduces to taking the inverse of the refined radon transform of the solution in the wave zone.

From Eq. (31) it is known that in the wave zone the solution of the wave equation is, apart from a factor $1/r$, a function of only $r - ct$ or $r + ct$, representing propagation along rays confined to a cone. The field in the wave zone, therefore, defines the range of the unit vector \hat{n} and the amplitude. This information is essentially equivalent to knowing the projections in different directions. The exact field may then be reconstructed from the set of projections.

D. Example of a Bullet

We conclude Section 7 by discussing an explicit example of a bullet that is a solution of the scalar wave equation.³⁸ An example of an electromagnetic bullet is given in Ref. 38.

A bullet that is confined to a finite volume in the wave zone is given by

$$f(r, t) = H(\sigma - \theta)[H(r - a - ct) - H(r - b - ct)]/r, \quad r \rightarrow \infty, \quad (32)$$

where H is the Heaviside function; a and b , with $b > a$, denote the boundaries of the bullet along the radius; and 2σ is the vertex angle of the cone containing the bullet. Note that this solution is causal and of finite energy and has a form that is consistent with the remarks following Eq. (31). It represents a packet of energy shot through a cone whose axis coincides with the z axis.

This solution can be easily verified by letting $f = g(r, \theta, t)/r$ and noting that

$$\left(\nabla^2 - c^{-2} \frac{\partial^2}{\partial t^2}\right)f = \left(\frac{\partial^2}{\partial r^2} - c^{-2} \frac{\partial^2}{\partial t^2}\right)g + \frac{1}{r^2 \sin \theta} \frac{\partial}{\partial \theta} \left(\sin \theta \frac{\partial}{\partial \theta} \right) g.$$

Assuming that $g(r, \theta, t) = h(r - ct - r_0)Y(\theta)$, one finds that

$$\left(\nabla^2 - c^{-2} \frac{\partial^2}{\partial t^2}\right)f = \frac{h}{r^2 \sin \theta} \frac{d}{d\theta} \left(\sin \theta \frac{d}{d\theta} Y \right), \quad (33)$$

which tends to zero for all continuous $Y(\theta)$ as $r \rightarrow \infty$. For the case when $Y(\theta) = \eta(\sigma - \theta)$, we let $-dY/d\theta = \exp[-(\sigma - \theta)^2/2\Delta^2]/(2\pi)^{1/2}\Delta$, with $\Delta \rightarrow 0$. Note that as $\Delta \rightarrow 0$, $dY/d\theta \rightarrow -\delta(\sigma - \theta) = d\eta(\sigma - \theta)/d\theta$. Substituting this form into Eq. (33), we notice that, as Δ is made to approach zero, r must increase indefinitely in order for the right-hand side of Eq.

(33) to approach zero. This shows very clearly that Eq. (32) is indeed a solution in the wave zone.

The spot size may be defined by

$$r_s^2 = \int dr d\theta d\phi / r^2 \sin \theta (2r \sin \theta)^2 \left/ \int dr d\theta d\phi / r^2 \sin \theta \right. \quad (34)$$

where $2r \sin \theta$ is the width of a cone of half-angle θ . Substituting Eq. (32) into Eq. (34), one obtains

$$r_s \rightarrow [(8 - 9 \cos \sigma + \cos 3\sigma)/3(1 - \cos \sigma)]^{1/2} ct, \quad t \rightarrow \infty, \quad (35)$$

indicating a linear increase with time for the spot size, as in the case of the Gaussian pulse in Eq. (14b), although the constants of proportionality are different. We mention in passing that the solutions given by Moses and Prosser³⁶⁻³⁸ are distinguished from the other solutions reviewed here by not having an explicit dependence on the frequency or the wave number.

As mentioned in Subsection 7.C, to obtain the exact solution everywhere one has merely to evaluate the inverse radon transform of the solution in the wave zone [Eq. (32)]. Since the derivation is lengthy we shall simply quote the result. The exact solution is given by

$$f(r, t) = f_a(r, t) - f_b(r, t), \quad (36a)$$

where

$$f_a(r, t) = H(\sigma - \theta) [H[a + ct - r \cos(\theta - \sigma)] - H[a + ct - r]/r + \nu_a [H[a + ct - r \cos(\theta + \sigma)] - H[a + ct - r \cos(\theta - \sigma)]]/\pi r, \quad (36b)$$

with

$$\nu_a = \cos^{-1}[(\cos \sigma - \cos \beta_a \cos \theta)/\sin \beta_a \sin \theta], \quad 0 < \nu_a < \pi$$

and

$$\beta_a = \cos^{-1}[(a + ct)/r], \quad 0 < \beta_a < \pi/2,$$

and where $f_b(r, t)$ is identical to $f_a(r, t)$ except that a is replaced by b .

The field in Eq. (36) is identically zero for all r upstream of the bullet, i.e., for all $r < a + ct$. The wave-zone limit is obtained by taking $r, t \rightarrow \infty$. Then, since Eq. (36) corresponds to propagation in the positive cone (Fig. 6), from $r - ct = \text{constant}$, Eq. (32) is recovered. The requirement that $r - ct$ be constant is equivalent to observing the bullet in a comoving frame. Close to the origin the exact solution in Eq. (36) spreads out of the cone significantly. However, in the wave zone the solution is confined to the cone and is independent of the angle θ therein. Finally, it has been shown in Ref. 38 that the difference between the exact solution in Eq. (36) and the wave-zone solution in Eq. (32) becomes small quite rapidly as r, ct increase, with $r - ct$ held fixed.

In principle, one can now use the inverse source method to determine the sources that lead to the bullet described by Eq. (32). To our knowledge, however, this computation has yet to be performed.

8. SUMMARY AND CONCLUDING REMARKS

The motivation for much of the research reviewed here stems from the need to propagate a beam of radiation over

long distances without an appreciable decrease in the intensity. Possible applications would include power beaming, advanced radar, laser acceleration of particles, and directed energy sources. This need has led to a great deal of interest in such fundamental subjects as diffraction and new solutions of the wave equation.

It has been reiterated that the physical basis for diffraction of waves is the well-known relation $\Delta k_i \Delta x_i \approx 1$, for $i = 1, 2, 3$. By virtue of this, it is simple to determine the scale length for the diffractive spreading of a beam with an arbitrary transverse profile. Thus a knowledge of the spectrum is sufficient to permit determination of the maximum propagation distance of the beam. Since diffraction is unavoidable, by concentrating the energy in the high frequencies one can only delay the spreading of the beam.

Four examples of the research effort on the subject of beam propagation have been reviewed here. The conclusions are as follows:

(1) **Electromagnetic missiles:** Experiment indicates that a suitably tailored pulse shape can be designed to have an energy decay rate limited by the highest frequencies present in the pulse. This is fully consistent with our understanding of diffraction.

(2) **Bessel beams:** It is shown that as far as propagation is concerned Bessel beams are not resistant to the diffractive spreading commonly associated with all wave propagation. These beams propagate no farther than Gaussian beams or plane waves with the same transverse dimensions.

(3) **Electromagnetic directed-energy pulse trains:** The diffractive properties of the pulse form studied most intensively under this general heading are described by diffraction theory. These pulse trains do not defeat diffraction.

(4) **Electromagnetic bullets:** Given a radiation wave packet in the wave zone that is confined to a suitable solid angle and extends over a finite radial extent, one can determine the source required to generate the wave packet. As of this writing, however, this problem has not been solved for a practical case.

In a recent study, Godfrey examined electromagnetic missiles, Bessel beams, and electromagnetic directed-energy pulse trains. His conclusions regarding the practical utility and the diffractive properties of these are identical to ours.³⁹ Anan'ev's analysis of Bessel beams and his conclusions regarding their diffractive properties are also similar to ours.⁴⁰

APPENDIX A

The purpose of this appendix is to examine the transition from the Fresnel to the Fraunhofer region for a clipped Bessel beam and a clipped Gaussian beam within the context of the Huygens-Fresnel approximation.⁴⁶ The clipping is assumed to be caused by a finite-sized aperture.

In the case of the Bessel beam the field distribution at the aperture has the form $u(r, z=0) = J_0(k_{\perp} r)$ within a circular aperture of radius d . Making use of expression (6), we find that the amplitude at a point on the axis of symmetry is given by

$$\psi \propto z^{-1} \int_0^d dr' r' J_0(k_{\perp} r') \exp(ikr'^2/2z). \quad (A1)$$

The limit $k_{\perp} = 0$ corresponds to the case of plane waves

incident upon a circular aperture, as in Section 3. The intensity, given by expression (9), falls off monotonically for $z > Z_R$, where

$$Z_R = 2\pi d^2/\lambda. \quad (\text{A2})$$

For $k_\perp > 0$, the oscillatory behavior of the Bessel function in expression (A1) tends to phase mix the integrand, effectively reducing the upper limit of the integration. Consequently, the boundary of the Fresnel region, beyond which the radiation appears to be emitted essentially from a point source, is reached before $Z_R = 2\pi d^2/\lambda$.

Since there is no simple analytical approximation to the integral in expression (A1), consider the case of a cosine beam $u(x, y, z=0) = \cos(k_x x)\cos(k_y y)$, which is the Cartesian equivalent of a Bessel beam. The aperture is a rectangular opening in the x - y plane defined by $[(x, y), |x| < X, |y| < Y]$. In terms of

$$\xi_\pm = (k/2z)^{1/2}(X \pm k_x z/k), \quad (\text{A3})$$

the amplitude on the z axis has the form $\psi = I_z I_y$, where

$$I_z = [C(\xi_+) + iS(\xi_+) + C(\xi_-) + iS(\xi_-)]\exp(-ik_x^2 z/2k) \quad (\text{A4})$$

and

$$S(t) = (2/\pi)^{1/2} \int_0^t dt \sin t^2, \quad C(t) = (2/\pi)^{1/2} \int_0^t dt \cos t^2$$

are the Fresnel integrals.⁴³ The expression for I_y is obtained from that for I_z by making the replacements $k_x \rightarrow k_y, X \rightarrow Y$.

We are interested in the intensity well within a nominal Fresnel region defined by the width of the aperture

$$z \ll k(X^2, Y^2)/2 \quad (\text{A5})$$

but sufficiently far from the aperture so that the radiation diffracted from one edge can reach the z axis:

$$z \simeq k(X/k_x, Y/k_y). \quad (\text{A6})$$

Taking the appropriate limits of the Fresnel integrals, we find that the intensity is $I \simeq I_0/16$, where I_0 is the intensity at the diffracting aperture. This analysis indicates that expression (A6) defines the boundary of the true Fresnel region. The terms proportional to $\pm k_x z/k$ in Eq. (A3) represent propagation at an angle $\pm \sin^{-1}(k_x/k)$ to the z axis. As a consequence the drop in intensity characterizing the transition to the Fraunhofer region takes place at the location indicated by expression (A6) rather than by the right-hand side of expression (A5).

Returning to the Bessel beam with $d \gg 1/k_\perp$, we find that, in the region of significant phase mixing in the integrand of expression (A1), the Bessel function has the asymptotic form⁴³ $J_0(z) \sim (2/\pi z)^{1/2} \cos(z - \pi/4)$. Substituting this into expression (A1) and comparing the phases, we find that the Fraunhofer region for the Bessel beam commences at $Z_B \simeq 2\pi d/k_\perp \lambda$. From the definition of Z_R in Eq. (A2) we note that $Z_B/Z_R = 1/k_\perp d \ll 1$ for the experimental parameters in Ref. 26. Thus we see that a Bessel beam is not optimum as far as the diffractive falloff of the intensity is concerned.

For the Gaussian beam, substituting $u(r)\exp(-r^2/w_0^2)$ into expression (6) and performing the integral, we find that the intensity on the axis of symmetry is given by

$$I \propto \frac{1 + \exp[-2(d/w_0)^2] - 2 \exp[-(d/w_0)^2] \cos(kd^2/2z)}{1 + (z/Z_R)^2}, \quad (\text{A7})$$

where Z_R is the Rayleigh range defined in Eq. (1). For the parameters in Ref. 26, $d/w_0 \gg 1$, and the scale length for the intensity to drop to a quarter its initial value is of the order of $2Z_R$, as in expression (4c). The same scale length is roughly applicable to the case of a wider Gaussian beam with $w_0 \simeq d$. For an infinitely wide beam, $w_0 \rightarrow \infty$, and expression (A7) goes over to the case of plane waves [expression (9)].

For the off-axis intensity of the cosine beam we limit the discussion to the case for which the observation point is an integral number of half-periods off the z axis. In analogy with Eq. (A3) we define

$$\xi_\pm = (k/2z)^{1/2}[X \pm (k_x z/k - n_x \pi/k_x)],$$

$$\eta_\pm = (k/2z)^{1/2}[X \pm (k_x z/k + n_x \pi/k_x)],$$

where $n_x \pi/k_x$, with n_x an integer, is the x coordinate of the observation point. We assume that $n_x \pi/k_x < X$. In terms of these variables, the amplitude has the form $\psi = I_z I_y$, where

$$I_z = [C(\xi_+) + iS(\xi_+) + C(\xi_-) + iS(\xi_-) + C(\eta_+) + iS(\eta_+) + C(\eta_-) + iS(\eta_-)], \quad (\text{A8})$$

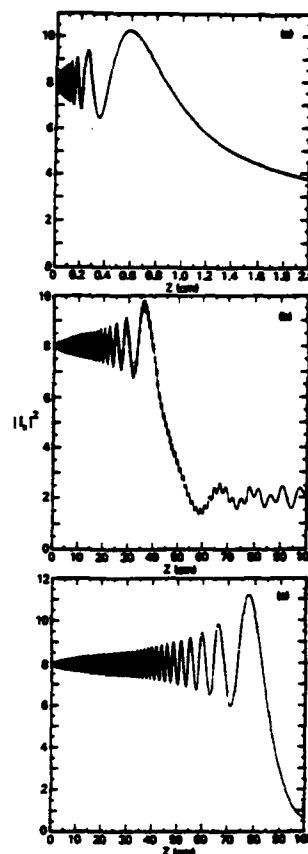


Fig. 7. Plot of $|I_z|^2$, in expression (A8), versus distance along the axis of symmetry z . Parameters are $X = 3.831$ mm, $\lambda = 6328$ Å, and $k_\perp = 41$ mm⁻¹: (a) penultimate lobe ($n_x = 49$); (b) lobe that is half-way between the z axis and the edge of the aperture ($n_x = 25$); (c) central lobe ($n_x = 0$). The Z coordinates in (a) extends to 2 cm only.

where C and S are the Fresnel integrals defined above and the expression for I_z is obtained from that for I_x by making the substitution $k_x \rightarrow k_y$, $X \rightarrow Y$, and $n_x \rightarrow n_y$.

For plane waves ($k_{x,y} \rightarrow 0$) and on the symmetry axis ($n_{x,y} \rightarrow 0$), the transition from the oscillatory to the monotonically falling behavior of the Fresnel integrals in expression (A8) takes place at $z \approx k(X^2, Y^2)/2$. This marks the boundary between the Fresnel and Fraunhofer regions. For the cosine beam and on the symmetry axis ($n_{x,y} \rightarrow 0$), expression (A8) reduces to Eq. (A4), and hence expression (A6) defines the boundary between the two regions. Away from the symmetry axis ($n_{x,y} > 0$) the behavior is somewhat more complicated. On the aperture, $z = 0$, and $\xi_{\pm}, \eta_{\pm} \rightarrow \infty$, whence $I_z = 2(1 + i)$. For z sufficiently large that $0 < \eta_- < 1$, but $\xi_+, \xi_-, \eta_+ \gg 1$, the last two terms in expression (A8) are small and $I_z \rightarrow 3(1 + i)/2$. From the definition of η_- we note that, as the observation point approaches the edge of the aperture ($n_x \pi/k_x \rightarrow X$), this reduction in the value of I_z is obtained at smaller values of z , according to the formula $z = k(X - n_x \pi/k_x)k_x$. Figure 7, which plots $|I_z|^2$ as a function of z , confirms this behavior for parameters similar to those of Ref. 26.

ACKNOWLEDGMENT

This research was supported by the U.S. Office of Naval Research, the U.S. Department of Energy, and the Defense Advanced Research Projects Agency.

* Permanent address, Science Applications International Corporation, McLean, Virginia 22102.

REFERENCES

- W. T. Welford, *Optics* (Oxford U. Press, New York, 1981), Chap. 3.
- C. J. Bouwkamp, "Diffraction theory," *Rep. Prog. Phys.* **17**, 35-100 (1954).
- A. E. Siegman, *An Introduction to Lasers and Masers* (McGraw-Hill, New York, 1971), Chap. 8.
- G. Toraldo di Francia, "Super-gain antennas and optical resolving power," *Nuovo Cimento Suppl.* **9**, 426-435 (1952).
- J. N. Brittingham, "Focus wave modes in homogeneous Maxwell's equations: transverse electric mode," *J. Appl. Phys.* **54**, 1179-1189 (1983).
- P. A. Belanger, "Packetlike solutions of the homogeneous-wave equation," *J. Opt. Soc. Am. A* **1**, 723-724 (1984).
- T. T. Wu and R. W. P. King, "Comment on 'Focus wave modes in homogeneous Maxwell's equations: transverse electric mode,'" *J. Appl. Phys.* **56**, 2587-2588 (1984).
- A. Sezginer, "A general formulation of focus wave modes," *J. Appl. Phys.* **57**, 678-683 (1985).
- T. T. Wu and H. Lehman, "Spreading of electromagnetic pulses," *J. Appl. Phys.* **58**, 2064-2065 (1985).
- P. Hillion, "More on focus wave modes in Maxwell equations," *J. Appl. Phys.* **60**, 2981-2982 (1986).
- P. Hillion, "Spinor focus wave modes," *J. Math. Phys.* **28**, 1743-1748 (1987).
- E. Heyman, B. Z. Steinberg, and L. B. Felsen, "Spectral analysis of focus wave modes," *J. Opt. Soc. Am. A* **4**, 2081-2091 (1987).
- L. B. Felsen and E. Heyman, "Discretized beam methods for focused radiation from distributed apertures," in *Microwave and Particle Beam Sources and Propagation*, N. Rostoker, ed., Proc. Soc. Photo-Opt. Instrum. Eng. **873**, 320-328 (1988).
- T. T. Wu, "Electromagnetic missiles," *J. Appl. Phys.* **57**, 2370-2373 (1985).
- H. M. Lee, "Rise and fall of directed transient: use of Mellin transformation in time domain problems," *Radio Sci.* **22**, 1102-1108 (1987).
- T. T. Wu, R. W. P. King, and H. M. Shen, "Spherical lens as a launcher of electromagnetic missiles," *J. Appl. Phys.* **62**, 4036-4040 (1987).
- T. T. Wu and H. M. Shen, "Radiation of an electromagnetic pulse from the open end of a circular waveguide," in *Microwave and Particle Beam Sources and Propagation*, N. Rostoker, ed., Proc. Soc. Photo-Opt. Instrum. Eng. **873**, 329-337 (1988).
- H. M. Shen, "Experimental study of electromagnetic missiles," in *Microwave and Particle Beam Sources and Propagation*, N. Rostoker, ed., Proc. Soc. Photo-Opt. Instrum. Eng. **873**, 338-346 (1988).
- J. M. Myers, "Pulsed radiation from a parabolic reflector," in *Microwave and Particle Beam Sources and Propagation*, N. Rostoker, ed., Proc. Soc. Photo-Opt. Instrum. Eng. **873**, 347-356 (1988).
- T. T. Wu, R. W. P. King, and H. M. Shen, "Generalized analysis of the spherical lens as a launcher of electromagnetic missiles," *J. Appl. Phys.* **63**, 5647-5653 (1988).
- T. T. Wu, R. W. P. King, and H. M. Shen, "Circular cylindrical lens as a line-source electromagnetic-missile launcher," *IEEE Trans. Antennas Propag.* **37**, 39-44 (1989).
- J. M. Myers, H. M. Shen, T. T. Wu, and H. E. Brandt, "Curved electromagnetic missiles," *J. Appl. Phys.* **65**, 2604-2610 (1989).
- H. M. Shen and T. T. Wu, "The transverse energy pattern of an electromagnetic missile from a circular current disk," in *Microwave and Particle Beam Sources and Directed Energy Concepts*, H. E. Brandt, ed., Proc. Soc. Photo-Opt. Instrum. Eng. **1061**, 352-360 (1989).
- T. T. Wu, H. M. Shen, and J. M. Myers, "A review of electromagnetic missiles," in *Microwave and Particle Beam Sources and Directed Energy Concepts*, H. E. Brandt, ed., Proc. Soc. Photo-Opt. Instrum. Eng. **1061**, 370-379 (1989).
- J. Durnin, "Exact solutions for nondiffracting beams. I. The scalar theory," *J. Opt. Soc. Am. A* **4**, 651-654 (1987).
- J. Durnin, J. J. Miceli, and J. H. Eberly, "Diffraction-free beams," *Phys. Rev. Lett.* **58**, 1499-1501 (1987).
- D. DeBeer, S. R. Hartman, and R. Friedberg, "Comment on 'Diffraction-free beams,'" *Phys. Rev. Lett.* **59**, 2611 (1987).
- J. Durnin, J. J. Miceli, and J. H. Eberly, "Comparison of Bessel and Gaussian beams," *Opt. Lett.* **13**, 79-80 (1988).
- R. W. Ziolkowski, "Exact solutions of the wave equation with complex source locations," *J. Math. Phys.* **26**, 861-863 (1985).
- R. W. Ziolkowski, "New electromagnetic directed energy pulses," in *Microwave and Particle Beam Sources and Propagation*, N. Rostoker, ed., Proc. Soc. Photo-Opt. Instrum. Eng. **873**, 312-319 (1988).
- R. W. Ziolkowski, "Localized transmission of electromagnetic energy," *Phys. Rev. A* **39**, 2005-2033 (1989).
- R. W. Ziolkowski, D. K. Lewis, and B. D. Cook, "Evidence of localized wave transmission," *Phys. Rev. Lett.* **62**, 147-150 (1989).
- R. W. Ziolkowski, "Localized transmission of wave energy," in *Microwave and Particle Beam Sources and Directed Energy Concepts*, H. E. Brandt, ed., Proc. Soc. Photo-Opt. Instrum. Eng. **1061**, 395-402 (1989).
- A. M. Shaarawi, I. M. Besieris, and R. W. Ziolkowski, "Localized energy pulse trains launched from an open, semi-infinite, circular waveguide," *J. Appl. Phys.* **65**, 805-813 (1989).
- H. E. Moses, "The time-dependent inverse source problem for the acoustic and electromagnetic equations in the one- and three-dimensional cases," *J. Math. Phys.* **25**, 1905-1923 (1985).
- H. E. Moses and R. T. Prosser, "Initial conditions, sources, and currents for prescribed time-dependent acoustic and electromagnetic fields in three dimensions. Part I: the inverse initial value problem. Acoustic and electromagnetic bullets, expanding waves, and imploding waves," *IEEE Trans. Antennas Propag.* **AP-34**, 188-196 (1986).
- H. E. Moses and R. T. Prosser, "A refinement of the radon transform and its inverse," *Proc. R. Soc. London Ser. A* **422**, 343-349 (1989); "Exact solutions of the three-dimensional scalar wave equation and Maxwell's equations from the approximate solutions in the wave zone through the use of the radon transform," *Proc. R. Soc. London Ser. A* **422**, 351-365 (1989).
- H. E. Moses and R. T. Prosser, "Acoustic and electromagnetic bullets. Derivation of new exact solutions of the acoustic and

- Maxwell's equations," SIAM J. Appl. Math. 50, 1325-1340 (1990).
39. B. B. Godfrey, "Diffraction-free microwave propagation," Sensor and Simulation Notes 320 (Weapons Laboratory, Kirtland Air Force Base, N.M., 1989).
 40. Yu. Yu. Anan'ev, "Nondiffracting light waves," Opt. Spectrosc. (USSR) 64, 722-723 (1988).
 41. R. Barakat, "Solution of the Luneberg apodization problems," J. Opt. Soc. Am. 52, 264-275 (1962).
 42. J. D. Jackson, *Classical Electrodynamics* (Wiley, New York, 1975), Chap. 9.
 43. I. S. Gradshteyn and I. M. Ryzhik, *Table of Integrals, Series, and Products* (Academic, San Diego, Calif., 1980).
 44. I. W. Kay and H. E. Moses, "The determination of the scattering potential from the spectral measure function. V. The Gelfand-Levitan equation for the three-dimensional scattering problem," Nuovo Cimento 22, 689-705 (1961).
 45. S. R. Deana, *The Radon Transform and Some of Its Applications* (Wiley, New York, 1983).
 46. W. H. Southwell, "Validity of the Fresnel approximation in the near field," J. Opt. Soc. Am. 71, 7-14 (1981).

Appendix M
Comment on Nondiffracting Beams

Comment on Nondiffracting Beams

Nondiffracting directed beams have been discussed by several authors.¹⁻⁷ Our intention is to comment on (i) the Bessel beam²⁻⁴ which has been called³ "remarkably resistant to the diffractive spreading" and (ii) the electromagnetic directed energy pulse train⁵⁻⁷ (EDEPT) which is claimed⁷ to be "significantly improved over conventional, diffraction-limited beams," and to⁵ "defeat diffraction." We find that diffraction is not reduced in either case and that conventional Gaussian beams will propagate at least as far for a given transmitting antenna dimension.

Durnin, Miceli, and Eberly³ have studied the field $\psi(r, z, t) = J_0(k_\perp r) \exp[i(k_z z - \omega t)]$, where J_0 is the Bessel function, k_\perp is the transverse wave number, ω is the frequency, and k_z is the axial wave number. Two properties of ψ are as follows: (i) The power contained in each lobe, between the adjacent zeros of J_0 , is of the same order, and (ii) J_0 is a superposition of plane waves propagating at an angle $\sim k_\perp/k_z$ to the z axis.⁸

Based on geometric optics, Durnin, Miceli, and Eberly³ found the propagation distance of the central lobe of an apertured Bessel beam of radius R to be $\sim 2Rr_0/\lambda$, where $r_0 \approx \pi/k_\perp$ is the spacing between zeros of J_0 and λ is the wavelength. They compare the propagation distance of the apertured Bessel beam with a Gaussian beam of spot size r_0 . The diffraction distance of the Gaussian beam is $Z_G \approx \pi r_0^2/\lambda$. Since $R \gg r_0$, they observed that the Bessel beam propagated $\sim (2/\pi)R/r_0$ times further than the Gaussian beam.

Our interpretation differs in a number of fundamental ways and shows that the comparison between the Bessel beam of radius R and the Gaussian beam of spot size r_0 is not appropriate. If $N \gg 1$ is the number of lobes, then $R \approx N r_0$. The diffraction length associated with the central lobe is

$$Z_B \approx R/\theta_B = 2N r_0^2/\lambda = 2R r_0/\lambda = (2/\pi) N Z_G,$$

where $\theta_B \approx k_\perp/k_z \approx \lambda/2r_0$ is the diffraction angle. The N lobes diffract away sequentially starting with the outermost one. The outermost lobe diffracts after a distance $\sim \pi r_0^2/\lambda$, the next one diffracts after a distance $2\pi r_0^2/\lambda$, and so on until the central lobe diffracts away after a distance $\sim N\pi r_0^2/\lambda \approx Z_B$. The central lobe persists as long as there are off-axis lobes to replenish its diffraction losses.

If we take a Gaussian beam having a spot size equal to the aperture R , it will propagate N times further than the apertured Bessel beam. By focusing the Gaussian beam, nearly all the power can be focused on a target of dimension r_0 in a distance Z_B . For the same power through the aperture, the focused Gaussian beam delivers $\sim N$ times more power than the Bessel beam.

Another solution to the wave equation which has been studied for its diffractive properties is the EDEPT.⁵⁻⁷ Ziolkowski, Lewis, and Cook⁶ have examined a particu-

lar pulse form both numerically and experimentally. The dominant radial profile of the modified-power-spectrum (MPS) pulse amplitude is $\exp[-br^2/\beta(z_0 + i\xi)]$, where $\xi = z - ct$, and b , β , and z_0 are constants. Ziolkowski, Lewis, and Cook use the minimum spot size, $w_0 = (\beta z_0/b)^{1/2}$, at the pulse center $\xi = 0$, to obtain the diffraction length $Z \approx \pi w_0^2/\lambda = \pi \beta z_0/b\lambda$. Their results indicate that the pulse propagates significantly further than $Z \approx \pi w_0^2/\lambda$.

In our interpretation the diffraction length is not $\sim \pi w_0^2/\lambda$, but is $Z_{MPS} = R/\theta_{MPS} \approx \pi w_0 R/\lambda$, where R is the transmitting antenna dimension and $\theta_{MPS} \approx \lambda/\pi w_0$ is the diffraction angle associated with a pulse having a typical transverse variation of $\sim w_0 < R$. As in the Bessel beam, the energy in the MPS pulse is radially spread out, typically over the full width R of the aperture. The scale length Z_{MPS} , derived here by a consistent application of diffraction theory to the MPS pulse, is fully consistent with the experimental and numerical results.^{6,7}

Utilizing the entire transmitting antenna radius R , an unfocused Gaussian beam would propagate a distance $\sim \pi R^2/\lambda$; this is greater than the MPS pulse propagation distance. A Gaussian beam can be focused to a dimension $\sim w_0$ in the distance $\sim Z_{MPS}$. Such a Gaussian beam focuses more power on the target than a corresponding MPS pulse.

This work was supported by the Office of Naval Research and the Defense Advanced Research Projects Agency.

P. Sprangle

Beam Physics Branch
Plasma Physics Division
Naval Research Laboratory
Washington, D.C. 20375-5000

B. Hafizi

Science Applications International Corporation
McLean, Virginia 22102

Received 5 March 1990

PACS numbers: 03.50.-z, 03.65.-w, 41.10.Hv, 42.10.Hc

¹See, for example, *Proceedings of the SPIE Conference on Microwave and Particle Beam Sources and Propagation, Los Angeles, 1988*, edited by N. Rostoker, SPIE Proceedings No. 873 (Society of Photo-Optical Instrumentation Engineers, Bellingham, WA, 1988).

²J. Durnin, J. Opt. Soc. Am. A 4, 651 (1987).

³J. Durnin, J. J. Miceli, Jr., and J. H. Eberly, Phys. Rev. Lett. 58, 1499 (1987).

⁴J. Durnin, J. J. Miceli, and J. H. Eberly, Opt. Lett. 13, 79 (1988).

⁵R. W. Ziolkowski, in Ref. 1, p. 312.

⁶R. W. Ziolkowski, D. K. Lewis, and B. D. Cook, Phys. Rev. Lett. 62, 147 (1989).

⁷R. W. Ziolkowski, Phys. Rev. A 39, 2005 (1989).

⁸See also D. DeBeer, S. R. Hartmann, and R. Friedberg, Phys. Rev. Lett. 59, 2611 (1987).

Durnin, Miceli, and Eberly Reply: A Bessel beam is not a Gaussian beam, and so it has a number of different properties, some of which were pointed out by us in Refs. 1-3. An *ideal* Bessel beam carries an infinite amount of energy and is totally nondiffracting, just like a plane wave, but it has a central intensity maximum (a beam spot) which a plane wave of course does not have. Experimental studies have shown that *laboratory realizations* of Bessel beams, which can be generated in several ways (see Refs. 1 and 4), retain some of the ideal beam's non-Gaussian properties.

Probably the most interesting of these properties is the relatively enormous depth of field of its central spot (i.e., the relatively great propagation distance over which the spot half-width remains constant). This distance, while great, is of course finite, but it is intrinsic to the beam, once formed, and does not depend on subsequent lenses or apertures. An example is the propagation of He-Ne laser light in the form of a Bessel beam with a 35- μm spot half-width, with less than 5- μm spreading over a propagation range of 100 cm (see Fig. 1). The least interesting of the Bessel beam's properties may be its comparative ability to carry energy onto a target, particularly if the distance to the target is accurately known in advance. Several estimates are given in Ref. 3.

Finally, with emphasis added to indicate the important element clearly, we give here the complete sentence from

Ref. 1 which has been only partially quoted in the first paragraph of Ref. 5: "We have confirmed that beams exist whose *central maxima* are remarkably resistant to the diffractive spreading commonly associated with all wave propagation."

J. Durnin and J. J. Miceli, Jr.

The Institute of Optics
University of Rochester
Rochester, New York 14627

J. H. Eberly

Department of Physics and Astronomy
University of Rochester
Rochester, New York 14627

Received 12 October 1990

PACS numbers: 03.50.-z, 03.65.-w, 41.10.Hv, 42.10.Hc

¹J. Durnin, J. J. Miceli, Jr., and J. H. Eberly, Phys. Rev. Lett. 58, 1499 (1987).

²J. Durnin, J. Opt. Soc. Am. A 4, 651 (1987).

³J. Durnin, J. J. Miceli, Jr., and J. H. Eberly, Opt. Lett. 13, 79 (1988).

⁴Y. Lin *et al.*, in Proceedings of the Joint Conference on Lasers and Electro-Optics and on Quantum Electronics (CLEO-IQEC '90) (to be published), paper CTuH55; Y. Lin, M.S. thesis, University of Rochester (unpublished).

⁵P. Sprangle and B. Hafizi, preceding Comment, Phys. Rev. Lett. 66, 837 (1991).

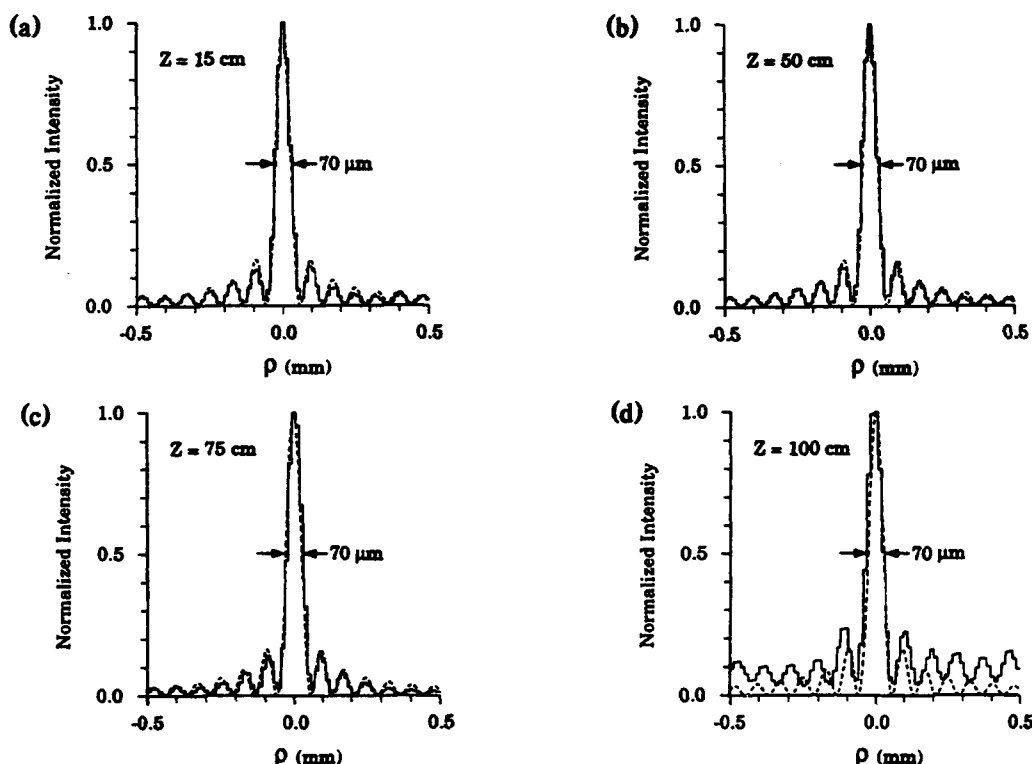


FIG. 1. Experimental data taken at 6328 Å showing the (lack of) transverse spreading of the central spot of the Bessel beam described in Ref. 2. A dashed line representing the ideal Bessel beam profile has been superimposed on a histogram of the actual beam intensity measured with a charge-coupled-device array. Even after 100 cm of propagation the central spot width is essentially unchanged, although growth of the beam wings has begun to be apparent.

Appendix N

Synchrotron-Betatron Parametric Instability in Free-Electron Lasers

Synchrotron-betatron parametric instability in free-electron lasers

B. Hafizi* and A. Ting

Beam Physics Branch, Plasma Physics Division, Naval Research Laboratory, Washington, D.C. 20375-5000

(Received 3 August 1989)

Analysis of the synchrotron-betatron coupling in a free-electron laser indicates that the particle motion is susceptible to an instability that is of a fundamentally different physical character to those examined previously. The domain of this instability, which is of a parametric type and causes an exponential growth of the betatron amplitude, is identified, and the growth rate therein determined.

I. INTRODUCTION

All electron beams have finite emittance; that is, there is a spread in the particle velocities transverse to the primary direction of motion. On traversing a wiggler, the inevitable presence of transverse gradients in the magnetic field leads to betatron oscillations of the particles. On the other hand, the beating of the wiggler and optical fields forms the ponderomotive potential wherein the particles perform synchrotron oscillations. Coupling of these two basic oscillatory degrees of freedom in a free-electron laser (FEL) may be deleterious to its efficient operation due either to detrapping out of the ponderomotive potential well or growth of betatron oscillation amplitude and emittance.

In Ref. 1 it is shown that the curvature of the optical wave fronts couples the synchrotron and betatron oscillations of the electrons and that under the proper resonance condition the amplitude of the synchrotron motion increases unstably. In subsequent work, the authors of Ref. 2 showed that a similar betatron-induced forcing of the synchrotron motion results in the case of planar optical wave fronts, provided the wiggler field is tapered.

In what follows it is shown that the particle motion is additionally susceptible to an instability that is dependent neither on the curvature of the wave fronts nor on a tapered wiggler field. The instability arises from the energy dependence of the betatron wave number. As a result, when the electrons undergo synchrotron oscillations, the betatron wave number is modulated at the synchrotron period, resulting in a parametric instability. This leads to an exponential growth of the betatron oscillation amplitude and velocity. The region of parameter space wherein this instability is operative is identified, and an analytical expression for the growth rate is obtained.

II. WIGGLER-AVERAGE EQUATIONS OF MOTION

It is assumed that the wiggler is linearly polarized, with the vector potential given by

$$A_w = A_w \cosh(k_w y) \sin(k_w z) \hat{e}_x,$$

where A_w is constant, $2\pi/k_w$ is the wiggler period, and \hat{e}_x is the unit vector along the x axis.

The optical field is assumed to be linearly polarized and

the vector potential is taken to correspond to the fundamental vacuum Gaussian mode:

$$A_s = A_s \cos \left[\frac{\omega}{c} z - \omega t + \phi \right] \hat{e}_x,$$

where ω is the angular frequency, c is the speed of light in vacuo,

$$\phi(y, z) = \omega y^2 / (2cR) - \frac{1}{2} \arctan(z/z_R) + \phi_0. \quad (1a)$$

$$R = z [1 + (z_R/z)^2] \quad (1b)$$

is the radius of curvature of the wave fronts,

$$z_R = \frac{\omega w_0^2}{2c} \quad (1c)$$

is the Rayleigh range, ϕ_0 is a constant,

$$A_s = \hat{A}_s \left[\frac{w_0}{w(z)} \right]^{1/2} \exp[-y^2/w^2(z)], \quad (1d)$$

\hat{A}_s is a constant, and $w(z)$, the spot size at z , is related to the waist w_0 at $z=0$ by

$$w(z) = w_0 [1 + (z/z_R)^2]^{1/2}. \quad (1e)$$

Following Ref. 1 the amplitude and phase of the optical field are assumed to be constant in time. This may be valid in the low-gain Compton or the trapped-particle regimes of the FEL. By writing out in detail the form of the optical field we shall be able to indicate clearly the region of applicability of the following analysis [cf. Eqs. (6) and (14)].

Following the standard procedure,³ the equations of motion in terms of the independent variable z are derivable from the Hamiltonian function $-p_z(y, p_y; z, -E; z)$, which is given by

$$p_z = \frac{E}{c} - \frac{m^2 c^3}{2E} [1 + (p_y/mc)^2 + a_x^2], \quad (2)$$

where E , the total energy of an electron of rest mass m and charge $-|e|$, is canonically conjugate to the time t , p_y is the momentum conjugate to the coordinate y , and a_x is the normalized, total vector potential:

$$a_x = a_w \cosh(k_w y) \sin(k_w z) + a_s \cos \left[\frac{\omega}{c} z - \omega t + \phi \right], \quad (3)$$

with $a_{w,s} = |e| A_{w,s} / (mc^2)$. Since the vector potential is not an explicit function of the coordinate x , the associated canonical momentum P_x is a constant. Equation (2) has been derived by choosing $P_x = 0$, and omitting terms on the order of $(mc^2/E)^{-2}$ and higher in the expansion of the Hamiltonian.

Upon squaring the expression in Eq. (3), averaging over the wiggler period, and retaining only the slowly varying contribution to the ponderomotive potential, it is found that

$$p_z = \frac{E}{c} - \frac{m^2 c^3}{2E} \left\{ 1 + (p_y/mc)^2 + \frac{1}{2} a_w^2 \cosh^2(k_w y) + a_w a_s \cosh(k_w y) \times \sin \left[\left(\frac{\omega}{c} + k_w \right) z - \omega t + \phi \right] \right\}.$$

Hamilton's equations are then given by

$$\frac{dy}{dz} = v, \quad (4a)$$

$$\frac{dv}{dz} = -k_\beta^2 \left[\frac{\sinh(2k_w y)}{2k_w} \right], \quad (4b)$$

$$\frac{d\psi}{dz} = k_w - \frac{\omega}{2\gamma^2 c} [1 + \frac{1}{2} a_w^2 \cosh^2(k_w y) + (\gamma v)^2], \quad (4c)$$

$$\frac{d\gamma}{dz} = \frac{-\omega}{2\gamma c} a_w a_s f_B \cosh(k_w y) \cos(\psi + \phi), \quad (4d)$$

where $\gamma = E/(mc^2)$, $\psi = (\omega/c + k_w)z - \omega t$, $v = p_y/(\gamma mc)$, $f_B = J_0(\xi) - J_1(\xi)$ is the usual difference of Bessel functions,⁴ $\xi = (a_w/2)^2 / (1 + a_w^2/2)$, and

$$k_\beta = \frac{a_w k_w}{\sqrt{2}\gamma} \quad (5)$$

is the betatron wave number. In arriving at Eq. (4b) it has been assumed that

$$\max \left\{ \frac{a_s}{a_w}, \frac{\gamma a_s}{1 + a_w^2/2}, \frac{a_s}{a_w (k_w w_0)^2} \right\} \ll 1, \quad (6)$$

where w_0 is the waist of the optical field, Eq. (1e). Additionally, the wave term, proportional to a_s/γ^2 , has been dropped from Eq. (4c).

III. ANALYSIS OF SYNCHROTRON-BETATRON COUPLING

Variation of the optical phase ϕ across the wave fronts underlies the instability investigated in Ref. 1. Specifically, the first term in (1a) leads to a linear increase with z of the synchrotron oscillation amplitude of deeply trapped electrons. Assuming the radius of curvature R of the wave fronts to be constant, the growth rate of this instability is proportional to y_β^2/R , where y_β is the amplitude of the betatron oscillation. In what follows it is assumed that $y_\beta^2/R \rightarrow 0$. This is the case for electrons confined to the central portion of the electron beam, or in the region where the curvature of the wave fronts is small. Assuming further that the z variation of ϕ is small on the scale length of the instability to be discussed, for a synchronous electron Eqs. (4c) and (4d) imply

$$\gamma = \hat{\gamma} = \text{const}, \quad (7a)$$

$$\hat{\psi} + \phi = (n + \frac{1}{2})\pi, \quad n = 0, \pm 1, \pm 2, \dots, \quad (7b)$$

whence, for $|k_w y| \ll 1$, Eqs. (4a) and (4b) integrate to

$$y = y_\beta \cos(\hat{k}_\beta z) + \hat{k}_\beta^{-1} v_\beta \sin(\hat{k}_\beta z), \quad (8)$$

where, from (5), $\hat{k}_\beta = a_w k_w / \sqrt{2}\hat{\gamma}$ is the betatron wave number for a synchronous electron, and y_β, v_β are constants. Upon substituting (8) into Eq. (4c) one obtains

$$\frac{1}{2} a_w^2 \cosh^2(k_w y) + (\gamma v)^2 \simeq \frac{1}{2} a_w^2 [1 + (k_w y)^2] + (\gamma v)^2 \rightarrow \frac{1}{2} a_w^2 + \hat{\gamma}^2 (\hat{k}_\beta^2 y_\beta^2 + v_\beta^2),$$

which is a constant in z , whence the synchronous energy follows from Eq. (4c) by setting $d\hat{\psi}/dz = 0$:

$$\hat{\gamma}^2 = \frac{1 + \frac{1}{2} a_w^2 [1 + (k_w y_\beta)^2]}{2ck_w/\omega - v_\beta^2}. \quad (9)$$

For an electron in the vicinity of the synchronous particle, $\gamma = \hat{\gamma} + \delta\gamma$, $\psi = \hat{\psi} + \delta\psi$, and Eqs. (4c) and (4d) imply synchrotron oscillations of $\delta\gamma$ and of $\delta\psi$. Through the γ dependence of the betatron wave number, Eq. (5), it follows from Eqs. (4a) and (4b) that under an appropriate resonance condition a parametric instability of the coupled betatron and synchrotron oscillations is then possible.

To examine this, the expression in (8) is generalized to

$$y = y_\beta(z) \cos[(\hat{k}_\beta + \epsilon)z] + (\hat{k}_\beta + \epsilon)^{-1} v_\beta(z) \sin[(\hat{k}_\beta + \epsilon)z], \quad (10)$$

where y_β and v_β are now functions of z and ϵ is a small wave-number shift to be determined. Assuming $|dy_\beta/dz| \sim \epsilon y_\beta$, $|dv_\beta/dz| \sim \epsilon v_\beta$, and omitting terms on the order of ϵ^2 , substitution of (10) into Eqs. (4a) and (4b) yields

$$(dv_\beta/dz - \epsilon \hat{k}_\beta y_\beta) \cos[(\hat{k}_\beta + \epsilon)z] - (\hat{k}_\beta dy_\beta/dz + \epsilon v_\beta) \sin[(\hat{k}_\beta + \epsilon)z] = \hat{k}_\beta^2 [y_\beta \cos[(\hat{k}_\beta + \epsilon)z] + (\hat{k}_\beta + \epsilon)^{-1} v_\beta \sin[(\hat{k}_\beta + \epsilon)z]] (\delta\gamma/\hat{\gamma}). \quad (11)$$

To obtain an expression for $\delta\gamma(z)$ to be used in Eq. (11), Eqs. (4c) and (4d) are perturbed about the synchronous values (7a) and (7b):

$$\frac{d}{dz}\delta\psi = k_w - \frac{\omega}{2c\hat{\gamma}^2} \left[1 + \frac{1}{2}a_w^2(1 + k_w^2y^2) + \hat{\gamma}^2v^2 \right] + \frac{\omega}{c\hat{\gamma}^3} \left[1 + \frac{1}{2}a_w^2(1 + k_w^2y^2) \right] \delta\gamma, \quad (12a)$$

$$\frac{d}{dz}\delta\gamma = (-1)^n \frac{\omega a_w a_s f_B}{2\hat{\gamma}c} (1 + \frac{1}{2}k_w^2y^2) \delta\psi, \quad (12b)$$

where n denotes an integer from the set defined in (7b). Substituting (10) and the forms

$$\delta\gamma = \Delta\gamma(z) \cos[2(\hat{k}_\beta + \epsilon)z + \eta], \quad (13a)$$

$$\delta\psi = \Delta\psi(z) \sin[2(\hat{k}_\beta + \epsilon)z + \eta], \quad (13b)$$

where η is a constant, into (12) and assuming that

$$k_w y_\beta \ll \hat{\gamma}^{-1/2}, \quad (14)$$

one obtains an identity whose consistency requires that $\Delta\gamma$ and $\Delta\psi$ be independent of z and that

$$2(\hat{k}_\beta + \epsilon) = \hat{k}_{\text{syn}}, \quad (15)$$

where

$$\hat{k}_{\text{syn}} = \left[\frac{\omega^2 a_w a_s f_B}{2\hat{\gamma}^4 c^2} (1 + \frac{1}{2}a_w^2) \right]^{1/2}$$

is the synchrotron wave number. In addition, it is required that the integer n in Eq. (12b) be odd. It should be noted that the constraint indicated by (14) is consistent with the neglect of the radiation field term in Eq. (4c) and the parameter restriction in (6).

Now substituting (13a) into Eq. (11) one again obtains an identity. Assuming $y_\beta, v_\beta \sim \exp(\lambda z)$, the consistency condition reduces to

$$\lambda = \pm \{ [\frac{1}{2}\hat{k}_\beta(\Delta\gamma/\hat{\gamma})\cos\eta]^2 - \epsilon^2 \}^{1/2}. \quad (16)$$

In general, the amplitude of the betatron motion of a given electron evolves as $c_+ \exp(+|\lambda|z) + c_- \exp(-|\lambda|z)$, where c_+ and c_- are constants. Clearly this leads to an

exponential growth of the betatron amplitude of the electrons (except those with $c_+ = 0$, which, however, belong to a set of measure zero).

IV. DISCUSSION

It is clear that the source of the instability discussed here lies in the energy dependence of the betatron wave number, Eq. (5). Previous studies of the synchrotron-betatron coupling have neglected this dependence. The results of Refs. 1 and 2 indicate a linear growth in the amplitude of the synchrotron motion ($\Delta\gamma, \Delta\psi$) for deeply trapped electrons. On the other hand, for the parametric instability discussed herein, $\Delta\gamma$ and $\Delta\psi$ are constants, whereas y_β and v_β grow exponentially fast. In all three cases, however, the resonance condition is essentially $\hat{k}_{\text{syn}} \simeq 2\hat{k}_\beta$.

From Eqs. (15) and (16) it follows that for a sufficiently large wave-number mismatch ϵ the growth rate vanishes. Maximum growth is obtained for $\epsilon = 0$:

$$\lambda_{\text{max}} = \frac{1}{2}\hat{k}_\beta |(\Delta\gamma/\hat{\gamma})\cosh\eta|. \quad (17)$$

It should be remarked that the growth rate in Eq. (17) depends on the laser intensity through the requirement that $2\hat{k}_\beta \simeq \hat{k}_{\text{syn}}$.

Since, at the order of approximation employed here, $\Delta\gamma$ and $\Delta\psi$ are constants, the parametric instability is expected to affect the extraction efficiency of the FEL mainly through increased electron-beam radius and particle detrapping from the ponderomotive potential, such as that described in Refs. 1 and 2, and would result once the betatron amplitude is sufficiently large. It must be remarked, however, that if the variation of the optical field amplitude or phase over the scale length indicated by (17) is large enough, then the resonance (15) may be crossed without an appreciable effect on the efficiency.^{5,6}

ACKNOWLEDGMENTS

This work was supported by the Office of Naval Research through the National Institute of Standards and Technology.

*Permanent address: Science Applications International Corp., McLean, VA 22102.

¹M. N. Rosenbluth, IEEE J. Quantum Electron. QE-21, 966 (1985).

²P. Sprangle and C. M. Tang, Phys. Fluids 28, 2019 (1985).

³N. M. Kroll, P. L. Morton, and M. N. Rosenbluth, IEEE J. Quantum Electron. QE-17, 1436 (1981).

⁴A. A. Kolomenskii and A. N. Lebedev, Kvant. Electron. 5, 1543 (1978) [Sov. J. Quantum Electron. 8, 879 (1978)].

⁵W. M. Fawley, D. Prosnitz, and E. T. Scharlemann, Phys. Rev. A 30, 2472 (1984).

⁶D. C. Quimby, Nucl. Instrum. Methods Phys. Res. A 250, 456 (1986).

Appendix O

Synchrotron-Betatron Parametric Instability in Free-Electron Lasers

SYNCHROTRON-BETATRON PARAMETRIC INSTABILITY IN FREE-ELECTRON LASERS

B. HAFIZI * and A. TING

Beam Physics Branch, Plasma Physics Division, Naval Research Laboratory, Washington, DC 20375-5000, USA

Analysis of the synchrotron-betatron coupling in a free-electron laser indicates that the particle motion is susceptible to an instability arising from the energy dependence of the betatron wave number. The domain of this instability, which is of a parametric type and causes an exponential growth of the betatron amplitude, is identified and the growth rate therein determined.

1. Introduction

Coupling of the various oscillatory degrees of freedom in a free-electron laser (FEL) may be deleterious to its efficient operation due either to detrapping out of the ponderomotive potential well or to growth of the betatron oscillation amplitude and emittance. In ref. [1] it is shown that the curvature of the optical wave fronts couples the synchrotron and betatron oscillations of the electrons and that under the proper resonance condition the amplitude of the synchrotron motion increases unstably. In subsequent work, the authors of ref. [2] showed that a similar betatron-induced forcing of the synchrotron motion results in the case of planar optical wave fronts provided the wiggler field is tapered.

Here it is shown that the particle motion is additionally susceptible to an instability which arises from the energy dependence of the betatron wave number. This leads to an exponential growth of the betatron oscillation amplitude and velocity. The region of parameter space wherein this instability is operative is identified and an analytical expression for the growth rate is obtained.

2. Wiggle-average equations of motion

It is assumed that the wiggler is linearly polarized, with the vector potential given by

$$A_w = A_w \cosh(k_w y) \sin(k_w z) e_x,$$

where A_w is constant and $2\pi/k_w$ is the wiggler period. The vector potential of the linearly polarized optical

field is taken to correspond to the fundamental vacuum Gaussian mode:

$$A_s = A_s \cos\left(\frac{\omega}{c}z - \omega t + \phi\right) e_x,$$

where ω is the angular frequency,

$$\phi(y, z) = \omega y^2 / (2cR) - \frac{1}{2} \arctan(z/z_R) + \phi_0, \quad (1a)$$

$$R = z \left[1 + (z_R/z)^2 \right] \quad (1b)$$

is the radius of curvature of the wave fronts,

$$z_R = \frac{\omega w_0^2}{2c} \quad (1c)$$

is the Rayleigh range, ϕ_0 is a constant,

$$A_s = \hat{A}_s \left[\frac{w_0}{w(z)} \right]^{1/2} \exp[-y^2/w^2(z)], \quad (1d)$$

\hat{A}_s is a constant, and $w(z)$, the spot size at z , is related to the waist w_0 at $z = 0$ by

$$w(z) = w_0 \left[1 + (z/z_R)^2 \right]^{1/2}. \quad (1e)$$

The equations of motion in terms of the independent variable z are derivable from the Hamiltonian function $-p_z(y, p_y, t, -E; z)$, which is given by [3]

$$p_z = \frac{E}{c} - \frac{m^2 c^3}{2E} \left[1 + \left(\frac{p_y}{mc} \right)^2 + a_x^2 \right], \quad (2)$$

where E is the total energy and a_x is the normalized total vector potential:

$$a_x = a_w \cosh(k_w y) \sin(k_w z) + a_s \cos\left(\frac{\omega}{c}z - \omega t + \phi\right), \quad (3)$$

with $a_{w,s} = |e| A_{w,s} / (mc^2)$.

Substituting eq. (3) into eq. (2), it is found that

$$p_z = \frac{E}{c} - \frac{m^2 c^3}{2E} \left\{ 1 + \left(\frac{p_y}{mc} \right)^2 + \frac{1}{2} a_w^2 \cosh^2(k_w y) + a_w a_s \cosh(k_w y) \times \sin\left[\left(\frac{\omega}{c} + k_w\right)z - \omega t + \phi\right] \right\}.$$

* Permanent address: Science Applications International Corp., McLean, VA, USA

Hamilton's equations are then given by

$$\frac{dy}{dz} = v, \quad (4a)$$

$$\frac{dv}{dz} = -k_B^2 \left[\frac{\sinh(2k_w y)}{2k_w} \right], \quad (4b)$$

$$\frac{d\psi}{dz} = k_w - \frac{\omega}{2\gamma^2 c} \left[1 + \frac{1}{2} a_w^2 \cosh^2(k_w y) + (\gamma v)^2 \right], \quad (4c)$$

$$\frac{d\gamma}{dz} = \frac{-\omega}{2\gamma c} a_w a_s f_B \cosh(k_w y) \cos(\psi + \phi), \quad (4d)$$

where $\gamma = E/(mc^2)$, $\psi = (\omega/c + k_w)z - \omega t$, $v = p_y/(\gamma mc)$, $f_B = J_0(\xi) - J_1(\xi)$ is the usual difference of Bessel functions [4], $\xi = (a_w/2)^2/(1 + a_w^2/2)$, and

$$k_B = \frac{a_w k_w}{\sqrt{2}\gamma} \quad (5)$$

is the betatron wave number. In arriving at eq. (4b) it has been assumed that

$$\max \left\{ \frac{a_s}{a_w}, \frac{\gamma a_s}{1 + a_w^2/2}, \frac{a_s}{a_w (k_w w_0)^2} \right\} \ll 1, \quad (6)$$

where w_0 is the waist of the optical field [eq. (1e)]. Additionally, the wave term, proportional to a_s/γ^2 , has been dropped from eq. (4c).

3. Analysis of synchrotron-betatron coupling

Variation of the optical phase ϕ across the wave fronts underlies the instability investigated in ref. [1]. Specifically, the first term in eq. (1a) leads to a linear increase with z of the synchrotron oscillation amplitude of deeply trapped electrons. Assuming the radius of curvature R of the wave fronts to be constant, the growth rate of this instability is proportional to y_B^2/R , where y_B is the amplitude of the betatron oscillation. In what follows it is assumed that $y_B^2/R \rightarrow 0$. This is the case for electrons confined to the central portion of the electron beam, or in the region where the curvature of the wave fronts is small. Assuming further that the z -variation of ϕ is small on the length scale of the instability to be discussed, for a *synchronous* electron eqs. (4c) and (4d) imply

$$\gamma = \hat{\gamma} = \text{constant}, \quad (7a)$$

$$\hat{\psi} + \phi = (n + \frac{1}{2})\pi, \quad n = 0, \pm 1, \pm 2, \dots, \quad (7b)$$

whence for $|k_w y| \ll 1$ eqs. (4a) and (4b) integrate to

$$y = y_B \cos(\hat{k}_B z) + \hat{k}_B^{-1} v_B \sin(\hat{k}_B z), \quad (8)$$

where, from eq. (5), $\hat{k}_B = a_w k_w / \sqrt{2}\hat{\gamma}$ is the betatron wave number for a synchronous electron, and y_B , v_B are constants. The synchronous energy follows from eq. (4c) by setting $d\hat{\psi}/dz = 0$:

$$\hat{\gamma}^2 = \frac{1 + \frac{1}{2} a_w^2 [1 + (k_w y_B)^2]}{2ck_w/\omega - v_B^2}. \quad (9)$$

For an electron in the vicinity of the synchronous particle, $\gamma = \hat{\gamma} + \delta\gamma$, $\psi = \hat{\psi} + \delta\psi$, and eqs. (4c) and (4d) imply synchrotron oscillations of $\delta\gamma$ and $\delta\psi$. Through the γ -dependence of the betatron wave number [eq. (5)] it follows from eqs. (4a) and (4b) that under an appropriate resonance condition a parametric instability of the coupled betatron and synchrotron oscillations is then possible.

To examine this, the expression in eq. (8) is generalized to

$$y = y_B(z) \cos[(\hat{k}_B + \epsilon)z] + (\hat{k}_B + \epsilon)^{-1} v_B(z) \sin[(\hat{k}_B + \epsilon)z],$$

where y_B and v_B are now functions of z and ϵ is a small wave-numbers shift. Assuming $|dy_B/dz| \approx \epsilon y_B$, $|dv_B/dz| \approx \epsilon v_B$, $k_w y_B \ll \hat{\gamma}^{-1/2}$, and omitting terms on the order of ϵ^2 , one finds that y_B and v_B grow like $\exp(\lambda z)$ when the following synchrotron-betatron resonance condition is satisfied:

$$2(\hat{k}_B + \epsilon) = \hat{k}_{\text{syn}}.$$

Here

$$\hat{k}_{\text{syn}} = \left[\frac{\omega^2 a_w a_s f_B}{2\hat{\gamma}^4 c^2} (1 + \frac{1}{2} a_w^2) \right]^{1/2}$$

is the synchrotron wave number, and

$$\lambda = \pm \left\{ \left[\frac{1}{2} \hat{k}_B (\Delta\gamma/\hat{\gamma}) \cos \eta \right]^2 - \epsilon^2 \right\}^{1/2},$$

is the growth rate of the instability.

4. Discussion

It is clear that the source of the instability discussed here lies in the energy dependence of the betatron wave number [Eq. (5)]. Previous studies of the synchrotron-betatron coupling have neglected this dependence. The results of refs. [1] and [2] indicate a linear growth in the amplitude of the synchrotron motion for deeply trapped electrons. On the other hand, for the parametric instability discussed here, the synchrotron motion is stable, whereas y_B and v_B grow fast exponentially. In all three cases, however, the resonance condition is essentially $\hat{k}_{\text{syn}} \approx 2\hat{k}_B$. Maximum growth is obtained for $\epsilon = 0$:

$$\lambda_{\text{max}} = \frac{1}{2} \hat{k}_B |(\Delta\gamma/\hat{\gamma}) \cos \eta|. \quad (10)$$

Since, at the order of approximation employed here, the synchrotron motion is stable, the parametric instability is expected to affect the extraction efficiency of the FEL mainly through an increased electron-beam radius, and particle detrapping from the ponderomotive potential, such as that described in refs. [1] and [2], would result once the betatron amplitude is sufficiently

large. It must be remarked, however, that if the variation of the optical-field amplitude or phase over the scale length indicated by eq. (10) is large enough, then the resonance may be crossed without an appreciable effect on the efficiency [5,6].

Acknowledgment

This work was supported by the Office of Naval Research through the National Institute of Standards and Technology.

References

- [1] M.N. Rosenbluth, *IEEE J. Quantum Electron* QE-21 (1985) 966.
- [2] P. Sprangle and C.M. Tang, *Phys. Fluids* 28 (1985) 2019.
- [3] N.M. Kroll, P.L. Morton and M.N. Rosenbluth, *IEEE J. Quantum Electron* QE-17 (1981) 1436.
- [4] A.A. Kolomenskii and A.N. Lebedev, *Kvantovaya Electron.* 5 (1978) 1543 [*Sov. J. Quantum Electron.* 8 (1978) 879].
- [5] W.M. Fawley, D. Prosnitz and E.T. Scharlemann, *Phys. Rev. A* 30 (1984) 2472.
- [6] D.C. Quimby, *Nucl. Instr. and Meth.* A250 (1986) 456.

Appendix P

Electron-Beam Quality in Free-Electron Lasers

ELECTRON-BEAM QUALITY IN FREE-ELECTRON LASERS

C.W. ROBERSON

Physics Division, Office of Naval Research, Arlington, VA 22217, USA

B. HAFIZI *

Beam Physics Branch, Plasma Physics Division, Naval Research Laboratory, Washington, DC 20375-5000, USA

The equilibrium electron-beam radius in a free-electron laser is determined by the emittance and focussing properties of the wiggler. The spot size of the radiation beam is determined by the optical guiding effects of the interaction. We have obtained a simple relationship connecting the beam emittance and the wavelength, with wiggler strength and current as parameters. Making use of the dispersion relation to define a scaled parallel thermal velocity, we then proceed to determine the limits on the velocity spreads to achieve a desired lasing wavelength.

The electron-beam quality in a free-electron laser (FEL) limits the efficiency and ultimately the wavelength at which it can be operated. Although the radiation and electron beam in the FEL are not constrained in the transverse direction by a slow-wave structure or a waveguide, the beam profiles must be closely matched to ensure an efficient interaction. The transverse emittance and wiggler focusing determine the radius of the electron beam, and the radius of the radiation beam is determined by optical guiding [1]. Here we consider the case of gain guiding in a planar wiggler. In this case, the relationship between the unnormalized electron-beam emittance ϵ and the radiation wavelength λ (for a filling factor of 1) is given by

$$\lambda = \left[\gamma v / (1 + a_w^2/2) \right]^{1/2} \epsilon, \quad (1)$$

where $v = I_b [\text{kA}] / 17\beta$ is Budker's parameter, $\gamma = 1/(1 - \beta^2)^{1/2}$, $\beta = v/c$, and $a_w = eA_w/mc^2$, A_w being the wiggler vector potential.

As is well-known, in vacuo the scale length for diffraction of a beam of waist w and wavelength λ is given by the Rayleigh range $Z_R = \pi w^2/\lambda$. Thus, for a given electron-beam emittance, higher gain and current are required to maintain a matched radiation beam at a longer wavelength, and the λ versus I_b scaling of eq. (1) is a reflection of this fact. This is to be contrasted with the classical result $\lambda = \pi\epsilon$ which is obtained by simply matching the waist of the electron and radiation beams when there is no optical focusing [2]. In fig. 1 we plot eq. (1) for two different cases, $\gamma I_b = 12 \text{ kA}$ (---) and $\gamma I_b = 60 \text{ kA}$ (....). Also shown is the nominal operating

point for the experiments at Boeing Aerospace Company (BAC).

Brightness has become a frequently used figure of merit for the electron beam in FELs. The normalized brightness is defined as [2]

$$B_n = \alpha I_b / \pi^2 \epsilon_n^2,$$

where $\epsilon_n = \beta\gamma\epsilon$ is the normalized emittance and α is a

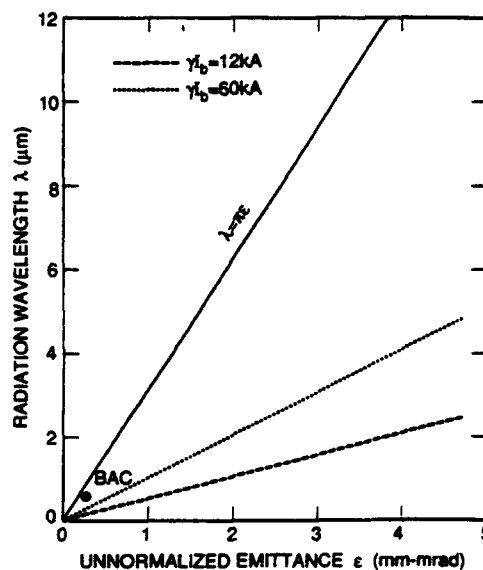


Fig. 1. Radiation wavelength versus unnormalized electron-beam emittance. The classical $\lambda = \pi\epsilon$ scaling is shown as a full line. The other lines show the scaling indicated by eq. (1). The point corresponding to the experiment at the Boeing Aerospace Company (BAC) is also shown.

* Permanent address: Science Applications Int. Corp., McLean, VA, USA.

form factor. (For a beam with a uniform ellipsoidal cross section, $\alpha = 2$.)

For a uniform circular cathode of radius r_c the thermal contribution to the emittance is $\epsilon = 2r_c(T/mc^2)^{1/2}$. For typical thermionic emitters, the average transverse energy of emitted electrons is 0.1 eV, which gives a peak brightness of (for $\alpha = 2$) $B_n = 8.2 \times 10^5 J_b / \gamma^2$, where J_b is the current density. The transverse emittance and brightness are useful parameters characterizing electron beams. Emittance filters preserve beam brightness while reducing beam emittance. However, the dynamics of the FEL is determined by the interaction of the wave with the axial component of the beam velocity. The axial energy spread in an electron beam can come from a variety of sources such as wiggler gradients, space charge and pitch-angle scattering. A useful definition of beam quality for the FEL that emphasizes the axial energy spread is

$$B_Q = J_b / \left(\frac{\delta \gamma_{\parallel}}{\gamma} \right),$$

where $\delta \gamma_{\parallel}$ is the total spread in the axial energy.

Although the beam parameters B_n , ϵ_n and B_Q are useful figures of merit for the electron beam, the FEL dispersion relation is required to obtain the scaling of the wavelength with emittance, as was done in eq. (1) for the case of gain guiding.

We have derived the dispersion relation in the high-gain Compton limit for an electron beam with a Lorentzian electron velocity distribution, and solved for the effective thermal velocity S [2]:

$$S = \left(\frac{\delta v_{\parallel}}{v_{\parallel}} \right) (4\omega^2 \gamma^3 \gamma_{\parallel}^2 / \omega_b^2 a_w^2)^{1/3}, \quad (2)$$

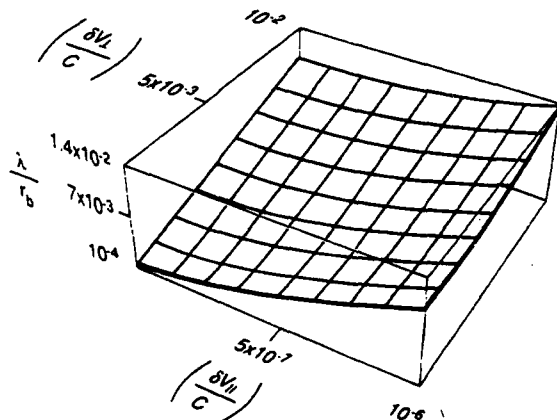


Fig. 2. Radiation wavelength versus parallel and perpendicular velocity spreads (normalized to the speed of light, c). The parameters are taken to be those of the Boeing experiment: a 170 MeV, 250 A electron beam of 1 mm radius, a 2.18 cm wiggler period and a wiggler field of 1 T.

where δv_{\parallel} is the axial velocity spread. When S approaches 1, the phase velocity of the ponderomotive wave lies within the velocity spread in the beam frame. Hence, we make the transition from the cold-beam limit, where all of the beam electrons are involved in the interaction, to the warm-beam or kinetic regime, where only a fraction of the beam particles are involved.

The scaled thermal velocity can be expressed in terms of the cold-beam efficiency η as

$$S = \gamma_{\parallel}^2 \delta v_{\parallel} / \eta v_{\parallel}.$$

We can combine eq. (1), connecting the wavelength and the emittance, with the expression for the scaled thermal velocity [Eq. (2)] to obtain an expression for the wavelength achievable for given parallel and perpendicular velocity spreads:

$$\frac{\lambda}{r_b} = \left[\frac{2\pi^2 \gamma_{\parallel}^4 \gamma^2}{S^3} \frac{1 + a_w^2/2}{a_w^2} \left(\frac{\delta v_{\parallel}}{c} \right)^3 + \frac{1}{2} \frac{\gamma^2}{1 + a_w^2/2} \left(\frac{\delta v_{\perp}}{c} \right)^2 \right]^{1/2}. \quad (3)$$

Here, if we let $S = 1$, we can find the bounding surface for transition to the kinetic regime of operation of an FEL. Note that the expression in eq. (3) has the virtue that it reduces to eq. (1) or eq. (2) in the appropriate limit.

In fig. 2 we have plotted the wavelength divided by the electron-beam radius as a function of the parallel and perpendicular velocity spreads. The parameters chosen are approximately those of the Boeing FEL: a 170 MeV, 250 A electron beam of 1 mm radius, with a wiggler period of 2.18 cm and a wiggler field of 1 T. If λ/r_b lies on the surface, then we are operating in the cold-beam regime for the parallel velocity spread and in a regime where the radiation beam spot size is matched to the electron beam for the given perpendicular velocity spread. Note that the requirement on δv_{\parallel} is about four orders of magnitude more severe than that on δv_{\perp} . This indicates a possible drawback of the technique of subharmonic bunching for operation at short wavelengths. Subharmonic bunching, which increases the peak current by axially compressing the beam, has the deleterious effect of increasing the axial velocity spread.

In conclusion, we have obtained an expression for the lasing wavelength of an optically guided FEL in the exponential-gain regime of operation. This expression, given by eq. (3), allows us to compare and evaluate the effect of the spreads in the electron distribution function in axial and perpendicular directions. Clearly, limitations on electron sources and problems in generating high-quality beams for free-electron lasers will continue to challenge accelerator scientists.

Acknowledgement

This work was supported by the Office of Naval Research.

References

- [1] B. Hafizi, P. Sprangle and A. Ting, *Phys. Rev. A* 36 (1987) 1739.
- [2] C.W. Roberson and P. Sprangle, *Phys. Fluids B* 1 (1989) 3.

Appendix 9

Efficiency Enhancement and Optical Guiding in a Tapered High-Power Finite-Pulse Free-Electron Laser

Efficiency Enhancement and Optical Guiding in a Tapered High-Power Finite-Pulse Free-Electron Laser

B. Hafizi,^(a) A. Ting, P. Sprangle, and C. M. Tang

Beam Physics Branch, Plasma Physics Division, Naval Research Laboratory, Washington, D.C. 20375-5000

(Received 13 July 1989)

We compare the radiation output from simulations of a finite-pulse high-power laser for several tapering rates. A fast taper leads to a tenfold increase in efficiency as compared to a slow taper, with little change in peak radiation intensity. The enhanced power for fast tapering rates is due to an increase in the optical-pulse cross section, brought about by a reduction in refractive guiding. This is analyzed by an envelope equation for the radiation beam. For the tapering rates leading to the highest powers, the optical pulse is virtually free of sideband modulation.

PACS numbers: 42.55.Tb, 52.75.Ms

One-dimensional free-electron-laser (FEL) theory predicts that the radiation intensity increases when the wiggler is tapered, leading to higher efficiency.¹⁻³ Thus, one would expect that a faster taper should lead to a higher output intensity and efficiency. Multidimensional results⁴ are generally reported as an increase in output power, without specifying the intensity, which is a key parameter in many applications. We have studied a high-power, finite-pulse FEL with a 3D, axisymmetric, time-dependent code. Comparison of the radiation at the wiggler exit for several tapering rates confirms the increase in power enhancement with faster tapering rates. Surprisingly, this improvement is not primarily due to an increase in the peak intensity within the pulse; rather, it is due to an increase in the radiation spot size. It turns out that the extra energy extracted from the electron beam is spread over a larger cross section due to a reduction in optical guiding.

Two causes of guiding,^{1-3,5-11} gain focusing and refractive guiding, have been distinguished based on the notion of a complex refractive index.⁸ In general, these two participate simultaneously and their combined effect on the spot size can be ascertained via the envelope equation for the radiation beam in an FEL.¹⁰ We find that refractive guiding, which dominates gain focusing, diminishes as the tapering rate is increased. As a result the wave fronts become more convex and the spot size increases.

To examine guiding, consider the FEL refractive index^{1-3,5-10}

$$\mu = 1 + (\omega_b/\omega)^2 (a_w/2|a|) \langle \exp(-i\xi)/\gamma \rangle,$$

where ω_b is the plasma frequency, and $a_w = |e|B_w/k_w mc^2$ and $a = |e|A/mc^2$ are the normalized vector potentials of the wiggler and radiation fields, with $-|e|$ the charge and m the mass of an electron with energy γmc^2 , B_w the amplitude, and $2\pi/k_w$ the period of the wiggler. The electron phase relative to the ponderomotive potential is ξ , and $\langle \dots \rangle$ denotes a beam average. The optical vector potential is represented by

$Ae^{i\omega(z/c-t)}\hat{e}_x/2 + \text{c.c.}$, where $A(x,t)$ is a slowly varying amplitude, ω is the frequency, and \hat{e}_x is the unit vector along the x axis. The real part of μ governs the refractive effect and the imaginary part describes the gain. Their combined role in the evolution of the radiation spot size $r_s(z,t)$ is expressed by the envelope equation¹⁰

$$r_s'' + K^2(z,t,r_s,|a_0|)r_s = 0,$$

$$K^2 \equiv (2c/\omega)^2 [-1 + 2C \cos \xi_r + C^2 \sin^2 \xi_r + (\omega/2c)r_s^2 C' \sin \xi_r] r_s^{-4},$$

where a_0 is the amplitude of the fundamental Gaussian mode, $C = (2I_b/17\gamma_r)Ha_w/|a_0|$, the prime symbol $\equiv \partial/\partial z + c^{-1}\partial/\partial t$, I_b is the beam current in kiloamperes, H , which is a form factor related to the transverse profile of the electron beam, is roughly a constant and close to unity herein, γ_r is the relativistic factor for a resonant electron, and ξ_r is the resonance phase approximation for $\langle \xi \rangle$. The -1 in the expression for K^2 is due to vacuum diffraction, $2C \cos \xi_r$ contributes to refractive guiding arising from the real part of μ , and the third and fourth terms, due to the imaginary part of μ , contribute to gain focusing. The relative importance of these will be discussed along with the simulation results.

The code employs the method of source-dependent expansion,¹⁰ using Gaussian Laguerre functions to evolve the optical field.¹² Betatron motion in a wiggler with parabolic pole faces is included. The initial electron distribution is a parabolic along the axial direction and in the transverse plane. The parameters for the computations, which are similar to those for the proposed rf-linac FEL experiment at the Boeing Aerospace Company, are listed in Table I.¹¹ The input power is sufficient to initially trap all the electrons. The tapering of the wiggler field, commencing at the entrance, is obtained by prescribing a constant rate of decrease of electron energy $d\gamma/dz < 0$.

For brevity, the results for only two tapering rates will be discussed. Case (a), $-d\gamma/dz = 0.1 \text{ m}^{-1}$ ($\xi_r \approx 1.8^\circ$), has a slow taper, and case (b), $-d\gamma/dz = 1.3 \text{ m}^{-1}$

TABLE 1. Parameters for a high-power, rf-linac FEL.

Energy γmc^2	175 MeV
Current I_b	450 A
Normalized edge emittance	153 mm mrad
E-beam radius	1 mm
E-beam pulse length	6.7 ps
Wiggler field B_w	6.4 kG
Wiggler period $2\pi/k_w$	4.7 cm
Wiggler length L	42 m
Radiation wavelength $2\pi c/\omega$	1 μ m
Initial spot size r_i	1.25 mm
Peak radiation input power	450 MW

($\xi_r \approx 18^\circ$), has a fast taper. Figure 1 shows the profiles of the optical pulse $|a(z, r=0)|$ and the electron pulse at the end of the wiggler for cases (a) and (b). Note that the peak intensity ($\sim |a|^2$) is about the same in both cases. The asymmetry of the optical pulse is due to the slippage of the electrons, which causes a greater amplification of the trailing side of the optical pulse as compared to the leading edge. Taking account of the finite transverse extent of the pulse, the slippage over a wiggler of length L is

$$\frac{1}{2} L [(1 + a_w^2/2)/\gamma_r^2 - (\pi c/\omega r_s)^2] \approx 1 \text{ mm},$$

where the second term is due to transverse effects. This is comparable to that observed in Fig. 1. Figure 1(a)

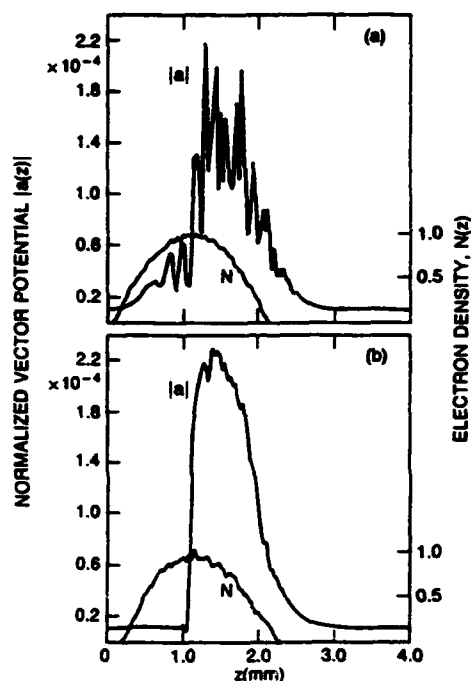


FIG. 1. Vector potential $|a(z, r=0)|$ and linear electron density $N(z)$ at wiggler exit. (a) Slow tapering rate, resonance phase $\xi_r \approx 1.8^\circ$ [case (a)]; (b) rapid tapering rate, resonance phase $\xi_r \approx 18^\circ$ [case (b)]. Note that intensity $\propto |a|^2$.

also illustrates the growth of sideband modulations from the leading to the trailing edge of the optical pulse. Note the sharp reduction in the modulation of the pulse in the more rapidly tapered case (b), Fig. 1(b), as in a recent experiment.¹³

Figure 2 shows the radiation spot size $r_s(z)$ (solid line) and wave-front curvature $\alpha(z)$ (dashed line), with $\alpha(z)$ normalized to $\omega r_s^2/2c$. Note that in the region where the field amplitude is significant the spot size is much smaller than in the surrounding regions where $\alpha \approx 0$, and r_s and α evolve as in *vacuum*. Note further that for case (a), shown in Fig. 2(a), $\alpha \approx 0$ within pulse, indicating roughly planar wave fronts. On the other hand, for case (b), shown in Fig. 2(b), $\alpha > 0$, indicating that the wave fronts are convex everywhere.

Figures 3 and 4 show the real and imaginary parts of $\mu(z)$ at the end of the wiggler. Comparing Figs. 3(a) and 3(b) it is apparent that $\text{Re}\mu$ is significantly larger in the former, case (a). On the other hand, noting that $\text{Im}\mu < 0$ corresponds to gain, Fig. 4(a) indicates that the net gain is approximately zero after averaging over the synchrotron modulations, whereas the more rapidly tapered case (b) of Fig. 4(b) is seen to have a net gain in the region where the optical field is significant.

The implication of these results with regard to the spot size may be ascertained by a consideration of the terms in K^2 in the envelope equation. Taking account of the fraction of trapped electrons, one finds that in going from case (a) to case (b) the gain-focusing term

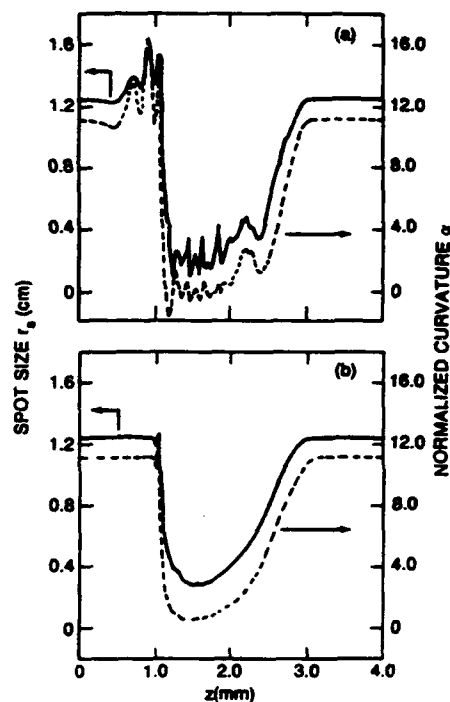


FIG. 2. Spot size $r_s(z)$ and normalized curvature $\alpha(z)$ at wiggler exit. (a) Slow taper [case (a)]; (b) rapid taper [case (b)].

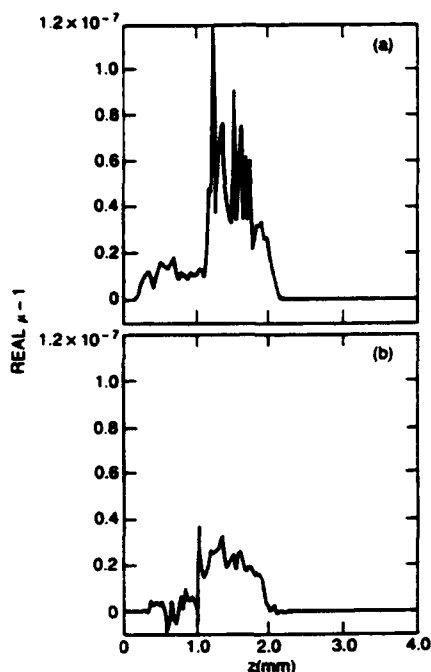


FIG. 3. Real $\mu(z, r=0)$ part of refractive index at wiggler exit. (a) Slow taper [case (a)]; (b) rapid taper [case (b)].

$C^2 \sin^2 \xi_r$ increases from 2.4×10^{-3} to 7×10^{-2} . The other term, $(\omega/2c)r_z^2 C' \sin \xi_r$, changes from -4.4×10^{-3} to -2.4×10^{-2} , the negative sign indicating a defocusing contribution. On the other hand, the refractive-guiding

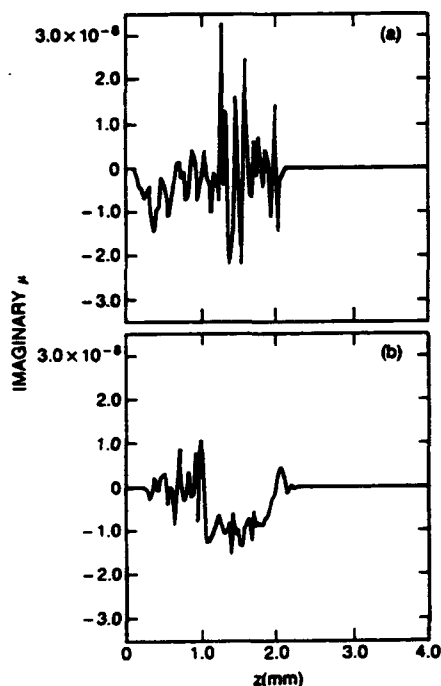


FIG. 4. Imaginary $\mu(z, r=0)$ part of refractive index at wiggler exit. (a) Slow taper [case (a)]; (b) rapid taper [case (b)].

term $2C \cos \xi_r$ decreases from 3.1 to 1.6. The increase in the magnitude of the gain-focusing terms in going from case (a) to case (b) is principally due to the increase in ξ_r . Concurrently, the 50% reduction in the refractive-guiding term is due to the increase in $|a_0|$ and the decrease in a_w . Since the refractive-guiding term is the dominant term, the reduction in its value leads to a decrease in K^2 , and hence to reduced optical guiding. The net effect is the increase in the spot size and the curvature observed in Fig. 2(b) as compared to Fig. 2(a). In other words, the wave fronts become increasingly convex with faster tapering rate.

Figure 5 summarizes the results for the nine tapering rates $-d\gamma_r/dz = 0.1, 0.3, \dots, 1.7 \text{ m}^{-1}$, corresponding to $\xi_r \approx 1.8^\circ, 3.5^\circ, \dots, 35^\circ$. Beyond $-d\gamma_r/dz = 0.3 \text{ m}^{-1}$, the amplitude $|a|$ is fairly constant up to $-d\gamma_r/dz = 1.3 \text{ m}^{-1}$, after which it decreases. However, there is a near-monotonic increase in the spot size. Therefore, it is the increased transverse extent of the optical field—and not an increase in intensity—that is responsible for the enhancement in the power ($\propto |r, a|^2$) observed in Fig. 5. Based on the desired output power and the constraint on the maximum spot size one can determine the optimal

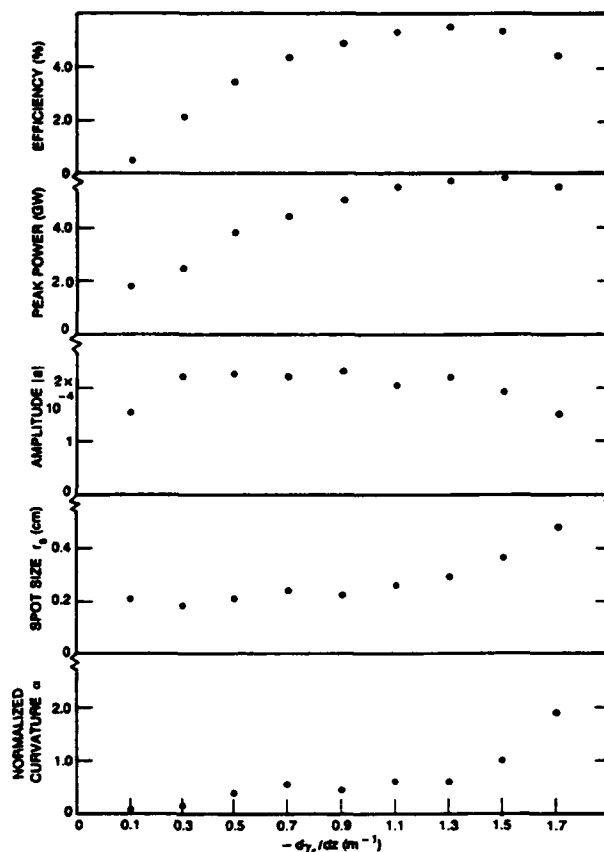


FIG. 5. Summary of results for various tapering rates $-d\gamma_r/dz$. Efficiencies are obtained from total energy in optical field. For other quantities, ordinate values correspond to peak-power point along the pulse, which varies somewhat between the different tapering rates.

tapering from Fig. 5.

Returning to Fig. 1, the period of the sideband modulation in Fig. 1 is within 10% of that given by theory.^{14,15} Tapering reduces sideband modulation by decreasing the trapping fraction and by distorting the synchrotron motion.^{12,16} The trapping fraction drops from ~40% in case (a) to ~35% in case (b). A measure of the distortion of electron orbits is given by¹² $R = |c(dy_r/dz) / (\Omega(\gamma - \gamma_r))|$ which is the ratio of the change in energy $c dy_r/dz$ due to tapering and the change in energy $(\Omega(\gamma - \gamma_r))$ due to synchrotron motion, where $\Omega = ck_\omega \times [2a_w |a| / (1 + a_w^2)]^{1/2}$ is the synchrotron frequency. For case (a), $R \approx 1\%$, indicating a slight distortion, whereas for case (b), $R \approx 25\%$, indicating significant modification of the synchrotron motion and thus, reduced sideband modulation, as is indeed observed in Fig. 1(b).

In summary, we find that tapering does not significantly affect the peak intensity in an FEL. Power enhancement is accomplished by spreading the radiation into a larger cross section due to reduced refractive guiding. It should be remarked that tapering can lead to an increase in the intensity if the spot size is held constant. From the envelope equation it can be shown that this may be achieved by suitable "tapering" of the electron-beam radius. For a tapered FEL with the parameters herein, distortion of electron orbits due to tapering is observed to be a significant cause for the reduction in sideband amplitude.

The authors are grateful to Dr. T. F. Godlove, Dr. I. Haber, Dr. W. P. Marable, and Dr. C. W. Roberson for valuable suggestions. This work was supported by ONR through the National Institute of Standards and Technology.

^(a)Permanent address: Science Applications Intl. Corp., McLean, VA 22101.

¹P. Sprangle, C. M. Tang, and W. M. Manheimer, Phys. Rev. Lett. 43, 1932 (1979); Phys. Rev. A 21, 302 (1980).

²N. M. Kroll, P. L. Morton, and M. N. Rosenbluth, IEEE J. Quantum Electron. 21, 1436 (1981).

³D. Prosnitz, A. Szoke, and V. R. Neil, Phys. Rev. A 24, 1436 (1981).

⁴E. T. Scharlemann, J. Appl. Phys. 58, 2774 (1985); R. A. Jong, E. T. Scharlemann, and W. M. Fawcett, Nucl. Instrum. Methods Phys. Res., Sect. A 272, 99 (1988); J. E. La Sala, D. A. G. Deacon, and J. M. J. Madey, Nucl. Instrum. Methods Phys. Res., Sect. A 272, 141 (1988); C. W. Roberson and P. Sprangle, Phys. Fluids B 1, 3 (1989).

⁵P. Sprangle and C. M. Tang, Appl. Phys. Lett. 39, 677 (1981).

⁶J. M. Slater and D. D. Lowenthal, J. Appl. Phys. 52, 44 (1981).

⁷G. T. Moore, Opt. Commun. 52, 46 (1984).

⁸E. T. Scharlemann, A. M. Sessler, and J. S. Wurtele, Nucl. Instrum. Methods Phys. Res., Sect. A 239, 29 (1985); Phys. Rev. Lett. 54, 1925 (1985).

⁹M. Xie and D. A. G. Deacon, Nucl. Instrum. Methods Phys. Res., Sect. A 250, 426 (1986).

¹⁰P. Sprangle, A. Ting, and C. M. Tang, Phys. Rev. Lett. 59, 202 (1987); Phys. Rev. A 36, 2773 (1987).

¹¹C. M. Tang, P. Sprangle, A. Ting, and B. Hafizi, J. Appl. Phys. 66, 1549 (1989).

¹²B. Hafizi, A. Ting, P. Sprangle, and C. M. Tang, Phys. Rev. A 38, 197 (1988).

¹³A. Bhattacharjee, S. Y. Cai, S. P. Chang, J. W. Dodd, and T. C. Marshall, in Proceedings of the Tenth International Free-Electron Laser Conference, Jerusalem, Israel, 29 August-2 September 1988 (to be published).

¹⁴J. C. Goldstein and W. B. Colson, in Proceedings of the International Conference on Lasers, New Orleans, LA, 1982, edited by R. C. Powell (STS, McLean, VA, 1983), p. 218; J. C. Goldstein, B. E. Newman, R. W. Warren, and R. L. Sheffield, Nucl. Instrum. Methods Phys. Res., Sect. A 250, 4 (1986).

¹⁵R. C. Davidson and S. Wurtele, Phys. Fluids 30, 557 (1987).

¹⁶W. B. Colson, Nucl. Instrum. Methods Phys. Res., Sect. A 250, 168 (1986).

Appendix R

Effect of Tapering on Optical Guiding and Sideband Growth in a Finite-Pulse Free-Electron Laser

EFFECT OF TAPERING ON OPTICAL GUIDING AND SIDEBAND GROWTH IN A FINITE-PULSE FREE-ELECTRON LASER

B. HAFIZI *, A. TING, P. SPRANGLE and C.M. TANG

Beam Physics Branch, Plasma Physics Division, Naval Research Laboratory, Washington, DC 20375-5000, USA

The radiation outputs from a finite-pulse high-power laser for several tapering rates are compared. Simulations reveal that fast tapering leads to increased efficiency as compared to slow tapering, but with little change in the peak radiation intensity. Increasing the tapering rate reduces refractive guiding and increases the spot size of the optical field. The enhanced power for fast tapering rates is due to the increase in the optical pulse cross section, rather than an increase in the amplitude. This is analyzed by an envelope equation for the radiation beam. Reduced sideband modulation due to distortion of the synchrotron motion by the tapering is also observed.

1. Introduction

One-dimensional free-electron laser (FEL) theory predicts that the radiation intensity increases when the wiggler is tapered, leading to higher efficiency [1-3]. Thus, one would expect that a faster taper should lead to a higher output intensity and efficiency. Multidimensional results [4] are generally reported as an increase in output power, without specifying the intensity, which is a key parameter in many applications. We have studied a high-power, finite-pulse FEL with a 3D, axisymmetric, time-dependent code. Comparison of the radiation at the wiggler exit for several tapering rates confirms the increase in power enhancement with faster tapering rates. Surprisingly, this improvement is not primarily due to an increase in the peak intensity within the pulse; rather, it is due to an increase in the radiation spot size. It turns out that the extra energy extracted from the electron beam is spread over a larger cross section due to a reduction in optical guiding [5].

Two causes of guiding [1-3,6-12], gain focusing and refractive guiding, have been distinguished based on the notion of a complex refractive index [9]. In general these two participate simultaneously and their combined effect on the spot size can only be ascertained via the envelope equation for the radiation beam in an FEL [11]. We find that refractive guiding, which dominates gain focusing, diminishes as the tapering rate is increased. As a result the wave fronts become more convex and the spot size increases.

2. Radiation envelope equation

To examine guiding, consider the FEL refractive index [1-3,6-12]

$$\mu = 1 + (\omega_b/\omega)^2 (a_w/2|a|) \langle \exp(-i\xi)/\gamma \rangle, \quad (1)$$

where ω_b is the plasma frequency, and $a_w = |e|B_w/k_w mc^2$ and $a = |e|A/mc^2$ are the normalized vector potentials of the wiggler and radiation fields, with $-|e|$ the charge and m the mass of an electron with energy γmc^2 , B_w the amplitude and $2\pi/k_w$ the period of the wiggler. The electron phase relative to the ponderomotive potential is ξ , and $\langle \dots \rangle$ denotes a beam-average. The optical vector potential is represented by $A \exp[i\omega(z/c - t)] \hat{e}_x/2 + c.c.$, where $A(r, t)$ is a slowly varying amplitude, ω the frequency and \hat{e}_x the unit vector along the x -axis. The real part of μ governs the refractive effect and the imaginary part describes the gain. Their combined role in the evolution of the radiation spot size $r_s(z, t)$ is expressed by the envelope equation [11]

$$r_s'' + K^2(z, t, r_s, |a_0|) r_s = 0, \quad (2)$$

$$K^2 = \left(\frac{2c}{\omega} \right)^2 \left[-1 + 2C \cos \xi_r + C^2 \sin^2 \xi_r \right. \\ \left. + \frac{\omega}{2c} r_s^2 C' \sin \xi_r \right] r_s^{-4},$$

where a_0 is the amplitude of the fundamental Gaussian mode, $C = (2I_b/17\gamma_r) H a_w / |a_0|$, $' \equiv \partial/\partial z + c^{-1} \partial/\partial t$, I_b is the beam current in kA, H , which is a form-factor related to the transverse profile of the electron beam, is roughly a constant and close to unity herein, γ_r is the relativistic factor for a resonant electron, and ξ_r is the resonance phase approximation for $\langle \xi \rangle$. The -1 in the expression for K^2 is due to vacuum diffraction,

* Permanent address: Science Applications Int. Corp., McLean, VA, USA.

$2C \cos \xi_r$ contributes to refractive guiding arising from the real part of μ , the third and the fourth terms, due to the imaginary part of μ , contribute to gain focusing. The relative importance of these will be discussed along with the simulation results in the following section.

3. Results and discussion

The code employs the method of source-dependent expansion [11], using Gaussian-Laguerre functions to evolve the optical field [13]. Betatron motion in a wiggler with parabolic pole faces is included. The initial electron distribution is parabolic along the axial direction and in the transverse plane. The parameters for the computations, appropriate for an FEL amplifier based on an rf linac [14], are listed in table 1. The input power is sufficient to initially trap all the electrons. The tapering of the wiggler field, commencing at the entrance, is obtained by prescribing a constant rate of decrease of electron energy, $d\gamma_r/dz < 0$.

For brevity, the results for only two tapering rates will be discussed. Case (a), $-d\gamma_r/dz = 0.1 \text{ m}^{-1}$ ($\xi_r = 1.8^\circ$), has a slow taper, and case (b), $-d\gamma_r/dz = 1.3 \text{ m}^{-1}$ ($\xi_r = 18^\circ$), has a fast taper. Fig. 1 shows the profiles of the optical pulse $|a(z, r=0)|$ and the electron pulse at the end of the wiggler for cases (a) and (b). Note that the peak intensity ($\propto |a|^2$) is about the same in both cases. The asymmetry of the optical pulse is due to the slippage of the electrons, which causes a greater amplification of the trailing side of the optical pulse as compared to the leading edge. Fig. 2 shows the longitudinal profiles of the power in the radiation pulse for cases (a) and (b). Note the clearly enhanced power in the rapidly tapered case (b). Taking account of the finite transverse extent of the pulse, the slippage over a wiggler of length L is $L[(1 + a_w^2/2)/\gamma_r^2 - (\pi c/\omega r_s)^2]/2 = 1 \text{ mm}$, where the second term is due to transverse effects. This is comparable to that observed in fig. 1. Fig. 1a also illustrates the growth of sideband modulations from the leading to the trailing edge of the

Table 1
Parameters for a high-power, rf-linac FEL

Energy γmc^2	175 MeV
Current I_0	450 A
Normalized edge emittance	153 mm mrad
E-beam radius	1 mm
E-beam pulse length	6.7 ps
Wiggler field B_w	6.4 kG
Wiggler period $2\pi/k_w$	4.7 cm
Wiggler length L	42 m
Radiation wavelength $2\pi c/\omega$	1 μm
Initial spot size r_s	1.25 mm
Peak radiation input power	450 MW

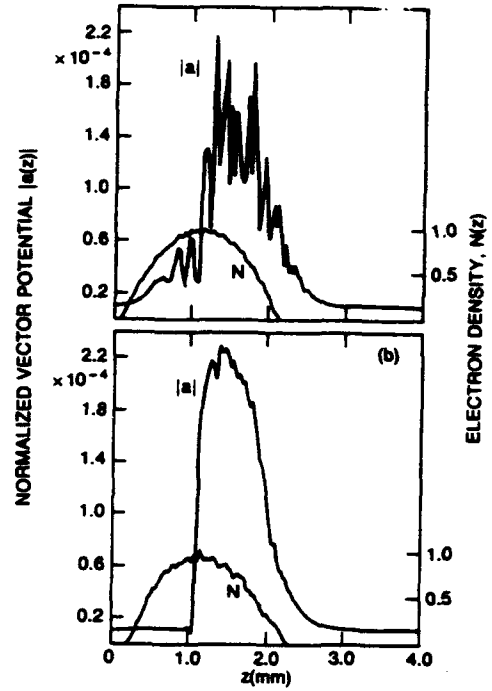


Fig. 1. Vector potential $|a(z, r=0)|$ and linear electron density $N(z)$ at wiggler exit. (a) Slow tapering rate, resonance phase $\xi_r = 1.8^\circ$, case (a); (b) rapid tapering rate, resonance phase $\xi_r = 18^\circ$, case (b). Note that intensity $\propto |a|^2$.

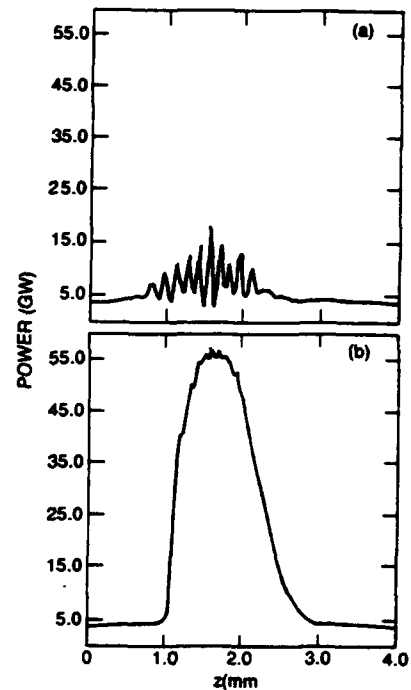


Fig. 2. Radiation power in GW at wiggler exit. (a) Slow taper, case (a); (b) rapid taper, case (b).

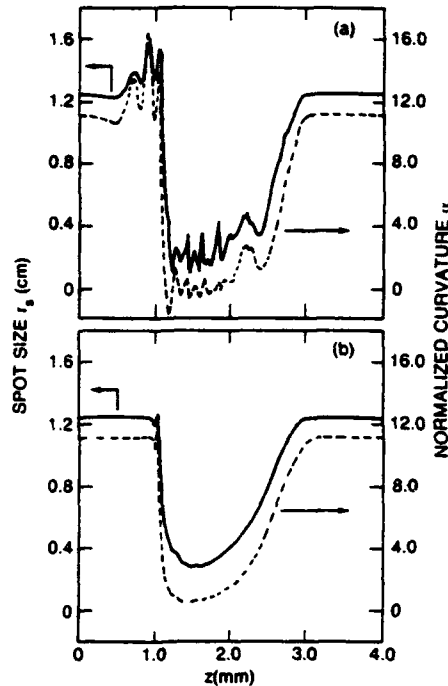


Fig. 3. Spot size $r_s(z)$ and normalized curvature $\alpha(z)$ at wiggler exit. (a) Slow taper, case (a); (b) rapid taper, case (b).

optical pulse. Note the sharp reduction in the modulation of the pulse in the more rapidly tapered case (b), as in a recent experiment [15].

Fig. 3 shows the radiation spot size $r_s(z)$ (solid line) and wave-front curvature $\alpha(z)$ (dashed line), with $\alpha(z)$ normalized to $\omega r_s^2/2c$. Note that in the region where the field amplitude is significant the spot size is much smaller than in the surrounding regions where $\alpha \approx 0$, and r_s and α evolve as in *vacuum*. Note further that for case (a), shown in fig. 3a, $\alpha \approx 0$ within the pulse, indicating roughly planar wave fronts. On the other hand, for case (b), shown in fig. 3b, $\alpha > 0$, indicating that the wave fronts are convex everywhere.

Figs. 4 and 5 show the real and the imaginary parts of $\mu(z)$ at the end of the wiggler. Comparing figs. 4a and 4b it is apparent that $\text{Re } \mu$ is significantly larger in the former, case (a). On the other hand, noting that $\text{Im } \mu < 0$ corresponds to gain, fig. 5a indicates that the net gain is approximately zero after averaging over the synchrotron modulations, whereas the more rapidly tapered case (b) of fig. 5b is seen to have a net gain in the region where the optical field is significant.

The implication of these results with regard to the spot size may be ascertained by a consideration of the terms in K^2 in the envelope equation, eq. (2). Taking account of the fraction of trapped electrons, one finds that in going from case (a) to case (b) the gain-focusing term $C^2 \sin^2 \xi$, increases from 2.4×10^{-3} to 7×10^{-2} .

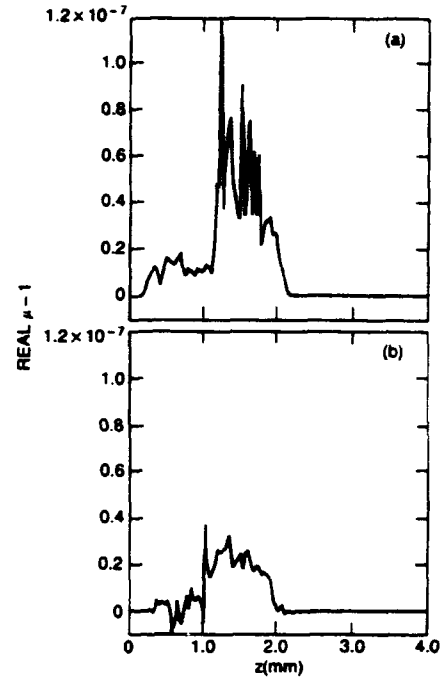


Fig. 4. Real part of refractive index $\mu(z, r=0)$ at wiggler exit. (a) Slow taper, case (a); (b) Rapid taper, case (b).

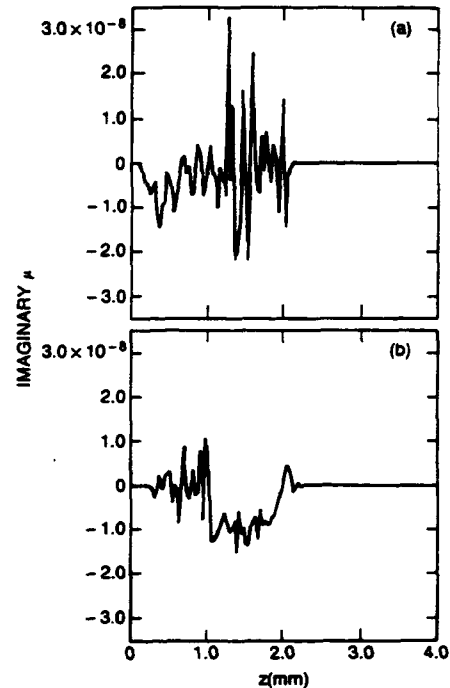


Fig. 5. $\mu(z, r=0)$ part of refractive index imaginary at wiggler exit. (a) Slow taper, case (a); (b) rapid taper, case (b).

The other term, $(\omega/2c)r_p^2 C' \sin \xi_r$, changes from -4.4×10^{-3} to -2.4×10^{-2} , the negative sign indicating a defocusing contribution. On the other hand, the refractive guiding term $2C \cos \xi_r$ decreases from 3.1 to 1.6. The increase in the magnitude of the gain focusing terms in going from case (a) to case (b) is principally due to the increase in ξ_r . Concurrently, the 50% reduction in the refractive guiding term is due to the increase in $|a_0|$ and the decrease in a_w . Since the refractive guiding term is the dominant term, the reduction in its value leads to a decrease in K^2 , and hence to reduced

optical guiding. The net effect is the increase in the spot size and the curvature observed in fig. 3b as compared to fig. 3a. In other words, the wave fronts become increasingly convex with faster tapering rate.

Fig. 6 summarizes the results for the nine tapering rates $-d\gamma_r/dz = 0.1, 0.3, \dots, 1.7 \text{ m}^{-1}$, corresponding to $\xi_r = 1.8^\circ, 3.5^\circ, \dots, 35^\circ$. Beyond $-d\gamma_r/dz = 0.3 \text{ m}^{-1}$, the amplitude $|a|$ is fairly constant up to $-d\gamma_r/dz = 1.3 \text{ m}^{-1}$, after which it decreases. However, there is a near-monotonic increase in the spot size. Therefore, it is the increased transverse extent of the optical field -

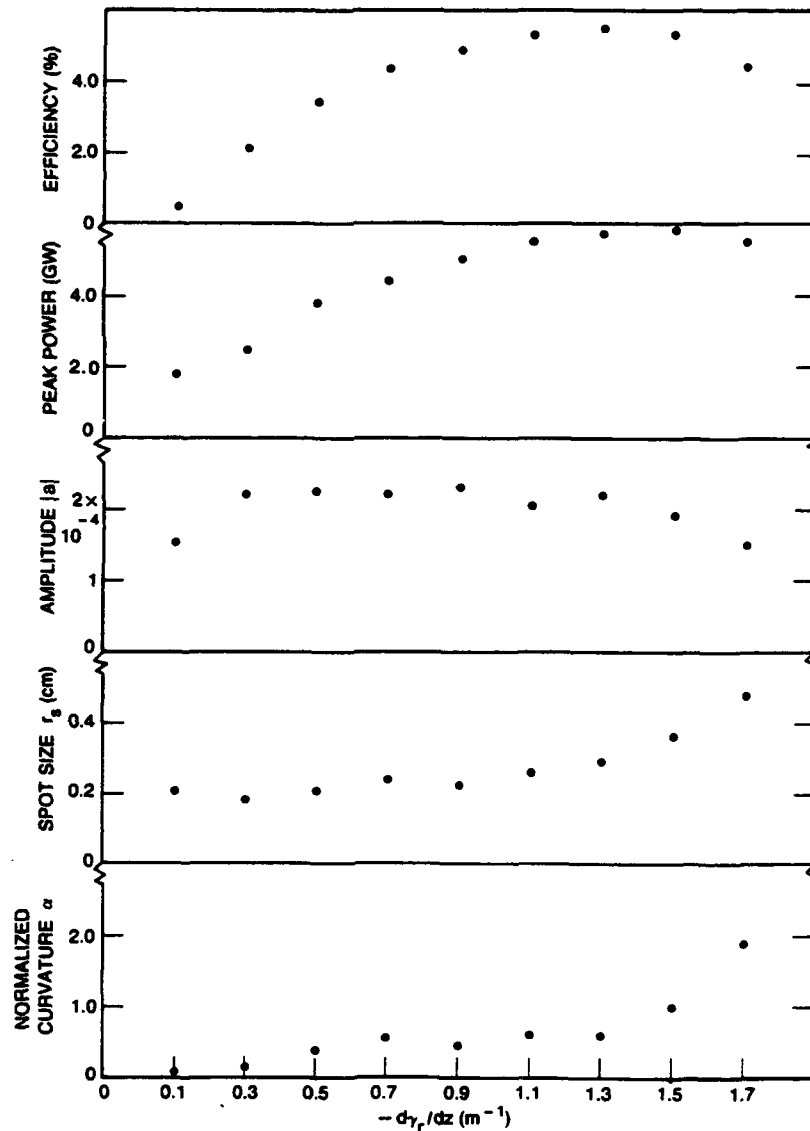


Fig. 6. Summary of results for various tapering rates $-d\gamma_r/dz$. Efficiencies are obtained from total energy in optical field. For other quantities, ordinate values correspond to peak-power point along the pulse, which varies somewhat between the different tapering rates.

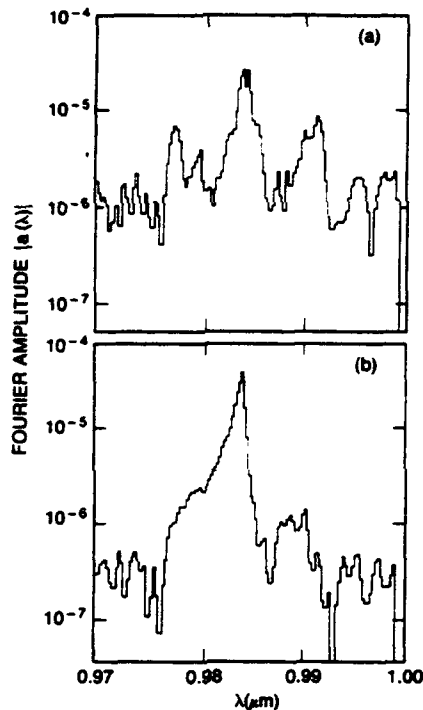


Fig. 7. Fourier spectrum of radiation amplitude $|a(\lambda)|$ at wiggler exit. (a) Slow taper, case (a); (b) rapid taper, case (b).

and not an increase in intensity – that is responsible for the enhancement in the power ($\approx |r_s a|^2$) observed in fig. 6. Based on the desired output power and the constraint on the maximum spot size one can determine the optimal tapering from fig. 6.

Returning to figs. 1 and 2, sideband modulation is seen to be sharply reduced. This is also shown in fig. 7 where the Fourier spectra of the radiation amplitude $|a(\lambda)|$ are plotted for cases (a) and (b). The wavelength of the sideband radiation is within 10% of that given by theory [16,17]. Tapering reduces sideband modulation by decreasing the trapping fraction and by distorting the synchrotron motion [13,18]. The trapping fraction drops from $\sim 40\%$ in case (a) to $\sim 35\%$ in case (b). A measure of the distortion of electron orbits is given by [13] $R \equiv |c(d\gamma_r/dz)/\langle\Omega(\gamma - \gamma_r)\rangle|$ which is the ratio of the change in energy $cd\gamma_r/dz$ due to tapering and the change in energy $\langle\Omega(\gamma - \gamma_r)\rangle$ due to synchrotron motion, where $\Omega = ck_w[2a_w|a|/(1 + a_w^2)]^{1/2}$ is the synchrotron frequency. For case (a), $R = 1\%$, indicating a slight distortion, whereas for case (b), $R = 25\%$, indicating significant modification of the synchrotron motion and thus reduced sideband modulation as is indeed observed in figs. 1b and 2b.

4. Conclusions

We find that tapering does not significantly affect the peak intensity in an FEL. Power enhancement is accomplished by spreading the radiation into a larger cross section due to reduced refractive guiding. It should be remarked that tapering can lead to an increase in the intensity if the spot size is held constant. From the envelope equation it can be shown that this may be achieved by suitable “tapering” of the electron beam radius. For a tapered FEL with the parameters herein, distortion of electron orbits due to tapering is observed to be a significant cause for the reduction in sideband amplitude.

Acknowledgements

The authors are grateful to Drs. T.F. Godlove, I. Haber, W.P. Marable and C.W. Roberson for valuable suggestions. This work was supported by ONR through the National Institute of Standards and Technology.

References

- [1] P. Sprangle, C.M. Tang and W.M. Manheimer, *Phys. Rev. Lett.* 43 (1979) 1932; *Phys. Rev. A* 21 (1980) 302.
- [2] N.M. Kroll, P.L. Morton and M.N. Rosenbluth, *IEEE J. Quantum Electron* QE-21 (1981) 1436.
- [3] D. Prosnitz, A. Szoke and V.R. Neil, *Phys. Rev. A* 24 (1981) 1436.
- [4] E.T. Scharlemann, *J. Appl. Phys.* 58 (1985) 2154; R.A. Jong, E.T. Scharlemann and W.M. Fawley, *Nucl. Instr. and Meth.* A272 (1988) 99; J.E. La Sala, D.A.G. Deacon and J.M.J. Madey, *Nucl. Instr. and Meth.* A272 (1988) 141; C.W. Roberson and P. Sprangle, *Phys. Fluids* B1 (1989) 3.
- [5] B. Hafizi, A. Ting, P. Sprangle and C.M. Tang, *Proc. 1989 IEEE Particle Accelerator Conf., Chicago, IL, IEEE Catalog no. 89CH-2669* (1989) p. 1234; B. Hafizi, A. Ting, P. Sprangle and C.M. Tang, *Phys. Rev. Lett.* 64 (1990) 180.
- [6] P. Sprangle and C.M. Tang, *Appl. Phys. Lett.* 39 (1981) 677.
- [7] J.M. Slater and D.D. Lowenthal, *J. Appl. Phys.* 52 (1981) 44.
- [8] G.T. Moore, *Opt. Commun.* 52 (1984) 46.
- [9] E.T. Scharlemann, A.M. Sessler and J.S. Wurtele, *Nucl. Instr. and Meth.* A239 (1985) 29; *Phys. Rev. Lett.* 54 (1985) 1925.
- [10] M. Xie and D.A.G. Deacon, *Nucl. Instr. and Meth.* A250 (1986) 426.
- [11] P. Sprangle, A. Ting and C.M. Tang, *Phys. Rev. Lett.* 59 (1987) 202; *Phys. Rev. A* 36 (1987) 2773.
- [12] P. Sprangle, A. Ting, B. Hafizi and C.M. Tang, *Nucl. Instr. and Meth.* A272 (1988) 536.
- [13] B. Hafizi, A. Ting, P. Sprangle and C.M. Tang, *Phys. Rev. A* 38 (1988) 197.

- [14] C.M. Tang, D. Sprangle, A. Ting and B. Hafizi, *J. Appl. Phys.* 66 (1989) 1549.
- [15] A. Bhattacharjee, S.Y. Cai, S.P. Chang, J.W. Dodd and T.C. Marshall, *Nucl. Instr. and Meth.* A285 (1989) 158.
- [16] J.C. Goldstein and W.B. Colson, *Proc. Int. Conf. on Lasers '82*, New Orleans, LA, 1982, ed. R.C. Powell (STS, McLean, VA, 1983) p. 218;
- J.C. Goldstein, B.E. Newnam, R.W. Warren and R.L. Sheffield, *Nucl. Instr. and Meth.* A250 (1986) 4.
- [17] R.C. Davidson and S. Wurtele, *Phys. Fluids* 30 (1987) 557.
- [18] W.B. Colson, *Nucl. Instr. and Meth.* A250 (1986) 168.

Appendix S

Final Report-The NRL Modified Betatron Accelerator Program



NRL/MR/6793--92-7161

Final Report—The NRL Modified Betatron Accelerator Program

C. A. KAPETANAKOS

L. K. LEN

T. SMITH

S. J. MARSH

P. LOSCHIALPO

D. DIALETIS

J. MATHEW

*Beam Physics Branch
Plasma Physics Division*

December 31, 1992

Approved for public release; distribution unlimited.

REPORT DOCUMENTATION PAGE			Form Approved OMB No. 0704-0188	
<small>Public reporting burden for this collection of information is estimated to average 1 hour per response, including the time for reviewing instructions, searching existing data sources, gathering and maintaining the data needed, and completing and reviewing the collection of information. Send comments regarding this burden estimate or any other aspect of the collection of information, including suggestions for reducing this burden, to Washington Headquarters Services, Directorate for Information Operations and Reports, 1215 Jefferson Davis Highway, Suite 1204, Arlington, VA 22202-4302, and to the Office of Management and Budget, Paperwork Reduction Project (0704-0188), Washington, DC 20503.</small>				
1. AGENCY USE ONLY (Leave Blank)		2. REPORT DATE December 31, 1992		3. REPORT TYPE AND DATES COVERED Final
4. TITLE AND SUBTITLE Final Report—The NRL Modified Betatron Accelerator Program			5. FUNDING NUMBERS WU - 1485 WU - 2835	
6. AUTHOR(S) C. A. Kapetanakis, L. K. Len,* T. Smith,* S. J. Marsh,† P. Loschialpo, D. Dialetis,** and J. Mathew				
7. PERFORMING ORGANIZATION NAME(S) AND ADDRESS(ES) Naval Research Laboratory Washington, DC 20375-5320			8. PERFORMING ORGANIZATION REPORT NUMBER NRL/MR/6793—92-7161	
9. SPONSORING/MONITORING AGENCY NAME(S) AND ADDRESS(ES) SPAWAR ONR Washington, DC 20363 Arlington, VA 22217			10. SPONSORING/MONITORING AGENCY REPORT NUMBER	
11. SUPPLEMENTARY NOTES This report is supported by ONR and SPAWAR. *FM Technologies, Inc., Fairfax, VA 22032 †SFA Inc., Landover, MD 20785 **Science Applications International Corp., 170 Goodridge Drive, McLean, VA 22102				
12a. DISTRIBUTION/AVAILABILITY STATEMENT Approved for public release; distribution is unlimited.			12b. DISTRIBUTION CODE	
13. ABSTRACT (Maximum 200 words) This final report summarizes the highlights of the NRL modified betatron accelerator program and documents the status at its termination of July 17, 1992. A substantial fraction of the results in this report has not been published previously.				
14. SUBJECT TERMS Final report Modified betatron accelerator			15. NUMBER OF PAGES 152	
			16. PRICE CODE	
17. SECURITY CLASSIFICATION OF REPORT UNCLASSIFIED	18. SECURITY CLASSIFICATION OF THIS PAGE UNCLASSIFIED	19. SECURITY CLASSIFICATION OF ABSTRACT UNCLASSIFIED	20. LIMITATION OF ABSTRACT SAR	

Table of Contents

I. Introduction.....	1
II. Historical Background	4
III. Experimental Results before the Installation of Strong Focusing (1985-1988).....	16
IV. Results after the Installation of Strong Focusing Windings (SFW)	36
a. Background on the SFW	36
b. Injection and Trapping	40
c. Beam Dynamics During Acceleration.....	44
d. Studies of the Cyclotron Resonances	48
e. Preliminary Beam Extraction Studies	57
V. Assessment of Results	71
References	83
Appendix: List of Publications by the NRL Research Staff	87

FINAL REPORT—THE NRL MODIFIED BETATRON ACCELERATOR PROGRAM

I. Introduction

This final report summarizes important experimental results from the NRL modified betatron program and documents its status at its termination on July 17, 1992. The objective of this program was to study the critical physics issues of the concept and to accelerate a 1 kA electron ring to 20 MeV with subsequent extraction of the ring. Critical physics issues associated with the concept are self field effects, image forces at the walls of the vacuum chamber, ring equilibrium, ring stability during acceleration, beam injection and finally extraction.

At the time of its termination the trapped current in the NRL device was in excess of 1 kA and the electron energy, as inferred from the main x-ray peak, above 20 MeV. Even more importantly, the NRL research effort furnished valuable information on the various critical physics issues of the concept. Twelve years ago i.e., at the commencement of the modified betatron program very little was known about the physics of high current, recirculating accelerators. Today, there is a solid, well documented, although incomplete data base.

During its life span, the NRL program addressed both theoretically and experimentally several important physical processes associated with the high current circular accelerators. Currently, the majority of these processes is reasonably well understood. However, there are some experimental observations, such as the toroidal distribution of the beam losses when the twelve resonant coils are activated, which, as of today, remain without a complete explanation. In addition, a critical physics issue, the extraction of the beam, has been addressed experimentally only temporarily and its data base is very limited.

Our experimental effort to develop a beam extraction scheme from the modified betatron accelerator proceeded at slower than expected pace, mainly because the technical approach had to be modified a few months before the termination of the program. In 1988, an extraction technique was reported by the NRL research staff that is easily realizable and has the potential to lead to high extraction efficiency. The hardware for this mainline extraction approach was designed and fabricated. However, it was never installed in the experiment because it requires a beam with low transverse velocity, since the aperture of the agitator is small. There is evidence that the beam in the NRL device has substantial transverse velocity caused by magnetic field disturbances. As a result of this difficulty, we had to pursue some alternate extraction approaches that do not require beams with low transverse velocity.

The alternate beam extraction approaches had to be terminated prematurely with the shutdown of the program. Still, these incomplete beam extraction studies have furnished some very interesting data on the toroidal beam loss distribution and the dependence of the beam loss rate on the amplitude and risetime of the current pulse that powers the twelve kicker coils. These results are discussed in Section IVe.

Although the conception and subsequent development of the modified betatron accelerator was motivated by defense oriented applications, it is likely that this device will be useful in some areas of civilian economy. As a result of its compactness, light weight and high-current carrying capability, the modified betatron can generate very intense electron beam that can provide high dose rates at reduced unit irradiation cost.

In this report, we have compiled several publications written by the NRL-MBA re-

search staff, which cover the highlights of the experimental effort. In addition, we have included recent unpublished experimental results. The bulk of the theoretical work is not included. This work is adequately documented in the published literature¹. The Appendix provides a list of all the publications, both theoretical and experimental, written by the NRL research staff on the MBA and other similar accelerators.

II. Historical Background

The modified betatron accelerator was the major component of the Advanced Accelerator Program (AAP) that formally started in FY 81. However, preliminary work on the modified betatron concept² was done before FY 81. At its commencement, the AAP was a Special Focus Program (later it was renamed Accelerated Research Initiative) and it was jointly supported by ONR and by in-house funds.

During FY 81 the modified betatron concept went through intensive theoretical evaluation. The objective of this evaluation was to assess the viability of the modified betatron as a high current accelerator and to derive a set of scaling laws that can be used in the design of the device.

The extensive theoretical and numerical studies were reviewed by the Modified Betatron Review Panel that was convened at NRL by Dr. T. Coffey on November 19 and 20, 1981. The panel made several recommendations. Probably the most important was the conceptual design of a proof-of-principle experiment. A key excerpt from the Panel's report.

As a general remark, the panel was impressed by the very high quality of the NRL presentations and technical programs. The technical progress during the past 11 months has been substantial in all areas, and provides a strong basis for expecting continued steady progress in the equilibrium, stability, injection and extraction properties of the modified betatron. While virtually all aspects of the high current modified betatron provide a very difficult technical challenge, it is the

strong recommendation of the panel that NRL proceed immediately with the conceptual design of a proof-of-principle experiment. The conceptual design should be completed no later than November 1982, with construction project approval to follow a design review at that time.

During the concept evaluation phase, it was brought to our attention that Donald Kerst³ in the U.S.A. and John Lawson³ in England have added weak toroidal fields to conventional betatrons⁴ to increase their current carrying capabilities. However, these quick experiments produced inconclusive results. In addition, in 1968 a USA patent was obtained by P.J. Gratreau⁵ for a betatron with a toroidal magnetic field and a radial electric field for deflecting the injected beam. The importance of the space charge effects is not addressed in Gratreau's patent. These effects have been included in an unpublished work by A.G. Bonch-Osmolovsky.⁶

A device similar to the modified betatron is the plasma betatron. In the modified betatron the high current circulating beam is generated by an external source and space charge effects and images on the wall play a dominant role in the confinement of the electron ring. In contrast, in plasma betatrons the circulating electrons are plasma runaway electrons and are produced from the plasma that fills the vacuum chamber. The space charge of the electron beam is neutralized by the background ions and thus does not play any role in the confinement of the beam. Suggested initially by Budker⁷, the plasma betatron was investigated by several groups including J.C. Linhart⁸ and C. Maisonnier, Reynold and Skarsgard⁹ and more recently by Rostoker's group¹⁰. The MBA Preliminary

Design Review Panel met at NRL on December 7 and 8, 1982 and made several general and detailed recommendations and approved the construction of the apparatus as presented by the NRL research staff, but under two constraints.

At the time of the review the objective of the modified betatron program was the formation of multikiloampere (5-10 kA) electron rings with subsequent acceleration from 3 to 50 MeV and the study of critical physics issues of such rings.

The most pressing Physics issues of the modified betatron concept, at the time, were:

1. Is it possible to efficiently inject a high current beam in a toroidal device?
2. Do equilibrium states exist for a high current ring?
3. Are these equilibrium states stable on the time scale of interest?
4. Is the orbit displacement resulting from the energy mismatch manageable?

Since a high quality 3 MeV, 10 - 20 kA injector accelerator required substantial development and could not be obtained at an affordable cost and in order to reduce the risk and the cost of the program, the initial objective was modified on March 29, 1983. According to the reformulated program the development of the modified betatron should proceed in two phases, with the following objectives:

Phase A: Formation of 1 kA, 1 MeV electron ring in a modified betatron configuration using an inexpensive vacuum chamber. Without accelerating the ring (DC ring experiment) study the critical physics issues associated with the concept, such as injection, equilibrium and short time stability.

Phase B: After the installation of a new vacuum chamber accelerate the ring to 20 MeV and study the critical physics issues associated with the acceleration, such as long time ring stability and radiation losses.

The construction and assembly of the accelerator was completed on February 11, 1985, and the testing of the various power systems on April 20, 1985. The first injection experiments started on April 22, 1985.

Phase A, i.e., the DC ring experiment was completed on July 29, 1986. Specifically, electron rings were formed with circulating current between 1 - 3 kA. The DC ring experiment has provided some valuable information on the physics of high current rings.^{11, 12}

In relation to Phase B, a substantial effort was made in the development of an inexpensive vacuum chamber. The novel chamber made of epoxy reinforced graphite fibers was installed in the experiment in the Summer of 1987. Attempts to accelerate the beam over a one year period, i.e., between the summer of 1987 and the summer of 1988, were unsuccessful. The ring confinement time was limited to a few microseconds, too short for imparting any measurable energy to the beam.

In August, 1988, the decision was made to proceed immediately with the design, fabrication and installation of strong focusing windings^{13, 14} in the device. At the time, Omicron Technology, Inc. had completed the design of a strong focusing system for the MBA. However, the cost (~ \$ 700k) and the time requested by the contractor to complete the fabrication and installation of the strong focusing system (~ 40 weeks) were

not compatible with the budget and time schedule of the MBA. Thus, we decided to develop the strong focusing system in-house. The installation of the stellarator windings was completed in December 1988. The next few months were invested to assemble the power supply for the SF windings and to carry out experiments with runaway electrons. The experiments with an injected beam were initiated in April 1989. Within approximately two months, i.e., when the Technical Review Panel convened at NRL by Dr. S. Ossakow on June 27-28, 1989, to review the program, the trapped current was ~ 0.5 kA and the beam energy¹⁵ ~ 10 MeV.

The Technical Review Panel made the recommendation that NRL management continues the MBA program for two more years, as it becomes apparent from the following excerpt taken from the Panel's report.

The Committee was impressed by the significant technical progress made during the past several months with the addition of a helical strong focusing field in the NRL modified betatron experiment. Dr. Kapetanakos and the entire experimental team are to be commended for achieving the difficult milestone of 10 MeV at 0.5 kA. It is anticipated that the improved physics understanding associated with these experiments will be substantial.

Needless to say, the recent experimental results had a favorable impact on the Committee's assessment. It is recommended that Laboratory management give high priority

to continuation of the modified betatron program, at least through the concept demonstration phase (20 MeV at 1 kA, including extraction) over the next twenty-four months.

The spiky x-ray signals produced by the lost electrons in the NRL device could be explained either by the cyclotron resonances or the cyclotron instability.¹⁵ However, measurements of the magnetic field components of the electromagnetic modes inside the toroidal chamber have shown¹⁶ that the amplitude of these modes was too small to excite the cyclotron instability. Thus, the definite conclusion was reached that the cyclotron resonance was the dominant beam loss mechanism.

During the next several months that followed the June 1989 review a concerted effort was made to locate and eliminate the field disturbances that may excite the cyclotron resonances.¹⁷ As a result of this effort and also by increasing the strong focusing and toroidal magnetic fields, the beam energy was raised above 20 MeV while the trapped current was in excess of 1 kA.

In late spring-early summer, 1991, while the beam dynamic stabilization experiments with twelve resonant coils were underway, we observed that the beam could be kicked out of the magnetic field of the device within a time interval that was comparable to the risetime of the current pulse that powered the resonant coils.^{18, 19} Three current pulses with risetimes 12, 5 and 0.4 μsec were used. With the 12 μsec risetime current pulse the FWHM of the x-ray signal was reduced from approximately 900 μsec to only 8 μsec , i.e., by more than two orders of magnitude while its amplitude increased by a factor of thirty.

Extensive studies of the spatial distribution of beam losses when the resonant coils are energized with the $0.4 \mu\text{sec}$ current pulse have shown that the beam strikes the wall at six very well defined toroidal positions that are 60° apart. Rotation of the vacuum chamber and thus of the strong focusing windings that are attached to the chamber by 30° as well as an $\ell = 1$ small radial displacement of the chamber had no effect on the beam distribution.¹⁹ However, in the absence of the strong focusing field when the resonant coils are energized, the experimental results show that the beam strikes the wall at a single toroidal position near $\theta = 70^\circ$.

Although the fabrication of the hardware for the resonant extraction²⁰ approach that was the mainline extraction scheme for the NRL device was completed by the end of FY 91, the resonant extraction was never tested experimentally. The reason is that this extraction technique is based on a single agitator with a very small aperture. Therefore, it requires a beam with low transverse velocity. However, this was not the case in the NRL experiment. The amplitude of the various field imperfections never was reduced to a low enough level to make the transverse velocity of the beam compatible with the small aperture of the agitator. To avoid this difficulty we had to invent a new agitator with large aperture. Among the various kickers considered, magnetic cusps were found to be the most promising. Extensive numerical studies of several cusp configurations have shown that a single layer, 24.2 cm long cusp surrounded by a resistive shroud could provide sufficient displacement to the beam over a 20 nsec time period. Unfortunately such a cusp could not be fabricated on time and thus we had to proceed with an inferior agitator that is based on three double cusps that are located 120° apart in the toroidal direction. This agitating

system was fabricated in-house and tested in the experiment for a short period of time just before the termination of the MBA program. These incomplete results are discussed in Section IVe.

Table I lists most of the important dates in the history of the MBA program and Table II lists the names of the technical staff on November 15, 1991, i.e., the day NRL decided to terminate the MBA program.

Table I
MODIFIED BETATRON ACCELERATOR
IMPORTANT DATES

EVENT AND DATE	COMMENTS
Start Date: 1 October 1980.	
Concept Review: 19-20 Nov. 1981.	Modified Betatron Concept was reviewed by a national panel of experts at NRL.
Design Review: 7-8 Dec. 1982.	The design of the device was reviewed by a national panel of experts, which recommended construction of a proof-of-principle experiment.
Program Reformulation: 29 March 1983.	To reduce cost and risk program objectives were modified (from 10 kA, 50 MeV to 1 kA, 20 MeV).
Diagnostic Devel. - Workshop: 6-7 Oct. 1983.	Modified Betatron diagnostics were reviewed by a national group of experts.
Construction Completed: 11 Feb. 1985.	Construction and assembly of the accelerator was completed.
Testing Completed: April 1985.	All power systems in operation.
DC Ring Experiments Started: 22 April 1985.	First injection experiment.
DC Ring Experiments Completed: July 1986.	Interesting results were obtained, but were limited to a few microseconds.
ARI Termination: 30 Sep. 1986	

MODIFIED BETATRON ACCELERATOR **IMPORTANT DATES (Cont'd)**

EVENT AND DATE

Installation of strong focusing windings (SFW) completed: Dec 1988.

Commencement of experiments with SFW and injected beam: April 1989.

First successful beam trapping exp: May 9, 1989.

First successful acceleration: May 19, 1989.

13 Technical Review: 27-29 June 1989.

Trapped current exceeds 1 kA and beam energy 20 MeV: June 1991.

COMMENTS

To reduce cost, the SFW were designed and fabricated in-house.

By June, 1989, the trapped current was ~ 0.5 kA and the beam energy ~ 10 MeV.

Progress was reviewed by a national panel of experts, which recommended that NRL management give high priority to the program.

MODIFIED BETATRON ACCELERATOR IMPORTANT DATES (Cont'd)

EVENT AND DATE

COMMENTS

Commencement of preliminary extraction experiments: Summer 1991.

Using twelve resonant kickers. Beam FWHM is comparable to risetime of the current pulse that drives the kickers.

CPB Accelerator Technology Review: 16-17 Oct., 1991.

Purpose of the review was to determine the strengths, potential shortcomings and weaponization potential of the various accelerator technologies.

14 NRL decided to terminate the MBA program before the end of FY 92: 15 Nov. 1991.

The University of Crete (Greece) offers to buy the MBA intact: January 1992.

MBA Program Terminated: 17 July 1992.

NRL decided to loan the major components of the MBA to the University of Crete: Aug. 1992

Table II

NRL MODIFIED BETATRON

RESEARCH STAFF

NOV. 15, 1991

C.A. Kapetanakis, P.I.

<u>Experiment</u>	<u>Theory and Simulation</u>	<u>Technicians</u>
L.K. Len (FMT)	D. Dialetis(SAIC)	R. Covington (SFA)
T. Smith (FMT)	J. Marsh (SFA)	D. Hardesty
J. Mathew		S. Krafsig (SFA)
P. Loschialpo		B. Lewis
J.H. Chang		
J. Golden (part-time) (BRA)	<u>Engineering</u>	
	K. Smith (SFA)	
	L. Seto (SFA)	
<u>Consultant</u>		
D. Kerst (SFA)		

III. Experimental Results Before the Installation of Strong Focusing (1985 - 1988).

This Section briefly describes the highlights of the experimental effort before the installation of the strong focusing windings. To make these results meaningful to the reader who is not familiar with the modified betatron, a short theoretical introduction has been included that addresses the transverse dynamics of the electron ring. Although the initial studies²¹⁻²³ of the transverse electron ring dynamics were based on the linearized equations of motion, here we have adopted a different approach that was developed later on and is based on the two constants of the motion.²⁴ The latter approach has several advantages; such as (i) It is easier and thus more transparent, (ii) allows the ring orbits to be determined over the entire minor cross section of the torus and not only near its minor axis, and (iii) the toroidal effects associated with the various fields can be included in a natural and straightforward way.

a. Beam Dynamics

Consider an electron ring inside a perfectly conducting torus of circular cross section as shown in Fig. 1. The center of the ring is located at a distance Δr , Δz from the minor axis of the torus. The kinetic energy γmc^2 of a reference electron that is located at the position r , z varies according to the equation

$$mc^2 \frac{d\gamma}{dt}(r, z) = -|e|\vec{v} \cdot \vec{E}(r, z), \quad (1)$$

where $\vec{E}(r, z)$ is the total electric field at the position of the reference electron. The electric field is related to the space charge Φ and magnetic vector potential \vec{A} by

$$\vec{E}(r, z) = -\nabla\Phi - \frac{1}{c} \frac{\partial \vec{A}}{\partial t}, \quad (2)$$

where the total time derivative of Φ is given by

$$\frac{d\Phi}{dt} = \frac{\partial\Phi}{\partial t} + \vec{v} \cdot \nabla\Phi. \quad (3)$$

For the problem of interest, the accelerating and self fields vary slowly in time and thus it is a reasonable approximation to assume

$$\frac{\partial \vec{A}}{\partial t} = \frac{\partial\Phi}{\partial t} \approx 0. \quad (4)$$

Combining Eqs. (1) to (4), we obtain

$$\frac{d\gamma(r, z)}{dt} - \frac{|e|}{mc^2} \frac{d\Phi(r, z)}{dt} = 0$$

or, after integration

$$\gamma(r, z) - \frac{|e|}{mc^2} \Phi(r, z) = \text{constant}. \quad (5)$$

According to Eq. (5) the sum of the kinetic and potential energy of the reference electron is conserved. In a subsequent more accurate calculation¹⁴ the approximation of Eq. (4) has been relaxed. It has been found that the partial time derivative of the potentials contributes a small term that is proportional to ν/γ^2 .

Since the fields of the modified betatron configuration are independent of the toroidal angle θ , the canonical angular momentum P_θ is also a constant of the motion, i.e.,

$$P_\theta = \gamma m r v_\theta - \frac{|e|\hbar}{c} r A_\theta = \text{constant}, \quad (6)$$

where A_θ is the toroidal component of the total magnetic vector potential and v_θ is the toroidal velocity of the reference electron. Assuming that $v_\theta \approx v$ and eliminating γ from Eqs. (5) and (6), it is obtained

$$\left\{ \left[\frac{P_\theta}{m c r} + \frac{|e|\hbar}{m c^2} A_\theta(r, z) \right]^2 + 1 \right\}^{1/2} - \frac{|e|\hbar}{m c^2} \Phi(r, z) = \text{constant}, \quad (7a)$$

or, at the centroid of the ring

$$\left\{ \left[\frac{P_\theta}{m c R} + \frac{|e|\hbar}{m c^2} A_\theta(R, Z) \right]^2 + 1 \right\}^{1/2} - \frac{|e|\hbar}{m c^2} \Phi(R, Z) = \text{constant}. \quad (7b)$$

For very high energy beams, i.e., when $\gamma^2 \gg 1$, Eq. (7b) is reduced to

$$\frac{P_\theta}{m c R} + \frac{|e|\hbar}{m c^2} [A_\theta(R, Z) - \Phi(R, Z)] = \text{constant}. \quad (7c).$$

This non-linear conservation law can furnish very useful information on the slow (drift) motion of the ring in the r, z plane, provided that the potentials A_θ and Φ at the center of the ring are known. It should be noticed that Eqs. (7) are independent of the toroidal magnetic field. This is a consequence of the assumption that $v \approx v_\theta$, i.e., to the omission of the fast motion of the electrons.

In Eq. (7), the total magnetic vector potential $A_\theta(r, z)$ is

$$A_\theta(r, z) = A_\theta^{\text{ext}}(r, z) + A_\theta^{\text{self}}(r, z),$$

where $A_\theta^{ext}(r, z)$ is the external and $A_\theta^{self}(r, z)$ is the self magnetic vector potential.

It is assumed that the betatron magnetic field is described by

$$A_\theta^{ext}(r, z) = B_{z0} \left[\left(\frac{r_0}{r} \right)^n \left(\frac{r}{2-n} \right) + \frac{r_0^2 (1-n)}{r (2-n)} + \frac{nz^2}{2r} \right], \quad (8)$$

where B_{z0} is the magnetic field at $r=r_0$, $z=0$ and n is the external field index, i.e.,

$$n = -\frac{r_0}{B_{z0}} \left(\frac{\partial B_z}{\partial r} \right)_{r_0, 0}.$$

For a cylindrical electron beam inside a straight, perfectly conducting cylindrical pipe, the self potentials can be computed exactly, even for large beam displacements from the minor axis. In the local coordinate system ρ, ϕ the self potentials inside the beam, i.e., for $|\vec{\rho} - \vec{\Delta}| \leq r_b$ are given by

$$A_\theta^{self}(\rho, \phi) = -2|e|N_e\beta_0 \left\{ 1/2 + \ell n \frac{a}{r_b} - \frac{[\rho^2 + \Delta^2 - 2\rho\Delta\cos(\phi - \alpha)]}{2r_b^2} - \sum_{\ell=1}^{\infty} \left(\frac{\rho}{a} \right)^\ell \left(\frac{\Delta}{a} \right)^\ell \ell^{-1} \cos(\phi - \alpha) \right\}, \quad (9a)$$

and

$$\Phi(\rho, \phi) = -2|e|N_e \left\{ 1/2 + \ell n \frac{a}{r_b} - \frac{[\rho^2 + \Delta^2 - 2\rho\Delta\cos(\phi - \alpha)]}{2r_b} - \sum_{\ell=1}^{\infty} \left(\frac{\rho}{a} \right)^\ell \left(\frac{\Delta}{a} \right)^\ell \ell^{-1} \cos(\phi - \alpha) \right\}. \quad (9b)$$

At the beam center, i.e., for $\rho = \Delta$ and $\phi = \alpha$, Eqs. (9a) and (9b) become

$$A_\theta^{self}(R, Z) = -2|e|N_e\beta_0 \left\{ 1/2 + \ell n \frac{a}{r_b} + \ell n \left[1 - \frac{(R - r_0)^2 + Z^2}{a^2} \right] \right\}, \quad (10a)$$

and

$$\Phi(R, Z) = -2|e|N_\ell \left\{ 1/2 + \ell n \frac{a}{r_b} + \ell n \left[1 - \frac{(R - r_o)^2 + Z^2}{a^2} \right] \right\}, \quad (10b)$$

where N_ℓ is the linear electron density, r_b is the minor radius of the beam, a is the minor radius of the conducting pipe and $\beta_\theta = v_\theta/c$.

To obtain a better understanding of the potentials inside a perfectly conducting torus, we solved the differential equations for Φ and \vec{A} to first order in the ratio a/R , but to any order²⁵ in the normalized displacement Δ/a . For a constant particle density n_o ring and to second order in Δ/a , the electrostatic potential at the center of the ring is given by

$$\Phi(R, Z) \approx -2N_\ell|e| \left[1/2 + \ell n(a/r_b) - \frac{(R - r_o)^2 + Z^2}{a^2} - \frac{r_b^2}{8a^2} \frac{(R - r_o)}{R} \right], \quad (11a)$$

and for $J_\theta = \text{constant}$, the stream function ψ is

$$\psi(R, Z) \simeq -2N_\ell|e|R\beta_\theta \left[1/2 + \ell n(a/r_b) - \frac{(R - r_o)^2 + Z^2}{a^2} - \frac{r_b^2}{8a^2} \frac{(R - r_o)}{R} \right]. \quad (11b)$$

Similarly, the image fields at the centroid of the ring are given by

$$E_r = -\frac{2|e|N_\ell}{a} \left[\frac{(R - r_o)}{a} + \left(\frac{a}{2R} \right) \ell n \frac{a}{r_b} + \frac{r_b^2}{8Ra} \right], \quad (12a)$$

$$E_z = -\frac{2|e|N_\ell}{a} \left(\frac{Z}{a} \right), \quad (12b)$$

$$B_r^{self} = -\frac{2|e|N_e\beta_\theta}{a} \left(\frac{Z}{a} \right), \quad (12c)$$

and

$$B_z^{self} = \frac{2|e|N_e\beta_\theta}{a} \left[\frac{(R-r_o)}{a} - \left(\frac{a}{2R} \right) \left(\ln \frac{a}{r_b} + 1 \right) + \left(\frac{r_b^2}{8Ra} \right) \right], \quad \text{for } J_\theta = \text{constant.} \quad (12d)$$

The toroidal term in Eq. (11) is very small for the parameters of interest and therefore the potentials at the center of the ring are approximately cylindrical.²⁴ For low energy rings the small toroidal term could be important and may have a profound effect on the shape of the orbits. However, when $\gamma \gg 1$, the potentials for $n_o = \text{constant}$ and $J_\theta = \text{constant}$ become approximately equal and hence they do not contribute substantially in Eq. (7c).

Equation (7b) has been solved numerically, using the potentials of Eqs. (8) and (11). Typical macroscopic beam orbits in the r, z plane are shown in Fig. 2. The various parameters for those runs are listed in Table III. Only orbits that are at least one beam minor radius away from the wall are shown. Each orbit corresponds to a different value of the constant in Eq. (7b). A striking feature of the results is the sensitivity of the orbits to the value of the constant.

The number marked in every fourth orbit is equal to $10^4 \cdot [\text{constant} - \langle \text{constant} \rangle]$, where the average value of the constant, i.e. $\langle \text{constant} \rangle$ for each run is shown at the top of the figure. For all the cases tested, less than 3% change in the constant of the motion was sufficient to generate orbits that extend over the entire minor cross-section of the torus. Orbits shown with solid lines correspond to a constant that is greater than

<constant> and those shown with a dashed line correspond to a constant that is less than <constant>. All the orbits close inside the vacuum chamber. However, a fraction of them lie inside the annular region that extends from the dotted-dashed line to the wall. This region has a width that is less than the beam radius and hence part of the beam will strike and wall.

In the general case, it is difficult to derive an explicit expression for the ring orbits in the transverse plane from Eqs. (7b) and (11). However, in the limit $\gamma^2 \gg 1$, $\beta_\theta/\beta \simeq 1$ and $\nu/\gamma \ll 1$, such an expression can be obtained near the minor axis of the torus.

Assuming that $\beta_\theta \simeq \beta$ and since $\gamma\beta \simeq \gamma - 1/2 \gamma$, Eqs. (5) and (6) give

$$\frac{P_\theta}{mcR} + \frac{|e|}{mc^2} A_\theta^{\text{ext}} + \frac{|e|}{mc^2} (A_\theta^{\text{self}} - \Phi) + \frac{1}{2\gamma} = \text{constant} = G. \quad (13)$$

Expanding γ near r_0 and using Eq. (5), it is obtained

$$\delta\gamma = \gamma - \gamma_0 = \frac{|e|}{mc^2} \frac{\partial \Phi}{\partial r} \Big|_{r_0} \Delta r + \frac{\partial G}{\partial r} \Big|_{r_0} \Delta r,$$

where $\Delta r = R - r_0$. It is shown later on that $\frac{\partial G}{\partial r} \Big|_{r_0} = 0$ and thus the above equation becomes

$$\delta\gamma = \gamma - \gamma_0 = \frac{|e|}{mc^2} \frac{\partial \Phi}{\partial r} \Big|_{r_0} \Delta r. \quad (14)$$

From Eqs. (11a) and (11b), the difference in the self potentials can be written as

$$A_\theta^{\text{self}} - \Phi = 2N_\ell |e| \left\{ 1/2 + \ell n \frac{a}{r_b} - \frac{(\Delta r^2 + \Delta z^2)}{a^2} - \frac{r_b^2}{8a^2} \frac{\Delta r}{R} \right\} (1 - \beta_\theta). \quad (15)$$

Since

$1 - \beta_\theta \simeq 1 - \beta \simeq 1/2\gamma^2$ and substituting $\delta\gamma$ from Eq. (14) in the expansion for $1/\gamma^2$, it is obtained

$$1 - \beta_\theta \simeq \frac{1}{2\gamma_o^2} \left[1 - \frac{2}{\gamma_o} \frac{|e|}{mc^2} \frac{\partial \Phi}{\partial r} \Big|_{r_o} \Delta r \right]. \quad (16)$$

Similarly, expanding $1/2\gamma$ as

$$\frac{1}{2\gamma} \approx \frac{1}{2\gamma_o} - \frac{|e|}{2\gamma_o^2 mc^2} \frac{\partial \Phi}{\partial r} \Big|_{r_o} \Delta r, \quad (17)$$

and $1/R$ as

$$\frac{1}{R} \approx \left(\frac{1}{r_o} \right) \left[1 - \frac{\Delta r}{r_o} + \left(\frac{\Delta r}{r_o} \right)^2 \right], \quad (18)$$

and using a linear expression for the external vector potential

$$A_\theta^{ext} \simeq B_{zo} r_o \left[1 + \frac{\Delta r^2 (1 - n)}{2r_o^2} + \frac{\Delta z^2 n}{2r_o^2} \right], \quad (19)$$

Eqs. (13) to (19) give.

$$\begin{aligned} & \left[\frac{P_\theta}{mcr_o} + \frac{\Omega_{zo}^{ext} r_o}{2c} (1 - n) - \frac{\nu r_o^2}{\gamma_o^2 a^2} \right] \left(\frac{\Delta r}{r_o} \right)^2 + \left[\frac{\Omega_{zo}^{ext} r_o}{2c} n - \frac{\nu r_o^2}{\gamma_o^2 a^2} \right] \left(\frac{\Delta z^2}{r_o} \right) \\ & - \left[\frac{P_\theta}{mcr_o} + \frac{\nu}{2\gamma_o^2} \left(\frac{r_b^2}{2a^2} + \ell n \frac{a}{r_b} \right) \right] \left(\frac{\Delta r}{r_o} \right) = \tilde{G}, \end{aligned} \quad (20)$$

where $\Delta r = R - r_o$, $\Delta z = Z$, \tilde{G} is a constant that is determined from the initial conditions and ν is the Budker's parameter.

Equation (20) describes the ring orbits near the minor axis, when $\gamma_o^2 \gg 1$. These orbits are centered around the minor axis of the torus when the coefficient of the $(\frac{\Delta r}{r_o})$ term is zero, i.e., when

$$\frac{P_{\theta o}}{mcr_o} + \frac{\nu}{2\gamma_o^2} \left[\left(\frac{r_b}{2a} \right)^2 + \ln \frac{a}{r_b} \right] \approx \frac{\delta P_{\theta}}{mcr_o} \approx 0. \quad (21)$$

For $(r_b/a)^2 \ll 1$ and $\gamma_o \gg 1$, Eq. (21) predicts that $\frac{P_{\theta}}{mcr_o} \approx 0$. Therefore, the orbits are circular when the external field index is approximately equal to 0.5, in agreement with the computer results shown in Fig. 2.

Equation (20) can be writtern as:

$$q_1 \left(\frac{\Delta r}{r_o} \right)^2 + q_2 \left(\frac{\Delta z}{r_o} \right)^2 - (2\delta P_{\theta}/mr_o^2\Omega_{zo}^{ext}) \left(\frac{\Delta r}{r_o} \right) = \frac{2\tilde{G}c}{\Omega_{zo}^{ext}r_o}, \quad (22)$$

where

$$q_1 = 1 - n - n^* + 2P_{\theta}/mr_o^2\Omega_{zo}^{ext}$$

$$q_2 = n - n^*,$$

and

$$n^* = 2\nu r_o c / \gamma_o^2 a^2 \Omega_{zo}^{ext}.$$

According to Eq. (22), the macroscopic beam orbits are stable, provided $q_1 q_2 > 0$.

Figure 3 shows the product $q_1 q_2$ as a function of n^* . Since $n^* \sim I_b/\gamma_o^3$, the parameter n^*

decreases rapidly during acceleration. Therefore, in order to avoid crossing the unstable region ($q_1 q_2 < 0$) when γ_0 increases, it is necessary to select the beam parameters during injection so that n^* is located to the left of the unstable region.

The extreme of Eq. (5) furnishes useful information on the dynamics of the ring in the r - z plane. First, we will show that this extreme is the radial balance equation of motion for the reference electron.

Setting the partial derivative of Eq. (5) with respect to r equal to zero

$$\frac{\partial \gamma}{\partial r} - \frac{|e|}{mc^2} \frac{\partial \Phi}{\partial r} = 0, \quad (23)$$

and using the relation $\gamma = (1 + \beta^2 \gamma^2)^{1/2}$ and Eq. (6), we obtain

$$\frac{\partial \gamma}{\partial r} = \beta \left[-\frac{P_\theta}{mcr^2} + \frac{|e|}{mc^2} \frac{\partial A_\theta^{ext}}{\partial r} + \frac{|e|}{mc^2} \frac{\partial A_\theta^{self}}{\partial r} \right], \quad (24)$$

where we have assumed that $\beta = v/c$ is approximately equal to $\beta_\theta = v_\theta/c$.

Substituting Eq. (6) into Eq. (24) and using the equations

$$B_z^{ext} = \frac{A_\theta^{ext}}{r} + \frac{\partial A_\theta^{ext}}{\partial r}, \quad (25a)$$

$$B_z^{self} = \frac{A_\theta^{self}}{r} + \frac{\partial A_\theta^{self}}{\partial r},$$

and

$$E_r = -\frac{\partial \Phi}{\partial r}, \quad (25c)$$

it is obtained

$$-\gamma m \frac{v_\theta^2}{r} = -|e| [E_r + \frac{v_\theta}{c} (B_z^{ext} + B_z^{self})], \quad (26)$$

i.e., the radial balance equation. This equation gives the equilibrium position of the ring, which is located along the \hat{e}_r axis. At this position the reference electron at the centroid of the ring moves only along the toroidal direction, i.e., $v_r = v_z = 0$.

When the equilibrium position is at $r = r_o$, the toroidal velocity of the reference electron can be determined from Eqs. (6) and (21) and is

$$v_{\theta o} = \frac{r_o \Omega_{zo}^{ext} / \gamma_o - \frac{\nu}{2\gamma_o} [(\frac{r_b}{2a})^2 + \ln \frac{a}{r_b}]}{[1 + \frac{2\nu}{\gamma_o} (1/2 + \ln \frac{a}{r_b})]}. \quad (27)$$

With the exception of the very small term on the numerator, Eq. (27) is the same with the expression reported previously^{21, 22} for beams with square current density profile.

The external magnetic field B_{zo}^{ext} required to confine the ring at $r = r_o$ and be readily found from Eq. (27). Omitting the small term in the numerator of Eq. (27), we obtain

$$B_{zo}^{ext} = B_{zo}^{sp} [1 + \frac{2\nu}{\gamma_o} (1/2 + \ln \frac{a}{r_b})], \quad (28)$$

where the single particle magnetic field is $B_{zo}^{sp} = \frac{\gamma_o \beta_{eo} m c^2}{r_o |e|}$.

The magnetic field required to maintain the beam at an equilibrium position that is different than r_o can also be determined from the radial balance equation. Substituting E_r and B_z^{self} from Eqs. (12a) and (12d) into Eq. (26), it is obtained

$$B_z^{ext} = B_z^{ep} \left\{ 1 + \frac{2\nu}{\gamma} \left[1/2 + \ell n \frac{a}{r_b} + \frac{R(R - r_o)}{a^2(\gamma\beta)^2} + \frac{r_b^2}{8a^2(\gamma\beta)^2} \right] \right\}. \quad (29)$$

Equation (29) has been derived under the assumption that ν is not a function of R .

As a consequence of the assumption that $\beta_\theta = \beta$ and $\gamma_\theta = \gamma$, the fast motion of the electrons has been neglected. This effect can be taken into account either by using the exact equations of motion or the relativistic guiding center equations of motion. It can be shown from the guiding center equations with linear external fields but non-linear image fields that for symmetric orbits with their center on the minor axis, the square of the bounce frequency ω_B^2 is given by

$$\omega_B^2 = \left(\frac{\Omega_{xo}}{\Omega_{\theta o}} \right)^2 \left(\frac{\beta_\theta c}{r_o} \right)^2 * \left[\left(n - \frac{2\nu}{\beta^2 \gamma^3} \frac{1 + \alpha^2 \gamma^2}{\frac{\Omega_{xo} r_o}{\gamma \beta_\theta c}} \frac{1}{1 - (\frac{\ell}{a})^2} \left(\frac{r_o}{a} \right)^2 \right) \right. \\ \left. * \left(1 - n - \frac{2\nu}{\beta^2 \gamma^3} \frac{1 + \alpha^2 \gamma^2}{\frac{\Omega_{xo} r_o}{\gamma \beta_\theta c}} \frac{1}{1 - (\frac{\ell}{a})^2} \left(\frac{r_o}{a} \right)^2 \right) \right], \quad (30)$$

with

$$\frac{\Omega_{xo} r_o}{\gamma \beta_\theta c} = \left(1 + \frac{1}{2} \alpha^2 \right) + \frac{2\nu}{\gamma} \left[\frac{1}{2} + \frac{1}{2} \left(1 + \frac{1 + \alpha^2}{\beta^2} \right) \ell n \frac{a}{r_b} + \ell n \left(1 - \frac{\rho^2}{a^2} \right) \right]. \quad (31)$$

In Eqs. (30) and (31)

$$\beta_\theta^2 = \frac{\beta^2}{1 + \alpha^2}, \quad \frac{1}{\beta_\theta^2 \gamma_\theta^2} = \frac{1 + \alpha^2 \gamma^2}{\beta^2 \gamma^2}, \quad \nu = \frac{I_b (kA)}{17.045 \beta_\theta},$$

$\beta^2 = 1 - \frac{1}{\gamma^2}$ and $\alpha = v_\perp / v_\theta$, where v_\perp is the transverse velocity component that is due to the fast motion.

b. Description of the Experiment and Results

In its initial form, i.e., before the installation of the strong focusing windings, the NRL modified betatron comprised two different external magnetic fields; the betatron field that is a function of time and is responsible for the acceleration of the electrons and the toroidal magnetic field that varies only slightly during acceleration²⁷. Figure 4 shows a photograph of the experiment.

The NRL modified betatron is an air-core device. Both the local field and the magnetic flux are produced by eighteen circular coils that are connected in series. Their total inductance is approximately $530\mu H$. The coils are powered by an 8.64 mF capacitor bank (48 capacitors each having $172\mu F$ nominal capacitance) that can be charged up to 17 kV. At full charge, the bank delivers to the coils a peak current of about 65 kA. The current flowing through the coils produces a field that varies sinusoidally with a quarter period risetime of 2.6 msec and an amplitude on the minor axis at peak charging voltage equal to 2.1 kG. Immediately after the peak the field is crowbarred with a 4.5 msec decay time.

The flux condition and field index are adjusted by two sets of trimmer coils that are connected in parallel to the main coils. The current through the trimmers is adjusted with series inductors. Typically $\sim 10\% - 15\%$ of the total current flows through the trimmers.

The toroidal magnetic field controls mainly the minor cross section of the electron ring and the growth rate of several unstable collective modes. This field is generated by twelve air-core, rectangular coils that are connected in series. The coils are made of aluminum square tubing and have a 150 cm height and 135 cm width. The total inductance of the twelve coils is $\sim 85\mu H$ and are powered by a 34-mF capacitor bank (85 capacitors each

having 400 μ F nominal capacitance) that can be charged to a peak voltage of 10.6 kV. At peak voltage, the bank delivers to the coils ~ 214 kA. This current produces a field that varies sinusoidally with a quarter period risetime of 2.3 msec and an amplitude on the minor axis in excess of 5.0 kG.

Demountable, high current joints allow removal of the outer legs of the coils. The high current density, low bolting force joints are attainable with multilam. The number and size of the coils has been selected in order to attain tolerable field errors. The discreteness of the coils produces a periodic field error that has all three components, i.e., ΔB_θ , ΔB_z , and ΔB_r . Recent measurement of the ΔB_r component with an accurate probe²⁶ have shown that its average value over a 30° span at $r=105$ cm is ~ 0.2 % of the toroidal field. Thus, when $B_\theta = 5$ kG, $\langle \Delta B_r \rangle \simeq 25$ G.

The coils are supported by a stiff structure that consists of two triangular decks, three aluminum legs, a central tension rod and a central spline. The decks are made of polytruded epoxy-glass beams and stainless steel plates that are not electrically continuous. The gaps in the stainless steel plates are necessary to avoid circulating currents from the changing magnetic flux.

Nested among the vertical field coils is the vacuum chamber. The 100 cm major radius, 15.2 cm-inside minor radius chamber has been constructed using epoxy-reinforced carbon fibers and has been briefly described previously. The diode that emits the injected beam is located inside the vacuum chamber and ~ 3.7 cm from the minor axis. Both the diode and the generator that powers the diode have been briefly discussed in previous publications.^{15, 28}

During the first few microseconds following injection, the macroscopic beam motion in the transverse plane is studied by monitoring the light emitted from a thin (2-10 μ m) polycarbonate foil that is stretched across the minor cross section of the vacuum chamber. The foil is carbon coated on the upstream side to avoid electrostatic charging. Figure 5 shows open-shutter photographs of the light emitted as the electron beam passes through the foil for various values of the vertical magnetic field. As the vertical magnetic field decreases, the equilibrium position of the beam, located approximately at the geometric center of the transverse orbit, also decreases. At $B_{z0} \approx 42$ G the center of the orbit is located very near the minor axis.

Figure 6 shows the vertical magnetic field B_{z0} required to keep the beam at its equilibrium position R_{eq} for five beam currents 3, 2.5, 2.0, 1.0 and 0 kA. These results have been obtained from Eq. (26) using the fields shown in Eqs. (12). Although the beam current varies from shot to shot and there is uncertainty in both the energy and radius of the beam, the qualitative agreement between experiment and theory is satisfactory. It is apparent that the image forces from the induced charge and current on the wall of the vacuum chamber play a very important role and dramatically change the shape of the B_{z0} vs. R_{eq} curve.

The bounce frequency²² ω_B , i.e., the angular frequency with which the beam moves on the macroscopic orbits of Fig. 2 has been measured in the NRL modified betatron accelerator under a wide range of experimental conditions. Figure 7 shows the bounce frequency squared vs. the circulating electron ring current. The solid lines have been computed from Eqs. (30) and (31) for $n = 0.5$ and for three values of the normalized

transverse velocity β_{\perp} . The solid circles are from the experiment. It is apparent that the measured ω_B^2 is substantially greater than that predicted by the theory for $\beta_{\perp}/\beta = 0$. A reasonable agreement between theory and experiment is obtained only under the assumption that $\beta_{\perp}/\beta \simeq 0.5$. As a rule, the measured ω_B is several times greater than that predicted by the cold beam theory. A satisfactory explanation of this discrepancy has been, so far, elusive.

Before the installation of the strong focusing windings, the operating point¹² in the NRL-MBA was to the right of the instability gap (see Fig. 3), i.e., in the high current regime. The low current regime was inaccessible because the beam could not drift enough over the first revolution to avoid the injector. It has been shown that an electron beam inside a resistive wave guide is drag instability unstable²⁹ when its current I_b exceed the critical current I_{crit} , i.e., when the beam is in the high current regime. The drag instability is due to the poloidal displacement of the electric and magnetic images that is caused by the finite resistivity of the chamber wall.

The growth rate Γ predicted by the linear theory²⁹, for $(b-a) < \delta < \sqrt{b(b-a)}$, is

$$(r_o \Gamma / c) = \frac{c(\gamma_o^2 - 1)}{2\pi} \left(\frac{r_o}{b} \right) \frac{\rho}{(b-a)} \frac{x}{(x-1)}, \quad (32)$$

where δ is the skin depth, ρ is the wall resistivity, $b-a$ is the wall thickness, $x = I_b/I_{crit}$ and $I_{crit} = 4.26(\gamma_o^2 - 1)^{3/2}(a/r_o)^2(kA)$. The rest of the parameters have been defined previously. The beam lifetime is computed from

$$t_o = \ell n(a/\Delta_o)/\Gamma, \quad (33)$$

where Δ_0 is the injection position.

Figure 8 shows the normalized ring lifetime $c t_0/2\pi r_0$ as a function of the electron ring current for several value of γ_0 . In effect, $ct_0/2\pi r_0$ is the number of revolutions around the major axis performed by the beam before it strikes the wall. The dashed line shows the number of revolution over a bounce period. When no attempt is made to trap the beam, only the portion of the solid curves to the left of the dashed curve are meaningful. According to Fig. 8, the maximum number of revolutions the beam could perform before striking the wall is limited to about 40. However, we have routinely observed in the experiment beam lifetimes that were five times longer.

The solid curves in Fig. 8 have been plotted under the assumption that on each curve the beam electrons have the same kinetic energy, independently of the beam current. This implies that the voltage on the diode of the injector V_d increases as the beam current increases. Figure 9 shows the normalized beam lifetime as a function of beam current for fixed voltage on the diode. This represents a realistic simulation of the experiment. The dramatic increase in the beam lifetime with beam current is due to the lower growth rate at lower γ_0 and also to the reduction of I_{crit} .

Several trapping techniques have been used to trap the beam in the modified betatron before the installation of the strong focusing windings. All these techniques required that the beam drifts a sufficient distance during the first revolution around the major axis that the beam misses the diode. In the three initial techniques, sufficient drift could be attained only when the beam current was high, i.e., when the beam was in the high current regime. However, in the high current regime the beam lifetime was limited by the drag instability.

To avoid this difficulty a technique was invented to enhance the drift motion of the beam during its first revolution around the major axis¹². This technique was based on the generation of a pulsed radial magnetic field that would drift the beam radially inward. In general, all four techniques were not very reliable and introduced additional complications.

In summary, the studies in the MBA before the installation of the strong focusing windings led to the formation of electron rings with circulating current ¹² as high as 3 kA. In addition, these studies furnished important information on the critical physics issues of the concept, such as

- demonstrated the beneficial effect of B_θ on the expansion of the ring's minor radius,
- unambiguously confirmed the bounce motion of the ring,
- verified the pronounced effect of image forces on the ring equilibrium,
- confirmed the existence of the macroscopic instability gap and the transformation of ring orbits from diamagnetic to paramagnetic,
- revealed, for symmetric orbits, that the bounce frequency is several times higher than the theoretical prediction, and
- shown that, at least for the drift trapping techniques, the low current regime is inaccessible.

Finally, these studies revealed that over a wide range of parameters the ring lifetime was limited to a few μsec which is comparable to the magnetic field diffusion time through the vacuum chamber. Thus, it became apparent from these results that the modified betatron had to be modified in order to increase the beam lifetime and thus to achieve

acceleration. In August 1988 the decision was made to proceed rapidly with the design, fabrication and installation of strong focusing windings.

Table III

Parameters for the results shown in Fig. 2

	Fig. 2a	Fig. 2b	Fig. 2c
External field index	0.35	0.5	0.65
Torus major radius (m)	100	100	100
Torus minor radius (cm)	16	16	16
Ring minor radius (cm)	3	3	3
Ring current (kA)	5	5	5
Electron energy (MeV)	3.123	3.123	3.123
Betatron field $B_{\pi 0}$ (G)	138.4	138.4	138.4
$P_{\theta}/\text{mc}r_0$	-0.0018	- 0.0020	- 0.0023

IV. Results After the Installation of Strong Focusing Windings (SFW)

a. Background on the SFW

The beneficial effect of the SFW on the confinement of charged particles has been known for some time. There are two basic configurations: The stellarator¹³ shown in Fig. 10 and the torsatron¹⁴ shown in Fig. 11. The stability properties of the stellarator windings for high current beams have been studied initially by Gluckstern³⁰ in linear geometry and by Roberson¹³ et al. in toroidal geometry. The beneficial effect of torsatron windings on high current electron beams has been addressed by Kapetanakis^{14, 31} et al.

To improve the confining properties of the MBA we considered both configurations. The stellarator configuration was selected not only because of the small net vertical field and the lower current per winding, but also because it is compatible with our contemplated extraction scheme.³²

Figure 12 shows the orbital stability diagram¹³ in the rotating frame for an external field index $n=0.5$. The two axes are:

$$U = \frac{b^2 + 2 - 4n_s r_b^2 / a^2}{(m + b)^2}, \quad (34)$$

and

$$V = \frac{|\mu|}{(m + b)^2}, \quad (35)$$

where

$$b = B_{\theta 0} / B_{z0}, \quad m = -2\alpha r_0, \quad n_s = \omega_b^2 / 2\gamma_0^2 \Omega_{z0}^2,$$

$$\mu = B_s^{\text{ex}} \epsilon_{st} \alpha r_0 / B_{s0},$$

$\Omega_s^{\text{ex}} \epsilon_{st} = 4\alpha \Omega_0 \rho_0 K'_2(2\alpha \rho_0)$, $\alpha = 2\pi/L$, $B_0 = \frac{8\pi I_{st}}{cL}$, ω_b is the beam plasma frequency ρ_0 is the winding radius, L is the axial pitch, I_{st} is the winding current, r_0 is the major radius and r_b is the beam minor radius.

We have decided to select the parameters of the windings in such a way that the experiment will operate in region 2, because it has been shown that the electron ring will be stable during acceleration if it is located in this region at injection.³¹

When $B_\theta > 0$ and $v_\theta > 0$, operation in region 2 requires that

$$0 < U \leq 1 - 4V, \quad (36)$$

or

$$|\mu| \leq \left(\frac{m}{4}\right)^2 + \frac{mb}{8} + \frac{1}{4} \left(\frac{n_s r_b^2}{a^2} - \frac{1}{2} \right), \quad (37)$$

and

$$\left(\frac{b}{2}\right)^2 + \frac{1}{2} \geq \frac{n_s r_b^2}{a^2}. \quad (38)$$

It can be shown from (37) that $m > 0$ or $m < -2b$. For $m > 0$ and since $m = -2\alpha r_0$, $\alpha < 0$ or the windings should be left-handed.

When $n \neq 1/2$, the entire region 2 is not stable. The parameters of the injected beam should be selected to the right of the dashed line of region 2 (shown in Fig. 13). Along this line the bounce frequency in the laboratory frame $\omega_B = \omega_- = 0$ (instability gap).

During the acceleration phase this dashed line moves to the left and eventually coincides with the vertical axis. The parameter V of injection goes to $2/m^2$ and thus never crosses the $\omega_- = 0$ line.

The exact stallarator field index¹³ is defined by

$$n_{st} = \frac{\mu^2}{m^2 + mb - \frac{1}{2} + \eta_s r_b^2/a^2}. \quad (39)$$

When $mb \gg m^2 - \frac{1}{2} + \eta_s r_b^2/a^2$, n_{st} becomes

$$n_{st} \simeq \frac{\mu^2}{mb} = -\frac{(\Omega_s^{ex} \epsilon_{st})^2 \alpha r_0}{2\Omega_{x0}\Omega_{\theta 0}}. \quad (40)$$

Figure (14) shows n_{st} , n_s , $n_s(r_b/a)^2$ and $\tilde{n}_s(r_b/a)^2$ for typical parameters of the NRL modified betatron accelerator. The index $\tilde{n}_s(r_b/a)^2$ scales as γ_o^{-1} and is applicable after the wall current induced by the injected beam has decayed. Figure (15) shows the same indices for $r_b = 2$ cm. It is apparent from these figures that $n_s > n_{st}$ at injection.

It can be shown that in the presence of strong focusing the linearized electron ring centroid orbit equation in the transverse plane is¹⁴

$$\left\{ \frac{\langle P_\theta \rangle}{mcr_0} - \frac{\nu r_0^2}{a^2 \beta_{\theta i} \gamma_i^2} + \frac{\Omega_{x0} r_0}{2c} (1 - n) - \frac{(\Omega_s^{ex} \epsilon_{st})^2 \alpha r_0^2}{4c\Omega_{\theta 0}} \right\} \left(\frac{X}{r_0} \right)^2 + \left\{ -\frac{\nu r_0^2}{a^2 \beta_{\theta i} \gamma_i^2} + \frac{\Omega_{x0} r_0}{2c} n - \frac{(\Omega_s^{ex} \epsilon_{st})^2 \alpha r_0^2}{4c\Omega_{\theta 0}} \right\} \left(\frac{Z}{r_0} \right)^2 - \frac{\delta P_\theta}{mcr_0} \left(\frac{X}{r_0} \right) = \Delta, \quad (41)$$

where:

$$\frac{\delta P_\theta}{mcr_0} = \frac{\langle P_\theta \rangle}{mcr_0} + \frac{\nu}{\beta_{\theta i} \gamma_i^2} \left(\ell n \frac{a}{r_b} + \frac{r_b^2}{4a^2} \right), \quad \langle P_\theta \rangle \text{ is the averaged, canonical angular}$$

momentum over the intermediate frequency,

$$\Delta \equiv \beta_{\theta i} \gamma_i - \frac{\langle P_{\theta} \rangle}{m c r_0} - \frac{\Omega_{x0} r_0}{c} + 2\nu \beta_{\theta i} \left[\frac{1}{2} + \ell n \frac{a}{r_b} - \frac{1}{\beta_{\theta i}^2} \left(1 - \frac{1}{2\gamma_i^2} \right) \left(\frac{X_i}{a} \right)^2 \right],$$

γ_i is the normalized beam energy at injection, $\beta_{\theta i}$ is the normalized beam velocity at injection and X_i is the injection position. In contrast with Eq. (20), Eq. (41) is not based on the assumption that $\gamma^2 \gg 1$ and $\frac{\partial \Phi}{\partial t} = \frac{\partial A_z}{\partial t} = 0$. The factor of two difference in the $\ell n \frac{a}{r_b}$ in the $\delta P_{\theta}/m c r_0$ term of Eqs. (20) and (41) could be traced to this approximation.

According the Eq. (41), a beam injected on the minor axis, i.e., $X_i = Z_i = 0$ will remain on the minor axis provided its energy is selected to satisfy the condition

$$\beta_{\theta i} \gamma_i = \beta_{\theta 0} \gamma_0 = \frac{\nu}{\beta_{\theta 0} \gamma_0^2} \left(\ell n \frac{a}{r_b} + \frac{r_b^2}{4a^2} \right)$$

$$+ \frac{\Omega_{x0} r_0}{c} - 2\nu \beta_{\theta 0} \left(\frac{1}{2} + \ell n \frac{a}{r_b} \right).$$

In the NRL device the strong focusing field¹⁵ is generated by four twisted windings carrying current in alternate directions. The left-handed windings are located 23.4 cm from the minor axis and have a 209.4-cm period, i.e., there are three periods over the circumference of the torus. They are supported by epoxy-reinforced graphite jackets and have been designed to carry up to 30 kA. The windings are connected in series and the current temporal profile is controlled by a ballast inductor. Since I_{st} , $\Omega_{\theta 0}$ and Ω_{x0}/γ remain approximately constant during acceleration, n_{st} scales inversely proportional to the relativistic factor γ .

b. Injection and Trapping

A challenging physics issue of the modified betatron concept was the capture of the injected beam into the closed magnetic field configuration of the device. For successful trapping the beam has to drift fast enough during the first revolution to avoid the injector and also its poloidal orbit has to be modified in such a way that the beam will not return to the injector after a bounce period. Modification of the beam's poloidal orbit can be achieved by either changing the equilibrium position of the gyrating electrons or by reducing the radius of the poloidal orbit.

At the time the decision was made to install strong focusing windings to the device, the NRL research staff was considering three different trapping schemes. The first was based on the resistivity of the vacuum chamber's wall³³, the second on a localized toroidal electric field³⁴ that is produced by a coaxial pulseline and the third on a pulsed vertical magnetic field that is generated by conductors¹⁴ located inside the vacuum chamber. According to the linear theory, the resistivity of the wall in the NRL device was not high enough to provide the required inward shift to the beam over a bounce period. Thus, the first trapping scheme was ignored. The second, i.e., the toroidal pulseline³⁴ was adopted as the mainline trapping scheme with the third as a backup.

The toroidal pulseline was constructed and tested. However, it was never installed in the experiment, because when the current of the strong focusing windings was raised to a high enough level and the direction of the poloidal orbit was changed from diamagnetic to paramagnetic the beam spiraled near the minor axis and was trapped. This interesting phenomenon has been observed over several thousands of shots and for a wide range of

parameters. However, its explanation remained elusive until February 1991.

At the beginning of 1991, a series of detailed experiments³⁵ were carried out to measure with accuracy the various parameters associated with the trapping of the beam. As a result of these experiments a revised model of resistive trapping was developed that is in agreement with the experimental results.

The predicted decay rate Γ^{-1} from the initial linear theory for the parameters of the experiment was between 15 and 20 μsec , i.e., too long to explain the experimental results. Two modifications were introduced to the original model. First, the analysis is not restricted to beam motion near the minor axis³⁶ and therefore nonlinear effects and the fast diffusion times that scale as $\mu_0(b-a)^2/\pi^2\rho$, where $(b-a)$ is the thickness of the chamber and ρ is the wall resistivity, become important. Second, in order to take into account the intermediate motion of the beam that has been omitted in the calculation of the image fields of the beam, the wall surface resistivity was computed using the skin depth that corresponds to the frequency of the intermediate mode and not the actual thickness of the chamber.

Results from the revised resistive model are shown³⁵ in Fig. 16. The various parameters for the run are listed in Table IV. Figure 16 (a) shows the projection of the centroid's orbit on the $\theta = 0$ plane. Both the intermediate and slow (bounce) modes are apparent. Since there are six field periods for $0 \leq \theta \leq 2\pi$, the electrons perform six oscillations during one revolution around the major axis. To take into account the intermediate motion that has been neglected in the calculation of the image fields, the surface resistivity in the code was computed using the skin depth that corresponds to the intermediate frequency and

not the actual thickness of the wall.

The solid circles in Fig. 16 (b) show the positions the beam crosses the $\theta = 240^\circ$ plane. This is a realistic simulation of the experimental situation. The time difference between two circles is equal to the period around the major axis, i.e., ~ 23 nsec. The parameters of this run are similar to those in Fig. 16 (c) and the similarity of the two orbits is quite apparent. When the crossing plane is moved from $\theta = 240^\circ$ to a different azimuthal position θ , the beam orbit rotates around the minor axis. The rotation predicted by the theory is very similar to that observed in the experiment.

In most of the experiments the center of the circular opening of the conical anode was located at the midplane and 8.7 cm from the minor axis of the toroidal chamber. In a series of experiments the diode moved to progressively larger radial positions from the minor axis. Successful trapping of the beam was observed as long as the radial distance was less than 10 cm.

Table IV

Parameters of the run shown in Fig. 16

Torus major radius r_o	100 cm
Torus minor radius a	15.2 cm
Relativistic factor γ	1.5
Winding radius ρ_0	23.4 cm
Winding current I_{st}	24 kA
Vertical field at injection B_{z0}	26 G
Toroidal field $B_{\theta 0}$	4 kG
Beam minor radius r_b	3 mm
Beam current I_b	1.2 kA
Wall resistivity	8 m Ω -cm
Intermediate frequency, ω_w	$1.8 \times 10^9 \text{ sec}^{-1}$

c. Beam Dynamics During Acceleration

Following trapping the beam settles at the radial distance of 98.5 - 99.0 cm and not on the minor axis, which is located at $r_0 = 100$ cm. Since the stellarator windings have been wound using a simple winding law $\varphi = 3\theta$, where φ is the poloidal and θ is the toroidal coordinate, the magnetic axis of the windings is located at $r=98.87$ cm as shown in Fig. 17. Therefore, this result is not surprising.

The x-ray traces indicate that the beam losses are negligibly small between injection and approximately 200 μ sec. Three different diagnostics, magnetic probes, x-rays from localized targets and fibers, have shown that the beam electrons strike the inner surface of the vacuum chamber slightly above the midplane.

Due to the finite resistivity of the vacuum chamber wall the return current induced by the beam at injection decays within two to three magnetic field loop times $\tau_{00} = \frac{4\pi\epsilon_0\Delta a}{\rho c^2} \left[\ell n \frac{8r_0}{a} - 2 \right]$, where a is the minor radius of the torus and Δa its thickness, r_0 is the major radius and ρ is the combined resistivity of the wall. As a consequence of the current decay, the magnetic field of the beam diffuses into the hole of the torus.

For a beam of minor radius r_b that is located on the minor axis of a torus of major radius r_0 and minor radius a , the magnetic flux ϕ that links the beam axis is related to the vector potential $A_{\theta 0}^{in}$ at the centroid of the beam by the relation

$$\phi = 2\pi r_0 A_{\theta 0}^{in}(r = r_0, z = 0), \quad (42)$$

where³⁶

$$A_{\theta 0}^{in}(r = r_0, z = 0) = \frac{I_b}{c} \left[2 \left(\ell n \frac{8r_0}{r_b} - \frac{3}{2} \right) - 2 \left(\ell n \frac{8r_0}{a} - 2 \right) e^{-t/\tau_{00}} \right]. \quad (43)$$

The loop voltage can be computed from Eqs. (42) and (43) and is

$$V_{loop} = \frac{4\pi r_0 I_b}{r_{00} c^2} \left[\ln \left(\frac{8r_0}{a} \right) - 2 \right] e^{-t/\tau_{00}}. \quad (44)$$

For $I_b = 1$ kA, $r_0 = 1$ m, $\tau_{00} = 40$ μ sec and $a = 15.2$ cm, Eq. (44) gives $V_{loop} = 61.6e^{-t/\tau_{00}}$ (volts), and the total energy loss within $5 \tau_{00}$, i.e., when the first beam losses are observed is 120 keV.

The energy gained by the beam during $5 \tau_{00}$, when the acceleration rate is 0.8 kV/turn, is 8.0 MeV. Since at injection the beam energy is approximately 0.5 MeV, its total energy is 8.5 MeV and thus the energy mismatch is $\Delta\gamma/\gamma = 1.4\%$. At $\gamma = 18$, Fig. 14 gives $n_{st} \simeq 1.55$ and $n_s(r_b/a)^2 \simeq 0$, thus the expected shift Δr in the beam centroid is

$$\Delta r = \frac{(\Delta\gamma/\gamma)r_0}{0.5 - n_s(r_b/a)^2 + n_{st}} \simeq 0.9 \text{ cm}$$

In addition to the reduction of the beam energy to build up the fields inside the loop, some beam energy is also lost to the heating of the wall. However, this loss is typically an order of magnitude smaller than the energy loss associated with the build up of the fields.

The Larmor radius of the fast motion in the toroidal magnetic field $B_{\theta 0}$ of 5 kG at $t = 200$ μ sec is only 3 cm, even when $\beta_{\perp} = 0.5$, which is an upper limit. For $\beta_{\perp} > 0.5$ the beam equilibrium will be lost and the entire beam will strike the wall in a short period of time. Therefore, the diffusion of the self field and the finite Larmor radius cannot provide sufficient radial displacement to the electrons to reach the wall at $t = 200$ μ sec.

Figure 18 shown a typical x-ray signal. This signal lasts for several hundred microseconds. The slow loss rate is a manifestation that individual particles strike the wall rather

than the entire beam. Figure 14 shows that the individual particle self index of 1 kA, 1 cm radius beam becomes equal to n_{st} ($I_{st} = 30$ kA), when $\gamma_0 = 6.5$. At this energy the individual particle orbital stability is lost, at least temporarily and theory^{22, 37} and computer simulations³⁸ predict a substantial increase in the beam radius, when the beam electrons have even a small axial energy spread. This crossing of the individual particle instability gap is consistent with several features of the experimental results. However, the time τ_z the x-ray signal initially appears is independent of the trapped current, which is inconsistent with the fact that n_s is proportional to the beam current.

The dependence of τ_z on the toroidal magnetic field is shown in Fig. 19. In all the shots shown in Fig. 19 the peak B_z field was kept constant. However, the current in the strong focusing windings had to be raised with rising B_θ in order to provide sufficient drift to the beam and thus to reduce beam losses at the diode during the first revolution. For fixed B_θ , τ_z varies inversely proportional to the acceleration rate dB_z/dt . Figure 20 shows τ_z as a function of the peak B_z field that occurs at about 2.6 msec. This quantity is proportional to dB_z/dt . It appears that τ_z varies with B_θ and dB_z/dt the same way as the peaks of the x-ray signal.

It has been shown theoretically and confirmed with extensive numerical work that the equilibrium position of the beam is not sensitive to the transverse velocity, provided that $\beta_\perp/\beta < 0.5$. In the absence of strong focusing and space charge, the radial change of the equilibrium position Δr with β_\perp is given by

$$\frac{\Delta r}{r_0} = 2 \left[1 - (1 - \alpha^2)^{-\frac{1}{2}} + \alpha^2/2(1 - \alpha^2) \right], \quad (45)$$

where $\alpha = \beta_{\perp}/\beta$.

Equation (45) is plotted in Fig. 21. It is apparent from these results that the equilibrium position of the beam will not change noticeably, even though the beam will acquire some transverse velocity as it crosses a large number of higher ℓ resonances.

It has been determined experimentally that a betatron flux condition of 2.3 provides the best confinement to the beam*. For the same parameters TRIDIF predicts a $\langle B_z \rangle / B_{z0}$ that is in good agreement with the experiment as shown in Fig. 22a. The vacuum chamber has small effect on the betatron flux condition and only for the first 200 μsec . EFFI, a static code predicts a slightly lower flux condition. The radial profile of the normalized flux is shown in Fig. 22b. The solid solid line gives the normalized flux at $t=50 \mu\text{sec}$ for a sinusoidally varying current with a peak value of 40 kA. The rest of the parameters are listed in the figure. The dashed line shows the total rA, immediately after the injection of a 1 kA hollow electron beam. The beam is injected at 100 cm and has a radius of 1 cm. When the missing flux inside the hollow beam is taken into account, Eq. (43) is in very good agreement with the results of Fig. 22b.

*It has been reported²⁸ previously that the best results have been obtained for $\langle B_z \rangle / B_{z0} \simeq 2.0$. Since then an error was found in the calibration of B_z probe that raised this value to 2.3.

d. Studies of the Cyclotron Resonances

In a modified betatron with strong focusing there are four characteristic transverse modes. In the laboratory frame these four modes $\omega_{\pm\pm}$ are given by³⁹

$$[\omega_{\pm\pm}/(\Omega_{x0}/\gamma)] = \pm \frac{(m+b)}{2} [U + 1 \pm 2(U + 4V^2)]^{1/2} + \frac{m}{2}, \quad (46)$$

where U and V have been defined in Eqs. (34) and (35), m is the number of field periods, $b=B_{\theta 0}/B_{x0}$ and Ω_{x0} is the cyclotron frequency of the vertical field.

When $n_s \ll (b/2)^2$, $b^2 \gg 1$ and for modest winding current, as that in the NRL device, the four modes become

$$\omega_{++} \approx m\Omega_z/\gamma + \Omega_\theta/\gamma \quad (\text{High Freq. Cyclotron}), \quad (a)$$

$$\omega_{--} \approx \omega_B \quad (\text{Bounce}), \quad (b) \quad (47)$$

$$\omega_{-+} \approx -\Omega_\theta/\gamma \quad (\text{Cyclotron}), \quad (c)$$

and

$$\omega_{+-} \approx m\Omega_z/\gamma - \omega_B \quad (\text{S.F.mode}). \quad (d)$$

Integer resonances occur when

$$\omega_{\pm\pm}/(\Omega_{x0}/\gamma) = k, \quad k = \pm 1, \pm 2, \pm 3, \dots \quad (48)$$

Equations (46) and (48) are plotted in Figs. 23 to 26. Figure 23 shows the centroid integer resonances associated with ω_{--} (bounce) and ω_{+-} (SF field mode) for typical parameters

of the NRL device and before the self magnetic field of the beam diffuses out of the vacuum chamber. Figure 24 shows the same resonances as Fig. 23 but after the self magnetic field of the beam has diffused out of the chamber. The individual particle integer resonances of the bounce and SF mode are shown in Fig. 25. Finally, Fig. 26 shows the centroid integer resonances associated with the cyclotron mode ω_{-+} . When Eq. (47) is valid, the cyclotron resonance condition takes the very simple form⁴⁰ $B_{\theta 0}/B_{x 0} \approx \ell$, where ℓ is an integer $\gg 1$. Therefore, the cyclotron resonance is due to the coupling, caused by a field error(s) of the cyclotron motion associated with the toroidal and vertical fields.

It is apparent from Fig. 26 that for $I_{st} < 30 \text{ kA}$ and $\ell > 7$, the strong focusing field does not have a noticeable effect on the cyclotron resonance condition. Thus, the resonance condition is simplified to

$$\frac{r_0 \Omega_{\theta 0}}{c \gamma \beta_{\theta}} = \frac{(2\ell^2 - 1)}{2\ell}, \quad \ell = 1, 2, 3, \dots, \quad (49)$$

and it is valid even when the beam is off the minor axis.

The x-rays are monitored by three collimated x-ray detectors (scintillator-photomultiplier tube) that are housed inside lead boxes. In the results shown in Fig. 27, the x-rays enter the scintillator through a 1.94 cm-dia. tube and the detector is located 10.8 m from the vacuum chamber. As a rule, the shape of the x-ray signal recorded by all three detectors is spiky and the peaks always occur at the same value of $B_{\theta 0}/B_{x 0}$, independent of the current flowing in the stellarator windings. In addition to the x-ray pulse, Fig. 27 shows the values of ℓ on the minor axis. These values have been computed from Eq. (49) by substituting $c \gamma \beta_{\theta}$ for $\Omega_{x 0} r_0$. The ratio $B_{\theta 0}/B_{x 0}$ is computed from the measured values of

fields. A perfect match between theory and experiment requires that the peaks occur at integer values of ℓ .

It is apparent from the resonant condition that when $B_{\theta 0}/B_{z0} = \text{constant} \neq \text{integer}$, the cyclotron resonance is not excited. To test this supposition, we installed 24 single-turn coils on the outside of the vacuum chamber, as shown in Fig. 28. These coils are powered by a capacitor bank and have a risetime of approximately 100 μsec . During this time period the coils generate a toroidal field ramp that increases linearly with time and the total toroidal field increases in synchronism with the betatron field. Results from the experiment are shown in Fig. 29, when the coils are energized at 800 μsec . Beam losses are suppressed for 100 μsec , i.e., as long as the condition $B_{\theta 0}/B_{z0} \neq \text{integer}$ is satisfied.

The damage done to the beam at each resonance depends on the speed with which the resonance is crossed. By increasing the acceleration rate the resonance is crossed faster and thus the damage inflicted to the beam is reduced. To achieve higher acceleration rate, the vertical field coils were divided into two halves with midplane symmetry and powered in parallel. Figure 30 shows the x-ray signal for three acceleration rates, (dB_{z0}/dt) peak = 0.69, 1.69 and 1.93 $G/\mu\text{sec}$, for a constant $B_{\theta 0} = 4kG$. At the lowest acceleration rate the x-ray peak that corresponds to $\ell = 12$ has the largest amplitude. At the intermediate acceleration rate the amplitude of $\ell = 12$ has been reduced by a factor of two and the $\ell = 8$ becomes the dominant peak. At the highest acceleration rate the amplitude of the $\ell = 12$ peak was further reduced while the amplitude of the lower ℓ value peaks has been substantially increased.

The crossing of the resonance can be speeded up by modulating the toroidal magnetic

field with a rapidly varying ripple. This is the dynamic stabilization or tune jumping technique and requires a carefully tailored pulse to be effective over many resonances. This stabilization technique has been tested experimentally using the 24 coils that are shown in Fig. 28. These results have been reported previously¹⁹ and in general they are in agreement with the theoretical predictions and the computer calculations.

The dynamic behavior of the electron beam as it crosses the various ℓ number resonances depends on the nature and the amplitude of the field error.⁴¹ The field error(s) that excites the resonance can be either vertical ΔB_z or axial (toroidal) ΔB_θ . In the case of a vertical field error and in the absence of acceleration and strong focusing field, the normalized transverse velocity β_\perp and thus the Larmor radius of the transverse motion of the gyrating particles grows linearly with time,⁴⁰ provided that nonlinear effects associated with the particle velocity are neglected. When nonlinear effects are taken into account, β_\perp is a periodic function of time.

In the presence of an accelerating field and a large vertical field error,⁴¹ β_\perp increases proportionally to the square root of time, while $\gamma\beta_\theta$ saturates, i.e., the electrons lock-in to a specific resonance (lock-in regime). When the amplitude of ΔB_z is below a threshold, β_\perp exhibits Fresnel behavior, i.e., β_\perp grows quickly for approximately 1 μsec and then saturates until the beam reaches the next resonance. The threshold value of ΔB_z can be made larger either by increasing the acceleration rate or by adding a low amplitude ripple to the main toroidal field.

In the case of an axial field error and in the absence of acceleration, β_\perp grows exponentially with the time only for a very short period. Since β_\perp increases at the expense of

β_θ the particles are kicked off resonance. Thus, β_\perp varies periodically with time. Similarly, in the presence of an accelerating field β_\perp behaves as in the case of the vertical field error.

The previous discussion is based on the assumption that the space charge is low and the strong focusing field is zero. In addition to introducing new characteristic modes, the strong focusing field makes the expression for the regular cyclotron mode more complicated. However, it can be shown that for the parameters of the NRL device and provided $\ell \gg 1$, the strong focusing has only minor effect on the cyclotron resonance. This is also supported by extensive computer calculations.

A typical example of this behavior is shown in Fig. 31. These results have been obtained from the numerical integration of exact equations of motion for the parameters listed in Table V. The threshold value of ΔB_z in the minor axis is approximately 0.2 G for the $\ell = 9$ mode. Figures 31a and 31c show β_\perp vs. time below and above threshold, while Figs. 31b and 31d shows the corresponding $\gamma\beta_\theta$ vs. time. Since in Fig. 31d $\gamma\beta_\theta$ remains constant the resonance is never crossed [see Eq. (49)], i.e., the entire beam is lost at the same ℓ mode.

The temporal behavior of the x-ray signal (see Fig. 27) clearly indicates that only a fraction of the beam electrons may be in the lock-in regime, since we observe several ℓ modes. However, we carried out extensive experimental studies¹⁹ with several, externally applied field errors of variable amplitude. These results indicate that the entire beam was lost in a single ℓ mode whenever the amplitude of the magnetic perturbation was above a threshold value. Details about these results are given in the next section.

In addition to the nature and amplitude of the field error, the dynamic behavior of

the beam depends on the initial conditions.⁴¹ Results from the theoretical predictions are shown in Fig. 32, for the parameters listed in Table VI. Figure 32 shows contour plots of the final β_{\perp} in the $\beta_{\perp}^{(0)}, \varphi_0$ plane, where $\beta_{\perp}^{(0)}$ and φ_0 are the amplitude and phase of the asymptotic initial value of transverse velocity and its phase. In Fig. 32a the amplitude of the field error has been chosen equal to ~ 0.2 G. By increasing the field error amplitude from 0.2 G to 0.3 G, the lock-in regime has expanded for low $\beta_{\perp}^{(0)}$ over the entire range of initial phase angles as shown in Fig. 32b. When the electrons in the beam are uniformly distributed over the initial phase angle, the resonance diagram of Fig. 32 gives, for each initial $\beta_{\perp}^{(0)}$, the percentage of the beam that crosses the resonance and the percentage that locks into it. Therefore, it is not surprising that only a fraction of the electrons in the experiment are in the lock-in regime.

Following the successful demonstration of acceleration a concerted effort was made¹⁷ to locate and eliminate or reduce the field disturbances that may excite the cyclotron resonances. The sources of field errors investigated included: 1. coil misalignment, 2. coil discreteness, 3. eddy currents induced in the modified betatron support structure and nearby components, 4. errors produced from the various portholes in the vacuum chamber, and 5. two contributions from the feeds of the vertical field coils. Reduction in many of these errors together with the operation at higher B_0 and strong focusing fields led to beam energies in excess of 20 MeV, while the trapped current was above 1 kA.

Although the cyclotron resonance is a potent mechanism that has the potential to disturb the beam at low acceleration rate and when the various fields are not carefully designed, it also may provide a powerful technique²⁰ for extracting the beam from the

magnetic field configuration of the modified betatron. Results from such initial and incomplete studies are presented in the next section.

Table V

Parameters of the runs shown in Figs. 31

Torus major radius r_0	100 cm
Toroidal magnetic field B_{θ_0}	2771 Gauss
Vertical magnetic field B_{z_0}	305 Gauss
Field index n	0.5
Rate of change of vertical field \dot{B}_{z_0}	2 Gauss/ μ sec
Resonance mode ℓ	9
Amplitude of VF-error ΔB_{z_0}	0.190, 0.195 Gauss
Initial normalized toroidal momentum $\gamma\beta_{\theta}$	17.922
Initial normalized vertical velocity β_{\perp}	0.0
Initial radial displacement $r - r_0$	0.0 cm
Initial vertical displacement z	0.0 cm

Table VI

Parameters for the results shown in Fig. 32

Torus major radius r_0	100 cm
Toroidal magnetic field $B_{\theta 0}$	2771 Gauss
Field index n	0.5
Rate of change of vertical field \dot{B}_{z0}	2 Gauss/ μ sec
Resonance mode ℓ	9
Amplitude of VF-error ΔB_{z0}	0.2, 0.3 Gauss
Initial normalized toroidal momentum $\gamma\beta_{\theta}$	17.922

e. Preliminary Beam Extraction Studies

The results of the NRL modified betatron accelerator have unambiguously demonstrated that the toroidal and strong focusing fields improve the current carrying capability of the device. However, these field also make the extraction of the beam from the magnetic field configuration substantially more involved.

In 1988, an extraction scheme was reported²⁰ by the NRL research staff that is easily realizable and has the potential to lead to high extraction efficiency. Briefly, this extraction scheme is based on the transformation of the circulating electron ring into a stationary helix, in the toroidal direction, by excitation of the resonance that naturally exists for some specific values of the ratio of the vertical to toroidal magnetic field. Transformation of the ring into a helix is achieved with a localized vertical magnetic field disturbance that is generated by an agitator coil. As the minor radius of the helix increases with each passage through the gap of the agitator coil, the electrons eventually reach the extractor, which has the property that all the magnetic field components transverse to its axis are equal to zero. Thus, the electron ring unwinds into a straight beam.

The hardware for this mainline extraction approach was designed and fabricated. However, it never was installed in the experiment. The reason is that it requires a beam with low transverse velocity because the aperture of the agitator is small. There is evidence that the beam in the NRL device has substantial transverse velocity. As a consequence of this difficulty we pursued some alternate extraction approaches that do not require beams with low transverse velocity.

At the beginning of summer in 1991, while the beam dynamic stabilization experiments¹⁹

with twelve external coils were underway, we observed that the beam could be kicked out^{18, 19} of the magnetic field within a time that is comparable to the risetime of the current pulse, whenever the twelve coils were initiated while the beam was crossing the $\ell = 12$ resonance. Figure 33a shows the x-ray pulse when the resonant coils are off and Fig. 33b when the coils are on. The amplitude of the current pulse is 9 kA and its full risetime 12 μsec . The measured amplitude of the axial field disturbance ΔB_z at the center of the coil is ~ 240 G and its risetime 32 μsec . It is apparent from these results that the full width at half maximum (FWHM) of the x-ray signal has been reduced from approximately 900 μsec to 8 μsec (Fig 33c), i.e., by more than two orders of magnitude while its amplitude has increased by a factor of thirty. In the results shown in both Figs. 33a and 33b the toroidal magnetic field on the minor axis $B_{\theta 0}$, at injection, is 4.2 kG, the current flowing through the strong focusing windings is approximately 26.5 kA and the trapped beam current about 1 kA.

In a series of experiments with the twelve external coils the current flowing through them was changed by more than a factor of two. The results show that the FWHM of the x-ray signal varies inversely with the current in the coils as shown in Fig. 34.

In the results described so far, the twelve coils were divided into two groups that were connected in parallel while the six coils of each group were connected in series. By connecting all the twelve coils in parallel the current pulse risetime was reduced to 5 μsec , while the field risetime was reduced to approximately 6 μsec . Even shorter risetime pulses have been obtained with a set of internal coils. These coils are wound on blue nylon forms and encapsulated with epoxy. The 21 cm radius, single turn coils were mounted at the

joints of the vacuum chamber sectors. Six new drivers that produced a current pulse with risetime of $0.4 \mu\text{sec}$ powered the twelve coils. Each driver powered a pair of coils connected in parallel, with a combined inductance of 270 nH . All the drivers were triggered by the same trigger generator. The circuit of a driver and the multiple trigger generator are shown in Fig. 35.

Figure 36 shows the axial component of the field in free space and also in the presence of lateral walls. The geometry and the parameters used in the TRIDIF Code are given as inserts in the figure. As expected, the walls substantially reduce the amplitude of the field even at the radial distance of 12 cm . On the minor axis the reduction is even greater.

The width of the x-ray pulse depends on the risetime of the current pulse. The results are shown in Fig. 37. In addition, the results indicate that for the twelve coil configuration, the amplitude of ΔB_z field pulse required to extract the entire beam during the risetime of the field pulse is approximately 80 G .

To determine the toroidal distribution of the beam losses when the internal coils are energized a $400\text{-}\mu\text{m}$ diameter optical fiber was mounted on the outside of the vacuum chamber. By the time the $\ell=12$ resonance is crossed, the electrons have acquired sufficient energy to penetrate the chamber. The light generated when the electrons strike the fiber is monitored with a PM tube. Initially, a small section of the fiber was placed in different poloidal positions at a fixed toroidal angle. These measurements confirmed our previous conclusion that the electrons strike the wall of the vacuum chamber at its inner radius. In all the subsequent measurements the active length of the fiber was selected equal to half the poloidal (minor) circumference of the chamber and was placed symmetrically around

the midplanes at the inner radius of the torus.

The results from scanning around the torus at 10° intervals are shown in Fig. 38. There are six distinct peaks, separated by 60° . The three dominant peaks have approximately the same amplitude.

Figure 39 shows results from the numerical integration of orbit equations for the beam centroid near the $\ell=12$ cyclotron resonance. The values of the various parameters for the run are listed in Table VII. Figure 39a shows the projection of the beam centroid orbit in the transverse plane and Fig. 39b shows the same orbit on an expanded scale. The arrows indicate the direction of motion. Since the ratio of the toroidal cyclotron frequency Ω_θ/γ to the intermediate frequency ω_w is equal to $\ell/m = 2$, the beam centroid performs two revolutions (fast motion) around its guiding center during a single revolution in the strong focusing fields of the windings. The projection of the orbit in the (r, θ) plane is shown in Fig. 39c. There are six radial minima that occur at approximately the same toroidal angle as those of Fig. 38. However, in contrast with Fig. 38, all the peaks have the same amplitude. Figure 40 shows similar results from the crossing of $\ell = 9$ resonance. In this case $\frac{\Omega_\theta/\gamma}{\omega_w} = \frac{3}{2}$. This ratio is also manifested in the results of Fig 40c. For every three peaks, two are the same.

Under normal operating conditions the current that produces the strong focusing field is passively crowbarred and the fields decay with a long time constant L/R , where L is mainly the inductance of a ballast inductor that is in series with the windings. To test the effect of the strong focusing field on the distribution of beam loss, the ballast inductor was removed and the circuit was actively crowbarred. The shape of the current pulse

is a half sine with a half period of $\sim 650 \mu\text{sec}$. The beam is injected near the peak of the pulse. Thus, the strong focusing field is practically zero when the resonant coils are energized. Under these conditions most of the beam is lost at a single toroidal position near $\theta=70^\circ$. Both the amplitude and the toroidal position of the peak remained intact when the vacuum chamber and thus the strong focusing windings that are permanently attached to it were rotated clockwise 30° . This result implies that neither field errors associated with the stellarator winding nor the return current are responsible for the formation of the peak. In addition, we have not observed any noticeable modification in the peak by shifting the vacuum chamber radially inward by $\sim 0.3 \text{ cm}$ along the radial line that passes through the $\theta=90^\circ$ and 270° toroidal positions.

However, we have observed a substantial modification in the loss spectrum when the feeds of the vertical coils that are located just above and below the midplane were rotated from $\theta=60^\circ$ to $\theta=270^\circ$. It has been determined using a very accurate, figure eight magnetic probe that the feeds of this coil pair produce a substantial radial field error.

To test the feasibility of driving the beam to the wall on the time scale of one revolution around the major axis, the risetime of the current pulse had to be shortened and a new low inductance agitator with large aperture to be invented. The low inductance, small aperture agitator of the mainline extraction approach was not suitable, because it requires beams with low transverse velocity. Unfortunately, the amplitude of the various field imperfections in the NRL device was never reduced to low enough level and thus the beam acquired substantial transverse velocity during its long confinement time.

Among the various concepts considered, magnetic cusps were found to be the most

promising. Extensive numerical studies of several cusp configurations have shown that a single layer, 24.2 cm long cusp surrounded by a resistive ($\sigma=60$ mho/cm) shroud could provide sufficient displacement to the beam over a 20 nsec time period. This wide, 12 coil cusp system is shown in Fig. 41. Unfortunately such a cusp could not be fabricated on time and thus we had to proceed with an inferior agitator that is based on three double cusps that are located 120° apart in the toroidal direction. This agitating system was fabricated in-house and tested in the experiment for a short period of time just before the termination of the MBA program.

Each of the three double cusps consists of four coils. The first pair of coils is located ± 3.73 cm from the symmetry plane of the cusp and the second ± 5.92 cm. The coils are wound on thin toroidal forms made of epoxy reinforced graphite fibers and are encapsulated with epoxy. An axial slot in the coil form allows fast penetration of the fields. The double cusps are mounted inside the vacuum chamber and are fed with demountable copper electrodes that enter the vacuum chamber at the ports. A photograph of one of the double cusps is shown in Fig. 42.

Figure 43 shows the axial profiles of radial and axial fields. The solid line is from the TRIDIF code. The code assumes that the temporal profile of the current I_c in the four coils is given by

$$I_c = 1000 \sin \left[\frac{\pi t(\text{nsec})}{2 \cdot 400} \right] \quad (A),$$

and the wall of the vacuum chamber consists of two materials with conductivity

$$\sigma = \begin{cases} 160 \text{ mho/cm, for } 15.2 \leq \rho \leq 15.45 \text{ cm,} \\ 800 \text{ mho/cm, for } 15.45 \leq \rho \leq 15.55 \text{ cm,} \end{cases} \quad (50)$$

where ρ is the radial distance from the minor axis. The conductivity and thickness have been selected to give the same surface conductivity as in the experiment. The peak magnetic energy is 0.77 joules that corresponds to a coil inductance of $1.54 \mu\text{H}$. The solid circles in Fig. 43 are the measured values of the fields at $\rho=10.8 \text{ cm}$. It is apparent that there is good agreement between the experiment and the code. All three double cusps were not identical. In two of them the coil minor cross section was a semi-circle with the flat surface of the copper away from the minor axis and at the radial distance of 14.7 cm.

Figure 44 gives the axial profiles of the fields for a double cusp when the coil radius is 14.7 cm, the compound wall has a conductivity as that given in Eq. (50), the peak current in the coils is 3 kA and its risetime (quarter period) 20 nsec. These fields have been used in the beam centroid code to determine the displacement of the centroid in three revolutions (60 nsec). Results are shown in Fig. 45 for the parameters listed in Table VIII. Figure 45a shows the projection of the beam centroid orbit in the transverse plane. At $t=0$ the centroid is located 10.0 cm away from the minor axis. During the last 20 nsec of the run, i.e., during one revolution around the major axis the centroid is displaced by 0.9 cm. This radial displacement is almost sufficient for a small radius beam to avoid hitting the septum of the extractor. Obviously, larger radial displacements can be obtained either by increasing the current of the cusps or by tapering the radii of the cusp coils to reduce the positive component of B_ρ . A top view of the orbit is shown in Fig. 45b.

Figure 46a shows the projection of the beam centroid orbit in the transverse plane for

the same parameters as the run of Fig. 45 but artificially setting the positive component of $B_p = 0$. Comparison of the two figures clearly demonstrates the advantage of using a single polarity cusp. The radial displacement of the beam centroid in one revolution has increased by $\sim 30\%$. Figure 46b shows a top view of the orbit.

In the runs of Figs. 45 and 46 the various parameters of the beam centroid have been carefully selected to satisfy the $\ell = 12$ resonance condition. During the initial phase, i.e., for about 10-20 nsec the centroid transverse velocity is low and the orbit projection in the transverse plane is a triangle as shown in Fig. 47a. This figure shows the projection of the orbit for 20 nsec. The values of the various parameters are the same as in the run shown in Fig. 45, except for the initial radial position that is 10.5 cm instead of 10.0 cm and the cusp current, which is zero. With the cusps off, the beam remains in resonance for a long time and the orbit precession is small. With the cusps on, the centroid acquires transverse velocity, falls off resonance and start to precess rapidly. Figure 47b shows the three component of the magnetic field seeing by the centroid. As a result of the proximity of the orbit to the windings, the magnetic field components at the orbit are substantially different than those listed in Table VIII.

It became apparent in the Spring of 1992 that because of severe time and several other constraints the experiment was operating under, the only realistic approach to obtain short risetime current pulses to drive the double cusps was the sharpening of the pulse of the existing drivers using ferrites. The sharpening results from the change of permeability that occurs when a ferrite material is driven into saturation. Ferrite pulse sharpeners have been built and tested by earlier workers and their results have been documented in

the published literature.⁴²

The ferrite loaded transmission line consists of a $5/32''$ - diameter inner conductor and a braided outer conductor slipped over an acrylic insulating tube. A cross sectional view of the line is shown in Fig. 48a. The inner diameter of the acrylic tube is $1/2''$ and its outer diameter is $5/8''$. The ferrites used were Krystinel K01 toroids with dimensions $3/16''$ ID, $3/8''$ OD and $1/8''$ thick. All intervening spaces were filled with epoxy or oil. The potted ferrite line was found to give results almost identical to those obtained from an oil immersed line.

Figure 48b shows a schematic diagram of the experiments setup used to develop the ferrite pulse sharpeners. An 80-nF capacitor charged to voltages ranging from 35 kV to 60 kV DC, delivers a voltage pulse into a 45-foot-long, $50\ \Omega$ cable. A Rogowski coil monitors the current delivered to the cable. A 3-foot long ferrite loaded line sharpens the pulse from the $50\ \Omega$ cable, and transmits the sharpened pulse to another 25-foot-long $50\text{-}\Omega$ cable short-circuited at one end. A Rogowski coil placed between the ferrite line and the 25-foot line, measured the waveshape of the sharpened current pulse.

At 50-kV charge voltage the amplitude of the first current step in the 45-foot, 50Ω cable is 1 kA. The ferrites saturate even before the current reaches 0.1 kA. The risetime of the current pulse, as measured by ROG1 is ~ 25 ns. The risetime of the sharpened pulse measured by ROG2 is ~ 3 ns. The presence of the Rogowski coil introduces added inductance in the cable connections. Since, the Rogowski coil has a response time of ~ 1 ns, the intrinsic risetime of the pulse is therefore ~ 2 ns. For optimum performance, the saturated characteristic impedance of the ferrite line needs to be the same as the impedance

of the cables on either end of the line. The impedance of the ferrite line shown in Fig. 48a appears to be 50Ω . However, this requires a relative permeability of ~ 3 after saturation, as opposed to the ideal value of unity.

The cables on either side of the ferrite line isolate it from reflections from the load (short-circuit, here) and the spark gap switch, for the duration of the round trip transit time in each cable. If the ferrite line is made longer than the length needed to erode the injected current risetime, then the flattop is also eroded and the 45-foot cable needs to be made longer to compensate for this effect.

Figure 48c shows the layout of the drivers that powered the double cusps. Two 50Ω ferrite sharpeners drive each coil. At 40 kV charge voltage the average amplitude of the first current step is 2.6 kA and the risetime is approximately 50 nsec and is solely determined by the effective inductance of the coil.

Typical results from the experiment are shown in Fig. 49. The important parameters are listed in Table IV. Figure 49a shows the x-ray signal with the cusps off and Fig. 49b shows the x-ray signal when the three cusps are energized at $480 \mu\text{sec}$, i.e., when the $\ell=12$ resonance is crossed. As in Fig. 33, most of the beam exits the magnetic field configuration in a single ℓ mode, although the current through the coils is substantially lower. The high frequency noise that is observed in Fig. 49b is a consequence of the fact that the $1.5 \mu\text{sec}$ integrator that has been used in the input of the digitizer in Fig. 49a was removed to avoid possible reduction of the sharp x-ray pulse when the cusps are activated.

A difficulty experienced during these studies was the substantial jitter of the drivers. Apparently, the cause of this difficulty was the roughness of the electrodes in the switches

of the drivers. Unfortunately, the overhauling of the spark gaps could not be fitted into the time schedule of the experiment.

Table VII

<u>Parameters</u>	<u>Fig. 39</u>	<u>Fig. 40</u>
Major radius r_0	100 cm	100 cm
Torus minor radius a	15.2 cm	15.2 cm
Winding radius ρ_0	23.4 cm	23.4 cm
α	0.03 cm^{-1}	0.03 cm^{-1}
Winding current I_{st}	20 kA	20 kA
Toroidal field $B_{\theta 0}$	3400 G	3400 G
Vertical field B_{z0}	308 G	410 G
Ext. field index n	0.5	0.5
dB_z/dt	$0.85 \text{ G}/\mu\text{sec}$	$0.85 \text{ G}/\mu\text{sec}$
Initial γ	16.555B	22.389
Initial radial position	-8.26 cm	-7.789
Initial vertical position	1.83 cm	0.283
Mode number ℓ	12	9

Table VIII

Major radius r_o	=	105 cm
Torus minor radius a	=	15.2 cm
Winding radius ρ_o	=	23.4 cm
α	=	0.029 cm^{-1}
Field periods m	=	6
Toroidal field $B_{\theta 0}$	=	3910 G
Vertical field B_{z0}	=	391 G
External field index	=	0.5
dB_z/dt	=	$0.656 \text{ G}/\mu\text{sec}$
Cusp radius	=	14.7 cm
Cusp current	=	3 kA
Initial position	=	-10 cm
Initial γ	=	20.25
Run duration	=	60 nsec
Initial β_{\perp}	=	0
Mode number ℓ	=	12

Table IX

Toroidal magnetic field at injection	4 kG
SF windings current at injection	28 kA
Driver voltage	35 kV
Average amplitude of the first current step	2.2 kA
Pressure	4×10^{-6} torr
Trapped beam current	1.2 kA

V. Assessment of results

The purpose of this section is to assess the results of the experimental effort. In addition to briefly addressing the major successes and failures of the project, we discuss the level of understanding of the various physical processes that dominate the beam dynamics in the device and we make a few recommendations about the direction of future research in this area.

In the absence of strong focusing, we were able to trap a large number of electron in the device. Although the trapped electron current was as high as 3 kA, the lifetime of the electron ring was limited to a few microseconds. With the exception of the high current rings (~ 3 kA), the beam was centroid unstable, i.e., the entire beam drifted quickly to the wall of the vacuum chamber. The high current rings were suffering initially individual particle losses, i.e., slow decay of their current. Eventually, after their current was reduced to a low level the loss became catastrophic.

Probably without exception all the electron rings formed were in the high current regime. Attempts to form rings in the low current regime have been unsuccessful. The reason is that the reduced beam current could not provide enough drift to the beam during the first revolution for the electrons to clear the diode of the injector.

There is convincing evidence, but no actual proof, that the catastrophic beam loss was due to the drag instability. There is a large amount of experimental results which supports this conclusion. If we had succeeded to form stable rings in the low current regime, such a conclusion would be more definite.

A quantity that can be measured accurately in the device is the bounce frequency. As

a rule, the bounce frequency measured in the experiment was higher than that predicted by the theory and the codes. It is likely that the beam energy used to compute the bounce frequency is not known with sufficient accuracy.

The addition of the strong focusing windings made a dramatic improvement in the confining properties of the device and established the modified betatron as the first and, as of today, the only successful recirculating high current accelerator. And this, in spite of the fact that the windings have not been carefully fabricated or accurately positioned in the device.

Needless to say that this was the outcome of a necessity rather of a choice and it is contrary to the accepted practice in the technology of particle accelerators. To improve the accuracy of the strong focusing windings a new vacuum chamber was designed with embedded modular windings. It incorporates a new winding law that has a highly desirable feature. The magnetic and geometric axes coincide. Before potting, the windings were positioned on the surface to the vacuum chamber with an estimated accuracy of $\sim \pm 0.5$ mm, using a winding machine. Unfortunately, the fabrication of the new vacuum chamber was not completed on time and thus the chamber never installed and tested in the experiment.

This is regrettable, because there are strong indications that the random spatial fluctuations of the stellarator windings are responsible for the excitation of the cyclotron resonance. Figure 50 shows β_- and $\gamma\beta_\theta$ of the beam centroid in the fields of the modified betatron. The model assumes that the stellarator windings are made of 10 cm long segments that are randomly positioned at each end, within a cube of ± 2 mm. The reference

particle is injected with $\gamma = 8.864$, just before it reaches the $\ell=24$ resonance. At $t=50$ μsec , the centroid locks in the $\ell=19$ mode and its $\gamma\beta_z$ remains constant. At $t=60$ μsec β_\perp is approximately 30% and the diameter of its fast orbit ~ 7 cm. The efficiency of transferring energy from the axial to the transverse direction by the random fluctuation of the strong focusing winding is remarkable.

The trapping of the injected beam into the closed magnetic field configuration of the device was one of the most challenging physics issues of the modified betatron program. For this reason a large fraction of the program's resources was invested to develop several injection schemes. Ironically, none of these trapping schemes was used in the device after the installation of strong focusing windings. The reason is that when the current of the strong focusing windings was raised to high enough level and the direction of the poloidal orbit was changed from diamagnetic to paramagnetic the beam spiraled from the injection position to the vicinity of the minor axis and was trapped.

This interesting phenomenon has been observed over several thousands of shots and for a wide range of parameters. However, its explanation remained elusive until the beginning of 1991. During January and February, 1991, a series of detailed experiments were performed that provided accurate data on the various processes associated with the trapping of the beam. As a result of these measurements, a revised model of resistive trapping was developed that is in agreement with the experimental results. The fact that the revised model explains not only the main features but also esoteric details of the experimental results, such as the rotation of the peaks of the poloidal orbit with the poloidal angle, makes us believe that the model is correct.

In most of the experiments the center of the circular opening of the conical node was located at the midplane and 8.7 cm from the minor axis of the toroidal chamber. In a series of experiments the diode moved to progressively larger radial positions from the minor axis. Successful trapping of the beam was observed as long as the radial distance was less than 10 cm. At this radial distance the stellarator fields are nonlinear and increase rapidly as the distance from the minor axis increases. Since the radius of the intermediate orbit is proportional to the strong focusing field, it is possible that the beam strikes the wall. Therefore, in order to successfully trap the beam the injection position should be carefully selected.

The slow electron loss rate during acceleration is a manifestation that individual particles, rather than the entire beam, strike the wall. The x-ray signal initially appears at approximately $t = \tau_z = 200 \mu\text{sec}$ and lasts for as long as 1 msec. Following trapping the beam settles on the magnetic axis of the strong focusing system, which is located about 1 cm off the minor axis. If the guiding center of the beam centroid had remained on the magnetic axis during acceleration, the Larmor radius of the fast motion could not bring the electrons to the wall of the vacuum chamber. Only sufficient axial energy spread in the beam can provide appreciable displacement to the electrons in order to reach the wall. This axial energy spread cannot be due to scattering of beam electrons with the background gas, because τ_z would be a function of the pressure, which is not the case. Random field fluctuations produced by random displacement of say the strong focusing windings have the potential to introduce large axial energy spread to the beam. This conclusion is supported by computer calculations but it has not been confirmed experimentally.

A beam radial drift in combination with the fast motion provide a second mechanism for the electrons to reach the wall. The diffusion of the self magnetic field of the beam cannot provide sufficient radial displacement to the electrons to reach the wall of the chamber. Random spatial fluctuations in the strong focusing windings can provide a potent mechanism for transferring energy to the transverse direction and also a radial inward drift to the beam.

Figure 51 shows very recent results from a 261 μsec long run for randomly positioned stellarator windings. The cube dimensions have increased from ± 2 mm to ± 4 mm. The rest of the parameters are listed in Table X. The column in the left shows the positions the beam centroid crosses the $\theta = 0$ plane in the time interval indicated in each frame. The column in the right shows the temporal profile of β_{\perp} and $\gamma\beta_{\theta}$. At $t \approx 8\mu\text{sec}$, the beam locks in the $\ell = 24$ mode and shortly thereafter $\gamma\beta_{\theta}$ remains constant up to 150 μsec . At this time and while β_{\perp} has reached 78%, the beam unlocks from the $\ell = 24$ resonance and its β_{\perp} starts to decrease. Simultaneously, the centroid starts to drift radially inward with a speed which is approximately 1 mm / μsec . At 261 μsec the beam centroid hits the wall just above the midplane. The similarity between these results and the experiment is striking. Several additional runs have shown that a substantial fraction of electrons inside the beam are not unstable to this kind of perturbations.

Although the mechanism that drives the electrons to the wall during acceleration has probably been identified, a definite proof is still missing. A diagnostic that can provide information on the beam position during acceleration would be very useful. The experimental results from the NRL device have unambiguously demonstrated that the electron

loss is reduced and the beam lifetime is prologued with increasing toroidal field. The beneficial effect of B_θ is not limited to the confinement of the beam during acceleration. As a rule, the trapped electron current is enhanced with increasing B_θ field.

Since the initial successful acceleration of electrons in the modified betatron, the x-ray signal is spiky and the peaks always occur at the same value of $B_{\theta 0}/B_{z0}$, independently of the current flowing in the stellarator windings. There is extensive experimental evidence that support the hypothesis that the spiky x-ray signal is caused by the excitation of the cyclotron resonances. During the last few years a large amount of work, both experimental and theoretical, has been done, mainly by the NRL research staff, on the crossing of cyclotron resonances and the subject appears to be well understood.

The cyclotron resonance is due to coupling, caused by field disturbances, between the cyclotron motions in the vertical and toroidal fields. Since the actual accelerating gradient in the present device is low, the electrons have to perform a large number of revolutions around the major axis in order to obtain large energies. Thus, cyclotron resonances are of special importance for the existing device, that has low tolerance to field errors.

Following the successful demonstration of acceleration a concerted effort was made to locate and eliminate, or at least reduce, the field disturbances that may excite the cyclotron resonances. Most of the errors detected were reduced to a level that was limited by the sensitivity of the magnetic field monitors ($\sim 2\%$). To reduce the errors produced by the mispositioned strong focusing windings a new vacuum chamber with very accurately positioned windings was constructed and partially fabricated. The large amplitude errors at the feeds of the vertical field coils were never corrected, mainly because the cost of

repair was beyond the limits of the project's budget.

Three different cyclotron resonance stabilization techniques were tested in the experiment. Among these techniques, acceleration of the beam at higher acceleration rate appears to have the highest practical potential. By increasing the acceleration rate the resonance is crossed faster and thus the damage inflicted to the beam is reduced. To achieve higher acceleration rate, the vertical field coils were divided into two halves with midplane symmetry and powered in parallel. The experimental results indicate that an increase in the acceleration rate by approximately a factor of 2.5 has a profound effect on the cyclotron resonances.

Although the cyclotron resonance is a potent mechanism that has the potential to disturb the beam at low acceleration rate and when the various fields are not carefully designed, it also may provide a powerful technique for extracting the beam from the magnetic field configuration of the modified betatron. As a matter of fact, this was realized well before the cyclotron resonances were observed in the NRL device.

Although the fabrication of the hardware for the resonant extraction approach that was the mainline extraction scheme for the NRL device was completed by the end of FY 91, the resonant extraction was never tested experimentally. The reason that this extraction technique is based on a low inductance (~ 4 nH) agitator with a very small aperture (~ 2 cm). Therefore, it requires a beam with low transverse velocity. However, this was not the case in the NRL experiment. The amplitude of the various field imperfections was never reduced to a low enough level to make the transverse velocity of the beam compatible with the small aperture of the agitator. Thus, we had to explore alternate extraction approaches

that are based on large aperture agitators.

Initially, twelve single turn coils were used either on the outside of the vacuum chamber or at the joints of twelve sectors. The coils were activated at the time the beam was crossing the $\ell=12$ mode. These resonant coils were powered with 12, 5 and 0.4 μsec risetime current pulses. The beam could be kicked out of the magnetic field of the device within a time that was comparable to the risetime of the current pulse. The required amplitude of axial field disturbances ΔB_z to extract the entire beam during the risetime of the field pulse is approximately 80 G.

Extensive studies of the spatial distribution of beam losses when the twelve internal resonant coils are energized with the 0.4 μsec current pulse have shown that the beam strikes the wall at six very well defined toroidal positions that are 60° apart. In the absence of the strong focusing field (when the resonant coils are energized) the beam strikes the wall at a single toroidal position near $\theta=70^\circ$. Although the results with the twelve resonant coils are very interesting and provided a valuable insight in the physics of extraction, this approach cannot lead to a practical extraction scheme, since it cannot form a single head in the beam. In addition to being capable of forming a single, well defined head in the beam, a practical agitator should have low inductance, large aperture and the capability to produce the required magnetic field disturbances at manageable voltages. Among the various agitator concepts considered, magnetic cusps were found to be the most promising.

Extensive numerical studies of several cusp configurations have shown that a single layer, 24.2 cm long cusp surrounded by a resistive shroud with a 21 cm radius could provide ~ 1.4 cm radial displacement to the beam over a 20 nsec time period, when the current

through the coil is 2.5 kA. Unfortunately such a cusp could not be fabricated on time and thus we had to proceed with an inferior agitator that is based on three double cusps that are located 120° apart in the toroidal direction. This agitating system was fabricated in-house and tested in the experiment for a short period of time just before the termination of the MBA program.

The numerical results indicate that the 14.7 cm radius double cusps could provide 0.9 cm radial displacement during the last 20 nsec of a 60 nsec wide, 3 kA height rectangular current pulse. These cusps have been powered with 2-3 nsec risetime current pulses produced from the existing drivers with ferrite sharpeners. At 40 kV charge voltages the amplitude of the current step was 2.6 kA and its risetime ~ 50 nsec and was solely determined by the inductance of the coil. Activation of these double cusps at 480 μ sec, i.e., when the $\ell=12$ resonance is crossed forced most of the beam to exit the magnetic field configuration in a single ℓ mode, as it is apparent from Fig. 49.

In contrast with the conventional accelerators that operate in the single-particle regime, the high current modified betatron operates in an uncharted territory, in which space charge effects from the self and image fields are as important as externally applied fields. Virtually, every aspect of the modified betatron has been a challenging technical task. As a result, the pace of progress has been slower than initially anticipated. However, the results have been very rewarding.

The extraction of the beam is presently the most important unresolved technical issue. Although some interesting results were obtained during the last few month with the NRL device, there are several fundamental questions that remain. Developing a large aperture

agitator with 1-2 nsec risetime that provides enough field to kick the beam radially by $\sim 2-3$ cm at a reasonable voltage is not, in principle, a difficult task. However, when the integration of such an agitator into the device is considered, the task becomes considerably more complex. Specifically, the penetration of the fast fields requires the agitator to be located inside the chamber. To avoid any interference with the circulating beam the agitator should be near the wall of the chamber. This wall has to be continuous to avoid disruption of the return currents. The induced current on the wall by the rapidly changing field of the cusp substantially reduces its various field components. However, the proximity of the coils to the wall diminishes the inductance of the kicker. Although the voltage required to produce a specific field amplitude within a specific time is smaller with an internal cusp, introducing the high voltage into the chamber without adding substantial inductance to the system is a challenging engineering task.

Our diagnostics that probe the beam dynamics during the first few microseconds following injection, have been found both reliable and sufficient. However, our diagnostics that provide information on the beam current, position, size, axial energy spread and emittance during the acceleration phase have been found very inadequate. The development of such diagnostics that provide reliable information on the millisecond time scale will be both difficult and expensive. Such a task, however, will be necessary in any serious future effort on the modified betatron or any other high current recirculating accelerator.

Our results have unambiguously demonstrated that the strong focusing windings improve the confining properties of the device at least in the intermediate time scale, i.e., during the first 100-200 μsec . In addition, these windings have increased substantially the

complexity of the accelerator. The loss of toroidal symmetry with the incorporation of the stellarator windings in the NRL initial system made our two dimensional particle simulation computer codes obsolete. The absence of a reliable 3-D computer simulation code to provide information on the dynamics of the individual particles inside the beam has inhibited our ability to completely understand the x-ray spectra. Any future investment in the modified betatron technology should include funds for either the development or the acquisition of a 3-D particle simulation code.

Undoubtedly, the modified betatron has several important advantages, in relation to other approaches, in the generation of high current beams. Among its shortcomings, its sensitivity to field errors is of concern. The port in the wall of the vacuum chamber that is required for any internal injection could be the source of a serious field error. By its nature, the injector porthole error cannot be eliminated as long as the diode is located inside the chamber. Therefore, it is advisable that an external injection scheme be developed that will eliminate or at least substantially reduce the size of the diode porthole. An additional advantage of the external injection is its compatibility with higher diode voltages. Such higher voltages will be necessary whenever the current of the device will be required to be raised well above the 1 kA level.

As a consequence of its sensitivity to field errors, any future device should be carefully designed to keep the field errors as low as possible but not much higher than 0.1%. Furthermore, it will be very advantageous to select the acceleration rate ten times higher than in the present device, i.e., about 8-10 G/ μ sec.

Table X

Major radius r_o	= 100 cm
Torus minor radius a	= 15.2 cm
Toroidal magn. field $B_{\theta o}$	= 3 kG
Vertical magn. field B_{zo}	= 120 G
Relativistic factor γ at inj.	= 7.02
α	= 0.03 cm ⁻¹
Minor radius of windings ρ_o	= 23.4 cm
Current in the St. windings	= 25 kA
dB_z/dt	= 0.69 G/ μ sec
Initial radial position (r-r _o)	= - 0.14 cm
Initial vertical position Z	= 0.0 cm
Initial transverse velocities $v_r = v_z$	= 0

References

- * FM Technologies, Inc., 10529-B Braddock Road, Fairfax, Virginia
- † SFA, Inc., Landover, Maryland 20785
- ** Science Applications International Corp., 170 Goodridge Drive, McLean, Virginia 22102
1. R. C. Davidson, *An Introduction to the Physics of Nonneutral Plasmas*, Addison-Wesley Publ. Co (1990). Chapter 4 of this book contains a comprehensive list of theoretical papers on the modified betatron.
 2. P. Sprangle and C.A. Kapetanakis, *J. Appl. Phys.* 49, 1 (1978).
 3. D. Kerst and J. Lawson, private communication.
 4. D. Kerst, *Phys. Rev.* 60, 47 (1941); also *Encycl. of Appl. Phys.* 2, 347 (1991).
 5. P. J. Gratreau, U. S. Patent Number 3, 377, 563 (1968).
 6. A. G. Bonch - Osmolovsky, Joint Institute for Nuclear Research, Dubna, USSR, Preprint No. P9-5299 (1970). Translated by G. Brodell and L. Jackson Laslett, UCRL- Trans. -1446 (1971).
 7. G. I. Budker, *Proc. of the CERN Symposium on High Energy Accel. and Pion. Phys.*, Geneva, Switzerland (1956).
 8. J. G. Linhart, *Proc. of the 4th Conf. on Ion. Phen. in Gases, Uppsala* (1959); Also *Plasma Phys.* (1960).
 9. P. Reynolds and H.M. Skarsgard, *J. Nucl. Energy Part. C1*, 36 (1959).

10. H. Ishizuka, R. Prohasko, A. Fisher, and N. Rostoker, in *Proceedings of the 7th International Conference on High-Power Particle Beams* (Kernforschungszentrum Karlsruhe GmbH, Karlsruhe, Germany, 1988), Vol II, p. 857; Also H. Ishizuka, G. Leslie, B. Mandelbaum, A. Fisher and N. Rostoker, *IEEE Trans. Nucl Sci.* NS-32, 2727 (1985).
11. J. Golden, F. Mako, L. Floyd, K. McDonald, T. Smith, D. Dialetis, S. J. Marsh and C.A. Kapetanacos, *Proc. of the 6th Intern. Conf. on High-Power Particle Beams*, Kobe, Japan, P. 709 (1986).
12. J. Golden, L. K. Len, A. V. Deniz, J. Mathew, T. J. Smith, P. Loschialpo, J. H. Chang, D. Dialetis, S. J. Marsh and C. A. Kapetanacos, *Proc. of the 7th Intern. Conf. on High Power Particle Beams*, 88 Karlsruhe, FRG, Vol. I, 221 (1988).
13. C. Roberson, A. Mondelli, and D. Chernin, *Phys. Rev. Lett.* 50, 507 (1983).
14. C. A. Kapetanacos, D. Dialetis and S. J. Marsh, *Part. Accel.* 21, 1 (1987).
15. C. A. Kapetanacos, L. K. Len, T. Smith, J. Golden, K. Smith, S. J. Marsh, D. Dialetis, J. Mathew, P. Loschialpo, and J. H. Chang, *Phys. Rev. Lett.* 64, 2374 (1990).
16. C.A. Kapetanacos, L. K. Len, T. Smith, D. Dialetis, S. J. Marsh, P. Loschialpo, J. Golden, J. Mathew and J. H. Chang, *Phys. Fluids B*, 3, 2396 (1991).
17. J. Golden, L. K. Len, T. J. Smith, J. Mathew, P. Loschialpo, L. Seto, J. H. Chang and C. A. Kapetanacos, *Proc. of SPIE*, Vol. 1407, p. 418 (1991).
18. L. K. Len, T. Smith, P. Loschialpo, J. Mathew, S. J. Marsh, D. Dialetis, J. Golden, J. H. Chang and C. A. Kapetanacos, *Proc. of the SPIE Conf.* Vol. 1629, p. 521 (1992).

19. C. A. Kapetanacos, L. K. Len, T. Smith, P. Loschialpo, J. Mathew, S. J. Marsh, D. Dialetis, J. Golden and J. H. Chang, NRL Memo Report NRL/MR/4795-92-6988 (1992).
20. C. A. Kapetanacos, S. J. Marsh, and D. Dialetis, *Phys. Rev. Lett.* **61**, 86 (1986).
21. P. Sprangle, C. A. Kapetanacos and S. J. Marsh *Proc. of the 4th Intern. Conf. on High Power Electron and Ion Beam Research and Tech.*, Vol. 2, p. 803 (1981).
22. C. A. Kapetanacos, P. Sprangle, D. P. Chernin, S. J. Marsh and I. Haber, *Phys. Fluids*, **26**, 1634 (1983).
23. D. P. Chernin and P. Sprangle, *Part. Accel.* **12**, 85 (1982).
24. C. A. Kapetanacos and S. J. Marsh, *Phys. Fluids* **28**, 2263 (1985).
25. C. A. Kapetanacos and P. Sprangle, NRL Memo Report No. 5388 (1984).
26. P. Loschialpo, S. J. Marsh, L. K. Len, T. Smith and C. A. Kapetanacos, Subm. to *Rev. Sc. Inst.* (1992).
27. C. A. Kapetanacos and P. Sprangle, U. S. Patent Number 4, 481, 475 (1984).
28. L. K. Len, T. Smith, J. Golden, K. Smith, S. J. Marsh, D. Dialetis, J. Mathew, P. Loschialpo, J. H. Chang, and C. A. Kapetanacos, *Proceedings of International Society for Optical Engineers (SPIE)* (SPIE, Bellingham, WA, 1990), Vol. 1226, p. 382.
29. P. Sprangle and C. A. Kapetanacos, **14**, 15 (1983).
30. R. L. Gluckstern, in *Proceedings of Linear Accelerator Conference* (Brookhaven Laboratory, Upton, NY, 1979), p. 245

31. C. A. Kapetanakos, P. Sprangle, S. J. Marsh, D. Dialetis and C. Agritellis, *Part. Accel.* 18, 73 (1985).
32. S. J. Marsh, J. Golden, C. A. Kapetanakos and D. Anderson, *J. Appl. Phys.* 64, 6138 (1988).
33. P. Sprangle and C. A. Kapetanakos, *Part. Accel.* 18, 203 (1986).
34. J. Mathew, S. J. Marsh, D. Dialetis and C. A. Kapetanakos, NRL Memo Report No. NRL/MR/4795-92-7114 (1992).
35. C. A. Kapetanakos, D. Dialetis, S. J. Marsh, L. K. Len and T. Smith, *Phys. Rev. A* 44, 3900 (1991).
36. D. Dialetis, S. J. Marsh and C. A. Kapetanakos, NRL Memo Report No. NRL/MR/4795-92-6985 (1992).
37. W. M. Manheimer and J. Finn, *Part. Accel.* 14, 29 (1983).
38. I. Haber, S. J. Marsh and P. Sprangle, *Proc. of the 5th Intern. Conf. on High Power Particle Beams*, p. 485 (1983).
39. C. W. Roberson, A. Mondelli, and D. Chernin, *Part. Accel.* 17, 79 (1985).
40. D. Chernin and P. Sprangle, *Part. Accel.* 12, 101 (1982).
41. D. Dialetis, S. J. Marsh and C. A. Kapetanakos, Subm. to *Phys. Rev. A* (1992).
42. M. Weiner, *IEEE Trans. on Magnetics*, Vol. Mag.-17, 1472 (1981).

Appendix
Publications by the NRL
research staff.

Publications by the NRL research staff

I. MODIFIED BETATRON ACCELERATOR (MBA)

(With and Without Strong Focusing)

A. THEORY

INJECTION

Injection of a High-Current Beam into a Modified Betatron Accelerator, C. A. Kapetanacos, P. Sprangle, and S. J. Marsh, Phys. Rev. Letts. 49, 741 (1982); Also, NRL Memo Report No. 4835 (1982).

External Injection into a High Current Modified Betatron, F. Mako, W. M. Manheimer, D. P. Chernin, F. Sandel, and C. A. Kapetanacos, Phys. Fluids 27, 2211 (1984); Also, NRL Memo Report No. 5196 (1983).

Simulation Studies on a Novel Modified Betatron Injection Scheme, W. Peter, R. J. Faehl, and F. Mako, Beams 83, 458, Proc. of the 5th Intl. Conf. on High Power Particle Beams (1983).

Beam Trapping in High Current Cyclic Accelerators with Strong Focusing Fields, P. Sprangle and C. A. Kapetanacos, Part. Accel. 18, 203 (1986); Also, NRL Memo Report No. 5458 (1985).

Beam Trapping in a Modified Betatron with Torsatron Windings, C. A. Kapetanacos, D. Dialetis and S. J. Marsh, Part. Accel., 21, 1 (1987); Also, NRL Memo Report No. 5619 (1985).

Beam Trapping in a Modified Betatron with Torsatron Windings, C. A. Kapetanakis, D. Dialetis, and S. J. Marsh, Proc. of the Compact Accelerators Technology Conference (Secret) Special Publication BRL-SP-52, p. 127 (1986).

A passive method to Trap an Electron Beam in a Stellatron Accelerator, A. V. Deniz, J. Appl. Phys. 69, 1151 (1991).

Dissipative Beam Trapping in a Modified Betatron with Strong Focusing, Y. Seo and P. Sprangle, Part. Accel. (1992).

Diffusion of the Self Magnetic Fields of an Electron Beam through a Resistive Toroidal Chamber, D. Dialetis, S. J. Marsh, and C. A. Kapetanakis, Submitted to J. of Th. Physics, (1992); Also, NRL Memo Report No. NRL/MR/4795-92-6985 (1992).

EQUILIBRIUM

Constant Radius Magnetic Acceleration of a Strong Non-neutral Proton Ring, P. Sprangle and C.A. Kapetanakis, J. Appl. Phys. 49, 1 (1978).

Dynamics of an Intense Electron Ring in a Modified Betatron Field, P. Sprangle, C. A. Kapetanakis, and S. J. Marsh, Proc. of the 4th Intl. Top. Conf. on High Power Electron and Ion Beam Research and Technology, Vol. 2, page 803 (1981); Also, NRL Memo Report No. 4666 (1981).

Equilibrium of a High Current Electron Ring in a Modified Betatron Accelerator, C. A. Kapetanakis, P. Sprangle, D. P. Chernin, S. J. Marsh, and I. Haber, Phys. Fluids, 26, 1634 (1983); Also, NRL Memo Report No. 4905 (1982).

Transverse Beam Dynamics in a Modified Betatron, D. P. Chernin and P. Sprangle, Part. Accel. 12, 85, (1982).

Self Consistent Theory of Equilibrium and Acceleration of a High Current Electron Ring in a Modified Betatron, W. M. Manheimer and J. Finn, Part. Accel. 14, 29 (1983).

The Stellatron - A high Current Betatron with Stellerator Fields, C. W. Roberson, A. Mondelli, and D. Chernin, Phys. Rev. Letters, 50, 507 (1983).

The Effect of Field Index Fluctuation on the Dynamics of a High Current Ring, C. Agritelis, S. J. Marsh, and C. A. Kapetanakos, Part. Accel. 16, 155 (1985); Also, NRL Memo Report No. 5141 (1983).

Self Potentials of an Electron Ring in a Torus for Large Displacement from the Minor Axis, C. A. Kapetanakos and P. Sprangle, NRL Memo Report No. 5388 (1984).

Non-linear Transverse Electron Beam Dynamics in a Modified Betatron Accelerator, C. A. Kapetanakos and S. J. Marsh, Phys. Fluids 28, 2263 (1985); Also, NRL Memo Report No. 5387 (1984).

Acceleration of an Electron Ring in a Modified Betatron with Transverse Pressure, J. M. Grossman, J. M. Finn, and W. M. Manheimer, Phys. Fluids 28, 695 (1985); Also, NRL Memo Report No. 5444 (1984).

Flux Diffusion and Acceleration in a High Current Modified Betatron, J. M. Grossman and W. M. Manheimer, Part. Accel. 16, 185 (1985).

The Plasma Assisted Modified Betatron, W. M. Manheimer, Part. Accel. 17, 157 (1985);
Also, NRL Memo Report No. 5459 (1984)

Improving the Current-Carrying Capability of the Modified Betatron, C. A. Kapetanakis,
D. Dialetis, and S. J. Marsh, Nucl. Inst. and Methods in Physics Research B24/25, 805
(1987).

Self Consistent Theory of Equilibrium and Adiabatic Evolution of a High Current Electron
Ring in a Modified Betatron, J. M. Finn and W. M. Manheimer, Phys. Fluids 26, 3400
(1983).

Studies of the Electron-Ring Dynamics in a Modified Betatron for Large Ring Displacement
from the Minor Axis, S. J. Marsh and C. A. Kapetanakis, Part. Accel. 23, (1988). Also,
NRL Memo Report No. 5933 (1987).

STABILITY

Longitudinal and Transverse Instabilities in a High Current Modified Betatron Electron
Accelerator, P. Sprangle and J. L. Vomrordis, Part. Accel. 18, 1 (1985); Also, NRL Memo
Report No. 4688 (1984).

Electron-Ion Instabilities in a High Current Modified Betatron, W. M. Manheimer, Part.
Accel. 13, 209 (1983).

Drag Instability in a Modified Betatron, P. Sprangle and C. A. Kapetanakis, Part. Accel.
14, 15 (1983); Also, NRL Memo Report No. 4950 (1983).

Integer Resonances in a Modified Betatron, D. Chernin and P. Sprangle, Part. Accel. 12, 101 (1982).

Beam Current Limitations Due to Instabilities in Modified and Conventional Betatrons, P. Sprangle and D. Chernin, Part. Accel. 15, 35 (1984); Also, NRL Memo Report No. 5176 (1983).

Emittance Growth in a Modified Betatron Crossing the Orbital-Turning-Point Transition, I. Haber, S. J. Marsh, and P. Sprangle, Proc. of the 5th Intl. Conf. on High Power Particle Beams, Page 485 (1983).

Self-Consistent Modified Betatron Equilibria and their Adiabatic Evolution, J. Grossman, W. M. Manheimer, and J. Finn, Proc. of the 5th Intl. Conf. on High Particle Beams, page 489 (1983).

Stabilization of the Negative Mass Instability in a Rotating Relativistic Electron Beam, Y. Y. Lau and D. Chernin, Phys. Rev. Letts. 52, 1425 (1984).

Mode Coupling in the Modified Betatron, D. P. Chernin, Part Accel. 14, 139 (1984); Also, NRL Report No. 5061 (1984).

Dynamic Behavior of an Electron Ring Close to a Cyclotron Resonance in a Modified Betatron Accelerator, D. Dialetis, S. J. Marsh, and C. A. Kapetanakis. Submitted to Phys. Rev. (1992).

Current Loss in Modified Betatrons Due to Field Error Resonances, E. Esarey, P. Sprangle, S. J. Marsh, and Y. H. Seo, NRL Memo Report No. 6694 (1992).

EXTRACTION

Injection and Extraction of a Relativistic Electron Beam in a Modified Betatron, B. Hui and Y. Y. Lau, Phys. Rev. Lett. 53 2024 (1984).

High Midplane Accessibility Stellarator Windings for High Current Toroidal Accelerators, S. J. Marsh, J. Golden, and C. A. Kapetanakis, J. Appl. Phys. 64, 6138 (1988); Also, NRL Memo Report No. 6025 (1987).

Beam Extraction Scheme from the Modified Betatron Accelerator, C. A. Kapetanakis, S. J. Marsh, and D. Dialetis, Phys. Rev. Lett. 61, 86 (1988); Also, NRL Memo Report No. 6214 (1988).

B. EXPERIMENT

Preliminary Design of the NRL Modified Betatron, J. Golden, J. A. Pasour, D. E. Pershing, K. Smith, F. Mako, S. Slinker, F. Mora, N. Orrick, R. Altes, A. Fliflet, P. Champney, and C. A. Kapetanakis, Proc. of IEEE Trans. Nucl. Science, NS-30, 2114 (1983).

Pulsed, Low-Error, High Current TF and VF Coils with Demountable Joints, F. Mako, K. Smith, J. A. Pasour, D. E. Pershing, K. McDonald, R. Altes, J. Golden, and C. A. Kapetanakis, Proc. of 10th Symp. on Fusion Eng., Philadelphia, PA. (1983).

The NRL Modified Betatron, J. Golden, F. Mako, L. Floyd, K. McDonald, T. Smith, P. Sprangle, and C. A. Kapetanakis, Proc. of the Compact Accelerators Technology Conference (Secret) Special Publication BRL-SP-52, p. 121 (1986).

Measurements of Fuse and Resistor Characteristics for Multimicrojoule Capacitor Bank Applications, K. F. McDonald, T. Smith, J. Golden, L. Floyd, and B. Conley, Rev. Sci. Instrum. 58, 1287 (1987).

Internal Injection into the NRL Modified Betatron, F. Mako, J. Golden, L. Floyd, K. McDonald, T. Smith, and C. A. Kapetanakis, IEEE Trans. on Nucl. Sci., Vol. NS-32, 3027 (1985).

Modified Betatron Data Acquisition and Control System, L. Floyd, J. Golden, T. Smith, E. Day and S. J. Marsh, IEEE Trans. Nucl. Sci. NS-32 #5, 2092 (1985).

Controls and Data Acquisition for the NRL Modified Betatron Accelerator, L. Floyd, J. Golden, T. Smith, E. Day and S. J. Marsh, LANL Accelerator Control Workshop Proc., Nucl. Methods and Instrum., A247, 68, (1986).

Progress in the Development of the NRL Modified Betatron Accelerator, J. Golden, F. Mako, L. Floyd, K. McDonald, T. Smith, D. Dialetis, S. J. Marsh, and C. A. Kapetanakis, Proc. of the 6th Intl. Conf. on High Power Beams, 709 (1986).

Beam "Self-Trapping" in the NRL Modified Betatron Accelerator, F. Mako, J. Golden, D. Dialetis, L. Floyd, N. King, and C. A. Kapetanakis, Proceedings of the High Brightness Accelerators 773 (1988).

The NRL Modified Betatron Accelerator Pulsed Power System, K. F. McDonald, F. Mako, T. Smith, L. Floyd, J. Golden and C. A. Kapetanakis, Proc. of the 5th Pulsed Power Conf. (1986).

A Novel Trapping Scheme in the Modified Betatron Accelerator, J. Golden, F. Mako, L. Floyd, T. Smith, D. Dialetis, S. J. Marsh, and C. A. Kapetanakis, IEEE Part. Accel. Conf. Vol. 2, 936 (1987).

Studies of a Multikiloampere Electron Ring Confined in a Modified Betatron Accelerator, J. Golden, L. K. Len, A. Deniz, J. Mathew, T. J. Smith, P. Loschialpo, J. H. Chang, D. Dialetis, S. J. Marsh, and C. A. Kapetanakis, Proc. of the 7th International Conference on High Power Particle Beams-Beams '88, Karlsruhe FRG, Vol. I, 221 (1988).

Progress in the Development of the NRL Modified Betatron Accelerator, L. K. Len, T. Smith, J. Golden, K. Smith, S. J. Marsh, D. Dialetis, J. Mathew, P. Loschialpo, J. H. Chang, and C. A. Kapetanakis, Proc. of SPIE Vol. 1226, p. 382 (1990).

Improved Beam Confinement in the Modified Betatron with Strong Focusing, C. A. Kapetanakis, L. K. Len, T. Smith, J. Golden, K. Smith, S. J. Marsh, D. Dialetis, J. Mathew, P. Loschialpo, and J. H. Chang, Phys. Rev. Lett. 64 2374 (1990).

Diffusion of magnetic Fields in a Toroidal Conducting Shell of Circular Cross Section, D. Dialetis, L. K. Len, J. Golden, and C. A. Kapetanakis, J. Appl. Phys., 69, 1813 (1991); Also, NRL Memo Report No. 6719 (1990).

Compact, High Current Accelerators and their Prospective Application, C. A. Kapetanakis, L. K. Len, T. Smith, D. Dialetis, S. J. Marsh, P. Loschialpo, J. Golden, J. Mathew, and J. H. Chang, Phys. Fluids B3 2396 (1991).

Studies of Synchrotron Radiation Emission from the NRL Modified Betatron, T. Smith,

J. Golden, and C. A. Kapetanacos, J. Appl. Phys. 69, 6836 (1991); Also, NRL Memo Report No. 6774 (1991).

The NRL Modified Betatron Accelerator, L. K. Len, T. Smith, J. Golden, S. J. Marsh, D. Dialetis, J. Mathew, P. Loschialpo, J. H. Chang and C. A. Kapetanacos, Proc. of Eur. Part. Accel. Conf. Vol. 1, p. 446 (1991).

Studies of the Integer Cyclotron Resonances in a Modified Betatron Accelerator, C. A. Kapetanacos, L. K. Len, T. Smith, P. Loschialpo, J. Mathew, S. J. Marsh, D. Dialetis, J. Golden, and J. H. Chang; To be published in the Proceedings of the DARPA/Services Conference (1992); Also, NRL Memo Report No. 6988 (1992).

Excitation of the $\ell = 12$ Cyclotron Resonance in the NRL Modified Betatron Accelerator, L. K. Len, T. Smith, P. Loschialpo, J. Mathew, S. J. Marsh, D. Dialetis, J. Golden, J. H. Chang, and C. A. Kapetanacos, Proc. of the SPIE Conf. Vol. 1629, p. 521 (1992).

Identification of Toroidal Field Errors in a Modified Betatron Accelerator, P. Loschialpo, S. J. Marsh, L. K. Len, T. Smith, and C. A. Kapetanacos, Submitted to Rev. of Sci. Inst., (1992).

Beam Trapping in a Modified Betatron Accelerator, C. A. Kapetanacos, D. Dialetis, S. J. Marsh, L. K. Len, and T. Smith, Phys. Rev. A 44, 3900 (1991); Also, NRL Memo Report No. 6808 (1991).

Recent Developments on the NRL Modified Betatron Accelerator, J. Golden, L. K. Len, T. J. Smith, J. Mathew, P. Loschialpo, L. Seto, J. H. Chang, and C. A. Kapetanacos, Proc. of SPIE Vol. 1407, p. 418 (1991).

Beam Trapping in a Modified Betatron with a Localized Bipolar Electric Field Pulse, J. Mathew, S. J. Marsh, D. Dialetis, and C. A. Kapetanakos, Submitted to J. Appl. Physics; Also, NRL Memo Report No. NRL/MR/4795-92-7114 (1992).

Output Switch for a Megavolt Electron Beam Generator, J. Mathew and J. Golden, Rev. Sci. Instrum. **62**, 1514 (1991).

II. OTHER HIGH CURRENT ACCELERATORS

High Current, High Voltage Accelerators as Free electron Lasers Drivers, C. W. Roberson, J. A. Pasour, C. A. Kapetanakos, P. Sprangle, J. Golden, F. Mako, and R. Lucey, Proc. of Free Electron Laser Conference in Sun Valley, ID, September (1981).

Energy Scaling Laws for the Racetrack Induction Accelerator, A. A. Mondelli, and C. W. Roberson, Part. Accel. **15**, 221 (1984); Also, NRL Report No. 5008 (1982).

Dynamics of a High-Current Electron Ring in a Conventional Betatron Accelerator, C. A. Kapetanakos, S. J. Marsh, and P. Sprangle, Part. Accel. **14**, 261 (1984); Also, NRL Memo Report 5108 (1983).

Recent Developments in Ultra-High Current Electron Induction Accelerators, C. A. Kapetanakos, and P. Sprangle. Phys. Today, February (1985); Also, NRL Memo Report No. 5259 (1984).

Studies of a Rapid Electron Beam Accelerator (REBATRON), C. A. Kapetanakos, P. Sprangle, S. J. Marsh, D. Dialetis, and C. Agritellis, Part. Accel. **18**, 73 (1985); Also, NRL Memo Report No. 5503 (1985).

The REBATRON as a High Energy Accelerator, D. Dialetis, S. J. Marsh, and C. A. Kapetanakos, NRL Memo Report No. 5655 (1986).

Recent Rebatron Studies, A. Prakash, S. J. Marsh, D. Dialetis, C. Agritellis, P. Sprangle, and C. A. Kapetanakos, IEEE Trans. on Nucl. Sci., Vol. NS-32, 3265 (1986).

Analysis of the Acceleration Process in a Rebatron, D. Dialetis, S. J. Marsh, and C. A. Kapetanakos, Part Accel. 21, 227 (1987).

Ultra-High Current Accelerators, C. A. Kapetanakos, McGraw-Hill Yearbook of Science and Technology 348-350 (1987).

The Fast Modified Betatron Accelerator, C. A. Kapetanakos, J. of Defense Res. 21, 541 (1992). (SECRET).

Ph.D Thesis

Study of the Synchrotron Radiation Emission from the NRL Modified Betatron Accelerator, Tab Smith, Doctor of Philosophy, Univ. of Maryland, 1990.

Patents

Betatron Accelerator having High Ratio of Budker Parameter to Relativistic Factor, C. A. Kapetanakos and P. Sprangle, U.S. Patent No. 4, 481, 475 (1984).

Low Perturbation Electron Injector for Cyclic Accelerators, F. Mako, W. Manheimer, C. A. Kapetanakos and F. Sandel, U.S. Patent No. 4, 608, 537 (1986).

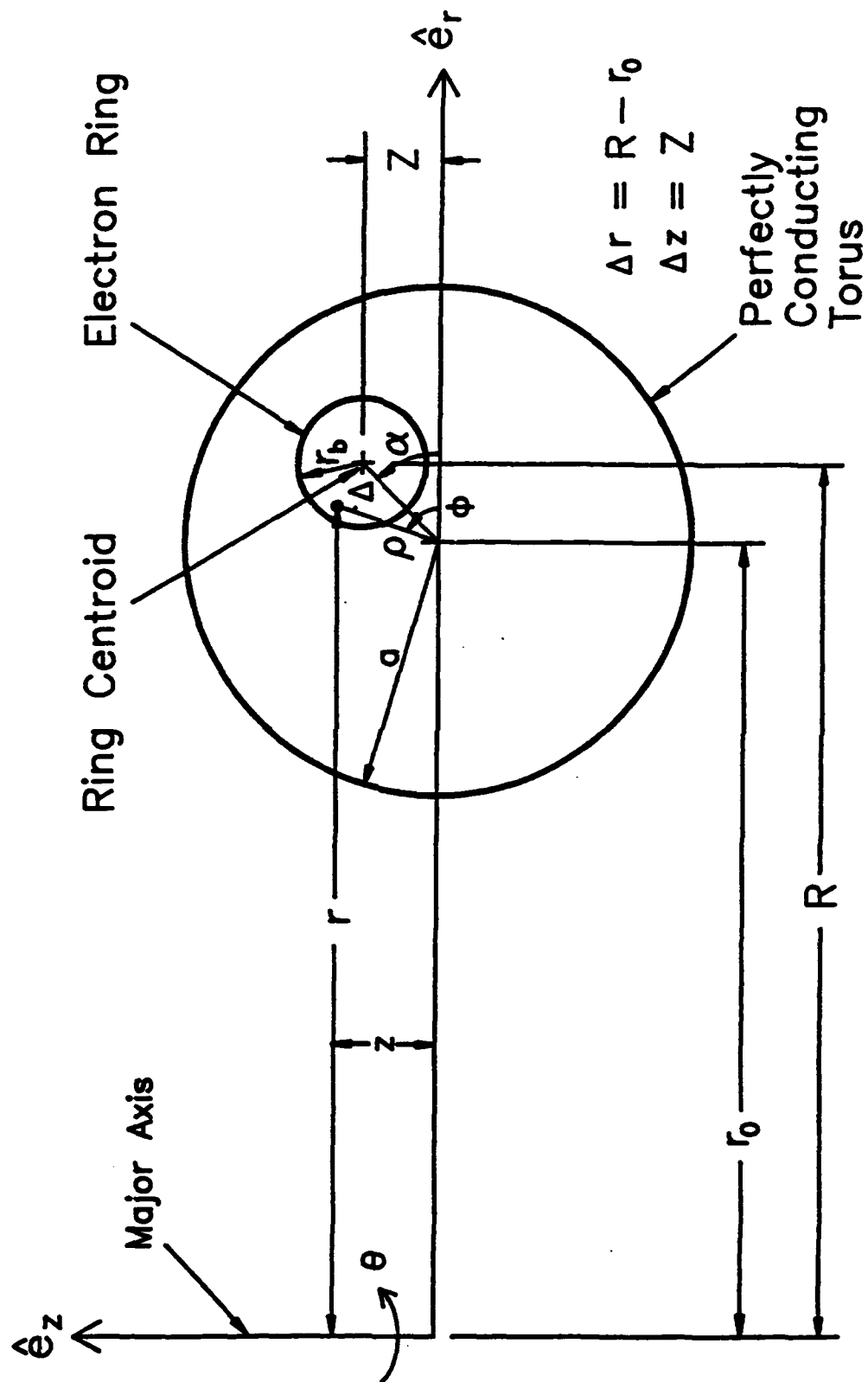


Fig. 1. System of coordinates.

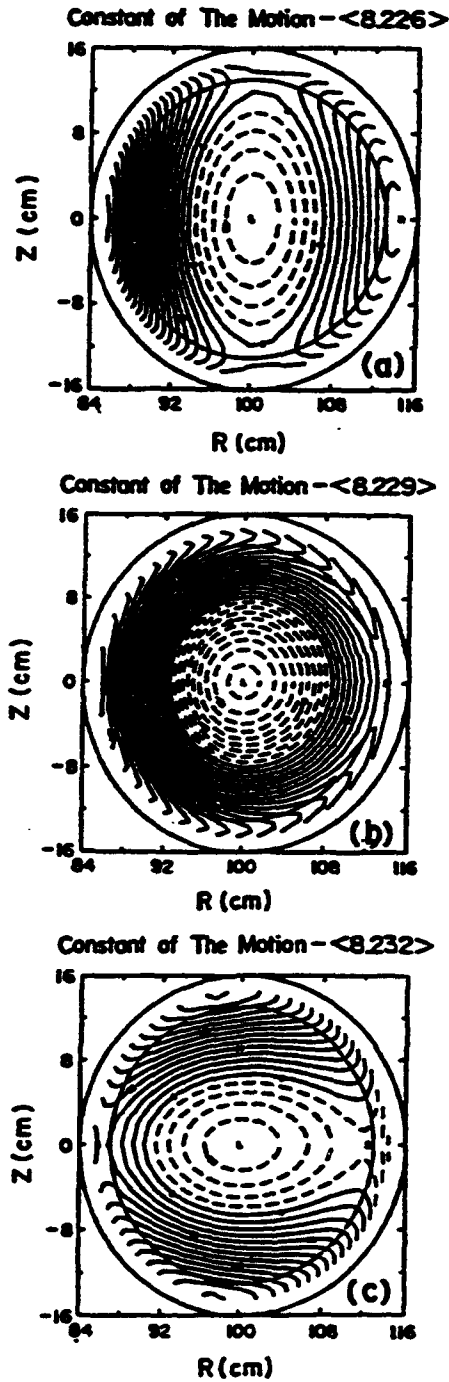


Fig. 2. Orbits of ring centroid in the transverse plane from Eq. (7b) and the potentials of Eq. (11). In (a) the external field index is 0.35, in (b) 0.5 and in (c) 0.65.

Modified Betatron without Strong Focusing Ring Centroid Orbital Stability Diagram

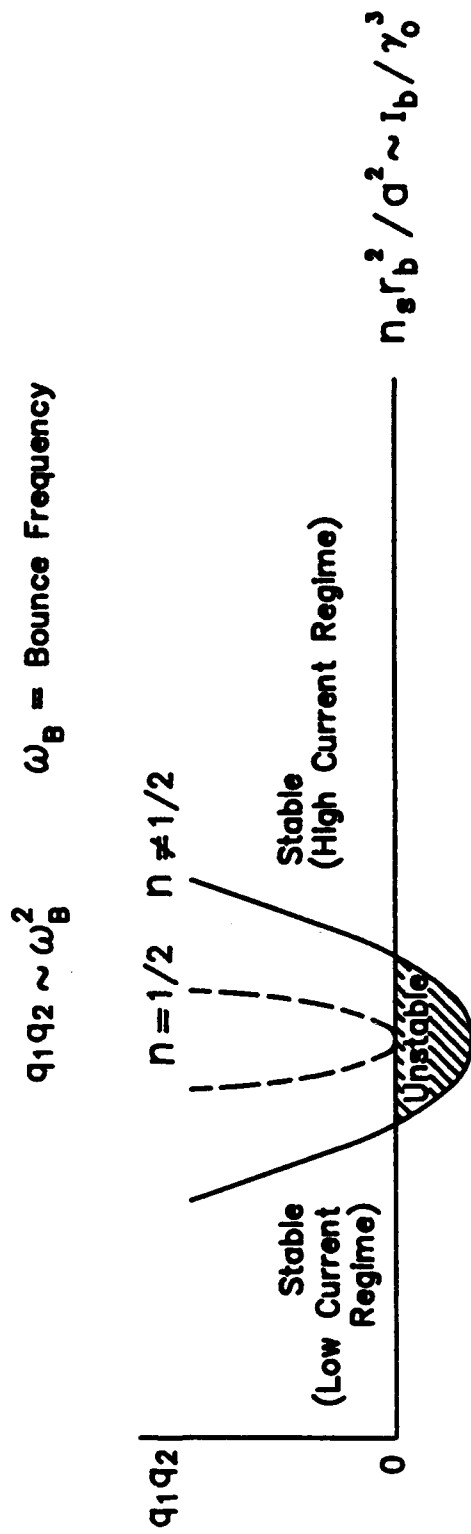


Fig. 3. Schematic of the ring centroid orbital stability diagram for a modified betatron without strong focusing.

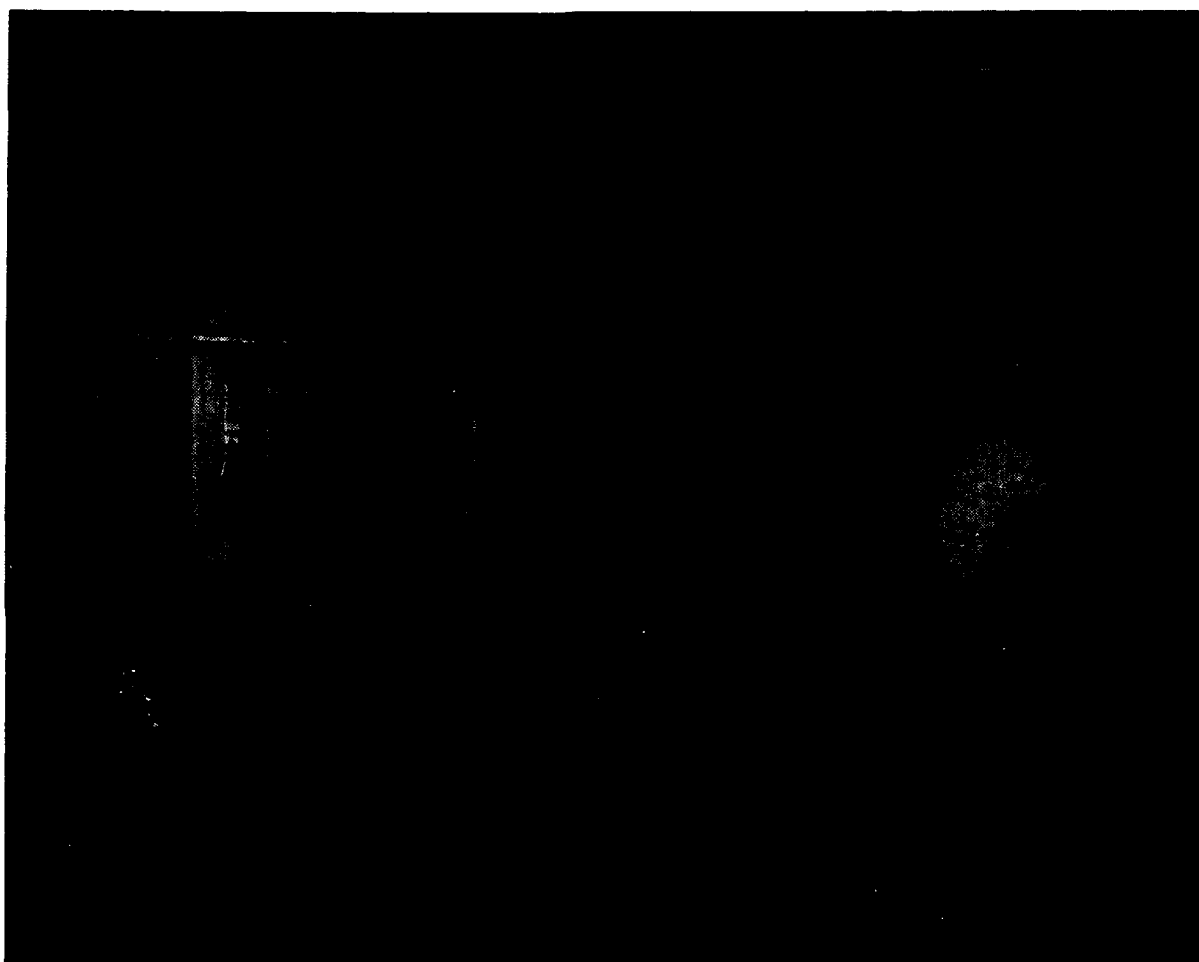


Fig. 4. Photograph of the NRL modified betatron accelerator.

NRL MODIFIED BETATRON - HIGH CURRENT REGIME RING ORBIT IN THE TRANSVERSE PLANE

$V_0 = 735$ kV, $B_0 = 2.88$ kG

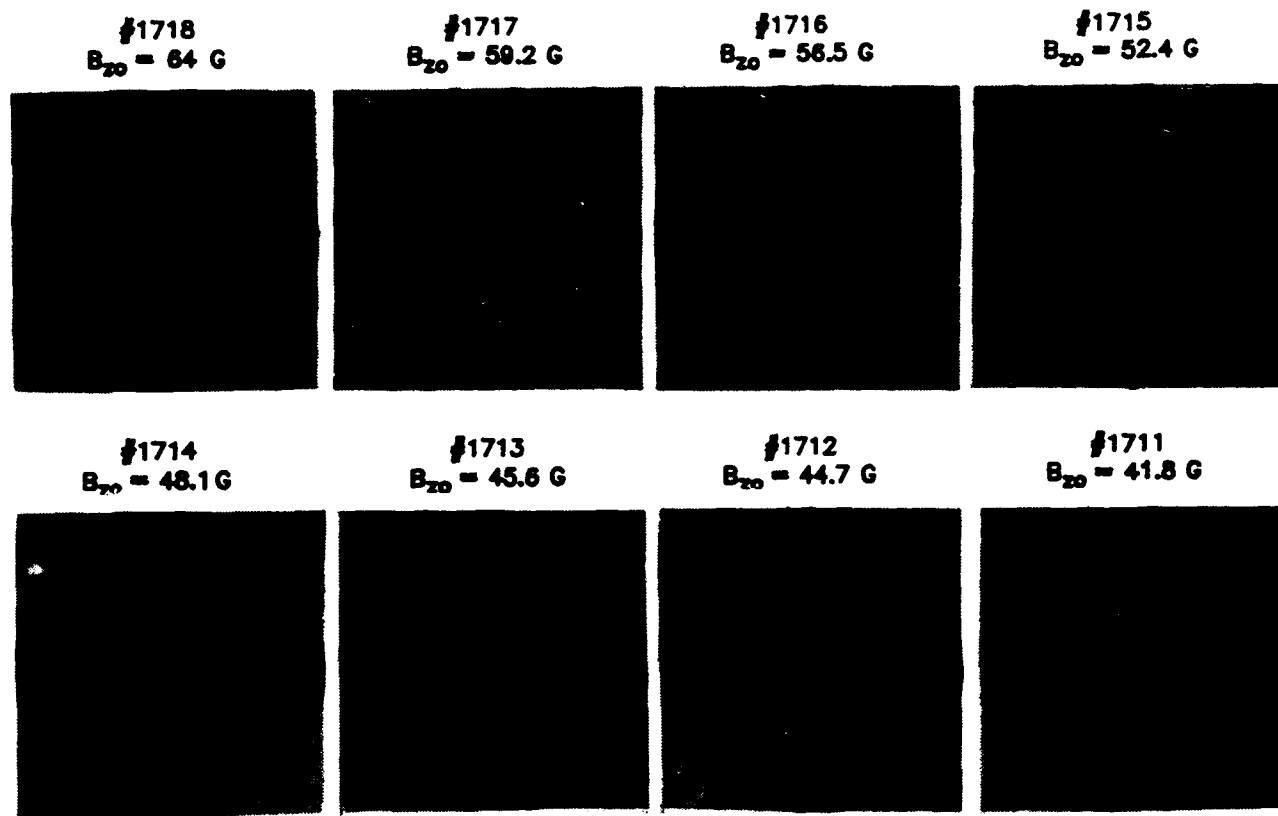
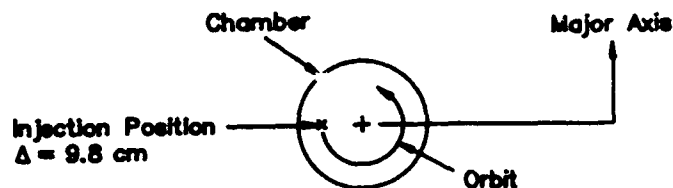


Fig. 5. Ring orbits in the transverse plane for several values of vertical magnetic field.

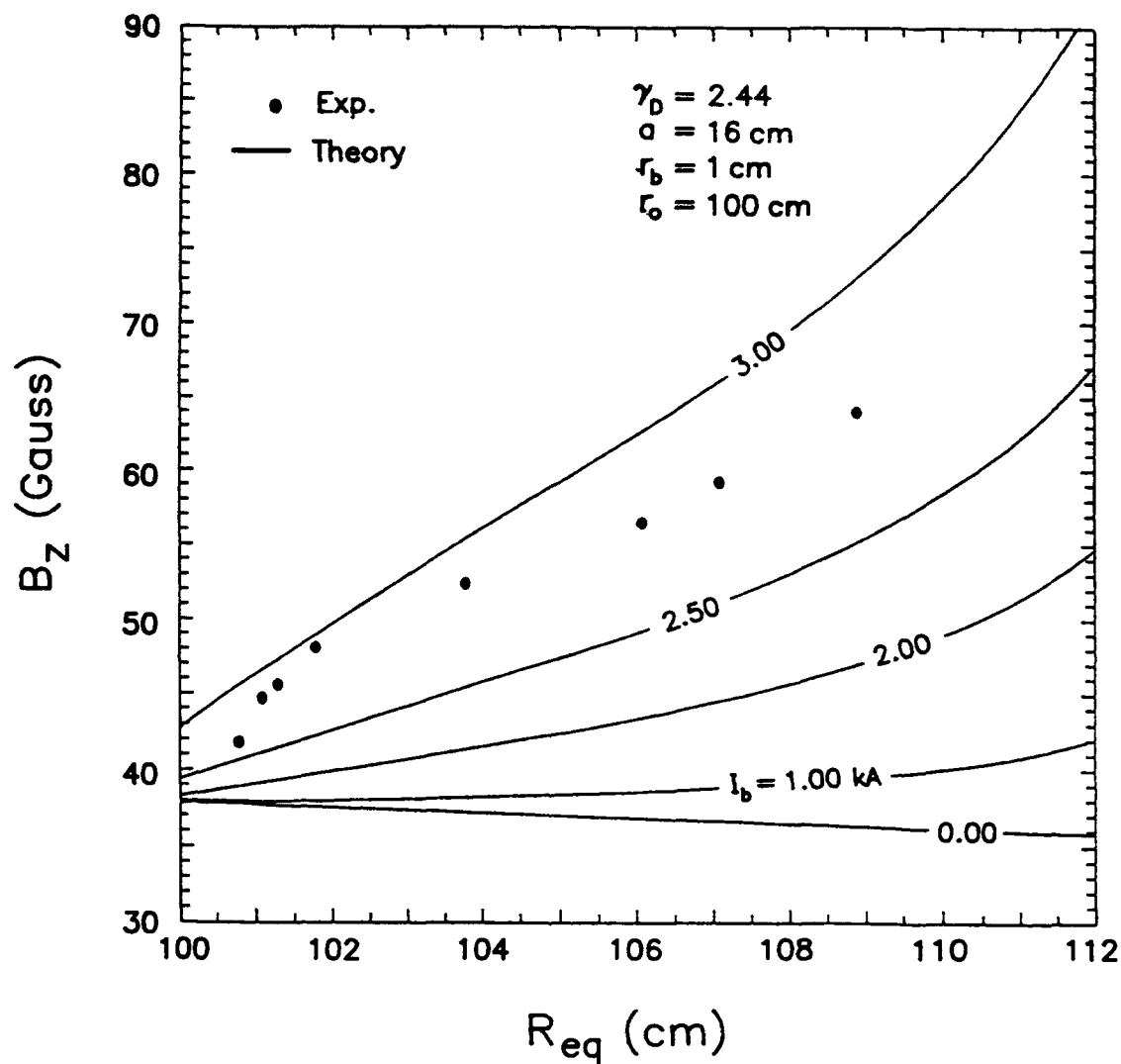


Fig. 6. Vertical magnetic field required to hold the electron ring at its equilibrium position for five different values of beam current.

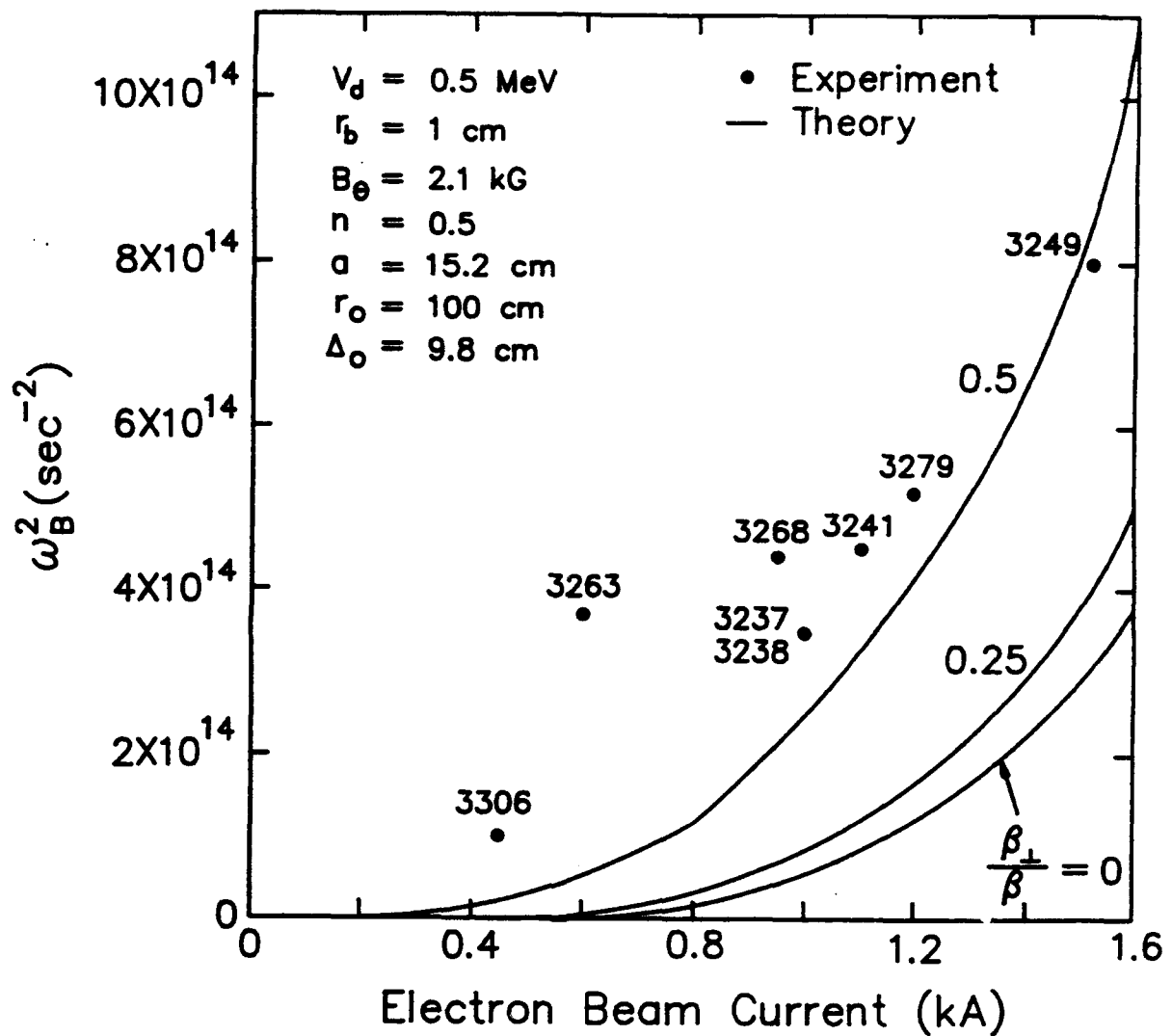


Fig. 7. Bounce frequency squared vs. electron beam current for three different values of transverse velocity.

Stellarator, Individual Particle and Centroid Indices

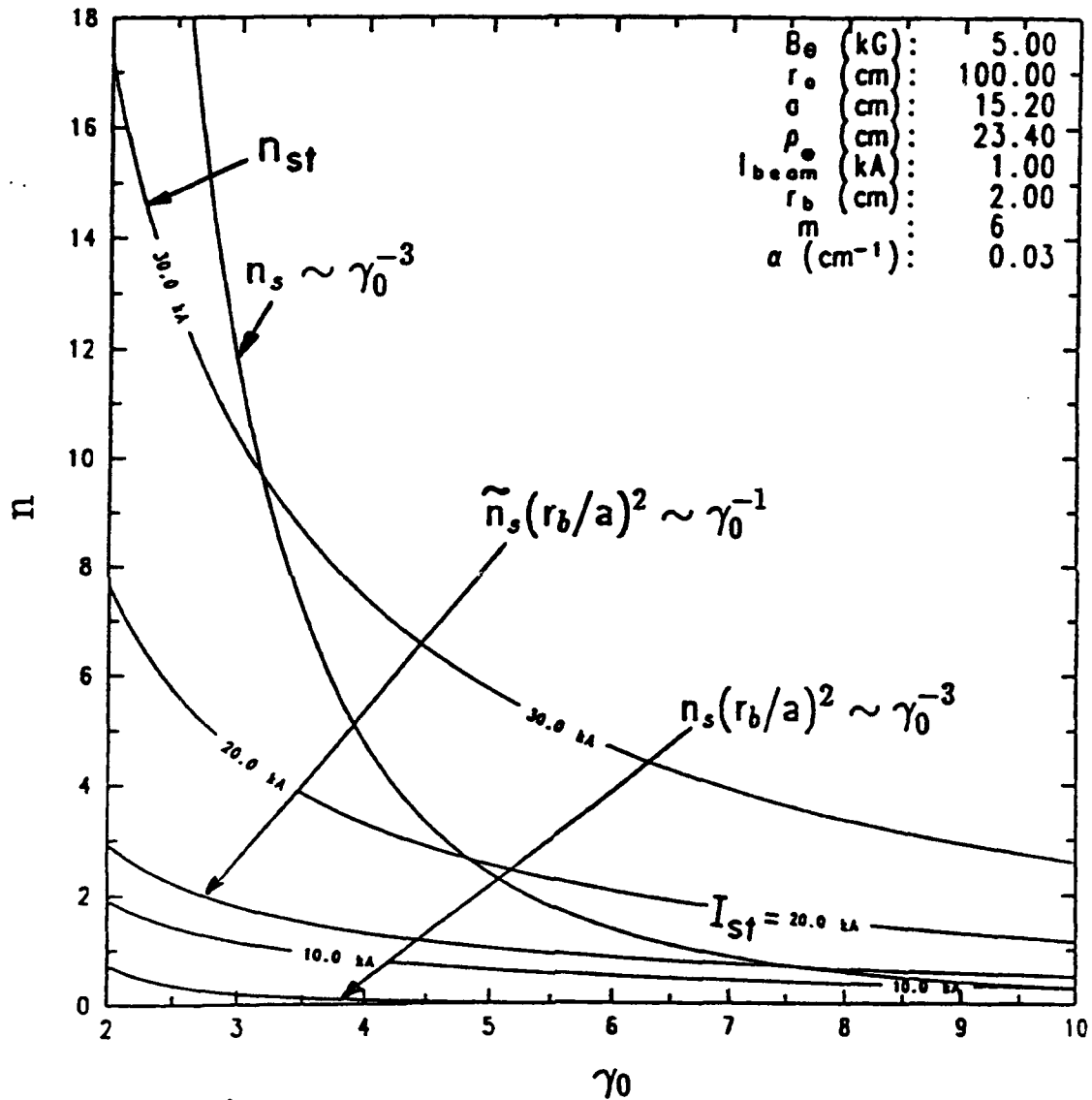


Fig. 8. Normalized ring lifetime vs. electron ring current for six different values of normalized beam energy γ_0 . The parameter γ_0 is the normalized beam energy after the ring has been formed and it is smaller than the normalized electron energy in the diode γ_d .

The Effect of Drag Instability on The Electron Ring Lifetime

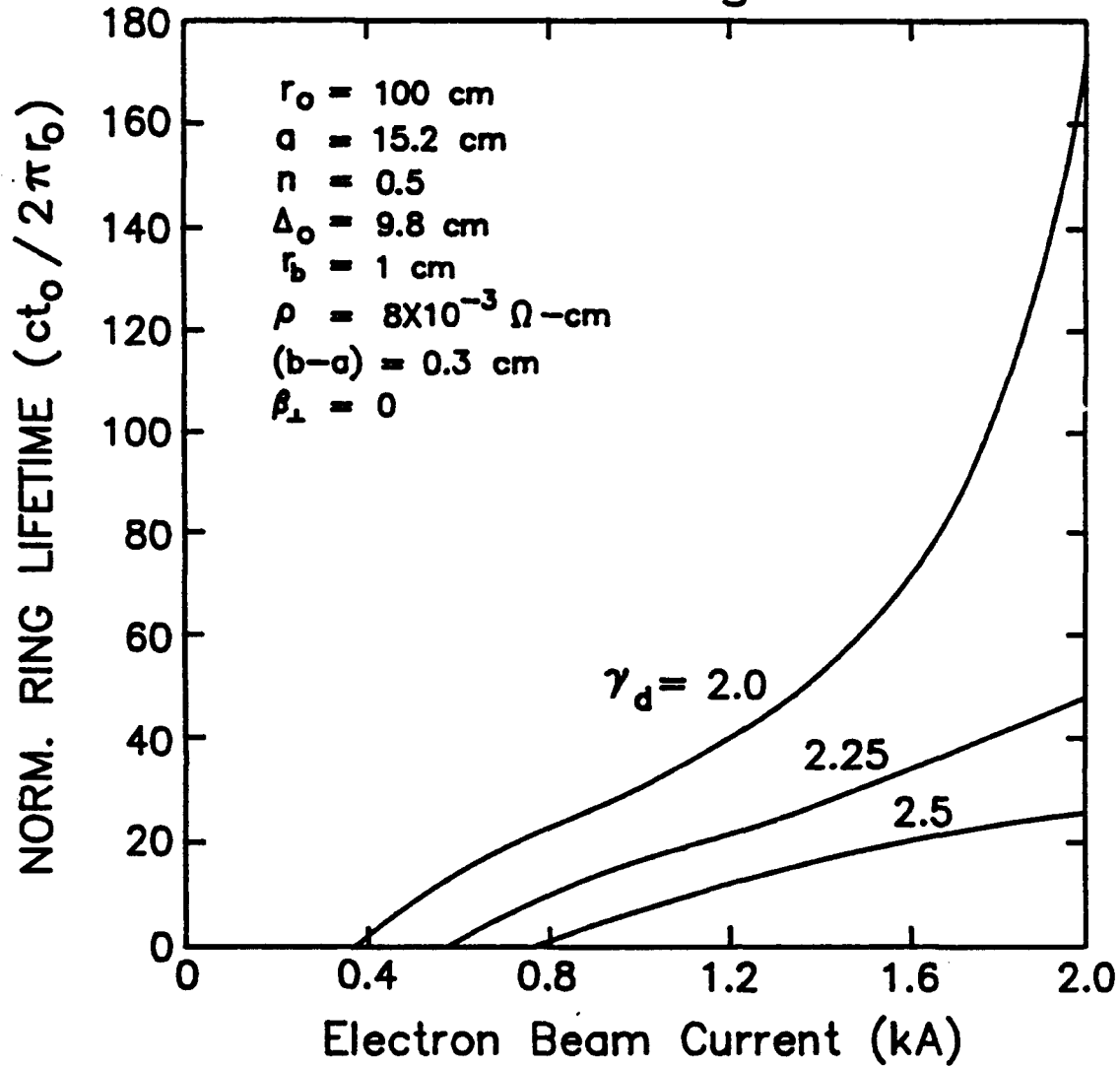


Fig. 9. Normalized ring lifetime vs. electron ring current for three values of the normalized electron energy at the diode γ_d . The beam is injected at the radial distance of $\Delta_0 = 9.8$ cm from the minor axis.

Modified Betatron with Stellarator Windings

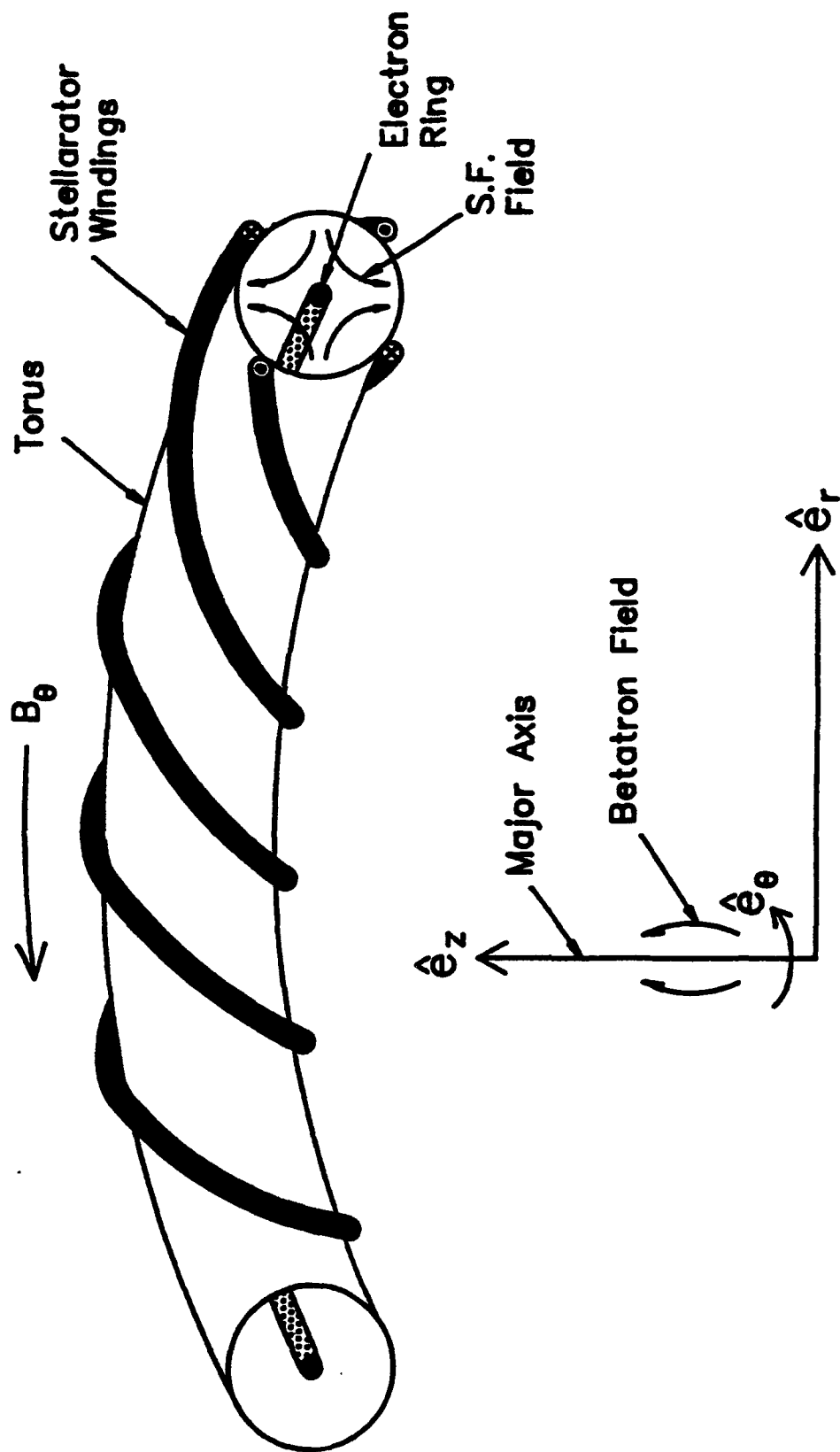


Fig. 10. Left-handed stellarator windings.

Modified Betatron with Torsatron Windings

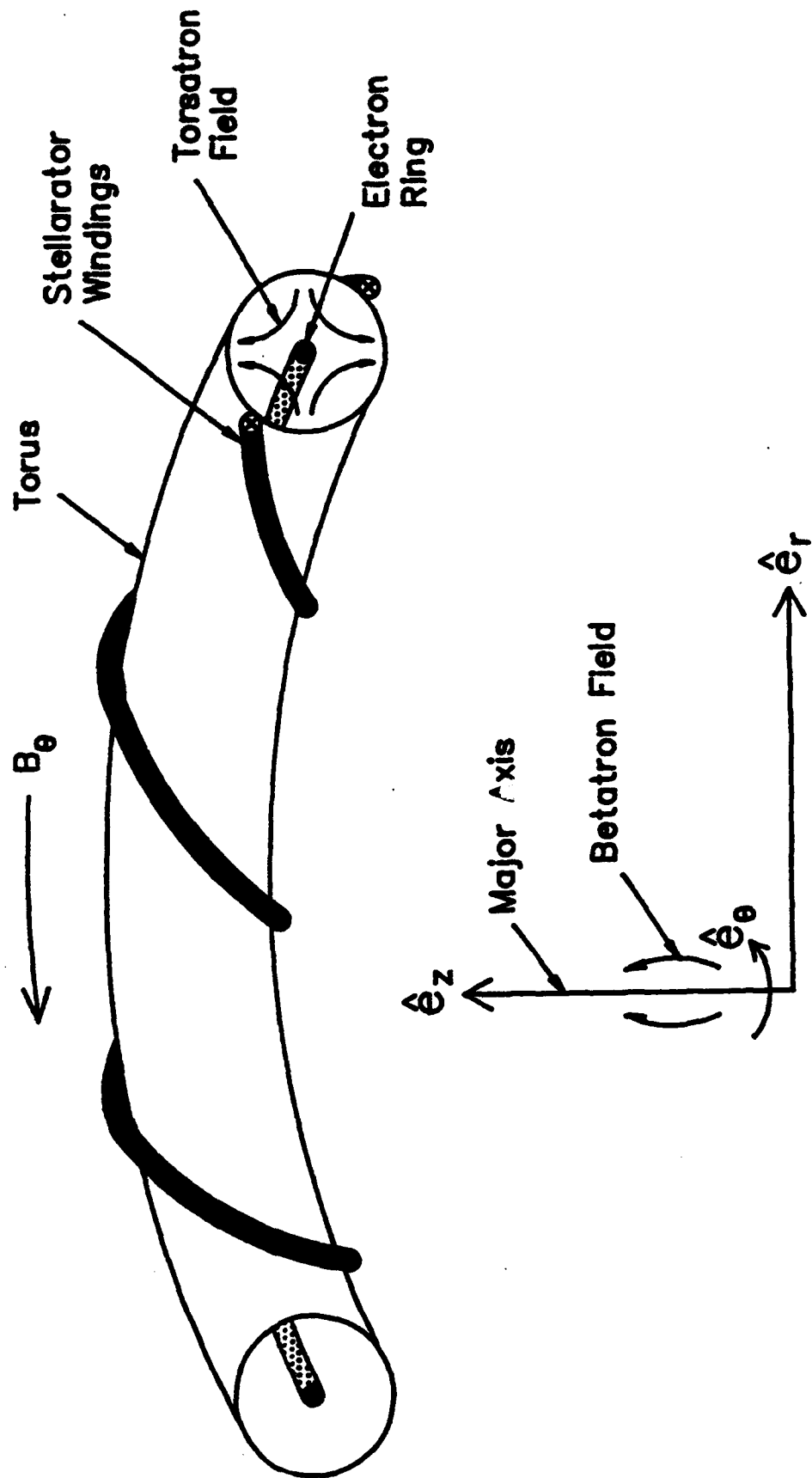


Fig. 11. Left-handed torsatron windings.

ORBITAL STABILITY DIAGRAM

Rotating Frame

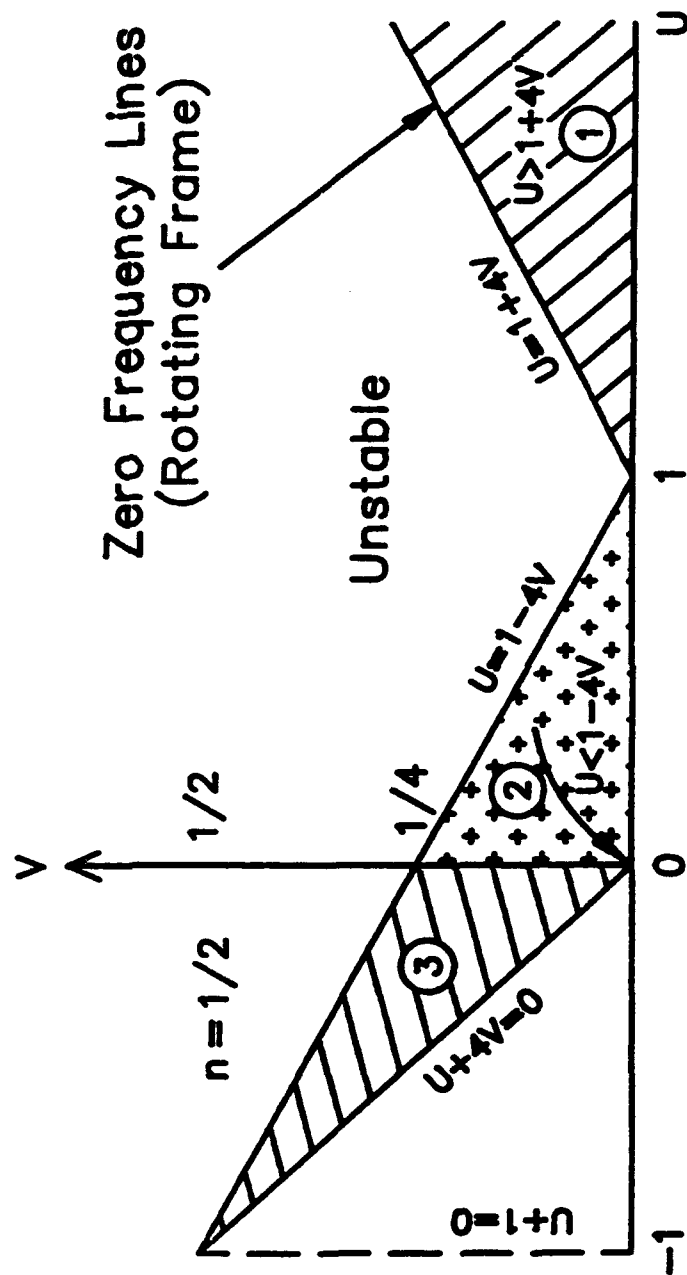


Fig. 12. Orbital stability diagram in the rotating frame from C.W. Roberson et al., Phys.

Rev. Letts. 50, 507 (1983).

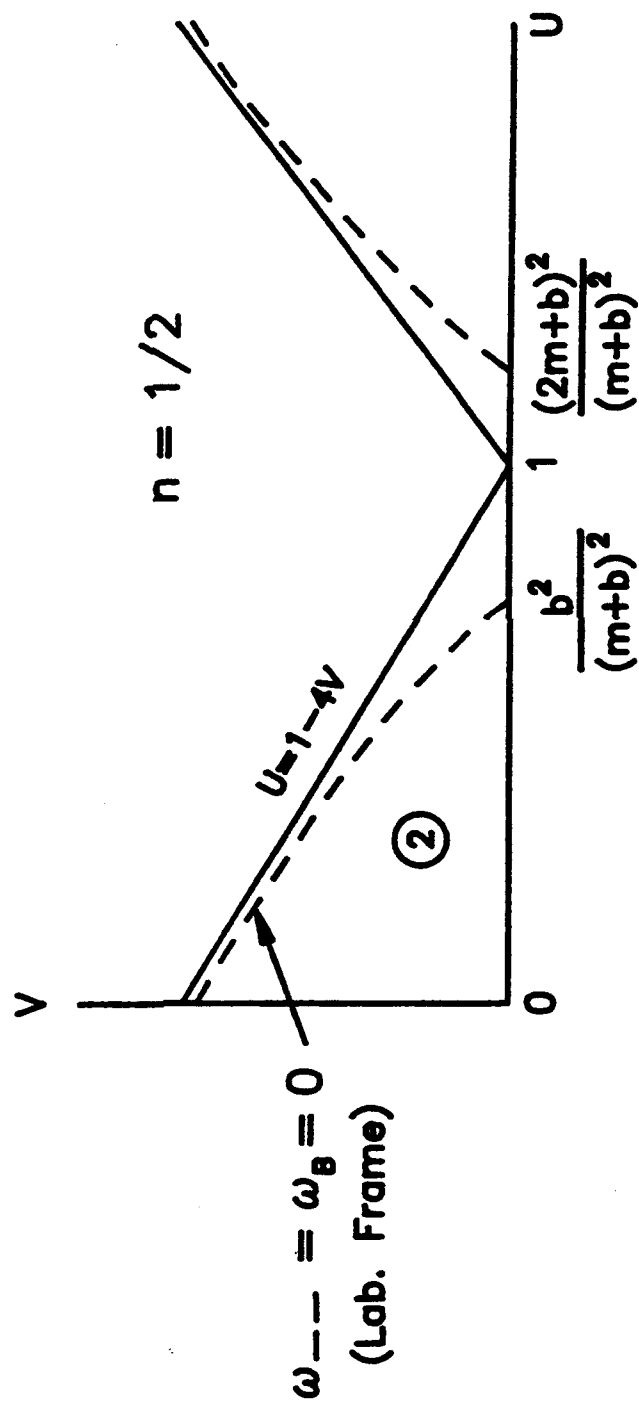


Fig. 13. Along the dashed lines the bounce frequency in the laboratory frame is equal to zero. At injection the values of U and V have to be selected to the right of the dashed line of region 2 for left-handed windings with B_0 and $v_0 > 0$.

Stellarator, Individual Particle and Centroid Indices

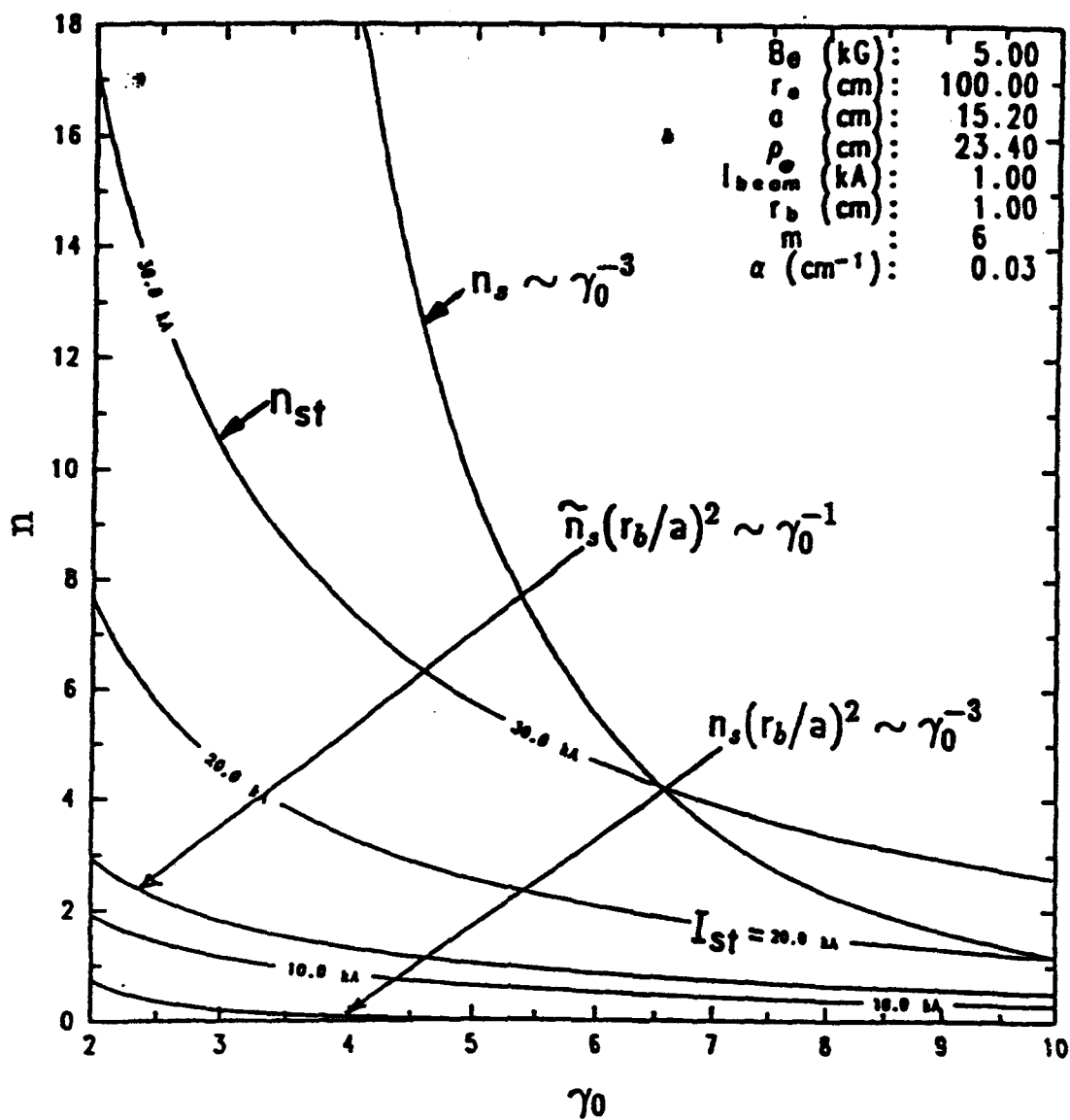


Fig. 14. Stellarator index n_{st} , individual particle self index n_s , and centroid self indices for typical parameters of the NRL modified betatron.

Stellarator, Individual Particle and Centroid Indices

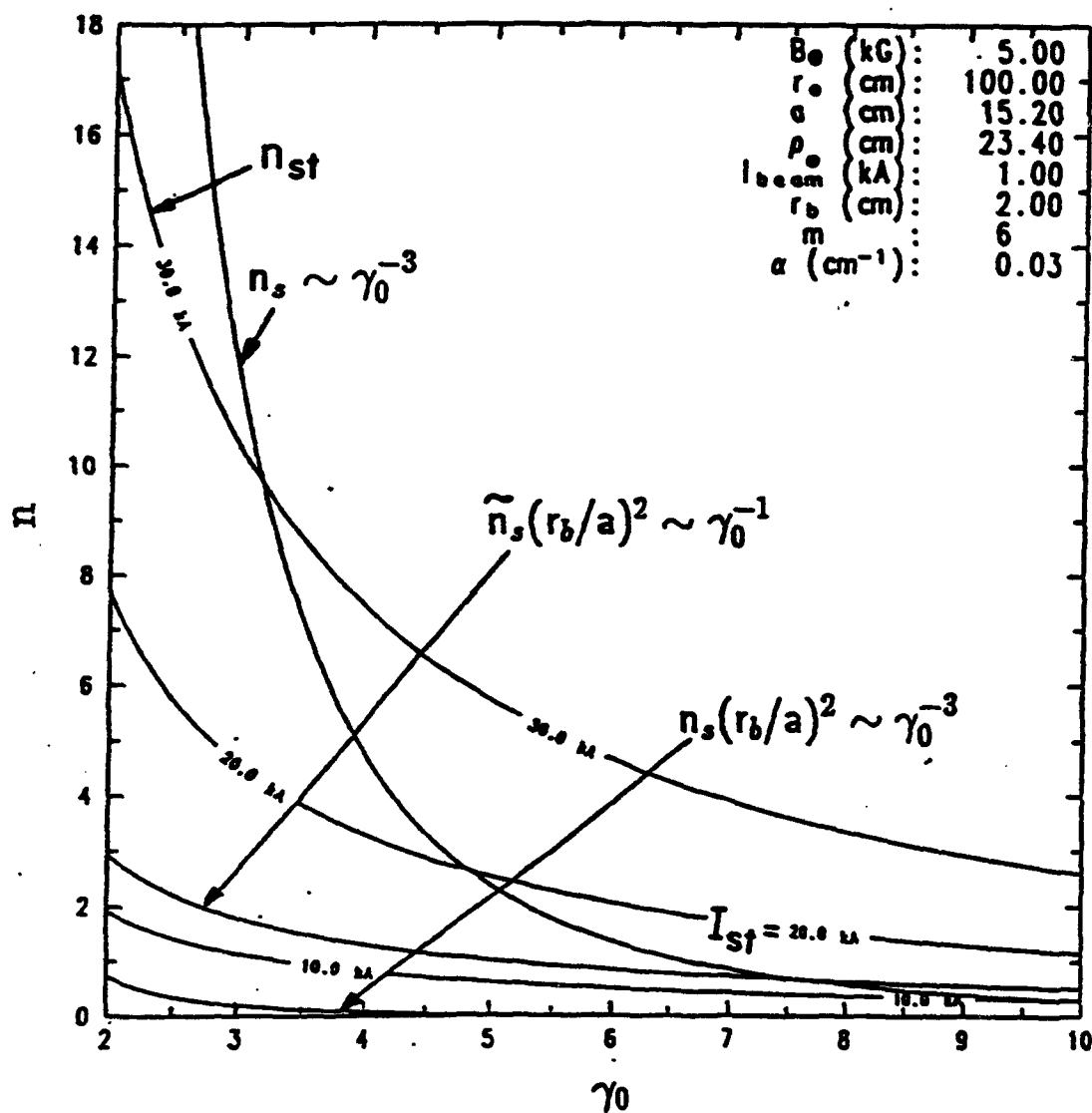


Fig. 15. As in Fig. (14) but with a beam radius of 2 cm instead of 1 cm.

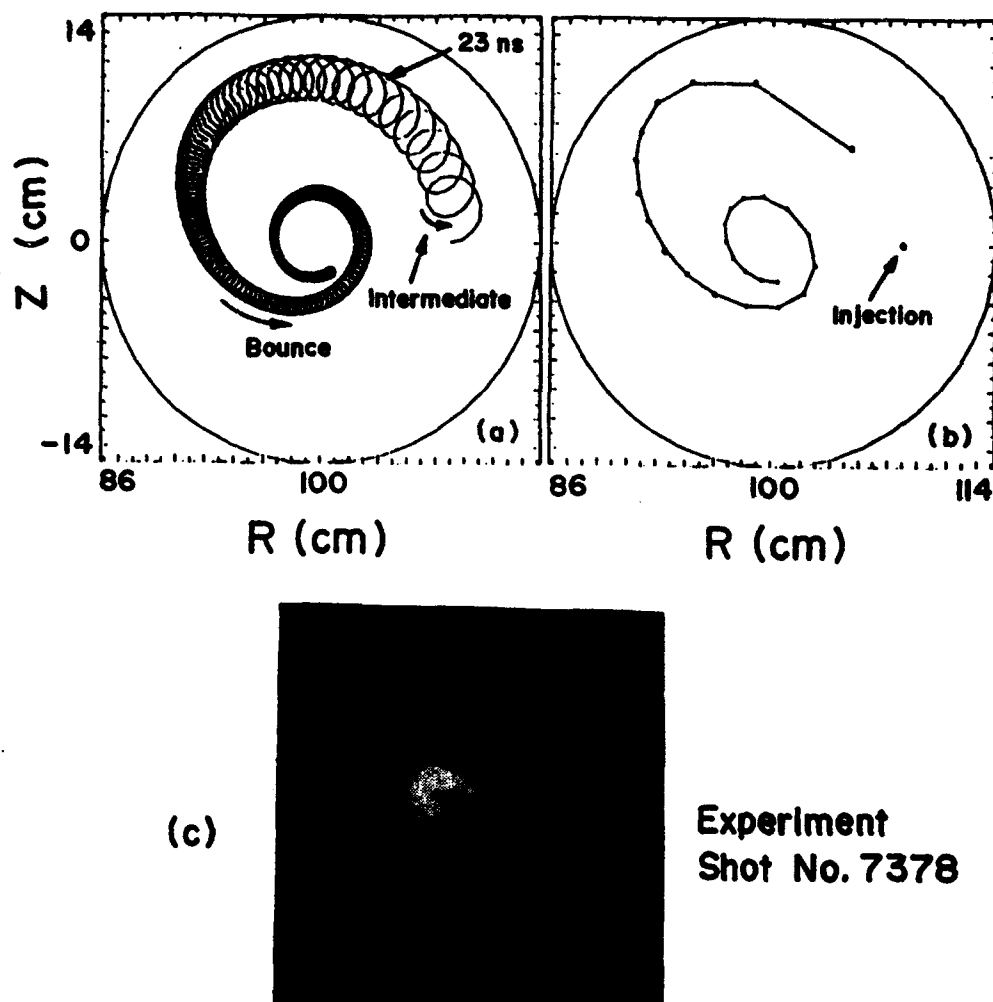


Fig. 16. Beam centroid orbit from the numerical integration of the equations of motion, using the image fields from the resistive shell model [(a) and (b)]. Results from the experiment (c).

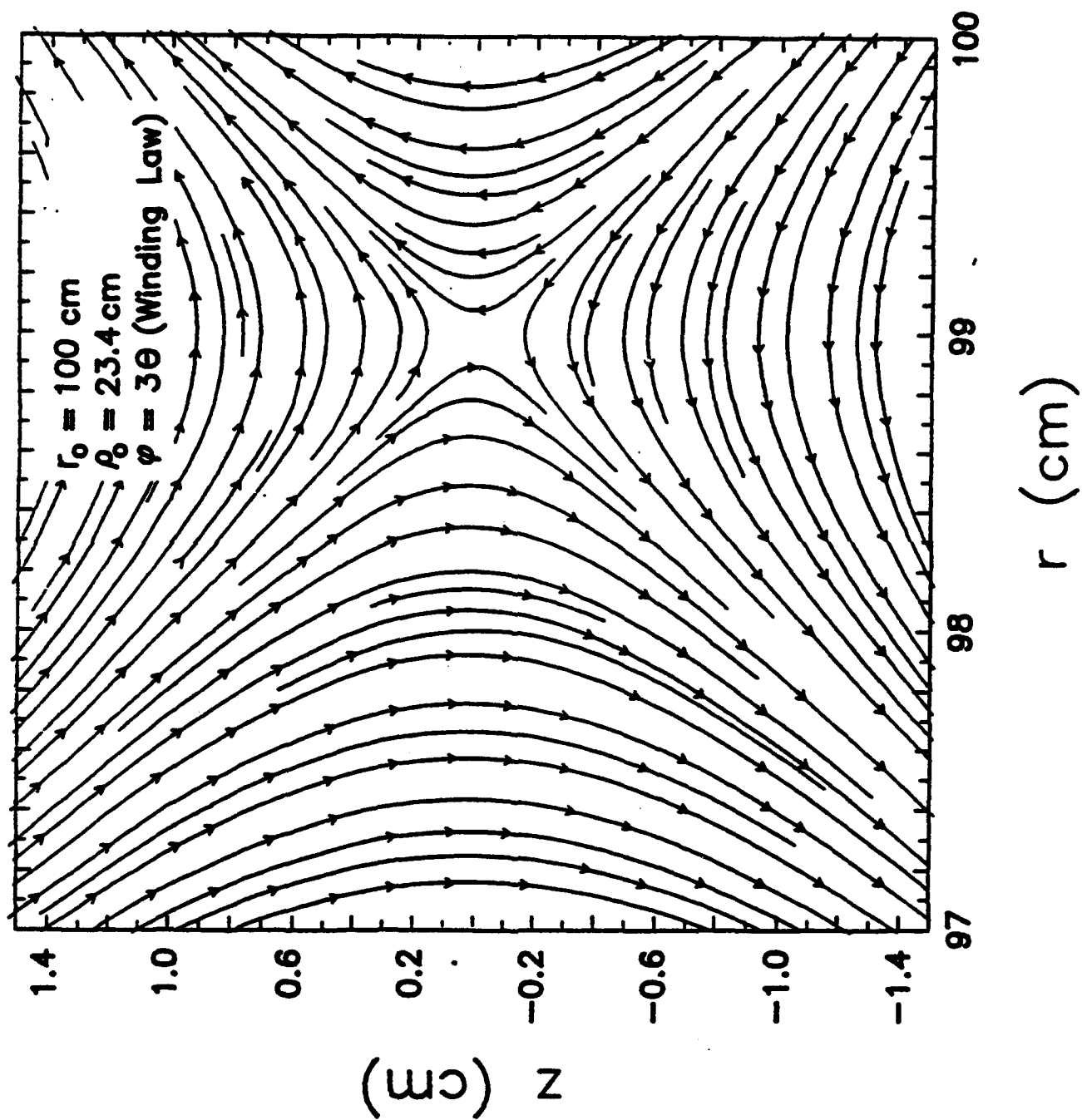


Fig. 17. Field lines in the vicinity of the magnetic axis (SF field).

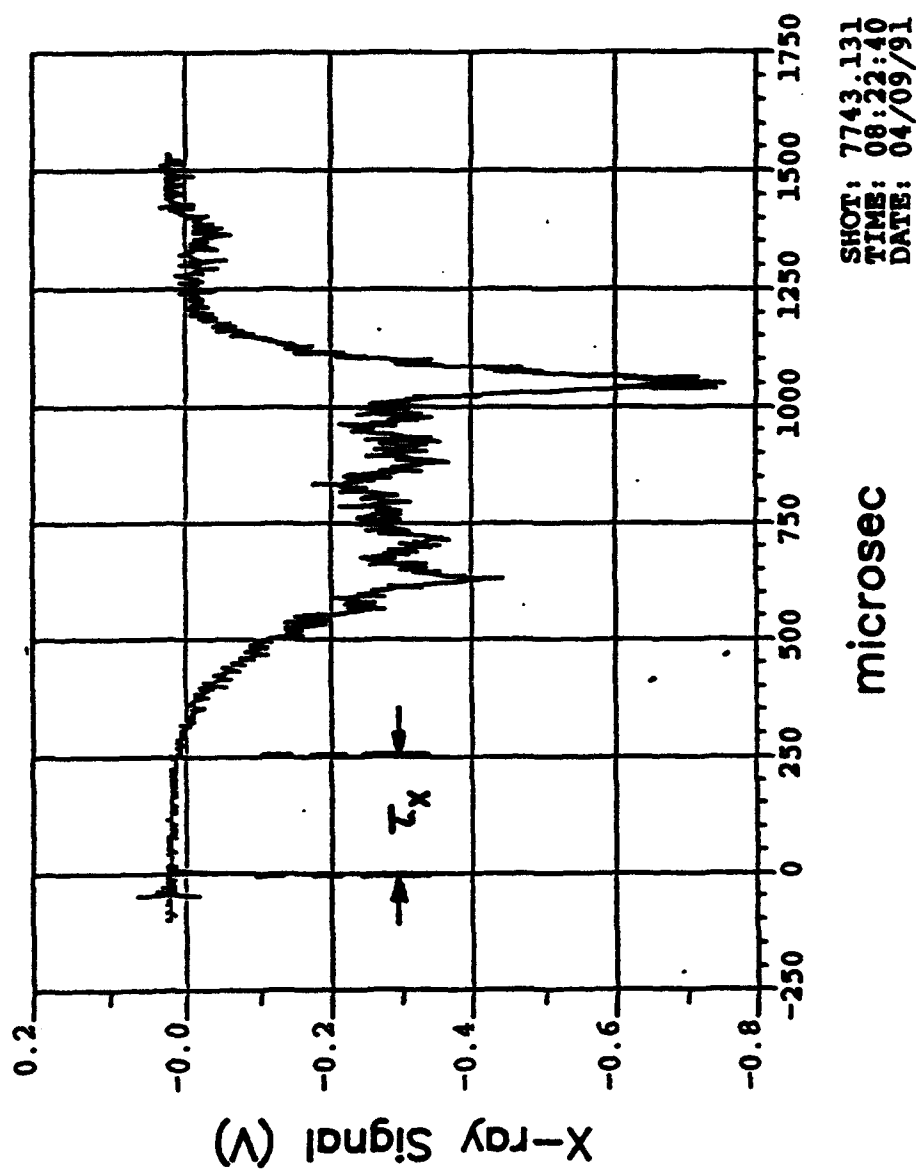


Fig. 18. X-ray signal as a function of time.

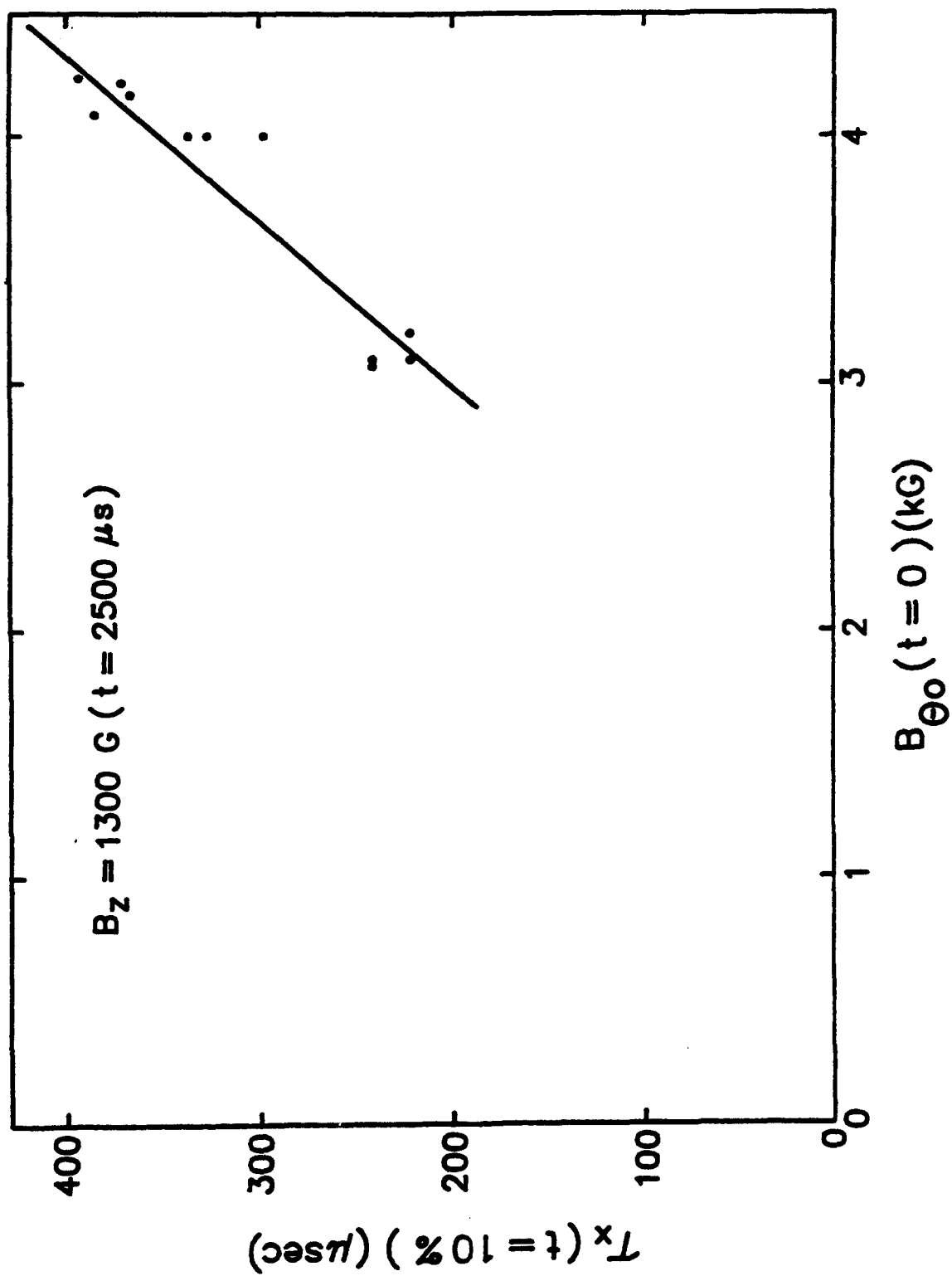


Fig. 19. The time the x-ray signal initially appears τ_z as a function of toroidal magnetic field for constant peak vertical field.

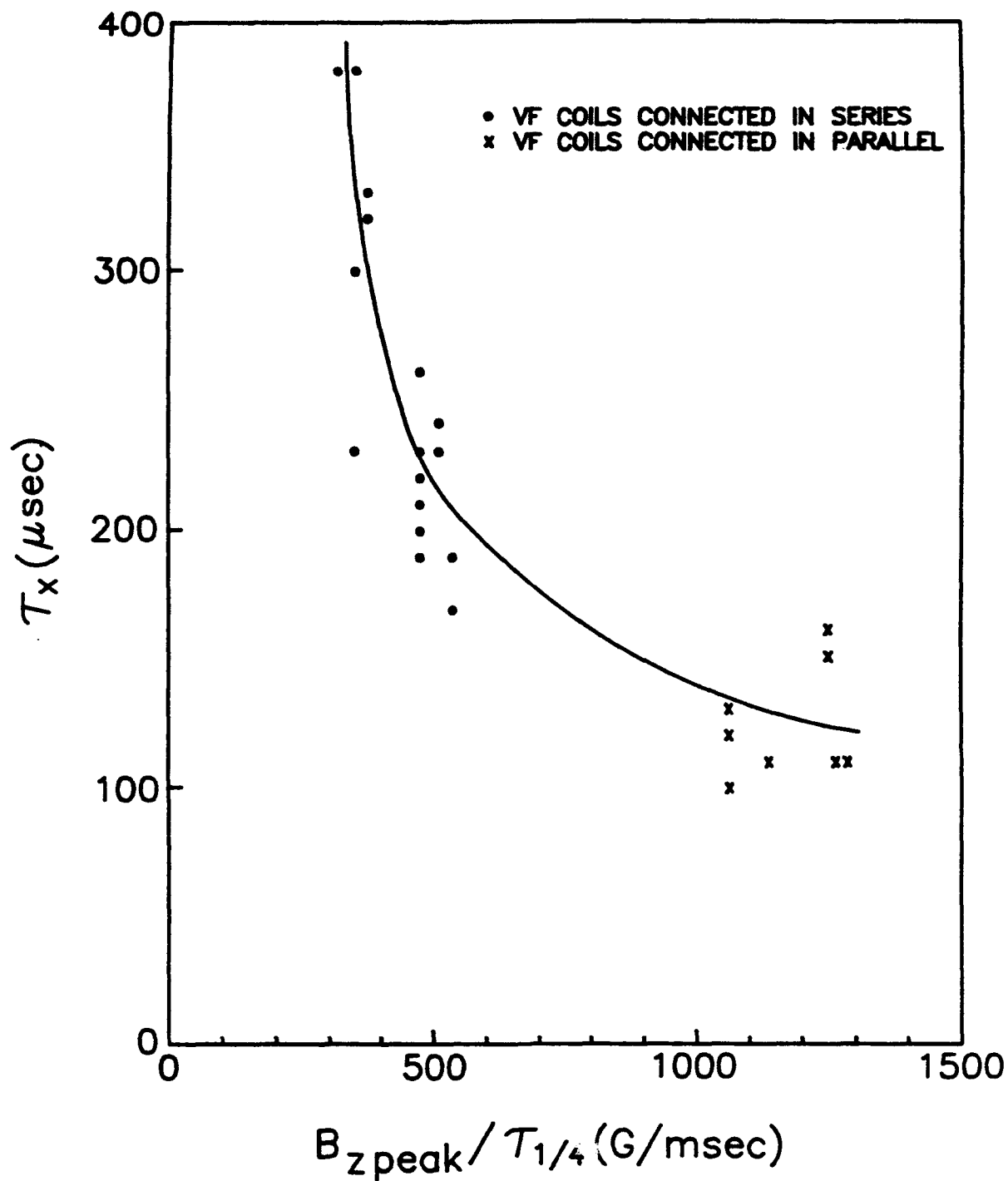


Fig. 20. The time τ_x as a function of the peak vertical magnetic field B_z peak divided by the risetime (quarter period) of the B_z waveform for $B_{00} \approx 4$ kG and a trapped beam current.

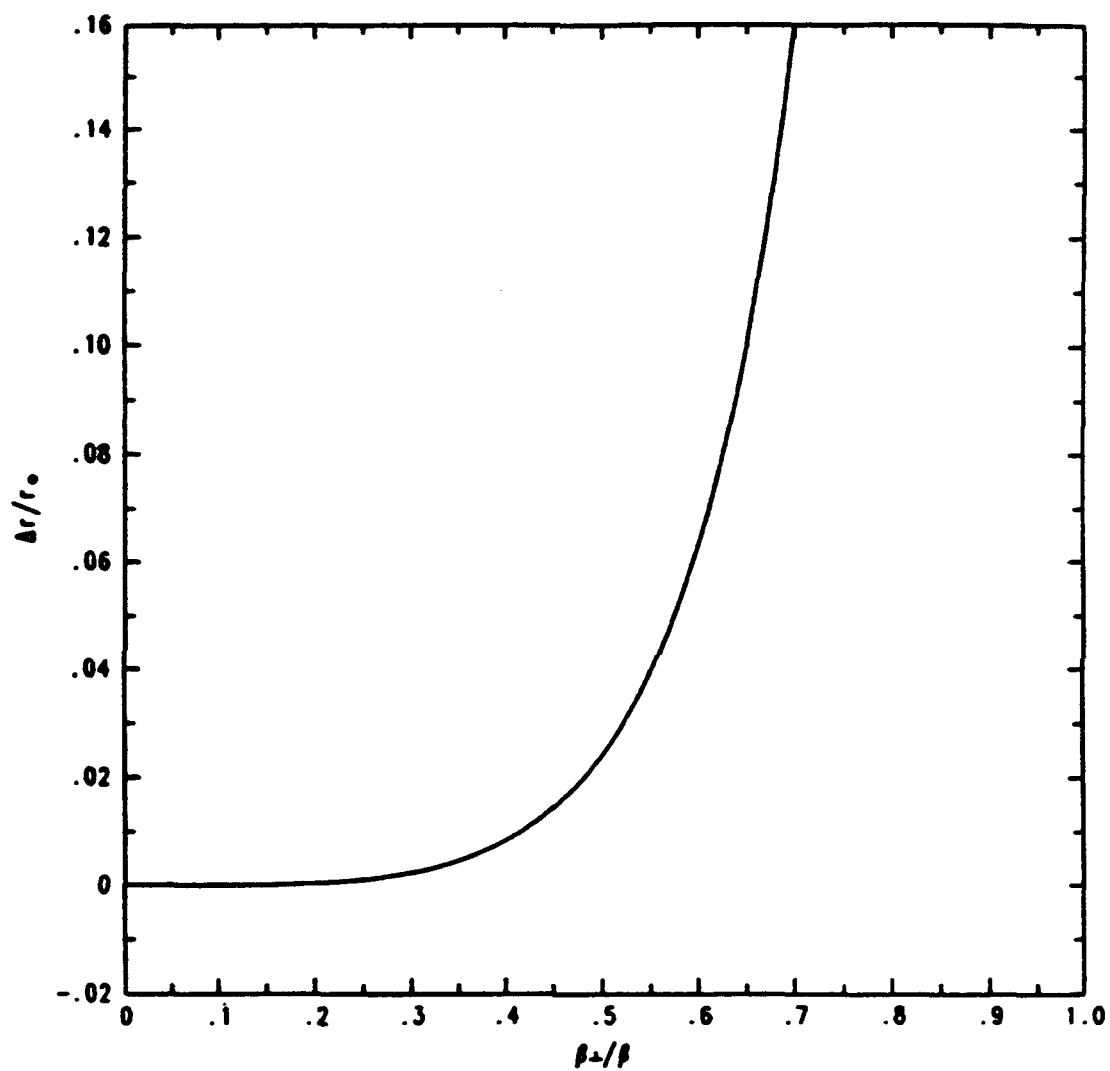


Fig. 21. Normalized radial displacement of the beam's equilibrium position vs. its normalized transverse velocity.

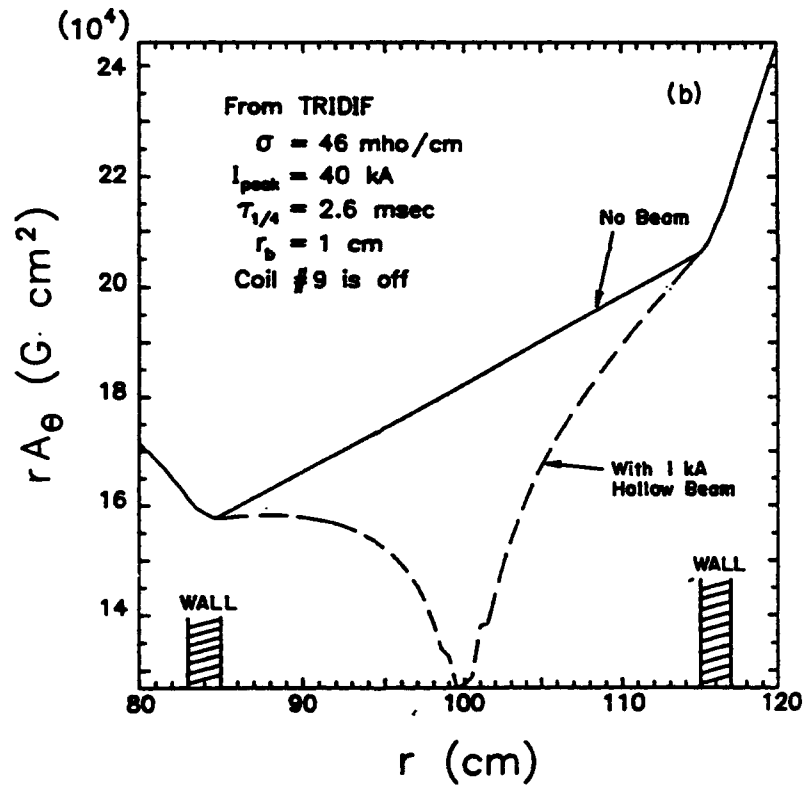
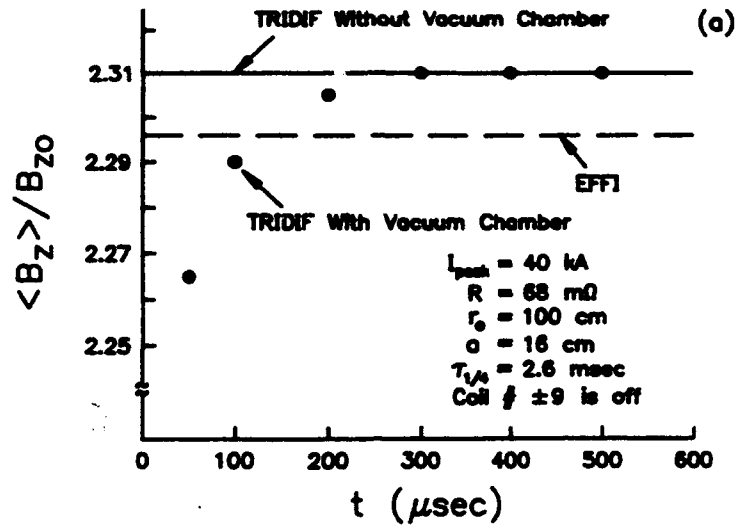
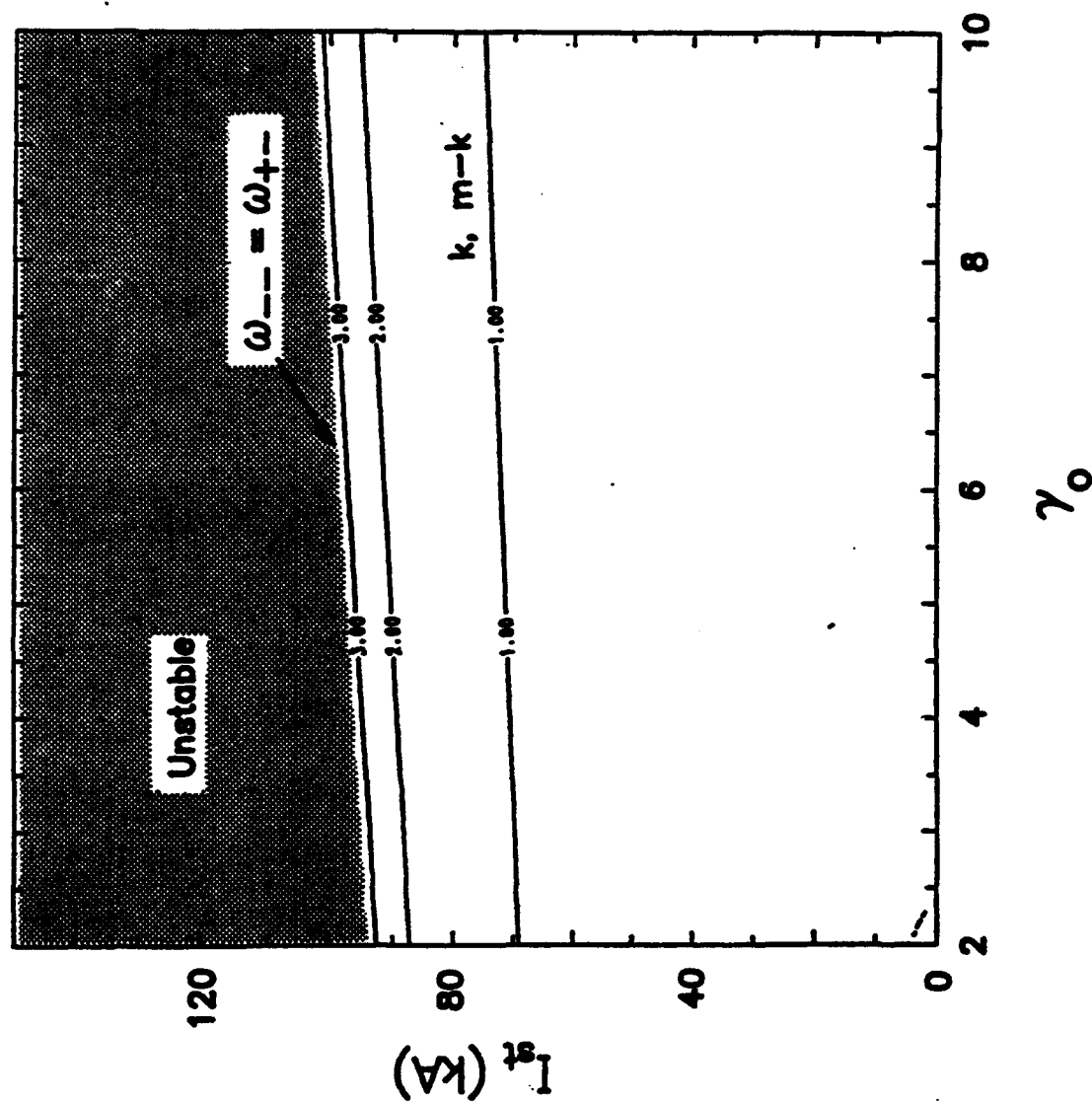


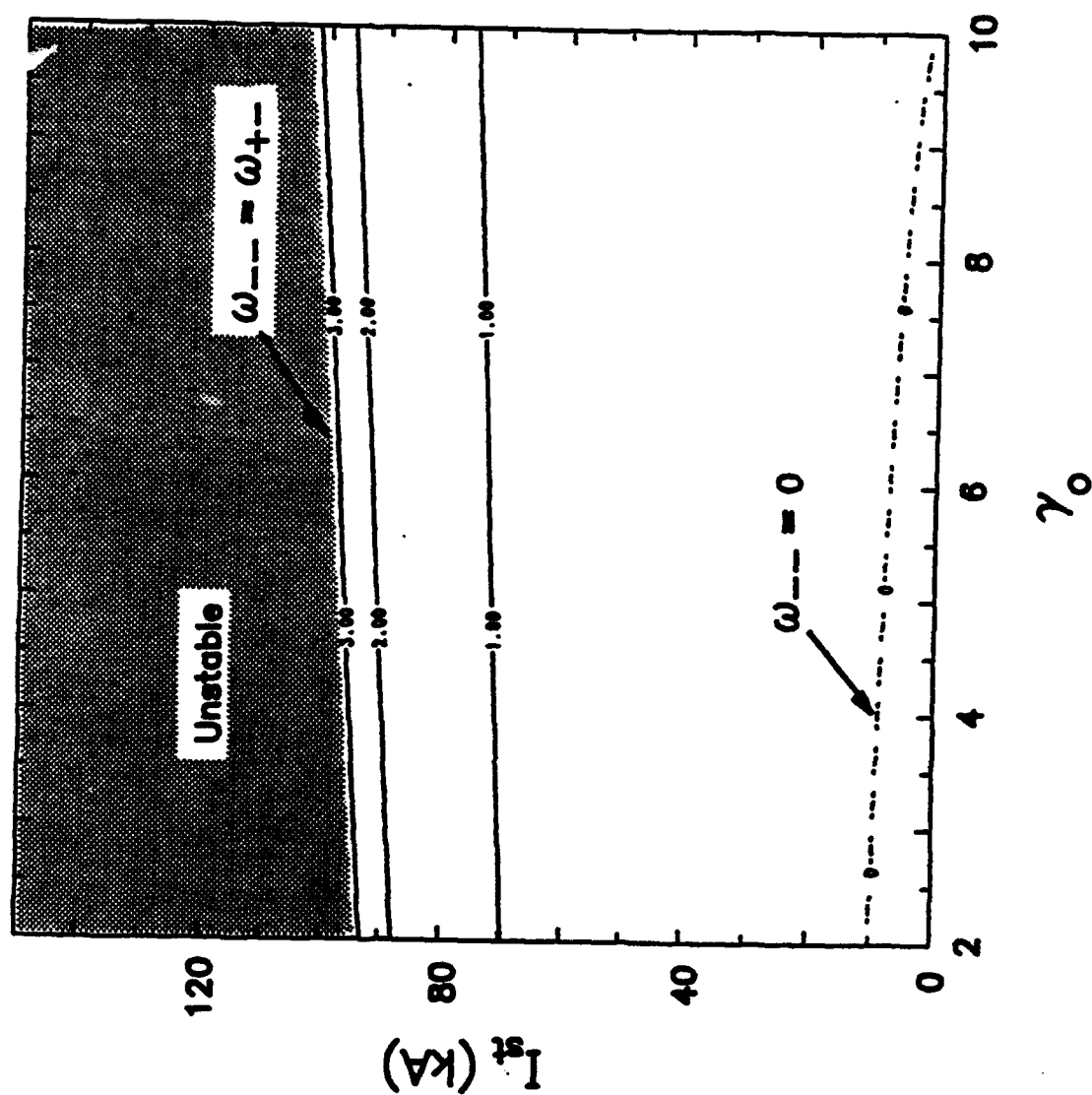
Fig. 22. (a) Betatron flux condition from TRIDIF and EFFI. The measured value of the betatron flux condition in the experiment is 2.3. (b) normalized magnetic flux vs. radial distance with and without the beam.



$$n_b(r_b/a)^2 \sim \gamma_0^{-3}$$

$$\begin{aligned} B_0 &= 4 \text{ kG} \\ I_b &= 1 \text{ kA} \\ r_0 &= 100 \text{ cm} \\ a &= 15.2 \text{ cm} \\ r_b &= 1 \text{ cm} \\ \rho_0 &= 23.4 \text{ cm} \\ m &= 6 \\ \alpha &= 0.03 \text{ cm}^{-1} \end{aligned}$$

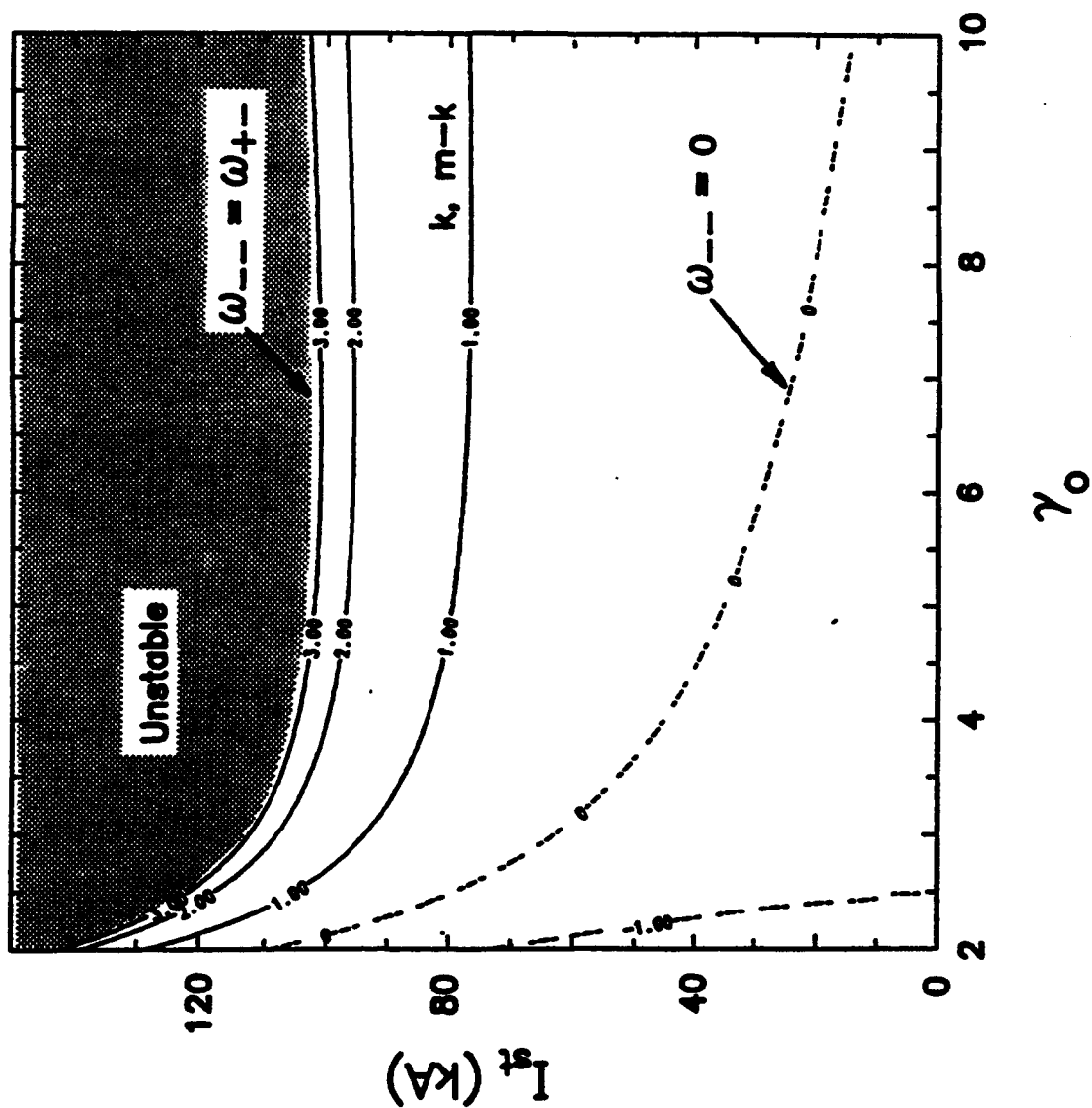
Fig. 23. Centroid integer resonances of the ω_{+-} low frequency modes ω_{+-} (bounce) and ω_{+-} (SF mode) before the image magnetic field of the beam diffused out of the vacuum chamber $n(r_b/a)^2 \sim \gamma_0^{-3}$.



$$\tilde{n}_e(r_b/a)^2 \sim \gamma_0^{-1}$$

$$\begin{aligned} B_0 &= 4 \text{ kG} \\ I_b &= 1 \text{ kA} \\ r_0 &= 100 \text{ cm} \\ a &= 15.2 \text{ cm} \\ r_b &= 1 \text{ cm} \\ \rho_0 &= 23.4 \text{ cm} \\ m &= 6 \\ \alpha &= 0.03 \text{ cm}^{-1} \end{aligned}$$

Fig. 24. As in Fig. (23) but after the image magnetic field of the beam diffused out of the vacuum chamber.



$B_\theta = 4$ kG
 $I_b = 1$ kA
 $r_o = 100$ cm
 $a = 15.2$ cm
 $r_b = 1$ cm
 $\rho_o = 23.4$ cm
 $m = 6$
 $\alpha = 0.03$ cm⁻¹

Fig. 25. Individual particle integer resonances of the two low frequency modes ω_{--} (bounce) and ω_{+-} (SF mode).

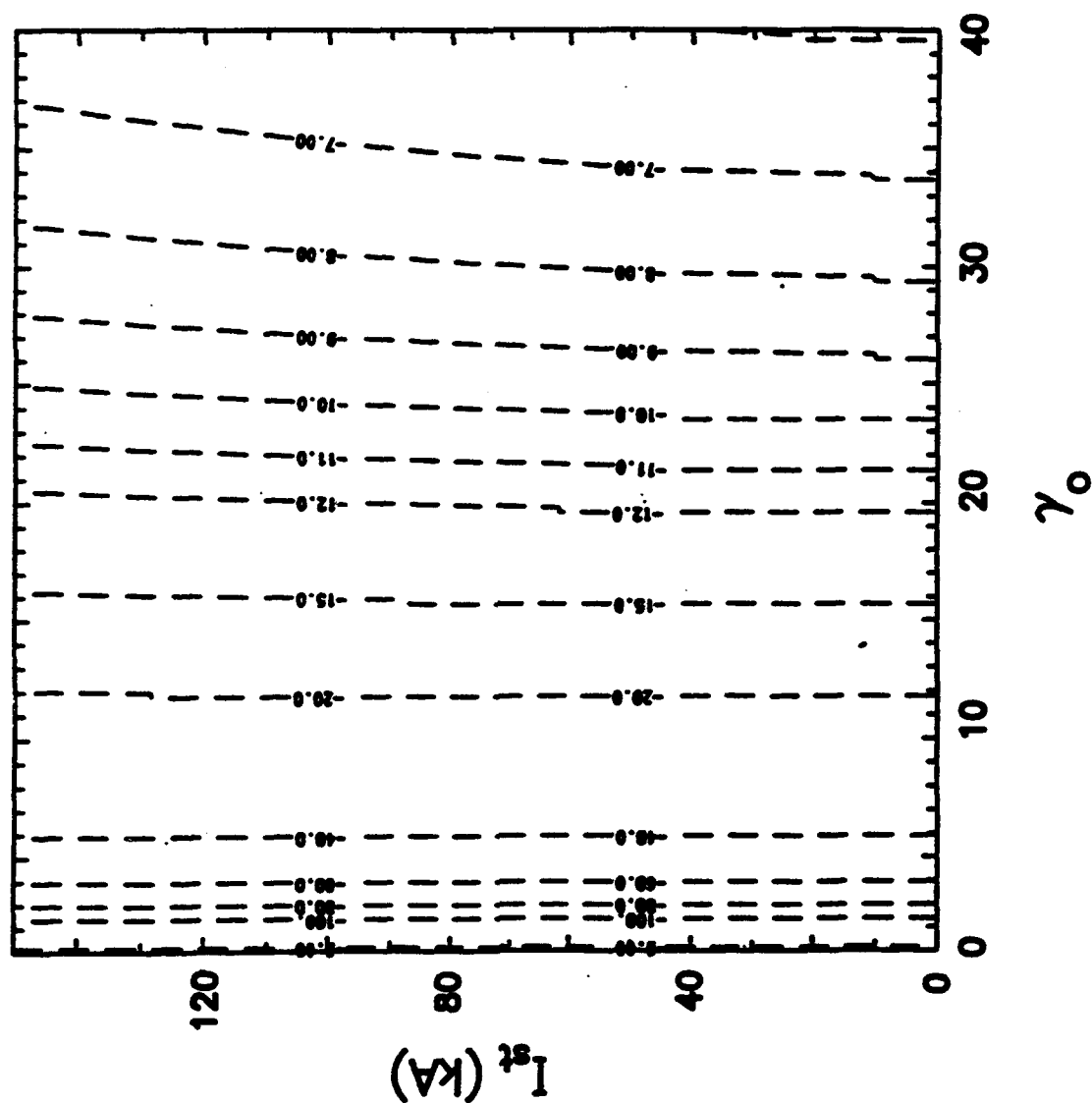


Fig. 26. Centroid integer resonances of the cyclotron mode ω_{-+} . For $\ell > 7$ and $I_{st} < 50$

kA these modes are independent of I_{st} .

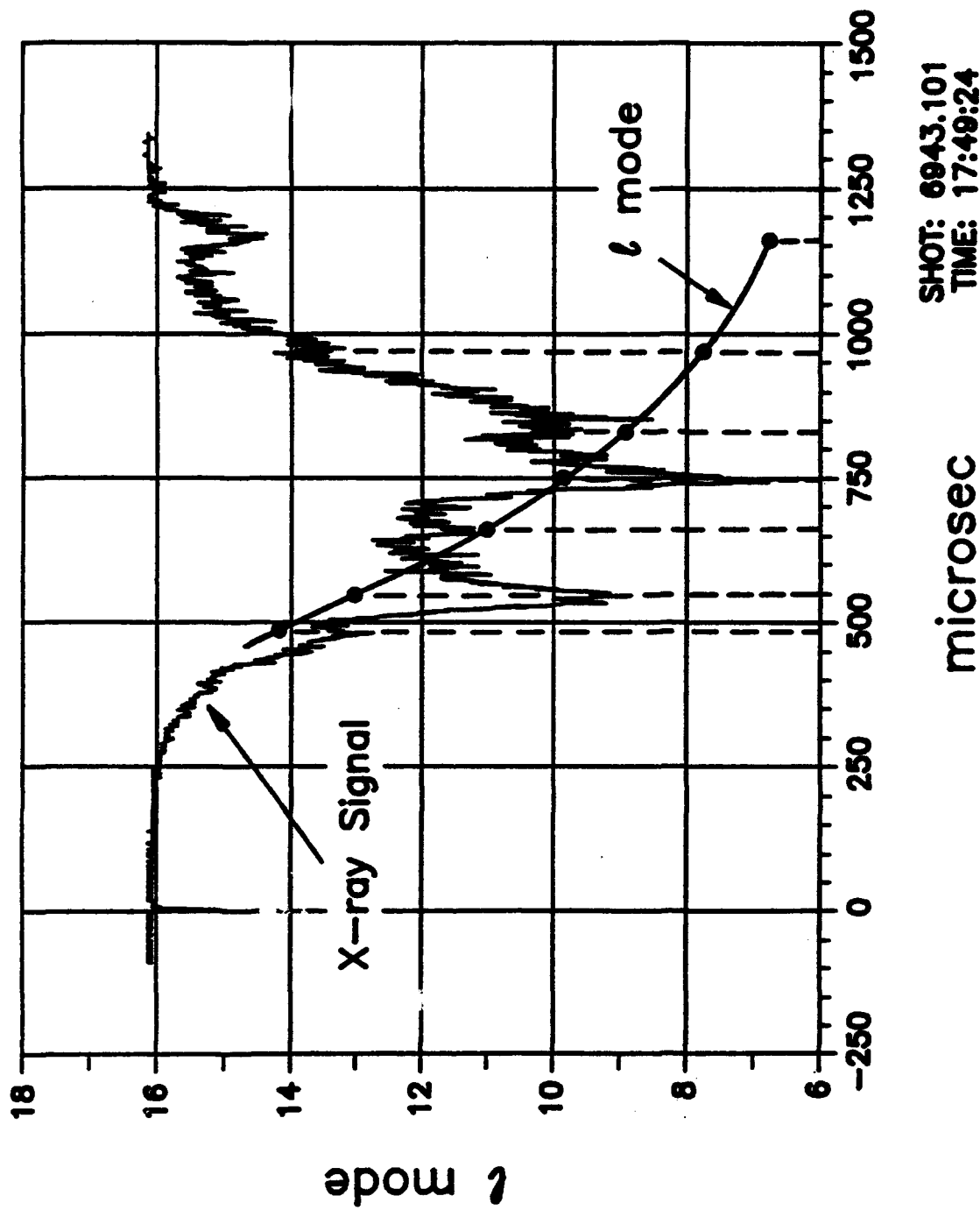


Fig. 27. X-ray signal as a function of time and l from Eq. (49), after replacing c/β_0 with

Ω_{rofo} .

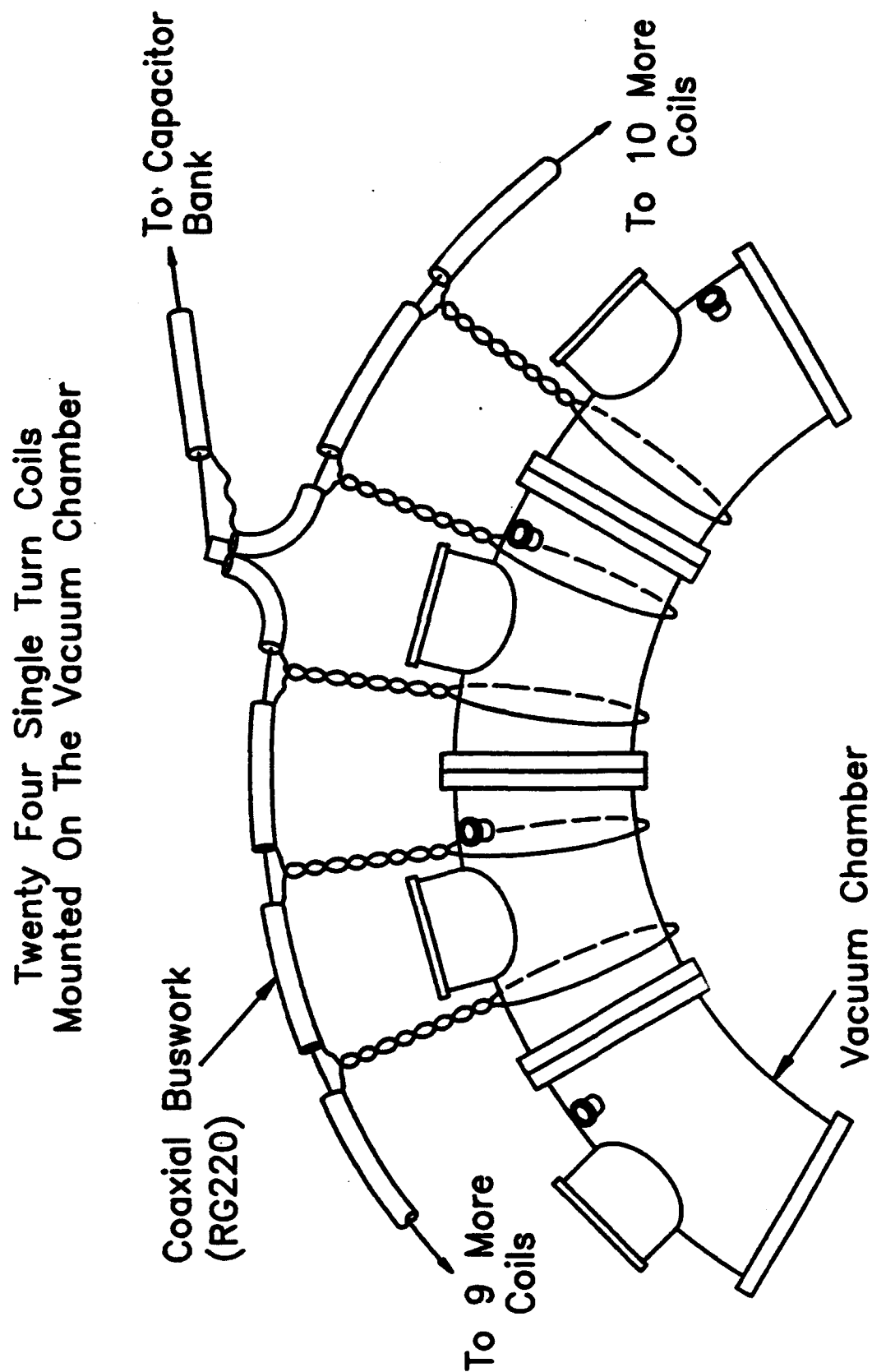


Fig. 28. Schematic of the initial twenty-four external resonant coils.

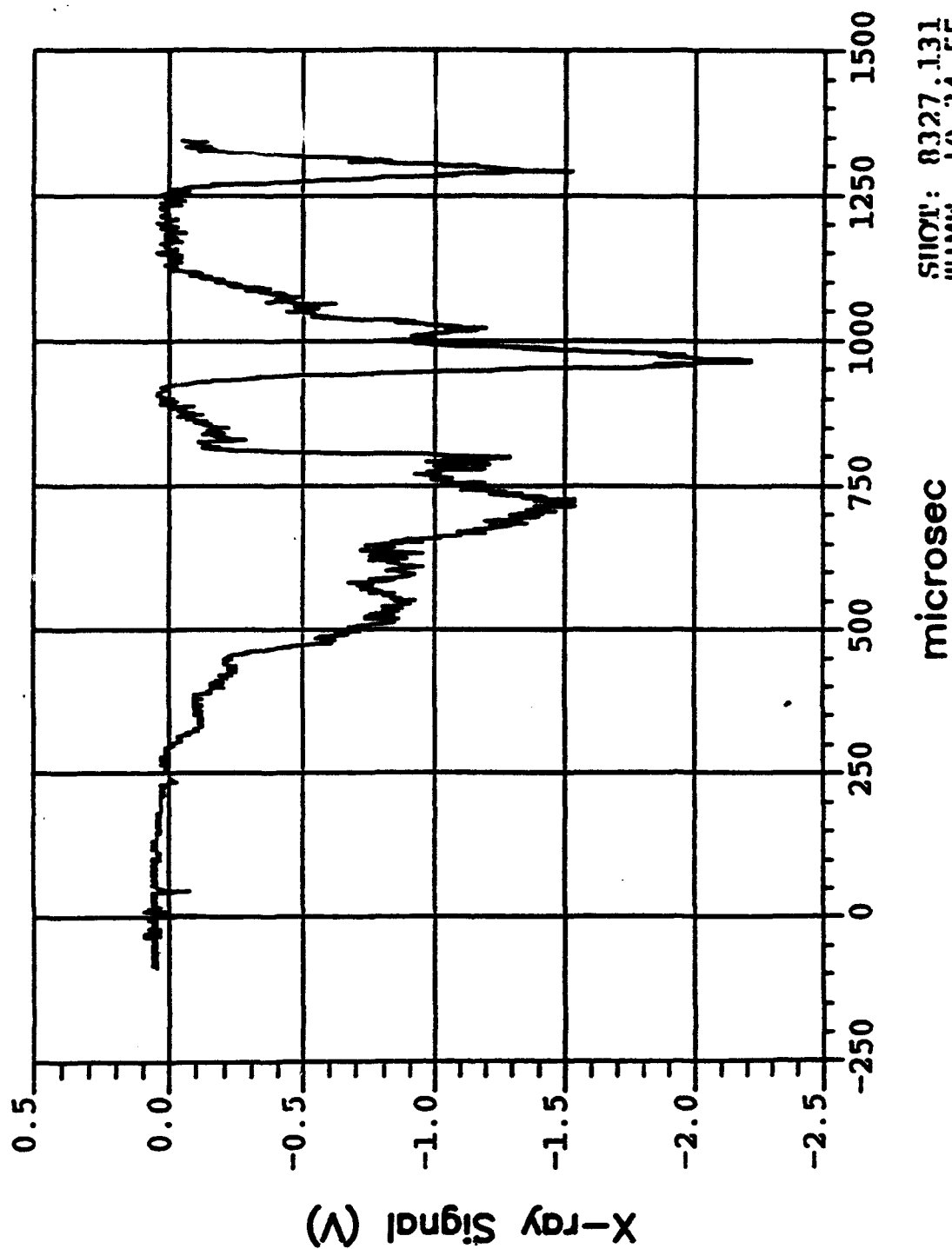


Fig. 29. X-ray signal vs. time. Between 800-900 μ sec the ratio $B_{90}/B_{20} \approx$ constant \neq integer.

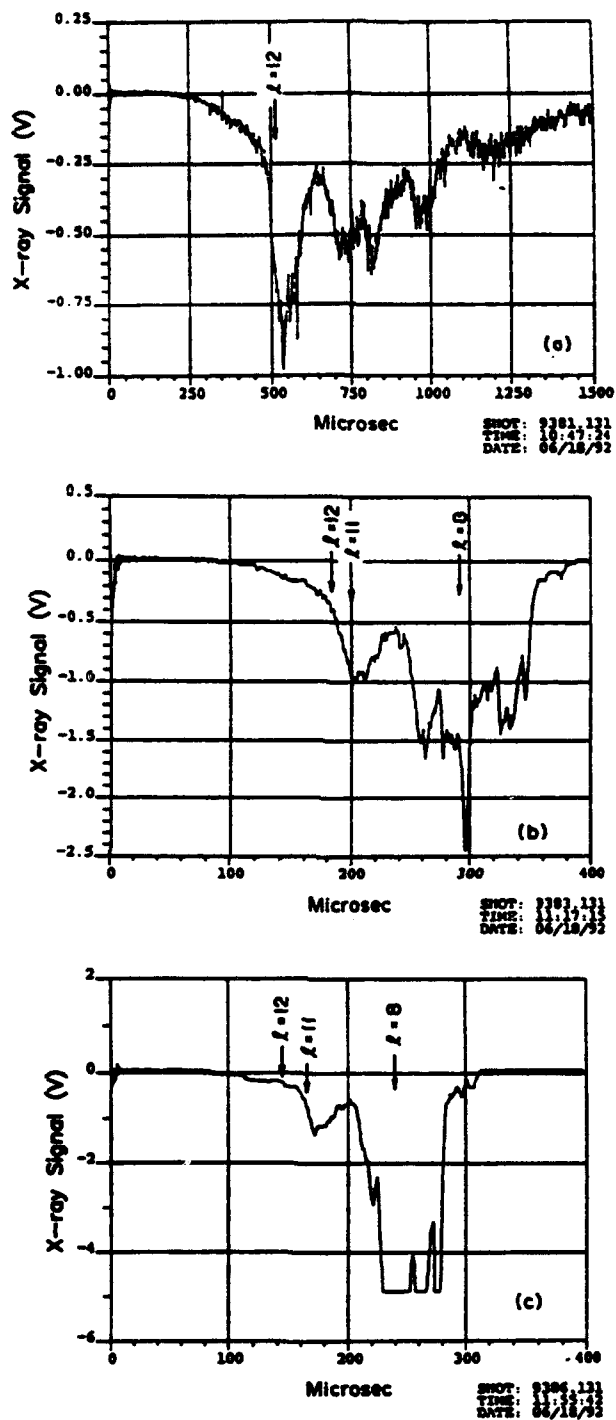


Fig. 30. X-ray signals as a function of time for three different acceleration rates: (a) $(\dot{B}_z)_{\text{peak}} = 0.69 \text{ G}/\mu\text{sec}$, (b) $1.69 \text{ G}/\mu\text{sec}$, and (c) $1.93 \text{ G}/\mu\text{sec}$. In all three runs $B_{\theta 0} \approx 4 \text{ kG}$.

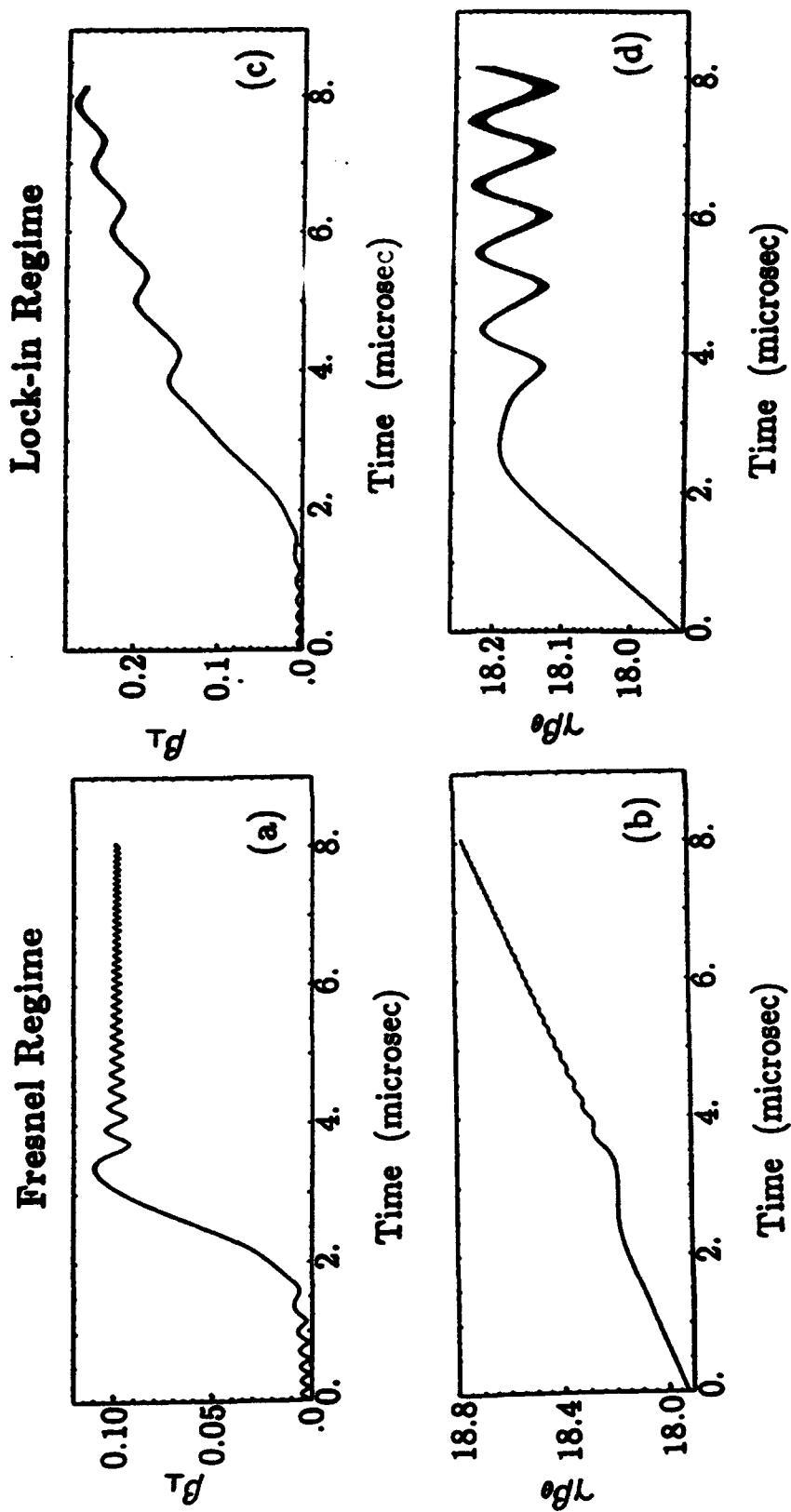


Fig. 31. Normalized transverse velocity β_L and $\gamma\beta_\theta$ vs. time in the Fresnel and Lock-in regimes.

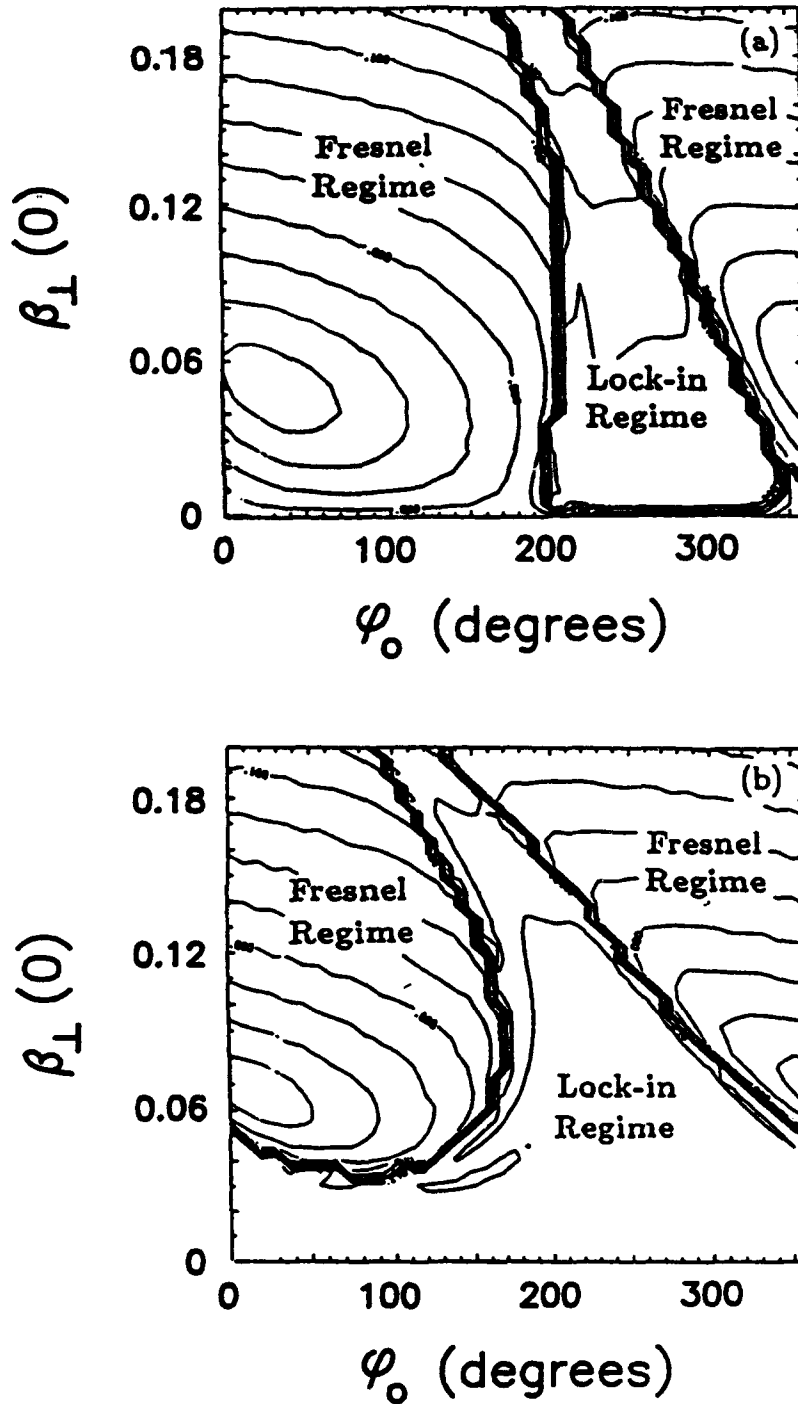


Fig. 32. Contour plots of the final β_{\perp} in the $\beta_{\perp}^{(0)}, \varphi_0$ plane where $\beta_{\perp}^{(0)}$ and φ_0 are the amplitude and phase of the initial value of transverse velocity and its phase. In (a) $\Delta B_{x0} = 0.2$ G and in (b) $\Delta B_{x0} = 0.3$ G.

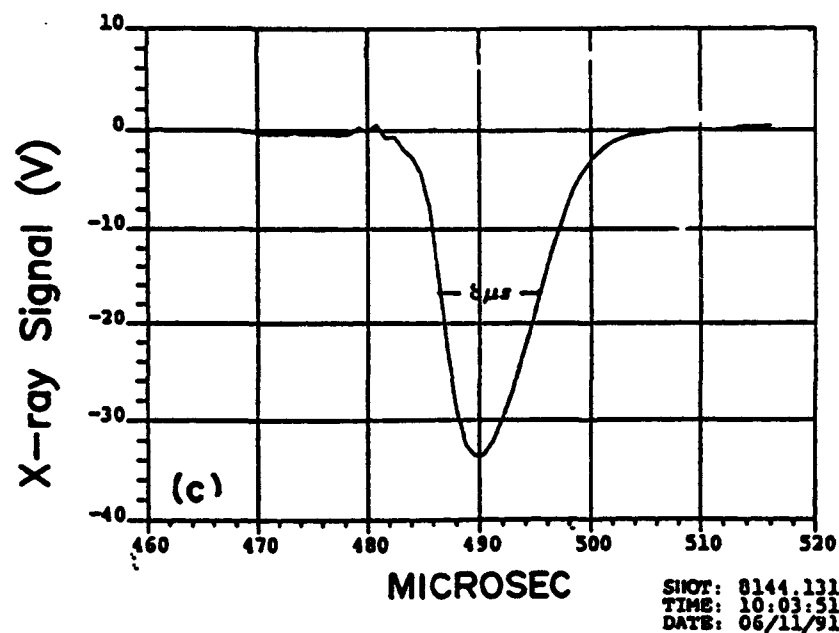
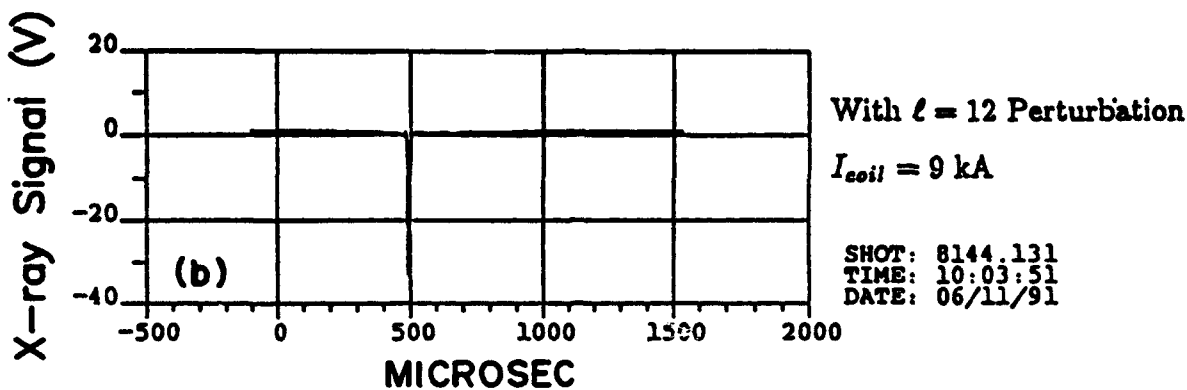
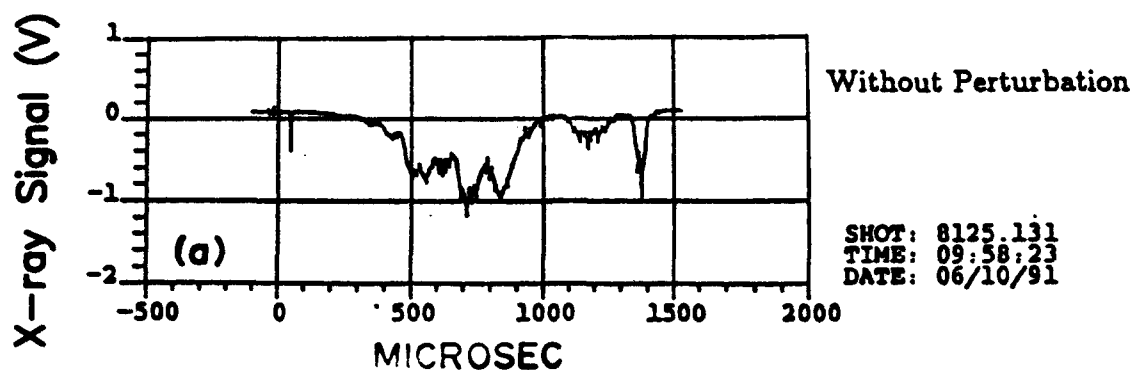


Fig. 33. X-ray signal vs. time: (a) Without the resonant coils, (b) when the resonant coils are activated and (c) the trace shown in (b) in a expanded time scale.

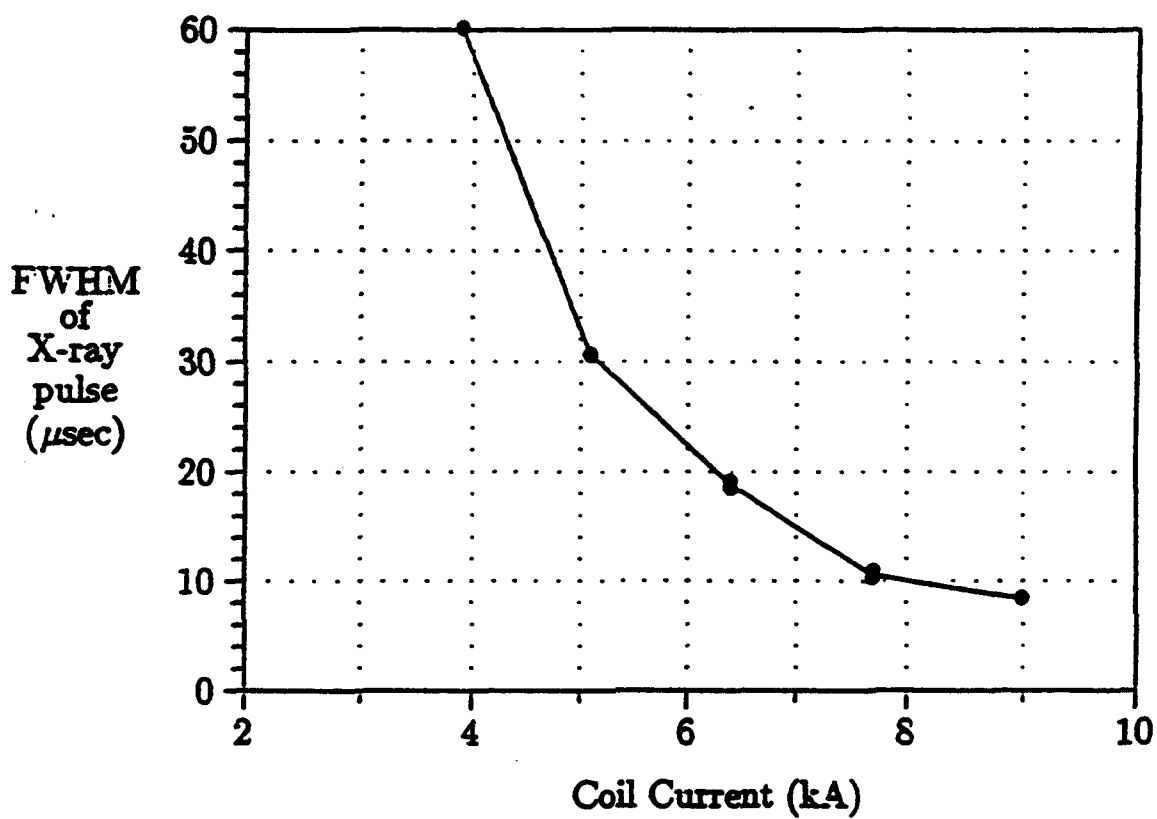
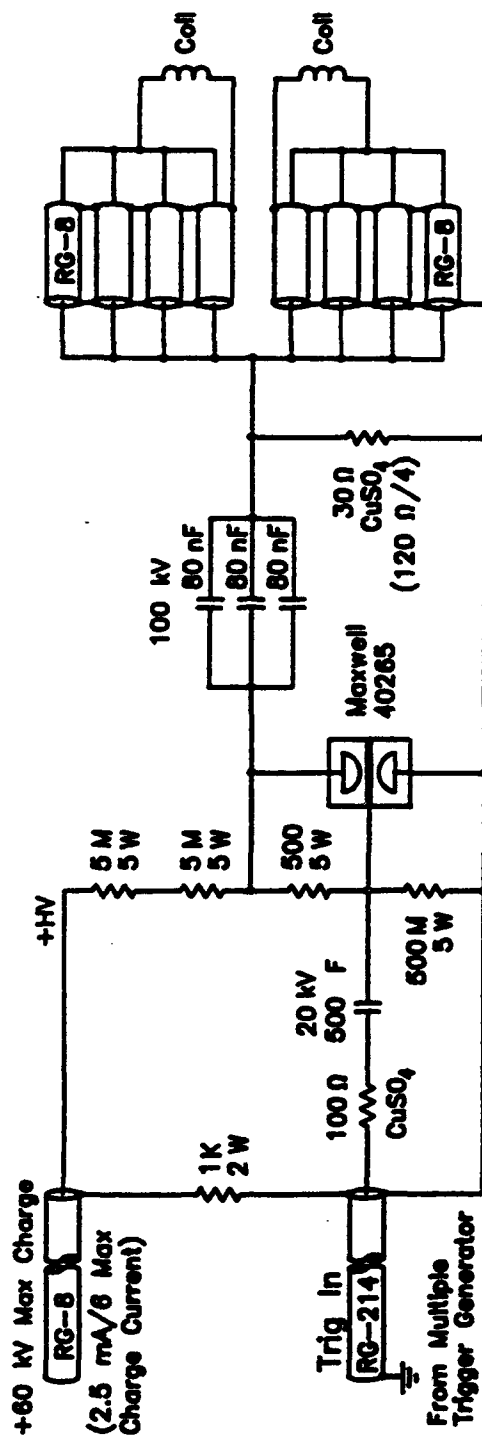


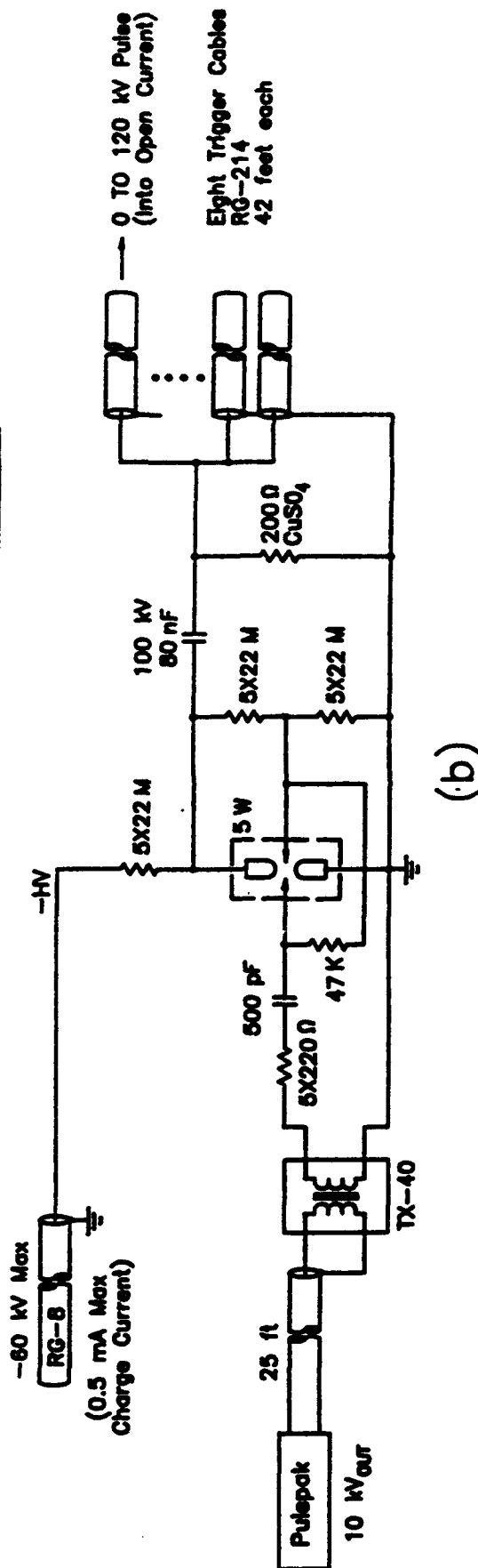
Fig. 34. Full width at half maximum (FWHM) of the x-ray pulse vs. resonant coil current when the coils are activated near the $\ell=12$ resonance.

Driver Circuit



(a)

Multiple trigger Generator



(b)

Fig. 35. Driver for the internal coils. (a) Driver circuit, (b) multitrigger generator circuit.

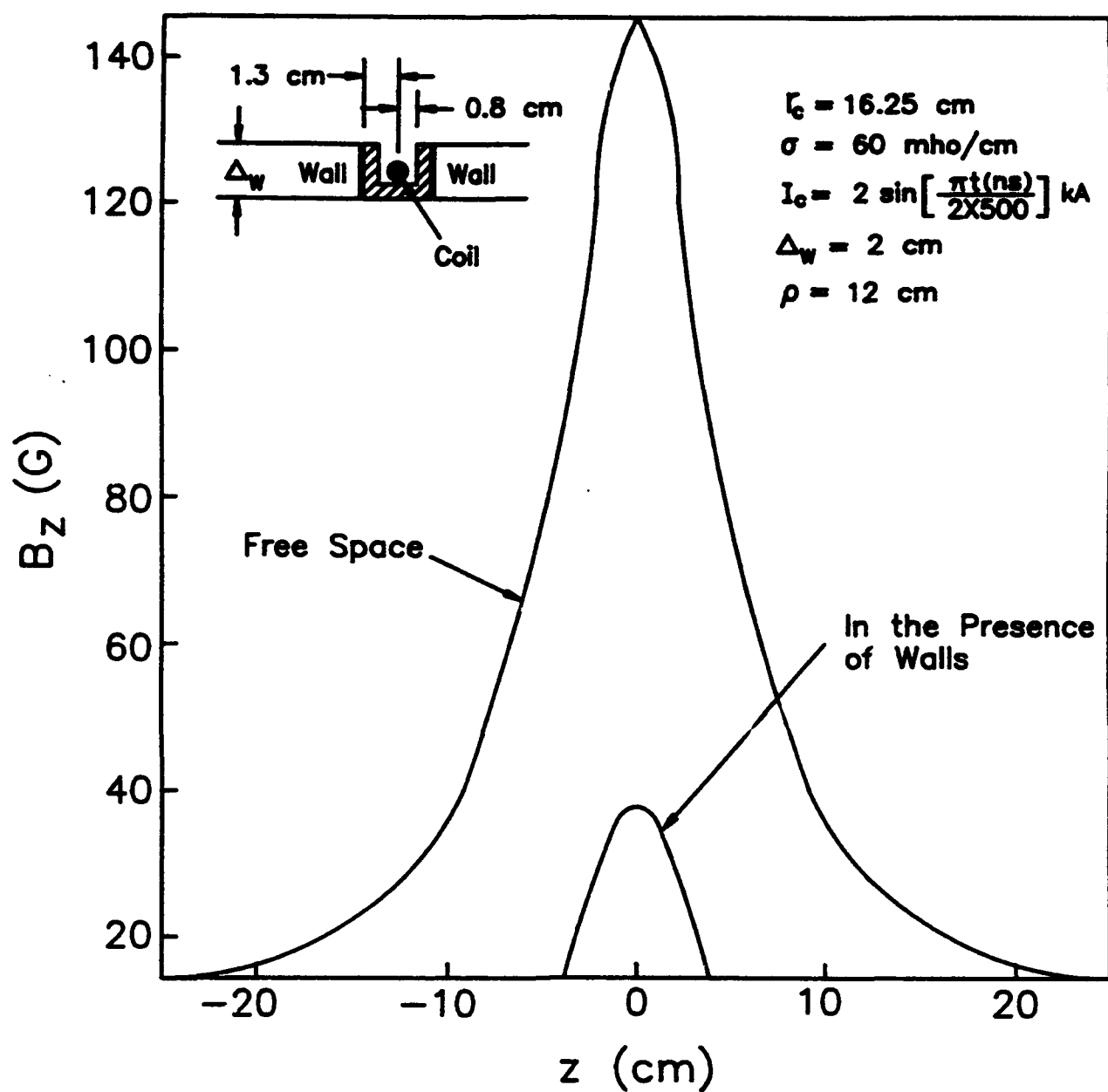


Fig. 36. Axial magnetic field at the radial distance of 12 cm from the minor axis in free space and in the presence of lateral walls.

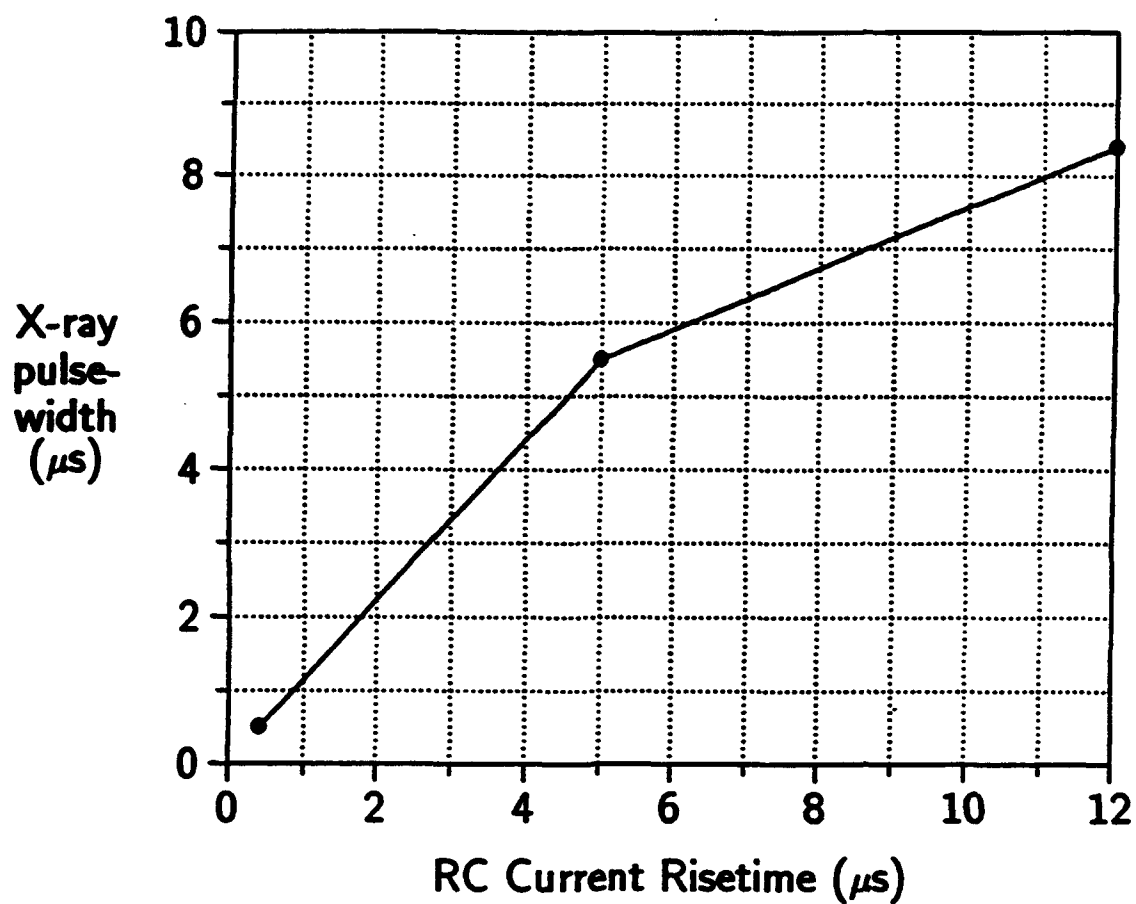


Fig. 37. FWHM of the x-ray signal vs. resonant coil current risetime.

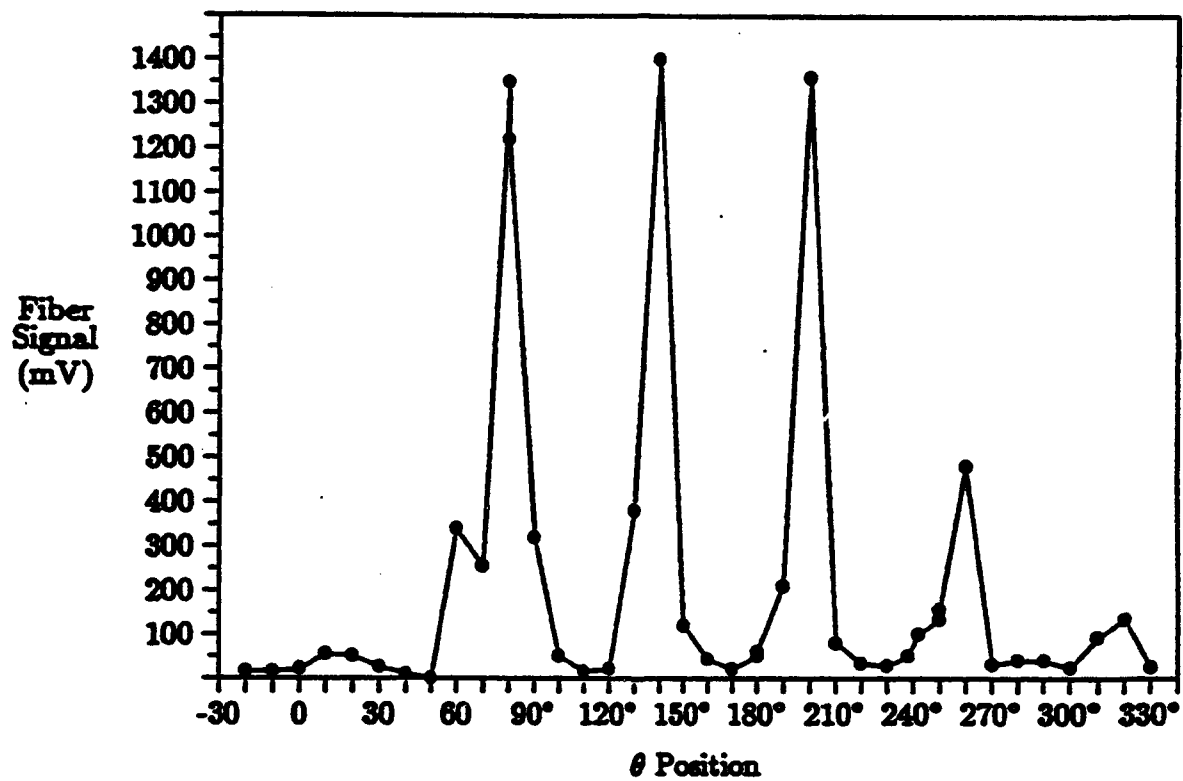


Fig. 38. Toroidal distribution of beam losses following the activation of the internal resonant coils.

From [pmt2.tex]

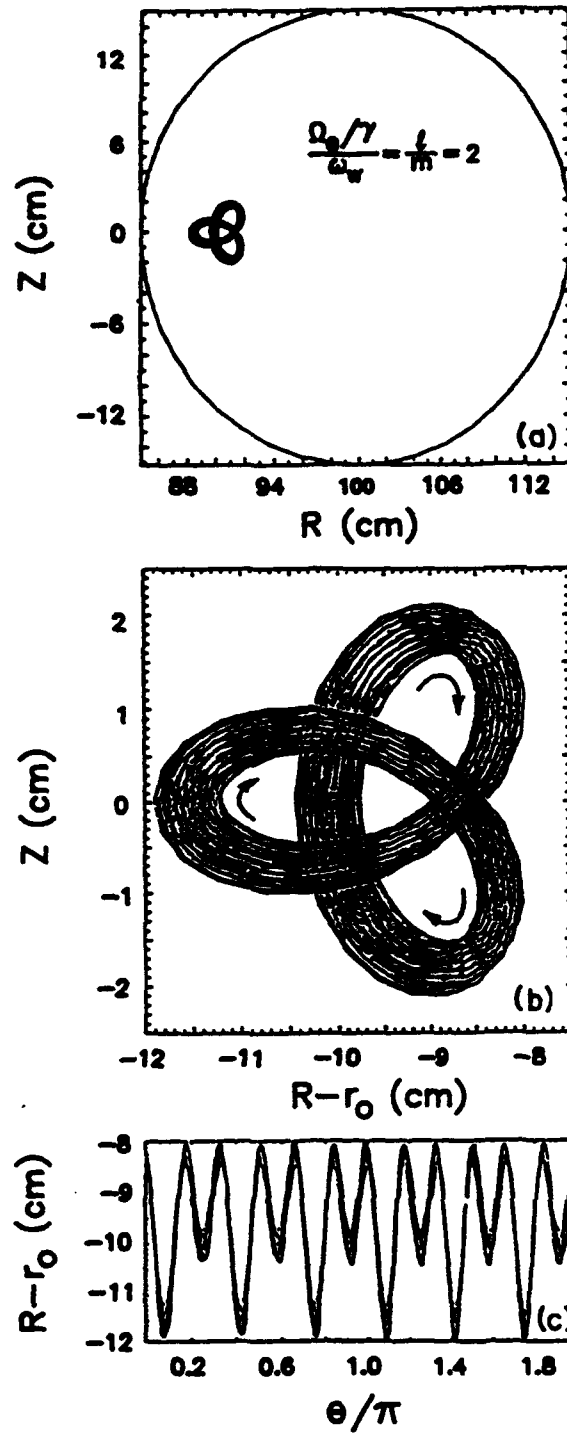


Fig. 39. Results from the numerical integration of orbit equations for the beam centroid near $\ell=12$. (a) Projection of the orbit in the (R, Z) plane for 160 nsec, (b) as in (a) but in a expanded scale, (c) projection of the orbit in the $(R - r_0, \theta)$ plane.

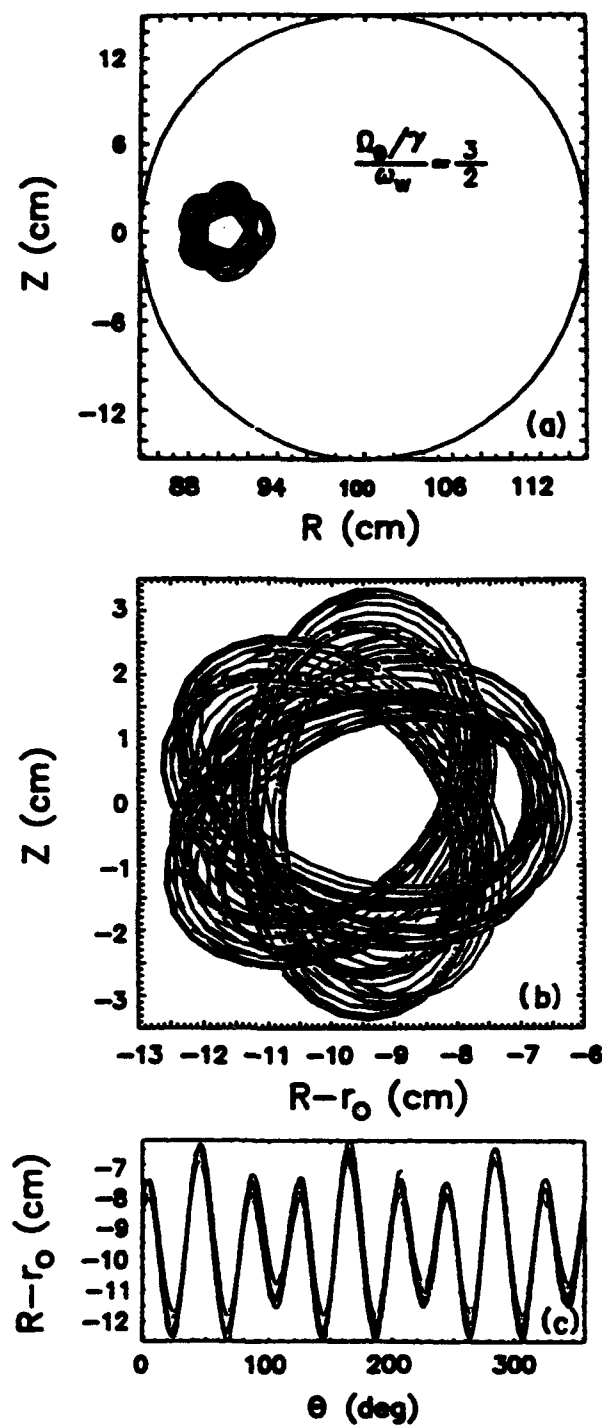


Fig. 40. Results from the numerical integration of orbit equations for the beam centroid near $\ell=9$. (a) projection of the orbit in the R,Z plane for 160 nsec, (b) as in (a) but in a expanded scale, (c) projection of the orbit in the $(R - r_0, \theta)$ plane.

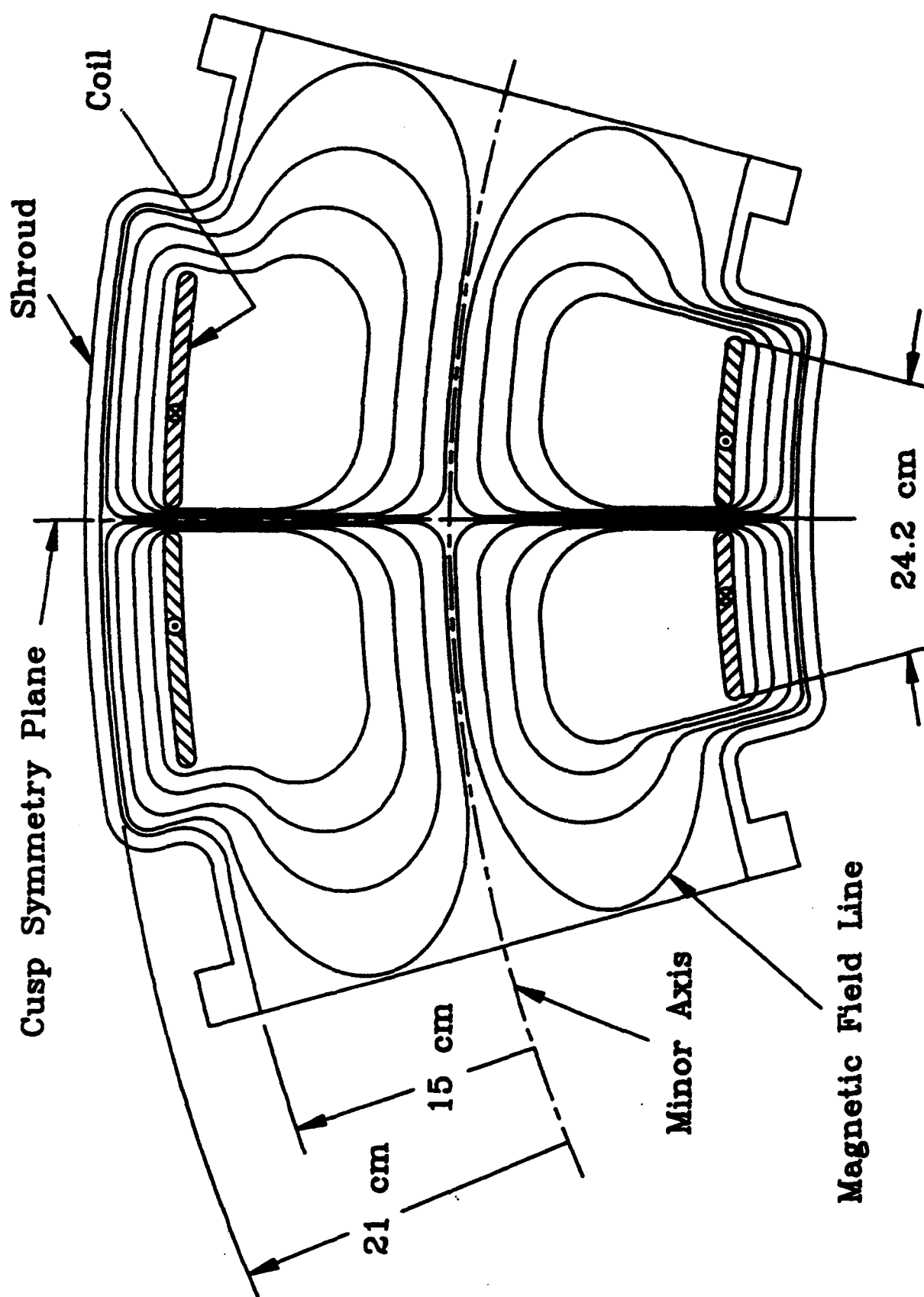


Fig. 41. Wide cusp and magnetic field lines.

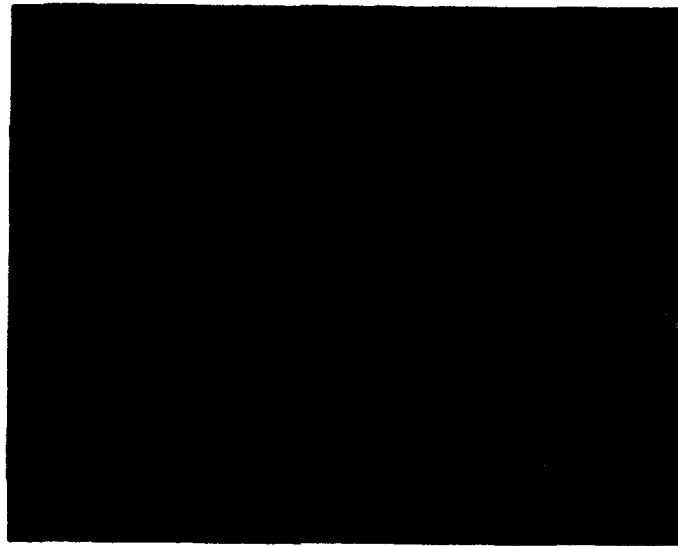


Fig. 42. Photograph of one of the double cusps.

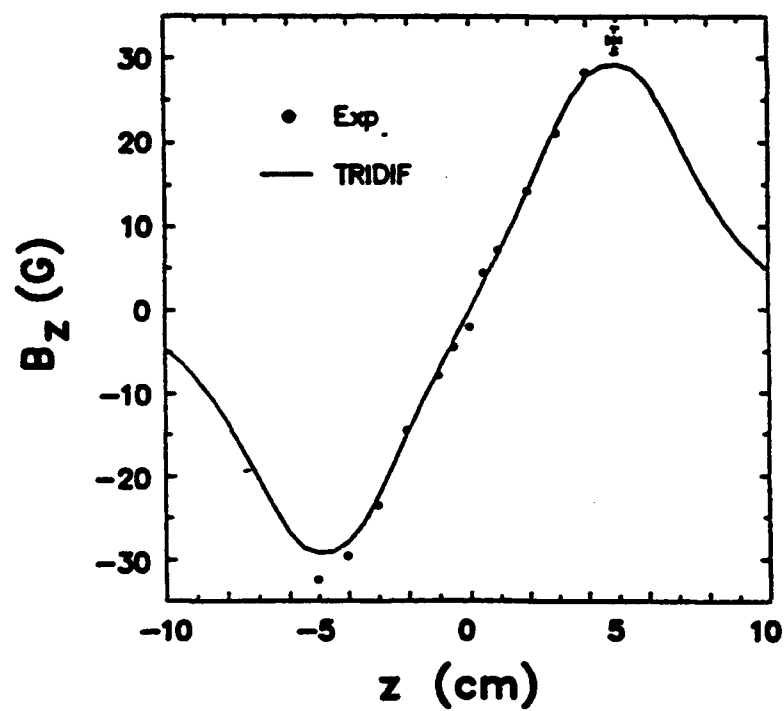
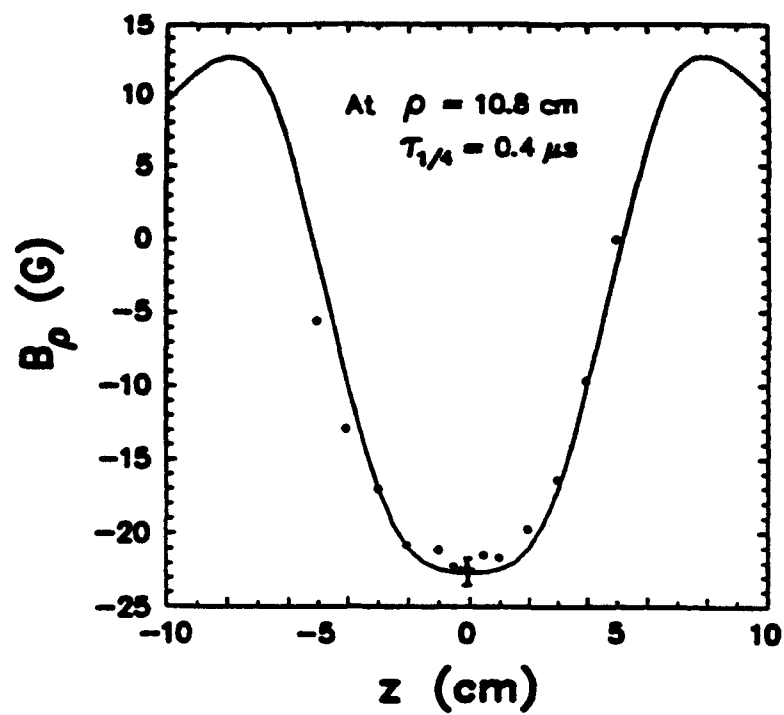


Fig. 43. Axial profile of radial (a) and axial (b) fields at $\rho=10.8 \text{ cm}$ from the minor axis.

Solid lines are from TRIDIF and solid circles from the experiment.

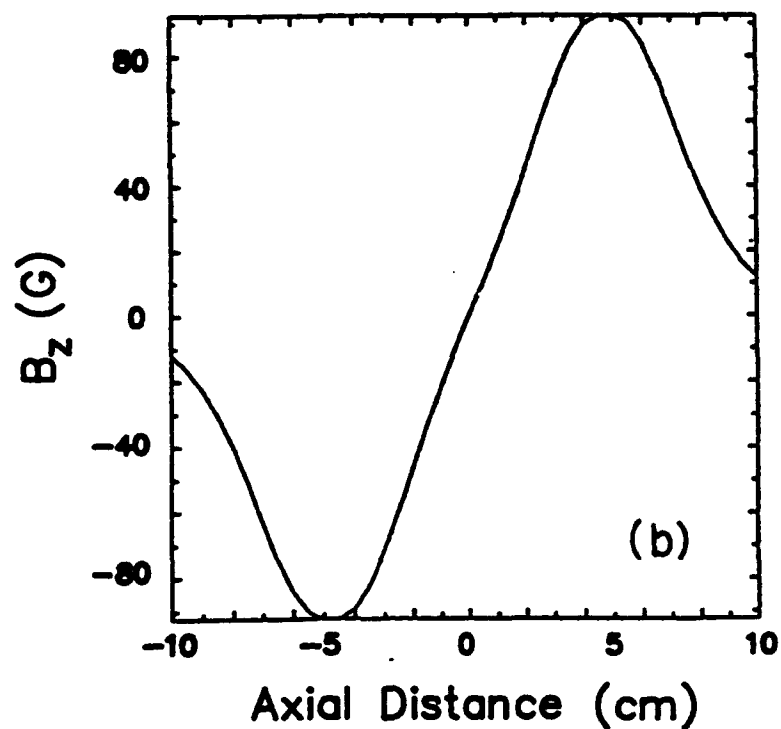
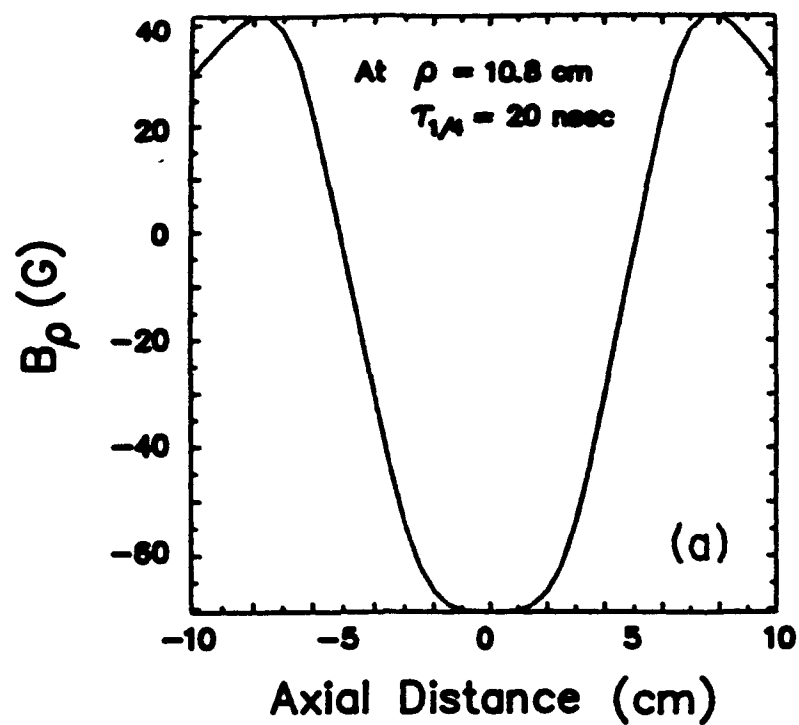


Fig. 44. Axial profile of radial (a) and axial (b) fields at $\rho=10.8$ cm from the minor axis.

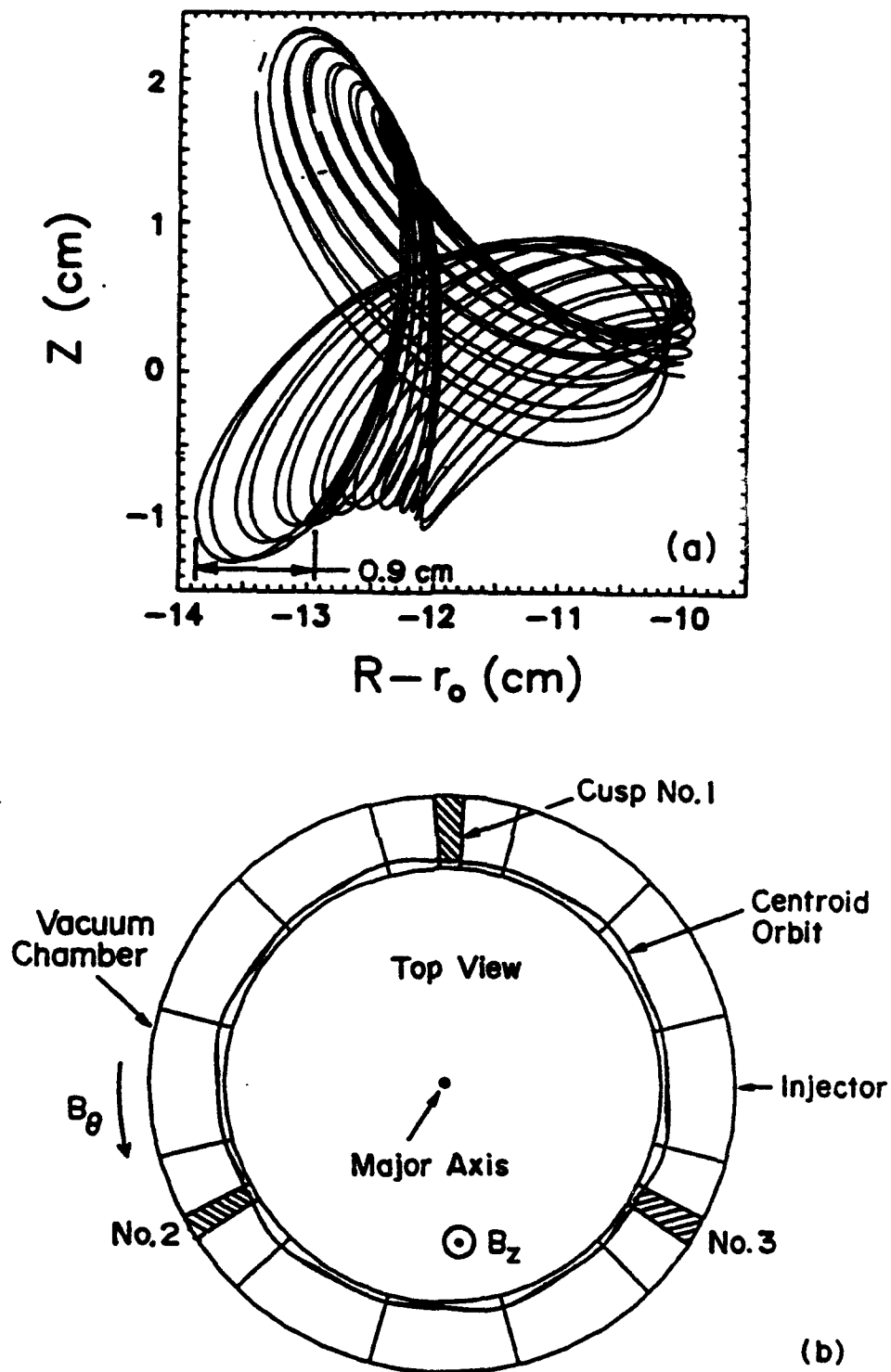


Fig. 45. (a) Projection of the beam centroid orbit in the transverse plane; (b) top view of the orbit.

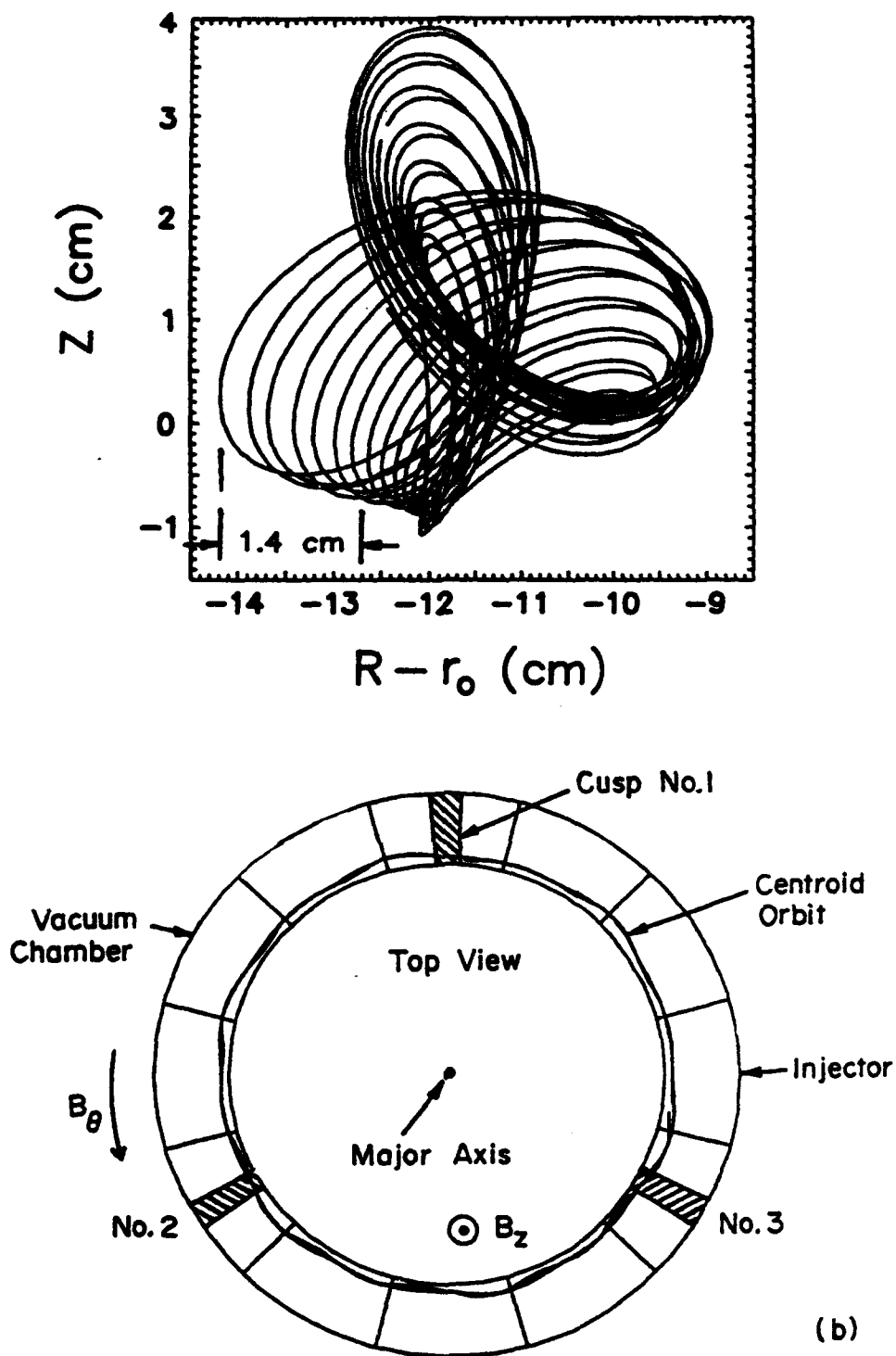


Fig. 46. (a) Projection of the beam centroid orbit in the transverse plane when $B_\theta = 0$; (b) top view of the orbit.

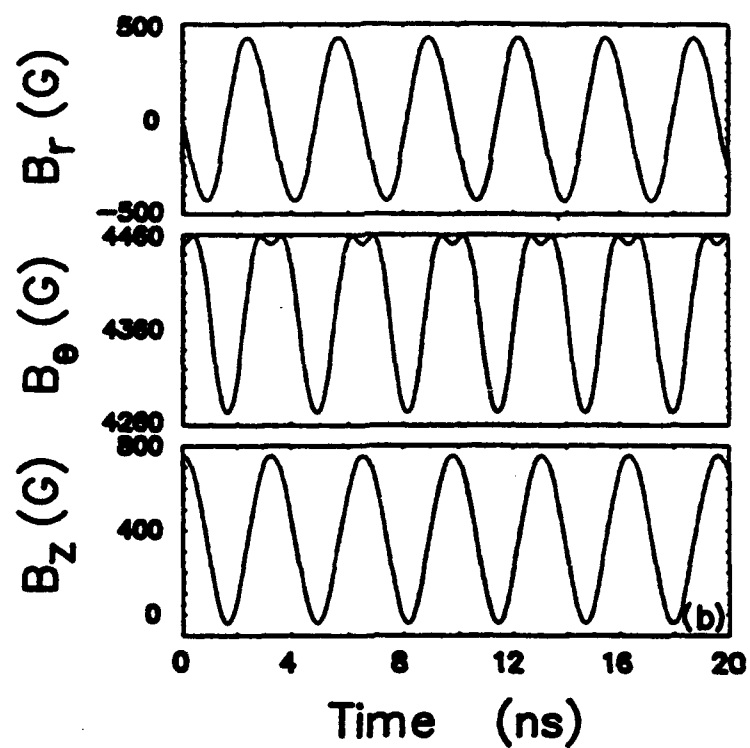
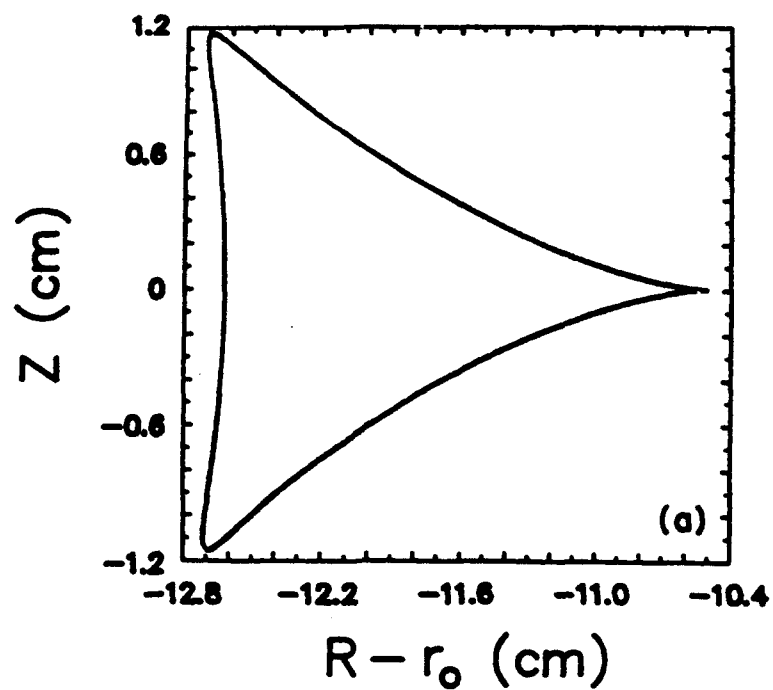
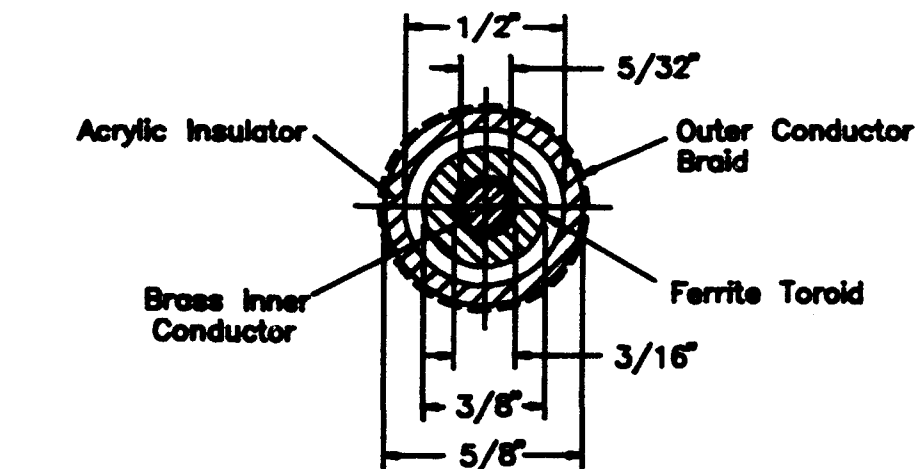
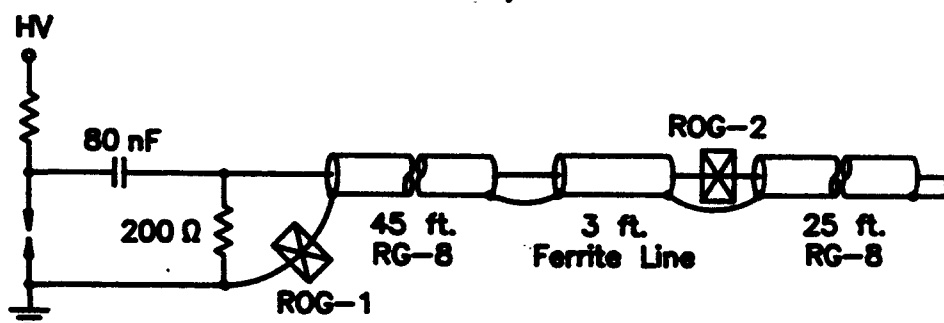


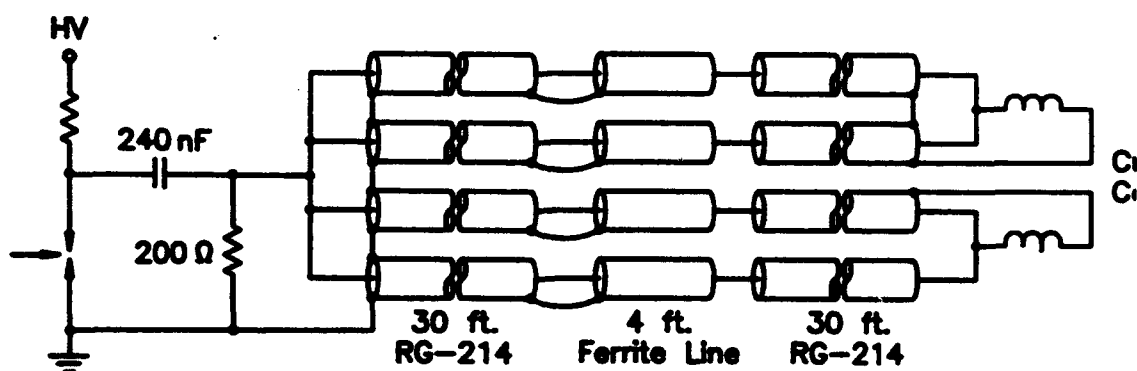
Fig. 47. (a) Projection of the beam centroid orbit in the transverse plane for 20 nsec when the cusps are off; (b) the three components of the magnetic field at the beam centroid.



(a)



(b)



(c)

Fig. 48. (a) Cross sectional view of the pulse sharpener, (b) set-up to test the sharpener and (c) layout of the drivers to power the double cusps.

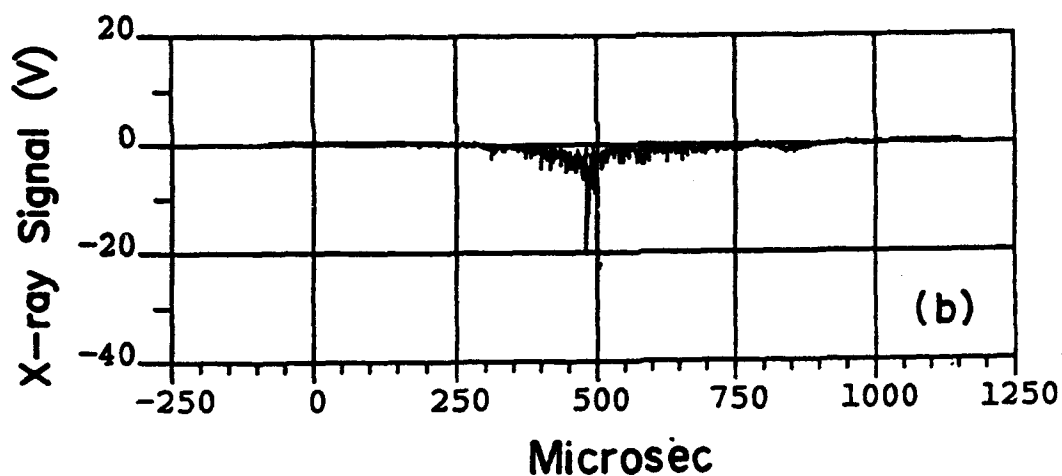
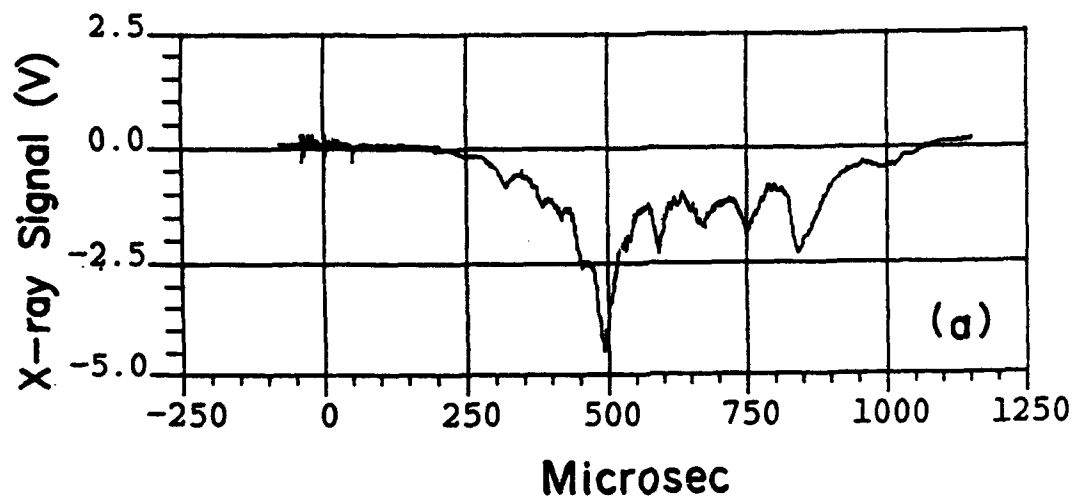


Fig. 49. X-ray signal vs. time: (a) With the double cusps off and (b) with the double cusps on. The amplitude of the signal in 49a is higher than that in Figs. 18 and 27 because of the copper wires in the double cusps.

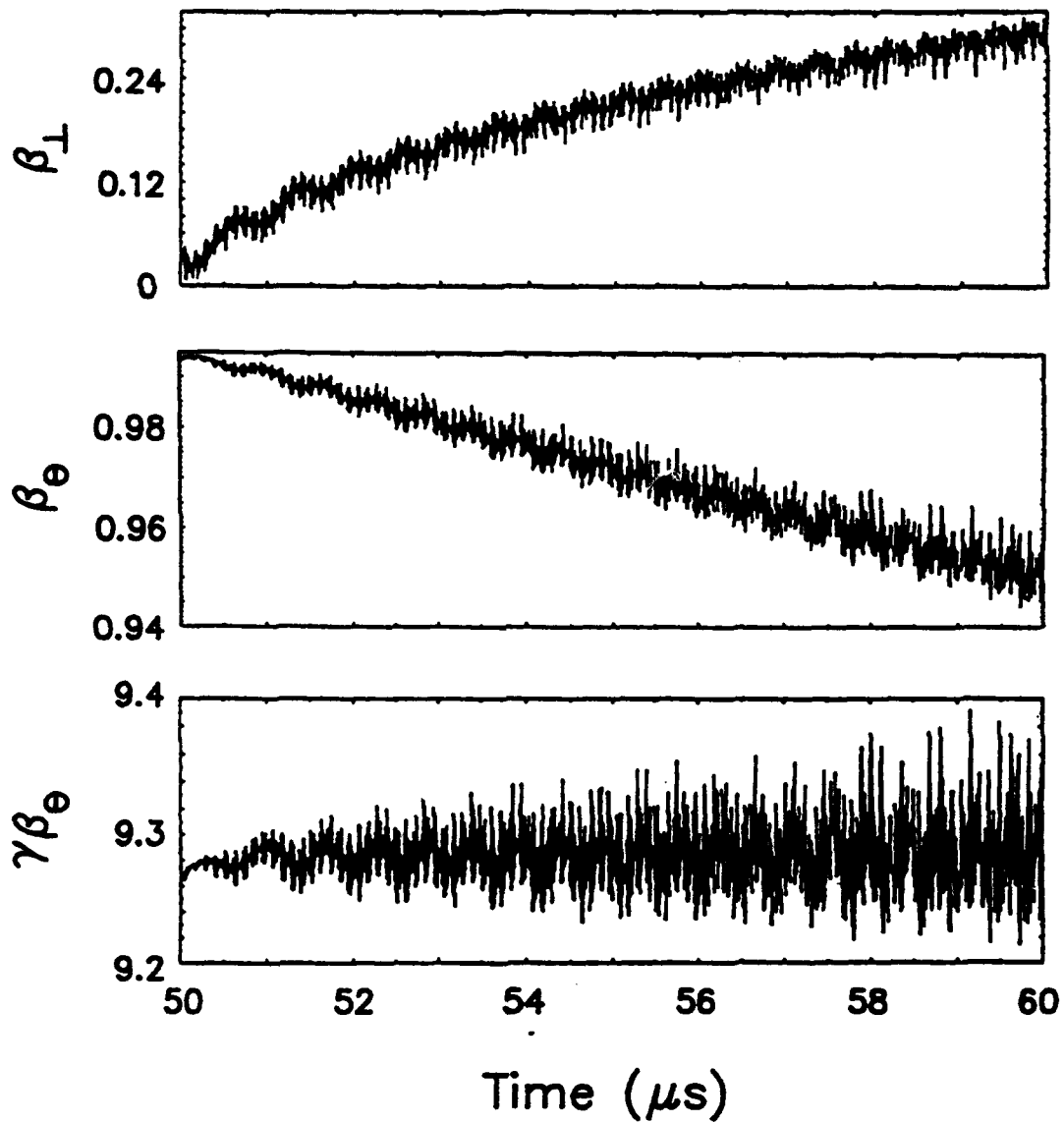


Fig. 50. Beam centroid transverse velocity β_{\perp} , axial velocity β_{θ} and $\gamma\beta_{\theta}$ between 50 and 60 μsec , immediately after the beam locks in the $\ell = 19$ mode. The assumed $\pm 2\text{mm}$ random spatial fluctuations in the stellarator windings are less than those in the experiment.

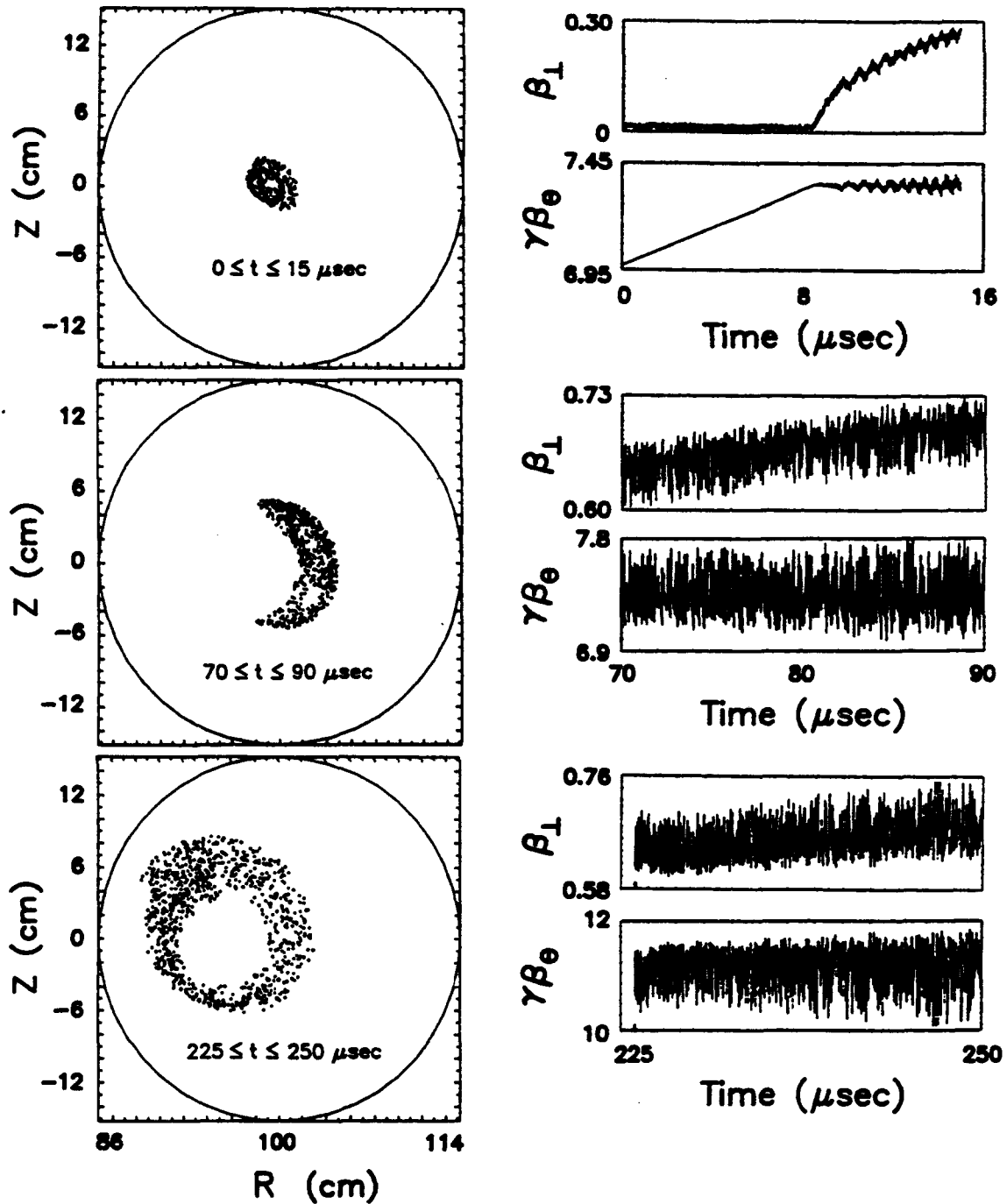


Fig. 51. The left column shows the positions the centroid crosses the $\theta = 0$ plane. The right column shows β_{\perp} and $\gamma\beta_{\theta}$ in the time intervals of interest. The beam locks in the $\ell = 24$ mode at $\sim 8 \mu\text{sec}$ and unlocks at $150 \mu\text{sec}$. During this time the equilibrium position remains still.

Appendix T

Resonance Extraction from the Modified Betatron

**NRL Modified Betatron Accelerator
Technical Review Workshop**

June 27-29, 1989

**Resonance Extraction from
the Modified Betatron**

**Presented by
D. Dialetis**

Collaborators:

**C.A. Kapetanakos
S.J. Marsh
P. Loschialpo**

THREE STAGES FOR THE RING EXTRACTION

Radial outward displacement of the ring equilibrium position by mismatching the vertical magnetic field to the electron energy with a local time dependent magnetic field ($\tau = 5 - 10 \mu sec$)

A local vertical magnetic field disturbance generated by the agitator coil transforms the ring into a helix in the toroidal direction. The minor radius of the helix increases with each passage through the agitator coil ($\tau = 40 - 60 nsec$)

Eventually, the electrons reach the extractor, which has the property that it cancels out the external magnetic fields transverse to its axis. Thus, the electron ring unwinds into a straight beam ($\tau = 2 nsec$)

RADIAL OUTWARD DISPLACEMENT OF THE RING

Numerical simulation of the ring dynamics showed that the energy mismatch should increase slowly in relation to the bounce period. Then, as the ring follows its equilibrium position, its radius of rotation around the equilibrium position remains small

Also, the initial energy mismatch of the ring should be very small, so that the initial amplitude of the bounce motion is very small.

Local vertical extraction field

$$B_z^{extr} = B_{z0}^{extr} (1 - e^{-t/\tau})$$

COMPUTER SIMULATION (MOBE - PIC)

RUN PARAMETERS

Initial beam energy $\gamma_0 = 100$ [99.98]

Major radius r_0 (cm) = 100

Initial beam minor radius r_b (cm) = 4.2 mm

Initial beam center position r_i (cm) = 100

Betatron magn. field at r_0 , $z = 0$, B_{0z} (G) = 1704.5

Toroidal magn. field at r_0 , $z = 0$, $B_{0\theta}$ (KG) = -4kG

Initial emittance ϵ (rad - cm) = 280 mradcm - normalized emittance

External field index $n = 0.5$

Wall diffusion time τ_D (nsec) = ∞

Time step (nsec) = 200 ps

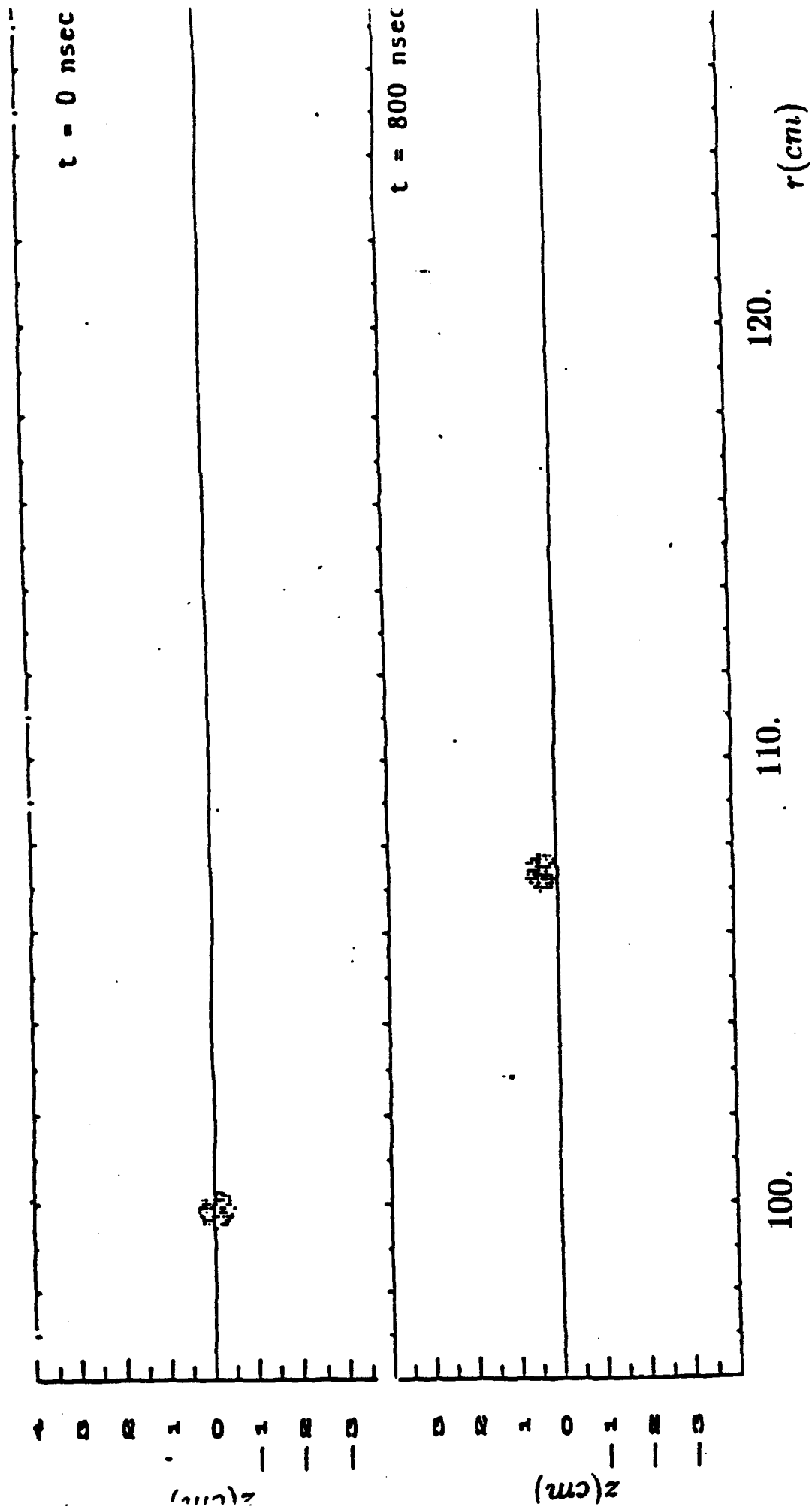
No. of particles = 128

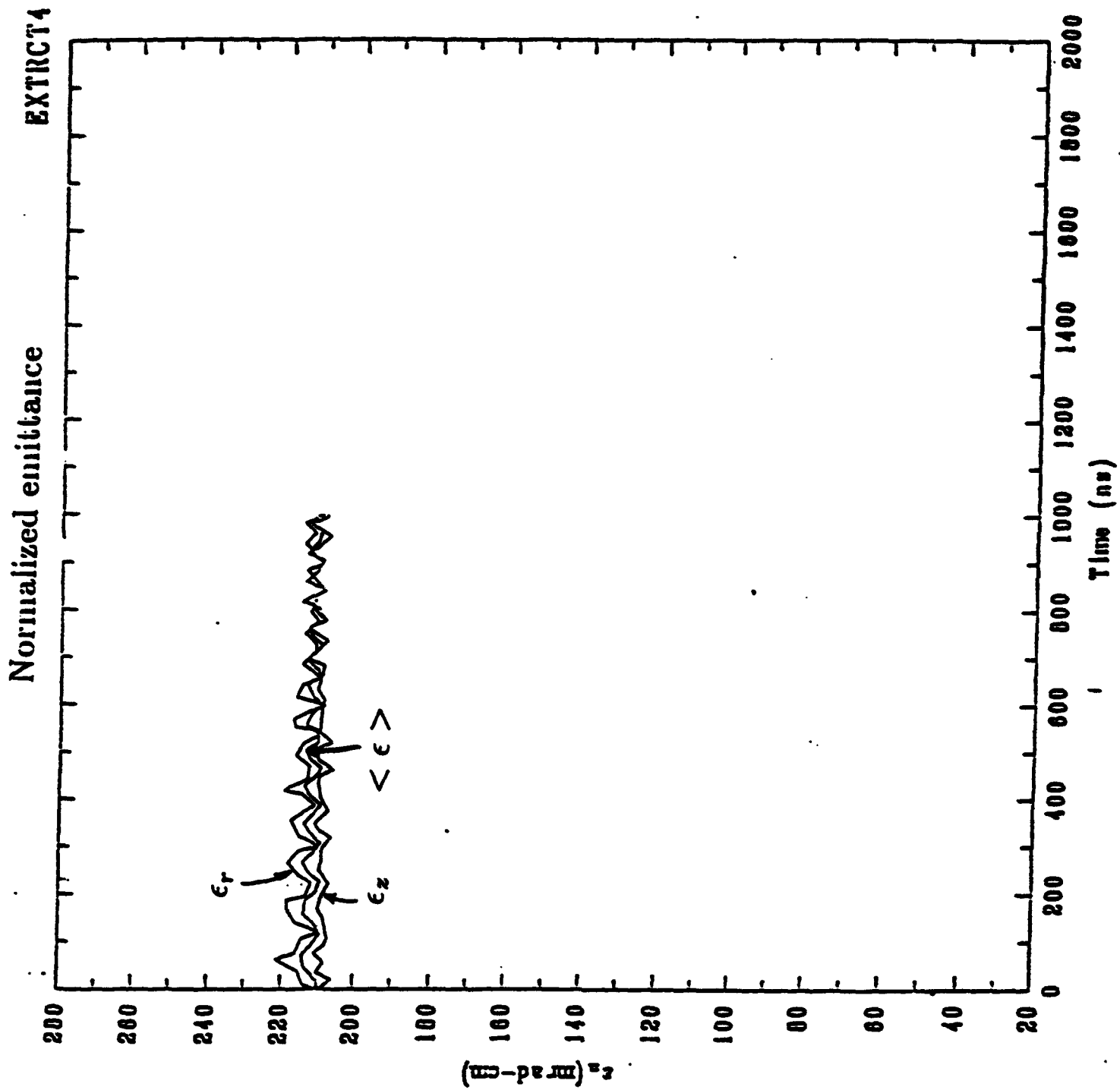
Trapping field $B_z^{\text{Trap}} = 204.5$ G

Time constant $\tau = 4$ μ sec

COMPUTER SIMULATION

Ring Envelope During Extraction





Ring Extraction

The NRL extraction technique

Basically, this technique consists of transforming the circulating electron ring into a stationary helix, in the toroidal direction, by exciting the resonance that naturally exists for some specific values of the ratio of the vertical to toroidal magnetic field.

Transformation of the ring into a helix is achieved with a localized vertical magnetic field disturbance that is generated by an agitator coil.

Two modes of operation:

- Pulsed
- Static

RESONANCE EXTRACTION

Electrons passing through the agitator are made to gyrate about the toroidal field, B_θ .

When the ratio B_z/B_θ at the agitator satisfies the resonance condition

$$B_z/B_\theta = 2\ell/(2\ell^2 - 1), \ell = 1, 2, 3, \dots$$

all the electrons execute identical helical orbits (Coherent Motion). The radius of the helical orbits can be determined by

$$\rho = 2(N/\ell)(\Delta\Omega_z^a/\Omega_z)r_a\Delta\theta.$$

where

N = number of passes through the agitator

ΔB_z^a = magnetic field of the agitator

$\Delta\theta$ = toroidal half width of the
agitator magnetic field

r_a = radial distance of the agitator from
the major axis

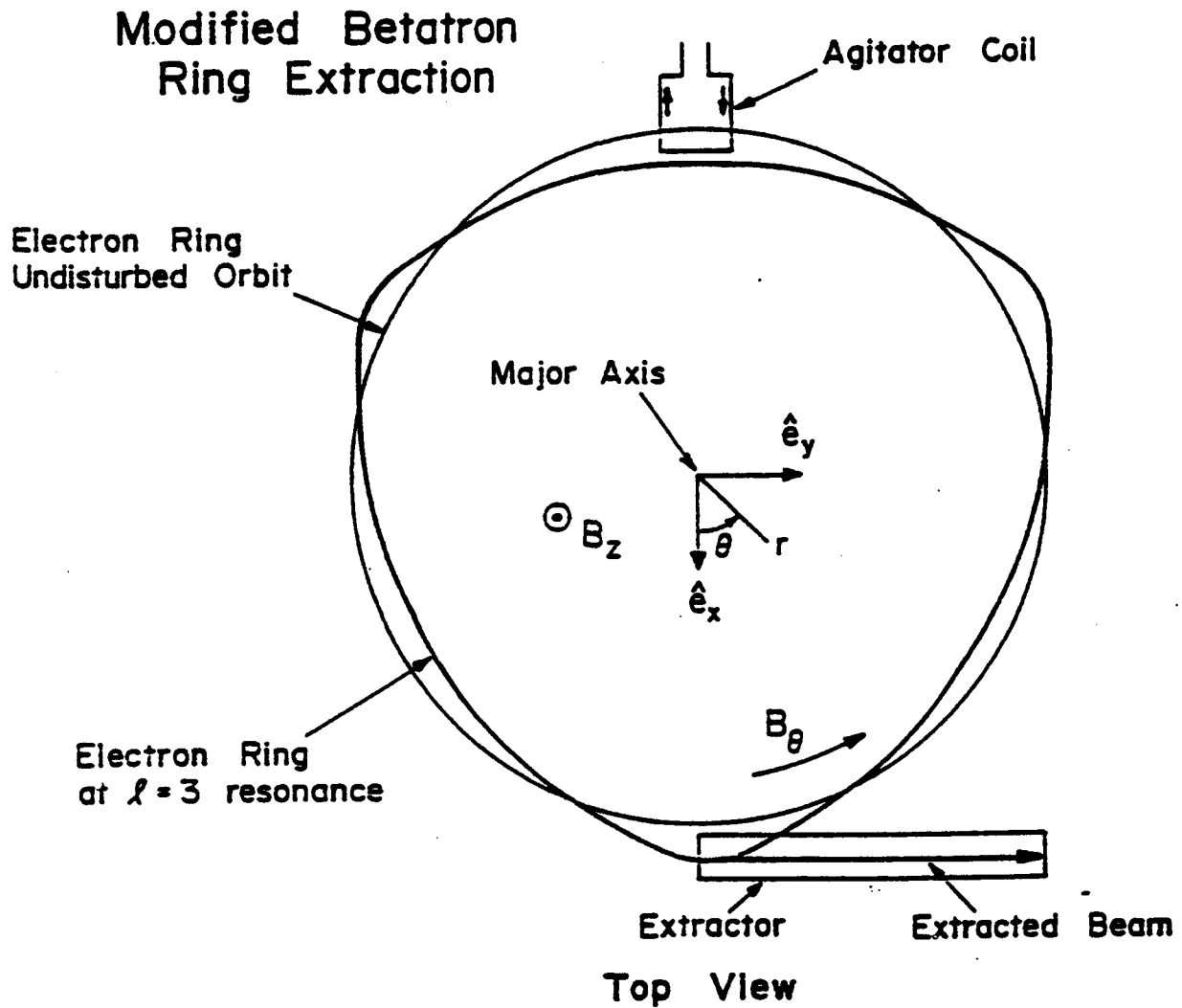
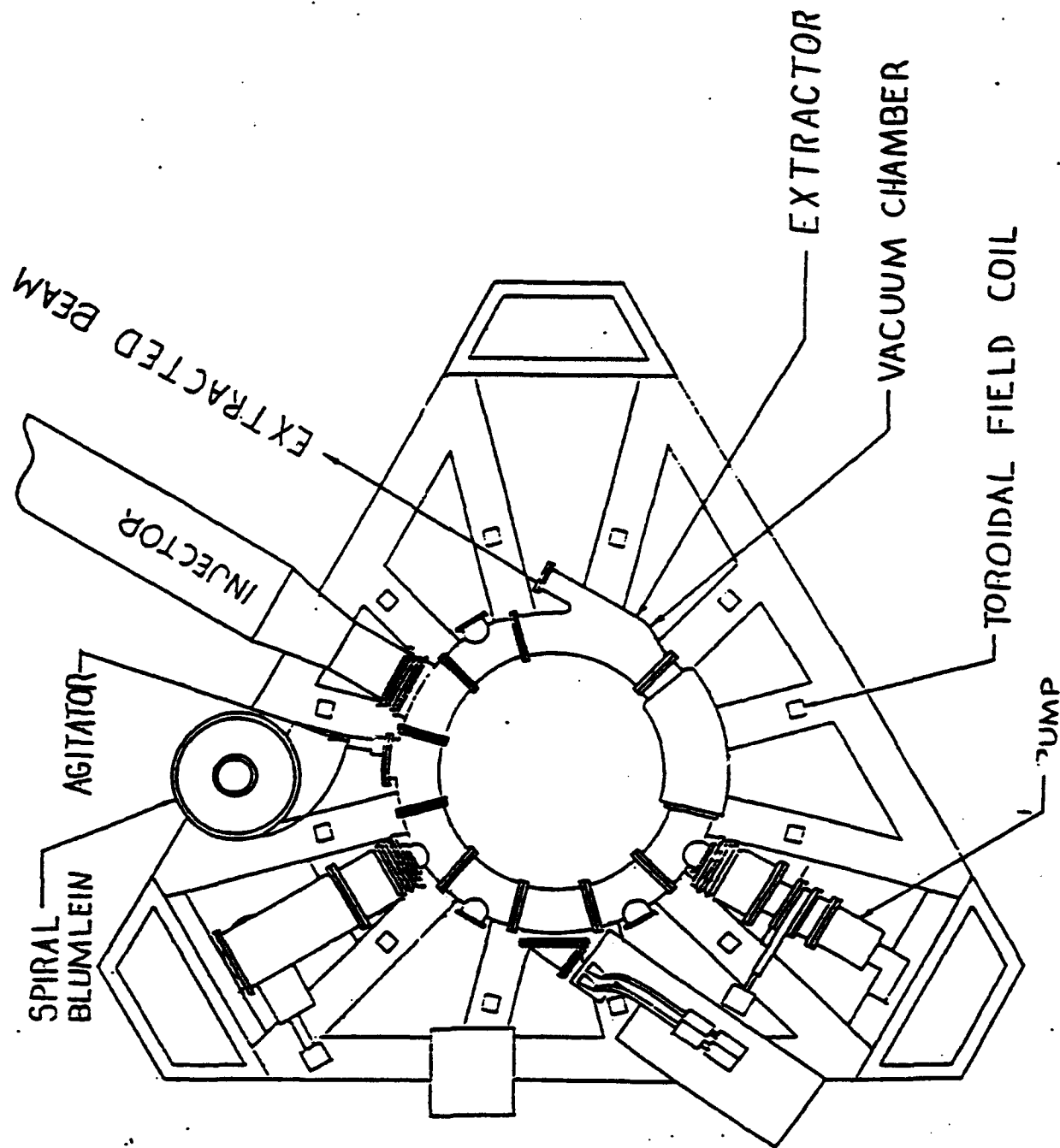
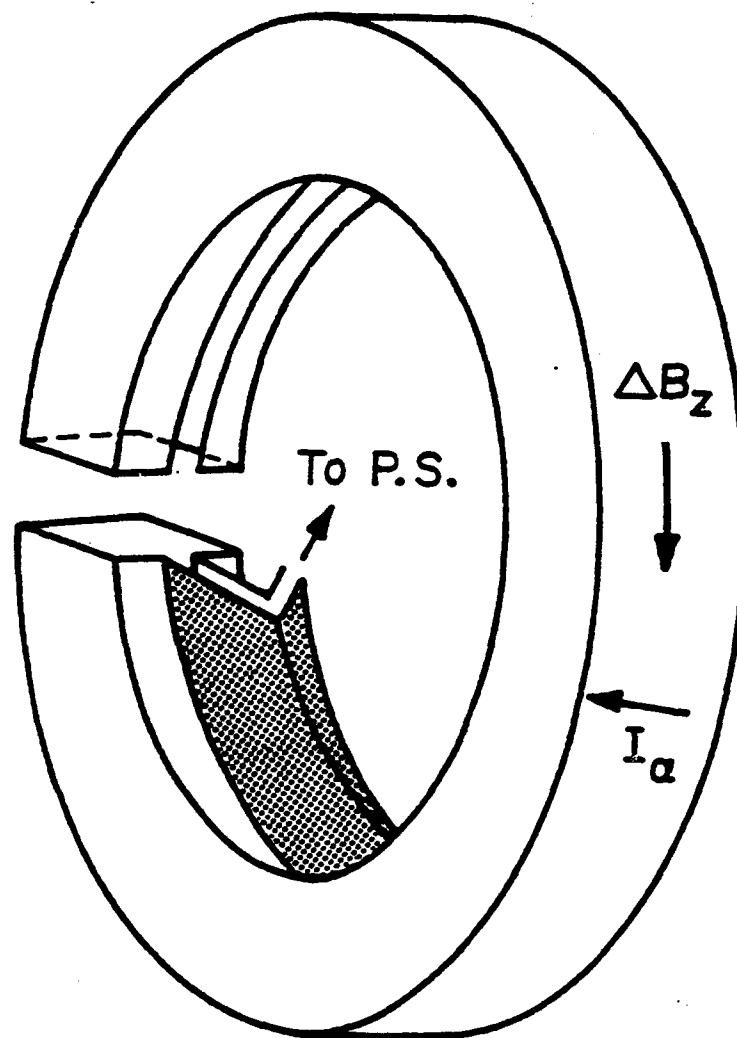


Fig. 1. Schematic of the proposed extraction scheme.

NRL MODIFIED BETATRON WITH EXTRACTION COMPONENTS

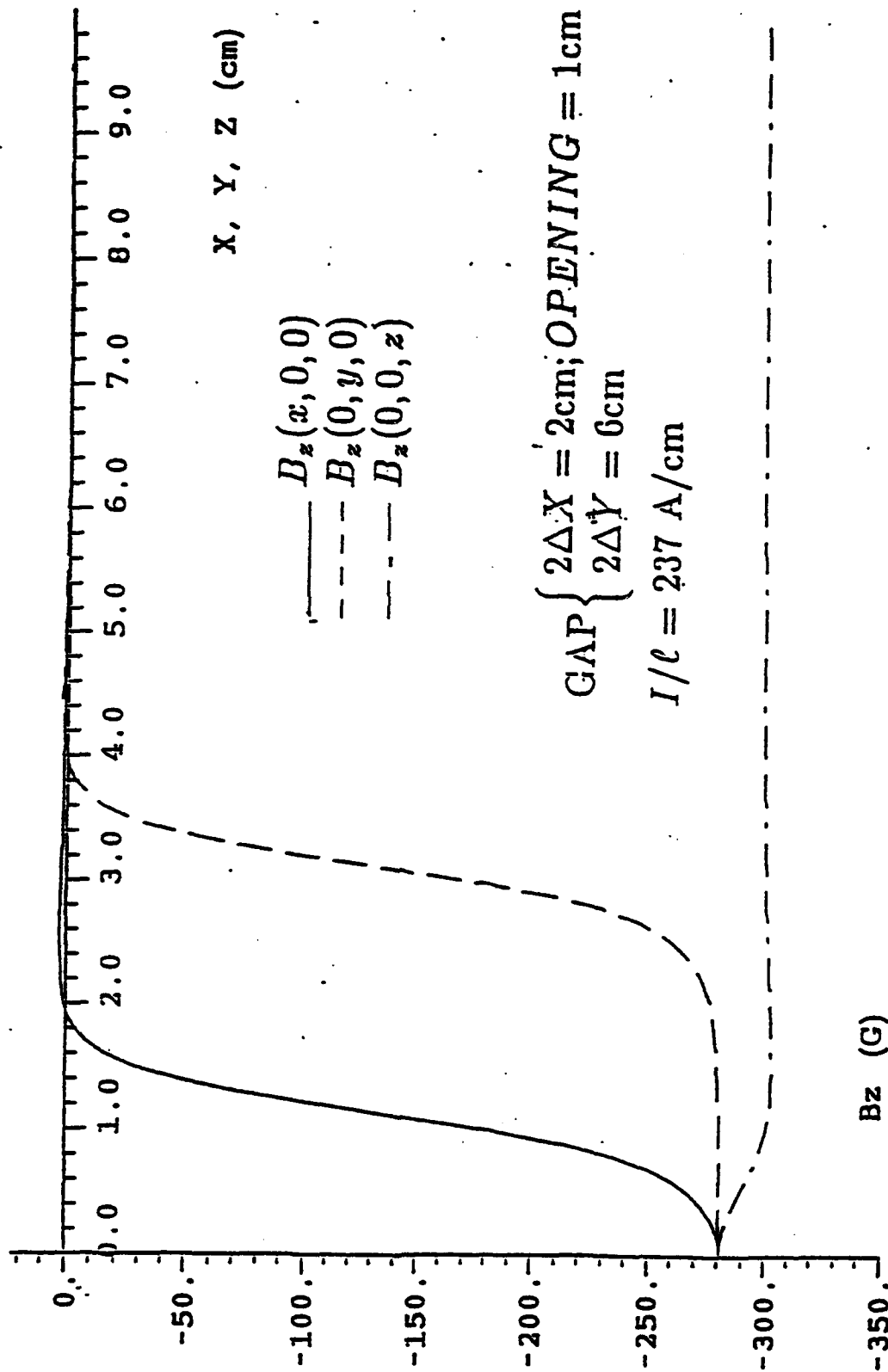




Agitator Coil

Fig. 2. Agitator coil that generates the localized disturbance.
It is powered by a coaxial transmission line.

COMPUTED AGITATOR-FIELD PROFILE WITH TRIMMER COILS FOR STATIC MODE



TABLE

List of various parameters for the runs # 266 and 270

RUN #	266	270
Agitator's mode	Static	Static
Relativistic factor γ	40	400
Major radius r_o (cm)	100	100
Vertical field at r_o (G)	649.9	6501
Toroidal field at r_o (G)	-1971	-19310
Field index n	0.5	0.5
Resonance integer 1	3	3
Amplitude of mismatching field (G)	60	600
Time constant of mismatching field (μsec)	10	10
Agitator's toroidal position	1.26π	1.26π
Agitator's toroidal width $2\Delta\theta$ (rad)	0.066	0.066
Agitator's inner radius (cm)	120	120
Agitator's outer radius (cm)	124	124
Agitator's opening (cm)	2	2.0
Agitator's linear current density (kA/cm)	0.375	3.75
Agitator's field ΔB_z^a (G)	-450	-4500
Extractor's opening toroidal position	0	0
Extractor's minimum inner radius (cm)	120.5	120.5
Extractor's minimum outer radius (cm)	124.5	124.5
Extractor's field ΔB_z^e (G)	-590	-5900

Ring Orbits for $\gamma = 40$

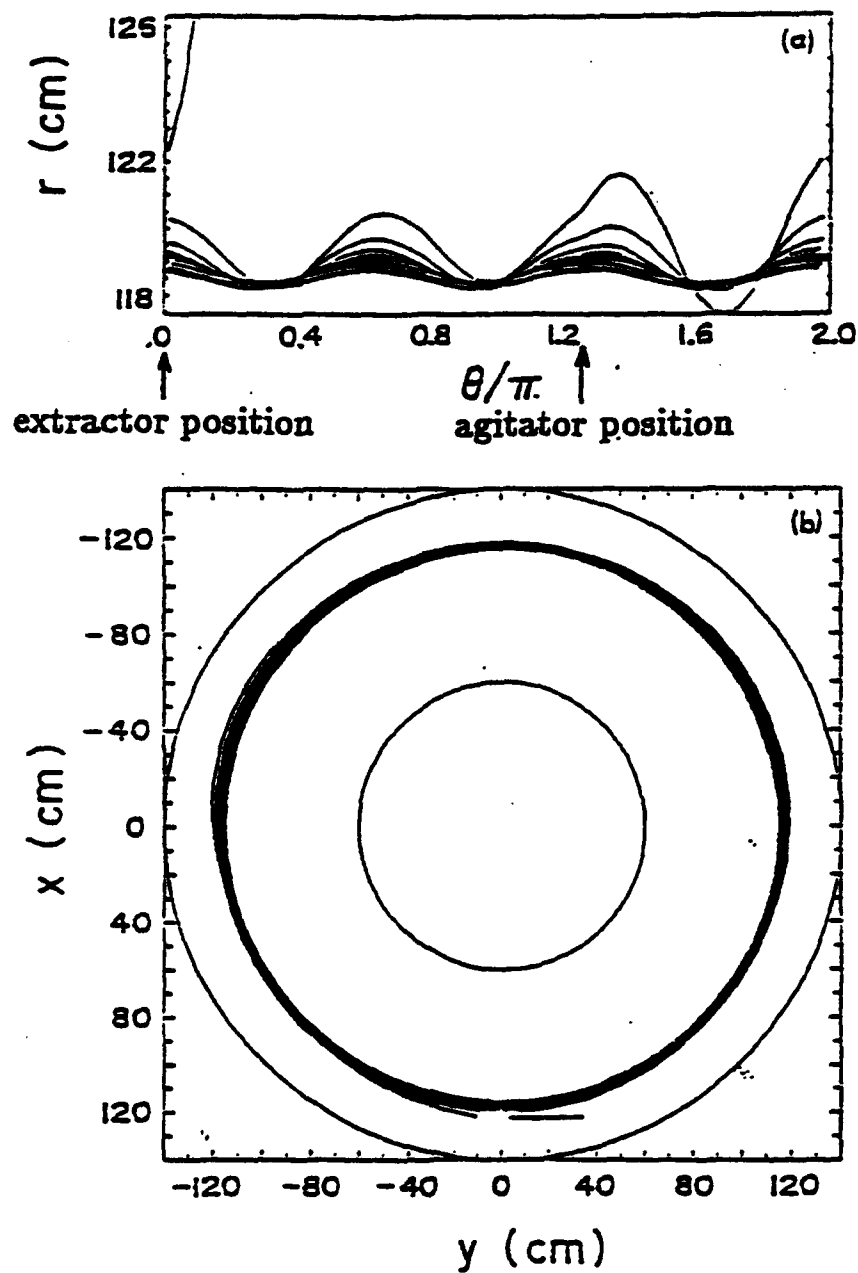


Fig. 5. Radial excursions of a typical electron (a) and top view of its trajectory in the x, y plane for the run 266.

Ring Orbits for $\gamma = 400$

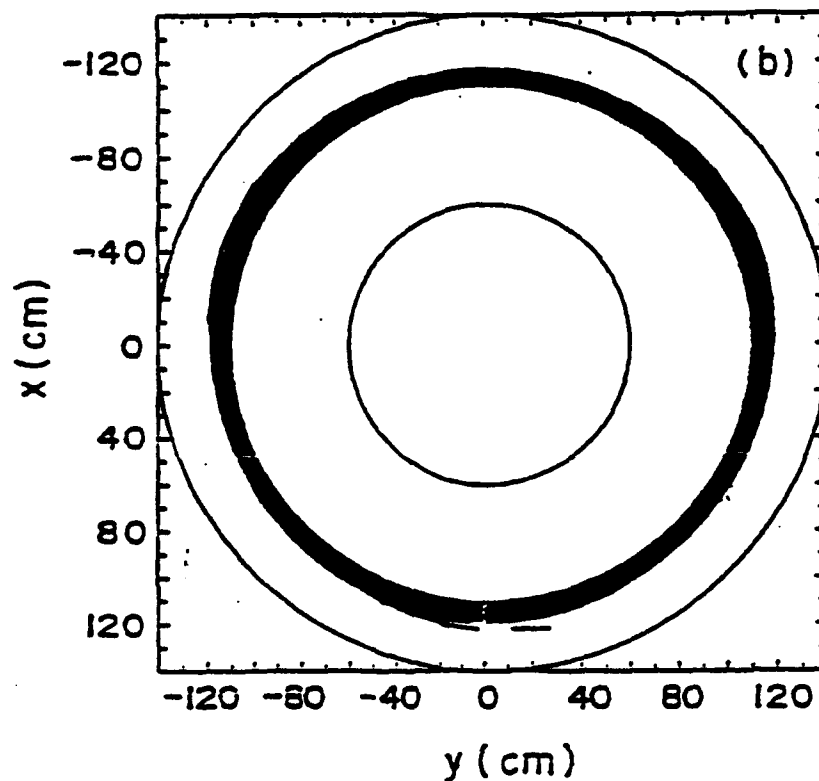
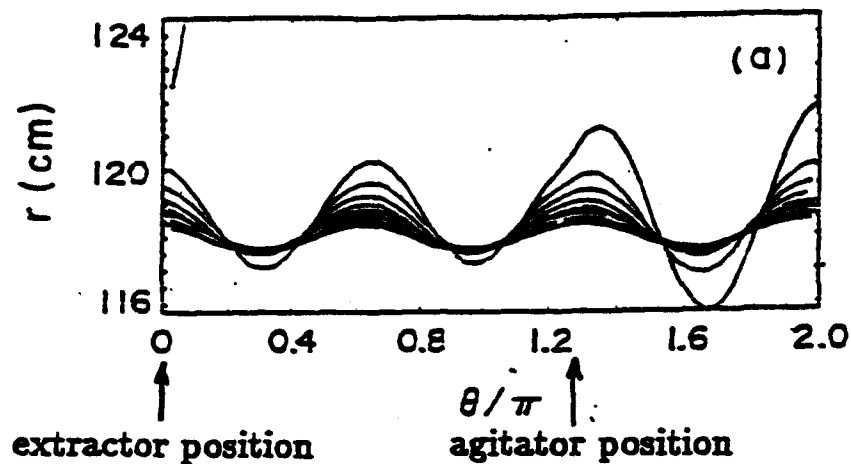


Fig. 7. Radial excursion of a typical electron (a) and top view of its trajectory in the x, y plane for the run 270.

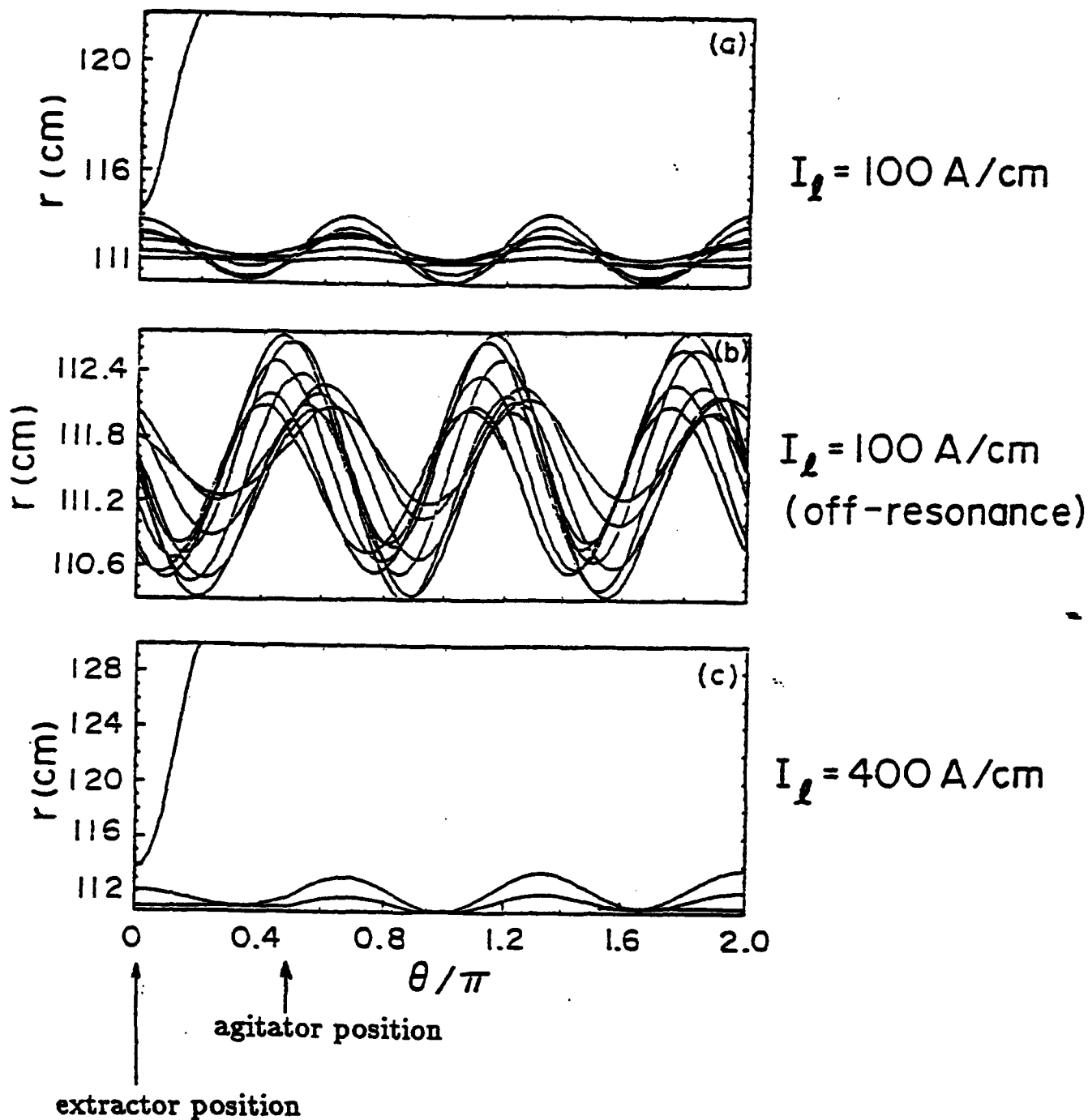
TABLE I
List of various parameters for the runs # 379-381

RUN #	379	380	381
Agitator's mode	Pulsed	Pulsed	Pulsed
Relativistic factor γ	39.9	39.9	39.9
Major radius r_o (cm)	100	100	100
Vertical field at r_o (G)	681	681	681
Toroidal field at r_o (G)	-1,920	-1970	-1,925
Field index n	0.5	0.5	0.5
Resonance integer ℓ	3	off	3
Agitator's toroidal position(rad)	0.493π	0.493π	0.493π
Agitator's toroidal width $2\Delta\theta$ (rad)	0.026	0.026	0.026
Agitator's inner radius (cm)	110.5	110.5	110.5
Agitator's outer radius (cm)	113.5	113.5	113.5
Agitator's opening (cm)	2.0	2.0	2.0
Agitator's linear current density (kA/cm)	0.1	0.1	0.4
Agitator's field ΔB_z^a (G)	-78	-78	-350
Extractor's opening toroidal position	0	0	0
Extractor's minimum inner radius (cm)	113.0	113.0	113.0
Extractor's minimum outer radius (cm)	116.0	116.0	116.0

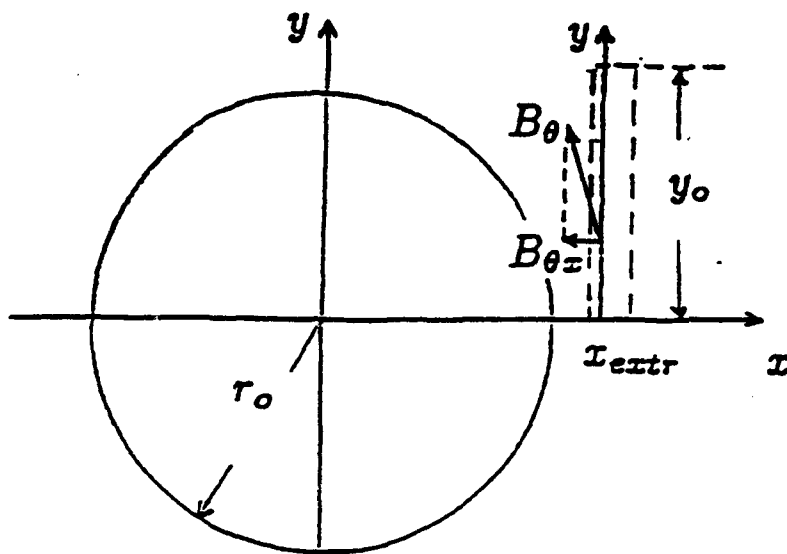
Ring Orbit in the r, θ Plane

$$\gamma = 40$$

Pulsed Mode



MAGNETIC FIELD COMPONENTS TO BE CANCELED OUT BY EXTRACTOR



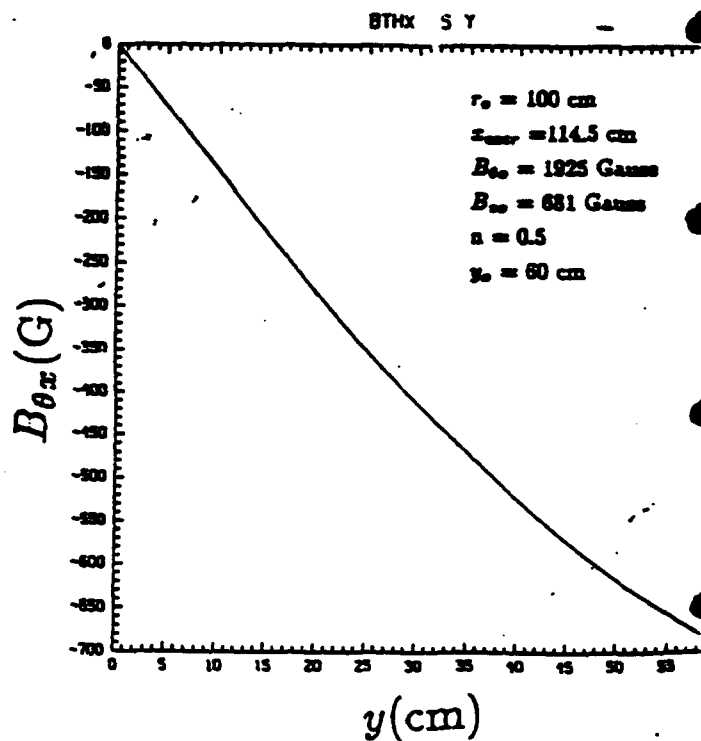
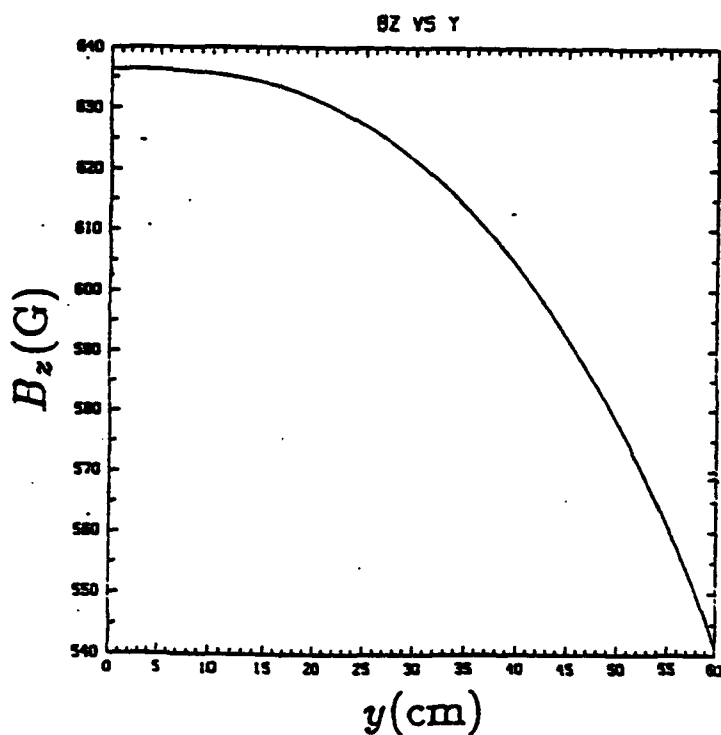
Top view

$$B_{\theta x} = -B_{\theta 0} \frac{r_0 y}{x_{extr}^2 + y^2}$$

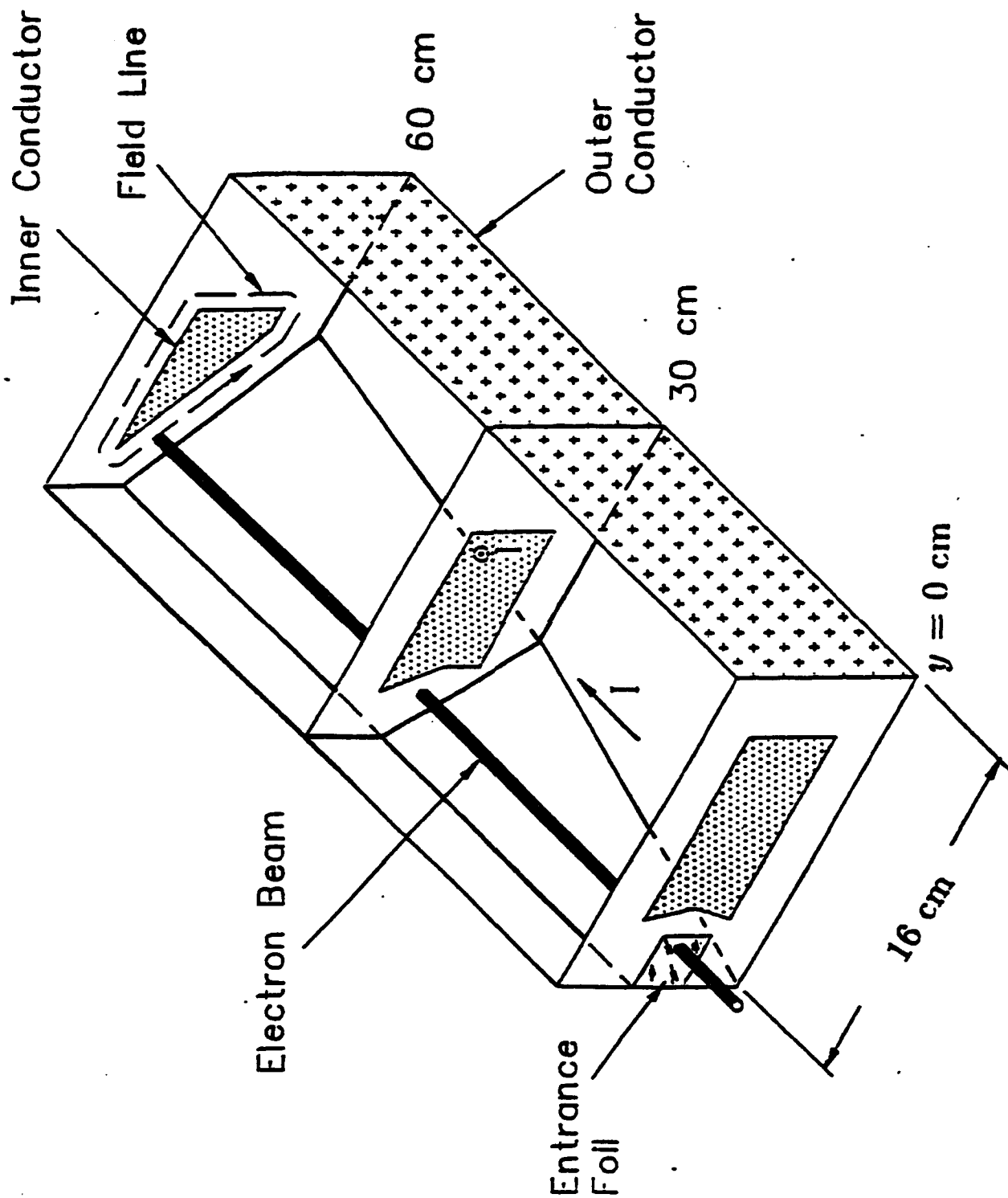
$$B_z = B_{z0} \left(\frac{r_0}{\sqrt{x_{extr}^2 + y^2}} \right)^{\frac{1}{2}}$$

$B_{\theta x}$ must be canceled inside the extractor

Otherwise there is a vertical force $F_z = -ev_y B_{\theta x}$

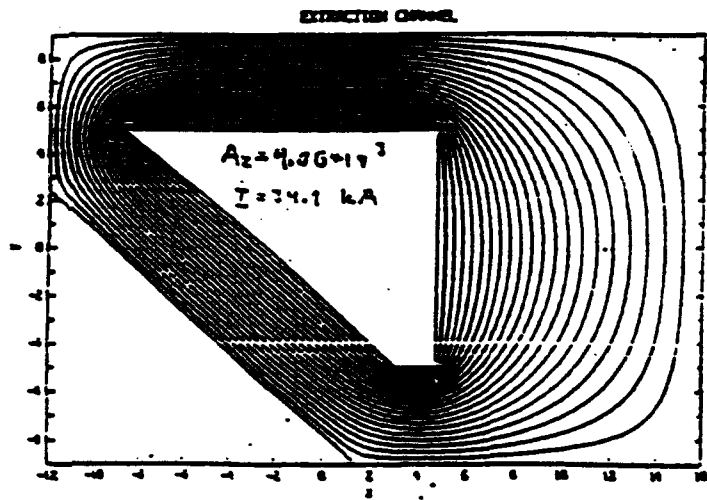


Extractor

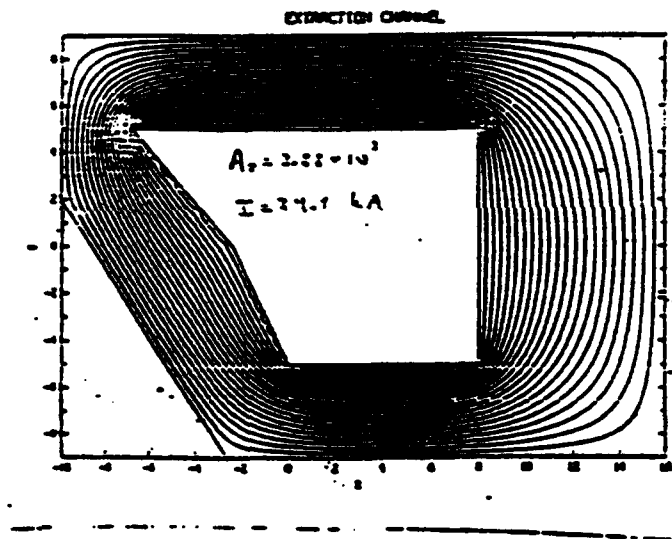


Extractor Field Structure

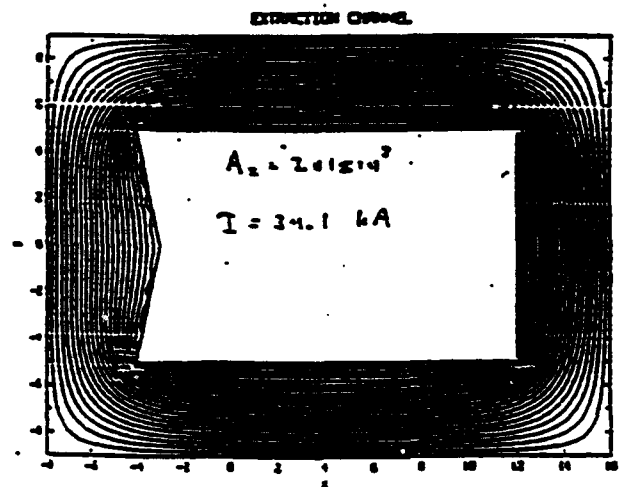
$y = 60 \text{ cm}$

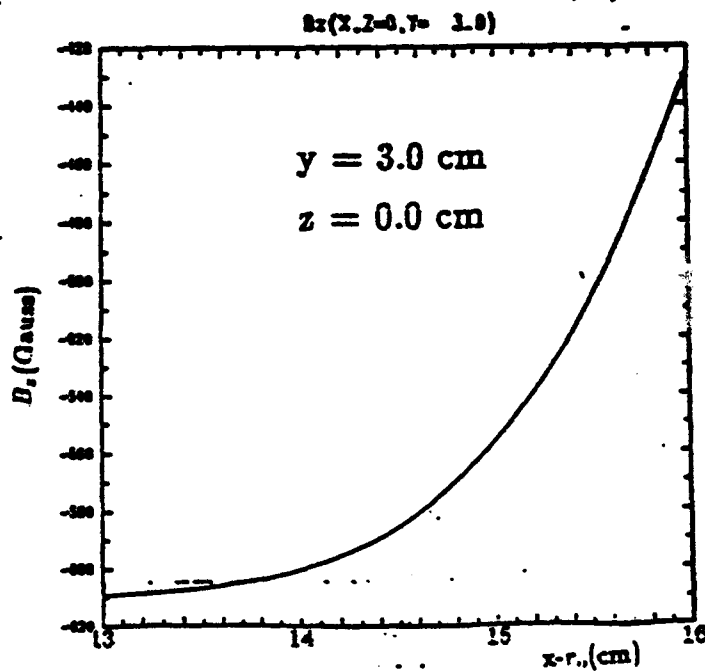
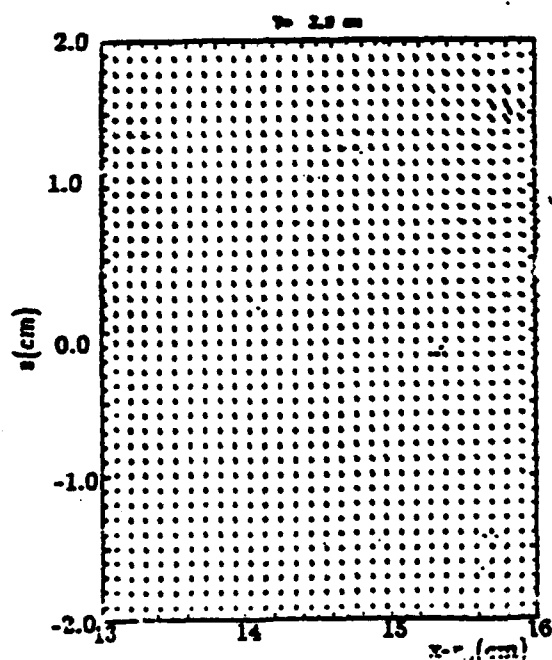
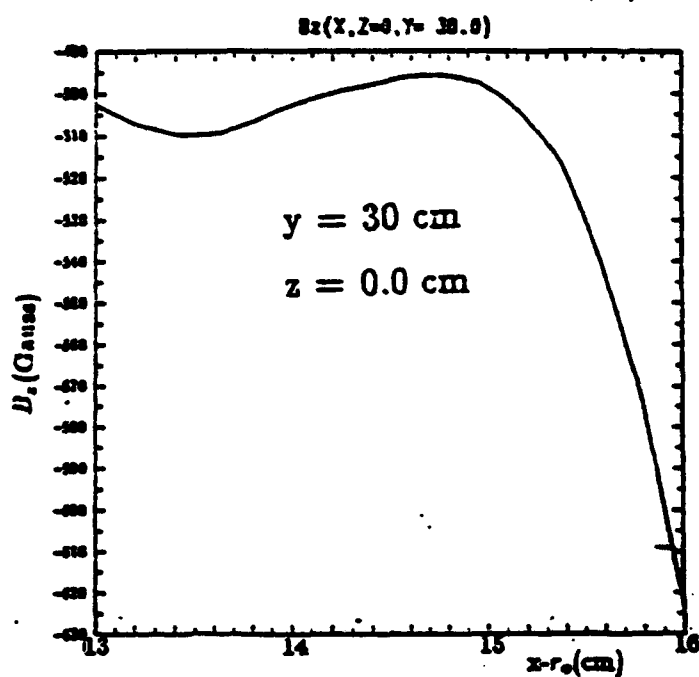
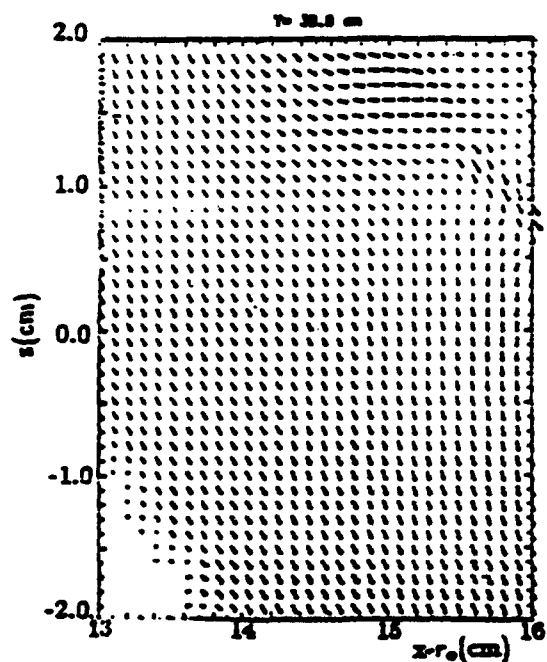
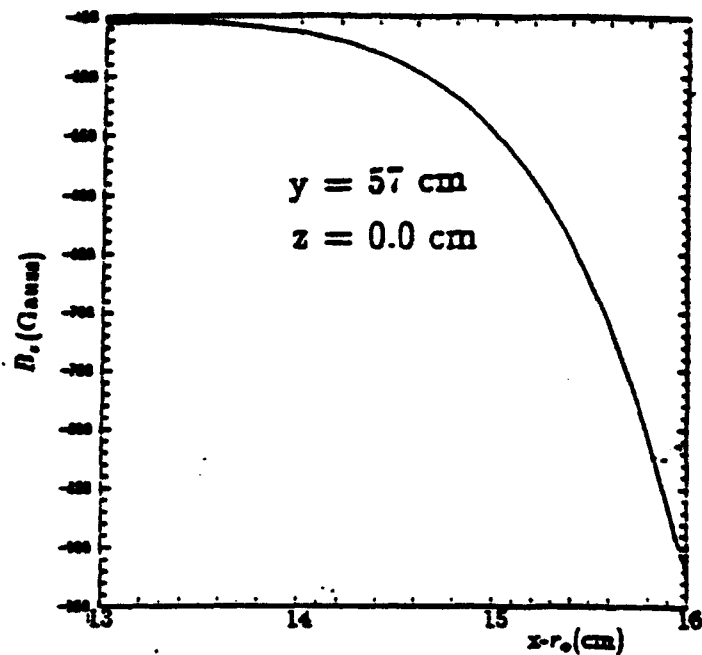
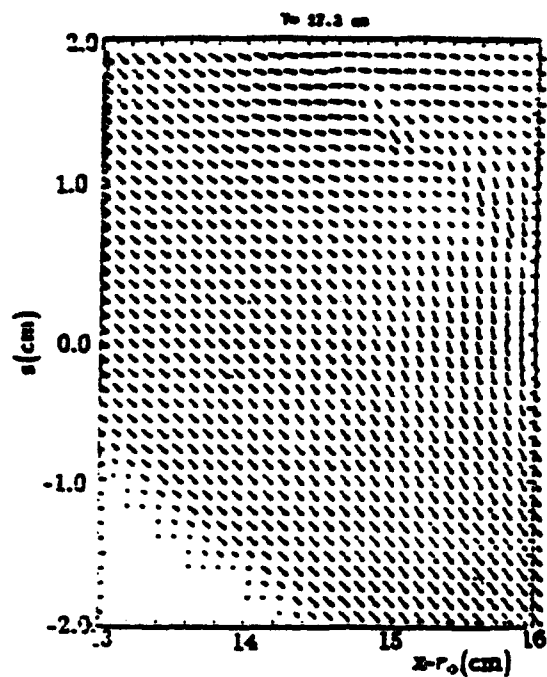


$y = 30 \text{ cm}$



$y = 0 \text{ cm}$





BEAM DYNAMICS INSIDE THE EXTRACTOR

For the numerical integration of the beam orbits, the magnetic fields inside the extractor were computed using the 3-D MAGNUS code

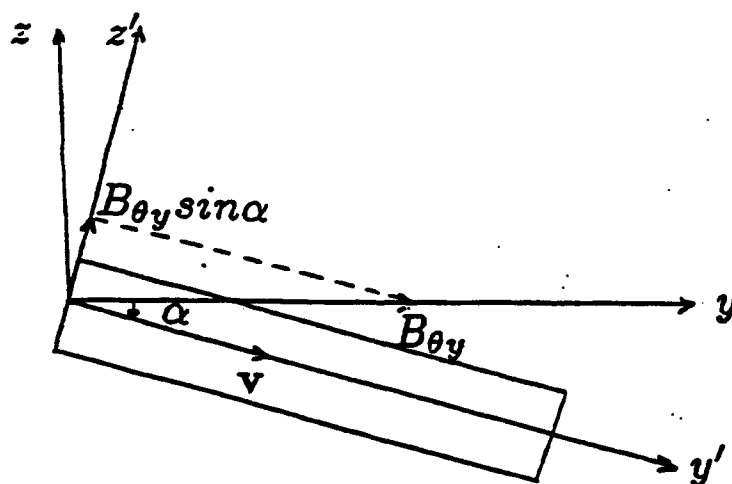
The inner conductor was replaced by a set of current filaments such that their current density was that computed by the POISSON code at each cross section of the extractor

The computed fields by the 3-D MAGNUS code were in very good agreement with those computed by the 2-D POISSON code

EFFECT OF SMALL VERTICAL VELOCITY AT THE ENTRANCE OF THE EXTRACTOR

$$v_z = -0.0332v_y$$

This small vertical velocity causes helical motion of the beam around the $B_{\theta y}$ component of the toroidal field



Side view of extractor

By tilting the extractor and by adjusting slightly its current to cancel the small $B_{\theta y} \sin \alpha$ component the beam orbit is almost linear

EFFECT OF ADJUSTING THE CURRENT IN THE EXTRACTOR

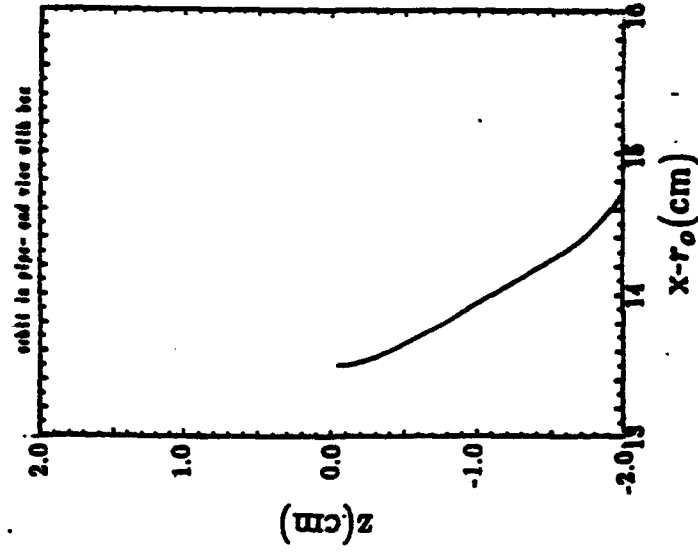
$$v_z = -0.0332v_y$$

$$\text{Tilt angle} = -2 \text{ cm} / 60 \text{ cm}$$

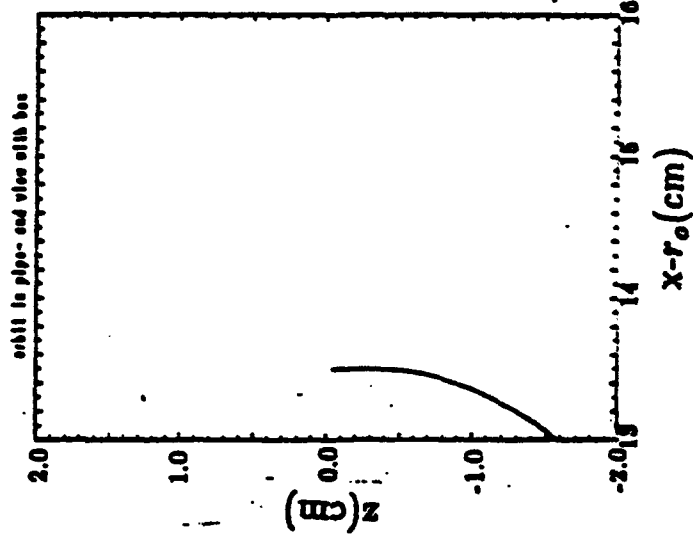
$$B_z^{\text{external}} (x = 114, y = 3, z = 0) = 600 \text{ Gauss}$$

Orbits shown from extractor end view (not tilted)

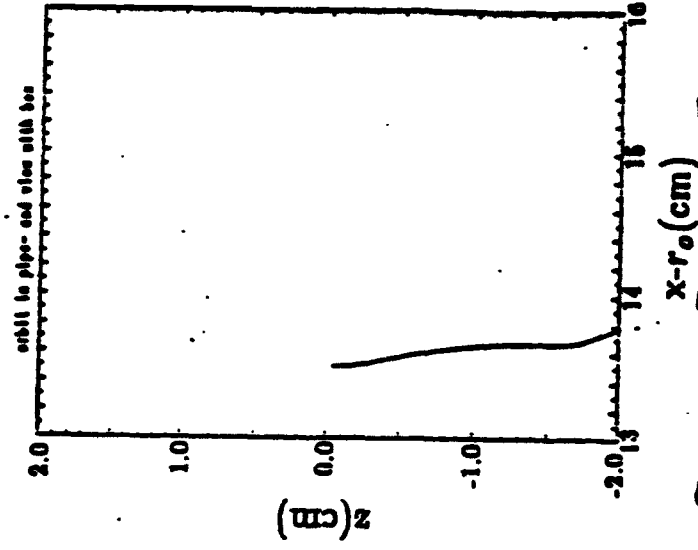
$B_z^{\text{extractor}} = -780 \text{ Gauss}$



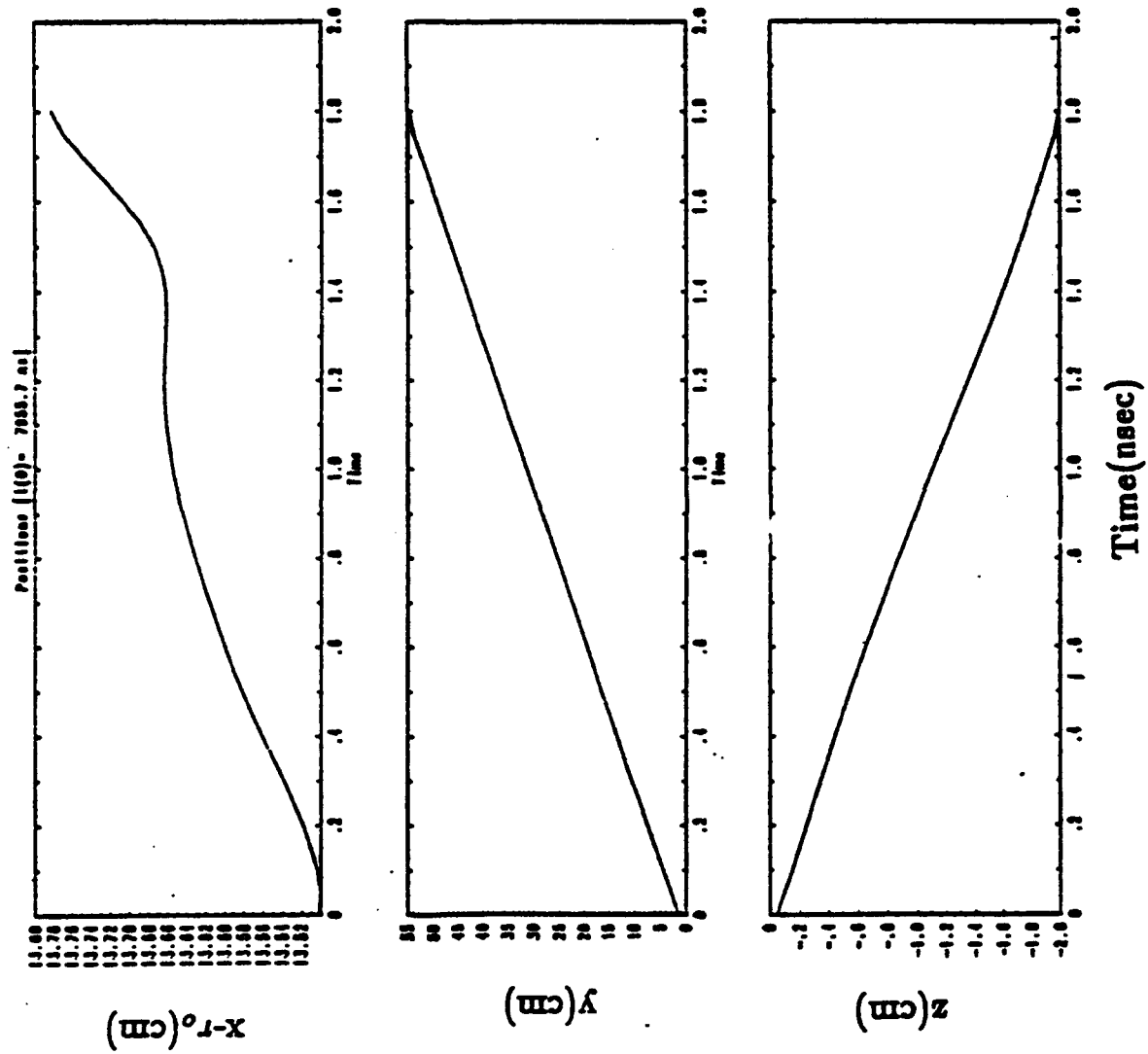
$B_z^{\text{extractor}} = -680 \text{ Gauss}$



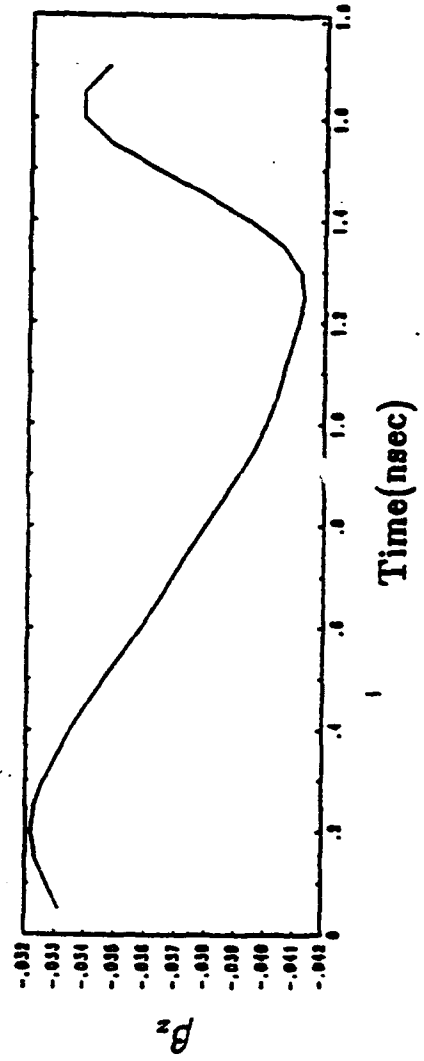
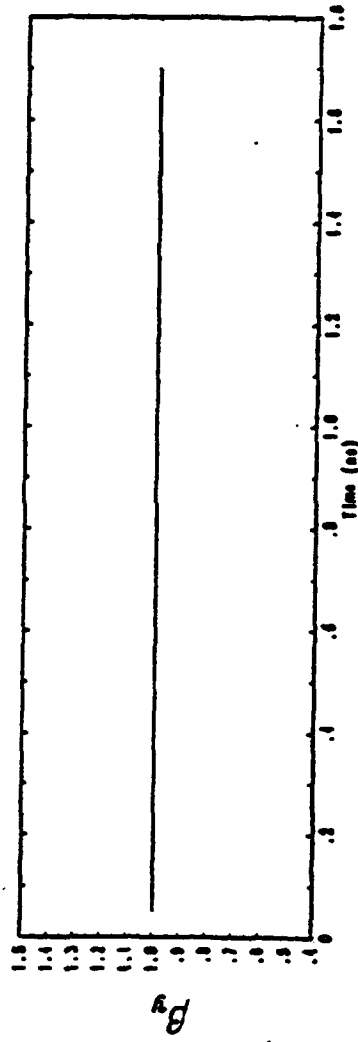
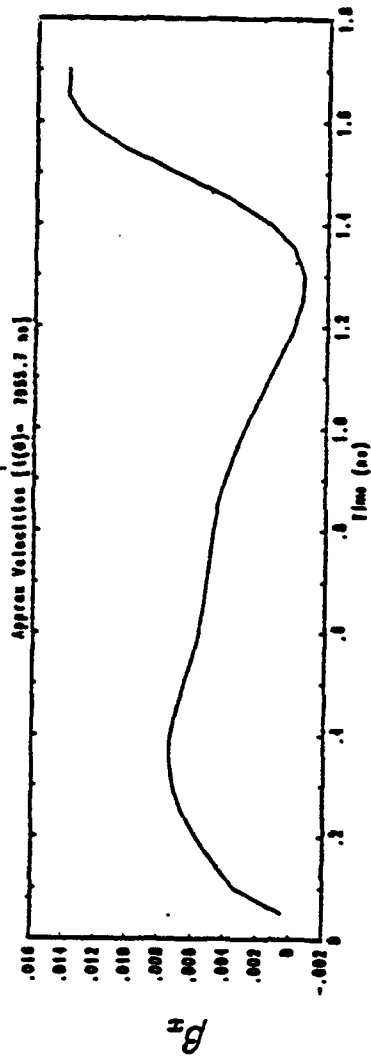
$B_z^{\text{extractor}} = -730 \text{ Gauss}$



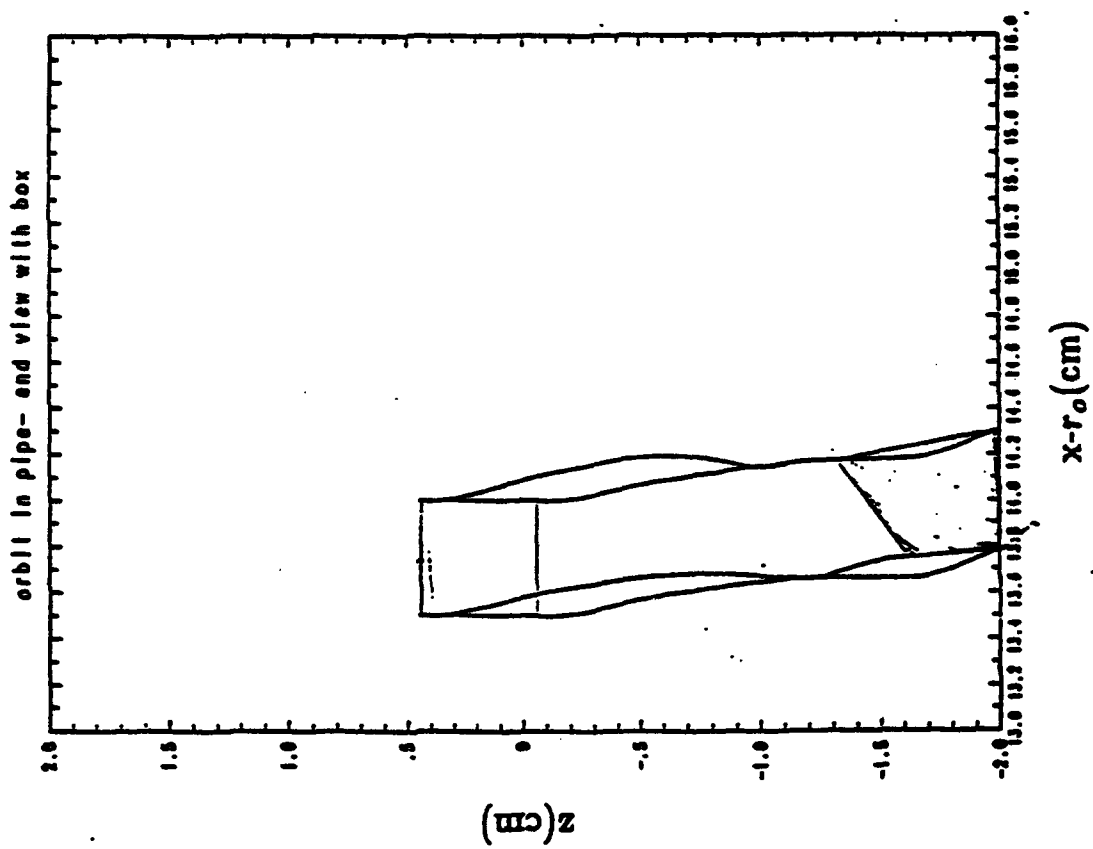
PARTICLE POSITION INSIDE THE EXTRACTOR VS TIME



PARTICLE NORMALIZED VELOCITY INSIDE THE EXTRACTOR VS TIME



END VIEW ORBITS OF FOUR PARTICLES INSIDE THE EXTRACTOR



CONCLUSION

An extraction technique has been conceptually developed for the modified betatron that is easily realizable and has the potential to lead to a very high efficiency, since all the electrons of the ring perform coherent motion

The design of most of the components of the extraction experiment has been completed and the fabrication and testing of some components is currently in progress

Appendix U

Intense Microwave and Particle Beams

PROCEEDINGS REPRINT

 SPIE—The International Society for Optical Engineering

Reprinted from

Intense Microwave and Particle Beams

**16-19 January 1990
Los Angeles, California**



Volume 1226

©1990 by the Society of Photo Optical Instrumentation Engineers
Box 10, Bellingham, Washington 98227 USA. Telephone 206/676-3290.

Progress in the development of the NRL modified betatron accelerator*

**L.K. Len[△], T. Smith, J. Golden⁺, K. Smith[°], S.J. Marsh[°],
D. Dialetis[†], J. Mathew, P. Loschialpo, J.H. Chang, and C.A. Kapetanakis**
Plasma Physics Division, Naval Research Laboratory
Washington, DC 20375

ABSTRACT

The lifetime of the circulating electron beam in the NRL modified betatron has been substantially increased from a few μsec to over 700 μsec by the addition of strong focusing windings to the device. The injected beam consistently spirals from the injector to the minor axis and is trapped. The ~ 0.5 kA trapped electron ring has been accelerated to ~ 12 MeV from the injection energy of ~ 0.5 MeV. The beam acceleration has been confirmed not only by the x-ray attenuation technique but also with the detection of photoneutrons from the reaction $D(\gamma, n)H$.

The experimental observations show that during acceleration the electrons cross initially higher order cyclotron resonances. Eventually, when the ratio of the vertical B_z to toroidal magnetic field B_θ is $\sim 1/9$, i.e., at $\ell = 9$, a substantial fraction of the ring electrons is lost. The remaining electrons are lost at higher B_z , that is, at lower ℓ values. Experiments are in progress to locate and eliminate the field error(s) that excite the resonances and thus to accelerate the electron ring to even higher energy.

1. INTRODUCTION

Accelerators that combine high current capability and high effective accelerating gradient are currently under development in several laboratories.¹⁻⁵ These accelerators have two common features, namely strong focusing that improves their current carrying capability and recirculation that enhances their effective accelerating gradient.

Among these accelerators is the modified betatron.⁶⁻⁸ This device is currently under investigation at the University of California, Irvine² and also at the Naval Research Laboratory¹ (NRL). In its original form the modified betatron consists of a strong toroidal magnetic field and a time varying betatron field that is responsible for the acceleration.

Extensive studies of beam capture and confinement in the NRL modified betatron led to formation of electron rings with circulating current as high as 3 kA. In addition, these studies furnished valuable information on the critical physics issues of the concept. For instance, they have

- demonstrated the beneficial effect of B_θ on the expansion of the ring's minor radius,
- unambiguously confirmed the bounce motion of the ring,
- verified the pronounced effect of image forces on the ring equilibrium,
- confirmed the existence of the macroscopic instability gap and the transformation of ring orbits from diamagnetic to paramagnetic,
- revealed, for symmetric orbits, that the bounce frequency is several times higher than the theoretical prediction, and

- shown that, at least for the drift trapping technique, the low current regime is inaccessible.

Finally, these studies divulged that over a wide range of parameters the ring lifetime was limited to a few μsec which is comparable to the magnetic field diffusion time through the vacuum chamber. Thus, it became apparent from these results that the modified betatron had to be modified in order to increase the beam lifetime and thus to achieve acceleration. In August 1988 the decision was made to proceed rapidly with the design, fabrication and installation of strong focusing windings.

Stellarator⁹ and Torsatron¹⁰ winding configurations were considered. Both configurations have some strong points. However, the stellarator configuration was selected not only because of the small net vertical field and the lower current per winding but also because it is compatible with our contemplated extraction scheme.^{11,12}

This paper describes in some detail the NRL modified betatron in its latest form and very briefly summarizes the results after the installation of the strong focusing windings.

2. DESCRIPTION OF THE EXPERIMENT

2.1. External magnetic fields

The NRL modified betatron comprises three different external magnetic fields; the betatron field that is a function of time and is responsible for the acceleration of the electrons, the toroidal magnetic field that varies only slightly during the acceleration of the electron ring and the strong focusing field that also has a very weak time dependence. As shown in Fig. 1, the coils that

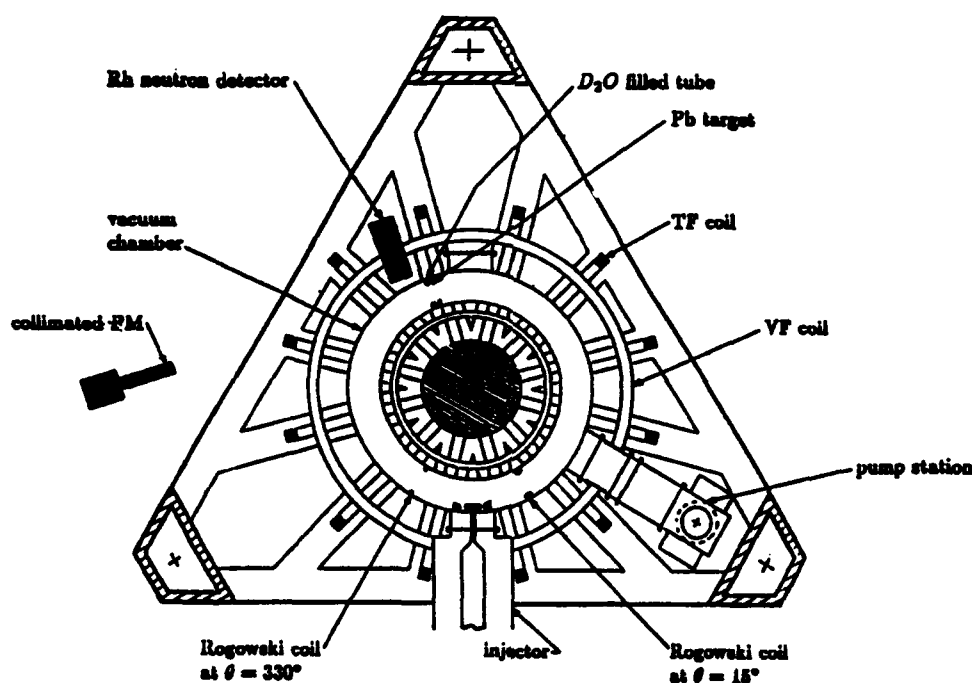


Figure 1: Schematic plan view of the NRL Modified Betatron.

generate these three fields are supported by a stiff structure in the form of an equilateral triangle with truncated vertices.

2.2. The betatron field

The betatron¹³ magnetic field controls mainly the major radius of the gyrating electron ring and is produced by 18 air core, circular coils connected in series. Their total inductance is approximately 530 μH . The coils are powered by an 8.64 mF capacitor bank that can be charged up to 17 kV. At full charge, the bank delivers to the coils about 45 kA peak current. The current flowing through the coils produces a sinusoidally varying field that has a quarter period of 2.5 msec and its amplitude on the minor axis, at peak charging voltage is 2.1 kG. Immediately after the peak the field is crowbarred with a 4.5 msec decay time.

The flux and index are adjusted by two sets of trimmers that are connected in parallel to the main coils. The current through the trimmers is limited by a 3.3 mH series inductor to $\sim 10 - 15\%$ of the total current.

The ratio of the average vertical magnetic field $\langle B_z \rangle$ to the local vertical magnetic field on the minor axis B_{z0} can be adjusted over a reasonably broad range. Figure 2a shows $\langle B_z \rangle$ and B_{z0} as a function of time with only 16 coils and one set of trimmers connected. The gains of the two channels in the oscilloscope have been adjusted to include the different sensitivity of the two probes and the factor of two in the ratio $\langle B_z \rangle / B_{z0}$. The complete overlapping of the two traces clearly demonstrates that the ratio $\langle B_z \rangle / B_{z0}$ is very near 2 over almost the entire acceleration time of the electron ring. In (b) the two traces are offset slightly for clarity.

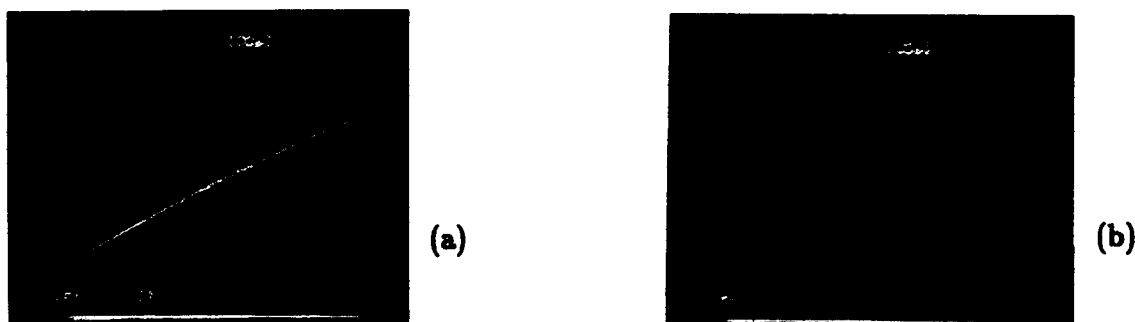


Figure 2: Time resolved measurement of the average $\langle B_z \rangle$ and local B_{z0} axial magnetic field. In (a), the oscilloscope is adjusted so that the channel recording B_{z0} has exactly twice the gain (including the probe sensitivity) as the channel which records $\langle B_z \rangle$. In (b), the traces are offset slightly for clarity.

Figure 3 shows the spatial variations of the field index at the toroidal position $\theta = 295^\circ$ at $t = 500$ and $1500 \mu\text{sec}$, i.e., after the field diffusion through the vacuum chamber has been completed. The experimental results are in good agreement with the predictions of EFFI, a static 3-D magnetic code.

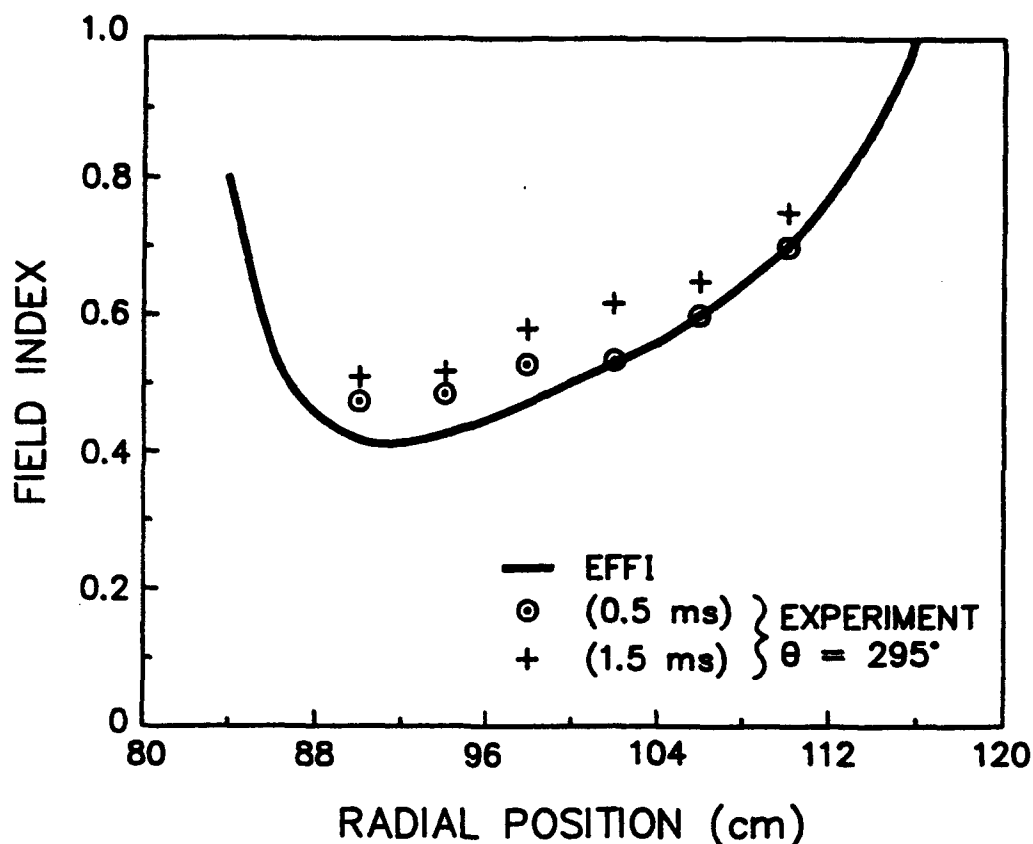


Figure 3: Radial variation of the field index. The measured values are compared to the profile obtained using a static, 3-D magnetic field code.

2.3. The toroidal field

The toroidal magnetic field controls mainly the minor cross section of the electron ring and the growth rate of several unstable collective modes. This field is generated by twelve air-core rectangular coils that are connected in series.

The coils are made of aluminum square tubing and have a 150 cm height and 135 cm width. The total inductance of the 12 coils is $\sim 85 \mu\text{H}$ and are powered by a 24 mF capacitor bank that can be charged to a peak voltage of 10.6 kV. At the peak voltage the bank delivers to the coils $\sim 180 \text{ kA}$ peak current. This current produces a sinusoidally varying field that has a quarter period of $T/4 = 1.9 \text{ msec}$ and its amplitude on the minor axis is 3.9 kG.

The toroidal field is not uniform but varies as $1/r$, where r is the radial distance from the major axis. In addition, as a result of the discreteness of the coils, the toroidal field has a 1-2% ripple (bumpy torus) along the minor axis.

2.4 The strong focusing field

The strong focusing field improves the confining properties of the two other fields by reducing the sensitivity of the centroid and individual particles to energy mismatch and energy spread.

In the NRL modified betatron the strong focusing is generated by four twisted windings that carry current in alternate directions.

The left handed windings are located 23.42 cm from the minor axis and have a 209.4 cm period, i.e., there are three winding periods over the length of the torus. The windings are supported by epoxy reinforced graphite jackets and have been designed to carry up to 25 kA. The windings are connected in series and the peak current and the temporal profile of the field is controlled by a ballast inductor.

For a stellarator configuration with an $\ell = 2$ poloidal number, the toroidal transform ι over a winding period L is given by

$$\frac{\iota}{2\pi} \simeq \frac{1}{2} \left[\frac{4\mu_0 I_{st}}{LB_\theta(\alpha\rho_0)^2} \right]^2, \quad (1)$$

where I_{st} is the current through the windings, B_θ is the toroidal field, ρ_0 is the distance of the windings from the minor axis and $\alpha = 2\pi/L$. For $\alpha = -0.03/\text{cm}$, $\rho_0 = 23.42$ cm, $B_\theta = 0.2 \text{ W/m}^2$, and $I_{st} = 20$ kA, Eq. (1) gives $\iota = 46.4^\circ$, over a winding period.

Another useful quantity is the stellarator field index n_{st} that is defined, in the linear approximation, as¹⁰

$$n_{st} = -\frac{(\Omega_z^{\epsilon z} \epsilon_{st})^2 \alpha r_0}{2\Omega_{x0}\Omega_{\theta 0}}, \quad (2)$$

where $\Omega_z^{\epsilon z} \epsilon_{st} \approx 4\alpha\Omega_0\rho_0 K'_2(2\alpha\rho_0)$, $\Omega_0 = \frac{|e|B_0}{m}$, $B_0 = \frac{2\mu_0 I_{st}}{L}$, r_0 is the major radius, K'_2 is the derivative of the modified Bessel function and Ω_{x0} and $\Omega_{\theta 0}$ are the cyclotron frequencies of the vertical and toroidal fields on the minor axis. Since in the NRL modified betatron I_{st} , $\Omega_{\theta 0}$ and Ω_{x0}/γ remain approximately constant during acceleration, Eq. (2) predicts that n_{st} scales inverse proportionally to γ , as shown in Fig. 4.

2.5. Injector accelerator and diode

The injection accelerator¹⁴ consists of a Marx generator, a pulse forming line, an output switch, a ballast resistor, a tail-biter switch and a vacuum transmission line.

The Marx is an oil insulated, 25 stage generator, charged to a peak voltage of ± 50 kV. The generator rises to 2.5 MV in ~ 550 nsec. The pulse forming line consists of a 16.8 cm inner and 59.7 cm outer conductor and is filled with glycol dielectric ($\epsilon = 40$). The output switch is a self-breaking SF_6 insulated switch. The switch body is constructed of plexiglass. The insulator has been carefully designed to provide good electric field grading in the interfaces with the glycol and SF_6 , while preserving the impedance in the glycol line.

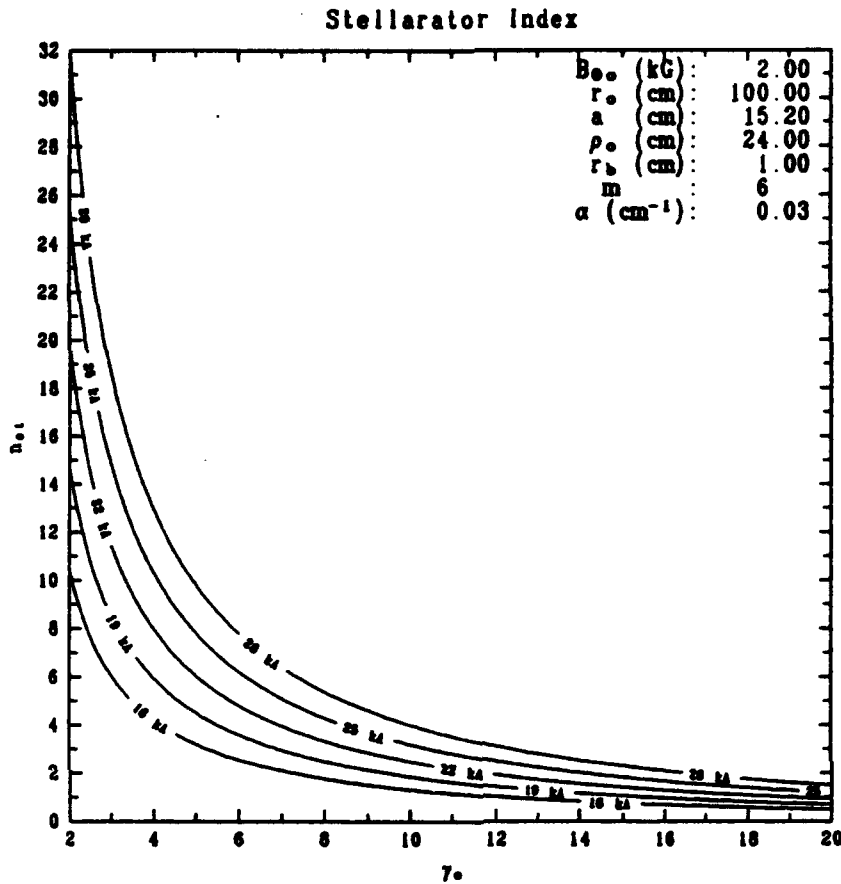


Figure 4: Plot of the stellarator field index n_{st} versus beam energy γ_0 . The field index is proportional to the square of the winding current and varies inversely with the beam energy.

A low impedance ($\sim 12 \Omega$) constant temperature, $CuSO_4$ ballast resistor is used in parallel with the diode in order to obtain diode voltage regulation by matching the load to the pulse forming line impedance. Thus, the voltage is held constant regardless of large variations in the diode impedance.

The pulse forming line is connected to the diode through a 120Ω vacuum transmission line. To increase the turn-on field and therefore to minimize parasitic emission, the inner conductor of the vacuum line is made of carefully polished 1.3 cm radius molybdenum tube.

Figure 5 shows a top view of the diode. To minimize the magnetic field component transverse to the emitting surface of the cathode the core of the cathode stalk is made out of high $\sigma\mu$ ferromagnetic material. The unsaturated state of the ferromagnetic material is prolonged by the copper housing. The main purpose of the molybdenum cladding is to reduce undesirable electron emission from the stalk.

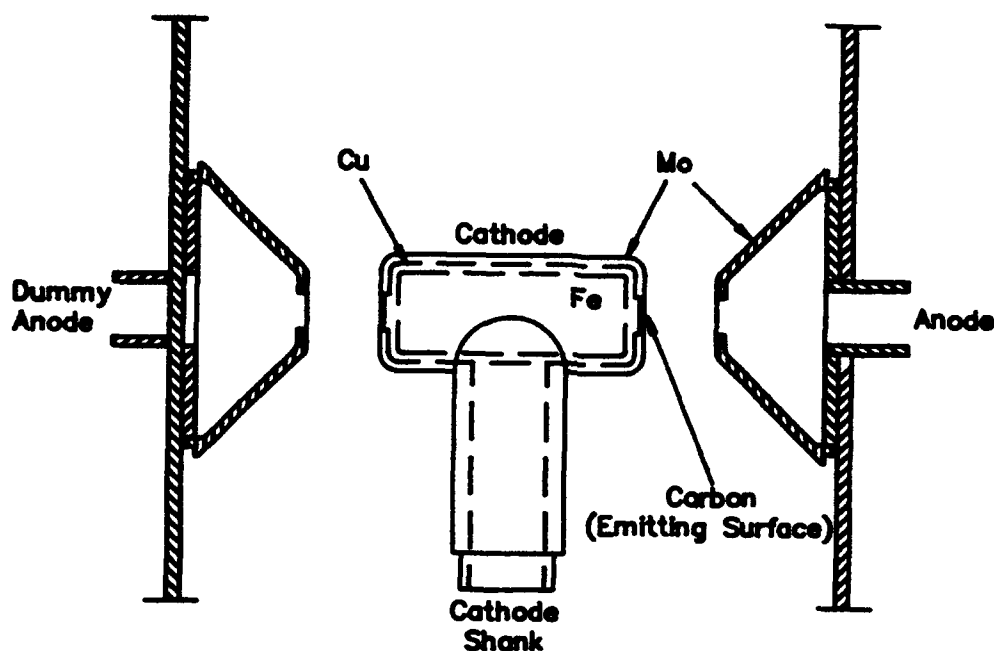


Figure 5: Partially immersed diode with dual emitting surfaces. The molybdenum cladding reduces parasitic electron emission.

Since the current flowing through the cathode stalk lasts longer than 23 nsec, i.e., the ring revolution around the major axis, the cathode stalk made symmetric in order to minimize the magnetic field perturbation from the stalk current on the electron ring orbit. However, only one electron beam is extracted from the diode because the second beam that is emitted in the opposite direction to B_0 is terminated at the anode hole by a thick metal stopper. For gaps with equal openings, we have been unsuccessful in generating consistently two equal intensity beams and thus, for the results reported in this paper, the gap of the dummy diode was increased to several cms.

2.6 The vacuum chamber

The 100 cm major radius, 15.2 cm inside minor radius vacuum chamber has been constructed using epoxy reinforced carbon fibers. The desired conductivity is obtained by inserting a phosphor bronze screen inside the body of the graphite. The graphite is 2.5 mm thick and has a surface resistivity of $26.6 \text{ m}\Omega$ in the square. The screen has 250×250 wires per inch and is made of $40 \text{ }\mu\text{m}$ diameter wire with an equivalent surface resistivity of $12.8 \text{ m}\Omega$ in the square. The calculated resistance for the entire vacuum chamber is $57 \text{ m}\Omega$. The measured D.C. resistance of the toroidal vacuum vessel is $68 \pm 2 \text{ m}\Omega$. The outside surface of the chamber is covered with a 6.3 mm thick, epoxy reinforced fiber glass layer.

This novel construction technique has several attractive features, including controllable resistivity and thus magnetic field penetration time, high stiffness and tensile strength, high radiation resistance (up to 500 Mrad) and low outgassing rate ($\sim 10^{-8}$ torr/sec-cm²).

3. EXPERIMENTAL RESULTS

During the first microsecond following injection, the beam dynamics is studied by monitoring the light emitted from a 10 μ m thick polycarbonate foil that is stretched across the minor cross section of the vacuum chamber¹. This foil is graphite coated on the upstream side to avoid electrostatic charging. Figure 6 is an open shutter photograph of the light emitted as the ring passes the foil.

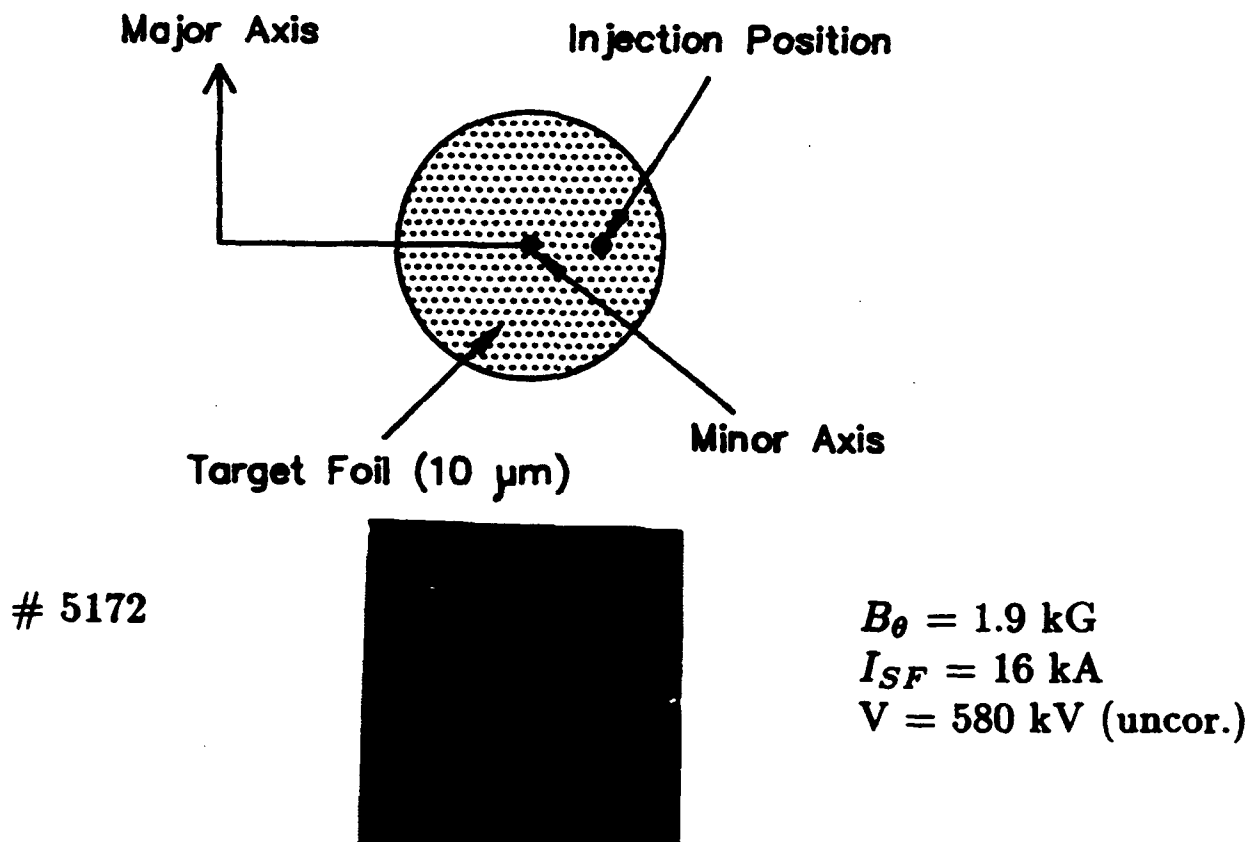


Figure 6: Open shutter photograph showing the electron beam spiraling toward the minor axis of the vacuum chamber. Visible light is emitted as the electron beam passes through the thin polycarbonate foil.

For several combinations of the injection parameters the beam spirals consistently from the injection position to the minor axis and is trapped. The transit time of the beam from the injection position to the minor axis is typically less than 0.5 μ sec. The transit time increases with increasing toroidal field.

The circulating electron ring current is monitored with two Rogowski coils that are located inside the vacuum chamber. A typical waveform is shown in Fig. 7. Although some losses occur immediately after injection, it is observed that the circulating current remains practically constant during the first 10 μsec . Observations are limited to less than 10 μsec by the 100 μsec passive integrator. Attempts to use active integrators have been, so far, unsuccessful.

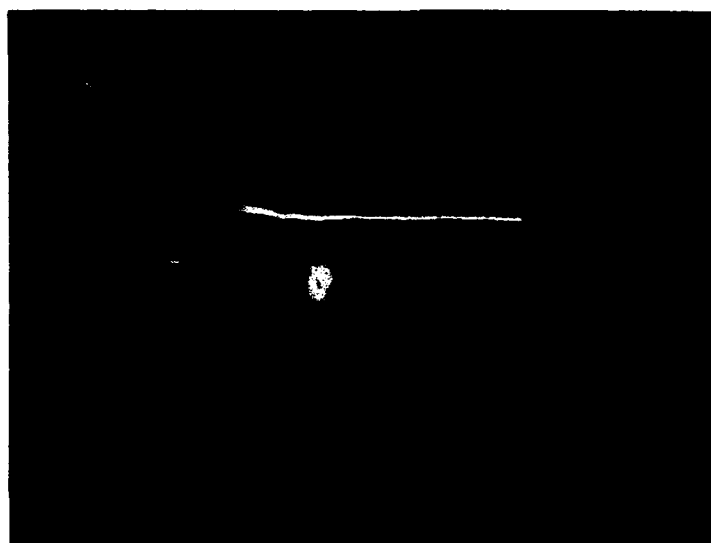


Figure 7: Circulating current measured by a passively integrated Rogowski coil that is located inside the vacuum chamber. In this shot, the total observation time is 2 μsec , and the trapped current is approximately 0.5 kA.

The ring lifetime is inferred from the x-rays produced when the beam strikes a 2.0 cm wide, 1 mm thick lead limiter. The x-rays are monitored by a collimating x-ray detector (scintillator/photomultiplier tube) that is located 2.5 m away from the target. A typical waveform of the x-ray monitor is shown in Fig. 8. From the value of B_z field it can be easily computed that the main peak of the x-ray signal corresponds to a particle energy near 11.5 MeV.

In addition, the acceleration of the ring has been confirmed with the x-ray attenuation technique and also with the observation of photoneutrons produced from the reaction $D(\gamma, n)H$.

The experimental observations show that the spiky shape of the x-ray signal and therefore the beam loss is due to the excitation of the cyclotron resonance^{15,16}. Experiments are in progress to locate and eliminate the field error(s) that excite the resonance and thus to accelerate the ring to higher energy.

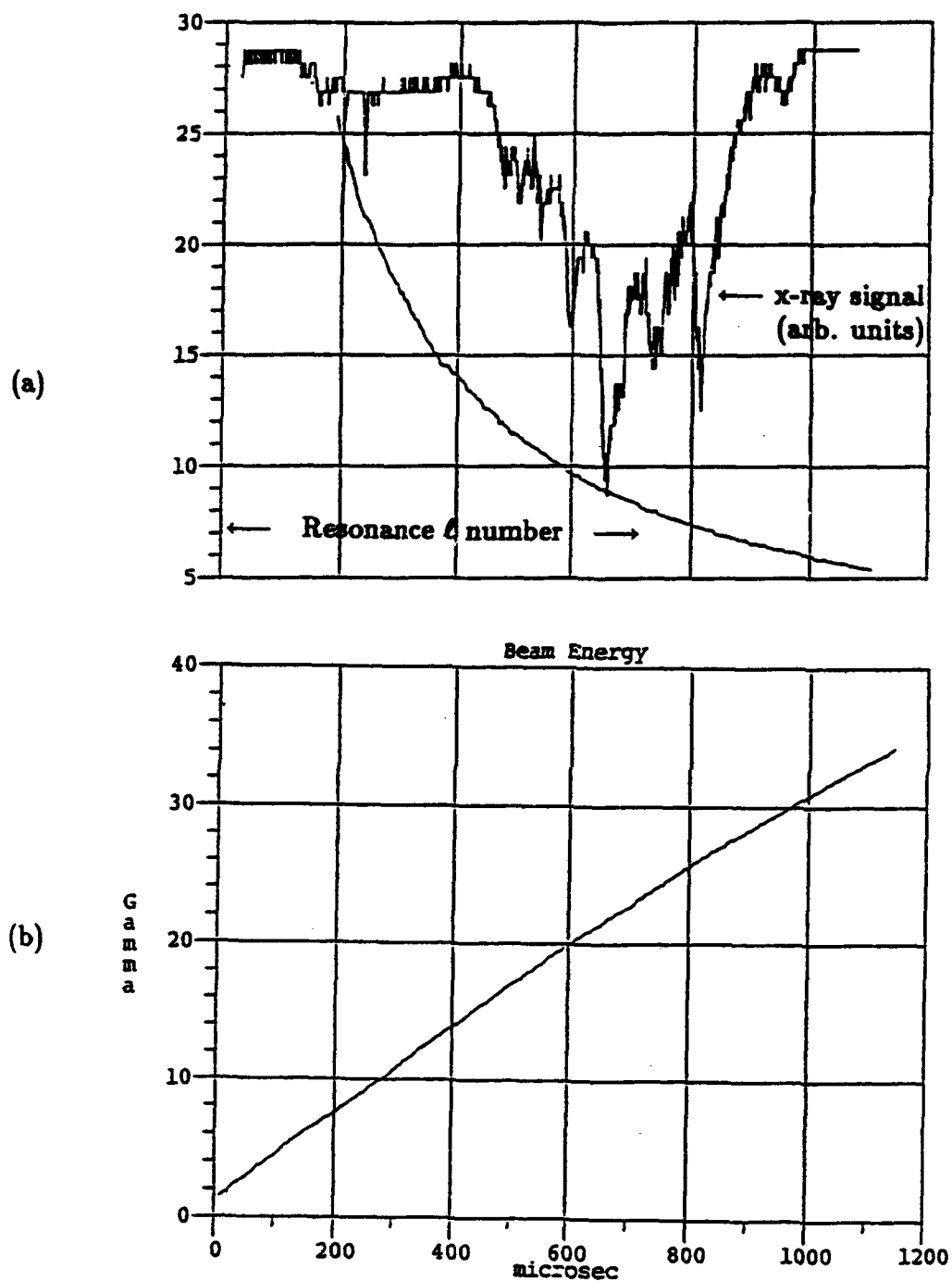


Figure 8: Measurements of the beam energy from X-ray emission. The time resolved x-ray signal (a) shows that the maximum electron loss occurs at approx 600-800 μsec . The corresponding beam energy (b) is inferred from the value of the vertical magnetic field at the same time.

4. REFERENCES

*Supported by ONR and SPAWAR.

^Δ FM Technologies, Inc., ⁺Berkeley Research Associates, [°]SFA, Inc., [†]SAIC.

1. J. Golden, L.K. Len, A.V. Deniz, J. Mathew, T.J. Smith, P. Loschialpo, J.H. Chang, D. Dialetis, S.J. Marsh and C.A. Kapetanakis, "Studies of a Multi-kiloampere Electron Ring Confined in a Modified Betatron Accelerator" Proceedings of the 7th Intern. Conf. on High-Power Particle Beams, Vol. I, p. 221 (1988).
2. H. Ishizuka, R. Prohasko, A. Fisher and N. Rostoker, "Suppression of Beam Instabilities in the UCI Stelleratron", Proceedings of the 7th Intern. Conf. on High-Power Particle Beams, Vol. II, p. 857 (1988).
3. S. Humphries, Jr. and L.K. Len, "High Current Betatron Research at the University of New Mexico", Proc. of 1987 IEEE Part. Accel. Conf., p. 914.
4. V. Bailey, L. Schlitt, M. Tiefenbank, S. Putnam, A. Mondelli, D. Chernin, and J. Petello, "An Experimental Program to Investigate the Strong Focussed, Spiral Line Recirculating Induction Accelerator", Proc. of 1987 IEEE Part. Accel. Conf., p. 920.
5. W.K. Tucker, S.L. Shope, and D.E. Hasti, "Recirculating Electron Beam LINAC", Proc. of 1987 IEEE Part. Accel. Conf., p. 957.
6. P. Sprangle and C.A. Kapetanakis, "Constant Radius Magnetic Acceleration of a Strong Non-Neutral Proton Ring", J. Appl. Phys. **49**, p. 1 (1978).
7. C.A. Kapetanakis, P. Sprangle, D.P. Chernin, S.J. Marsh, and I. Haber, "Equilibrium of a High-Current Electron Ring in a Modified-Betatron Accelerator", Phys. Fluids **26**, p. 1634, (1983).
8. N. Rostoker, "High-Current Betatron", Comments on Plasma Physics **6**, p. 91 (1980).
9. C. Roberson, A. Mondelli, and D. Chernin, "High-Current Betatron with Stellarator Fields", Phys. Rev. Letts. **50**, p. 507, (1983).
10. C.A. Kapetanakis, D. Dialetis, and S.J. Marsh, "Beam Trapping in a Modified Betatron with Torsatron Windings", Part. Accel. **21**, p. 1, (1987).
11. C.A. Kapetanakis, S.J. Marsh, and D. Dialetis, "Beam Extraction Scheme from the Modified Betatron Accelerator", Phys. Rev. Letts. **61**, p. 86, (1988).
12. S.J. Marsh, J. Golden, C.A. Kapetanakis and David Anderson, "High Midplane Accessibility Stellarator Windings for High-Current Toroidal Accelerators", J. Appl. Phys. **64**, p. 6138 (1988).
13. D.W. Kerst, "Historical Development of the Betatron", Nature **157**, pp. 90-95, (1946).
14. K.F. McDonald, F. Mako, T. Smith, L. Floyd, J. Golden, and C.A. Kapetanakis, "The NRL Modified Betatron Accelerator Pulsed Power Systems", Proc. of the 5th Pulsed Power Conf., (1986).
15. D. Chernin and P. Sprangle, "Integer Resonances in the Modified Betatron", Part. Accel. **12**, p. 101 (1982).
16. C.W. Roberson, A. Mondelli, and D. Chernin, "The Stelleratron Accelerator", Part. Accel. **17**, p. 79, (1985).

Appendix V

Improved Beam Confinement in the Modified Betatron with Strong Focusing

Improved Beam Confinement in the Modified Betatron with Strong Focusing

C. A. Kapetanakos, L. K. Len,^(a) T. Smith, J. Golden,^(b) K. Smith,^(c) S. J. Marsh,^(c) D. Dialetis,^(d)
J. Mathew, P. Loschialpo, and J. H. Chang

Plasma Physics Division, Naval Research Laboratory, Washington, D.C. 20375

(Received 16 January 1990)

The lifetime of the circulating electron beam in the Naval Research Laboratory modified betatron has been increased by more than 2 orders of magnitude with the addition of strong focusing windings to the device. The injected beam consistently spirals from the injector to the minor axis and is trapped. The ~0.5-kA trapped electron ring has been accelerated above 10 MeV from the injection energy of 0.5 to 0.6 MeV. The beam acceleration has been confirmed not only by the x-ray attenuation technique but also with the detection of photon neutrons.

PACS numbers: 41.80.Ee, 29.20.Fj

Accelerators that combine high-current capability and high effective accelerating gradient are currently under development in several laboratories.¹⁻⁵ These accelerators have two common features, namely, strong focusing that improves their current-carrying capability and recirculation that enhances their effective accelerating gradient.

Among these accelerators is the modified betatron.⁶⁻⁸ This device is currently under investigation at the University of California, Irvine² and also at the Naval Research Laboratory¹ (NRL). In its original form the modified betatron consists of a strong toroidal magnetic field and a time-varying betatron field that is responsible for the acceleration.

Extensive studies of beam capture and confinement in the NRL modified betatron led to the formation of electron rings with circulating current as high as 3 kA and have furnished valuable information on the critical physics issues of the concept. In addition, these studies have shown that over a wide range of parameters the ring lifetime was limited to a few microseconds which is comparable to the magnetic-field diffusion time through the vacuum chamber. Thus, it became apparent from these results that the magnetic-field configuration of the device had to be modified to increase the beam lifetime and thus to achieve acceleration. A decision was made to proceed rapidly with the design, fabrication, and installation of strong focusing windings.

Stellarator⁹ (four twisted windings that carry current in alternate directions) and Torsatron¹⁰ (two twisted windings that carry current in the same direction) winding configurations were considered. Both configurations have advantages and shortcomings. The stellarator configuration was finally selected not only because of the small net vertical field and the lower current per winding but also because it is compatible with our contemplated extraction scheme.^{11,12}

This paper briefly describes the NRL modified betatron in its latest form and summarizes the most impor-

tant experimental results after the installation of the strong focusing windings. Although experiments were carried out at various background pressures, most of the results reported in this paper were limited to pressures between 2×10^{-6} and 8×10^{-6} Torr. In this pressure range the electron-beam electrical neutralization time by direct collisional ionization of the background gas has been estimated to be between 180 and 45 μ sec. Work is in progress to reduce the background pressure by at least an order of magnitude and thus avoid substantial plasma formation over the entire beam lifetime. This is in contrast to the main effort in the Stellatron at Irvine² that is focused on the formation of runaway electron beams and therefore the pressure is incidentally high.

Description of the experiment.—(1) External magnetic fields: The NRL modified betatron comprises three different external magnetic fields; the betatron field that is a function of time and is responsible for the acceleration of the electrons, the toroidal magnetic field that varies only slightly during the acceleration of the electron ring, and the strong focusing field that also has a very weak time dependence. The coils that generate these three fields are shown schematically in Fig. 1.

(2) The betatron field: The betatron¹³ magnetic field controls mainly the major radius of the gyrating electron ring and is produced by eighteen air-core, circular coils connected in series. Their total inductance is approximately 530 μ H. The coils are powered by an 8.64-mF capacitor bank that can be charged up to 17 kV. At full charge, the bank delivers to the coils a peak current of about 45 kA. The current flowing through the coils produces a field that varies sinusoidally with time having a quarter period of 2.5 msec and an amplitude on the minor axis at peak charging voltage equal to 2.1 kG. Immediately after the peak the field is crowbarred with a 4.5-msec decay time.

The flux condition and field index are adjusted by two sets of trimmer coils that are connected in parallel to the main coils. The current through the trimmers is adjust-

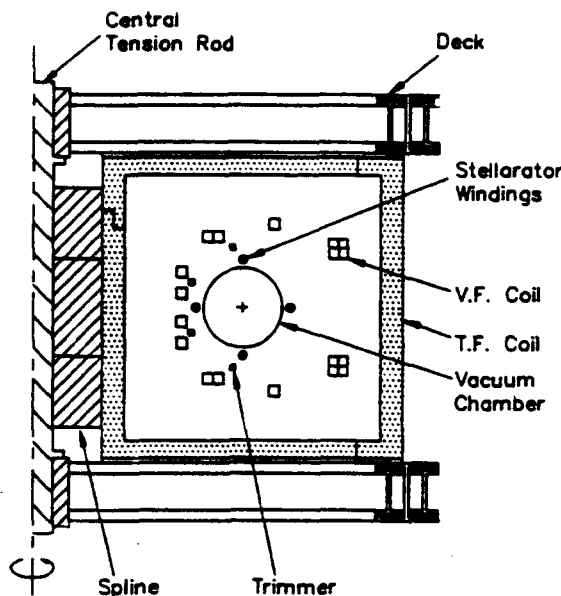


FIG. 1. Elevation of the device showing the vertical field (V.F.), toroidal field (T.F.), stellarator windings, and some structural components.

ed with series inductors. Typically $\sim 10\%$ – 15% of the total current flows through the trimmers.

(3) The toroidal field: The toroidal magnetic field controls mainly the minor cross section of the electron ring and the growth rate of several unstable collective modes. This field is generated by twelve air-core, rectangular coils that are connected in series.

The coils are made of aluminum square tubing and have a 150 cm height and 135 cm width. The total inductance of the twelve coils is $\sim 85 \mu\text{H}$ and are powered by a 24-mF capacitor bank that can be charged to a peak voltage of 10.6 kV. At peak voltage, the bank delivers to the coils ~ 180 kA. This current produces a field that varies sinusoidally with time having a quarter period of 1.9 msec and an amplitude on the minor axis equal to 3.9 kG.

(4) The strong focusing field: The strong focusing field improves the confining properties of the other two fields by reducing the sensitivity of the beam centroid and individual electrons to energy mismatch and energy spread.

In the NRL modified betatron the strong focusing field is generated by four twisted windings carrying current in alternate directions. The left-handed windings are located 23.4 cm from the minor axis and have a 209.4-cm period, i.e., there are three periods over the circumference of the torus. They are supported by epoxy-reinforced graphite jackets and have been designed to carry up to 25 kA. The windings are connected in series and the current temporal profile is controlled by a ballast inductor.

The stellarator field index n_{st} is defined, in the linear

approximation, as¹⁰

$$n_{st} = -(\Omega_z^{\text{ex}} \epsilon_{st})^2 a r_0 / 2 \Omega_{r0} \Omega_{\theta 0},$$

where

$$\Omega_z^{\text{ex}} \epsilon_{st} \approx 4 \alpha \Omega_0 \rho_0 K'_2(2 \alpha \rho_0),$$

$\Omega_0 = |e| B_0 / m$, $B_0 = 2 \mu_0 I_{st} / L$, $\alpha = 2\pi / L$, r_0 is the major radius, K'_2 is the derivative of the modified Bessel function, and Ω_{r0} and $\Omega_{\theta 0}$ are the cyclotron frequencies of the vertical and toroidal fields on the minor axis. Since in the NRL modified betatron I_{st} , $\Omega_{\theta 0}$, and Ω_{r0} / γ remain approximately constant during acceleration, n_{st} scales inversely proportional to the relativistic factor γ . The stellarator field index is related to the maximum gradient $g = (\partial B_z / \partial r)_{\text{max}} = (\partial B_z / \partial z)_{\text{max}}$ of the stellarator field by $n_{st} = -g^2 r_0 / 2 \alpha B_{r0} B_{\theta 0}$. For $B_{\theta 0} = 2.0$ kG, $B_{r0} = 25$ G, $\alpha = -0.03/\text{cm}$, $\rho_0 = 23.42$ cm, and $I_{st} = 19$ kA, $n_{st} \approx 14$, and $g \approx 20$ G/cm.

(5) The vacuum chamber and diode: The 100-cm major radius, 15.2-cm-inside minor radius vacuum chamber has been constructed using epoxy-reinforced carbon fibers. The desired conductivity is obtained by embedding a phosphor bronze screen inside the body of the graphite. The graphite is 2.5 mm thick and has a surface resistivity of 26.6 m Ω on a square. The screen has 250 \times 250 wires per inch and is made of 40- μm -diam wire with an equivalent surface resistivity of 12.8 m Ω on a square. The calculated resistance for the entire vacuum chamber is 57 m Ω . The measured dc resistance of the toroidal vacuum vessel is 68 ± 2 m Ω . The outside surface of the chamber is covered with a 6.3-mm-thick, epoxy-reinforced fiberglass layer.

This novel construction technique has several attractive features, including controllable resistivity and thus magnetic-field penetration time, high stiffness, and tensile strength, high-radiation resistance (up to 500 Mrad) and low-outgassing rate ($\sim 10^{-8}$ Torr/sec cm²).

The electrons are emitted from a thin carbon disk mounted at one end of a 2.5-cm-diam cylindrical cathode stalk clad with molybdenum. The carbon disk is flush with the molybdenum cladding and faces the circular opening of the conical anode, that is located 8.7 cm from the minor axis of the toroidal chamber. To minimize the magnetic-field component transverse to the emitting surface of the cathode the core of the cathode stalk is made out of high $\sigma\mu$ ferromagnetic material. The unsaturated state of the ferromagnetic material is prolonged by a thin copper housing.

Experimental results.—During the first microsecond following injection, the beam transverse motion is studied by monitoring the light emitted from a 10- μm -thick polycarbonate foil that is stretched across the minor cross section of the vacuum chamber.¹ The foil is graphite coated on the upstream side to avoid electrostatic charging. Figure 2 shows two open-shutter photographs of the light emitted as the ring passes through the foil.

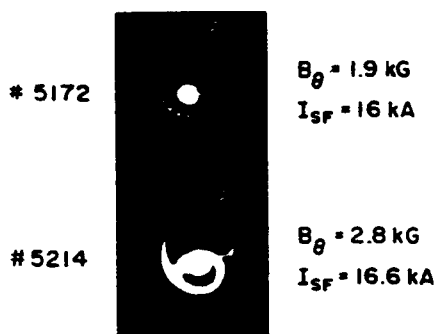
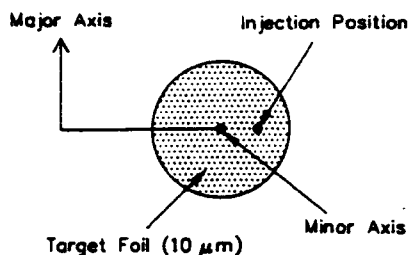


FIG. 2. Open-shutter photographs of the light emitted when the beam passes a 10- μ m-thick foil.

The light spots near the edges of the photograph are position fiducials produced by a ring of light-emitting diodes located approximately 0.7 cm from the vacuum chamber wall. Reflections from the wall are also noticeable near the upper edge of the photograph.

For several combinations of injection parameters the beam consistently spirals from the injection position to the minor axis and is trapped. The transit time of the beam to the minor axis is typically less than 0.5 μ sec. In shot No. 5172 both the beam current and B_θ are low and thus the bounce frequency is high. As the beam spirals from the diode to the minor axis it creates distinct light spots as it passes through the foil. By increasing the beam current and B_θ the bounce frequency is reduced and thus the light spots start to overlap and the spiral becomes continuous as in shot No. 5214.

The trapping mechanism is presently unknown. A likely candidate is the wall resistivity. However, the predicted decay rate Γ^{-1} from the linear theory¹⁴ for the parameters of the experiment is between 10 and 20 μ sec, i.e., too long to explain the experimental results.

The circulating electron ring current is monitored with two Rogowski coils that are located inside the vacuum chamber. A typical wave form is shown in Fig. 3. Although some losses occur immediately after injection, the circulating current remains practically constant during the first 10 μ sec. Observations are limited to 10 μ sec by the signal level and the 100- μ sec passive integrator. Attempts to use active integrators have been, so far, unsuccessful.

In the results reported here the injected electron beam is produced by a diode with a 1-cm-diam carbon cathode



FIG. 3. Output from a Rogowski coil that is located 15° downstream of the diode. The plateau (trapped current) corresponds to 525 A.

disk that is matched to a 1-cm-diam anode hole. For such a beam radius the maximum trapped current is between 0.5 and 0.6 kA. The results indicate that the trapped current increases as the beam diameter increases. Experiments with larger radius beams are presently in progress.

The ring lifetime is inferred from the x rays produced when the beam strikes a 2.5-cm-wide, 1-mm-thick lead limiter. The x rays are monitored by a collimated x-ray detector (scintillator-photomultiplier tube) that is housed inside a lead box. In the results reported in this paper, the x rays enter the scintillator through a 1.94-cm-diam hole and the detector is located 10.8 m from the target. A typical wave form of the x-ray monitor is shown in Fig. 4. From the value of the B_z field it can be easily computed that the main peak of the x-ray signal corresponds to a particle energy near 11.0 MeV. The energy of the electrons that are lost at a later time is obviously higher.

The x-ray signal is very reproducible in both amplitude and shape. For the first 200–300 μ sec we do not observe any x rays. The time at which x rays are initially observed and the times the various signal peaks occur are directly proportional to B_θ and inversely proportional to dB_z/dt . In addition, the temporal occurrence of the

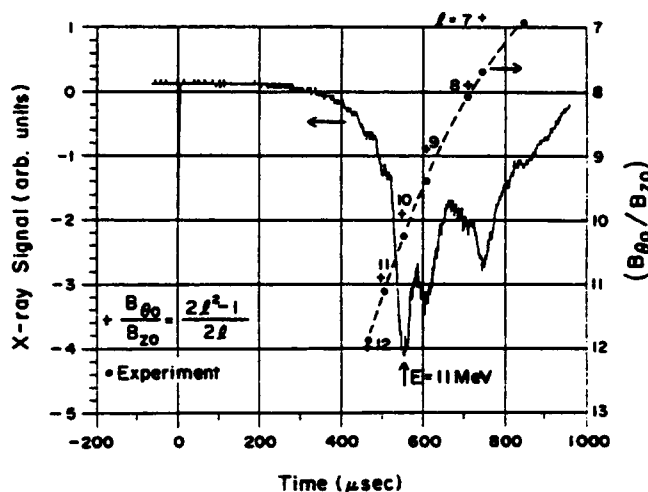


FIG. 4. Output of the x-ray detector vs time and B_θ/B_z at the peaks of the x-ray signal for $B_\theta = 3.6$ kG, $I_{SF} = 20$ kA, and $(B_z)/B_{z0} = 1.9$.

x-ray signal appears to be independent of the trapped current for at least up to 0.5 kA and also of the background pressure up to 6×10^{-5} Torr. However, the amplitude of the x-ray signal decreases rapidly with increasing pressure above 8×10^{-6} Torr. For the results of Fig. 4, the electrons gain energy at the rate of 0.39 keV/revolution. Those electrons lost at the main x-ray peak have performed in excess of 28000 revolutions around the major axis. In our best results the corresponding number is ~ 35000 revolutions and the electron energy about 12 MeV.

The spiky shape of the x-ray signal and therefore the beam loss is consistent with the excitation of the cyclotron resonance.^{15,16} Figure 4 also shows the ratio B_z/B_r versus time. The solid circles are from the experiment and the crosses are the prediction of the theory. The poor agreement between theory and experiment for low- I values is probably associated with the omission of toroidal effects in the theoretical model. The results are also consistent with the excitation of the electron-cyclotron instability.¹⁷ This instability is caused by the coupling of the electron-cyclotron mode to the TE_{11} waveguide mode of the torus. Work is in progress to pinpoint the exact cause of the beam loss.

The x-ray signal has been studied with the usual attenuation technique. A layer of lead more than 5 cm thick is needed to completely eliminate the signal. A 1.3-cm-thick layer does not have any effect on the signal except on the initial spike that is due to the injected beam. In addition to the x-ray attenuation technique, the beam acceleration has been confirmed with the photoneutrons produced from the $D(\gamma, n)H$ reaction. A plastic tube in the form of a ring containing heavy water was inserted behind the limiter. The photons produced on the target photodisintegrate the deuterium and produce neutrons that are monitored with a rhodium activation detector.¹⁸ The number of counts measured during the first minute exceeds 7 standard deviations.

The intensity and polarization of the synchrotron radiation has been computed numerically. At low energy (≤ 1 MeV) the radiation spectrum is dominated by a peak at the Doppler-shifted B_z cyclotron frequency. As the electron energy increases the effect of the B_z cyclotron motion is reduced and the spectrum approaches that of a purely circular orbit.

Two high-gain (50 db) heterodyne receivers are used to monitor the emitted radiation in the bands 26.5–28.5 and 36.5–38.5 GHz during acceleration. The measurements show that the amplitude of the radiation scales linearly with the trapped ring current. During the first 200 nsec, both the amplitude and polarization are consistent with the predicted single-particle emission. In addition, the temporal shift of the first peak is in good agreement with the predicted toroidal field and energy

dependence of the Doppler-shifted cyclotron frequency. However, the late-time behavior of the radiation signals is not presently well understood. The radiation signal starts to decay after ~ 200 μ sec, contrary to the prediction of the theory. It is likely that electron losses, plasma formation, or beam displacement out of the field of view of the detectors are responsible for the observed discrepancy.

The authors are grateful to Professor D. Kerst, Dr. P. Sprangle, and Dr. Y. H. Seo for many illuminating discussions. This work was supported by the ONR and the Space and Naval Warfare Systems Command.

Note added.—Since the submission of the paper, the trapped current increased to 0.9–1.0 kA and the beam energy to 15–16 MeV.

^(a)Permanent address: FM Technologies, Inc., 10529-B Braddock Road, Fairfax, VA 22032.

^(b)Permanent address: Berkeley Research Associates, 5532 Hempstead Way, Springfield, VA 22151.

^(c)Permanent address: Sachs/Freeman Associates, Inc., Landover, MD 20785.

^(d)Permanent address: Science Applications, Inc., 1710 Goodridge Drive, McLean, VA 22102.

¹J. Golden *et al.*, in *Proceedings of the Seventh International Conference on High-Power Particle Beams, Karlsruhe, Germany, July 1988*, edited by W. Bauer and W. Schmidt (Kernforschungszentrum Karlsruhe GmbH, Karlsruhe, 1988), Vol. I, p. 221.

²H. Ishizuka *et al.*, in *Proceedings of the Seventh International Conference on High-Power Particle Beams* (Ref. 1), Vol. II, p. 857.

³S. Humphries, Jr., and L. K. Len, in *Proceedings of the 1987 Particle Accelerator Conference, Washington, DC, March 1987*, edited by E. R. Lindstrom and L. S. Taylor (IEEE, New York, 1987), p. 914.

⁴V. Bailey *et al.*, in *Proceedings of the 1987 Particle Accelerator Conference* (Ref. 3), p. 920.

⁵W. K. Tucker *et al.*, in *Proceedings of the 1987 Particle Accelerator Conference* (Ref. 3), p. 957.

⁶P. Sprangle and C. A. Kapetanakis, *J. Appl. Phys.* **49**, 1 (1978).

⁷C. A. Kapetanakis *et al.*, *Phys. Fluids* **26**, 1634 (1983).

⁸N. Rostoker, *Comments Plasma Phys.* **6**, 91 (1980).

⁹C. Roberson *et al.*, *Phys. Rev. Lett.* **50**, 507 (1983).

¹⁰C. A. Kapetanakis *et al.*, *Part. Accel.* **21**, 1 (1987).

¹¹C. A. Kapetanakis *et al.*, *Phys. Rev. Lett.* **61**, 86 (1987).

¹²S. J. Marsh *et al.*, *J. Appl. Phys.* **64**, 6138 (1988).

¹³D. W. Kerst, *Nature (London)* **157**, 90 (1946).

¹⁴P. Sprangle and C. A. Kapetanakis, *Part. Accel.* **18**, 203 (1986).

¹⁵D. Chernin and P. Sprangle, *Part. Accel.* **12**, 101 (1982).

¹⁶C. W. Roberson *et al.*, *Part. Accel.* **17**, 79 (1985).

¹⁷P. Sprangle (private communication).

¹⁸F. C. Young, *IEEE Trans. Nucl. Sci.* **22**, 718 (1975).

Appendix W

Compact, High-Current Accelerators and Their Prospective Applications

Compact, high-current accelerators and their prospective applications*

C. A. Kapetanakis,[†] L. K. Len,[‡] T. Smith, D. Dialetis,[§] S. J. Marsh,^{||} P. Loschialpo, J. Golden,[¶] J. Mathew, and J. H. Chang

Plasma Physics Division, Naval Research Laboratory, Washington, DC 20375-5000

(Received 5 December 1990; accepted 1 April 1991)

This paper briefly surveys the three compact, high-current accelerators that are presently under development in the United States in support of a national program. In addition, it reports recent experimental results from the Naval Research Laboratory (NRL) modified betatron [Phys. Rev. Lett. 64, 2374 (1990)] with emphasis on the electron-cyclotron resonance that presently limits the energy of the beam to approximately 18 MeV. Finally, it briefly addresses selective existing and prospective applications of accelerators.

I. INTRODUCTION

Over the last 60 years the technology of high-energy accelerators has advanced to a remarkable level of sophistication.¹ These conventional accelerators are designed to operate reliably at high energies but at relatively low current, primarily to avoid complications related to beam self-field effects. Thus the beam dynamics in conventional accelerators is determined mainly by the externally applied fields.

Over the last several years, it has become apparent that accelerators with both high current and high-average power could have interesting applications not only in national defense² but also in several areas of the civilian economy.¹

In contrast with the conventional accelerators that operate in the single-particle regime, high-current accelerators operate in an uncharted territory, in which space charge effects from the self and image fields are as important as externally applied fields. The free energy stored in the intense self fields of these beams can drive collective instabilities and strong magnetic fields are needed to reduce the rapid growth rate of these unstable modes. Several of the key physics issues associated with the high-current accelerators are similar to those in plasma physics. Therefore it is not accidental that the majority of researchers that are presently developing this technology have been trained in plasma physics and not in conventional accelerator technology.

Compact, high-current accelerators are currently under development in several laboratories.³⁻⁷ As a result of their compactness and light weight, these devices are expected to be substantially less costly than conventional accelerators of comparable power. In addition, because of their high-current carrying capability, these accelerators have the potential to generate very powerful electron beams that can provide high dose rates at reduced unit irradiation cost.

During the last several years several applications have

been suggested,^{1,8} such as water purification, sludge disinfection, cracking of crude oil, and excavation of tunnels, all requiring high-average power and low unit irradiation cost. These applications are presently on hold waiting for the development of inexpensive beams.

In this paper, we briefly survey the three compact accelerators that are currently under development in support of the DARPA/services program and report recent experimental results from the NRL modified betatron. The last section briefly addresses existing and prospective applications of accelerators.

II. REVIEW OF COMPACT, HIGH-CURRENT ACCELERATORS

Compact, high-current accelerators are currently under development at the University of California, Irvine,⁴ University of New Mexico,⁵ Pulse Sciences Inc.⁶ (PSI), Sandia National Laboratory⁷ (SNL), and the Naval Research Laboratory³ (NRL). All these concepts are induction accelerators. The reason is that induction accelerators are inherently low-impedance devices and thus are ideally suited to drive high-current beams. The acceleration process is based on the electric field produced by a time-varying magnetic field. The electric field can be either continuous or localized along the accelerating path.

This section briefly reviews the three electron acceleration concepts that are part of the national program: The spiral line induction accelerator (SLIA) developed at PSI, the recirculating linear accelerator (RLA) developed at SNL, and the modified betatron accelerator (MBA) developed at NRL. In addition to being inductive, these three accelerators utilize strong focusing in order to improve their current carrying capability and recirculation to enhance their accelerating gradient.

A. Spiral line induction accelerator⁶

The SLIA concept is shown schematically in Fig. 1(a). The beam is injected at one end of the spiral line and is accelerated at the advanced test accelerator (ATA) type accelerating cells. The minor radius of the beam is controlled by an axial magnetic field and the beam is guided at the bends by a static vertical and strong focusing field. At the exit, the beam

* Paper 116, Bull. Am. Phys. Soc. 35, 1919 (1990).

[†] Invited speaker.

[‡] Permanent address: FM Technologies, Inc., 10529-B Braddock Road, Fairfax, Virginia 22032.

[§] Permanent address: Science Applications, Inc., 170 Goodridge Drive, McLean, Virginia 22102.

^{||} Permanent address: SFA, Inc., Landover, Maryland 20785.

[¶] Permanent address: Berkeley Research Associates, 5532 Hampstead Way, Springfield, Virginia 22151.

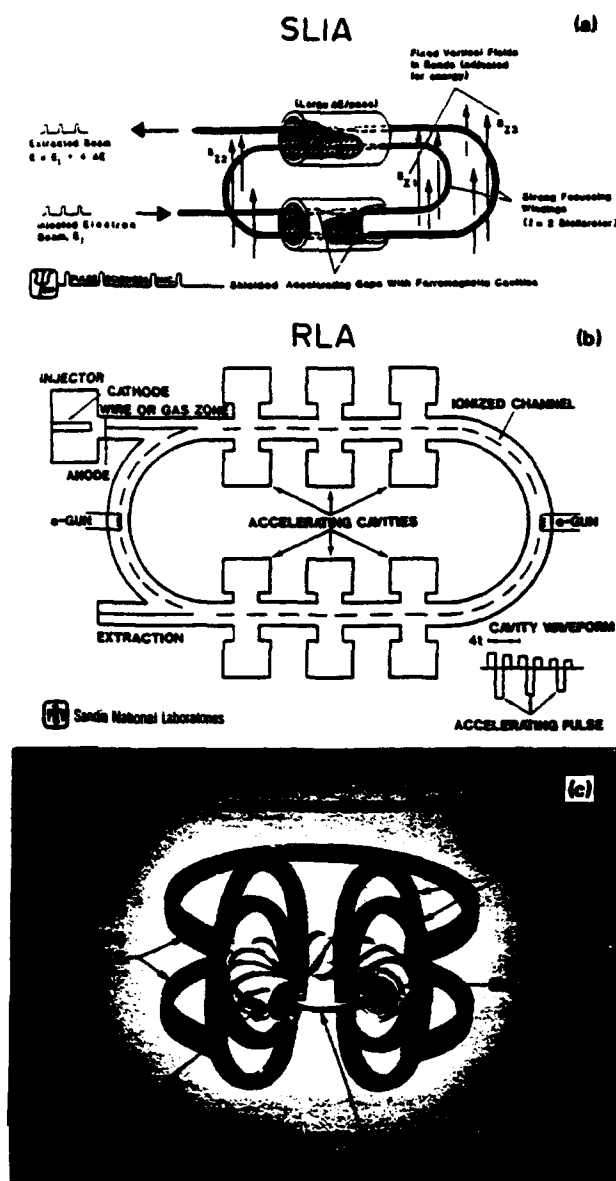


FIG. 1. Schematics of the three compact, high-current accelerators presently under development in support of the national compact accelerator development program.

TABLE I. Parameters of proof-of-concept (POC) experiments.

SLIA	RLA	MBA
Injected beam Energy ~ 3.5 MeV Current ~ 10 kA Duration ~ 35 nsec Axial mag. field 5.5 kG Vert. mag. field < 0.32 kG S.F. gradient < 0.25 kG/cm No. of passes 2 No. of acc. units 2 Energy gain/acc. unit 1.5 MeV	Injected beam Energy 3.5 MeV Current 10 kA Duration 40 nsec Channel radius 1.5 cm Channel density/beam density 0.4 No. of passes 3 No. of cavities 2 Energy gain/cavity 1 MeV	Injected beam Energy 0.6–0.7 MeV Current < 2 kA Duration ~ 40 nsec Torus major radius 100 cm Torus minor radius 15 cm Toroidal mag. field 2–5 kG Vertical mag. field B_z 0–2 kG Current in S.F. windings 20–25 kA No. of S.F. field periods 6 $dB_z/dt < 1.5$ G/ μ sec

energy is equal to the injection energy plus the energy gain per pass times the number of passes.

Since the SLIA is open-ended, difficulties associated with injection and extraction are avoided. Furthermore, this configuration provides flexibility in the selection of shape of the electron pulses. Important outstanding technical issues associated with the SLIA concept are the excitation of the beam breakup instability (BBU), the matching of fields between the straight sections and the bends, and the development of high-frequency power supply for driving and resetting the ferromagnetic cores.

A proof-of-concept (POC) experiment is presently under design and construction. Its most important parameters are listed in Table I. The 3.5 MeV, 10 kA, 35 nsec duration injected beam pulse will be accelerated to 9.5 MeV by passing twice through the two, 1.5 MeV accelerating units.

B. Recirculating linear accelerator⁷

The RLA is shown schematically in Fig. 1(b). The injected beam is accelerated by dielectric cavities that are placed in tandem along the straight sections of the race track. Beam focusing is provided by an ion channel formed by a low-energy, low-current electron beam. A time-rising vertical magnetic field guides the beam at the bends.

Important advantages of RLA concept are the suppression of BBU and the wide energy bandwidth provided by the ion channel. In addition to injection and extraction, maintaining the integrity and centering of the ion channel during acceleration and avoiding beam erosion are key technical issues.

A POC experiment is currently under construction. Its most important parameters are listed in Table I. The 3.5 MeV, 10 kA, 40 nsec duration electron beam pulse will be accelerated to 8–10 MeV by passing three times through the two, 1 MeV dielectric cavities.

C. The modified betatron accelerator^{8–11}

In both the SLIA and the RLA, the accelerating electric field is localized at the gaps. In contrast, the electric field in the MBA is continuous along the entire beam path and thus

the accelerator is constrained to circular shape. An artist's conception of the MBA is shown in Fig. 1(c). The injected beam is accelerated by the time-varying vertical (betatron) magnetic field B_z . The toroidal magnetic field B_θ controls mainly the minor radius of the beam and the growth rate of the various unstable modes while the vertical and strong focusing fields control mainly the major radius of the electron ring. The stability properties of the stellarator windings for high-current beams were studied initially by Gluckstern¹² in linear geometry and by Roberson¹³ *et al.* in toroidal geometry.

Important advantages of the MBA are the natural synchronization of B_z and particle energy, the absence of the BBU mode and its compact size and light weight. Outstanding technical issues are the suppression of the cyclotron resonances, collective instabilities, and the extraction of the beam.

A POC experiment is currently in operation at NRL. The various parameters of the device are listed in Table I. Its objective is to study the critical physics issues associated with the concept and to accelerate at 1 kA, 20 nsec electron beam pulse to 20 MeV with subsequent extraction of the beam.¹⁴ Presently, the trapped electron beam has been accelerated to between 17–18 MeV from the injected energy of 0.6–0.7 MeV. The maximum trapped current is up to 1.5 kA and the trapping efficiency is as high as 75%.

III. RECENT EXPERIMENTAL RESULTS FROM THE MBA

The NRL modified betatron accelerator has been described previously^{3,15,16} and a summary of the initial experimental results has been published.^{3,16} In this paper, we summarize the highlights of the most recent results.

During the first microsecond following injection, the beam motion is inferred from the light emitted when the electrons pass through a thin ($3\ \mu\text{m}$) plastic foil stretched across the minor cross section of the vacuum chamber. The open shutter photographs show that for a wide range of experimental parameters and after fine tuning the fields, the injected beam consistently spirals from the injector to the vicinity of the minor axis and is trapped. The beam travel time from the injector to the minor axis depends on the values of the various fields and is typically between 300–1000 nsec.

The trapping of the beam is most likely due to the wall resistivity of the vacuum chamber. The physical mechanism of the resistive trapping can be understood as follows. Consider a pencil-like electron beam inside a cylindrical pipe with finite resistivity wall. Because of the resistivity of the wall, the electric and magnetic images do not coincide and thus the centroid of an off-axis beam experiences a negative radial magnetic field component. This field component crossed with the axial velocity of the beam produces a poloidal force, which is in the opposite direction to the poloidal motion of the beam. In the absence of the strong focusing and when the self-fields dominate the external fields (high-current regime), the poloidal force in conjunction with the axial (toroidal) magnetic field drives the beam to the wall (drag instability). However, in the presence of strong focus-

ing, the direction of the poloidal motion can be reversed and the beam spirals to the minor axis.

The resistive wall trapping mechanism has been analyzed previously.¹⁷ The linear theory was done for a beam near the minor axis. In this case, the relevant diffusion time is $\tau_1 = \mu_0 a / 2\rho$, where a is the minor radius of the torus and ρ its surface resistivity. For the parameters of the NRL-MBA, $\tau_1 \approx 10\ \mu\text{sec}$. The linear decay rate Γ^{-1} from the theory is between 10–15 μsec , as expected. This time is at least a factor of 30 too long to explain the results.

In contrast to the analysis that assumes the beam is near the minor axis, the beam in the experiment during injection is near the wall and therefore the relevant diffusion time is $\tau_2 = \mu_0 \Delta / \pi^2 \rho$, where Δ is the thickness of the wall. The ratio $\tau_1 / \tau_2 = \pi^2 a / \Delta \approx 300$. The fact that τ_2 is substantially shorter than the observed trapping time is not surprising since the beam remains near the wall only for a short period of time. Experiments are presently under way to test the hypothesis of the resistive trapping.

The x rays are monitored by three collimated x-ray detectors (scintillator-photomultiplier tube) that are housed inside lead boxes. In the results shown in Fig. 2, the x rays enter the scintillator through a 1.94 cm diam tube and the detector is located 10.8 m from the vacuum chamber. As a rule, the shape of the x-ray signal recorded by all three detectors is spiky and the peaks always occur at the same value of $B_{\theta 0} / B_{z 0}$ ($B_{\theta 0}$ is the toroidal and $B_{z 0}$ the vertical magnetic fields on the minor axis) independently of the current flowing in the stellarator windings.

In addition to the x-ray pulse, Fig. 2 shows the ratio of $B_{\theta 0} / B_{z 0}$ at the peaks of the signal. The solid circles are from the experiment and the crosses are from the resonance condition $B_{\theta 0} / B_{z 0} = (2l^2 - 1) / 2l$, $l = 1, 2, \dots$, of the cyclotron resonance.^{18,19} The solid line shows the trend of the experimental results with time. For $l = 8, 9$, and 10, experiment and theory are in good agreement. However, for the remaining l values there is noticeable divergence between the theoretical predictions and the experiment.

The theory of the cyclotron resonance has been developed under the assumption that the beam is located on the

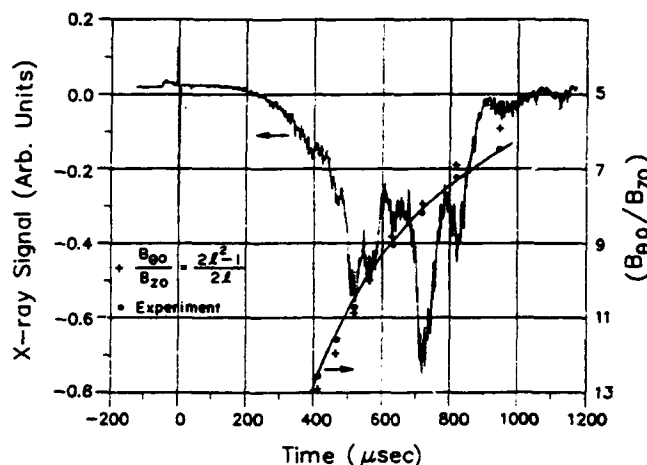


FIG. 2. X-ray pulse and ratio of $B_{\theta 0} / B_{z 0}$ at the peaks of the x-ray signal. The main peak corresponds to 17.2 MeV.

minor axis. However, the experimental observations indicate that the electron ring starts to move off axis after 200–300 μsec . Recently, the theory of the cyclotron resonance has been extended to a beam that is located on the midplane but off the minor axis. For such a beam the resonance conditions becomes

$$r_0 \Omega_{\theta 0} / c \gamma \beta_{\theta} = (2l^2 - 1) / 2l, \tag{1}$$

where r_0 is the major radius, $\Omega_{\theta 0}$ is the cyclotron frequency of the toroidal field, γ is the relativistic factor, and β_{θ} is the normalized toroidal velocity. Perfect match between the experimental results and the revised theory is obtained if it is assumed that the equilibrium position of the beam moves initially toward the major axis and then away from it with a constant outward radial speed of 0.23 mm/ μsec , starting at about 460 μsec .

In a modified betatron with strong focusing windings, there are four characteristic transverse modes $\omega_{\pm \pm}$. Integer resonances occur when the frequency of these modes, in the laboratory frame, over the relativistic cyclotron frequency of the vertical field Ω_z / γ on the minor axis is an integer, i.e., when

$$\omega_{\pm \pm} / (\Omega_z / \gamma) = K, \text{ where } K = \pm 1, \pm 2, \dots$$

The cyclotron resonance occurs when $\omega_{+ +} / (\Omega_z / \gamma) = K$, and, for the parameters of the NRL modified betatron listed in Table II, the cyclotron resonances are shown in Fig. 3. It is apparent from this figure that as the beam energy increases, the beam centroid crosses progressively lower-integer number resonances.

In the general case, the expressions for the four characteristic modes $\omega_{\pm \pm}$ are very complicated. However, for modest beam and strong focusing winding currents, as those found in the NRL device, the modes are considerably simplified. Under these conditions, $\omega_{- +} \approx -\Omega_{\theta 0} / \gamma$, where m is the number of field periods. In addition, when $B_{\theta 0} \gg B_z$, the resonance condition takes the very simple form $B_{\theta 0} / B_z \approx l$, where $l = 1, 2, \dots$. Therefore the cyclotron resonance is due to the coupling, caused by a field error(s), of the cyclotron motions associated with the toroidal and vertical fields.

The physical mechanism of the cyclotron resonance can be easily understood with the help of Fig. 4. Consider an electron rotating in a uniform vertical field B_z in the presence of a toroidal field B_{θ} . When this electron is at its equilibrium position, its orbit is a circle, centered around the major axis, and the velocity vector is tangential to the circular or-

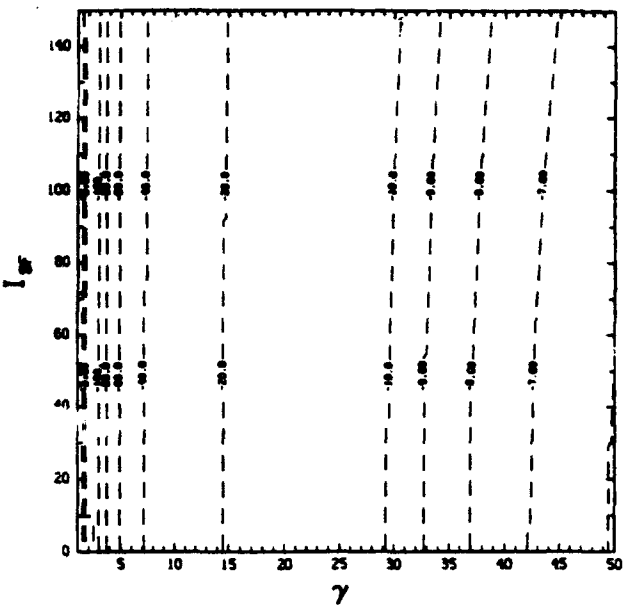


FIG. 3. Beam centroid integer cyclotron resonances for the parameters listed in Table II.

bit. Now, let us assume that a negative vertical field disturbance ΔB_z is introduced at a short segment of the orbit with toroidal half-width $\Delta \theta$. As the electron crosses the disturbance, it sees a reduced B_z and tries to acquire a larger radius. Thus, its velocity vector rotates clockwise and the electron develops a radial velocity component. As a result, the electron starts to rotate around B_{θ} and its orbit is transformed from a circle into a helix. When the resonance condition is satisfied, the electron will return to the disturbance on phase and it will acquire additional radial velocity and the radius of the helix will further increase.

The combined motion of the electron around B_z and B_{θ} is very similar to the motion of the Earth around the Sun and its axis. Fortunately, the time it takes the Earth to orbit the Sun (1 yr) over the time it takes the Earth to spin around its axis (1 day) is 365.242 199, i.e., is not an integer. By select-

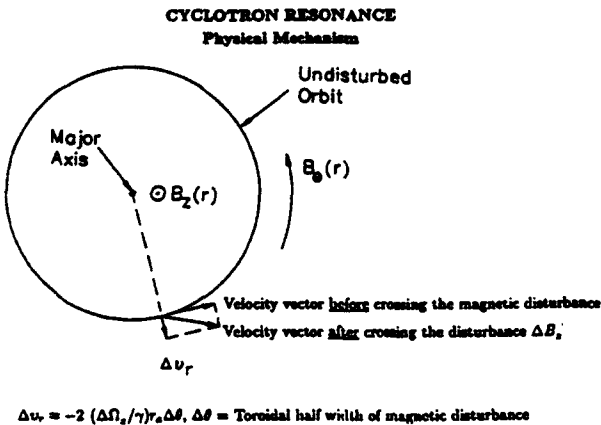


FIG. 4. Physical mechanism of the cyclotron resonance. The disturbance is located at approximately 5 o'clock at radius r_s .

TABLE II. Parameters used in the computation of cyclotron modes shown in Fig. 3.

Toroidal magnetic field B_{θ}	5 kG
Beam current	1 kA
Torus major radius	100 cm
Torus minor radius	15 cm
Beam minor radius	1 cm
S.F. field periods	6

ing the ratio year/day \neq integer, nature has avoided the excitation of a resonance from gravitational disturbances. As a consequence of this selection, the calendar had to be reformed three times (Caesar, Augustus, Pope Gregory XIII) over the last 2000 years. However, this is a rather small price to pay.

Since the initial observation of the cyclotron resonance in the NRL device, we have uncovered several field disturbances. By correcting these field deficiencies, a substantial increase in the beam lifetime has been observed with subsequent increase in the beam energy. One of the most important field errors was caused by the ports of the vacuum chamber. The ports disturb the flow pattern of the current induced by the rising B_z and create magnetic dipole-type field errors. The measured field errors from the ports and their Fourier modes are shown in Figs. 5(a) and 5(b), respectively. Figures 5(c) and 5(e) show the normalized transverse velocity components and 5(d) shows the normalized toroidal velocity as a function of time from the numerical solution of orbit equations. It is apparent that both transverse velocity components increase at the expense of the toroidal velocity as the beam crosses the $l = 10$ and 9 resonances.

It has been suggested that the beam loss in the modified betatron may be caused by the excitation of the cyclotron instability²⁰ instead of the cyclotron resonance. This instability results from the coupling of the cyclotron mode to the TE_{11p} modes of the toroidal chamber and is characterized by the resonance condition $[B_{\theta 0}/B_{z0} = (x_{||}^2 r_0^2/a^2 + p^2)^{1/2} - p\beta_{\theta}]$, where $x_{||} = 1.841$ and p is an integer. Figure 6 shows the cavity modes ω_{11p} and the cyclotron mode ω for several values of $\Omega_{\theta 0}/\Omega_{z0}$. The parameter

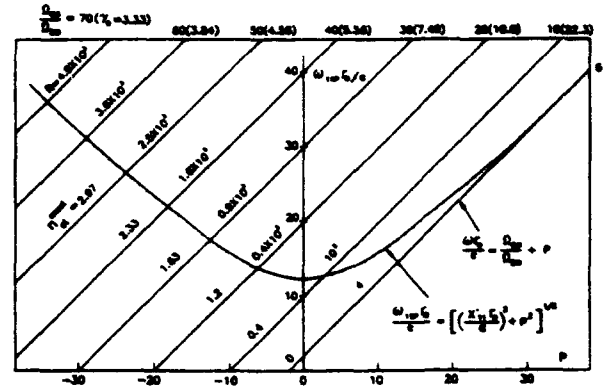


FIG. 6. TE_{11p} modes of the toroidal chamber and cyclotron mode. The cyclotron mode moves from left to right as the vertical magnetic field B_z rises while the toroidal magnetic field remains practically constant.

$R = -(r_0/c\Omega_{\theta 0})(d\omega/dt)/(d\Omega_{z0}/dt)$ is the normalized time rate of the cyclotron mode caused by the rising B_z field. The parameter n_{st}^{exact} is the exact stellarator field index.¹³ Strong interaction is expected when the cyclotron mode crosses the cavity modes near cutoff because both R and n_{st}^{exact} are small.

To determine the importance of the cyclotron instability, an attempt was made to measure both the poloidal B_{θ}^d and toroidal B_{ϕ}^d magnetic field components of the electromagnetic modes inside the toroidal chamber using a fast, broadband \vec{B} probe. The results of these measurements indicate that the peak of B_{θ}^d is less than 3×10^{-5} G near cutoff

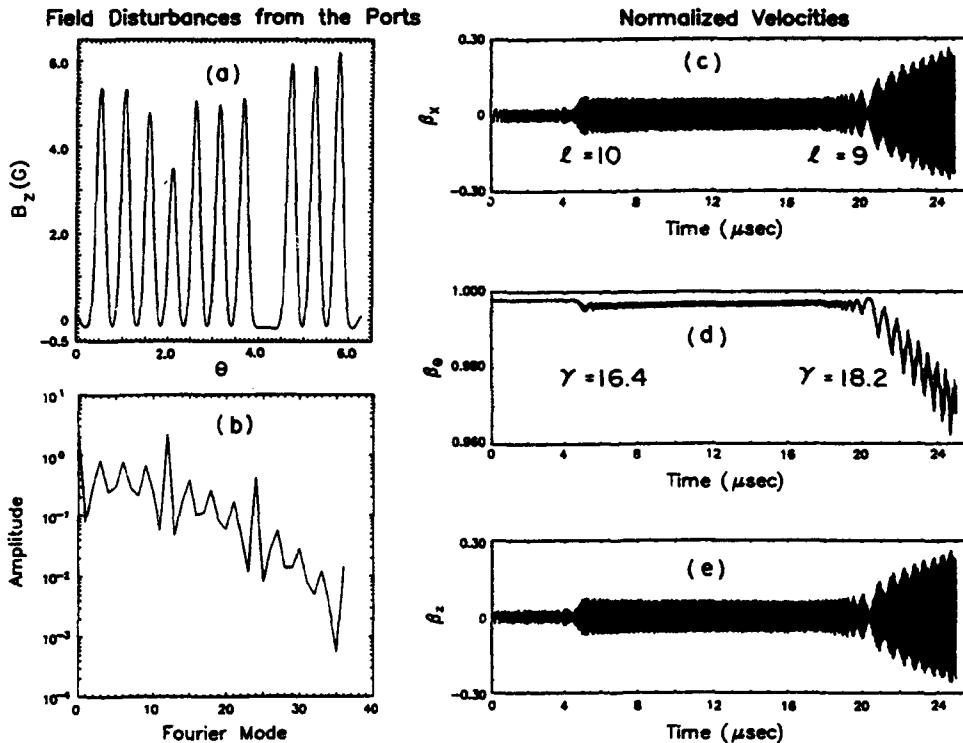
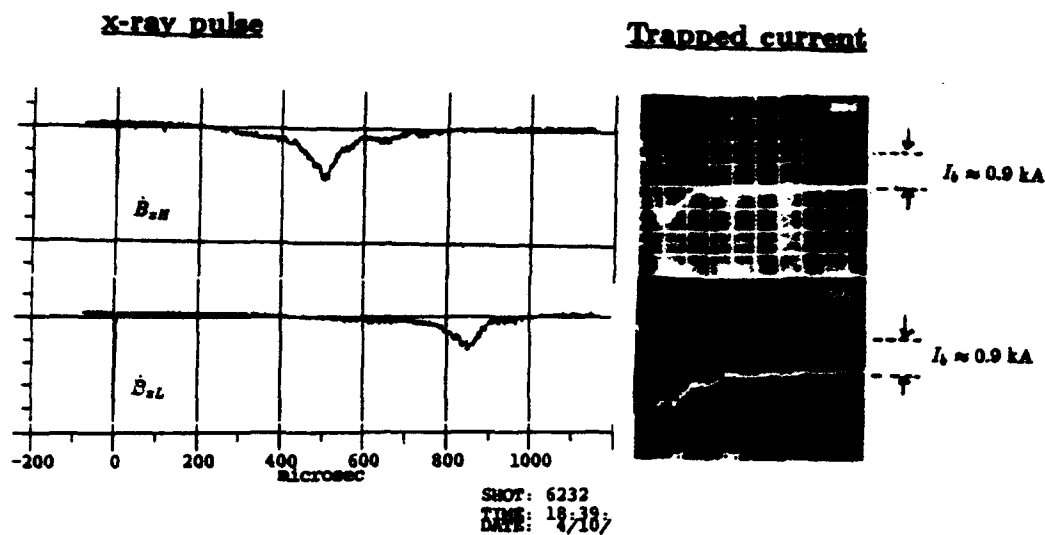


FIG. 5. Crossing of $l = 10$ and 9 cyclotron resonance during acceleration. (a) Measured field disturbances from the ports of the vacuum chamber, (b) Fourier modes of the disturbances, (c) and (e) normalized transverse velocity, and (d) normalized toroidal velocity versus time.



$$\left(\dot{B}_{zH} / \dot{B}_{zL} \right) = 1.82$$

$$B_{\theta 0} = 3.8 \text{ kG}$$

$$I_{SF} = 21 \text{ kA}$$

FIG. 7. Two x-ray signals taken under identical conditions except for the time rate of the vertical field \dot{B}_z . The electron ring lifetime varies approximately inverse proportionally to \dot{B}_z .

(580 MHz), i.e., the amplitude of the electromagnetic modes inside the torus is negligibly small. Since the B_{θ}^{el} required to excite the cyclotron instability is between 3–10 G, it is very unlikely that the beam loss is due to the cyclotron instability. In addition, the absence of electromagnetic modes with appreciable amplitude inside the toroidal cavity precludes the parametric instability²¹ as a serious beam loss mechanism.

The hypothesis that the beam loss is due to the cyclotron resonance is also supported by the fact that for a fixed toroidal magnetic field, the ring lifetime varies approximately inverse proportionally to the time rate of the vertical magnetic field dB_z/dt . Figure 7 shows the x-ray pulses for two shots with identical parameters, including the beam-trapped current, except for dB_z/dt . By reducing dB_z/dt by a factor of 1.82, the beam lifetime increased by approximately the same amount.

IV. EXISTING AND POTENTIAL APPLICATIONS OF ACCELERATORS

Table III lists selective existing and potential applications of accelerators. The first column shows the application, the second the dose or dose rate, and the third the desired average power. The required dose varies from a fraction of a Gy for radiation therapy to ~1 MGy for cracking of crude oil, i.e., it spans approximately seven orders of magnitude.

With the exception of the last application listed in Table III, the rest of them have already been discussed in the scientific literature.^{1,8,22}

The radiation-induced cross-linkage of polymers is probably the most important industrial application of accel-

erators today and is used extensively by several companies both in the U.S. and abroad. For example, the Cryovac Division of W. R. Grace utilizes in excess of 40 electron accelerators with an aggregate beam power in excess of 1 MW. The annual value of irradiated products is ~\$800 M. Raychem

TABLE III. Application of accelerators.

Application	Dose or dose rate	Desired average power ^a
(1) Radiation therapy	0.25–1.4 Gy/min	VL
(2) Sterilization		
Pharmaceuticals	20–30 kGy	H
Human transplants	10–20 kGy	L
Musical instruments	10 kGy	L
Potable water	1 kGy	H
(3) Radiative processing		
Sludge disinfection	4–10 kGy	H
Food preservation	1.0–25 kGy	H
Cellulose depolymerization	5–10 kGy	H
Graft copolymerization	10–20 kGy	H
Curing of coatings	20–50 kGy	M
Vulcanization of silicones	50–150 kGy	H
Cross-linkage of polymers	100–300 kGy	H
Vulcanization of rubber	100–300 kGy	H
Flue-gas clean up	20–30 kGy	H
Cracking of crude oil	1000 kGy	H
Radiography	10–100 Gy/min	M
Excavation of tunnels	100–200 kGy	VH
Burning of nuclear wastes		VH

^a VH > tens of MW, H = several hundred kW, M = 10–100 kW, L ~ kW, VL < kW.

Corporation utilizes more than 20 accelerators in the energy range 0.3–10 MeV. The annual value of the irradiated products is ~\$1000 M. Accelerators are also used extensively by Western Electric to irradiate telephone wires. However, the company is unwilling to release any information related to this activity.

Recently, accelerators have been utilized to induce curing of composites.²³ These fiber-reinforced polymers²⁴ are presently used in several applications, including aircraft frames and wings, automobile bodies and doors, rocket motor cases, oxygen tanks, printed circuits, and tennis rackets. Curing the composites with electron beams has two important advantages: (1) Curing time is reduced by almost two orders of magnitude (from 4 days to 2 h), and (2) thermal stresses are reduced and thus the quality of the product is substantially improved.

Aerospace has recently purchased two, 10 MeV, 20 kW accelerators from CGR to irradiate rocket motor cases at 5 Mrad.

The last application listed in Table III is presently under development at Los Alamos National Laboratory.²⁵ Briefly, it requires a 1.6 GeV, 25 mA proton beam that strikes a Pb-Bi target producing 55 neutrons per proton. The long half-life nuclear wastes are separated from those with short half-life and are irradiated by the neutron flux. Transmutation reduces the half-life of wastes. The higher atomic weight actinides form fissionable products that produce power in excess of that required to drive the accelerator. The contemplated radio-frequency quadrupole (RFQ) linear accelerator is 1/4 mile long, requires a 55 ft wide tunnel, and its cost has been estimated at \$500 M.

Substantial savings in the cost of the accelerator and the housing facility may result if high-current, compact accelerators could be used to generate the high-energy proton beam. The potential of high-current accelerator technology to this important application is presently under evaluation. Results will be reported in a future publication.

In conclusion, accelerators have several interesting industrial applications. However, the majority of these applications require low unit irradiation cost. High-current, compact accelerators have the potential to reduce the unit irradiation cost, and therefore their development is a step in the right direction.

ACKNOWLEDGMENTS

This research was supported by the Office of Naval Research (ONR) and the Space and Naval Warfare Systems

Command (SPAWAR).

- ¹ W. Scharf, in *Particle Accelerators and their Uses*, edited by F. T. Cole (Harwood Academic, London, 1986), p. 839.
- ² G. B. Lubkin (Editor), *Phys. Today* **36**(8), 17 (1983).
- ³ C. A. Kapetanakis, L. K. Len, T. Smith, J. Golden, K. Smith, S. J. Marsh, D. Dialetis, J. Mathew, P. Loschialpo, and J. H. Chang, *Phys. Rev. Lett.* **64**, 2374 (1990).
- ⁴ H. Ishizuka, R. Prohasko, A. Fisher, and N. Rostoker, in *Proceedings of the 7th International Conference on High-Power Particle Beams* (Kernforschungszentrum Karlsruhe GmbH, Karlsruhe, Germany, 1988), Vol. II, p. 857.
- ⁵ S. Humphries, Jr. and L. K. Len, in *Proceedings of 1987 IEEE Particle Accelerator Conference* (IEEE, New York, 1987), p. 914.
- ⁶ V. Bailey, L. Schlitt, M. Tiefenbank, S. Putnam, A. Mondelli, D. Chernin, and J. Petello, in *Proceedings of 1987 IEEE Particle Accelerator Conference* (IEEE, New York, 1987), p. 920.
- ⁷ W. K. Tucker, S. L. Shope, and D. E. Hasti, in *Proceedings of 1987 IEEE Particle Accelerator Conference* (IEEE, New York, 1987), p. 957.
- ⁸ M. R. Cleland (private communication).
- ⁹ P. Sprangle and C. A. Kapetanakis, *J. Appl. Phys.* **49**, 1 (1978).
- ¹⁰ C. A. Kapetanakis, P. Sprangle, D. P. Chernin, S. J. Marsh, and I. Haber, *Phys. Fluids* **26**, 1634 (1983).
- ¹¹ N. Rostoker, *Comments Plasma Phys.* **6**, 91 (1980).
- ¹² R. L. Gluckstern, in *Proceedings of Linear Accelerator Conference* (Brookhaven Laboratory, Upton, NY, 1979), p. 245.
- ¹³ C. Roberson, A. Mondelli, and D. Chernin, *Phys. Rev. Lett.* **50**, 507 (1983).
- ¹⁴ C. A. Kapetanakis, S. J. Marsh, and D. Dialetis, *Phys. Rev. Lett.* **61**, 86 (1988).
- ¹⁵ J. Golden, L. K. Len, A. V. Deniz, J. Mathew, T. J. Smith, P. Loschialpo, J. H. Chang, D. Dialetis, S. J. Marsh, and C. A. Kapetanakis, in *Ref. 4*, Vol. I, p. 221.
- ¹⁶ L. K. Len, T. Smith, J. Golden, K. Smith, S. J. Marsh, D. Dialetis, J. Mathew, P. Loschialpo, J. H. Chang, and C. A. Kapetanakis, *Proceedings of International Society for Optical Engineers (SPIE)* (SPIE, Bellingham, WA, 1990), Vol. 1226, p. 382.
- ¹⁷ P. Sprangle and C. A. Kapetanakis, *Part. Accel.* **18**, 203 (1986).
- ¹⁸ D. Chernin and P. Sprangle, *Part. Accel.* **12**, 101 (1982).
- ¹⁹ C. W. Roberson, A. Mondelli, and D. Chernin, *Part. Accel.* **17**, 79 (1985).
- ²⁰ P. Sprangle, J. Krall, C. M. Tang, and C. A. Kapetanakis, *Bull. Am. Phys. Soc.* **35**, 1005 (1990).
- ²¹ T. P. Hughes and B. B. Godfrey, *Phys. Fluids* **29**, 1698 (1986).
- ²² See National Technical Information Service Document No. DE84001632 (U.S. Department of Energy Report No. DOE/ER-0176, 1983). Copies may be obtained from the National Technical Information Service, Springfield, Virginia 22161. The price is \$23.00 plus a \$3.00 handling fee. All orders must be prepaid.
- ²³ J. Silverman (private communication).
- ²⁴ P. K. Mallick, *Fiber-Reinforced Composites* (Marcel Dekker, New York, 1988).
- ²⁵ C. D. Bowman (private communication).

Appendix X

Diffusion of Magnetic Fields in a Toroidal Conducting Shell of Circular Cross Section

Diffusion of magnetic fields in a toroidal conducting shell of circular cross section

D. Dialetis,^{a)} L. K. Len,^{b)} J. Golden,^{c)} and C. A. Kapetanakis
Plasma Physics Division Naval Research Laboratory, Washington, DC 20375

(Received 23 July 1990; accepted for publication 23 October 1990)

The diffusion of an external magnetic field through a toroidal conducting shell is studied under the assumption of a small aspect ratio. The external magnetic field can have an arbitrary field index and magnetic flux on the minor axis of the torus. The diffused field, field index, magnetic flux, and wall current are computed analytically and compared with the numerical results from the TRIDIF code. The analytical and numerical results are in good agreement.

Measurements in the toroidal chamber of the NRL modified betatron gave a delay time of 34 μsec , which is less than 10% from the theoretical prediction of 37 μsec .

I. INTRODUCTION

Over the years abundant analytical work has been done on the diffusion of the magnetic field in hollow circular cylindrical conductors of infinite length,¹⁻³ and has led to the understanding of the diffusion process in such a geometry. Much less attention has been given to the diffusion of fields in toroidal vessels. As a rule, the diffusion problem through toroidal chambers is more complex than through cylindrical conductors. The difficulty in toroidal geometry is due mainly to the application of the boundary conditions in the inner and outer surfaces of the torus. However, when the wall thickness of the torus becomes small in comparison to its minor radius, i.e., for a conducting shell, then the problem simplifies considerably. The toroidal shell approximation has been used to compute analytically the magnetic field of two toroidal segments, that carry known time-independent currents. In this paper, we have extended the work of P. Rolicz *et al.*⁴ to study the diffusion of fields through toroidal conducting shells.

The analytic results are further simplified under the additional assumption of a small aspect ratio toroidal conducting shell. To the lowest order on the aspect ratio, our work indicates that the diffusion of fields through a conducting shell of conductivity σ , major radius r_0 , minor radius a and thickness d_w , depend on three characteristic times τ_0 , τ_1 and τ_2 , where $\tau_1 = \mu_0 \sigma a d_w / 2$ (diffusion time), $\tau_0 = 2\tau_1 [\ln(8r_0/a) - 2]$ (L/R time), and $\tau_2 = \tau_1/2$. In contrast, the diffusion process in cylindrical shells depends on a single characteristic time (τ_1).

It is well known that there is a time lag between the magnetic field in the interior of the conducting shell and the externally applied magnetic field. This time lag can be easily measured in the laboratory and therefore is a useful physical quantity. When the transient phase of the diffusion process is over, the time lag becomes independent of time and is called

the delay time τ_d . For a linearly rising applied magnetic field the delay time for a cylindrical conducting shell is equal to τ_1 . On the other hand, in a toroidal conducting shell the delay time depends on both τ_0 and τ_1 and also on the flux condition, i.e., the ratio of the average field to the local field on the minor axis. Specifically $\tau_d = (\tau_0 + 3\tau_1)/2$ for the special case of a field that satisfies the betatron flux condition, i.e., when the value of the flux condition is equal to two.

In contrast to the field, the current flowing on the wall of the conducting shell depends only on τ_0 . Thus, by measuring experimentally the delay time of the fields and also the rise time of the wall current, all characteristic times can be determined.

The results of the analysis have been compared with the predictions of the two-dimensional finite difference numerical code TRIDIF.⁵ The agreement between theory and numerical computation is fairly good, in spite of the fact that the theory was done for a toroidal conducting shell, while in the numerical computation the torus had finite thickness. Specifically, the delay time predicted by the analysis is approximately 5% longer than the prediction of the code. Similarly, the temporal profile of the wall current from the analysis and the TRIDIF code agree to within a few percent. However, the temporal profile of the external field index and flux predicted by the theory and the code are in good agreement after a few delay times but not initially.

The delay time predicted by the theory and the code has been compared with the delay time measured in the toroidal chamber of the NRL modified betatron. For the parameters of the NRL device, the computed delay time is 37 μsec , while the measured delay time is 34 μsec . The less than 10% difference between the two delay times is probably within the uncertainty of the measurement.

In Sec. II, the theory is developed and a comparison is made with the numerical results obtained from the TRIDIF code. Section III contains a description of the NRL toroidal device and of the coils that generate the external magnetic field, and the measured quantities are compared with the theoretical results. Finally, in Sec. IV, the conclusions are presented.

^{a)} Science Applications International Corporation.

^{b)} FM Technologies, Inc.

^{c)} Berkeley Research Associates.

II. THEORY AND COMPARISON WITH NUMERICAL RESULTS

The diffusion fields are computed near the minor axis of the circular cross section, toroidal conducting shell. As shown in Fig. 1, the conductor has a major radius r_0 , a minor radius a , wall thickness d_w , where $d_w \ll a$, and conductivity σ . In the presence of an external magnetic field which is axisymmetric and time dependent, the diffused magnetic field inside the conductor is described by the diffusion equation

$$\nabla \times \nabla \times \mathbf{A} = -\mu_0 \sigma \frac{\partial \mathbf{A}}{\partial t}, \quad (1)$$

where the vector potential \mathbf{A} has only one nonzero component A_z that depends only on the cylindrical components (r, z) and on the time. The magnetic field components are given by

$$B_r = -\frac{\partial A_z}{\partial z}, \quad (2a)$$

$$B_z = \frac{1}{r} \frac{\partial r A_z}{\partial r}, \quad (2b)$$

while the electric field is equal to

$$E_z = -\frac{\partial A_z}{\partial t}. \quad (3)$$

Equation (1) is identical to Ampere's law combined with Ohm's law inside the conductor. In the special case, when the toroidal conductor is a shell, i.e., when $d_w \ll a$, this equation can be integrated and provides the first boundary condition, i.e.,

$$\mathbf{n} \times (\mathbf{B}^{\text{out}} - \mathbf{B}^{\text{in}}) = \mu_0 \sigma d_w \mathbf{E}^{\text{in}}, \quad (4)$$

where \mathbf{n} is the unit vector normal to the conducting wall and directed towards the region outside the conductor and μ_0 is the permeability of the vacuum. The second boundary condition is obtained from the requirement that the electric field is continuous across the boundary, i.e.,

$$\mathbf{E}^{\text{in}} = \mathbf{E}^{\text{out}}. \quad (5)$$

For a small aspect ratio a/r_0 vessel, it is appropriate to

use toroidal coordinates. The cylindrical coordinates (r, z) are related to the toroidal coordinates (η, ξ) by

$$r = b \frac{\sinh \eta}{\cosh \eta - \cos \xi}, \quad (6a)$$

$$z = b \frac{\sin \xi}{\cosh \eta - \cos \xi}, \quad (6b)$$

where b is a constant. These relations can be easily inverted, namely

$$e^{-2\eta} = \left(\frac{r_1}{r_2} \right)^2 = \frac{(r-b)^2 + z^2}{(r+b)^2 + z^2}, \quad (7a)$$

$$e^{-\eta} \cos \xi = \frac{1}{2} \left(1 - \frac{b}{r} \right) + \frac{1}{2} \left(1 + \frac{b}{r} \right) e^{-2\eta}. \quad (7b)$$

From Eq. (7a), we see that for fixed η , the coordinates (r, z) describe a circle whose radius is $b/\sinh \eta$. If for $\eta = \eta_0$ this circle coincides with the toroidal shell whose minor radius is a , then it is straightforward to show that $b = r_0 [1 - (a/r_0)^2]^{1/2}$. The points (η, ξ) outside the toroidal shell are determined by the inequality $\eta < \eta_0$, while the points inside the hollow region of the shell are determined by $\eta > \eta_0$. In both regions, the right-hand side of Eq. (1) is zero and, in toroidal coordinates, this equation reduces to

$$\frac{1}{h_\eta h_\xi h_\theta} \left[\frac{\partial}{\partial \eta} \left(\frac{h_\xi h_\theta}{h_\eta} \frac{\partial A_\theta}{\partial \eta} \right) + \frac{\partial}{\partial \xi} \left(\frac{h_\theta h_\eta}{h_\xi} \frac{\partial A_\theta}{\partial \xi} \right) \right] - \frac{1}{h_\theta^2} A_\theta = 0, \quad (8)$$

where

$$h_\eta = h_\xi = \frac{b}{\cosh \eta - \cos \xi}, \quad (9a)$$

$$h_\theta = \frac{b \sinh \eta}{\cosh \eta - \cos \xi}. \quad (9b)$$

If we set $A_\theta = b(\cosh \eta - \cos \xi)^{1/2} F(\eta, \xi)$, then the differential equation satisfied by $F(\eta, \xi)$ is a separable equation and its solution can be expressed in terms of the toroidal functions. Specifically, the solutions of Eq. (8) in the two regions inside and outside the toroidal shell are

$$A_\theta^{\text{in}} = b(\cosh \eta - \cos \xi)^{1/2} \sum_{m=0}^{\infty} \epsilon_m a_m(t) \times Q_{m-1/2}^1(\cosh \eta) \cos m\xi, \quad (10a)$$

$$A_\theta^{\text{out}} = A_\theta^{\text{ext}} + b(\cosh \eta - \cos \xi)^{1/2} \sum_{m=0}^{\infty} \epsilon_m b_m(t) \times P_{m-1/2}^1(\cosh \eta) \cos m\xi, \quad (10b)$$

where $\epsilon_0 = 1$, $\epsilon_m = 2$ when $m = 1, 2, 3, \dots$, $P_{m-1/2}^1(\cosh \eta)$, $Q_{m-1/2}^1(\cosh \eta)$ are the associated Legendre functions of the first and second kind, respectively, and $A_\theta^{\text{ext}}(\eta, \xi, t)$ is the vector potential associated with the applied external field. The time-dependent parameters $a_m(t)$ and $b_m(t)$ are determined from the boundary conditions. Since the ξ component of the magnetic field is equal to

$$B_\xi = -\frac{1}{h_\eta h_\theta} \frac{\partial}{\partial \eta} h_\theta A_\theta, \quad (11)$$

and the external field is zero at $t = 0$, the boundary condi-

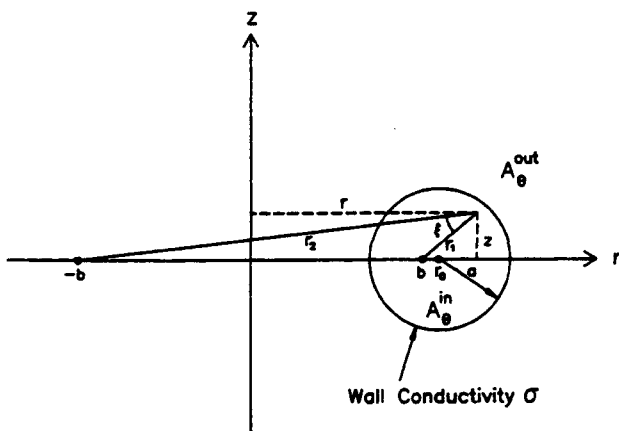


FIG. 1. Toroidal shell and coordinate systems used in the analysis.

tions of Eqs. (4) and (5), expressed in terms of the vector potential A_m , become

$$A_m^{\text{out}}(\eta_0, \xi, t) = A_m^{\text{out}}(\eta_0, \xi, t), \quad (12a)$$

$$\begin{aligned} & (\cosh \eta_0 - \cos \xi)^{3/2} \frac{\partial}{\partial \eta} \\ & \times \left(\frac{A_m^{\text{out}}(\eta, \xi, t) - A_m^{\text{in}}(\eta, \xi, t)}{(\cosh \eta - \cos \xi)^{1/2}} \right) \Big|_{\eta = \eta_0} \\ & = -\tau \frac{\partial A_m^{\text{in}}(\eta_0, \xi, t)}{\partial t} \end{aligned} \quad (12b)$$

where $\tau = \mu_0 \sigma d_m b$.

In the following, we shall assume that there are no external current coils very near the toroidal conductor or inside it. If η_c is the toroidal coordinate of the coil nearest to the minor axis, and such that $\eta_c < \eta_0$, then the external vector potential A_m^{ext} is given by

$$\begin{aligned} A_m^{\text{ext}} &= b(\cosh \eta - \cos \xi)^{1/2} \sum_{m=0}^{\infty} \epsilon_m a_m^{\text{ext}}(t) \\ & \times Q_{m-1/2}^1(\cosh \eta) \cos m\xi, \end{aligned} \quad (13)$$

for all $\eta > \eta_c$. The time-dependent parameters $a_m^{\text{ext}}(t)$ are known and are associated with physical properties of the external field, such as external field index, flux condition, etc.

Now, it is straightforward to compute the unknown coefficients a_m, b_m from the boundary conditions. From Eq. (12a) we obtain

$$b_m = \frac{(a_m - a_m^{\text{ext}}) Q_{m-1/2}^1(\cosh \eta_0)}{P_{m-1/2}^1(\cosh \eta_0)}. \quad (14)$$

Similarly, Eq. (12b) together with Eq. (14) and the identity⁶

$$\begin{aligned} & Q_{m-1/2}^1(u) \frac{dP_{m-1/2}^1(u)}{du} - P_{m-1/2}^1(u) \\ & \times \frac{dQ_{m-1/2}^1(u)}{du} = -\frac{4m^2 - 1}{4(u^2 - 1)}, \end{aligned} \quad (15)$$

leads to the following set of coupled differential equations for a_m

$$\begin{aligned} \dot{a}_0 &= -\frac{1}{\tau_0} (a_0 - a_0^{\text{ext}}) + \frac{1}{\tau_1} \frac{1}{\cosh \eta_0} \\ & \times \frac{Q_{1/2}^1(\cosh \eta_0)}{Q_{-1/2}^1(\cosh \eta_0)} (a_1 - a_1^{\text{ext}}), \end{aligned} \quad (16a)$$

$$\begin{aligned} \dot{a}_m &= -\frac{1}{\tau_m} (a_m - a_m^{\text{ext}}) + \frac{1}{\tau_{m-1}} \frac{1}{2 \cosh \eta_0} \\ & \times \frac{Q_{m-3/2}^1(\cosh \eta_0)}{Q_{m-1/2}^1(\cosh \eta_0)} (a_{m-1} - a_{m-1}^{\text{ext}}) + \frac{1}{\tau_{m+1}} \\ & \times \frac{1}{2 \cosh \eta_0} \frac{Q_{m+1/2}^1(\cosh \eta_0)}{Q_{m-1/2}^1(\cosh \eta_0)} (a_{m+1} - a_{m+1}^{\text{ext}}), \end{aligned} \quad (16b)$$

where $m = 1, 2, 3, \dots$ and

$$\tau_m = -\frac{4\tau \tanh \eta_0}{4m^2 - 1} Q_{m-1/2}^1(\cosh \eta_0) P_{m-1/2}^1(\cosh \eta_0). \quad (17)$$

The toroidal functions $P_{m-1/2}^n$ and $Q_{m-1/2}^n$ appearing in Eqs. (16a), (16b) and (17) are given by the following exact expressions⁶

$$\begin{aligned} P_{m-1/2}^n(\cosh \eta) &= \frac{2^n \Gamma(m)}{\pi^{1/2} \Gamma(m - n + \frac{1}{2})} (\sinh \eta)^n e^{(m-n-1/2)\eta} \times (1 - \delta_{m0}) \sum_{s=0}^{m-1} \frac{(n + \frac{1}{2})_s (n - m + \frac{1}{2})_s}{s!(1-m)_s} e^{-2s\eta} \\ &+ \frac{(-1)^n 2^{n+1} \Gamma(m + n + \frac{1}{2})}{\pi^{3/2} \Gamma(m + 1)} (\sinh \eta)^n e^{-(m+n+1/2)\eta} \sum_{s=0}^{\infty} \frac{(n + \frac{1}{2})_s (m + n + \frac{1}{2})_s}{s!(m+1)_s} e^{-2s\eta} \\ &\times [\ln(4e^\eta) + u_s + u_{m+s} - v_{n+s} - v_{m+n+s}], \end{aligned} \quad (18a)$$

$$Q_{m-1/2}^n(\cosh \eta) = \frac{(-1)^n 2^n \Gamma(m + n + \frac{1}{2}) \pi^{1/2}}{\Gamma(m + 1)} (\sinh \eta)^n e^{-(m+n+1/2)\eta} \times \sum_{s=0}^{\infty} \frac{(n + \frac{1}{2})_s (m + n + \frac{1}{2})_s}{s!(m+1)_s} e^{-2s\eta}, \quad (18b)$$

where

$$(a)_s = a(a+1)(a+2)\dots(a+s-1), \quad (a)_0 = 1, \quad (19a)$$

$$u_n = \frac{1}{2} \sum_{k=1}^n \frac{1}{k}, \quad u_0 = 0, \quad (19b)$$

$$v_n = \sum_{k=1}^n \frac{1}{2k-1}, \quad v_0 = 0. \quad (19c)$$

For $m = 0$, the first term in Eq. (18a) is omitted, since $\delta_{mnn} = 1$ for $m = n$, and $\delta_{mnn} = 0$ for $m \neq n$. The expressions above are appropriate for the region inside the toroidal conductor, i.e., for $\eta > \eta_0$, as well as on its surface.

Up to this point the results are exact. For small aspect ratio a/r_0 , $e^{-\eta} = (r_0 + a - b)/(r_0 + a + b) \approx a/2r_0 \ll 1$. Thus, to the lowest order in the aspect ratio, Eq. (17) becomes

$$\tau_0 = 2\tau_D \left(\ln \frac{8r_0}{a} - 2 \right), \quad (20a)$$

$$\tau_m = \frac{\tau_D}{m}, \quad (20b)$$

where $m = 1, 2, 3, \dots$, and

$$\tau_D = \frac{\mu_0 \sigma d_w a}{2}. \quad (21)$$

The time τ_0 is the L/R time of the toroidal conductor, while τ_m are the higher order diffusion times.

An approximate expression for A_θ^m can be obtained from Eq. (10a) by keeping terms up to order $e^{-2\eta}$, i.e., up to second order toroidal corrections. Making use of the identity⁹

$$(\cosh \eta - \cos \xi)^{1/2} = \sum_{m=0}^{\infty} \epsilon_m C_m(\eta) \cos m\xi, \quad (22)$$

where

$$C_0(\eta) = \frac{\sqrt{2}}{2\pi} e^\eta (1 + e^{-2\eta}) \times \left(Q_{-1/2}(\cosh \eta) - \frac{2e^{-\eta}}{1 + e^{-2\eta}} Q_{1/2}(\cosh \eta) \right), \quad (23a)$$

$$C_m(\eta) = \frac{\sqrt{2}}{2\pi} e^\eta (1 + e^{-2\eta}) \times \left(Q_{m-1/2}(\cosh \eta) - \frac{e^{-\eta}}{1 + e^{-2\eta}} \times [Q_{m-3/2}(\cosh \eta) + Q_{m+1/2}(\cosh \eta)] \right), \quad (23b)$$

and also of Eq. (18b), a lengthy calculation leads to the approximate expression

$$A_\theta^m \approx -\frac{\pi}{2\sqrt{2}} b \left[a_0 + \frac{3}{2} (a_0 - a_1) e^{-2\eta} - (a_0 - 3a_1) e^{-\eta} \cos \xi - \frac{1}{4} \times (a_0 + 6a_1 - 15a_2) e^{-2\eta} \cos 2\xi \right]. \quad (24)$$

Using Eqs. (7a), (7b) and keeping terms up to order $(1 - b/r)^2$ and $(z/r)^2$, Eq. (24) reduces to

$$A_\theta^m \approx -\frac{\pi}{2\sqrt{2}} b \left[a_0 - \frac{1}{2} (a_0 - 3a_1) \left(1 - \frac{b}{r} \right) + \frac{1}{16} (a_0 + 15a_2) \left(1 - \frac{b}{r} \right)^2 + \frac{3}{16} (a_0 + 4a_1 - 5a_2) \left(\frac{z}{r} \right)^2 \right], \quad (25)$$

i.e., the approximate A_θ^m has been expressed in terms of the

cylindrical coordinates (r, z) . The magnetic field components near the minor axis are determined from Eqs. (2a) and (2b) and are equal to

$$B_r^m \approx -B_{z0} n_D \frac{z}{r}, \quad (26a)$$

$$B_z^m \approx B_{z0} \left[1 - n_D \left(1 - \frac{b}{r} \right) \right], \quad (26b)$$

where

$$B_{z0} = -\frac{\pi}{4\sqrt{2}} (a_0 + 3a_1), \quad (27a)$$

is the vertical field component near the minor axis and

$$n_D = \frac{3}{4} \frac{a_0 + 4a_1 - 5a_2}{a_0 + 3a_1}, \quad (27b)$$

is the field index. To first order in a/r_0 , the magnetic flux Φ_0 through the area πr_0^2 on the midplane is

$$\Phi_0 = 2\pi r_0 A_\theta^m(r_0, 0, t) \approx -2\pi r_0^2 \frac{\pi}{2\sqrt{2}} a_0 \quad (28)$$

Defining ϵ_D by means of the relation $\Phi_0 \equiv 2\pi r_0^2 B_{z0} (1 - \epsilon_D)$, the vertical component of the field on the minor axis can be written

$$B_{z0} (1 - \epsilon_D) = -\frac{\pi}{2\sqrt{2}} a_0. \quad (29)$$

The parameter ϵ_D is a measure of the flux condition. When $\epsilon_D = 0$, the betatron flux condition is satisfied.

The quantities a_0, a_1, a_2 are determined completely by the magnetic field, the field index and the flux on the minor axis, and, therefore, are parametric representations of these physical quantities. But the vector potential that describes the external field in Eq. (13) has exactly the same form as A_θ^m in Eq. (10a). Therefore, if B_0, n , and Φ_0^{ext} are the external field, external field index, and external flux on the minor axis, then $a_0^{\text{ext}}, a_1^{\text{ext}}$ and a_2^{ext} can be expressed as follows.

$$a_0^{\text{ext}} = -\frac{2\sqrt{2}}{\pi} B_0 (1 - \epsilon), \quad (30a)$$

$$a_1^{\text{ext}} = -\frac{2\sqrt{2}}{3\pi} B_0 (1 + \epsilon), \quad (30b)$$

$$a_2^{\text{ext}} = -\frac{2\sqrt{2}}{15\pi} B_0 (7 - 8n + \epsilon), \quad (30c)$$

where ϵ is defined now by the relation $\Phi_0^{\text{ext}} = 2\pi r_0^2 B_0 (1 - \epsilon)$.

These expressions are used in solving Eqs. (16a), (16b). It is assumed that only B_0 is time dependent. This is a valid assumption provided that the coils that generate the external field carry the same current and are filaments, i.e., there is no diffusion process associated with them.

All the physical quantities of interest have been computed to first order in toroidal corrections. Therefore, it is sufficient to compute the parameters a_0 , a_1 , a_2 to first order in a/r_0 . If all terms of order $e^{-2\eta_0}$ or higher are omitted, Eqs. (16a), (16b) become

$$\dot{a}_0 \approx -\frac{1}{\tau_0} (a_0 - a_0^{\text{ext}}), \quad (31a)$$

$$\dot{a}_m \approx -\frac{1}{\tau_m} (a_m - a_m^{\text{ext}}) + \frac{1}{\tau_{m-1}} \frac{2m}{2m+1} (a_{m-1} - a_{m-1}^{\text{ext}}), \quad (31b)$$

where $m = 1, 2$. This system of equations can be integrated

$$n_D = \frac{\left(\frac{3}{8} + \frac{\alpha}{2-\alpha}\right) (1-\epsilon) A_0 + \left[n - \left(\frac{3}{8} + \frac{\alpha}{2-\alpha}\right) (1-\epsilon)\right] A_2}{\left(\frac{1}{2} + \frac{\alpha}{1-\alpha}\right) (1-\epsilon) A_0 + \left[1 - \left(\frac{1}{2} + \frac{\alpha}{1-\alpha}\right) (1-\epsilon)\right] A_1}. \quad (34b)$$

Another interesting physical quantity is the surface wall current density, which is given by

$$J_{\phi} = -\sigma d_w \frac{\partial A_w^m(\eta_0, \xi, t)}{\partial t}. \quad (35)$$

To first order in toroidal corrections, Eqs. (25), (31a), (31b), (32a), and (32b) give

$$J_{\phi} \approx \frac{2r_0}{\mu_0 a} \left\{ \alpha (1-\epsilon) (A_0 - B_0) - \left[\left(4 + \alpha - \frac{2\alpha}{1-\alpha}\right) (1-\epsilon) (A_0 - B_0) - \left(1 + \epsilon - \frac{2\alpha}{1-\alpha} (1-\epsilon)\right) (A_1 - B_0) \right] \frac{a}{r_0} \cos \phi \right\}, \quad (36)$$

where $\cos \phi = (r - r_0)/a$ and r is the radial position of any point on the wall chamber. The wall current is equal to

$$I = \int_0^{2\pi} J_{\phi} a d\phi = \frac{4\pi r_0}{\mu_0} \alpha (1-\epsilon) (A_0 - B_0). \quad (37)$$

As a first application, consider a rising external magnetic field that reaches a constant value, i.e.,

easily. Under the initial conditions $a_m(0) = 0$, the solutions for $\tau_2 = \tau_1/2$ are

$$a_0 = -\frac{2\sqrt{2}}{\pi} (1-\epsilon) A_0, \quad (32a)$$

$$a_1 = -\frac{2\sqrt{2}}{3\pi} \left[\left(1 + \epsilon - \frac{2\alpha}{1-\alpha} (1-\epsilon)\right) A_1 + \frac{2\alpha}{1-\alpha} (1-\epsilon) A_0 \right], \quad (32b)$$

$$a_2 = -\frac{2\sqrt{2}}{15\pi} \left[\left(7 - 8n + \epsilon - 4(1+\epsilon) + \frac{8\alpha}{2-\alpha} \times (1-\epsilon)\right) A_2 + \left(4(1+\epsilon) - \frac{8\alpha}{1-\alpha} (1-\epsilon)\right) A_1 + \frac{8\alpha}{(1-\alpha)(2-\alpha)} (1-\epsilon) A_0 \right], \quad (32c)$$

where

$$\alpha = \frac{\tau_1}{\tau_0}, \quad (33a)$$

and

$$A_m = \frac{1}{\tau_m} e^{-t/\tau_m} \int_0^t e^{t'/\tau_m} B_0(t') dt'. \quad (33b)$$

Substitution of a_0 , a_1 , a_2 into Eqs. (27a), (27b) leads to

$$B_{\phi} = \left(\frac{1}{2} + \frac{\alpha}{1-\alpha}\right) (1-\epsilon) A_0 + \left[1 - \left(\frac{1}{2} + \frac{\alpha}{1-\alpha}\right) (1-\epsilon)\right] A_1, \quad (34a)$$

$$B_0(t) = \hat{b}_0 (1 - e^{-t/\tau_{\text{ext}}}). \quad (38)$$

From Eq. (33b), we have:

$$A_m = \hat{b}_0 \left[1 - \frac{1}{1 - \frac{\tau_m}{\tau_{\text{ext}}}} e^{-t/\tau_{\text{ext}}} + \frac{\tau_m/\tau_{\text{ext}}}{1 - \frac{\tau_m}{\tau_{\text{ext}}}} e^{-t/\tau_m} \right]. \quad (39)$$

For $t \gg \tau_{\text{ext}}$ and $t \gg \tau_m$, the coefficient $A_m \approx \hat{b}_0$ and from Eqs.

(34a), (34b), $B_{z0} \approx \hat{b}_0$ and $n_D \approx n$. Also the wall current goes to zero. All three conclusions are as expected.

For a sinusoidally varying field

$$B_0(t) = \hat{b}_0 \sin \omega t, \quad (40)$$

the coefficients A_m are given by

$$A_m = \frac{\hat{b}_0}{1 + (\omega\tau_m)^2} [\sin \omega t - \omega\tau_m \cos \omega t + \omega\tau_m e^{-t/\tau_m}] \quad (41)$$

After a long time, i.e., for $t \gg \tau_m$, the external field and the field on the minor axis are not in phase, but their phase difference remains constant. On the other hand, for small times, i.e., for $\omega t \ll 1$ and $t \ll \tau_m$, the coefficients $A_m \approx \hat{b}_0 \omega t^2 / 2\tau_m$ and the field index becomes

$$n_D(t=0) = \frac{16n - (5\alpha + 6)(1 - \epsilon)}{4[2 - (1 + \alpha)(1 - \epsilon)]}. \quad (42)$$

Furthermore, assuming that $\omega\tau_m \ll 1$ and $\omega t \ll 1$, but not $t \gg \tau_m$, we obtain

$$A_m \approx \hat{b}_0 \omega [t - \tau_m(1 - e^{-t/\tau_m})], \quad (43)$$

and

$$B_{z0} \approx \hat{b}_0 \left[t - \tau_d + \frac{\tau_d - \tau_1}{\tau_0 - \tau_1} \tau_0 e^{-t/\tau_0} - \frac{\tau_d - \tau_0}{\tau_0 - \tau_1} \tau_1 e^{-t/\tau_1} \right], \quad (44)$$

where the delay time τ_d is equal to

$$\tau_d = \frac{(1 - \epsilon)\tau_0 + (3 - \epsilon)\tau_1}{2}. \quad (45)$$

In contrast, the delay time for a cylinder of infinite length is equal to the diffusion time. It is apparent from Eq. (45) that in the case of the toroidal conducting shell, the delay time depends linearly on both the L/R time τ_0 and the diffusion time τ_1 . In addition, for a toroidal shell, B_{z0} has an exponentially decreasing dependence on both times τ_0 and τ_1 , while the wall current, from Eq. (37), depends only upon τ_0 , i.e.,

$$I = -\frac{4\pi r_0}{\mu_0} \omega \tau_1 \hat{b}_0 (1 - \epsilon)(1 - e^{-t/\tau_0}), \quad (46)$$

i.e., it reaches exponentially its maximum value with the L/R time τ_0 .

A direct comparison has been made between the theory presented above and the numerical results from the two-dimensional TRIDIF code. The set of parameters used for the comparison are listed in Table I. For these parameters, Eqs. (20a), (20b), (45), give $\tau_0 = 11.28 \mu\text{sec}$, $\tau_1 = 2.95 \mu\text{sec}$, $\alpha = 0.26$, and $\tau_d = 10.42 \mu\text{sec}$. The solid curves in Figs. 2(a)–2(d) show B_{z0} , n_D , $\Phi_0/(\pi r_0^2 B_{z0})$, and I as a function of time. In the computer run, the inner minor radius of the toroidal conductor is 15 cm and the outer minor radius is 17 cm. In the region of the chamber, the mesh has a cell size $\Delta r = 0.5 \text{ cm}$, $\Delta z = 1.0 \text{ cm}$, but further out it is much less dense. Thus, in the radial direction there are 157 mesh points over a distance of 300 cm, while in the vertical direction there are 71 mesh points over a distance of 200 cm, and the time step used is $\Delta t = 0.5 \mu\text{sec}$. Advantage is taken of the midplane symmetry, i.e., the calculation is confined to the region $z > 0$. The external field is generated by current filaments (coils) located at the same positions as in the modified betatron experiment. All the coils carry the same current and have the same sinusoidal dependence. In the absence of the toroidal chamber the maximum vertical field generated by these coils on the minor axis, i.e., at $r = 100 \text{ cm}$, $z = 0$, is $B_0 = 1267 \text{ Gauss}$, when the maximum current through the coils is 40 kA. This is the value of \hat{b}_0 used in the theory. In the absence of the toroidal chamber, these coils generate a field index of 0.54 on the minor axis and an $\epsilon = -0.067$, but the values chosen in the theory are slightly different, so that at times $t > 30 \mu\text{sec}$ the theoretical and numerical n_D and $\Phi_0/(\pi r_0^2 B_{z0})$ are identical.

The dashed curves in Figs. 2(a)–2(d) give the predictions of the code for B_{z0} , n_D , $\Phi_0/(\pi r_0^2 B_{z0})$ and I as a function of time. The straight line in Fig. 2(a) is B_{z0} , when $\sigma = 0$. The numerical delay time, obtained from Fig. (2a), is $9.7 \mu\text{sec}$ as compared to the theoretical value of $10.42 \mu\text{sec}$. The small difference is attributed to the fact that τ_0 and τ_1 depend on the volume of the numerical integration. It should be noticed that in the numerical calculation the integration has been carried inside a cylinder of radius 300 cm and of half-height 200 cm, while in the theoretical work the integration has been carried out over the whole space. To obtain some insight into this effect, let us look at the diffusion through a cylindrical conducting shell of infinite length, where the region of the numerical integration is limited within a perfect conductor located at a radius r_1 . The diffusion time is equal to $\tau_D [1 - (a/r_1)^2]$, where a is the radius of the conductor and τ_D is given by Eq. (21). It is apparent that the diffusion time decreases as the volume of the integration region decreases, and, therefore, the inductance of the system decreases. As another example consider a toroidal conducting shell, with a region of integration confined within a perfect conductor located at $\eta = \eta_1$ and therefore the radial positions r are limited to the values between $r_{1 \min} = b \tanh(\eta_1/2)$ and $r_{1 \max} = b \coth(\eta_1/2)$. All the theoretical results obtained above remain the same except for the L/R time in Eq. (20a) that is replaced by $2\tau_D [\ln 8r_0/a - 2 - (\pi r_0/2r_{1 \max})^2]$. Again, the L/R time (but not the times τ_1 , τ_2) decreases as the volume of the integration region decreases and so does τ_d . In the example given above the region for $r < r_{1 \min}$ is excluded, while in the

TABLE I. Parameters for the diffusion theory.

Torus major radius, r_0 (cm)	100
Torus minor radius, a (cm)	16
Chamber wall thickness, d_w (cm)	2
Torus wall conductivity, σ (mho/cm)	14.666
Amplitude of sinusoidal external magnetic field, b_0 (Gauss)	1267
Period of external magnetic field, T (μsec)	10^4
Field index of external magnetic field, n	0.53
Flux condition parameter of external magnetic field, ϵ	-0.05

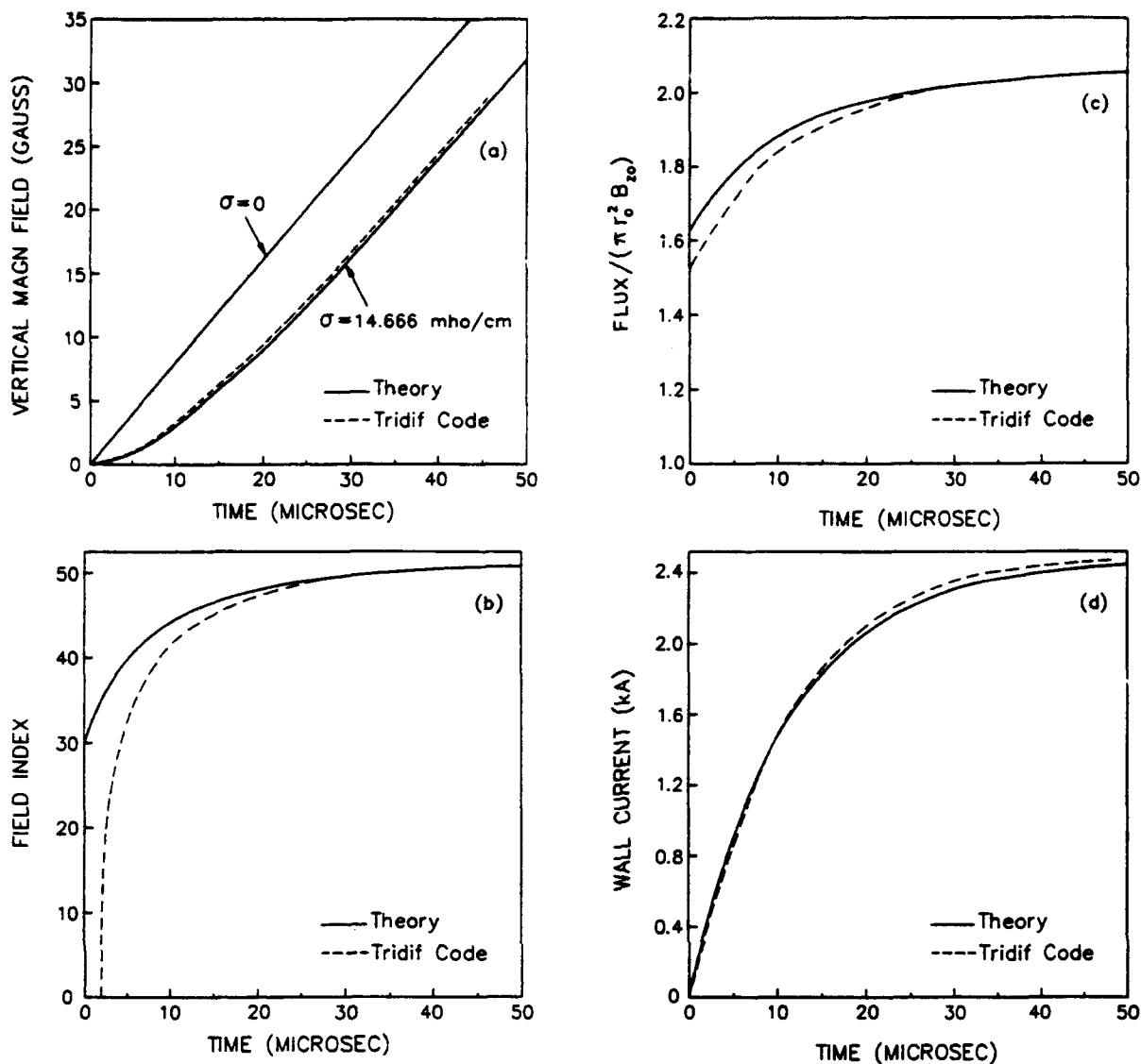


FIG. 2. Temporal profiles from analysis (solid line) and computer code (dashed line). (a) vertical (betatron) field, (b) field index, (c) flux condition, and (d) wall current.

numerical results this region is included. For this reason, the comparison of the numerical results is made with the theoretical results for the whole space rather than a finite region of integration. The largest discrepancy between theory and numerical computation is in the field index for small times. This could be due to the large time step ($0.5 \mu\text{sec}$) that was used in the numerical integration or to the fact that the field index is computed from the second derivative of the stream function rA_θ and this function is not accurately computed initially by the code. The same argument is applicable to the smaller discrepancy, for short times, in the quantity $\Phi_0/(\pi r_0^2 B_{z0})$. Over all, however, the agreement is fairly good between theory and numerical computation with the TRIDIF code.

III. EXPERIMENTAL RESULTS

This section briefly summarizes the measurements on the time delay of the vertical magnetic field caused by the

vacuum chamber of the device and compares the experimental results with the predictions of the theory and that of the computer code.

The NRL modified betatron comprises three different external magnetic fields: the betatron field that is a function of time and is responsible for the acceleration of the electrons, the toroidal magnetic field that varies only slightly during the acceleration of the electron ring and the strong focusing field that also has a very weak time dependence. These three fields have been described previously. However, for completeness we briefly describe in this paper the vertical field and the vacuum chamber.

The betatron magnetic field controls mainly the major radius of the gyrating electron ring and is produced by a set of 18 air core (see Fig. 3), circular coils connected in series. Sixteen main coils and four trimmers are used to generate a field configuration with a flux condition equal to 1.92. Their total inductance is approximately $343 \mu\text{H}$. The coils are powered by an 8.64 mF capacitor bank that can be charged

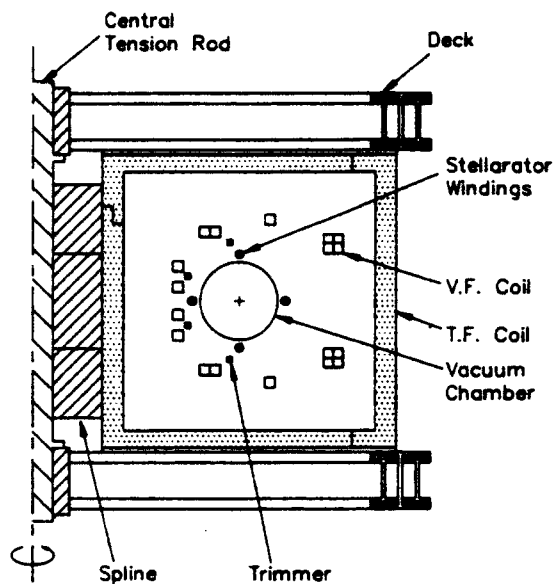


FIG. 3. Elevation of the experiment.

up to 17 kV. At full charge, the bank delivers to the coils a peak current of about 45 kA. The current flowing through the coils produces a sinusoidally varying field having a quarter period of 2.6 msec and its amplitude on the minor axis at peak charging voltage is 2.1 kG. Immediately after the peak the field is crowbarred with a 4.5 msec decay time. The temporal profile of the vertical field is shown in Fig. 4.

The flux condition and field index are adjusted by two sets of trimmers that are connected in parallel to the main coils. The current through the trimmers is adjusted with series inductors. Typically 10–15% of the total current flows through the trimmers.

The 100 cm major radius, 15.2 cm inside minor radius vacuum chamber has been constructed using epoxy reinforced carbon fibers. The desired conductivity is obtained by embedding a phosphor bronze screen in the outer layer of the graphite as shown in Fig. 5. The graphite is 2.5 mm thick and

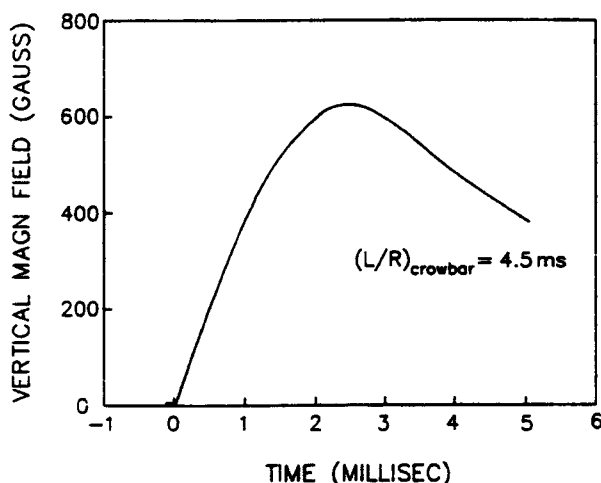


FIG. 4. Vertical (betatron) field vs time.

VACUUM CHAMBER WALL COMPOSITION

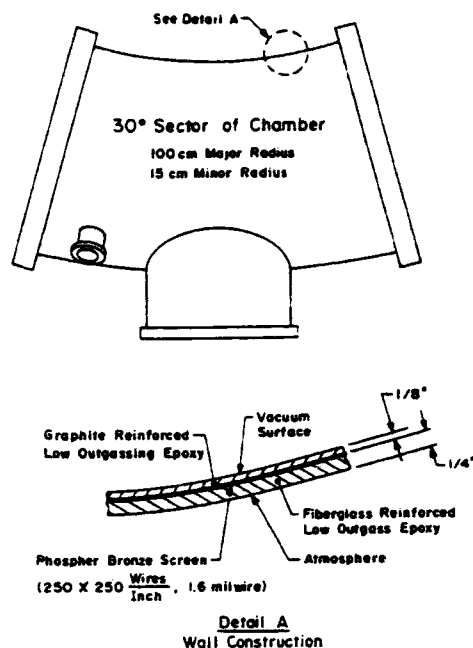


FIG. 5. 30° sector of the vacuum chamber and details of wall construction.

has a surface resistivity of 26.6 mΩ on a square. The screen has 250×250 wires per inch and is made of 40-μm-diam wire with an equivalent surface resistivity of 12.8 mΩ on a square. The calculated resistance for the entire vacuum chamber is 57 mΩ. The measured D.C. resistance of the toroidal vacuum vessel is 68 ± 2 mΩ. The outside surface of the chamber is covered with a 6.3-mm-thick, epoxy reinforced fiberglass layer. Figure 6 is a photograph of the vacuum chamber.

This novel construction technique has several attractive features, including controllable resistivity and thus magnetic field penetration time, high stiffness and tensile strength,

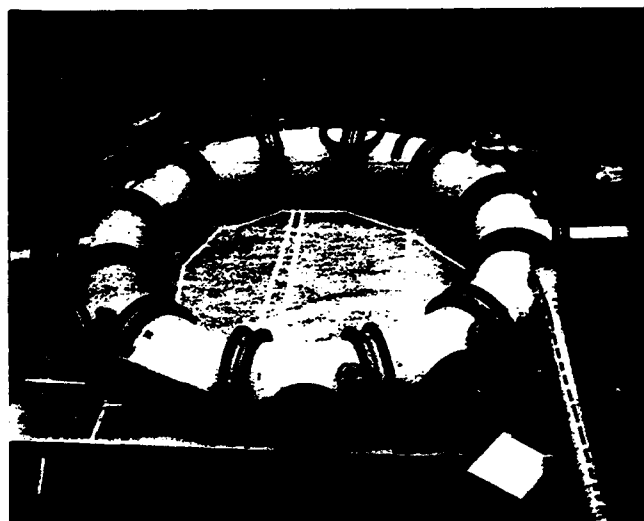


FIG. 6. Photograph of the epoxy reinforced-carbon fiber vacuum chamber.

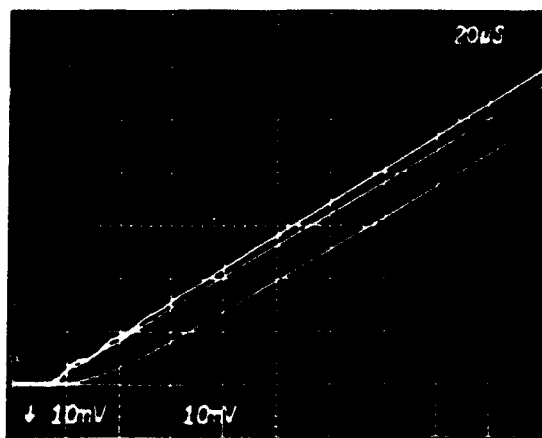


FIG. 7. Measured vertical magnetic field vs time on the minor axis ($r = 100$ cm, $z = 0$) of the torus. Bottom trace: Inside the complete vacuum chamber. Intermediate trace: Inside the chamber with a gap. Top trace: After the removal of the chamber (vacuum field).

high radiation resistance (up to 500 Mrad) and low outgassing rate ($\sim 10^{-8}$ Torr/sec-cm²).

The vertical magnetic field is monitored with a small magnetic probe that is located on the minor axis. The probe has been wound of gauge 35 copper wire, has approximately 600 turns, its measured inductance being 6.2 mH and its measured internal resistance being 43 Ω . The output of the probe is fed to a passive integrator with a time constant of 20.5 msec.

To improve the time response of the probe the 50 Ω terminator at the input of the integrator has been omitted. Oscillations in the output signal have been avoided by locating the oscilloscope approximately 2 m away from the probe, inside an aluminum housing clad with mu metal.

Results from the measurements are shown in Fig. 7. The lower trace is the output of the probe when it is located inside the vacuum chamber and the upper trace is the output of the probe after the chamber is removed (vacuum field). It is apparent from the oscillogram that after approximately 60 μ sec the two signals are parallel and the lower is delayed from the upper by 34 μ sec.

For the parameters of the vacuum chamber, and when the flux condition $\Phi_0/\pi r_0^2 B_{z0}$ is equal to 1.92, i.e., for $\epsilon = 0.04$ both the theory and the computer code predict a time delay of 37 μ sec. The less than 10% difference between the two delay times is probably within the uncertainty of the measurement.

In addition, we broke the electrical continuity of the vacuum chamber by unbolting the joint of two adjacent sec-

tors. The probe was placed on the minor axis with its axis of symmetry on the vertical plane that passes through the symmetry plane of the gap. The intermediate trace in Fig. 7 shows the output of the probe for this measurement.

It is expected that at the symmetry plane of the gap the magnetic field to be identical to the vacuum field. However, due to various constraints, the diameter of the probe and the gap width are approximately equal and thus the measured field is lower than the vacuum field.

IV. CONCLUSION

The diffusion of the magnetic field through a toroidal conducting shell has been studied under the assumption of a small aspect ratio. The external magnetic field can have an arbitrary field index and magnetic flux on the minor axis of the torus. The diffused field, field index, magnetic flux, and wall current were computed analytically and compared with the numerical results from the TRIDIF code. Three time constants determine the evolution in time of the diffusion process, namely, the L/R time τ_0 , the diffusion time τ_1 , and $\tau_2 = \tau_1/2$. The delay time depends linearly on τ_0 , τ_1 and also on the flux condition of the external field. The analytic delay time was larger than that computed from the TRIDIF code. The difference is attributed to the finite volume of the region of integration in the numerical computation which causes the inductance of the system to be smaller. In general, the agreement between the theoretical and numerical results is quite good.

A measurement of the delay time in the toroidal chamber of the NRL modified betatron gave a delay time approximately equal to 34 μ sec, i.e., less than 10% smaller from the theoretical value of 37 μ sec.

In conclusion, we have seen that the diffusion process in the toroidal conducting shell is much more complicated than that in a conducting cylinder. Therefore, the results for a cylinder cannot be generalized to apply to a toroidal device. The case of the torus should be investigated on its own merit.

ACKNOWLEDGMENTS

This work was supported by ONR and SPAWAR.

¹ J. C. Jaeger, *Philos. Mag.* **29**, 18 (1940).

² C. A. Kapetanakis, University of Maryland, Department of Physics and Astronomy Technical Report No. 70-113, June 1970.

³ H. Knoepfel, *Pulsed High Magnetic Fields* (North-Holland, Amsterdam, 1970).

⁴ P. Rolicz, J. Purczynski, and R. Sikora, *J. Appl. Phys.* **47**, 4127 (1976).

⁵ J. R. Freeman, *J. Comput. Phys.* **41**, 142 (1981).

⁶ A. Erdelyi, *Higher Transcendental Functions* (McGraw-Hill, New York, 1953), Vol. 1.

Appendix Y

Beam Trapping in a Modified Betatron Accelerator

Beam trapping in a modified betatron accelerator

C. A. Kapetanakis, D. Dialectis,* S. J. Marsh,[†] L. K. Len,[‡] and T. Smith[‡]
Plasma Physics Division, Naval Research Laboratory, Washington, D.C. 20375-5000

(Received 24 May 1991)

The experimental results on the trapping of the beam in the Naval Research Laboratory modified betatron accelerator are in good agreement with a revised model of resistive trapping, and thus it may be concluded that the wall resistivity is responsible for the inward spiral motion of the beam after injection.

INTRODUCTION

Currently, several laboratories [1-5] are engaged in studies to assess the feasibility of compact, high-current accelerators. Among the various accelerating schemes presently under investigation is the modified betatron accelerator (MBA) [6-8]. This device is under study at the University of California, Irvine [2] and also at the Naval Research Laboratory (NRL). Since the initial successful demonstration of acceleration [1] approximately two years ago, the NRL-MBA has achieved [11] trapped currents as high as 1.5 kA and energies approximately 18 MeV. The beam lifetime that is typically 700-900 μ sec is limited by the cyclotron resonance.

Following the installation of strong focusing windings [9,10] in the NRL device it is routinely observed [1,11] that for several combinations of injection parameters the beam consistently spirals from the injection position to the magnetic minor axis and is trapped. The explanation of this interesting phenomenon has been so far elusive. However, a fair understanding of the trapping mechanism is not only of academic interest but a necessity for any upgrading of the existing or the construction of a new device.

In this paper we report recent experimental results on the trapping of the beam in the NRL-MBA. The results are in agreement with a revised model of resistive trapping [12]. Two modifications have been introduced to the original model. First, the beam motion is not limited near the minor axis and therefore nonlinear effects and the fast diffusion times that scale as $\mu_0(b-a)^2/\pi^2\rho$, where $b-a$ is the thickness of the chamber and ρ is the wall resistivity, become important. Second, in order to take into account the intermediate motion [10] of the beam that has been omitted in the calculation of the image fields of the beam, the wall surface resistivity is computed using the skin depth that corresponds to the frequency of the intermediate mode and not the actual thickness of the chamber.

There are three distinct groups of diffusion times with which the self-magnetic-field of the beam leaks out of a resistive torus. The shortest are the "plane" characteristic times

$$\tau_{mk} \approx \mu_0(b-a)^2/\pi^2\rho k^2 = \frac{\tau_{01}}{k^2} \equiv \frac{\tau_p}{k^2},$$

where $k=1,2,3,\dots$. The "plane" diffusion times are important when the beam is near the wall. The "cylinder" diffusion times are

$$\tau_{m0} \approx \tau_{10}/m = \tau_c/m = \mu_0 a(b-a)/2\rho m,$$

where $m=1,2,3,\dots$. Both τ_p and τ_c determine the speed with which the self-magnetic-field of the beam penetrates the wall of the chamber and are instrumental in the resistive trapping of the beam. Finally, the "loop" diffusion time $\tau_{00} \equiv \tau_l = 2\tau_c(\ln(8r_0/a)-2)$, where r_0 is the major radius of the torus, determines the speed with which the beam field diffuses into the hole of the doughnut. The "loop" diffusion time does not play any role in the resistive trapping of the beam.

The resistive trapping is due to the negative radial component of the image magnetic field of the beam that acts on its centroid, when such a beam moves poloidally inside a resistive chamber. This field component crossed with the axial (toroidal) velocity of the beam produces a poloidal force, which is in the opposite direction to the poloidal motion of the beam. In the absence of the strong focusing and when the self-fields dominate the external fields (high-current regime), the poloidal force in conjunction with the axial (toroidal) magnetic field drives the beam to the wall (drag instability [13]). However, in the presence of strong focusing the direction of the poloidal motion can be reversed and the beam spirals to the minor axis [12].

BRIEF DESCRIPTION OF THE EXPERIMENT

The NRL modified betatron has been described [1,14] previously. In this paper we give, for completeness, a short description of its basic components. The NRL-MBA is a toroidal device that comprises three different external magnetic fields; the betatron field B_z that can vary from 0-2.7 kG, the toroidal field B_θ that can vary between 0-5.1 kG, and the strong focusing field that has a maximum gradient between 0-31 G/cm, when the current I_{SF} in the windings varies from 0-30 kA.

The 100-cm major radius, 15.2-cm-inside minor radius vacuum chamber has been constructed using epoxy-reinforced carbon fibers. The desired conductivity is obtained by embedding in the outer layer of graphite a phosphor bronze screen. The measured dc resistance of the toroidal vessel is 68 ± 2 m Ω and the corresponding

Work of the U. S. Government
 Not subject to U. S. copyright

surface resistivity is 10.3 m Ω on a square. The graphite surface resistivity is 26.6 m Ω on a square.

The electrons are emitted from one end-face of a cylindrical carbon cathode. The other end-face is mounded on the cathode stalk. The emitting surface of the cathode faces the circular opening of the conical anode, which is located on the midplane of the device, 8.7 cm from its minor axis.

EXPERIMENTAL RESULTS

Over a wide range of parameters and after fine tuning the external fields the beam spirals from the injector near the minor axis and is trapped. The beam trapping time, i.e., the time it takes the beam to travel from the injection position to the vicinity of the minor axis is determined by measuring the time delay between the x-ray peaks that are generated at injection and at a 1×1.1 -cm, 0.8-mm-thick lead target that is located on the magnetic minor axis. The lead target is mounted on the front surface of a 3- μ m-thick polycarbonate foil that is stretched across the minor cross section of the vacuum chamber as shown in Fig. 1(a). The x rays are monitored by a collimated x-ray detector that is located 4 m away from the lead target. The scintillator-photomultiplier tube is housed inside a lead box and the x rays enter the scintillator through a 3-mm-diam hole. The foil is graphite coated on the upstream side to avoid charging. Figure 1(b) shows an open-shutter photograph of the light emitted as the beam passes through the foil. The x rays emitted as the beam

strikes the diode and the lead target are shown in the upper trace of Fig. 1(c). The trapping time τ_{tr} for this shot is 1.25 μ sec. The lower trace of Fig. 1(c) shows the output of the Rogowski coil that monitors the beam current. The peak of the signal corresponds to 1.2 kA.

The results shown in Fig. 1 were taken with a 0.5-cm hole in the anode. This hole is by a factor of 3 smaller than that used regularly in the NRL device. Thus, the trapped current has been reduced by a factor of 2–3. This reduction in the beam current was necessary in order to achieve satisfactory resolution in the open-shutter photographs.

To determine the effect of the foil on the transverse beam orbit, we carried out a series of experiments in which the 3- μ m-thick foil was replaced with a foil of the same composition but with only half its thickness. The results show that the equilibrium position of the beam is slightly larger in the case of 1.5- μ m-thick foil. It requires approximately 1–2 G higher vertical field (~ 4 –8%) to shift the equilibrium to its original position and make the orbits identical.

As the electrons pass through the plastic foil, they suffer both inelastic and elastic scattering. The stopping power [15] of 0.6 MeV electrons passing through polyethylene (data for polycarbonate are not available) is ~ 2 (MeV cm²)/gm. Thus, the energy loss per pass is 0.6 keV. The total energy loss in 1.2 μ sec, i.e., in sixty revolutions around the major axis, is 36 keV or $\sim 6\%$. The energy loss in the thinner foil is only 18 keV and therefore the equilibrium position is expected to increase by

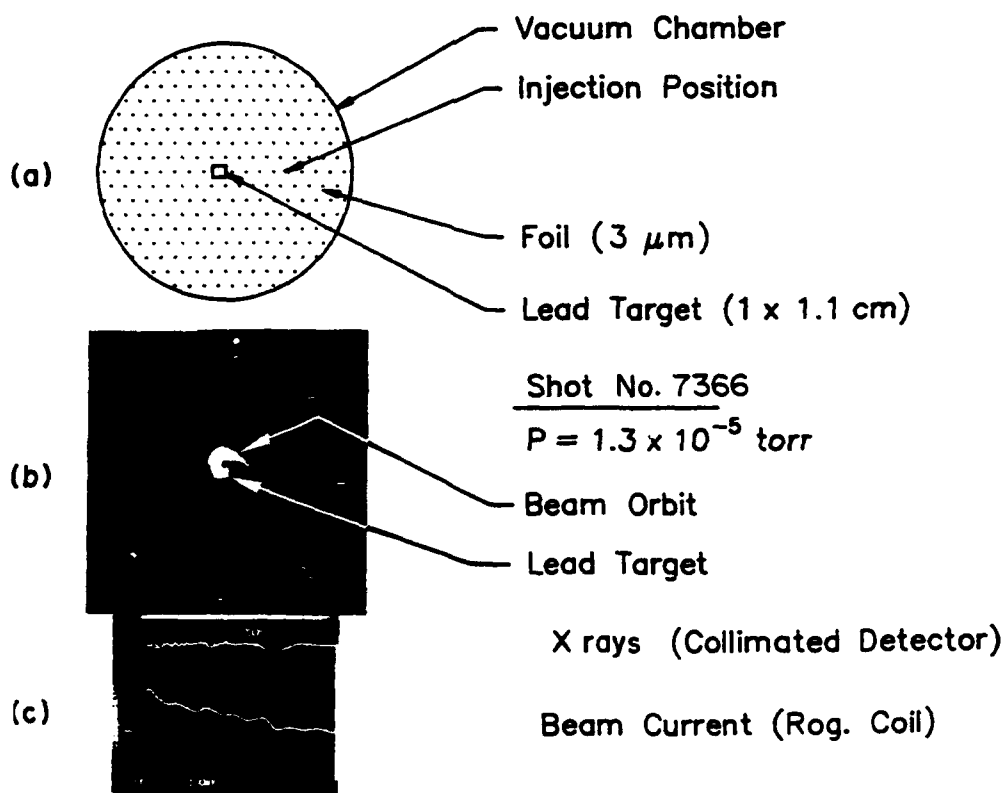


FIG. 1. Beam trapping time.

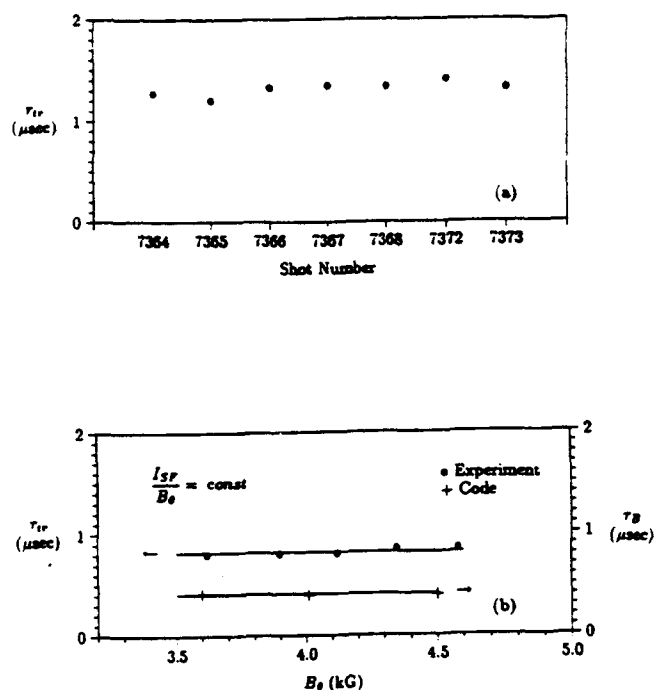


FIG. 2. (a) Trapping time reproducibility and (b) dependence of τ_{tr} and τ_B on B_θ for constant I_{SF}/B_θ .

3% when the thickness of the foil is reduced to half. This shift is not substantially different from that observed in the experiment. The elastic-scattering induced RMS angle is 0.9° for the first pass through the $1.5\text{-}\mu\text{m}$ -thick foil. Although substantial, the elastic scattering does not contribute to the shift of the equilibrium position.

The beam orbits are very reproducible and τ_{tr} shows only modest variations for the same operating parameters. Figure 2(a) shows τ_{tr} for seven shots taken with the same values of the fields. It is apparent from this figure that τ_{tr} varies by $\pm 7\%$. In a second run with five shots the variation was even smaller. Figure 2(b) shows τ_{tr} vs B_θ for constant I_{SF}/B_θ , where I_{SF} is the current of the strong-focusing windings. For all practical purposes τ_{tr} remains constant in the narrow range tested.

In addition to τ_{tr} , the bounce period τ_B , i.e., the time the beam takes to perform a complete revolution in the poloidal direction, is of special interest. To determine τ_B , the foil target was removed and replaced with a 1.1-cm -wide, 1-mm -thick, 16-cm -long lead strip. The lead target is backed on the upstream side by a thin plastic strip and is mounted on a half lucite ring that is carbon coated. The symmetry axis of the target lies on the midplane of the device as shown in Fig. 3(a).

The light emitted from the upstream side of the target when the beam strikes it is monitored with an open

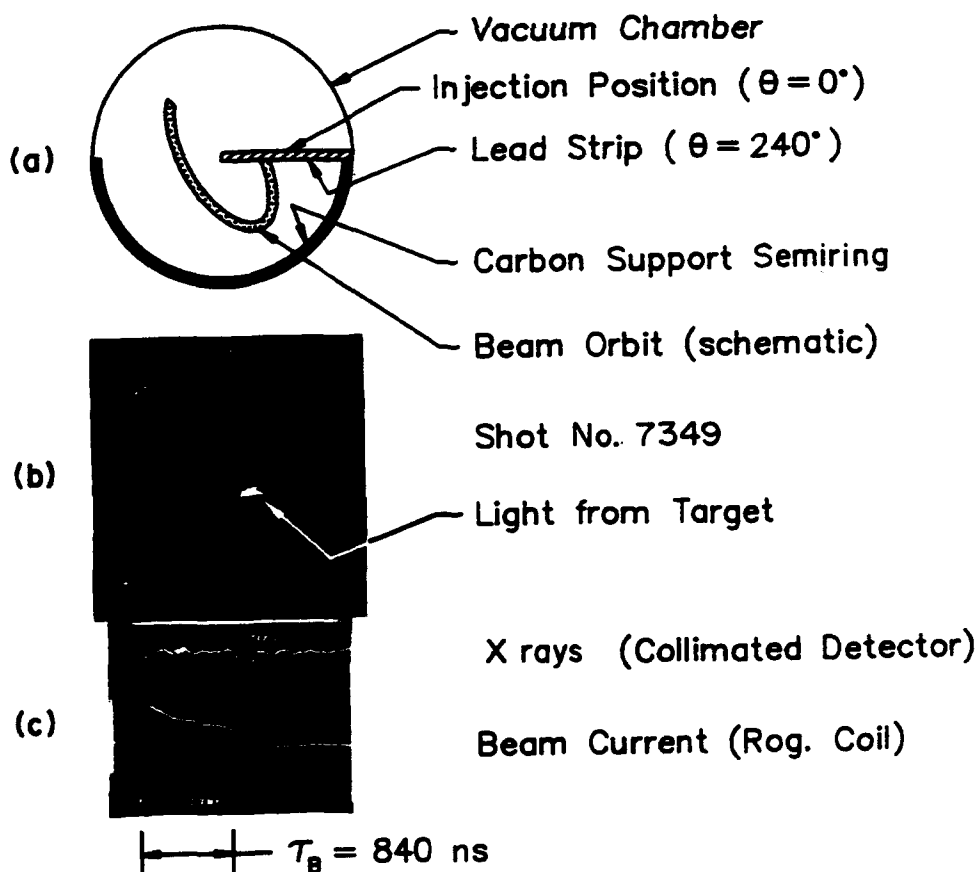


FIG. 3. Beam bounce period.

shutter camera. Results are shown in Fig. 3(b). The x-ray signal and the output of the Rogowski coil that monitors the beam current are shown in Fig. 3(c). The bounce period is inferred from the time delay of the two x-ray peaks, as indicated in Fig. 3(c), and in this shot is 840 nsec. The damage pattern on the lead strip has a diameter that is equal to the diameter of the anode hole. This implies that the diameter of the beam has not changed after about 40 revolutions around the major axis. In addition, we observe that the damage pattern is a semicircle that is always located near the lower edge of the strip. From this observation it may be concluded that the beam drifts 3 mm over 20 nsec, i.e., its bounce speed near the strip is $\sim 15 \text{ cm}/\mu\text{sec}$.

To verify that there is no correlation between τ_r and τ_l , i.e., with the speed the beam magnetic field diffuses into the hole of the doughnut, the vacuum chamber was unbolted in two joints that are located 180° apart in the toroidal direction and a ring insulator was inserted in each of these joints. Sixty carbon resistors, 51Ω each, were symmetrically mounted on the outer surface of one of the two rings as shown in Fig. 4(a). To improve its voltage holding capabilities the inner surface of the blue nylon insulator was angled and a 0.6-cm-deep groove was machined at its plane of symmetry. In addition, its inner surface was protected from stray electrons by a 0.8-mm-thick lead strap that is supported by an epoxy reinforced

carbon fiber belt. The purpose of the second insulator was only to minimize the distortion of the toroidal chamber and thus shorting wide straps, instead of resistors, were installed on its outer surface.

There are two distinct currents flowing on the wall of the vacuum chamber. The first i_w is due to the rising vertical field and the second I_r is induced by the beam. Since the vertical field during the first quarter period varies as $B_z(t) = B_p \sin(2\pi t/\tau)$, where B_p is the peak field and τ is the period, the induced voltage in the chamber is $V = -V_0 \cos(2\pi t/\tau)$, where $V_0 = (4\pi^2 r_0^2 / \tau) B_p$, and r_0 is the major radius of the torus. The current flowing on the wall of the chamber is described by the equation $V = L(di_w/dt) + Ri_w$, where L is the inductance and R the resistance of the torus. The instantaneous value of i_w can be found by integrating the above equation and is given by

$$i_w = - \frac{V_0}{R \left[1 + \left(\frac{2\pi L/R}{\tau} \right)^2 \right]} \times \left[\cos(2\pi t/\tau) + \frac{2\pi L/R}{\tau} \sin(2\pi t/\tau) - e^{-t/(L/R)} \right], \quad (1)$$

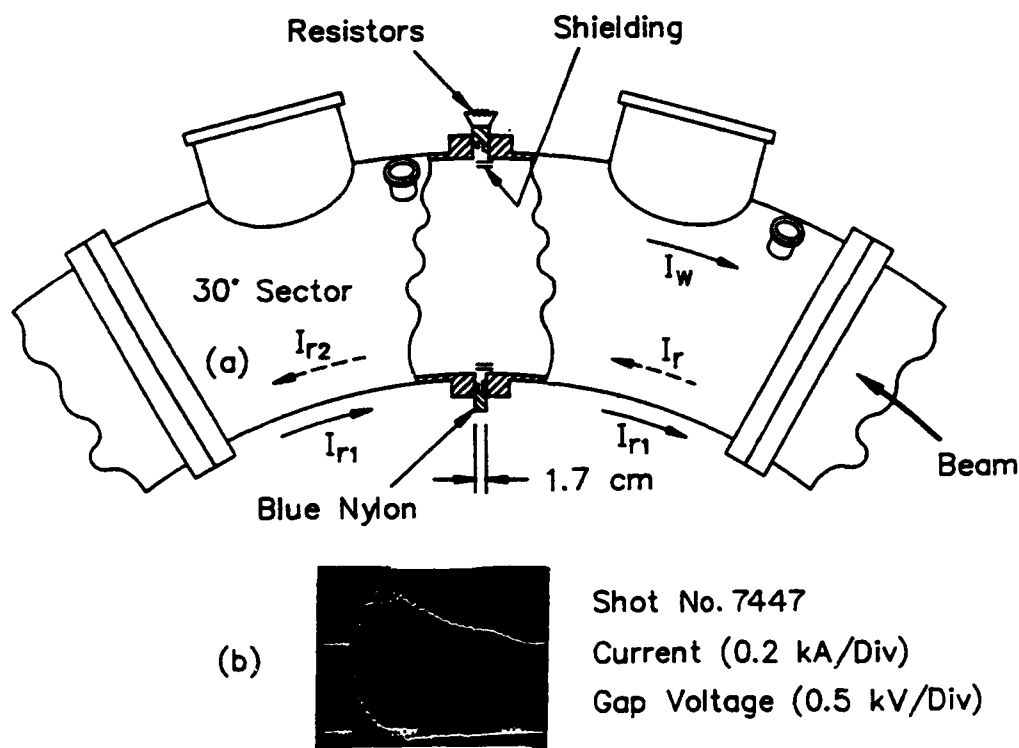


FIG. 4. (a) Schematic of the vacuum chamber joint with the insulator in place. (b) Current and gap voltage waveforms.

with the initial condition $i_w(t=0)=0$.

The temporal profile of i_w predicted by the above simple model is identical to that predicted from the exact solution of the diffusion problem for a toroidal resistive shell [16] and also is in good agreement with the results of the TRIDIF code for a finite thickness toroidal vessel. According to Eq. (1), i_w has a maximum at time t_p , which for $\alpha \equiv 2\pi(L/R)/\tau \ll 1$ is determined from $\alpha^2[1-t_p/(L/R)] = -e^{-t_p/(L/R)}$. The peak value of the current is $i_{wp} = V/R$. The measured peak value of the current in the experiment is in good agreement with the above theoretical prediction and scales, as expected, with the value of the resistance at the gap.

The return current of the beam is measured with a fast Rogowski coil ($\tau_{rise} \approx 20$ nsec) that is located outside the vacuum chamber. With the resistors at the gap shorted, the Rogowski coil shows a slowly rising current that is consistent with the decay of I_r . However, when the shorting clips are removed the Rogowski coil shows a current pulse that rises to $\sim \frac{2}{3}$ of its peak value in less than 100 nsec as shown in Fig. 4(b). The lower trace in fig. 4(b) shows the voltage across the resistors V_g as measured directly by a Tektronix 7844 oscilloscope after a 100X attenuation. The shape of the time-integrated V_g is very similar to the current waveform resisted by the Rogowski coil, i.e., V_g is proportional to the time derivative of the current.

COMPARISON WITH THEORY

The equations that describe the motion of the beam centroid have been solved numerically using analytical expressions for B_z and B_θ . The stellarator fields are determined numerically from Biot-Savart law by dividing each period of the windings into 20 segments. The image fields on the beam centroid have been computed analytically for a uniform density electron ring that is located inside a large major radius torus with resistive wall of thickness $b-a$, where a is the inner and b the outer radii of the torus. In contrast with previous calculation [12], the beam is not limited near the minor axis.

In the local cylindrical coordinate system (ρ, ϕ, z) with its origin on the geometric minor axis, the electrostatic potential inside the ring is given by [17]

$$\Phi_0 = \frac{Q_l}{2\pi\epsilon_0} \left\{ \ln \frac{a}{r_b} + \frac{1}{2} - \frac{1}{2} \frac{\rho^2 + \Delta^2 - 2\Delta\rho \cos(\phi - \alpha)}{2r_b^2} + \frac{1}{2} \ln \left[1 + \left(\frac{\Delta\rho}{a^2} \right)^2 - 2 \frac{\Delta\rho}{a^2} \cos(\phi - \alpha) \right] \right\}, \quad (2)$$

where Δ and α define the beam position on the transverse plane, r_b is the minor radius of the beam, and Q_l is the charge per unit length. Similarly, the magnetic vector potential inside the beam is [17]

$$A_{\theta 0} = \frac{\Phi_0 \beta_\theta}{c} + \sum_{k=0}^{\infty} A_{0k} U_{0k}^{(c)}(t) + \sum_{m=1}^{\infty} \sum_{k=0}^{\infty} A_{mk} \left[\frac{\rho}{a} \right]^m [U_{mk}^{(c)}(t) \cos m\phi + U_{mk}^{(s)}(t) \sin m\phi], \quad (3)$$

where β_θ is the normalized toroidal beam velocity.

The time-dependent coefficients $U_{mk}^{(c)}(t)$, $U_{mk}^{(s)}(t)$ are zero at $t=0$ and are determined by the differential equations

$$\dot{U}_{mk}^{(c)} + \frac{1}{\tau_{mk}} U_{mk}^{(c)} = \frac{Q_l \beta_\theta}{2\pi\epsilon_0 c \tau_{mk}} \left[\frac{\Delta}{a} \right]^m \cos m\alpha, \quad (4)$$

$$\dot{U}_{mk}^{(s)} + \frac{1}{\tau_{mk}} U_{mk}^{(s)} = \frac{Q_l \beta_\theta}{2\pi\epsilon_0 c \tau_{mk}} \left[\frac{\Delta}{a} \right]^m \sin m\alpha,$$

where

$$\frac{1}{\tau_{mk}} = \frac{\alpha_{mk}^2}{\mu_0 \sigma}, \quad m=0,1,2,\dots, \quad k=0,1,2,\dots,$$

σ is the wall conductivity of the toroidal chamber, and α_{mk} are the zeros of the function

$$f_0(\alpha) = \frac{\pi}{2} x_0 [J_1(x_0) Y_0(x_1) - Y_1(x_0) J_0(x_1)] - \frac{\pi}{2} \left[\ln \frac{8R_b}{b} - 2 \right] x_0 x_1 [J_1(x_0) Y_1(x_1) - Y_1(x_0) J_1(x_1)] \quad (5)$$

when $m=0$, and

$$f_m(\alpha) = \frac{\pi}{4} x_0 x_1 [J_{m+1}(x_0) Y_{m-1}(x_1) - Y_{m+1}(x_0) J_{m-1}(x_1)] \quad (6)$$

when $m=1,2,3,\dots$. The arguments of Bessel functions in (5) and (6) are $x_0 = a\alpha$, $x_1 = ab$ and R_b is the major radius of the beam. For each m there is an infinite number of zeros denoted by the index $k=0,1,2$. The time-dependent coefficients A_{0k} , A_{mk} that appear in the vector potential are equal to

$$A_{mk} = - \frac{2g_m(\alpha_{mk})}{\alpha_{mk} f'_m(\alpha_{mk})},$$

where $f'_m(\alpha)$ is the derivative of $f_m(\alpha)$ and

$$g_0(\alpha) = \frac{\pi}{2} [J_0(x_0) Y_0(x_1) - Y_0(x_0) J_0(x_1)] - \frac{\pi}{2} \left[\ln \frac{8R_b}{b} - 2 \right] x_1 [J_0(x_0) Y_1(x_1) - Y_0(x_0) J_1(x_1)]$$

when $m=0$, and

$$g_m(\alpha) = \frac{\pi}{2} x_1 [J_m(x_0) Y_{m-1}(x_1) - Y_m(x_0) J_{m-1}(x_1)]$$

when $m = 1, 2, 3, \dots$. The image fields at the beam centroid, i.e., when $\rho = \Delta$ and $\phi = \alpha$, are obtained from the expressions of Φ_0 and A_{0k} given above.

The radial components $B_\rho^{(c)}$ at the beam centroid is of special interest because it is responsible for the inward radial motion of the beam. This component is given by

$$B_\rho^{(c)} = \sum_{m=1}^{\infty} \sum_{k=0}^{\infty} \frac{m}{a} A_{mk} \left[\frac{\Delta(t)}{a} \right]^{m-1} \times [-U_{mk}^{(s)}(t) \cos m\alpha(t) + U_{mk}^{(c)}(t) \sin m\alpha(t)] . \quad (7)$$

Since $B_\rho^{(c)}$ is independent of A_{0k} and $U_{0k}^{(c)}$, i.e., it is independent of loop time $\tau_l = \tau_{00}$, the beam trapping time should also be independent of τ_l as observed in the experiment.

$$B_\rho^{(c)}(\text{shell}) = \frac{\sin \alpha}{R_b} \left\{ \frac{Q_l \beta_\theta}{4\pi\epsilon_0 c} \left[\ln \frac{a}{r_b} + 1 \right] + \frac{Q_l \beta_\theta}{4\pi\epsilon_0 c} \ln \left[1 - \left[\frac{\Delta(t)}{a} \right]^2 \right] - \frac{Q_l \beta_\theta}{16\pi\epsilon_0 c} \left[\frac{r_b}{a} \right]^2 \frac{1}{\left[1 - \left[\frac{\Delta}{a} \right]^2 \right]^2} \right. \\ \left. + \frac{1}{2} \sum_{m=1}^{\infty} \frac{1}{m} \left[\frac{\Delta(t)}{a} \right]^m [U_{cm}^{(0)}(t) \cos m\alpha(t) + U_{sm}^{(0)}(t) \sin m\alpha(t)] + \frac{1}{2} \left[\ln \frac{8R_b}{a} - 2 \right] U_0^{(0)}(t) + U_0^{(1)}(t) \right\} \\ + \frac{1}{a} \sum_{m=1}^{\infty} \left[\frac{\Delta(t)}{a} \right]^{m-1} \{ -[U_{sm}^{(0)}(t) + U_{sm}^{(1)}(t) + V_{sm}^{(1)}(t)] \cos m\alpha + [U_{cm}^{(0)}(t) + U_{cm}^{(1)}(t) + V_{cm}^{(1)}(t)] \sin m\alpha(t) \} , \quad (8)$$

where the time-dependent parameters $U_0^{(0)}(t)$, $U_0^{(1)}(t)$, $U_{cm}^{(0)}(t)$, $U_{sm}^{(0)}(t)$, $U_{cm}^{(1)}(t)$, $U_{sm}^{(1)}(t)$, $V_{cm}^{(1)}(t)$, and $V_{sm}^{(1)}(t)$ are zero at $t=0$ and are determined by the differential equations

$$\begin{aligned} \dot{U}_0^{(0)} + \frac{1}{\tau_l} \left[1 + \tau_c \frac{\dot{x}_c}{R_b} \right] U_0^{(0)} &= \frac{2Q_l \beta_\theta}{4\pi\epsilon_0 c} \frac{1}{\tau_l} \left[1 + \frac{x_c}{2R_b} \right] , \\ \dot{U}_0^{(1)} + \frac{1}{\tau_c} U_0^{(1)} &= \frac{1}{2\tau_c} U_0^{(0)} , \\ \dot{U}_{cm}^{(0)} + \frac{m}{\tau_c} U_{cm}^{(0)} &= \frac{2Q_l \beta_\theta}{4\pi\epsilon_0 c} \frac{m}{\tau_c} \left[\frac{\Delta}{a} \right]^m \cos m\alpha , \\ \dot{U}_{sm}^{(0)} + \frac{m}{\tau_c} U_{sm}^{(0)} &= \frac{2Q_l \beta_\theta}{4\pi\epsilon_0 c} \frac{m}{\tau_c} \left[\frac{\Delta}{a} \right]^m \sin m\alpha , \\ \dot{U}_{cm}^{(1)} + \frac{m}{\tau_c} U_{cm}^{(1)} &= -\frac{\dot{x}_c}{2R_b} U_{cm}^{(0)} , \\ \dot{U}_{sm}^{(1)} + \frac{m}{\tau_c} U_{sm}^{(1)} &= -\frac{x_c}{2R_b} U_{sm}^{(0)} , \\ \dot{V}_{cm}^{(1)} + \frac{m}{\tau_c} V_{cm}^{(1)} &= \frac{Q_l \beta_\theta}{16\pi\epsilon_0 c} \frac{1}{\tau_c} \frac{a}{R_b} \left[\frac{r_b}{a} \right]^2 \\ &\quad \times \left[\frac{\Delta}{a} \right]^{m-1} \cos(m-1)\alpha , \end{aligned} \quad (9)$$

TABLE I. Parameters of the run shown in Fig. 5.

Torus major radius r_0	100 cm
Torus minor radius a	15.2 cm
Relativistic factor γ	1.5
SF radius ρ_0	23.4 cm
SF current I_{sf}	24 kA
Vertical field at injection B_{z0}	26 G
Toroidal field $B_{\theta 0}$	4 kG
Beam minor radius r_b	3 mm
Beam current I_b	1.2 kA
Wall resistivity	8 mΩ cm
Intermediate frequency, ω_W	$1.8 \times 10^9 \text{ sec}^{-1}$

To gain further insight, we have computed the image fields, including first-order toroidal corrections, at the beam centroid for a beam inside a resistive toroidal shell—in this case $B_\rho^{(c)}$:

$$\dot{V}_{sm}^{(1)} + \frac{m}{\tau_c} V_{sm}^{(1)} = \frac{Q_l \beta_\theta}{16\pi\epsilon_0 c} \frac{m^2}{\tau_c} \frac{a}{R_b} \left[\frac{r_b}{a} \right]^2 \times \left[\frac{\Delta}{a} \right]^{m-1} \sin(m-1)\alpha ,$$

where

$$\tau_0 = 2\tau_c \left[\ln \frac{8R_b}{a} - 2 - \frac{x_c}{2R_b} \right] ,$$

and

$$x_c = \Delta \cos \alpha \equiv R_b - r_0 .$$

It is apparent from Eqs. (8) and (9) that the toroidal correction term of $B_\rho^{(c)}$ is a function of τ_l . However, this term is multiplied by $\sin \alpha(t)$ and therefore averages to zero in a poloidal period.

In the limit $(b-a) \ll a$, the toroidal electric field E_θ on the outer surface of the chamber for a stationary beam has a relatively simple, closed form. At $t=0$, $E_\theta=0$ and peaks within a few fast diffusion times τ_p . For a longer time, E_θ decays to zero with τ_l . This form of the electric field is consistent with the observed return current after the beam injection. When the resistors at the gap are shorted the current measured with the external Rogowski coil should rise at the same rate the beam return current

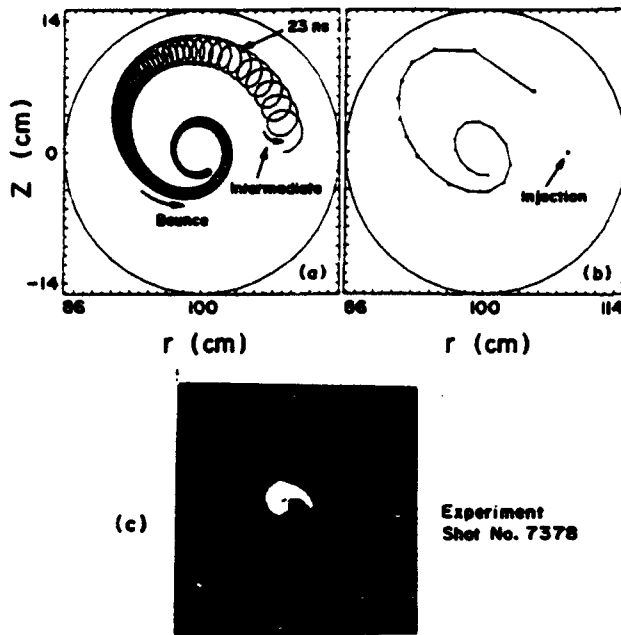


FIG. 5. Beam centroid orbit from the numerical integration of the equations of motion, using the image fields from the resistive shell model [(a) and (b)]. Results from the experiment (c).

decays. However, when the resistors at the gap are not shorted, a portion (I_{r1}) of the return current (I_r) flows on the outer wall of the chamber as shown in Fig. 4. I_{r1} rises considerably faster because the beam magnetic field can leak locally out of the resistive gap considerably faster than it can leak out of a uniform chamber.

Results from the numerical integration of orbit equations are shown in Fig. 5. The various parameters for the run are listed in Table I. Figure 5(a) shows the projection of the centroid's orbit on the $\theta=0$ plane. Both the intermediate and slow (bounce) modes are apparent. Since there are six field periods between $0 \leq \theta \leq 2\pi$, the electrons perform six oscillations during one revolution around the major axis. To take into account the intermediate motion that has been neglected in the calculation of the image fields, the surface resistivity in the code is

computed using the skin depth that corresponds to the intermediate frequency and not the actual thickness of the wall.

The solid circles in Fig. 5(b) show the positions the beam crosses the $\theta=240^\circ$ plane. This is a realistic simulation of the experimental situation. The time difference between two circles is equal to the period around the major axis, i.e., ~ 23 nsec. The parameters of this run are similar to those in Fig. 5(c) and the similarity of the two orbits is quite apparent. When the crossing plane is moved from $\theta=240^\circ$ to a different azimuthal position θ , the beam orbit rotates around the minor axis. The rotation predicted by the theory is very similar to that observed in the experiment.

There is some ambiguity, both in the experiment and theory, in the determination of the beam trapping time, because its exact value depends on the position and size of the target. However, this is not the case with τ_B , which can be measured very accurately. We made four computer runs for different values of B_θ keeping $I_{SF}/B_\theta = \text{constant}$. Figure 2(b) shows τ_B vs B_θ for three of these runs. For all practical purposes τ_B remains constant as B_θ varies. In the fourth run B_θ was reduced to 2 kG and although the beam orbit changed substantially τ_B was lower only by 7%.

As a rule, the theory predicts a τ_B and τ_{tr} that are approximately a factor of 2 shorter than those observed in the experiment. With the exception of these two times the revised model of resistive trapping is in agreement with the experiment observations, although in the analysis the beam current remains constant while in the experiment the current decays. This decay is observed whenever there is a target inside the chamber but in general is absent during the acceleration experiments when the various targets are removed.

ACKNOWLEDGMENTS

This work is supported by the Office of Naval Research and the Space and Naval Warfare Command.

*Permanent address: Science Applications International Corporation, 1710 Goodridge Drive, McLean, VA 22102.

†Permanent address: SFA, Inc., Landover, MD 20785.

‡Permanent address: FM Technologies, Inc., 10529-B Braddock Road, Fairfax, VA 22032.

- [1] C. A. Kapetanakis *et al.*, Phys. Rev. Lett. 64, 2374 (1990).
- [2] H. Ishizuka *et al.*, in *Proceedings of the Seventh International Conference on High-Power Particle Beams, Karlsruhe, Germany, 1988*, edited by W. Bauer and W. Schmidt (Kernforschungszentrum Karlsruhe GmbH, Karlsruhe, 1988), Vol. II, p. 857.
- [3] S. Humphries, Jr., and L. K. Len, in *Proceedings of the 1987 Particle Accelerator Conference, Washington, D.C., 1987*, edited by E. R. Lindstrom and L. S. Taylor (IEEE,

New York, 1987), p. 914.

- [4] V. Bailey *et al.*, in *Proceedings of the 1987 Particle Accelerator Conference* (Ref. 3), p. 920.
- [5] W. K. Tucker *et al.*, in *Proceedings of the 1987 Particle Accelerator Conference* (Ref. 3), p. 957.
- [6] P. Sprangle and C. A. Kapetanakis, J. Appl. Phys. 49, 1 (1978).
- [7] C. A. Kapetanakis *et al.*, Phys. Fluids 26, 1634 (1983).
- [8] N. Rostoker, Comments Plasma Phys. 6, 91 (1980).
- [9] C. Roberson *et al.*, Phys. Rev. Lett. 50, 507 (1983).
- [10] C. A. Kapetanakis *et al.*, Part. Accel. 21, 1 (1987).
- [11] C. A. Kapetanakis *et al.*, Phys. Fluids (to be published).
- [12] P. Sprangle and C. A. Kapetanakis, Part. Accel. 18, 203 (1986); Y. Seo and P. Sprangle, *ibid.* (to be published).

- [13] P. Sprangle and C. A. Kapetanakos, *Part. Accel.* 14, 15 (1983).
- [14] L. K. Len *et al.*, in *Intense Microwave and Particle Beams*, Proceedings of the International Society for Optical Instrumentation Engineers, Los Angeles, CA, January 1990 (SPIE, Bellingham, WA, 1990), Vol. 1226, p. 38.
- [15] M. J. Berger and S. M. Seltzer, NASA Report No. SP-3012, 1964 (unpublished).
- [16] D. Dialetis *et al.*, *J. Appl. Phys.* 69, 1813 (1991).
- [17] D. Dialetis *et al.* (unpublished).

Appendix Z

Diffusion of the Self Magnetic Fields of an Electron Beam Through a Resistive Toroidal Chamber



NRL/MR/4795-92-6985

Diffusion of the Self Magnetic Fields of an Electron Beam through a Resistive Toroidal Chamber

D. DIALETIS,* S. J. MARSH, AND C. A. KAPETANAKOS**

*Beam Physics Branch
Plasma Physics Division*

**Science Applications International Corp.
McLean, VA 22102*

***Sachs-Freeman Assoc., Inc.
Landover, MD 20785*

July 16, 1992

REPORT DOCUMENTATION PAGE			Form Approved OMB No. 0704-0188	
<small>Public reporting burden for this collection of information is estimated to average 1 hour per response, including the time for reviewing instructions, searching existing data sources, gathering and maintaining the data needed, and completing and reviewing the collection of information. Send comments regarding this burden estimate or any other aspect of this collection of information, including suggestions for reducing this burden, to Washington Headquarters Services, Directorate for Information Operations and Reports, 1215 Jefferson Davis Highway, Suite 1204, Arlington, VA 22202-4302, and to the Office of Management and Budget, Paperwork Reduction Project (0704-0188), Washington, DC 20503.</small>				
1. AGENCY USE ONLY (Leave blank)	2. REPORT DATE July 16, 1992	3. REPORT TYPE AND DATES COVERED Interim		
4. TITLE AND SUBTITLE Diffusion of the Self Magnetic Fields of an Electron Beam through a Resistive Toroidal Chamber		5. FUNDING NUMBERS		
6. AUTHOR(S) D. Dialetis,* S. J. Marsh,** and C. A. Kapetanakos				
7. PERFORMING ORGANIZATION NAME(S) AND ADDRESS(ES) Naval Research Laboratory Washington, DC 20375-5000		8. PERFORMING ORGANIZATION REPORT NUMBER NRL/MR/4795-92-6985		
9. SPONSORING/MONITORING AGENCY NAME(S) AND ADDRESS(ES) Office of Naval Research Arlington, VA 22217-5000		10. SPONSORING/MONITORING AGENCY REPORT NUMBER SPAWAR Washington, DC 20362-5100		
11. SUPPLEMENTARY NOTES *Science Applications International Corp., McLean, VA 22102 **Sachs-Freeman Assoc., Inc., Landover, MD 20785				
12a. DISTRIBUTION/AVAILABILITY STATEMENT Approved for public release; distribution unlimited.		12b. DISTRIBUTION CODE		
13. ABSTRACT (Maximum 200 words) We have studied the diffusion of the self magnetic field of a relativistic electron beam through a resistive toroidal chamber. In contrast with previous calculations, the solution is not limited near the minor axis of the torus. Under the assumptions of small aspect ratio, thin conducting wall and to zero order in toroidal corrections, it has been found that there are three characteristic times with which the magnetic field leaks out of the resistive torus. The computed fields have been used to determine the beam centroid orbit during trapping that follows the beam injection in the NRL modified betatron accelerator. The predicted orbit is in very good agreement with the results of the experiment.				
14. SUBJECT TERMS Diffusion Resistive toroidal chamber		Modified betatron accelerator		15. NUMBER OF PAGES 66
				16. PRICE CODE
17. SECURITY CLASSIFICATION OF REPORT UNCLASSIFIED	18. SECURITY CLASSIFICATION OF THIS PAGE UNCLASSIFIED	19. SECURITY CLASSIFICATION OF ABSTRACT UNCLASSIFIED		20. LIMITATION OF ABSTRACT UL

CONTENTS

I.	Introduction	1
II.	Formulation of the Diffusion Problem	4
III.	Vector Potential of a Current Ring	7
IV.	Homogeneous Solution of the Vector Potential	16
V.	Initial Conditions of the Vector Potential	20
VI.	Diffusion Fields Inside and Outside the Toroidal Conductor	22
VII.	Approximate Results for a Thin Conducting Wall	36
VIII.	Two Applications for the Shell Model	49
IX.	Conclusion	54
	Appendix	55
	References	59

DIFFUSION OF THE SELF MAGNETIC FIELDS OF AN ELECTRON BEAM THROUGH A RESISTIVE TOROIDAL CHAMBER

I. Introduction

Extensive work has been done in the past on the diffusion of external magnetic fields into hollow circular cylindrical conductors of infinite length¹⁻⁵ and also on the diffusion of the self magnetic field of beams out of hollow cylinders.⁶⁻⁹ The beam self magnetic field diffusion studies have also considered the effect of the diffusing fields on the beam dynamics and have furnished interesting results on the beam stability⁶⁻⁸ and beam trapping.⁹ However, these studies are linear and the expressions for the fields are valid only near the axis of the cylinder.

Following the installation of strong focusing windings in the NRL modified betatron accelerator it is routinely observed that for several combinations of injection parameters the injected beam consistently spirals from the injection position to the magnetic minor axis and is trapped.^{10,11} Attempts to explain this interesting phenomenon using the existing linear resistive model have been unsuccessful.¹¹ The decay rate predicted by the linear theory⁹ for the parameters of the experiment is at least 10-20 times longer than that observed in the experiment, even when wake field effects are taken into account.¹²

In contrast to the analysis^{9,12} that assumes the beam to be near the minor axis, the beam in the experiment during injection is at least temporarily near the wall. In addition, the geometry of the NRL device is toroidal¹⁰ and not cylindrical and, therefore, there are additional characteristic times⁵ that may modify the diffusion process.

The present work extends the results of the linear theory. The expressions for the diffusing fields are valid not only near the axis but almost over the entire cross-section of the chamber and toroidal effects

are included to lowest order. The results have been obtained under the following assumptions. First, it is assumed that the toroidal vacuum chamber has a small aspect ratio, i.e., the results are valid provided that the ratio of the minor to the major radius is much less than unity and the radial distances of the observation point from the minor axis is considerably smaller than the major radius of the torus. Second, since the results are confined in the vicinity of the toroidal chamber, propagation effects do not play any role, i.e., the displacement current is omitted in Maxwell's equations. Third, in order to obtain tractable analytical results, it is assumed that the conducting wall is thin, i.e., its thickness is much smaller than the minor radius of the torus. In this case, the analytical results are not valid very near the conducting wall. In the limit when the ratio of the wall thickness to the minor radius of the torus tends to zero, i.e., for a toroidal conducting shell, the analytical results are exact everywhere inside of the toroidal vessel. Finally, the analytical results on the beam dynamics are further simplified under the assumption that the current ring moves slowly in comparison to the fastest of the characteristic times that dictate the diffusion process.

Under the assumptions mentioned above, it is found that there are three characteristic times with which the magnetic field leaks out of a resistive torus, when a current ring turns on at $t = 0$ inside the torus. The shortest is the "plane" or "fast" diffusion time $\tau_{FD} = \mu_0 \sigma (b-a)^2 / \pi^2$, where σ is the wall conductivity, a and b are the inner and outer minor radii of the conducting wall and μ_0 is the permeability of the vacuum. The terms associated with τ_{FD} are responsible for the electric field to be zero at $t=0$ outside the torus since no leakage has occurred as yet. The "cylinder" diffusion time $\tau_D = \mu_0 \sigma (b-a) a / 2$ together with τ_{FD} determines the speed with which the fields penetrate the wall chamber so that the images

of these fields gradually disappear. Finally, the "loop" diffusion time $\tau_{00} = 2\tau_D [\ln(8r_0/a) - 2]$, where r_0 is the major radius of the torus, determines the speed with which the fields diffuse into the hole of the doughnut and is responsible for the gradual disappearance of the wall current. It turns out that the radial component of the self magnetic field, which is responsible for the beam trapping in the MBA, is independent of τ_{00} , and, therefore, the "loop" diffusion time does not play any role in the resistive trapping of the beam. The expressions of the fields predicted by the present work have been used to compute the beam centroid orbit and several other trapping parameters measured in recent detailed beam trapping studies ¹³ in the NRL modified betatron accelerator. The shape of the computed orbits is very similar to those observed in the experiment.

In Section II, the diffusion problem for a current ring inside a toroidal conductor is formulated. In Section III, the vector potential for a current ring in the absence of the conductor is derived. This is the particular solution of the problem. In Section IV, the homogeneous solution inside and outside the torus (but not inside the conductor) is derived in toroidal geometry. The toroidal geometry removes the ambiguity on the value of certain constants associated with the logarithmic dependence of the solutions. In Section V, the initial conditions are established that determine the time-dependent arbitrary parameters in the homogeneous solutions. In Section VI, the solution inside the conductor is derived and the boundary conditions are applied. The vector potential is computed in the three regions inside and outside the torus and inside the conductor. In Section VII, approximate results are obtained under the assumption of a thin conducting wall. Section VIII contains exact analytic results for the shell model and Section IX provides a summary of the main results and lists the most important conclusions of the present study.

II. Formulation of the Diffusion Problem

The configuration and system of coordinates is shown in Fig. 1. The toroidal chamber has a major radius r_0 , an inner and outer minor radius a and b , respectively, and conductivity σ . In the presence of an external driver, namely, a current ring which is axisymmetric, time-dependent and is located inside the torus, the magnetic vector potential in that region is determined by the equation

$$\vec{\nabla} \times \vec{\nabla} \times \vec{A}^{in} = -\mu_0 \vec{J}, \quad (1)$$

where the vector potential \vec{A} has only one nonzero component A_θ^{in} that depends only on the cylindrical components (r, z) and on time. The current density \vec{J} of the current ring has only one nonzero component J_θ which is equal to $J_\theta = I_c / \pi r_c^2$ inside the ring and zero outside it. Here, I_c is the ring current and r_c is its minor radius.

The magnetic field inside the conductor is determined from the vector potential \vec{A}^{con} that is described by the diffusion equation

$$\vec{\nabla} \times \vec{\nabla} \times \vec{A}^{con} = -\mu_0 \sigma \frac{\partial \vec{A}^{con}}{\partial t}, \quad (2)$$

where, again, \vec{A}^{con} has only one component A_θ^{con} , which depends on (r, z) and on time. Finally, the vector potential outside the torus is determined by the homogeneous equation

$$\vec{\nabla} \times \vec{\nabla} \times \vec{A}^{out} = 0 \quad (3)$$

where the component A_θ^{out} of \vec{A}^{out} depends on (r, z) and on time. The magnetic and electric field components, in each region, are given by

$$B_r = - \frac{\partial A_\theta}{\partial z}, \quad (4a)$$

$$B_z = \frac{1}{r} \frac{\partial r A_\theta}{\partial r}, \quad (4b)$$

$$E_\theta = - \frac{\partial A_\theta}{\partial t}, \quad (4c)$$

where A_θ is one of the components defined above, depending on the region of interest. Notice that Eq. (2) is identical to Ampere's law combined with Ohm's law inside the conductor.

It is convenient to express the vector potential and the fields in terms of the local cylindrical coordinates (ρ, ϕ) which are related to the global cylindrical coordinates (r, z) by:

$$r = r_0 + \rho \cos \phi, \quad (5a)$$

$$z = \rho \sin \phi. \quad (5b)$$

Then, in the region inside the conductor, Eq. (2) reduces to

$$\begin{aligned} \frac{1}{\rho} \frac{\partial}{\partial \rho} \rho \frac{\partial A_\theta^{\text{con}}}{\partial \rho} + \frac{1}{\rho^2} \frac{\partial^2 A_\theta^{\text{con}}}{\partial \phi^2} + \frac{\cos \phi \frac{\partial A_\theta^{\text{con}}}{\partial \rho} - \sin \phi \frac{1}{\rho} \frac{\partial A_\theta^{\text{con}}}{\partial \phi}}{r_0 + \rho \cos \phi} \\ - \frac{A_\theta^{\text{con}}}{(r_0 + \rho \cos \phi)^2} = + \mu_0 \sigma \frac{\partial A_\theta^{\text{con}}}{\partial t}, \end{aligned} \quad (6)$$

after taking account of the fact that A_θ^{con} is independent of the toroidal angle θ . Also, in the local coordinate system Eqs. (4a), (4b) are replaced by

$$B_\rho = - \frac{1}{\rho} \frac{\partial A_\theta}{\partial \phi} + \frac{\sin \phi}{r_0 + \rho \cos \phi} A_\theta, \quad (7a)$$

$$B_{\phi} = \frac{2A_{\theta}}{3\rho} + \frac{\cos\phi}{r_0 + \rho\cos\phi} A_{\theta}, \quad (7b)$$

while Eq. (4c) remains the same.

At the surface of the toroidal conductor, i.e., at $\rho = a$ and $\rho = b$, the tangential components of the electric and magnetic fields are continuous. Therefore, in the local coordinate system, the boundary conditions are:

$$E_{\theta}^{\text{in}}(\rho = a, \phi, t) = E_{\theta}^{\text{con}}(\rho = a, \phi, t), \quad (8a)$$

$$E_{\theta}^{\text{out}}(\rho = b, \phi, t) = E_{\theta}^{\text{con}}(\rho = b, \phi, t), \quad (8b)$$

$$B_{\phi}^{\text{in}}(\rho = a, \phi, t) = B_{\phi}^{\text{con}}(\rho = a, \phi, t), \quad (8c)$$

$$B_{\phi}^{\text{out}}(\rho = b, \phi, t) = B_{\phi}^{\text{con}}(\rho = b, \phi, t). \quad (8d)$$

Since the vector potential is zero at $t = 0$, the first two boundary conditions can also be expressed as

$$A_{\theta}^{\text{in}}(\rho = a, \phi, t) = A_{\theta}^{\text{con}}(\rho = a, \phi, t), \quad (9a)$$

$$A_{\theta}^{\text{out}}(\rho = b, \phi, t) = A_{\theta}^{\text{con}}(\rho = b, \phi, t). \quad (9b)$$

Thus, the diffusion fields in the three regions inside and outside the torus and inside the conductor are determined by the solutions of Eqs. (1), (3) and (6) with the boundary conditions given by Eqs. (9a), (9b), (8c) and (8d) on the inner and outer surface of the toroidal conductor.

III. Vector Potential of a Current Ring

In this section, an approximate expression for the vector potential of a current ring external driver is obtained. This is the particular solution of Eq. (1). For that purpose, the toroidal coordinate system associated with the current ring is used. Toroidal coordinates are most appropriate for a toroidal conductor and their significance will become evident in the next section when the arbitrariness as to the value of certain constants in the solution is removed.

The global cylindrical coordinates (r, z) are related to the ring toroidal coordinates (η', ξ') by:

$$r = b_c \frac{\sinh \eta'}{\cosh \eta' - \cos \xi'}, \quad (10a)$$

$$z = b_c \frac{\sin \xi'}{\cosh \eta' - \cos \xi'}, \quad (10b)$$

where b_c is a constant. These relations can be easily inverted, namely:

$$e^{-2\eta'} = \frac{(r - b_c)^2 + z^2}{(r + b_c)^2 + z^2}, \quad (11a)$$

$$e^{-\eta'} \cos \xi' = \frac{1}{2} \left(1 - \frac{b_c}{r}\right) + \frac{1}{2} \left(1 + \frac{b_c}{r}\right) e^{-2\eta'}, \quad (11b)$$

$$e^{-\eta'} \sin \xi' = \frac{z}{2r} (1 - e^{-2\eta'}). \quad (11c)$$

According to Eq. (11a), when η' is fixed, the coordinates (r, z) describe a circle whose radius is $b_c / \sinh \eta'$. If for $\eta' = \eta'_c$ this circle coincides with the current ring surface whose major radius is R_c , then it is straightforward to show that $b_c = [R_c^2 - r_c^2]^{1/2}$. The points (η', ξ') outside

the ring are determined by the inequality $\eta' < \eta'_c$, while the points inside the ring are determined by $\eta' > \eta'_c$.

In the absence of the toroidal conductor, the solution of Eq. (1) for a current ring with constant current density $J_\theta = I_c / \pi r_c^2$ is equal to

$$A_\theta^{\text{ext}} = \frac{\mu_0 I_c}{4\pi^2 r_c^2} \int_V \frac{\cos(\theta' - \theta'')}{|\vec{x}' - \vec{x}''|} d^3x'', \quad (12)$$

where \vec{x}' and \vec{x}'' are the observation point and a point inside the ring, respectively, and the integration is over the volume V of the ring. The Green's function of $|\vec{x}' - \vec{x}''|^{-1}$, in toroidal geometry is equal to ¹⁴

$$\begin{aligned} \frac{1}{|\vec{x}' - \vec{x}''|} &= \frac{1}{\pi b_c} (\cosh \eta' - \cos \xi')^{1/2} (\cosh \eta'' - \cos \xi'')^{1/2} \\ &\times \sum_{m,n=0}^{\infty} \varepsilon_n \varepsilon_m (-1)^n \frac{\Gamma(m-n+\frac{1}{2})}{\Gamma(m+n+\frac{1}{2})} \cos n(\theta' - \theta'') \cos m(\xi' - \xi'') \\ &\times \left\{ \begin{array}{ll} P_m^n - 1/2 (\cosh \eta') Q_m^n - 1/2 (\cosh \eta''); & \eta'' > \eta' \\ P_m^n (\cosh \eta'') Q_m^n - 1/2 (\cosh \eta'); & \eta'' < \eta' \end{array} \right\}, \quad (13) \end{aligned}$$

where $\varepsilon_0 = 1$, $\varepsilon_m = 2$ when $m = 1, 2, 3, \dots$, $\Gamma(x)$ is the gamma function, and $P_m^n - 1/2 (\cosh \eta)$, $Q_m^n - 1/2 (\cosh \eta)$ are the associated Legendre functions of the first and second kind, respectively. Without giving the details of the calculation, substitution of Eq. (13) into Eq. (12) leads to the following expression of the vector potential of the current ring:

$$A_\theta^{\text{ext}} = b_c (\cosh \eta' - \cos \xi')^{1/2} \sum_{m=0}^{\infty} \varepsilon_m a_m^{\text{ext}} Q_m^1 - 1/2 (\cosh \eta') \cos m \xi'$$

$$+ b_c (\cosh \eta' - \cos \xi')^{1/2} \sum_{n=0}^{\infty} \epsilon_n c_n^{\text{ext}} P_n^{1/2} - 1/2 (\cosh \eta') \cos n \xi', \quad (14a)$$

inside the current ring, i.e., when $\eta' > \eta'_c$, and

$$A_{\theta}^{\text{ext}} = b_c (\cosh \eta' - \cos \xi')^{1/2} \sum_{n=0}^{\infty} \epsilon_n b_n^{\text{ext}} P_n^{1/2} - 1/2 (\cosh \eta') \cos n \xi', \quad (14b)$$

outside the current ring, i.e., when $\eta' < \eta'_c$, where

$$a_n^{\text{ext}} = - \frac{4\sqrt{2}\mu_0 I_c b_c}{3\pi^2 r_c^2} \frac{1}{n^2 - \frac{1}{4}} \int_{\eta'_c}^{\eta'} P_n^{1/2} - 1/2 (\cosh \eta'') Q_n^2 - 1/2 (\cosh \eta'') \frac{d\eta''}{\sinh \eta''}, \quad (15a)$$

$$c_n^{\text{ext}} = - \frac{4\sqrt{2}\mu_0 I_c b_c}{3\pi^2 r_c^2} \frac{1}{n^2 - \frac{1}{4}} \int_{\eta'}^{\infty} Q_n^{1/2} - 1/2 (\cosh \eta'') Q_n^2 - 1/2 (\cosh \eta'') \frac{d\eta''}{\sinh \eta''} \quad (15b)$$

$$b_n^{\text{ext}} = - \frac{4\sqrt{2}\mu_0 I_c b_c}{3\pi^2 r_c^2} \frac{1}{n^2 - \frac{1}{4}} \int_{\eta'_c}^{\infty} Q_n^{1/2} - 1/2 (\cosh \eta'') Q_n^2 - 1/2 (\cosh \eta'') \frac{d\eta''}{\sinh \eta''}, \quad (15c)$$

and $\eta'_c = \ln [(R_c + r_c + b_c)/(R_c + r_c - b_c)]$. In the derivation of Eqs. (14a), (14b) from Eq. (12), use was made of the identity¹⁴

$$\int_0^{\pi} \frac{\cos n \xi''}{(\cosh \eta'' - \cos \xi'')^{5/2}} d\xi'' = \frac{4\sqrt{2}}{3 \sinh^2 \eta''} Q_n^2 - 1/2 (\cosh \eta''). \quad (16)$$

The toroidal functions $P_m^n - 1/2 (\cosh \eta)$ and $Q_m^n - 1/2 (\cosh \eta)$ appearing in Eqs. (13), (14a), (14b), (15a), (15b) and (15c) are given by the following exact expressions: 15

$$\begin{aligned}
 P_m^n - 1/2 (\cosh \eta) &= \frac{2^n \Gamma(m)}{\pi^{1/2} \Gamma(m - n + \frac{1}{2})} (\sinh \eta)^n e^{(m - n - \frac{1}{2})\eta} \\
 &+ (1 - \delta_{m0}) \sum_{s=0}^{m-1} \frac{(n + \frac{1}{2})_s (n - m + \frac{1}{2})_s}{s! (1 - m)_s} e^{-2s\eta} \\
 &+ \frac{(-1)^n 2^{n+1} \Gamma(m+n+\frac{1}{2})}{\pi^{3/2} \Gamma(m+1)} (\sinh \eta)^n e^{-(m+n+\frac{1}{2})\eta} \\
 &+ \sum_{s=0}^{\infty} \frac{(n+\frac{1}{2})_s (m+n+\frac{1}{2})_s}{s! (m+1)_s} e^{-2s\eta} [\ln(4e^\eta) + u_s + u_{m+s} - v_{n+s} - v_{m+n+s}],
 \end{aligned}
 \tag{17a}$$

$$\begin{aligned}
 Q_m^n - 1/2 (\cosh \eta) &= \frac{(-1)^n 2^n \pi^{1/2} \Gamma(m+n+\frac{1}{2})}{\Gamma(m+1)} (\sinh \eta)^n \\
 &- (m+n+\frac{1}{2})\eta \sum_{s=0}^{\infty} \frac{(n+\frac{1}{2})_s (m+n+\frac{1}{2})_s}{s! (m+1)_s} e^{-2s\eta},
 \end{aligned}
 \tag{17b}$$

where

$$(a)_s = a(a+1)(a+2)\dots(a+s-1), \quad (a)_0 = 1, \tag{18a}$$

$$u_n = \frac{1}{2} \sum_{k=1}^n \frac{1}{k}, \quad u_0 = 0, \tag{18b}$$

$$v_n = \sum_{k=1}^n \frac{1}{2k-1}, \quad v_0 = 0. \quad (18c)$$

For $n=0$, the first term in Eq. (17a) is omitted, since $\delta_{nn} = 1$ for $n = n$, and $\delta_{nn} = 0$ for $n \neq n$. The expressions above are appropriate for the region inside as well as outside the torus but on its vicinity.

Up to this point, the results given above are exact. In the following, an approximate expression of A_θ^{ext} will be obtained from Eqs. (14a) and (14b) under the assumption of a small aspect ratio r_c/R_c of the current ring by keeping terms up to order $e^{-\eta'_c}$. Notice that, when $r_c/R_c \ll 1$, then to first order in the aspect ratio, or to first order in the toroidal corrections, we have the approximate relations: $b_c \approx R_c$, $e^{-\eta'_c} \approx r_c/2R_c$ and $e^{-\eta'} \approx \rho'/2R_c$. Here, (ρ', ϕ') are the local cylindrical coordinates with respect to the ring position, i.e.,

$$r = R_c + \rho' \cos \phi', \quad (19a)$$

$$z = \rho' \sin \phi'. \quad (19b)$$

Making use of the identity

$$(\cosh \eta' - \cos \xi')^{1/2} = \sum_{n=0}^{\infty} \epsilon_n D_n(\eta') \cos n \xi', \quad (20)$$

where

$$D_0(\eta') = \frac{\sqrt{2}}{2\pi} e^{\eta'} (1 + e^{-2\eta'}) \left[Q_{-1/2}(\cosh \eta') - \frac{2 e^{-\eta'}}{1 + e^{-2\eta'}} Q_{1/2}(\cosh \eta') \right], \quad (21a)$$

$$D_m(\eta') = \frac{\sqrt{2}}{2\pi} e^{\eta'} (1 + e^{-2\eta'}) \left[Q_{m-1/2}(\cosh \eta') - \frac{e^{-\eta'}}{1 + e^{-2\eta'}} (Q_{m-1/2}(\cosh \eta') + Q_{m+1/2}(\cosh \eta')) \right], \quad (21b)$$

and also of Eq. (17b), a straightforward calculation leads to the approximate expression, to first order in toroidal corrections,

$$b_c (\cosh \eta' - \cos \xi')^{1/2} \sum_{m=0}^{\infty} \epsilon_m a_m^{\text{ext}} Q_{m-1/2}^1(\cosh \eta') \cos m \xi' \\ = - \frac{\pi}{2\sqrt{2}} b_c \left[a_0^{\text{ext}} - (a_0^{\text{ext}} - 3 a_1^{\text{ext}}) e^{-\eta'} \cos \xi' \right]. \quad (22)$$

The number of terms kept on the right hand side of Eq. (22) was determined by the fact that the quantities $b_c a_m^{\text{ext}}$ are of zero order in toroidal corrections, as is indicated by Eqs. (15a), (17a) and (17b). Similarly, the quantities $b_c b_m^{\text{ext}}$ and $b_c c_m^{\text{ext}}$ are of order $(b_c/r_c)^2 e^{-2(m+1)\eta'}$ or $(b_c/r_c)^2 e^{-2(m+1)\eta'_c}$ and, consequently, we have the approximate expression

$$b_c (\cosh \eta' - \cos \xi')^{1/2} \sum_{m=0}^{\infty} \epsilon_m b_m^{\text{ext}} P_{m-1/2}^1(\cosh \eta') \cos m \xi' \\ = - \frac{\sqrt{2}}{2\pi} b_c \left[b_0^{\text{ext}} (\ln(4e^{\eta'}) - 2) - b_0^{\text{ext}} (\ln(4e^{\eta'}) - 2) e^{-\eta'} \cos \xi' - 2b_1^{\text{ext}} e^{\eta'} \cos \xi' \right], \quad (23)$$

to first order in toroidal corrections. The same relation above holds for the quantities $b_c c_m^{\text{ext}}$.

From Eqs. (14a), (14b), (19a), (19b), (22) and (23), it follows that in the local coordinate system (ρ', ϕ') of the current ring and to first order in r_c/R_c , we have inside the ring, i.e., when $\rho' \leq r_c$:

$$\begin{aligned}
A_{\theta}^{\text{ext}} = & -\frac{\pi}{2\sqrt{2}} R_c \left[a_0^{\text{ext}} - \frac{1}{2} (a_0^{\text{ext}} - 3 a_1^{\text{ext}}) \frac{\rho' \cos \phi'}{R_c} \right] \\
& - \frac{\sqrt{2}}{2\pi} R_c \left[c_0^{\text{ext}} \left(\ln \frac{8R_c}{\rho'} - 2 \right) + \frac{c_0^{\text{ext}}}{2} \left(\frac{\rho' \cos \phi'}{R_c} - \frac{r_c^2 \cos \phi'}{R_c \rho'} \right) \right. \\
& \left. - \frac{c_0^{\text{ext}}}{2} \frac{\rho' \cos \phi'}{R_c} \left(\ln \frac{8R_c}{\rho'} - 2 \right) - 4c_1^{\text{ext}} \frac{R_c \cos \phi'}{\rho'} \right], \quad (24a)
\end{aligned}$$

while outside the ring, i.e., when $\rho' \geq r_c$, we have:

$$\begin{aligned}
A_{\theta}^{\text{ext}} = & -\frac{\sqrt{2}}{2\pi} R_c \left[b_0^{\text{ext}} \left(\ln \frac{8R_c}{\rho'} - 2 \right) + \frac{b_0^{\text{ext}}}{2} \left(\frac{\rho' \cos \phi'}{R_c} - \frac{r_c^2 \cos \phi'}{R_c \rho'} \right) \right. \\
& \left. - \frac{b_0^{\text{ext}}}{2} \frac{\rho' \cos \phi'}{R_c} \left(\ln \frac{8R_c}{\rho'} - 2 \right) - 4b_1^{\text{ext}} \frac{R_c \cos \phi'}{\rho'} \right]. \quad (24b)
\end{aligned}$$

Next, we need the approximate expressions, to first order in r_c/R_c , for the quantities $R_c a_m^{\text{ext}}$, $R_c c_m^{\text{ext}}$ and $R_c b_m^{\text{ext}}$, when $m = 0, 1$. From Eqs. (15a), (15b), (15c), (17a), and (17b), it is easy to show that

$$R_c a_0^{\text{ext}} = -\frac{\sqrt{2} \mu_0 I_c}{\pi^2} \left[\ln \frac{8R_c}{r_c} - \frac{3}{2} - \left(\frac{\rho'}{r_c} \right)^2 \left(\ln \frac{8R_c}{\rho'} - \frac{3}{2} \right) \right], \quad (25a)$$

$$R_c a_1^{\text{ext}} = \frac{5 \sqrt{2} \mu_0 I_c}{6\pi^2} \left[\left(\frac{\rho'}{r_c} \right)^2 - 1 \right], \quad (25b)$$

$$R_c c_0^{\text{ext}} = -\frac{\sqrt{2}}{2} \mu_0 I_c \left(\frac{\rho'}{r_c} \right)^2, \quad (25c)$$

$$R_c c_1^{\text{ext}} = \frac{5 \sqrt{2} \mu_0 I_c}{64} \frac{\rho'^4}{R_c^2 r_c^2}, \quad (25d)$$

$$R_{c b_0}^{\text{ext}} = -\frac{\sqrt{2}}{2} \mu_0 I_c, \quad (25e)$$

$$R_{c b_1}^{\text{ext}} = \frac{5 \sqrt{2} \mu_0 I_c}{64} \left(\frac{r_c}{R_c} \right)^2. \quad (25f)$$

Substitution of Eqs. (25a) through (25f) into Eqs. (24a) and (24b) leads to the following expressions for A_θ^{ext} to first order in r_c/R_c in the local coordinate system of the ring:

$$\begin{aligned} A_\theta^{\text{ext}} = & \frac{\mu_0}{2\pi} I_c \left[\ln \frac{8R_c}{r_c} - \frac{3}{2} - \frac{1}{2} \left(\frac{\rho'}{r_c} \right)^2 \right] \\ & - \frac{\mu_0}{4\pi} I_c \frac{\rho' \cos \phi'}{R_c} \left[\ln \frac{8R_c}{r_c} - 3 - \frac{1}{4} \left(\frac{\rho'}{r_c} \right)^2 \right], \end{aligned} \quad (26a)$$

when $\rho' \leq r_c$, and

$$\begin{aligned} A_\theta^{\text{ext}} = & \frac{\mu_0}{2\pi} I_c \left[\ln \frac{8R_c}{\rho'} - 2 \right] \\ & - \frac{\mu_0}{4\pi} I_c \frac{\rho' \cos \phi'}{R_c} \left[\ln \frac{8R_c}{\rho'} - 3 - \frac{1}{4} \left(\frac{r_c}{\rho'} \right)^2 \right], \end{aligned} \quad (26b)$$

when $\rho' \geq r_c$. Let (Δ, α) be the ring position in the local cylindrical coordinates of the toroidal conductor (cf. Eqs. (5a), (5b)). Then, in the relation above, R_c , ρ' and $\rho' \cos \phi'$ are replaced by

$$R_c = r_0 + \Delta \cos \alpha, \quad (27a)$$

$$\rho' = \left[\rho^2 + \Delta^2 - 2 \rho \Delta \cos (\phi - \alpha) \right]^{1/2}, \quad (27b)$$

$$\rho' \cos \phi' = \rho \cos \phi - \Delta \cos \alpha. \quad (27c)$$

Equations (26a) and (26b) are useful in the diffusion problem of a current ring inside a toroidal conducting shell with first order toroidal corrections. This will be reported elsewhere. Here, only the zero order solution to the diffusion problem is considered. In this case, the vector potential of the current ring, in the absence of the conductor, is equal to

$$A_{\theta 0}^{\text{ext}} = \frac{\mu_0}{2\pi} I_c \left[\ln \frac{8r_0}{r_c} - \frac{3}{2} - \frac{1}{2} \left(\frac{\rho'}{r_c} \right)^2 \right], \quad (28a)$$

inside the ring, and

$$A_{\theta 0}^{\text{ext}} = \frac{\mu_0}{2\pi} I_c \left[\ln \frac{8r_0}{\rho'} - 2 \right], \quad (28b)$$

outside the ring. Equation (28b) can also be written as:

$$\begin{aligned} A_{\theta 0}^{\text{ext}} &= \frac{\mu_0}{2\pi} I_c \left(\ln \frac{8r_0}{\rho} - 2 \right) \\ &- \frac{\mu_0}{4\pi} I_c \ln \left[1 + \left(\frac{\Delta}{\rho} \right)^2 - 2 \frac{\Delta}{\rho} \cos (\phi - \alpha) \right]. \end{aligned} \quad (28c)$$

This expression of the ring vector potential is used in the application of the boundary conditions at the inner surface of the toroidal conductor.

IV. Homogeneous Solution of the Vector Potential

Inside the torus, the most general solution of Eq. (1) is

$$A_{\theta}^{\text{in}} = A_{\theta}^{\text{ext}} + A_{\theta h}^{\text{in}}, \quad (29)$$

where $A_{\theta h}^{\text{in}}$ is the homogeneous solution of Eq. (1). The exact homogeneous solution can be expressed most appropriately in toroidal coordinates with respect to the toroidal conductor rather than the current ring. For that purpose, we replace ξ', η', b_c by $\xi_1, \eta_1, b_1 = [r_0^2 - a^2]^{1/2}$, in Eqs. (10a), (10b), (11a), (11b), and (11c). When $\eta_1 = \eta_{1c}$, where $\eta_{1c} = \ln[(r_0 + a + b_1)/(r_0 + a - b_1)]$, the coordinates (r, z) describe a circle which coincides with the inner surface of the toroidal conductor. In terms of the toroidal coordinates (η_1, ξ_1) , the exact homogeneous solution of Eq. (1) inside the torus is

$$A_{\theta h}^{\text{in}} = b_1 (\cosh \eta_1 - \cos \xi_1)^{1/2} \sum_{m=0}^{\infty} \epsilon_m Q_m^{-1/2} (\cosh \eta_1) * [\tilde{a}_m^{(c)} \cos m \xi_1 + \tilde{a}_m^{(s)} \sin m \xi_1]. \quad (30)$$

For small aspect ratio a/r_0 , and, to lowest order in this ratio, we have the approximate relations:

$$b_1 = r_0, \quad e^{-\eta_{1c}} = a/2r_0 \quad \text{and} \quad e^{-(\eta_1 + i\xi_1)} = \rho e^{-i\phi/2r_0},$$

where (ρ, ϕ) are the local cylindrical coordinates with respect to the toroidal conductor (cf. Eqs. (5a), (5b)). Moreover, if it is assumed that each of the coefficients $b_1 \tilde{a}_m^{(c)}, b_1 \tilde{a}_m^{(s)}$ is of order $(r_0/a)^m$, then it follows from Eqs. (17b) and (30) that the homogeneous solution of Eq. (1), to zero order in toroidal corrections, is equal to

$$A_{\theta 0}^{\text{in}} = b_1 \sum_{m=0}^{\infty} \epsilon_m \frac{\pi^{1/2} \Gamma(m + \frac{3}{2})}{2^{1/2} \Gamma(m + 1)} \left(\frac{\rho}{2r_0}\right)^m$$

$$* \left[\tilde{a}_m^{(c)} \cos m\phi + \tilde{a}_m^{(s)} \sin m\phi \right]. \quad (31)$$

By redefining the coefficients $\tilde{a}_m^{(c)}$, $\tilde{a}_m^{(s)}$, in terms of the zero order coefficients a_0 , $a_m^{(c)}$, $a_m^{(s)}$, we conclude from Eqs. (29) and (31) that the most general solution inside the torus (inside and outside the current ring) and to zero order in toroidal corrections is

$$A_{\theta 0}^{\text{in}} = A_{\theta 0}^{\text{ext}} + a_0 + \sum_{m=1}^{\infty} \left(\frac{\rho}{a}\right)^m \left[a_m^{(c)} \cos m\phi + a_m^{(s)} \sin m\phi \right] \quad (32)$$

The undefined coefficients a_0 , $a_m^{(c)}$, $a_m^{(s)}$ will be determined from the boundary conditions.

The homogeneous zero order solution $A_{\theta 0}^{\text{in}}$ satisfies also the zero order homogeneous equation

$$\frac{1}{\rho} \frac{\partial}{\partial \rho} \rho \frac{\partial A_{\theta 0}}{\partial \rho} + \frac{1}{\rho^2} \frac{\partial^2 A_{\theta 0}}{\partial \phi^2} = 0, \quad (33)$$

which follows from Eq. (1) by expressing it in the local coordinates of the toroidal conductor (cf. Eq. (6)) and neglecting the terms with toroidal corrections.

For the vector potential outside the torus, we define the toroidal coordinates (η_0, ξ_0) in a similar fashion, i.e., we replace ξ' , η' and b_c by ξ_0 , η_0 , $b_0 = [r_0^2 - b^2]^{1/2}$, in Eqs. (10a), (10b), (11a), (11b) and (11c). When $\eta_0 = \eta_{0c}$, where $\eta_{0c} = \ln[(r_0 + b + b_0)/(r_0 + b - b_0)]$, the coordinates (r, z) describe a circle which coincides with the outer surface of the toroidal conductor. In terms of the toroidal coordinates (η_0, ξ_0) , the exact solution of Eq. (3) outside the torus is

$$A_{\theta}^{\text{out}} = b_0 (\cosh \eta_0 - \cos \xi_0)^{1/2} \sum_{m=0}^{\infty} \epsilon_m P_m^1 - 1/2 (\cosh \eta_0) \\ * [\bar{b}_m^{(c)} \cos m \xi_0 + \bar{b}_m^{(s)} \sin m \xi_0]. \quad (34)$$

As before, for small aspect ratio b/r_0 , we have the approximate relations:

$b_0 = r_0$, $e^{-\eta_0} = b/2r_0$ and $e^{\eta_0 + i\xi_0} = 2r_0 e^{i\phi/\rho}$. If it is assumed that each of the coefficients $b_0 \bar{b}_m^{(c)}$, $b_0 \bar{b}_m^{(s)}$ is of order $(b/r_0)^m$, then it follows from Eqs. (17a) and (34) that the solution of Eq. (3), to zero order in toroidal corrections, is equal to

$$A_{\theta 0}^{\text{out}} = \left(\ln \frac{8r_0}{\rho} - 2 \right) b_0 + \sum_{m=1}^{\infty} \left(\frac{b}{\rho} \right)^m [b_m^{(c)} \cos m\phi + b_m^{(s)} \sin m\phi]. \quad (35)$$

Here, the coefficients $\bar{b}_m^{(c)}$, $\bar{b}_m^{(s)}$ have been redefined in terms of the zero order coefficients b_0 , $b_m^{(c)}$, $b_m^{(s)}$. These undefined coefficients will be determined from the boundary conditions.

It is apparent that Eq. (35) satisfies the zero order homogeneous equation (33), but the solution of Eq. (33) does not provide all the information included in Eq. (35). The most general solution of Eq. (33) which is independent of the toroidal angle ϕ is equal to $C_0 + C_1 \ln \rho$ where C_0 and C_1 are arbitrary constants. But Eq. (35) indicates that these two constants are related to each other and their dependence on each other is established only by solving the problem in toroidal geometry rather than making some ad hoc assumption. For example, if we assumed that, at infinite time, the vector potential outside the conductor is equal to that of the current ring in the absence of the conductor, we would probably obtain the correct relationship between C_0 and C_1 , but this assumption

would be imposed on the solution of the diffusion problem rather than coming out naturally as a result from the solution.

V. Initial Conditions of the Vector Potential

When I_c , Δ and α are time dependent quantities, the coefficients a_0 , $a_n^{(c)}$, $a_n^{(s)}$, b_0 , $b_n^{(c)}$, and $b_n^{(s)}$ in Eqs. (32) and (35) are also time dependent. Since outside the torus the vector potential is zero at $t = 0$, $b_0(t)$, $b_n^{(c)}(t)$ and $b_n^{(s)}(t)$ are also zero at $t = 0$. In addition, the vector potential is zero at $t = 0$ inside the conductor. From the continuity of the vector potential at the inner surface of the conductor and from Eq. (32), it follows that the coefficients $a_0(t)$, $a_n^{(c)}(t)$, $a_n^{(s)}(t)$ are not zero at $t = 0$. Since the image fields constitute a zero order homogeneous solution inside the torus, it is convenient to redefine the as yet undetermined coefficients

$a_n^{(c)}(t)$, $a_n^{(s)}(t)$ by subtracting the image solution from them, so that they are zero at $t = 0$. As to the coefficient $a_0(t)$, in order that it becomes zero at $t = 0$, it is convenient to redefine it by replacing it with $a_0(t) - (\mu_0/2\pi)I_c(t) (\ln 8r_0/a - 2)$. Then, Eq. (32) should be replaced by

$$\begin{aligned} A_{\theta 0}^{\text{in}}(\rho, \phi, t) = & \frac{\mu_0}{4\pi} I_c(t) \left[2 \left(\ln \frac{a}{r_c} + \frac{1}{2} \right) \right. \\ & - \frac{\rho^2 + \Delta^2(t) - 2\rho \Delta(t) \cos(\phi - \alpha(t))}{r_c^2} \\ & + \ln \left(1 + \left(\frac{\rho \Delta(t)}{a^2} \right)^2 - 2 \frac{\rho \Delta(t)}{a^2} \cos(\phi - \alpha(t)) \right) \Big] \\ & + a_0(t) + \sum_{n=1}^{\infty} \left(\frac{\rho}{a} \right)^n \left[a_n^{(c)}(t) \cos n\phi + a_n^{(s)}(t) \sin n\phi \right], \end{aligned} \quad (36a)$$

inside the ring, and

$$\begin{aligned}
 A_{\theta 0}^{\text{in}}(\rho, \phi, t) = & \frac{\mu_0}{4\pi} I_c(t) \left[2 \ln \frac{a}{\rho} \right. \\
 & - \ln \left(1 + \left(\frac{\Delta(t)}{\rho} \right)^2 - 2 \frac{\Delta(t)}{\rho} \cos(\phi - \alpha(t)) \right) \\
 & + \ln \left(1 + \left(\frac{\rho \Delta(t)}{a^2} \right)^2 - 2 \frac{\rho \Delta(t)}{a^2} \cos(\phi - \alpha(t)) \right) \Big] \\
 & + a_0(t) + \sum_{n=1}^{\infty} \left(\frac{\rho}{a} \right)^n \left[a_n^{(c)}(t) \cos n\phi + a_n^{(s)}(t) \sin n\phi \right],
 \end{aligned} \tag{36b}$$

outside the current ring but inside the torus. The vector potential from the image has a logarithmic singularity at the image position $(a^2/\Delta(t), \alpha(t))$, which lies outside the inner surface of the conductor. Therefore, inside the torus, it is a zero order homogeneous solution of Eq. (33).

When $\Delta(t)/\rho < 1$, Eq. (36b) is equivalent to

$$\begin{aligned}
 A_{\theta 0}^{\text{in}}(\rho, \phi, t) = & \frac{\mu_0}{2\pi} I_c(t) \left[\ln \frac{a}{\rho} \right. \\
 & - \sum_{n=1}^{\infty} \frac{1}{n} \left(\frac{\Delta(t)}{a} \right)^n \left(\left(\frac{\rho}{a} \right)^n - \left(\frac{a}{\rho} \right)^n \right) \cos n(\phi - \alpha(t)) \Big] \\
 & + a_0(t) + \sum_{n=1}^{\infty} \left(\frac{\rho}{a} \right)^n \left[a_n^{(c)}(t) \cos n\phi + a_n^{(s)}(t) \sin n\phi \right], \tag{37}
 \end{aligned}$$

where $a_0(t)$, $a_n^{(c)}(t)$, $a_n^{(s)}(t)$ are zero at $t = 0$. The zero initialization of these coefficients will lead to simple expressions when the boundary conditions will be applied in the next Section.

VI. Diffusion Fields Inside and Outside the Toroidal Conductor

In order to compute the fields, the zero order diffusion equation must be solved inside the conductor and the boundary conditions be applied on its inner and outer surface. The zero order diffusion equation is obtained from Eq. (6) by omitting the toroidal corrections, namely,

$$\frac{1}{\rho} \frac{\partial}{\partial \rho} \rho \frac{\partial A_{\theta 0}^{\text{con}}}{\partial \rho} + \frac{1}{\rho^2} \frac{\partial^2 A_{\theta 0}^{\text{con}}}{\partial \phi^2} - \mu_0 \sigma \frac{\partial A_{\theta 0}^{\text{con}}}{\partial t} = 0 \quad (38)$$

In general, let

$$\hat{f}(p) = \int_0^\infty f(t) e^{-pt} dt, \quad (39)$$

be the Laplace transform of $f(t)$. Then, in the Laplace transform domain, Eq. (38) becomes

$$\frac{1}{\rho} \frac{\partial}{\partial \rho} \rho \frac{\partial \hat{A}_{\theta 0}^{\text{con}}}{\partial \rho} + \frac{1}{\rho^2} \frac{\partial^2 \hat{A}_{\theta 0}^{\text{con}}}{\partial \phi^2} - \mu_0 \sigma p \hat{A}_{\theta 0}^{\text{con}} = 0, \quad (40)$$

where $A_{\theta 0}^{\text{con}}(\rho, \phi, t)$ was assumed to be zero at $t = 0$. The most general solution of Eq. (40) is

$$\begin{aligned} \hat{A}_{\theta 0}^{\text{con}}(\rho, \phi, p) = & \hat{c}_0(p) I_0(\lambda \rho) \\ & + \sum_{m=1}^{\infty} I_m(\lambda \rho) \left[\hat{c}_m^{(c)}(p) \cos m\phi + \hat{c}_m^{(s)}(p) \sin m\phi \right] \\ & + \hat{d}_0(p) K_0(\lambda \rho) + \sum_{m=1}^{\infty} K_m(\lambda \rho) \left[\hat{d}_m^{(c)}(p) \cos m\phi + \hat{d}_m^{(s)}(p) \sin m\phi \right], \quad (41) \end{aligned}$$

where

$$\lambda = [\mu_0 \sigma p]^{1/2}, \quad (42)$$

and $I_m(x)$, $K_m(x)$ are the modified Bessel functions of order m .

The boundary conditions, to zero order in toroidal corrections, follow from Eqs. (7a), (7b), (8c), (8d), (9a), (9b) and (39). They are given by

$$\hat{A}_{\theta 0}^{\text{in}}(a, \phi, p) = \hat{A}_{\theta 0}^{\text{con}}(a, \phi, p), \quad (43a)$$

$$\left. \frac{\partial \hat{A}_{\theta 0}^{\text{in}}(\rho, \phi, p)}{\partial \rho} \right|_{\rho=a} = \left. \frac{\partial \hat{A}_{\theta 0}^{\text{con}}(\rho, \phi, p)}{\partial \rho} \right|_{\rho=a}, \quad (43b)$$

and the same two relations at $\rho=b$. Defining $\hat{F}_m^{(c)}(p)$ and $\hat{F}_m^{(s)}(p)$ to be the Laplace transforms of $(\Delta(t)/a)^m \cos m \alpha(t)$ and $(\Delta(t)/a)^m \sin m \alpha(t)$, respectively, the boundary conditions at $\rho=a$ and $\rho=b$, using Eqs. (35), (37) and (41), lead to the following algebraic system of equations:

$$\hat{a}_0(p) = \hat{c}_0(p)I_0(\lambda a) + \hat{d}_0(p)K_0(\lambda a), \quad (44a)$$

$$-\frac{\mu_0}{2\pi} \hat{I}_c(p) = \lambda a [\hat{c}_0(p)I'_0(\lambda a) + \hat{d}_0(p)K'_0(\lambda a)], \quad (44b)$$

$$\left(\ln \frac{8r_0}{b} - 2 \right) \hat{b}_0(p) = \hat{c}_0(p)I_0(\lambda b) + \hat{d}_0(p)K_0(\lambda b), \quad (44c)$$

$$-\hat{b}_0(p) = \lambda b [\hat{c}_0(p)I'_0(\lambda b) + \hat{d}_0(p)K'_0(\lambda b)], \quad (44d)$$

when $m=0$, and

$$\hat{a}_m^{(i)}(p) = \hat{c}_m^{(i)}(p)I_m(\lambda a) + \hat{d}_m^{(i)}(p)K_m(\lambda a), \quad (45a)$$

$$- \frac{\mu_0}{\kappa} \hat{f}_m^{(i)}(p) + m \hat{a}_m^{(i)}(p) - \lambda a \left[\hat{c}_m^{(i)}(p) I'_m(\lambda a) + \hat{d}_m^{(i)}(p) K'_m(\lambda a) \right] \quad (45b)$$

$$\hat{b}_m^{(i)}(p) = \hat{c}_m^{(i)}(p) I_m(\lambda b) + \hat{d}_m^{(i)}(p) K_m(\lambda b) \quad (45c)$$

$$- m \hat{b}_m^{(i)}(p) = \lambda b \left[\hat{c}_m^{(i)}(p) I'_m(\lambda b) + \hat{d}_m^{(i)}(p) K'_m(\lambda b) \right], \quad (45d)$$

when $m = 1, 2, \dots$, and $i = c, s$. Also, $I'_m(x)$, $K'_m(x)$ are the derivatives of $I_m(x)$, $K_m(x)$. The solution of the first algebraic system of Eqs. (44a) - (44d) is

$$\hat{a}_0(p) = \frac{\mu_0}{2\kappa} \hat{I}_c(p) \frac{\tilde{g}_0(\lambda)}{\tilde{f}_0(\lambda)}, \quad (46a)$$

$$\hat{b}_0(p) = \frac{\mu_0}{2\kappa} \hat{I}_c(p) \frac{1}{\tilde{f}_0(\lambda)}, \quad (46b)$$

$$\hat{c}_0(p) = \hat{b}_0(p) \left[\left(\ln \frac{8r_0}{b} - 2 \right) \lambda b K_1(\lambda b) - K_0(\lambda b) \right], \quad (46c)$$

$$\hat{d}_0(p) = \hat{b}_0(p) \left[\left(\ln \frac{8r_0}{b} - 2 \right) \lambda b I_1(\lambda b) + I_0(\lambda b) \right], \quad (46d)$$

where

$$\begin{aligned} \tilde{f}_0(\lambda) = & \left(\ln \frac{8r_0}{b} - 2 \right) \lambda a \lambda b \left[K_1(\lambda a) I_1(\lambda b) - I_1(\lambda a) K_1(\lambda b) \right] \\ & + \lambda a \left[K_1(\lambda a) I_0(\lambda b) + I_1(\lambda a) K_0(\lambda b) \right], \end{aligned} \quad (47a)$$

$$\tilde{g}_0(\lambda) = \left(\ln \frac{8r_0}{b} - 2 \right) \lambda b \left[K_0(\lambda a) I_1(\lambda b) + I_0(\lambda a) K_1(\lambda b) \right]$$

$$+ K_0(\lambda a) I_0(\lambda b) - I_0(\lambda a) K_0(\lambda b). \quad (47b)$$

Similarly, the solution of the second algebraic system of Eqs. (45a) - (45d) is

$$\hat{a}_m^{(i)}(p) = \frac{\mu_0}{2K} \hat{p}_m^{(i)}(p) \frac{\tilde{g}_m(\lambda)}{\tilde{f}_m(\lambda)}, \quad (48a)$$

$$\hat{b}_m^{(i)}(p) = \frac{\mu_0}{2K} \hat{p}_m^{(i)}(p) \frac{1}{\tilde{f}_m(\lambda)}, \quad (48b)$$

$$\hat{c}_m^{(i)}(p) = \hat{b}_m^{(i)}(p) \lambda b K_{m-1}(\lambda b), \quad (48c)$$

$$\hat{d}_m^{(i)}(p) = \hat{b}_m^{(i)}(p) \lambda b I_{m-1}(\lambda b), \quad (48d)$$

where

$$\tilde{f}_m(\lambda) = -\frac{\lambda a \lambda b}{2} [I_{m+1}(\lambda a) K_{m-1}(\lambda b) - K_{m+1}(\lambda a) I_{m-1}(\lambda b)], \quad (49a)$$

$$\tilde{g}_m(\lambda) = \lambda b [I_m(\lambda a) K_{m-1}(\lambda b) + K_m(\lambda a) I_{m-1}(\lambda b)], \quad (49b)$$

and $m = 1, 2, 3, \dots, i = c, s$.

The inverse Laplace transforms of the coefficients given above are determined from the sum of the residues at the poles of these coefficients. The poles are computed at the zeroes of $\tilde{f}_m(\lambda_{mk}) = 0$, where $m = 0, 1, 2, \dots, k = 0, 1, 2, \dots$. Since all the zeroes occur for imaginary values of λ , we define the real quantities α_{mk} by means of the relation $\lambda_{mk} = i\alpha_{mk}$. Then a pole occurs at $p_{mk} = -\alpha_{mk}^2/\mu_0\sigma$ (cf. Eq. (42)) and the inverse Laplace transform $h_m(t)$ of $\tilde{g}_m(\lambda)/\tilde{f}_m(\lambda)$ is

$$h_n(t) = \sum_{k=0}^{\infty} \frac{\tilde{g}_n(i\alpha_{nk})}{\left. \frac{d\lambda}{dp} \right|_{\lambda=i\alpha_{nk}}} \frac{F'_n(i\alpha_{nk})}{F'_n(i\alpha_{nk})} e^{-\frac{\alpha_{nk}^2}{\mu_0 \sigma} t} \Theta(t), \quad (50)$$

where $F'_n(z)$ is the derivative of $F_n(z)$ and $\Theta(t) = 1$, when $t > 0$, while $\Theta(t) = 0$, when $t < 0$. Using the convolution theorem in the Laplace transform domain, we obtain the following expressions for the coefficients inside and outside the torus:

$$a_0(t) = \sum_{k=0}^{\infty} A_{ok} U_{ok}(t), \quad (51a)$$

$$b_0(t) = \sum_{k=0}^{\infty} B_{ok} U_{ok}(t), \quad (51b)$$

$$a_n^{(i)}(t) = \sum_{k=0}^{\infty} A_{nk} U_{nk}^{(i)}(t), \quad (51c)$$

$$b_n^{(i)}(t) = \sum_{k=0}^{\infty} B_{nk} U_{nk}^{(i)}(t), \quad (51d)$$

where $n = 1, 2, \dots$, $i = c, s$, and

$$U_{ok}(t) = \frac{1}{\tau_{ok}} e^{-t/\tau_{ok}} \int_0^{t/\tau_{ok}} e^{t'/\tau_{ok}} \frac{\mu_0}{2\pi} I_c(t') dt', \quad (52a)$$

$$U_{nk}^{(c)}(t) = \frac{1}{\tau_{nk}} e^{-t/\tau_{nk}} \int_0^{t/\tau_{nk}} e^{t'/\tau_{nk}} \frac{\mu_0}{2\pi} I_c(t') \left(\frac{\Delta(t')}{a} \right)^m \cos m\alpha(t') dt', \quad (52b)$$

$$U_{mk}^{(s)}(t) = \frac{1}{\tau_{mk}} e^{-t/\tau_{mk}} \int_0^t e^{t'/\tau_{mk}} \frac{\mu_0}{2\pi} I_c(t') \left(\frac{\Delta(t')}{a} \right)^m \sin m\alpha(t') dt', \quad (52c)$$

Also,

$$\frac{1}{\tau_{mk}} = \frac{\alpha_{mk}^2}{\mu_0 \sigma}, \quad (53a)$$

$$A_{mk} = - \frac{2g_m(\alpha_{mk})}{\alpha_{mk} f'_m(\alpha_{mk})}, \quad (53b)$$

$$B_{mk} = - \frac{2}{\alpha_{mk} f'_m(\alpha_{mk})}, \quad (53c)$$

where $m = 0, 1, 2, \dots$ $k = 0, 1, 2, \dots$ Finally, the functions $f_m(\alpha)$, $g_m(\alpha)$ and the derivative $f'_m(\alpha)$ of $f_m(\alpha)$ are as follows:

$$f_0(\alpha) = \tilde{f}_0(i\alpha) \quad (54a)$$

$$= \frac{\pi}{2} x_0 [J_1(x_0)Y_0(x_1) - Y_1(x_0)J_0(x_1)]$$

$$- \frac{\pi}{2} \left(\ln \frac{8r_0}{b} - 2 \right) x_0 x_1 [J_1(x_0)Y_1(x_1) - Y_1(x_0)J_1(x_1)],$$

$$f_m(\alpha) = \tilde{f}_m(i\alpha) = \frac{\pi}{2} \frac{x_0 x_1}{2} [J_{m+1}(x_0)Y_{m-1}(x_1) - Y_{m+1}(x_0)J_{m-1}(x_1)], \quad (54b)$$

$$g_0(\alpha) = \tilde{g}_0(i\alpha) = \frac{\pi}{2} [J_0(x_0)Y_0(x_1) - Y_0(x_0)J_0(x_1)] \quad (55a)$$

$$- \frac{\pi}{2} \left(\ln \frac{8r_0}{b} - 2 \right) x_1 [J_0(x_0)Y_1(x_1) - Y_0(x_0)J_1(x_1)],$$

$$g_m(\alpha) = \tilde{g}_m(i\alpha) = \frac{\pi}{2} x_1 [J_m(x_0)Y_{m-1}(x_1) - Y_m(x_0)J_{m-1}(x_1)], \quad (55b)$$

$$\alpha f'_0(\alpha) = i\alpha f'_0(i\alpha) \quad (56a)$$

$$\begin{aligned} &= f_0(\alpha) + \frac{\pi}{2} x_0^2 [J_0(x_0)Y_0(x_1) - Y_0(x_0)J_0(x_1)] \\ &+ \frac{\pi}{2} \left(\ln \frac{8r_0}{b} - 2 \right) x_0 x_1 [J_1(x_0)Y_1(x_1) - Y_1(x_0)J_1(x_1)] \\ &- \frac{\pi}{2} \left[\left(\ln \frac{8r_0}{b} - 2 \right) x_1^2 + 1 \right] x_0 [J_1(x_0)Y_0(x_1) - Y_1(x_0)J_0(x_1)] \\ &- \frac{\pi}{2} \left(\ln \frac{8r_0}{b} - 2 \right) x_0^2 x_1 [J_0(x_0)Y_1(x_1) - Y_0(x_0)J_1(x_1)], \end{aligned}$$

$$\alpha f'_m(\alpha) = i\alpha f'_m(i\alpha) \quad (56b)$$

$$\begin{aligned} &= \frac{\pi}{2} \frac{x_0^2 x_1}{2} [J_m(x_0)Y_{m-1}(x_1) - Y_m(x_0)J_{m-1}(x_1)] \\ &- \frac{\pi}{2} \frac{x_0^2 x_1^2}{2} [J_{m+1}(x_0)Y_m(x_1) - Y_{m+1}(x_0)J_m(x_1)], \end{aligned}$$

where $x_0 = \alpha a$, $x_1 = \alpha b$, $m = 1, 2, \dots$ and $J_m(x)$, $Y_m(x)$ are the Bessel functions of order m . Notice that α_{mk} are the zeroes of $f_m(\alpha_{mk}) = 0$, for $m = 0, 1, 2, \dots$, $k = 0, 1, 2, \dots$

From Eqs. (36a), (36b), (35), (51a)-(51d), we conclude that the zero order vector potential inside the ring is equal to

$$\begin{aligned} A_{\Theta 0}^{in}(\rho, \phi, t) &= \frac{\mu_0}{4\pi} I_c(t) \left[2 \left(\ln \frac{a}{r_c} + \frac{1}{2} \right) \right. \\ &\left. - \frac{\rho^2 + \Delta^2(t) - 2\rho\Delta(t)\cos(\phi - \alpha(t))}{r_c^2} \right] \end{aligned} \quad (57a)$$

$$\begin{aligned}
& + \ln \left(1 + \left(\frac{\rho \Delta(t)}{a^2} \right)^2 - 2 \frac{\rho \Delta(t)}{a^2} \cos (\phi - \alpha(t)) \right) \Bigg] \\
& + \sum_{k=0}^{\infty} A_{ok} U_{ok}(t) + \sum_{m=1}^{\infty} \sum_{k=0}^{\infty} A_{mk} \left(\frac{\rho}{a} \right)^m \left[U_{mk}^{(c)}(t) \cos m\phi + U_{mk}^{(s)}(t) \sin m\phi \right].
\end{aligned}$$

Outside the ring and inside the torus (i.e., $\rho \leq a$), it is equal to

$$\begin{aligned}
A_{\theta 0}^{\text{in}}(\rho, \phi, t) &= \frac{\mu_0}{4R} I_c(t) \left[2 \ln \frac{a}{\rho} \right. \\
&- \ln \left(1 + \left(\frac{\Delta(t)}{\rho} \right)^2 - 2 \frac{\Delta(t)}{\rho} \cos (\phi - \alpha(t)) \right) \\
&+ \ln \left(1 + \left(\frac{\rho \Delta(t)}{a^2} \right)^2 - 2 \frac{\rho \Delta(t)}{a^2} \cos (\phi - \alpha(t)) \right) \Bigg] \\
&+ \sum_{k=0}^{\infty} A_{ok} U_{ok}(t) + \sum_{m=1}^{\infty} \sum_{k=0}^{\infty} A_{mk} \left(\frac{\rho}{a} \right)^m \left[U_{mk}^{(c)}(t) \cos m\phi + U_{mk}^{(s)}(t) \sin m\phi \right]
\end{aligned} \tag{57b}$$

and outside the torus (i.e., $\rho \geq b$) it is equal to

$$\begin{aligned}
A_{\theta 0}^{\text{out}}(\rho, \phi, t) &= \left(\ln \frac{8r_0}{\rho} - 2 \right) \sum_{k=0}^{\infty} B_{ok} U_{ok}(t) \\
&+ \sum_{m=1}^{\infty} \sum_{k=0}^{\infty} B_{mk} \left(\frac{\rho}{b} \right)^m \left[U_{mk}^{(c)}(t) \cos m\phi + U_{mk}^{(s)}(t) \sin m\phi \right].
\end{aligned} \tag{58}$$

From Eqs. (52a), (52b) and (52c) it is easy to show that the time dependent coefficients $U_{ok}(t)$, $U_{mk}^{(c)}(t)$, $U_{mk}^{(s)}(t)$ satisfy the first order differential equations

$$\dot{U}_{ok}(t) + \frac{1}{\tau_{ok}} U_{ok}(t) = \frac{1}{\tau_{ok}} \frac{\mu_0}{2R} I_c(t), \tag{59a}$$

$$\dot{U}_{mk}^{(c)}(t) + \frac{1}{\tau_{mk}} U_{mk}^{(c)}(t) = \frac{1}{\tau_{mk}} \frac{\mu_0}{2\pi} I_c(t) \left(\frac{\Delta(t)}{a} \right)^m \cos m\alpha(t) \quad (59b)$$

$$\dot{U}_{mk}^{(s)}(t) + \frac{1}{\tau_{mk}} U_{mk}^{(s)}(t) = \frac{1}{\tau_{mk}} \frac{\mu_0}{2\pi} I_c(t) \left(\frac{\Delta(t)}{a} \right)^m \sin m\alpha(t) \quad (59c)$$

with initial conditions $U_{ok}(0) = U_{mk}^{(c)}(0) = U_{mk}^{(s)}(0) = 0$, for $m = 1, 2, \dots, k = 0, 1, 2, \dots$. These differential equations are very useful when the current ring moves and its equations of motion depend on the diffusion fields, i.e., when the ring dynamics is coupled to the diffusion fields. Then, the state vector of the system consists not only of the position and velocity of the ring, but also of the diffusion coefficients $U_{ok}(t)$, $U_{mk}^{(c)}(t)$, $U_{mk}^{(s)}(t)$, for $m = 1, 2, \dots, k = 0, 1, 2, \dots$, and its time derivative is determined by the ring dynamics, as well as by Eqs. (59a)-(59c). Notice that it is much easier to solve in the computer a set of coupled first order differential equations rather than a set of coupled first order differential equations and the convolution integrals given by Eqs. (52a)-(52c).

Next, four exact identities will be established for the time independent coefficients A_{mk} , B_{mk} . For a motionless, step function ring current, i.e., when $I_c(t) = I_0 \Theta(t)$, Eqs. (51a)-(51d) and Eqs. (52a)-(52c) give

$$a_0(t) = \frac{\mu_0}{2\pi} I_0 \sum_{k=0}^{\infty} A_{ok} \left(1 - e^{-t/\tau_{ok}} \right), \quad (60a)$$

$$b_0(t) = \frac{\mu_0}{2\pi} I_0 \sum_{k=0}^{\infty} B_{ok} \left(1 - e^{-t/\tau_{ok}} \right), \quad (60b)$$

$$a_m^{(c)}(t) + i a_m^{(s)}(t) = \frac{\mu_0}{2\pi} I_0 \left(\frac{\Delta}{a}\right)^m e^{im\alpha} \sum_{k=0}^{\infty} A_{mk} (1 - e^{-t/\tau_{mk}}), \quad (60c)$$

$$b_m^{(c)}(t) + i b_m^{(s)}(t) = \frac{\mu_0}{2\pi} I_0 \left(\frac{\Delta}{a}\right)^m e^{im\alpha} \sum_{k=0}^{\infty} B_{mk} (1 - e^{-t/\tau_{mk}}), \quad (60d)$$

The Laplace transform of $I_c(t)$ is $\hat{I}_c(p) = I_0/p$, and we have from Eqs. (46a), (46b), (48a), (48b):

$$\hat{a}_0(p) = \frac{\mu_0}{2\pi} I_0 \frac{1}{p} \frac{\tilde{g}_0(\lambda)}{\tilde{f}_0(\lambda)}, \quad (61a)$$

$$\hat{b}_0(p) = \frac{\mu_0}{2\pi} I_0 \frac{1}{p} \frac{1}{\tilde{f}_0(\lambda)}, \quad (61b)$$

$$\hat{a}_m^{(c)}(p) + i \hat{a}_m^{(s)}(p) = \frac{\mu_0}{2\pi} I_0 \left(\frac{\Delta}{a}\right)^m e^{im\alpha} \frac{1}{p} \frac{\tilde{g}_m(\lambda)}{\tilde{f}_m(\lambda)}, \quad (61c)$$

$$\hat{b}_m^{(c)}(p) + i \hat{b}_m^{(s)}(p) = \frac{\mu_0}{2\pi} I_0 \left(\frac{\Delta}{a}\right)^m e^{im\alpha} \frac{1}{p} \frac{1}{\tilde{f}_m(\lambda)}, \quad (61d)$$

From the well-known theorem of Laplace transforms it follows that $\lim_{t \rightarrow 0} f(t) = \lim_{p \rightarrow \infty} p f(p)$. Eqs. (47a), (47b), (49a), (49b), give

$$\lim_{\lambda \rightarrow 0} \tilde{f}_0(\lambda) = 1, \quad (62a)$$

$$\lim_{\lambda \rightarrow 0} \tilde{g}_0(\lambda) = \ln \frac{8r_0}{a} - 2, \quad (62b)$$

$$\lim_{\lambda \rightarrow 0} \tilde{f}_m(\lambda) = m \left(\frac{b}{a}\right)^m, \quad (62c)$$

$$\lim_{\lambda \rightarrow 0} \bar{g}_m(\lambda) = \left(\frac{b}{a}\right)^m. \quad (62d)$$

Application of the theorem just mentioned in Eqs. (60a)-(60d) and Eqs. (61a)-(61d), in conjunction with Eqs. (62a)-(62d) leads to the following identities:

$$\sum_{k=0}^{\infty} A_{ok} = \ln \frac{8r_o}{a} - 2, \quad (63a)$$

$$\sum_{k=0}^{\infty} B_{ok} = 1, \quad (63b)$$

$$\sum_{k=0}^{\infty} A_{mk} = \frac{1}{m}, \quad (63c)$$

$$\sum_{k=0}^{\infty} B_{mk} = \frac{1}{m} \left(\frac{a}{b}\right)^m. \quad (63d)$$

These identities have been verified by the computer for a thin as well as a thick conducting wall. Substitution of these identities into Eqs. (60a)-(60d) when $t \rightarrow \infty$, leads to

$$\lim_{t \rightarrow \infty} a_o(t) = \frac{\mu_o}{2\pi} I_o \left(\ln \frac{8r_o}{a} - 2 \right), \quad (64a)$$

$$\lim_{t \rightarrow \infty} b_o(t) = \frac{\mu_o}{2\pi} I_o, \quad (64b)$$

$$\lim_{t \rightarrow \infty} \left[a_m^{(c)}(t) + i a_m^{(s)}(t) \right] = \frac{\mu_o}{2\pi} I_o \frac{1}{m} \left(\frac{\Delta}{a}\right)^m e^{im\alpha}, \quad (64c)$$

$$\lim_{t \rightarrow \infty} \left[b_m^{(c)}(t) + i b_m^{(s)}(t) \right] = \frac{\mu_o}{2\pi} I_o \frac{1}{m} \left(\frac{\Delta}{b}\right)^m e^{im\alpha}. \quad (64d)$$

With the help of these identities and Eqs. (35), (36a) and (36b), it is easy to show that, as $t \rightarrow \infty$, the zero order vector potential inside and outside the toroidal conductor (as well as inside the ring) becomes equal to that of the current ring in the absence of the conductor, i.e., it becomes equal to $A_{\theta 0}^{\text{ext}}$, due to the diffusion process. This conclusion demonstrates the importance of the identities (63a)-(63d).

The magnetic and electric fields inside and outside the torus can be computed from Eqs. (57a), (57b) and (58). Thus, the self-magnetic and self-electric fields, i.e., the fields of the ring at its centroid $\rho = \Delta(t)$, $\phi = \alpha(t)$, are equal to

$$B_{\theta \rho}^{\text{self}}(t) = \sum_{n=1}^{\infty} \sum_{k=0}^{\infty} \frac{n}{a} A_{nk} \left(\frac{\Delta(t)}{a} \right)^{n-1} \quad (65a)$$

$$* \left[-U_{nk}^{(s)}(t) \cos n\alpha(t) + U_{nk}^{(c)}(t) \sin n\alpha(t) \right],$$

$$B_{\theta \phi}^{\text{self}}(t) = -\frac{\mu_0}{2\pi} I_c(t) \frac{\Delta(t)}{a^2} \frac{1}{1 - \left(\frac{\Delta(t)}{a} \right)^2} \quad (65b)$$

$$+ \sum_{n=1}^{\infty} \sum_{k=0}^{\infty} \frac{n}{a} A_{nk} \left(\frac{\Delta(t)}{a} \right)^{n-1}$$

$$* \left[U_{nk}^{(c)}(t) \cos n\alpha(t) + U_{nk}^{(s)}(t) \sin n\alpha(t) \right],$$

$$E_{\theta 0}^{\text{self}}(t) = -\frac{\mu_0}{2\pi} \dot{I}_c(t) \left[\ln \frac{a}{r_c} + \frac{1}{2} + \ln \left(1 - \left(\frac{\Delta(t)}{a} \right)^2 \right) \right]$$

$$+ \frac{\mu_0}{2\pi} I_c(t) \frac{\frac{x_c(t)\dot{x}_c(t) + z_c(t)\dot{z}_c(t)}{a^2}}{1 - \left(\frac{\Delta(t)}{a} \right)^2}$$

$$- \sum_{k=0}^{\infty} \frac{A_{ok}}{\tau_{ok}} \left[\frac{\mu_0}{2R} I_c(t) - U_{ok}(t) \right] \quad (65c)$$

$$- \sum_{n=1}^{\infty} \sum_{k=0}^{\infty} \frac{A_{nk}}{\tau_{nk}} \left(\frac{\Delta(t)}{a} \right)^n \left[\frac{\mu_0}{2R} I_c(t) \left(\frac{\Delta(t)}{a} \right)^n \right.$$

$$\left. - U_{nk}^{(c)}(t) \cos n\alpha(t) - U_{nk}^{(s)}(t) \sin n\alpha(t) \right],$$

where $x_c(t) = \Delta(t) \cos \alpha(t)$ and $z_c(t) = \Delta(t) \sin \alpha(t)$.

The last three relations, and in particular the B_{op}^{self} component were useful in providing an analytical model for the beam trapping that occurs after injection in the modified betatron accelerator.

A typical example of the effect that the diffusion process has on the ring dynamics, immediately after injection is shown in Fig. 2. The numerical integration of the ring equations of motion coupled with the diffusion fields was done for the parameters listed in Table I. Figure 2(a) shows the projection of the centroid orbit on the r - z plane that moves with the same toroidal angular velocity as the ring centroid. There is a slow (bounce) motion and, due to the presence of the stellarator windings (i.e., strong focusing), there is also an intermediate motion. Both of these modes are indicated in Fig. 2(a). Since there are six field periods of the stellarator field in the range $0 \leq \theta \leq 2\pi$, the electrons perform six oscillations during one revolution around the major axis. To take into account the intermediate motion that has been neglected in the diffusion model presented in this paper, the resistivity in the code is computed

using the skin depth that corresponds to the intermediate frequency and not the actual thickness of the wall. The dots in Fig. 2(b) show the positions the beam crosses the r-z plane at $\theta = 0^\circ$. The time difference between two dots is equal to the period around the major axis, i.e., ~ 27 nsec, and therefore the speed of the ring on the r-z plane can be inferred from the relative position of the dots. Fig. 2(c) provides the relativistic factor γ vs. time and the reduction in γ is obvious due to the energy lost on the resistive wall and to establish the electromagnetic field outside the torus. Another example is given in reference 13, which refers to the beam trapping in the modified betatron accelerator and is in good agreement with the experimental results.

VII. Approximate Results for a Thin Conducting Wall

The results presented in the previous Sections are approximate in the sense that they include only zero order toroidal corrections, i.e., are valid only for small aspect ratio vessels. Otherwise, they are exact. In this Section, the additional assumption is made that the conducting wall is thin. This assumption allows us to compute approximate expressions of the zeroes α_{mk} of $f_m(\alpha_{mk}) = 0$ (cf. Eqs. (54a), (54b)) and of the vector potential and the fields.

When the conducting wall is thin, i.e., $(b-a)/a \ll 1$, both $x_0 = \alpha a$ and $x_1 = \alpha b$, where α is a zero of $f_m(\alpha) = 0$, are very large numbers and the asymptotic expansions of the Bessel functions can be used in Eqs. (54a), (54b). This is valid only up to some maximum value of m . Keeping terms up to order $1/z$, the asymptotic expansions of $J_n(z)$, $Y_n(z)$ are: ¹⁶

$$J_n(z) \sim \sqrt{\frac{2}{\pi z}} \left[\cos X_n - \frac{4n^2 - 1}{8z} \sin X_n \right], \quad (66a)$$

$$Y_n(z) \sim \sqrt{\frac{2}{\pi z}} \left[\sin X_n + \frac{4n^2 - 1}{8z} \cos X_n \right], \quad (66b)$$

where $X_n = z - (n + 1/2) \pi/2$. We substitute these expansions into Eqs. (54a), (54b). Then, the zeroes of $f_0(\alpha_{ok}) = 0$ are determined from

$$\tan(x_1 - x_0) = \frac{1}{\left(\ln \frac{8r_0}{b} - 2 \right) x_0}, \quad (67a)$$

while the zeroes of $f_m(\alpha_{mk}) = 0$ are determined from

$$\tan(x_1 - x_0) = \frac{2m}{x_0}. \quad (67b)$$

A more accurate expression for the zeroes of $f_m(\alpha_{mk}) = 0$, correct to order $(m/x_0)^2$, is derived in the Appendix, and is given by

$$\tan(x_1 - x_0) = \frac{\frac{2m}{x_0} - \frac{3}{2} \frac{m^2 - \frac{1}{4}}{x_0^2} + \frac{1}{2} \left(\frac{b-a}{a}\right)^2 x_0}{1 - \left(m - \frac{1}{2}\right) \frac{b-a}{a} + \left(m - \frac{3}{2}\right) \left(m + \frac{1}{2}\right) \left(\frac{b-a}{a}\right)^2} x_0. \quad (67c)$$

If $x_0 \gg 1$, we see from Eq. (67a) that $|x_1 - x_0| \ll 1$. Therefore, $\tan(x_1 - x_0) = x_1 - x_0 = (b-a)\alpha$, and one of the zeroes is

$$\alpha_{00} = \left[\frac{1}{\left(\ln \frac{8r_0}{b} - 2 \right) a(b-a)} \right]^{1/2}, \quad (68a)$$

while the others are given by

$$\alpha_{0k} = \frac{k\pi}{b-a}, \quad (68b)$$

where $k = 1, 2, \dots$. The small additive correction term $1/[k\pi(\ln(8r_0/b) - 2)a]$ has been omitted in Eq. (68b). The zeroes of Eq. (67b) can be obtained in a similar fashion, except when m is as large or larger than x_0 . Let $m = 1, 2, \dots, M$, where $M = \text{Int}[a/4(b-a)]$, and $\text{Int}(x)$ is the integral part of x . Then one set of zeroes of Eq. (67b) is approximately given by

$$\alpha_{m0} = \left[\frac{2m}{a(b-a)} \right]^{1/2}, \quad (69a)$$

with an error of only a few percent when $(b-a)/a \leq 10^{-2}$. For m as specified above and $k = 1, 2, \dots, K$, where $K = \text{Int}[a/\pi(b-a)]$, the rest of the zeroes are given by

$$\alpha_{mk} = \frac{k\pi}{b-a}. \quad (69b)$$

The small correction term $[2m + (k\kappa)^2/2]/(k\kappa a)$ has been omitted in Eq. (69b). For values of m and k larger than M and K , respectively, the zeroes should be computed numerically from Eq. (54b). Notice that the presence of the terms $(\rho/a)^m$ and $(b/\rho)^m$ in the series expansions of the vector potential and the fields indicates that the large values of m become important when these quantities are computed close to the conducting wall, where ρ/a and b/ρ become almost equal to 1 and more m -terms must be included in the sums to converge within a prescribed accuracy. An estimate of the minor radius ρ_1 within which the vector potential and the fields are sufficiently accurate is determined by $\rho_1/a = [(b-a)/a]^{1/M}$. Since $(b-a)/a \ll 1$, all the terms associated with $(\rho/a)^m$, for $m = M+1, M+2, \dots$ in the series expansions of the vector potential and the fields, have a negligible contribution, provided $\rho \leq \rho_1$. A similar argument can be made for the vector potential and the fields outside the torus. Their accuracy is within a few percent when $\rho \geq \rho_0$, where $\rho_0/a = [a/(b-a)]^{1/M}$. Within the distances $d_1 = a - \rho_1$ and $d_0 = \rho_0 - b$ from the inner and outer conducting walls the zeroes (and, therefore, the vector potential and the fields) cannot be computed analytically in terms of a simple expression. In this case they should be computed numerically from Eq. (54b) and then use the analytic expressions for the vector potential and the fields. As an example, when $(b-a)/a = 10^{-3}$, then $M = 250$, $K = 318$, $d_1/a = 0.027$, $d_0/a = 0.028$, but when $(b-a)/a = 10^{-2}$, then $M = 25$, $K = 31$, $d_1/a = 0.17$, $d_0/a = 0.20$. In the following, the various quantities will be computed to order $(b-a)/a$, with the understanding that they are not accurate close to the conducting wall. But in the limit when the ratio $(b-a)/a$ tends to zero (but $\sigma(b-a)/a$ remains finite), i.e., when the toroidal conductor becomes a toroidal conducting shell, the distances d_1, d_0 are zero and the results become exact, to zero order in toroidal corrections, everywhere inside as well as outside and in the vicinity of the torus.

Under the assumptions stated above, the time constants τ_{mk} in Eq. (53a) become

$$\tau_{00} = 2 \tau_D \left(\ln \frac{8r_0}{b} - 2 \right), \quad (70a)$$

$$\tau_{0k} = \frac{\tau_{FD}}{k^2}, \quad (70b)$$

$$\tau_{m0} = \frac{\tau_D}{m}, \quad (70c)$$

$$\tau_{mk} = \frac{\tau_{FD}}{k^2}, \quad (70d)$$

where

$$\tau_D = \frac{\mu_0 \sigma (b - a) a}{2}, \quad (71a)$$

$$\tau_{FD} = \frac{\mu_0 \sigma (b - a)^2}{\pi^2}, \quad (71b)$$

and $m = 1, 2, \dots$, $k = 1, 2, \dots$. Therefore, there are three characteristic time constants associated with the diffusion process. The "loop" diffusion time τ_{00} is the slowest and determines the speed with which the external field of the ring diffuses into the hole of the doughnut. This time is present because of the toroidal geometry of the conductor. The "cylinder" diffusion time τ_D and the "fast" diffusion time τ_{FD} are associated with the diffusion process in a cylinder and determine the speed with which the field of the ring penetrates the conducting wall. Notice that, in the limit of a toroidal conducting shell, any terms associated with the fast diffusion time τ_{FD} diffuse instantaneously at $t = 0$ outside the torus.

This explains the origin of the electric field that is immediately established at $t = 0$ outside the torus for the shell model (cf. statement after Eq. (90) in the next section). On the other hand, we know from Eq. (58), that the magnetic field does not diffuse instantaneously at $t = 0$ outside the torus.

Under the same assumptions stated above and to lowest order in $(b - a)/a$, we have the following approximate relations

$$A_{00} = \ln \frac{8r_0}{a} - 2 - \frac{1}{3} \frac{b - a}{a}, \quad (72a)$$

$$A_{0k} = \frac{2}{(k\pi)^2} \frac{b - a}{a}, \quad (72b)$$

$$A_{m0} = \frac{1}{m} - \frac{2}{3} \frac{b - a}{a}, \quad (72c)$$

$$A_{mk} = \frac{4}{(k\pi)^2} \frac{b - a}{a}, \quad (72d)$$

$$B_{00} = 1 + \frac{1}{6 \left(\ln \frac{8r_0}{b} - 2 \right)} \frac{b - a}{a}, \quad (73a)$$

$$B_{0k} = \frac{2 (-1)^k}{\left(\ln \frac{8r_0}{b} - 2 \right) (k\pi)^2} \frac{b - a}{a}, \quad (73b)$$

$$B_{m0} = \frac{1}{m} + \frac{4}{3} \frac{b - a}{a}, \quad (73c)$$

$$B_{mk} = \frac{4 (-1)^k}{(k\pi)^2} \frac{b - a}{a}, \quad (73d)$$

for $m = 1, 2, \dots$, $k = 1, 2, \dots$. The relations (73b), (73d) were derived directly from Eqs. (56a), (56b), while the relations (72b), (72d) were derived with the help of Eqs. (73b), (73d) and the relations $g_0(\alpha_{0k}) = (-1)^k (\ln 8r_0/a - 2)$, $g_m(\alpha_{mk}) = (-1)^k$, for $m = 1, 2, \dots$, $k = 1, 2, \dots$

Finally, A_{oo} , A_{mo} , B_{oo} , B_{mo} were derived using the identities (63a) - (63d).

As mentioned above, the terms associated with the fast diffusion time τ_{PD} vary in time on a much faster time scale than the terms associated with the times τ_{oo} and τ_D . If the ring current $I_c(t)$ and its position ($\Delta(t)$, $\alpha(t)$) vary slowly within a few e-folds of τ_{PD} , then the part of the vector potential (or the fields) which is associated with τ_{PD} can be simplified considerably.

First, let us consider the self-magnetic field. Substitution of Eqs. (70b), (70d) and Eqs. (72a) - (72d) into Eqs. (65a), (65b) leads to the relations

$$B_{op}^{self}(t) = \frac{1}{a} \sum_{n=1}^{\infty} \left(1 - \frac{2n}{3} \frac{b-a}{a}\right) \left(\frac{\Delta(t)}{a}\right)^{n-1} \quad (74a)$$

$$\begin{aligned} & * \left[-U_{mo}^{(s)}(t) \cos n\alpha(t) + U_{mo}^{(c)} \sin n\alpha(t) \right] \\ & + \frac{4}{\pi^2} \frac{b-a}{a^2} \sum_{k=1}^{\infty} \frac{1}{\tau_{PD}} \int_0^t h_s^{self}(t, t-t') e^{-\frac{t'}{\tau_{PD}} k^2} dt', \end{aligned}$$

$$\begin{aligned} B_{o\phi}^{self}(t) = & -\frac{\mu_0}{2\pi} I_c(t) \frac{\Delta(t)}{a^2} \frac{1}{1 - \left(\frac{\Delta(t)}{a}\right)^2} \\ & + \frac{1}{a} \sum_{n=1}^{\infty} \left(1 - \frac{2n}{3} \frac{b-a}{a}\right) \left(\frac{\Delta(t)}{a}\right)^{n-1} \quad (74b) \end{aligned}$$

$$* \left[U_{mo}^{(c)}(t) \cos n\alpha(t) + U_{mo}^{(s)}(t) \sin n\alpha(t) \right]$$

$$+ \frac{4}{\pi^2} \frac{b-a}{a^2} \sum_{k=1}^{\infty} \frac{1}{\tau_{FD}} \int_0^t h_c^{\text{self}}(t, t-t') e^{-\frac{t'}{\tau_{FD}} k^2} dt',$$

where

$$h_c^{\text{self}}(t, t') = \frac{\mu_0}{2\pi} I_c(t') \frac{\Delta(t')}{a} \quad (75a)$$

$$\star \frac{\left[1 + \left(\frac{\Delta(t)\Delta(t')}{a^2}\right)^2\right] \cos(\alpha(t) - \alpha(t')) - 2 \frac{\Delta(t)\Delta(t')}{a^2}}{\left[1 + \left(\frac{\Delta(t)\Delta(t')}{a^2}\right)^2 - 2 \frac{\Delta(t)\Delta(t')}{a^2} \cos(\alpha(t) - \alpha(t'))\right]^2},$$

$$h_s^{\text{self}}(t, t') = \frac{\mu_0}{2\pi} I_c(t') \frac{\Delta(t')}{a} \quad (75b)$$

$$\star \frac{\left[1 - \left(\frac{\Delta(t)\Delta(t')}{a^2}\right)^2\right] \sin(\alpha(t) - \alpha(t'))}{\left[1 + \left(\frac{\Delta(t)\Delta(t')}{a^2}\right)^2 - 2 \frac{\Delta(t)\Delta(t')}{a^2} \cos(\alpha(t) - \alpha(t'))\right]^2}.$$

If $I_c(t - t')$, $\Delta(t - t')$, $\alpha(t - t')$ vary only slightly as t' varies within a few e-folds of τ_{FD} , they can be replaced by $I_c(t)$, $\Delta(t)$ and $\alpha(t)$, except in the sine in Eq. (75b) we should set $\alpha(t) - \alpha(t - t') = \alpha'(t)t'$ to get the lowest order contribution. Here $\alpha'(t)$ is the derivative of $\alpha(t)$.

Equations (74a) and (74b) then become

$$B_{op}^{\text{self}}(t) = \frac{1}{a} \sum_{m=1}^{\infty} \left(1 - \frac{2m}{3} \frac{b-a}{a}\right) \left(\frac{\Delta(t)}{a}\right)^{m-1}$$

$$\star \left[-U_{mo}^{(s)}(t) \cos m\alpha(t) + U_{mo}^{(c)}(t) \sin m\alpha(t) \right]$$

$$\begin{aligned}
& + \frac{b-a}{a} \frac{2\mu_0}{\pi^3} I_c(t) \alpha'(t) \tau_{FD} \frac{\Delta(t)}{a^2} \frac{1 + \left(\frac{\Delta(t)}{a}\right)^2}{\left[1 - \left(\frac{\Delta(t)}{a}\right)^2\right]^3} \\
& * \sum_{k=1}^{\infty} \frac{1}{k^2} \left(1 - \frac{t}{\tau_{FD}} e^{-\frac{t}{\tau_{FD}} k^2} \right), \tag{76a}
\end{aligned}$$

$$\begin{aligned}
B_{o\phi}^{\text{self}}(t) &= - \frac{\mu_0}{2\pi} I_c(t) \frac{\Delta(t)}{a^2} \frac{1}{1 - \left(\frac{\Delta(t)}{a}\right)^2} \\
& + \frac{1}{a} \sum_{n=1}^{\infty} \left(1 - \frac{2n}{3} \frac{b-a}{a} \right) \left(\frac{\Delta(t)}{a} \right)^{n-1} \\
& * \left[U_{m0}^{(c)}(t) \cos n\alpha(t) + U_{m0}^{(s)}(t) \sin n\alpha(t) \right] \\
& + \frac{b-a}{a} \frac{2\mu_0}{\pi^3} I_c(t) \frac{\Delta(t)}{a^2} \frac{1}{\left[1 - \left(\frac{\Delta(t)}{a}\right)^2\right]^2} \\
& * \sum_{k=1}^{\infty} \frac{1}{k^2} \left(1 - e^{-\frac{t}{\tau_{FD}} k^2} \right). \tag{76b}
\end{aligned}$$

After a few e-folds of τ_{FD} , the sum over k becomes equal to $\pi^2/6$ and there is a residual contribution in the self-magnetic field from the fast diffusing terms. Since $(b-a)/a \ll 1$, Eqs. (76a), (76b) indicate that this contribution is small unless the ring is close to the conducting wall. But in that region, these relations are no longer valid and, therefore, they provide only a hint as to the significance of the fast diffusing terms when the ring is close to the conducting wall.

From Eqs. (65c), (70b) (70d) and Eqs. (72a) - (72d), and to lowest order in $(b - a)/a$, the electric field at the ring centroid is given by

$$\begin{aligned}
 E_{\theta 0}^{\text{self}}(t) = & -\frac{\mu_0}{2\pi} \dot{I}_c(t) \left[\ln \frac{a}{r_c} + \frac{1}{2} + \ln \left(1 - \left(\frac{\Delta(t)}{a} \right)^2 \right) \right] \\
 & + \frac{\mu_0}{2\pi} I_c(t) \frac{\frac{x_c(t)\dot{x}_c(t) + z_c(t)\dot{z}_c(t)}{a^2}}{1 - \left(\frac{\Delta(t)}{a} \right)^2} \\
 & + \frac{1}{2\tau_D} \left[U_{00}(t) + 2 \sum_{m=1}^{\infty} \left(\frac{\Delta(t)}{a} \right)^m \left[U_{m0}^{(c)}(t) \cos m\alpha(t) + U_{m0}^{(s)}(t) \sin m\alpha(t) \right] \right] \\
 & - \frac{1}{\tau_D} \left[\frac{\mu_0}{4\pi} I_c(t) + h_e^{\text{self}}(t, t) \right] \quad (77) \\
 & - \frac{1}{\tau_D} \frac{\mu_0}{4\pi} 2 \sum_{k=1}^{\infty} \left[I_c(t) - \frac{k^2}{\tau_{FD}} \int_0^t I_c(t-t') e^{-\frac{t'}{\tau_{FD}} k^2} dt' \right] \\
 & - \frac{1}{\tau_D} 2 \sum_{k=1}^{\infty} \left[h_e^{\text{self}}(t, t) - \frac{k^2}{\tau_{FD}} \int_0^t h_e^{\text{self}}(t, t-t') e^{-\frac{t'}{\tau_{FD}} k^2} dt' \right],
 \end{aligned}$$

where

$$\begin{aligned}
 h_e^{\text{self}}(t, t') = & \frac{\mu_0}{2\pi} I_c(t') \frac{\Delta(t)\Delta(t')}{a^2} \quad (78) \\
 & * \frac{\cos(\alpha(t) - \alpha(t')) - \frac{\Delta(t)\Delta(t')}{a^2}}{1 + \left(\frac{\Delta(t)\Delta(t')}{a^2} \right)^2 - 2 \frac{\Delta(t)\Delta(t')}{a^2} \cos(\alpha(t) - \alpha(t'))}.
 \end{aligned}$$

When $I_c(t)$, $\Delta(t)$, $\alpha(t)$ vary slowly, in a similar fashion as for the self-magnetic field, we obtain the simplified equation for the self-electric field

$$\begin{aligned}
 E_{\theta 0}^{\text{self}}(t) = & -\frac{\mu_0}{2\pi} \dot{I}_c(t) \left[\ln \frac{a}{r_c} + \frac{1}{2} + \ln \left(1 - \left(\frac{\Delta(t)}{a} \right)^2 \right) \right] \\
 & + \frac{\mu_0}{2\pi} I_c(t) \frac{\frac{x_c(t)\dot{x}_c(t) + z_c(t)\dot{z}_c(t)}{a^2}}{1 - \left(\frac{\Delta(t)}{a} \right)^2} \\
 & + \frac{1}{2\tau_D} \left[U_{00}(t) + 2 \sum_{m=1}^{\infty} \left(\frac{\Delta(t)}{a} \right)^m \left[U_{m0}^{(c)}(t) \cos m\alpha(t) + U_{m0}^{(s)}(t) \sin m\alpha(t) \right] \right] \\
 & - \frac{\mu_0}{4\pi} \frac{I_c(t)}{\tau_D} \theta_3(0, e^{-t/\tau_{FD}}) \left[1 + 2 \frac{\left(\frac{\Delta(t)}{a} \right)^2}{1 - \left(\frac{\Delta(t)}{a} \right)^2} \right], \quad (79)
 \end{aligned}$$

where $\theta_3(z, q)$ is the theta function of order 3,¹⁶ i.e.,

$$\theta_3(z, q) = 1 + 2 \sum_{k=1}^{\infty} q^{k^2} \cos 2kz. \quad (80)$$

Notice that $\theta_3(0, q)$ can be expressed in terms of the complete elliptic integral of the first kind $K(m)$, i.e., $\theta_3(0, q) = [2K(m)/\pi]^{1/2}$. Here, m is related with the nome q by the relation $q = \exp[-\pi K(1-m)/K(m)]$ and when q tends to 1, then m tends also to 1. When $t/\tau_{FD} \ll 1$, the nome q is very close to 1, and in this case $K(1-m) \approx K(0) = \pi/2$, so that

$[2K(m)/\pi]^{1/2} \approx [\pi/\ln(1/q)]^{1/2}$. Therefore, $\theta_3(0, e^{-t/\tau_{FD}}) \approx [\pi/(t/\tau_{FD})]^{1/2}$, i.e., the self-electric field is proportional to $I_c(t)[\tau_{FD}/t]^{1/2}$ when $t/\tau_{FD} \ll 1$. If the ring current is a step function of time, i.e., $I_c(t) = I_0 \theta(t)$, then the self-electric field is infinite at $t = 0$ (actually, it is infinite everywhere inside the torus). This result is not surprising if we

take into account that the vector potential rises in time instantaneously at $t = 0$, because the ring current does so. When $t/\tau_{FD} \gg 1$, we have $\theta_3(0, e^{-t/\tau_{FD}}) \approx 1$ and the fast diffusing part in E_{∞}^{self} provides a residual contribution.

Finally, consider the electric field outside the torus, i.e., when $\rho \geq b$. From Eqs. (4c), (58), (59a)-(59c), (70d) and Eqs. (72a)-(72d) we see that, to lowest order in $(b-a)/a$, it is given by

$$\begin{aligned}
 E_{\infty}^{out}(\rho, \phi, t) = & \frac{1}{2\tau_D} \left[\frac{\ln \frac{8r_0}{\rho} - 2}{\ln \frac{8r_0}{b} - 2} U_{00}(t) \right. \\
 & \left. + 2 \sum_{m=1}^{\infty} \left(\frac{b}{\rho} \right)^m \left(U_{m0}^{(c)}(t) \cos m\phi + U_{m0}^{(s)}(t) \sin m\phi \right) \right] \\
 & - \frac{1}{\tau_D} \left[\frac{\ln \frac{8r_0}{\rho} - 2}{\ln \frac{8r_0}{b} - 2} \frac{\mu_0}{4\pi} I_c(t) + h_0(\rho, \phi, t) \right] \\
 & - \frac{1}{\tau_D} \frac{\ln \frac{8r_0}{\rho} - 2}{\ln \frac{8r_0}{b} - 2} \frac{\mu_0}{4\pi} 2 \sum_{k=1}^{\infty} (-1)^k \left[I_c(t) - \frac{k^2}{\tau_{FD}} \int_0^t I_c(t-t') e^{-\frac{t'}{\tau_{FD}} k^2} dt' \right] \\
 & - \frac{1}{\tau_D} 2 \sum_{k=1}^{\infty} (-1)^k \left[h_0(\rho, \phi, t) - \frac{k^2}{\tau_{FD}} \int_0^t h_0(\rho, \phi, t-t') e^{-\frac{t'}{\tau_{FD}} k^2} dt' \right],
 \end{aligned} \tag{81}$$

where

$$h_0(\rho, \phi, t) = \frac{\mu_0}{2\pi} I_c(t) \frac{b\Delta(t)}{\rho a} \tag{82}$$

$$* \frac{\cos(\phi - \alpha(t)) - \frac{b\Delta(t)}{pa}}{1 + \left(\frac{b\Delta(t)}{pa}\right)^2 - 2 \frac{b\Delta(t)}{pa} \cos(\phi - \alpha(t))}.$$

When $I_c(t)$, $\Delta(t)$, $\alpha(t)$ vary slowly, Eq. (81) simplifies to

$$\begin{aligned} E_{\theta 0}^{\text{out}}(\rho, \phi, t) = & \frac{1}{2\tau_D} \left[\frac{\ln \frac{8r_0}{\rho} - 2}{\ln \frac{8r_0}{b} - 2} U_{00}(t) \right. \\ & \left. + 2 \sum_{n=1}^{\infty} \left(\frac{b}{\rho}\right)^n \left(U_{n0}^{(c)}(t) \cos n\phi + U_{n0}^{(s)}(t) \sin n\phi \right) \right] \\ & - \theta_4\left(0, e^{-t/\tau_{FD}}\right) \frac{1}{\tau_D} \left[\frac{\ln \frac{8r_0}{\rho} - 2}{\ln \frac{8r_0}{b} - 2} \frac{\mu_0}{4\pi} I_c(t) + h_0(\rho, \phi, t) \right] \end{aligned} \quad (83)$$

where $\theta_4(z, q)$ is the theta function of order 4,¹⁶ i.e.,

$$\theta_4(z, q) = 1 + 2 \sum_{k=1}^{\infty} (-1)^k q^{k^2} \cos 2kz. \quad (84)$$

Notice that $\theta_4(0, q) = [(1-m)^{1/2} 2 K(m)/\pi]^{1/2}$. When $t/\tau_{FD} \ll 1$, the nome q is very close to 1 and in this case, $K(m) \approx (1/2) \ln[16/(1-m)]$ and $2 K(m)/\pi \approx \pi/\ln(1/q)$. Therefore, we have

$$\theta_4\left(0, e^{-t/\tau_{FD}}\right) \approx 2 \left[\frac{\pi}{t/\tau_{FD}} e^{-\frac{\pi^2}{2(t/\tau_{FD})}} \right]^{1/2}, \quad (85)$$

i.e., when the ring current is a step function of time, the electric field is zero at $t = 0$ outside the torus. On the other hand, when

$t/\tau_{PD} \gg 1$, then $\theta_4(0, e^{-t/\tau_{PD}}) = 1$ and the electric field reduces to that computed from the shell model. It appears, therefore, that the fast diffusing part in $E_{\theta 0}^{out}$ contributes the exact amount needed for $E_{\theta 0}^{out}$ to vanish at $t = 0$, but very quickly $E_{\theta 0}^{out}$ increases to the value predicted by the shell model when the conducting wall is thin.

To calculate the wall current density $J_{\theta 0}^{wall}(\rho, \phi, t) = \sigma E_{\theta 0}^{con}(\rho, \phi, t)$, the electric field inside the conductor is needed. From the continuity of the electric field at the inner and outer surfaces of the conductor and when $t/\tau_{PD} \ll 1$, $E_{\theta 0}^{con}$ varies from a very large value at the inner surface to a very small value at the outer surface. However, when $t/\tau_{PD} \gg 1$, but $t/\tau_D \ll 1$, and in the special case of a thin conducting wall, it is easy to show from Eqs. (57b), (72a), (72c) and (83) that the electric fields at the inner and outer surface are approximately equal to each other. In the extreme case of the shell model, they become exactly equal to each other, and the surface wall current density is equal to $J_{\theta s}^{wall}(\phi, t) = \sigma(b-a)E_{\theta 0}^{out}(a, \phi, t)$, where $E_{\theta 0}^{out}(a, \phi, t)$ is given by Eq. (83). The surface wall current $I_s^{wall}(t)$ is computed by integrating $J_{\theta s}^{wall}(\phi, t)$ over the poloidal angle ϕ .

VIII. Two Applications for the Shell Model

When $(b-a)/a$ tends to zero but $\sigma(b-a)/a$ remains finite, i.e., for the shell model, Eqs. (57a), (57b) and (58) simplify considerably, i.e.,

$$\begin{aligned}
 A_{\theta 0}^{\text{in}}(\rho, \phi, t) = & \frac{\mu_0}{4\pi} I_c(t) \left[2 \left(\ln \frac{a}{r_c} + \frac{1}{2} \right) - \left(\frac{\rho'}{r_c} \right)^2 \right. \\
 & \left. + \ln \left(1 + \left(\frac{\rho \Delta(t)}{a^2} \right)^2 - 2 \frac{\rho \Delta(t)}{a^2} \cos(\phi - \alpha(t)) \right) \right] \\
 & + \left(\ln \frac{8r_0}{a} - 2 \right) U_{00}(t) + \sum_{n=1}^{\infty} \frac{1}{n} \left(\frac{\rho}{a} \right)^n \left(U_{n0}^{(c)}(t) \cos n\phi + U_{n0}^{(s)}(t) \sin n\phi \right),
 \end{aligned} \tag{86a}$$

inside the ring ($\rho' \leq r_c$),

$$\begin{aligned}
 A_{\theta 0}^{\text{in}}(\rho, \phi, t) = & \frac{\mu_0}{4\pi} I_c(t) \left[2 \ln \frac{a}{\rho'} \right. \\
 & \left. + \ln \left(1 + \left(\frac{\rho \Delta(t)}{a^2} \right)^2 - 2 \frac{\rho \Delta(t)}{a^2} \cos(\phi - \alpha(t)) \right) \right] \\
 & + \left(\ln \frac{8r_0}{a} - 2 \right) U_{00}(t) + \sum_{n=1}^{\infty} \frac{1}{n} \left(\frac{\rho}{a} \right)^n \left(U_{n0}^{(c)}(t) \cos n\phi + U_{n0}^{(s)}(t) \sin n\phi \right)
 \end{aligned} \tag{86b}$$

outside the ring but inside the torus ($\rho \leq a$), and

$$\begin{aligned}
 A_{\theta 0}^{\text{out}}(\rho, \phi, t) = & \left(\ln \frac{8r_0}{\rho} - 2 \right) U_{00}(t) \\
 & + \sum_{n=1}^{\infty} \frac{1}{n} \left(\frac{a}{\rho} \right)^n \left(U_{n0}^{(c)}(t) \cos n\phi + U_{n0}^{(s)}(t) \sin n\phi \right),
 \end{aligned} \tag{87}$$

outside the torus ($\rho \geq a$), where ρ' is defined by Eq. (27b).

First, consider the case of a motionless ring, i.e., Δ and α are constant, and its current is a step function of time, i.e., $I_c(t) = I_0 \Theta(t)$. From Eqs. (52a)-(52c) we have:

$$U_{00}(t) = \frac{\mu_0}{2\pi} I_0 \left(1 - e^{-t/\tau_{00}}\right), \quad (88a)$$

$$U_{00}^{(c)}(t) + i U_{00}^{(s)}(t) = \frac{\mu_0}{2\pi} I_0 \left(\frac{\Delta}{a}\right)^2 e^{im\alpha} \left(1 - e^{-\frac{m}{\tau_D} t}\right), \quad (88b)$$

and the vector potential becomes:

$$\begin{aligned} A_{\Theta 0}^{in}(\rho, \phi, t) = & \frac{\mu_0}{4\pi} I_0 \left[2 \left(\ln \frac{8r_0}{r_c} - \frac{3}{2} \right) - \left(\frac{\rho'}{r_c} \right)^2 \right. \\ & \left. - 2 \left(\ln \frac{8r_0}{a} - 2 \right) e^{-t/\tau_{00}} + \ln \left(1 + \left(\frac{\rho \Delta}{a^2} e^{-t/\tau_D} \right)^2 - 2 \frac{\rho \Delta}{a^2} e^{-t/\tau_D} \cos(\phi - \alpha) \right) \right] \end{aligned} \quad (89a)$$

inside the ring ($\rho' \leq r_c$),

$$\begin{aligned} A_{\Theta 0}^{in}(\rho, \phi, t) = & \frac{\mu_0}{4\pi} I_0 \left[2 \left(\ln \frac{8r_0}{\rho'} - 2 \right) \right. \\ & \left. - 2 \left(\ln \frac{8r_0}{a} - 2 \right) e^{-t/\tau_{00}} + \ln \left(1 + \left(\frac{\rho \Delta}{a^2} e^{-t/\tau_D} \right)^2 - 2 \frac{\rho \Delta}{a^2} e^{-t/\tau_D} \cos(\phi - \alpha) \right) \right] \end{aligned} \quad (89b)$$

outside the ring but inside the torus ($\rho \leq a$), and

$$\begin{aligned} A_{\Theta 0}^{out}(\rho, \phi, t) = & \frac{\mu_0}{4\pi} I_0 \left[2 \left(\ln \frac{8r_0}{\rho} - 2 \right) \right. \\ & \left. - 2 \left(\ln \frac{8r_0}{\rho} - 2 \right) e^{-t/\tau_{00}} + \ln \left(1 + \left(\frac{\Delta}{\rho} e^{-t/\tau_D} \right)^2 - 2 \frac{\Delta}{\rho} e^{-t/\tau_D} \cos(\phi - \alpha) \right) \right] \end{aligned} \quad (90)$$

outside the torus ($\rho \geq a$). Notice that although $A_{\theta 0}^{\text{out}}(\rho, \phi, t)$ is zero at $t = 0$, its partial time derivative is not zero at $t = 0$, because, as explained in the previous section, the fast diffusing terms which render the electric field zero at $t = 0$ outside the torus, are missing in the shell model. Also, notice that at $t=0$ the vector potential is the sum of the external vector potential of the ring and its image, but for $t \gg \tau_{00}$ only the vector potential of the ring remains present.

As a second application, consider the case in which the ring moves on a circle, i.e., Δ is constant, $\alpha = \omega t$, and its current is a step function of time, i.e., $I_c(t) = I_0 \theta(t)$. From Eqs. (52a)-(52c) we have:

$$U_{00}(t) = \frac{\mu_0}{2\pi} I_0 \left(1 - e^{-t/\tau_{00}}\right), \quad (91a)$$

$$U_{m0}^{(c)}(t) = \frac{\mu_0}{2\pi} I_0 \left(\frac{\Delta}{a}\right)^m \frac{\cos m\omega t + \omega\tau_D \sin m\omega t - e^{-\frac{t}{\tau_D}}}{1 + (\omega\tau_D)^2}, \quad (91b)$$

$$U_{m0}^{(s)}(t) = \frac{\mu_0}{2\pi} I_0 \left(\frac{\Delta}{a}\right)^m \frac{\sin m\omega t - \omega\tau_D \cos m\omega t + \omega\tau_D e^{-\frac{t}{\tau_D}}}{1 + (\omega\tau_D)^2}, \quad (91c)$$

and the vector potential becomes:

$$\begin{aligned} A_{\theta 0}^{\text{in}}(\rho, \phi, t) = & \frac{\mu_0}{4\pi} I_0 \left[2 \left(\ln \frac{8r_0}{r_c} - \frac{3}{2} \right) - \left(\frac{\rho'}{r_c} \right)^2 \right. \\ & - 2 \left(\ln \frac{8r_0}{a} - 2 \right) e^{-t/\tau_{00}} + \ln \left(1 + \left(\frac{\rho\Delta}{2} \right)^2 \right) - 2 \frac{\rho\Delta}{a^2} \cos(\phi - \omega t) \\ & \left. - \frac{1}{1 + (\omega\tau_D)^2} \left(\ln \left(1 + \left(\frac{\rho\Delta}{2} \right)^2 \right) - 2 \frac{\rho\Delta}{a^2} \cos(\phi - \omega t) \right) \right] \end{aligned} \quad (92a)$$

$$\begin{aligned}
& - \ln \left(1 + \left(\frac{\rho \Delta}{a} e^{-t/\tau_D} \right)^2 - 2 \frac{\rho \Delta}{a} e^{-t/\tau_D} \cos(\phi - \omega t) \right) \Bigg) \\
& - \frac{2\omega\tau_D}{1 + (\omega\tau_D)^2} \left(\text{Arctan} \frac{\frac{\rho \Delta}{a} \sin(\phi - \omega t)}{1 - \frac{\rho \Delta}{a} \cos(\phi - \omega t)} - \text{Arctan} \frac{\frac{\rho \Delta}{a} e^{-t/\tau_D} \sin \phi}{1 - \frac{\rho \Delta}{a} e^{-t/\tau_D} \cos \phi} \right) \Bigg]
\end{aligned}$$

inside the ring ($\rho' \leq r_c$),

$$\begin{aligned}
A_{\theta 0}^{\text{in}}(\rho, \phi, t) &= \frac{\mu_0}{4\pi} I_0 \left[2 \left(\ln \frac{8r_0}{\rho'} - 2 \right) \right. \\
& - 2 \left(\ln \frac{8r_0}{a} - 2 \right) e^{-t/\tau_{00}} + \ln \left(1 + \left(\frac{\rho \Delta}{a} \right)^2 - 2 \frac{\rho \Delta}{a} \cos(\phi - \omega t) \right) \\
& - \frac{1}{1 + (\omega\tau_D)^2} \left(\ln \left(1 + \left(\frac{\rho \Delta}{a} \right)^2 - 2 \frac{\rho \Delta}{a} \cos(\phi - \omega t) \right) \right. \\
& \left. \left. - \ln \left(1 + \left(\frac{\rho \Delta}{a} e^{-t/\tau_D} \right)^2 - 2 \frac{\rho \Delta}{a} e^{-t/\tau_D} \cos(\phi - \omega t) \right) \right) \right] \\
& - \frac{2\omega\tau_D}{1 + (\omega\tau_D)^2} \left(\text{Arctan} \frac{\frac{\rho \Delta}{a} \sin(\phi - \omega t)}{1 - \frac{\rho \Delta}{a} \cos(\phi - \omega t)} - \text{Arctan} \frac{\frac{\rho \Delta}{a} e^{-t/\tau_D} \sin \phi}{1 - \frac{\rho \Delta}{a} e^{-t/\tau_D} \cos \phi} \right) \Bigg],
\end{aligned} \tag{92b}$$

outside the ring, but inside the torus ($\rho \leq a$), and

$$\begin{aligned}
A_{\theta 0}^{\text{out}}(\rho, \phi, t) &= \frac{\mu_0}{4\pi} I_0 \left[2 \left(\ln \frac{8r_0}{\rho} - 2 \right) \right. \\
& \left. - 2 \left(\ln \frac{8r_0}{\rho} - 2 \right) e^{-t/\tau_{00}} + \ln \left(1 + \left(\frac{\Delta}{\rho} \right)^2 - 2 \frac{\Delta}{\rho} \cos(\phi - \omega t) \right) \right]
\end{aligned} \tag{93}$$

$$\begin{aligned}
& - \frac{1}{1 + (\omega\tau_D)^2} \left(\ln \left(1 + \left(\frac{\Delta}{\rho} \right)^2 - 2 \frac{\Delta}{\rho} \cos(\phi - \omega t) \right) \right. \\
& \left. - \ln \left(1 + \left(\frac{\Delta}{\rho} e^{-t/\tau_D} \right)^2 - 2 \frac{\Delta}{\rho} e^{-t/\tau_D} \cos(\phi - \omega t) \right) \right) \\
& - \frac{2\omega\tau_D}{1 + (\omega\tau_D)^2} \left(\operatorname{Arctan} \frac{\frac{\Delta}{\rho} \sin(\phi - \omega t)}{1 - \frac{\Delta}{\rho} \cos(\phi - \omega t)} - \operatorname{Arctan} \frac{\frac{\Delta}{\rho} e^{-t/\tau_D} \sin\phi}{1 - \frac{\Delta}{\rho} e^{-t/\tau_D} \cos\phi} \right),
\end{aligned}$$

outside the torus ($\rho \geq a$). There are two extreme cases of interest:

i) when $\omega\tau_D \ll 1$; then the vector potential is the same as that of a motionless ring. ii) when $\omega\tau_D \gg 1$; then there is diffusion of the terms associated with the loop time τ_{00} , but the image fields do not dissipate to zero, but they follow in phase the circular motion of the ring.

IX. Conclusion

The diffusion of the self magnetic field of a beam inside a toroidal conductor is governed by three different diffusion times. The loop time τ_{oo} is responsible for the diffusion of the fields into the hole of the doughnut and, after a few e-folds of the fast diffusion time, the time behavior of the wall current is completely determined by τ_{oo} . The "cylinder" diffusion time τ_D is responsible for the dissipation of the image fields which are present initially, but they vanish after a few e-folds of τ_D , if the ring current does not vary with time. Finally, the fast diffusion time is responsible for the electric field outside the conductor to be zero initially, but it acquires approximately the value associated with the shell model after a few e-folds of τ_{FD} .

After a few e-folds of the loop time and if the ring current does not vary with time, the vector potential becomes equal to that in the absence of the conductor. In addition, to zero order in the toroidal corrections, the radial component of the self-magnetic field, which is responsible for the beam trapping, is independent of the loop time. Therefore, the time scale of the trapping mechanism should be independent of τ_{oo} . Reliable results close to the conducting wall can be obtained only by numerical computation of the poles and by including a very large number of terms in the series expansions of the vector potential and the fields. But in the extreme case of the shell model, the results are exact everywhere inside as well as outside and in the vicinity of the torus. This model provides quite an accurate description of the diffusion process for a toroidal conductor with a thin wall, except during the first few e-folds of τ_{FD} , since the effect of the fast diffusing terms is not included. Due to the simplicity of the shell model, it is rather easy to compute the first order toroidal corrections. These results will be reported in a future publication.

Appendix

An expression for $f_m(\alpha)$, given by Eq. (54b), will be derived here, correct to second order in m/x_0 . Using the multiplication theorem for the Bessel functions, we obtain the relation ¹⁶

$$\begin{aligned} \frac{2}{\pi} \frac{1}{x_0 x_1} f_m(\alpha) &= J_{m+1}(x_0) Y_{m-1}(x_1) - Y_{m+1}(x_0) J_{m-1}(x_1) \quad (A1) \\ &= \left(\frac{b}{a}\right)^m \sum_{k=0}^{\infty} \frac{(-1)^k}{k!} \left(\frac{b^2 - a^2}{2a^2} x_0\right)^k [J_{m+1}(x_0) Y_{m-1+k}(x_0) - Y_{m+1}(x_0) J_{m-1+k}(x_0)]. \end{aligned}$$

With the help of the identities

$$J_\ell(x_0) Y_{\ell+1}(x_0) - Y_\ell(x_0) J_{\ell+1}(x_0) = -\frac{2}{\pi x_0}, \quad (A2a)$$

$$Z_{\ell-1}(x_0) + Z_{\ell+1}(x_0) = \frac{2\ell}{x_0} Z_\ell(x_0), \quad (A2b)$$

where $Z_\ell(x_0)$ is either $J_\ell(x_0)$ or $Y_\ell(x_0)$, we can show that

$$J_{m+1}(x_0) Y_{m-1}(x_0) - Y_{m+1}(x_0) J_{m-1}(x_0) = \frac{2m}{x_0} \frac{2}{\pi x_0}, \quad (A3a)$$

$$J_{m+1}(x_0) Y_m(x_0) - Y_{m+1}(x_0) J_m(x_0) = \frac{2}{\pi x_0}, \quad (A3b)$$

$$J_{m+1}(x_0) Y_{m+2}(x_0) - Y_{m+1}(x_0) J_{m+2}(x_0) = -\frac{2}{\pi x_0}, \quad (A3c)$$

and for $\ell = 1, 2, \dots$ we can also show that

$$\begin{aligned} &J_{m+1}(x_0) Y_{m+4\ell-1}(x_0) - Y_{m+1}(x_0) J_{m+4\ell-1}(x_0) \\ &= \frac{2}{\pi x_0} \left[-\frac{2(2\ell-1)(m+2\ell)}{x_0} + O\left(\frac{1}{x_0^3}\right) \right], \end{aligned} \quad (A4a)$$

$$J_{m+1}(x_0) Y_{m+4\ell}(x_0) - Y_{m+1}(x_0) J_{m+4\ell}(x_0)$$

$$= \frac{2}{\pi x_0} \left[1 - \frac{4\ell(2\ell-1)(m+2\ell)(m+2\ell+1)}{x_0^2} + o\left(\frac{1}{x_0^4}\right) \right], \quad (A4b)$$

$$\begin{aligned} & J_{m+1}(x_0) Y_{m+4\ell+1}(x_0) - Y_{m+1}(x_0) J_{m+4\ell+1}(x_0) \\ &= \frac{2}{\pi x_0} \left[\frac{4\ell(m+2\ell+1)}{x_0} + o\left(\frac{1}{x_0^3}\right) \right], \end{aligned} \quad (A4c)$$

$$\begin{aligned} & J_{m+1}(x_0) Y_{m+4\ell+2}(x_0) - Y_{m+1}(x_0) J_{m+4\ell+2}(x_0) \\ &= \frac{2}{\pi x_0} \left[1 + \frac{4\ell(2\ell+1)(m+2\ell+1)(m+2\ell+2)}{x_0^2} + o\left(\frac{1}{x_0^4}\right) \right]. \end{aligned} \quad (A4d)$$

Therefore, we conclude that

$$\begin{aligned} & \left(\frac{a}{b}\right)^m \frac{1}{x_0} f_m(\alpha) = \frac{2m}{x_0} - \sin \left(\frac{b^2 - a^2}{2a^2} x_0 \right) \\ & - \frac{2}{x_0} \sum_{k=0}^{\infty} (-1)^k \frac{(k+1)(m+k+2)}{(2k+4)!} \left(\frac{b^2 - a^2}{2a^2} x_0 \right)^{2k+4} \\ & + \frac{4}{x_0^2} \sum_{\ell=1}^{\infty} \frac{\ell(2\ell-1)(m+2\ell)(m+2\ell+1)}{(4\ell+1)!} \left(\frac{b^2 - a^2}{2a^2} x_0 \right)^{4\ell+1} \\ & - \frac{4}{x_0^2} \sum_{\ell=1}^{\infty} \frac{\ell(4\ell+1)(m+2\ell+1)(m+2\ell+2)}{(4\ell+3)!} \left(\frac{b^2 - a^2}{2a^2} x_0 \right)^{4\ell+1}. \end{aligned} \quad (A5)$$

where terms of order $1/x_0^3$ and higher have been omitted. A straightforward

and lengthy calculation leads to the relations

$$\sum_{k=0}^{\infty} (-1)^k \frac{(k+1)(m+k+2)}{(2k+4)!} z^{2k+4} \quad (A6a)$$

$$= m - \frac{z}{2} \left(m - \frac{1}{2} \right) \sin z - \left(m + \frac{z^2}{4} \right) \cos z,$$

$$\sum_{\ell=1}^{\infty} \frac{\ell(2\ell-1)(m+2\ell)(m+2\ell+1)}{(4\ell+1)!} z^{4\ell+1} \quad (A6b)$$

$$- \sum_{\ell=1}^{\infty} \frac{\ell(2\ell+1)(m+2\ell+1)(m+2\ell+2)}{(4\ell+3)!} z^{4\ell+3}$$

$$= \frac{1}{8} \left[\frac{z^4}{4} - \left(m - \frac{3}{2} \right) \left(m + \frac{1}{2} \right) z^2 + \frac{3}{4} \right] \sin z$$

$$- \left(m + \frac{1}{2} \right) \frac{z}{8} \left[z^2 + 3 \left(m - \frac{1}{2} \right) \right] \cos z.$$

Substituting Eqs. (A6a), (A6b) into Eq. (A5), we conclude that

$$\left(\frac{a}{b} \right)^m \frac{1}{x_1} f_m(\alpha) = - \left[1 - \left(m - \frac{1}{2} \right) \left(\frac{b^2 - a^2}{2a^2} \right) \right] \quad (A7)$$

$$- \frac{1}{2x_0^2} \left(\frac{9}{4} - \left(m - \frac{3}{2} \right) \left(m + \frac{1}{2} \right) \left(\frac{b^2 - a^2}{2a^2} x_0 \right)^2 + \frac{1}{4} \left(\frac{b^2 - a^2}{2a^2} x_0 \right)^4 \right) + 0 \left(\left(\frac{m}{x_0} \right)^3 \right) \right]$$

$$* \sin \left(\frac{b^2 - a^2}{2a^2} x_0 \right)$$

$$+ \left[\frac{2}{x_0} \left(m + \frac{1}{4} \left(\frac{b^2 - a^2}{2a^2} x_0 \right)^2 \right) - \frac{1}{2x_0^2} \left(m + \frac{1}{2} \right) \left(3 \left(m - \frac{1}{2} \right) + \left(\frac{b^2 - a^2}{2a^2} x_0 \right)^2 \right) \right]$$

$$+ 0 \left(\left(\frac{m}{x_0} \right)^3 \right) \cos \left(\frac{b^2 - a^2}{2a^2} x_0 \right)$$

We see that the zeroes of $f_m(\alpha)$ are given by the relation

$$\tan \left(\frac{b^2 - a^2}{2a^2} x_0 \right) = A/B, \quad (A8)$$

where

$$A = \frac{2m}{x_0} + \frac{1}{2} \left(\frac{b^2 - a^2}{2a^2} \right)^2 x_0 - \frac{1}{2} \left(m + \frac{1}{2} \right) \left(\frac{3(m - \frac{1}{2})}{x_0^2} + \left(\frac{b^2 - a^2}{2a^2} \right)^2 \right)$$

$$B = 1 - \left(m - \frac{1}{2} \right) \left(\frac{b^2 - a^2}{2a^2} \right) - \frac{1}{2} \frac{9}{4x_0^2} - \left(m - \frac{3}{2} \right) \left(m + \frac{1}{2} \right) \left(\frac{b^2 - a^2}{2a^2} \right)^2 + \frac{1}{4} \left(\frac{b^2 - a^2}{2a^2} \right)^4 x_0^2,$$

correct to order $(m/x_0)^2$. If $(b - a)/a \ll 1$, and $x_0 \gg 1$, the relation above simplifies to

$$\tan (x_1 - x_0) \approx \frac{\frac{2m}{x_0} - \frac{3}{2} \frac{m^2 - \frac{1}{4}}{x_0^2} + \frac{1}{2} \left(\frac{b - a}{a} \right)^2 x_0}{1 - \left(m - \frac{1}{2} \right) \frac{b - a}{a} + \left(m - \frac{3}{2} \right) \left(m + \frac{1}{2} \right) \left(\frac{b - a}{a} \right)^2}. \quad (A9)$$

References

*Supported by ONR and SPAVAR.

^AScience Applications International Corporation, McLean, VA 22102.

^SSFA, Inc., Landover, MD 20785.

- 1 J.C. Jaeger, *Phil. Mag.* 29, 18 (1940).
- 2 C.A. Kapetanakos, University of Maryland, Department of Physics and Astronomy Technical Report No. 70-113, June 1970.
- 3 H. Knoepfel, Pulsed High Magnetic Fields (North-Holland Publishing Co., Amsterdam, 1970).
- 4 P. Rolicz, J. Purczynski, and R. Sikora, *J. Appl. Phys.* 47, 4127 (1976).
- 5 D. Dialetis et al., *J. Appl. Phys.* 69, 1813 (1991).
- 6 S. Bodner, V.K. Neil, and L. Smith, *Part. Accel.* 1, 327 (1970).
- 7 V.K. Neil, University of California, Lawrence Livermore Laboratory Report No. 17976, November 1978.
- 8 P. Sprangle and C.A. Kapetanakos, *Part. Accel.*, 14, 15 (1983).
- 9 P. Sprangle and C.A. Kapetanakos, *Part. Accel.*, 18, 203 (1986).
- 10 C.A. Kapetanakos, L.K. Len, T. Smith, J. Golden, K. Smith, S.J. Marsh, D. Dialetis, J. Mathew, P. Loschialpo, and J.H. Chang, *Phys. Rev. Letters*, 64, 2374 (1990).
- 11 C.A. Kapetanakos, L.K. Len, T. Smith, D. Dialetis, S.J. Marsh, P. Loschialpo, J. Golden, J. Mathew and J.H. Chang, *Phys. Fluids*, B3, 2396 (1991).
- 12 Y. Seo and P. Sprangle, *Part. Accel.*(accepted for publication, 1991).
- 13 C.A. Kapetanakos, D. Dialetis, S.J. Marsh, L.K. Len and T. Smith, *Phys. Rev.*, 44, 3900 (1991).
- 14 E.W. Hobson, The Theory of Spherical and Ellipsoidal Harmonics (Cambridge University Press, 1931).
- 15 A. Erdelyi, Higher Transcendental Functions (McGraw-Hill, New York, 1953), Vol 1.
- 16 M. Abramowitz and A. Stegun, Handbook of Mathematical Functions (National Bureau of Standards, 1970).

Table I. Parameters of the run shown in Fig. 2

Torus major radius r_0	100 cm
Torus inner minor radius a	15.2 cm
Torus outer minor radius b	15.217 cm
Strong focusing radius ρ_0	23.4 cm
Strong focusing current I_{SF}	24 kA
Strong focusing Periodicity n	6
Vertical magnetic field B_{z0}	26 Gauss
Toroidal magnetic field $B_{\theta 0}$	4000 Gauss
Beam relativistic factor γ	1.69714
Beam minor radius r_c	3 mm
Beam current I_c	0.5 kA
Wall resistivity	8.84 m Ω cm
Intermediate frequency ω_v	$1.8 \times 10^9 \text{ sec}^{-1}$

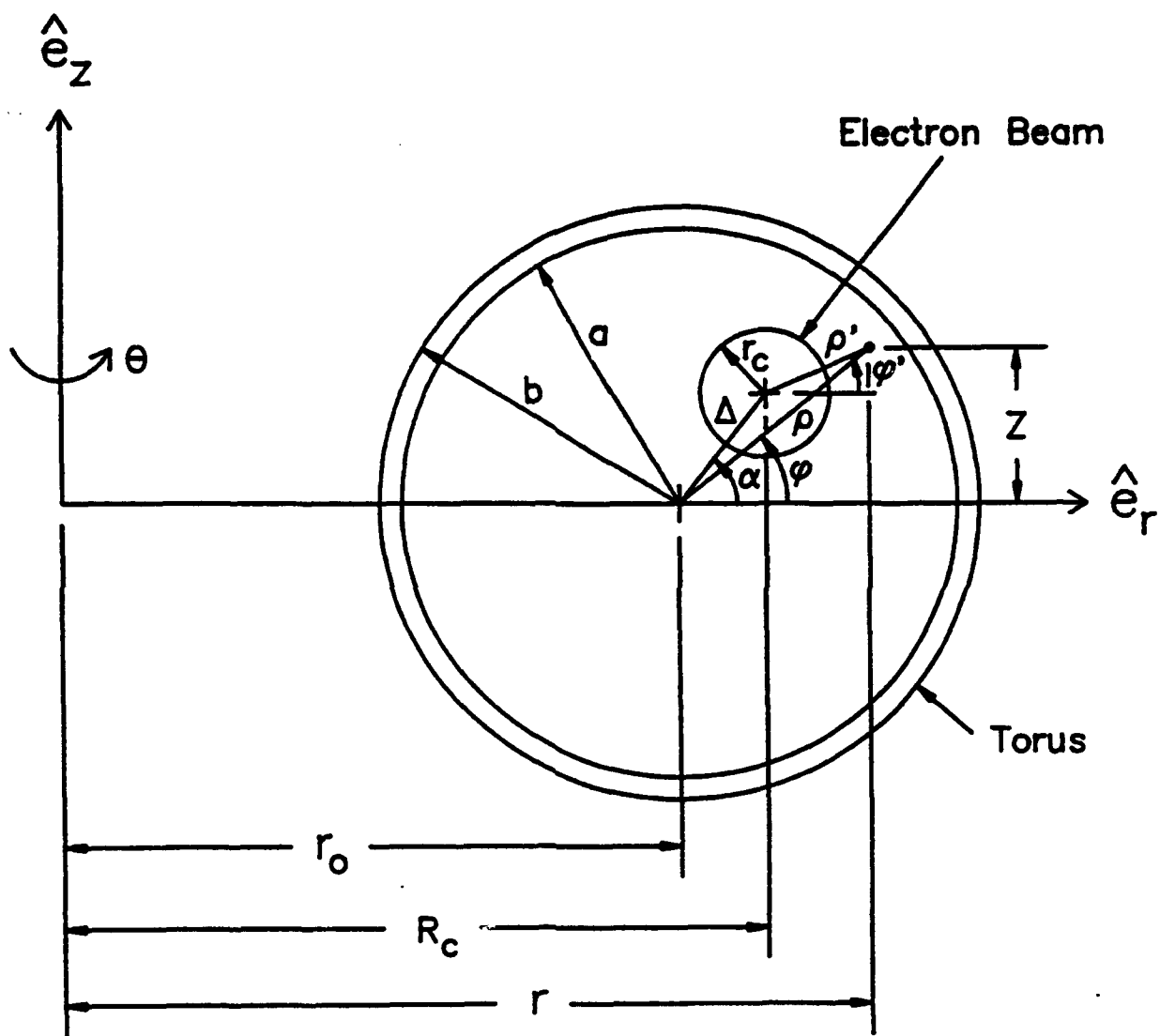


Fig. 1 System of coordinates

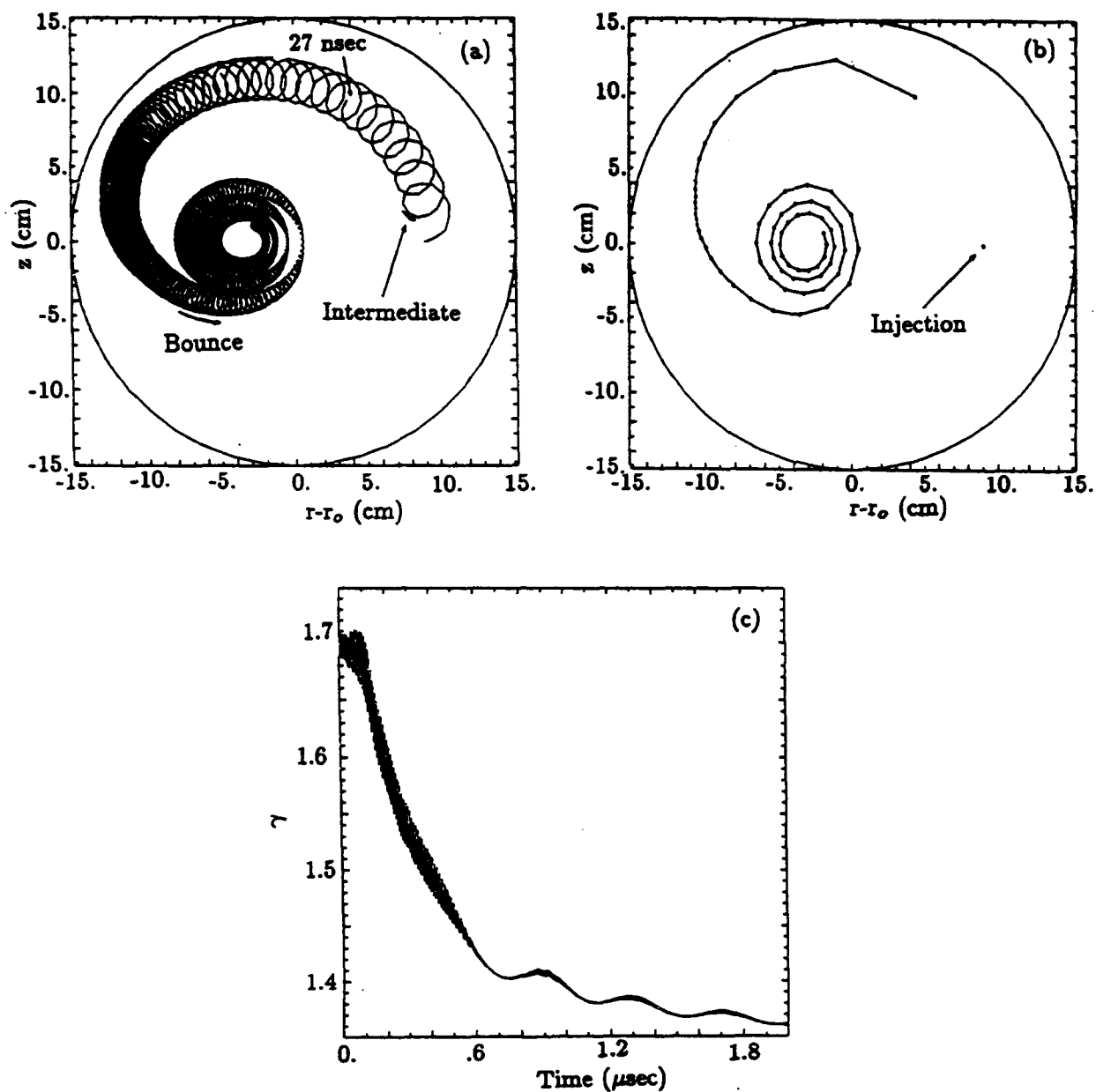


Fig. 2 Beam centroid orbit [(a) and (b)] and relativistic factor vs. time [(c)] from the numerical integration of the ring equations of motion coupled with the diffusion fields.

Appendix AA

Beam Trapping in a Modified Betatron With a Localized Bipolar Electric Field Pulse



NRL/MR/4795-92-7114

Beam Trapping in a Modified Betatron With a Localized Bipolar Electric Field Pulse

J. MATHEW AND C. A. KAPETANAKOS

*Beam Physics Branch
Plasma Physics Division*

S. J. MARSH

*SFA Inc.
Landover, MD 20785*

AND

D. DIALETIS

*SAIC
McLean, VA 22102*

August 24, 1992

Supported by SPAWAR and the Office of Naval Research

Public reporting burden for this collection of information is estimated to average 1 hour per response, including the time for reviewing instructions, searching existing data sources, gathering and maintaining the data needed, and completing and reviewing the collection of information. Send comments regarding this burden estimate or any other aspect of this collection of information, including suggestions for reducing this burden, to Washington Headquarters Services, Directorate for Information Operations and Reports, 1215 Jefferson Davis Highway, Suite 1204, Arlington, VA 22202-4302, and to the Office of Management and Budget, Paperwork Reduction Project (0704-0188), Washington, DC 20503.

1. AGENCY USE ONLY (Leave Blank)		2. REPORT DATE August 24, 1992		3. REPORT TYPE AND DATES COVERED Interim	
4. TITLE AND SUBTITLE Beam Trapping in a Modified Betatron With a Localized Bipolar Electric Field Pulse				5. FUNDING NUMBERS	
6. AUTHOR(S) J. Mathew, S. J. Marsh, ¹ D. Dialetis, ² and C. A. Kapetanakis					
7. PERFORMING ORGANIZATION NAME(S) AND ADDRESS(ES) Naval Research Laboratory Washington, DC 20375-5320				8. PERFORMING ORGANIZATION REPORT NUMBER NRL/FR-4795-92-7114	
9. SPONSORING/MONITORING AGENCY NAME(S) AND ADDRESS(ES) SPAWAR Washington, DC 20363 ONR Arlington, VA 22217				10. SPONSORING/MONITORING AGENCY REPORT NUMBER	
11. SUPPLEMENTARY NOTES ¹ SFA Inc., Landover, MD 20785 ² SAIC, McLean, VA 22102					
12a. DISTRIBUTION/AVAILABILITY STATEMENT Approved for public release; distribution is unlimited.				12b. DISTRIBUTION CODE	
13. ABSTRACT (Maximum 200 words) This paper describes a scheme for trapping the injected beam in a modified betatron accelerator using a localized inductive electric field pulse generated by a charged coaxial pulseline. The average canonical angular momentum $\langle P_\theta \rangle$ is not conserved in this scheme. Numerical simulations demonstrate trapping over a wide range of operating parameters. A 0.84-Q, 45-ns water dielectric pulseline has been built for testing the trapping concept. The pulseline is switched using triggered vacuum surface flashover switches. By crowbarring the pulseline, its output is limited to a single bipolar pulse that has a ~22 ns rise time.					
14. SUBJECT TERMS Modified betatron Beam trapping Toroidal pulseline				15. NUMBER OF PAGES 52	
				16. PRICE CODE	
17. SECURITY CLASSIFICATION OF REPORT UNCLASSIFIED	18. SECURITY CLASSIFICATION OF THIS PAGE UNCLASSIFIED	19. SECURITY CLASSIFICATION OF ABSTRACT UNCLASSIFIED	20. LIMITATION OF ABSTRACT SAR		

CONTENTS

I. INTRODUCTION	1
II. THE ELECTRIC FIELD PULSE	2
III. WAVE PROPAGATION IN TOROIDAL GEOMETRY	6
IV. NUMERICAL RESULTS	15
V. PULSELINE CONSTRUCTION	17
VI. EXPERIMENTAL RESULTS	21
VII. DISCUSSION	26
VIII. SUMMARY AND CONCLUSIONS	29
REFERENCES	30
DISTRIBUTION LIST	49

BEAM TRAPPING IN A MODIFIED BETATRON WITH A LOCALIZED BIPOLAR ELECTRIC FIELD PULSE

I. INTRODUCTION

Compact, high-current accelerators are currently under development in several laboratories.¹⁻⁵ Among these accelerators is the modified betatron.⁶⁻⁸ This accelerator is a toroidal, closed orbit device that utilizes three different magnetic fields to accelerate and confine the high current electron ring; the time varying betatron or vertical field that controls mainly the major radius of the electron ring and also is responsible for the acceleration, the quasi-static toroidal magnetic field that controls primarily the minor radius of the ring and also the growth rate of the various unstable modes and finally the quasi-static strong focusing (SF) field that reduces the sensitivity of the electron orbits to energy mismatch and spread.

A challenging physics issue of the modified betatron concept is the capture of the injected beam into the closed magnetic field configuration of the device. Capture of the beam requires that its poloidal orbit be modified within a bounce period τ_B , i.e., within a poloidal revolution around the equilibrium position. Modification of the beam's poloidal orbit can be achieved by either changing the equilibrium position of the gyrating electrons or by reducing the radius of the poloidal orbit.

The strong focusing field in the modified betatron is generated by a set of stellarator windings. Since this field is a function of the toroidal angle, the canonical angular momentum P_θ is not conserved. However, when P_θ is averaged over the intermediate frequency mode of the system ω_w ($= 4\pi v_\theta / L_{sf}$, where v_θ is the toroidal velocity and L_{sf} is the period of the SF windings), the averaged $\langle P_\theta \rangle$ is an approximate constant of the motion.¹⁰ Two different schemes¹⁰⁻¹² have been developed, so far, for trapping the beam

in the modified betatron. In both schemes $\langle P_\theta \rangle$ is an approximate invariant. In this paper, we discuss an additional trapping approach, in which $\langle P_\theta \rangle$ is not conserved. The proposed trapping scheme is based on the change of the centroid's equilibrium position by a localized electric field. This electric field pulse is produced by a coaxial pulseline and has a pulsewidth comparable to the bounce period of the beam.

This paper is organized as follows: Section II briefly reviews the generation of the localized electric field pulse. Section III treats the propagation of electromagnetic waves in toroidal geometry. Beam centroid orbits from the numerical integration of equations of motion are presented in Section IV. Section V describes the constructional details of the pulseline and the experimental data are presented in Section VI. An interesting feature observed in the experiment is discussed in Section VII, and Section VIII contains a brief summary of the results and some important conclusions.

II. THE ELECTRIC FIELD PULSE

Although the pulseline that is described in Section V is toroidal, the discussion in this Section is limited for simplicity to the coaxial, cylindrical pulseline shown in Fig. 1. This pulseline is similar to the radial line initially employed by Pavlovskii *et al.*,¹³ and analyzed by Eccleshall and Temperley.¹⁴ In this Section, we briefly review the pulseline for completeness.

The voltage at the gap V_g of the pulseline after the switch closes can be found by integrating the equation $\nabla \times \vec{E} = -\partial \vec{B} / \partial t$ along the dash line of Fig. 1. Assuming that the resistivity of the conductor can be neglected, then

$$V_g = \oint \vec{E} \cdot d\vec{\ell} = -\frac{\partial \Phi}{\partial t}, \quad (1)$$

where Φ is the magnetic flux through the area A surrounded by the dash line.

The magnetic field of the propagating wave is found by integrating the equation $\nabla \times \vec{B} = \mu \vec{j} + \mu \epsilon (\partial \vec{E} / \partial t)$ in the circular area D that is located just behind the wave front.

The result is

$$B = -\mu I_\ell / 2\pi R, \quad (2)$$

where I_ℓ is the current of the line, and R is the radius of the circular area.

The magnetic flux Φ can be computed from

$$\Phi = \int_A \vec{B} \cdot d\vec{S}, \quad (3)$$

where B is given by Eq. (2). Substituting (2) into (3), we obtain

$$\Phi = \begin{cases} -\frac{\mu I_\ell U t}{2\pi} \ln \left(\frac{R_3}{R_2} \right), & \text{for } t \leq \tau \\ -\frac{\mu I_\ell U}{2\pi} \ln \left(\frac{R_3}{R_2} \right) (2\tau - t), & \text{for } \tau \leq t \leq 3\tau, \end{cases} \quad (4)$$

where U is the speed of the electromagnetic wave, $\tau = 2\ell/U$ is the one-way transit time, ℓ is the length of the pulseline (see Fig. 1), and it has been assumed that $R_2 = \sqrt{R_3 R_1}$.

Since the characteristic impedance Z_o of the line is given by

$$Z_o = \frac{1}{2\pi} \sqrt{\frac{\mu}{\epsilon}} \ln \left(\frac{R_3}{R_2} \right), \quad (5)$$

and $V_o = I_\ell Z_o$, where V_o is the initial voltage of the line, Eqs. (1) and (4) give

$$V_g = \begin{cases} V_o, & \text{for } t \leq \tau \\ -V_o, & \text{for } \tau \leq t \leq 3\tau. \end{cases}$$

Up to this point the effect of the beam (load) has been neglected. The beam induces a voltage V_b at the gap and thus the accelerating voltage is reduced, i.e.,

$$V_g = V_o - V_b. \quad (6)$$

Since $V_b = I_b Z_o$, where I_b is the beam current and assuming that the beam is matched to the line, i.e., $V_g = I_b Z_o$, Eq. (6) gives $V_g = V_o/2$. When the beam is matched to the line all the energy that is initially stored in the line is transferred to the beam and thus the efficiency of the system is 100%.

If ΔE is the beam energy change required to move the beam equilibrium position by a few centimeters, and τ_o is the period of revolution around the major axis, then

$$\Delta E = \left(\frac{V_o}{2} \right) \frac{2\tau}{\tau_o}, \quad (7)$$

for the case where the injected beam interacts with the pulseline during the period $\tau \leq t \leq 3\tau$. Since $I_b = V_o/2Z_o$, Eq. (7) together with the expressions for τ and Z_o given previously, yield

$$\ell \ln \frac{R_3}{R_2} = \frac{\Delta E \tau_o \pi}{2\mu I_b}. \quad (8)$$

In the NRL modified betatron the ratio R_3/R_2 is restricted to values close to unity by the presence of the strong focusing windings. Therefore, the length of the line is unac-

ceptably large. This difficulty can be avoided by mismatching the beam. In this case, the initial voltage of the line is made larger than the value needed for matching, namely $2I_b Z_o$. Then the voltage at the gap is $V_g = V_o - I_b Z_o$, and the length of the line is given by

$$\ell = \frac{\Delta E \tau_o c}{4\sqrt{\epsilon/\epsilon_o} [V_o - I_b Z_o]}. \quad (9)$$

For $\Delta E = 60$ keV, $\tau_o = 24$ ns, $\epsilon/\epsilon_o = 80$, $V_o = 20$ kV, $I_b = 2$ kA, $R_1 = 16.8$ cm, $R_2 = 19.0$ cm and $R_3 = 21.6$ cm, $Z_o = 0.84 \Omega$ and Eq. (9) gives $\ell = 0.66$ m. Although lower than in the case of the matched beam, the system efficiency is still resonable and is given by

$$\epsilon_f = \frac{4Z_o I_b}{V_o^2} (V_o - I_b Z_o). \quad (10)$$

For the parameters listed above $\epsilon_f \simeq 31\%$.

Plots of Z_o , ℓ , ϵ_f , and τ as a function of ϵ/ϵ_o for the parameters given above are shown in Fig. 2. For a matched beam, Eq. (10) gives an efficiency of 100%, and at time $t = 3\tau$ there is no energy left in the pulseline. The interaction of a beam with a charged pulseline cavity can be better understood using superposition. It can be shown that the gap voltage is the sum of the open circuit voltage at the gap of the charged pulseline in the absence of the beam, and the gap voltage induced by the beam in the absence of any charge voltage. If the beam is present beyond $t = 3\tau$ (as is the case with a cyclic accelerator like the modified betatron), energy will be transferred from the beam back to the pulseline during the period $3\tau \leq t \leq 5\tau$. This is the case regardless of whether the beam is matched to the pulseline or not. Fig. 3 shows the gap voltage for a matched beam injected at $t = \tau$.

To avoid beam interactions beyond $t = 3\tau$, the pulseline needs to be crowbarred by firing a set of switches located in the insulating gap region. This isolates the pulseline from the circulating electron beam. Pulselines used in linear accelerators do not need crowbar switches because the beam duration is usually less than 2τ .

III. WAVE PROPAGATION IN TOROIDAL GEOMETRY

Let (r, θ, z) be the cylindrical coordinates and $\vec{e}_r, \vec{e}_\theta, \vec{e}_z$ be the unit vectors in cylindrical geometry. Then the electromagnetic field can be decomposed into its toroidal components E_θ, B_θ and its transverse components \vec{E}_t, \vec{B}_t , namely:

$$\vec{E} = \vec{E}_t + E_\theta \vec{e}_\theta, \quad (11a)$$

$$\vec{B} = \vec{B}_t + B_\theta \vec{e}_\theta, \quad (11b)$$

where

$$\vec{E}_t = E_r \vec{e}_r + E_z \vec{e}_z, \quad (12a)$$

$$\vec{B}_t = B_r \vec{e}_r + B_z \vec{e}_z, \quad (12b)$$

It is assumed that the electromagnetic field can be expressed in the form

$$\vec{E} = \vec{E}(r, z) e^{-i\omega t + im\theta}, \quad (13a)$$

$$\vec{B} = \vec{B}(r, z) e^{-i\omega t + im\theta}, \quad (13b)$$

where ω is the frequency and m is an integer ($m \neq 0$). Then, it is possible to show from Maxwell's equations (in MKS units) that the transverse components can be expressed in terms of the toroidal components as follows:

$$\vec{E}_t = \frac{1}{k^2 - (m/r)^2} \left[\frac{im}{r} \nabla_t E_\theta - i\omega \vec{e}_\theta \times \nabla_t B_\theta + \frac{im}{r^2} E_\theta \vec{e}_r + i\omega \frac{1}{r} B_\theta \vec{e}_z \right], \quad (14a)$$

$$\vec{B}_t = \frac{1}{k^2 - (m/r)^2} \left[\frac{im}{r} \nabla_t B_\theta + \frac{ik^2}{\omega} \vec{e}_\theta \times \nabla_t E_\theta + \frac{im}{r^2} B_\theta \vec{e}_r - \frac{ik^2}{\omega} \frac{1}{r} E_\theta \vec{e}_z \right], \quad (14b)$$

where

$$\nabla_t = \vec{e}_r \frac{\partial}{\partial r} + \vec{e}_z \frac{\partial}{\partial z}, \quad (15)$$

$k = \sqrt{\mu_r \epsilon_r} (\omega/c)$, μ_r and ϵ_r are the relative permeability and relative permittivity of the medium, and c is velocity of light in vacuum.

After a lengthy computation, it can be shown that the toroidal components satisfy the following coupled set of differential equations:

$$\begin{aligned} \left(\frac{1}{r} \frac{\partial}{\partial r} r \frac{\partial}{\partial r} + \frac{\partial^2}{\partial z^2} \right) E_\theta - \frac{2m^2}{k^2 - (m/r)^2} \frac{1}{r^3} \frac{\partial E_\theta}{\partial r} + \left[k^2 - \frac{m^2 + 1}{r^2} - \frac{2m^2}{k^2 - (m/r)^2} \frac{1}{r^4} \right] E_\theta \\ + \frac{2m\omega}{k^2 - (m/r)^2} \frac{1}{r^2} \frac{\partial B_\theta}{\partial z} = 0, \end{aligned} \quad (16a)$$

$$\begin{aligned} \left(\frac{1}{r} \frac{\partial}{\partial r} r \frac{\partial}{\partial r} + \frac{\partial^2}{\partial z^2} \right) B_\theta - \frac{2m^2}{k^2 - (m/r)^2} \frac{1}{r^3} \frac{\partial B_\theta}{\partial r} + \left[k^2 - \frac{m^2 + 1}{r^2} - \frac{2m^2}{k^2 - (m/r)^2} \frac{1}{r^4} \right] B_\theta \\ - \frac{2m(k^2/\omega)}{k^2 - (m/r)^2} \frac{1}{r^2} \frac{\partial E_\theta}{\partial z} = 0. \end{aligned} \quad (16b)$$

These equations indicate that it is not possible to have pure TE or TM modes in a toroidal cavity. But it is possible to have solutions with a small E_θ or B_θ component, inversely proportional to r . In the first case, the solutions determine the pseudo-TE modes

and in the second case, the pseudo-TM modes. Notice that when Eqs. (16a) and (16b) are solved, the transverse components can be computed from Eqs. (14a) and (14b).

In order to solve Eqs. (16a) and (16b), we shall make use of the following theorem:

Let G_m and H_m be the solutions of the differential equation

$$\left(\frac{1}{r} \frac{\partial}{\partial r} r \frac{\partial}{\partial r} + \frac{\partial^2}{\partial z^2} \right) F_m + \left[k^2 - \frac{m^2}{r^2} \right] F_m = 0. \quad (17)$$

Then the set of toroidal components

$$E_\theta = \frac{\partial}{\partial z} [G_{m-1}(r, z) + H_{m+1}(r, z)] e^{-i\omega t + im\theta}, \quad (18a)$$

$$B_\theta = \frac{1}{\omega} \left[\left(k^2 - \frac{m^2}{r^2} \right) (G_{m-1}(r, z) - H_{m+1}(r, z)) + \frac{m}{r} \left(\frac{\partial}{\partial r} + \frac{1}{r} \right) (G_{m-1}(r, z) + H_{m+1}(r, z)) \right] e^{-i\omega t + im\theta}, \quad (18b)$$

satisfies the differential equations (16a) and (16b). The same is true for the set

$$B_\theta = \frac{\partial}{\partial z} [G_{m-1}(r, z) + H_{m+1}(r, z)] e^{-i\omega t + im\theta}, \quad (19a)$$

$$E_\theta = -\frac{\omega}{k^2} \left[\left(k^2 - \frac{m^2}{r^2} \right) (G_{m-1}(r, z) - H_{m+1}(r, z)) + \frac{m}{r} \left(\frac{\partial}{\partial r} + \frac{1}{r} \right) (G_{m-1}(r, z) + H_{m+1}(r, z)) \right] e^{-i\omega t + im\theta}, \quad (19b)$$

The first set (Eq. (18)) is appropriate for the computation of the pseudo-TE modes and the second set (Eq. (19)) is appropriate for the pseudo-TM modes, although both modes can be derived from either set.

All the results given above are valid for any toroidal cavity. In the following we shall confine ourselves to a toroidal conductor with rectangular cross section. Figure 4 illustrates the geometry of the problem. The inner and outer surfaces of the conductor are at $r = a$ and $r = b$, while the lower and upper surfaces lie at $z = 0$ and $z = D$. By direct inspection of Maxwell's equations it is easy to show that for such a toroidal conductor the boundary conditions are:

$$E_\theta = 0, \quad (20a)$$

$$\frac{\partial}{\partial r} r B_\theta = 0 \quad (20b)$$

at $r = a$ and $r = b$, and

$$E_\theta = 0, \quad (21a)$$

$$\frac{\partial B_\theta}{\partial z} = 0, \quad (21b)$$

at $z = 0$ and $z = D$. For a rectangular toroidal conductor, the solution of Eq. (7) is separable. First, let us consider the pseudo-TE modes. A solution of Eq. (17) is

$$G_m(r, z) = \frac{1}{2} (AJ_m(\beta r) + BY_m(\beta r)) \cos \frac{q\pi z}{D}, \quad (22)$$

where $J_m(x)$, $Y_m(x)$ are the Bessel functions of the first and second kind, and

$$\beta^2 = k^2 - \left(\frac{q\pi}{D}\right)^2 = \mu_r \epsilon_r \left(\frac{\omega}{c}\right)^2 - \left(\frac{q\pi}{D}\right)^2 \quad (23)$$

Let us also choose $H_m(r, z) = G_m(r, z)$. Then,

$$G_{m-1} + H_{m+1} = \frac{m}{\beta r} (AJ_m(\beta r) + BY_m(\beta r)) \cos \frac{q\pi z}{D}, \quad (24a)$$

$$G_{m-1} - H_{m+1} = (AJ'_m(\beta r) + BY'_m(\beta r)) \cos \frac{q\pi z}{D}, \quad (24b)$$

and substituting these relations into Eqs. (18a) and (18b) we obtain

$$E_\theta = -\frac{q\pi}{D} \frac{m}{\beta r} (AJ_m(\beta r) + BY_m(\beta r)) \left(\sin \frac{q\pi z}{D} \right) e^{-i\omega t + im\theta}, \quad (25a)$$

$$B_\theta = \frac{k^2}{\omega} (AJ'_m(\beta r) + BY'_m(\beta r)) \left(\cos \frac{q\pi z}{D} \right) e^{-i\omega t + im\theta}. \quad (25b)$$

By choosing q to be an integer, i.e., $q = 1, 2, \dots$, the boundary conditions at $z = 0$ and $z = D$ are satisfied. The boundary condition (20a) leads to the relations

$$AJ_m(x_1) + BY_m(x_1) = 0, \quad (26a)$$

$$AJ_m(x_2) + BY_m(x_2) = 0, \quad (26b)$$

where $x_1 = \beta a$ and $x_2 = \beta b$. It is easy to show that the boundary condition (20b) is satisfied when Eqs. (26a) and (26b) are true. The determinant of the algebraic system (26a), (26b) must be zero, and, therefore, the unknown parameter β is determined from the zeroes of the relation

$$J_m(x_1)Y_m(x_2) - J_m(x_2)Y_m(x_1) = 0, \quad (27)$$

for pseudo-TE modes.

Next, let us consider the pseudo-TM modes. A solution of Eq. (17) is

$$G_m(r, z) = \frac{1}{2} (PJ_m(\beta r) + QY_m(\beta r)) \sin \frac{q\pi z}{D}, \quad (28)$$

where β is given by Eq. (23). We choose $H_m(r, z) = G_m(r, z)$, as before, and substituting into Eqs. (19a) and (19b), we obtain

$$B_\theta = \frac{q\pi}{D} \frac{m}{\beta r} (PJ_m(\beta r) + QY_m(\beta r)) \left(\cos \frac{q\pi z}{D} \right) e^{-i\omega t + im\theta}, \quad (29a)$$

$$E_\theta = -\omega \left(PJ'_m(\beta r) + QY'_m(\beta r) \right) \left(\sin \frac{q\pi z}{D} \right) e^{-i\omega t + im\theta}, \quad (29b)$$

for the TM modes. Again, by choosing $q = 1, 2, \dots$, the boundary conditions at $z = 0$, and $z = D$ are satisfied. Either of the boundary conditions (20a), (20b) leads to the algebraic system

$$PJ'_m(x_1) + QY'_m(x_1) = 0, \quad (30a)$$

$$PJ'_m(x_2) + QY'_m(x_2) = 0, \quad (30b)$$

where x_1 and x_2 have been defined. For the pseudo-TM modes, the parameter β is determined from the zeroes of the relation

$$J'_m(x_1)Y'_m(x_2) - J'_m(x_2)Y'_m(x_1) = 0. \quad (31)$$

The final task is the computation of the parameter β from Eq. (27) for the pseudo-TE modes and Eq. (31) for the pseudo-TM modes. This will be done under the assumption that the aspect ratio d/a , where $d = b - a$, is much less than unity. First, let us investigate for zeroes such that the quantity $\delta = x_2 - x_1$ is much less than unity. A Taylor expansion, to third order in δ , of Eq. (27) yields

$$\frac{2d}{\pi a} \left[1 - \frac{1}{2} \frac{d}{a} + \frac{m^2 + 2}{6} \left(\frac{d}{a} \right)^2 - \frac{\delta^2}{6} \right] = 0, \quad (32)$$

and Eq. (31) to second order in δ , yields

$$\frac{2d}{\pi a} \left[1 - \frac{m^2}{x_1^2} - \frac{1}{2} \frac{d}{a} \left(1 - \frac{3m^2}{x_1^2} \right) \right] = 0. \quad (33)$$

These equations are obtained using the identity

$$J_{m+1}(x_1)Y_m(x_1) - J_m(x_1)Y_{m+1}(x_1) = \frac{2}{\pi x_1}, \quad (34)$$

and the recursion formulas for the Bessel functions. Equation (32) does not have a zero for small δ , while Eq. (33) has a zero when $x_1 \approx m$. In this case, we have $\delta \approx md/a$, and for m not very large, the parameter δ is small as originally assumed. More accurately, it follows from Eq. (33) that $x_1 \approx m(1 - d/2a)$. Therefore, when δ is small, the pseudo-TE modes do not have zeroes, while for the pseudo-TM modes $\beta \approx (m/a)(1 - d/2a)$ and from Eq. (23),

$$k^2 = \mu_r \epsilon_r \left(\frac{\omega}{c} \right)^2 \approx \left(\frac{m}{a} \right)^2 \left(1 - \frac{d}{a} \right) + \left(\frac{q\pi}{D} \right)^2. \quad (35)$$

For moderate values of δ and small d/a , the arguments x_1 , x_2 of the Bessel functions are large (at this point this is an assumption that will be justified after the zeroes have been computed). Using the asymptotic expressions for the Bessel functions, Eq. (27) gives to lowest order in d/a

$$\delta \tan \delta \approx \frac{4m^2 - 1}{8} \left(\frac{d}{a} \right)^2, \quad (36)$$

while Eq. (31) reduces to

$$\delta \tan \delta \approx \frac{4m^2 + 3}{8} \left(\frac{d}{a} \right)^2. \quad (37)$$

An approximate solution of the relations above can be obtained by setting $\delta = p\pi + \epsilon$, where $p = 1, 2, \dots$, and ϵ is a small parameter. Then Eqs. (36) and (37) have the approximate solutions

$$\delta \approx p\pi + \frac{4m^2 - 1}{8p\pi} \left(\frac{d}{a} \right)^2, \quad (38)$$

and

$$\delta \approx p\pi + \frac{4m^2 + 3}{8p\pi} \left(\frac{d}{a} \right)^2, \quad (39)$$

for values of m that are not very large. From Eqs. (38) and (39) it follows that $x_1 \approx p\pi a/d$ and $x_2 \approx p\pi b/d$, i.e., both x_1 and x_2 are very large and the use of the asymptotic expansions is justified in the derivation of the zeroes. The eigenfrequencies of the psuedo-TE modes can be obtained from Eqs. (23) and (38), and are given by

$$k^2 = \mu_r \epsilon_r \left(\frac{\omega}{c} \right)^2 \approx \left(m^2 - \frac{1}{4} \right) \frac{1}{a^2} + \left(\frac{p\pi}{d} \right)^2 + \left(\frac{q\pi}{D} \right)^2, \quad (40)$$

Similarly, the eigenfrequencies of the pseudo-TM modes can be obtained from Eqs. (23) and (39), and are given by

$$k^2 = \mu_r \epsilon_r \left(\frac{\omega}{c} \right)^2 \approx \left(m^2 + \frac{3}{4} \right) \frac{1}{a^2} + \left(\frac{p\pi}{d} \right)^2 + \left(\frac{q\pi}{D} \right)^2. \quad (41)$$

Eqs. (40) and (41) indicate that the eigenfrequencies for a toroidal rectangular conductor are similar to those of a straight rectangular cavity.

It is apparent from Eqs. (35) and (41) that ω does not vary linearly with m and that the system is dispersive, i.e., the phase velocity is a function of ω . However, when $D \rightarrow \infty$, i.e., for a curved stripline of infinite width satisfying the relation $(b - a)/a \ll 1$, Eq. (35) gives

$$\frac{\omega}{c} \approx \frac{1}{\sqrt{\mu_r \epsilon_r}} \left(\frac{m}{a} \right) \left(1 - \frac{d}{2a} \right),$$

which implies that the phase velocity of the propagating wave is not a function of frequency and thus the various frequency components of the wave propagate with the same speed. Figure 5 shows a sketch of the electric field lines in the stripline. In this geometry, a quasi-TEM mode propagates. The dominant fields are B_z and E_r with a small E_θ component and all other components, namely E_z , B_r and B_θ are zero.

The pulseline described in Section V has a topology different from that of the curved stripline of infinite width and thus it is not clear if the results of the stripline model

are applicable. Obviously, a complete 3-D analysis is required for the actual topology of the toroidal pulseline before a definitive conclusion can be reached about its properties. However, it should be noticed that the wave equation in toroidal geometry is separable in the variables t and θ and thus its solution is a superposition of eigenfunctions of the forms $F(\mu, \xi)e^{i\omega t - im\theta}$, where μ , ξ and θ are the toroidal variables. Unfortunately, the eigenfrequencies of the toroidal pulseline cannot be easily obtained. It is expected that in the general case the pulseline is dispersive. However, for the special case where the separation between the pulseline conductors is much smaller than their minor radii, and the minor radii are also small compared with the major radius of the line, the dispersive effects are likely to be negligible for quasi-TEM modes.

IV. NUMERICAL RESULTS

The beam dynamics in the modified betatron have been studied for the bipolar pulse shown in Fig. 6. The pulse is negative (accelerating) for the first 50 ns, and positive (decelerating) for the subsequent 100 ns. In a Pavlovskii line¹³ only the second pulse is used for acceleration. Here, both the positive and negative polarity components of the pulse are used because more efficient trapping occurs with this choice. The orbit for the beam centroid is obtained by integrating the equations of motion with JAX, a 3-D particle integrator code. The toroidal pulseline electric fields are computed from a cylindrical model with a simple $1/r$ toroidal correction to ensure that $\oint E_{\theta} r d\theta$ is the same for any path. The stellarator fields are calculated from Biot-Savart's law by dividing each period of the winding into twenty segments. The image electric and magnetic fields used in the code have been discussed in previous publications⁷.

Successful trapping in the modified betatron requires that 1) the beam does not hit the injector after the first toroidal revolution around the major axis and 2) the beam does not return to the injector after a poloidal (bounce) period. Numerical results for various amplitude pulses are shown in Figs. 7, 8 and 9. The parameters for the three runs are listed in Table I. The figures show the projection of the beam centroid on the $\theta = 0$ plane. The small circular motion in these figures is associated with the stellarator field (intermediate frequency mode). Since there are six stellarator field periods between $0 \leq \theta \leq 2\pi$, the beam centroid performs six oscillations during a revolution around the major axis. The beam moves approximately 1 m in the toroidal direction for each small orbit.

Results with the 80 kV bipolar pulse are shown in Fig. 7. At the end of the first revolution around the major axis ($t \approx 25$ ns), the beam has moved almost 5 cm which is more than enough to miss the injector and its shroud. At the end of the first bounce period, the beam is on an orbit with a radius of just over 3 cm centered at 100.6 cm. Thus both trapping criteria have been met.

As the beam passes through the gap, its energy changes. This change in γ will cause the center of the bounce (slow) motion to move according to

$$\frac{\Delta r}{r} = \frac{\Delta\gamma/\gamma}{n - n_s(r_b/a)^2 + n_{sf}},$$

where $\Delta\gamma$ is the energy mismatch, n is the external field index, n_s is the self field index, n_{sf} is the strong focusing index¹⁰, r_b is the beam radius, and a is the minor radius of the vacuum chamber.

For the parameters of Fig. 7, Δr is ± 0.9 cm. Its sign depends on the polarity of the pulse. At $t = 0$ the center of the bounce motion is at $r = 102.4$ cm. After $t = 50$ ns, the electron beam has been accelerated twice by the negative voltage and the equilibrium position is at 104.2 cm. This change in the center of the motion results in a smaller radius of curvature than it would have otherwise. During the second (positive) phase of the bipolar pulse, the beam is decelerated 4 times with a net change in equilibrium position of 3.6 cm and the center of the orbit is at 100.6 cm. The bipolar pulse, properly timed, has the effect of chasing the particle and continuously decreasing the size of the orbit.

An even better final orbit is obtained by increasing the pulseline voltage to 100 kV as shown in Fig. 8. Because of the larger $\Delta\gamma$ the final equilibrium position is at 100.2 cm and is closer to the beam. The final radius of the poloidal orbit is considerably larger when the amplitude of the bipolar pulse is reduced to 60 kV, as shown in Fig. 9. If the toroidal field and the strong focusing current are halved, the required bipolar pulse amplitudes are also roughly halved for similar trapping characteristics. However, the beam radius r_b is larger at the lower toroidal field.

V. PULSELINE CONSTRUCTION

The modified betatron vacuum chamber consists of twelve flange coupled 30° sectors with a major radius of 100 cm, and a minor radius of 15 cm. The pulseline was designed as an integral part of a 60° sector, and it is intended to replace two 30° vacuum chamber sectors. Fig. 10 shows a simplified drawing of the pulseline. The insulating spacer across which the gap voltage is developed is shown at the leftmost end. The pulseline looks like a toroidal coaxial equivalent of a folded stripline. The radii of the inner and outer conductors

are $R_1 = 16.8$ cm and $R_3 = 21.6$ cm. The radius R_2 of the middle conductor is chosen to make the characteristic impedance between the inner and middle conductors equal to that between the outer and middle conductors. Thus $R_2 = \sqrt{R_1 R_3} = 19.0$ cm. The choice of values for R_1 and R_3 is severely limited by the available space between the vacuum chamber and the coils of the modified betatron.

Deionized water is used as the dielectric medium between the pulseline conductors. This choice yields the maximum practical pulselength for given geometric dimensions. Since the dielectric constant of water is ~ 80 , the mean one-way transit time τ is 45 ns. To avoid field errors, the magnetic field penetration time of the pulseline needs to be the same as for the rest of the vacuum chamber. The pulseline is constructed from fiberglass and epoxy-reinforced carbon fibers. The modified betatron vacuum chamber is constructed similarly. The inner pulseline conductor is made of seven layers of carbon fiber cloth with a total thickness of 1.5 mm. However, a major portion of the line current is carried by a sheet of phosphor-bronze wire cloth embedded between the outer two carbon layers. The surface resistivity of the wire cloth is $32 \text{ m}\Omega$ on a square. The measured resistivity of the carbon fiber matrix is $\sim 8 \text{ m}\Omega\text{-cm}$. The middle conductor is also made of carbon fiber with an overall thickness of 1.5 mm, but it has two sheets of phosphor-bronze wire cloth to simulate the folded nature of the pulseline. Finally, the outer conductor is similar in construction to the inner conductor.

The middle conductor is perforated with a large number of 3-mm-diam. holes to facilitate free circulation of water within the pulseline. The hole spacing is ~ 2.5 cm. Water is admitted through five holes at the bottom. After circulating through the pulseline, the

water exits through five holes at the top, and then passes through a deionizer before returning to the inlet holes. The water resistivity is maintained above $8 \text{ M}\Omega\text{-cm}$. Also, the initial filling is done gradually, typically taking 20-30 minutes. This minimizes bubbles in the pulseline and in the circulating water.

Switching is done by a set of triggered vacuum surface flashover switches. Cast polyurethane annular disks separate the vacuum flashover region from the outside, and from the water dielectric medium. Spark gap switches cannot be used here for several reasons. The capacitance of the middle conductor with respect to the inner and outer conductors is 50 nF . For a typical charge voltage of 20 kV , the stored energy in the pulseline is only 10 J . It is doubtful if spark gaps can switch the pulseline with a total switch resistance loss less than 0.5 J . Another disadvantage of spark gaps is their inability to perform at low voltages as crowbar switches. Ideally, during the crowbar phase, the switch needs to close when there is no voltage between its electrodes. The vacuum surface flashover switches used here perform admirably well under these conditions as will be shown in the next section. Because of the tight space restrictions, a spark gap switch might take the form of an annular rail-gap switch. But the machining tolerances that would be necessary to ensure multichannel operation at these low voltages, would be quite impractical for a rail-gap switch. The surface flashover switches also offer the added convenience of almost complete isolation between the trigger and pulseline charge circuits.

Eight surface flashover sites on the vacuum side of the outer polyurethane disk initiate pulse propagation in the water lines. Each site is triggered by plasma emanating from the end of an overvolted 0.64-cm-diam. semi-rigid coaxial cable. A simplified circuit diagram of

the initiation driver circuit is shown in Fig. 11. The spacing between the end of the trigger coax and the polyurethane surface is typically 8 mm. The inductance of each flashover switch is roughly 50 nH. If all eight switches fire synchronously, the net inductance is $50/8 = 6.3$ nH. Using Eq. (5) the pulseline characteristic impedance is 0.84Ω . So the risetime due to inductance alone is $2.2 \times 6.3/0.84 = 16.5$ ns. The crowbar switches are a similar set of eight triggered flashover sites on the inner polyurethane disk. The crowbar driver circuit is also similar to the initiation circuit shown in Fig. 11. All electrical connections between pulseline conductors are made via spiral wound RF gaskets. Gold plated, 1.3-cm-wide stainless steel strips on the conductor walls provide the mating surfaces for the RF gaskets.

Four capacitive probes in the outer conductor wall monitor the electric field between the middle and outer conductors. Each probe is a gold plated stainless steel disk with a diameter of 1.25 cm. The probe surface is in intimate contact with the water and is flush with the inside surface of the outer conductor. Thus field perturbations due to these probes are kept to a minimum. Of the four probes, two namely CAP1 and CAP4 are on the horizontal midplane. CAP1 is the capacitive probe closest to the initiation switches. Its distance from the switching plane, measured along the inside surface of the outer conductor, is ~ 27 cm, and the distance of CAP4 from the switching plane is ~ 80 cm. The probes CAP2 and CAP3 are located midway between the other two probes, but CAP2 is displaced 60° in poloidal angle above the horizontal midplane, and CAP3 is 60° below the midplane. Their distance from the switching plane is ~ 53 cm.

VI. EXPERIMENTAL RESULTS

Before discussing the pulseline results, it is instructive to review some of the results obtained from an earlier experiment set up to study the characteristics of the vacuum surface flashover switch. A 2.5-cm-high block of polyurethane supported between brass plates, formed the flashover switch for this experiment. The plates were connected to a 3-m-long semi-rigid coaxial cable charged to 30 kV. Plasma from another overvolted semi-rigid coaxial cable triggered the main switch. The driver circuit for the trigger coax is similar to that shown in Fig. 11, and typical charging voltages ranged from 15 kV to 30 kV. The flashover switch current was measured with a shielded Rogowski coil. The risetime appeared to be ~ 10 ns. The calculated rise time due to switch and lead inductances is only 5 ns. Thus a substantial part of the rise time needs to be attributed to the resistive phase of the switch. Resistive rise times usually depend on the magnitude of the voltage across a switch, while inductive rise times show no such dependence. The presence of the resistive phase was confirmed when the rise time increased to 20 ns for charge voltages below 15 kV. For a 10 mm spacing between the trigger coax end and the flashover surface, switch current was observed roughly 50 ns after the trigger coax end overvolted. This delay may be attributed to the finite plasma propagation velocity, which appears to be on the order of 10^7 cm/s. When the spacing was increased to 13 mm the delay increased to ~ 65 ns, and for a spacing of 6 mm the delay appeared to be ~ 35 ns. The switch voltage was 30 kV and the driver charge voltage was -25 kV. The switch performance showed a weak dependence on the polarities of these voltages. The sixteen initiation and crowbar switches used on the pulseline are roughly similar in dimensions to the switch described above. Thus comparable performance can be expected.

The pulseline cannot be dc charged because of resistive losses due to the relatively high water conductivity. For a 20-kV charge voltage, the resistive loss in the pulseline is 1.3 J if the voltage is applied for 4 μ s and the water resistivity is 8 M Ω -cm. This needs to be compared with the 10 J stored energy in the electric fields. The pulse charge time is therefore chosen to be less than 2 μ s, and the charge voltage is near its maximum only for about 1 μ s. Figure 12(a) shows the charging voltage on the middle conductors as measured by capacitive probe CAP1. The pulse charge circuit consists of an 80-nF capacitor dc charged to 18 kV and discharged by a spark gap into a short length of coaxial cable the other end of which connects to the middle and outer pulseline conductors. Since the pulseline capacitance is 50 nF, the charging waveform is expected to have a $[1 - \cos(\omega t)]$ dependence, which appears to be the case in Fig. 12(a), and the peak voltage is $18 \times 2 \times 30.8/50 = 22$ kV. The equivalent series inductance is ~ 8.7 μ H.

The initiation switches fire at ~ 2 μ s when the charge voltage reaches its peak. A gap voltage appears immediately after initiation as shown in Fig. 12(b). The gap voltage is shown on an expanded time scale in Fig. 13(b). It is measured using a capacitive probe located close to the insulating gap spacer. The signals in Fig. 12 are integrated with a 10- μ s passive integrator. For the waveforms in Figs. 12 and 13, the pulseline is not crowbarred and there is no load (beam current). When the initiation switches fire, a quasi-TEM wave is excited in the outer water line. The wavefront propagates away from the switches until it reaches the end of the middle conductor. Here the wave makes a 180° turn and most of the wave energy propagates in the inner water line toward the crowbar switches. Because of the open-circuit condition at the gap, the wave reflects and proceeds towards the initiation switches where it reflects again because of the short-circuit, and the

cycle repeats. The period of the cycle is the two-way transit time in the pulseline, i.e., 90 ns.

The gap voltage in Fig. 12(b) appears to decay with an e-folding time of 0.7 μ s. The decay rate can be calculated from the known resistivities of the conductors used. The gap voltage is obtained by integrating the rate of change of the magnetic flux enclosed by the dashed line in Fig 1. This voltage is also equal to the magnitude of the propagating voltage wavefront, if a one-dimensional approximation is employed for the pulseline. A propagating wavefront in an infinitely long line is described by $V \exp(-\gamma z)$, where $\gamma^2 = (R + Ls)(G + Cs)$. R , L , G and C are the line resistance, inductance, conductance and capacitance per meter and s is the Laplace transform time variable. Since the gap voltage is roughly sinusoidal after the first oscillation, one can substitute $j\omega$ for s and write $\gamma = \alpha + j\beta$, where $\omega/2\pi$ is the frequency of the oscillation. If $R \ll \omega L$ and $G \ll \omega C$, $\alpha \cong R/(2Z_o) + GZ_o/2$, where $Z_o = \sqrt{L/C}$. Using the known resistivities for the carbon-fiber matrix and the phosphor-bronze screen, $R = 33.5 \text{ m}\Omega/\text{m}$. G can be used to account for losses in the water. For a resistivity of 8 $\text{M}\Omega\text{-cm}$, the conductance G is $6 \times 10^{-4} \text{ mho/m}$, and since $Z_o = 0.84 \Omega$, the attenuation constant α is 0.02 Neper/m. Losses in water account for only 1.3% of the total losses. The calculated value of α predicts an e-folding time of 1.5 μ s for the decay rate of the gap voltage. This is roughly twice the observed time in Fig. 12(b).

The higher resistive losses in the experiment may be due to several factors. Potential sources for this discrepancy include joint resistances, perforations in the middle conductor, additional losses when the wave makes the 180° turn around the edge of the middle con-

ductor, losses in the switches, and losses due to skin effect. The correction for skin effect is likely to be small because the diameter of the individual wires forming the phosphor-bronze screen, is $38\text{ }\mu\text{m}$, while the skin depth for the dominant frequency is $\sim 50\text{ }\mu\text{m}$.

Figure 13 shows the pulseline waveforms on an expanded timescale. Only the initiation switches fire for this sequence of shots. Figure 13(a) shows the current in one of the trigger coaxes at the driver end of the line (see Fig. 11). The current is measured using a shielded Rogowski coil and integrated with a passive $2\text{-}\mu\text{s}$ integrator. This waveform triggers the oscilloscope and serves as the time reference for all other waveforms in Fig. 13. The dc charge voltage on the 80-nF driver capacitor is -24 kV . Waveforms (b) thru (e) are integrated with a $10\text{-}\mu\text{s}$ passive integrator. Figure 13(b) shows a two-shot overlay of the gap voltage. The dip at 330 ns does not appear to be quite reproducible, probably because of variations or lack of synchronism in the initiation switch firings. Waveforms (c), (d) and (e) show the voltages measured by capacitive probes CAP1, CAP3 and CAP4. There is a certain amount of shifting of the zero-level baseline in these signals. This is readily apparent in Fig. 12(a), and it is due to the inadequate RC time of the $10\text{-}\mu\text{s}$ integrator. This effect is absent in the gap voltage waveforms because they are approximately symmetrical voltages. Signals (b) thru (e) use a common-mode rejector¹⁵ while (a) does not. The common-mode rejector was made by winding 97 turns of RG-174 cable on a ferrite core, and it adds a delay of 90 ns . Additionally, since the Rogowski coil measures the current at the driver end, it can "sense" the trigger coax flashover event only after 45 ns , which is the one-way transit time of the trigger cables. The flashover event occurs at $t = 120\text{ ns}$ in Fig. 13(a), and the gap voltage appears at $t = 230\text{ ns}$ in Fig. 13 (b). The delay in the firing of the initiation switches is therefore $(230 - 120) - (90 - 45) = 65\text{ ns}$. This is consistent with

the finite plasma propagation velocities and delays measured for the prototype flashover switch described at the beginning of this section.

The rise time of the gap voltage waveform in Fig. 13(b) appears to be ~ 22 ns as indicated by the first negative going pulse. This could be the result of only six out of eight switches firing simultaneously, in which case the predicted risetime is $2.2 \times 8.3 / 0.84 = 22$ ns. Because of the transit time isolation between switches, there is a high probability that all eight switches fire on every shot, but two switches may fire, say 5 ns later. This is a likely event, in view of the fact that the delay due to trigger plasma propagation time, is roughly 65 ns. A more detailed comparison of the waveforms in Fig. 13 with simulated waveforms, is carried out in the next section.

Figure 14 shows the effect of crowbarring. The delay between the initiation and crowbar switch firings can be continuously varied. Figure 14(a) shows the gap voltage when the crowbar switches fire at the right time. The waveform is close to the desired waveform (see Fig. 6). In Fig. 14(b) the pulseline was crowbarred ~ 20 ns later. The delay can be arbitrarily varied to essentially short-circuit the gap voltage at any point in time. Even though there is energy stored in the pulseline during the post-crowbar phase, no gap voltage appears because both ends of the line have been short-circuited. Figure 14(a) appears to indicate that the flashover switches perform satisfactorily even when there is very little voltage across them. It is extremely difficult to achieve similar performance with spark gaps.

Following the installation of the strong focusing windings in the NRL device it has been routinely observed that for several combinations of injection parameters, the beam consis-

tently spirals from the injection position to the magnetic minor axis and is trapped.^{1, 12} Thus, trapping experiments using the pulseline have not yet been performed. If successful, the trapping of the beam with the pulseline is expected to make the modified betatron more versatile because it will allow a wider choice of the values of the toroidal and strong focusing fields during injection.

VII. DISCUSSION

In this section, the experimental data are compared with results from a computer simulation for a straight coaxial transmission line, which is known to obey the one dimensional wave equation. An interesting outcome of this comparison is the possibility that three dimensional effects in the toroidal pulseline counteract some of the distortions in pulse shape due to switch inductance. The net result is a superior pulse shape in comparison with the pulse that would have been obtained with a straight coaxial pulseline.

There are several features in the experimental data that do not agree with the computer simulations. These differences are described in more detail later in this section. The gap voltage waveform (Fig. 13 (b)) is of special interest. Although, the initial falling edge of the bipolar gap voltage waveform indicates a rise time of ~ 22 ns, which is close to the predicted value, the subsequent rising edge at ~ 300 ns lacks a "shoulder" and has a rise time of ~ 32 ns which is much larger than expected. Also, the dip at ~ 350 ns is considerably smoothed out. These, and other smoothing effects become apparent when waveforms (b) thru (e) in Fig. 13 are compared with the simulated waveforms appearing in Fig. 16.

The 1-D simulations are performed using a transmission line code that is routinely

used for the analysis of transient in electrical circuits. The code successfully reproduces the current waveform in Fig. 13(a), where wave propagation takes place in a 9-m long, RG-214 coaxial cable, and three dimensional effects are absent. Figure 15 shows the transmission line representation of the toroidal pulseline, as used in the 1-D code. The voltages V_1 , V_3 and V_4 at the junction nodes correspond to the voltages measured by the capacitive probes CAP1, CAP3 and CAP4, and the electrical lengths of the four transmission lines are appropriately chosen. Also, $\sum_{i=1}^4 \tau_i = 45$ ns, which is the one-way transit time of the pulseline. All lines are assumed to be lossless. The switch inductance L_s is assumed to be 8 nH, corresponding to the case where six out of eight switches fire simultaneously.

The topology of the pulseline is interesting in the sense that the gap voltage responds immediately to the closure of the initiation switches. Therefore, the rise time of the gap voltage is directly related to the switch closure time. Figure 16(a) shows that the rise time of the first negative going pulse is ~ 25 ns, which agrees with the experimental value. However, the fall time of the negative pulse shows a well defined shoulder at ~ 45 ns. This shoulder is absent, or is considerably smoothed out in the experiment (see Fig. 13(b)). The shoulder occurs when the propagating wavefront reaches the crowbar switches, and reflects due to the open circuit condition at the gap. The dispersive resistive losses in the pulseline can also cause smoothing, but this is not applicable here because resistive losses modify the pulse shape only over long periods of time, while the smoothing described above occurs almost instantaneously. Traces (b), (c) and (d) in Fig. 16 show the calculated voltages corresponding to those measured by capacitive probes CAP1, CAP3 and CAP4. These waveforms show well defined shoulders (for example, the shoulder in (b) is at ~ 85 ns),

which are delayed signatures of the reflection event at the gap. Again, all these shoulders are smoothed out in the experimental data.

Another distinguishing feature is the large dip in the calculated gap voltage waveform in Fig. 16(a) at ~ 100 ns. This occurs when the wavefront returns to the initiation switches and reflects. The dip would be absent if an ideal, distributed, radial switch with zero inductance is employed in place of the eight surface flashover switches used in the experiment. If the switch inductance L_s is reduced, the depth of the dip is unaffected, but its width is reduced. This can also be shown analytically. The gap voltage dip is considerably smoothed out in the observed waveform.

An explanation of the observed smoothing is the possibility that the three dimensional geometry of the pulseline causes substantial wavefront distortions, and the toroidal pulseline may indeed be dispersive. There may also be other mechanisms that distort the waveforms in the experiment. However, the distortions cannot be attributed to the capacitive probes used for the measurements, because these probes are known to have adequate frequency response. In an earlier analysis of curved transmission lines,¹⁶ expressions for the characteristic impedance of a deformed line have been derived, but the analysis does not treat the details of wave propagation inside the line. It is well known that a sharp bend in a coaxial cable distorts the shape of a pulse sent through it. The distortion is usually analyzed in terms of the impedance mismatch introduced by the bend. In practice, mechanical considerations limit the bend radius of cables. As a result, the observed distortions in cables are usually negligibly small.

The gap voltage waveform of a straight coaxial pulseline is expected to have a pro-

nounced dip as shown in Fig. 16(a). This dip is considerably smoothed out in the toroidal pulseline and the gap voltage waveform bears closer resemblance to the ideal waveform. The accelerated electron beam interacts with the pulseline only via the gap voltage and the beam cannot "sense" the higher order modes or other nonideal conditions existing inside the pulseline. So, in a restricted sense, the toroidal pulseline might be superior to a straight coaxial pulseline.

VIII. SUMMARY AND CONCLUSIONS

Numerical results from the integration of orbit equations indicate that the injected electron beam in a modified betatron accelerator can be trapped using a charged pulseline over a wide range of operating parameters. Trapping is accomplished by modifying the poloidal orbit within a bounce period. This orbit modification is due to the change of beam energy. A distinctive feature of this trapping scheme is that the average canonical angular momentum $\langle P_\theta \rangle$ is not conserved. Trapping is achieved over a wide range of pulseline voltages from 30 kV to 100 kV.

A toroidal coaxial version of the Pavlovskii line is used to change the energy of the beam. A $0.84\text{-}\Omega$ water dielectric line has been built and tested. The toroidal pulseline is successfully switched using triggered vacuum surface flashover switches. The rise time of the crowbarred, bipolar pulse is typically 22 ns. The gap voltage waveform of a straight coaxial pulseline is expected to have a pronounced dip due to switch inductance. Experimental data show that this dip is considerably smoothed out in the toroidal pulseline.

REFERENCES

1. C. A. Kapetanacos *et al.*, Phys. Rev. Lett. **64**, 2374 (1990).
2. H. Ishizuka *et al.*, in *Proceedings of the Seventh International Conference on High-Power Particle Beams, Karlsruhe, Germany, 1988*, edited by W. Bauer and W. Schmidt (Kernforschungszentrum Karlsruhe GmbH, Karlsruhe, 1988), Vol. II, p. 857.
3. S. Humphries, Jr., and L. K. Len, in *Proceedings of the 1987 Particle Accelerator Conference, Washington, D.C., 1987*, edited by E. R. Lindstrom and L. S. Taylor (IEEE, New York, 1987), p. 914.
4. V. Bailey *et al.*, in *Proceedings of the 1987 Particle Accelerator Conference* (Ref. 3), p. 920.
5. W. K. Tucker *et al.*, in *Proceedings of the 1987 Particle Accelerator Conference* (Ref. 3), p. 957.
6. P. Sprangle and C. A. Kapetanacos, J. Appl. Phys. **49**, 1 (1978).
7. C. A. Kapetanacos *et al.*, Phys. Fluids **26**, 1634 (1983).
8. N. Rostoker, Comments Plasma Phys. **6**, 91 (1980).
9. C. Roberson *et al.*, Phys. Rev. Lett. **50**, 507 (1983).
10. C. A. Kapetanacos *et al.*, Part. Accel. **21**, 1 (1987).
11. P. Sprangle and C. A. Kapetanacos, Part. Accel. **18**, 203 (1986); Y. Seo and P. Sprangle, *ibid.* (to be published).
12. C. A. Kapetanacos *et al.*, Phys. Rev. A. **44**, 3900 (1991).

13. A. I. Pavlovskii *et al.*, Sov. Phys. Dokl. **20**, 441 (1975).
14. D. Eccleshall and J. K. Temperley, J. Appl. Phys. **49**, 3649 (1978).
15. J. Mathew, Rev. Sci. Instrum. **61**, 1926 (1990).
16. H. H. Meinke, Arch. Elekt. Uber. **5**, 106 (1951).

Table I. Parameters used for the beam trapping simulations.

	Fig. 7	Fig. 8	Fig. 9
Relativistic factor γ	2.36	2.36	2.36
Bipolar pulse amplitude (kV)	∓ 80	∓ 100	∓ 60
$\Delta\gamma/\text{pass}$	± 0.157	± 0.196	± 0.117
Beam current I_b (kA)	1.36	1.36	1.36
Injection radius r_i (cm)	108	108	108
Beam radius r_b (cm)	1	1	1
Self field index $n_s(r_b/a)^2$	0.6	0.6	0.6
Torus major radius r_o (cm)	100	100	100
Torus minor radius a (cm)	15.2	15.2	15.2
SF radius ρ_o (cm)	23.4	23.4	23.4
SF current I_{sf} (kA)	20	20	20
SF index n_{sf}	8	8	8
Vertical field at injection B_z (G)	34	34	34
Vertical field index n	0.5	0.5	0.5
Toroidal Field B_θ (G)	4000	4000	4000

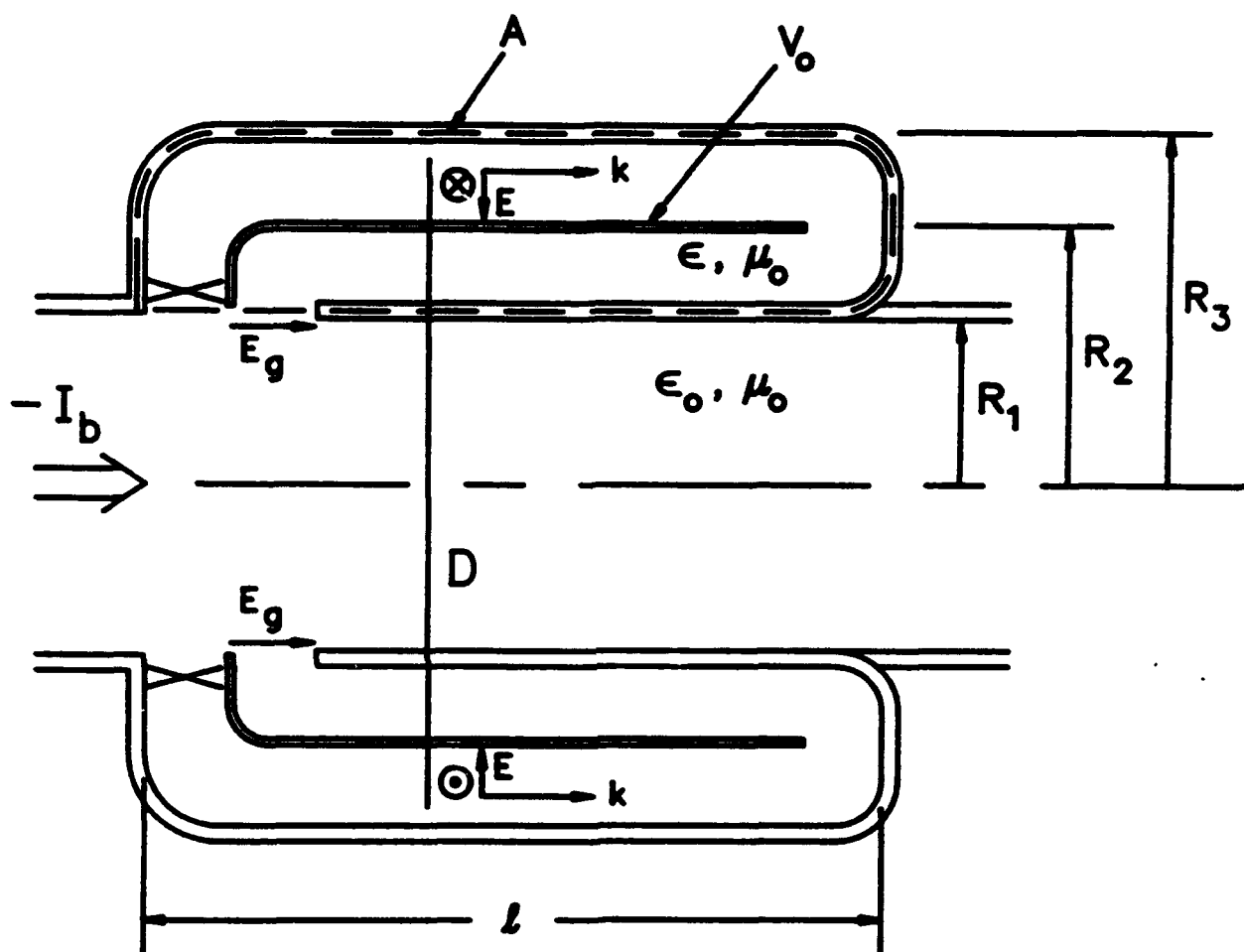


FIG. 1. Simplified cross sectional view of the coaxial pulseline.

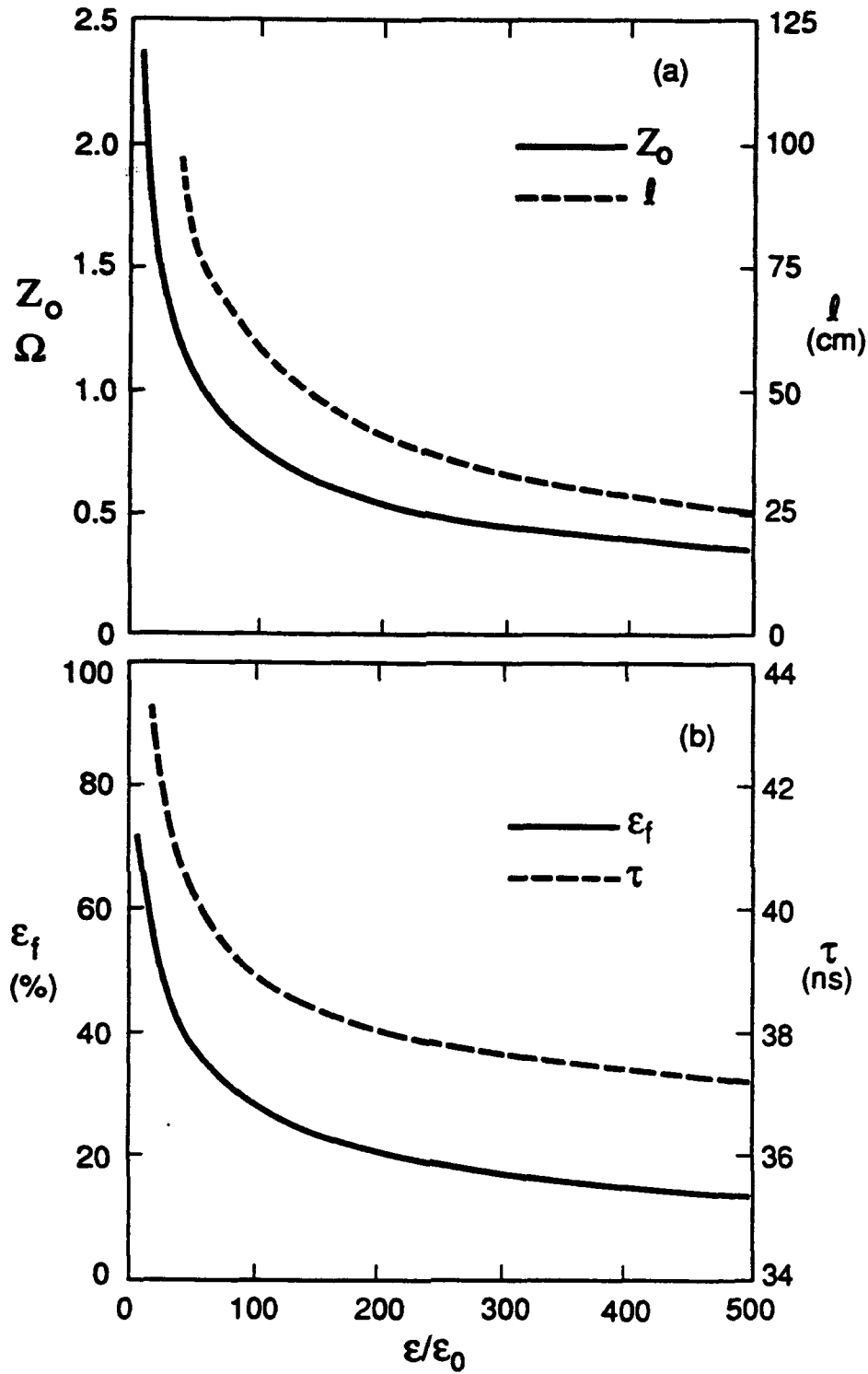


FIG. 2. Pulseline characteristics for $\Delta E = 60$ keV, $\tau_o = 24$ ns, $V_o = 20$ kV, $I_b = 2$ kA, $R_1 = 16.8$ cm, $R_2 = 19.0$ cm and $R_3 = 21.6$ cm. (a) Plots of Z_o and l versus ϵ/ϵ_o . (b) Plots of ϵ_f and τ versus ϵ/ϵ_o .

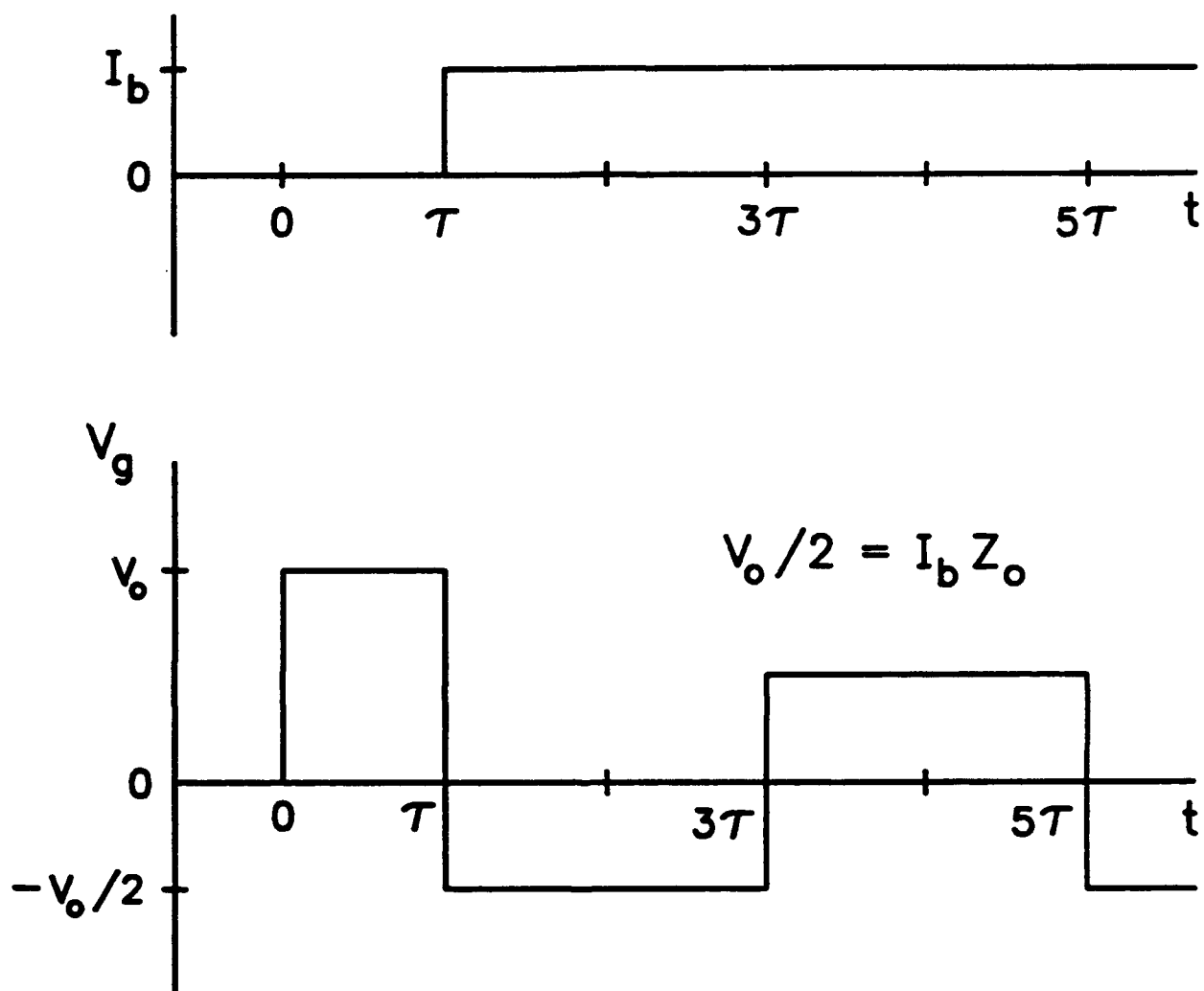


FIG. 3. Injected beam current and gap voltage waveforms for the matched condition.

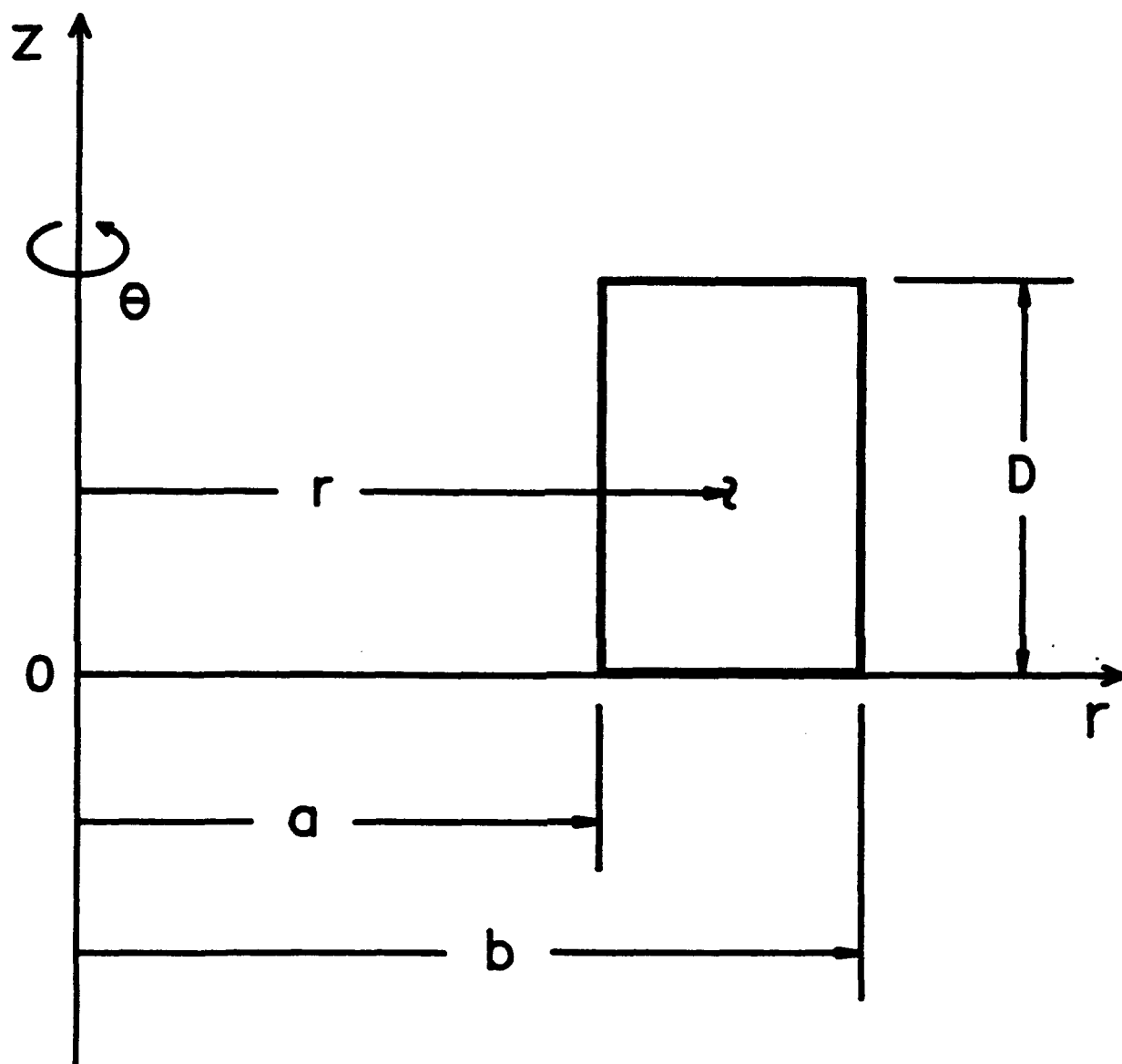


FIG. 4. Coordinate system for a toroidal waveguide with rectangular cross section.

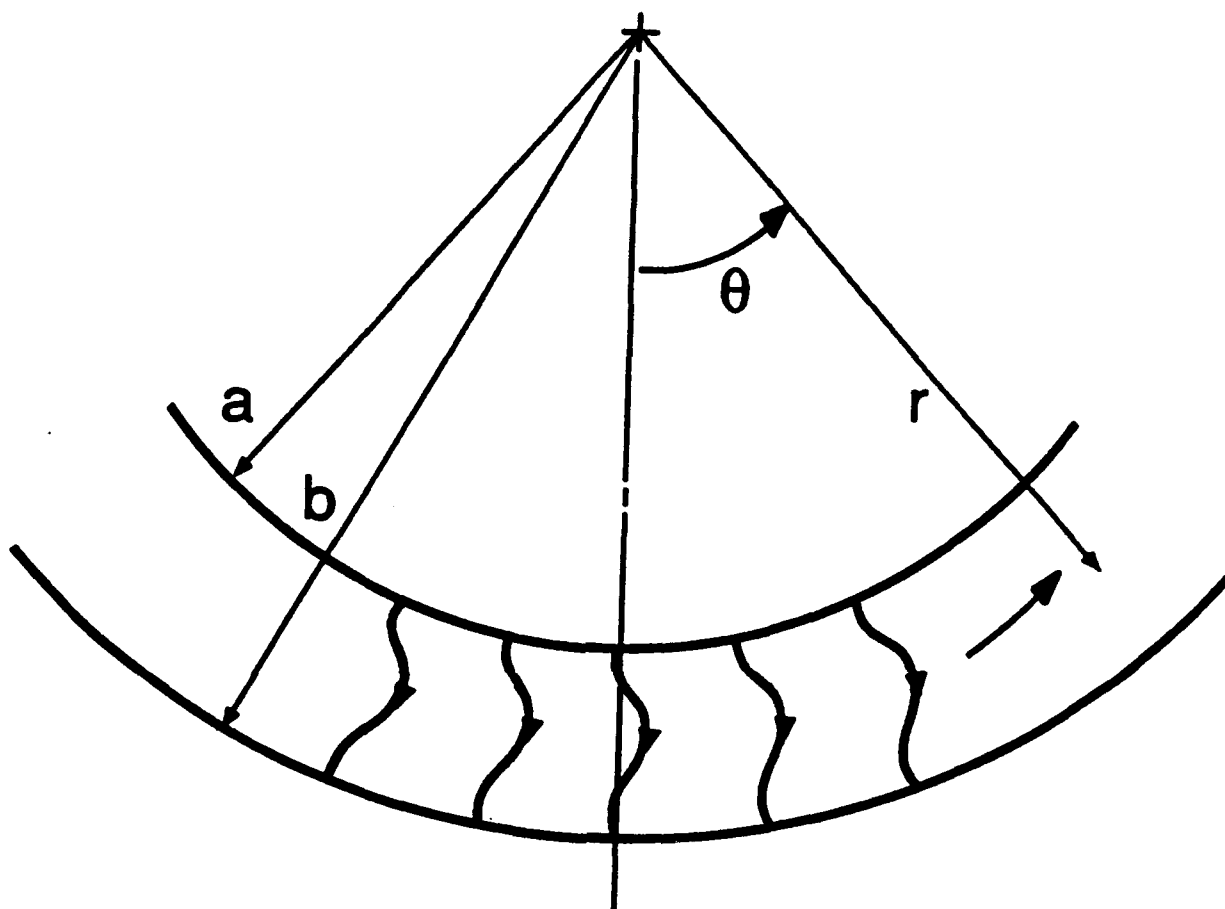


FIG. 5. Sketch of quasi-TEM wave propagation in a curved stripline of infinite width.

Only electric field lines are shown, and E_θ is shown exaggerated for clarity.

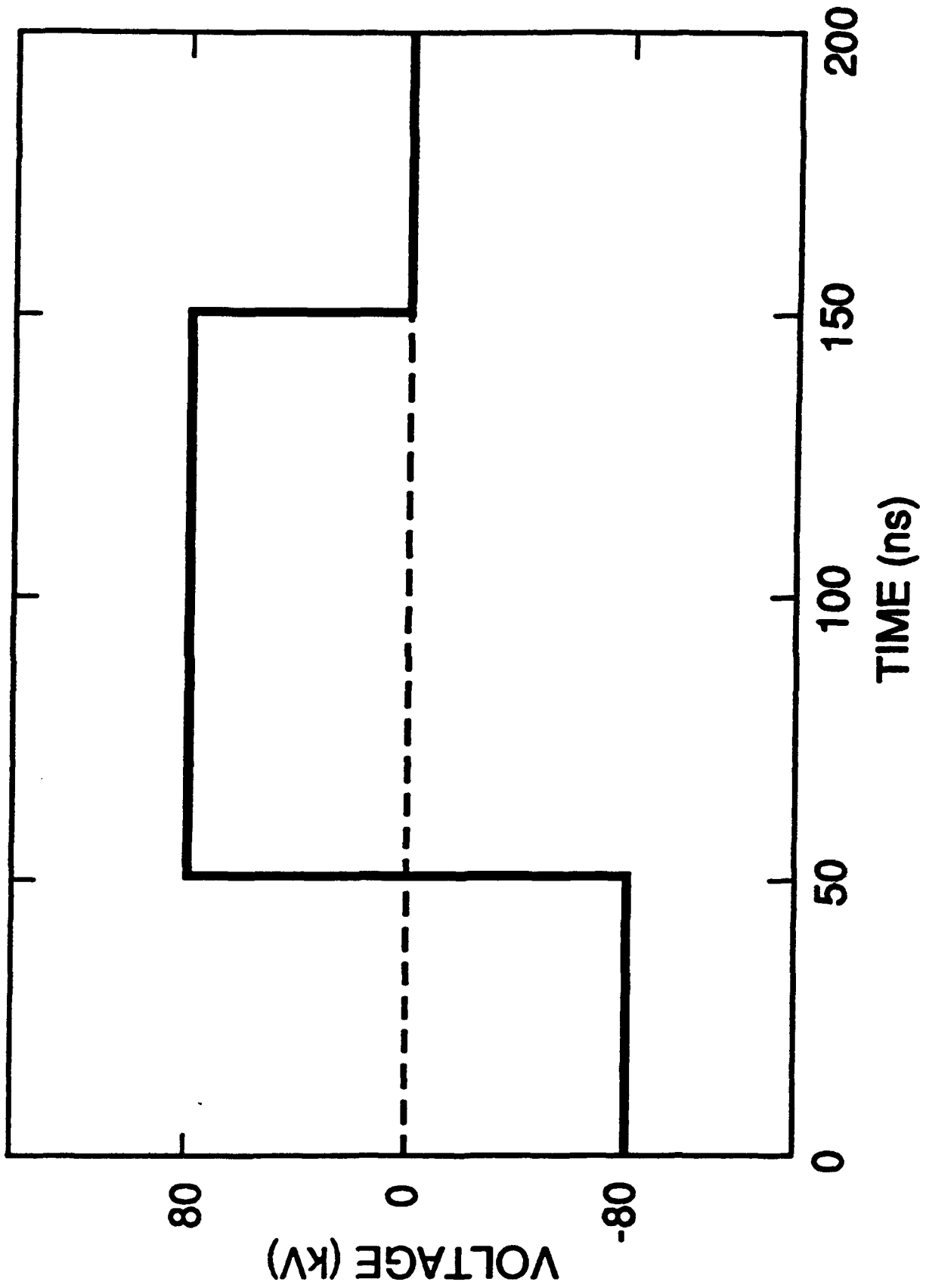


FIG. 6. Bipolar gap voltage pulse used for numerical simulations.

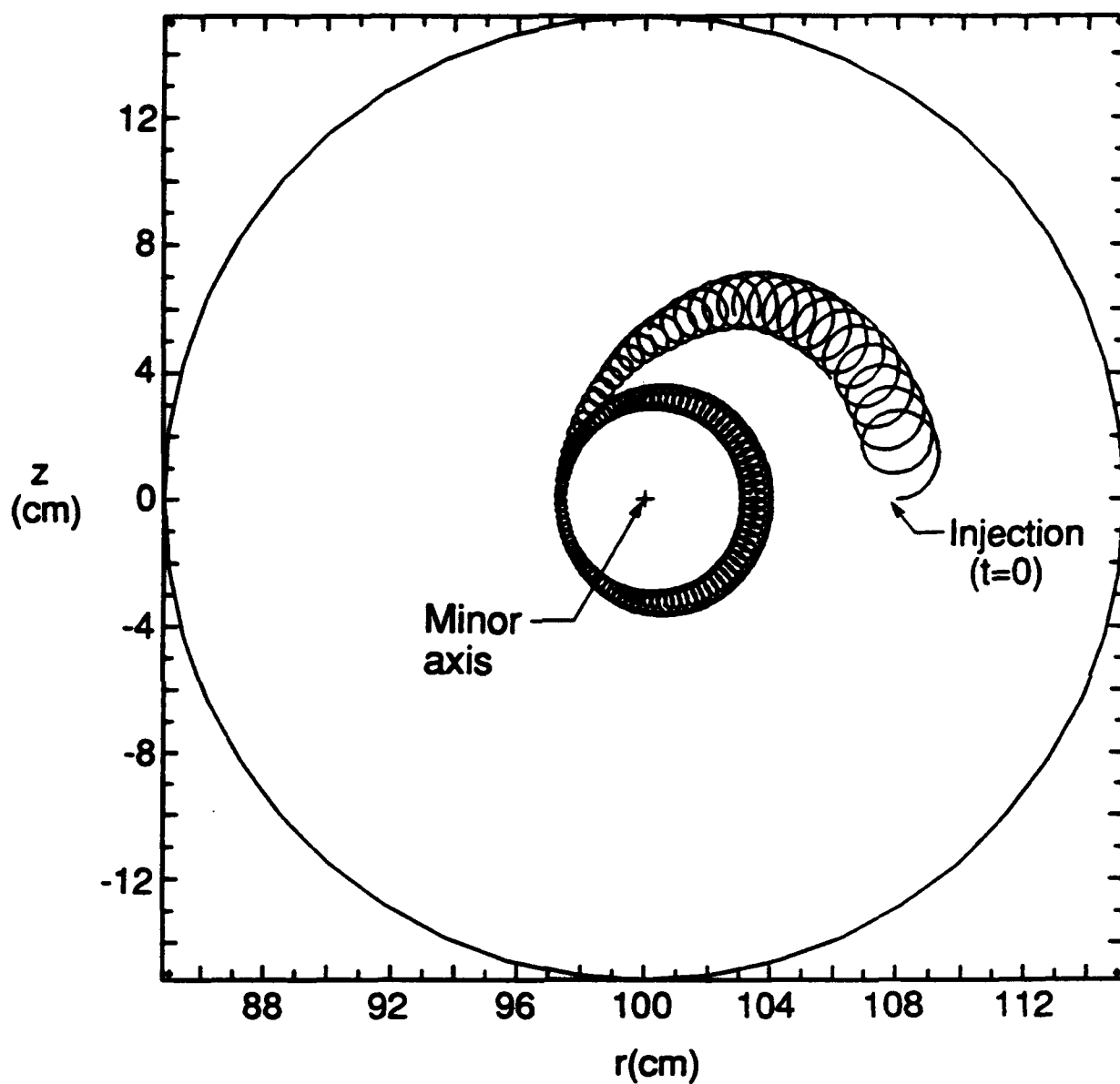


FIG. 7. Beam trapping simulation for an 80-kV bipolar pulse. The minor axis is at $r = 100$ cm. Other parameters are listed in Table I.

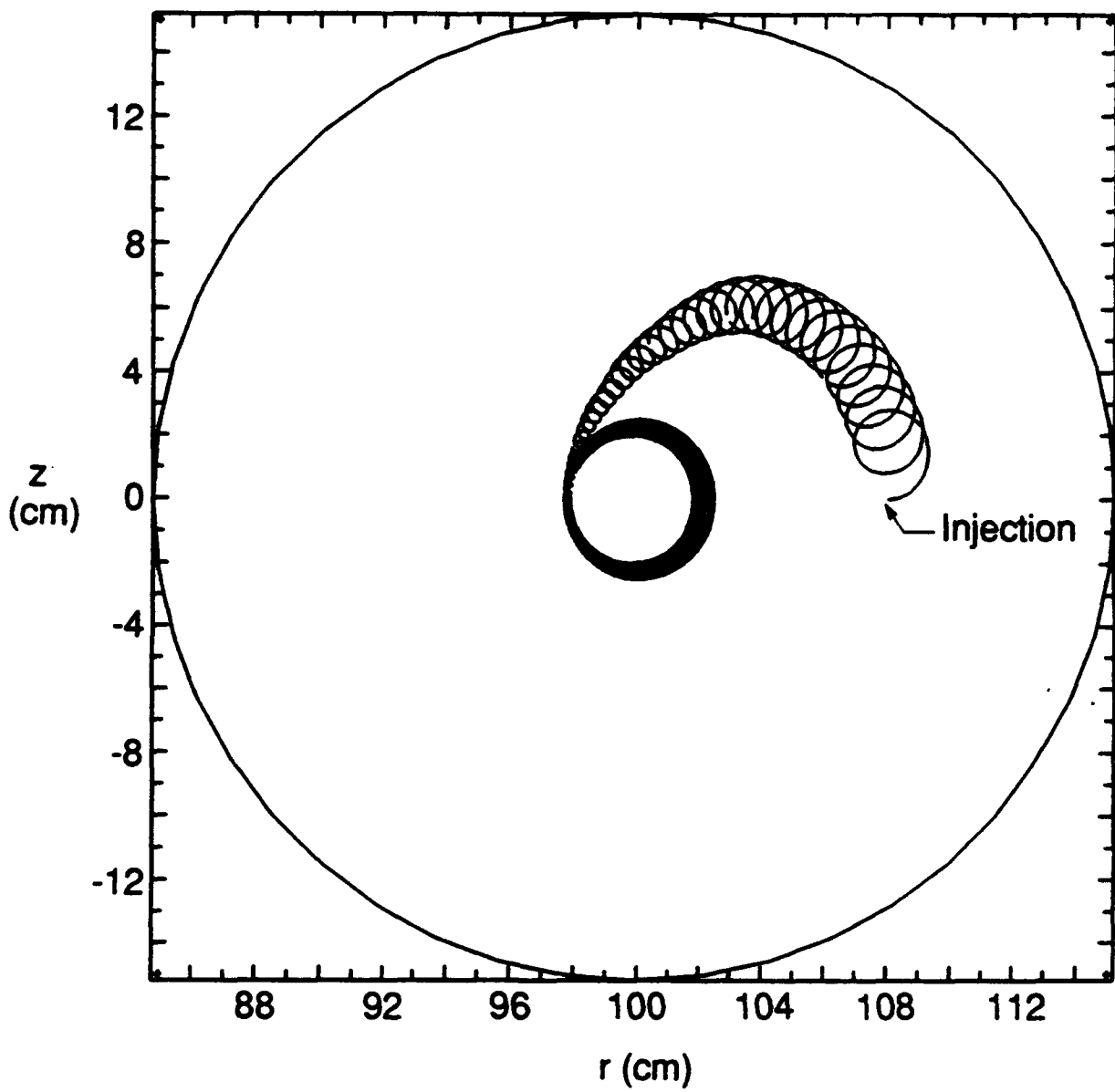


FIG. 8. Beam trapping for a 100-kV pulse.

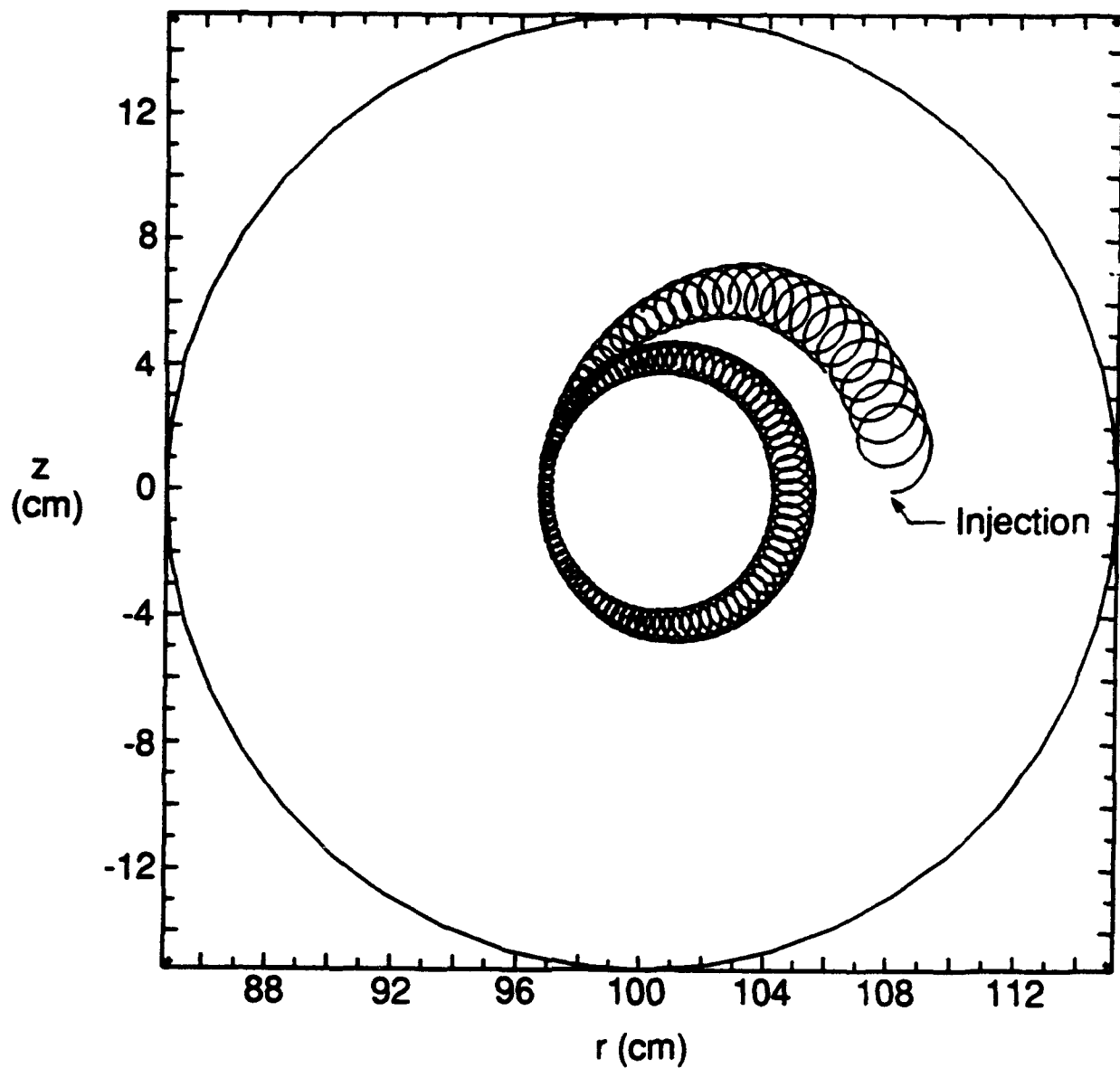


FIG. 9. Beam trapping for a 60-kV pulse.

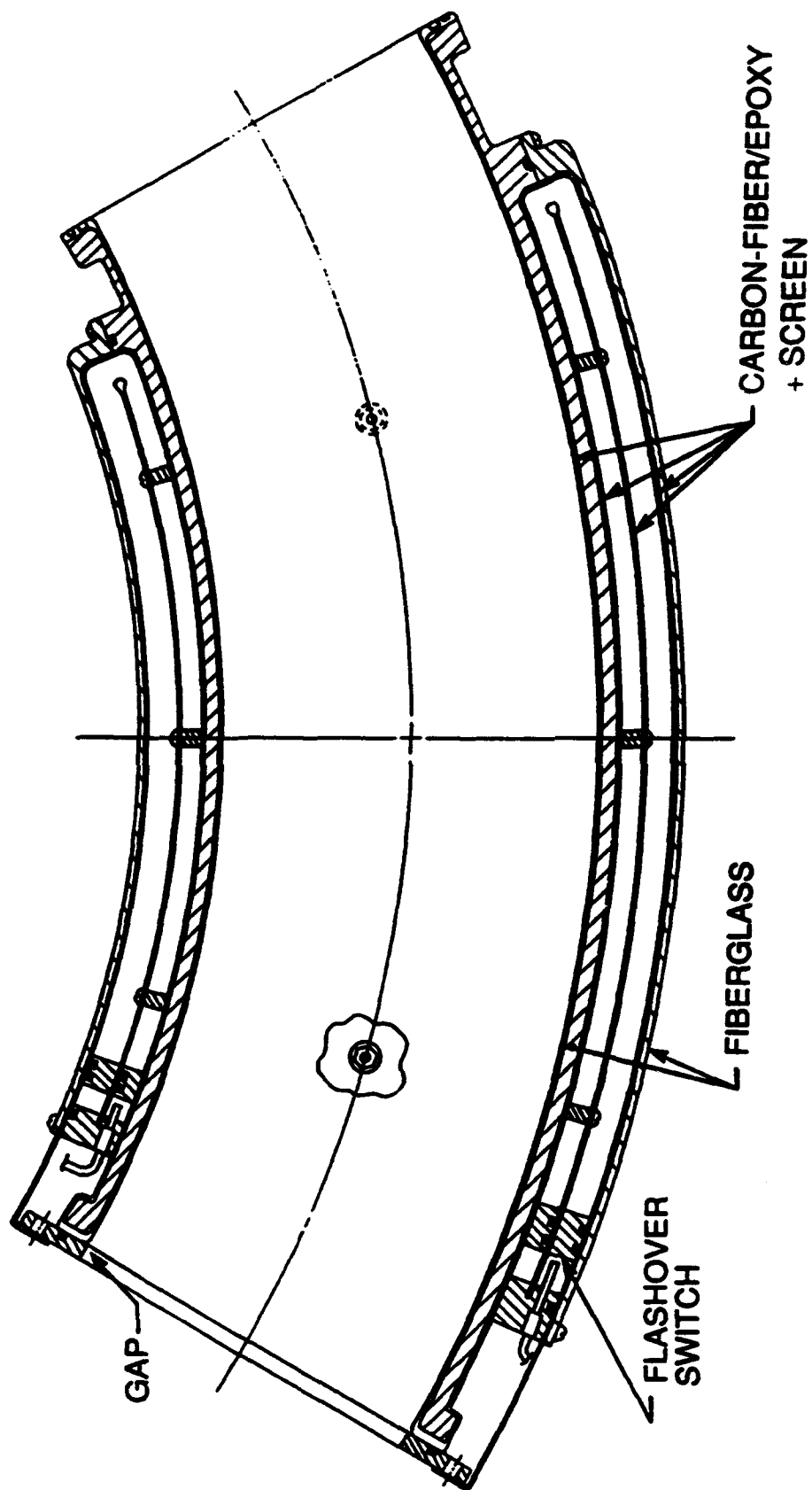


FIG. 10. Cross sectional view of the toroidal coaxial pulseline.

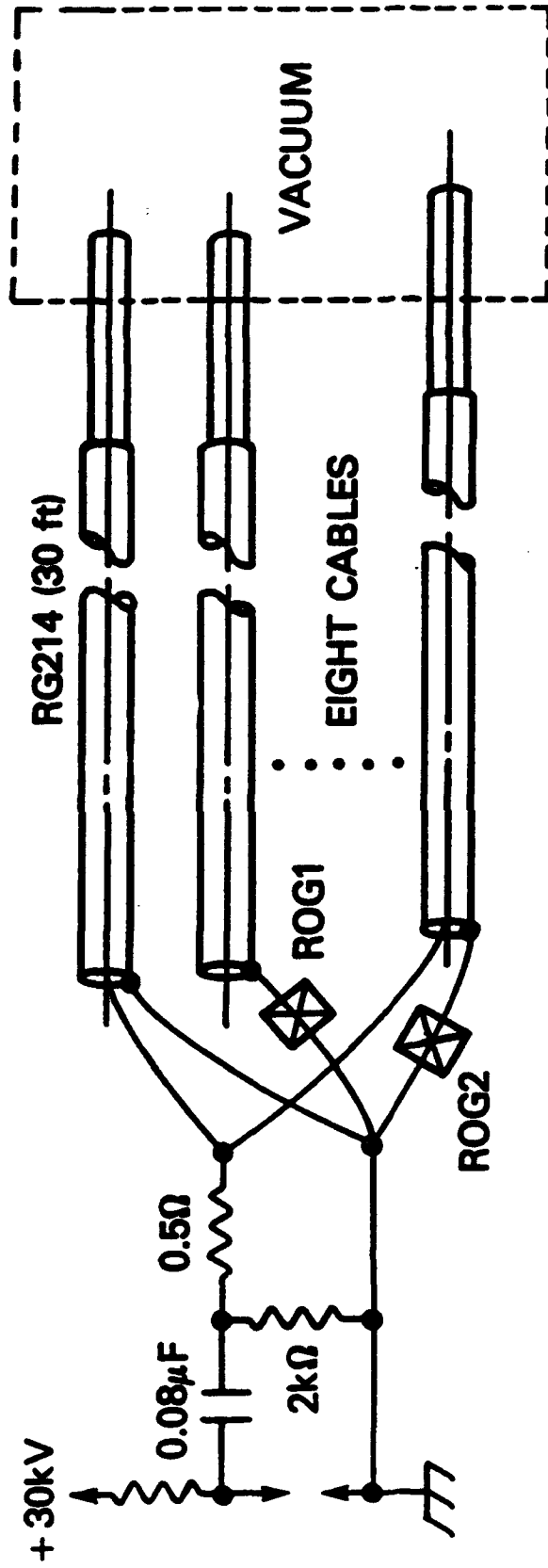


FIG. 11. Simplified circuit diagram of the initiation driver circuit used to trigger eight surface flashover sites in the pulseline.

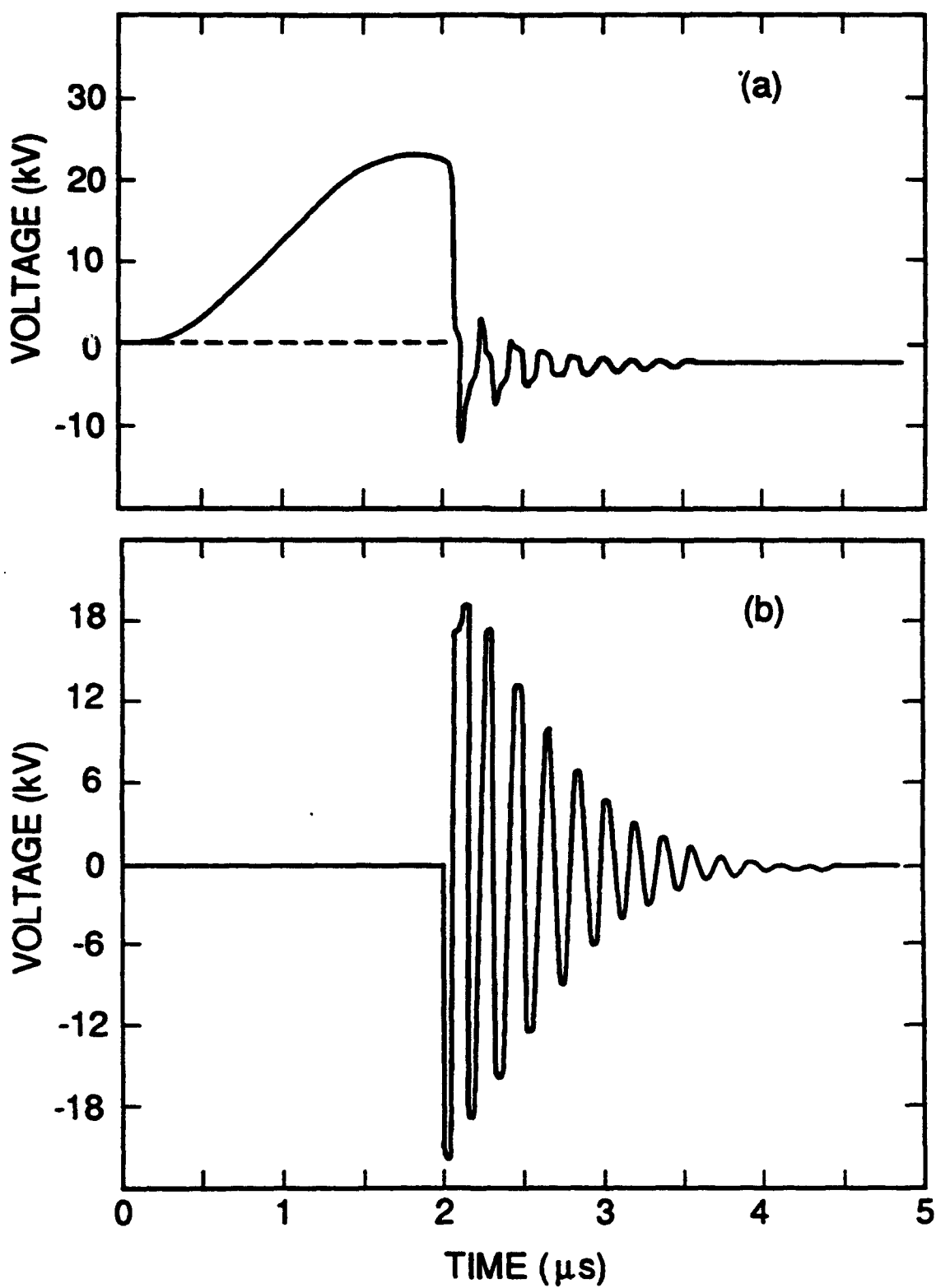


FIG. 12. (a) Pulseline charge voltage measured by capacitive probe CAP1. (b) Gap voltage waveform.

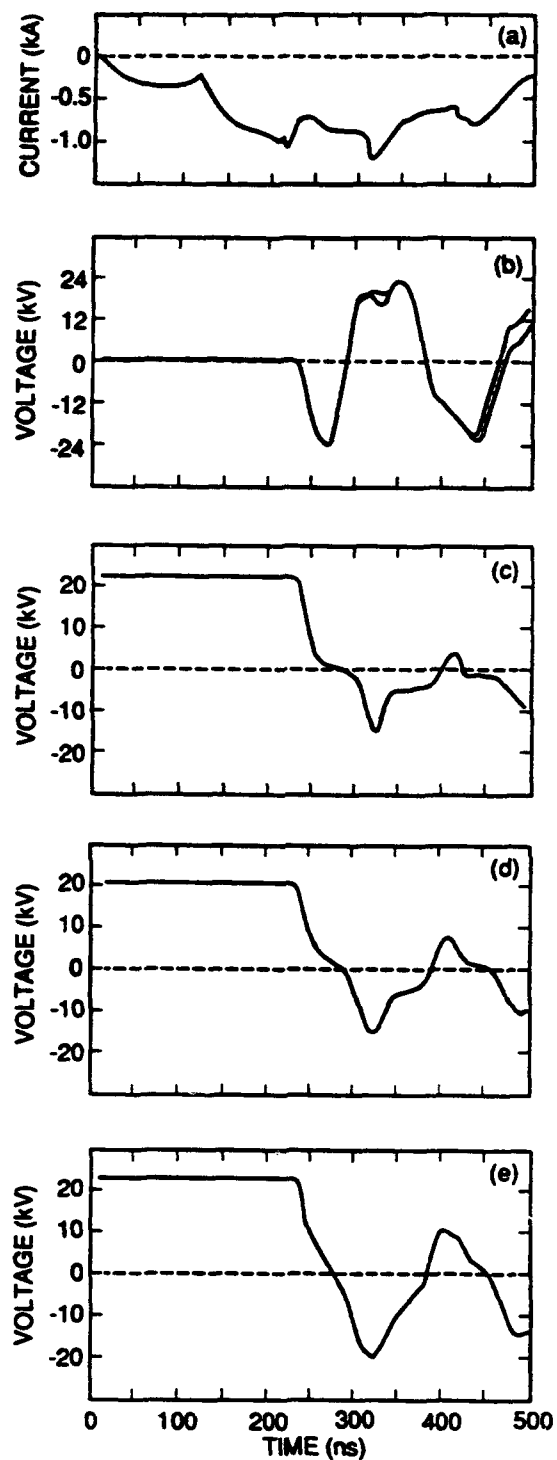


FIG. 13. Noncrowbarred pulseline waveforms for 22-kV charge voltage. (a) Trigger coax current, (b) gap voltage waveform (two shot overlay), (c) voltage measured by capacitive probe CAP1 in water, (d) voltage measured by CAP3 and (e) voltage measured by CAP4.

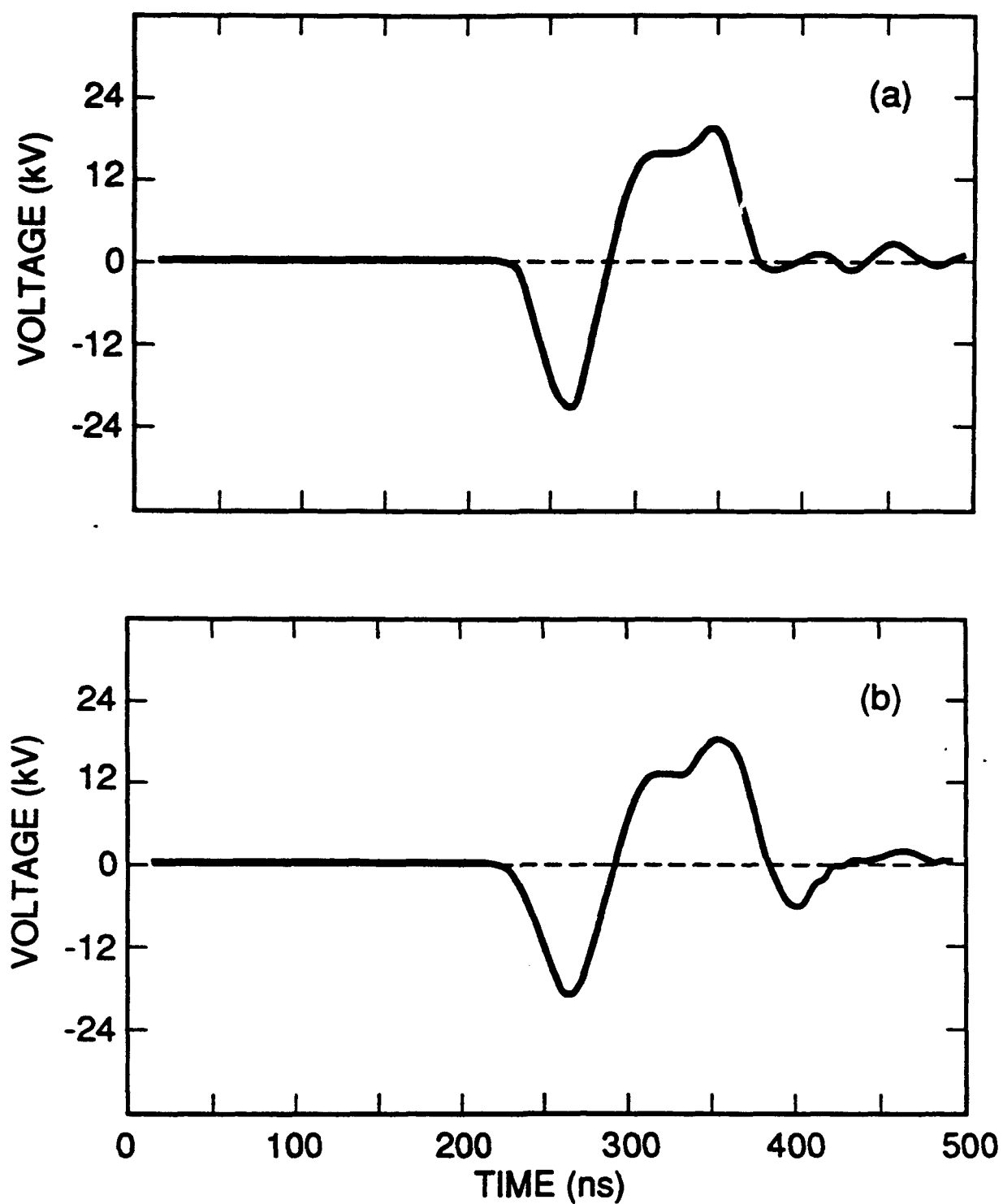
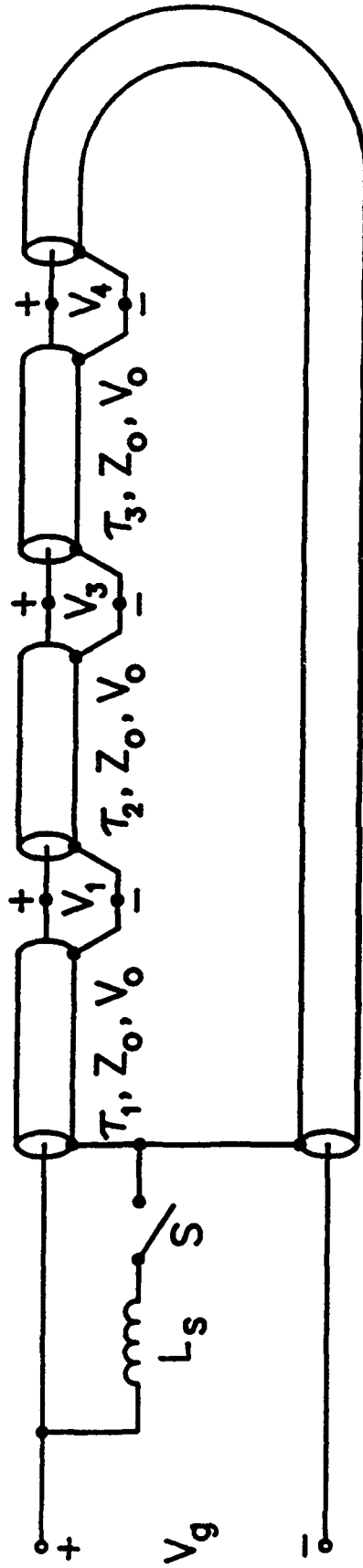


FIG. 14. Crowbarred gap voltage waveforms for 22-kV charge voltage. The crowbar switches fire 20 ns later for (b).



$$T_4, Z_0, V_0$$

FIG. 15. Transmission line representation of the toroidal pulseline for 1-D simulations.

$$\tau_1 = 6.0 \text{ ns}, \tau_2 = 6.3 \text{ ns}, \tau_3 = 6.3 \text{ ns}, \tau_4 = 26.4 \text{ ns}, \sum_{i=1}^4 \tau_i = \tau = 45 \text{ ns}, Z_0 = 0.84$$

Ω , $V_0 = 25 \text{ kV}$ and $L_s = 8 \text{ nH}$. V_g represents the gap voltage. V_1 , V_3 and V_4 represent the voltages measured by probes CAP1, CAP3 and CAP4. The switch

S closes at $\tau = 0$.

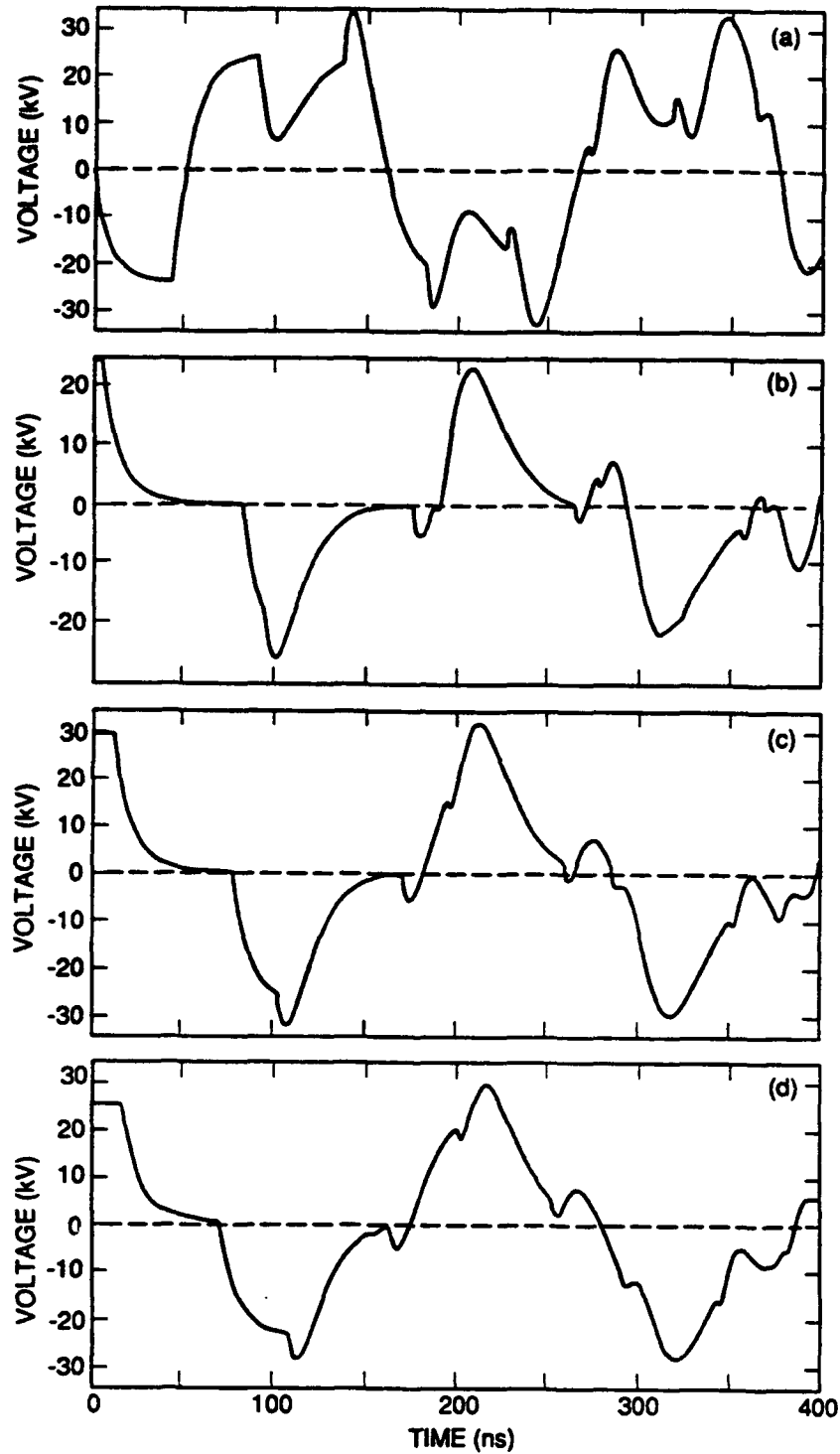


FIG. 16. (a) Simulated gap voltage waveform using the 1-D transmission line code. (b) thru (d) show the simulated waveforms corresponding to the voltages measured by CAP1, CAP3, and CAP4.

Appendix BB

Dynamic Behavior of an Electron Ring Close to a Cyclotron Resonance in a Modified Betatron Accelerator

Dynamic behavior of an electron ring close to a cyclotron resonance in a modified betatron accelerator

D. Dialetis,* S. J. Marsh,[†] and C. A. Kapetanakos

Plasma Physics Division, Naval Research Laboratory, Washington, D.C. 20375-5000

(Received 15 June 1992)

The effect on the electron-ring dynamics when a cyclotron resonance is crossed in a modified betatron accelerator has been studied analytically and numerically. It has been found that, in the presence of small vertical field errors, there is a field-error-amplitude threshold below which the normalized transverse velocity β_1 of the gyrating electrons is bounded (Fresnel regime) and above which it is unbounded (lock-in regime). In the lock-in regime, the average value of the normalized axial (toroidal) momentum $\gamma\beta_\theta$, where γ is the relativistic factor and β_θ is the normalized axial velocity, remains constant, i.e., the resonance is never crossed. In addition, above threshold, β_1 increases proportionally to the square root of the time. The threshold value of the vertical field error amplitude can be made larger either by increasing the acceleration rate or by adding a small oscillatory toroidal field to the main toroidal field. The multiple crossing of the same resonance, in the presence of such a small oscillatory toroidal field, was also studied with some interesting results.

PACS number(s): 41.75.Fr, 41.85.Lc, 29.27.Bd

I. INTRODUCTION

There is extensive experimental evidence suggesting that the gradual beam loss that is observed in the Naval Research Laboratory (NRL) modified betatron accelerator (MBA) is a consequence of crossing various cyclotron resonance modes during acceleration [1,2]. The cyclotron resonance is due to the excitation of the cyclotron motion by field errors associated with the toroidal and vertical magnetic fields. Consequently, these field errors can be either a vertical-field δB_z (VF) error or an axial-(toroidal) field δB_θ (TF) error or both.

Recirculating accelerators with low accelerating gradient such as the existing NRL modified betatron are sensitive to field errors, because the electrons have to perform a large number of revolutions around the major axis in order to obtain the desired peak energy. Successful detection and elimination or reduction of several field errors in the NRL device led to beam energies in excess of 20 MeV, while the trapped current is above 1 kA [3].

Although the cyclotron resonance is a potent mechanism with the potential to disturb the beam at a low acceleration rate and when the various fields are not carefully designed, it also may provide a powerful technique for extracting the beam from the magnetic-field configuration of the modified betatron [4]. The study of the cyclotron resonances is facilitated by introducing the detuning factor $w = r_0 \Omega_{\theta 0} / \gamma \beta_\theta c - l$, where r_0 is the major radius of the torus, c is the velocity of light, γ is the relativistic factor, β_θ is the normalized toroidal velocity, $\Omega_{\theta 0} = |e| B_{\theta 0} / mc$, $B_{\theta 0}$ is the toroidal magnetic field on the minor axis, e and m are the charge and mass of the electron, and l is the mode number of the resonance. The l mode of the cyclotron resonance occurs when the ratio of the toroidal field $B_{\theta 0}$ to the vertical field B_{z0} is approximately equal to l . Since at equilibrium the ratio

$r_0 \Omega_{\theta 0} / \gamma \beta_\theta c$ is approximately unity, at least when the beam current is low and in the absence of strong focusing, the l -mode cyclotron resonance is crossed when the detuning factor is zero. Furthermore, the detuning factor appears naturally in the slow equations of motion derived by averaging out the fast cyclotron motion. The fact that $w + l$ is inversely proportional to $\gamma \beta_\theta$ has a profound effect on the ring dynamics. The quantity $\gamma \beta_\theta$ has a nonlinear dependence on the normalized perpendicular velocity β_1 , and, as a consequence, there is a threshold for the vertical field error amplitude below which β_1 is bounded (Fresnel regime) and above which β_1 increases continuously (lock-in regime) with time. In the lock-in regime, the detuning factor remains almost zero long after the resonance has been reached and, therefore, the resonance is never crossed. In addition, above threshold, β_1 increases proportionally to the square root of time while $\gamma \beta_\theta$ remains, on the average, a constant. The threshold value of the vertical field error amplitude can be made larger either by increasing the acceleration rate or by adding a small oscillatory toroidal field to the main toroidal field. The latter method is called dynamic stabilization of the resonance.

In the case of a vertical field error and in the absence of acceleration, space charge, and strong focusing field, our studies of the cyclotron resonances show that the normalized transverse velocity β_1 and thus the Larmor radius of the transverse motion of the gyrating particles grows linearly with time [5], provided that nonlinear effects associated with $\gamma \beta_\theta$ are neglected. When such effects are taken into account, β_1 is periodic and bounded.

As mentioned previously, in the presence of an accelerating field and of a large vertical field error, β_1 increases proportionally to the square root of time while $\gamma \beta_\theta$ saturates, i.e., the electrons lock into a specific resonance (lock-in regime). When the amplitude of δB_z is

below the threshold, β_1 exhibits Fresnel behavior, i.e., β_1 grows quickly for approximately 1 μ sec and then saturates until the beam reaches the next resonance.

In the case of an axial field error and in the absence of acceleration, when the ring is initially at exact resonance, β_1 grows exponentially with time only for a very short period. Since β_1 increases at the expense of β_0 , the particles are kicked off resonance and β_1 varies cyclicly with time. Similarly, in the presence of an accelerating field β_1 behaves as in the case of the vertical field error, i.e., below threshold it exhibits the Fresnel behavior and above threshold the ring locks into the resonance. The same is also true during acceleration even in the absence of a vertical or toroidal field error, but in the presence of stellarator fields of periodicity m , when the quasiequilibrium position of the ring is off the magnetic axis of the strong focusing system and the resonance mode is equal to m . The results of the studies with axial field error will be reported in a future publication. In the absence of a toroidal magnetic field, nonlinear effects associated with the crossing of resonances in synchrotrons have been considered previously by DePackh [6].

The preceding discussion is based on the assumption that the space charge is low and the strong focusing field is zero. In addition to introducing new characteristic modes, the strong focusing field makes the expression for the regular cyclotron mode more complicated [7]. However, it can be shown that for the parameters of the NRL device and provided $l \gg 1$, the strong focusing has only a minor effect on the cyclotron resonance. This conclusion is supported by extensive computer calculations.

This paper is organized as follows. The theoretical model is formulated in Sec. II. Section III A contains examples of both the Fresnel and lock-in state from the exact equations of motion. The slow equations of motion are derived in Sec. III B, and the simplified slow equations of motion with linearized detuning factor are given in Sec. III C. The asymptotic behavior in the Fresnel and lock-in state as well as the appropriate initial conditions to be used in the subsequent sections are presented in Sec. IV, while Sec. V contains a discussion of possible ways to cross a resonance without locking into it. Resonance diagrams for nonzero initial perpendicular velocity are displayed in Sec. VI, and the multiple crossing of the same resonance is demonstrated in Sec. VII. Finally, Sec. VIII contains the summary and conclusions.

II. MODEL WITH A VERTICAL-FIELD ERROR

Imperfections in the coils that generate the betatron field could result in a field error. A typical example is given in Fig. 1, which shows the VF error per kiloampere of the current circulating in the coils as a function of the toroidal angle, at $r = 100$ cm. This error is due to a small straight section in each coil that generates the betatron field in the vicinity of the power feeds. Table I provides the Fourier decomposition of the error. The values are the actual error amplitudes (in G) for a toroidal field $B_{\theta 0} = 4650$ G as each particular resonance is reached during acceleration.

Obviously, near a resonance, only the mode associated with that resonance is acting on the ring. The contribu-

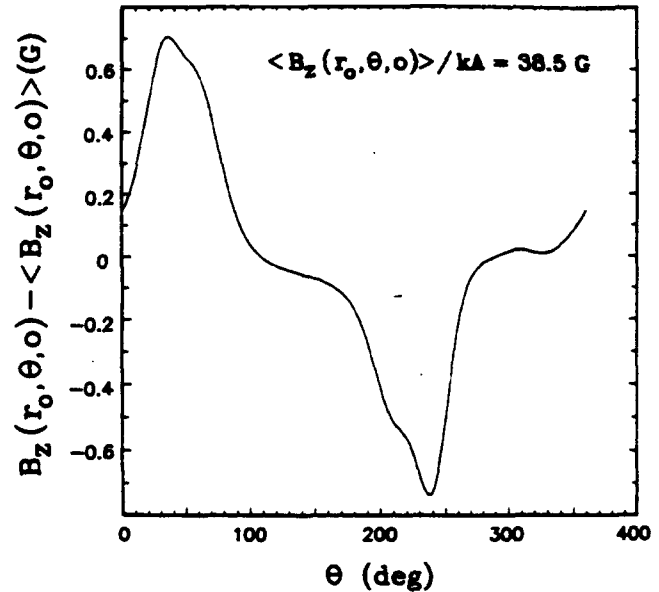


FIG. 1. Vertical field error per kiloampere of current in the coils that generate the betatron field, as a function of the toroidal angle θ , at $r = 100$ cm, $z = 0.0$ cm.

tion of all the other modes, being far away from the resonance, averages out to zero due to their fast oscillatory behavior. Therefore the VF error will be expressed in terms of the particular l mode associated with the resonance under study, i.e.,

$$\delta B_r = \delta B_{z0} K_{r0} \frac{r - r_0}{r_0} \sin(l\theta + \theta_0), \quad (1a)$$

$$\delta B_z = \delta B_{z0} \left[1 + K_{r0} \frac{r - r_0}{r_0} \right] \sin(l\theta + \theta_0), \quad (1b)$$

TABLE I. Fourier decomposition of VF error. Actual values of the VF error at each l mode for $B_{\theta 0} = 4650$ G are listed.

Fourier mode	Fourier amplitude	cos (Fourier amplitude)	sin (Fourier amplitude)
1	108.2698	81.6151	71.1430
2	1.2152	0.3749	1.1559
3	8.8142	-6.5489	5.8994
4	0.9985	0.0905	0.9944
5	1.0148	-0.3835	-0.9395
6	0.5915	-0.5915	0.0000
7	0.3350	-0.0856	0.3238
8	0.3188	0.0884	-0.3063
9	0.3226	-0.2428	-0.2124
10	0.0759	0.0640	0.0407
11	0.1301	0.0868	-0.0970
12	0.0243	-0.0243	0.0000
13	0.0373	0.0264	0.0264
14	0.0112	0.0088	-0.0069
15	0.0062	-0.0045	0.0042
16	0.0034	0.0008	0.0033
17	0.0010	-0.0010	-0.0002
18	0.0012	-0.0012	0.0000
19	0.0002	-0.0002	0.0000
20	0.0000	0.0000	0.0000

$$\delta B_\theta = \delta B_{\theta 0} \frac{z}{r_0} \cos(l\theta + \theta_0). \quad (1c)$$

In Eqs. (1), $\delta B_{\theta 0}$, θ_0 , and K_{r0} are the amplitude, the phase, and the gradient in the radial direction of the l mode and r_0 is the major radius around which the analysis is carried out. It should be noticed that Eqs. (1a)–(1c) satisfy Maxwell's equations to first order in toroidal correlations.

The magnetic fields acting on the ring in the MBA are the betatron, the toroidal, and the stellarator field. For simplicity, the stellarator field is omitted in the present analysis. At high energies its contribution to the confinement of the ring is diminished and abundant computer runs have shown that the main results presented here are not altered in the presence of the stellarator field except for resonances $l = km$, where m is the field period of the stellarator and $k = 1, 2, \dots$. In the analysis, the betatron field is approximated by

$$B_r^{(b)} = -nB_{\theta 0} \frac{z}{r_0}, \quad (2a)$$

$$B_z^{(b)} = B_{\theta 0} \left[1 - n \frac{r - r_0}{r_0} \right], \quad (2b)$$

where n is the field index and $B_{\theta 0}$ the field on the minor axis. Similarly, the toroidal magnetic field is given by

$$B_\theta = B_{\theta 0} \frac{r_0}{r}, \quad (3)$$

where $B_{\theta 0}$ is the field at $r = r_0$.

Since the VF error is a sinusoidal function of the toroidal angle θ , it is convenient to express the equations of motion in terms of the independent variable θ rather than time. In their transformed state, the equations of motion become

$$\begin{aligned} \xi'' + \left[i \frac{r_0 \Omega_{\theta 0}}{\gamma \beta_\theta c} + \frac{1}{\gamma \beta_\theta} (\gamma \beta_\theta)' - \frac{1}{2} \frac{\xi' + \xi^{*'}}{1 + P} \right] \xi' \\ = i \frac{r_0 (\Omega_r + i \Omega_z)}{\gamma \beta_\theta c} (1 + P)^2 + 1 + P, \end{aligned} \quad (4)$$

where the complex variable $\xi = [(r - r_0) + iz]/r_0$, $\xi' = d\xi/d\theta$, ξ^* is the complex conjugate of ξ , and Ω is the cyclotron frequency, i.e., $\Omega = |e|B/mc$. The position of the ring centroid is given by

$$P \equiv \frac{r - r_0}{r_0} = \frac{1}{2} (\xi + \xi^*), \quad (5a)$$

$$Q \equiv \frac{z}{r_0} = \frac{1}{2i} (\xi - \xi^*). \quad (5b)$$

The quantity $\gamma \beta_\theta$ can be expressed as

$$\gamma \beta_\theta = \left[\frac{\gamma^2 - 1}{1 + \frac{1}{(1 + P)^2} \xi' \xi^{*'}} \right]^{1/2}, \quad (6)$$

where γ is the relativistic factor and its derivative with respect to θ is equal to

$$\begin{aligned} \frac{1}{\gamma \beta_\theta} (\gamma \beta_\theta)' &= \frac{\gamma \gamma'}{(\gamma \beta_\theta)^2} - \frac{r_0 \Omega_r}{\gamma \beta_\theta c} \frac{1}{2i} (\xi' - \xi^{*'}) \\ &\quad - \left[1 - \frac{r_0 \Omega_z}{\gamma \beta_\theta c} (1 + P) \right] \frac{1}{2} \frac{\xi' + \xi^{*'}}{1 + P}. \end{aligned} \quad (7)$$

The accelerating electric field is given by

$$E_\theta = -\frac{1}{c} r_0 \dot{B}_{\theta 0}, \quad (8)$$

where $\dot{B}_{\theta 0}$ is the time derivative of the betatron field at $r = r_0$. Using the rate of change of time that is given by $t' = (r_0/c\beta_\theta)(1 + P)$, it can be shown that

$$\gamma' = \left[\frac{r_0}{c} \right]^2 \dot{\Omega}_{\theta 0} (1 + P) \quad (9)$$

and

$$\Omega'_{\theta 0} = \frac{r_0}{c} \dot{\Omega}_{\theta 0} \frac{\gamma}{\gamma \beta_\theta} (1 + P). \quad (10)$$

In the equations given above Ω_r and Ω_z include both the betatron field and the VF error. Notice that Eq. (4) is a second-order nonlinear differential equation of the complex quantity ξ . In terms of ξ , the position of the ring centroid is given by Eqs. (5), while its normalized velocity components v_r, v_z are

$$B_r + iB_z = \frac{\gamma \beta_\theta}{\gamma} \frac{1}{1 + P} \xi'. \quad (11)$$

Obviously, the exact set of nonlinear equations given above is very complicated and difficult to handle. However, for a ring that has a bounce motion with a small amplitude, i.e., for small mismatch, and for large l -mode values, it is easy to show that near the resonance $|\xi| \approx |\xi'|/l$ and therefore $|\xi|$ is much smaller than $|\xi'|$. In this case, it is appropriate to linearize Eq. (4) with respect to ξ and ξ^* . Under such conditions, Eq. (4) simplifies to

$$\xi'' + iB_1 \xi' + K_1 \xi = f_1, \quad (12)$$

where

$$\begin{aligned} f_1 &= \Delta + \left[\frac{1}{2} (1 + \Delta) (\xi' + \xi^{*'}) + iB_1 \xi (\xi' + \xi^{*'}) - \frac{\gamma}{(\gamma \beta_\theta)_1^2} \gamma' - \frac{1}{2} (1 - nC) (\xi \xi' + \xi^* \xi^{*'}) - \frac{1}{2} (\xi^* \xi' + \xi \xi^{*'}) \right] \xi' \\ &\quad - K_2 \xi^* + \xi C (\xi + \xi^*) - \delta C [1 + \xi + (1 + K_{r0}) \xi^* + \frac{1}{2} (\xi' + \xi^{*'}) \xi'] \sin(l\theta + \theta_0), \\ \frac{1}{(\gamma \beta_\theta)_1} &= \left[\frac{1 + \xi' \xi^{*'}}{\gamma^2 - 1} \right]^{1/2}, \end{aligned} \quad (13a)$$

$$b = \frac{r_0 \Omega_{x0}}{(\gamma \beta_\theta)_1 c}, \quad (13b)$$

$$C = \frac{r_0 \Omega_{x0}}{(\gamma \beta_\theta)_1 c}, \quad (13c)$$

$$\delta C = \frac{r_0 \delta \Omega_{x0}}{(\gamma \beta_\theta)_1 c}, \quad (13d)$$

$$\zeta = \frac{1}{2} \frac{\xi \xi^*}{1 + \xi \xi^*}, \quad (13e)$$

$$\Delta = 1 - C, \quad (13f)$$

$$K_1 = C - \frac{1}{2}, \quad (13g)$$

$$K_2 = (1 - n)C - \frac{1}{2}. \quad (13h)$$

When the mismatch term Δ is small, then $C \approx 1$ and $K_2 \approx \frac{1}{2} - n$. Since the term $K_2 \xi^*$ in f_1 will be treated as a perturbation in the derivation of the slow equations of motion, K_2 must be small. Therefore we assume that n is close to $\frac{1}{2}$. Also, since we consider only values of $|\xi'| < 0.2$, before the resonance is crossed, terms proportional to $|\xi'|^2 |\xi|$ are omitted when compared to one. The simplified Eq. (12) is complemented by the derivatives with respect to θ of γ and $r_0 \Omega_{x0}/c$, which are given by

$$\gamma' = \left[\frac{r_0}{c} \right]^2 \dot{\Omega}_{x0} \left[1 + \frac{\xi + \xi^*}{2} \right] \quad (14a)$$

and

$$\frac{r_0 \Omega'_{x0}}{c} = \left[\frac{r_0}{c} \right]^2 \dot{\Omega}_{x0} \frac{\gamma}{(\gamma \beta_\theta)_1} \left[1 + \frac{\xi + \xi^*}{2} \right]. \quad (14b)$$

Results from the numerical integration of Eq. (12) and the exact Eq. (4) are in very good agreement, provided the initial values of $|\xi| < 0.30 \times 10^{-2}$ and $|\xi'| < 0.2$. Therefore Eq. (12) will be used in the derivation of the slow equations by averaging out the fast cyclotron oscillatory motion.

III. DYNAMIC BEHAVIOR NEAR A RESONANCE: FRESNEL AND LOCK-IN REGIMES

A. Numerical results from the exact equations

The results from the numerical integration of the exact equations of motion, i.e., Eq. (4), as a resonance is crossed during acceleration indicate the following consistent behavior: there is a threshold value of the VF error amplitude δB_{x0} , below which the perpendicular velocity β_\perp of the gyrating electrons increases by a certain amount as the resonance is crossed and then it remains relatively constant, after the resonance has been crossed. Above the threshold value, β_\perp keeps increasing with time while $\gamma \beta_\theta$ remains, on the average, constant, and the resonance is never crossed, i.e., the ring is locked into the resonance. A typical example of this behavior is shown in Fig. 2 for the parameters listed in Table II. The threshold value of δB_{x0} is between 0.19 and 0.195 G. Figures 2(a) and 2(c) show β_\perp versus time below and above threshold, while Figs. 2(b) and 2(d) show the corresponding $\gamma \beta_\theta$ versus time.

It is rather difficult to find from the exact equations of motion the source of the dynamic behavior shown in Fig. 2. This behavior can be explained by the slow equations of motion derived in Sec. III B.

To derive the slow equations of motion the instantaneous

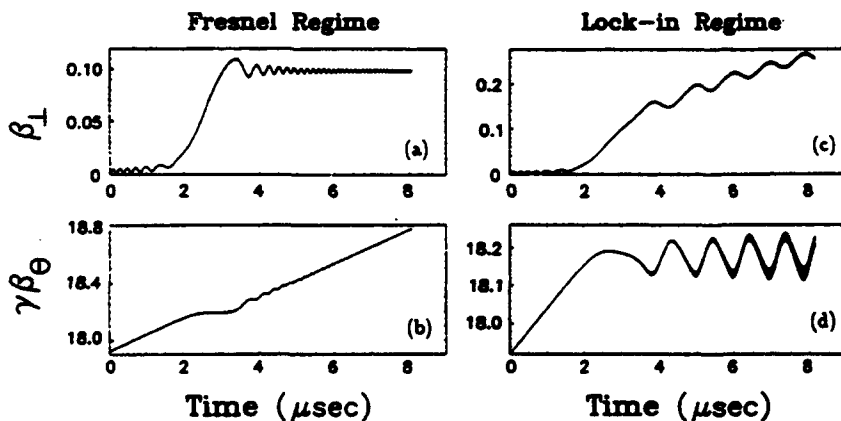


FIG. 2. β_\perp and $\gamma \beta_\theta$ vs time obtained from the exact equations of motion [Eq. (4)], in the Fresnel and lock-in regimes and close to the threshold, for the parameters in Table II.

TABLE II. Parameters of the runs shown in Figs. 2-6.

Parameter	Value
Torus major radius r_0	100 cm
Toroidal magnetic field $B_{\theta 0}$	2771 G
Vertical magnetic field B_{z0}	305 G
Field index n	0.5
Rate of change of vertical field \dot{B}_{z0}	2 G/ μ sec
Resonance mode l	9
Amplitude of VF error δB_{z0}	0.190, 0.195 G
Constant phase of VF error θ_0	0.0
Gradient of VF error K_{z0}	0.0
Initial normalized toroidal momentum $\gamma\beta_\theta$	17.922
Initial normalized vertical velocity β_z	0.0
Initial phase of vertical velocity φ_0	0.0
Initial radial displacement $r - r_0$	0.0 cm
Initial vertical displacement z	0.0 cm
Integration time t_f	8 μ sec

ous position of the particle ξ is decomposed into two components. The first is associated with the bounce motion and the second with the cyclotron or fast motion, i.e., $\xi = \xi_b + \xi_c$, where $\xi_b = \xi_b^{(s)} \exp(-i\nu_b \theta)$, $\xi_c = \xi_c^{(s)} \exp(-i\nu_c \theta)$, and ν_b and ν_c are the two characteristic frequencies of the system. Specifically, $\nu_b = \nu_-$ and $\nu_c = \nu_+$, where

$$\nu_{\pm} = \frac{b}{2} \pm \left[\left(\frac{b}{2} \right)^2 + K_1 \right]^{1/2}. \quad (15)$$

The complex amplitudes $\xi_b^{(s)}$ and $\xi_c^{(s)}$ are, in general, slowly varying quantities, provided that the perturbation is not very large. Since these two amplitudes vary slowly, the corresponding derivatives with respect to θ are equal to $\dot{\xi}_b = -i\nu_b \xi_b$ and $\dot{\xi}_c = V_c^{(s)} \exp[-i(l\theta + \theta_0)]$, provided that $\nu_c \approx l$. The amplitude $V_c^{(s)}$ is a slowly varying quantity because ξ_c has been expressed in a frame that rotates with angular velocity lc/r_0 . As a consequence of $|V_c^{(s)}| \ll |\xi|$, the position of the cyclotron mode is given by $\xi_c \approx -(1/i\nu_c) V_c^{(s)} \exp[-i(l\theta + \theta_0)]$.

From the previous discussion, the complex position ξ and its derivative $\dot{\xi}$ can be expressed as follows:

$$\xi = \xi_b - (1/i\nu_c) V_c^{(s)} e^{-i(l\theta + \theta_0)}. \quad (16a)$$

and

$$\dot{\xi} = -i\nu_b \xi_b + V_c^{(s)} e^{-i(l\theta + \theta_0)}. \quad (16b)$$

It is apparent from Eqs. (16) that it is possible to extract the bounce and (slow) cyclotron motion in the rotating frame by inverting Eqs. (16). Specifically,

$$\xi_b = \frac{\nu_c}{\nu_c - \nu_b} \left[\xi - \frac{i}{\nu_c} \dot{\xi} \right] \quad (17a)$$

and

$$V_c^{(s)} = \frac{\nu_c}{\nu_c - \nu_b} (i\nu_b \xi + \dot{\xi}) e^{i(l\theta + \theta_0)}. \quad (17b)$$

Figures 3(a) and 3(b) show the real and imaginary components of $\beta_\theta V_c^{(s)}$ for the parameters listed in Table II. For these same parameters, the actual orbit in the r - z plane, during the first 2 μ sec, is given in Fig. 4(a), while Fig. 4(b) gives the bounce motion associated with the actual orbit, as computed from Eq. (17a).

B. Slow equations of motion

The method that is used in this section to obtain the equations of motion of the slowly varying quantities asso-

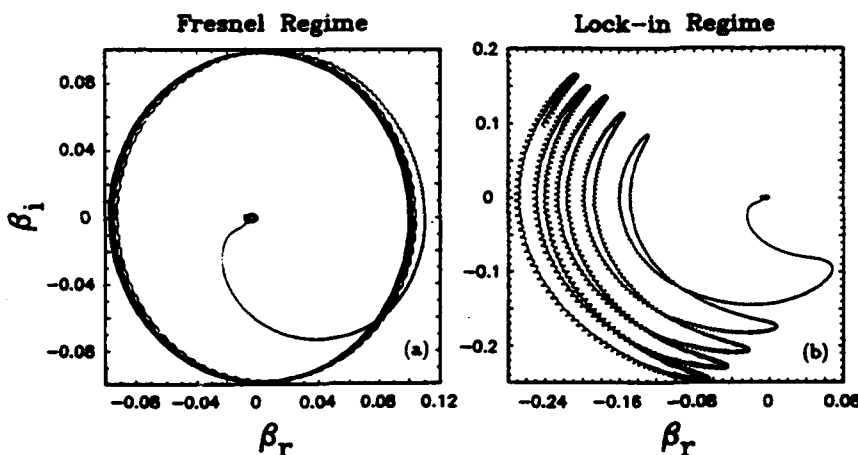


FIG. 3. Normalized perpendicular velocity in velocity space and in the rotating frame [Eq. (17b)] obtained from the exact equations of motion in the Fresnel and lock-in regimes (for the same parameters as in Fig. 2).

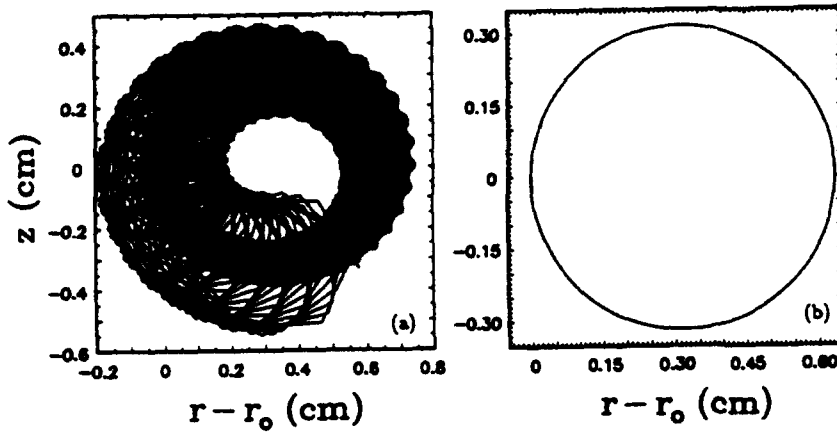


FIG. 4. (a) Exact orbit and (b) bounce motion orbit obtained from the exact equations of motion during the first $2 \mu\text{sec}$, and for the same parameters as in Figs. 2 and 3.

ciated with the cyclotron and bounce motions has been devised by Bogoliubov and Mitropolsky [8] and is a perturbation approach to the problem. Before this method can be applied, the simplified Eq. (12) should be written in a suitable form. For this purpose we express ξ, ξ' in terms of the quantities ξ_b, V_c as follows:

$$\xi = \xi_b + \frac{i}{v_+} V_c, \quad (18a)$$

$$\xi' = -iv_- \xi_b + V_c, \quad (18b)$$

where

$$v_{\pm} = \frac{b_0}{2} \pm \left[\left(\frac{b_0}{2} \right)^2 + K_{10} \right]^{1/2}, \quad (19a)$$

$$b_0 = \frac{r_0 \Omega_{\theta 0}}{(\gamma \beta_{\theta 0})_c}, \quad (19b)$$

$$C_0 = \frac{r_0 \Omega_{x0}}{(\gamma \beta_{\theta 0})_c}, \quad (19c)$$

$$K_{10} = C_0 - \frac{1}{2}, \quad (19d)$$

$$\frac{1}{(\gamma \beta_{\theta 0})_0} = \left[\frac{1 + |V_0|^2}{\gamma^2 - 1} \right]^{1/2}, \quad (19e)$$

In Eq. (19e), V_0 is the zero order, slowly varying quantity associated with V_c [see Eq. (26a)]. In addition, v_{\pm} are definitely slowly varying quantities, since they depend on $|V_0|^2$.

The equations of motion of V_c and ξ_b are

$$V_c' + iv_+ V_c = \frac{v_+}{v_+ - v_-} \left[f + \delta f + iv_- \xi_b - \frac{v'_+}{v_+} \frac{v_-}{v_+} V_c \right], \quad (20a)$$

$$\xi_b' + iv_- \xi_b = -\frac{i}{v_+ - v_-} \left[f + \delta f + iv_- \xi_b - \frac{v'_+}{v_+} V_c \right], \quad (20b)$$

where

$$f = \Delta_0 + \frac{1}{2}(1 + \Delta_0)(\xi' + \xi^{*'})\xi' - \delta C_0 \sin(l\theta + \theta_0), \quad (21a)$$

$$\delta f = \Delta - \Delta_0 + \left[-i(b - b_0) + \frac{1}{2}(\Delta - \Delta_0)(\xi' + \xi^{*'}) + ib\xi(\xi + \xi^*) - \frac{\gamma}{(\gamma \beta_{\theta 0})_1^2} \gamma' \right. \\ \left. - \frac{1}{2}(1 - nC)(\xi\xi' + \xi^*\xi^{*'}) - \frac{1}{2}(\xi^*\xi' + \xi\xi^{*'}) \right] \xi' - (K_1 - K_{10})\xi - K_2\xi^* + \xi C(\xi + \xi^*) \\ - \delta C[\xi + (1 + K_{10})\xi^* + \frac{1}{2}(\xi' + \xi^{*'})\xi'] \sin(l\theta + \theta_0) - (\delta C - \delta C_0) \sin(l\theta + \theta_0). \quad (21b)$$

$$\Delta_0 = 1 - C_0, \quad (22a)$$

$$\delta C_0 = \frac{r_0 \delta \Omega_{x0}}{(\gamma \beta_{\theta 0})_c}, \quad (22b)$$

and b_0, C_0, K_{10} have already been defined.

To implement the perturbation theory, we introduce the parameter ϵ , which indicates the relative smallness of the various terms. In terms of ϵ , Eqs. (20) can be written as follows:

$$V_c' + iV_c = \epsilon[f_c - i(v_+ - l)V_c], \quad (23a)$$

$$\xi_b' + i\epsilon v_- \xi_b = \epsilon f_b, \quad (23b)$$

where

$$f_c = \frac{v_+}{v_+ - v_-} [f + \delta f], \quad (24a)$$

$$f_b = -\frac{i}{v_+ - v_-} [f + \delta f]. \quad (24b)$$

Assuming that the field error $\delta B_{x0} \ll B_{x0}$, $|\Delta_0| \ll 1$, and since $l \gg |V_0|$ and $v_+ \approx l$, the right-hand side of Eqs. (23) is at least of order ϵ . In addition, since $|v_-| \ll 1$, the term $iv_- \xi_b$ in Eq. (23b) is of order ϵ . The terms that are proportional to the derivatives of v_{\pm} have been omitted because they are of higher order.

Furthermore, for high l -mode numbers $|\xi| \ll |\xi'|$ and in light of Eqs. (18), in terms of ϵ , ξ and ξ' can be written as follows:

$$\xi = \epsilon \left[\xi_b + \frac{i}{v_+} V_c \right], \quad (25a)$$

$$\xi' = -iv_- \xi_b \epsilon + V_c. \quad (25b)$$

The perturbation method is applied on Eqs. (23) and (25) by setting

$$V_c = V_0 e^{-i(l\theta + \theta_0)} + \epsilon V_1(\xi_0, \xi_0^*, V_0, V_0^*, \theta) + \dots, \quad (26a)$$

$$\xi_b = \xi_0 + \epsilon \xi_1(\xi_0, \xi_0^*, V_0, V_0^*, \theta) + \dots, \quad (26b)$$

$$V_0' = \epsilon A_1(\xi_0, \xi_0^*, V_0, V_0^*) + \epsilon^2 A_2(\xi_0, \xi_0^*, V_0, V_0^*) + \dots, \quad (26c)$$

$$\xi_0' = \epsilon B_1(\xi_0, \xi_0^*, V_0, V_0^*) + \epsilon^2 B_2(\xi_0, \xi_0^*, V_0, V_0^*) + \dots, \quad (26d)$$

where V_0, ξ_0 are the slowly varying quantities associated with V_c, ξ_b , respectively. Then, the slowly varying quantities A_1, A_2, \dots and B_1, B_2, \dots are determined by inserting the equations above into Eqs. (23) and eliminating the terms that lead to secular terms for each order of the perturbation parameter ϵ .

The computation is carried out to second order in ϵ and it is tedious but straightforward and will not be given here. To that order, the quantities V_1, ξ_1 , are equal to

$$V_1 = \frac{v_+}{v_+ - v_-} \frac{1}{il} \left[\Delta_0 + \frac{1}{2}(1 + \Delta_0)|V_0|^2 + \frac{i}{4}\delta C_0 e^{i(l\theta + \theta_0)} - \frac{1}{2}(1 + \Delta_0)V_0^2 e^{-2i(l\theta + \theta_0)} \right], \quad (27a)$$

$$\xi_1 = -\frac{i}{v_+ - v_-} \frac{1}{2l} \left[\delta C_0 e^{-i(l\theta + \theta_0)} + \delta C_0 e^{i(l\theta + \theta_0)} + \frac{i}{2}(1 + \Delta_0)V_0^2 e^{-2i(l\theta + \theta_0)} \right]. \quad (27b)$$

Also, to second order in ϵ , the slow equations for V_0 and ξ_0 are

$$V_0' + i(v_+ - l)V_0 = f_c^{(s)}, \quad (28a)$$

and

$$\xi_0' + iv_- \xi_0 = f_b^{(s)}, \quad (28b)$$

where

$$f_c^{(s)} = i \frac{v_+}{v_+ - v_-} \left\{ i \frac{\gamma \gamma'}{(\gamma \beta_\theta)_0^2} V_0 - v_- \xi_0 V_0 + b_0 \xi_0 (\xi_0 + \xi_0^*) V_0 - \left[\Delta_0 + \frac{\xi_0 C_0}{2} \right] v_- (\xi_0 - \xi_0^*) V_0 + \frac{C_0}{2v_+} [\xi_0(1 - |V_0|^2) - \Delta_0(1 + 2\xi_0 - \Delta_0(1 + \frac{3}{2}|V_0|^2))] V_0 - \frac{\delta C_0}{2} \left[1 + \xi_0 + (1 + K_{r0})\xi_0^* + \frac{1}{2}|V_0|^2 - \frac{1}{2}V_0^2 - \frac{\delta C_0}{8v_+} \frac{1}{1 + |V_0|^2} V_0 \right] \right\}, \quad (29a)$$

and

$$f_b^{(s)} = -\frac{i}{v_+ - v_-} \left\{ \Delta_0 + \frac{1}{2}|V_0|^2 - (b_0 v_- + \Delta_0 + |V_0|^2)\xi_0 \xi_0^* - \left[K_{20} - \frac{nC_0}{2}|V_0|^2 + (\Delta_0 + |V_0|^2)\xi_0 \right] \xi_0^* - \frac{\delta C_0}{2v_+} \left[\left(1 + \frac{1}{2}\Delta_0 + \xi_0 - \frac{1}{2} \frac{K_{10}\xi_0}{1 + |V_0|^2} \right) (V_0 + V_0^*) + K_{r0}V_0^* - \frac{\delta C_0}{4}\xi_0 V_0 \right] \right\}. \quad (29b)$$

The quantities for ξ_0 and K_{20} are given in Eqs. (13e) and (13h) with $|\xi'|^2$ replaced by $|V_0|^2$ and C replaced by C_0 . The slow Eqs. (28) and (29) should be complemented by the derivatives of γ and $r_0 \Omega_{x0}/c$. Keeping only the zero order nonoscillatory parts in Eqs. (14a) and (14b), we obtain

$$\gamma' \approx \left[\frac{r_0}{c} \right]^2 \dot{\Omega}_{x0} \left[1 + \frac{\xi_0 + \xi_0^*}{2} \right] \quad (30)$$

and

$$\frac{r_0 \Omega_{x0}'}{c} \approx \left[\frac{r_0}{c} \right]^2 \dot{\Omega}_{x0} \frac{\gamma}{(\gamma \beta_\theta)_0} \left[1 + \frac{\xi_0 + \xi_0^*}{2} \right]. \quad (31)$$

Solutions of the slow equations are shown in Fig. 5 for the same input parameters (see Table II) used in the solution of the exact Eq. (4). Figures 5(a) and 5(c) show the zero order $\beta_1^{(0)} \equiv (\gamma \beta_\theta)_0 |V_0|/\gamma$ versus time, below and

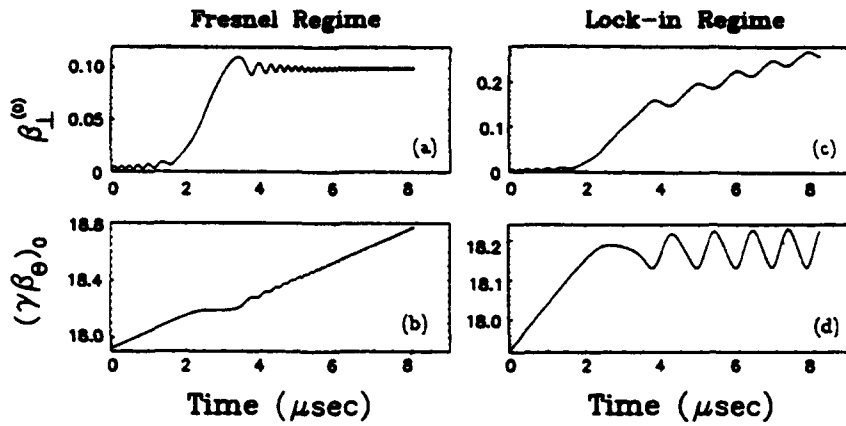


FIG. 5. β_{\perp} and $\gamma\beta_{\perp}$ vs time obtained from the slow equations of motion [Eqs. (28) and (29)], in the Fresnel and lock-in regimes and close to the threshold, for the parameters in Table II.

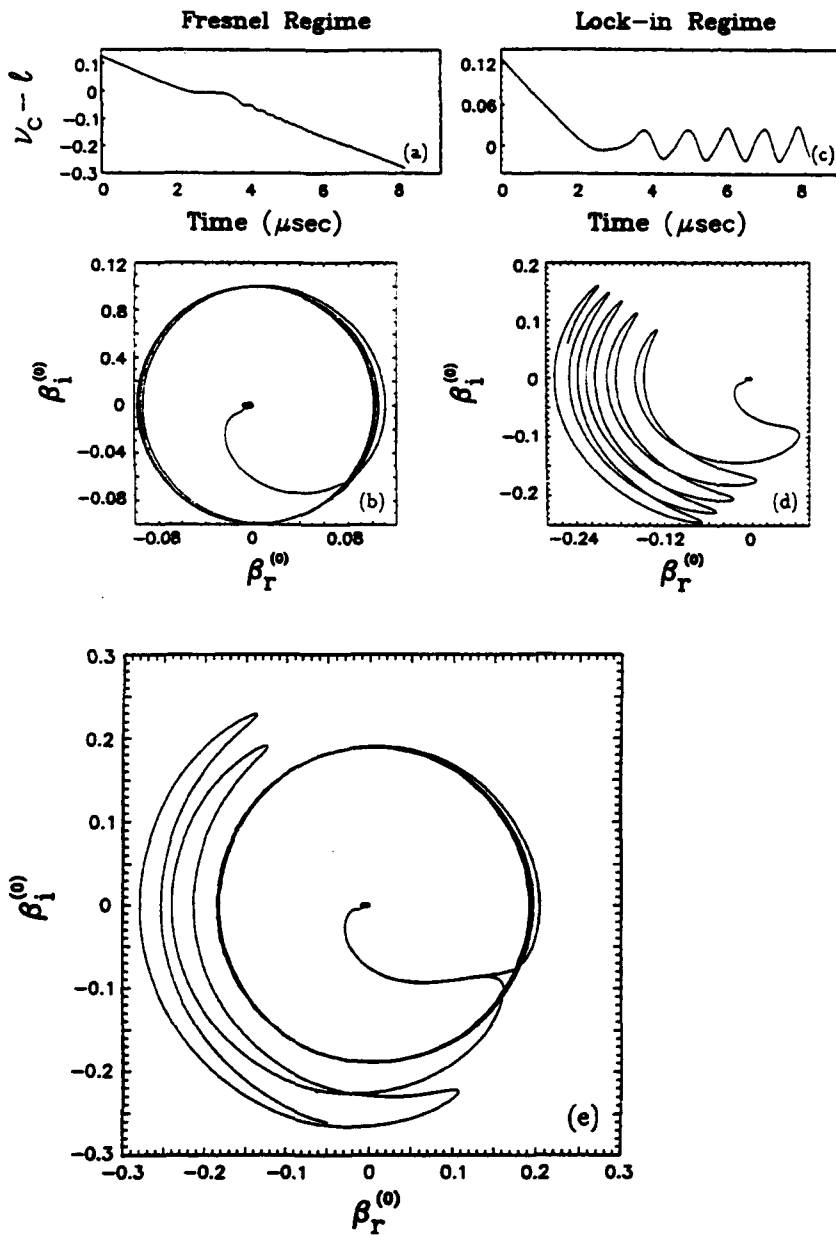


FIG. 6. Detuning factor vs time and normalized perpendicular velocity in velocity space obtained from the slow equations of motion in the Fresnel and lock-in regimes (for the same parameters as in Fig. 5).

above threshold, while Figs. 5(b) and 5(d) show the corresponding zero order $(\gamma\beta_\theta)_0$ versus time. Figure 6 shows the detuning factor $w = v_- - l$ and the real and imaginary parts of $(\gamma\beta_\theta)_0 V_0 / \gamma$, below and above threshold. By comparing Figs. 5 and 6 to Figs. 2 and 3 it is apparent that the slow equations predict accurately β_1 and $\gamma\beta_\theta$ when the initial perpendicular velocity is zero. Above threshold the detuning factor locks into the resonance, with only a small variation around zero. A plot of ξ_0 is not given, since it is exactly the same as that in Fig. 4(b). Obviously, the numerical integration of the slow equations is much faster than that of the exact Eq. (4) or (12), since the oscillatory terms have been averaged out.

C. Slow equations of motion with linearized detuning factor

The slow equations of Sec. III B are still too lengthy to provide insight into the origin of the threshold behavior. When $\delta B_{x0} |V_0| / |B_{x0}| \ll 1$, the last term in Eq. (29b) can be neglected and the equation for the bounce motion simplifies to the equation

$$\begin{aligned} \xi'_0 + i v_- \left[1 + \frac{1}{K_{10}} (b_0 v_- + \Delta_0 + |V_0|^2) \right] \xi_0 \\ + i \frac{v_-}{K_{10}} \left[K_{20} - \frac{\pi C_0}{2} |V_0|^2 + (\Delta_0 + |V_0|^2) \xi_0 \right] \xi_0^* \\ = i \frac{v_-}{K_{10}} (\Delta_0 + \frac{1}{2} |V_0|^2), \end{aligned} \quad (32)$$

where we have used the fact that $|v_-| \ll v_+$, and the relation $v_- v_+ = -K_{10}$. Equation (32) indicates that the equilibrium position of the bounce motion is proportional to the generalized mismatch $\Delta_0 + \frac{1}{2} |V_0|^2$. Without exception the computer runs have shown that during the crossing of the resonance the equilibrium position of the bounce motion hardly changes when the gradient factor $K_{r0} = 0$. That is not the case when $K_{r0} \neq 0$. Therefore, if both the initial mismatch and the initial bounce position ξ_0 are zero, the latter quantity remains very small. Under these conditions, the slow equation for V_0 simplifies to the equation

$$\begin{aligned} V'_0 + i \left[v_+ - l + \frac{C_0}{2v_+} (\Delta_0 - \frac{1}{2} |V_0|^2) \right] V_0 \\ = i \left[i \frac{\gamma\gamma'}{(\gamma\beta_\theta)_0^2} V_0 - \frac{\delta C_0}{2} (1 + \frac{1}{2} |V_0|^2 - \frac{1}{2} V_0^2) \right], \end{aligned} \quad (33)$$

where terms proportional to $\Delta_0^2 |V_0|^4$, and $\Delta_0 |V_0|^2$ or higher have been omitted.

To simplify further Eq. (33), it is convenient to introduce the quantity U_0 by means of the relation

$$V_0 = \frac{U_0}{[\gamma^2 - 1 - |U_0|^2]^{1/2}}. \quad (34)$$

Since, to zero order, V_0 is equal to $[(\beta_r + i\beta_z)/\beta_\theta] \exp[i(l\theta + \theta_0)]$, U_0 is, to the same order, equal to $\gamma(\beta_r + i\beta_z) \exp[i(l\theta + \theta_0)]$, and it is easy to show

from Eqs. (19e) and (34) that

$$(\gamma\beta_\theta)_0 = [\gamma^2 - 1 - |U_0|^2]^{1/2}. \quad (35)$$

A straightforward transformation of Eq. (33) from the V_0 to the U_0 variable leads to the slow equation for U_0 , namely

$$U'_0 + i \left[v_+ - l + \frac{C_0}{2v_+} \left[\Delta_0 - \frac{1}{2} \frac{|U_0|^2}{(\gamma\beta_\theta)_0^2} \right] \right] U_0 = -iB_0, \quad (36)$$

where

$$B_0 = \frac{1}{2} \frac{r_0 \delta \Omega_{x0}}{c}. \quad (37)$$

Equation (36) indicates that the detuning factor $w = v_+ - l$ should be redefined by adding to it the small correction term

$$C_0 \left[\Delta_0 - \frac{1}{2} \frac{|U_0|^2}{(\gamma\beta_\theta)_0^2} \right] / 2v_+.$$

Above threshold, the small correction term is important because it compensates for the small time-dependent contribution of K_{10} in v_+ [cf. Eq. (19a)]. If the small correction term is omitted in either Eq. (36) or (33), then, above threshold, the average value of $(\gamma\beta_\theta)_0$ does not remain constant but increases with θ . This is contrary to the solution of either Eqs. (28) and (29) or the exact Eq. (4) or (12).

When the mismatch $\Delta_0 + \frac{1}{2} |V_0|^2 \approx 0$ and the initial ξ_0 is also zero, then $\xi_0 \approx 0$ and the relativistic factor γ is equal to $\gamma = \gamma_0 + \gamma' \theta$ [cf. Eq. (30)], where γ_0 and γ' are the initial values of γ and the acceleration rate [assumed to be a constant, and given by Eq. (30) with $\xi_0 = 0$], respectively. Assuming that $\gamma' \theta \ll \gamma_0$ and $||U_0|^2 - |U_{00}|^2| \ll 1$, where U_{00} is the initial value of U_0 , the detuning factor can be linearized with respect to $\gamma' \theta$ and $|U_0|^2 - |U_{00}|^2$, namely

$$w = w_0 - \alpha \theta + \frac{1}{2} \delta [|U_0|^2 - |U_{00}|^2], \quad (38)$$

where

$$w_0 = v_{+0} - l + \frac{C_{00}}{2v_{+0}} \left[\Delta_{00} - \frac{1}{2} \frac{|U_{00}|^2}{(\gamma\beta_\theta)_{00}^2} \right], \quad (39a)$$

$$\alpha = v_{+1} \frac{\gamma_0 \gamma'}{(\gamma\beta_\theta)_{00}^2}, \quad (39b)$$

$$\delta = v_{+1} \frac{1}{(\gamma\beta_\theta)_{00}^2}, \quad (39c)$$

$$v_{+1} = \frac{b_{00}}{2} \left[1 + \frac{\frac{b_{00}}{2}}{\left[\left(\frac{b_{00}}{2} \right)^2 + K_{100} \right]^{1/2}} \right], \quad (39d)$$

$$(\gamma\beta_\theta)_{00} = [\gamma_0^2 - 1 - |U_{00}|^2]^{1/2}, \quad (39e)$$

and $v_{+0}, b_{00}, C_{00}, \Delta_{00}, K_{100}$ are the initial values of $v_+, b_0, C_0, \Delta_0, K_{10}$, respectively. The dependence of K_{10}

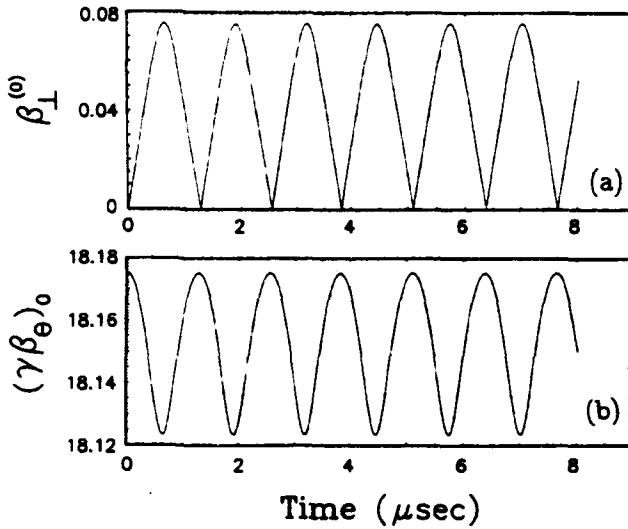


FIG. 7. β_1 and $\gamma\beta_\theta$ vs time obtained from the slow equations of motion without acceleration, for the parameters in Table III.

on θ and on $(\gamma\beta_\theta)_0$ has been neglected, since v_+ is weakly dependent on K_{10} when $b_0 \approx l \gg 1$. Also, since $\Delta_0 \approx -\frac{1}{2}|U_0|^2/(\gamma\beta_\theta)_0^2$, $C_0 \approx 1$, and $\delta \approx l/(\gamma\beta_\theta)_0^2$, the small correction term that is added to the detuning factor in Eq. (36) provides such a small contribution to δ , of order $1/l^2$, that it has been neglected. Therefore the slow equation for U_0 with linearized detuning factor is

$$U_0' + i[\omega_0 - \alpha\theta + \frac{1}{2}\delta(|U_0|^2 - |U_{00}|^2)]U_0 = -iB_0. \quad (40)$$

This equation predicts the same temporal behavior for β_1 and $\gamma\beta_\theta$ as the original slow Eqs. (28) and (29). The cause of this behavior is the nonlinear term proportional to $|U_0|^2 - |U_{00}|^2$ (it will be shown shortly that when $\delta=0$, the solution is the Fresnel integral, which is bounded). We conclude that the existence of the Fresnel and lock-in regimes in the exact Eq. (4) or in Eq. (12) is due to the dependence of the term $r_0\Omega_{e0}/\gamma\beta_\theta c$ upon $\gamma\beta_\theta$ and the fact that $\gamma\beta_\theta$ depends nonlinearly on the perpendicular velocity.

It is interesting to examine the case when there is no acceleration ($\alpha=0$), the particles are at exact resonance ($\omega_0=0$) and the initial perpendicular velocity is zero ($|U_{00}|^2=0$). Then Eq. (40) becomes

$$U_0' + i\frac{1}{2}\delta|U_0|^2U_0 = -iB_0, \quad (41)$$

and it can be solved exactly. For that purpose, define $A \equiv |U_0|^2$. Then, separating the real and imaginary parts of Eq. (41), it is easy to show that

$$U_{0r} = -\frac{\delta}{8B_0}A^2, \quad (42a)$$

$$U_{0i} = -\frac{1}{2B_0}A', \quad (42b)$$

and from the definition of A it follows that

$$A' = \left[A \left(4B_0^2 - \frac{\delta^2}{16}A^3 \right) \right]^{1/2}. \quad (43)$$

The exact solution of this differential equation is

$$\int_0^{\lambda^2 A} \frac{dx}{[x(1-x)(x^2+x+1)]^{1/2}} = 2B_0\lambda\theta, \quad (44)$$

where $\lambda = (\delta/8B_0)^{1/3}$. The integral can also be expressed in terms of the elliptic integral of the first kind [9] $F(\phi, k)$, i.e.,

$$F \left[2 \operatorname{arccot} \frac{1}{3^{1/4}} \left(\frac{1-\lambda^2 A}{\lambda^2 A} \right)^{1/2}, \frac{\sqrt{2-\sqrt{3}}}{2} \right] = 3^{1/4} 2B_0\lambda\theta. \quad (45)$$

For very small or very large values of the argument of the arccot, the approximate solution is

$$A \equiv (\gamma\beta_1)^2 = \left[\frac{8B_0}{\delta} \right]^{2/3} \frac{\tan^2 \mu\theta}{\sqrt{3} + \tan^2 \mu\theta}, \quad (46)$$

where $\mu = 3^{1/4}\lambda B_0$. The solution of Eq. (43) is bounded. When $\mu\theta \ll 1$, $A \approx (B_0\theta)^2$ and β_1 is proportional to θ , which is the usual linear secular solution. But the nonlinear dependence of $\gamma\beta_\theta$ on β_1 forces the solution to be bounded. Figure 7 shows β_1 and $\gamma\beta_\theta$ versus time for the parameters listed in Table III, by integrating either the

TABLE III. Parameters of the run shown in Fig. 7.

Parameter	Value
Torus major radius r_0	100 cm
Toroidal magnetic field $B_{\theta 0}$	2771 G
Initial generalized mismatch $\Delta_0 + 0.5 V_0 ^2$	0.0
Field index n	0.5
Rate of change of vertical field \dot{B}_{z0}	0.0 G/ μ sec
Resonance mode l	9
Amplitude of VF error δB_{z0}	0.3 G
Constant phase of VF error θ_0	0.0
Gradient of VF error K_{z0}	0.0
Initial normalized toroidal momentum $\gamma\beta_\theta$	18.1753
Initial normalized vertical velocity β_1	0.0
Initial phase of vertical velocity ϕ_0	0.0
Initial normalized radial bounce displacement ξ_{0r}	0.0
Initial normalized vertical bounce displacement ξ_{0z}	0.0
Integration time t_f	8 μ sec

slow Eq. (40) or (36), or Eqs. (28) and (29). Integration of the exact Eq. (4) for the same parameters also gives identical results. The peak value of β_1 and the period $(\pi/\mu)r_0/c$ as computed from the approximate Eq. (46) are 0.0757 and 1.247 μsec , respectively, in good agreement with Fig. 7.

In conclusion, our analysis indicates that there is a completely different behavior near a resonance with or without acceleration. Even at exact resonance, β_1 is always bounded without acceleration, but it is unbounded with acceleration and in the presence of a large field error.

IV. ASYMPTOTIC BEHAVIOR IN THE FRESNEL AND LOCK-IN REGIMES

In order to study the asymptotic behavior of Eq. (40), it is convenient to transform it into dimensionless form. For this purpose, when $\alpha > 0$, we introduce the quantities $\sigma = \sqrt{\alpha}\theta$, $\sigma_0 = w_0\sqrt{\alpha}$, $\hat{\epsilon} = (\delta/2\alpha^{3/2})^{1/2}B_0$, and $\hat{U}_0 = (\delta/2\alpha^{1/2})U_0$.

Then, Eq. (40) becomes

$$\frac{d\hat{U}_0}{d\sigma} + i[\sigma_0 - \sigma + |\hat{U}_0|^2 - |\hat{U}_{00}|^2]\hat{U}_0 = -i\hat{\epsilon}, \quad (47)$$

where \hat{U}_{00} is not equal to the initial value of \hat{U}_0 and will be defined shortly. Let $\hat{\epsilon}_{\text{thr}}$ be the threshold value of $\hat{\epsilon}$. When $\hat{\epsilon} \ll \hat{\epsilon}_{\text{thr}}$, i.e., when $B_0\delta/(2\alpha^{3/2}) \ll \hat{\epsilon}_{\text{thr}}$, the change in \hat{U}_0 associated with the crossing of the resonance is small, i.e., $||\hat{U}_0|^2 - |\hat{U}_{00}|^2| \ll 1$, and Eq. (47) simplifies to

$$\frac{d\hat{U}_0}{d\sigma} + i(\sigma_0 - \sigma)\hat{U}_0 = -i\hat{\epsilon}. \quad (48)$$

The crossing of the resonance occurs at $\sigma = \sigma_0$, i.e., at $\theta_0 = w_0/\alpha$. The solution of this equation is

$$\hat{U}_0 = e^{i(1/2)(\sigma - \sigma_0)^2} \left[\hat{U}_{00} e^{-i(1/2)\sigma_0^2} - i\hat{\epsilon} \int_{-\sigma_0}^{\sigma - \sigma_0} e^{-i(1/2)\sigma'^2} d\sigma' \right], \quad (49)$$

i.e., the particular solution can be written in terms of the Fresnel integral. When $\sigma_0 \gg 1$, the asymptotic expression of the Fresnel integral leads to the approximate solution

$$U_0 \approx e^{i(w^2/2\alpha)} \left[\left(U_{00} + \frac{B_0}{w_0} \right) e^{-i(w_0^2/2\alpha)} - i \frac{B_0}{\sqrt{\alpha}} \int_{-\infty}^{-w/\sqrt{\alpha}} e^{-i(1/2)\xi^2} d\xi \right], \quad (50)$$

where the solution has been transformed to the original variables and $w = w_0 - \alpha\theta$. U_0 is very sensitive to the phase $w_0^2/2\alpha$, when $U_{00} + B_0/w_0 \neq 0$. Since $\alpha \ll 1$, a small change in the initial time interval $\tau_0 \equiv (r_0/c)w_0/\alpha$ from the resonance [e.g., a small change in the initial value of $(\gamma\beta_g)_0$] will cause a very different behavior of $|U_0|$ versus time. To alleviate this problem, we define the

initial condition of Eq. (50), and also of Eq. (40), by means of the initial variable \bar{U}_{00} , i.e.,

$$U_{00} = \bar{U}_{00} e^{i(w_0^2/2\alpha)} - \frac{B_0}{w_0}, \quad (51)$$

where $\bar{U}_{00} = (\delta/2\alpha^{1/2})^{-1}\hat{U}_{00}$ and \hat{U}_{00} is the value in Eq. (47) around which the detuning factor is linearized. Then Eq. (50) becomes

$$U_0 = e^{i(w^2/2\alpha)} \left[\bar{U}_{00} - i \frac{B_0}{\sqrt{\alpha}} \int_{-\infty}^{-w/\sqrt{\alpha}} e^{-i(1/2)\xi^2} d\xi \right], \quad (52)$$

and is independent of τ_0 , but it does depend on the initial phase of \bar{U}_{00} . Equation (52) indicates that as θ tends to minus infinity, $||U_0|^2 - |\bar{U}_{00}|^2|$ tends to zero. Therefore $|\bar{U}_{00}|$ is the appropriate constant around which the detuning factor should be linearized, and w_0, α, δ become functions of \bar{U}_{00} (and not of U_{00}). Because $|U_0|$ tends to $|\bar{U}_{00}|$ as $\theta \rightarrow -\infty$ we shall call \bar{U}_{00} the asymptotic initial value of U_0 . When $\theta \gg 1$ (or $|w|/\sqrt{\alpha} \gg 1$), the asymptotic value of $|U_0|$ is

$$|U_0| \sim |\bar{U}_{00} - iB_0\sqrt{\pi/\alpha}(1+i)|. \quad (53)$$

Therefore, when $\bar{U}_{00} \neq 0$, the final value of $|U_0|$ could be smaller than its asymptotic initial value $|\bar{U}_{00}|$. When $\bar{U}_{00} = 0$, the asymptotic value of β_1 is

$$\beta_1(\theta \gg 1) = \sqrt{2\pi/\alpha} \frac{B_0}{\gamma_0 + \gamma'\theta}, \quad (54)$$

where $|\gamma'\theta| \ll \gamma_0$. Since the width of the Fresnel integral is $\Delta\sigma = 2\pi^{1/2}$, we conclude that the time Δt it takes for the resonance to be crossed is

$$\Delta t = 2 \frac{r_0}{c} \sqrt{\pi/\alpha}. \quad (55)$$

Therefore the final β_1 and Δt are inversely proportional to the square root of the acceleration rate in the Fresnel regime, provided $\hat{\epsilon} \ll \hat{\epsilon}_{\text{thr}}$. Figure 8 shows $\beta_1^{(0)}$ and $(\gamma\beta_g)_0$ versus time for the parameters of Table II, except that $\delta B_{z0} = 0.1$ G, i.e., far away from the threshold. Notice the smooth variation of $\beta_1^{(0)}$ during the first microsecond and compare to the oscillatory behavior that occurs in Fig. 5(a). The difference is due to the choice of the initial condition. In Fig. 8(a), $\bar{U}_{00} = 0$, while in Fig. 5(a), $U_{00} = 0$. When $w > 0$ and $|w|/\sqrt{\alpha} \gg 1$, i.e., well before the resonance crossing, the asymptotic value of U_0 , as given by Eq. (52), is

$$U_0 \sim \bar{U}_{00} e^{i(w^2/2\alpha)} - \frac{B_0}{w}. \quad (56)$$

When $\bar{U}_{00} = 0$, we have $|U_0| = -B_0/|w|$, which explains the smooth variation of $\beta_1^{(0)}$ in Fig. 8(a).

We have shown above that if the initial condition, given by Eq. (51), is chosen the solution of Eq. (40), in either the Fresnel or the lock-in regime, is independent of the initial time interval τ_0 from the resonance, when $w_0/\sqrt{\alpha} \gg 1$. This is no longer true if the initial condition given by Eq. (51) is chosen for the solution of Eq.

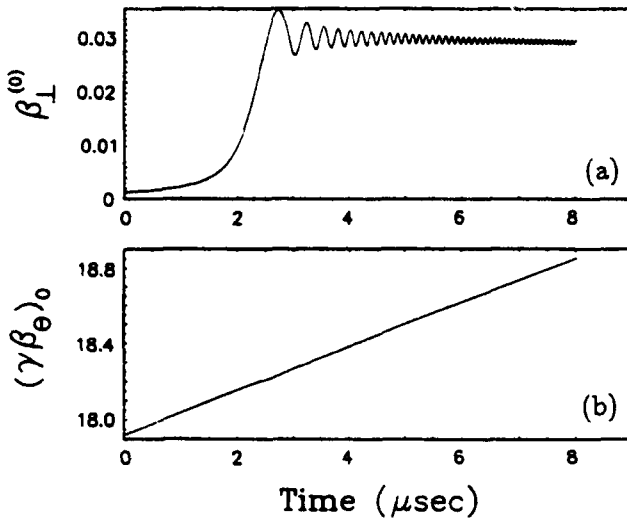


FIG. 8. β_1 and $\gamma\beta_\theta$ vs time from the slow equations of motion in the Fresnel regime far away from the threshold, i.e., for the parameters of Table II, except that $\delta B_{z0} = 0.1$ G [the initial condition is given by Eq. (51), with $\bar{U}_{00} = 0$].

(36), which has a nonlinear detuning factor w . The nonlinear dependence of w on θ causes the solution to depend on τ_0 . To second order in θ , the detuning factor is given by

$$w = w_0 - \alpha\theta + \frac{1}{2}\alpha_2\theta^2 + \frac{1}{2}\delta[|U_0|^2 - |\bar{U}_{00}|^2], \quad (57)$$

where w_0, α, δ have already been defined, \bar{U}_{00} will be redefined shortly, and

$$\alpha_2 = \left[3 - \frac{(\gamma\beta_\theta)_{00}^2}{\gamma_0^2} \right] \frac{\gamma_0\gamma'}{(\gamma\beta_\theta)_{00}^2} \alpha. \quad (58)$$

When $w/\sqrt{\alpha} \gg 1$, i.e., well before the resonance crossing, the term proportional to δ can be neglected in Eq. (57), and the asymptotic solution of Eq. (40) is

$$U_0 \sim \exp \left[-i \int_0^\theta w d\theta \right] \left[U_{00} + \frac{B_0}{w_0} \right] - \frac{B_0}{w}, \quad (59a)$$

where

$$w = w_0 - \alpha\theta + \frac{1}{2}\alpha_2\theta^2. \quad (59b)$$

Inverting Eq. (59b), we get (since $\alpha_2\theta^2 \ll 1$)

$$\theta = -\frac{w - w_0}{\alpha} + \frac{\alpha_2}{2\alpha^2}(w - w_0)^2, \quad (60)$$

and, therefore,

$$\int_0^\theta w d\theta = \left[1 + \frac{\alpha_2 w_0}{6\alpha^2} \right] \frac{w_0^2}{2\alpha} - \left[1 + \frac{\alpha_2}{\alpha^2} \left(w_0 - \frac{2}{3}w \right) \right] \frac{w^2}{2\alpha}. \quad (61)$$

Instead of Eq. (51), where $\alpha_2 = 0$, if we redefine the initial condition by the relation

$$U_{00} = \bar{U}_{00} e^{i \left[1 + \alpha_2 w_0 / 6\alpha^2 \right] w_0^2 / 2\alpha} - \frac{B_0}{w_0}, \quad (62)$$

then Eq. (59a) becomes

$$U_0 \sim \bar{U}_{00} e^{i \left[1 + (\alpha_2/\alpha^2) \{ w_0 - (2/3)w \} \right] w^2 / 2\alpha} - \frac{B_0}{w}. \quad (63)$$

Notice that U_0 depends on w_0 and, therefore, on τ_0 . However, if $\alpha_2 w_0 / \alpha^2 \ll 1$, then the dependence is weak and the solution of Eq. (36) with the initial condition given by Eq. (62) is also weakly dependent on τ_0 . Equation (63) indicates that as θ tends to minus infinity, $||U_0|^2 - |\bar{U}_{00}|^2|$ tends to zero, and, therefore, \bar{U}_{00} is the appropriate parameter around which the detuning factor should be expanded. Also, $w_0, \alpha, \alpha_2, \delta$ are functions of \bar{U}_{00} . As before, we call \bar{U}_{00} the asymptotic initial value of U_0 . From this point on, the solutions of Eqs. (28) and (29) are obtained using the initial condition computed from Eq. (62). If such an approach is not followed, each small change in the initial parameters, e.g., $(\gamma\beta_\theta)_{00}, B_{00}$, etc., would produce a different U_0 which could be either in the Fresnel or the lock-in regime, to the extent that one might get the impression that the behavior is random.

An analytic expression of $\beta_1^{(0)}$ on θ , above threshold, can be easily obtained assuming that $(\gamma\beta_\theta)_0$ remains almost constant. This assumption is justified by the numerical solution of either Eqs. (28) and (29) or Eq. (36). Results are shown in Fig. 9(b) for the same parameters listed in Table II, except that $\delta B_{z0} = 0.4$ G. In contrast to the solutions of Eqs. (28) and (29) or Eq. (36), Eq. (40) predicts that $(\gamma\beta_\theta)_0$ initially behaves in the same manner, but gradually increases as θ (or time) increases to very large values. The exact Eq. (4) or (12) gives also an average $\gamma\beta_\theta$ that varies as in Fig. 9(b). Since $\gamma\beta_\theta$ remains constant, on the average, after the resonance has been reached, we conclude that

$$(\gamma_0 + \gamma'\theta)^2 - 1 - |U_0|^2 = \text{const}. \quad (64)$$

If the initial value $\bar{U}_{00} = 0$, then at $\theta = \theta_0 \equiv w_0/\alpha$, we have $|U_0| \approx 0$ and $\gamma = \gamma_0 + \gamma'\theta_0$, and Eq. (64) leads, to zero or-

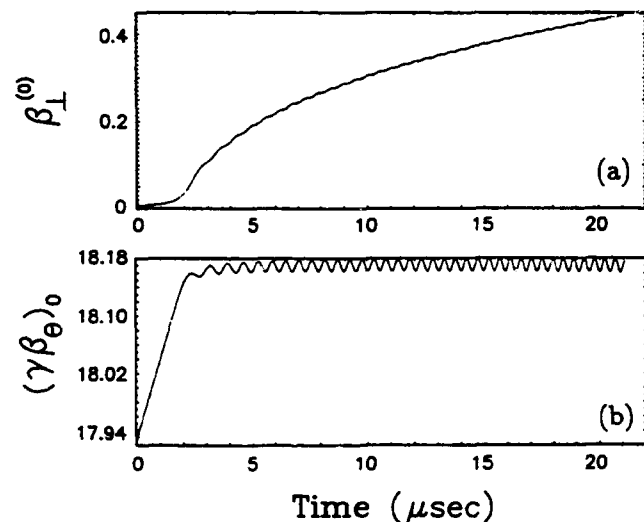


FIG. 9. Asymptotic behavior of β_1 and $\gamma\beta_\theta$ above the threshold (lock-in regime) for the parameters of Table II, except that $\delta B_{z0} = 0.4$ G.

der in β_1 , to the expression

$$\beta_1^2 \approx \frac{1 + \frac{\gamma'}{2\gamma_0}(\theta + \theta_0)}{\left[1 + \frac{\gamma'}{\gamma_0}\theta\right]^2} \frac{2\gamma'}{\gamma_0}(\theta - \theta_0). \quad (65)$$

When $\gamma'\theta \ll \gamma_0$, β_1 is proportional to the square root of time, which is demonstrated in Fig. 9(a) and also β_1 is proportional to the square root of the acceleration rate γ' . In contrast, below threshold, it has been shown that β_1 is inversely proportional to the square root of γ' .

V. DYNAMIC STABILIZATION AND THRESHOLD LAW

There are at least three possible ways to cross a cyclotron resonance without locking into it: (a) by reducing or eliminating the field errors, (b) by accelerating fast through the resonance, and (c) by adding a small time-dependent toroidal field that provides dynamic stabilization. In effect, it will be shown that the dynamic stabilization is equivalent to increasing the acceleration rate. The effectiveness of the second stabilizing mechanism is discussed at the end of this section. Here, we analyze the effectiveness of the stabilizing toroidal field, which is assumed to be sinusoidal with amplitude $\delta B_{\theta 0}$, and period τ which is much larger than the time Δt it takes to cross the resonance. The total toroidal field is described by

$$B_{\theta 0}(t) = B_{\theta 0} + \delta B_{\theta 0} \sin \frac{2\pi(t - t_d)}{\tau}, \quad (66)$$

where t_d is the time delay. Inserting Eq. (66) into Eqs. (13b) and (19b) [with the initial value $B_{\theta 0}(0)$ in b_{00}] and linearizing the detuning factor in Eq. (36), the parameters α, α_2 become

$$\alpha = v_{+1} \left[\lambda_0 - \kappa_0 \frac{\delta \Omega_{\theta 0}}{\Omega_{\theta 0}(0)} \cos \left[\frac{2\pi t_d}{\tau} \right] \right], \quad (67a)$$

$$\alpha_2 = \left[3 - \frac{(\gamma \beta_{\theta 0})_{00}^2}{\gamma_0^2} \right] \lambda_0 \alpha + \frac{r_0 \delta \Omega_{\theta 0}}{(\gamma \beta_{\theta 0})_{00} c} \kappa_0^2 \sin \left[\frac{2\pi t_d}{\tau} \right], \quad (67b)$$

where

$$\lambda_0 = \frac{\gamma_0 \gamma'}{(\gamma \beta_{\theta 0})_{00}^2}, \quad (68a)$$

$$\kappa_0 = \frac{2\pi}{\tau} \frac{r_0}{c} \frac{\gamma_0}{(\gamma \beta_{\theta 0})_{00}}, \quad (68b)$$

and w_0, δ, v_{+1} are given by Eqs. (39a), (39c), and (39d). The expansion of the detuning factor in Eq. (36) is done around \bar{U}_{00} and not around the initial value U_{00} , so that all the parameters given above depend on \bar{U}_{00} . For simplicity, let us assume that $t_d = 0$. If the toroidal field decreases as the resonance is being crossed, i.e., if $\delta B_{\theta 0} < 0$, then according to Eq. (67a) α becomes larger. This is equivalent to replacing γ' in α with a larger effective value. It is shown shortly that the larger the acceleration

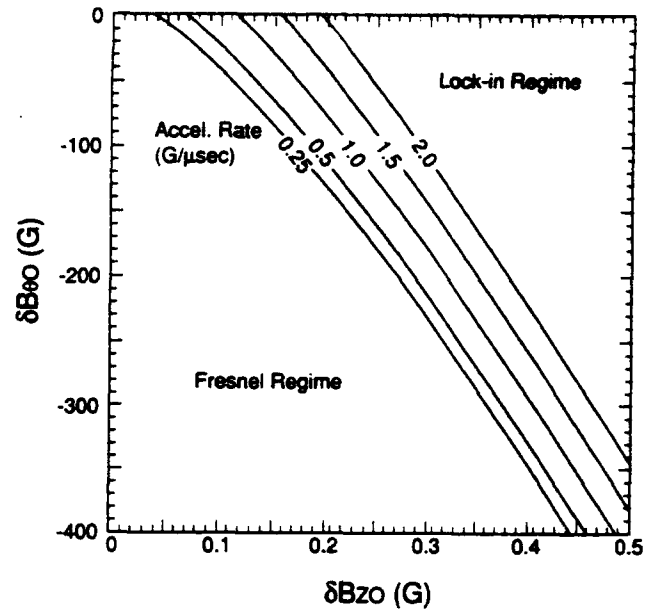


FIG. 10. Threshold law in the presence of a stabilizing time-dependent toroidal magnetic field, i.e., $\delta B_{\theta} = \delta B_{\theta 0} \sin(2\pi t/\tau)$ and zero initial perpendicular velocity ($\bar{U}_{00} = 0$).

rate, the larger becomes the threshold value. Therefore a small time-dependent toroidal field with negative time derivative does provide dynamic stabilization.

The threshold law is obtained by determining numerically the threshold value of ϵ in the dimensionless Eq. (47) in the special case when $\bar{U}_{00} = 0$. Then the threshold law is expressed by the relation

$$\frac{\delta}{2\alpha^{3/2}} B_{0\text{thr}}^2 = \epsilon_{\text{thr}}^2 \equiv 1.36. \quad (69)$$

Figure 10 gives the threshold values of δB_{z0} as a function of $\delta B_{\theta 0}$ for different acceleration rates, when $B_{\theta 0} = 2771$ G, $\tau = 50 \mu\text{sec}$, and $l = 9$. The beneficial effect of a large acceleration rate or a small time-dependent toroidal field becomes obvious from this figure. Each line in the figure separates the Fresnel from the lock-in regimes for each different value of the acceleration rate.

VI. DYNAMIC BEHAVIOR WITH INITIAL PERPENDICULAR VELOCITY

When the asymptotic initial value of U_0 is not zero, the display of the dynamic behavior close to the resonance becomes more difficult, because the dynamics depend on the initial phase as well as on the initial amplitude of \bar{U}_0 . The results are conveniently presented as contour plots (i.e., the resonance diagrams) of the final $\beta_1 \equiv |U_0|/\gamma$ in the $\beta_1^{(0)}(0), \varphi_0$ plane, where $\beta_1^{(0)}(0)$ and φ_0 are the amplitude and phase of the asymptotic initial value \bar{U}_{00}/γ_0 . The rest of the parameters, including the interval of integration over θ or time, are kept constant. Since the final β_1 becomes large in the lock-in regime while it is bounded in the Fresnel regime, the contours are very dense at the boundary between the two regions.

Figure 11 shows the two regimes for the parameters listed in Table IV. Although the results shown in Fig. 11

TABLE IV. Parameters of the run shown in Figs. 11 and 12.

Parameter	Value
Torus major radius r_0	100 cm
Toroidal magnetic field $B_{\theta 0}$	2771 G
Initial generalized mismatch $\Delta_0 + 0.5 V_0 ^2$	0.0
Field index n	0.5
Rate of change of vertical field \dot{B}_{z0}	2.4 G/ μ sec
Resonance mode l	9
Amplitude of VF error δB_{z0}	0.195, 0.3 G
Constant phase of VF error θ_0	0.0
Gradient of VF error K_{z0}	0.0
Amplitude of stabilizing toroidal field $\delta B_{\theta 0}$	0, -200 G
Period of stabilizing toroidal field τ	70 μ sec
Time delay of stabilizing toroidal field t_d	0.0 μ sec
Initial normalized toroidal momentum $\gamma\beta_{\theta 0}$	17.922
Initial normalized radial bounce displacement ξ_{0r}	0.0, 0.003, -0.003
Initial normalized vertical bounce displacement ξ_{0z}	0.0
Integration time t_f	8 μ sec

have been obtained by integrating Eqs. (28) and (29), Eq. (36) or (40) gives the same results, provided that there is negligible bounce motion. In Fig. 11(a), δB_{z0} has been chosen equal to 0.195 G, which is very close to the threshold value when $\beta_1^{(0)}(0)$. By increasing the field error amplitude from 0.195 to 0.3 G, the lock-in regime dominates for small initial $\beta_1^{(0)}(0)$ for the entire range of

initial phase angles as shown in Fig. 11(b). By turning on the stabilizing field, the Fresnel region increases at the expense of the lock-in region. Results are shown in Fig. 11(c) for $\delta B_{z0}=0.195$ G and $\delta B_{\theta 0}=-200$ G. This figure should be compared with Fig. 11(a) that has the same field error amplitude but not stabilizing field. Finally, in Fig. 11(d) the acceleration rate has been increased from

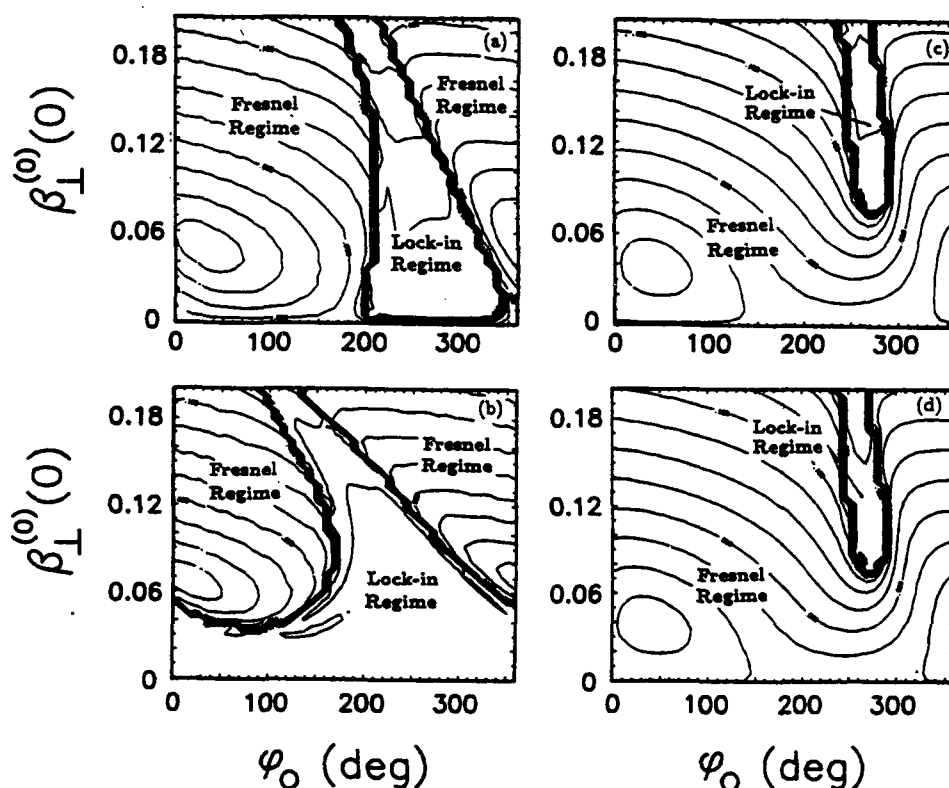


FIG. 11. Resonance diagrams, i.e., contour plots of the final β_1 , when the initial amplitude and phase of the normalized perpendicular velocity \bar{U}_{00}/γ_0 are not zero, for the parameters in Table IV, and in (a) $\delta B_{z0}=0.195$ G, $\delta B_{\theta 0}=0.0$ G, $\dot{B}_{z0}=2$ G/ μ sec; (b) $\delta B_{z0}=0.3$ G, $\delta B_{\theta 0}=0.0$ G, $\dot{B}_{z0}=2$ G/ μ sec; (c) $\delta B_{z0}=0.195$ G, $\delta B_{\theta 0}=-200$ G, $\tau=70$ μ sec, $\dot{B}_{z0}=2$ G/ μ sec; (d) $\delta B_{z0}=0.195$ G, $\delta B_{\theta 0}=0.0$ G, $\dot{B}_{z0}=4$ G/ μ sec.

$\dot{B}_{z0} = 2$ to 4 G/ μ sec, while $\delta B_{z0} = 0.195$ G and $\delta B_{\theta 0} = 0$. Again, comparison of Fig. 11(d) with Fig. 11(a) shows that the Fresnel region has increased at the expense of the lock-in region. When the electrons in the ring are uniformly distributed over the initial phase angle, the resonance diagrams give, for each initial $\beta_1^{(0)}(0)$, the percentage of the ring that crosses the resonance and the percentage that locks into it.

In all the results presented so far, the equilibrium position of the bounce motion was located at the origin of the coordinate system [i.e., $\Delta_{00} + |\bar{U}_{00}|^2/2(\gamma\beta_{\theta 0})^2 = 0$] and the amplitude of the bounce motion was selected negligibly small (since the initial $\xi_0 = 0$). If the equilibrium position is chosen off the origin [i.e., $\Delta_{00} + |\bar{U}_{00}|^2/2(\gamma\beta_{\theta 0})^2 \neq 0$], and the amplitude of the bounce motion is negligibly small, by judiciously choosing ξ_{00} , the resonance diagrams remain the same for the same set of parameters. When $\Delta_{00} + |\bar{U}_{00}|^2/2(\gamma\beta_{\theta 0})^2 \neq 0$, and in the special case of a field index $n = \frac{1}{2}$, the parameters γ' and r_0/c in Eqs. (68a) and (68b) should be replaced by $(1 + \Delta_{10})\gamma'$ and $(1 + \Delta_{10})r_0/c$, respectively, where $\Delta_{10} = [\Delta_{00} + |\bar{U}_{00}|^2/2(\gamma\beta_{\theta 0})^2]/K_{100}$. Also, the initial bounce position must be equal to $\xi_{00} = \Delta_{10}$, to have bounce motion with negligible amplitude. Finally, the term

$$(\nu_- - 2b_0\xi_0) \left[\Delta_0 + \frac{1}{2} \frac{|U_0|^2}{(\gamma\beta_{\theta 0})^2} \right] / K_{10}$$

should be added to the detuning factor in Eq. (36), and, therefore, the term $(\nu_- - 2b_0\xi_{00})\Delta_{10}$ should be added to ω_0 in Eq. (39a), where ν_- is the initial value of the bounce frequency.

When there is a small bounce motion superimposed to the cyclotron motion there is a modest change of the resonance diagrams. This becomes apparent by comparing Fig. 11(a) with Fig. 12. These figures have been obtained from Eqs. (28) and (29) with the same parameters, except for the initial bounce position. In Fig. 11(a), the initial position of the bounce motion is at the origin, while in Fig. 12(a), it is at (0.30 cm, 0.0 cm) and in Fig. 12(b) it is at (-0.30 cm, 0.0 cm). In the latter two cases, the amplitude of the bounce motion is 0.30 cm.

VII. MULTIPLE CROSSING OF A RESONANCE

When a small toroidal field with sinusoidal time dependence is added to the main toroidal field $B_{\theta 0}$, the detuning factor may become zero more than once, as time evolves, for the same resonance mode l . This is defined as a multiple crossing of the resonance mode l . Results are shown in Fig. 13. These results have been obtained from Eqs. (28) and (29) for the parameters listed in Table V and $\delta B_{z0} = 0.35$ G. Figure 13(a) shows that the detuning factor w becomes zero five times and a Fresnel jump occurs each time the resonance mode l is crossed. It is not necessary that all the crossings have a Fresnel jump. A lock into the resonance could occur at some crossing if

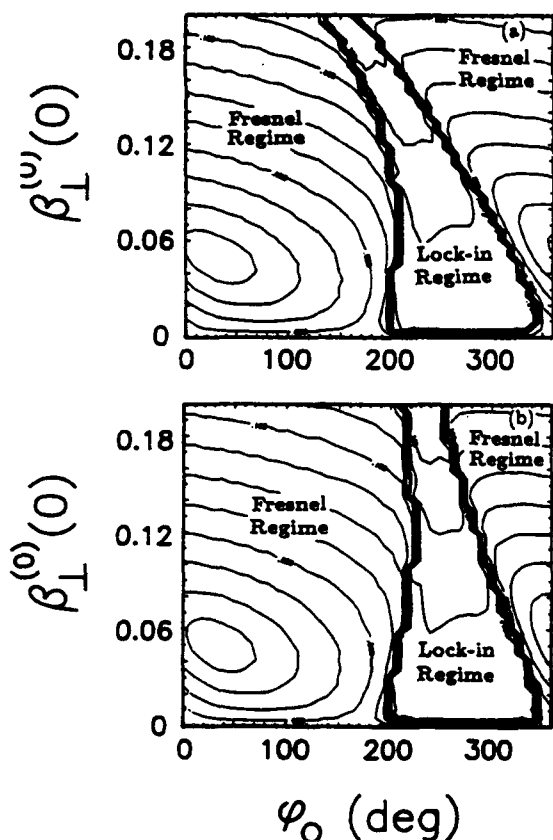


FIG. 12. Resonance diagrams for the same parameters as in Fig. 11(a), except that the radius of the bounce motion is 0.3 cm in both (a) and in (b) and in (a) the initial position of the bounce motion, i.e., $\xi_{00} = (0.3 \text{ cm}, 0.0 \text{ cm})$; in (b) $\xi_{00} = (-0.3 \text{ cm}, 0.0 \text{ cm})$.

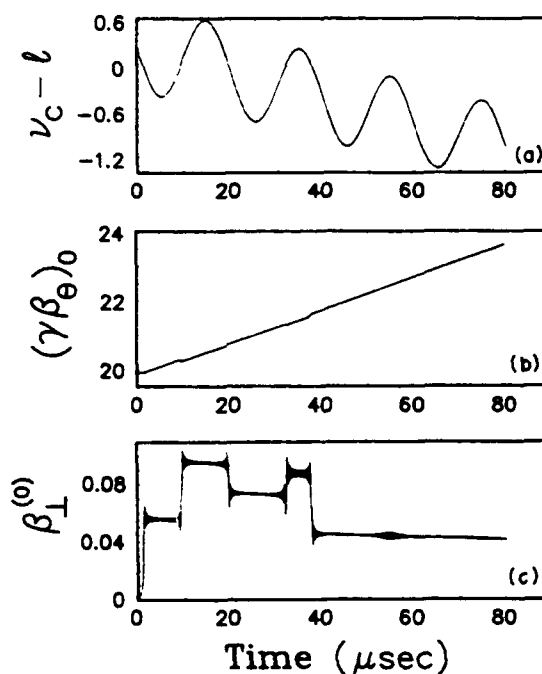


FIG. 13. $\nu_c - l$, $\gamma\beta_{\theta}$, and β_1 vs time during a multiple crossing of the resonance $l = 8$, obtained from the slow equations of motion [Eqs. (28) and (29)], for the parameters of Table V, and $\delta B_{z0} = 0.35$ G.

TABLE V. Parameters of the run shown in Fig. 7.

Parameter	Value
Torus major radius r_0	100 cm
Toroidal magnetic field $B_{\theta 0}$	2771 G
Initial generalized mismatch Δ_0	0.0
Field index n	0.5
Rate of change of vertical field \dot{B}_{z0}	0.8 G/ μ sec
Resonance mode l	8
Amplitude of VF error δB_{z0}	0.35, 1.0 G
Constant phase of -VF error θ_0	0.0
Gradient of VF error K_{z0}	0.0
Amplitude of stabilizing toroidal field $\delta B_{\theta 0}$	-200 G
Period of stabilizing toroidal field τ	20 μ sec
Time delay of stabilizing toroidal field t_d	0.0 μ sec
Initial normalized toroidal momentum $\gamma\beta_\theta$	19.875
Initial normalized vertical velocity β_1	0.0
Initial phase of vertical velocity φ_0	0.0
Initial normalized radial bounce displacement ξ_{0r}	0.0
Initial normalized vertical bounce displacement ξ_{0z}	0.0
Integration time t_f	80 μ sec

the asymptotic initial velocity is in the lock-in regime of the resonance diagram. As a rule, the detuning factor follows the time-dependent toroidal field. Figure 13(b) shows that when all the crossings are in the Fresnel regime, $\gamma\beta_\theta$ follows γ between crossings, while Fig. 13(c) shows that there are five Fresnel jumps in β_1 . In contrast, when the ring locks into the resonance, then $\gamma\beta_\theta$ follows the time-dependent toroidal field while w remains very small. This is shown in Fig. 14, obtained by integrating Eqs. (28) and (29), for the parameters listed in Table V and $\delta B_{z0} = 1.0$ G. According to Fig. 14(a) the first cross-

ing occurs at 1 μ sec and the ring locks into the resonance up to approximately 10 μ sec. As long as it remains locked, $w \approx 0$, while $\gamma\beta_\theta$ follows the time varying toroidal field [Fig. 14(b)]. Figure 14(c) shows that just before 10 μ sec, β_1 decreases to zero, while $\gamma\beta_\theta$ increases at a faster rate than γ . Since at this time $(\gamma\beta_1)^2 = \gamma^2 - 1 - (\gamma\beta_\theta)^2 \approx 0$, a continuously rising $\gamma\beta_\theta$ would require a negative $(\gamma\beta_1)^2$, which is an unphysical situation. Thus the ring unlocks from the resonance. The same cycle is repeated up to 45 μ sec, when β_1 , due to

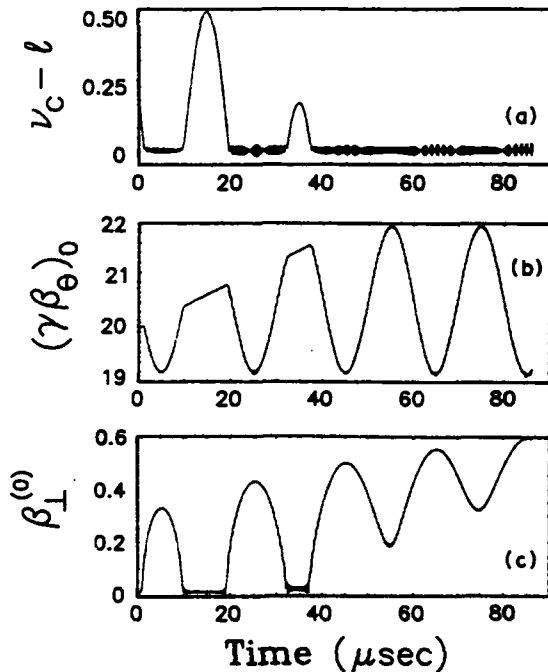


FIG. 14. $\nu_c - l$, $\gamma\beta_\theta$, and β_1 vs time during a multiple crossing of the resonance $l=8$ under the same conditions as in Fig. 13, except that $\delta B_{z0} = 1.0$ G.

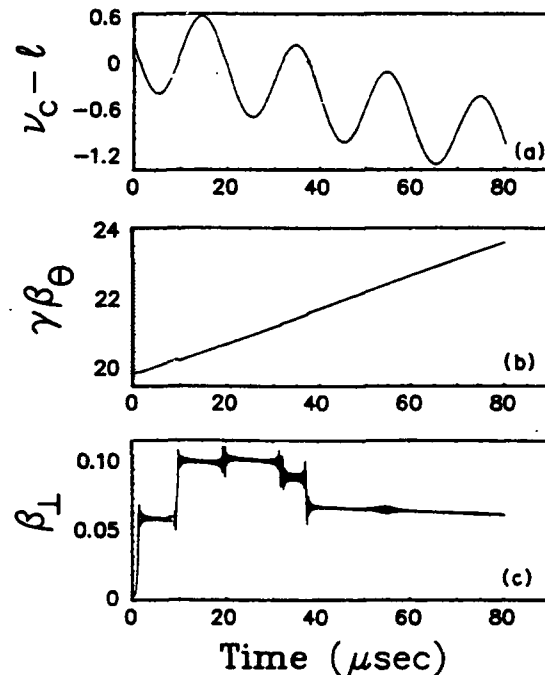


FIG. 15. $\nu_c - l$, $\gamma\beta_\theta$, and β_1 vs time during a multiple crossing of the same resonance $l=8$, under the same conditions as in Fig. 13, but obtained by integrating the exact equations of motion [Eq. (4)].

the rise of its average value, cannot become zero. After this time, $\gamma\beta_\theta$ remains locked to the sinusoidal variation of the field, while w remains almost zero. Therefore the next resonance mode $l+1$ is never reached, in spite of the fact that γ keeps increasing. The energy is transferred to $\gamma\beta_1$ rather than $\gamma\beta_\theta$. The exact Eq. (4) or (5) or the nonlinear slow Eq. (36), give identical results to those obtained from Eqs. (28) and (29) which are shown in Fig. 14. However, this is not the case with Fig. 13. Results from the integration of the exact Eq. (4) for the parameters listed in Table V and $\delta B_{z0}=0.35$ G are shown in Fig. 15. The detuning factor and $\gamma\beta_\theta$ in Fig. 15(a) and 15(b) are very similar to the results shown in Figs. 13(a) and 13(b). However, the transverse velocity in Fig. 15(c) is similar to that of Fig. 13(c) until the third crossing occurs at $19 \mu\text{sec}$. The difference is due to the fact that the slow Eqs. (28) and (29) are approximate, and the phase of β_1 computed from the exact and the slow equations becomes gradually different for long times. Therefore, for long times, when many resonances are to be crossed or multiple crossing occurs, the exact Eq. (4) should be used. The slow equations provide a valuable insight in the dynamic behavior close to a particular resonance, but are not reliable over long periods of time.

VIII. SUMMARY AND CONCLUSIONS

Magnetic-field errors excite resonances that the electron ring must cross during acceleration. In the presence of a VF error, there is a threshold value of the field error amplitude that separates two distinct regimes. Below threshold (Fresnel regime) and for zero initial \bar{U}_{00} , the perpendicular velocity increases by a finite amount as the resonance is crossed. The increase as well as the time it takes to cross the resonance are inversely proportional to the square root of the acceleration rate. Above threshold (lock-in regime), the perpendicular velocity is proportional to the square root of the acceleration rate and increases with the square root of time, while $\gamma\beta_\theta$ remains on the average constant, and the detuning factor remains extremely small. Therefore the ring locks into the resonance. The dynamic behavior without acceleration is entirely different even at exact resonance. The perpendicular velocity is proportional to time initially, but, due to the nonlinearities in the equations of motion, it reaches a maximum, then it decreases to zero and repeats periodically the same cycle. Therefore it is bounded.

The threshold is predicted by the slow equations of motion that have been derived by averaging out the fast cyclotron motion. The origin is the nonlinear dependence of $\gamma\beta_\theta$ on the perpendicular velocity and the fact that the cyclotron frequency is inversely proportional to $\gamma\beta_\theta$. By the appropriate choice of the initial conditions it was shown that the solutions of the slow or the exact equations of motion could be made weakly dependent on the initial time interval from the resonance. Possible ways to increase the threshold have been discussed. It has been shown, that the threshold value of the VF error amplitude is proportional to the $\frac{1}{4}$ power of the acceleration rate. Dynamic stabilization, i.e., the addition of a small time-dependent field to the main toroidal field, also

provides an effective increment to the acceleration rate, if it has a negative time derivative, and, therefore, increases the threshold. When the initial perpendicular velocity is not zero, the dynamic behavior has been presented by means of the resonance diagrams. These diagrams predict that a small bounce motion has only a modest effect on the Fresnel and lock-in regimes. Finally, the multiple crossing of the same resonance has been analyzed in the presence of dynamic stabilization and we have concluded that for long periods of time the exact equations of motion should be used.

Following the successful demonstration of acceleration in the NRL device, a concerted effort was made to locate and eliminate or reduce the various field disturbances that may excite the cyclotron resonance. Reduction in many of these field errors, together with the operation of higher toroidal and strong focusing fields led to beam energies in excess of 20 MeV, while the trapped current was above 1 kA.

In addition, three different cyclotron resonance stabilization techniques were tested in the NRL modified batatron: enhancement of the acceleration rate, dynamic stabilization or tune jumping, and avoidance of the resonance.

The damage done to the beam at each resonance depends on the speed with which the resonance is crossed. By enhancing the acceleration rate the resonance is crossed faster and thus the damage inflicted to the beam is reduced. To achieve higher acceleration rate, the vertical field coils were divided into two halves with midplane symmetry and powered in parallel. The experimental results show a striking reduction of the beam losses at $l=12$, 11, and 10, when the acceleration rate increased from 0.69 to 1.93 G/ μsec .

The crossing of the resonance can be also speeded up by modulating the toroidal magnetic field with a rapidly varying ripple. This is the dynamic stabilization or tune jumping technique and requires a carefully tailored pulse to be effective over many resonances. These results have been reported [10] previously and in general they are in agreement with the predictions of Sec. V and extensive computer calculations.

It is apparent from the resonance condition that when $B_{\theta 0}/B_{z0}=\text{const}\neq\text{integer}$, the cyclotron resonance is not excited. To test this prediction, a linearly rising toroidal field ramp ΔB_θ was superimposed on the main toroidal field. During the rise time of the ramp ($\sim 100 \mu\text{sec}$), the ratio $B_{\theta 0}+\Delta B_\theta/B_{z0}\approx\text{const}\neq\text{integer}$. The experimental results indicate that during this time period the beam losses are completely suppressed. Although very powerful, the resonance avoidance technique by keeping the ratio $B_{\theta 0}/B_{z0}=\text{const}\neq\text{integer}$ is not practical because to be effective over the entire spectrum of l requires very high toroidal field. Among the three stabilization techniques tested, acceleration of the beam at a higher acceleration rate appears to have the highest practical potential.

ACKNOWLEDGMENT

This work was supported by the U.S. Office of Naval Research and by SPAWAR.

- *Also at Science Applications International Corporation, McLean, VA 22102.
†Also at SFA, Inc., Landover, MD 20785.
- [1] C. A. Kapetanacos, L. K. Len, T. Smith, J. Golden, K. Smith, S. J. Marsh, D. Dialetis, J. Mathew, P. Loschialpo, and J. H. Chang, *Phys. Rev. Lett.* **64**, 2374 (1990).
 - [2] C. A. Kapetanacos, L. K. Len, T. Smith, D. Dialetis, S. J. Marsh, P. Loschialpo, J. Golden, J. Mathew, and J. H. Chang, *Phys. Fluids B* **3**, 2396 (1991).
 - [3] L. K. Len, T. Smith, P. Loschialpo, J. Mathew, S. J. Marsh, D. Dialetis, J. Golden, J. H. Chang, and C. A. Kapetanacos, *Proc. SPIE, Intense Microwave and Particle Beams III* **1629**, 521 (1992).
 - [4] C. A. Kapetanacos, S. J. Marsh, and D. Dialetis, *Phys. Rev. Lett.* **61**, 86 (1988).
 - [5] D. Chernin and P. Sprangle, *Part. Accel.* **12**, 101 (1982).
 - [6] D. C. DePackh, *NRL Report No. 4608*, 1955 (unpublished).
 - [7] C. W. Roberson, A. Mondelli, and D. Chernin, *Part. Accel.* **17**, 79 (1985).
 - [8] N. N. Bogoliubov and Y. A. Mitropolaky, *Asymptotic Methods in the Theory of Nonlinear Oscillations* Hindustan, Delhi, 1961).
 - [9] I. S. Gradshteyn and I. M. Ryzhik, *Table of Integrals, Series and Products* (Academic, New York, 1980), Sec. 3.145, Eq. 2.
 - [10] C. A. Kapetanacos, L. K. Len, T. Smith, P. Loschialpo, J. Mathew, S. J. Marsh, D. Dialetis, J. Golden, and J. H. Chang, *NRL Memo Report No. 6988*, 1992 (unpublished).

Appendix CC

Intense Microwave and Particle Beams II

PROCEEDINGS REPRINT

 SPIE—The International Society for Optical Engineering

Reprinted from

Intense Microwave and Particle Beams II

**21–24 January 1991
Los Angeles, California**



Volume 1407

©1991 by the Society of Photo-Optical Instrumentation Engineers
Box 10, Bellingham, Washington 98227 USA. Telephone 206/676-3290.

Recent Developments on the NRL Modified Betatron Accelerator*

J. Golden[†], L. K. Len^{*}, T. J. Smith, D. Dialetis[△],
S. J. Marsh[‡], K. Smith[‡], J. Mathew,
P. Loschialpo, L. Seto[‡], J. H. Chang,
and C. A. Kapetanakis

Plasma Physics Division
Naval Research Laboratory
Washington, DC 20375

ABSTRACT

Since the previously reported successful demonstration of acceleration of electrons to ~ 12 MeV, higher trapped beam current and longer beam lifetime have been obtained. The improved confinement has led to a higher peak energy ~ 18 MeV, and is the result of increasing the strong focusing and toroidal magnetic fields, reducing magnetic field errors, and optimizing the betatron flux condition. Modifications to the electromagnet buswork are in progress to further reduce field errors, and a fast pulsed magnet system to provide dynamic stabilization of the the cyclotron resonances is being studied.

1. INTRODUCTION

The Modified Betatron Accelerator is a compact (major radius=1 m), cyclic, high current electron accelerator which is of interest for several civilian and military applications. The device uses a toroidal magnetic field B_θ and a strong-focusing, quadrupole stellarator field B_{sf} as well as the weak focusing conventional betatron field B_z to confine a ring of electrons. The electrons are injected with an initial energy of 0.6-0.7 MeV and are accelerated to peak energy $\simeq 18$ MeV. Ring currents of ~ 1.5 kA are trapped near the minor axis following injection. The experimental observations indicate that the ring lifetime is apparently limited by the excitation of the cyclotron orbital resonances.¹ Measurements of x-rays emitted when electrons strike the wall of the vacuum chamber show that electrons are lost from the ring for specific values of the ratio of the magnetic fields B_z/B_θ . The measured amplitude of the magnetic field associated with the circulating electromagnetic modes inside the torus reveal that these modes are several orders of magnitude too weak to excite the cyclotron instability² or the parametric instability³ and therefore, cause the electron loss. Measurements of x-rays emitted when the electrons strike the beam injector that protrudes into the chamber, and observations of the 'single particle', classical synchrotron radiation⁴ suggest that electrons move away from the minor axis during the latter part of the acceleration.

In this paper, efforts to improve confinement and extend the beam lifetime to higher energy are reported. The steps taken include the following measures. The B_{sf} and B_θ magnetic fields have been increased. The higher B_{sf} reduces the sensitivity of the beam centroid and individual particles to a mismatch of B_z and the particle energy, and the higher B_θ provides better confinement of the beam minor radius. Also field errors that may excite the cyclotron resonance have been reduced. The alignment of the vacuum chamber and magnetic

field coils has been improved substantially, and the stray fields associated with the buswork feeding currents to the betatron field coils have been analyzed and are being corrected. In addition, a concept to dynamically stabilize the cyclotron resonances is being studied.

2. THE EXPERIMENTAL APPARATUS

A plan view and elevation of the modified betatron are shown in Figs. 1 and 2. The applied magnetic fields, B_z , B_θ , and B_{sf} , are generated by three sets of pulsed electromagnet coils. The B_z and B_θ coils are supported by a structure made of polyester/fiberglass composite and stainless steel, and is nearly magnetically transparent. The B_{sf} coils are mounted on the toroidal vacuum chamber which is made of graphite/epoxy and fiberglass/epoxy composite. The beam is generated by a field emission diode that is located inside the vacuum chamber. Power for the coils is provided by capacitor discharge. The risetimes are 2.5 ms, 1.0 ms, and 2.4 ms for the B_z , B_{sf} , and B_θ fields, respectively.

The B_z magnets comprise 18 air core circular coils having a total series inductance of $530\mu\text{H}$. At full charge (17 kV), a peak field of 2.1 kG is achieved with a peak current $\simeq 45$ kA. Two pairs of trimmer coils and a parallel shunt inductance across the two B_z -coils closest to the midplane provide adjustment of the field index n and flux condition ξ . The field index is defined as $n = -[r_0/B_{z0}]dB_z/dr$ where r_0 and B_{z0} are the major radius and betatron field at the minor axis, and the flux condition is $\xi = d\langle B \rangle/dt/dB_{z0}/dt$ where $d\langle B \rangle/dt$ is the time derivative of the average magnetic field linked by the minor axis.

Twelve rectangular single turn coils produce B_θ . These coils are connected in series and powered by a 33 mF capacitor bank. At the peak current $\simeq 210$ kA, $B_\theta \simeq 5.1$ kG. Because of the discreteness of the coils, the B_θ has a $\sim 1\%$ ripple inside the chamber.

The strong focusing field is generated by left handed windings that are located 23.412 cm from the minor axis and have three winding periods (six field periods) around the major axis. A peak current $I_{sf} > 25$ kA can be passed through the windings. Additional details have been previously reported in comprehensive descriptions of the modified betatron apparatus.⁵

3. OBSERVATION OF THE CYCLOTRON RESONANCES

Since the first observation of the 'spiked' x-ray waveform produced by the electrons accelerated in the NRL modified betatron, it has been apparent that beam loss is associated with resonances. These resonances result when an eigenfrequency $\omega_{\pm\pm}$ of the motion in the transverse (r-z) plane is equal to a harmonic of the frequency of revolution around the major axis. The beam motion in the transverse plane is characterized by four modes⁶ which are very complex. However, when $(B_\theta/B_z)^2 \gg n_s$ (n_s is the self field index) and the current in the strong focusing windings is low, these modes are considerably simplified. In this case there are the cyclotron modes, $\omega_{-+} = -\Omega_\theta/\gamma$ and $\omega_{++} = s\Omega_z/\gamma + \Omega_\theta/\gamma$ (where $\Omega_\theta = eB_\theta/m$, $\Omega_z = eB_z/m$, e and m are the electron charge and mass, and γ is the relativistic energy parameter), the 'bounce' frequency, $\omega_{--} \simeq \omega_B$, and the intermediate frequency, $\omega_{+-} \simeq s\Omega_z/\gamma - \omega_B$ (where $s = 6$ is the number of strong focusing field periods). The cyclotron resonance condition is that $\omega_{++} = \ell\Omega_z/\gamma$, and is equivalent to

$$\frac{B_\theta}{B_z} = \frac{2\ell^2 - 1}{2\ell}, \quad (1)$$

where $\ell = \pm 1, \pm 2, \dots$

The physical mechanism is that the electrons return to a spatially localized field disturbance with the same phase. Thus, the motion is coherent, and the perturbation of the electron orbit is reinforced each time the disturbance is encountered. With sufficient perturbation, electrons strike the chamber wall where they produce the Bremsstrahlung.

The x-rays are observed with collimated scintillator/photomultiplier detectors that are housed in lead shields. Each has 10 cm thick walls and a 0.5 m long collimating pipe. The detector circuit is specially constructed with sufficient capacitance across the dynodes of the photomultiplier so that the dynode bias voltage and the detector gain do not 'droop' during the ~ 0.5 ms duration pulse. To limit the signal amplitude, the detector is typically located several meters from the torus (e.g., 10 m), and the detector aperture is limited to 1 – 3 cm. The x-ray signal produced by injection electrons which are not trapped is clipped by an integrating filter that has an RC-time of one microsecond.

The x-ray signal is shown in Fig. 3 along with the values of ℓ for which eqn. (1) is satisfied. It is seen that the peaks in the x-ray waveform agree well with the theory for the electron cyclotron resonances. In earlier observations, significant excitation of resonances with $\ell \simeq 15$ were seen. In the recent experiments, the first serious resonance encountered is when $\ell = 10$ where a large fraction of the beam is lost. Remarkably, the surviving portion of the beam remains sufficiently intact so that subsequent resonances at $\ell = 9 \rightarrow 6$ are routinely observed. For the data shown (shot 6933), $B_\theta = 4.3$ kG, $I_{ef} \simeq 25.4$ kA, and the $\ell = 9$ resonance occurs at an energy of 14 MeV.

To determine if the observed resonances could be the result of coupling between the cyclotron mode and the TE_{11p} modes of the chamber, attempts were made to measure the poloidal \bar{B}_ϕ and toroidal \bar{B}_θ fields of the electromagnetic modes inside the torus. Measurements with wideband magnetic probes have yielded null results; the peak measured field is $\bar{B}_\theta < 3 \times 10^{-5}$ G at 580 MHz. This places an upper bound ≤ 16 W on the power inside the chamber. Because a circulating power of ~ 1 MW is required to produce a magnetic field of a few Gauss, the cyclotron instability² and the parametric instability³ can be excluded as the cause of beam loss.

Instead, the most likely explanation is that the electron cyclotron resonance is driven by field errors. Numerical modelling has shown that threshold field errors for the excitation of these resonances are on the order of 1 % of the B_θ or B_z fields.^{7,8}

For example, when the beam encounters a 'bump' in B_z as the $\ell = 9$ resonance is encountered, the transverse velocity increases. This is shown in Fig. 4 where the upper frame shows the beam centroid β_\perp (transverse velocity divided by the speed of light) as a function of time for two cases that have slightly different amplitude 'bumps' in B_z . In case #1, the amplitude of the field disturbance is 5.30 G, for case #2, it is 5.44 G. It is seen that case #1 is stable, but case #2 is not. In the lower frame of Fig. 4, $\gamma\beta_\theta$ (\propto forward momentum) is shown as a function of time. For case #1 the acceleration of the beam continues, but for case #2, $\gamma\beta_\theta$ remains close to the value at resonance, i.e., the beam remains stuck at the resonance. (Note that the strong focusing field was omitted in this particular simulation because of its small effect at high energy, $\gamma \sim 18$.)

4. MAGNETIC FIELD ERRORS

During the past several months, a concerted effort has been made to locate and eliminate the field disturbances that may excite the cyclotron resonance. The sources of field errors that

have been investigated include the following, (1) coil misalignment, (2) coil discreteness, (3) eddy currents induced in the modified betatron support structure and nearby components, (4) porthole induced eddy current and image errors in the toroidal vacuum chamber, and (5) contributions from the buswork and current feeds of the coils. Many of these field errors were identified during the initial design of the modified betatron apparatus when it was recognized that field errors posed a potential problem. During the last year, improved measurement and correction techniques have resulted in a substantial reduction in many of these errors. The steps to measure and reduce the errors are described below.

The errors produced by misalignment of the toroidal field (TF) and vertical (betatron) field (VF) coils have been the most straightforward to reduce. This is because the coils were manufactured to a 'true position' tolerance of ± 1.5 mm, which includes the small, measured variation of coil insulation thickness. The initial installation was performed to an accuracy of approximately ± 3 mm. However, because coil supports and shims loosened over several thousand shots, some of the VF coils were found to have a radial shift approaching 1 cm and be tilted out of the horizontal plane by an angle of several milliradians. For individual coil misalignments, such radial displacements produce $\ell = 1$ errors of a few tenths of a Gauss, and the tilt produces comparable $\ell = 2$ errors. With several VF coils misaligned, higher mode errors can result.

In the case of the TF coils, the principal error is from misalignment out of the vertical plane. Because the inner vertical segment of each TF coil is tightly constrained within a vertical groove in an accurately machined phenolic cylinder at the center of the machine (the 'spline', see Fig. 2), these inner 'legs' of the TF coil set are parallel with the central axis of the structure. However, it was found that the rubber shock absorbing pads on which rest each corner of the lower deck had partially collapsed. This resulted in a tilt angle to the central axis of ~ 5 mrad. Furthermore, the TF coils are subject to a tilting force in the $\pm \hat{\theta}$ -direction because of their radial currents interacting with the vertical betatron field B_z . Although the radial segments of each TF coil were held by sturdy clamps mounted on the structurally stiff 'decks,' these clamps could not originally be located far enough radially outboard to prevent deformation of the coil out of the vertical plane. Thus, several TF coils had become tilted by as much as 7 mrad. Calculations with the computer program EFFI⁹ have shown that this tilt generates a several Gauss vertical field at the minor axis.

To correct these misalignments, the decks were jacked into a level position as surveyed using a Sokkisha/Lietz optical transit level. The structure was regouted and tightened. Additional VF and TF coil clamps were installed to permit higher field operation and to provide redundancy to prevent future coil misalignment as individual clamps occasionally loosen. With these modifications, the coils were repositioned to within ± 1.5 mm. The chamber was then positioned and clamped in place to a similar tolerance.

Although the $\ell = 12$ resonance does not appear to pose a significant problem, an effort was made to reduce the errors produced by coil discreteness that correspond to the B_θ field lines bulging radially outward between the 12 TF coils. An EFFI calculation predicts the B_θ variation was $\sim 1\%$ in a region within 10 cm of the minor axis. Thus, error fields of several tens of Gauss were present. To reduce these 'bumpy torus' bulges, a diamagnetic coil was placed directly under each TF coil. These 12 correction coils consisted of two turns of #2 AWG wire wrapped poloidally around the outside of the chamber. By connecting each coil

in series with an appropriate inductance, the circuit inductance L and resistance R could be selected. In practice, the series inductance comprised ten turns of wire placed in the r - z plane below the lower deck where no fringing or return flux of the main coil sets would be linked. The wire gauge determined the resistance. By adjusting the L/R magnetic diffusion time, B_θ inside the chamber could be slightly reduced under each coil so that the $\ell = 12$ bumps in B_θ are nearly eliminated.

A third source of error fields was found in the eddy currents induced in the structural elements of the decks. The decks are made of non-magnetic (304 alloy), stainless steel plates embedded in polyester-glass extruded structural shapes. Although in the original design, the radial spokes and perimeter edge beams were to have breaks in the steel plates so that eddy currents would be avoided, some of these breaks were omitted or shorted during construction. Rogowski coil measurements of the eddy currents revealed that B_z induced up to 1.6 kA in the radial spokes and ~ 25 kA in the edge beams. Such currents produce error fields ~ 2.5 G and ~ 15 G, respectively, at the chamber. The remedy was to place an insulating sleeve around bolts at the ends of the members to interrupt the eddy currents.

The errors produced by currents and images in the vacuum chamber proved far more difficult to reduce. The carbon/epoxy/glass composite chamber consists of 12 sectors, 11 of which have a 20 cm diameter porthole and two 2.5 cm diameter diagnostic ports. A sector is shown schematically in Fig. 5. To obtain a magnetic diffusion time ($L/R \sim 8\mu s$) for the B_z field to penetrate the chamber wall, a phosphor-bronze screen is embedded in the wall of the chamber. Thin gold plated inconel flanges and electrical gauze gaskets connect the screens of adjacent sectors so that beam induced image currents in the wall and screen can flow in the toroidal direction. The B_z eddy currents also flow in the toroidal direction.

Errors arise because of the perturbation of these wall currents by the portholes. An estimate of the magnetic field error is obtained by modelling the diversion of the chamber current around the porthole as two semicircular arcs and a straight current segment. Using EFFI and estimating the fraction of current that is diverted, (typically ~ 1 kA), it is found that errors ~ 25 G can result when $B_z \simeq 600$ G. The existence of these errors was confirmed by measurements made with a pair of effectively identical small probe coils having $\simeq 2$ cm diameter, $N=600$ turns, and a turn-area product of 0.2 turn- m^2 . The probe signals were integrated with matched integrators with a time constant, $RC=20.5$ ms. Placing one probe near a porthole and the other near the end of a sector, the error field was monitored as the differential signal. Field errors ~ 33 G at $r = 110$ cm were measured when $B_z \simeq 600$ G.

Partial correction of the porthole errors was accomplished by placing a disk of phosphor-bronze screen mounted on a supporting insert frame into each port and connecting it via gauze gasketing to sheet metal tabs soldered to the screen in the chamber wall. This reduced the errors by 50 %. To reduce the field disturbances by ~ 80 %, brass and stainless steel wires oriented in the $\hat{\theta}$ -direction were soldered to the edges of the screen. Each porthole insert was customized to obtain a satisfactory reduction in the the error field. The errors, now ~ 5 G are shown in Fig. 5.

A still uncorrected set of field errors is produced by the buswork current feeds to the VF coils. Although the buswork is coaxial and contributes little to the field, the transition from coax to the hoops comprising the VF coils produces an error of several percent. This error results because the transition segments of the current feeds are not circular arcs at the

radius of the coil but are instead straight chords. Over these chords, the current flows at a radial position that is displaced as much as 5 cm inward from the correct position. An EFFI calculation of these errors is shown in Fig. 6. New buswork leads (see Fig. 2, 'risers') that are circular arcs should eliminate these errors. Presently, such leads are under development.

5. EXPERIMENTAL RESULTS

Of the modifications described above, three have resulted in improved beam confinement and higher peak energy. These are the optimization of ξ , the reduction of the field errors associated with the portholes of the vacuum chamber, and the increase in B_θ and B_{zf} . The effect of stronger B_θ is to provide better confinement of the beam minor radius and leads to higher trapped beam current. The higher B_{zf} reduces the sensitivity of the beam centroid position to energy. However, the two fields cannot be varied arbitrarily because they affect the trapping of the beam. During the first revolution of the beam around the major axis, the beam must drift a sufficient distance poloidally so that the electrons do not strike the injection diode. This drift depends on the stellarator field index η_{st} which is a measure of the strong focusing forces. The stellarator field index η_{st} is proportional to $I_{zf}^2/(\gamma B_\theta)$. It is found that a relatively narrow range of I_{zf}^2/B_θ leads to efficient trapping.

Over the past year, the operating value of the B_θ field has been increased from ~ 3 kG to ~ 5.1 kG. With this increase, a trapped beam current in excess of 1.5 kA is typical for an optimal value of $I_{zf}^2/(\gamma B_\theta)$. Moreover, the value of B_z is now larger for which is reached a given ratio B_θ/B_z corresponding to a particular ℓ -value resonance. Thus, a serious encounter with the $\ell \leq 10$ resonance still occurs, but this is at an electron energy ~ 14 MeV (instead of ~ 11).

Another manifestation of the improved confinement is the reduction in x-rays produced by electrons striking the injection diode long after injection during the acceleration pulse and prior to the x-ray pulses produced as the beam strikes the wall because of the disruptive resonances. At the lower values of B_θ , x-rays from the diode are routinely observed. However, at the higher B_θ , some shots yield a very small pulse of diode x-rays which indicates that few electrons are lost before the principal resonances occur.

Experiments were also performed to determine the flux condition (ξ) which resulted in the longest beam lifetime. As the electrons are accelerated, an incorrect ξ can shift the equilibrium position to the chamber wall or into the injection diode that protrudes into the chamber. Furthermore, when the beam is not near the minor axis, resonances may also be excited by the strong focusing field.

Flux adjustment is obtained with a combination of the trimmer coils which are powered by shunting some of the current flowing to the main VF coil set through a parallel circuit branch with a large inductance that has no mutual inductance coupling to the VF coils, and by removing some of the larger radius VF coils from the circuit. Table I displays some of the configurations used in the experiment. Given are the minimum and maximum values of the index within 10 cm of the minor axis as predicted by EFFI calculations. Simultaneous measurement of the loop voltage ($\propto d\langle B \rangle/dt$) and dB_z/dt at the minor axis indicate that the EFFI calculation leads to an overestimate for ξ by 17 %. This discrepancy might result from the neglect of flux exclusion by the conductors of various coils and structural elements. The table gives the measured values of ξ .

TABLE I. Various B_z -field Configurations

#	$n_{min}-n_{max}$	ξ	configuration
15.3	0.41-0.64	1.7	all trimmers at 15 % I_{vf}
17.7	0.42-0.71	1.9	w/o VF ± 9 , no trimmers
17.6	0.59-0.88	2.0	w/o VF ± 9 , all trimmers 15 % I_{vf}
17.3	0.42-0.64	2.0	w/o VF ± 9 , no trimmers

where I_{vf} is the series current through the VF coils.

Using the configurations listed in Table I, it was found that $\xi = 1.9$ is best. This is illustrated in Fig. 7, where the x-ray signal versus time is shown for two flux conditions, $\xi = 1.9$ and 2.0. In both cases, the field amplitudes and the trapped current ~ 1.5 kA were the same. It was found that beam trapping is not very sensitive to the flux condition, but confinement is. If the flux condition is not optimal, the beam is expected to move away from the minor axis during acceleration. The observed temporal reduction in the synchrotron radiation emitted by the beam,⁴ and the x-rays emitted as beam scrapes the injector are consistent with such an excursion.

While the beam lifetime has proven to be sensitive to the amplitudes of the fields and to the flux condition, only a modest increase in lifetime has resulted from the efforts to reduce field errors. Thus, although several field disturbances have been greatly reduced, e.g., the errors produced by the chamber portholes, it appears that significant perturbations remain.

6. DISCUSSION

Avoidance of unstable excitation of the cyclotron resonances will likely require reduction of all field errors below threshold values. To further improve the field configuration towards this goal, new buswork connections to the VF coils are under construction. However, it is uncertain whether these improvements will be sufficient remedies to avoid the resonances. Therefore, in addition to continuing the refinement of the fields, a scheme for dynamic stabilization of the resonances is being investigated.⁸

The basic concept of dynamic stabilization is to avoid locking the beam into a resonance by applying a temporal modulation of B_θ . The modulation is switched on just prior to the beam's encounter with the disruptive resonance. The concept is being studied analytically and numerically. The engineering development of the hardware to produce the modulation field is underway.

7. REFERENCES

- * Work supported by ONR and SPAWARS.
 - † Berkeley Research Associates, Inc., Springfield, VA 22150
 - * F-M Technologies, Fairfax, VA 22032
 - Δ SAIC, McLean, VA 22102
 - ‡ Sachs-Freeman Associates, Inc., Landover, MD 20785
1. C. A. Kapetanacos, L. K. Len, T. Smith, J. Golden, K. Smith, S. J. Marsh, D. Dialetis, J. Mathew, P. Loschialpo, and J. H. Chang, *Phys. Rev. Lett.* **64**, 2374 (1990).
 2. C. M. Tang, P. Sprangle *et al*, *Bul. Am. Phys. Soc.* **34**, 1996 (1989).
 3. T. P. Hughes and B. B. Godfrey, *Phys. Fluids* **29**, 5 (1986).
 4. T. J. Smith, J. Golden, and C. A. Kapetanacos, Memorandum Report 6774, NRL, Wash. DC (1991).
 5. L. K. Len, T. Smith, J. Golden, K. Smith, S. J. Marsh, D. Dialteis, J. Mathew, P. Loschialpo, J. H. Chang, and C. A. Kapetanacos, *Intense Microwave and Particle Beams*, conf. proc. of OE LASE 90, 16-19 January 1990, Los Angeles, SPIE, vol **1226**, 382 (1990).
 6. C. W. Roberson, A. Mondelli, and D. Chernin, *Part. Accel.* **17**, 79 (1985).
 7. S. J. Marsh, D. Dialetis, and C. A. Kapetanacos, *Bul. Am. Phys. Soc.*, **35**, abstr 6S23, 2073 (1990).
 8. D. Dialetis, S. J. Marsh, and C. A. Kapetanacos, *Bul. Am. Phys. Soc.* **35**, abstr. 6S22, 2073 (1990).
 9. S. J. Sackett, Report UCRL-52402, Lawrence Livermore Nat'l. Lab., Livermore, CA (1978).

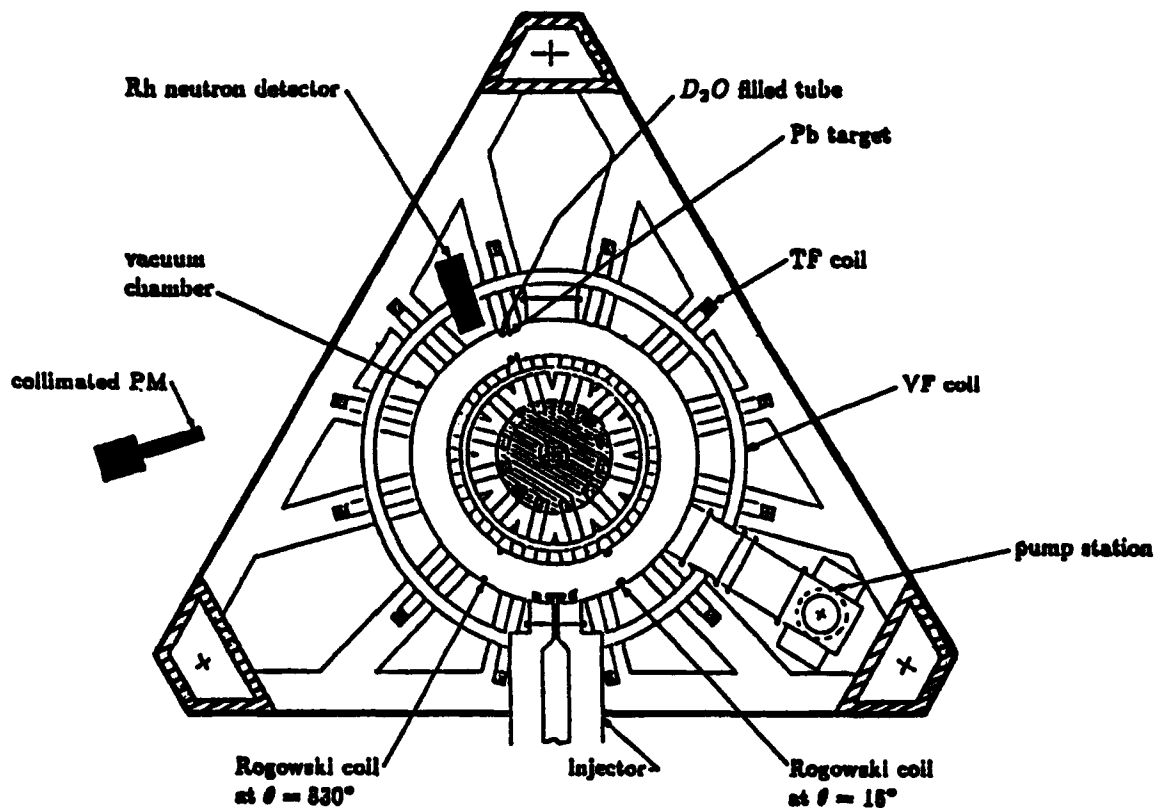


Fig. 1. Plan view of the NRL modified betatron.

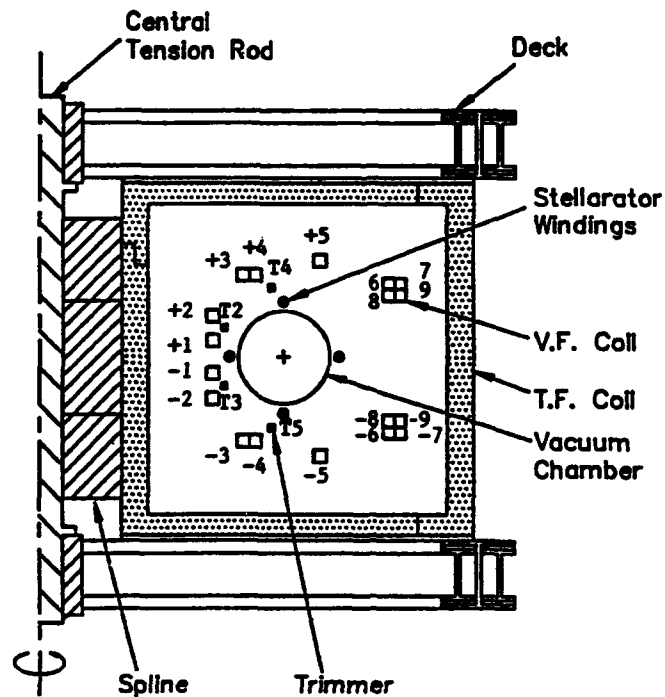


Fig. 2. Elevation of the modified betatron showing the vertical betatron field (VF) coils, toroidal field (TF) coils, stellarator windings, and some structural components.

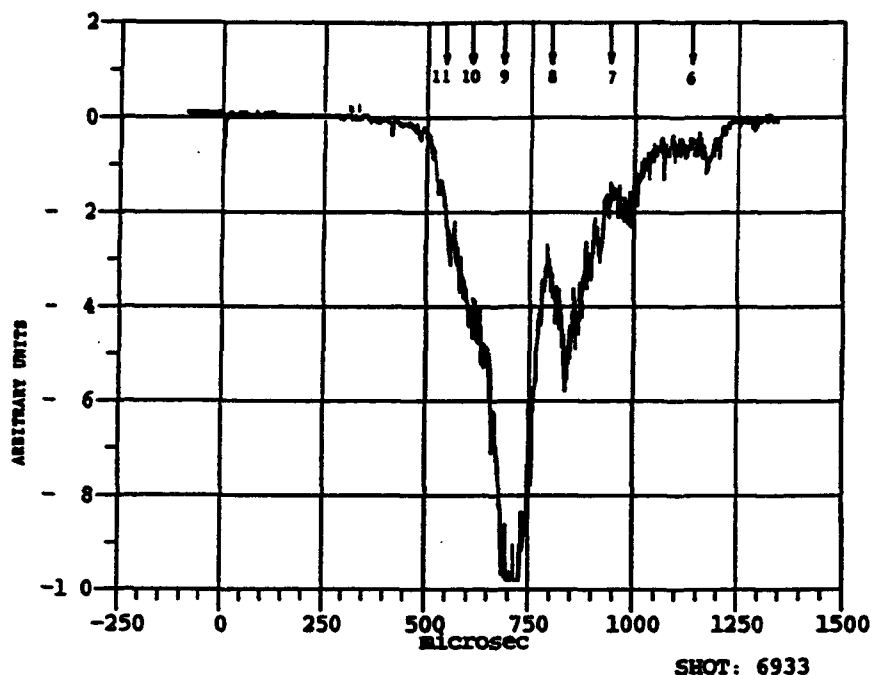


Fig. 3. X-ray signal vs. time for $B_0 = 4.3$ kG, $I_{ef} \approx 25.4$ kA. The arrows indicate resonance number where $B_0/B_z = (2\ell^2 - 1)/(2\ell)$.

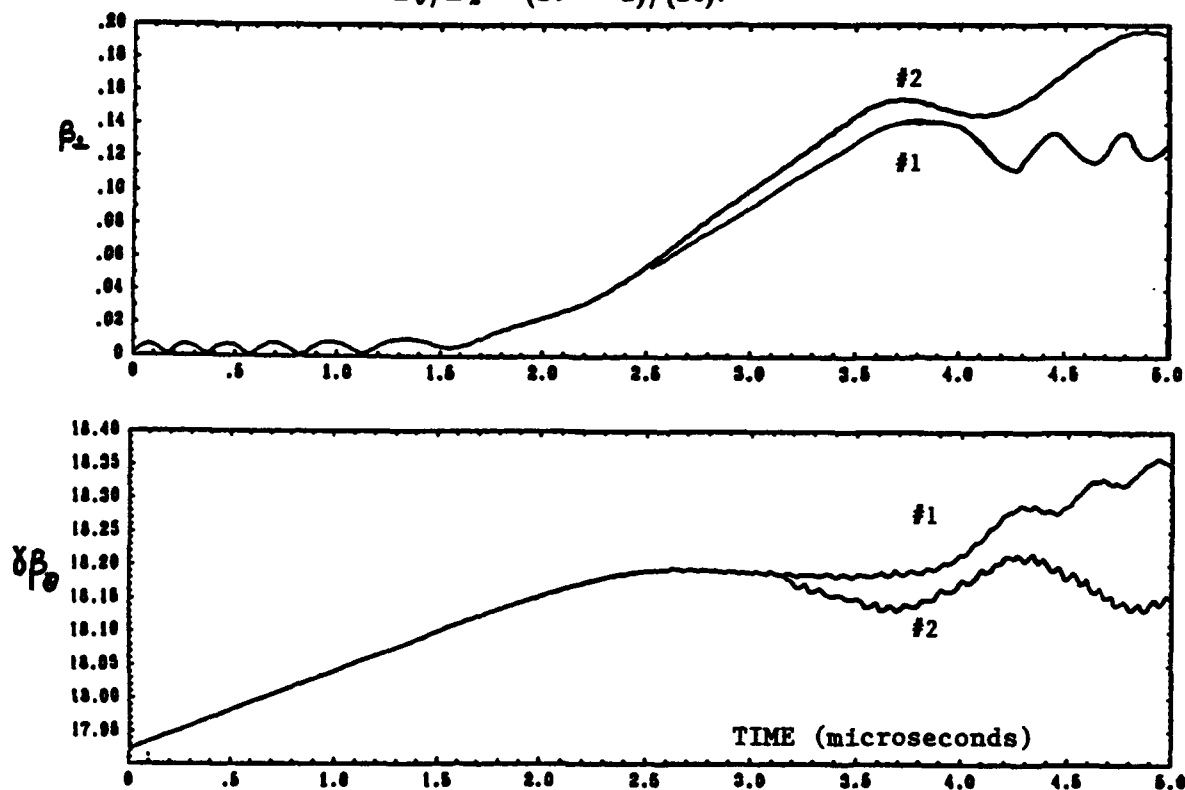


Fig. 4. Results of numerical modelling the beam centroid motion in a modified betatron without strong focusing as the $\ell = 9$ resonance is encountered in the presence of a 'bump' δB_z in B_z . Case #1 is stable, $\delta B_z = 5.30$ G; case #2 is unstable, $\delta B_z = 5.44$ G.



Field Disturbances from the Ports

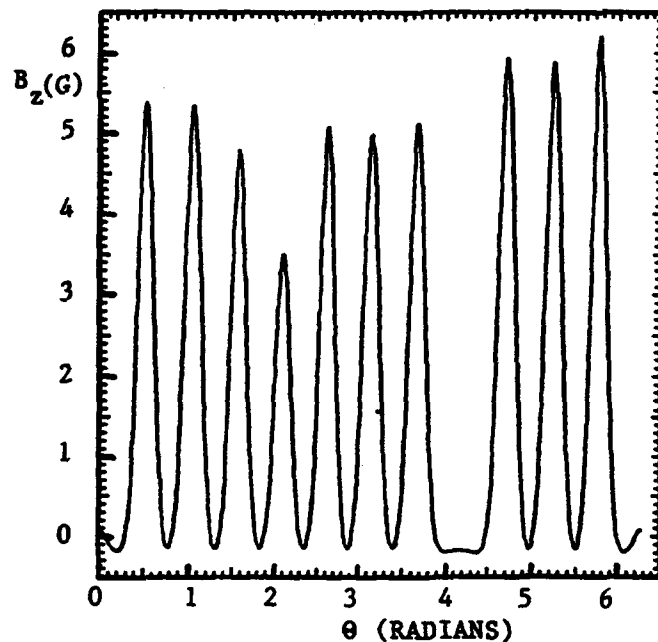


Fig. 5. The portholes of the vacuum chamber produce disturbances in the B_z field. (upper) Plan view of one of the 12 chamber sectors. (lower) The field disturbances vs. toroidal angle. Note the small error near the injector ($\theta = 0$) and a sector with no large port ($\theta = 4.2$ rad).

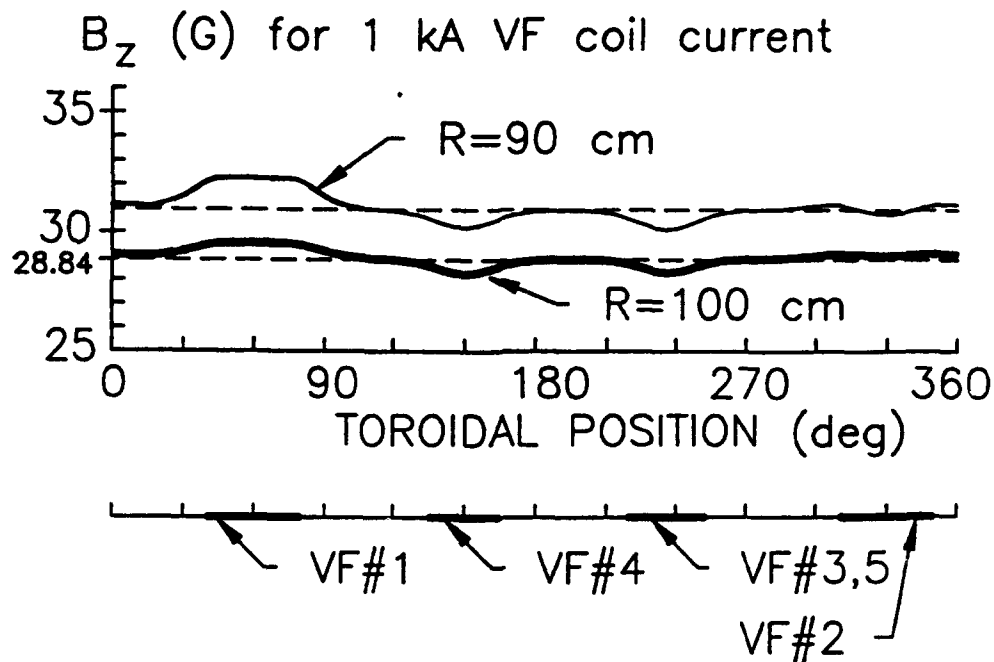


Fig. 6. The field disturbances resulting from the bus connections to the VF coils.

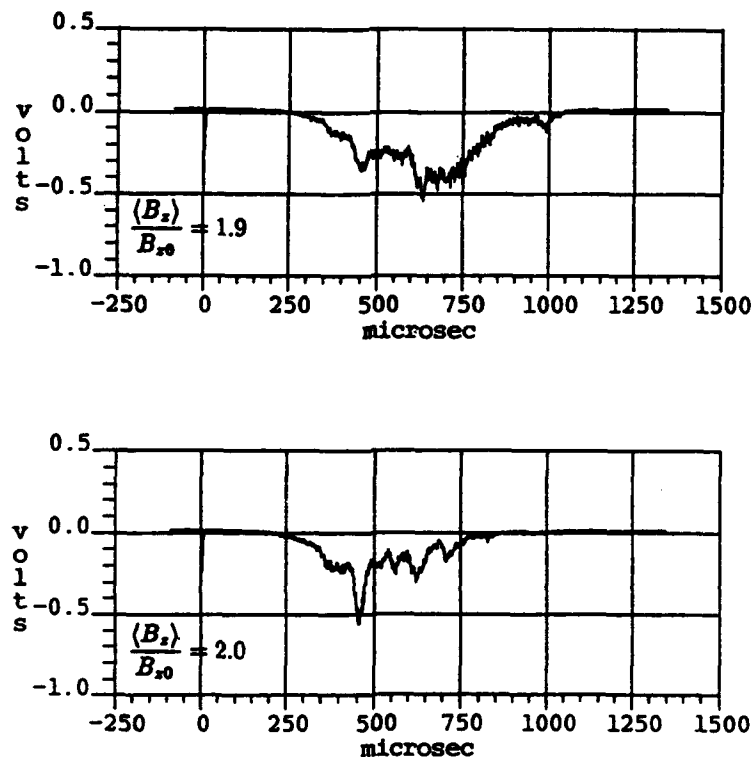


Fig. 7. Comparison of x-ray signals for two different flux conditions.

Appendix DD

Intense Microwave and Particle Beams III

PROCEEDINGS REPRINT



SPIE—The International Society for Optical Engineering

Reprinted from

Intense Microwave and Particle Beams III

20–24 January 1992
Los Angeles, California



Volume 1629

©1992 by the Society of Photo-Optical Instrumentation Engineers
Box 10, Bellingham, Washington 98227 USA. Telephone 206/676-3290.

Excitation of the $\ell = 12$ Cyclotron Resonance in the NRL Modified Betatron Accelerator*

L. K. Len,^{a)} T. Smith,^{a)} P. Loschialpo, J. Mathew, S. J. Marsh,^{b)} D. Dialetis,^{c)}
J. Golden,^{d)} J.H. Chang and C. A. Kapetanakis

Plasma Physics Division, Naval Research Laboratory, Washington, DC 20375-5000

The basic periodicity in the NRL device is twelve-fold. There are twelve toroidal field coils, twelve sectors, and so on. For a long time, the $\ell = 12$ resonance was the dominant resonance in the experiment. To test the importance of the $\ell = 12$ resonance, we have intentionally introduced an $\ell = 12$ field error using twelve resonant coils. By activating these coils when the resonance is observed, the duration of x-rays produced by beam loss was reduced from 900 μ s to 5.5 μ s, while the amplitude of the signal increased from 0.5 to ~ 40 volts. The full width of the x-ray pulse at half maximum is inversely proportional to the current through the resonant coils and proportional to the risetime of the pulse. Work is in progress with a set of twelve internal coils that have a risetime of 300 – 400 ns. The results with these coils have confirmed the importance of the $\ell = 12$ resonance. In addition, it has been shown experimentally that by adding a ΔB_θ such that the ratio of the total toroidal magnetic field to the vertical field is not an integer, the cyclotron resonance is not excited. These experiments have extended the beam lifetime by more than 100 μ s, which is approximately equal to the risetime of the applied ΔB_θ pulse. In the presence of such a pulse, the beam lifetime is 1 ms and the electron beam energy is 22 MeV, while the trapped current is in excess of 1 kA.

I. INTRODUCTION

The lifetime of the electron beam in the NRL modified betatron accelerator has been limited by the excitation of the cyclotron resonances.¹ These resonances occur whenever the condition $(B_{\theta 0}/B_{z 0}) = (2\ell^2 - 1)/2\ell$ is satisfied, with ℓ taking integer values.^{2,3} Here $B_{\theta 0}$ and $B_{z 0}$ are the toroidal and vertical magnetic fields on the minor axis of the chamber. In this paper, we present results from several experiments related to the excitation of electron cyclotron resonances. The first experiment deals specifically with the $\ell = 12$ resonance and the second addresses the spatial distribution of the beam losses. In the third experiment, a time rising ΔB_θ has been added to the main B_θ field. This has effectively resulted in a total $B_{\theta T}$ that maintains the condition of $B_{\theta T}/B_z = \text{constant} \neq \text{integer}$ over the risetime of the ΔB_θ pulse, and thus the beam does not cross any resonance.

II. EXPERIMENTAL APPARATUS

Detailed description of the NRL modified betatron accelerator can be found in previous publications^{1,4-7} where various experimental results, including observation of the electron cyclotron resonances were reported. There are three main external magnetic fields that provide confinement to the high current beam, namely, the toroidal (B_θ), the strong focusing (B_{sf}), and the vertical (B_z) fields. They are generated by pulsed, aircore

electromagnets and have risetimes equal to 2.3 ms, 1.0 ms, and 2.6 ms respectively. The peak value of B_θ is ~ 5 kG and that of B_z is ~ 2 kG. The strong focusing windings can be operated at peak currents as high as ~ 30 kA.

Two sets of resonant coils have been used in the experiments reported in this paper. A set of 12 single-turn coils are installed on the outside of the vacuum chamber (external resonant coils). They are approximately equally spaced around the toroidal chamber. The drivers for these coils can be configured to generate ΔB_θ with risetime of 12 and 5 μ s. To generate a faster resonant pulse, these coils have been replaced with 12 single-turn internal coils that are located accurately at the joints between sectors as shown in Fig. 1. The internal coils are wound on a blue nylon housing and encapsulated with epoxy.

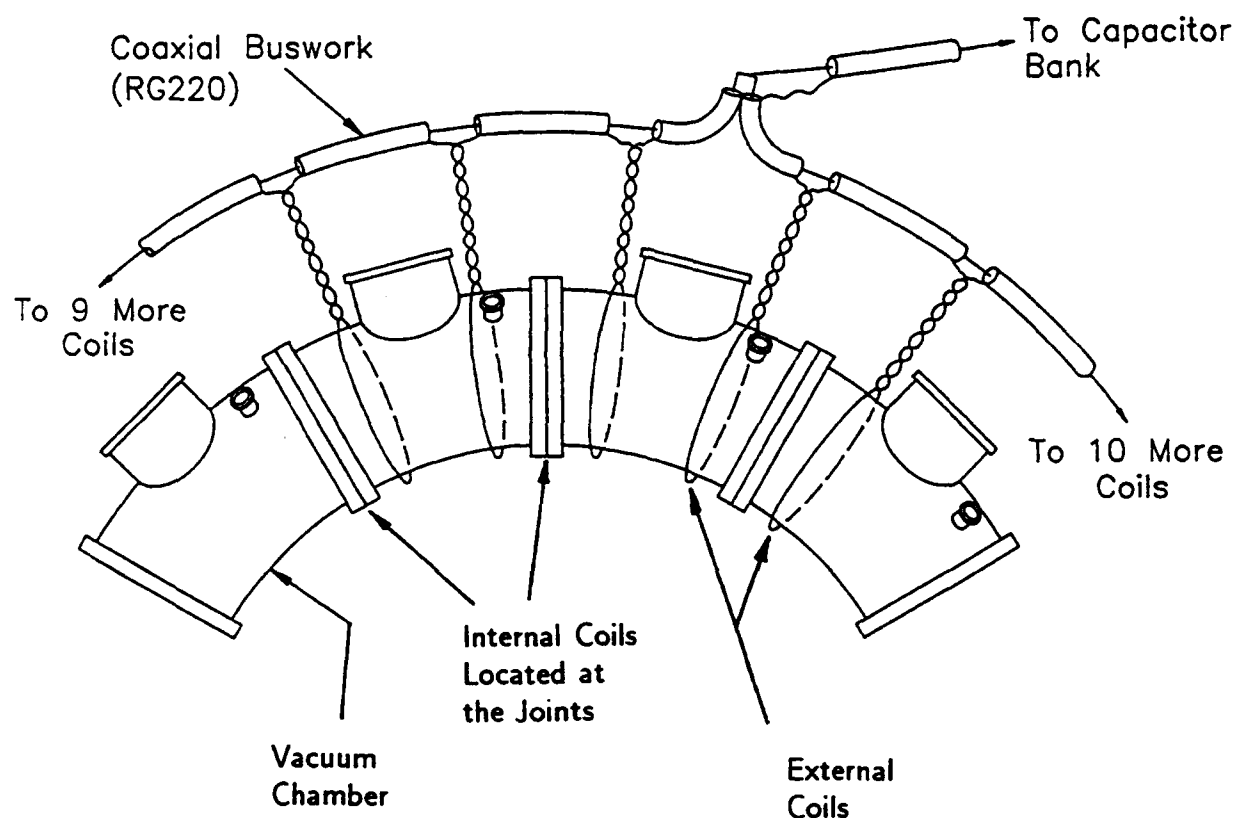


FIG. 1. Schematic view of the resonant coils with respect to the vacuum chamber sectors.

In the experiment with $B_{\theta T}/B_z = \text{constant} \neq \text{integer}$, the number of external coils was increased to 24 in order to produce a smoother ΔB_θ . In addition, the pulsed power driver was modified to increase the quarter period risetime to ~ 100 μ s.

Beam injection is initiated near the peak of the toroidal and strong focusing fields. The injector diode is located inside the vacuum chamber 8.6 cm from the minor axis. When the ratio of B_θ to B_z is nearly 12, the resonant coils are energized to produce the ΔB_θ disturbance. Diagnostics includes the following: Magnetic field probes to measure B_θ and B_z , three NPM-54 x-ray detectors that monitor the x-rays generated when the beam strikes the chamber wall, a Rogowski belt to measure the electron beam current and optical fibers that are located on the outside of the vacuum chamber. The light emitted when the energetic electrons strike these fibers is monitored with photomultiplier tubes. This technique has allowed us to determine accurately the beam dump positions.

III. EXPERIMENTAL RESULTS

In the modified betatron the electron beam performs a complicated motion following injection. To avoid hitting the diode or/and the wall as the beam spirals onto the minor axis during the trapping process, it is necessary to select the operating parameters carefully to maximize the beam trapping efficiency. The signals from the x-ray detectors looking at the diode and the lead shielding around the Rogowski belt are used in conjunction with the beam current monitor as a guide to arrive at the optimum field settings. The beam lifetime is inferred from the x-ray signal such as that shown in Fig. 2. The main peak at 800 μs corresponds to an energy of 20 MeV while the last peak at 1300 μs is 28 MeV.

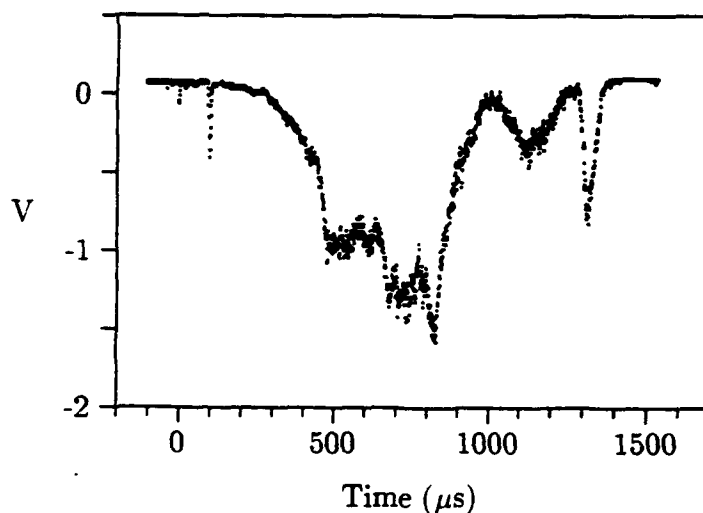


FIG. 2. Typical x-ray signal

For a long time, the $\ell = 12$ resonance has been the dominant cause of beam loss. Even after a careful realignment of the field coils, vacuum chamber, the injector, the supporting deck structures and reductions of other possible field errors, the $\ell = 12$ resonance remains significant. It is the first major resonance encountered as can be seen in Fig. 2.

The $\ell = 12$ resonance is of special interest because the NRL device has a twelve-fold periodicity. There are twelve sectors in the vacuum chamber and twelve toroidal field coils.

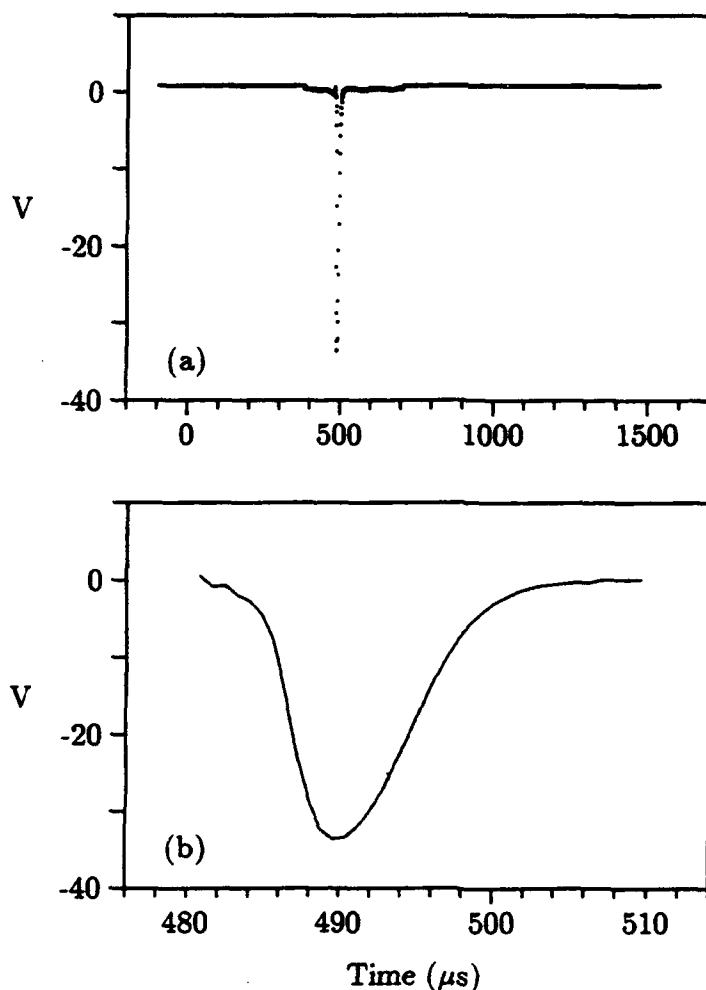


FIG. 3. X-ray signal when the resonant coils are activated at $\ell=12$. (a) Full trace; (b) Expanded trace.

To enhance this resonance, we have installed twelve resonant coils to generate a periodic field perturbation.

Initially, a set of twelve resonant coils was installed on the outside of the chamber (external coils). These coils are initiated at $\tau = 430 \mu\text{s}$, i.e., when the $\ell = 12$ condition is reached. A ΔB_θ pulse with a quarter period risetime of $12 \mu\text{s}$ and amplitude of 200 G is generated on the minor axis when the current in the coils is 9 kA. As it is apparent from Figs. 2 and 3(a), the width of the x-ray signal (a measure of rate of beam loss) is reduced from approximately $900 \mu\text{s}$ to $8 \mu\text{s}$, i.e., by more than two orders of magnitude while its amplitude has increased by a factor of twenty. The width of the x-ray signal varies inversely to the current in the resonant coils as shown in Fig. 4. The loss rate is also dependent on the risetime of the resonant coil pulse.

By connecting the coils in parallel instead of in series, the risetime was reduced to $5 \mu\text{s}$, and even shorter risetime pulses have been produced with a set of internal coils. The internal coils are powered by new drivers with a risetime of 400 ns. Being faster and nearer

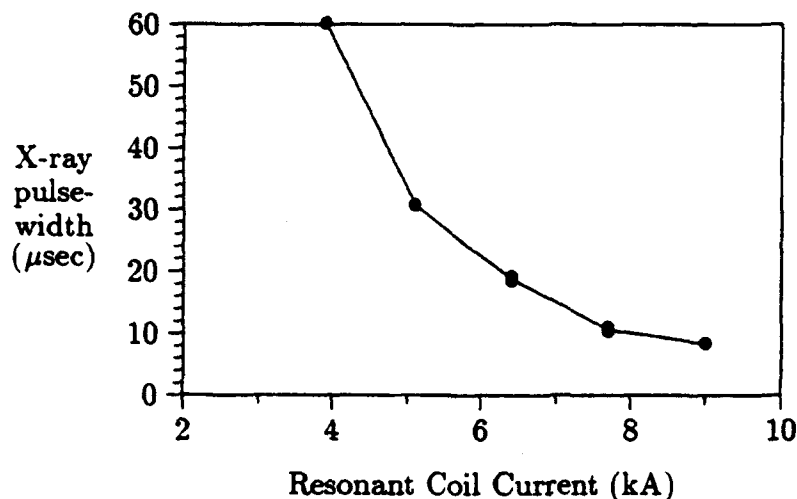


FIG. 4. Full width of the x-ray pulse at half-maximum versus the current in the resonant coils. The peak ΔB_θ generated in the chamber corresponds to 28 G/kA.

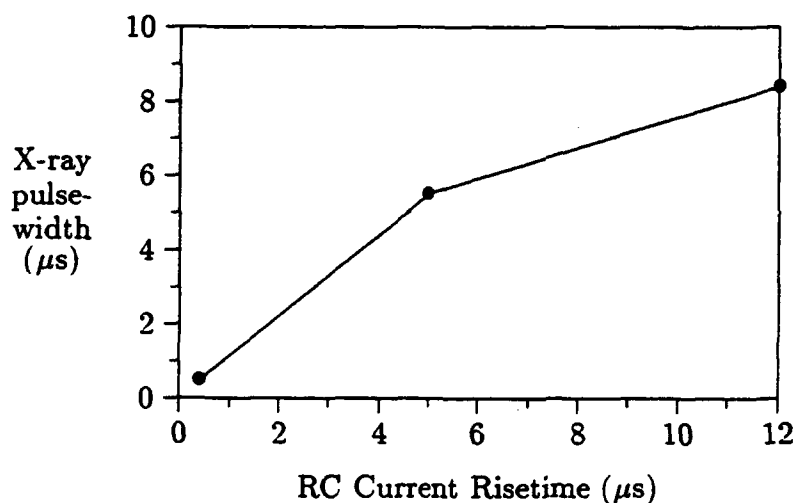


FIG. 5. Full width of the x-ray pulse at half maximum versus the current risetime of the resonant coils.

to the sector flanges, the internal coils require substantially higher voltage and current to produce the required field perturbations. The results from this experiment are shown in Fig. 5.

To determine the spatial distribution of beam losses when the resonant coils are energized, several 400- μm -diameter optical fibers were mounted on the outside of the vacuum chamber. By the time the $\ell = 12$ resonance is crossed, the electrons have acquired sufficient energy to penetrate the chamber. The light generated when the electrons strike the fiber is monitored with a photomultiplier tube. The results from scanning around the torus at 10° intervals are shown in Fig. 6. Only six peaks instead of the expected twelve are observed. This is most likely due to the beating between the $\ell = 12$ and $\ell = 6$ mode that is excited by the six field periods of the stellarator windings. Computer simulation

shows that the strong focusing modulates the $\ell = 12$ peaks in such a way that only every other strikes the wall as shown in Fig. 7. It is still not clear at this time why three of the peaks are higher than the rest. Experiments are in progress to clarify this issue.

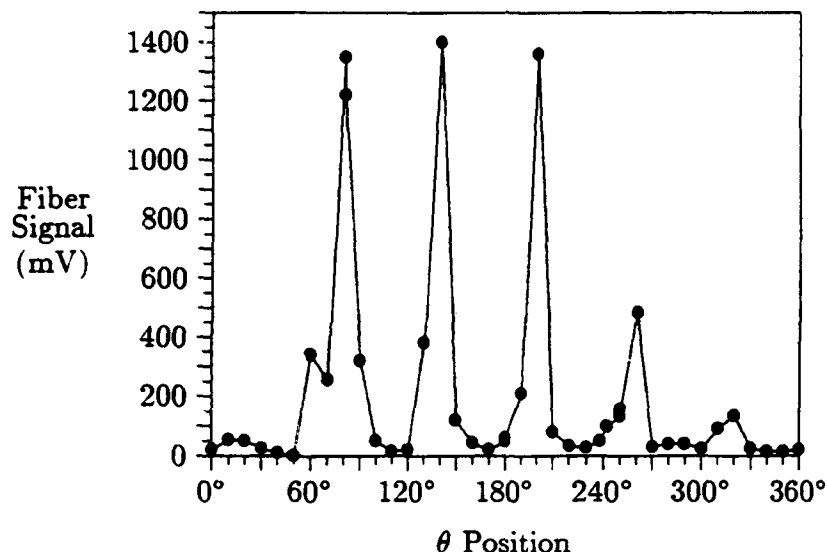


FIG. 6. Distribution of beam loss on the inner wall around the torus.

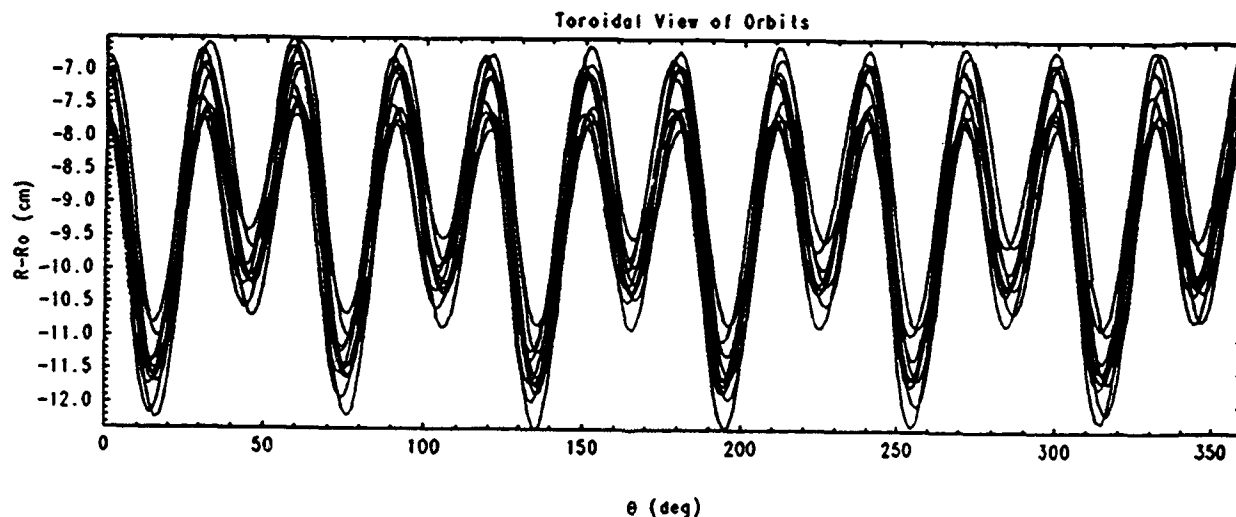


FIG. 7. Results from computer simulation. R_0 is the major radius.

Finally, we present the results from an experiment in which a time-rising ΔB_θ is used to extend the beam lifetime. It is well known that when $B_\theta/B_z = 2\ell^2/(2\ell-1) \approx \ell = \text{integer}$ (for the ℓ values relevant to our observation), resonances are excited and beam losses are observed. Therefore, by using an applied ΔB_θ to maintain $B_{\theta T}/B_z = \text{constant} \neq \text{integer}$,

where $B_{\theta T} = B_{\theta} + \Delta B_{\theta}$, crossing of resonances can be avoided. A set of 24 single-turn external coils, powered by a larger capacitor bank generates the ΔB_{θ} ramp. Results from the experiment are shown in Fig. 8 where the ΔB_{θ} was introduced at $\tau = 800 \mu\text{s}$. Beam loss is suppressed for $100 \mu\text{s}$, which is the risetime of the applied B_{θ} .

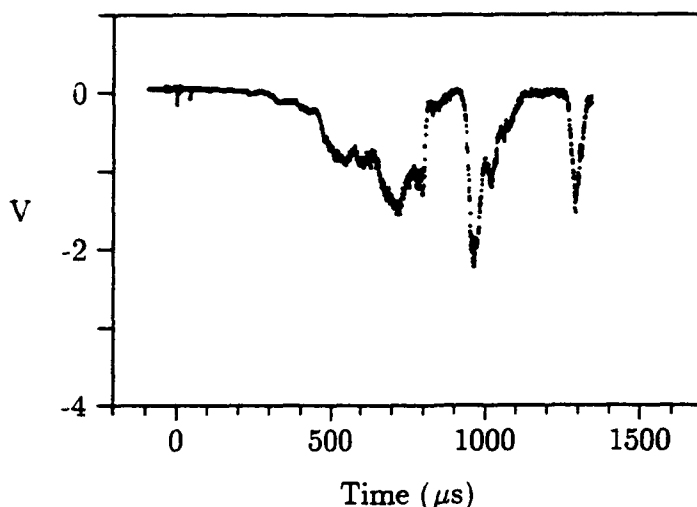


FIG. 8. X-ray signal for the case where a ΔB_{θ} has been added to extend the peak at $830 \mu\text{s}$ to $950 \mu\text{s}$.

IV. REFERENCES

- * This work was supported by ONR and SPAWAR.
- a) Permanent address: FM Technologies, Inc., 10529-B Braddock Road, Fairfax, Virginia 22032.
- b) Permanent address: SFA, Inc., Landover, Maryland 20785.
- c) Permanent address: Science Applications International Corporation, 170 Goodridge Drive, McLean, Virginia 22102.
- d) Permanent address: Berkeley Research Associates, 5532 Hampstead Way, Springfield, Virginia 22151.
- ¹ C. A. Kapetanacos, L. K. Len, T. Smith, J. Golden, K. Smith, S. J. Marsh, D. Dialetis, J. Mathew, P. Loschialpo, and J. H. Chang, *Phys. Rev. Lett.* **64**, 2374 (1990).
- ² D. Chernin and P. Sprangle, *Part. Accel.* **12**, 101 (1982).
- ³ C. W. Roberson, A. Mondelli, and D. Chernin, *Part. Accel.* **17**, 79 (1985).
- ⁴ L. K. Len, T. Smith, J. Golden, K. Smith, S. J. Marsh, D. Dialetis, J. Mathew, P. Loschialpo, J. H. Chang, and C. A. Kapetanacos, *Intense Microwave and Particle Beams, SPIE*, **1226**, 382 (1990).
- ⁵ L. K. Len, T. Smith, J. Golden, S. J. Marsh, D. Dialetis, J. Mathew, P. Loschialpo, J. H. Chang, and C. A. Kapetanacos, *Proceedings of the 2nd European Particle Accelerator Conf.*, **1**, 446 (1990).
- ⁶ J. Golden, L. K. Len, T. J. Smith, D. Dialetis, S. J. Marsh, K. Smith, J. Mathew, P. Loschialpo, L. Seto, J. H. Chang, and C. A. Kapetanacos, *Intense Microwave and*

Particle Beams II, SPIE, 1407, 418 (1991).

- ⁷ C. A. Kapetanacos, D. Dialetis, S. J. Marsh, L. K. Len, and T. Smith, *Phys. Rev. A*, 44 (6), 3900 (1991).

Appendix EE

**Studies of the Integer Cyclotron Resonances
in a Modified Betatron Accelerator**



NRL/MR/4795-92-6988

Studies of the Integer Cyclotron Resonances in a Modified Betatron Accelerator

C. A. KAPETANAKOS AND J. H. CHANG

*Beam Physics Branch
Plasma Physics Division*

L. K. LEN AND T. SMITH

*FM Technologies Inc.
Fairfax, VA 22032*

P. LOSCHIALPO, J. MATHEW, AND J. MARSH

*Sachs-Freeman Associates, Inc.
Landover, MD 20785*

D. DIALETIS

*Science Applications International Corporation
McLean, VA 22102*

AND

J. GOLDEN

*Berkeley Research Associates
Springfield, VA 22151*

July 28, 1992

This work was supported by ONR and SPAWAR.

REPORT DOCUMENTATION PAGE			Form Approved OMB No 0704-0188	
<small>Public reporting burden for this collection of information is estimated to average 1 hour per response, including the time for reviewing instructions, searching existing data sources, gathering and maintaining the data needed, and completing and reviewing the collection of information. Send comments regarding this burden estimate or any other aspect of this collection of information, including suggestions for reducing this burden, to Washington Headquarters Services, Directorate for Information Operations and Reports, 1215 Jefferson Davis Highway, Suite 1204, Arlington, VA 22202-4302, and to the Office of Management and Budget, Paperwork Reduction Project (0704-0188), Washington, DC 20503</small>				
1. AGENCY USE ONLY (Leave blank)	2. REPORT DATE July 28, 1992	3. REPORT TYPE AND DATES COVERED Interim		
4. TITLE AND SUBTITLE Studies of the Integer Cyclotron Resonances in a Modified Betatron Accelerator		5. FUNDING NUMBERS		
6. AUTHOR(S) C.A. Kapetanacos, L.K. Len,* T. Smith,* P. Loschialpo,** J. Mathew,** S.J. Marsh,** D. Dialetis,† J. Golden,‡ and J.H. Chang				
7. PERFORMING ORGANIZATION NAME(S) AND ADDRESS(ES) Naval Research Laboratory Washington, DC 20375-5320		8. PERFORMING ORGANIZATION REPORT NUMBER NRL/MR/4795-92-6988		
9. SPONSORING/MONITORING AGENCY NAME(S) AND ADDRESS(ES) Office of Naval Research SPAWAR Arlington, VA 22217-5000 Washington, DC 20362-5100		10. SPONSORING/MONITORING AGENCY REPORT NUMBER		
11. SUPPLEMENTARY NOTES This work was supported by ONR and SPAWAR. *FM Technologies, Inc., Fairfax, VA 22032, **SFA, Inc., Landover, MD 20785, †SAIC, McLean, VA 22102, and ‡Berkeley Research Associates, Springfield, VA 22151				
12a. DISTRIBUTION/AVAILABILITY STATEMENT Approved for public release; distribution unlimited.		12b. DISTRIBUTION CODE		
13. ABSTRACT (Maximum 200 words) This paper briefly summarizes recent experimental results from the studies of the integer cyclotron resonances in the NRL modified betatron accelerator. Special emphasis is given to the $\ell=12$ resonance, because the NRL device has a twelve-fold symmetry. To test the importance of the $\ell=12$ resonance, we have intentionally introduced an $\ell=12$ field error using twelve resonant coils. By activating these coils when the resonance is observed, the duration of x-rays produced by beam loss was reduced from 900 μ s to 5.5 μ s, while the amplitude of the signal increased from 0.5 to ~40 volts. The full width of the x-ray pulse at half maximum is inversely proportional to the current through the resonant coils and proportional to the risetime of the pulse. Work is in progress with a set of twelve internal coils that have a risetime of 300-400 ns. Studies of the spatial distribution of beam losses at $\ell=12$ show that the beam is always lost in six well defined toroidal positions. In addition, it has been shown experimentally that when the ratio of the total toroidal magnetic field to the vertical field is not an integer, the cyclotron resonance is not excited.				
14. SUBJECT TERMS Integer cyclotron resonances Modified betatron accelerator		15. NUMBER OF PAGES 13		
		16. PRICE CODE		
17. SECURITY CLASSIFICATION OF REPORT UNCLASSIFIED	18. SECURITY CLASSIFICATION OF THIS PAGE UNCLASSIFIED	19. SECURITY CLASSIFICATION OF ABSTRACT UNCLASSIFIED	20. LIMITATION OF ABSTRACT UL	

Studies of the integer cyclotron resonances in a modified betatron accelerator*

I. INTRODUCTION

The cyclotron resonance is due to the coupling, caused by a field error(s), of the cyclotron motions associated with the toroidal and vertical fields. The field error(s) that excites the resonance can be either vertical ΔB_z or axial (toroidal) ΔB_θ . In the case of a vertical field error and in the absence of acceleration and strong focusing field, the normalized transverse velocity β_\perp and thus the Larmor radius of the transverse motion of the gyrating particles grows linearly with time¹, provided that nonlinear effects associated with the particle velocity are neglected. When such effects are taken into account, β_\perp exhibits cycloidal behavior.²

In the presence of an accelerating field and a large vertical field error, β_\perp increases proportionally to the square root of time, while $\gamma\beta_\theta$ saturates, i.e., the electrons lock-in to a specific resonance (lock-in state). When the amplitude of ΔB_z is below a threshold, β_\perp exhibits Fresnel behavior, i.e., β_\perp grows quickly for approximately 1 μsec and then saturates until the beam reaches the next resonance.²

In the case of an axial field error and in the absence of acceleration, β_\perp grows exponentially with time only for a very short period. Since β_\perp increases at the expense of β_θ , the particles are kicked off resonance. Thus, β_\perp varies cycloidally with time. Similarly, in the presence of an accelerating field β_\perp behaves as in the case of the vertical field error.

The previous discussion is based on the assumption that the strong focusing field is zero. In addition to introducing new characteristic modes, the strong focusing field makes the expression for the regular cyclotron mode more complicated.³ However, it can be shown that for the parameters of the NRL device and provided $\ell \gg 1$, the strong focusing has only minor effect on the cyclotron resonance. This is also supported by extensive computer calculations.

In this paper, we present results from several experiments related to the excitation of cyclotron resonances, for both vertical and toroidal field errors. The last Section addresses possible remedies for the suppression of the cyclotron resonances in the modified betatron accelerator.

II. EXPERIMENTAL APPARATUS

Detailed description of the NRL modified betatron accelerator can be found in previous publications⁴⁻⁶, where various experimental results, including observation of the electron cyclotron resonances were reported. There are three main external magnetic fields that provide confinement to the high current beam, namely, the toroidal (B_θ), the strong focusing (B_{sf}), and the vertical (B_z) fields. They are generated by pulsed, aircore electromagnets with risetimes equal to 2.3 ms, 1.0 ms, and 2.6 ms respectively. The peak value of B_θ is ~ 5 kG and that of B_z is ~ 2 kG. The strong focusing windings can be operated at peak currents as high as ~ 30 kA. A photograph of the experiment is shown in Fig. 1.

III. EXPERIMENTAL RESULTS

In a modified betatron with strong focusing windings there are four characteristic transverse modes³ $\omega_{\pm\pm}$. Integer resonances occur when the frequency of these modes, in the laboratory frame, over the relativistic cyclotron frequency of the vertical field Ω_{z0}/γ on the minor axis is an integer, i.e., when

$$\frac{\omega_{\pm\pm}}{(\Omega_{z0}/\gamma)} = k, \quad \text{where } k = \pm 1, 2, \dots \quad (1)$$

The four characteristic modes $\omega_{\pm\pm}$ are in general very complex. However, for modest beam and strong focusing currents, as those in the NRL device and when $B_\theta/B_z \gg 1$ the modes are considerably simplified. Under these conditions the mode that is responsible for the cyclotron resonance becomes $\omega_{-+} \approx \Omega_{\theta0}/\gamma$, where $\Omega_{\theta0}$ is the cyclotron frequency that corresponds to the toroidal magnetic field. Under these conditions Eq. (1) takes the very simple form $B_{\theta0}/B_{z0} \approx \ell$, where $\ell = 1, 2, \dots$, and $B_{\theta0}$ and B_{z0} are the toroidal and vertical fields on the minor axis. Therefore, the cyclotron resonance is due to the coupling, caused by a field error(s), of the cyclotron motions associated with the toroidal and vertical fields.

The x-rays are monitored by three collimated x-ray detectors (scintillator-photo-multiplier tube) that are housed inside lead boxes. In the results shown in Fig. 2, the x-rays enter the scintillator through a 1.94 cm-dia. tube and the detector is located 10.8 m from the vacuum chamber. As a rule, the shape of the x-ray signal recorded by all three detectors is spiky and the peaks always occur at the same value of $B_{\theta 0}/B_{x 0}$, independently of the current flowing in the stellarator windings.

In addition to the x-ray pulse, Fig. 2 shows the ratio of $B_{\theta 0}/B_{x 0}$ at the peaks of the signal. The solid circles are from the experiment and the crosses are from the resonance condition $B_{\theta 0}/B_{x 0} = (2\ell^2 - 1)/2\ell$, $\ell = 1, 2, \dots$ of the cyclotron resonance. For $\ell = 8, 9$ and 10, experiment and theory are in good agreement. However, for the remaining ℓ values there is noticeable divergence between the theoretical predictions and the experiment.

The theory of the cyclotron resonance has been developed under the assumption that the beam is located on the minor axis. However, the experimental observations indicate that the electron ring starts to move off axis after 200-300 μsec . Recently, the theory of the cyclotron resonance has been extended to a beam that is located on the midplane but off the minor axis. For such a beam the resonance conditions becomes

$$\frac{r_0 \Omega_{\theta 0}}{c \gamma \beta_{\theta}} = \frac{2\ell^2 - 1}{2\ell}, \quad (2)$$

where r_0 is the major radius, and β_{θ} is the normalized toroidal velocity. The agreement between the experimental results and the theory is improved when the radial motion of the beam is taken into account.

It is apparent from the resonant condition that when $B_{\theta 0}/B_{x 0} = \text{constant} \neq \text{integer}$, the cyclotron resonance is not excited. To test this supposition, we have installed 24 single-turn coils on the outside of the vacuum chamber, as shown in Fig. 3. These coils are powered by a capacitor bank and have a risetime of approximately 100 μsec . During this time period the coils generate a toroidal field ramp that increases linearly with time and the total toroidal field increases in synchronism with the betatron field. Results from the experiment are shown in Fig. 4, when the coils are energized at 800 μsec . Beam losses are suppressed for 100 μsec , i.e., as long as the condition $B_{\theta 0}/B_{x 0} \neq \text{integer}$ is satisfied.

The damage done to the beam at each resonance depends on the speed with which the resonance is crossed. By modulating the toroidal field with a rapidly varying ripple the resonance is crossed quickly and thus the damage inflicted to the beam is reduced. This

is the dynamic stabilization or tune jumping technique and requires a carefully tailored pulse to be effective over many resonances.

Results from the numerical integration of orbit equations are shown in Fig. 5. The left column shows the transverse velocity β_{\perp} , axial velocity β_{θ} and the product $\gamma\beta_{\theta}$ as a function of time when the coils that produce the ripple are not energized. As the beam crosses the $\ell=10$ resonance, its transverse velocity increases by a few percent while at $\ell=9$, β_{\perp} reaches 18%. At the same time β_{θ} decreases. Even more importantly, the product $\gamma\beta_{\theta}$ saturates at $\ell=10$, i.e., all the energy from the accelerating fields goes to β_{\perp} instead of β_{θ} . This interesting phenomenon is due to nonlinear effects and will be called "lock-in" state. The corresponding results with the stabilizing coils on are shown in the right column of Fig. 5. At both $\ell=10$ and $\ell=9$ the transverse velocity of the beam increases modestly but $\gamma\beta_{\theta}$ does not saturate.

Results from the experiment are shown in Fig. 6. The toroidal field modulation is produced by the 24 coils that are mounted on the exterior surface of the vacuum chamber, two coils on each sector. The period of the under damped LRC circuit is 70 μsec . The decay of the current waveform is mainly due to the resistance of the vacuum chamber that plays the role of the secondary.

Figure 6a shows the x-ray waveform in the absence of modulation. The corresponding x-ray waveform when the coils are energized at 430 μsec and the first peak of the modulation is positive is shown in Fig. 6b. It is apparent that the x-ray signal is modulated with the period of the ΔB_{θ} field and the two modulations are in phase. An interesting feature of these results is the drastic reduction of the x-ray signal following the initiation of the ΔB_{θ} ripple. Typically, the x-ray signal goes to zero, temporarily, when the amplitude of ΔB_{θ} exceeds a threshold. When the polarity of the ΔB_{θ} field is reversed, the x-ray waveform exhibits similar characteristics as in the case of positive first peak and is shown in Fig. 6c. However, in contrast with the previous case, the beam losses are accelerated immediately after the initiation of the ΔB_{θ} ripple.

The experimental results appear to be in agreement with the theoretical predictions and the computer calculations shown in Fig. 5. When the beam is in the lock-in state and the amplitude of the modulation is not large enough, $\gamma\beta_{\theta}$ remains locked and tracks the modulation, as required by the resonance condition of Eq. (1). For positive first peak, $\gamma\beta_{\theta}$ increases and thus β_{\perp} is reduced. The smaller Larmor radius results in reduced

particle losses. For negative first peak, $\gamma\beta_\theta$ is reduced and thus β_θ increases. The larger Larmor radius drives the electrons to the wall and the x-ray signal increases. It should be emphasized, however, that the above interpretation of the experimental results is not unique. There is at least one more model that is consistent with the results.

The basic periodicity in the NRL device is twelve-fold. There are twelve toroidal field coils, twelve sectors, and so on. For a long time, the $\ell=12$ resonance was the dominant resonance in the experiment. To test the importance of the $\ell=12$ resonance, we have intentionally introduced an $\ell=12$ axial field error using twelve resonant coils.

Initially, the set of twelve resonant coils was installed on the outside of the chamber (external coils). These coils are initiated at $t=430 \mu\text{s}$, i.e., when the $\ell=12$ condition is reached. A ΔB_θ pulse with a quarter period risetime of $12 \mu\text{sec}$ and amplitude of 200 G is generated on the minor axis when the current in the coils is 9 kA . Figure 7a shows the x-ray pulse when the resonant coils are off and Fig. 7b when the coils are on. It is apparent from these results that the width of the x-ray signal is reduced from approximately $900 \mu\text{sec}$ to $8 \mu\text{sec}$, i.e., by more than two orders of magnitude while its amplitude has increased by a factor of thirty. The width of the x-ray signal varies inversely with the current in the resonant coils as shown in Fig. 8 and also depends on the risetime of the resonant coil pulse.

By connecting the coils in parallel instead of in series, the risetime was reduced to $5 \mu\text{sec}$, and even shorter risetime pulses have been produced with a set of internal coils. The internal coils are wound on a blue nylon housing and encapsulated with epoxy (Fig. 9) and are powered by new drivers with a risetime of 400 ns . Being faster and nearer to the sector flanges, the internal coils require substantially higher voltage and current to produce the required field perturbations. The dependence of the x-ray pulse width on the risetime of the current pulse is shown in Fig. 10.

To determine the spatial distribution of beam losses when the resonant coils are energized, several $400\text{-}\mu\text{m}$ -diameter optical fibers were mounted on the outside of the vacuum chamber. By the time the $\ell=12$ resonance is crossed, the electrons have acquired sufficient energy to penetrate the chamber. The light generated when the electrons strike the fiber is monitored with a photomultiplier tube. The results from scanning around the torus at 10° intervals are shown in Fig. 11. Only six peaks instead of the expected twelve are observed. This is most likely due to the beating between the $\ell=12$ and $\ell=6$ mode that

is excited by the six field periods of the stellarator windings. Computer simulation shows that the strong focusing modulates the $\ell=12$ peaks in such a way that only every other peak strikes the wall as shown in Fig. 12. It is still not clear at this time why three of the peaks are higher than the rest.

Under normal operating conditions the current that produces the strong focusing field is passively crowbarred and the fields decay with a long time constant L/R , where L is mainly the inductance of a ballast inductor that is in series with the windings. To test the effect of the strong focusing field on the distribution of beam loss, the ballast inductor was removed and the circuits were actively crowbarred. The shape of the pulse is a half sine with a half period of $\sim 650 \mu\text{sec}$. The beam is injected near the peak of the pulse. Thus, the strong focusing field is practically zero when the resonant coils are energized. Under these conditions most of the beam is lost at a single toroidal position near $\theta = 90^\circ$. These experiments are currently in progress.

IV. REMEDY

Although the effective accelerating gradient in the present device is large, its actual accelerating gradient is low ($\sim 150\text{V}/m$). As a result the electrons have to perform a large number of revolutions around the major axis in order to obtain the desired peak energy of 20 MeV. Thus, the existing modified betatron is sensitive to field errors. Possible remedies for the problem of the cyclotron resonances are listed in Table I. Computer calculations show that at the contemplated acceleration rate of $300 \text{ G}/\mu\text{sec}$ for the advanced devices the cyclotron resonance is not excited, provided that the various fields have been designed with an accuracy better than 0.1%.

Table I

Possible remedies for the cyclotron resonance

<u>Remedy</u>	<u>Comments</u>
• Design the device carefully to avoid field errors	Increase cost.
• Carry out accurate mapping of fields ($\sim 0.1\%$). Use trim coils to eliminate field errors.	Tedious and time consuming. Standard technique in accelerators.
• Keep ratio $B_\theta/B_z = \text{const.} \neq \text{integer}$ during acceleration.	Powerful approach. Requires high B_θ .
• When dB_z/dt is large the cyclotron resonance is not excited.	In contemplated advanced devices $dB_z/dt \approx 300 \text{ G}/\mu\text{sec}$. Thus, the cyclotron resonance will not be excited.
• Modulate B_θ field to cross resonances quickly and thus to reduce damage. (Dynamic Stabilization or tune jumping).	Requires carefully tailored pulse to be effective over many resonances.

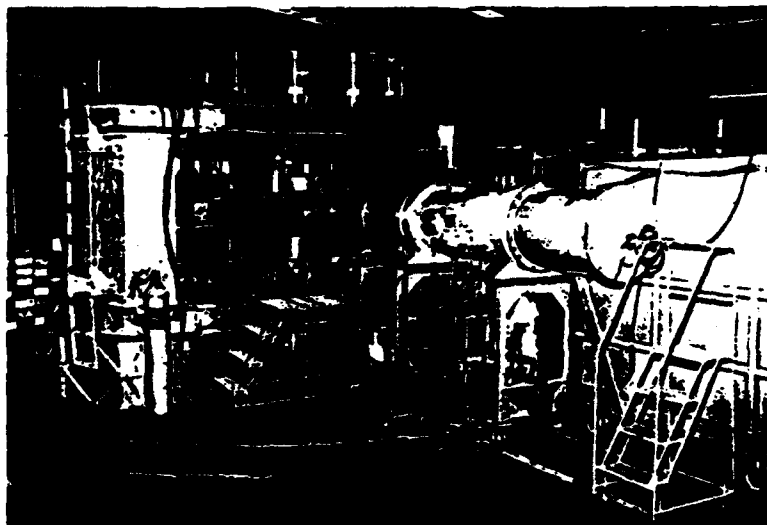


Fig. 1. Photograph of the NRL modified betatron accelerator.

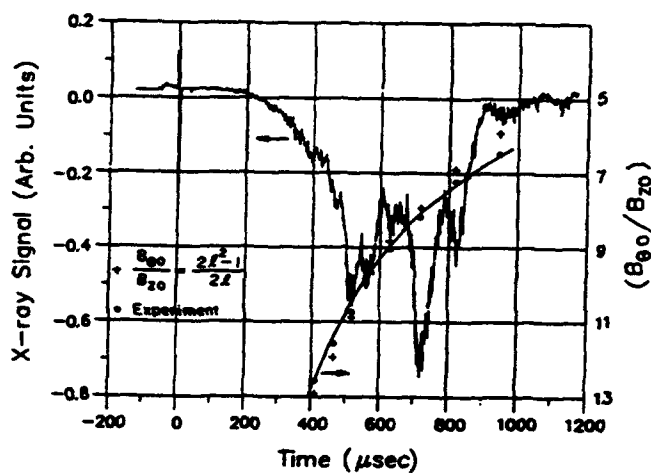


Fig. 2. X-ray pulse and ratio of $B_{\theta 0}/B_{z0}$ at the peaks of the x-ray signal.

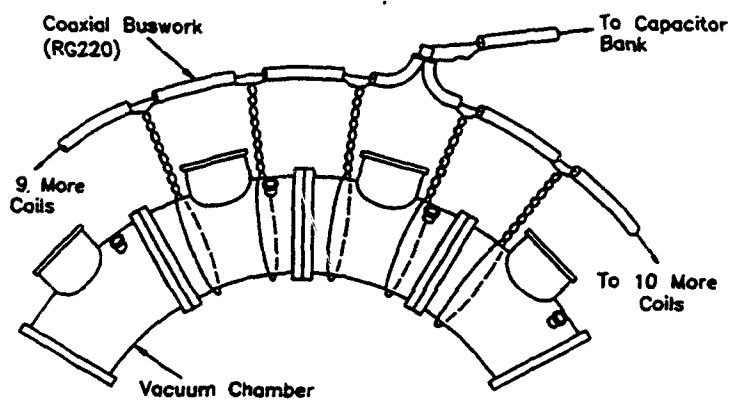


Fig. 3. External resonant coils.

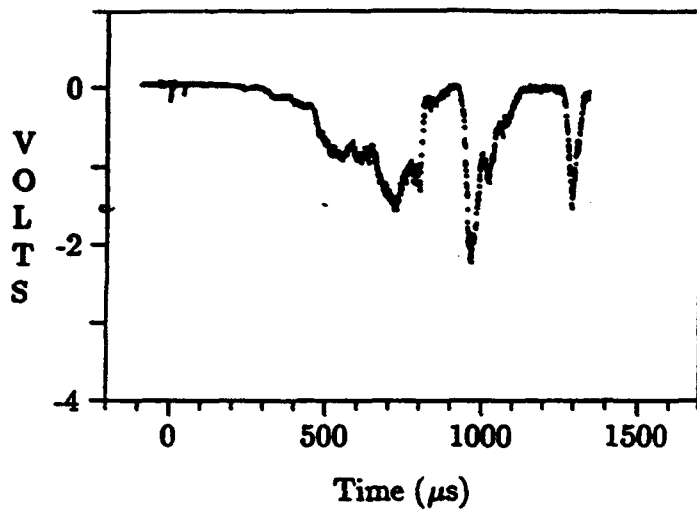


Fig. 4. X-ray signal. Between 800-900 μs
 $B_{\theta 0}/B_{x0} = \text{constant} \neq \text{integer}$

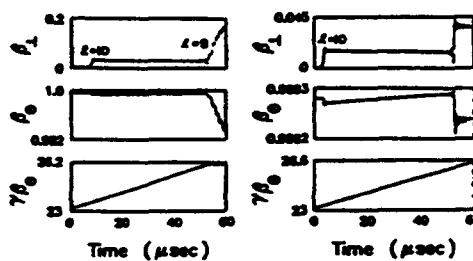


Fig. 5. Results from the
 numerical integration
 of orbit equations

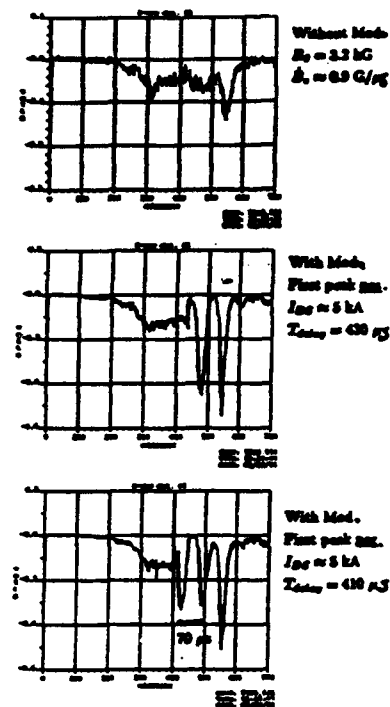


Fig. 6. X-ray signals
 vs. time at reduced
 toroidal field.

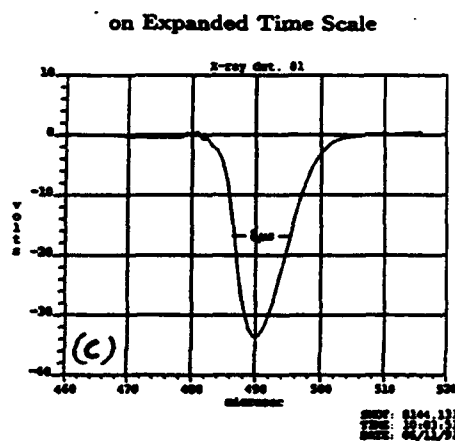
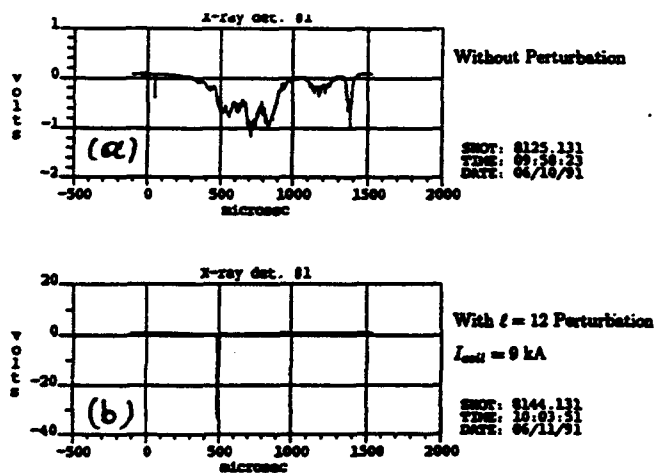


Fig. 7. X-ray signal with the resonant coils off (a)
 and when the coils are activated: (b) full trace; (c) expanded.

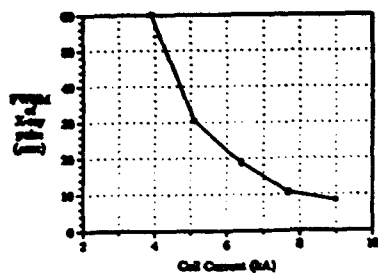


Fig. 8. Width (at halfmax.) of the x-ray pulse vs. resonant coil current at $\ell=12$. Peak $\Delta B_\theta = 28G/kA$

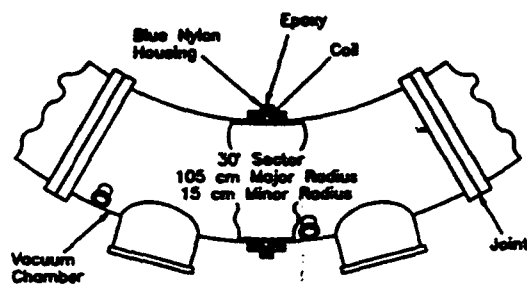


Fig. 9. Internal coils

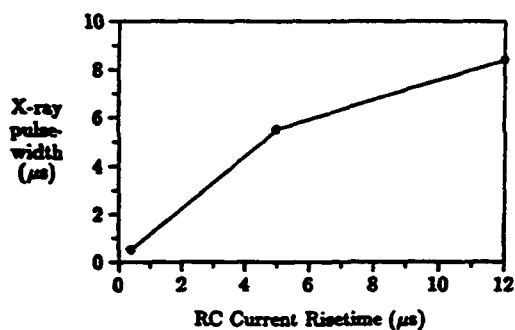


Fig. 10. Width (at half max.) of the x-ray pulse vs. current risetime.

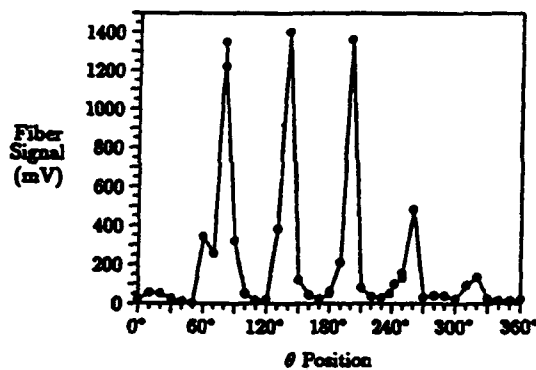


Fig. 11. Distribution of beam losses.

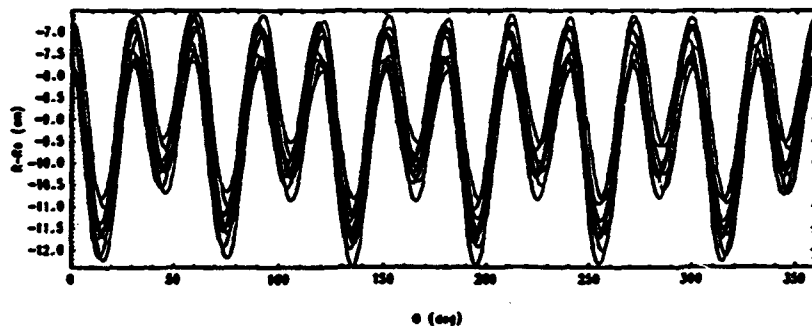


Fig. 12. Computer results that show the radial displacement of the beam from the minor axis vs. toroidal angle.

Appendix FF

**Reduction of $3\omega_0/2$ Emission from Laser-Produced
Plasmas with Broad Bandwidth,
Induced Spatial Incoherence at $0.53\text{ }\mu\text{m}$**

Reduction of $3\omega_0/2$ emission from laser-produced plasmas with broad bandwidth, induced spatial incoherence at $0.53\ \mu\text{m}$

T. A. Peyser^{a)}

Science Applications International, Corp., McLean, Virginia 22102

C. K. Manka,^{b)} S. P. Obenshain, and K. J. Kearney

Laser Plasma Branch, Plasma Physics Division, Naval Research Laboratory, Washington, DC 20375-5000

(Received 12 October 1990; accepted 5 February 1991)

Measurements of the $3\omega_0/2$ emission from laser-irradiated targets at $0.53\ \mu\text{m}$ were made at three angles over a wide range of laser bandwidths with and without induced spatial incoherence (ISI) echelons. The $3\omega_0/2$ emission was found to be correlated with hard x rays but not Raman spectra, suggesting that the $3\omega_0/2$ radiation was due to two-plasmon decay. Reduction of both $3\omega_0/2$ emission and the accompanying hard x rays by ISI required five to ten times larger bandwidths than needed to suppress stimulated Raman scattering and stimulated Brillouin scattering.

I. INTRODUCTION

Induced spatial incoherence (ISI) was first proposed as a beam smoothing technique to provide the highly uniform illumination required for direct-drive laser fusion.^{1,2} ISI has been found, however, not only to provide uniform illumination but also to suppress a number of deleterious plasma instabilities associated with the reflection and absorption of the incident laser energy such as stimulated Raman scattering (SRS) and stimulated Brillouin scattering (SBS).³⁻⁵ In this paper, we present the first detailed experimental study of the effect of ISI on the two-plasmon decay instability as inferred from three-halves harmonic ($3\omega_0/2$) emission correlated with x-ray measurements.

The importance of beam smoothing for direct-drive laser fusion has been widely recognized especially with respect to minimizing initial perturbations that can lead to hydrodynamic instabilities and reducing filamentation that may enhance parametric instabilities. There are now a number of other optical beam-smoothing techniques in addition to ISI—random phase plates (RPP),⁶ lens arrays,⁷ smoothing by spectral dispersion (SSD),⁸ and echelon-free ISI.^{9,10} All of the extant beam-smoothing techniques achieve much improved illumination uniformity over generic unsmoothed laser beams. There are differences, however, between the various techniques in the extent and nature of the laser bandwidth. The degree of laser bandwidth required to achieve substantial decreases in potentially catastrophic laser-plasma instabilities may be an important criterion determining the use of one or the other of the above-mentioned beam-smoothing techniques. The RPP approach to beam smoothing does not utilize broad laser bandwidth. The lens array technique does not rely on broad laser bandwidth, but it does not preclude its use. ISI, SSD, and echelon-free ISI, on the other hand, all rely heavily on broadened laser band-

width. They differ in the mechanism by which the bandwidth is generated and possibly in the technological feasibility of achieving a given degree of bandwidth.

Recent experiments on the backscattered fractions of stimulated Raman and Brillouin scattering have attributed a measured 25-fold reduction in instability levels with ISI as compared with RPP to corresponding decreases in the filamentation instability.¹¹ In the experiments described herein, ISI was observed to reduce the $3\omega_0/2$ and hard x rays associated with the two-plasmon instability. However, the details of the effects of ISI on the two-plasmon decay instability were very different from that observed with SBS and SRS. At the largest bandwidth used here ($\Delta\lambda = 10\ \text{\AA}$ at $0.53\ \mu\text{m}$ or $\Delta\omega/2\pi = 1.2 \times 10^{13}\ \text{sec}^{-1}$), SBS and SRS were completely suppressed by ISI under our experimental conditions and greatly reduced at an intermediate bandwidth ($\Delta\lambda = 1\ \text{\AA}$)—a factor of 10 times smaller. In contrast, the $3\omega_0/2$ emission was observed to be reduced, but not completely suppressed, only by using ISI with the broadest bandwidths. These results suggest that the mechanism by which ISI affects the two-plasmon decay instability may be different than that for SBS and SRS.

In the two-plasmon decay instability, an incident laser photon at frequency ω_0 undergoes a parametric decay at the quarter-critical density surface into two electron plasma waves or plasmons each at a frequency approximately equal to $\omega_0/2$. Three-halves harmonic emission occurs when an $\omega_0/2$ plasmon interacts with an ω_0 photon in the vicinity of the quarter-critical surface giving a photon at the $3\omega_0/2$ frequency. Three-halves harmonic emission from laser-irradiated targets has been extensively studied both theoretically¹²⁻¹⁶ and experimentally.¹⁷⁻²⁸ The importance of the two-plasmon decay to inertial fusion lies in the fact that electrons, accelerated to high energies by electron plasma waves, can preheat the target thus preventing efficient pellet compression.

The threshold for two-plasmon decay instability in a spatially inhomogeneous plasma is given by $(v_e/v_e)^2 k_0 L > \alpha$, where v_e is the electron oscillatory veloc-

^{a)} Present address: Charged Particle Physics Branch, Naval Research Laboratory, Washington, DC 20375-5000.

^{b)} Present address: Space Plasma Branch, Naval Research Laboratory, Washington, DC 20375-5000.

ity, v_e is the electron thermal velocity, k_0 is the wave number of the pump, L is the density scale length, and $\alpha = 2$ to $\alpha = 4$ depending on the value of a parameter $\beta = v_e^2/v_{te}^2$.^{12,14,15} Hydrodynamic simulations of the effect of the laser-target interactions under our conditions give typical density scale lengths for 0.53 μm irradiation of approximately 150 μm at quarter-critical density and temperatures of 900 eV.^{29,30} These parameters give $\alpha \approx 3$ and an intensity threshold for absolute two-plasmon decay in the green of $1.3 \times 10^{13} \text{ W/cm}^2$. The collisional threshold for the two-plasmon instability is given by the condition that the growth rate $\gamma_0 \approx k_0 v_0/4$ exceed $\nu_{ei}/2$ where ν_{ei} is the electron-ion collision frequency. Assuming an electron density at the quarter-critical density surface of $1.5 \times 10^{21} \text{ cm}^{-3}$, an electron temperature of 900 eV and a $Z_{\text{eff}} \approx 5$, the intensity threshold for the collisional two-plasmon instability is $1.3 \times 10^{13} \text{ W/cm}^2$ —essentially the same as the threshold calculated above for a spatially inhomogeneous plasma. The present experiment was carried out at time-integrated average intensities between 2.5×10^{13} and $2.5 \times 10^{14} \text{ W/cm}^2$, above both the estimated collisional and spatially inhomogeneous two-plasmon decay thresholds.

II. EXPERIMENTAL SETUP

The experiment was performed with two beams of the Pharos III Nd-glass laser with $f/11$ focusing lenses. Both beams were frequency converted to the green at 527 nm.³¹ The laser pulse duration was 2 nsec (FWHM) and the energy was varied from 10 to 250 J on target. One beam contained ISI echelons, the other did not. The ISI beam smoothing used in the present experiment utilized a set of orthogonal transmissive and reflective echelons for spatial incoherence and broad laser bandwidth for temporal incoherence.^{1,2} The echelons break the 20 cm diameter laser beam into approximately 300 $1 \times 0.8 \text{ cm}$ beamlets. Optical delays on the order of 2 psec were introduced into each adjacent beamlet by incrementing the optical path length in each step of the echelon. If the laser bandwidth $\Delta\omega$ is sufficiently large that the laser coherence time $\tau_c = 2\pi/\Delta\omega$ is shorter than the optical delays introduced by the ISI echelons, then the resulting focal distribution on target will be smooth on time scales long compared to the laser coherence time.

Measurements of $3\omega_0/2$ radiation from the target were taken with the ISI echelons in place at four distinct laser bandwidths covering a range of three orders of magnitude. At the broadest two bandwidths, $\Delta\lambda = 10$ and 5 \AA , the laser coherence times τ_c satisfied the criteria ($\tau_c < 2 \text{ psec}$) for beam smoothing with our echelons. At the intermediate bandwidth cases, $\Delta\lambda = 1 \text{ \AA}$, τ_c is approximately five times greater than the minimum optical delay between beamlets introduced by the ISI echelons, but some residual beam smoothing does occur. Finally in the extreme narrow bandwidth case, in which the laser pulse is time-bandwidth limited, the laser bandwidth is $\Delta\lambda = 0.01 \text{ \AA}$. The laser coherence time τ_c here is approximately 500 times greater than the minimum optical delay introduced by the ISI echelons and the resulting beam intensity profile on target is highly non-uniform.

The experimental configuration of both beams, target,

x-ray detectors, and harmonic emission detectors is shown in Fig. 1. Each beam was incident on a flat 200 μm thick CH target at an angle of 4° to the normal. Measurements of $3\omega_0/2$ emission were also taken at the same four bandwidths for targets irradiated by a beam without ISI echelons. Three fiber-optic collectors each with a 6 cm focal length lens were situated at a distance of 50 cm from the target location at 180° , 150° , and 130° collection angles with respect to the target normal. Quartz fibers from each fiber-optic collection position were input into a $\frac{1}{4} \text{ m}$ spectrograph whose output was matched to an optical multichannel analyzer (OMA) with a two-dimensional intensified vidicon array operating in a time-integrating mode. Neutral density filters as well as selected bandpass interference filters were used in front of the collection optics. The magnitude of the $3\omega_0/2$ signal for each collection angle was obtained by integrating the OMA detector signal over both the red- and blue-shifted wavelength components. Finally, the Raman backscatter at the 180° collection angle was measured with an array of fast silicon photodiodes with 50 nm bandwidth interference filters centered at 650, 750, 850, and 950 nm.

III. EXPERIMENTAL RESULTS

A. Differences in $3\omega_0/2$ spectra

Two time-integrated $3\omega_0/2$ spectra at the 150° collection angle are shown in Fig. 2 for targets irradiated at broad bandwidth and narrow bandwidth ($\Delta\lambda = 10$ and 0.01 \AA) at intensity approximately equal to $7.5 \times 10^{13} \text{ W/cm}^2$. The peak of the $3\omega_0/2$ emission in the spectrum with the narrow bandwidth laser is almost two orders of magnitude greater than in the spectrum obtained with broad bandwidth. In addition, the measurements show a significant difference in the relative amplitudes of the red and blue components of the $3\omega_0/2$ spectrum. The $3\omega_0/2$ spectrum from the narrow bandwidth case contains a blue component with a magnitude less than 10% that of the red component, whereas in the

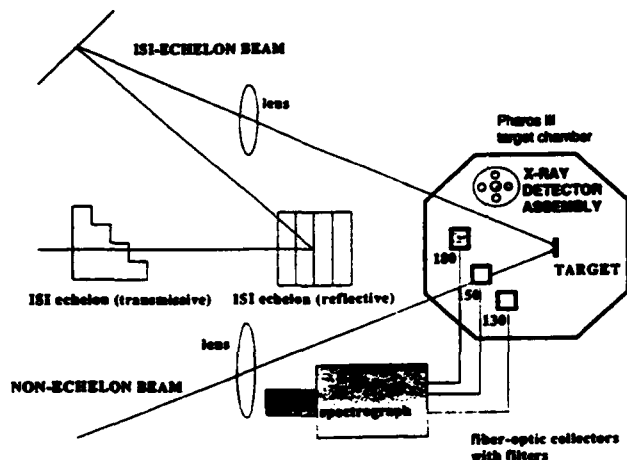


FIG. 1. Experimental arrangement for $3\omega_0/2$ ISI interaction experiment showing two beams, with and without ISI echelons, and position of the fiber-optic $3\omega_0/2$ collectors, spectrograph, and OMA as well as the x-ray detector assembly.

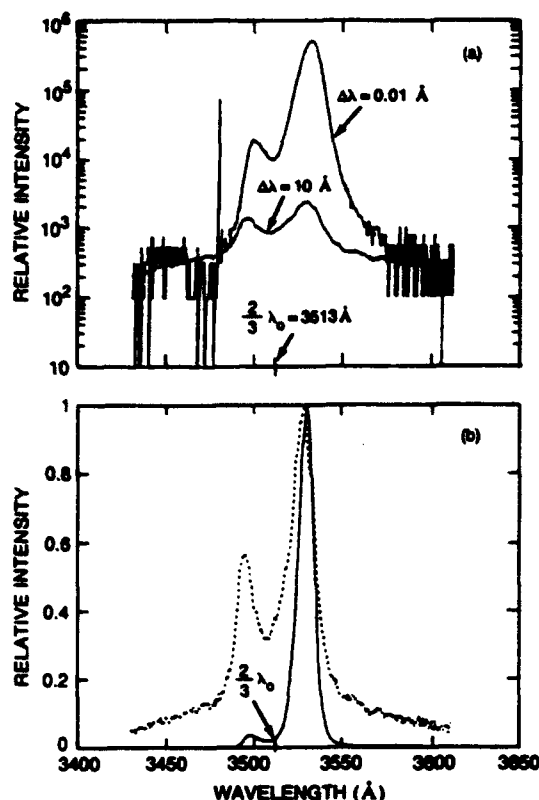


FIG. 2. (a) Time-integrated spectra of the $3\omega_0/2$ emission at the 150° observation angle for two shots with ISI echelons: one, at narrow bandwidth 0.01 Å ; the other, broad bandwidth 10 Å . (b) The same spectra, narrow bandwidth 0.01 Å (—), and broad bandwidth 10 Å (---), shown normalized to their maximum values. The wavelength corresponding to the $3\omega_0/2$ frequency is indicated as $2\lambda_0/3$.

broad bandwidth case the blue component is over 50% the amplitude of the red component. Although the effect of broad bandwidth ISI is to reduce the overall level of emission, the red component carrying most of the energy seems to be damped more strongly than the blue component. The wavelength shift from the nominal $2\lambda_0/3$ value for the red and blue components is virtually the same for the two shots.

B. Relative amplitudes of the $3\omega_0/2$ emission

The use of broad bandwidth ISI results in a significant reduction in the overall level of the $3\omega_0/2$ radiation. Figure 3 shows the effect of bandwidth variation in conjunction with ISI echelons on the overall level of the $3\omega_0/2$ emission observed at the 180° and 150° collection angles. The incident laser intensity was determined by fitting densitometer line-outs of the equivalent focal plane distribution to the ideal ISI intensity profile $I = I_0 \text{sinc}^2(2\pi x/d)$ and then calculating the average intensity within the full width at half-maximum where d is the diffraction envelope width. The use of broad laser bandwidth ($\Delta\lambda = 10$ and 5 Å) reduced not only the amplitude of the $3\omega_0/2$ emission as compared with the intermediate ($\Delta\lambda = 1 \text{ Å}$) and narrow bandwidth ($\Delta\lambda = 0.01 \text{ Å}$) cases, but also the rate of increase of the amplitude with increasing average laser intensity. Data points in Fig. 3 indi-

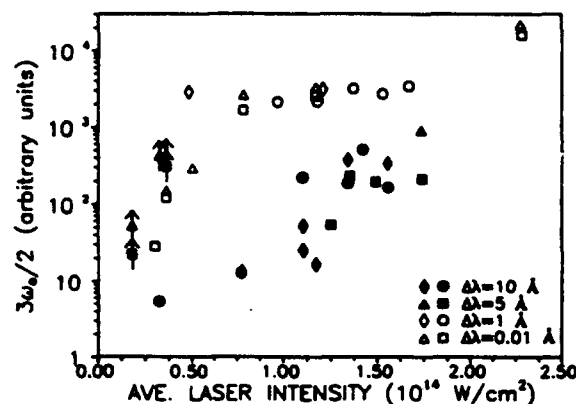


FIG. 3. Time- and spectrally integrated $3\omega_0/2$ signal for beam with ISI echelons at four bandwidths for two collection angles: circles and squares denote 180° , diamonds and triangles denote 150° .

cated by upward arrows may be below the actual values by as much as a factor of 2 due to detector saturation, however, this does not alter the qualitative picture described above.

In the limit of bandwidth $\Delta\omega$ much greater than the growth rate γ ($\Delta\omega \gg \gamma$), Thomson's theoretical treatment of bandwidth effects on parametric instabilities predicts that reductions in growth rates by a factor $\gamma/\Delta\omega$ can be achieved.³² Although Thomson's theory includes temporal bandwidth only whereas ISI involves both spatial and temporal incoherence, it is interesting to examine the predicted effects of bandwidth alone. The maximum two-plasmon decay growth rate is given by $\gamma = k_0 v_0/4$.¹²⁻¹⁵ At the parameters of the present experiment, the maximum growth rate at incident laser intensities of $1 \times 10^{14} \text{ W/cm}^2$ is $\gamma = 5.7 \times 10^{12} \text{ sec}^{-1}$ compared with values of bandwidth of $3.45 \times 10^{12} \text{ sec}^{-1}$ for the $\Delta\lambda = 5 \text{ Å}$ case and $6.68 \times 10^{12} \text{ sec}^{-1}$ for the $\Delta\lambda = 10 \text{ Å}$ case. At the irradiances of the experiment reported here, the growth rate of the two-plasmon decay instability is roughly comparable or only slightly less than the largest laser bandwidths—a region where present theories of the effects of bandwidth on parametric instabilities do not strictly apply.

Experiments have been reported showing suppression of $3\omega_0/2$ emission in filamentary channels using broad bandwidth (30 Å), low energy (10 J) and short pulses at 1.06 μm .²⁵ In that study, however, time-integrated laser intensity distributions at an equivalent focal plane appear highly non-uniform for narrow bandwidth and smooth at broad bandwidth suggesting that the combination of low $f\#$ optics and chromatic aberration of the final focusing lens may have smoothed the laser profile in a manner analogous to ISI. It is therefore unclear whether the reported suppression of the harmonic emission in that experiment can be attributed to bandwidth or beam-smoothing effects. Similarly, in the present experiment, it is not possible to clearly distinguish between bandwidth and beam-smoothing effects because of the large illumination nonuniformities present in both the ISI-echelon beam at narrow bandwidth and the no-echelon beam at all bandwidths. Nonetheless it is interesting to examine the intensity dependence of the $3\omega_0/2$ emission at the

four bandwidths for a laser with no ISI echelons.

A comparison of results at the four bandwidths with a regular beam (no echelons) is shown in Fig. 4 for the 130° collection angle. The laser intensity given here is the average value over the flat-top portion of the intensity pattern at the equivalent focal plane. The three-halves harmonic emission levels in Fig. 4 show little difference between the four bandwidths. At the lower intensities in particular, where the ratio of growth rate to bandwidth is the smallest, and the largest finite bandwidth effect might be expected, virtually no difference between broad and narrow bandwidths in the $3\omega_0/2$ emission is observed on the no-echelon beam. The slopes and amplitudes for the $3\omega_0/2$ emission across all four bandwidths for the no-echelon beam are comparable to the intermediate and narrow bandwidth with the ISI-echelon beam. In the presence of large illumination nonuniformities characteristic of the no-echelon beam, broad bandwidth alone does not reduce the level of the underlying two-plasmon decay instability. As in Fig. 3 above, data points in Fig. 4 indicated by upward arrows may be below the actual values by as much as a factor of 2 due to detector saturation.

C. Raman and hard x-ray data

An array of photodiode detectors with narrow band interference filters as well as time-integrated spectroscopy were used to monitor Raman spectra in the region 6500 to 9500 Å. The peak Raman signal was obtained near the 750 nm wavelength. Copious Raman emission was observed for both the no-echelon beam at all bandwidths and the ISI-echelon beam at the narrowest bandwidth $\Delta\lambda = 0.01$ Å. Finally, time- and space-integrated hard x-ray measurements were also made using a set of silicon *p-i-n* diodes and scintillator/photomultiplier detectors with broadband k-edge filtering techniques. The hard x-ray signals were fit to a Maxwellian energy distribution and the energy in hot electrons determined accordingly following the procedure outlined by Keck *et al.*³³ Figure 5 shows the correlation between the x-ray data and the $3\omega_0/2$ data at 130° at the broad bandwidth

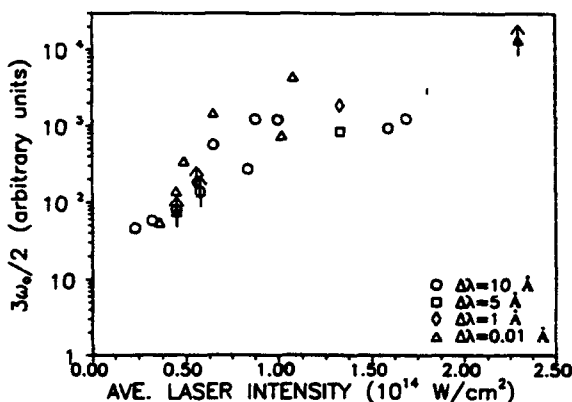


FIG. 4. Comparison of time- and spectrally integrated $3\omega_0/2$ signal for the beam without echelons at four bandwidths for the collection angle of 130° with respect to the target normal.

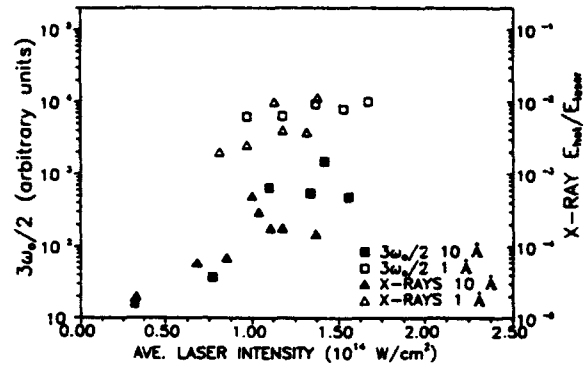


FIG. 5. Correlation between time- and space-integrated hard x-ray measurements (ratio of hot electron energy to the incident laser energy) and the 130° collection angle $3\omega_0/2$ data at broad bandwidth (10 Å) and narrow bandwidth (1 Å) for the ISI-echelon beam.

(10 Å) and the intermediate bandwidth (1 Å) for the ISI-echelon beam.

Hard x rays produced by suprathermal electrons undergoing collisions with the cooler background plasma can be a signature of either Raman or two-plasmon decay.³³ In contrast to the x-ray data and the $3\omega_0/2$ data, the Raman spectra was nearly completely suppressed at the $\Delta\lambda = 1$ Å bandwidth in agreement with earlier reported results. Figure 6 compares the Raman backscatter near 750 nm and the $3\omega_0/2$ emission backscatter for an ensemble of shots with incident laser intensity from 7.5×10^{13} to 1.40×10^{14} W/cm². There is significant reduction of Raman at narrow bandwidth (1 Å) in contrast with the $3\omega_0/2$ radiation which did not exhibit any substantial reduction in emission amplitude except at full laser bandwidth (10 Å). A similar bandwidth effect to that observed with Raman was also seen with simulated Brillouin.⁵ Although three-halves harmonic radiation can be generated from Raman occurring at $n_e/4$ as well as two-plasmon decay, the lower threshold and the charac-

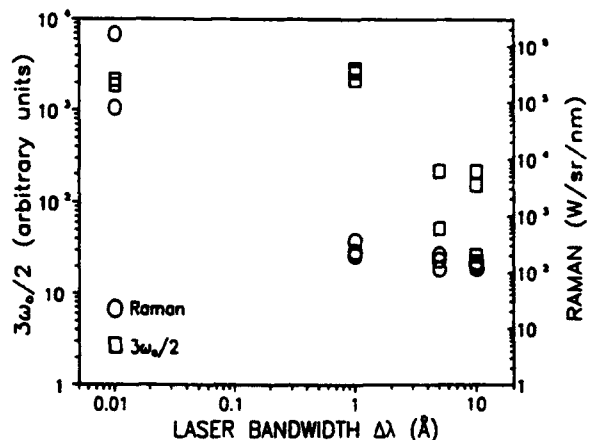


FIG. 6. Comparison of Raman and $3\omega_0/2$ signal levels at four bandwidths for an ensemble of shots with incident intensity I between 7.5×10^{13} and 1.40×10^{14} W/cm² showing significant reduction of Raman at narrow bandwidth (1 Å) compared with $3\omega_0/2$, which did not exhibit any substantial reduction in emission amplitude except at full laser bandwidth (10 Å).

teristic red and blue spectral components of the emission observed in the present experiment suggest that the two-plasmon decay is responsible for the observed $3\omega_0/2$ emission.¹⁷ The anticorrelation between the x-ray and Raman data for the $\Delta\lambda = 1 \text{ \AA}$ bandwidth is additional evidence that two-plasmon decay at quarter-critical is indeed the instability responsible for the x rays as well as the $3\omega_0/2$ emission. It is interesting to note that the maximum theoretical growth rate for Raman is comparable to two-plasmon decay. If temporal bandwidth alone were important for both instabilities, one might expect instability amplitude reduction for both at the same bandwidth. The observed difference in bandwidth effect on Raman and $3\omega_0/2$ emission shown in Fig. 6 may be due to differences in intensity thresholds for the two instabilities as well as differences in the nature of the instabilities (absolute versus convective). A recent paper by Guzdar *et al.* on the effect of ISI on absolute Raman has suggested that the effect of bandwidth variation may affect absolute instabilities differently than convective instabilities.³⁴ This issue is further complicated by the observation made with unsmoothed lasers that Raman occurring well below quarter-critical density may be an absolute instability associated with density fluctuations in the plasma.³⁵ At present there is no well-established theory that can explain these phenomena.

IV. SUMMARY AND CONCLUSIONS

Theoretical and numerical studies indicate that ISI can suppress filamentation at $0.53 \mu\text{m}$ for intensities comparable to those in the present experiment.³⁰ In both the present and previous experiments at the intermediate (1 \AA) bandwidth, the reduction of SRS and SBS has been attributed at least in part to the predicted decrease in filamentation with ISI.^{3,5} In the case of two-plasmon decay, however, neither the $3\omega_0/2$ emission nor the hard x rays are reduced until the bandwidth is increased an additional factor of 5 to 10 times ($\Delta\lambda = 5$ and 10 \AA), hence it is possible that the reduction of the instability is due as much to direct bandwidth effects on the instability as to the absence of filamentation. The experimental observation that larger bandwidth is required to suppress two-plasmon decay than SRS or SBS is in qualitative agreement with a recent theoretical analysis of the direct effect of ISI on parametric instabilities, especially at the quarter-critical density surface.³⁶ The strong correlation between the x-ray data and the $3\omega_0/2$ emission further suggests that the observed reduction in the three-harmonic emission is related to reduction in the underlying two-plasmon decay instability rather than the harmonic generation process.

In conclusion, we have made the first detailed study of the two-plasmon decay instability as inferred from $3\omega_0/2$ and hard x-ray emission with and without ISI echelons over a range of bandwidths at intensities relevant to laser fusion. The use of ISI echelons at broad bandwidths leads to significant decreases in the level of emission as compared with both no-echelon beams and echelon beams with intermediate and narrow laser bandwidths. In contrast to SRS and SBS, however, two-plasmon decay is not completely suppressed by broad bandwidth and ISI. As in the previous ISI interaction

experiments, it is not clear whether the observed reduction in plasma instabilities with ISI is due to a decrease in filamentation or whether there is an additional effect due to bandwidth. The difference between two-plasmon and other previously observed laser-plasma instabilities discussed above, however, suggests that very large bandwidth may be important for interaction physics with any beam-smoothing technique.

ACKNOWLEDGMENTS

The authors are pleased to acknowledge useful discussions with and assistance from Dr. S. E. Bodner, Dr. R. Lehmburg, Dr. A. J. Schmitt, Dr. P. N. Guzdar, and Dr. A. N. Mostovych. Technical assistance from L. Daniels, J. Ford, N. Nocerino, M. Rogawski, MD, and J. L. Gavreau is gratefully acknowledged.

This work was supported by the U.S. Department of Energy.

- ¹ R. H. Lehmburg and S. P. Obenshain, *Opt. Commun.* **46**, 27 (1983).
- ² R. H. Lehmburg, A. J. Schmitt, and S. E. Bodner, *J. Appl. Phys.* **62**, 2680 (1987).
- ³ S. P. Obenshain, J. Grun, M. J. Herbst, K. J. Kearney, C. K. Manka, E. A. McLean, A. N. Mostovych, J. A. Stamper, R. R. Whitlock, S. E. Bodner, J. H. Gardner, and R. H. Lehmburg, *Phys. Rev. Lett.* **56**, 2807 (1986).
- ⁴ S. P. Obenshain, C. J. Pawley, A. N. Mostovych, J. A. Stamper, J. H. Gardner, A. J. Schmitt, and S. E. Bodner, *Phys. Rev. Lett.* **62**, 768 (1989).
- ⁵ A. N. Mostovych, S. P. Obenshain, J. H. Gardner, J. Grun, K. J. Kearney, C. K. Manka, E. A. McLean, and C. J. Pawley, *Phys. Rev. Lett.* **59**, 1193 (1987).
- ⁶ Y. Kato, K. Mima, N. Miyanaga, S. Aringa, Y. Kitagawa, M. Naktsuka, and C. Yamanka, *Phys. Rev. Lett.* **53**, 1057 (1984).
- ⁷ X. Deng, X. Liang, Z. Chen, W. Yu, and R. Ma, *Appl. Opt.* **25**, 377 (1986).
- ⁸ S. Skupsky, R. W. Short, T. Kessler, R. S. Craxton, S. Letzring, and J. M. Soures, *J. Appl. Phys.* **66**, 3456 (1989).
- ⁹ R. H. Lehmburg and J. Goldhar, *Fusion Technol.* **11**, 532 (1987).
- ¹⁰ D. Veron, H. Ayrat, C. Goudeard, D. Husson, J. Laurion, O. Martin, B. Meyer, M. Rostaing, and C. Sauteret, *Opt. Commun.* **65**, 42 (1988).
- ¹¹ O. Willi, T. Afshar, and S. Coe, *Phys. Fluids B* **2**, 1318 (1990).
- ¹² C. S. Liu and M. N. Rosenbluth, *Phys. Fluids* **19**, 967 (1976).
- ¹³ C. S. Liu, in *Advances in Plasma Physics*, edited by A. Simon and W. B. Thompson (Wiley, New York, 1976), Vol. 6, p. 176.
- ¹⁴ See National Technical Information Service Document No. DE83011875. [Lawrence Livermore National Laboratory, Laser Program Annual Report 1981 (UCRL-50021-81) pp. 4-49, by B. F. Lasinski and A. B. Langdon] Copies may be ordered from the National Technical Information Service, Springfield, Virginia 22161. The price is \$53.00 plus a \$3.00 handling fee. All orders must be prepaid.
- ¹⁵ A. Simon, R. W. Short, E. A. Williams, and T. Dewandre, *Phys. Fluids* **26**, 3107 (1983).
- ¹⁶ S. J. Karttunen, *Lasers Part. Beams* **3**, 157 (1985).
- ¹⁷ A. I. Avrov, V. Yu. Bychenkov, O. N. Krokhin, V. V. Pustovalov, A. A. Rupakov, V. P. Silin, G. V. Skilzov, V. T. Tikhonchuk, and A. S. Shikanov, *Sov. Phys. JETP* **45**, 507 (1977).
- ¹⁸ P. D. Carter, S. M. L. Sim, H. C. Barr, and R. G. Evans, *Phys. Rev. Lett.* **44**, 1407 (1980).
- ¹⁹ H. A. Baldis and C. J. Walsh, *Phys. Fluids* **26**, 1364 (1983).
- ²⁰ L. V. Powers and R. J. Schroeder, *Phys. Rev. A* **29**, 2298 (1984).
- ²¹ R. E. Turner, D. W. Phillion, B. F. Lasinski, and E. M. Campbell, *Phys. Fluids* **27**, 511 (1984).
- ²² D. M. Villeneuve, H. A. Baldis, and C. J. Walsh, *Phys. Fluids* **28**, 1454 (1985).
- ²³ V. Aboites, T. P. Hughes, E. McGoldrick, S. M. L. Sim, S. J. Karttunen, and R. G. Evans, *Phys. Fluids* **28**, 2555 (1985).

- ²⁴ W. Seka, B. B. Afeyan, R. Boni, L. M. Goldman, R. W. Short, K. Tanaka, and T. W. Johnston, *Phys. Fluids* **28**, 2570 (1985).
- ²⁵ L. Zunqi, T. Weihai, G. Min, M. Guang, P. Chengming, Y. Wenyan, and D. Ximing, *Lasers Part. Beams* **4**, 223 (1986).
- ²⁶ F. Amiranoff, F. Briand, and C. Labaune, *Phys. Fluids* **30**, 2221 (1987).
- ²⁷ P. E. Young, B. F. Lasinski, W. L. Kruer, E. A. Williams, K. G. Estabrook, E. M. Campbell, R. P. Drake, and H. A. Baldis, *Phys. Rev. Lett.* **61**, 2766 (1988).
- ²⁸ P. E. Young, H. A. Baldis, B. A. Remington, and K. G. Estabrook, *Phys. Fluids B* **2**, 1228 (1990).
- ²⁹ A. J. Schmitt, *Phys. Fluids* **31**, 3079 (1988).
- ³⁰ J. Gardner (private communication).
- ³¹ M. S. Pronko, R. H. Lehmberg, S. Obenschain, C. J. Pawley, C. K. Manka, and E. Echardt, *IEEE J. Quantum Electron.* **QE-26**, 337 (1990).
- ³² J. J. Thomson, *Nucl. Fusion* **15**, 237 (1975).
- ³³ R. L. Keck, L. M. Goldman, M. C. Richardson, W. Seka, and K. Tanaka, *Phys. Fluids* **27**, 2762 (1984).
- ³⁴ P. N. Guzdar, W. Tan, Y. C. Lee, and C. S. Liu, *Phys. Fluids B* **3**, 776 (1991).
- ³⁵ R. P. Drake, E. A. Williams, P. E. Young, K. Estabrook, and W. L. Kruer, *Phys. Rev. Lett.* **60**, 1018 (1988).
- ³⁶ R. L. Berger, *Phys. Rev. Lett.* **65**, 1207 (1990).

Appendix GG

**Electron-Ion Hybrid Instability in Laser-Produced Plasma
Expansion Across Magnetic Fields**

Electron-ion hybrid instability in laser-produced plasma expansions across magnetic fields

T. A. Peyser^{a)}

Science Applications International Corp., McLean, Virginia 22102

C. K. Manka, B. H. Ripin, and G. Ganguli

Space Plasma Branch, Plasma Physics Division, Naval Research Laboratory, Washington, D.C. 20375-5000

(Received 20 February 1992; accepted 21 April 1992)

High-intensity laser irradiation of hollow glass cylinders immersed in a magnetic field results in plasma expansions strongly collimated in the direction transverse to both the initial flow and the magnetic field, but jetlike in the direction parallel to the initial flow. Magnetic fields from $B=0$ kG to $B=10$ kG produced plasmas with markedly different geometrical features. Fast framing camera photographs show the plasmas propagating across magnetic field lines and undergoing structuring indicative of transverse velocity shear-driven instabilities. Comparison is made between the observed instability characteristics and predictions of Rayleigh-Taylor, classical Kelvin-Helmholtz, and the electron-ion hybrid instabilities. Only the electron-ion hybrid instability is consistent with the experimental results.

I. INTRODUCTION

The propagation and stability of collimated streams or jets of plasmas in magnetic fields is central to a number of important physical problems, including beam heating of magnetically confined thermonuclear plasmas,¹ the interaction of the solar wind with planetary magnetospheres,² bipolar flows associated with young stellar objects,³ and the formation and equilibrium properties of extragalactic jets.^{4,5} Streaming or counterstreaming plasma flows have velocity shears that can give rise to a number of plasma instabilities such as the Kelvin-Helmholtz instability.⁶ The presence of velocity shear in a plasma can dominate the flow dynamics and the evolution of structures within the plasma.

In this paper, we report laser-produced plasmas that propagate across magnetic fields and undergo dramatic structuring instabilities. Although both Rayleigh-Taylor (magnetic interchange instabilities) and Kelvin-Helmholtz instabilities are possible in the present experiment, their growth rates are much lower than those observed in the experiment. A modified form of the Kelvin-Helmholtz instability, i.e., the electron-ion hybrid instability,⁷ has a growth rate consistent with the observations. Kelvin-Helmholtz plasma instabilities have been observed previously in the laboratory.⁸⁻¹¹ However, recent experiments have uncovered short-scale-length velocity-shear-driven lower-hybrid instabilities with faster growth rates in laser-produced plasmas.¹² The present results are the first detailed observations of large-scale-length electron-ion hybrid instabilities in a laser-produced plasma.

II. EXPERIMENTAL SETUP

The experiments used beams from the Pharos III Nd-glass laser¹³ operating with wavelength 1054 nm, 2 nsec pulses [full width at half-maximum (FWHM)] and energies between 30 and 300 J. The intense laser pulse is focused onto the interior wall of a hollow glass cylinder to intensities ranging from 5×10^{11} to 5×10^{12} W/cm². The cylinders had length 3 mm, diameter 1 mm, and wall thickness 50 μ m. The cylinder axis is oriented at approximately 16° from the incident laser beam axis. The cylinder interior wall is illuminated in an elliptical pattern by the circular laser focal spot, as shown in Fig. 1(a). Ablation plasma is produced directly in the laser-light-solid-target interaction process at the cylinder wall. Shadowgraphic images reveal that the ablation plasma emerges from the cylinder ends well before the breakup or disassembly of the cylinder. Thus, the cylinder provides some degree of collimation of the plasma emerging symmetrically from both ends. The production of a directed plasma expansion by interior illumination of a hollow cylinder is a novel feature of the present work. The extent of the collimation can be further enhanced by immersing the cylinder in a magnetic field, as discussed below.

The expanding plasma is observed in its self-luminosity with an ultrafast framing camera—a single-frame Kentech instruments gated optical imager (GOI) with exposure times between 200 psec and 5 nsec.¹⁴⁻¹⁶ Most of the photographs reported here were obtained with 1 or 2 nsec exposure times, which were sufficient to freeze plasma motion to within 100–200 μ m. Some images were acquired with 200 psec exposures to verify that there was no loss of information at the longer exposures. Plasma expansion were photographed at various times from 150 to 2000 nsec after the laser pulse struck the target. The GOI was coupled to a Nikkor $f/5.6$ zoom telephoto lens (100–300 mm) and the focal length adjusted to give different magnifica-

^{a)}Permanent address: Lawrence Livermore National Laboratory, University of California, Livermore, California 94550.

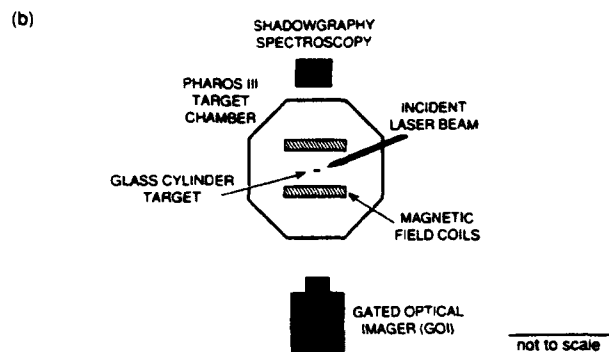
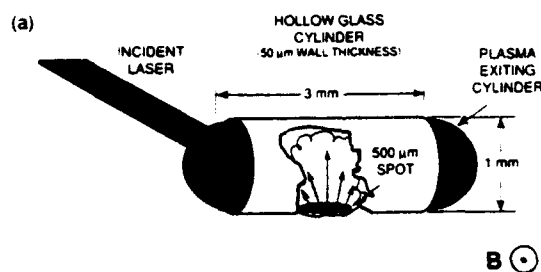


FIG. 1. Experimental setup. (a) The laser strikes the interior walls of a 1 mm diam, 3 mm long hollow glass cylinder at an angle of approximately 16° . The high-velocity plasma expands outward from the laser focal spot, undergoes collisions with the still-intact cylinder, and is ejected out of the cylinder ends. (b) The laser is incident onto the cylinder located at the center of the Helmholtz coil. The principle diagnostic used in these experiments is a single-frame ultrafast framing camera or gated optical imager (GOI).

tions, as required. The spectral response of the GOI was from 300 to 900 nm, determined by the S-25 photocathode. The photographs shown below were obtained by coupling the GOI output phosphor to high-speed, high dynamic range Kodak TMAX P3200 negative film placed on top of Polaroid high-speed Type 667 positive film. The Polaroid exposure was used as a guide for processing of the Kodak negative film.

The cylindrical targets were located at the center of a 24 cm diam pair of coils in a Helmholtz configuration. The coils provided a uniform central magnetic field adjustable from $B=0$ kG to $B=10$ kG, which was effectively steady state on the time scale of the experiment. The usual viewing orientation of the GOI was along the external applied magnetic field direction and approximately perpendicular to both the incident laser beam and the axis of the cylindrical target. This orientation allowed study of the cross-field plasma motion. Data were also taken perpendicular to the magnetic field to provide a view of the plasma expansion along the field lines.

Optical spectra were obtained from different regions of the plasma expansion with an EGG PARC optical multi-channel analyzer with a silicon-enhanced intensified linear array. Both time-integrated and time-resolved data were obtained. Spectroscopic measurements made 100 nsec or more after the laser was incident on the target show that the dominant line emission is from neutral and singly ionized silicon atoms placing the plasma temperature in the 8–16 eV range. Time-of-flight ion detectors were used to

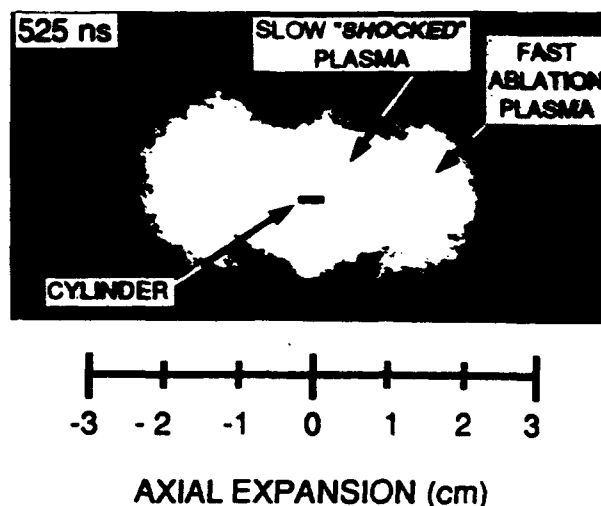


FIG. 2. GOI image of plasma expansion into the zero magnetic field taken 525 nsec after the laser is incident on the target with a 2 nsec exposure. The position of the cylindrical target and its relative scale compared with the plasma expansion is shown. The plasma expands into two hemispheres, one at each cylinder end. The two components of the plasma velocity—the slower "shocked" plasma and the fast ablation plasma—are clearly visible in the GOI image. There is no evidence of collimation.

measure the plasma expansion velocity distribution. The orientation of the glass cylinder targets, laser axis, GOI in the parallel viewing configuration, ion time-of-flight detectors, and external magnetic field coils is shown schematically in Fig. 1(b).

III. PLASMA EXPANSION DATA

In the absence of an applied magnetic field, the plasma rapidly expands in the transverse as well as axial direction. Figure 2 shows a photograph of the plasma expansion with no applied magnetic field. The photograph was taken 525 nsec after the laser pulse struck the target. The photograph reveals that there are two major plasma components of the expansion centered along the cylinder axis: a fast component with velocity $5.5 \pm 0.5 \times 10^6$ cm/sec followed by a slower component with velocity $2.2 \pm 0.5 \times 10^6$ cm/sec. These two velocity components in the magnetic-field-free expansion are also observed as a clear double-peaked structure in ion time-of-flight detector signals.

The faster plasma is most likely the ablation plasma from the original laser-plasma interaction at the cylinder wall, although its speed is a factor of 5 or more below that expected for an ablation plasma at the given laser irradiance.¹⁷ A decrease in the ablation plasma velocity would be one obvious consequence of collisions between the expanding plasma and the cylinder wall opposite to the laser focal spot in the first 5–10 nsec after the beam is incident on the target. The slower component probably originates from the denser, shock-created plasma from the inside of the cylinder wall caused by the intense pressure pulse (≈ 1 Mbar) occurring during the laser-target interaction.

When a magnetic field is applied perpendicular to the cylinder axis, however, there is a significant reduction in

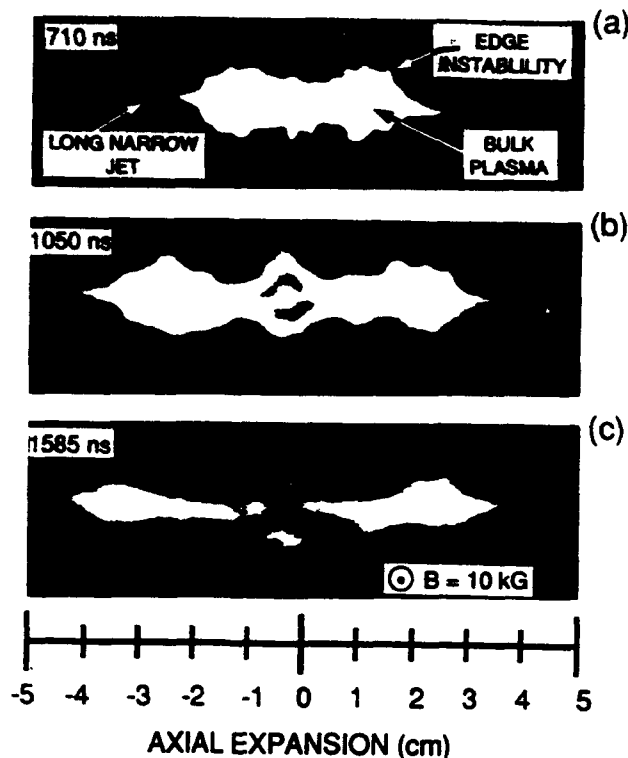


FIG. 3. GOI photographs of plasma expansion into high (10 kG) magnetic fields, showing the long narrow jet phenomena, the instability in the edge regions of the plasma, and the bulk plasma expansion across the magnetic field (a) taken 710 nsec after the laser is incident on the target with 2 nsec exposure, showing early development of the jets and the edge instability (b) taken at 1150 nsec with shorter 200 psec exposure (c) taken at 1585 nsec with 2 nsec exposure.

the plasma flow perpendicular to the magnetic field and the cylinder axis. Cross-magnetic field plasma expansions were observed over a range of magnetic fields ($0 \text{ kG} < B < 10 \text{ kG}$), times (100–2000 nsec) and incident laser energies (30–300 J). The dynamics of the expansions are, in general, insensitive to the incident laser energy, but do depend considerably on the magnitude of the magnetic fields. In the case of the 10 kG applied magnetic fields, the cross-field velocity along the cylinder axis is about four times the transverse cross-field velocity, resulting in the appearance of a highly collimated expansion.

There are three distinct features of these expansions, which are discussed further below: first, the long narrow jets leading the fast plasma component across the magnetic field (in the high magnetic field cases); second, the propagation of the bulk of the slow plasma at constant velocity across the magnetic field; and, third, an instability that appears along the edges of the bulk plasma expansion.

A. Plasma expansion across high (10 kG) magnetic fields

The general features of the expansion across high fields are shown in Fig. 3. In these photographs, the laser is incident on the target from the left and the magnetic field is pointed out of the plane of the picture. In the earliest frame shown (710 nsec), Fig. 3(a), the long narrow jets

are well formed and extend a distance of approximately 3.4 cm from the original target location corresponding to a maximum velocity in the axial direction of about $4.8 \times 10^6 \text{ cm/sec}$. Behind the jets, the center of mass of the bulk plasma expansion (from the fast component of the plasma) is moving with an axial velocity of about $2.5 \times 10^6 \text{ cm/sec}$. There are undulations with a wavelength of 3–5 mm on both the top and bottom surfaces of the bulk plasma, indicative of an instability. Figure 3(b), taken on a nearly identical shot to that shown in Fig. 3(a), shows the development of the expansion at $t = 1050 \text{ nsec}$. The long narrow jets continue to travel at a velocity $v = 4.8 \times 10^6 \text{ cm/sec}$. The bulk plasma expansion, which has an axial velocity of about $2.2 \times 10^6 \text{ cm/sec}$ also has maintained its speed. The bulk plasma surface instability is still evident, although it has not evolved significantly from 200–300 nsec earlier. Finally, Fig. 3(c) shows a similar expansion at a still later time (1585 nsec) in which the long narrow jets are still evident, but their full extent is not visible due to occlusion by the Helmholtz magnetic field coils. The bulk plasma expansion on this shot has a maximum axial velocity of about $2.1 \times 10^6 \text{ cm/sec}$. The original edge instability has lost its distinctness and has taken on the form of a wedge- or diamond-shaped structure. Also at this time, an even slower plasma component can be seen to be expanding from the original target location at a velocity of about $6.5 \times 10^5 \text{ cm/sec}$. This very slow plasma component is most likely residual cylindrical target debris.

B. Plasma expansion across moderate (6 kG) magnetic fields

The plasma expansions across 6 kG magnetic fields are qualitatively similar to the higher 10 kG case. There are subtle but interesting differences, however, in the long narrow jet propagation and in the onset time and character of the edge instability. Figure 4 shows a series of 6 kG expansion photographs. The long narrow jets are clear in the earliest of the sequence, Fig. 4(a) at 600 nsec, but the jets are less pronounced than in the 10 kG case at this time. The aspect ratio or collimation of the plasma, that is the length to width ratio, is smaller for the 6 kG expansions than for the 10 kG cases. In contrast to the expansions at the 10 kG case, there is no visible evidence of the edge instability in the earliest image. At 1000 nsec, however, the edge instability is pronounced, as shown in Fig. 4(b), with a wavelength of 3–6 mm. At later times (1585 nsec), the bulk plasma exhibit the same wedge or diamond structure as in the higher 10 kG case, although the overall degree of lateral constriction appears to be less in Fig. 4(c) as compared with Fig. 3(c).

C. Plasma expansion across low (<3 kG) magnetic fields

The plasma expansion into still lower magnetic fields, specifically 3 kG fields, has some important qualitative as well as quantitative differences from the higher field expansions. Figure 5 shows a series of 3 kG expansion photographs. Long narrow jets, which were a pronounced fea-

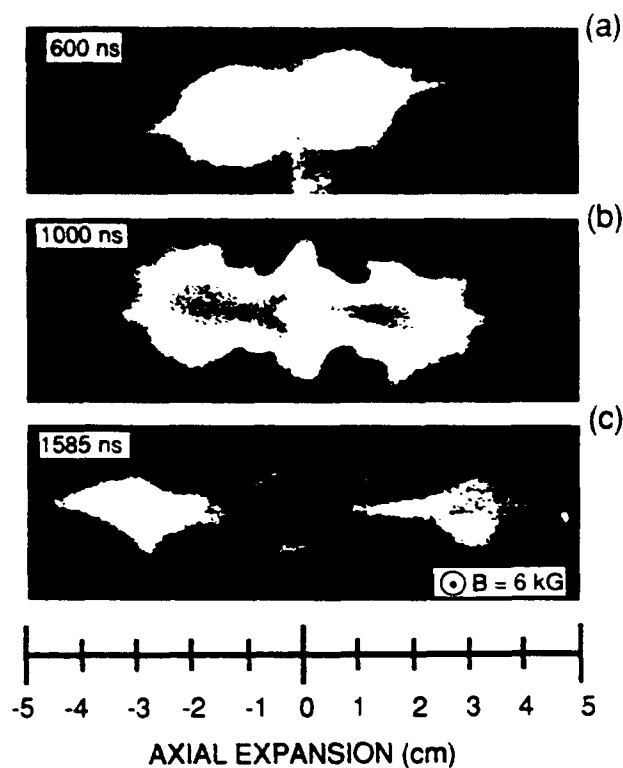


FIG. 4. GOI photographs of plasma expansion into a 6 kG applied magnetic field all with 2 nsec exposures: (a) 600 nsec; (b) 1000 nsec; (c) 1585 nsec.

ture of the higher field expansions, are not seen at low magnetic fields. Rather, only a small protuberance appears along the cylinder axis, as seen in Fig. 5(a). The velocity of the expansion at this point, about 5.3×10^6 cm/sec, however, is comparable to the maximum long narrow jet velocities seen at the higher magnetic fields and the ablation plasma velocities seen at zero fields. In contrast to the higher field cases in which the magnetic field appears to greatly constrain the transverse motion of the bulk plasma across the field, at low fields the bulk plasma expansion velocity of 5.0×10^6 cm/sec is more characteristic of the maximum velocities seen in the zero-field fast-component expansion. The edge instability can still be observed in the 3 kG expansions, although it appears at later times (1200 nsec) and with reduced amplitudes, as compared to higher field expansions, as shown in Fig. 5(b). Finally, the characteristic late time wedge or diamond shape develops by 1800 nsec as shown in Fig. 5(c), although the lower transverse collimation of the plasma relative to the higher field cases makes these structures less dramatic in appearance.

Expansions into still lower (1 kG) magnetic fields show no evidence of jet formation or instability, yet do show some effect of magnetic collimation as illustrated in Fig. 5(d) taken at 1200 nsec. It is possible that the development of other features characteristic of the high-field expansions would occur at later times if our experiment was of comparably larger dimension.

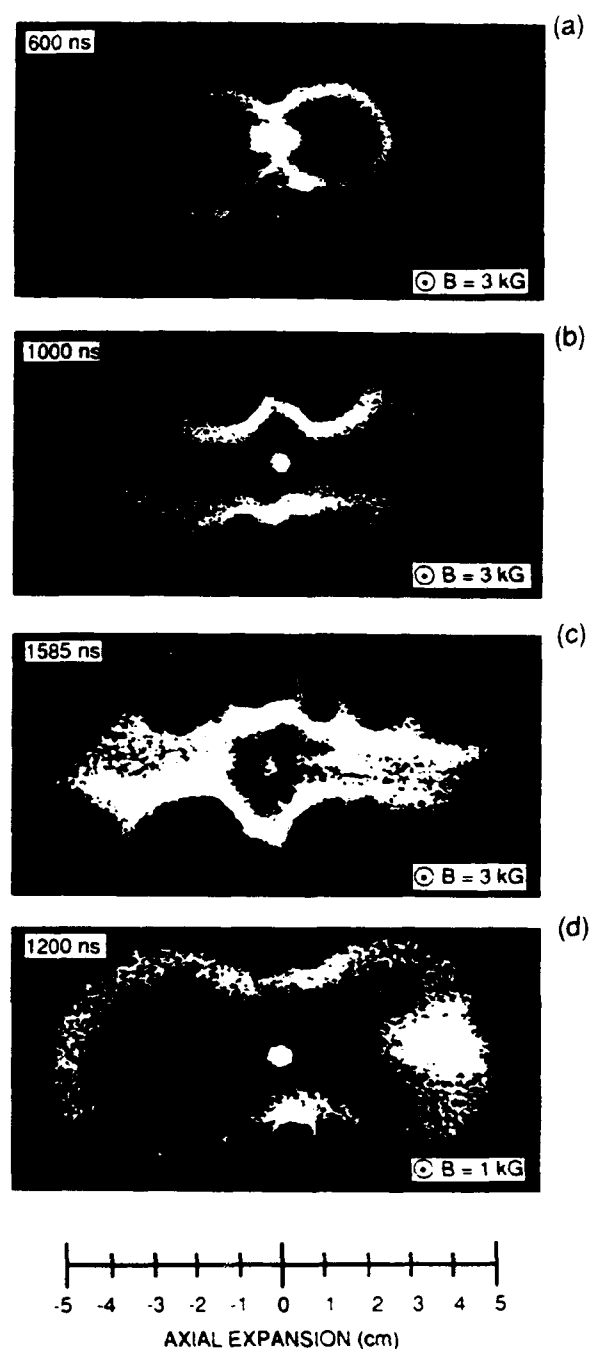


FIG. 5. GOI photographs of plasma expansion into low applied magnetic fields, showing some collimation and jet formation, but at a reduced rate compared to the high field cases: (a) 3 kG magnetic field at 600 nsec; (b) 3 kG magnetic field at 1200 nsec; (c) 3 kG magnetic field at 1800 nsec; (d) 1 kG magnetic field at 1200 nsec.

D. Plasma expansion along the magnetic field

Images of the plasma expansion taken with the GOI viewing orientation perpendicular to the magnetic field and cylinder axis show that the plasma is free streaming along the field lines, even though its flow is restricted in the transverse direction. Figure 6(a) illustrates this behavior at time 1200 nsec for a plasma expansion across a 6 kG magnetic field. The bumps and wiggles evident on the

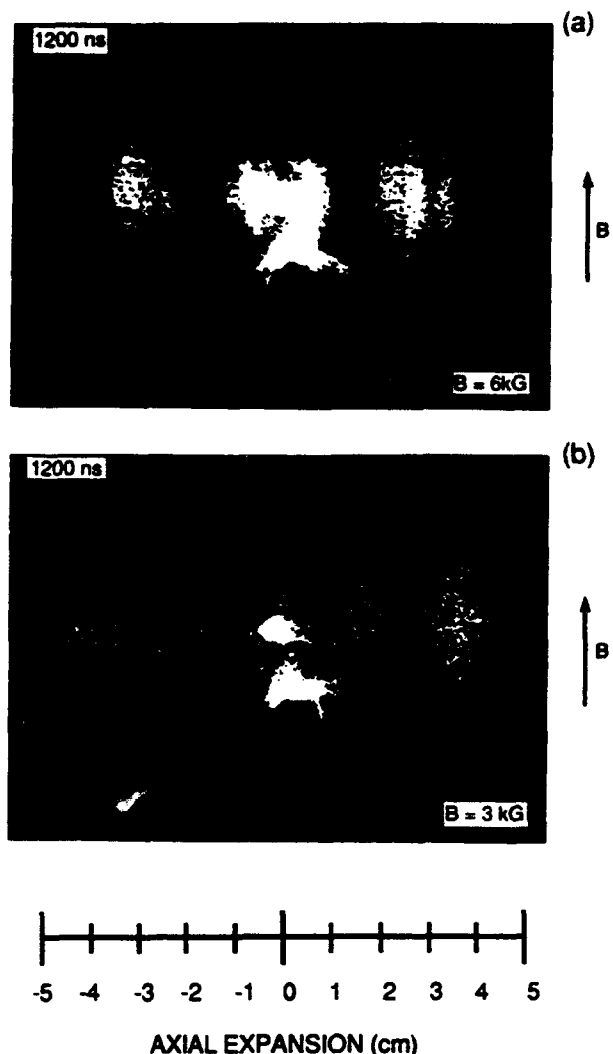


FIG. 6. GOI photo perpendicular to the magnetic field showing free-streaming along the field lines and continued evidence of flutelike instability in the pattern of light and dark stripes parallel to the magnetic field: (a) 6 kG magnetic field at $t=1200$ nsec with a 1 nsec exposure; (b) 3 kG magnetic field at $t=1200$ nsec with a 2 nsec exposure.

plasma boundaries in the parallel-field viewing configuration now appear in Fig. 6(a) as bright and dark field-aligned striations with a 4–6 mm wavelength. These intensity variations are presumably due to relative increases or decreases in the optical line-of-sight path length through the luminous plasma. These striations are much less pronounced in a photograph taken at 1200 nsec of an expansion into a $B=3$ kG magnetic field shown in Fig. 6(b). This is consistent with the parallel magnetic field images, which show a much less developed edge instability for 3 kG than 6 kG at this time.

E. Summary of plasma expansion features

Plasma motion across the magnetic field lines occurs for all applied field strengths. There are striking differences, however, in the geometry and stability properties in the high and low magnetic fields. We examine the behavior of the two most salient physical features—the long narrow

jets leading the plasma expansion across the magnetic field along the cylinder axis and the expansion of the bulk plasma perpendicular to the magnetic field immediately behind the jets.

Figure 7 gives the axial distance versus time for the long narrow jets (LNJ) and the bulk plasma leading edge (BPLE) from an ensemble of shots for the 10, 6, and 3 kG magnetic fields. At early times, the scatter in the data shown in Fig. 7 may be due either to actual differences in axial velocity on different shots or to differences in the convolution of framing camera gain and film sensitivity. At later times ($t > 1200$ nsec), the change in plasma luminosity may be responsible for the apparent decrease in the expansion velocity. The linear curve fits shown in Fig. 7 are therefore weighted to early times.

In all cases, the tips of the long narrow jets initially propagate across the magnetic field lines (along the cylinder axis) at a velocity comparable to the peak zero magnetic field ablation velocity ($\approx 5.5 \pm 0.5 \times 10^6$ cm/sec). Immediately behind the jets, there is, on most shots, a distinct leading edge to the remaining bulk plasma. Whereas the jets propagate large distances at near the ablation plasma speed, and have almost no dependence on the magnetic field strength, the bulk plasma leading edge has a weak inverse dependence on the magnetic field. The mean bulk plasma expansion velocity is about 2.4×10^6 cm/sec for the 10 kG ensemble of shots, 3.3×10^6 cm/sec for the 6 kG shots, and about 4.0×10^6 cm/sec for the 3 kG shots. A similar analysis of the bulk plasma leading edge velocity gives about 4.8×10^6 cm/sec for the 1 kG shots.

Although the jets in the 3 kG case cannot be characterized as “long and narrow” as in the higher field cases, the velocity of the small protuberance at the expected location of the jet is comparable at the more well-developed long narrow jets observed in the high-field cases. The bulk plasma leading edge velocity appears to be only slightly reduced compared with the long narrow jet velocity. No jet formation is observed at the lowest magnetic field (1 kG).

IV. PLASMA PROPAGATION ACROSS THE MAGNETIC FIELD

Plasma propagation into and across strong transverse magnetic fields has been the subject of many experimental and theoretical investigations in both space and laboratory plasmas.^{18–39} Plasma expansion across a magnetic field occurs in both the diamagnetic and nondiamagnetic limits. In the diamagnetic limit, an expanding high- β plasma ($m n V^2 \gg B^2/4\pi$) effectively displaces the magnetic field from its volume, bending the field lines in the process. The plasma expansion continues until it reaches the magnetic stagnation point, where the displaced magnetic energy is approximately equal to the kinetic energy of the plasma expansion.^{20,21,25,33} In the nondiamagnetic limit, the magnetic field is able to diffuse into the plasma on time scales short compared with the relevant experimental time scale.

Cross-field propagation of a plasma mass can proceed due to the formation of a polarization electric field that causes a bulk plasma $E \times B$ drift. In the simplest model, the initial plasma mass can be considered as a rectangular slab

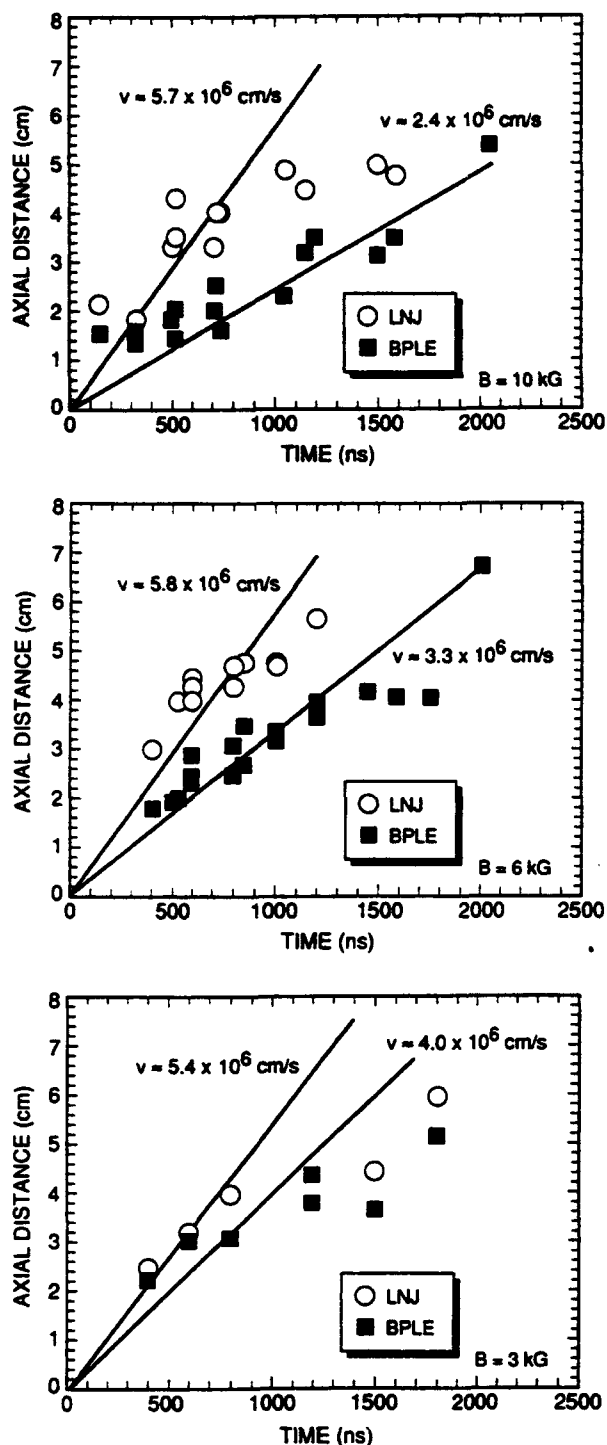


FIG. 7. Time evolution of the long narrow jets (LNJ) and the bulk plasma leading edge (BPLE) for applied magnetic fields of 3, 6, and 10 kG. The long narrow jets appear to propagate across the magnetic field lines (along the cylinder axis) at a velocity approximately equal to 5.5×10^6 cm/sec comparable to the peak zero-field axial expansion velocity. Behind the jets, the leading edge of the remaining bulk plasma expands at reduced velocities, depending on the applied magnetic field. The bulk plasma leading edge velocity is reduced to about 2.5×10^6 cm/sec at 10 kG, 3.3×10^6 cm/sec at 6 kG, and 4.0×10^6 cm/sec at $B = 3$ kG.

moving at a velocity V normal to the magnetic field.^{18,24} The action of the Lorentz force on the ions and electrons in the plasma leads to a charge separation and to a polariza-

tion of the plasma, giving rise to an internal electric field satisfying the equation

$$E + (1/c)V \times B = 0. \quad (1)$$

The plasma is then able to continue moving across the transverse magnetic field at the $E \times B$ velocity given by

$$V = E \times B / B^2, \quad (2)$$

that is, at nearly its initial velocity.

Both the density and the velocity are important in determining the cross-field propagation dynamics of the plasma. In the present experiment, the density can be estimated from models of mass ablation rates for incident intensities comparable to those in the present experiment and from simple geometric considerations related to the increase in volume of an expanding sphere or cylinder of plasma at a given velocity for a given time. Using the experimental mass ablation scaling $dm/dt \propto I^{0.6}$ found by Grun *et al.*,¹⁷ assuming a velocity on the order of 5×10^6 cm/sec, and taking silicon as the principal atomic constituent, the density ranges from 3×10^{19} cm⁻³ at early times ($t \approx 10$ nsec) to 2×10^{14} cm⁻³ at later times ($t \approx 500$ nsec). The directed- β ($4\pi mnV^2/B^2$) in the present experiment thus depends not only on the value of the applied field, but also on the change in both density and velocity in time. At $t \approx 250$ nsec into the expansion, the density is on the order of 2×10^{15} cm⁻³, hence the directed β goes from $\beta = 30$ for the low-field $B = 1$ kG to $\beta = 0.30$ for the high-field $B = 10$ kG. In view of the fact, however, that both the density and the velocity in the present experiments are rapidly changing functions of space and time, the directed plasma β will also be a highly dynamic quantity, and may vary considerably over the duration of the expansion at a given applied magnetic field.

The plasma β per se is not the only factor governing the nature of the expansion. The degree of magnetic field penetration into or exclusion from the expanding plasma does not depend on the plasma β alone. The diffusion of the magnetic field into the plasma, as determined by the plasma temperature and other transport parameters, may be equally important in permitting cross-field propagation to occur by $E \times B$ drifts. The magnetic diffusion time,

$$\tau = (4\pi/\eta)L^2/c^2, \quad (3)$$

depends both on the plasma resistivity η and the density scale length L . The expansion dynamics may be determined when the plasma first exits the collimating cylinder. The maximum spatial extent of the plasma 10 nsec after the laser is incident on the target is on the order of 1 mm or less. The scale length for magnetic diffusion may be as little as 100 μ m at this time. Assuming classical Spitzer resistivity at an initial electron temperature of 100 eV, the diffusion time is on the order of 25 nsec. Hence the initial plasma expansion from the cylinder ends is permeated by the magnetic field from very early times. Since the initial expansion occurs primarily in the axial direction due to the effects of the presence of the cylinder, the induced electric field is in the transverse direction to both the applied magnetic field and the initial flow velocity. Collimation effects

on the expanding plasma are apparent on the framing camera photographs as early as 150 nsec after the laser incident on the target.

We have seen that the long narrow jet velocity remains approximately constant for all applied magnetic fields at about 5.5×10^6 cm/sec—approximately the initial maximum plasma velocity from the cylinder ends. This is consistent with the velocity preserving $E \times B$ cross-field drift mechanism discussed above. The long narrow jet geometry results from focusing of the ablation plasma front toward the axis as it propagates across the magnetic field. The focusing long narrow jets have the same appearance, as observed in low- β cross-field $E \times B$ propagation experiments described in Ref. 12. There, the focusing is caused by the $E \times B$ force from small axial components of the polarization electric field that naturally arise from the curvature of the plasma boundary and the axial velocity gradient. The focusing mechanism that causes the long narrow jet features in these (higher- β) experiments is likely the same as in the low- β cases, since the same arguments apply. There is some magnetic field penetration into the plasma boundary, even though we are dealing with high- β cases, due to the diffusion, which allows an inward (focusing) $E \times B$ body force on the boundary-layer plasma.

The bulk plasma velocity is less than the field-free ablation velocity and is a decreasing function of the applied magnetic field, as indicated in Fig. 7. For the 10 kG case, the directed velocity is reduced almost twofold compared to the 1 kG case. The bulk plasma propagates close to a constant velocity for a given magnetic field, but at a reduced velocity compared with the long narrow jets. The bulk plasma mass speed is close enough, however, to the jet speed that both most likely originate in the ablation plasma. The bulk plasma has lost more of its directed energy component than the jet plasma. The bulk plasma behavior observed may be related to the increase in magnetic diffusion time as the plasma dimension and magnetic field diffusion scale length increase. A more rapid magnetic field diffusion in the long narrow jets and edge region than in the bulk plasma could explain the different properties of the jets and bulk plasma, respectively. A rapid magnetic field penetration in the jets permits motion across the magnetic field at the initial ejection velocity via the $E \times B$ drift, as discussed above. The slower diffusion of the magnetic field into the bulk plasma, however, would result in a lower $E \times B$ drift due to reduced internal field strengths.

The data show only that the bulk plasma expansion velocity decreases at increased applied magnetic fields. Given the otherwise fixed velocity of the long narrow jets at all magnetic fields strengths, it is this difference in the long narrow jet velocity and the bulk plasma velocity that produces the dramatic elongated structures seen at the higher magnetic fields.

It is not possible on the basis of framing camera photographs alone to provide a definitive explanation of the difference between the long narrow jet and bulk plasma propagation. Direct measurement in future experiments of the magnetic field in the jet and bulk plasma regions of the plasma would be helpful in elucidating the differences be-

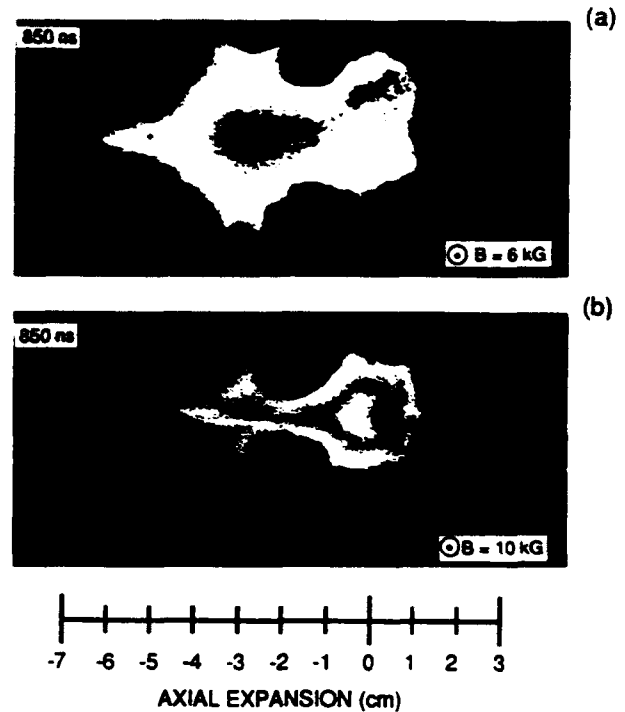


FIG. 8. GOI photographs of plasma expansion from a closed cylindrical target with the laser beam incident from left, showing dramatic vortex structure and rollup: (a) 6 kG magnetic field at 850 nsec with a 1 nsec exposure; (b) 10 kG magnetic field at 850 nsec with 1 nsec exposure.

tween the two phenomena. The use of simple magnetic probes and diamagnetic loops in laser-plasma expansion experiments is complicated by the perturbations introduced in the flow dynamics by the probes themselves. Non-perturbative space- and time-resolved optical magnetic-field measurements using Faraday rotation techniques, such as that reported recently by Dimonte and Wiley, would be more appropriate for the present experiment.³⁹

V. EDGE INSTABILITY

The instability observed in the present experiment consist of "bumps and wiggles" with a 3–5 mm wavelength occurring primarily on the edges of the bulk plasma expansion. The earliest time these are observed varies from 600 to 1200 nsec depending on the magnetic field strength. In the standard open cylinder targets used for most of the experiment, the instability amplitude appears to stop growing approximately 200–300 nsec after initial observation and saturate at ≈ 5 mm amplitude (peak to valley). At still later times, the instability amplitudes decrease below the level of the instrument resolution (typically 100 μ m). In the case of cylindrical targets in which the end opposite to the incident laser was closed by means of an epoxy plug, the onset of the instability occurs at an earlier time and grows with larger amplitude. In both the open- and plugged-cylinder targets, the instability exhibits a vortex-like rollup characteristic of transverse flow-driven shear instabilities. This vortex structure is especially pronounced in the closed targets, as shown in Figs. 8(a) and 8(b).

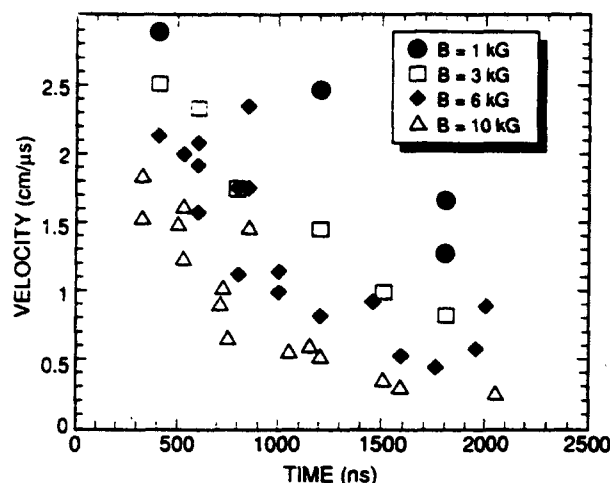


FIG. 9. Transverse velocity of expanding plasma at the location of a structuring instability for $B=1, 3, 6$, and 10 kG from which the plasma deceleration can be derived.

There are three candidates for the mechanism driving the observed instability: the Rayleigh–Taylor instability, the Kelvin–Helmholtz instability, and a lower-hybrid, non-local velocity-shear instability. The first two instabilities are the well-known and extensively studied classical hydrodynamic instabilities. In the present experiment, the observed instability has a vortex or eddy structure, and does not appear to have the classic spike and bubble morphology usually associated with Rayleigh–Taylor. The presence of a strong velocity field in conjunction with magnetic interchange could, however, produce vortexlike structures similar to the classical Kelvin–Helmholtz instability. It is therefore useful to make a rudimentary comparison of the relevant growth rates for each of the two instabilities.

The classical Rayleigh–Taylor growth rate λ_{RT} for a plasma decelerated by a magnetic field in the short-wavelength limit ($kL_n > 1$) is given by

$$\lambda_{RT} \propto (g_{eff}/L_n)^{-1/2}, \quad (4)$$

where g_{eff} is the effective deceleration due to the magnetic field and L_n is the density scale length. In principle, the effective deceleration can be estimated by equating the plasma kinetic energy decrease to the excluded magnetic field energy in the volume. Assuming a radial expansion at each cylinder end,

$$g_{eff}(t) = B^2 R^2(t) / 2m_0,$$

where $R(t)$ is the radius of the plasma expansion and m_0 is the total plasma blob mass. The plasma mass (i.e., the plasma that undergoes both the cross-field propagation and the structuring instability) could not be reliably determined with the diagnostics available on the experiment. However, the magnetic deceleration can be obtained directly from the GOI photographic data. Figure 9 gives the transverse velocity of the expanding plasma at the location of the structuring instability as a function of time for all four magnetic field strengths (1, 3, 6, and 10 kG). Linear fits to the data give decelerations $g_{eff} = 2.0 \times 10^{12}$ cm/sec²

for the 10 kG magnetic field and $g_{eff} = 1.5 \times 10^{12}$ cm/sec² for the 6 kG magnetic field. The Rayleigh–Taylor growth time, i.e., the inverse of the growth rate given by Eq. (4) above, corresponding to these decelerations for a scale length L_n of 5 mm, is on the order of 2–3 μ sec; this is much larger than the entire duration of the experiment, and hence classical Rayleigh–Taylor is not strong enough to be important here.

Large Larmor radius versions of the Rayleigh–Taylor instability are predicted theoretically to proceed on faster time scales than the classical (small Larmor radius) Rayleigh–Taylor instability.^{36,37} There are two Larmor radii that are relevant here—the thermal Larmor radius r_{LT} given by v_{Ti}/ω_{ci} and the directed Larmor radius r_{LD} given by V/ω_{ci} where v_{Ti} is the ion thermal speed, V is the plasma flow velocity, and ω_{ci} is the ion cyclotron frequency. Assuming singly ionized silicon ($Z=1$) and ion temperatures of 10 eV (consistent with the later time spectroscopic observations), the thermal Larmor radius in the present experiment is approximately 5.7 mm for $B=3$ kG, 2.8 mm for $B=6$ kG, and 1.7 mm for $B=10$ kG. This is comparable to the density scale length (≈ 5 mm) and small relative to the expansion radius. The directed Larmor radius for $V=2 \times 10^6$ cm/sec and $B=10$ kG is somewhat larger, $r_{LD} \approx 5.8$ mm, but is still comparable to the scale length. The most important condition for the large Larmor interchange instability is that the Larmor radius be large compared with the density scale length of the expanding plasma. This is not clearly satisfied in the present experiment, using either the thermal or directed velocity. The onset criterion for the instability is $\gamma_0 > \omega_{ci}$ where $\gamma_0 \approx (g_{eff}/L_n)^{1/2}$ is the maximum growth rate of the instability.^{36,37} Using the experimental value for g_{eff} and assuming $L_n \approx 5$ mm, this criterion is similarly not satisfied. Smaller values of L_n make γ_0 comparable to ω_{ci} but there are additional reasons why the observed instability is unlikely to be the large Larmor interchange instability. These include the restriction of the instability to the edges of the plasma, the apparent saturation of the instability after several hundred nanoseconds and the lack of bifurcated structures, which are all in contrast with observations made of the instability from a planar target in an applied magnetic field.^{26,27}

The Kelvin–Helmholtz instability depends on the free energy in a velocity shear layer and does not require a transverse deceleration of the plasma. The vortex rollup feature of the Kelvin–Helmholtz instability (and any transverse flow-driven velocity shear instability) is an important signature, although, as noted above, it can be mimicked by interchange instabilities in the presence of velocity fields. The growth rate of the instability is more relevant, and definitive, for identifying the nature of the instability. The classical Kelvin–Helmholtz instability is characterized by a velocity shear length L_v greater than the Larmor radius ρ_i (i.e., ions are magnetized) and a wavelength parallel to the flow (or transverse to the applied field) greater than the shear scale length (i.e., $k_y L_v \approx 1$, $k_y = 2\pi/\lambda_y$). This instability is driven by the gradient in the transverse flow shear on the ions, i.e., $d^2 V_E / dx^2$, where V_E is the velocity of the

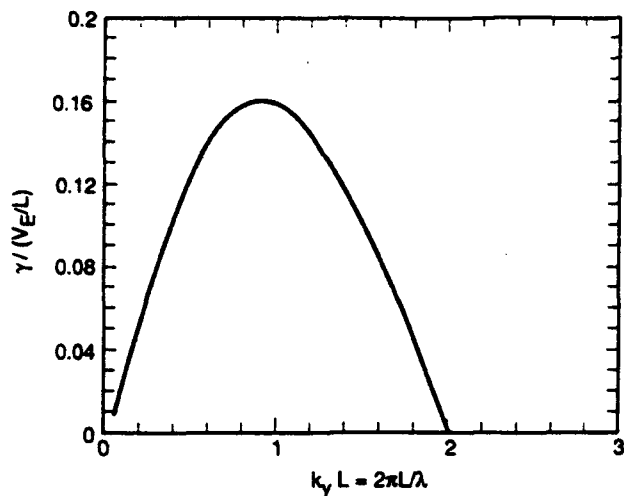


FIG. 10. The Kelvin-Helmholtz growth rate obtained from numerical analysis with velocity profile $V_E = V_0 \text{sech}^2(x/L_v)$.

edge layer and x is the direction transverse to both the flow and the magnetic field. The electrons do not play a major role. We assume a profile, given by

$$V_E(x) = V_E^0 \text{sech}^2(x/L_v). \quad (5)$$

The differential equation for the Kelvin-Helmholtz dispersion relation can then be solved numerically,

$$\left(\frac{d^2}{dx^2} - k_y^2 + \frac{k_y V_E''(x)}{\omega - k_y V_E(x)} \right) \Phi = 0, \quad (6)$$

where the magnetic field is in the z direction, the nonuniform cross-field flow V_E is in the y direction, while the dominant inhomogeneity is in the x direction. The growth rate for classical Kelvin-Helmholtz γ_{KH} is shown in Fig. 10.

The relevant velocity for estimating the growth rate of the shear-driven instability in the present experiments, the edge velocity (V_E) can be obtained from the mean velocity of the plasma expansion at the approximate location of the observed instability. The shear length similarly can be estimated from the thickness of the edge layer itself. Table I gives a tabulation of the edge velocity (V_E), shear scale length (L_v), the thermal Larmor radius (ρ_{iT}), the ratio of edge velocity to shear scale length or the shear frequency

(V_E/L_v), and a maximum growth time (τ_{KH}) for a number of experimental conditions. Figure 10 indicates that the maximum Kelvin-Helmholtz growth rate occurs for $k_y L_v \approx 1$, and the corresponding growth time can be obtained from

$$\tau_{KH} = \frac{2\pi}{\gamma} = \frac{2\pi}{0.16(V_E/L_v)}. \quad (7)$$

The growth time, therefore, for the first of the 10 kG shots listed in Table I with an edge velocity V_E of 2.2×10^6 cm/sec and a velocity shear scale length $L_v \approx 1.5$ mm is $\tau_{KH} = 2.6 \mu\text{sec}$; this is also longer than the experiment duration and therefore not in agreement with the observed onset times. A slightly higher growth rate can be obtained by taking the maximum plasma velocity rather than the mean edge velocity, $V_E \approx 4.4 \times 10^6$ cm/sec, but it still gives a growth time far in excess of the experiment duration. If we assume that a minimum of 3–5 e -foldings are needed for the instability amplitudes to become large enough for observation, then we need a growth time $\tau \approx 100$ –300 nsec, as opposed to microseconds, as estimated above.

While the classical Kelvin-Helmholtz has a growth rate far too small to account for the observed instability, there are both fluid and kinetic treatments of a modified version of the Kelvin-Helmholtz instability with appreciably larger growth rates. Ganguli *et al.*^{7,40,41} and Nishikawa *et al.*^{42,43} have developed a kinetic theory that predicts the existence of a faster growing velocity-shear-driven instabilities in the limit of large or comparable ion Larmor radius relative to the velocity shear scale length. There is also a fluid treatment of the Kelvin-Helmholtz instability in the limit of large Larmor radius that predicts the existence of a faster growing instability mode, albeit with a growth rate at the ion cyclotron frequency Ω_i —considerably slower than required to explain the structure seen in the present experiment.⁴⁴

Ganguli *et al.*⁷ assume unmagnetized ions and magnetized electrons, and then write the Poisson equation as a dispersion relation of exactly the same form as the classical Kelvin-Helmholtz given above,

$$\left(\frac{d^2}{dx^2} - k_y^2 + F(\omega) \frac{k_y V_E''(x)}{\omega - k_y V_E(x)} \right) \Phi = 0, \quad (8)$$

TABLE I. Plasma expansion parameters required for calculation of classical Kelvin-Helmholtz growth rates, including the edge velocity (V_E), shear scale length (L_v), thermal Larmor radius (ρ_{iT}), ratio of edge velocity to shear scale length or the shear frequency (V_E/L_v), and maximum growth time (τ_{KH}). The figure numbers in column one identify the GOI images used for these calculations. The growth rate τ_{KH}^{-1} for classical Kelvin-Helmholtz is far too small to account for the observed instability.

Figure	(B) (kG)	ρ_{iT} (mm)	V_E (cm/ μsec)	L_v (mm)	V_E/L_v (MHz)	τ_{KH} (μsec)	Target
3(b)	10	1.7	2.20	1.5	14.67	2.67	open
3(a)	10	1.7	2.00	1.5	13.33	2.95	open
4(b)	6	2.8	2.00	3.0	6.67	5.89	open
5(b)	3	5.7	2.00	6.0	3.33	11.79	open
8(b)	10	1.7	3.5	1.5	14.0	2.80	plug
8(a)	6	2.8	3.50	2.5	23.33	1.68	plug

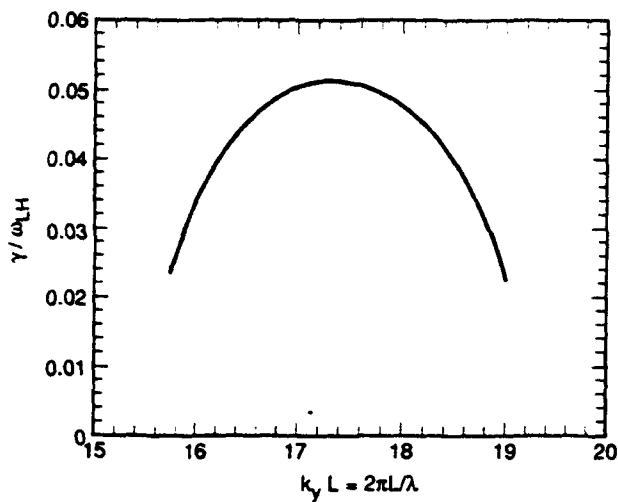


FIG. 11. Electron-ion hybrid growth rate obtained from numerical analysis for silicon with an electron-ion mass ratio of 5.125×10^4 and velocity shear parameter $\alpha \approx 10^{-4}$.

where $F(\omega) = \delta^2 / \{(\delta^2 + 1)[1 - (\omega_{LH}/\omega)^2]\}$, $\delta = \omega_{pe}/\Omega_e$, and $\omega_{LH} = \omega_{pe}\Omega_e/(\omega_{pe}^2 + \Omega_e^2)^{1/2}$ is the lower-hybrid frequency. The important difference in this dispersion condition, as compared with classical Kelvin-Helmholtz, is that there is an additional resonance at $\omega = \omega_{LH}$ that is introduced via $F(\omega)$. This mode is driven by the gradient of the transverse flow shear of the electrons, but unlike the classical Kelvin-Helmholtz instability here the other species, the ions, play an important role by introducing the resonance around the lower-hybrid frequency. Furthermore, unlike the classical Kelvin-Helmholtz, this instability is sensitive to the ion to electron mass ratio and is characterized by a higher frequency and shorter wavelength than the Kelvin-Helmholtz instability. A recent detailed analysis of this instability indicates that it is not stabilized by sharp density gradients and does not require a net cross-field current.⁴⁵

This equation can be evaluated numerically, as shown in Fig. 11, for conditions similar to those in our experiment, namely $\delta = \omega_{pe}/\Omega_e \approx 5$ and $\alpha = V_E/L_e\Omega_e \approx 1-2.5 \times 10^{-4}$, where V_E is the maximum flow velocity, L_e is the shear scale length, and Ω_e is the electron cyclotron frequency. The parameter α is a measure of the magnitude of the velocity shear—larger values of α imply stronger instability. In addition, we have used the electron to ion mass ratio for silicon, namely $m_e/28m_p \approx 5.152 \times 10^4$, where m_e is the electron mass and m_p is the proton mass. The growth rate for the electron-ion hybrid instability for $\alpha \approx 10^{-4}$ is $\gamma = 0.05\omega_{LH}$ from Fig. 11. At applied magnetic fields of 10 kG and densities on the order of 10^{14} cm^{-3} , characteristic of the time in the expansion at which the instability is observed, $\omega_{LH} \approx 7.5 \times 10^8 \text{ rad/sec}$. The maximum growth time for the instability according to Fig. 11 is given by

$$\tau = 2\pi/0.05\omega_{LH}, \quad (9)$$

which gives $\tau \approx 170 \text{ nsec}$ for our case. This is in good agreement with the experimental onset times ($t \approx 500-600$

nsec), where again it is assumed that several e-folding times are needed before the instability is observed. The experimental $k_y L_e \approx 12$ is close to the maximum growth rate according to the numerical solution of the dispersion relation above, which gives $k_y L_e \approx 18$. It should be noted here that the theory above is linear and pertains to the conditions at the instability onset that are not directly observable in the present experiment with the available diagnostics. By the time the instability reported here is observed, it is near the fully developed, nonlinear state and hence the shear (i.e., the value of the α parameter) may have already relaxed from its peak value. However, even at this reduced value of α ($\approx 10^{-4}$), the growth rates predicted by the theory are consistent with the experimental data. The observed difference in instability onset time for the different magnetic field strengths is due primarily to the change in the shear parameter α caused by the increase in shear scale lengths at lower applied magnetic fields. Although plasma velocities remain relatively high in the low magnetic field expansions, the lack of sufficient $E \times B$ collimation appears to reduce α below levels required for observation of the instability.

Plugging one end of the cylinder produces dramatic changes in both the expansion parameters and the resulting instability, as seen in Figs. 8(a) and 8(b) and summarized in Table I. The GOI photographs show that the plasma velocity in the plugged cylinder expansions is considerably greater than in the open cylinder expansions. This may be due to differences in the geometry of the thermalization process of the ablation plasma within the two types of targets. The increase in the expansion velocity from the plugged cylinders is especially interesting, in view of the fact that the plasma expansions from the open cylinders did not exhibit any dependence on the incident laser energy. It would be useful in future experiments with the plugged cylindrical targets to decrease the incident laser energy and compare the expansion dynamics with that of the open targets. The instability is also observed to persist to longer times for plasma expansions with the plugged cylinder targets. Finally, there is an increase in either the temperature or density (or both), leading to an increase in the luminous emission compared with the open cylinder plasmas. It should be noted that while the edge velocity has increased by almost a factor of 2, the scale size of the velocity shear either remains of the same order or becomes smaller with the plugged targets, as compared with the open cylinders. The increase in the edge velocity at a given applied magnetic field with the same or reduced shear scale length results in a larger value of the shear parameter α and hence a stronger instability, i.e., a more abundant source of free energy to drive the instability, resulting in earlier onset, greater amplitudes, and longer persistence times.

VI. SUMMARY AND CONCLUSIONS

Laser-produced plasmas from the inside of small, hollow glass cylinders immersed in a magnetic field evolve into plasma structures that are strongly collimated in the direction transverse to the cylinder axis and magnetic field

and jetlike in the direction along the cylinder axis. These jets propagate across the magnetic field at their initial velocity via the mechanism of $E \times B$ drift. Immediately behind the jets, the bulk plasma propagates across the magnetic field, but at a reduced constant velocity, depending on the applied magnetic field. The magnetic field in the edge region of the bulk plasma gives rise to a velocity shear, and the plasma undergoes a dramatic structuring instability. While there are a number of possible explanations for the plasma structure, detailed analysis of the data is in good agreement with the theory of electron-ion hybrid instabilities, especially as regards the growth rates observed in the present experiment. Both the jet structure associated with the cross-field plasma propagation and the structuring instability may be relevant to a range of astrophysical phenomena.

ACKNOWLEDGMENTS

Technical assistance on the experiments was provided by L. Daniels, J. Ford, N. Nocerino, and L. Shirey. The authors wish to extend special thanks to Dr. J. D. Hares of Kentech Instruments, Ltd. for design and construction of the GOI as well as for technical support relating to the instrument, and to E. McLean of the Naval Research Laboratory for his foresight in acquiring the GOI, without which the present work would not have been possible.

This work was supported by the Office of Naval Research and the Defense Nuclear Agency.

- ¹E. Ott and W. M. Mannheimer, Nucl. Fusion 17, 1057 (1977).
- ²D. J. Southwood, Planet. Space Sci. 16, 587 (1968).
- ³*Galactic and Extragalactic Star Formation*, edited by R. Pudritz and M. Fich, NATO ASI Series C (Reidel, Dordrecht, 1988).
- ⁴M. C. Begelman, R. D. Blandford, and M. J. Rees, Rev. Mod. Phys. 56, 255 (1984).
- ⁵J. O. Burns, M. L. Norman, and D. A. Clarke, Science 253, 522 (1991).
- ⁶S. Chandrasekhar, *Hydrodynamic and Hydromagnetic Stability* (Oxford U.P., London, 1961).
- ⁷G. Ganguli, Y. C. Lee, and P. J. Palmadesso, Phys. Fluids 31, 2753 (1988).
- ⁸N. D'Angelo, Phys. Fluids 8, 1748 (1965).
- ⁹D. L. Jassby and F. W. Perkins, Phys. Rev. Lett. 24, 256 (1970).
- ¹⁰G. I. Kent, N. C. Jen, and F. F. Chen, Phys. Fluids 12, 2140 (1969).
- ¹¹J. C. Glowienka, W. C. Jennings, and R. L. Hickok, Phys. Fluids 31, 2704 (1988).
- ¹²A. N. Mostovych, J. A. Stamper, and B. H. Ripin, Phys. Rev. Lett. 62, 2837 (1989).
- ¹³M. S. Pronko, R. H. Lehmberg, S. Obenschain, C. J. Pawley, C. K. Manka, and E. Eckardt, IEEE J. Quantum Electron. QE-26, 337 (1990).
- ¹⁴J. D. Hares, *X-Rays from Laser Plasmas* (SPIE, Bellingham, WA, 1987), Vol. 831, p. 165.
- ¹⁵P. E. Young, J. D. Hares, J. D. Kilkenny, D. W. Phillon, and E. M. Campbell, Rev. Sci. Instrum. 59, 1457 (1988).
- ¹⁶Single and multiframe gated optical imager (GOI) systems are available commercially from Grant Applied Physics, Inc., 2011 Los Angeles Avenue, Berkeley, CA 94707.
- ¹⁷J. Grun, S. P. Obenschain, B. H. Ripin, R. R. Whitlock, E. A. McLean, J. Gardner, M. J. Herbst, and J. A. Stamper, Phys. Fluids 26, 588 (1983).
- ¹⁸G. Schmidt, Phys. Fluids 3, 961 (1960).
- ¹⁹D. A. Baker and J. E. Hammel, Phys. Fluids 8, 713 (1965).
- ²⁰P. D. Markovic and F. R. Scott, Phys. Fluids 14, 1742 (1971).
- ²¹S. Okada, K. Sato, and T. Sekiguchi, Jpn. J. Appl. Phys. 20, 157 (1981).
- ²²G. Jellison and C. R. Parsons, Phys. Fluids 26, 1171 (1983).
- ²³Yu. P. Zakharov, A. M. Orishich, A. G. Ponomarenko, and V. G. Posukh, Sov. J. Plasma Phys. 12, 674 (1987).
- ²⁴J. E. Borovsky, Phys. Fluids 30, 2518 (1987).
- ²⁵M. Galvez, Phys. Fluids 30, 2729 (1987).
- ²⁶B. H. Ripin, E. A. McLean, C. K. Manka, C. Pawley, J. A. Stamper, T. A. Peyser, A. N. Mostovych, J. Grun, A. B. Hassam, and J. Huba, Phys. Rev. Lett. 59, 2299 (1987).
- ²⁷B. H. Ripin, C. K. Manka, T. A. Peyser, E. A. McLean, J. A. Stamper, A. N. Mostovych, K. Kearney, J. R. Crawford, A. B. Hassam, and J. D. Huba, Laser Part. Beams 8, 183 (1990).
- ²⁸M. Galvez and C. Barnes, Phys. Fluids 31, 863 (1988).
- ²⁹M. Galvez and J. E. Borovsky, Phys. Fluids 31, 857 (1988).
- ³⁰M. Galvez, G. Gisler, and C. Barnes, Phys. Fluids B 1, 2516 (1989).
- ³¹F. J. Wessel, R. Hong, J. Song, A. Fisher, N. Rostoker, A. Ron, R. Li, and R. Y. Fan, Phys. Fluids 31, 3778 (1988).
- ³²F. J. Wessel, N. Rostoker, A. Fisher, H. U. Rahman, and J. J. Song, Phys. Fluids B 2, 1467 (1990).
- ³³K. Akimoto, M. Galvez, S. P. Gary, A. G. Sgro, and D. Winske, J. Geomag. Geoelectr. 40, 1161 (1988).
- ³⁴G. Gisler and D. S. Lemons, J. Geophys. Res. 94, 10145 (1989).
- ³⁵E. V. Mishin, R. A. Treumann, and V. Ya. Kapitanov, J. Geophys. Res. 91, 10, 183 (1986).
- ³⁶J. D. Huba, J. G. Lyon, and A. B. Hassam, Phys. Rev. Lett. 59, 2971 (1987).
- ³⁷J. D. Huba, A. B. Hassam, and D. Winske, Phys. Fluids B 2, 1676 (1990).
- ³⁸K. Papadopoulos, A. Mankofsky, R. C. Davidson, and A. T. Drobot, Phys. Fluids B 3, 1075 (1991).
- ³⁹G. Dimonte and L. G. Wiley, Phys. Rev. Lett. 67, 1755 (1991).
- ⁴⁰G. Ganguli, Y. C. Lee, and P. J. Palmadesso, Phys. Fluids 31, 823 (1988).
- ⁴¹G. Ganguli, Y. C. Lee, P. J. Palmadesso, and J. D. Huba, in *Proceedings of 1989 International Conference on Plasma Physics*, New Delhi, India 1989, edited by A. Sen and P. K. Kaw (Indian Academy of Sciences, Bombay, 1991), pp. 197-200 (distributed by Oxford University Press).
- ⁴²K.-I. Nishikawa, G. Ganguli, Y. C. Lee, and P. J. Palmadesso, Phys. Fluids 31, 1568 (1988).
- ⁴³K.-I. Nishikawa, G. Ganguli, Y. C. Lee, and P. J. Palmadesso, J. Geophys. Res. 95, 1029 (1990).
- ⁴⁴E. N. Opp and A. B. Hassam, Phys. Fluids B 3, 885 (1991).
- ⁴⁵H. Romero, G. Ganguli, Y. C. Lee, and P. J. Palmadesso, Phys. Fluids B 4, 1078 (1992).

Appendix HH

Sub-Alfvenic Plasma Expansion

Sub-Alfvénic plasma expansion

B. H. Ripin, J. D. Huba, E. A. McLean, C. K. Manka, T. Peyser,^{a)} H. R. Burris,^{b)} and J. Grun

Plasma Physics Division, Naval Research Laboratory, Washington D.C. 20375-5346

(Received 28 May 1993; accepted 30 June 1993)

A large ion Larmor radius plasma undergoes a particularly robust form of Rayleigh–Taylor instability when sub-Alfvénically expanding into a magnetic field. Results from an experimental study of this instability are reported and compared with theory, notably a magnetohydrodynamic (MHD) treatment that includes the Hall term, a generalized kinetic lower-hybrid drift theory, and with computer simulations. Many theoretical predictions are confirmed while several features remain unexplained. New and unusual features appear in the development of this instability. In the linear stage there is an onset criterion insensitive to the magnetic field, initial density clumping (versus interchange), linear growth rate much higher than in the “classic” MHD regime, and dominant instability wavelength of order of the plasma density scale length. In the nonlinear limit free-streaming flutes, apparent splitting (bifurcation) of flutes, curling of flutes in the electron cyclotron sense, and a highly asymmetric expansion are found. Also examined is the effect on the instability of the following: an ambient background plasma (that adds collisionality and raises the expansion speed/Alfvén speed ratio), magnetic-field line tying, and expansion asymmetries (that promotes plasma cross-field jetting).

I. INTRODUCTION

Plasma expanding into a magnetic field can undergo several forms of the classic Rayleigh–Taylor instability, as depicted in Fig. 1. The Rayleigh–Taylor instability, originally formulated for ordinary fluids,¹ occurs when a heavy fluid is decelerated (or supported) by a less dense fluid; the fluids tend to interchange positions into a lower energy state via classic bubble-and-spike formation. The analogous Rayleigh–Taylor instabilities for a conducting liquid² and magnetohydrodynamic (MHD) plasma³ (heavy fluids) moving across a magnetic field (light fluid) were formulated in the 1950s. MHD theory is applicable to plasmas with Debye lengths and Larmor radii much smaller than any characteristic dimensions and time scales much longer than an ion cyclotron period. The Rayleigh–Taylor growth rates for these MHD fluids are the same as for ordinary fluids with greatly differing densities, namely, $\gamma_{\text{MHD}} = (kg)^{1/2}$ for sharp interfaces and $\gamma_{\text{MHD}} = (g/L_n)^{1/2}$ for interfaces with a density gradient length, $L_n^{-1} = \partial \ln(n)/\partial x$, where $k > L_n^{-1}$. Another way of stating the instability criterion is that the effective acceleration, g , be opposite to the density gradient at the location of the interface between the two fluids. There can be several sources for the adverse acceleration as shown in Fig. 1, although the primary effective g that will concern us in this work is deceleration of the plasma by the excluded magnetic field.

The Rayleigh–Taylor instability (also known as interchange instability) was first observed clearly in a laboratory plasma-gun experiment by Dickinson *et al.*,⁴ and in many of the early magnetic fusion experiments.⁵ When the plasma ion Larmor radius is comparable to the density

gradient length, the Rayleigh–Taylor instability in the MHD regime is predicted to stabilize.⁶ Although there is substantial indirect evidence that finite Larmor radius (FLR) stabilization occurs, there has not been, to our knowledge, direct experimental verification. Curiously, when the ion Larmor radii becomes large compared to L_n (i.e., unmagnetized ions but magnetized electrons), a Rayleigh–Taylor-like instability returns in a particularly robust form.^{7–9} This new regime is the primary focus of this paper. Instability was observed in this regime during the course of the Active Magnetospheric Particle Tracer Experiment (AMPTE) barium-release experiment¹⁰ and in the recent Combined Release and Radiation Effects Satellite (CRRES) magnetospheric barium releases,¹¹ and in laser-produced-plasma experiments.¹² We expand upon the large Larmor radius (LLR) instability study described by Ripin *et al.* in Ref. 12; we point out several new features found in subsequent experiments and extend comparisons with theory and computer calculations.

The paper is organized as follows. We introduce sub-Alfvénic plasma expansion in a magnetic field concepts in the next section. The experimental arrangement and results are then described and the results are compared in detail with theory. Finally, a summary and conclusions are offered.

II. SUB-ALFVÉNIC PLASMA EXPANSION

We review theory relevant to understanding expanding plasma/magnetic field Rayleigh–Taylor instability, particularly in the large ion Larmor radius regime. Most of the results come from the modified MHD treatments of Hassam and Huba⁹ and computer simulations.¹¹ We also point out some features of alternative descriptions such as a gen-

^{a)}Present address: Lawrence Livermore National Laboratory, Livermore, California.

^{b)}Present address: RSI Inc., Alexandria, Virginia.

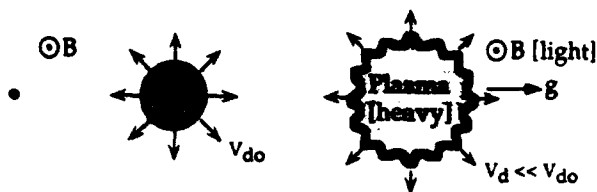


FIG. 1. Rayleigh-Taylor instability of a plasma expanding into a magnetic field. (a) Field aligned plasma flutes appear in the expansion front during deceleration by the magnetic field. Rayleigh-Taylor instability can be driven by radial deceleration, centripetal acceleration, or pressure gradients at plasma boundary (drift instability).

eralized lower-hybrid drift instability¹³ (GLHDI), and others.¹⁴ We begin with estimates of the expansion properties of the bulk plasma.

A. Plasma expansion in a uniform magnetic field

As the plasma expands, it pushes the magnetic field ahead of it because internal diamagnetic currents arise to exclude the field from its interior. The plasmas we consider here are sufficiently conductive that field exclusion should be nearly complete and the collisionless skin depth, c/ω_{pe} , determines the field penetration into the plasma boundary. If, maximum expansion is determined predominantly by the work the plasma does to push the magnetic field out of its volume, then the stopping radius can be simply estimated from conservation of energy relation,

$$E_0 = \frac{1}{2} M V_d^2 + \frac{B^2 \Sigma}{2 \mu_0}, \quad (1)$$

where, Σ is the volume of the excluded field (plasma volume), V_d is the expansion speed ($V_d=0$ at the magnetic confinement radius, R_b), M is the total plasma mass, B is the magnetic field, and E_0 is the total plasma energy. Of course, we are neglecting radiation losses, thermal energy, incomplete field exclusion, internal Ohmic heating losses, etc., here; but, these corrections are small for the plasmas we consider. Assuming spherical symmetry ($\Sigma = 4\pi R_b^3/3$), the nominal magnetic confinement radius obtained from Eq. (1) is

$$R_b = \sqrt[3]{\frac{3 \mu_0 E_0}{2 B_0^2 \pi}}, \quad (2)$$

where B_0 is the initial ambient magnetic field.

The effective gravitational acceleration associated with the plasma deceleration, $g = -dV/dt$, obtained from Eq. (1), is

$$g = -\frac{2\pi B^2 R^2}{\mu_0 M}, \quad (3)$$

where spherical symmetry has again been assumed. Thus, the effective deceleration is proportional to $B^2 R^2$ and the magnetic confinement radius has a $B^{-2/3}$ dependence. The coefficients of Eqs. (2) and (3) are modified in a straightforward way when the expansion is not totally spherically symmetric, as is the case in some of the experiments.

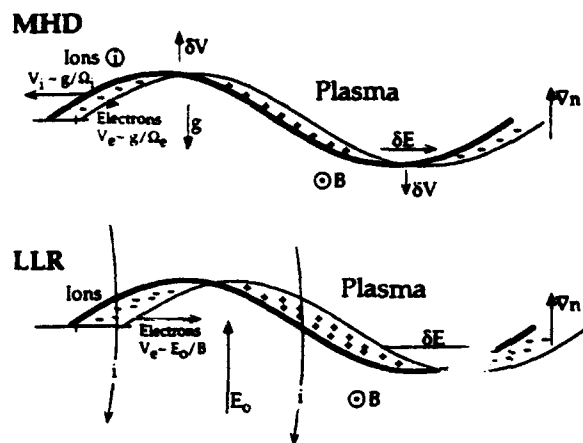


FIG. 2. Models of drift forces driving the growth of the MHD-regime Rayleigh-Taylor instability (top) and LLR-regime Rayleigh-Taylor instability (bottom). Drift motion of the electron population caused by large ambipolar electric fields set up by the energetic ions at the plasma boundary result in a LLR growth rate much higher than the conventional MHD growth rate (which is driven primarily by ion drifts driven by gravitational force).

B. Linear LLR-Rayleigh-Taylor instability theory

A physical picture of forces driving the Rayleigh-Taylor instability is depicted in Fig. 2. The plasma/magnetic field interface perturbations grow in response to electron and ion component drifts, $V_{de,di} = F_{de,di} \times B / q B^2$, induced by forces, $F_{de,di}$, acting on the populations at the unstable interface boundary. The ions and electrons drift in direct response to the effective gravitational force in the conventional MHD-Rayleigh-Taylor instability, indicated in Fig. 2(a). The ion-to-electron drift ratio is large, approximately the mass ratio. The resulting charge separation creates local electric fields, δE , which then drive the perturbation amplitude larger through $\delta E \times B$ drift. In contrast, the large ion Larmor radius situation, shown in Fig. 2(b), has in a similar charge separation and perturbation growth, but driven by a much different mechanism. Here, the electrons are restrained by the magnetic field and "feel" the adverse deceleration, but the unmagnetized ions can stream ahead of the plasma front and create a strong inward-directed electric field, E_0 , at the boundary. The electrons respond to the large $E_0 \times B$ drift, but the ions, being effectively unmagnetized, do not. The resulting force on the perturbations in the LLR limit are in the same sense as that of the MHD regime but are much stronger. This results in a much higher instability growth rate than the conventional MHD-Rayleigh-Taylor. Additionally, the different sources of the driving drifts in the two cases, cause many different instability growth characteristics.

Hassam and Huba⁷ first described this instability using a nonideal MHD treatment that allows terms proportional to ρ/L_n or ω/ω_{ci} to be larger than unity, i.e., the Hall term is included. Their papers should be consulted for details of the derivation. The ion cyclotron frequency is denoted by ω_{ci} and the directed ion Larmor radius by ρ_i . They obtain

a dispersion relation which includes the standard magnetosonic waves and a LLR term (Hall term) that dominates in the large Larmor ($\rho/L_n \gg 1$) or high-frequency ($\omega/\omega_{ci} \gg 1$) limit. In the short wavelength ($kL_n \gg 1$) limit, the Rayleigh-Taylor growth rate becomes,

$$\gamma_{LLR} = kL_n \gamma_{MHD} \quad \text{for } k > L_n^{-1}, \quad (4)$$

where $\gamma_{MHD} = (g/L_n)^{1/2}$ is the usual MHD-Rayleigh-Taylor growth rate. The growth rate increases linearly with wave number k . In the long wavelength ($kL_n \ll 1$) and LLR limits the growth rate is $\gamma \approx (kg/A)^{1/2}$, where A is the Atwood number [$A = (n_2 - n_1)/(n_2 + n_1)$, where the subscripts denote the plasma on either side of the boundary].¹⁵ This growth rate is quite different from the usual MHD growth rate in the long wavelength limit [$\gamma \approx (kgA)^{1/2}$]. One interesting difference is that the instability proceeds at a lower rate for higher gradients (or Atwood number) in the long wavelength limit because in this case more mass is accelerated than for a weaker gradient over the same scale size.

A characteristic of the LLR-instability development distinct from the usual MHD mode is density clumping. Density clumping occurs in the LLR limit because fluid flows are nearly irrotational ($\nabla \times \mathbf{u} \approx 0$) and allow $n \approx \nabla \cdot \mathbf{u}$ flow. Thus, density clumping, rather than pure density/B-field interchanges (as in the usual MHD case, where $\nabla \times \mathbf{u} \neq 0$ and $\nabla \cdot \mathbf{u} = 0$) is the expected action in the LLR-instability development.⁷

Another, interesting property to come out of this LLR treatment is the existence of an onset criterion, which turns out to be independent of magnetic field strength. A delayed, magnetic-field insensitive, onset was originally found in the experiment¹² and subsequently shown to drop naturally out of the dispersion relation.⁹ The onset criterion requires that the growth rate be sufficiently high to overcome the FLR stabilization terms that tend to quench the instability. The requirement for instability onset is

$$\gamma_{MHD} > \omega_{ci}/2, \quad (5)$$

which, using Eq. (3) for g , predicts a magnetic-field independent onset at a critical radius, R_c , expressed by

$$R_c = \sqrt{\frac{L_n M e Z}{2 m_i}}. \quad (6)$$

The criterion for the instability to occur at all is, naturally, that the onset radius, R_c , be smaller than the magnetic confinement radius, R_b , given by Eq. (2). Thus, the LLR instability will not appear if the total plasma energy content is too low, below a critical energy E_c given by

$$E_c = R_c^3 B_0^2 / 2. \quad (7)$$

C. Generalized lower-hybrid-drift instability approach

The initial theory of the LLR instability was based upon Hall MHD theory.^{7,9} However, a number of kinetic calculations have since been performed.^{13,16} The most detailed kinetic calculation is given by Huba *et al.*¹³ In addition to plasma drift caused by the gravitational acceleration ($V_g = g/\omega_{ci}$), the kinetic treatments include the

diamagnetic drift ($V_{di} = cT/eBL_n$) and the Pederson drift [$V_p = (v_{in}/\omega_{ci})V_n$, where v_{in} is the ion-neutral collision frequency and V_n is the neutral flow velocity]. Because of its similarity to the lower-hybrid-drift instability (driven by V_{di}), the LLR instability has been referred to as the generalized lower-hybrid-drift instability.¹⁶ The theory also included finite- β effects, collisional effects, and neutral flows. The major differences between kinetic theory and fluid theory are the following: First, the kinetic treatment predicts the maximum linear growth rate at $k\rho_{ei} \approx O(1)$, where the thermal electron Larmor radius is given by $\rho_{ei} = (T_e/m_i)^{1/2}/\omega_{ci}$; this is a finite electron Larmor radius effect that is not included in the fluid theory. Second, the instability is driven by an ion-wave resonance (i.e., inverse Landau damping) in the weak drift regime ($V_g < v_{ti}$ and $V_d < v_{ti}$, where v_{ti} is the ion-thermal velocity); again, an effect not included in fluid theory.

D. Collisional limit

The effect of collisions on the LLR instability is discussed in detail in Huba *et al.*¹³ They find that electron collisions ($\nu_e = \nu_{ei} + \nu_{en}$, where ν_{ei} is the electron-ion collision frequency and ν_{en} is the electron-neutral collision frequency) are stabilizing. This is primarily a diffusion effect which smoothes out density perturbations; a damping term is introduced $\propto k^2 D_e$, where $D_e = \nu_e \rho_e^2$ is the electron diffusion coefficient. The effect of ion-neutral collisions on the instability depends upon ion temperature. In the cold ion limit (i.e., when $V_g > v_{ti}$; the fluid limit), ion-neutral collisions are stabilizing. In the strong collisional ($\nu_{in} \gg \omega$), low-frequency limit ($\omega \ll \omega_{lh}$, where ω_{lh} is the lower-hybrid frequency) the growth rate is $\gamma \approx k^2 g L_n / \nu_{in}$ where it is also assumed that $\omega_{lh}^2 \gg \nu_{in} \omega$ and $\nu_{in} \gg k L_n \omega_{ci}$. However, in the warm ion limit (i.e., where $V_g < v_{ti}$; the kinetic limit), ion-neutral collisions are destabilizing. The reason for this is as follows. In the weak drift regime the instability is driven by inverse Landau damping of the ions in the presence of a negative energy wave; ion dissipation provided by the ion Landau resonance causes the wave to grow. Ion-neutral collisions provide an additional dissipation mechanism, and thus, enhance the growth rate of the instability.

E. Nonlinear LLR-Rayleigh-Taylor computer simulations

Computer simulations have been primarily used to follow the instability development into the nonlinear regime,^{8,11,16-20} although some analytic theory was reported in Ref. 19. The first nonlinear simulations of the Rayleigh-Taylor instability in the large Larmor radius limit were reported in Huba *et al.*⁸ It is evident that the basic character of the LLR instability is quite different from the usual MHD-Rayleigh-Taylor instability in the nonlinear regime. Simulations of the laser experiments presented here are based upon a two-dimensional (2-D) MHD code which includes the Hall term. Details of the code structure, its limitations for describing the three-dimensional (3-D) problem, and its initialization for these

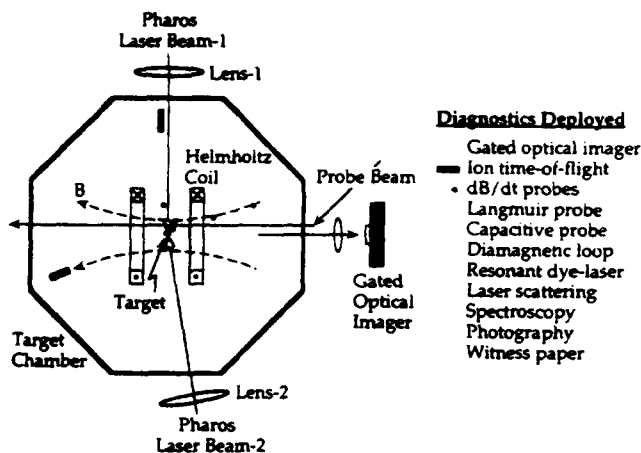


FIG. 3. Experimental arrangement for instability studies. Ion time-of-flight detectors (rectangles), B , capacitance, and Langmuir probes (circles) are deployed various distances from the target position.

simulations are described in the Appendix. Specific results from the simulations will be described later in the paper in the experimental context.

III. EXPERIMENT

The large Larmor radius regime is easily accessed by using an energetic laser-produced plasma which expands radially outward into a uniform magnetic region in an evacuated chamber. These experiments are extensions of those first reported by Ripin *et al.*¹² in 1987. There have been several previous laser-produced-plasma expansion experiments in a magnetic field,²¹⁻²⁹ but, most of these were in different regimes or did not focus on the present instability.

A schematic of the experimental arrangement is shown in Fig. 3. The plasma is formed by placing a small (typically, $2\text{ }\mu\text{m}$ thick, 0.3 to 1 mm diameter) Al disk target in the focal region of one or two beams of the Pharos III Nd laser. Each laser beam is focused to give an intensity of about $5 \times 10^{12}\text{ W/cm}^2$ yielding a plasma with an expansion speed of $5.4 \pm 1.8 \times 10^7\text{ cm/sec}$, $Z \approx 10$, and a total mass of about $0.2\text{ }\mu\text{g}$ for a typical 30 J , 3.5 nsec duration, incident laser pulse. When two beams are used to form a more symmetric expansion, they simultaneously strike the disk target from opposite sides. In most cases the target chamber is evacuated to pressures below 0.1 mTorr to ensure that the dominant plasma interaction is with the magnetic field and not through collisions. Additionally, we choose parameters to be in a low expansion-velocity/Alfvén-velocity ratio regime, i.e., $V_e/V_A \ll 1$. In some experiments described later, we relax these conditions by adding hydrogen gas up to 2 Torr pressure to look for collisional and $V_e/V_A \sim 1$ effects. A more complete description of the experimental arrangement, the expansion plasma, and its use in other experiments can be found in Refs. 30-33.

A uniform magnetic field up to 11 kG in the interaction region is provided by a 25 cm interior diameter pair of Helmholtz coils. The coil current is pulsed on with a 16

msec quarter-period rise time and is essentially steady state on the time scale of the laser-pulse (3.5 nsec) and expansion/instability dynamics ($< 1\text{ }\mu\text{sec}$).

Several diagnostics are used to measure the properties of the initial plasma and the development of the plasma/magnetic-field expansion and instability dynamics. The primary diagnostic in this experiment is the gated optical imager (GOI) used to image the plasma during the expansion. The GOI camera's optical system consists of a lens which focuses a demagnified (2.5 to 6 times) image of the plasma onto the S25 photocathode of a Grant Applied Physics fast-gated microchannel-plate optical imager. Although capable of shutter times as short as 120 psec , we typically set the shutter times at 1 – 2 nsec due to the low levels of emitted light from the plasma. The viewing direction in most of the experiments was either parallel or antiparallel to the magnetic field as sketched in Fig. 3. The plasma was viewed perpendicular to the magnetic field in some experiments. Several time-of-flight ion charge collectors, positioned about 50 cm from the target, were used to measure the velocity distribution of the expansion plasma in the absence of magnetic field or plasma flowing along the applied magnetic field.

Arrays of small (1 mm) induction loops were located at various positions to measure the magnetic field dynamics in the expanding plasma and magnetic field front. Langmuir and capacitive probes were used to measure the plasma front density profiles and electromagnetic noise; a large diamagnetic loop measured the electrical conductivity of the expanding plasma was used to infer the average plasma temperature. Several lens/fiber-optic/spectrometer detectors were arranged to detect plasma light emission at various distances from the target. These provided spectrally and (sometimes) temporally resolved information about the plasma front conditions. Open-frame photography and plasma witness plates also provided qualitative time-integrated information.

A. Plasma expansion conditions

We now describe the laser-produced plasma employed in these experiments. The initially hot (500 – 1000 eV) but small ($< 1\text{ mm}$) laser-produced plasma evolves into a self-similar expansion within a couple of millimeters from the target.³⁴ In the absence of collisions with residual gas in the chamber, ions recoup over 90% of the total plasma energy in directed kinetic energy and have frozen-in high-charge states ($Z=10$ for Al). Computer simulations indicate that the electron temperature is in the few-eV range at 3 cm radius.³⁵ Diamagnetic loop measurements of the plasma resistivity with a 100 G magnetic field are consistent with electron temperatures of 1 to 2 eV , assuming the ions have charge $Z=10$.³⁶ The velocity distribution, spread, and angular distribution of mass and energy is typical of ablation plasmas measured previously.^{32,37} Single-sided planar target irradiations that are wider than the focal spot and thick compared to the ablation depth results in half the incident laser energy contained in the plasma within $\alpha \pm 40^\circ$ cone angle about the target normal. Double-sided irradiations of small limited-mass targets, on the other hand, create a

TABLE I. Parameters for a representative 30 J, 0.3 T single-sided experiment. All these parameters were varied widely during the full course of the experimental series.

Laser parameters		
Energy	E_i	30 J
Pulse duration	τ_i	3.5 nsec
Focal spot diameter	$2r_i$	300 μm
Irradiance	I_0	5×10^{12} W/cm ²
Plasma parameters		
Magnetic field	B_0	3.0 kG
Plasma expansion velocity	V_{∞}	6.2×10^7 cm/sec
Mass of plasma	M	0.2 μg
Ion specie	A, Z	Aluminum
Magnetic confinement radius	R_b	6.2 cm (at 3 kG)
Directed ion larmor radius	ρ_i	6.0 cm
Density scale length (at plasma edge)	L_n	1.0 cm
LLR critical radius	R_c	1.2–3.0 cm
LLR-instability growth time	τ	≈ 10 nsec
Dimensionless ratios		
Larmor radius/confinement radius	ρ_i/R_b	1.0
Critical radius/confinement radius	R_c/R_b	0.2
(c/ω_{pi}) /confinement radius	$(c/\omega_{pi})/R_b$	0.2
Density scale length/confinement radius	L_n/R_b	0.2

more nearly 4π -steradian uniform expansion. Extensive previous studies of ablation plasmas have shown the following parametric dependencies for the plasma speed, $V_{\infty} = V_0(I/I_0)^{0.2}$, and mass ablation rate, $\dot{M} = \dot{M}_0(I/I_0)^{0.6}$, where V_0 is 6.2×10^7 cm/sec, \dot{M}_0 is 7×10^6 g/sec cm², I_0 is 10^{13} W/cm² ($I_0 = E_0/\text{focal-spot area-pulse duration}$).³² Thus, it is possible to independently vary the plasma mass and directed expansion velocity by using various combinations of incident energy and focal-spot diameter. The ion velocity spread can also be independently varied,³⁴ but this was not done in this series of experiments.

As the plasma expands, its density falls and it cools adiabatically. Table I lists approximate parameters for the most frequent type of shot in this study, i.e., 30 J, single-sided irradiation. The plasma density is estimated by using the known total mass of the ablation plasma, its angular distribution and width of the expansion shell. The estimate is relatively insensitive to the mass distribution within the central portion of the plasma shell due to the R^3 dependence of the volume. The plasma ion density is of the order of 10^{15} /cm³ when the expansion front is 3 cm from the origin and electron density is about an order of magnitude higher (assuming $Z=10$). At early times in the expansion when R is small with respect to the magnetic containment radius, R_b , the magnetic field influence is weak and zero-field parameters are valid.

Most of the optical plasma light emitted and detected in our experiment is from a family of Al II and Al III lines. At first blush this appears inconsistent with our assertion that the predominant ionization state is $Z=10$. However, even at our relatively low chamber pressures, a small portion of the target plasma encounters enough charge exchange collisions to end up in low Z states. Indeed, when the background pressure is lowered/raised, the optical sig-

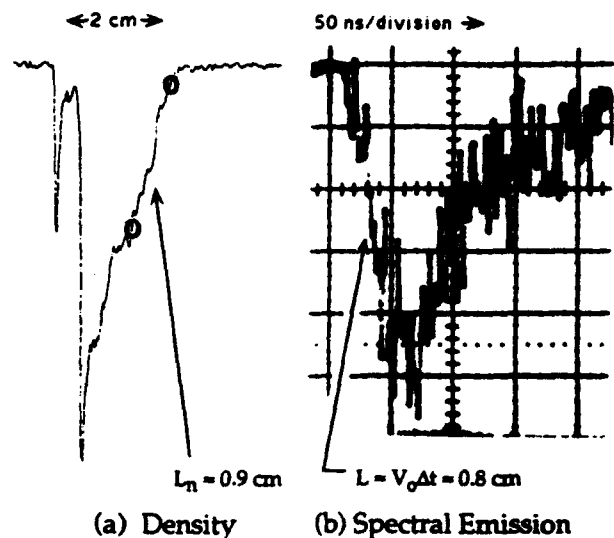


FIG. 4. Plasma front density-gradient measurements at $R=3$ cm. (a) Densitometer trace of plasma emission taken with the gated optical imager. (b) Rise time of Al III spectral line detected with the fiber-optic detector.

nal decreases/increases in concert. We believe that these ions are following the dynamics of the bulk plasma because of the consistency with other independent measurements, such as dB/dt probes, Langmuir probes, and ion detectors.

The density gradient, L_n , at the plasma-magnetic-field interface is a particularly important parameter because it appears to determine the dominant instability wavelength. L_n was measured three ways and was found to be $L_n = 1.0 \pm 0.3$ cm. One method to obtain L_n came from densitometering the leading edge of the plasma front observed in the optical framing images recorded on Tri-X film; Fig. 4(a) is such an example at $R=3$ cm, $B=0.5$ T. The second method used to measure the density gradient is from the rise time of the fiber-optic signals detecting the plasma front as it passes by the observation radius; Fig. 4(b) shows an example of this. The third method used to estimate L_n is inferred from the magnetic-field exclusion gradient, L_b , as measured with loop dB/dt signals; these are also in the 1 cm range [see Fig. 5(a) for example]. The magnetic-field diffusion length in the plasma front is assumed to be nearly equal to L_n since they are in approximate pressure balance. All three methods for obtaining L_n agree within experimental error.

B. Magnetic-field dynamics

Multiple dB/dt probes deployed at several positions in the expansion region give the general features of the magnetic-field dynamics. Particularly germane features are summarized here whereas more extensive descriptions of magnetic-field dynamics are published elsewhere.^{30,33,38} Magnetic-field dynamics exhibits the following features: (1) The expanding plasma pushes the excluded magnetic field ahead of it with a small peak above the vacuum field level [Fig. 5(a)], as expected in a sub-Alfvénic expansion. (2) The magnetic-field exclusion fraction is inversely pro-

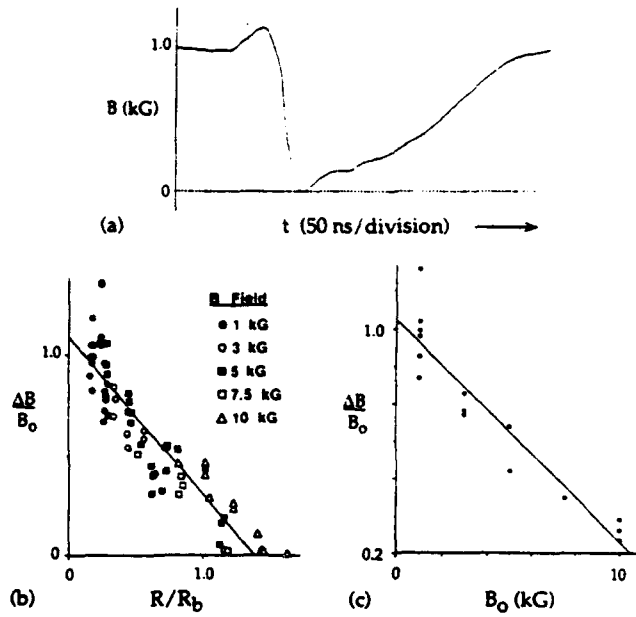


FIG. 5. Features of the magnetic-field dynamics. (a) Magnetic field vs time 5.4 cm from the target ($B_0 = 1$ kG, 32 J one-sided irradiation, Al target, $V_{\text{pl}} = 5 \times 10^7$ cm/sec). (b) Excluded field fraction $\Delta B/B_0$ vs R/R_b for a range of vacuum magnetic field strengths. (c) Excluded field fraction $\Delta B/B_0$ vs B_0 ; solid line is a linear fit to the data.

portional to the expansion radius to confinement radius ratio, i.e., $\Delta B/B_0 \propto (R/R_b)^{-1}$, as plotted in Fig. 5(b). (3) Field exclusion fraction is also inversely proportional to the vacuum field, i.e., $\Delta B/B_0 \propto 1/B_0$. (4) The magnetic field penetrates the plasma front well beyond the collisionless skin depth, typically to a depth $L_b \sim c/\omega_{pi}$. (5) Alfvén disturbances propagating with $V_A \propto B/n^{1/2}$ along the magnetic field lines were also directly observed, as predicted to occur in sub-Alfvénic plasma expansions. The observed magnetic disturbance velocity was proportional to the magnetic field and increased with distance from the target (consistent with a decreasing plasma density going away from the target).³⁸

Why the measured field penetration depth L_b is substantially larger than the collisionless skin depth is an interesting question. The magnetic-field penetration depth is nominally set by the electron skin depth c/ω_{pe} in a collisionless plasma, or the resistive scale length in a collisional plasma. On the other hand, anomalous resistivity caused by microturbulence is often invoked for collisionless plasmas to explain scale lengths greater than the electron skin depth. Alternatively, rapid field penetration in collisionless plasmas associated with Hall term dynamics has received considerable attention recently.³⁹ However, at late time ($t > 100$ nsec) the plasma is collisional. Consider the following parameters: $T_e \approx 0.5$ eV, $n_i \approx 10^{14}$ cm⁻³, $n_e \approx 10^{15}$ cm⁻³, $B \approx 0.1$ T, $A = 28$, and $Z = 10$. The electron-ion collision frequency is $\nu_{ei} \approx 2.0 \times 10^{10}$ sec⁻¹ which is comparable to the ion plasma frequency $\omega_{pi} \approx 2.3 \times 10^{10}$ rad/sec and the electron cyclotron frequency $\omega_{ce} \approx 1.8 \times 10^{10}$ rad/sec. The magnetic diffusion coefficient (i.e., resistivity) is $\eta = \nu_{ei}(c/\omega_{pe})^2 \approx 8.9 \times 10^6$

cm²/sec and the ion inertia length is $c/\omega_{pi} \approx 1.3$ cm. The time for the magnetic field to diffuse this distance is $\tau \approx (c/\omega_{pi})^2/\eta \approx 300$ nsec, which is too long to explain the experimental observations. The most likely explanation for the relatively large magnetic gradient length, L_b , is that the magnetic field is structured on scale lengths comparable to the plasma structure. The plasma has observed density flutes and irregularities with characteristic lengths of 1 to 2 cm at times $t \approx 100$ to 200 nsec for $B = 0.1$ T (see Fig. 13). This issue will be discussed in detail in the following section.

C. Instability development

When the magnetic field is turned on in the experiment, the instability is readily seen in the framing images viewing along the magnetic field lines, such as shown in Fig. 6. Figure 6 shows representative GOI images for one-sided irradiation examples with $B = 0$ and with $B = 0.1$ T. When $|B| > 0$, prominent plasma projections emerge from the plasma boundary. The degree of plasma expansion asymmetry can be varied by doing two-sided irradiations; targets large compared to the laser focal spots produce expansions that are more asymmetric (more like one-sided shots) than when the two laser spots overfill the target (that are reasonably spherical). Figure 6 (bottom) shows examples of plasma expansion for both cases with $B = 0$ and $B = 1.0$ T impressed. Note, that although the gross expansion symmetry is quite different, the instability amplitude and characteristic lengths are similar. For this reason, one-sided experiments are used most frequently in these studies.

The overall expansion and deceleration dynamics, as well as instability development, is mapped out by taking a sequence of framing images taken on individual shots at different times or on a single shot by using our four-frame GOI. With no magnetic field present, the plasma expands radially outward from the focal region with the expected directed velocity and spread. With a magnetic field impressed, the plasma front increasingly slows as the expansion approaches R_b . This was observed in Ref. 12 and, recently, by Dimonte and Wiley⁴⁰ who used a unique Faraday rotation magnetic-field probe. Figure 7 is a distance-time plot of data that demonstrates deceleration of the plasma front with 1 and 0.1 T ambient fields.¹² Note that although the plasma strongly decelerates as it approaches R_b , it does not stop there or show signs of rebounding. Observed decelerations are lower than the ideal case estimated by Eq. (3). For the 1 T case shown in Fig. 7, the experimentally measured deceleration (5×10^{14} cm/sec²) is lower than ideal by about a factor of 4, even after accounting for the expansion asymmetry. Some factors that can decrease deceleration include: incomplete exclusion of the field inside the plasma, $E \times B$ motion of plasma in the boundary layer of an asymmetric plasma expansion, collisional and enhanced "anomalous" instability diffusion of plasma. Deceleration is less apparent in the 0.1 T experiments since we observe it for $R_c < R_b$, but it is still present.

At intermediate magnetic fields, the observed confinement distance follows the expected $B^{-2/3}$ dependency rea-

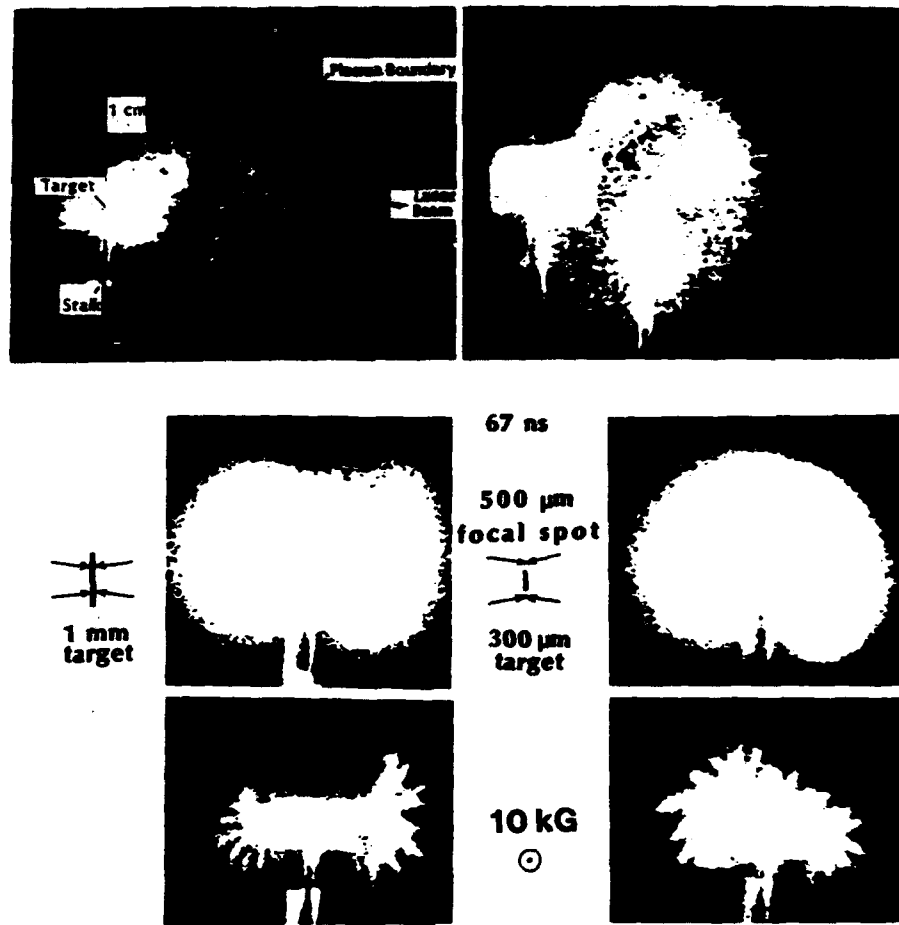


FIG. 6. GOI images of plasma expansions with and without an applied magnetic field. (top left) One-sided irradiation with $B=0$ and (top right) one-sided irradiation with $B=0.1$ T applied (30 J/beam, $t=115$ nsec). The bottom set of four frames shows two-sided irradiations of limited-mass Al-target-disks ($2.7 \mu\text{m}$ thick) with $B=0$ (top row) and 1.0 T (bottom row) that are made asymmetric (left) and symmetric (right) by under or overfilling the target with the laser beams, respectively (30 J/beam, $t=67$ nsec).

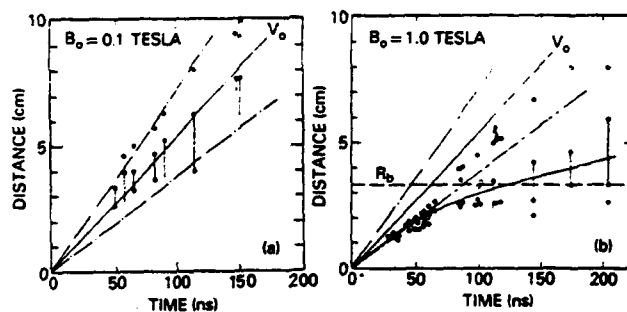


FIG. 7. Development of the instability. Distance from the target vs time of instability flute tips (open circles) and main plasma boundary (closed circles) for (a) a low-field (0.1 T) case and (b) a high-field (1.0 T) case. Shots denoted by triangles are plasma boundaries with zero applied magnetic field (free-streaming plasma) (25–30 J single-sided irradiations, $V_{\infty} = 5.4 \times 10^7$ cm/sec, and $P < 0.1$ mTorr).

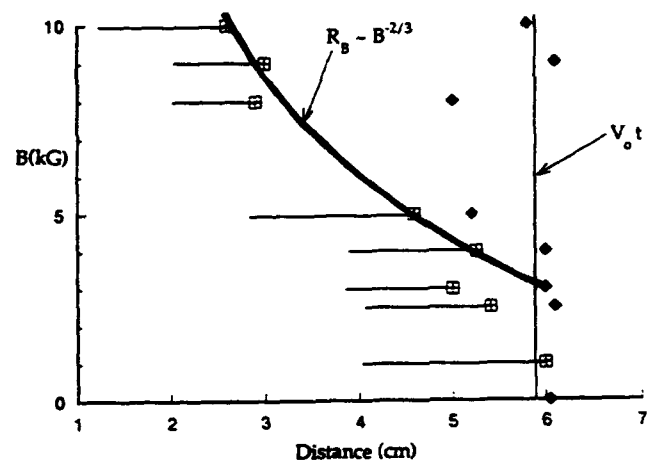


FIG. 8. Dependence of main plasma and instability tip locations upon applied magnetic field. The main plasma boundary (squares) approximately follows the expected $R_B = B^{-2/3}$ dependence whereas the instability tips (diamonds) free-stream out to a distance $V_{\infty} t$ (30 J, one-sided irradiations, $t=110$ nsec).



FIG. 9. A single-shot sequence of four GOI images of the instability development. This was a single-sided irradiation of a planar Al target by a laser beam coming in from the right side. The dark circle in the center is due to light blocked by a light shield. The two straight objects coming from the top are light reflected from two dB/dt probes.

sonably well, as seen in Fig. 8. The tips of the instability flutes, on the other hand, continue to extend ahead of the bulk plasma by about $v_{d0}t$, i.e., they are not strongly impeded by the magnetic field. Figure 7 shows that the flute tips are essentially free-streaming outward at the initial plasma speed while the bulk plasma is being decelerated.

Development of the LLR instability is illustrated in Figs. 9 and 10. Figure 9 shows a sequence of four GOI images of the instability development in a 0.5 T case (aluminum target, 35 J, $V_{d0} = 6 \times 10^7$ cm/sec) taken on the same shot. The flute amplitude already is past the linear stage at 75 nsec. The wavelength of the instability measured near the bulk plasma tends to be comparable to the density gradient length, $L_n = 1$ cm. Figure 10 shows a sequence of individual two-beam 1 T shots. For the first 30 nsec the plasma expands without obvious structure, then the instability goes through a rapid linear growth stage

from 50 to 70 nsec. From then on, the flutes continue to stream away from the target; their shape becomes increasingly intricate. We discuss the unusual high-field nonlinear regime later.

1. Linear phase

Figure 11 is a graph of the flute amplitude development for a range of magnetic field experiments. The instability onsets at about 35 to 50 nsec in most cases. The e -folding growth time of the 1 T linear phase was measured to be about 10 nsec or less.¹² (Reference 12 shows a clearer plot of the linear growth phase for 0.1 and 1 T cases.) The measured growth rate agrees with LLR-instability theory prediction of $\gamma_{LLR} = 1.2 \times 10^8$ /sec if the *measured* deceleration, wavelength, and density gradient are used in the estimate. The accuracy of the growth-rate measurement is

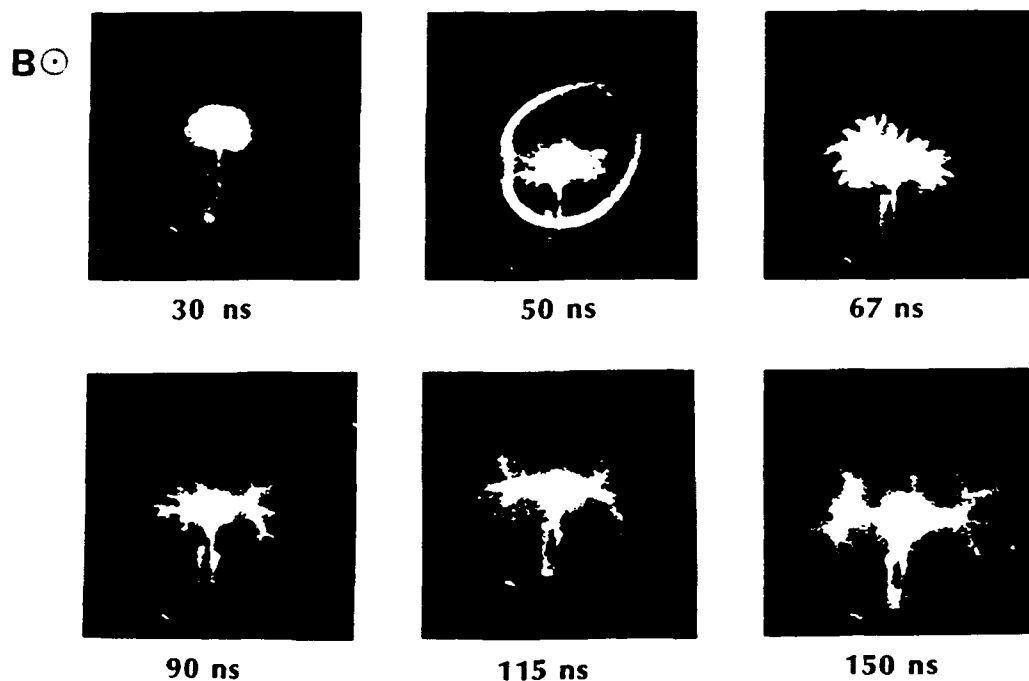


FIG. 10. Instability development with 1 T applied field. A sequence of individual two-sided irradiation shots shows the initial instability onset between 30 and 50 nsec and the later time nonlinear development. (The circle seen in 50 nsec case photograph is a reflection from a diamagnetic loop diagnostic and is not a feature of the instability.)

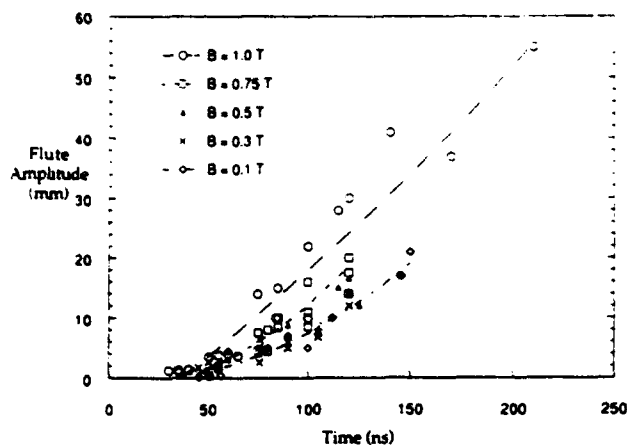


FIG. 11. Flute amplitude (tip-to-bubble) vs time for several magnetic-field cases. There is a critical turn-on time (radius) and brief linear phase at 35–50 nsec (2–3 cm) with largely free-streaming growth thereafter.

limited to a factor of 2 due to the brevity of the linear phase and shot-to-shot reproducibility. The observed growth rate is much faster than the MHD-regime Rayleigh–Taylor prediction of $\gamma_{\text{MHD}} = 2 \times 10^7/\text{sec}$. Figure 11 also clearly shows that the instability onset radius (time) is nearly independent of magnetic field, even though the effective acceleration is proportional to B^2 and, hence, $\gamma \sim B$. This behavior agrees with the instability onset condition, Eq. (5), which is also independent of the magnetic field. Equation (5) predicts onset at about $R_c = 2$ cm, compared to the experimentally observed values of 2–3 cm (if the experimental deceleration is used). If the magnetic field were increased sufficiently high ($R_b < R_c$) then the instability would not appear.

The instability structure often appears initially as density clumps in the leading edge of the expansion plasma, such as shown in Fig. 3 of Ref. 12. This clumping behavior is another predicted characteristic of the LLR instability. Density clumping is a consequence of the $\nabla \cdot \mathbf{u}$ fluid motion allowed in the LLR regime (but not allowed in the usual MHD regime).

We have also proven that the instability projections are flutelike in geometry and are not, for instance, narrow spikes. Figure 12 presents two views of the unstable plasma, end-on and across the magnetic field, which demonstrates flute geometry. The cross-field view of the plasma front is featureless except for curvature of plasma flowing along the magnetic field in response to the expansion, as expected of flutes.

The initial wavelength or characteristic periodicity of the instability was found to be insensitive to most experimental parameters. For instance, Fig. 13 shows that the LLR-instability wavelength as measured near the bulk plasma front (distance between the bottoms of the flutes) is relatively insensitive to the applied magnetic field in our experiments. The data plotted in Fig. 13 are from a combination of shots with: one-sided and two-sided irradiations, various incident laser energies, and observation times from 50 to 150 nsec. Our observations of approximately

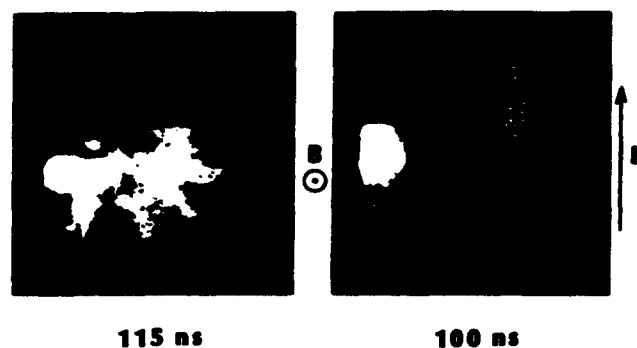


FIG. 12. Flutes imaged along the 0.5 T magnetic field (left) and across the field (right). The smooth curving front in the cross-field view indicates the instability is flutelike geometry, not spikelike (30 J).

constant wavelength finding is in contrast to observations in other experiments and the dependency expected for the conventional lower-hybrid drift instability (where $\lambda \propto B^{-1}$). As time proceeds the instability wavelength also tends to remain fixed, even though the plasma continues to expand radially. This is unusual since it suggests that the effective mode number of the instability may increase during the expansion. This behavior will be discussed further in the next section.

An additional puzzle is that the instability wavelength is much larger than predicted for peak growth of the LLR instability in the linear regime (a few times the electron gyroradius). The observed instability wavelength, $\lambda = 5.5 \pm 1$ mm, appears to be set by the density-gradient or B -field-gradient length, which is 10 ± 3 mm. One possible explanation is that processes occurring on smaller plasma spatial scales might simply see reduced instability driving fields and increased diffusion due to whatever is causing the rapid magnetic field penetration at the plasma edge. A second possible explanation for the observations is that they are made primarily in the large amplitude nonlinear regime and we simply cannot distinguish the short wave-

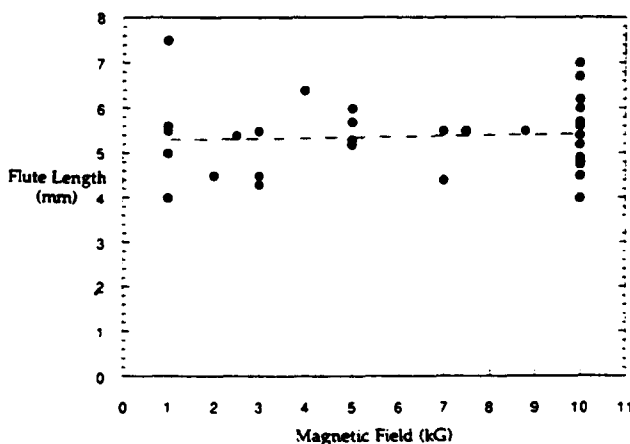


FIG. 13. Instability wavelength vs applied magnetic field. The distance between the instability valleys is not sensitive to applied magnetic field strength.

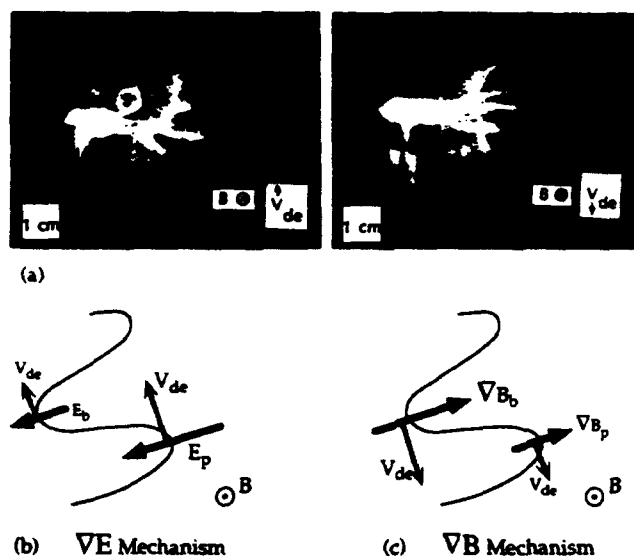


FIG. 14. Flutes curl in electron $E \times B$ drift sense. Note the reversal of curvature sense when the 1.0 T field is switched from out of the paper [(a), left] to into the paper [(a), right]. The curvature is also evident in two-beam irradiations. Possible mechanisms causing the curvature may arise from electron force $F \times B$ drift velocity shears from: (b) higher radial electric fields at flute tips than bubbles, or a (c) higher magnetic-field gradient in the bubble than the flute tip.

lengths that may be present early in the instability development. Computer simulations suggest that coalescence occurring in the nonlinear phase leads to the longer wavelengths observed.^{8,18,20} Still another possible explanation is that another instability actually sets in earlier than the LLR instability in the plasma expansion and causes a long wavelength to grow. When the critical radius for LLR-instability onset is crossed, the observed wavelength mode already present is amplified, much like a test wave, and dominates the spectrum. For instance, possible early-time instabilities include the lower-hybrid drift instability,⁴¹ the modified-two-stream instability,⁴² and the electron-ion-hybrid shear instability.⁴³⁻⁴⁸ Although the wavelength of these modes are short, they would develop very early in time and have mode numbers comparable to those observed at LLR onset. More research is needed to clarify these conjectures.

2. Nonlinear phase

After the brief period of linear growth, when the flute amplitude exceeds the wavelength, the flute amplitude grows approximately linearly in time at the free-streaming rate, as seen in Figs. 7 and 11. In addition to the plasma flutes growing very large as they cut across the magnetic field, the nonlinear phase exhibits other interesting behavior.

The flutes, particularly at the higher magnetic field strengths, frequently show a slight curvature when viewed end-on to the field lines. Figure 14 shows examples of this curvature, two one-sided irradiation shots with oppositely directed magnetic fields, and a more symmetric two-sided irradiation case. The flute curvature, which is not sensitive

to gross expansion symmetry, curls in the electron-cyclotron, or electron $E \times B$ drift, sense. It reverses with magnetic field direction. It has not as yet been determined whether the curl arises from the flute tips moving upward or the bubble region downward. (Similarly appearing curvature is seen in some computer simulations of the instability, however it is frequently in the opposite sense to that observed.) Two mechanisms that could cause the observed flute curvature are illustrated in Figs. 14(b) and 14(c). The electric-field gradient mechanism, sketched in Fig. 14(b), would occur if the radial electric field which drives the LLR instability is higher at the tips than in the bubble regions; this would cause a shear in the electron drift and, hence, properly curved flutes (flute tips move upward in this model). A depressed electric field in the bubble region might occur due to shielding of the plasma flutes on each side and the presence of low-density plasma in the bubble region. Electron $E \times B$ drift motion in the plasma front may also explain the flute curvature. Both the direction and the approximate magnitude ($\sim 0.2 v_{te}$) of the velocity drift necessary for this instability, as described later, are consistent with the experimental observations. The other possibility considered, the magnetic-field gradient mechanism, is also due to electron-drift velocity shear but, as depicted in Fig. 14(c), derived from larger magnetic-field gradients in the bubble than in the tip region (bubble regions would move downward in this case); however, the observed B -field gradients seem too small for this mechanism to adequately account for the observed curvature.

Another interesting effect observed, most evident in the nonlinear stage, is the relatively constant instability wavelength (measured as the distance between flute bottoms) noted earlier. We discussed possible reasons why the observed instability wavelength is larger than predicted. But, why does the initial wavelength persist as the plasma expands outward, when one might expect the effective mode number ($m = 2\pi R/\lambda$) to be fixed instead? Two effects tend to maintain a constant wavelength in the system. The most curious process is the bifurcation or splitting of flute tips. A secondary effect seen in asymmetric expansion geometry is a gentle curvature of the flutes toward the target normal with distance.

The above effects were initially noted by placing witness plates (black Polaroid film) perpendicular to the magnetic field a few centimeters to one side of single-side illuminated targets. Time-integrated impressions of the plasma running down the field lines etched the surface of the plates. Flutes were observed beyond 8 cm from the target normal on these films. Long spikes that curve toward the midplane were recorded on the witness plates; additional projections formed toward the sides of the pattern with increasing distance from the source. Several instances of flute splitting (bifurcation) were also seen. Flute curvature, formation of new flutes at the sides, and bifurcation evidently permit the instability wavelength to remain fixed near L_n or L_b . The effective instability mode number therefore increases with radius. Now the question is: Is the same thing happening in the more symmetric two-sided irradiation shots, that have no preferred expansion direc-

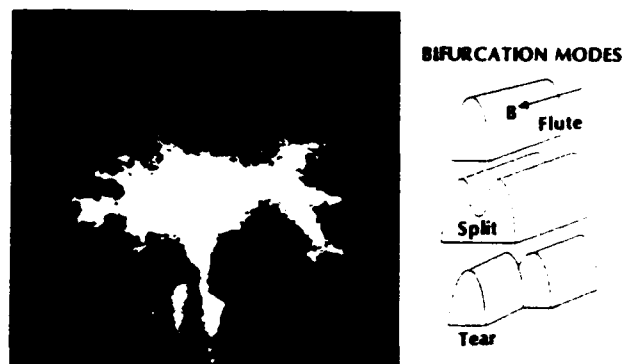


FIG. 15. Flute-tip bifurcation and division. Example of a 1.0 T two-sided target irradiation at 90 nsec whose flute tips are undergoing division. Possible modes of division are shown schematically on the right.

tion? A qualified answer is that in moderately symmetric expansion cases flute tip division also occurs. Figure 15 shows an example of flute splitting obtained with the time-resolved optical imager along with an illustration of two possible modes. To our knowledge, plasma instability bifurcation has rarely, if ever, been seen in the laboratory.

The mechanism of flute division has and the mechanisms have not been definitively identified, but several possibilities come to mind. A relatively simple explanation may be that when the wavelength exceeds the "natural" instability wavelength, determined by the gradient length at the radial diverging plasma front, the LLR instability generates new flutes to form in between the existing flutes. Another factor that may promote bifurcation is the $\nabla \cdot \mathbf{u} \neq 0$ property of the LLR instability. As we shall show later, 2-D computer simulations found splittinglike structures forming on the LLR flutes in contrast to pure MHD flutes simply exhibiting the usual Kelvin-Helmholtz-like rotational curl-up of the flute tips. Still another possible origin of bifurcation stems from the observation that each free-streaming flute tip may eventually behave like an independent cross-field plasma jet. Jets are driven across magnetic fields by the same sort of $\mathbf{E} \times \mathbf{B}$ force that drives the LLR instability; curved and fringe E-field lines tend to deflect the plasma near the leading edge into a wedge shape in both low- β ($\beta \ll 1$) jets⁴⁹ and moderate- β ($\beta > 1$) jets.⁵⁰ In both cases,^{49,50} the jet boundaries were unstable to the nonlocal velocity drift (EIH) instability with k perpendicular to \mathbf{B} and parallel to V_d . However, no gross splitting perpendicular to V_d , is observed in the present experiments. Nonetheless, plasma jetting across magnetic fields is a relatively unexplored topic and more investigation is clearly warranted.

3. Energy dependence

The plasma energy content affects the gross features of its expansion across a magnetic field. For one thing, the magnetic confinement radius is a function of the plasma energy content, $R_b \propto E_p^{1/3}$. Radius versus time characteristics also depend upon whether the increased plasma energy content is due to additional mass or velocity. Nominally

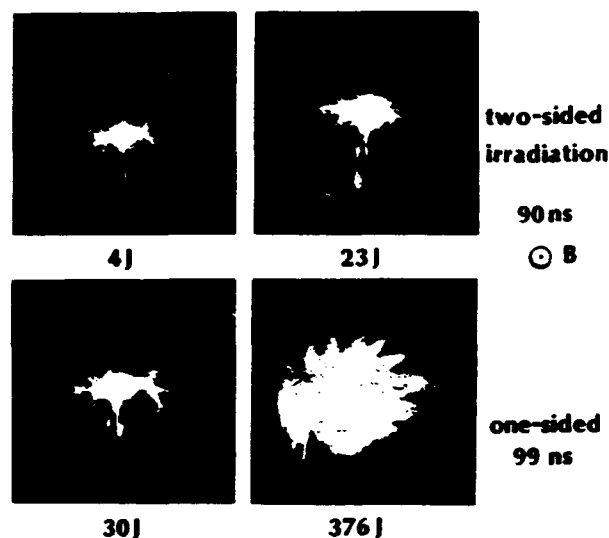


FIG. 16. Instability characteristics with varying plasma energies. These are two-sided irradiations (except for the lower-right highest energy shot) in a 1.0 T magnetic field.

the LLR instability is predicted to have little dependence upon plasma energy except, perhaps, through its onset criteria, Eq. (7), or the density-gradient length if it is a function of energy. Here we constrain ourselves to the cases in which the expansion remains very sub-Alfvénic.

Figure 16 shows a set of 1.0 T field shots in which the incident laser energy on target ranged from 4 to 376 J. The radial extent of the main bulk plasma approximately follows the expected $E_p^{1/3}$ dependence. Signs of the flute instability are seen in all these images, although its appearance varies considerably. The LLR-instability onset condition, Eq. (7), has both an explicit and implicit functional dependence upon plasma energy. The implicit dependence is in the total plasma mass, M , which, as mentioned earlier, has an $I^{0.2}$ times focal-area functional dependence. The net result is that all the shots in Fig. 16, including the lowest energy shot (4 J), satisfy Eq. (7) and are predicted to be unstable. Additional experiments are required to verify whether a minimum plasma energy is required for instability as predicted by Eq. (7). The instability wavelength is not a strong function of plasma energy, presumably because the density-gradient lengths are comparable at all four energies.

4. Line-tying effects

We now try to address the question of whether the LLR instability can be suppressed if the magnetic-field-line ends were line tied, i.e., anchored in a good conductor. Line tying has been proposed to stabilize interchange instabilities in open-ended fusion systems, such as mirror machines, in the MHD limit⁵¹ and later extended to include effects of lowered conductivity due to sheath formation,⁵² finite Larmor radius effects,⁵³ and surface line tying.⁵⁴ No line-tying theory has been formulated in the large Larmor radius limit as yet. Natural physical situa-

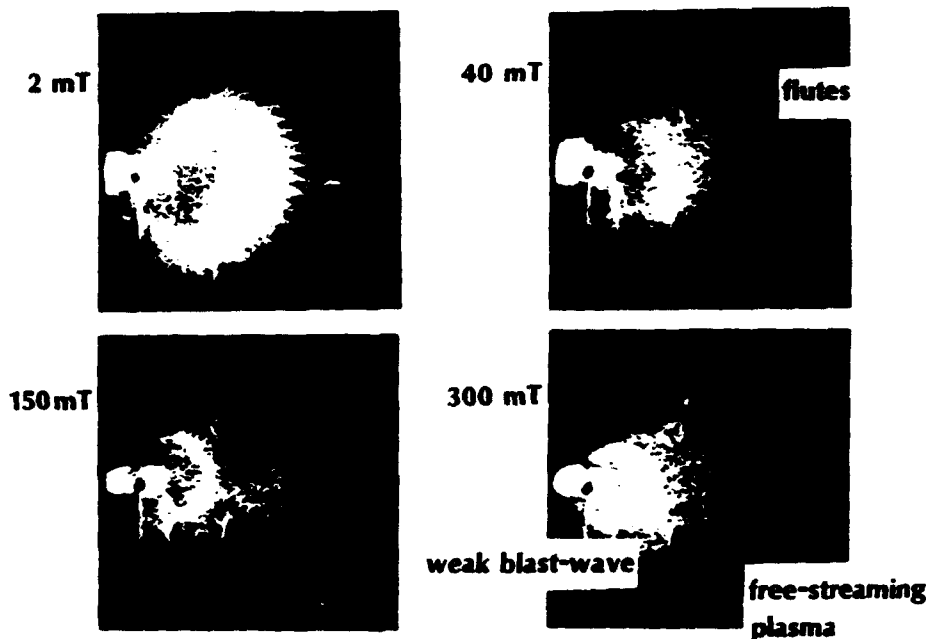


FIG. 17. Quenching of the LLR instability due to collisions with background gas and plasma. All signs of instability disappear above 150 mTorr H_2 when collisional effects appear, such as blast-wave formation (30 J, $B=0.1$ T, hydrogen gas, $t=150$ nsec).

tions in which this instability might be affected by having a highly conducting region nearby include the F layer of the Earth's ionosphere or solar corona. We could not demonstrate the line tying in our experiments, but we did gain some insight into it.

A first attempt to look for line-tying effects was made by shorting out one side of the magnetic field lines with a copper disk and allowing the other side to remain open. The shorting plate was placed perpendicular to the magnetic field lines and displaced about 5 cm from the target. The plasma expansion dynamics were viewed, as usual, along the free field-line side. We took shots with the plate bare and grounded, bare and floating, insulated and grounded, and insulated and floating. The insulation was witness-plate paper placed on the target side of the plate to allow visualization of time-integrated structure at the plate.

However, the instability was not quenched by the conducting plate in any of our shots. The flaw in this line-tying experiment may be that the plasma does not sense the highly conductive metal plate, but rather is insulated from it by the plasma sheath that forms in front of it.⁵² Sheath resistivity has hampered similar line-tying experiments elsewhere.⁵⁵ Heated electron emissive endplates would overcome the sheath complication, but doing this was outside the scope of the present study. A more detailed investigation of line-tying effects is needed.

5. Background plasma effects

Thus far we have been studying a single plasma component expanding into a magnetic field. Here, we introduce a second magnetized plasma through which the laser-

produced plasma expands. We look for effects of plasma collisionality, increased V_{d0}/V_A , and cold plasma line tying on the instability.

The background plasma is produced by bleeding gas into the target chamber and allowing the radiation from the laser-target-plasma interaction to photoionize the surrounding gas. The production process and properties of the photoionized plasma are described in detail elsewhere.⁵⁶ The photoionized ambient plasma is fully ionized within a few millimeters of the target and has an ionization fraction decreasing as R^{-2} beyond it; at 1 cm from the target the fractional ionization is about 1% for our parameters. The temperature of the photoionized plasma is 1 to 2 eV. The applied magnetic field is imbedded in this plasma since the field is already present during plasma production. In the present studies hydrogen (H_2) gas is used at pressures up to 2 Torr.

The interaction between the laser-produced plasma and an ambient photoionized plasma has been studied extensively both in the absence of a magnetic field^{30,31,33} and with a magnetic field present.^{12,33} In the 100 to 1 Torr range the interaction makes a transition from collisionless to collisional nature. Collisional features include the formation of a blast wave (energy and momentum conserving strong shock, also known as a Sedov shock). We find that the LLR instability quenches in the same pressure regime that collisionality starts to affect the coupling between the two plasma components. The effect of increased background gas pressure and collisionality can be seen in Figs. 17 and 18. With a 2 mTorr H_2 , gas fill the instability can be seen clearly, its character has not changed from corresponding vacuum shots. At 40 mTorr the instability is still

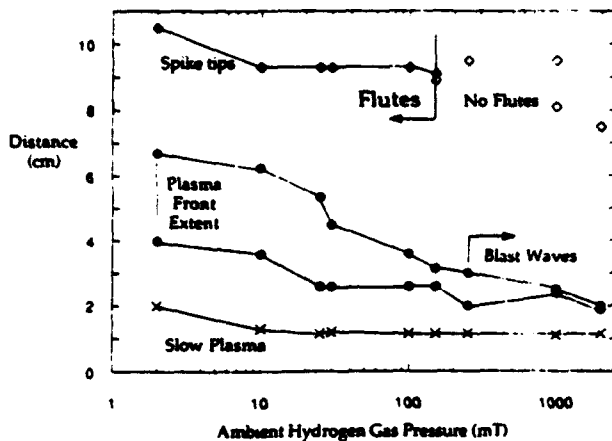


FIG. 18. Plasma expansion characteristics vs background gas pressure. Plotted are distances from the target of: slow target debris, inner and outer extents of main plasma front, and extent of spike tips, \bullet , and uncoupled freely expanding plasma boundary, \diamond (25–30 J, $B=0.1$ T, $R_0=11$ cm, $t=150$ nsec).

clearly visible but some energy has been collisionally coupled to the H_2 gas. However, at 150 mTorr pressure, a weak blast wave forms and the instability structure is almost washed out. Although the coupling is still not totally collisional at 300 mTorr as evidenced by the presence of free-streaming target plasma, the LLR instability is completely quenched. At still higher pressures collisions dominate the interaction and only sharp smooth blast waves are observed. The general observations that collisions act to stabilize the LLR instability are consistent with the theoretical finding earlier in the paper. Recall that collisional stabilization occurs if plasma is in the cold ion limit, where the ion thermal speed is small compared to the plasma drift due to the gravitational acceleration (i.e., $v_i < V_g$). An interesting extension of the present experiments would be to warm the ions to the point where the instability is predicted to destabilized according to theory.¹³

A second effect of adding a plasma background in front of the expanding laser plasma is that the effective Mach number of the expansion is increased. In a vacuum or very low density plasma, the ratio V_{exp}/V_A is very small and the expansion is subsonic. In this case, the regime of primary interest in this paper, there is little magnetic field compression ahead of the expansion front. Additionally, most interactions tend to be electrostatic as opposed to electromagnetic. As the background density is raised, however, the expansion can approach sonic or even supersonic conditions. The whole interaction may be totally changed from subsonic conditions. Higher Mach-number regimes will be the subject of future investigation. In the present experiment, our opinion is that the quenching of the instability is a consequence of collisional effects and not due to finite or supersonic expansion effects. This is because the fractional ionization is too low in the present experiment to lower V_A to the order of V_{exp} . Experiments to uniformly ionize a large volume of gas surrounding the target to in-

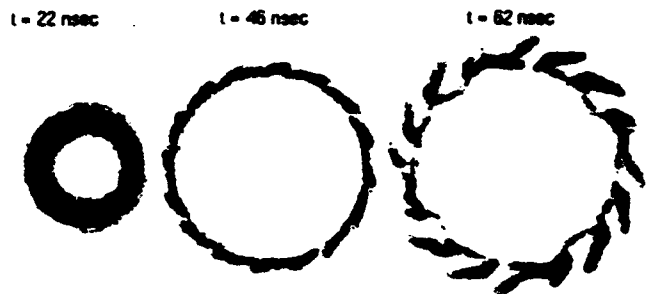


FIG. 19. Laser plasma expansion 2-D MHD computer simulations including Hall term. Density contours are shown at times 22, 46, and 62 nsec.

dependently vary V_A should provide additional clarification.

IV. ADDITIONAL THEORY AND SIMULATIONS SUPPORTING EXPERIMENT

In this section we show results from computer simulations of the LLR instability that help clarify and interpret some of the experimental observations.

A description of the computer code used to simulate the LLR instability in the experiment is in the Appendix. A gray-scale contour plot of the plasma density from the simulation is shown in Fig. 19 at times 22, 46, and 62 nsec. Black corresponds to the maximum density $n_{\text{max}} \approx 2 \times 10^{14} \text{ cm}^{-3}$ while white corresponds to the ambient density $n_0 \approx 5 \times 10^{11} \text{ cm}^{-3}$. At 22 nsec the initial perturbation in the density is already apparent. At 46 nsec the expanding density shell has thinned and structuring has begun. The number of density enhancements is consistent with the initial mode number (16) of the perturbation. At 62 nsec the instability is in the nonlinear phase. There is significant distortion of flute tips indicated by the curvature of the flutes caused by the Hall term. The sense of the curvature is opposite to the experimental observations however. Two other comments are in order. First, simulations were also performed using a colder Gaussian plasma distribution ($v_{\text{th}} = 5 \times 10^6 \text{ cm/sec}$). For this situation the instability developed faster and with a higher mode number ($m \sim 32$). This behavior is consistent with earlier simulations of the CRRES barium releases which found the shortest wavelength modes to dominate the early dynamics of the expansion.⁵⁷ Second, simulations were also performed with the Hall term arbitrarily turned off. The expanding plasma did not structure noticeably and the plasma reached a maximum radius of about 2.9 cm before recompressing. This is consistent with the theoretical stopping distance $R_p \approx 2.8$ cm. When parameters are adjusted to allow the MHD (no Hall term) Rayleigh–Taylor instability development it exhibits substantial rotational flow characteristics, including the eventual Kelvin–Helmholtz roll-up of the flute tips. On the other hand, in the nonlinear regime of the LLR–Rayleigh–Taylor instability the initial plasma clumps evolve into long, slender striations, such as observed in the experiment.

Finally detailed 2-D Hall MHD simulations of the CRRES G-4 and G-10 barium releases in the magnetosphere were described by Huba *et al.*⁶. In both cases the plasma rapidly structured, mode coalescence occurred forming larger scale-size plasma blobs that could free-stream across the magnetic field through $E \times B$ drift. The magnetic field also developed structure obtained from the simulations was shown to be in good agreement with *in-situ* magnetometer data.⁵⁷

V. SUMMARY AND DISCUSSION

We have experimentally demonstrated linear and nonlinear properties of a robust flutelike instability in the important regime of large ion Larmor radius and sub-Alfvénic expansion speed. The instability has many of the features predicted by modified MHD and kinetic theories and computer simulations. The LLR instability onsets at a critical radius that is insensitive to magnetic field, even though the growth rate is a strong function of magnetic field. The instability onset can occur well before the plasma front reaches its maximum deceleration, near the magnetic confinement radius. The growth rate during the brief linear phase was measured to be consistent with LLR-instability theoretical prediction, which is much higher than the corresponding MHD-regime growth rate. The wavelength of the instability is slightly less than the density or magnetic-field gradient lengths. When the flute amplitude approaches the density-gradient length the instability goes into the nonlinear regime. Here, the flute tips subsequently free-stream with a speed nearly that of the initial plasma expansion speed. The nonlinear regime has some very unusual features. The flute tips tend to curl in the electron $E \times B$ drift direction, perhaps due to a drift velocity shear caused by nonuniform radial electric fields. Even more striking is the observation that the instability wavelength tends to remain fixed at approximately the density scale length with most parameter changes. A mechanism that allows this to occur is bifurcation or division of the flutes that sets in when the wavelength tends to expand beyond L_n . Collisions quench the instability, but attempts to short out field lines (magnetic-field line tying) on one side of the plasma expansion failed to suppress the instability.

Many of the predictions and observations in these experiments agree with current theory and simulation of the LLR instability. It is concluded that the LLR instability is the predominant mechanism. It may be possible that another instability occurs early in the expansion that seeds the dominant instability wavelength. Even so, many unresolved issues remain. It is also important to extend these studies into other important regimes. For instance, a systematic investigation in which the ion Larmor radius is reduced to the order of the density gradient length would examine the transition from the large-Larmor radius regime into the finite-Larmor radius regime, where considerably different behavior is expected. Addition of a uniform high-density plasma in the expansion region would allow a systematic transition across the sonic-supersonic expansion regimes. A thorough study of the onset criteria for these instabilities would be important. Finally, the nonlin-

ear stage of the LLR instability exhibits some very unusual behavior that has some resemblance to cross-field jetting of plasmas. This phenomenon should also be explored in greater depth.

ACKNOWLEDGMENTS

The authors are pleased to acknowledge contributions of J. Stamper, G. Ganguli, H. Romero, N. Nocerino, L. Daniels, J. Ford, C. Brown, A. Mostovych, C. Fawley, and J. Crawford.

This work was sponsored by the Office of Naval Research.

APPENDIX: 2-D MHD COMPUTER SIMULATION INCLUDING HALL TERM

The simulations are based upon the following set of one fluid equations

$$\frac{\delta n}{\delta t} + \nabla \cdot n\mathbf{u} = 0, \quad (\text{A1a})$$

$$nm_i \frac{d\mathbf{u}}{dt} = -T\nabla n - \nabla \left(\frac{B^2}{8\pi} \right), \quad (\text{A1b})$$

$$\frac{\delta \mathbf{B}}{\delta t} = \nabla \times (\mathbf{u} \times \mathbf{B}) - \frac{\nabla \times (\mathbf{j} \times \mathbf{B})}{ne}, \quad (\text{A1c})$$

where \mathbf{u} is the center of mass velocity, m_i is the ion mass, and \mathbf{j} is the current density. The isothermal equation of state is chosen for simplicity. Equations (A1) are derived directly from the ion and electron Vlasov equations under the following assumptions.⁹ We assume (1) $\rho_e/L_n \ll 1$ and $\omega/\omega_{ce} \ll 1$ (i.e., the electrons are strongly magnetized), (2) the electron and ion pressure tensors are isotropic, (3) the electron and ion fluids are isothermal with $T = T_e = T_i$, and (4) the Debye length is very small. The final term in Eq. (A1c) is the Hall term.

Equations (A1) are solved numerically on a cylindrical-like grid with $(r \times \theta)$ resolution of 50×40 . The grid is uniform in the r direction for 40 grid cells; the final ten grid cells are stretched. We consider plasma motion only in the plane transverse to the magnetic field ($\mathbf{B} = B\hat{e}_z$). Hard wall conditions are used for the inner r boundary, zero gradient conditions are used for the outer r boundary, and periodic boundary conditions are used in the θ direction. The mesh in the θ direction ranges from 0° to 90° . The mesh size is chosen such that no field or density disturbances reach the outer boundary. The algorithm used solves Eqs. (A1) in conservation form using a total variation decreasing (TVD) nonlinear switch between a first-order transport scheme and an Adams-Bashforth, centered eighth-order spatial scheme.

In order to make quantitative comparisons with the experiments, the mass of the expanding plasma is scaled so the magnetic confinement distance (R_b) is the same for both 2-D cylindrical and 3-D spherical expansions. The difference between the 3-D and 2-D expansions is simply geometrical and is due to the scaling of magnetic energy. We find that $R_b = (3MV_{\infty}^2/B_0^2)^{1/3}$ in three dimensions; however, $R_b = (4MV_{\infty}^2/B_0^2)^{1/2}$ in two dimensions. Thus, the mass in the simulations is chosen to be

$M^* = (3MB_0/8V_{d0})^{2/3}$. Although this choice of mass will allow the 2-D code to provide the appropriate length and time scales for the evolution of the diamagnetic cavity, there is a significant difference between 2-D and 3-D expansions that cannot be removed by scaling arguments: the radial dependence of the deceleration. The effective gravity felt by the expanding plasma is $g_{\text{eff}} = B_0^2 R^2 / 2M$ for a 3-D spherical expansion, while it is $g_{\text{eff}} = B_0^2 R / 4M$ for a 2-D cylindrical expansion. Thus, the 2-D simulation model does not predict the same onset radius and time of instability as the 3-D model.

The initial velocity distribution of the expanding plasma is a drifting Gaussian with $V_{d0} = 6 \times 10^7$ cm/sec and $v_{th} = 1 \times 10^7$ cm/sec. The minimum velocity included in the calculation is $v_{\min} = 3 \times 10^7$ cm/sec and the maximum velocity used is $v_{\max} = 9 \times 10^7$ cm/sec. The simulations start at $t = t_0$ and the inner boundary is given by $r_i = v_{\min} t_0$. The plasma is assumed to have free-streamed and is deposited accordingly. The magnetic field is initialized as follows:

$$B = \begin{cases} B_0 \left(\frac{n_{\max} - n}{n_{\max} - n_0} \right)^4, & r > r_{\max}, \\ 0, & r < r_{\max}, \end{cases} \quad (\text{A2})$$

where r_{\max} is the position of maximum density (i.e., $n = n_{\max}$) at the start of the simulation, and n_0 is the background density. The parameters used in the simulation are as follows: $B_0 = 10$ T, $M = 6.84 \times 10^{-4}$ g (corresponds to a mass of $M = 2 \times 10^{-7}$ g in 3-D), Alfvénic Mach number $M_A = 0.1$, $c_s = 1.0 \times 10^5$ cm/sec, $n_0 = 4.7 \times 10^{11}$ cm $^{-3}$, $A = 28$, $Z = 10$, and $t_0 = 20$ nsec. The initial radial grid begins at 0.6 cm and extends to a radius 10.9 cm; the radial grid is uniform for $n_i < r < 3.6$ cm with a spacing $\Delta r = 7.5 \times 10^{-2}$ cm, and has a stretched mesh with ten radial grid cells for $3.6 \text{ cm} < r < 10.9$ cm. The simulation is initialized with a 2% perturbation of mode 16 in the density.

- ¹Lord Rayleigh, Proc. London Math. Soc. 14, 170 (1883); G. I. Taylor, Proc. R. Soc. London Ser. A 201, 192 (1950).
- ²M. Kruskal and M. Schwarzschild, Proc. R. Soc. London Ser. A 223, 348 (1948).
- ³M. N. Rosenbluth and C. L. Longmire, Ann. Phys. (NY) 1, 120 (1957).
- ⁴H. Dickinson, W. H. Bostick, J. N. DiMarco, and S. Koslov, Phys. Fluids 5, 1048 (1962).
- ⁵See for instance: D. J. Rose and M. Clark, Jr., *Plasmas and Controlled Fusion* (Wiley, New York, 1961).
- ⁶M. N. Rosenbluth, N. A. Krall, and N. Rostocker, Nucl. Fusion Suppl. 1, 143 (1962).
- ⁷A. B. Hassam and J. D. Huba, Geophys. Res. Lett. 14, 60 (1987).
- ⁸J. D. Huba, J. G. Lyon, and A. B. Hassam, Phys. Rev. Lett. 59, 2971 (1987).
- ⁹A. B. Hassam and J. D. Huba, Phys. Fluids 31, 318 (1988).
- ¹⁰P. A. Bernhardt, R. Roussel-Dupre, M. B. Pongratz, G. Haerendel, A. Valenzuela, D. A. Gurnett, and R. R. Anderson, J. Geophys. Res. 92, 5777 (1987).
- ¹¹J. D. Huba, P. A. Bernhardt, and J. D. Lyon, J. Geophys. Res. 97, 11 (1992).
- ¹²B. H. Ripin, E. A. McLean, C. K. Manka, C. Pawley, J. A. Stamper, T. A. Peyser, A. N. Mostovych, J. Grun, A. B. Hassam, and J. D. Huba, Phys. Rev. Lett. 59, 2299 (1987).
- ¹³J. D. Huba, A. B. Hassam, and D. Winske, Phys. Fluids B 2, 1676 (1990).

- ¹⁴S. P. Gary, and M. F. Thomsen, J. Plasma Phys. 28, 551 (1982).
- ¹⁵J. D. Huba, A. B. Hassam, and P. Satyanarayana, Phys. Fluids B 1, 931 (1989).
- ¹⁶D. Winske and J. Geophys. Res. 93, 2539 (1988); See also: S. H. Brecht and N. T. Gladd, IEEE Trans. Plasma Sci. PS-20, 678 (1992).
- ¹⁷J. D. Huba, Phys. Fluids B 3, 3217 (1991).
- ¹⁸D. Winske, Phys. Fluids B 1, 1900 (1989).
- ¹⁹A. B. Hassam and J. D. Huba, Phys. Fluids B 2, 2001 (1990).
- ²⁰A. G. Sgro, S. P. Gary, and D. S. Lemons, Phys. Fluids B 1, 1890 (1989).
- ²¹F. W. Suvov, J. L. Pack, A. V. Phelps, and A. G. Engelhardt, Phys. Fluids 10, 2035 (1967).
- ²²J. Bruneteau, E. Fabre, H. Lamain, and P. Vasseur, Phys. Fluids 13, 1795 (1970).
- ²³T. Matoba and S. Ariga, J. Phys. Soc. Jpn. 30, 1477 (1971).
- ²⁴D. Koopman, Phys. Fluids 19, 670 (1976).
- ²⁵S. Okada, K. Sato, and T. Sekiguchi, J. Phys. Soc. Jpn. 46, 355 (1979); also, Jpn. J. Appl. Phys. 20, 157 (1981).
- ²⁶G. Jellison and C. R. Parsons, Phys. Fluids 24, 1787 (1981); 26, 1171 (1983).
- ²⁷Y. A. Bykovskii, S. M. Sil'nov, and G. A. Sheroziya, Fiz. Plazmy 12, 237 (1986) [Sov. J. Plasma Phys. 12, 140 (1986)].
- ²⁸V. A. Rozhanskii, Fiz. Plazmy 12, 294 (1986) [Sov. J. Plasma Phys. 12, 170 (1986)].
- ²⁹Yu. P. Zakharov, A. M. Orishich, A. G. Ponomarenko, and V. G. Posukh, Fiz. Plazmy 12, 1170 (1986) [Sov. J. Plasma Phys. 12, 674 (1986)]; also, Fiz. Plazmy 14, 203 (1988) [Sov. J. Plasma Physics 14, 114 (1988)].
- ³⁰B. H. Ripin, A. W. Ali, H. R. Griem, J. Grun, S. T. Kacenjar, C. K. Manka, E. A. McLean, A. N. Mostovych, S. P. Obenschain, and J. A. Stamper, in *Laser Interaction and Related Plasma Phenomena*, edited by H. Hora and G. Miley (Plenum, New York, 1986), Vol. 7, p. 855.
- ³¹B. H. Ripin, J. Grun, T. N. Lee, C. K. Manka, E. A. McLean, A. N. Mostovych, C. Pawley, T. A. Peyser, and J. A. Stamper, in *Laser Interaction and Related Plasma Phenomena*, edited by H. Hora and G. Miley (Plenum, New York, 1988), Vol. 8, pp. 417-433.
- ³²J. Grun, S. P. Obenschain, B. H. Ripin, R. R. Whitlock, E. A. McLean, J. Gardner, M. J. Herbst, and J. A. Stamper, Phys. Fluids 26, 588 (1983).
- ³³S. Kacenjar, M. Haussman, M. Keskinen, A. W. Ali, J. Grun, C. K. Manka, E. A. McLean, and B. H. Ripin, Phys. Fluids 29, 2007 (1986).
- ³⁴J. Grun, R. Stellingwerf, and B. H. Ripin, Phys. Fluids 29, 3390 (1986).
- ³⁵J. L. Giuliani, Jr., M. Mulbrandon, and E. Hyman, Phys. Fluids B 1, 1463 (1989).
- ³⁶A. M. Mostovych (private communication, 1988).
- ³⁷B. H. Ripin, C. M. Armstrong, S. E. Bodner, R. Decoste, S. Gold, J. Grun, R. H. Lehmberg, E. A. McLean, J. M. McMahon, D. J. Nagel, S. P. Obenschain, J. A. Stamper, R. R. Whitlock, and F. C. Young, Phys. Fluids 23, 1012 (1980); 24, 990 (1981).
- ³⁸H. R. Burris, C. K. Manka, B. H. Ripin, J. Grun, J. Resnick, J. Stamper, and J. Huba, Bull. Am. Phys. Soc. 35, 2095 (1990); 36, 2465 (1991).
- ³⁹A. S. Kingsep, K. V. Chukbar, and V. V. Yan'kov, in *Reviews of Plasma Physics*, edited by B. B. Kadomtsev (Consultants Bureau, New York, 1990), Vol. 16; A. Fruchtman, Phys. Fluids B 3, 1908 (1991); L. I. Rudakov, C. E. Seyler, and R. N. Sudan, Comm. Plasma Phys. Controlled Fusion 14, 171 (1991); J. D. Huba, Phys. Fluids B 3, 3217 (1991); R. J. Mason, P. L. Auer, R. N. Sudan, B. V. Oliver, C. E. Seyler, and J. B. Greenly, Phys. Fluids B 5, 1115 (1993).
- ⁴⁰G. Dimonte and L. G. Wiley, Phys. Rev. Lett. 67, 1755 (1991).
- ⁴¹N. A. Krall and P. C. Liewer, Phys. Rev. A 4, 2094 (1971).
- ⁴²J. B. McBride, E. Ott, J. P. Boris, and J. H. Orens, Phys. Fluids 15, 2367 (1972).
- ⁴³G. Ganguli, Y. C. Lee, and P. J. Palmadesso, Phys. Fluids 31, 2753 (1988).
- ⁴⁴H. Romero, G. Ganguli, Y. C. Lee, and P. J. Palmadesso, Phys. Fluids B 4, 1708 (1992).
- ⁴⁵H. Romero, G. Ganguli, and Y. C. Lee, Phys. Rev. Lett. 69, 3503 (1992); H. Romero and G. Ganguli, Phys. Fluids B 5, 3163 (1993).
- ⁴⁶G. Ganguli, Y. C. Lee, and P. J. Palmadesso, Phys. Fluids 31, 823 (1988).
- ⁴⁷H. Romero and G. J. Morales, Phys. Fluids B 1, 1805 (1989).

- ⁴⁸H. Romero, G. Ganguli, P. Palmadesso, and P. B. Dusenbery, *Geophys. Res. Lett.* **17**, 2313 (1990).
- ⁴⁹A. N. Mostovych, J. A. Stamper, and B. H. Ripin, *Phys. Rev. Lett.* **62**, 2837 (1989).
- ⁵⁰T. A. Peyser, C. K. Manka, B. H. Ripin, and G. Ganguli, *Phys. Fluids B* **4**, 2448 (1992).
- ⁵¹J. Berkowitz, H. Grad, and H. Rubin, in *Proceedings of the 2nd United Nations International Conference on Peaceful Uses of Atomic Energy* (United Nations, Geneva, 1958), Vol. 31, p. 177.
- ⁵²W. B. Kunkel and J. U. Guillory, in *Proceedings of the 7th International Conference on Phenomena in Ionized Gases*, edited by B. Perovic and D. Tosic (Gradevinsk Knjiga, Beograd, Yugoslavia, 1966), Vol. II, p. 702.
- ⁵³J. C. Riordan and C. W. Hartman, *Phys. Fluids* **20**, 1378 (1977).
- ⁵⁴S. Fornaca, Y. Kiwamoto, and N. Rynn, *Phys. Rev. Lett.* **42**, 772 (1979).
- ⁵⁵R. J. Colchin, J. L. Dunklap, and H. Postma, *Phys. Fluids* **13**, 501 (1970).
- ⁵⁶A. W. Ali and E. A. McLean, *J. Quant. Spectrosc. Radiat. Transfer* **33**, 381 (1985).
- ⁵⁷J. D. Huba, P. A. Bernhardt, and J. L. Lyon, *J. Geophys. Res.* **97**, 11 (1992).

Appendix II

A Segmented Concentric Faraday Cup for Measurement of Time-Dependent Relativistic Electron Beam Profiles

A segmented concentric Faraday cup for measurement of time-dependent relativistic electron beam profiles

T. A. Peyser,^{a)} J. A. Antoniadis,^{b)} M. C. Myers, M. Lampe, R. E. Pechacek, D. P. Murphy, and R. A. Meger

Plasma Physics Division, Naval Research Laboratory, Washington, DC 20375-5000

(Received 14 June 1991; accepted for publication 12 August 1991)

A multi-element segmented concentric Faraday collector has been developed for measuring the time evolution of the beam half-current radius ($a_{1/2}$) of an intense relativistic electron beam. Each collector segment measures the total current within its radius. The data analysis procedure fits the data from all five segments at a given time to a prescribed beam profile and calculates $a_{1/2}$ from the parameters of the fitted curves. The effect of beam centroid offsets on the data analysis was investigated numerically. Beam centroid offsets as large as half the beam radius produce only a 10% error in the experimental measurement of $a_{1/2}$. The use of a thin graphite overlayer followed by range-thick stainless steel reduces scattering from one collector element to the next. The instrument has been used extensively on the SuperIBEX relativistic electron beam accelerator for measurement of the half-current radius as a function of time. Radius variations in excess of 4:1 have been measured over the duration of the beam pulse for beams with 5-MeV energy, 20-kA peak current and 1-cm final half-current radii.

I. INTRODUCTION

The propagation of high-current relativistic electron beams ($E \approx 5$ MeV, $I > 10$ kA) in uniform density background gas is relevant to a number of applications including heating of magnetically confined plasmas, ion-driven inertial fusion, strategic defense and basic particle accelerator research. Stable propagation over any appreciable distance, however, is severely limited by a convective instability known as the resistive hose instability.¹ The growth rate of the resistive hose may be reduced to tolerable levels by introducing a temporal variation in the beam radius thereby "detuning" the instability between one portion of the beam and another.²⁻⁴ Measurement of the temporal variation of the beam radius $a(t)$, or more generally the beam current density profile $J_b(r,t)$, is complicated by the simultaneous change in the total current as well as the radius necessitating an instrument capable of resolving current densities over two orders of magnitude or more.

The instrument on which we report is a variation on an old theme—a multielement Faraday collector. The segmented concentric Faraday collector (SCFC) discussed here consists of a central range-thick cylinder surrounded by four range-thick collecting rings. Each collector segment measures the total current enclosed within its radius. Figure 1 shows the current within the five segments for an intense relativistic electron beam ($I \approx 15$ kA, $E \approx 5$ MeV) produced by the Naval Research Laboratory (NRL) SuperIBEX accelerator. The Faraday collector was placed immediately downstream of a 10 cm diameter, 40-cm-long low-pressure gas cell filled with 3–10 mTorr of argon. The current in each collector segment can be normalized to the

area of the collector to give an average beam current density $J_b(\langle r \rangle, t)$ where $\langle r \rangle$ is the mean radius of each segment. The beam radial current profile can be obtained from detailed analysis of the data from all five segments. A novel feature of the instrument discussed in greater length below, is that numerical analysis of the data directly gives the time evolution of the beam half-current radius, $a_{1/2}(t)$, defined as the radius containing one-half of the total current.

II. DESCRIPTION OF THE INSTRUMENT

In its simplest incarnation, a Faraday cup consists of a single-range-thick collector in which incident charged particles are deposited and then the collected current shunted to ground through a current-measuring device.⁵ Other versions of segmented Faraday cups have been used in previous experiments to diagnose various relativistic electron beam parameters.⁶⁻¹² The Faraday collector reported here is unique in its geometry, data inversion routines, and capability to directly give $J_b(r,t)$ and $a_{1/2}(t)$.

The principal design requirement for the instrument was the ability to measure $>4:1$ variation in the beam radius over a pulse of approximately 40 ns in duration. A complete time history of the beam radius required optimizing the detector sensitivity to be able to measure large radii early in the beam pulse while retaining the ability to resolve small radii at later times. This dictated the largest possible collector areas consistent with the required spatial resolution, namely, a nested circular or concentric array of collectors. In addition, the concentric collector geometry is a cost-efficient alternative to the use of multi-element collectors on a Cartesian grid which would require at least twice the number of collector segments and the associated expensive high-bandwidth channels to achieve the same spatial resolution as obtained with the five-element concentric collector. The outer radii of the five elements of the

^{a)}Permanent address: Science Applications International Corporation, Inc., McLean, VA 22102.

^{b)}Permanent address: Sachs-Freeman Associates, Inc., Landover, MD, 20785.

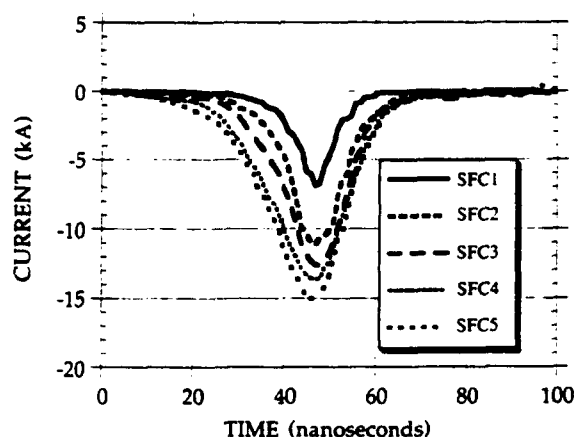


FIG. 1. Time dependence of the current collected within each of the five concentric Faraday collector segments designated SFC1 (inner collector) through SFC5 (outer collector). This data was taken from an intense relativistic electron beam ($I \approx 15$ kA, $E = 5$ MeV) produced by the NRL SuperIBEX accelerator.

segmented concentric Faraday collector are, respectively: 0.76, 1.67, 2.59, 3.50, and 4.62 cm. A schematic diagram of the five-element segmented concentric Faraday collector is shown in Fig. 2(a).

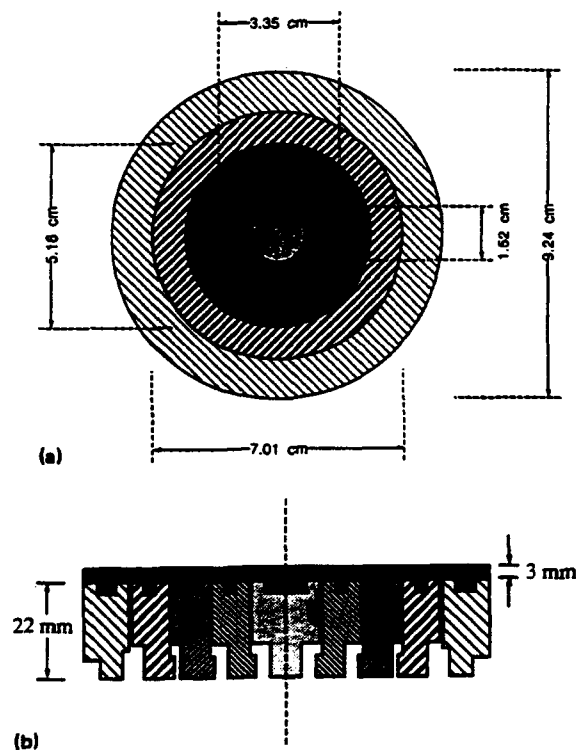


FIG. 2. (a) Top view of the five-element segmented concentric Faraday collector (SCFC) giving the diameters of each collector segment; (b) cross-sectional view of the SCFC consisting of a 3-mm graphite overlayer followed by a 22-mm-range-thick layer of stainless steel. The thin graphite layer reduces surface damage and secondary electron production, while the thicker stainless-steel layer captures the electrons in each Faraday collector segment with only minimal scattering from one to the next.

At the beam energies used in the present experiments, there are distinct advantages to the use of a thin layer of low- Z material such as graphite followed by a thicker range-thick layer of a higher- Z material such as stainless steel. The initial graphite layer is especially important at high currents for limiting surface damage due to melting and spalling. The graphite also suppresses secondary electron emission which can give erroneous values for the measured incident beam current. The subsequent thicker high- Z material captures the incident beam electrons in the shortest possible distance preventing intra-element scattering and thereby preserving the spatial resolution of the instrument as discussed below. In the final design, a thin layer of graphite (3 mm) was used on each collector face followed by thick (22 mm) stainless-steel cylinders or rings. A cross section of the five-element Faraday collector showing the composite graphite and stainless steel design is shown in Fig. 2(b). As discussed below, this design was found experimentally and theoretically to greatly reduce scattering between collector segments as compared with collectors made entirely of range-thick graphite.

Each element is separated by 0.5 mm from adjacent elements and electrically isolated with 5-mil Kapton insulation. The charge deposited in each element is then separately shunted to ground through an array of nested Rogowski coils. Five Rogowski coils are mounted within concentric grooves in an aluminum base plate to which all the collector segments are attached as shown in Fig. 3. The n th Rogowski coil from the center measures the total current enclosed within the first n segments. The output of each Rogowski coil is digitized on a Tektronix 7912 A or B digitizer at a GHz sample rate.

The Faraday collector is placed in a high vacuum enclosure centered with respect to the nominal beam axis. There is a 1.5-mil-thick titanium entrance foil 5 mm from the front surface of the collectors. The combination of the high vacuum and the presence of a foil which is range thick for any low-energy plasma electrons associated with the return current enable the Faraday collector to measure the true beam current rather than the net current (beam current minus the plasma return current). The Faraday collector diagnostic can be placed at any axial position in the beam line.

III. CALIBRATION

The Rogowski coils were made by hand winding magnet wire onto RG-174 cable that had been stripped of its outer braid. The winding ends were then soldered to the center conductor and the outer braid of the cable and insulated with shrink tubing. SMA connectors were attached to the coil before potting the coils in the aluminum base plate with low viscosity epoxy. The time response of the coils was tested by observing their response as a cable termination using time-delay reflectometry.¹³ The measured time response of the coils was in excess of 350 MHz.

The calibration of the five Rogowski coil array used in the segmented concentric Faraday collector was performed on the same 5-MeV SuperIBEX electron beam accelerator as used in the experiments. A single large-element Faraday

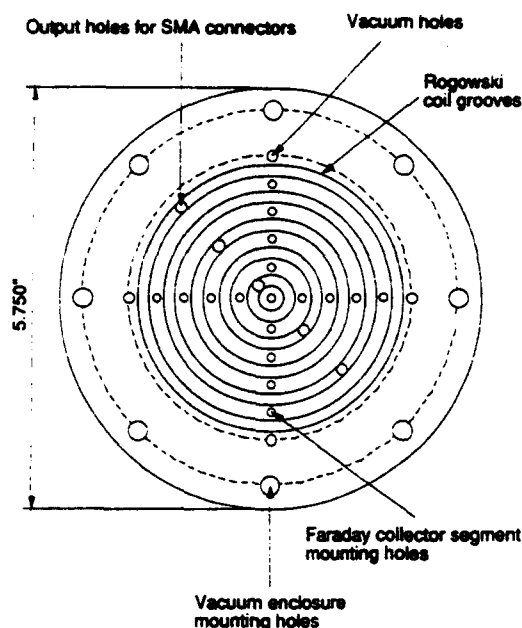


FIG. 3. A half-inch thick aluminum base plate contains the five Rogowski coils mounted within concentric grooves (shaded grey in the figure). The n th Rogowski coil from the center measures the total current enclosed within the first n segments. The smaller through holes arranged on the vertical and horizontal axis are for mounting the five Faraday collector segments to the base plate. The four through holes on the same pattern outside the fifth Rogowski coil groove are for vacuum pumpout of the collector segment array from the back of the base plate. The five holes on a diagonal are for the Rogowski coil outputs to SMA connectors on the rear of the base plate. The eight through holes towards the edge of the plate are for mounting the assembled detector plate and Faraday collector array to the vacuum enclosure.

collector consisting of range-thick graphite was constructed for the purpose of calibrating the five nested Rogowski coils. The outer diameter of the calibration Faraday cup was approximately equal to the diameter of the outermost multi-element Faraday collector. All the current collected in the large single-element Faraday cup was shunted to ground through the center of the coil array thus insuring that all five concentric Rogowski loops measured the same input current. The current on each of the Rogowski loops was then compared with current monitors 1.5 cm upstream of the Faraday collector. The coil sensitivity for the five coils ranged from 2.8 kA/V for the center collector to 4.2 kA/V for the outermost collector with an average error of less than $\pm 5\%$ of the calibration value for all five coils.

IV. DATA ANALYSIS PROCEDURE

A data analysis procedure was developed to obtain the time dependence of the electron beam half-current radius $a_{1/2}(t)$, defined as the radius containing half of the total instantaneous current. Expressions for the half-current ra-

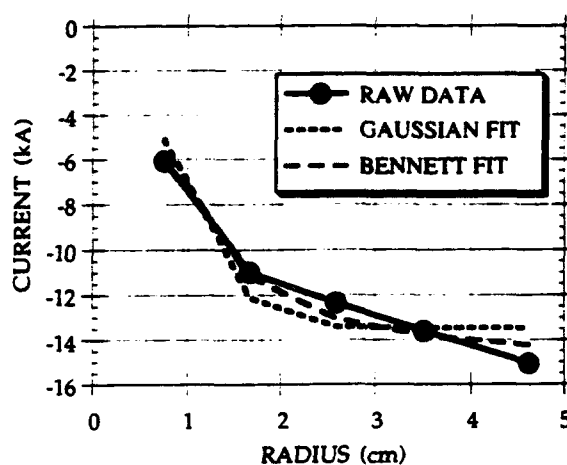


FIG. 4. The raw data from the five Faraday collector segments at a time $t \approx 46$ ns is fit to analytic expressions for the total current enclosed within a given radius $I(r_0)$ for both a Gaussian and a Bennett current density profile. There is a 10% difference in the value of the total current determined by the Gaussian and Bennett fits, but less than 5% difference in the value of the half-current radius given by the two fits.

dus can be obtained from standard analytic models of cylindrical beam equilibria such as Gaussian and Bennett profiles.¹⁴⁻¹⁶

The current density for a centered Gaussian profile is given by

$$J(r) = J_0 \exp(-r^2/a_G^2), \quad (1)$$

where a_G is the Gaussian radius. The total current collected within a radius r_0 is given by

$$I(r_0) = I_0 [1 - \exp(-r_0^2/a_G^2)], \quad (2)$$

where $I_0 = J_0 \pi a_G^2$ is the total beam current. The half-current radius can be obtained directly from the equation for the total current and is given by $a_{1/2} = a_G (\ln 2)^{1/2}$. In a beam with a centered Bennett current density profile

$$J(r) = J_0 [1 + (r^2/a_B^2)]^{-2}, \quad (3)$$

the total current collected within a radius r_0 is

$$I(r_0) = I_0 r_0^2 / (a_B^2 + r_0^2), \quad (4)$$

where a_B is the Bennett radius, $I_0 = J_0 \pi a_B^2$ is the total beam current, and the half-current radius $a_{1/2} = a_B$.

The half-current radius at a given time t_0 is obtained by fitting a Gaussian or Bennett profile from Eq. (2) or Eq. (4) above to the instantaneous values of the currents in the five Faraday collector segments. A computer program which fits the data in nanosecond increments was written to give the time evolution of the beam radius. The curve fits are thus performed to an integral quantity, the total current within the outer radius of each collector segment, which makes the curve fit results less susceptible to error from random noise. The data inversion is done with NRL's ASYST-based scientific data acquisition and analysis system using a modified version of the Newton-Raphson least-squares minimization method.^{17,18} Figure 4 gives the raw data and fits to both a centered Gaussian and Bennett

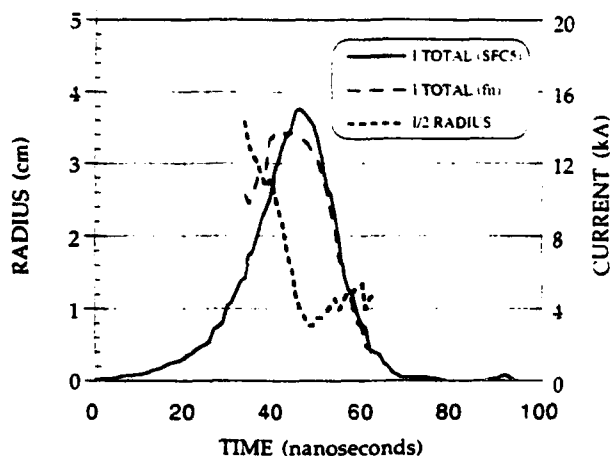


FIG. 5. Time dependence of the half-current radius and total current obtained from a Gaussian fit to the data from an intense relativistic electron beam produced by the SuperIBEX accelerator. Also shown is the total current measured by the outer Faraday collector SFC5.

profile at a time $t \approx 46$ ns into the beam pulse shown in Fig. 1. The data are fit to Eqs. (2) and (4) above, i.e., to the expression for the total current enclosed within a given radius $I(r_0)$ assuming a centered Gaussian or Bennett current density profile. Although there is a 10% difference in the value of the total current determined by the Gaussian and Bennett fits, there is less than 5% difference in the value of the half-current radius given by the two fits. The result of the fit to a Bennett profile is a total current of 14.8 kA and a half-current radius 0.96 cm, compared with the results of a fit to a Gaussian profile with a total current of 13.5 kA and a half-current radius of 0.92 cm. Figure 5 shows the half-current radius $a_{1/2}$ and axial current density from fitting the data to a Gaussian current density profile from the same shot on the SuperIBEX accelerator as shown in Figs. 1 and 4. Figure 5 illustrates the variation in the beam radius induced by the low-pressure gas cell from $a_{1/2} \approx 3.6$ cm early in the pulse to $a_{1/2} \approx 0.9$ cm shortly after the peak current. Also shown in Fig. 5 is the total current measured by the outer Faraday collector SFC5.

V. TESTS OF DATA INVERSION ROUTINES: EFFECT OF BEAM OFFSET, NOISE AND MISSING DATA POINTS

The most important source of nonsystematic error for the instrument is beam centroid position offset from the nominal beam axis. Other sources of error include electromagnetic pickup in the signal cables as well as inaccuracies in the calibration of Rogowski coils. Finally there can be additional uncertainty in the half-current radius determination at various times during the beam pulse due to missing data points caused by low signal-to-noise on a given collector signal or redundant signals on two or more collectors. Simulated input data were used to test the data inversion routines for the effects of beam centroid offset, random noise and missing data on the reconstructed half-current radius.

The beam centroid in most intense relativistic electron beams, including the beam produced by the SuperIBEX accelerator, is subject to some degree of motion or sweep away from the nominal beam axis. The actual beam position can be determined experimentally by a number of independent diagnostics, including magnetic beam centroid location monitors,^{19,20} time-integrated exposures of radiachromatic film as well as time-resolved streak and framing camera images of Cerenkov emission from thin Teflon[®] foils immediately upstream of the Faraday collector. In the accelerator configuration used for the Faraday collector experiments, the beam sweep on the SuperIBEX accelerator was found on average to be less than or equal to ± 5 mm.

The Faraday collector data analysis procedure assumes that the beam incident on the collector is both axisymmetric and well-centered. A computer program was written that produced simulated input data for a beam of a prescribed current density profile displaced a fixed distance along the positive x axis. The program calculates the current that would be collected by each collector segment for the test beam. These results are then used as the input to the fitting program precisely in the same manner as the experimental data. The data inversion was found to be insensitive to beam centroid offsets as much as one-half to one times the radius of the center of the Faraday collector (r_{c1}) depending on the beam radius as discussed below.

The data simulation program finds the current collected in each Faraday collector segment for a beam displaced a fixed distance Δr from the nominal beam axis. The beam offset (Δr) is given in terms of the smallest Faraday collector segment radius (r_{c1}). Figure 6(a) shows the current measured by each Faraday collector segment as a function of beam centroid offset ($\Delta r/r_{c1}$) for a beam with a Gaussian current density profile. SFC1 is the innermost collector and SFC5 is the outermost collector. The Gaussian radius $a_G = 2r_{c1}$ where r_{c1} is the radius of SFC1. Figure 6(b) gives the percentage change in the measured current on each of the five collectors as a function of beam offset ($\Delta r/r_{c1}$) relative to a centered beam ($\Delta r=0$). Beam offsets $\Delta r < 0.5 r_{c1}$ result in changes in the measured current on all five collectors relative to a centered beam of approximately 5%. As the magnitude of the beam offset increases, the discrepancy between the measured current for the offset beam compared with a centered beam increases. The most serious problems occur with the centermost collectors. This problem is also most severe for beams with small Gaussian radii. Figure 7 shows the discrepancy in the current collected by the center collector (SFC1) as a function of beam offset ($\Delta r/r_{c1}$) for beams with Gaussian radius a_G equal to 1, 1.5, 2, 2.5, and 3 times the center collector radius (r_{c1}). As the beam radius increases, the change in the current collected by the center segment decreases sharply and accordingly the error in the radius determination caused by the beam centroid offset decreases as well. Figure 8 gives the fitted value of the Gaussian radius as a function of beam offset from the data inversion routines for beams with the same set of input Gaussian radii. Again it is clear that the error is most significant for beams with

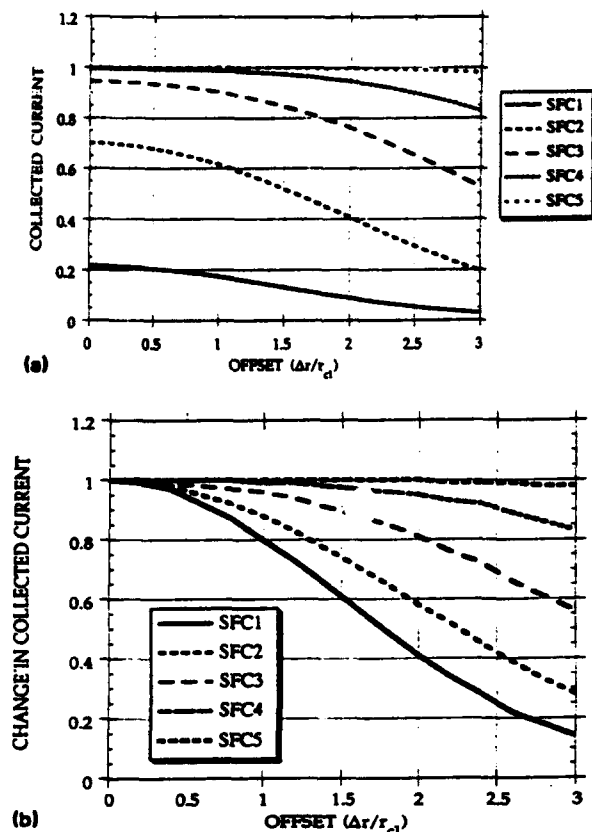


FIG. 6. (a) Variation in the measured current on each of the five Faraday collectors as a function of beam offset ($\Delta r/r_{cl}$) where Δr is the beam centroid offset and r_{cl} is the radius of the center Faraday collector. These curves were calculated for a Gaussian beam profile with a Gaussian radius $a_G = 2r_{cl}$. The total current incident on the Faraday collector was normalized to one; (b) the percentage change in the measured current on each of the five collectors as a function of beam offset ($\Delta r/r_{cl}$) relative to a centered beam ($\Delta r=0$). The discrepancies in the collected current between offset beams and a centered beam are largest for the smaller radii collector segments.

Gaussian radii small compared to the beam offset ($a_G/\Delta r < 1$). The simulations show, however, that even for small beams ($a_G/r_{cl} \approx 1$), beam centroid offsets of $0.5 r_{cl}$ result in no more than 10% error in the radius determination. A detailed examination of Fig. 8 suggests a more general result, namely that the error is fixed at approximately 10% for beam center offsets equal to one-half the beam radius. The simulation results show that for the typical ± 5 mm beam offsets encountered in SuperIBEX, the Faraday collector data inversion routine correctly gives the beam half-current radius to within 10% of the actual value for small beams and to within even greater accuracy for larger beams.

The two sources of random noise in the signals are an average $\pm 5\%$ uncertainty in the Rogowski coil calibration values and a 10-mV background due primarily to electromagnetic pickup in the cables. Random noise at the digitizer sampling rate frequency at various percentages of the instantaneous total current amplitude was added to the simulated input signal. This test was intended to study the

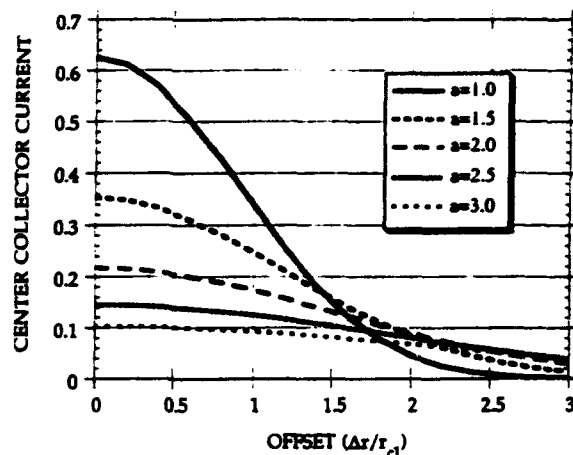


FIG. 7. Variation in the percentage of the total current measured by the center collector as a function of beam offset ($\Delta r/r_{cl}$) for beams with Gaussian radii equal to 1, 1.5, 2, 2.5, and 3 times the center collector radius (r_{cl}). The larger the Gaussian radius, the less a given offset changes the percentage of the total current measured by the center collector.

effect not only of noise on the actual experimental signals, but in addition the effects of small calibration errors in the Rogowski coils. For random noise levels $<10\%$ of the input signals, the data analysis routines were found to reproduce the input beam current and radius profiles to within the same percentage error as in the input signals. Sensitivity of the calculated half-current radius to the choice of an analytic beam profile—Gaussian or Bennett—was found to be minimal. The use of a Gaussian function to fit simulated Bennett profile data resulted in an error of only 3% in the calculated half-current radius—an accuracy better than that of the experimental measurement.

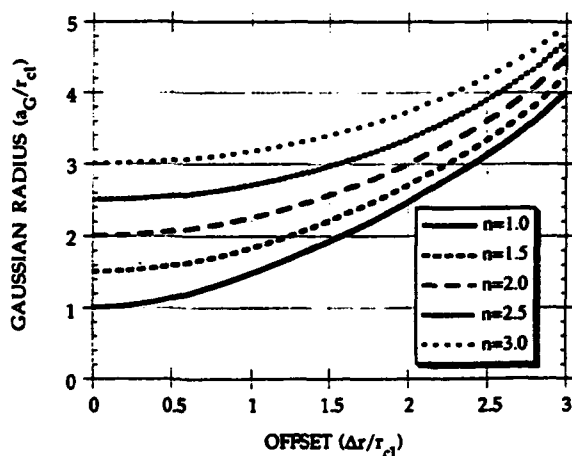


FIG. 8. The reconstructed half-current radii from the data inversion routines as a function of beam offset ($\Delta r/r_{cl}$) assuming a Gaussian beam profile with Gaussian radius $a_G = n r_{cl}$ ($n = 1, 1.5, 2, 2.5$, and 3) where r_{cl} is the radius of the center collector (SFC1). If the beam centroid offset is one-half the Gaussian radius or less, then the fitted half-current radius is within 10% of the actual half-current radius.

Numerical simulation of the detector response suggested that this collector geometry could resolve the large half-current radii ($a_{1/2} \approx 5$ cm) characteristic of the beam head as well as small half-current radii ($a_{1/2} < 1$ cm) characteristic of the beam radius at peak current. The combination of low current-density and large half-current radii ($a_{1/2} \approx 5$ cm), which would be characteristic of the beam head, resulted in signal amplitudes comparable to background noise levels for the center collector. Data on the four remaining collectors were sufficient, however, to allow the fitting algorithms to produce fits to the input data good to within the accuracy of the measurement ($\pm 5\%$). Similarly, small half-current radii ($a_{1/2} < 1.5$ cm), which would be characteristic of the peak current, produced redundant signals on the fourth and fifth collectors due to the low current density in the wings of a Gaussian profile, but gave distinct signals on the first four collector segments which were sufficient to determine the half-current radius again to within the accuracy of the experimental measurement.

VI. COMPETITION BETWEEN SCATTERING AND RANGE EFFECTS

The low degree of ionization, surface damage and secondary electron emission make graphite a commonly employed material for use as beam dumps as well as for Faraday cup applications involving intense relativistic electron beams. Preliminary experiments with the segmented concentric Faraday collector on the SuperIBEX accelerator used collector segments made entirely of range-thick graphite. At times late in the beam pulse, when optical diagnostics viewing Cerenkov emission from a thin Teflon[®] foil gave beam radii typically of 1.2 cm, the Faraday collector indicated a radius as much as 20% larger. This discrepancy appears to have been due to electron scattering within the graphite from one collector segment to another giving an anomalously large value for the half-current radius. Since the radial current profile is typically peaked on axis, the scattering from one graphite Faraday collector segment to the next statistically redistributes the beam current distribution towards higher values for the half-current radius. The effect of electron scattering from one segment to the next in the Faraday collector was investigated both theoretically and experimentally.

The range and scattering of charged particles incident on matter are old problems in physics that were treated extensively in the early days of particle accelerators.²¹⁻²³ Energy loss or stopping of energetic electrons in a dense medium is given by²⁴

$$\frac{d\gamma}{dt} = -4\pi NZ \left(\frac{e^2}{mc^2} \right)^2 \frac{\gamma^2}{\gamma^2 - 1} \left[\ln \left(\frac{2mc^2}{\hbar\langle\omega\rangle} \right) - 1 + \frac{1}{\gamma^2} + \ln(\gamma^2 - 1) \right], \quad (5)$$

where $\gamma = (1 - v^2/c^2)^{-1/2}$ is the usual relativistic factor, v is the particle velocity, N is the number density of atoms in the collector, Z is the atomic number, e and m are the electron charge and mass, $\hbar\langle\omega\rangle \approx 10$ eV is a typical atomic

excitation energy, and t is the penetration distance or path length in the material. The stopping power increases proportionally to NZ , i.e., nearly proportionally to the mass density; thus, the range of 5-MeV electrons is approximately 12 mm in graphite ($N = 9.0 \times 10^{22}$ cm⁻³ and $Z=6$), but only about 3 mm in stainless steel ($N = 8.6 \times 10^{22}$ cm⁻³ and $Z=26$ where the principal atomic constituent of stainless steel is iron).

As the electrons slow in the collector material, they suffer numerous small-angle scattering collisions resulting in substantial deviations from their initial straight-line trajectory. This is of little concern in single-element large-area Faraday collectors or multi-element devices with large separation between elements. However, in small-area, closely spaced, multi-element Faraday collectors such as the one described here, an electron incident on one segment may deposit its charge in another segment giving an erroneous measurement of the beam radial current density distribution. The velocity vector of an individual electron scatters into a Gaussian probability distribution of angles q about its original direction,

$$P(\vartheta) = -(\pi\Theta)^{-1/2} \exp(-\vartheta^2/\Theta^2), \quad (6)$$

where Θ increases as²⁵

$$\frac{d\Theta^2(t)}{dt} = 8\pi NZ^2 \left(\frac{e^2}{mc^2} \right)^2 \frac{\gamma^2}{(\gamma^2 - 1)^2} \times \ln \left(\frac{192}{Z^{1/3}} + \frac{1}{2} \ln(\gamma^2 - 1) \right). \quad (7)$$

The scattering rate varies as NZ^2 and thus increases rapidly with the Z of the material.

To determine the degree to which a beam spreads out radially while stopping, it is necessary to solve Eqs. (6) and (7) self-consistently. A Fokker-Planck-type equation which incorporates stopping and scattering could be derived and solved numerically. Equivalently, one could use a Monte Carlo numerical approach to calculate the electron transport. We do not need such an elaborate treatment here. Our objective is merely to understand the circumstances in which scattering from one collector segment to another is excessive and choose material for which this will be a negligible effect. To this end, we present in the Appendix an approximate solution in closed form of the scattering and stopping problem. For electrons with initial energy 5 MeV, we find that the rms radius of the beam electrons at stopping R_{stop} is given by

$$R_{\text{stop}}^2 = R_0^2 + 1.0\Theta_0^2 + 0.21 \text{ cm}^2 \quad (8)$$

in graphite and

$$R_{\text{stop}}^2 = R_0^2 + 0.0017\Theta_0^2 + 0.012 \text{ cm}^2 \quad (9)$$

in stainless steel. Here R_0 is the rms radius and Θ_0 is the rms spread in velocity angles at the entrance plane to the Faraday collector.

The solution shows that beam spreading falls off rapidly with the Z of the collector material, mainly because range shortening is the dominant effect. Equation (8) indicates that spreading in a graphite collector is quite ap-

preciable for beam radii $R_0 < 1$ cm, a regime of primary interest in the SuperIBEX experiments. In stainless steel, by contrast, spreading is only appreciable if $R_0 < 2$ to 3 mm well below the typical minimum beam radii encountered in our experiments. In both cases, the term proportional to Θ_0^2 , which represents simply the effect of straight-line beam trajectories of electrons whose initial velocity is oblique, is a small correction to the scattering term; for 5-MeV electrons propagating in gas prior to striking the Faraday collector, typically $\Theta_0 < 0.05$.

These calculations led to the design of the composite collector segment consisting of a thin graphite overlayer followed by range-thick high-Z material such as stainless steel. The stainless steel is the primary material for stopping and collecting the incident electrons, whereas the purpose of the graphite is to limit melting, spalling, and secondary electron emission.

VII. COMPARISON OF GRAPHITE VERSUS COMPOSITE COLLECTORS (EXPERIMENTAL RESULTS)

Experiments were conducted to verify the theoretical prediction of appreciable scattering across collector elements with the low-Z graphite collector and negligible scattering with higher-Z stainless-steel elements. These experiments also served to test whether the 3-mm graphite overlayer was sufficient to limit surface damage to the underlying stainless steel. A range-thick stainless-steel aperture with radius equal to the center segment was placed immediately in front of the Faraday cup. The outer collectors were thus prevented from collecting any beam current except that scattered outward from the center collector. In the absence of scattering from one element to the next, nearly all the beam current which passes through the aperture would be collected by the center element and all the Rogowski coils would measure the same current within the limit of their calibration accuracy. If scattering is an important effect, then there will be substantial beam current losses in the center collector relative to the adjacent collector.

The experiment was performed on SuperIBEX with peak currents on the order of 2–10 kA. In the first group of experiments, the center collector was made entirely of graphite. In the second group of experiments, the center collector consisted of a 3-mm-thick graphite disk placed on top of a range-thick stainless-steel cylinder. In both experiments, radiachromic film was wrapped azimuthally around the center collector to detect any electrons scattered from the center collector to the adjacent collector. Whereas the outer Faraday collector Rogowski loops measure 30% higher current than the center collector loop for the case of graphite only, the composite collector consisting of a thin graphite overlayer followed by range-thick stainless shows scattered current of less than 5%. Figure 9(a) shows the discrepancy between the current measured in the first collector and an average of the current measured in the surrounding collectors for the center Faraday collector made entirely of graphite. Figure 9(b) shows the result for the center Faraday collector made of a 3-mm

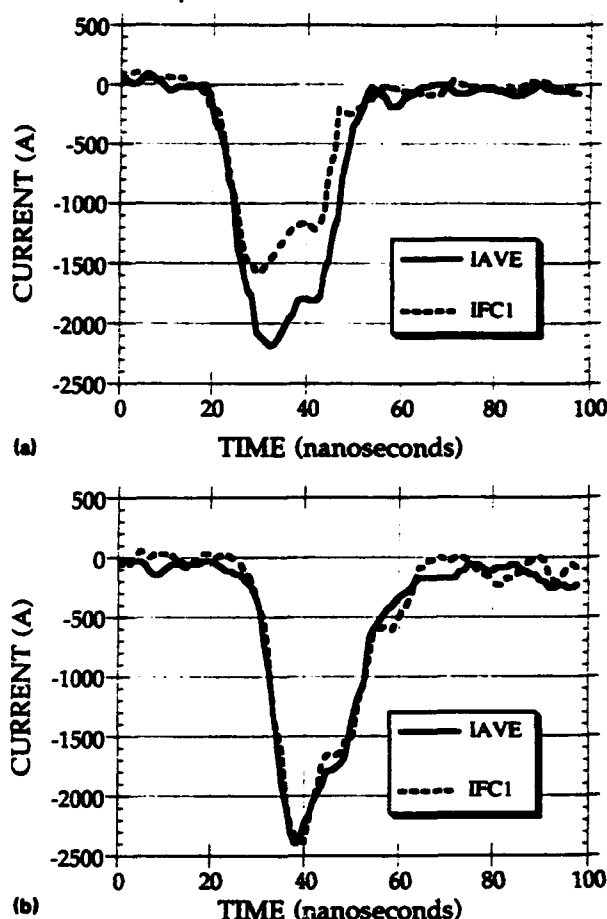


FIG. 9. (a) Current traces for a beam incident on a graphite-only Faraday collector after passing through a range-thick aperture with radius equal to that of the center Faraday collector—IFC1 is the current measured in the center Faraday collector and IAVE is an average of the current measured in the four surrounding collectors. There is a discrepancy of greater than 30% between IFC1 and IAVE due to scattering of electrons from the center collector to the outer collectors. (b) The same measurement made on a Faraday collector consisting of range-thick stainless steel with a thin graphite overlayer. Here the scattering has been greatly reduced and the discrepancy between IFC1 and IAVE is small, indicative merely of the noise level in the measurement.

graphite overlayer on top of range-thick stainless steel. In this case, there is little or no additional current read in the surrounding collectors compared with the current measured on the center collector. The radiachromic film surrounding the graphite center collector showed a significant degree of exposure due to radially scattered electrons, whereas the film surrounding the composite graphite and stainless-steel collector showed essentially no exposure. In addition, disassembly of the graphite and stainless-steel collector showed no visible surface damage to the underlying stainless-steel cylinder for current densities up to 4 kA/cm².

ACKNOWLEDGMENTS

This work was supported by the Defense Advanced Research Project Agency (DARPA), ARPA Order Number 7781, and the Office of Naval Research (ONR). The

authors wish to acknowledge valuable discussions and technical assistance from Dr. R. Hubbard and Dr. R. Fernsler. Additional technical support was provided by A. Noll, G. Littlejohn, W. Dolinger, C. Spohr, and J. Santos.

APPENDIX: CALCULATION OF BEAM SCATTERING IN THE COLLECTOR SEGMENTS

In order to avoid the complexities of a full Fokker-Planck treatment, we shall argue that the process of beam stopping and scattering can be separated into two disparate regimes which we shall treat as appropriate limiting cases. In the first regime, Regime (A), which applies to the early part of the beam electron trajectory in the collector, the beam is well collimated with axial velocities v_z much larger than transverse velocities v_1 . Scattering can then be treated as velocity diffusion in the two-dimensional transverse plane. In the second regime, Regime (B), which applies later in the trajectories, the beam electron velocities have been nearly isotropized. Scattering is then appropriately treated as a random walk in three-dimensional position space. In both cases, energy loss must be treated self-consistently with scattering.

Regime A: Velocity diffusion

The beam enters the collector with only a small spread Θ_0 in velocity angles θ ; typically this is on the order of 5% for the 5-MeV, 10–20 kA beams produced by the Super IBEX accelerator. In this situation, the principal effect of scattering is to add random velocity increments to the transverse electron velocity v_1 . This comes at the expense of the axial velocity v_z , but the decrease in v_z due to the scattering is small until Θ becomes a large angle. Thus the process at work is velocity diffusion in the transverse plane, which is directly represented by Eq. (7) for $d\Theta^2/dt$. This equation must be integrated simultaneously with Eq. (5) for γ .

Equation (5) can be approximated by setting $\ln(2mc^2/\hbar(\omega)) \approx \ln(10^5)$, and using an average value for the small time-dependent correction $\gamma^{-2} + \ln(\gamma^2 - 1)$. For initial value $\gamma_0 \approx 11$, this gives

$$\frac{d\gamma}{dt} = -K_{\text{stop}} \approx -1.37 \times 10^{-23} NZ. \quad (\text{A1})$$

Although (A1) neglects various γ -dependent factors on the right-hand side, it is remarkably accurate; errors are on the order of 10%. It follows that

$$\gamma = \gamma_0 - K_{\text{stop}} t, \quad (\text{A2})$$

where the subscript zero indicates the value at the entrance to the collector. K_{stop} can be regarded as a very weakly dependent function of γ_0 ; for $\gamma_0 = 11$, K_{stop} has a numerical value of 7.4 for graphite and 30 for stainless steel.

In the same spirit, Eq. (7) for Θ^2 can be approximated as

$$\frac{d\Theta^2(t)}{dt} = \frac{K_{\text{scat}}}{\gamma^2} = 1.20 \times 10^{-23} \frac{NZ^2}{\gamma^2}, \quad (\text{A3})$$

where K_{scat} is similarly a very weak function of γ_0 , with the value at $\gamma_0 = 11$ of 39 for graphite and 630 for stainless steel. Inserting (A2) into (A3) and integrating then gives

$$\Theta^2 = \Theta_0^2 + \frac{K_{\text{scat}} t}{\gamma_0(\gamma_0 - K_{\text{stop}} t)}. \quad (\text{A4})$$

For a velocity space diffusion process, the evolution of the rms radius R is related to the velocity-angle rms spread Θ by

$$\frac{d^2 R^2}{dt^2} = 2\Theta^2(t). \quad (\text{A5})$$

Upon inserting (A4) for Θ^2 , Eq. (A5) can be integrated twice to give

$$R^2(t) = R_0^2 + \left(\Theta_0^2 - \frac{K_{\text{scat}}}{K_{\text{stop}} \gamma_0} \right) t^2 - \frac{2K_{\text{scat}} \gamma_0}{K_{\text{stop}}^3} \times \left[\left(1 - \frac{K_{\text{stop}} t}{\gamma_0} \right) \left[1 - \ln \left(1 - \frac{K_{\text{stop}} t}{\gamma_0} \right) \right] - 1 \right]. \quad (\text{A6})$$

It is reasonable to expect that this treatment is valid qualitatively up to the value of t determined by

$$\Theta^2(t_1) = 1. \quad (\text{A7})$$

According to Eqs. (A4) and (A2), this is given by

$$t_1 = \frac{\gamma_0^2}{\gamma_0 K_{\text{stop}} + K_{\text{scat}}} \quad (\text{A8})$$

and the value of γ is then

$$\gamma_1 \equiv \gamma(t_1) = \frac{K_{\text{scat}} \gamma_0}{K_{\text{scat}} + K_{\text{stop}} \gamma_0}. \quad (\text{A9})$$

For graphite with $\gamma_0 = 11$, $t_1 = 1.00$ cm, $\gamma_1 = 3.6$, and

$$R_1^2 = R_0^2 + 1.00 \Theta_0^2 + 0.17 \text{ cm}^2. \quad (\text{A10})$$

For stainless steel with $\gamma_0 = 11$, $t_1 = 0.13$ cm, $\gamma_1 = 7.1$, and

$$R_1^2 = R_0^2 + 0.0017 \Theta_0^2 + 0.006 \text{ cm}^2. \quad (\text{A11})$$

At the point t_1 , the beam velocities have been largely isotropized. We see that this occurs far along in the trajectory for graphite, but early for stainless steel. It is also apparent that the radial spreading in real space at this point is much greater for the graphite than for stainless.

Regime B: Random walk in three-dimensional position space

For $t > t_1$, we shall treat the beam electrons as if they were isotropic in velocity distribution (although this is still only roughly true at t_1). Thus scattering no longer provides a net transfer of energy from v_z^2 to v_1^2 , and two-dimensional velocity-space diffusion for v_1 is no longer an appropriate model. From this point on, individual electrons can be regarded as doing a random walk with constant speed c (we neglect the decrease in speed for $\gamma \approx 1$) and with the time-step t equal to the time for an electron to scatter additionally through $\Theta = \pi/2$, and thus lose the memory

of its velocity direction. According to Eq. (A4), τ is a decreasing function of t given by

$$\tau = \frac{\gamma^2(t)}{\gamma(t)K_{\text{stop}} + (4/\pi^2)K_{\text{scat}}} \quad (\text{A12})$$

Since the transverse speed $v_{\perp} = (v_x^2 + v_y^2)^{1/2}$ is $(2/3)^{1/2}c$ for an isotropic velocity distribution, this random walk causes the transverse rms radius $R(t)$ to increase according to

$$\frac{dR^2}{dt} = D(t), \quad (\text{A13})$$

where the diffusion coefficient $D(t)$ is given by

$$D(t) = \frac{v_{\perp}^2}{c^2} \tau(t) = \frac{2}{3} \frac{\gamma^2(t)}{\gamma(t)K_{\text{stop}} + (4/\pi^2)K_{\text{scat}}} \quad (\text{A14})$$

Equations (A13) and (A14) can be integrated in closed form, using (A1) to relate γ to t . Performing the integral from t_1 to the point where the electrons stop ($\gamma = 1$), we find

$$R_{\text{stop}}^2 - R^2(t_1) = \frac{2}{3K_{\text{stop}}} \left[\frac{\gamma_1^2 - 1}{2} - \frac{4}{\pi^2} K(\gamma_1 - 1) + \frac{16K^2}{\pi^4} \ln \left(\frac{\gamma_1 + (4/\pi^2)K}{1 + (4/\pi^2)K} \right) \right], \quad (\text{A15})$$

where $K = K_{\text{scat}}/K_{\text{stop}}$. The value of the right-hand side of (A15) is 0.04 cm^2 for graphite and 0.006 cm^2 for stainless steel. Thus, combining this result with (A10) or (A11), we have for graphite

$$R_{\text{stop}}^2 = R_0^2 + 1.00\theta_0^2 + 0.21 \text{ cm}^2 \quad (\text{A16})$$

and for stainless steel

$$R_{\text{stop}}^2 = R_0^2 + 0.0017\theta_0^2 + 0.012 \text{ cm}^2. \quad (\text{A17})$$

It is apparent that radial spreading is significant in graphite for beams with $R_0 < 1 \text{ cm}$, but in stainless steel only for beams with $R_0 < 3 \text{ mm}$.

- ¹E. P. Lee, *Phys. Fluids* **21**, 1327 (1978).
- ²W. M. Fawley, *Bull. Am. Phys. Soc.* **35**, 1054 (1990).
- ³R. F. Hubbard, S. P. Slinker, R. F. Fernsler, M. Lampe, and G. Joyce, *Bull. Am. Phys. Soc.* **35**, 2083 (1990).
- ⁴M. Lampe, R. F. Fernsler, R. F. Hubbard, and S. P. Slinker, *Bull. Am. Phys. Soc.* **35**, 2083 (1990).
- ⁵K. L. Brown and G. W. Tautfest, *Rev. Sci. Instrum.* **27**, 696 (1956).
- ⁶E. J. Lauer, R. J. Briggs, T. J. Fessenden, R. E. Hester, and E. P. Lee, *Phys. Fluids* **21**, 1344 (1978).
- ⁷A. Luches, V. Nassisi, and M. R. Perrone, *Rev. Sci. Instrum.* **56**, 758 (1985).
- ⁸H. Matsuzawa and T. Akitsu, *Rev. Sci. Instrum.* **58**, 140 (1987).
- ⁹M. G. Mazarakis, R. B. Miller, J. W. Poukey, and R. J. Adler, *J. Appl. Phys.* **62**, 4024 (1987).
- ¹⁰D. Pellinen, *Rev. Sci. Instrum.* **41**, 1347 (1970).
- ¹¹R. L. Schuch and J. G. Kelly, *Rev. Sci. Instrum.* **43**, 1097 (1972).
- ¹²T. P. Starke, *Rev. Sci. Instrum.* **51**, 1473 (1980).
- ¹³W. Stygar and G. Gerdin, *IEEE Trans. Plasma Sci.* **10**, 40 (1982).
- ¹⁴R. B. Miller, *Introduction of the Physics of Intense Charged Particle Beams* (Plenum, New York, 1982), p. 150.
- ¹⁵S. Humphries, Jr., *Charged Particle Beams* (Wiley, New York, 1990), p. 583.
- ¹⁶E. P. Lee, *Phys. Fluids* **19**, 60 (1976).
- ¹⁷D. A. H. Jacobs, Ed., *The State of the Art in Numerical Analysis* (Academic, London, 1977), p. 269.
- ¹⁸W. H. Press, B. P. Flannery, S. A. Teukolsky, and W. T. Vetterling, *Numerical Recipes: The Art of Scientific Computing* (Cambridge University Press, Cambridge, 1986), p. 254.
- ¹⁹T. J. Fessenden, B. W. Stallard, and G. G. Berg, *Rev. Sci. Instrum.* **43**, 1789 (1972).
- ²⁰R. E. Pechacek (private communication).
- ²¹H. A. Bethe, M. E. Rose, and L. P. Smith, *Proc. Am. Phil. Soc.* **78**, 573 (1938).
- ²²W. A. Fowler, C. C. Lauritsen, and T. Lauritsen, *Rev. Mod. Phys.* **20**, 236 (1948).
- ²³R. R. Wilson, *Phys. Rev.* **84**, 100 (1951).
- ²⁴J. D. Jackson, Jr., *Classical Electrodynamics*, 1st ed. (Wiley, New York, 1962), p. 440.
- ²⁵J. D. Jackson, Jr., *Classical Electrodynamics*, 1st ed. (Wiley, New York, 1962), p. 457.

Appendix JJ

Enhanced Mixing from Shock-Generated Turbulence in Dusty Air

Enhanced mixing from shock-generated turbulence in dusty air

P. Boris, J. Boris, R. Hubbard, E. Oran, and S. Slinker

Laboratory for Computational Physics & Plasma Physics Division, Naval Research Laboratory, Washington, DC 20375-3000, USA

Abstract. Rapid, localized deposition of energy in air accompanies the propagation of laser beams, lightning bolts, and charged-particle beams. Unless the beam and the ionized channel in which it propagates are perfectly symmetric, uniform, and coaxial, there is misalignment between pressure gradients generated by the shocks associated with the energy deposition and the density gradients induced by the rapid expansion of the heated beam channel. This results in persistent vorticity rapidly cascading into turbulence. This shock-generated turbulence mixes cold gas from outside the channel with the beam-heated gas, quenching and broadening the channel much faster than thermal conductivity would suggest. This "anomalous thermal conduction," which in lightning bolts accounts for much of the Earth's nitrogen fixation, was first observed without explanation in experiments (Grieg et al. 1985). It was subsequently explained theoretically and simulated computationally in a number of two-dimensional cases (Picone et al. 1981, Picone and Boris 1983, 1988). Recent experiments at Livermore, discussed in (Hubbard 1990) with very uniform symmetric beams in clean gas, however, showed markedly less turbulence than earlier experiments, suggesting that possibly the purity of the propagation gas may have been a factor. This paper reports 2-D and 3-D simulations including the enhanced turbulence arising from dust particles exploded by the beam in air.

Key words: Dusty air, Mixing, Turbulence

1. Description of the simulation codes

Compressible gasdynamic problems involving both rotational effects (vortices, turbulence) and compressible effects (sound waves, shocks) are described by a set of multidimensional continuity equations which express the physical laws of mass, momentum, and energy conservation. In 2-D gasdynamics there are four continuity equations all having basically the same form. In 3-D there are five. Each of these equations requires an accurate, high-resolution algorithm for its solution because fluid problems usually generate very steep gradients in the solution such as at shocks and vortex interaction boundaries (Boris and Book 1976).

Each of the individual continuity equations, in each of the Cartesian directions is solved by a single, highly optimized algorithm called Flux-Corrected Transport which guarantees the physically important positivity property of fluid mass and energy densities. We use the most recent one-dimensional version of the FCT algorithm, LCPFCT (Boris et al. 1991) to solve the set of coupled continuity equations. This flexible general module is used with direction and timestep splitting to construct two-dimensional and three-dimensional simulations which allow physically realistic boundary conditions in a number of non-periodic geometries. The kernel of the algorithm consists of about 30 lines of C-star which has been specifically designed and optimized for parallel computation on the Connection Machine.

A Connection Machine consists of many thousands of individual scalar processors connected in a hypercube configuration (Oran et al. 1990a, 1990b). Communication to and control of these processors is through a front-end computer. The user controls the 16,384 processors on the CM through a front-end computer; at NRL these are Suns. Each of the individual processors can be reconfigured into a larger number of virtual processors, typically in powers of two. The actual

investigation of weak
Proc 15th Intl Symp

n. Adiabatic waves in

reflection of a shock
29-248:422

of planar shock waves
on Shock Tubes and

gas in a shock tube.

nonlinear hypersonic

computational grid.
pipelined processing
comparable to that

Table 1. Form factor terms

L	κ	τ_{eq}	f
0.0	0.0 (cm^2/sec)	$\approx 90 \mu\text{s}$	0.0
0.05	44.5 (cm^2/sec)	$\approx 90 \mu\text{s}$	0.06
0.20	143.2 (cm^2/sec)	$\approx 90 \mu\text{s}$	0.21
0.35	224.3 (cm^2/sec)	$\approx 100 \mu\text{s}$	0.35
0.50	258.7 (cm^2/sec)	$\approx 110 \mu\text{s}$	0.44
0.75	235.8 (cm^2/sec)	$\approx 110 \mu\text{s}$	0.40
1.00	146.3 (cm^2/sec)	$\approx 120 \mu\text{s}$	0.28
1.20	62.3 (cm^2/sec)	$\approx 120 \mu\text{s}$	0.12

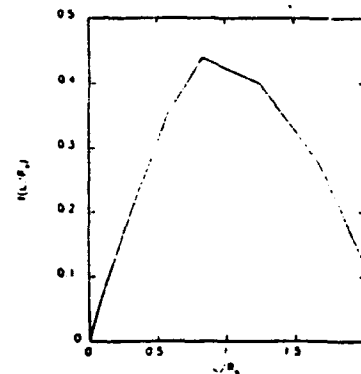


Fig. 1. Form factor curve

-D FCT gasdynam-
convective cooling in
cooling process and
ects in the recently
OE beams had mod-
patterns. However,
tric deposition pro-
ve first describe 2-D
s massively-parallel
much longer than
l. these simulations
ly is to estimate the

ral sets of possible
he turbulence prob-
oth a stretching and
flected shock waves
imulations assumed
calculations began
re. In the five pulse
th. Each pulse after
at a distance L =
erent uncertainty in

nel radius, $R_c = .800$
0.89 mg/cm^3 , and
to a cell size of 0.1
The multi-pulse case
eristic beam radius,
erpressure, $\delta P_b = 2$
e x and y directions

ation given by f =
ted vortex filament
e to its final radius
 τ_{eq} was the equilibra-
nd channel densities,
of f, κ , and τ_{eq} are
yielded the graph in
he form factor. The
ne and Boris and for

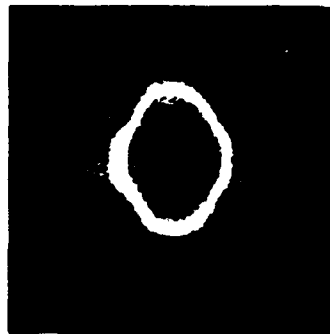


Fig. 2. Two-pulse density contour



Fig. 3. Two-pulse vorticity contour



Fig. 4. Multi-pulse density contour



Fig. 5. Multi-pulse vorticity contour

The pictures in Figs. 2-5 show graphically the turbulent effects that can occur with multiple particle beams in air. The first set of parameters was for a two pulse simulation and Figs. 2 and 3 show density contours and vorticity contours. The second set of parameters was for a five pulse

case where Figs. 4 and 5 correspond to the same quantities as described in the two pulse case. Figure 2 showed that over the 2 ms time scales of relevance for ATA/MPPE the channel did not deform significantly for the listed parameters. This figure, coupled with the lack of turbulence seen on the vorticity plot in Fig. 3 and with the velocity data taken from the FCT code (V_{\max} after equilibrium of 2-3 m/s) lead to the conclusion that turbulence won't be a factor in the two pulse experiments.

The five pulse case was very different, however. Figure 4 showed much greater channel deformation after the fifth pulse than was seen in the two pulse case. This deformation, added to the complex vorticity pattern shown in Fig. 5 and the large maximum fluid velocities (10-15 m/s), lead to the conclusion that turbulence would play a major role in the beam propagation experiment modeled by this simulation. The turbulence effect could be lessened if the beam-channel offsets are kept small (i.e. less than $\approx 0.1 R_0$) and interpulse separation short (i.e. less than ≈ 1 ms).

3. Three-dimensional simulations

The recent symmetric beam experiments at Livermore (Hubbard 1990) in uniform clean gas showed much less turbulence than earlier experiments. Several different reasons were postulated for this difference: 1) large, undiagnosed differences between the two sets of experiments such as two-dimensional filamentation of the earlier beams, 2) high sensitivity to three-dimensional beam instability effects not treated in previous theoretical work nor accessible to earlier computations, and 3) the generation of small-scale turbulence by micron-scale particulate inclusions in the gas which explode in the beam. Earlier generations of laser experiments, in fact, employed particulates to cause the initial channel ionization and breakdown.

We now present 3-D time-dependent numerical simulations of shock-generated turbulence in the presence of suspended dust particles. Because of the obvious differences in the attention to the purity of the propagation gases in the various experiments, this third alternative was a priori considered to be the most likely explanation and the subject of the 3-D numerical experiments reported here. Previous research on shock-generated turbulence had avoided the specifically 3-D effects such as particle inclusion asymmetries because digital computing hardware, until the last two or three years, has been too small and slow to permit adequate treatment of the 3-D problem. The inclusion problem is particularly difficult in 3-D because of the wide range of space scales involved. With the arrival of multiprocessor Crays in the scientific community with millions of words of memory, and in particular, with the arrival of the massively parallel TMC Connection Machine at NRL, such computations became possible.

The 3-D effects of particle inclusions in beam-generated turbulence were studied in several long computations using our optimized Flux-Corrected Transport model FAST3D with a $256 \times 128 \times 128$ grid on the CM. The computational cells were 0.1 mm on a side. The straight beam channel, initially at rest, had a linear density profile from 0.43 mg/cm³ inside of 2.0 mm radius increasing to 1.29 mg/cm³ at 2.5 mm radius and beyond. 25 lower density pockets (particulate inclusions) were added on a helix of radius 1.5 mm. Each inclusion had a factor of two density reduction in an expanded radius of 0.4 mm, representing a dust particle already exploded by the initial beam. A second beam pulse was represented by a 1.0 mm radius 10:1 overpressure in a mode 3 oscillating path in the center of the channel with a displacement of 1.0 mm. This roughly represents a hose-like perturbation of about 8.5 mm wavelength. The density initial conditions are shown in Fig. 6 for a number of slices along the length of the beam channel. The inclusions are seen as dark spots near the periphery of the channel.

After the initial rapid expansion to pressure equilibrium, a residual flow of complex vortex filaments remains and linearly increases the area of the well mixed region. The large-scale vorticity pattern generated by the expansion shock, and the well-developed turbulent state after 4000

two pulse case. channel did not of turbulence T code (Vmax ctor in the two

channel deformation, added to the (10-15 m/s), agation experiment beam-channel less than ≈ 1

form clean gas were postulated iments such as ensional beam computations, ions in the gas ed particulates

l turbulence in ne attention to ive was a priori al experiments specifically 3-D , until the last e 3-D problem. of space scales ith millions of IC Connection

died in several) with a $256 \times$ straight beam 2.0 mm radius ts (particulate of two density xploded by the erpressure in a). This roughly itial conditions The inclusions

omplex vortex -scale vorticity ate after 4000

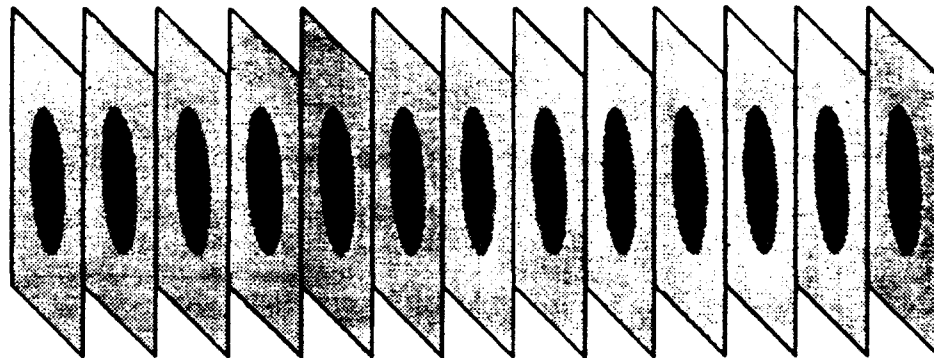


Fig. 6. Density initial contour



Fig. 7. Heated channel at 250 μsec

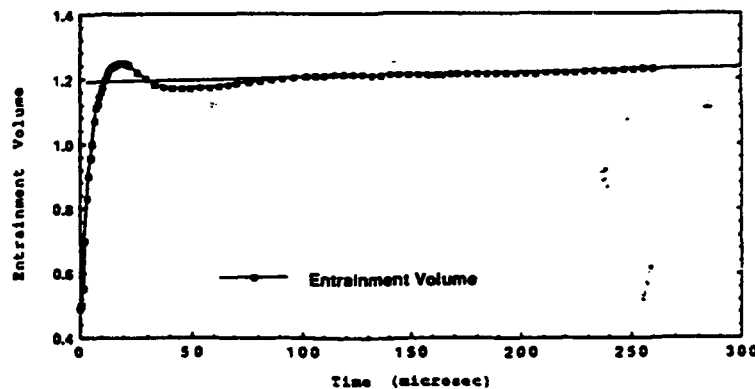


Fig. 8. Channel cross-section vs. time

timesteps (250 μs) are shown in Fig. 7 where a remnant of the large-scale sinusoidal perturbation is overlaid with appreciable small-scale turbulence from the inclusions. The long-term linear growth of the beam-channel area corresponds to an anomalous diffusion coefficient of $140 \text{ cm}^2/\text{s}$ as shown

in Fig. 8. Although the detailed simulations left residual turbulence velocities of about 40 m/s four or five times faster than previously observed in 2-D simulations, these flows are still slow compared to the sound speed and thus require many short timesteps. To deal with this, the timestep stretching algorithm developed and implemented in the original 2-D CM beam-channel code (Picone and Boris 1983) was adapted to the FAST3D model. Since the residual turbulent flows exceed 40 m/s, the time stretching factor was limited to 4:1 and could only be applied after the initial fast shock solutions from the second beam overpressure had exited the computational domain. The method of application, essentially an artificial compression algorithm, was designed to guarantee no numerical vorticity generation in isentropic regions.

Using this algorithm and completely filling the 16K processor NRL Connection Machine the first 200 μ s of the beam channel evolution will be simulated. The mixing diagnostic used was the time evolution of the entrainment volume, defined as the volume of the gas in the initial beam channel plus the volume of any background air entrained out to the 5% channel gas contour level. The results of these simulations show that dust particles can indeed contribute significantly to the shock-generated turbulence due to the exceedingly sharp gradients and small scales which they induce.

Acknowledgements

The authors would like to thank J.M. Picone, C. Li, and A. Whaley for their help during the course of this research which was sponsored by the Office of Naval Research through the Naval Research Laboratory and the Defense Advanced Research Projects Agency.

References

- Boris JP, Book PI (1976) Solution of the continuity equation by the method of flux-corrected transport. *Meth in Comp Phys*. 16:85-129
- Boris JP, Gardner JH, Oran ES, Zalesak S, Ellsey J, Patnaik G, Book DL, Guirgnis RH (1989) LCPFCT - A monotone algorithm for solving continuity equations, to appear as a Nav Res Lab Memorandum Report.
- Greig JR, Pechacek RE, Raleigh M (1985) *Phys Fluids* 28:2357.
- Hubbard RF, Ali AW, Boris JP, Boris PR, Fernsler RF, Joyce G, Oran ES, Picone JM, Sinker SP, Taylor RD (1990) NRI 1989 beam propagation studies in support of the ATA multi-pulse propagation experiment. US Nav Lab Mem Report, pp 6677
- Keeley D, Welch D (1990) private communications
- Oran ES, Boris JP, Boris PR, Brown E, Li C (1990a) Fluid dynamic computations on a connection machine - preliminary timings and complex boundary conditions. Presentation & AIAA Paper 90-0335, AIAA 28th Aerospace Sciences Meeting, Reno NV
- Oran ES, Boris JP, Whaley RO, Brown EF (1990b), Supercomputing review. *The Magazine of High-Performance Computing*, pp 52-60
- Picone JM, Boris JP, Greg JR, Raleigh M, Fernsler RF (1981), *J Atmospheric Sci* 38:2056-2062
- Picone JM, Boris JP (1983) *Phys Fluids* 2:365-382
- Picone JM, Boris JP (1988) Vorticity generation by shock propagation through bubble in a gas. *J Fluid Mech* 189:23-51

Int

T. F
1. In
2. Hal

Abst
focu
bubt
moti
the r
in air

Key

1. Ir

Unti
in th
(Cok
of re-
these
theor
a rea
The
pres
inter:
Test:
inter:
focu
inter

2. Es

The s
simul
beam
chan
obser-
200 μ s
circui

3. Re

Figur
which
upper
two b
respec
the w

Appendix KK

Reverberation Modeling with the Adiabatic Normal Mode Model Applications to the ARSRP Experiments

Reverberation Modeling with the Adiabatic Normal Mode Model Applications to the ARSRP Experiments

**Dalcio K. Dacol, Paul Boris (SAIC), Edward Jennings,
Elisabeth Kim (PSI).**

**Naval Research Laboratory
Acoustics Division
Washington, D.C. 20375-5350**

1. INTRODUCTION

Our objective is to develop a model for the long range reverberation in the ARSRP natural laboratory that is able to reproduce the major qualitative features of the data and provide a reasonable quantitative estimate of such reverberation levels. We have been using the adiabatic normal modes model to estimate the transmission loss. A full wave backscattering calculation allows us to estimate also the scattering strenghts.

2. REVERBERATION MODELING

Once we compute the transmission loss and the scattering coefficients using an approach discussed by the authors in previous meeetings, we follow a procedure similar to the one used by Makris [1] to map the experimental reverberation to the bathymetry. Since the geometry for the Acoustics Reconnaissance experiment was to a good aproximation monostatic we consider here only this case.

From our approximate solution to the Helmholtz equation for the acoustic field we obtain estimates for the intensity of the acoustic field at the bottom and for the backscattered field at the bottom. Then we carry out a spatial convolution of the product of the intensities of the incident and the backscattered fields at the bottom with the beam pattern of the receiving array. This procedure involves computing for each point on the reverberation map at a distance R from the source, an integral over an annulus with the same radius on the horizontal plan, centered on the source, and with width equal to a pulse lenght. This quantity is then plotted on the horizontal plane covering the region of interest.

3. CONCLUSIONS

We present five plots. The first one, labeled Bathymetry, shows the bathymetry in the natural laboratory, with the SW corner at coordinates 25.3 N - 47.4 W and the NE corner at coordinates 27.4N - 45.0W, corresponding to a 240 km by 240 km area. This is the high resolution bathymetry and it differs significantly from the one in the DB5 database. Just below it is a experimentally obtained reverberation map extracted by N. Makris from the data collected at the ARSRP Acoustics Reconnaissance experiment. The other three plots represent our attempt to simulate this data set. The parameters are those of the experiment, with the frequency being

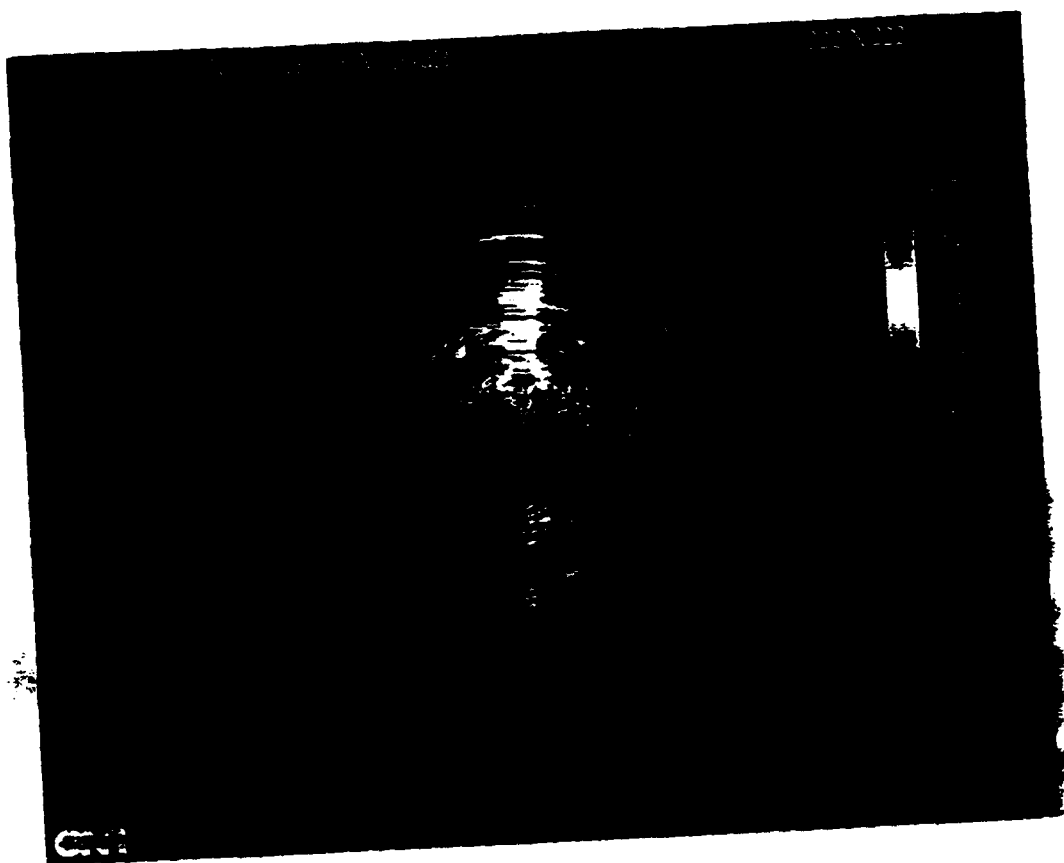
270 Hz. The third plot is the transmission loss at the bottom over the same area as in the bathymetry plot. The fourth plot is the dB level of the backscattered field at the bottom, also over the 240 km by 240 km region. Finally, the fifth plot, entitled Reverberation Map, presents our attempt to reproduce the experimental data mentioned above. Noticed that area has been reduced to conform with the data, instead of a 240 km by 240 km area, we present the reverberation over a 222 km by 222 km region. Some of the qualitative features of the data are reproduced, including the returns from the big spot on the left side, near mid-height in the empirical reverberation map. But the reverberation level is quite off. While the reverberation level in the data ranges from 40 dB to 100 dB, ours ranges from 3 dB to 46 dB. At this moment we do not know whether this huge difference is due to the omission of some factor in our processing of the synthetic data or in the acoustic field modeling itself.

4. ACKNOWLEDGEMENTS

One of the authors (DKD) is grateful to Dr. N. Makris for discussions on the data analysis and a suggestion for the computation of the spatial convolution integral. This work was supported by the Office of Naval Research.

5. REFERENCES

- 1) N. C. Makris, "Imaging ocean-basin reverberation via inversion", submitted to JASA.
- 2) W. A. Kuperman, M. B. Porter, J. S. Perkins and R. B. Evans, "Rapid computation of acoustic fields in three-dimensional ocean environments", J. Acoust. Soc. Am. 89, 125, 1991.
- 3) R. B. Evans and K. E. Gilbert, "Acoustic propagation in a refracting ocean waveguide with an irregular interface", Comp. & Maths. with Appls., 11, No. 7/8, 1985.
- 4) A. D. Pierce, "Extension of the method of normal modes to sound propagation in an almost stratified medium", J. Acoust. Soc. Am. 37, 19, 1965.
- 5) M. V. Berry and K. E. Mount, "Semiclassical approximations in wave mechanics", Rep. Prog. Phys., 35, 315, 1972.
- 6) H. Bremmer, "The WKB approximation as the first term of a geometric-optical series", Commun. Pure and Appl. Math., 4, 105, 1951.
- 7) P. C. Etter, "Underwater Acoustic Modeling", published by Elsevier Applied Science, New York, 1991.



Appendix LL

**Hydrodynamic Simulations of Beam-Generated
Turbulence in Channels**

HYDRODYNAMIC SIMULATIONS OF BEAM-GENERATED TURBULENCE IN CHANNELS*

P. Boris**, J. Boris, R. Hubbard, E. Oran, J. Picone, S. Slinker
Naval Research Laboratory, Washington, DC 20375-5000

INTRODUCTION

Heated columns or channels have been produced at several laboratories using lasers, guided discharges, or propagating relativistic electron beams. These experiments¹ have shown that turbulent or convective mixing of the hot air with the cooler gas outside the channel causes the channels to cool much more rapidly than expected from classical thermal conduction. Picone and Boris² modeled this process using a standard 2-D FCT hydro code and developed simple phenomenological models for incorporating convective cooling in axisymmetric models. These simple models use a form factor f to model the cooling process and have been used by several groups^{3,4} to predict range extension effects in the upcoming ATA Multi-Pulse Propagation Experiment (ATA/MPPE).

ATA/MPPE will attempt to produce beams which can propagate with modest hose instability growth, thus producing nearly axisymmetric deposition patterns. However, most previous experiments and simulations treated cases with highly asymmetric deposition profiles, so relatively little is known in the regime of interest to ATA/MPPE. In this paper, we describe 2-D hydro calculations using a new FCT⁵ algorithm developed for NRL's massively-parallel Connection Machine. Since the time scales of interest for ATA/MPPE are much longer than those in the original Picone-Boris study² and a finer spatial grid is required, these simulations would have been very expensive to run on a CRAY. A major goal of this study is to estimate the scaling of the Picone-Boris form factor f in the nearly-axisymmetric regime.

PROBLEM DEFINITION

A version of the LCPFCT⁶ code was run for several sets of possible ATA/MPPE parameters. Both two pulse and five pulse cases were studied. The turbulence problems were set up on a 256 by 256 grid with periodic boundary conditions. Both a stretching and a damping factor were added to the grid in order to limit errors caused by reflected shock waves feeding back into the calculations through the boundary conditions. The simulations assumed that the first pulse generated a smooth gaussian density depression, and the calculations began at the arrival of the second pulse, which created an offset gaussian overpressure. In the five pulse cases, a third pulse was added after 2.0 ms, a fourth after 4.0 ms, and so forth. Each pulse after the second was offset from the channel center randomly in a square pattern at a distance L , 0.5 cm in this case. The random placement of these pulses simulated the inherent uncertainty in aiming the particle beam in the experiment.

The physical parameters for the two pulse case were: characteristic channel radius, $R_c = .800$ cm, characteristic beam radius, $R_b = .600$ cm, channel center density, $\rho_c = 8.90 \times 10^{-4}$ gm/cc, and beam center overpressure, $\delta P_b = 2 \times P_a$. The numerical parameters were set to a cell size of 0.1 cm in both the x and y directions and to a simulation run time of 2.0 ms.

The multi-pulse case had these parameters: characteristic channel radius, $R_c = .888$ cm, characteristic beam radius, $R_b = .600$ cm, channel center density, $\rho_c = 5.90 \times 10^{-4}$ gm/cc, and beam center overpressure, $\delta P_b = 2 \times P_a$. The numerical parameters were set to a cell size of 0.1 cm in both the x and y directions and to a simulation run time of 6.8 ms.

DESCRIPTION OF CODE

Compressible gasdynamic problems generally involve both rotational effects (vortices, turbulence, etc.) and compressible effects (sound waves, shocks, etc.) but are described by a set of multidimensional continuity equations (partial differential equations) which express the physical laws of mass, momentum, and energy conservation. In 2-D gasdynamics there are four continuity equations all having basically the same form. Each of these equations requires an accurate, high-resolution algorithm for its solution because fluid problems generally generate very steep gradients in the solution such as at shocks and vortex interaction boundaries.⁷

Each of the four individual continuity equations, in each of the two Cartesian directions is solved by a single, highly optimized algorithm called Flux-Corrected Transport which guarantees the physically important positivity property of fluid mass and energy densities. This fluid convection module to solve the set of coupled continuity equations, is the most recent one-dimensional version of the FCT algorithm⁵, LCPFCT. This flexible general module is used with direction and timestep splitting to construct two-dimensional simulations which allow physically realistic boundary conditions in a number of non-periodic geometries. The kernel of the algorithm consists of about 30 lines of C-star which has been specifically designed and optimized for parallel computation on the Connection Machine.

A Connection Machine consists of many thousands of individual scalar processors connected in a hypercube configuration⁸. Communication to and control of these processors is through a front-end computer. At NRL, there are two Connection Machines, one with 16,384 (16K) processors and one with 8,192 (8K) processors. The user controls these through one of several kinds of front ends: a VAX, a Symbolics, or a Sun. Each of the individual processors can be reconfigured into a larger number of virtual processors, typically in powers of two, the actual number limited by the storage required for the algorithm and the size of the computational grid. Floating-point arithmetic is carried out by Weitek chips, each of which does pipelined processing of the floating-point operations for 32 of the scalar processors.

RESULTS

In order to estimate the Picone-Boris form factor, f : the equation given by $f = \kappa / g (\delta P_b / P_a) (R_b^2 / \tau_{eq}) \ln(\rho_a / \rho_c)$ must be solved. Here, κ was the integrated vortex filament strength, $g = (R_{bf} - R_b)^2 / R_b^2$ was a measure of the beam expansion rate to its final value R_{bf} , δP_b was the beam-generated overpressure, P_a was the ambient pressure, τ_{eq} was the equilibration time for the vortex filament strength, and ρ_a and ρ_c were the ambient and channel densities, respectively. For the parameters listed above, the quantity $g = 0.23$.

Values of f , κ , and τ_{eq} are listed in table 1 for various values of the beam-channel offset, L. Table 1, yielded the graph in figure 1 which represented one curve of the family of curves that make up the form factor. The curve obtained by this code strongly resembled the curves generated by Picone and Boris and for $L < R_b$, f was proportional to L, thus supporting the

assumptions made in Ref. 3.

The following pictures show graphically the turbulent effects that can occur with multiple particle beams in air. The first set of parameters was for a two pulse simulation and figures 2 and 3 show density contours and vorticity contours. The second set of parameters was for a five pulse case where figures 4 and 5 correspond to the same quantities as described in the two pulse case.

CONCLUSIONS

Figure 2 showed that over the 2 ms time scales of relevance for ATA/MPPE the channel did not deform significantly for the listed parameters. This figure, coupled with the lack of turbulence seen on the vorticity plot in figure 3 and with the velocity data taken from the FCT code (vmax after equilibrium of 2-3 meters/second) lead to the conclusion that turbulence won't be a factor in the two pulse experiments.

The five pulse case was very different, however. Figure 4 showed much greater channel deformation after the fifth pulse than was seen in the two pulse case. This deformation, added to the complex vorticity pattern shown in figure 5 and the large maximum fluid velocities (10-15 meters/second) lead to the conclusion that turbulence would play a major role in the beam propagation experiment modeled by this simulation. The turbulence effect could be lessened if the beam-channel offsets are kept small (i.e. less than $\approx 0.1 R_b$) and interpulse separation short (i.e. less than ≈ 1 ms).

The beam-channel offset used for the five pulse simulations in this paper was probably too large for the ATA/MPPE experiment. The pulse to pulse overpressure ratio in the actual experiment will decrease with pulse number. As a result of these factors, more simulations will have to be conducted to better model the experiment.

REFERENCES

1. J.R. Greig, R.E. Pechacek, and M. Raleigh, *Phys. Fluids* **28**, 2357 (1985).
 2. J.M. Picone and J.P. Boris, *Phys. Fluids* **26** 365-382 (1983).
 3. S. Slinker et al, Poster I-27, these proceedings.
 4. D. Keeley and D. Welch, (private communications).
 5. J.P. Boris, and D.L. Book, Solution of the Continuity Equation by the Method of Flux-Corrected Transport, *Methods in Computational Physics*, 16, 85-129, 1976.
 6. *LCPFCT - A Monotone Algorithm for Solving Continuity Equations*, J.P. Boris, J.H. Gardner, E.S. Oran, S. Zalesak, J. Ellzey, G. Patnaik, D.L. Book, R.H. Guirguis, to appear as a Naval Research Laboratory Memorandum Report, 1989.
 7. *Fluid Dynamic Computations on a Connection Machine - Preliminary Timings and Complex Boundary Conditions*, E.S. Oran, J.P. Boris, P.R. Boris, E. Brown, and C. Li, Presentation & AIAA Paper 90-xxxx, AIAA 28th Aerospace Sciences Meeting, Reno NV, 8-11 January 1990.
 8. *Connection Machine, Model CM-2 Technical Summary*, Thinking Machines Corporation, Cambridge, MA, 1989.
- * Supported by the Defense Advanced Research Projects Agency, ARPA Order No. 4395, Amendment 80, monitored by the Naval Surface Warfare Center.
- ** Science Applications International Corp., Mclean, VA

Table 1: Form Factor Terms

L	κ	τ_{eq}	f
0.0	0.0 (cm^2/sec)	$\approx 90 \mu s$	0.0
0.05	44.5 (cm^2/sec)	$\approx 90 \mu s$	0.06
0.20	148.2 (cm^2/sec)	$\approx 90 \mu s$	0.21
0.35	224.3 (cm^2/sec)	$\approx 100 \mu s$	0.35
0.50	258.7 (cm^2/sec)	$\approx 110 \mu s$	0.44
0.75	235.8 (cm^2/sec)	$\approx 110 \mu s$	0.40
1.00	146.3 (cm^2/sec)	$\approx 120 \mu s$	0.28
1.20	62.3 (cm^2/sec)	$\approx 120 \mu s$	0.12

Fig. 1: Form Factor Curve

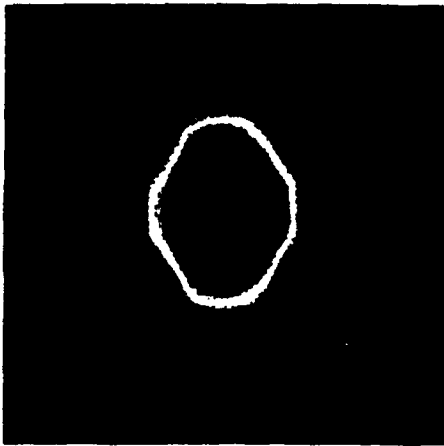
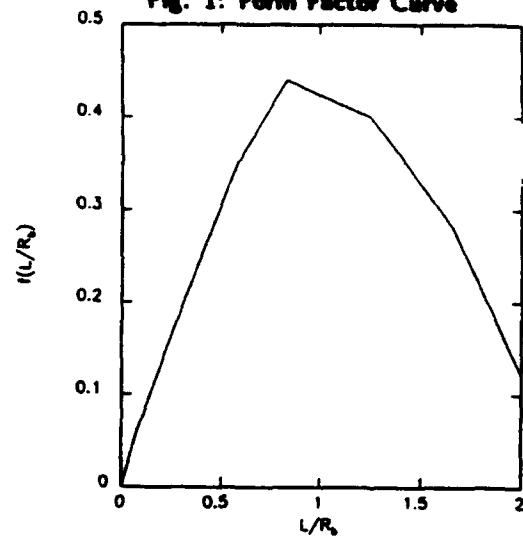


Fig. 2: Two-Pulse Density Contour



Fig. 3: Two-Pulse Vorticity Contour

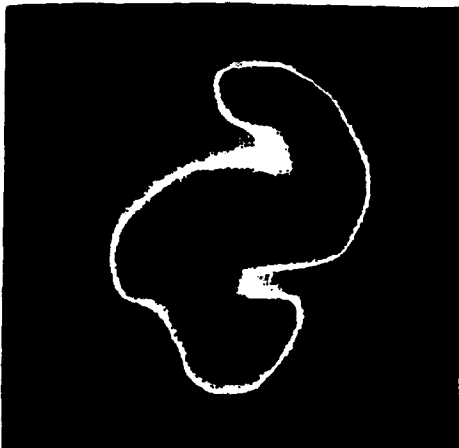


Fig. 4: Multi-Pulse Density Contour



Fig. 5: Multi-Pulse Vorticity Contour

Appendix MM
Beam Propagation in Channels

BEAM PROPAGATION IN CHANNELS^{*}

R. F. Hubbard, S. P. Slinker, R. D. Taylor,^{**} R. F. Fernsler
A, W. Ali, G. Joyce and P. Boris^{***}

Naval Research Laboratory, Washington, DC 20375-5000

I. INTRODUCTION

Beam propagation in density channels is a major focus of the current DARPA experimental program. The ATA Multi-Pulse Propagation Experiment (MPPE) will attempt to demonstrate stability, tracking and range extension in the channel formed by a five-pulse burst of 10 MeV, 6-8 kA beams. Also in progress are tracking experiments at NRL using the PULSERAD and SuperIBEX beams in laser-guided electric discharge (LGED) channels. This paper provides an overview of theoretical work at NRL in support of these propagation experiments. More detail can be found in Refs. 1-7.

II. ATA MULTI-PULSE PROPAGATION STUDIES

Overview: Detailed predictions for an ATA/MPPE burst require treatment of the complicated coupling between beam propagation and channel physics over times scales up to 5 msec. To address these problems, we have carried out five-pulse axisymmetric simulations which combine the SIMMO beam propagation code, the CHMAIR II detailed air chemistry code and the HINT long-time-scale chemistry and hydro code.¹ The results are used to predict the range of each pulse and to provide realistic channels for SARLAC hose instability simulations. Supporting these simulations are more detailed studies of certain air chemistry effects² and convective cooling.³ We have also studied the sensitivity of lead pulse hose instability growth to the amplitude of BBU and corkscrew-induced perturbations⁴ and choice of emittance tailoring method.⁵ Finally, we have assessed the feasibility of an ATA pulse-decoupling experiment.⁶

Typical parameters for these studies are beam energy $E_0 = 10$ MeV, peak current $I_0 = 5$ kA, nominal beam radius $a_0 = 0.5$ cm, pulse length $\tau_p = 33$ nsec, pulse separation $t_s = 1.25$ msec and an emittance variation of 4:1.

multi-pulse axisymmetric propagation and channel dynamics:¹ In these simulations, the SIMMO particle code is used for $\tau < \tau_p$ to propagate the beam and dump beam current density $J_b(r, \zeta, z)$. Here $\zeta = c\tau = ct - z$ is the distance from the beam head and z is the propagation distance in air. CHMAIR II uses the J_b input from SIMMO to calculate beam and ohmic deposition and detailed air chemistry for $\tau_p < \tau < 2\tau_p$ at several z -locations. HINT is then used to calculate the long-time-scale behavior of the channel ($\tau < \tau_s$), including the effects of hydrodynamic expansion, thermal and convective cooling, and vibrational relaxation. This generates a density profile $\rho(r, z)$ which is input into Simm0 for the next pulse in the burst, and the process is repeated.

Six simulations were run to determine the sensitivity of the channel depth and the transported beam fluence to model assumptions. The fluence $Q_n(R, z)$ is defined as the transported beam charge for the n^{th} pulse within a radius R of the beam axis at a fixed location z . The ratio Q_5/Q_1 for $R = 1.1$ cm and $z = 6$ m varied between 1.4 and 1.85, indicating modest range extension. The channel depth at $z = 0$ was very sensitive to the assumed Picone-Boris form factor f for convective cooling:³ the on-axis density at the fifth pulse was a factor of two higher when f was raised from 0 to 0.05. However, the predicted fluence at $z = 6$ m changed by less than 15% because the convectively-cooled channel was significantly broader. Changes in the assumed chemistry model for SIMMO and the inclusion of enhanced vibrational cooling from CO_2 produced modest but noticeable changes in the fluence.²

Chemistry effects in ATA/MPPE:² A new air chemistry model for SIMMO and SARLAC was developed using these same basic approach as in the standard "VIPER" model. The new model includes attachment and revised rate coefficients benchmarked against detailed CHRAIR II calculations in the ATA/MPPE regime. The new model gives similar axisymmetric behavior and generates slightly more hose instability growth. The second major focus of the air chemistry studies was a treatment of the transfer of the energy stored in N_2 vibrational excitations to gas heating. This process occurs on the millisecond time scale but can be speeded up by adding a small amount of CO_2 or water vapor.

Convective cooling in heated air channels:³

Fig 1. Initial displacement $X(\zeta, 0)$ and $Y(\zeta, 0)$ (solid and dashed lines): Case A2

Fig 2. $X(\zeta)$ and $Y(\zeta)$ at $z = 6\text{m}$ for Case A2. BBU-induced hose is stronger (solid line).

Fig 3. $X(\zeta)$ and $Y(\zeta)$ at $z = 8\text{m}$ or Case A3. I_0 is raised to 8 kA; beam is more unstable.

III. RADLAC HOSE INSTABILITY SIMULATIONS

Overview: Both HF and LF perturbations are produced in RADLAC even though BBU is thought to be unimportant. A series of SARLAC simulations were performed using a 0.02 cm 830 MHz HF perturbation in x and a 0.2 cm (at $\zeta = 900\text{ cm}$) sweep perturbation in y . Nominal beam parameters in the simulations were $I_0 = 10\text{ kA}$, $\gamma_0 = 41$ (ramped in some cases), beam radius $a_b = 2\text{ cm}$, rise length $\zeta_r = 300\text{ cm}$ and normalized emittance tapering by a factor η_t of 2-4 over a characteristic length of 200 cm.

RADLAC simulation results: Six simulations were performed as described in the table below. The energies E_{\min} and E_{\max} define the range of the energy ramp, and X_{\max} and Y_{\max} are the maximum hose amplitudes at $\zeta = 900\text{ cm}$ exhibited in 12 m of propagation.

Case	E_{\min}	E_{\max}	η_t	Comment	X_{\max}	Y_{\max}
R1	20 MeV	40 MeV	4	-	0.5 cm	0.5 cm
R2	20	20	4	$a_b = 1.5\text{ cm}$	2.5	0.8
R3	5	20	2	-	> 20	> 5
R4	5	20	4	-	4.5	1.5
R5	5	20	4	$Y_0 = 0.02\text{ cm}$	4.5	0.6
R6	10	20	4	Faster γ -ramp	1.1	0.4

As in the ATA simulations the high frequency modes dominate even though they are initiated at a smaller amplitude. Comparing Cases R1 and R3, it is apparent that relying on the natural tailoring which comes about from the energy ramp may lead to unacceptably large hose amplitudes. This is in part

because the head is so hot that it is quickly lost, leaving behind a poorly-tailored beam. Even when the 4:1 emittance variation is restored to a beam with a γ -ramp (Case R4), the beam is more unstable than in the constant energy case. Figure 4 plots $X(z)$ and $Y(z)$ at $\zeta = 675$ cm for Case R4, showing an initial damping of the LF mode followed by an eventual coupling to the faster-growing HF mode. Hose amplitudes versus ζ at $z = 120$ cm are shown for this case (Fig.5) and for the more unstable weakly-tapered Case R3 (Fig. 6).

Fig 4 $X(z)$ and $Y(z)$ at $\zeta = 675$ cm for RADLAC Case R4. Note initial decay in Y (dash line).

Fig 5. $X(\zeta)$ and $Y(\zeta)$ at $z = 12$ m for Case R4. HF mode (solid line) dominates.

Fig. 6. $X(\zeta)$ and $Y(\zeta)$ at $z = 12$ m for Case R4 (weaker taper). Note shorter pulse length.

IV. CONCLUSIONS AND REFERENCES

For both ATA and RADLAC, high frequency perturbations appear to couple more strongly to the resistive hose instability and should be suppressed if possible even at the expense of higher sweep amplitudes.

1. G. Joyce, R. Hubbard, M. Lampe and S. Slinker, J. Comp. Phys. 81, 193 (1989).
2. G. Caporaso, A. Cole and K. Struve, LLNL Report UCID-88262 (1983).
3. D. Keeley, these proceedings.
4. R. Hubbard, et al Poster I-11, these proceedings.

*Supported by the Defense Advanced research Projects Agency, ARPA Order No. 4395, Amendment 80, Monitored by the Naval Surface Warfare Center,

**Berkeley Research Associates, Springfield, VA 22150

Appendix NN

Foil Focusing for Transport and Conditioning

FOIL FOCUSING FOR TRANSPORT AND CONDITIONING*

R. Fernsler, R. Hubbard, S. Slinker
Naval Research Laboratory, Washington, D.C.

P. Boris,
SAIC, McLean, VA.

INTRODUCTION

Adler¹ and Humphries² have proposed foil focusing as a means of transporting electron beams, while Fawley³ has proposed foil focusing for conditioning. In this paper we address various issues relating to the use of foils for transporting and conditioning ultrarelativistic beams.

FOCAL LENGTH

An isolated foil may be treated as a thin lens of focal length f_ℓ provided $f_\ell \gg b$ and $b \partial/\partial \zeta \ll 1$, where the pipe radius b characterizes the axial range of the foil fields and $\zeta = ct - z$ measures distance behind the beam head. We have extended the analysis of Adler to compute f_ℓ for four beam profiles: flat-topped, Gaussian, parabolic, and Bessel. Plots of f_ℓ in units of $RI_A/(1-f_c)I_b$ versus r/R are shown below for three values of b/R ; here R is the rms beam radius, $I_A = 17\gamma$ kA is the Alfvén current, and f_c ($= 0$ in vacuum) is a plasma charge-neutralization fraction. We conclude from these plots that: (i) f_ℓ is relatively insensitive to beam profile; (ii) the

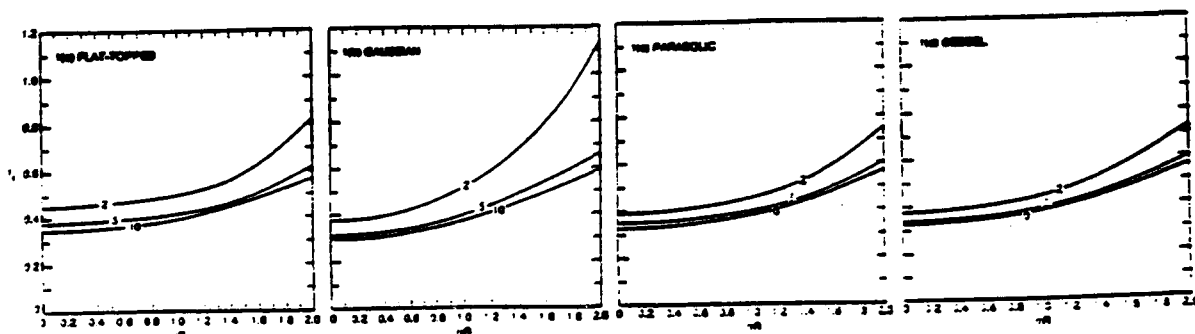


Fig. 1. Focal length f_ℓ in units of $RI_A/(1-f_c)I_b$ for $b/R = 2, 5, 10$.

* Work supported by the Defense Advanced Research Projects Agency ARPA Order No. 4395, Amendment No. 80, monitored by the Naval Surface Warfare Center.

paraxial treatment ($f_\ell \gg b$) is valid only if $(1-f_c)I_b/I_A \ll 0.2$; and (iii), foils are imperfect lenses with $\partial f_\ell / \partial r \neq 0$.

EMITTANCE GROWTH

We have found that a thin lens alters the normalized beam emittance ϵ by

$$\delta \epsilon^2 = \epsilon_{fo}^2 + \epsilon_{f1}^2$$

where

$$\epsilon_{fo}^2 = \gamma^2 [R^2 \langle (r/f_\ell)^2 \rangle - \langle r^2/f_\ell \rangle^2]$$

and

$$\epsilon_{f1}^2 = 2\gamma^2 [R^2 \langle u_r r / c f_\ell \rangle - \langle r^2 / f_\ell \rangle \langle u_r r / c \rangle].$$

Here $u_r(r)$ is the radial fluid velocity at r . Some general properties are: (i) $\delta \epsilon = 0$ for a perfect lens (constant f_ℓ); (ii) $\delta \epsilon$ is independent of the thermal velocity, $\delta \underline{v}_\perp = \underline{v}_\perp - u_r \hat{r}$; and (iii), $\epsilon_{f1} = 0$ if the beam expands self-similarly ($u_r \propto r$). Hence, unless the beam profile changes radically, the emittance increases quadratically by ϵ_{fo}^2 .

Using the previous results for f_ℓ , we find that for foils

$$\epsilon_{fo} = g_3 R (1-f_c) I_b / 17 \text{ kA}$$

where $g_3 = 0.1$ for flat-topped profiles, $g_3 = 0.2$ for parabolic and Bessel profiles, and $g_3 = 0.5$ for Gaussian profiles. The use³ of flat-topped profiles may thus considerably underestimate the emittance increase produced by anharmonic foil focusing. Observe that ϵ_{fo} , like the emittance increase from foil scattering, is independent of beam energy γ . A foil thus tailors ϵ only if R (or I_b) varies with ζ .

MULTI-FOIL TRANSPORT:

Interactions between adjacent foils become important at foil spacings $d \leq b$. The preceding theory of foil focusing can, however, be readily adapted provided the focal length within each foil cell satisfies $f_\ell \gg d$. This condition becomes the new paraxial condition and allows the foil cells to be treated as separate thin lenses.

Simple ray optics⁴ shows that a beam passing through a series of lenses at fixed spacing d and constant f_ℓ is stable provided $d < 4f_\ell$. For a harmonic lens but with $f_\ell \propto R$, we find that stability requires $d < 2f_\ell$, twice as restrictive as for constant f_ℓ . At very large R , saturation occurs. We have also derived a general "matching condition" for a beam of given emittance ϵ :

$$d = 2f_\ell \{1 + [1 - (\gamma R_{\min}^2 / f_\ell \epsilon)^2]^{1/2}\} > 2f_\ell,$$

where R_{\min} is the (minimum) radius between foils. Because this condition violates the stability criterion, we conclude that a matched, stable beam is not possible with foils - i.e., the beam must vary from one foil cell to another. Moreover, emittance growth from anharmonic focusing or foil scattering eventually causes the radius to grow linearly with foil number n .

FRIEZR SIMULATIONS

We have run two types of FRIEZR simulations: those that explicitly compute the foil fields, and those that use the thin-lens formalism. The former can treat a broader class of problems, but it requires small spatial and temporal steps to resolve the foil fields. The full code typically agrees with the theoretical calculations for the focal length and emittance growth to within 20%. Moreover, simulations of multi-foil transport are consistent with the analytical predictions for stability and radius growth, even at high I_b/I_A where the paraxial approximation and the analysis fail.

The use of foils for conditioning was examined using the thin-lens approximation in FRIEZR. Shown below are typical results for ATA using 2-mil carbon foils at $z = 0, 39, 60$ cm and 30-mil at $z = 78$ cm in an evacuated tank of radius 7 cm. The beam parameters were $\gamma = 21$, $I_b = 6$ kA with a 10 ns rise, $R = 1$ cm, and $\epsilon = 0.46$ rad-cm. Although R and ϵ are well tailored at exit, ϵ is higher than desired in the tail. Such overheating worsens at higher I_b/I_A .

CONCLUSIONS

Our analysis and simulations indicate that foil transport and conditioning work best at low I_b/I_A and short distances. At high I_b/I_A , emittance growth from scattering or anharmonic focusing becomes excessive,

and this growth accelerates as the beam expands. For transport, we have found that the foil spacing must be kept small to prevent unstable growth.

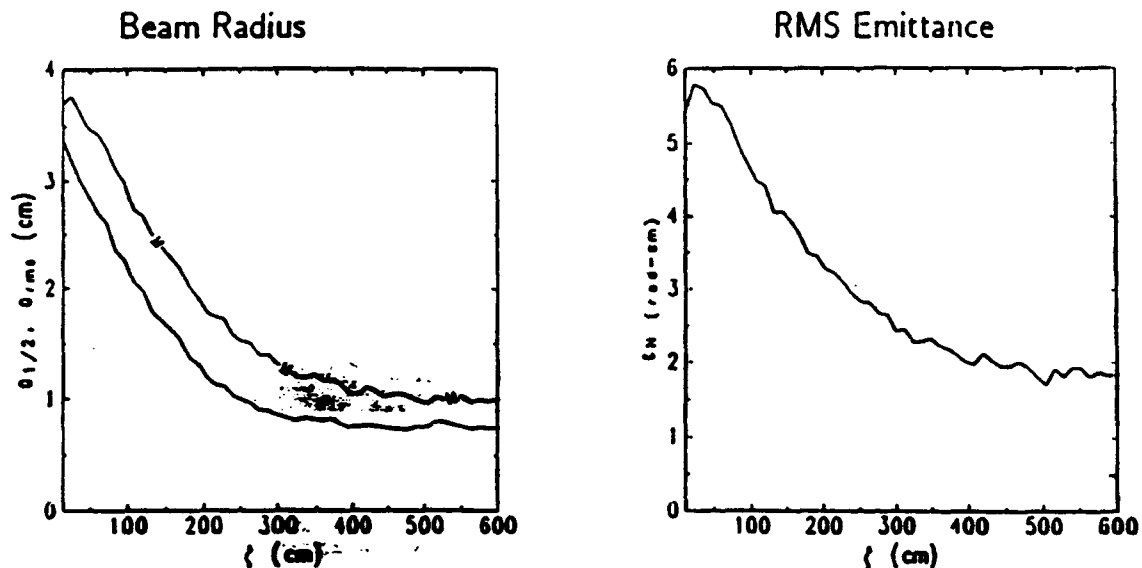


Fig. 2. ATA Multi-Foil Tailoring Cell ($z = 78$ cm).

REFERENCES

1. R. J. Adler, Part. Accel. 12, 39 (1982).
2. S. Humphries, Jr., Part. Accel. 13, 247 (1983).
3. V. M. Fawley, private communication.
4. S. Humphries, Jr., Principles of Charged Particle Acceleration, John Wiley & Sons, New York, 1986, p. 182. The condition given by Humphries, $d \leq 4f_\ell$, pertains only to exponential growth. Linear (unstable) growth occurs at $d = 4f_\ell$. In general, $d < 4f_\ell$ is required for stability.

Appendix OO
Wire Cells I: Vacuum

WIRE CELLS I: VACUUM*

R. Fernsler, S. Slinker
Naval Research Laboratory, Washington, D.C.
P. Boris
SAIC, McLean, VA

INTRODUCTION

In this paper we summarize our present theoretical understanding of active and passive vacuum wire cells as devices for centering or tailoring relativistic electron beams. The analytic theory is reviewed first, followed by numerical simulations. Gas-filled wire cells are considered separately in the companion paper, "Wire Cells II: Gas."

THEORY

In this section we present results from analytic calculations. We begin with a brief description of passive and active wire cells.

A passive vacuum wire cell consists of a thin resistive wire centered in an evacuated pipe with conducting end plates.¹ The beam induces a charge λ_v and current I_v on the wire. The wire resistance R_v resistively damps I_v in a time L_v/R_v , where L_v is the wire inductance. As a consequence, an electrostatic pinch force (from λ_v) develops with time.

An active vacuum wire cell uses a highly conducting wire with an external current.² Because $R_v = 0$, the attractive and repulsive forces from the induced wire charge and current nearly cancel, leaving the magnetic force from the external current, I_{ext} , to pinch and center the beam.

Away from the end plates and to order γ^{-2} , the only force on the beam electrons is the wire force, $F_v = -2T_v/r$ where $T_v = e(I_v/c - \lambda_v)$. The large spread in electron oscillation frequency, $\omega_\beta \propto 1/r$, causes rapid phase-mix damping so that the beam quickly centers and equilibrates about the wire.

Inside the wire cell, the average equilibrium beam temperature is given, independent of injection conditions, by

$$T = -\frac{1}{2} \int_0^{\infty} dr \frac{2\pi r J_b}{I_b} r F_v(r) = T_v$$

*Work supported by the Defense Advance Research Projects Agency, ARPA Order No. 4395, Amendment 80, monitored by the Naval Surface Warfare Center.

to order $a_v^2/a_b^2 \ll 1$. Here a_v is the wire radius, a_b is the beam radius, J_b is the beam current density, and I_b is the beam current. By contrast, the equilibrium temperature of a self-pinched, self-similar beam in air is given by $T_B = eI_{\text{eff}}/2c$, where $I_{\text{eff}} < I_b$ is the effective current. An active wire cell thus does not overheat the beam ($T_v \leq T_B$) provided

$$I_{\text{ext}} \leq I_{\text{eff}}/2.$$

However, in a passive wire cell, $I_v \rightarrow 0$ while $\lambda_v \rightarrow \sim -I_b/2c$. Hence, a passive cell overheats the beam by a factor

$$T_v/T_B \approx I_b/I_{\text{eff}} > 1.$$

Adding a thick exit foil overheats the beam further.

The $1/r$ dependence of F_v produces beam profiles strongly peaked about the wire. For example, for an isothermal beam about a hollow wire,

$$J_b(r) \rightarrow J_b(0) (a_v/r)^{2x},$$

where

$$x = H(a_v - r)/(1 - a_v^2/a_b^2).$$

Here H is the Heaviside step function, and $a_b^2 \equiv I_b/\pi J_b(0)$. For $r > a_v$ and $a_b \gg a_v$, $x = 1$. For a beam that is injected cold and nearly flat-topped, the equilibrium beam current density still peaks about $r = 0$ but falls off more gradually with a sharp cut-off at the initial edge radius, $a_i \gg a_v$:

$$J_b(r) \rightarrow (I_b/\pi a_i^2) [(a_i - r)/(r + a_v)] H(a_i - r).$$

The minimum beam emittance can be estimated by showing that a cold beam at injection contracts according to

$$\langle r^n \rangle = (n+1)^{-1/2} \langle r_i^n \rangle,$$

where $\langle r_i^n \rangle$ is the n th radial moment at injection. Combining this result with the result for $T = T_v$ yields a minimum normalized emittance given by

$$\epsilon_n^{(\min)} = \gamma R_i [(I_w - c\lambda_w)/I_A]^{1/2},$$

where R_i is the rms radius at injection and $I_A = 17\gamma$ kA is the Alfven current. The passive wire cell thus inverse tailors ϵ_n . On the other hand, the active wire cell tailors ϵ_n , for constant I_{ext} , only if R_i flares in the head (or γ falls with ζ). Note that a γ -ramp produces inverse tailoring for both cells and is therefore usually detrimental.

Losses to the walls and wire are a major concern for solid beams. By considering the turning radii of the electron orbits, we have concluded that the wall losses are small provided the beam temperature at injection is small, $T_i < T_w/2$, and the wall radius large, $b > 2 R_i$. Losses to the wire should be small provided $T_i \geq T_w/5$ and $a_w \leq 0.01 R_i$; here, finite T_i imparts angular momentum to the beam electrons, causing most to miss the wire (much as occurs for hollow, rotating beams such as RADLAC). A related concern is wire durability which typically is poor at high beam currents and long pulses; the wire must then be replaced after each shot.

SIMULATIONS

We have used the PEWW code to simulate both the passive and active wire cells. This code combines a fully relativistic particle pusher (courtesy of G. Joyce) and an ultrarelativistic circuit equation to compute I_w and λ_w . End-plate effects are not included in the simulations presented.

A passive wire cell of length $L = 1$ m and radius $b = 14.8$ cm, with a wire resistance $R_w = 1$ Ω /cm and radius $a_w = 0.05$ cm, is simulated below. The beam current I_b rose to 10 kA in 5 ns with $\gamma = 10$, half-radius $R_{1/2} = 1$ cm, and $\epsilon_n = 2.3$ rad-cm. The beam was injected off-axis at $\bar{x} = -0.5$ cm. Plotted at cell exit are $R_{1/2}$ and R , ϵ_n , and the centroid \bar{x} . Observe that the cell flares R , inverse tailors ϵ_n , and centers the beam body but not the head. The cell overheats the beam by $\sim 30\%$, relative to the Bennett temperature in air. Adding a thick exit foil to tailor ϵ_n would overheat the beam further.

We next show a simulation of an active cell with $L = 1$ m, $b = 20$ cm, $R_w = 0$, $a_w = 0.08$ cm, and $I_{\text{ext}} = 5$ kA. I_b rose to 20 kA in 12 ns with $\gamma = 10$ and a matching current $I_m = 1.7$ kA. The beam was injected off-axis at $\bar{x} = -0.5$ cm with R flared as shown. The beam at exit is well centered and emittance tailored.

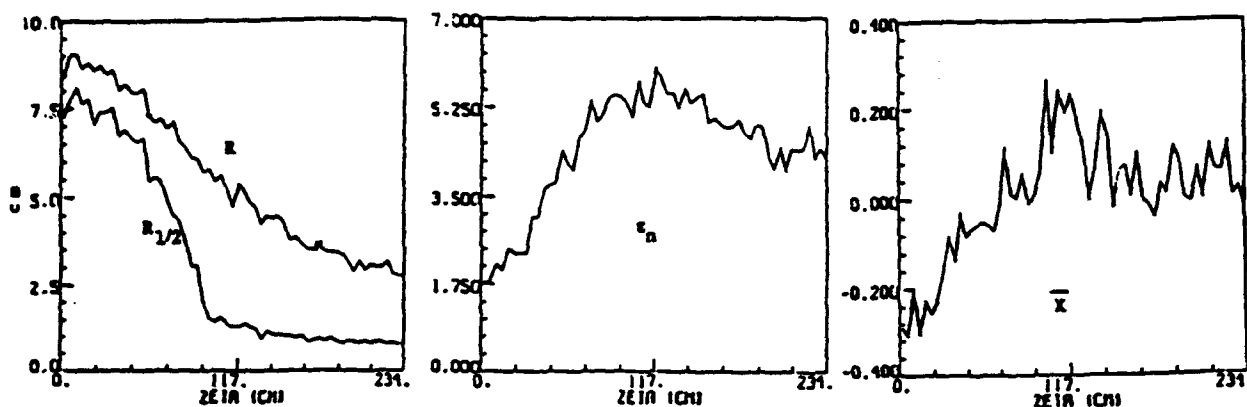


Fig. 1. A passive vacuum wire cell.

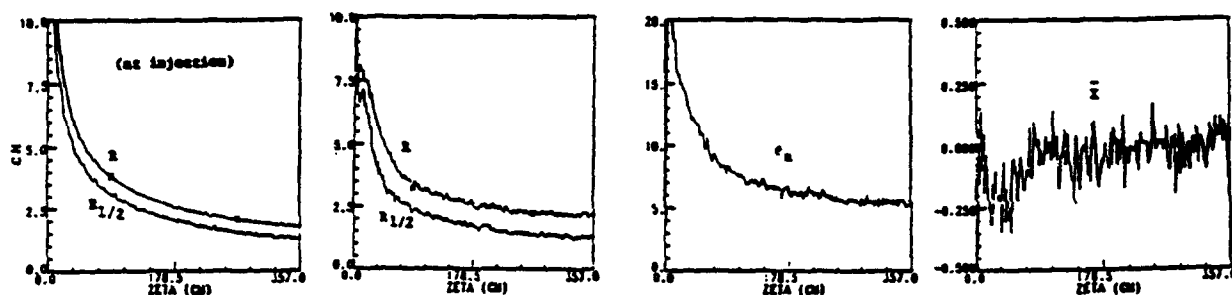


Fig. 2. An active vacuum wire cell (flared beam at injection).

CONCLUSION

A passive vacuum wire cell flares the radius, centers the body but not head, and overheats the body. The overheating becomes substantial at beam currents above 10 kA. An active cell centers the entire beam without overheating, and tailors the emittance if the beam is flared at injection.

REFERENCES:

1. D.S. Prono, et al., IEEE Trans. Nuc. Sci. NS-30, 2510 (1983).
2. J.R. Freeman, et al., Proc. 1988 DARPA Review 1, 147 (1989).

Appendix PP

Beam Stability and Range Extension Predictions for the ATA Multi-Pulse Propagation Experiment

BEAM STABILITY AND RANGE EXTENSION PREDICTIONS
FOR THE ATA MULTI-PULSE PROPAGATION EXPERIMENT*

S. Slinker, R. Hubbard, A.W. Ali, R. Fernsler and G. Joyce
Naval Research Laboratory

R.D. Taylor
Berkeley Research Associates

P. Boris
Science Applications Int. Corp.

Introduction. This paper summarizes our predictions for the ATA MPPE. For the nominal parameters, $I_b = 6$ kA, $r_b = 0.5$ cm, $\tau_p = 33$ ns, $N_p = 5$ pulses, we predict that range extension can be shown by: charge collection diagnostics at propagation distances of 3-6 meters into full density dry air. Longer propagation distances were not analyzed. For maximum initial hose perturbations under 0.1 mm, hose amplification of under 70 is seen for 6 meters of propagation. Stability, measured as an offset at a fixed laboratory position, is comparable for the first and fifth pulses. A 4 to 1 emittance tailoring over 12 ns was assumed. It also appears that hose displacement, at least for moderate propagation distances, is determined more by the initial perturbation than by the channel.

Other papers¹⁻³ in these proceedings discuss various aspects of this experiment.

Simulation Model. Several codes, which have been developed over the years, were combined to model this problem. Propagation was done with the particle simulation codes SIMMO, for axisymmetric cases, or SARLAC, for non-axisymmetric studies. These codes dumped the beam current density at specified propagation distances. For SARLAC, the current density was symmetrized because the hydro models were one dimensional. The current density and channel profile were input to the detailed air chemistry code CHMAIR II. This code calculates the beam deposition, population of species, and channel temperatures but does not assume hydrodynamic expansion. CHMAIR II simulated about 100 ns, enough time for ohmic deposition to finish and for the electron and vibrational temperatures to equilibrate. The particle densities are then consolidated and used as input to HINT. HINT is a one dimensional hydro code which calculates the channel for the rest of the interpulse time (~1ms). The channel for the next pulse is then input to the propagation code and the process repeats for the next pulse. HINT has a simplified air chemistry model which includes 7 species and the gas and vibrational temperatures. It has cooling by thermal conduction, but not by radiation. Non-axisymmetric cooling is modeled by the Picone-Boris⁴ theory. The fields are assumed to have decayed away.

*Work supported by the Defense Advanced Research Projects Agency, ARPA Order No. 4395, Amendment 80, monitored by the Naval Surface Warfare Center.

Axisymmetric Studies. The following table summarizes the results of six axisymmetric simulations of the MPPE:

5 PULSE AXISYMMETRIC PROPAGATION RESULTS

Case	Chem.	Enhanced Cool. (f)	Enhanced Vib. Rel.	ρ_{\min} $z=0m$	ρ_{\min} $z=4m$	Q_1	Q_5
A	Old	0.0	No	.25	.64	11.0	20.4
B	Old	0.05	No	.53	.73	11.0	18.5
J	New	0.0	No	.26	.80	12.5	18.0
K	New	0.0	Yes	.25	.66	12.5	21.4
KM	New	0.05	Yes	.53	.74	12.5	18.9
KL	New	0.05	Yes	.55	.80	12.1	17.2

For Cases A and B the pulse separation was 1 ms; for the other cases it was 1.25 ms. In Case KL the nominal beam radius was 0.6 cm. The "Old" air chemistry is the standard VIPER model. The "New" air chemistry was obtained by benchmarking MPPE-type beams with the detailed air chemistry code CHMAIR II². The enhanced cooling factor f is the phenomenological form factor in the Picone-Boris cooling theory which models non-axisymmetric hydrodynamic effects by using an enhanced thermal diffusivity.³ "Enhanced Vibrational Relaxation" means the inclusion of carbon dioxide in the propagation chamber to thermalize the vibrational energy of nitrogen to aid hole boring.² ρ_{\min} is the minimum fractional density at the entrance of the fifth pulse. Q_1 and Q_5 are the transported charges (μc) for pulses 1 and 5 within 1.125 cm of the chamber axis at a propagation distance of $z=6$ m. Six meters is roughly twice the Nordsieck length of the initial pulse.

By comparing columns 7 and 8, all of these cases show at least an almost 50% increase in transported charge clearly verifying range extension.

Cases A and J differ in two ways: pulse separation time and air chemistry model. Case A shows slightly better range extension properties, particularly in channel depth at large propagation ranges. Its shorter pulse separation time allowed less thermal cooling, but the major reason for the deeper channel is a 15% greater direct deposition rate used with the "old" chemistry.

Non-axisymmetric hydrodynamic effects are modeled by using an enhanced thermal conduction

$$\lambda_T = \rho c_p c_s^2 \tau \frac{1}{4\pi} \ln \left[\frac{\rho_\infty}{\rho_0} \right] f, \quad \text{ergs/cm-sec-}^\circ K,$$

where τ is the pressure equilibration time and f is a form factor.^{3,4} We have chosen $f = 0.05$ assuming an individual pulse has a symmetric

deposition and the offsets between pulses are small compared to a beam radius. Cases A and B and Cases K and KM differ only in the value of f . A large difference in channel depth at the nozzle is shown even for $f = 0.05$. The channels with the nonzero f are slightly broader. At 4 m, the contrast is not as great. Charge transported 6 m is 10-15% lower with enhanced cooling but it is still appreciably higher for the fifth pulse than the first one. The amount of cooling is difficult to predict and the MPPE results will be very valuable.

The only difference between Cases J and K is the addition of carbon dioxide in the propagation chamber to aid in the thermalization of the vibrational energy of nitrogen. The channels at the nozzle at the entrance of the fifth pulse are very similar although the Case K channel opened much sooner². At larger propagation distances Case K is definitely better and 15% better transport to 6 m is predicted. The use of carbon dioxide is recommended, though levels should be kept as low as possible, say ~ 1%, to avoid other air chemistry effects.

Cases KL and KM differ only in the nominal beam radius, which was 0.5 cm for KM and 0.6 cm for KL. The broader beam showed only slightly worse range extension at 6 m.

Non-axisymmetric Studies. Three of the non-axisymmetric simulations will be discussed here. The first modeled the beam into ambient air. The other two considered the fifth pulse. In one case into the (axisymmetric) channel of Case KM and the other into the channel of Case K. The initial maximum perturbation was 0.1 mm in the x or y direction with the standard form. Sensitivity to the exact form of the initial perturbation is discussed in Reference 1. The following table shows the total charge and deposition centroids for several propagation distances.

Z(M)	CHARGE CENTROID						DEPOSITION CENTROID					
	PULSE 1		PULSE 5-KM		PULSE 5-K		PULSE 1		PULSE 5-KM		PULSE 5-K	
	X(CM)	Y(CM)	X	Y	X	Y	X	Y	X	Y	X	Y
1	.03	.03	.03	.04	.04	.05	.03	.04	.03	.04	.03	.04
2	-.12	-.10	-.15	-.15	-.16	-.17	-.13	-.12	-.16	-.16	-.15	-.16
3	-.10	-.15	-.03	-.10	.00	-.06	-.10	-.16	-.02	-.11	.00	-.06
4	.10	.04	.20	.15	.25	.20	.11	.04	.21	.16	.23	.19
5	.28	.25	.28	.28	.22	.36	.30	.27	.29	.30	.21	.33
6	.15	.19	-.06	-.06	-.06	-.23	.16	.20	-.07	-.07	-.07	-.21

Through 5 m the centroids of all three pulses track each other to within a millimeter. This indicates that the hose displacement is determined more by the initial perturbation than by the presence of the channel. Thus employing a moveable charge collection diagnostic to catch the hosing beams may be successful. The maximum offset of any beam slice in the beam body is around 0.5-0.7 cm for all three cases over the 6 m range.

Conclusions. If the design parameters are met, the MPPE should be successful. The beam will be stable enough to travel over 6 m and dig enough of a channel to show range extension. Beam stability will not be very sensitive to the channel. The greatest unknown will be the effect of anomolous cooling.

References.

1. R.F. Hubbard, et al., "Sensitivity of Hose Instability to Frequency of Initial Perturbations in Low and High Current Beams", these proceedings.
2. S. Slinker, et al., "Air Chemistry Aspects of the ATA Multipulse Experiment", these proceedings.
3. P. Boris, et al., "Hydrodynamic Simulations of Beam-Generated Turbulence in Channels", these proceedings.
4. J.M. Picone and J.P. Boris, Phys. Fluids 26 365-382 (1983); J.M. Picone, et al., "PHAZR: A Phenomenological Code for Holeboring in Air", NRL Memo Rpt. 5647 (1985).